

REPORT DOCUMENTATION PAGE

Form Approved
OMB No. 0704-0188

Public reporting burden for this collection of information is estimated to average 1 hour per response, including the time for reviewing instruction, searching existing data sources, gathering and maintaining the data needed, and completing and reviewing the collection of information. Send comments regarding this burden estimate or any other aspect of this collection of information, including suggestions for reducing this burden, to Washington Headquarters Services, Directorate for Information Operations and Reports, 1215 Jefferson Davis Highway, Suite 1204, Arlington, VA 22202-4302, and to the Office of Management and Budget, Paperwork Reduction Project (0704-0188), Washington, DC 20503.

1. AGENCY USE ONLY (Leave Blank)		2. REPORT DATE 1 September 1997		3. REPORT TYPE AND DATES COVERED Scientific, Fiscal Year 1997	
4. TITLE AND SUBTITLE Proceedings of the 19 th Annual Seismic Research Symposium on Monitoring a Comprehensive Test Ban Treaty, 23-25 September 1997				5. FUNDING NUMBERS PE 35145F	
6. AUTHORS(S) Various: Editors: Michael J. Shore Rong-Song Jih Anton Dainty Joan Erwin					
7. PERFORMING ORGANIZATION NAME(S) AND ADDRESS(ES) Defense Special Weapons Agency 6801 Telegraph Road Alexandria, VA 22310-3398				8. PERFORMING ORGANIZATION REPORT NUMBER	
9. SPONSORING/MONITORING AGENCY NAME(S) AND ADDRESS(ES) Nuclear Treaty Programs Office, OSD HQ Air Force Technical Applications Center Department of Energy Defense Special Weapons Agency				10. SPONSORING/MONITORING AGENCY REPORT NUMBER	
11. SUPPLEMENTARY NOTES This research was supported by DSWA under PE 35145F (Air Force), AFTAC under PE 35999F, NTPO under PE 35134, DOE, ACDA, USGS and NSF.					
12a. DISTRIBUTION/AVAILABILITY STATEMENT Approved for Public Release; distribution unlimited				12.b DISTRIBUTION CODE	
13. ABSTRACT (Maximum 200 words) These Proceedings contain papers presented at the Nineteenth Annual Seismic Research Symposium on Monitoring a Comprehensive Test Ban Treaty (CTBT), held 23-25 September 1997, in Orlando, Florida. This Symposium represents the combined annual review for the research programs funded by DSWA, HQ AF Technical Applications Center (AFTAC), Department of Energy (DOE), the Nuclear Treaty Programs Agency, the Arms Control and Disarmament Agency (ACDA) and the National Science Foundation (NSF). In addition, representatives from five of the DOE National Laboratories participate in the Symposium to provide insight on the internal DOE CTBT R&D program. The scientific objectives of the research programs are to improve the United States' capability to detect, locate, identify, and characterize nuclear explosions under the CTBT. The purpose of the Symposia is to provide the sponsoring agencies an opportunity to review research, particularly contractor research, accomplished during the preceding year and to outline areas of investigation for the coming year. For the researchers, it provides a forum for the exchange of scientific information to help achieve program goals and an opportunity to meet DSWA, HQ AFTAC, DOE, NTPO, ACDA and NSF staff to discuss results and future plans. In addition, the Symposium and the technical presentations serve as an important avenue for technology transition to the Air Force and OSD user. The paper topics include subjects discussed by the Symposium panels; seismic regionalization and calibration; detection and location of sources; identification of sources and discrimination between different types of sources; wave propagation from source to receiver; the nature of seismic sources, including mining practices; hydroacoustic, infrasound and radionuclide methods and on-site inspection; and data processing and other topics.					
14. SUBJECT TERMS underground nuclear explosions, discrimination, regional seismology, seismic sources, detection and location, mining practices, hydroacoustics, data processing and analysis				15. NUMBER OF PAGES	
				16. PRICE CODE	
17. SECURITY CLASSIFICATION OF REPORT UNCLASSIFIED	18. SECURITY CLASSIFICATION OF THIS PAGE UNCLASSIFIED	19. SECURITY CLASSIFICATION OF ABSTRACT UNCLASSIFIED	20. LIMITATION OF ABSTRACT Unlimited		

SN 7540-01-2880-5500



DEPARTMENT OF THE AIR FORCE
AIR FORCE RESEARCH LABORATORY (AFMC)

27 July 2012

MEMORANDUM FOR: DEFENSE TECHNICAL INFORMATION CENTER
ATTN: DTIC-O
8725 JOHN J. KINGMAN RD, SUITE 0944
FT BELVOIR, VA 22060-6218

FROM: AFRL/RVOP
3550 Aberdeen Avenue, SE
Kirtland AFB, NM 87117-5776

SUBJECT: Submittal of Document to DTIC Collection

1. Enclosed please find a hard copy submittal of the Proceedings of the 19th Annual Seismic Research Symposium on Monitoring a Comprehensive Test Ban Treaty, 23-25 September 1997. This document was received in my office in November 2011, and includes an SF Form 298 as its second page.
2. Request processing and posting of this document to the DTIC collection.
3. I would appreciate it if I could receive notification via email upon your receipt of this document since hard copies do not generate an electronic receipt. My email address is lisa.drown@kirtland.af.mil. If you require anything further or have any questions pertaining to this submittal, please contact me at the email address above, or (505) 846-1328/DSN 246-1328.

LISA DROWN, GS-11
STINFO Officer
Space Vehicles Directorate

Enclosure:
Proceedings of the 19th Annual Seismic
Research Symposium

Proceedings of the 19th Annual Seismic Research Symposium on Monitoring a Comprehensive Test Ban Treaty

23-25 September 1997

Editors:

Michael J. Shore
Rong Song Jih
Anton Dainty
Joan Erwin

5 September 1997

APPROVED FOR PUBLIC RELEASE; DISTRIBUTION UNLIMITED.



Defense Special Weapons Agency/Special Programs
6801 Telegraph Road
Alexandria, VA 22310



HQ Air Force Technical Applications Center
Nuclear Treaty Monitoring Directorate
Patrick Air Force Base, FL 32925-3002



Department of Energy
Office of Nonproliferation & National Security
Washington, DC 20585

20120808430

Block 9 (Continued)

Nuclear Treaty Programs Office
1901 N. Moore St, Suite 609
Arlington, VA 22209

HQ AFTAC/TT
1030 South Highway A1A
Patrick AFB, FL 32925-3002

DOE
Office of R&D, NN-20
1000 Independence Avenue, SW
Washington, DC 20585

Defense Special Weapons Agency
Special Programs Office
6801 Telegraph Road
Alexandria, VA 22310

Table of Contents

Page

Panel Discussion Abstracts

Panel Members	1
Randall, Dr. George E. <i>Seismic Regionalization Panel Discussion</i>	2
Ryall, Dr. Alan S., Jr. <i>Panel on Calibration and Testing to Improve Location Capability of the CTBT International Monitoring System Seismic Network</i>	4
Stump, Brian <i>Special Panel on Mining Practices</i>	7
Wallace, Prof. Terry C. <i>Seismic Discrimination</i>	8
Harris, Dr. David B. <i>Monitoring the Oceans with the IMS Hydroacoustic Network</i>	9
Willemann, Dr. Ray <i>Infrasound Panel</i>	13a

Regionalization/Calibration

Baumgardt, Douglas R. <i>Multivariate Canonical Correlation of P/S Ratios and Propagation Path Parameters for Iran</i>	14
Cong, Lianli and Brian J. Mitchell <i>Regional Q Variations in the Middle East from Fundamental-Mode and Higher-Mode Surface-Wave Attenuation</i>	24
Jenkins, Richard D. and Thomas J. Sereno, Jr. <i>Frequency-Dependent Attenuation of Regional Phases in Australia</i>	34
Jones, Laura E. and Howard J. Patton <i>High Resolution Surface-Wave Dispersion Studies in China</i>	44

Kennett, B.L.N.	
<i>3-D Structure from Seismic Tomography - Implications for Event Locations</i>	51
Lay, Thorne and Guangwei Fan	
<i>Crustal Waveguide Effects on Regional Phases in China and Southeast Asia</i>	57
Levshin, A.L., M.H. Ritzwoller, L.I. Ratnikova, M.P. Silitch, R.C. Kelly and B. O'Sullivan	
<i>Intermediate Period Group Velocity Maps (15 - 30 s) across Central Asia, Western China, and Parts of the Middle East</i>	67
Mayeda, Kevin and William R. Walter	
<i>Preliminary Regional Magnitude Results in the Middle East Region Using Narrowband Lg Coda Envelopes</i>	77
McNamara, Daniel E. and William R. Walter	
<i>Surface Wave Group Velocity Dispersion Across Northern Africa, Southern Europe and the Middle East</i>	83
Mooney, Walter D., Gabi Laske and T. Guy Masters	
<i>A Global Crustal Model for CTBT Monitoring: Crust 5.1</i>	93
Mooney, Walter D. and Songlin Li	
<i>Crustal Structure of China from Deep Seismic Sounding Profiles</i>	104
North, Robert G., Istvan Bondar and Vladislav Ryaboy	
<i>New Regional Travel-Time Tables for the Baltic Shield Inferred from DSS Observations for Calibration of the International Monitoring System (IMS)</i>	115
Phillips, W.S., G.E. Randall, H.E. Hartse, S.R. Taylor and H.J. Patton	
<i>Source and Path Effects on Regional Phases in China</i>	125
Rapine, Richard R., James F. Ni and Thomas M. Hearn	
<i>Regional Wave Propagation in China and its Surrounding Regions</i>	135
Rodgers, Arthur and William Walter	
<i>Regionalization and Calibration of Seismic Discriminants, Path Effects and Signal-to-Noise for Station ABKT (Alibek, Turkmenistan)</i>	14
Ryaboy, Vladislav (U.S. Working Group)	
<i>Joint RF/US Research Program of Seismic Calibration of the International Monitoring System in Northern Eurasia and North America</i>	15

51	Shapira, Avi, Vladimir Pinsky, Yefim Gitterman and Alona Malitzky <i>Improvements in Monitoring the CTBT in the Middle East with the Israel Seismic Network</i>	162
----	---	-----

57	Stevens, Jeffry L. and K.L. McLaughlin <i>Improved Methods for Regionalized Surface Wave Analysis</i>	171
----	---	-----

Detection/Location

67	Alexander, Shelton S. and Chih-Chieh Yang <i>Accurate Depth Determinations and other Diagnostic Event Characteristics in Near-Real Time from Regional Signals</i>	181
----	---	-----

77	Ayala, Rodolfo and Lawrence A. Drake <i>Earthquake Location with a 3-D Velocity Model for the Region of the Bolivian Andes</i>	191
----	--	-----

83	Baker, G. Eli and Terry Barker <i>Source and Propagation Characterization for Network Performance Simulations in the Middle East</i>	201
----	--	-----

93	Clauter, Dr. Dean and Dr. Robert Blandford <i>Capability Modeling of the Proposed International Monitoring System 60-Station Infrasonic Network</i>	211
----	---	-----

104	Ekström, Göran, Adam M. Dziewonski and Gideon P. Smith <i>Strategies for Improving Seismic Event Location at Regional and Teleseismic Distances</i>	221
-----	---	-----

115	Hipp, Jim, Chris Young, and Ralph Keyser <i>Travel-Time Correction Surface Generation for the DOE Knowledge Base</i>	231
-----	--	-----

125	Husebye, Eystein S. and Bent O. Ruud <i>Seismic Wave Propagation in the Crust - Event Location in a Semiautomatic Manner</i>	242
-----	--	-----

135	Jih, Rong-Song <i>Epicenter Estimation using Erroneous Crustal Model(s) and Skew Regional Networks</i>	252
-----	--	-----

143	Kvaerna, Tormod and Frode Ringdal <i>Event Magnitudes, Capability Maps and Magnitude Thresholds</i>	262
-----	---	-----

Pulliam, Jay, Cliff Frohlich and Stephen P. Grand <i>Factors Controlling Single-Station Location</i>	272
Saikia, C.K., H-K Thio, B.B. Woods and D.V. Helmberger <i>Waveform Complexity as a Possible Depth Discriminant for the Automated IDC System</i>	281
Schultz, Craig A., Stephen C. Myers, and Stanley D. Ruppert <i>Event Location in the Middle East and North Africa</i>	291
Shearer, Peter M. and Luciana Astiz <i>Locating Nuclear Explosions using Waveform Cross-Correlation</i>	301
Sweeney, Jerry J. <i>Relocation of Gulf of Aqaba Earthquakes using the JSOP Bulletin</i>	310
Tinker, Mark Andrew and Terry C. Wallace <i>Epicenter Determination with Sparse Broadband Arrays at Regional Distances using only Azimuthal Information: The Incorporation of Surface Waves</i>	320
Young, Christopher J., Judy I. Beiriger, J. Mark Harris, Susan G. Moore, and Julian R. Trujillo <i>Testing the Waveform Correlation Event Detection System: Teleseismic, Regional, and Local Distances</i>	329

Discrimination/Identification

Armstrong, Russell A., Trella H. McCartor, Walter A. Lyons and Earle R. Williams <i>Optical and ELF Signatures of Lightning, Sprites, Elves and Jets Detection and Discrimination</i>	339
Barker, Terrance G., G. Eli Baker, and Keith L. McLaughlin <i>Identification Performance of the IMS in the Middle East and North Africa</i>	349
Bennett, T.J., K.L. McLaughlin, R.W. Cook and J.A. Carter <i>Regional Discrimination using L_g/P and Regional Phase Spectral Ratios: Studies of Physical Basis and Transportability</i>	359
Gitterman, Yefim, Vladimir Pinsky and Avi Shapira <i>Application of Spectral Semblance and Ratio Discriminants to Regional and Teleseismic Events Recorded by ISN and NORESS</i>	369

272	Harkrider, David G. <i>Evaluation of Intermediate-Period Rayleigh Wave Group Velocity Models</i>	400
281	Hartse, Hans E., Steven R. Taylor, W. Scott Phillips, and George E. Randall <i>Applying Source and Path Corrections to Improve Discrimination in China</i>	379
291	Hedlin, Michael A.H. <i>A Global Test of a Time-Frequency Small-Event Discriminant</i>	390
301	Herrin, Eugene <i>Ground Truth for Regional Seismic Events Recorded at TXAR</i>	412
310	Murphy, J.R., D.D. Sultanov, B.W. Barker, I. O. Kitov, and M.E. Marshall <i>Applications of Soviet PNE Data to the Assessment of the Transportability of Regional Discriminants</i>	422
320	Pinsky, Vladimir, Yefim Gitterman, and Avi Shapira <i>Multivariate Discrimination of Regional and Teleseismic Events, Using the Israel Seismic Network Recordings</i>	432
329	Pulli, Jay J. <i>Transportable Seismic Discriminants: Stabilizing Spectral Ratios Using Source Deconvolution</i>	442
	Shumway, Robert H. <i>Detecting Ripple-Firing in Time and Frequency</i>	451
	Walter, William R., David B. Harris and Steven C. Myers <i>Seismic Discrimination Between Earthquakes and Explosions in the Middle East and North Africa</i>	459
339	Woods, Bradley B. and C.K. Saikia <i>An Alternative Short-Period P/S Discriminant using Phase-Weighted Ratios</i>	469

Wave Propagation

349	Cormier, Vernon F. and Thomas Anderson <i>Lg Blockage and Scattering at Central Eurasian Arrays CNET and ILPA</i>	479
359	Goldstein, Peter, Craig Schultz, and Shawn Larsen <i>The Influence of Deep Sedimentary Basins, Crustal Thinning, Attenuation, and Topography on Regional Phases: Selected Examples from the Eastern Mediterranean and the Caspian Sea Regions</i>	486

Herrmann, R.B., T.A. Mokhtar, M. Raoof and C. Ammon <i>Wave Propagation - 16 Hz to 60 sec</i>	495
Jones, Eric M., Fred N. App, and Randy J. Bos <i>The Effects of Major Structural Features in Western China on Explosion Seismograms</i>	504
McLaughlin, Keith L. and Darin Wilkins <i>Progress in Numerical Methods for Wave Propagation</i>	514
Morozov, I.B., E.A. Morozova, and S.B. Smithson <i>L_g Propagation, Upper Mantle Structure and Attenuation along the Profile "Quartz," Russian Eurasia</i>	524
Priestley, Keith <i>Anomalous Wave Propagation across the South Caspian Basin</i>	534
Srinivasan, C. <i>Seismic Attenuation in the Mines of Kolar Gold Fields</i>	543
Wu, Ru-Shan, Shengwen Jin, Xiao-Bi Xie, and Thorne Lay <i>Verification and Applications of GSP (Generalized Screen Propagators) Method for Regional Wave Propagation</i>	552
Xu, Heming, Steven M. Day, and Jean-Bernard H. Minster <i>Nonlinear Wave Propagation in the Half Space</i>	562

Seismic Regionalization

Ahrens, T. J. and C. Liu <i>Shear Wave Generation from Rock Cracking Induced by Explosions in Spherical Cavities</i>	572
Barker, Terrance G. and Keith L. McLaughlin <i>Physical Mechanisms of Quarry Blast Sources</i>	581
Ben-Menahem, Ari <i>Model of Nonspherical Underground Nuclear Explosions in Nonlinear and Inhomogeneous Environments</i>	591
Gupta, Indra N. and Robert A. Wagner <i>Low and High Frequency L_g From Explosions - New Insights</i>	594

	Harris, David B.	
	<i>Waveform Correlation Methods for Identifying Populations of Calibration Events</i>	604
4	Imhof, Matthias C. and Nafi M. Toksoz	
	<i>Calculating Seismic Radiation Patterns for Explosions in and Around Cavities</i>	615
4	Johnson, Lane R.	
	<i>Generation of S Waves by Explosions</i>	625
4	Khalturin, Vitaly L. and Paul G. Richards	
	<i>The Seismic Signal Strength of Chemical Explosions</i>	632
14	Leith, William; Douglas Baumgardt; Nikolai M. Syrnikow; and Yjuri S. Rybnov	
	<i>The Kirovskiy Explosion of September 29, 1996: Example of a CTB Event Notification for A Routine Mining Blast</i>	642
3	Pasyanos, Michael; Doug Dreger, and Barbara Romanowicz	
	<i>Moment Tensor Inversion Codes for the International Data Center Using Regional and Teleseismic Broadband Data</i>	652
52	Sammis, Charles G.	
	<i>Observational Constraints on Non-Linear Source Models in the Damage Regime</i>	662
162	Stump, Brian W. and D. Craig Pearson	
	<i>Comparison of Single-Fired and Delay-Fired Explosions at Regional and Local Distances</i>	668
	Walter, William R.; Francois Heuze, and Douglas Dodge	
572	<i>Seismic Signals From Underground Cavity Collapses and other Mining-Related Failures</i>	678
581	Xie, Jiakang	
	<i>Quantification of Regional Wave Excitation and Propagation Central Asia</i>	688
	Yang, Xiaoning; Brian W. Stump, and W. Scott Phillips	
591	<i>The Unique Source Mechanism of an Explosively Induced Mine Collapse</i>	697
594	Hydroacoustics/Infrasound/Radionuclide/OSI	
	Adushkin, Vitaliy V. and Alexandr A. Spivak	
	<i>Use of Seismic Microarrays for On-Site Inspection Monitoring</i>	707

Blackman, Donna K. and John A. Orcutt <i>Characterization of T-Waves from Small Earthquakes in the Norwegian Sea</i>	716
Clarke, Douglas B., Philip E. Harben, Donald W. Rock and John W. White <i>Energy Coupling of Nuclear Bursts in and above the Ocean Surface: Source Regional Calculations and Experimental Validation</i>	723
deGroot-Hedlin, Catherine D. and John A. Orcutt <i>Observations of T-Phases from North Pacific Events: Determination of Epicentral Locations from T-Phases</i>	732
Farrell, Ted, Jeff Angell, Kevin LePage and Rob Gibson <i>Components of the Hydroacoustic Knowledge Database</i>	741
Hanson, Jeffrey A. and Holly K. Given <i>Accurate Arrival Azimuth for Earthquakes using T-Phase Waveforms from a Large Aperture Hydrophone Array</i>	750
Masters, Stephen E. <i>Source Identification using Meteorological and Statistical Modeling</i>	760
Miley, H. S., K.H. Abel, S.M. Bowyer, T.W. Bowye, C.W. Hubbard, A.D. McKinnon, M.E. Panisko, R.W. Perkins, P.L. Reeder, R.C. Thompson, and R.A. Warner <i>Radionuclide Measurements for the Comprehensive Test Ban Treaty</i>	770
Rooney, B., K. Gross, R. Nietert, J. Valentine and W. Russ <i>A Fluid-Based Measurement System for Airborne Radionuclide Surveillance</i>	778
Whitaker, Rod, Tom Sandoval, Dale Breeding, Dick Kromer, and Tim McDonald <i>Evaluation of a Prototype Infrasound System</i>	788

Data Processing and Others

Ahern, Tim and Tom McSweeney <i>Distribution of International Monitoring System Data to the General Research Community</i>	794
Ahern, Tim and Ken Creager <i>Fissures - A New Approach in Software Development</i>	801
Armstrong, Hillary M. and Ralph G. Keyser <i>The Browser Prototype for the CTBT Knowledge Base</i>	809

Beiriger, Judy I., Susan G. Moore, Julian R. Trujillo, and Chris J. Young <i>Software Design and Operational Model for the WCEDS Prototype</i>	819
Der, Zoltan A. <i>Automatic Phase Identification and Onset Time Estimation at Regional Distances using the CUSUM Algorithm and Generalized Polarization Analysis</i>	829
Doser, Diane I., G. Randy Keller, Paul Dial, Kate C. Miller and Steven Harder <i>Development of a Lithospheric Model and Geophysical Data Base for North Africa</i>	839
Edwards, Tony L., J. Mark Harris, Randall W. Simons, and Christopher J. Young <i>Visualization Tools for Comprehensive Test Ban Treaty Research</i>	848
Goldstein, Peter, Doug Dodge, and Mike Firpo <i>Recent Developments in SAC2000</i>	858
Grant, Lori, Robert Wagner, Florianna Ryall, Wilmer Rivers, and Ivan Henson <i>Ground Truth Database for Regional Seismic Discrimination Research in the Middle East and North Africa</i>	867
Herrington, Pres, Tim Draelos, and Rick Craft <i>A Key Management Concept for the CTBT International Monitoring System</i>	877
Leach, Richard R., Jr., Craig Schultz, and Farid Dowla <i>Optimized Filtering of Regional and Teleseismic Seismograms: Results of Maximizing SNR Measurements from the Wavejet Transform and Filter Banks</i>	886
Ruppert, Stanley D., Teresa F. Hauk, and Richard Leach <i>LLNL Middle East and North Africa Research Database</i>	896
Sandvol, Eric, Dogan Seber, David Steer, and Muawia Barazangi <i>Seismological Research in Support of CTBT for the Middle East and North Africa Region</i>	906
Seber, Dogan, David Steer, Eric Sandvol, Marisa Vallvé, Christine Orgren, and Mauwia Barazangi <i>Database Development for the Middle East and North Africa Region</i>	916
Shepherd, Ellen R., Ralph G. Keyser, Hillary M. Armstrong, Eric P. Chael, and Christopher J. Young <i>The Data Dictionary: A View into the CTBT Knowledge Base</i>	925

Steer, David, Dogan Seber, Christine Orgren, Marisa Vallvé, and Mauwia Barazangi <i>Global Database Development for the International Data Center</i>	934
---	-----

Regionalization Panel: George Randall (LANL), Chair

John Filson(USGS)
Paul Richards(LDEO)
Thorne Lay(UCSC)
Bill Walter(LLNL)
Vindell Hsu(AFTAC)
Chris Young(SNL)

Calibration Panel: Alan Ryall (LLNL), Chair

Dave Russell(AFTAC)
Gene Herrin(SMU)
Dave Harris(LLNL)
Brian Kennett(ANL)
Bob North(SAIC)
Craig Pearson(LANL)
Craig Schultz(LLNL)

Mining Practices Panel: Brian Stump (SMU), Chair

Gene Herrin(SMU)
Paul Richards(LDEO)
Bill Leith(USGS)
Dave Harris(LLNL)
Vindell Hsu(AFTAC)
Bill Walter(LLNL)
Michael Hedlin(UCSD)

Seismic Discrimination Panel: Terry Wallace (Univ of Ariz), Chair

Don Helmberger(CIT)
Steve Taylor(LANL)
Jack Murphy(Maxwell)
Doug Baumgardt(ENSCO)
Eric Chael(SNL)
Tom Ahrens(CIT)

Hydroacoustic Panel: Dave Harris (LLNL), Chair

Jeff Hanson(Scripps)
Ray Willemann(CMR)
John Orcutt(Scripps)
Doug Clarke(LLNL)
Phil Harben(LLNL)

Infrasound Panel: Ray Willemann (CMR), Chair

Mike Hedlin(UCSD)

Bob Blandford(AFTAC)

Terry Barker(Maxwell)

Brian Kennett(ANU)

Rod Whitaker(LANL)

Ted Farrell(BBN)

Seismic Regionalization Panel Discussion

G.E. Randall

Geophysics Group EES-3, Los Alamos National Laboratory

Sponsored by the U.S. Department of Energy, Contract W-7405-ENG-36
Comprehensive Test Ban Treaty Research and Development Program, ST482A

As part of the DOE CTBT Research and Development regional characterization effort, seismic, geological, and geophysical data must be assembled and organized for inclusion in a knowledge base for the US National Data Center at AFTAC. The seismic research community must characterize the regional excitation and propagation of seismic waves in regions of interest with sufficient accuracy to explain observed seismic data, and to detect, locate, and discriminate seismic events for the verification of a Comprehensive Test Ban Treaty (CTBT). Seismic waveform data is available for many primary and secondary CTBT stations from archives such as IRIS. Seismicity catalogs are available from a number of sources such as the USGS PDE. In seismic regions, using seismic waveforms and event locations we can identify Pn, Pg, Sn, Lg, Love and Rayleigh phases and pick arrival times and amplitudes for the body waves. Analysis of these arrival times will provide travel time and travel time corrections for large well located events to improve regional location. Amplitudes are analyzed to calibrate magnitude scales and for use in discrimination research. Aseismic regions or regions with a limited record of seismic activity will require additional active regional calibration programs based on dedicated explosions or well known mining and industrial explosions.

A key element in all CTBT seismic research is the available ground truth data of event locations, times and types. Large earthquakes (above a magnitude threshold that will vary by region) are located with a sufficiently small error ellipsoid to satisfy CTBT goals of 1000 km² epicentral error. Systematic mislocations may still exist in some regions. Event depths and origin times are less certain for most crustal events. Accurate catalogs of mining or industrial explosions may exist for some regions, but information may not be available for regions of interest. Improving the accuracy of ground truth data is important to reducing systematic biases in event location, and accurately categorizing events as earthquakes, mining or industrial explosions or nuclear tests. Improved ground truth for seismic event location and origin time may be available from dense local or regional networks or dense aftershock networks used for earthquake hazard work in some regions of interest, but obtaining the information may be politically difficult. Improving ground truth for mining and industrial seismic events will require cooperation of mine operators and the use of near in recording to document event time, location, and blasting pattern.

Qualitative categories and quantitative measures of ground truth are essential, but we must also define the accuracy of ground truth needed for regional characterization. Event location may require very accurate ground truth to develop travel times and corrections; magnitude calibration and discriminant calibration can probably be done with existing teleseismic event locations. We need to define strategies to obtain more accurate ground truth estimates of event location, origin time and depth. International exchange of data and collaborative research may provide event locations from regional and local seismic networks for more accurate event location. As a community we need to develop improved ground truth data in a timely manner to meet the needs of the US NDC to monitor the CTBT.

**PANEL ON CALIBRATION AND TESTING
TO IMPROVE LOCATION CAPABILITY OF THE
CTBT INTERNATIONAL MONITORING SYSTEM SEISMIC NETWORK**

Alan Ryall, Chairman
Lawrence Livermore National Laboratory

Calibration of the Comprehensive Test Ban Treaty International Monitoring System (CTBT IMS) encompasses a broad array of techniques and activities, the use of which are dependent on the type of station and/or tectonic region being calibrated. Calibration to improve seismic event location capability includes such issues as location accuracy needed for CTBT monitoring; formal error estimation vs. accuracy; need for regional and/or wholeearth velocity models; weighting various levels of "ground truth;" quantifying the degradation in location capability as functions of increasing source-receiver distance and decreasing event size; prescription of calibration procedures for seismic, aseismic and oceanic regions; strengths and weaknesses of different location methods; uncertainties connected with secondary phase onsets, and expert-system picks for small events at far-regional distance; use of waveform correlation to minimize phase-picking errors for repeated quarry blasts, aftershocks and swarms; situations requiring special calibration shots; confidence-building measures by host countries; effects of including uncalibrated regional network stations in the location procedure; usefulness of quarry blasts and/or crustal refraction data; evaluating the reliability and/or usefulness of various types of studies published in the geophysical literature. The following presentations will attempt to briefly identify the scope of calibration activities that will be required to achieve acceptable location capability for the IMS seismic network, with particular emphasis on research issues that still remain as obstacles to this effort.

Seismic Location Errors
Eugene T. Herrin
Southern Methodist University

The non-linear, least square method used for hypocenter location at the PIDC initially assumes that the errors associated with each station-time are normally and independently distributed with zero means and common variance. The method can be extended to allow for differences in variances provided prior knowledge of the ratio of these variances is known. Non-zero means lead to more serious problems. These means are hopefully reduced by calibration; i.e., by the use of station corrections or source-station traveltime corrections. If this is done properly, confidence ellipses can be computed that provide reasonable estimates of location errors.

Using Monte Carlo techniques we calculated the errors to be expected when uncalibrated station data is mixed with calibrated data. The calculations show the errors expected under these conditions for stations in the southwest Pacific and in North America. The results clearly show the effects of bias that arise from the use of uncalibrated data and show the failure of the confidence ellipse to accurately represent the location errors when uncalibrated station data is used.

Calibration Procedures at the PIDC

Robert G. North

Center for Monitoring Research

Software has been developed for the Prototype International Data Center (PIDC) to allow the operational application of various kinds of corrections aimed at improving seismic event location. A particular challenge for the PIDC is the sparse network it uses, with nearly all observations being at teleseismic and far-regional distances. The methods used by the PIDC to derive corrections and associated errors, and to extensively test their applicability and usefulness, will be described.

Use of Kriging in Empirical Calibration

David R. Russell

Air Force Technical Applications Center

A modified method of "Ordinary Kriging" is presented, which is useful for spatial interpolation between sparsely distributed seismic calibration events. Ordinary Kriging can be defined as a statistical "best linear unbiased estimate" between calibration events, given travel time corrections, variances, and correlation of calibration points. It is modified to reflect a-priori information on the confidence of calibration points as a function of distance and/or geological differences to the interpolant locations. Including interpolate information makes it possible to spatially interpolate very sparse data sets.

Ground Truth Hierarchy

David B. Harris

Lawrence Livermore National Laboratory

Ground truth information is crucial for developing seismic calibrations of all kinds, yet is frequently hard to obtain. Ground truth information is, for developing location calibrations: epicenter, depth, and origin times of events, and for developing discrimination calibrations: event source identities, and source parameters such as earthquake mechanisms and explosion types (e.g. ripple firing).

In the absence of hard ground truth information, various grades of inferred ground truth may have to be substituted. The grades of hard and inferred ground truth can be ordered into a hierarchy that indicates their value to calibration. Generally the most desirable grades of ground truth are the most difficult to obtain. For example, nuclear or dedicated calibration explosions are harder to acquire than earthquakes with teleseismically-constrained source and location parameters. This presentation proposes hierarchies of ground truth for developing location and discrimination calibrations, and suggests some approaches for ground truth collection.

Regional Calibration

Brian L.N. Kennett
Australian National University

It is doubtful that least-squares methods are appropriate for regional location unless array observations are available. Calibration at regional distance depends on having good reference locations which may be obtainable in seismically active areas with a high density of local stations, but not in more stable areas. Depths for calibration need to be treated carefully because they can be a strong function of the reference model used. Correction schemes need to take account of the different types of phases used—e.g. a small change in S_n velocity can give 10s residuals at 12 degrees.

Use of Earth Models in Calibration

Craig A. Schultz
Lawrence Livermore National Laboratory

The accurate location of seismic events is heavily dependent on our ability to estimate travel-time corrections in regions of interest. Where calibration data are available this can be accomplished through the generation of travel-time correction surfaces. Where such data are not available travel-time modeling may be required, especially in regions where an event occurs outside the correlation distance (zone of influence) of any surrounding calibration events. A number of modeling approaches have been proposed to predict travel-time corrections in these regions, some requiring a large research effort. Although the cost is high for some of these approaches, it may be justified for certain cases where interest is high and calibration information is limited.

Quarry Blasts, Refraction Lines, and Other "Targets of Opportunity" in Calibration

D. Craig Pearson
Los Alamos National Laboratory

Active calibration of IMS stations throughout the world can be accomplished in a timely and cost efficient manner assuming that targets of opportunity can be identified and host countries are receptive to active calibration activities. Targets of opportunity which could be utilized include mining related events (large overburden removal shots and engineered collapses of underground mines), shots conducted in cooperative mines specifically for calibration purposes (25 to 50 tons simultaneously detonated), long line crustal mapping refraction profiles, and unique applications as represented by the tunnel and borehole closure program at the Degelen Mountain and Shagan River former Russian test sites.

These active calibration techniques are attractive since they offer the highest possible level of ground-truth information, specifically accurate location and time of occurrence, and the opportunity to observe the broad-band source characteristics using deployments of portable seismic stations. The application of these techniques would be dependent on the availability of mining regions, the level of earthquake activity, and the level of cooperative confidence building measures which can be reasonably expected within the region.

Special Panel on Mining Practices

Brian Stump, Chairman
Los Alamos National Laboratory

Panel Members:

Bill Walter	LLNL
Gene Herrin	SMU
Michael Hedlin	UCSD
Brian Stump	LANL/SMU
Paul Richards	Columbia
Bill Leith	USGS
Dave Harris	LLNL
Vindell Hsu	AFTAC

Outstanding Issues:

1. How many seismic events reported by the IDC will be from mine related activities? What will be the magnitude range of these events? (Richards)
2. Can mining explosions be used as sources of ground truth information? Can these sources be used as surrogates for single-fired explosions in regions where no such sources exist? (Stump)
3. Is there a single regional discriminant that will work for all mining explosions or will it be necessary to apply a suite of discriminants? What are the candidate discriminants? How transportable are the discriminants? (Hedlin)
4. How can the Confidence Building Measures in the Treaty be used to take advantage of mining sources as Ground Truth information? Is it possible to use such information to "finger print" mines or mining activities? (Harris)
5. What will the impact of the Treaty be on the mining industry? Will there be any impact? (Hsu)
6. Do we know how to identify mining collapses and rockbursts using regional seismic observations? (Walter)
7. What is the synergy that exists between seismic and acoustic data from mining explosions? What are possible problems with the techniques? (Herrin)
8. Are there differences between US and foreign mining practices that may be important to regional observations from these sources? How much is known about signals from foreign mining operations? (Leith)

SEISMIC DISCRIMINATION

Terry C. Wallace

Department of Geosciences

University of Arizona Tucson, AZ 85721

Sponsored by the Defense Special Weapons Agency

ABSTRACT

Seismic monitoring of a Comprehensive Test Ban Treaty (CTBT) is a three-step process: (1) detection of a seismic event, (2) location of the event, and (3) identification of the type of the seismic source. The identification, or discrimination, of seismic sources is based on differences in the seismic wavefields generated by explosions, earthquakes, and some exotic sources such as bolides and asteroids. There are two basic classes of seismic discriminants used to identify explosions. The first of these is based on the spectral content of the wavefield. Explosions tend to have significantly enriched short-period energy (>1 Hz) relative to long-period energy levels (≤ 0.2 Hz) as compared to earthquakes of similar size. These differences were manifested in one of the first discriminants, the ratio of m_b to M_s . The second class of discriminants is based on the reduced generation of SH-wave-type energy in explosions. Although tectonic release can result in significant SH waves, these waves disappear as coherent arrivals at high frequencies.

Monitoring of a CTBT requires discrimination of relatively small seismic events ($ML < 4.0$). The wavefields of these small events are only well recorded at regional distances (< 1500 km). The regional distance wavefield propagates within the extremely heterogeneous crustal and upper mantle waveguide, and thus the wavefield is very complex, complicating discrimination. In this panel we will discuss the state of the art for regional discrimination with examples and experience. We will also discuss the limits of discrimination and how some evasion scenarios may affect discrimination procedures. We will also discuss the problem of exotic sources such as bolides exploding near the Earth's surface as meteorite impacts.

Seismic Discrimination Panel

Terry C. Wallace (U of A)
Steve Taylor (LANL)
Doug Baumgardt (ENSCO)
Don Helmberger (CIT)
Jack Murphy (Maxwell)
Eric Chael (SNL)

Monitoring the Oceans with the IMS Hydroacoustic Network

Dave Harris, Panel Chair
Lawrence Livermore National Laboratory

The IMS hydroacoustic network was conceived under cost constraints to detect underwater nuclear tests and assist their location and identification. The system that emerged from negotiations in Geneva is a sparse global network of 6 hydrophone stations, and five T-phase (special island seismic) stations. Four new hydrophone stations were allocated to the southern hemisphere, where their greater sensitivity could be used to monitor the vast open ocean areas of the southern seas. Four of the five T-phase stations were placed in the northern hemisphere to extend coverage there.

The sparseness of the network presents significant monitoring challenges, especially if the network is pushed to assist detection and analysis of explosions in the low atmosphere. Events will be observed over very long acoustic paths; path attenuation and velocity calibrations and synergy with the seismic and infrasound networks are crucial to detection, location and event identification. The transient-rich underwater acoustic channel may present an association challenge; techniques to estimate back-azimuth from widely-spaced hydrophones may reduce ambiguity. T-phase stations, embraced as a cost-saving measure, are significantly less sensitive than hydrophones; under what circumstances is their performance adequate?

The coupling of earthquakes and explosions in the low atmosphere to the SOFAR channel is only beginning to be understood. Empirical work with SOSUS and MILS observations of underwater earthquake T-phases establishes some parameters of the acoustic earthquake signature; numerical modeling may yield the physical basis for observed features. A combination of numerical modeling and experimentation with scaled charges is determining the coupling characteristics of explosions in the low atmosphere. Estimates of their spectra and time histories at long range may provide guidance for designers of detection algorithms and discriminants.

The question of how to integrate the hydroacoustic data stream with data from the other three networks for detection, event formation, location and identification is being resolved empirically. The sparseness of the hydroacoustic network makes joint processing a necessity. Issues remain as to whether the hydroacoustic network should be used in look-back mode (essentially triggered by seismic and infrasound detections) or whether the network should act as a trigger. The answer depends on whether the hydroacoustic threshold is set for detecting underwater or above-water explosions, and, in the latter case, the resulting false alarm rate and prospects for screening detections. The PIDC has adapted the GSETT-3 seismic detector to process hydroacoustic data, and is implementing a variety of algorithms for screening detections based on automatically-extracted signal features. Experience with this system and other NDC systems should establish practical strategies for event detection and determine tolerable false alarm rates.

Hydroacoustic Network Calibration

Ted Farrell

BBN, Inc.

Adequate calibration of the hydroacoustic network is required to obtain the desired location accuracy. Current efforts have focused on incorporating available environmental databases from standard oceanographic sources and the effects of horizontal refraction into travel time and attenuation predictions. This year, normal mode calculations were performed for both a world-wide grid and 51 high-resolution ocean areas such as coastlines, islands and seamounts; where rapid changes in phase speed cause significant horizontal refraction. The modal grids for each season are then used to predict the travel time, attenuation and travel time variance from a world-wide grid of source locations to each station in the IMS. The grids are generated for several frequencies and four seasons. These grids will be contained in the hydroacoustic knowledge database used by operational monitoring systems for both location and discrimination functions. They are also used to estimate the likely detection and location performance of the monitoring network. The status of this effort, including the likely reduction in localization bias errors and remaining issues will be presented.

Azimuth Estimation with IMS Hydrophone Stations and the Sensitivity of T-Phase Stations

Jeff Hanson

Scripps Institution of Oceanography

The sensitivity of hydrophones and the great efficiency of ocean acoustic propagation suggests that large numbers of acoustic detections may complicate hydroacoustic event association and location. Knowing the azimuth of an arriving T-phase signal greatly enhances the ability to associate that arrival with an event (LeBras and Sereno, 1996). The Ascension Island MILS (Missile Impact Location System) operated by the USAF provides an opportunity to investigate how well azimuth can be estimated from the widely-spaced hydrophones of a typical IMS hydrophone station. The hydrophone spacing (> 30 km) is larger than the coherence length of the T-phase signal, eliminating coherent array processing options. Instead, incoherent delay estimation among signal envelopes may provide azimuth constraints. We estimated T-phase arrival azimuths with incoherent methods for regional and teleseismic earthquakes and compared these with known great-circle back-azimuths. Typically the estimates are within 3 degrees of the known back-azimuths. We also examined the performance of different array configurations with varying numbers of elements.

The role oceanic island seismic (T-phase) stations may play in hydroacoustic monitoring of the oceans is not yet clear. T-phase stations have advantages: many exist already as part of the Global Seismic Network (GSN), and they are inexpensive compared to hydrophone stations. However, their sensitivity to T phases is not well understood. T-phase signal strength at seismic stations depends on the amplitude of the signal in the water column, the hydroacoustic-seismic conversion efficiency, and loss on the seismic portion of the path through the island. Ascension

Island provides an excellent laboratory for studying coupling between the water column and an island. It hosts a broad band seismic instrument (ASCN) and is surrounded by the 5 MILS hydrophones. We have collected a large set of earthquakes recorded both on the hydrophones and the seismic station. In general most of the useful T-phase signal at ASCN is between 2 and 8 Hz; the signal to noise ratio typically is 10 to 50 times less than that of the hydrophones. However, conversion efficiency is not a simple function of frequency and azimuth. We see variations among events from the same direction within similar frequency bins. These differences may be due to source and path effects partitioning energy differently among acoustic modes, which may result in different acoustic-seismic conversion efficiencies.

Scripps/IGPP Experience in Monitoring the Norwegian Sea and Pacific Ocean

John Orcutt

Scripps Institution of Oceanography

We have examined earthquake data from SOSUS arrays in the Norwegian Sea and (single hydrophones) Pt. Sur in the Pacific as well as data from the Wake Island MILS array. We have found, in the Pacific, that the length and onset times of slope-generated T-phase coda are consistent with seismic coupling occurring over a distributed, shallow region of the ocean floor in the vicinity of the earthquake epicenter. A simple expression involving sea floor depth, depth of the SOFAR channel, distance from the earthquake hypocenter to the sea floor coupling points, and travel times, was used to model T-phase amplitudes. We have found, for events with little path blockage from event to receiver, that we could model the onset times and T-phase duration quite accurately with this simple expression. The success achieved with this simple expression provides a clear direction for more accurate modeling which will involve large-scale computations. The T-phase coda recorded at a given hydrophone are not strongly dependent upon earthquake magnitude and do not vary widely for sources within a given region. In the Norwegian Sea, many more events are recorded by the SOSUS hydrophones than the seismic arrays on land in Norway and Svalbard. An earthquake swarm which occurred in 95-96 has provided important data on the behavior of earthquakes along a slow-spreading volcanic ridge axis. We have begun to record data from all the hydrophones in the Pt. Sur array which will allow analysis of these data well beyond the work to date with single hydrophones.

Source Phenomenology, Signatures, Discrimination

Phil Harben and Doug Clarke

Lawrence Livermore National Laboratory

Above-ocean nuclear explosions represent a likely evasion scenario and pose a complex problem for determining the eventual coupling of acoustic energy into the SOFAR channel. Using LLNL hydrodynamic modeling codes to model details of the source function and eventual coupling of acoustic energy into the ocean, we are attempting to quantify expected acoustic signatures at large distances from potential above-water explosive detonations.

One aspect of these modeling efforts is the validation of model predictions with experimental data. The Wyoming source modeling validation experiments were conducted to produce a data set that can be used to compare coupling - from fully-coupled underwater explosions to decoupled air shots - with model predictions. Data resulting from a series of 15 lb. high explosive detonations above and below a biologically dead lake were recorded by a nearby string of hydrophones. The resulting data set has been compared with model predictions. Future validation data is required on larger source sizes. Some data may be found in old above-water nuclear tests and other data sets may come from add-on experiments to tests such as Navy ship shock trials.

Hydroacoustic Detection, Phase Identification and Event Location at the IDC

Raymond Willeman
Center for Monitoring Research

The STA/LTA detector used for processing seismic data for GSETT-3 has been successfully reconfigured to process hydroacoustic data. The most important change, extending the length of the STA window to about 20 seconds in most cases, was required to limit the false detection rate. No important hydroacoustic detections are missed with this longer window, since it is still less than the duration of signals of interest. Selection of unique frequency bands for detection processing is required for each station in order to exclude bands with biologic noise typical of the area, for example based on the whale species typical of a region. Due to seasonal variation in local biologic activity, seasonal variations in the false detection rate occur. Some species produce short-period, broad band signals that are difficult to reject with the STA/LTA detector.

A newly implemented set of features, extracted for each detection, is derived from a "sonar clue set". Extracted features include onset and termination times, moments of the energy distribution, amplitude and time of the peak signal, complexity metrics, and cepstral measurements. With the exception of cepstral measurements, each feature is extracted in multiple frequency bands. Dispersion of the signal can be measured by comparison of onset, peak, or termination times in different bands. Spectral ratios can be measured by comparison of peak amplitude or total energy in different bands. Phase identification, based on the newly implemented feature extraction, has been implemented to distinguish noise detections from two different paths for signals of interest - pure ocean paths and ground/ocean coupled paths.

Phase identification is based on the newly implemented features. Default rules using duration and spectral ratios have been established, which accurately identify signals from a few in-ocean explosions and underwater volcanic eruptions as having a purely oceanic path and almost all signals from earthquakes as ground/ocean coupled paths. Artificial neural nets using a larger set of the extracted features have been trained for a few stations. The training set for the neural nets consists of automatic detections manually identified as noise by experienced analysts, hydroacoustic signals associated with events from the Reviewed Event Bulletin, and synthetically generated in-ocean explosion waveforms.

Event formation and location rules are the same for both automatic processing and manual analysis. Signals identified as ground/ocean coupled paths are associated with events already defined by seismic arrivals, but their times are not used to constrain the location because the ground/ocean coupling point is uncertain. Signals identified as having pure oceanic paths can be used to form and locate events in conjunction with either pure oceanic path signals at other stations or seismic signals. Because the network is sparse and because pure-ocean path signals are exceedingly rare, no events have been formed with pure-ocean path signals in IDC operations.

Infrasound Panel Abstract

Ray Willemann, Chairman
Center for Monitoring Research

Panel Members:

Terrance Barker	Maxwell Technologies
Robert Blandford	HQ AFTAC
Michael Hedlin	UCSD
Robert Gibson	BBN
Brian Kennett	Australian National University
Rodney Whitaker	LANL
Raymond Willemann	Center for Monitoring Research

Topics of Discussion:

- Network design
- Array design
- Noise reduction devices
- Signal detection in noise and clutter
- Signal measurement (feature extraction)
- Signal classification (phase identification)
- Association and event formation
- Event location
- Event screening

Abstract

Research in infrasound has been neglected over the past two decades, compared with the efforts invested in the other monitoring technologies of the CTBT IMS. Nevertheless, planning for infrasonic site surveys and station installation are underway, as is development of software for processing infrasonic data. Scientific expertise is urgently needed to support these planning and development efforts. There are fundamental questions for which only incomplete answers are available.

- What is the nature of wind-generated noise? What site features are most likely to be characteristic of low noise sites? What types of noise reduction devices are most effective under different conditions?
- What features characterize signals of interest? What frequency band is required to measure these features? How can arrays be designed to optimize measurement of these features? What detection algorithms are most sensitive to signals with these features? How should these features be measured, and how should they be used in signal classification? Among events formed from signals initially presumed to be important,

what features of the associated signals might indicate events more likely than others to be treaty violations?

- How do upper atmospheric conditions influence signal propagation? How does this influence effect network capability? Are higher capability stations required at some sites? What types of wind corrections are required to use azimuth and arrival time for accurate event locations? How does variability in upper atmospheric structure alter the features of signals? What information about the upper atmosphere is available quickly enough for use in processing infrasonic data? How should this information be used to associate signals from different stations with a common event, and to accurately locate events?

Data from a variety of sources and studies by different organizations are available to give at least partial answers to most of these questions. Panel members will be prepared to briefly review several of these topics in order to stimulate discussion, but the emphasis will be on discussing topics of interest in depth rather than covering all of the questions. Terry Barker can describe methods for evaluating alternative devices for noise reduction, including pipes and hoses. Bob Blandford can describe what is known from historical infrasound data about how long distance propagation influences signals. Rod Whitaker can describe the DOE prototype IMS infrasound station at Los Alamos, as well as upper atmospheric wind models and how promptly they are available. Michael Hedlin can describe criteria used in site surveys. Brian Kennett can describe the current understanding of local wind and noise at stations. Ray Willemann can describe the organization of processing and analysis at the IDC and alternative detection algorithms.

MULTIVARIATE CANONICAL CORRELATION OF P/S RATIOS AND PROPAGATION PATH PARAMETERS FOR IRAN

Douglas R. Baumgardt
Christopher M. Schneider

ENSCO, Inc.
5400 Port Royal Road, Springfield, VA 22151

Sponsored by U.S. Department of Energy
Office of Nonproliferation and National Security
Office of Research and Development
Contract No. F19628-95-C-0203

ABSTRACT

Spatial distributions of Pn/Sn and Pn/Lg ratios, recorded at the Iranian Long Period Array (ILPA), have been characterized in terms of spatial variations in characteristics of the crustal structure. Crustal structure parameters include elevation, depth to basement (sediment thickness), and depth to Moho (crustal thickness) and estimates of the gradients (roughness) of these parameters. Pn/Sn and Pn/Lg ratios, measured in eight frequency bands, were corrected for distance from the station and the residual variance was then regressed against six path parameters. The Pn/Sn and Pn/Lg amplitude ratios were found to best correlate with depth to basement, with correlation coefficients greater than 0.4. Moreover, comparison of contour gray level plots of Pn/Sn and Pn/Lg levels with the crustal structure maps indicate that closed contours of high values of Pn/Sn and Pn/Lg, or weak Sn and Lg, tend to be found associated with sedimentary basins in the eastern and central parts of Iran. These correlations indicate that strong attenuation or blockage of Sn and Lg amplitudes relative to Pn seem to be caused by sudden changes in the shallow crust, mainly sediment thickness.

We have used a multivariate canonical correlation analysis (CCA) program to examine the statistical properties and significance of correlations of signal fields and path-parameter fields. CCA finds linear combinations of path features, or *predictors*, which produce maximum correlation with linear combinations of signal features, or *predictands*. The correlation properties observed qualitatively were also found with CCA, i.e., the best predictor of signal features seems to have the highest weight on sediment thickness parameters. In addition to being a useful tool for examining statistical properties of correlation of signal and propagation-path features, CCA may also provide an empirical mechanism for predicting signal features from path features. This capability may be useful in CTBT monitoring for transporting regional discriminants to new regions and for optimally siting seismic stations in new regions so as to avoid blockage effects.

Keywords: Regional Seismic Discrimination, Crustal Structure, Regional Phases, Lg Blockage, Seismic Attenuation, Canonical Correlation Analysis

OBJECTIVE

Seismic discrimination between earthquakes and small explosions relies extensively on measurements of amplitude ratios of regional P (Pn, Pg) wave amplitudes to regional S (Sn, Lg) wave amplitudes which are known to be strongly affected by propagation-path effects. Modeling techniques have not yet been able to properly account for the effects of laterally heterogeneous crustal structure on amplitude ratios. However, recent empirical studies (e.g., Baumgardt and Der, 1994, Lay et al, 1997, Hartse, et al, 1997) have demonstrated that correlations appear to exist between quantitative measures of amplitude-ratio signal features and propagation-path parameters, and that such correlations apparently reduce the scatter in the amplitude-ratio. Hartse, et al, (1997) have argued that this reduced variance apparently improves discrimination

The primary objective of this study has been to investigate patterns regional P/S amplitude ratios measured for earthquakes in Iran recorded at the Iranian Long Period Array (ILPA). Following on an earlier study of Lg blockage in the Caspian Sea, reported by Baumgardt (1996), we continue to investigate more subtle variations in amplitude-ratio patterns to determine if the correlations observed in other regions also exist in Iran. The secondary objective is to investigate a new statistical correlation technique, called canonical correlation analysis (CCA) for predicting signal features from path features.

RESEARCH ACCOMPLISHED

The dataset used in this study comes from the Ground Truth Database (GTDB) assembled by Lori Grant of Multimax (Grant et al, 1996). Figure 1 shows the locations of the earthquakes recorded at the IR1 sensor of the ILPA which were studied in this paper. The array originally consisted of 7 sensors, designated IR1 through IR7. For most of the earthquakes, data is only available for a few of the sensors. The ILPA site IR1 had the most data and its location is shown in Figure 1.

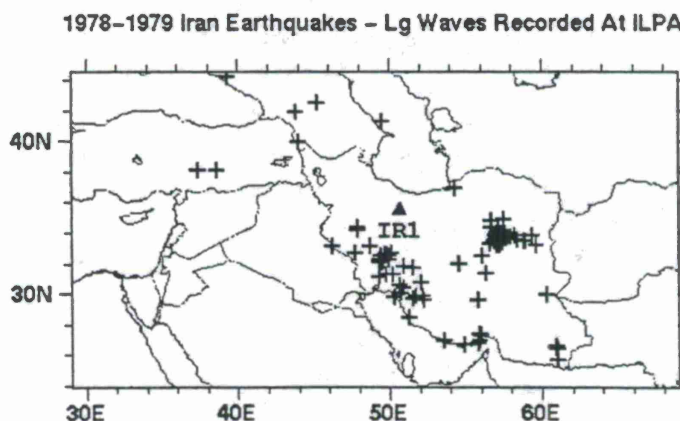


Figure 1: Locations of earthquake in Iran and the ILPA site IR1.

Figure 2 shows an example of one of the waveforms passed through several bandpass filters. This plot shows the evident decay in the amplitude of shear waves, especially Lg, as a function of fre-

quency. Above the 2 to 4 Hz band, Lg appears to be below the noise level. However, energy is apparent in both Pn and Sn at frequencies out to the 8 to 10 Hz band.

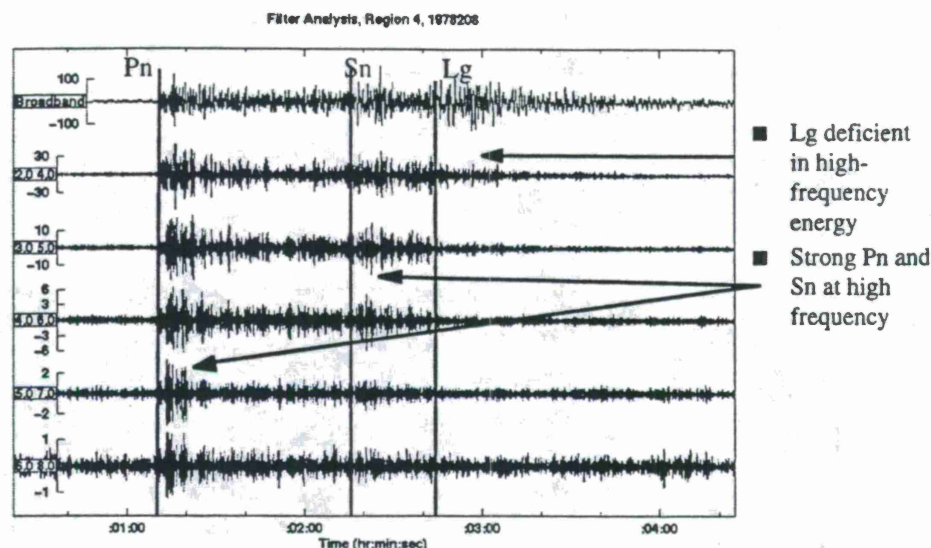


Figure 2: Example of waveform for Zagros region earthquake, recorded at IR1 of ILPA, in different frequency bands. Note that Lg loses energy at higher frequency.

For each of the earthquakes shown in Figure 1, multiple-frequency Pn/Lg amplitude ratios were determined. These ratios were measured in 8 different bands, 0.5-2.5 Hz, 2-4 Hz, 2.5-4.5 Hz, 3-5 Hz, 4-6 Hz, 5-7 Hz, 6-8 Hz, and 8-10 Hz. These measurements were made for all the available data from the IR1, IR2, IR3, IR4, IR5, and IR7 channels of ILPA whenever the data is available. However, in this paper, we will focus primarily on IR1.

Figure 3 shows shaded contour plots of elevation, depth to basement, and depth to Moho, for the Iranian part of the Cornell GIS database (Fielding et al, 1992). The major geological features in the regions are the Zagros mountains in the west, the Lut depression in central Iran (Giese et al, 1983), and the Caspian Basin in northern Iran. Baumgardt (1996) has argued that substantial sedimentary-thickness variations in the Caspian Basin may cause the blockage of Lg in the region. Variations in sediment thickness are less dramatic in other parts of Iran. The sediments in the Lut depression, for example, only reach 5 to 10 km, although there are sudden changes in sediment depth. The Moho depth thickens from about 40 km in the southwest to about 50 km under the Zagros Mountains, in the Caspian Basin and Caucasus Mountains, and in the Lut depression. The underlying sediments of the Zagros mountains are mainly platform cover and shelf type (Berberian and King, 1981). To the west, the sedimentary rocks are thickest in the Mesopotamian Fordeep, at about 13 km, and gradually thin to the west into the Arabian Shield, where there are no sediments (Beydoun, 1989).

Propagation-path parameters, described by Baumgardt and Der (1994) and also used in other more recent studies (e.g., Fan and Lay, 1997), were computed for cross sections in elevation, depth to basement, and depth to Moho for the great-circle paths from each earthquake in Figure 1

to each ILPA channel. The amplitude ratios P_n/S_n and P_n/L_g ratios were corrected for distance by regressing the amplitude ratios against distance and removing the linear trend. In general, the data exhibited high scatter when plotted versus distance because many of the measurements were made on noisy data, particularly at high frequency for L_g as shown in Figure 2. Correlation coefficients for the regressions usually did not exceed 0.5.

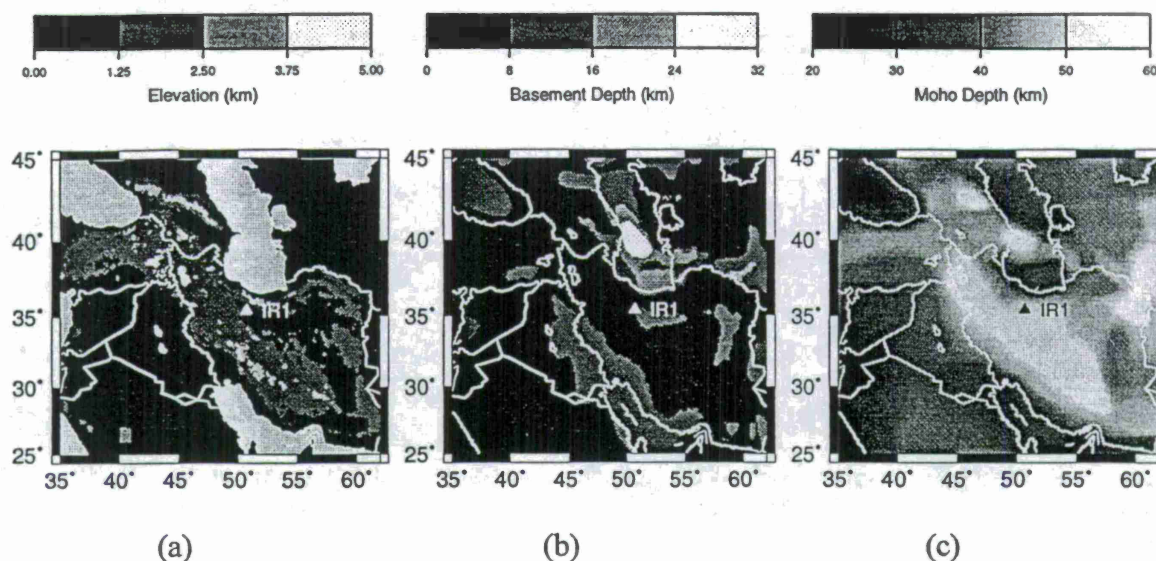


Figure 3: GIS databases for the ILPA study region from the Cornell database. (a) Elevation, (b) sediment thickness, and (c) crustal thickness.

Figures 4 and 5 show the plots of the base-10 logarithms of distance corrected P_n/S_n and P_n/L_g amplitude ratios, in 2 frequency bands, 2-4 Hz and 5-7 Hz, as a function of 6 path parameters: average Moho depth, average Moho depth gradient, average elevation, average elevation gradient, average basement depth, and average basement depth gradient.

These plots summarize the degree of correlation of the ratios with path parameters at low (2-4 Hz) and high (5-7 Hz) frequencies although these same ratios have been regressed for six other frequency bands. In most cases, the scatter is high and sometimes, correlations are low. As we mentioned above, we have found data quality problems, including low signal-to-noise ratios at the higher frequencies, mostly for L_g , and data spikes which appear at high frequency. We are now in the process of cleaning out the low-quality ratios.

However, the current data set shows some interesting trends, most notably the strong correlation of P_n/S_n and P_n/L_g ratios with sediment thickness, with correlation coefficients in excess of 0.4. Also, the ratios have weaker correlation with elevation statistics, with higher mean elevation corresponding to higher ratios or lower S_n and L_g values. Correlations with roughness statistics (gradients) are variable, usually low, although the highest correlations indicate that high basement-depth and elevation gradients cause lower ratios, or stronger S_n and L_g . The weakest correlations are with Moho depth. However, this may be because the Moho depth range for most of the paths is only about 6 km.

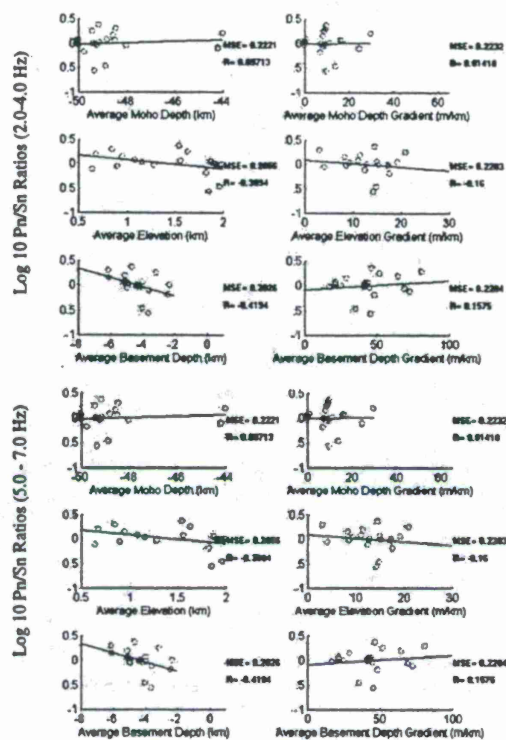


Figure 4: Regressions of distance-corrected Pn/Sn ratios versus path parameter for earthquakes recorded at ILPA bands in two frequency bands, 2-4 Hz (Top) and 5-7 Hz (bottom)

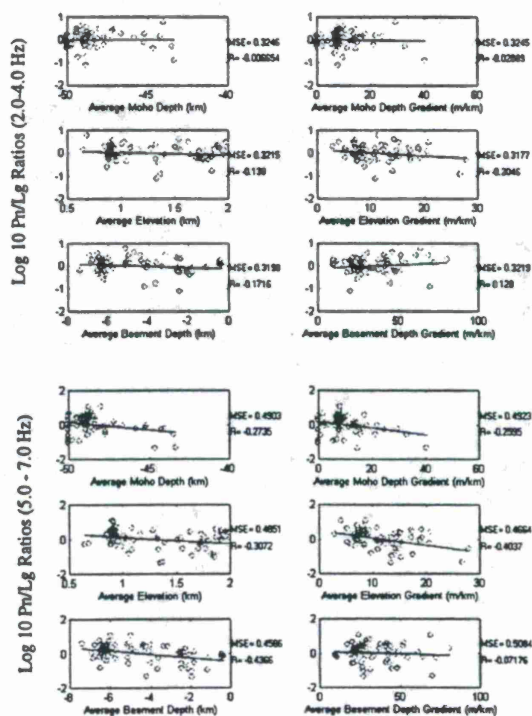


Figure 5: Regressions of distance-corrected Pn/Lg ratios versus path parameters for earthquakes recorded at ILPA for two frequency bands, 2-4 Hz (Top) and 5-7 Hz (bottom).

In order to examine patterns of ratio variations and to explore possible correlations with crustal structure variations, the Pn/Sn and Pn/L log 10 amplitude ratios are plotted as gray scale contour maps in Figures 6 and 7, respectively. Three frequency bands are shown, 0.5-2.5 Hz, 2-4 Hz, and 5-7 Hz. The white stars show the locations of the events. The shaded contours are only shown in regions where there are events and extrapolations are shown out to 2.5 degrees from any of the data points.

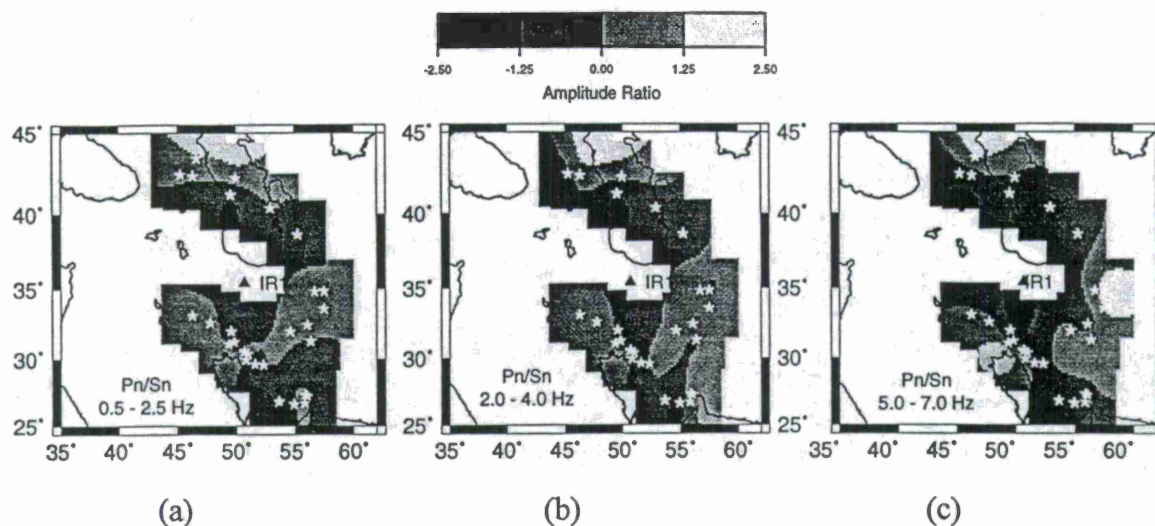


Figure 6: Shaded contour plots for log Pn/Sn ratios earthquakes in Iran, indicated by the stars to the IR1 sensor of the ILPA array. (a) 0.5-2.5 Hz, (b) 2-4 Hz, (c) 5-7 Hz.

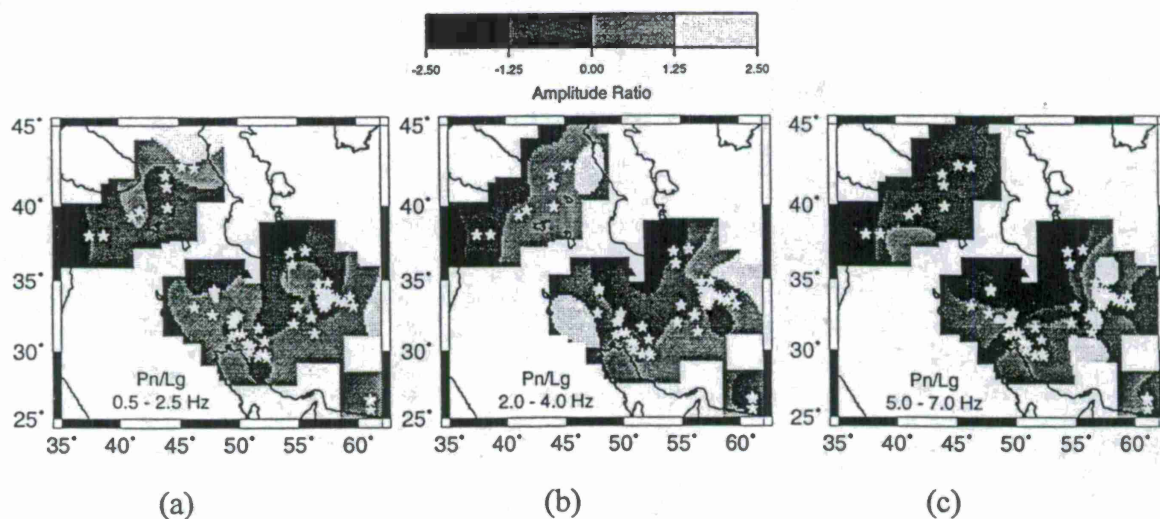


Figure 7: Shaded contour plots for log Pn/Lg ratios earthquakes in Iran, indicated by the stars to the IR1 sensor of the ILPA array. (a) 0.5-2.5 Hz, (b) 2-4 Hz, (c) 5-7 Hz.

Regions of blockage or non-observed phases are shown by the regions where there are no contours. This explains, for example, why no contours are shown near IR1 for Sn (Sn is not observed at close-in distances.) and for Lg in the Caspian Sea region (Lg is blocked for paths crossing the

Caspian Basin). Comparison of these plots shows the apparent tradeoff between Sn and Lg blockage, as discussed by Baumgardt (1996).

An interesting feature of these plots is the appearance of enclosed contours (gray or white spots) in regions of high Pn/Sn and Pn/Lg ratios. In Figure 6 (c), for example, there are enclosed contour regions of high Pn/Sn ratio at the eastern edge and in the center of the region. In Figure 7 (a), (b), and (c), enclosed regions of high Pn/Lg amplitude ratio appear in the vicinity of the Caspian Sea and in the eastern and central part of the regions. Comparing with Figure 2, these enclosed contour regions appear to coincide with the sedimentary basins in central and eastern Iran and reflect the high correlation of these ratios with basement depth in Figures 4 and 5. Admittedly, our data set is sparse and these contour patterns cannot be overly interpreted. However, the fact that high ratios, caused by weak or attenuated Sn and Lg, seem to concentrate in the sedimentary basins supports the argument of Baumgardt (1996) that these basins are the main cause of Lg and Sn blockage.

We now statistically examine this data using canonical correlation analysis (CCA). CCA is an empirical method for optimally correlating linear combinations for *predictor* and *predictand* fields of multivariate features. In our case the predictor fields are propagation path features and the predictand fields are seismic signal features. CCA is a multivariate correlation approach, first developed by Hotelling (1936) and Anderson (1984), which determines linear combinations of *predictor* vectors that have maximum correlation with linear combinations of *predictand* fields. The application of CCA to this problem has been inspired by the use of the method for meteorological and climate prediction (e.g., Bretherton et al, 1992). In climate prediction, statistical correlation approaches, using empirical knowledge, provide more skillful predictions than computer model predictions because of limitations of physical modeling. We believe an analogous situation exists for the transporting of the regional *P/S* ratios. Because the state-of-the-art in regional waveform modeling has not yet been demonstrated to reproduce the high frequency discriminants observed in data, and therefore, cannot be relied upon yet for predictions of *P/S* ratios in new geographic regions, empirical prediction approaches need to be used.

The initial CCA algorithm used in this study was programmed from the theory in Johnson and Wichern (1988) using Matlab. The algorithm looks for two sets of weight vectors, \mathbf{a}_i and \mathbf{b}_i , whose components are coefficients of linear combinations of the 6 path parameters, plus distance, and the 8 linear combinations of signal features, respectively. These linear combinations on the principal canonical component should provide the maximum correlation.

Figure 8 shows the results of canonical analysis applied to the correlation of Pn/Lg ratios and path parameters. In this case, the data has been distance corrected, but the parameter distance has still been included as a path parameter. In each case, the weight on the distance parameter as a predictor is 0, as it should be since the distance dependence was removed from the data prior to applying this analysis. The CCA analysis increased the correlation of the principal canonical variable to 0.73, still somewhat low but much better than the original correlations of 0.4.

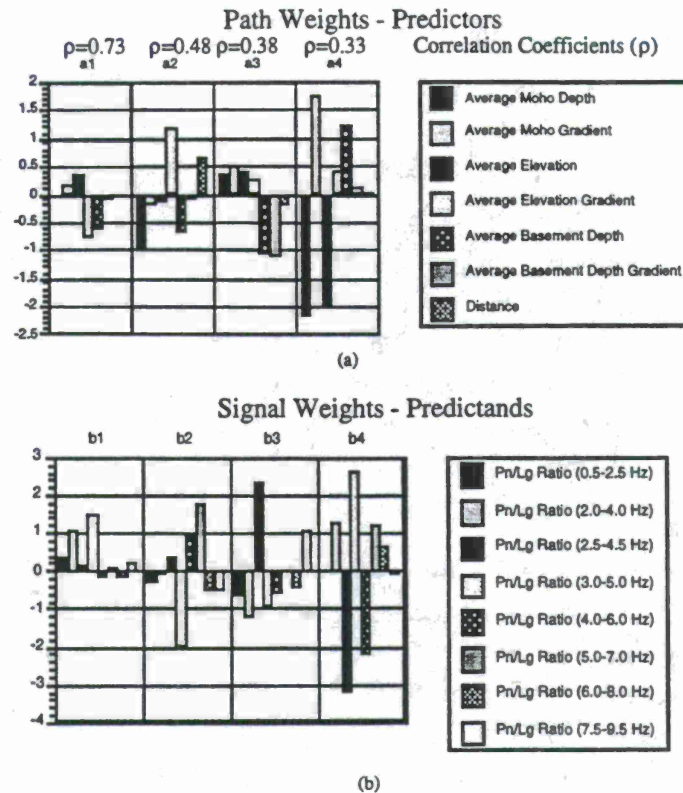


Figure 8: GIS path predictions of Pn/Lg ratios canonical correlation loadings distance corrected data. (a) Path weights or predictors. Most of the correlation (0.73) is accounted for by a1. Dominant path features are elevation, elevation gradient, basement depth. Least important are Moho depth, depth to basement gradient, and distance. (b) Signals weights or predictands. Path parameters are best correlated with Pn/Lg ratios in the 0.5-2.5 Hz, 2-4 Hz, and 3-5 Hz bands.

The CCA analysis shows that the Pn/Lg ratios in the 0.5-2.5 H, 2-4 Hz, and 3-5 Hz bands were best predicted by the data. The dominant predictor path features were the elevation, elevation gradient, and basement depth.

Finally, Figure 9 shows the CCA analysis applied to the data without distance-trend correction. In this case, it can be clearly seen that the distance parameter is non-zero, although its weight is not as strong as the weight on other path features, especially elevation gradient and basement depth. It is notable that the depth-to-Moho weight is very small, which suggests that the lower crust is not as important as the upper crust in controlling variations in the Pn/Lg ratios. Also, this may have been because the range of variation in Moho depth in Iran is only 10 km, which may not be a great enough range to produce significant correlation.

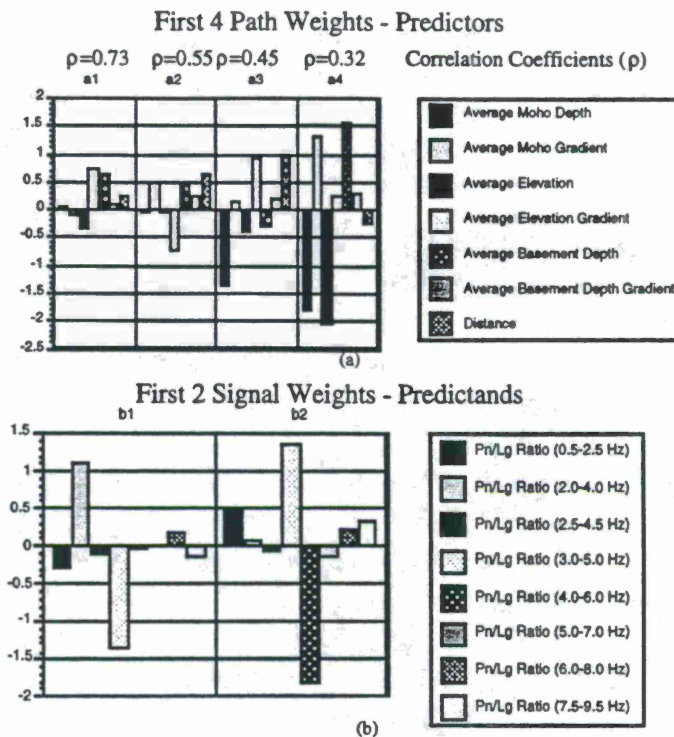


Figure 9: GIS path predictions of Pn/Lg Ratios canonical correlation loadings ratios uncorrected for distance. (a) Path weights or predictors. (b) First 2 signal weights or predictands.

These results show that a multivariate CCA prediction model can be derived which has stronger correlation and, therefore, more sensitive predictive power than the original path parameters. We expect that better results will be obtained by more judicious selection of feature vectors. We are also applying to the analysis of the Pn/Sn ratios.

CONCLUSIONS AND RECOMMENDATIONS

This paper has summarized the work in progress on the investigation of correlation of regional P/S ratios with propagation path parameters for earthquakes in Iran recorded at the ILPA array. We find a spatial correlation between sedimentary basins and large values of Pn/Sn and Pn/Lg ratio caused by strongly attenuated Sn and Lg. Sudden changes in sediment depth within the sedimentary basins in Iran can disrupt the crustal waveguide and block the propagation of Sn and Lg waves. The depth to the Moho does not appear to be strongly correlated with the ratios, although crustal thickness does not vary significantly in most of Iran. Multivariate canonical correlation analysis (CCA) provides a statistical approach for assessing correlations of complex fields of signal measurements with propagation-path parameters and determining the confidence of such correlations. CCA may provide an empirical model for predicting the P/S ratios from path parameters from path parameters. With regard to CTBT monitoring, CCA may provide an empirical signal feature prediction tool which can be useful for transporting regional discriminants to new regions of limited seismic record and for predicting paths that might have strong Sn or Lg

blockage or attenuation. This latter capability would be useful for optimally siting new stations to avoid such blockages for new regions of the world which need to be monitored.

REFERENCES

- Baumgardt, D.R. (1996). Investigation of Lg blockage and the transportability of regional discriminants, Scientific Report No. 1, PL-TR-96-2294, 11 November 1996, ENSCO, Inc., Springfield, VA.
- Baumgardt, D.R. and Z. Der (1995). Investigation of the transportability of the P/S ratio discriminant to different tectonic regions, *Scientific Report No. 1*, PL-TR-94-2299, 6 December 1994, ENSCO, Inc.
- Berberian, M. and G. King (1981). Towards a paleogeography and tectonic evolution of Iran, *Can. J. Earth Sci.*, **18**, 210-265.
- Beydoun, Z. R. (1989). Hydrocarbon potential of the deep (pre-Mesozoic) formation in the Middle-East Arab countries, in *Technical Papers Presented at the Seminar on Deep Formations in the Arab Countries: Hydrocarbon Potential and Exploration Techniques*, Abu Dhabi National Oil Company, Abu Dhabi, UAE.
- Bretherton, C.S., C. Smith, and J.M. Wallace (1992). An intercomparison of methods for finding coupled patterns in climate data, *J. Climate*, **5**, 541-560.
- Fan, G. and T. Lay (1997). Statistical analysis of irregular waveguide influences on regional seismic discriminants in China, submitted to *Bull. Seism. Soc. Am.*
- Fielding, E.J., B.L. Isacks, and M. Barazangi (1992). A geological and geophysical information system for Eurasia, *Technical Report No. 2*, Cornell University, Ithaca, New York.
- Giese, P., J. Makris, B. Akashe, P. Röwer, H. Letz, M. Mostaanpour (1983). Seismic crustal studies in Southern Iran between the Central Iran and the Zagros belt, in *Geodynamic Project (geotraverse) In Iran*, Final Report, Report No. 51.
- Grant, L., F. Ryall, I. Henson, and W. Rivers (1996). Ground truth database for seismic discrimination research, Proceedings of the 18th Annual Seismic Research Symposium on Monitoring a Comprehensive Test Ban Treaty, 4-6 September 1996, PL-TR-96-2153, Environmental Research Papers, No. 1195, J.F. Lewkowicz, J.M. McPhetres, D.T. Reiter, eds., pp 997-1006.
- Hartze, H.E., R. A. Flores, and P. A. Johnson (1997). Correcting regional discriminants for path effects in Western China, submitted to *Bull. Seism. Soc. Am.*, LAUR- 9701978, Los Alamos National Laboratory, Los Alamos, NM.
- Hotelling, H. (1935). Relations between two sets of variates, *Biometrika*, **28**, 321-377.
- Johnson, A. and D.W. Wichern (1988). *Applied Multivariate Statistical Analysis*, Prentice Hall, Englewood Cliffs, New Jersey.
- Lay, T., G. Fan, and A. Rodgers (1997). Crustal waveguide effects on regional phases in China and Southeast Asia, Scientific Report No. 1, PL-TR-97-2028.

REGIONAL Q VARIATIONS IN THE MIDDLE EAST FROM FUNDAMENTAL-MODE AND HIGHER-MODE SURFACE-WAVE ATTENUATION

Lianli Cong and Brian J. Mitchell
Department of Earth & Atmospheric Sciences
Saint Louis University

Sponsored by U.S. Department of Energy
Office of Nonproliferation and National Security
Office of Research and Development
Contract No. F19628-95-K-0004

ABSTRACT

Fundamental-mode Rayleigh-wave attenuation in the Middle East exhibits large lateral variations, being highest in regions surrounding the Black and Caspian Seas and lowest in Saudi Arabia. Models obtained from an inversion of two-station attenuation data show that crustal shear-wave Q throughout the entire Middle East is lower than that reported, in previous studies, for any stable continental region. Extreme values range from about 50 at mid-crustal depths in the Turkish and Iranian Plateaus to about 200 in the upper crust of the Arabian Peninsula. Models obtained from single-station studies of multi-mode Rayleigh-wave attenuation provide more detailed information of regional variation of crustal shear-wave Q . They show that Q is higher in the western (and shield) portion of Saudi Arabia than it is in the central and eastern portions. Throughout the entire Middle East the lower crust exhibits values no greater than about 150. This contrasts sharply with results from other continental regions (which are not undergoing compressional deformation) where shear-wave Q may be as high as several hundred to a thousand or more. These low values may indicate that fluids reside in faults, cracks, and permeable rock at lower crustal, as well as upper crustal, depths due to continental convergence and intense deformation at all depths in the Middle Eastern crust.

The regional variation of L_g coda Q at 1 Hz is consistent with variations in the shear-wave Q models derived from surface-waves at lower frequencies. It is lowest in regions surrounding the Black and Caspian Seas (150-250) and highest (~ 450) in the western, and shield, portion of the Arabian Peninsula. Low L_g coda Q (~ 250) also occurs in the Osman folded zone in the southeastern Arabian Peninsula. Q decreases from west (~ 450) to east (~ 350) across the Arabian Peninsula with the lower values coinciding with the deep sedimentary basins along the Persian Gulf.

Keywords: Q , Rayleigh waves, L_g , attenuation, Middle East

OBJECTIVE: Seismic wave attenuation throughout the entire Middle East is known to be high, but reliable models of the quality factor, Q , for that region are few. In addition to being characterized by high attenuation, that region is also geologically complex, a situation that suggests the presence of lateral variations of elastic properties that may cause focusing/defocusing and scattering of seismic waves that propagate through it. This study attempts to find surface-wave data for which the effects of those complexities is minimized so that we can obtain reliable models of shear-wave Q (Q_p) for the crust and upper mantle of the Middle East and to determine how those models vary from region to region. Further, we wish to determine whether or not the regional variation in attenuation of regional phases, such as Lg, at higher frequencies, is consistent with those models.

RESEARCH ACCOMPLISHED

Regionalization and Data Acquisition

The Middle East, as indicated by the map of Figure 1, is a geologically complex region. That complexity is being influenced by the collision of the Arabian and African plates with Eurasia as well as by spreading of the Red Sea and the Gulf of Aden. The most stable portion of the region is the Arabian Plate consisting of a shield in the west, a central shelf, and platforms and basins in the east. This plate is bounded on the northwest by the Dead Sea fault, and on the northeast by the Zagros thrust belt. The North Anatolian fault extends in an east-west direction across almost all of Turkey.

In order to model the regional variation of attenuation in the Middle East, we have divided it into three regions, based upon the availability of data for two-station attenuation studies. Region 1 is represented by those paths (Figure 2) in the northern portion of the map that are strictly confined to continents. Data for Region 1 is therefore restricted to that acquired for the station pairs ANTO-GNI, KIV-GNI, and ABKT-BGIO. Paths through the Black and Caspian Seas are excluded from this region and are assigned to Region 2. Region 2 data was acquired for the station pairs ANTO-KIV, GNI-ABKT, and KIV-ABKT. For Region 3 we use data from station pairs in Saudi Arabia as well as one station in Israel (BGIO-RAYN, BGIO-HALM, AFIF-SODA, HALM-RANI, and HALM-SODA). For all of these paths we measured the attenuation of spectral amplitudes between the two stations of each pair for the period range between about 5 seconds and 70 seconds.

To improve regional coverage we used a multi-mode method that requires only a single station (Cheng and Mitchell, 1981). Figure 3 displays the paths for each event-station pair used when applying that method. Groups of paths were selected to correspond to each of the three regions studied using the two-station method.

All stations outside Saudi Arabia are permanent IRIS stations and provided broadband data in digital form. The stations in Saudi Arabia were deployed temporarily by the University of California at San Diego and Boise State University. They also provided broadband digital data.

Two-station Results

Figure 4 displays a multiple-filter plot of spectral amplitudes for Rayleigh waves generated by an earthquake on 22 April 1995 and recorded at station GNI. The maximum amplitudes delineate a fundamental-mode Rayleigh wave at periods between about 6 seconds and 50 seconds. In addition, there is a well-defined higher mode between about 3 and 6 seconds. The higher mode is not used for two-station studies but will be employed

in the single-station studies discussed in the next section. Figure 5 displays Rayleigh wave attenuation coefficients for periods between about 5 and 70 seconds for Region 1 and between about 5 and 80 seconds for Region 3. With the exception of one path the coefficients for Region 3 are quite consistent whereas those for Region 1 show a greater variability. This difference is expected since Region 1 much more geologically complex than Region 3.

Inverting attenuation coefficients for shear-wave Q_β as a function of depth requires knowledge of the velocity structure of the region of study. Models for all three regions have been obtained from surface-wave phase and group velocities reported earlier (Cong et al., 1996). With that information, and assuming that Q_β is independent of frequency, we inverted for Q_β structure for each of the three regions. The models appear in Figure 6. Lowest Q_β values are associated with Region 1, especially in the depth range between 10 and 30 km. Highest crustal values occur in the model for Region 3, the Arabian plate, a stable and partly shield region. Crustal Q_β in Region 3, however, lies between about 150 and 400, values that are lower than those found for other stable regions. Q_β in these models attains high values at depths greater than 70 or 80 km in the upper mantle. This may, however, be illusory since the resolution of our method at these depths is poor.

An interesting result of this research is that Q_β is low in both the upper and lower portions of the crust of the Middle East. In other continental regions we found that Q_β increases rapidly with depth at mid-crustal depths, usually having values as high as several hundred to one thousand. Lower crustal Q_β in the Middle East do not appear to be greater than about 150 anywhere. Mitchell (1995) proposed that regional variations of Q_β in the upper crust of continents are due to variations in the volume of fluids in cracks and permeable rock and Q_β is high in the lower crust because those cracks close at greater depths. Since the Middle East is a region of plate convergence in the north and high upper mantle temperatures and uplift in Saudi Arabia (Mitchell, 1997) fluid-filled cracks may occur at lower crustal depths because metamorphic fluids were recently generated there.

Single-station Results

The single-station multi-mode method (Cheng and Mitchell, 1981) requires seismic events with known depths and focal mechanism solutions. It works best in regions of low Q , such as the Middle East. The procedure consists of trial-and-error forward modeling, trying various Q_β models until one is found that produces theoretical fundamental-mode and higher-mode spectra that match observed spectra. Models consisting of only two to four layers are usually sufficient to explain the spectral data.

Figure 7 shows the models obtained using the single-station method for all three regions and compares them to models obtained using the two-station method. Although the models obtained with the single-station method all show much less detail than that present for the models obtained from two-station studies, the agreement in all three cases is excellent. We found that is some regional variation in the crustal values of Q_β also occurs within Region 1. Four variations of the model were required to explain all of the observed spectral data for that region. Similarly, Region 3 required three different models. Model 1 corresponds to most of eastern and central Saudi Arabia while either Model 2 or Model 3, with low Q_β near the surface is required to explain the data for eastern Saudi Arabia where thick young sediments are present.

Figure 8 shows comparisons of theoretical and observed spectra obtained from the analysis of nine seismograms for Region 1. In all nine cases we have achieved good

agreement between observed and theoretical spectra if we allowed some variation in models within Regions 1 and 3.

Lg Coda Q

Lg coda Q has been mapped for nearly all of Eurasia (Mitchell et al., 1997). We have tried to map it in detail for the Middle East so that we could compare that variation with the models of Q_p obtained from surface-waves studies at longer periods. Figure 9 shows our data coverage as given by assumed scattering ellipses for Lg coda. The resulting Lg coda Q map appears in Figure 10. The lowest values lie in the regions surrounding the Black and Caspian where Q_p is lowest. It is also low in the Osman folded zone in southeastern Saudi Arabia. In addition, Lg coda Q varies from west to east across Saudi Arabia in the same wave as that indicated by our Q_p models.

CONCLUSIONS AND RECOMMENDATIONS

Seismic wave attenuation in the Middle East is very high (and Q_p is very low) throughout the Turkish and Iranian Plateaus. In the stable regions of Saudi Arabia Q_p is much lower than would be expected on the basis of results from other stable regions. Q_p in the lower crust throughout all of the Middle East is much lower than it is in the lower crust of other continental regions. This may occur because crustal deformation was so severe in the recent past that it generated metamorphic fluids that reside in cracks and permeable rock through the entire crust there. Two-station and single-station studies of surface-wave attenuation yield similar Q_p models for each of three regions of the Middle East. Measurements of Lg coda Q show the same variation of attenuative properties as that obtained from models of Q_p .

The high attenuative properties of the crust and upper mantle throughout the Middle East makes it difficult to observe seismic waves generated by small earthquakes and nuclear explosions in that region, at least along some paths, and thus to discriminate between them. It will be important to regionalize those properties in greater detail to see if there are optimum sites for emplacement of seismographs that might take advantage of higher than average Q_p in some portions of the crust in the Middle East.

REFERENCES

- Cheng, C.C., and B.J. Mitchell, Crustal Q structure in the United States from multi-mode surface waves, *Bull. Seism. Soc. Am.*, 71, 161-181, 1981.
- Cong, L., J. Ni, and B.J. Mitchell, Seismic surface attenuation studies in the Middle East, Rpt. PL-TR-96-2153, Proc. of the 18th Annual Seismic Research Symp. on Monitoring a Comprehensive Test Ban Treaty, 4-6 Sept. 1996, 16-25, 1996.
- Mitchell, B.J., Anelastic structure and evolution of the continental crust and upper mantle from seismic surface wave attenuation, *Rev. Geophys.*, 33, 441-462, 1995.
- Mitchell, B.J., Y. Pan, J. Xie, and L. Cong, Lg coda Q variation and the crustal evolution of Eurasia, *J. Geophys. Res.*, in press, 1997.
- Seeber, D., M. Vallve, E. Sandvol, D. Steer, and M. Barazangi, Middle East tectonics: Applications of geographic information systems (GIS), *GSA Today*, 7, 1-5, 1997.

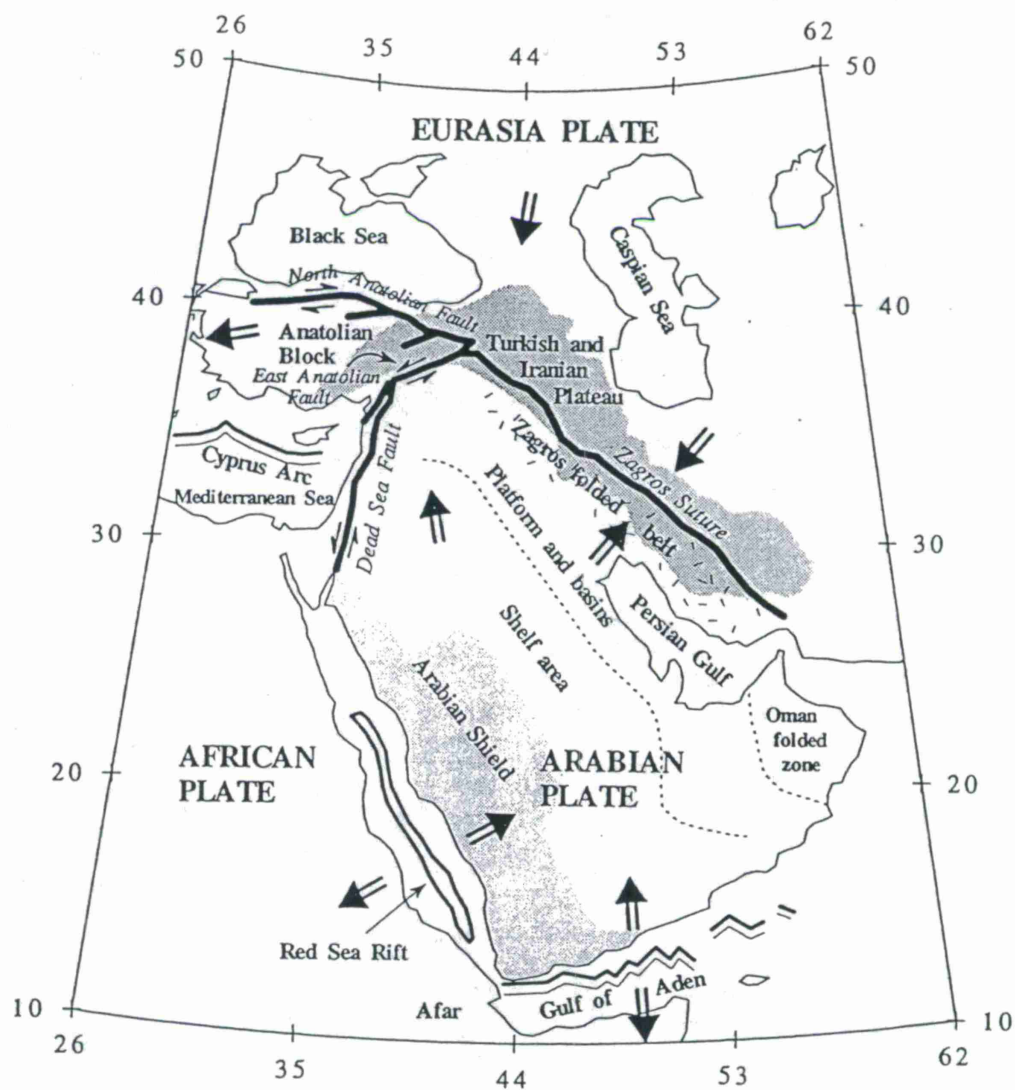


Figure 1. Tectonic map of the Middle East (Modified from Seber et al., 1997).

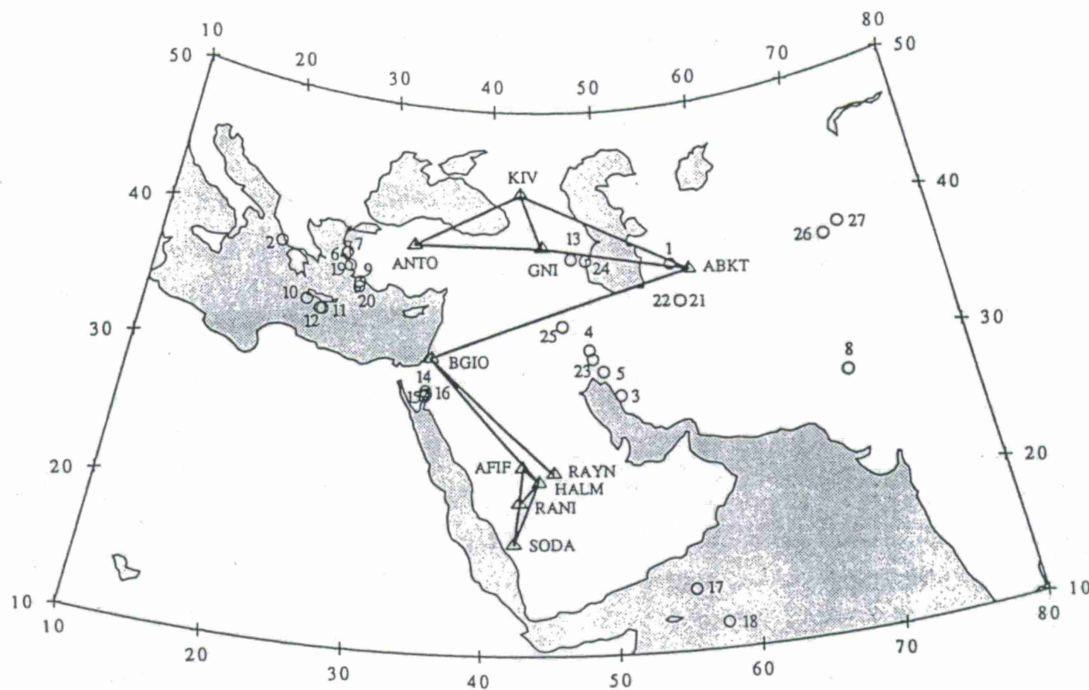


Figure 2. Paths used for two-station determinations of Rayleigh wave attenuation.

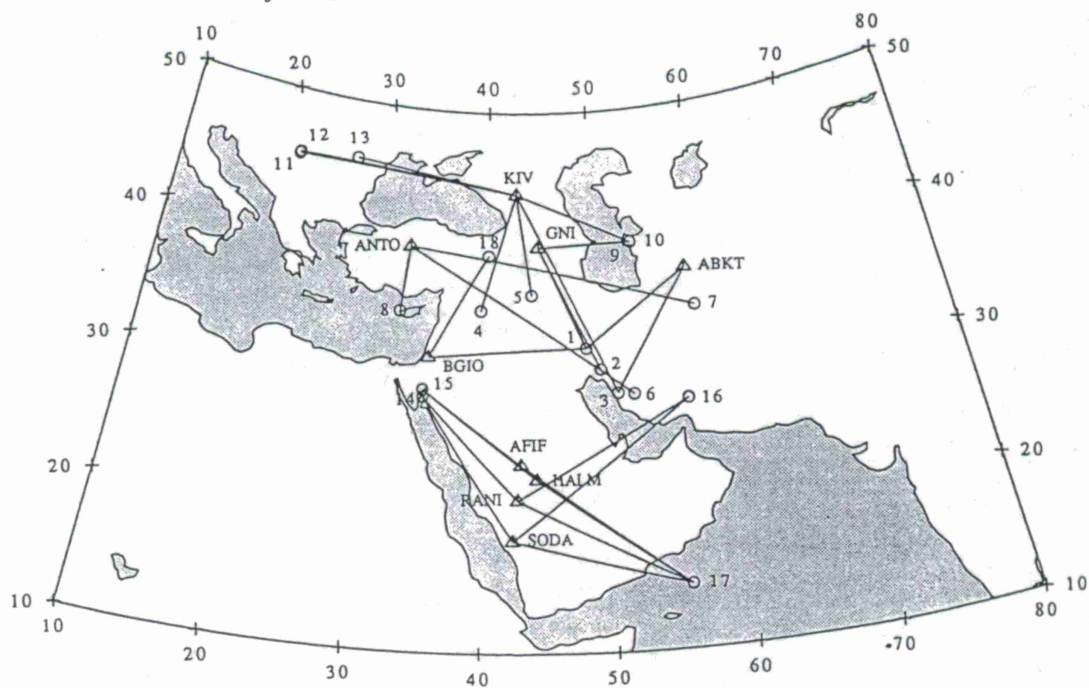


Figure 3. Paths used for single-station studies of multi-mode Rayleigh wave attenuation.

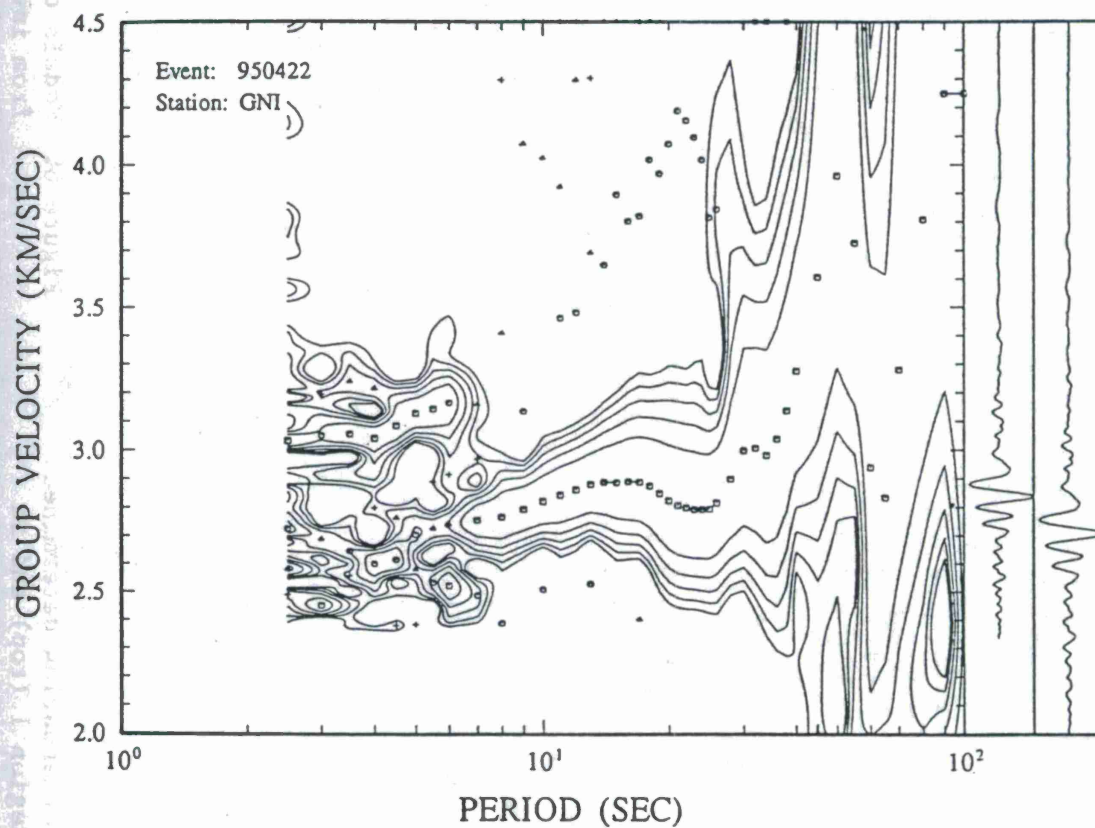


Figure 4. Contoured spectral amplitudes of fundamental-mode and higher-mode Rayleigh waves recorded at station GNI for an earthquake that occurred on 22 April 1995.

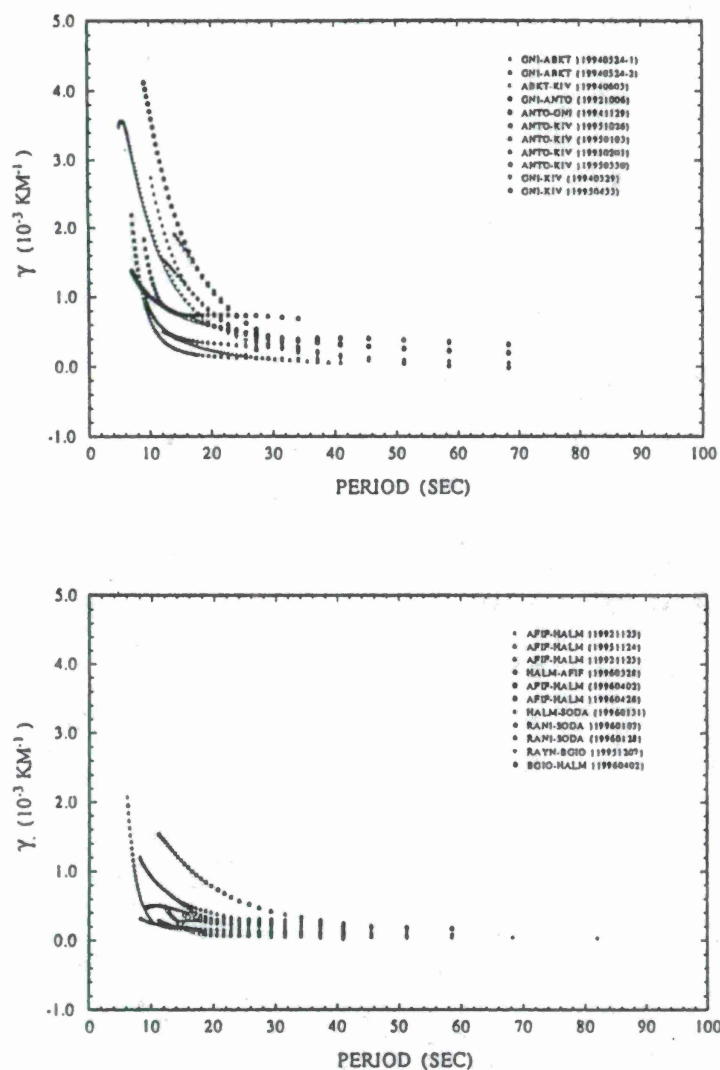


Figure 5. Rayleigh wave attenuation determined for paths in Region 1 (top) and in Region 3 (bottom).

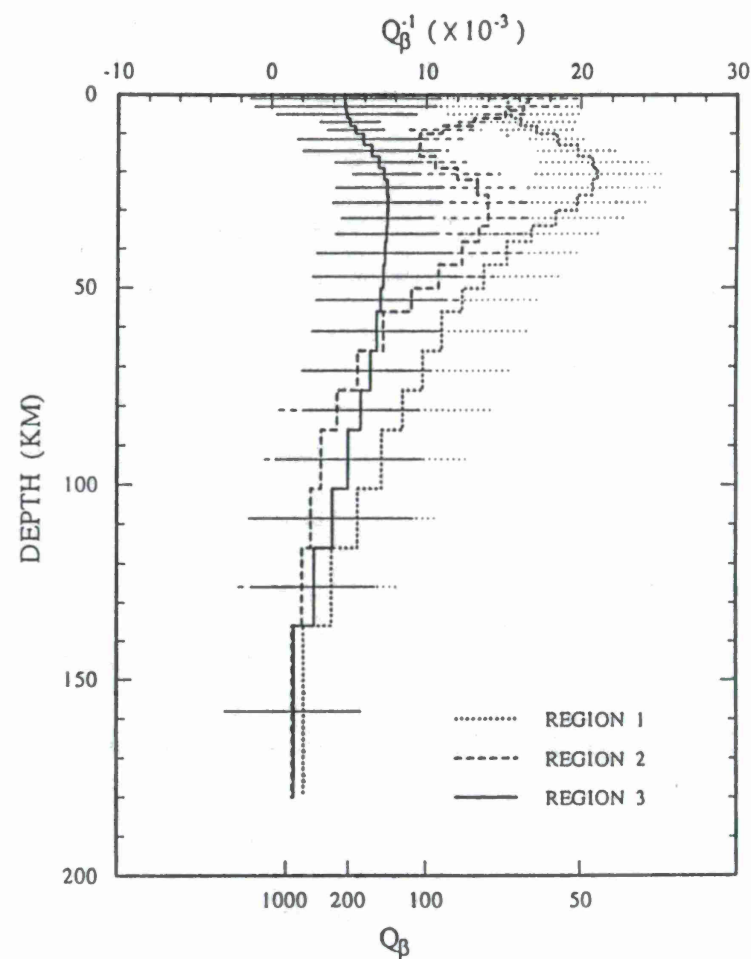


Figure 6. Models of shear-wave Q obtained from inversion of two-station determinations of Rayleigh-wave attenuation for three regions.

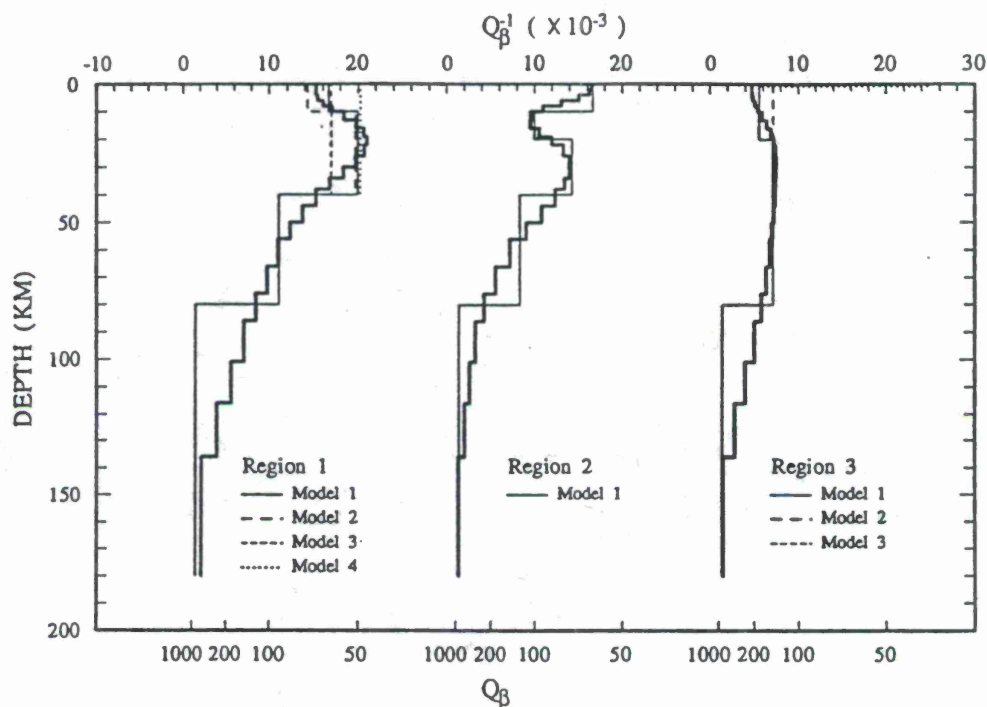


Figure 7. Q models obtained using the single-station method (light lines) compared to models obtained using the two-station method (heavy lines).

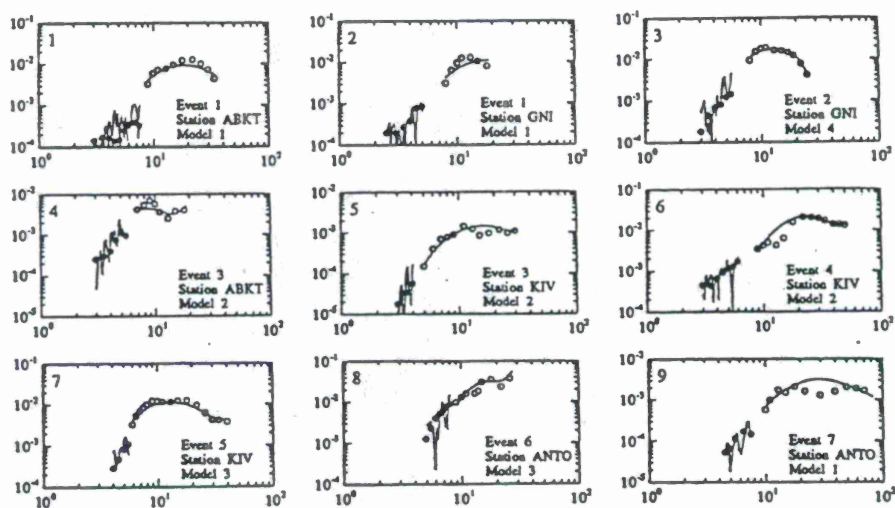


Figure 8. Comparison of theoretical multi-mode spectra for models of region 1 with observed spectra. Fundamental-mode observations are shown with open symbols and higher-mode observations are denoted by closed symbols.

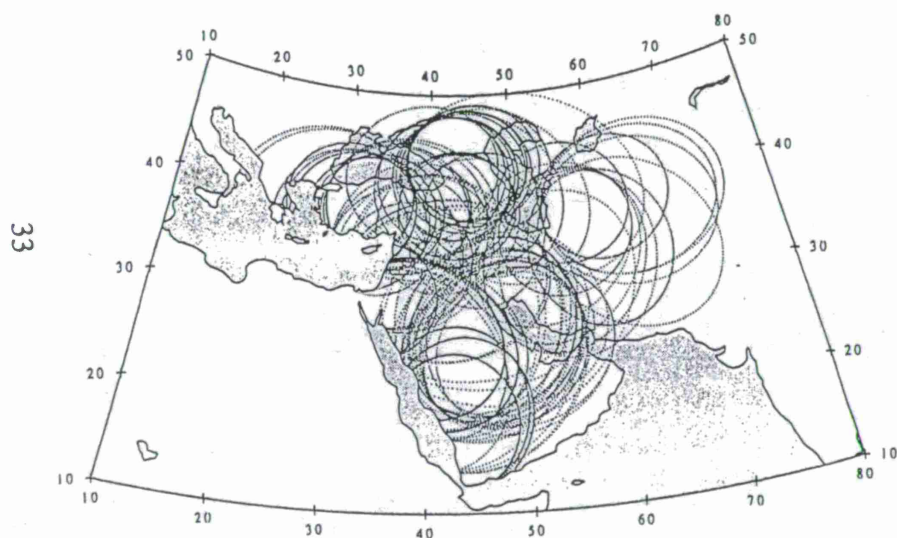


Figure 9. Scattering ellipses indicating assumed areal coverage obtained using Lg coda at a late time in the coda. For each ellips the two foci lie at the epicenter and recording station for a recorded event.

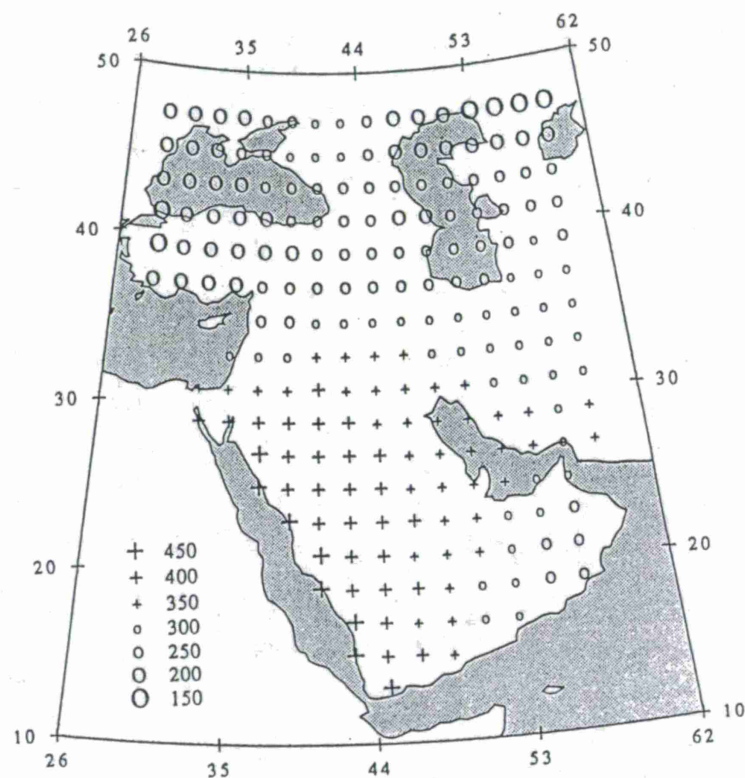


Figure 10. Distribution of Lg coda Q in the Middle East obtained using events that provided the coverage shown in Figure 9.

FREQUENCY-DEPENDENT ATTENUATION OF REGIONAL PHASES IN AUSTRALIA

Richard D. Jenkins and Thomas J. Sereno, Jr
Science Applications International Corporation
10260 Campus Point Drive
San Diego, California 92121

Sponsored by U.S. Department of Energy
Office of Nonproliferation and National Security
Office of Research and Development
Contract No. F19628-95-C-0097

ABSTRACT

Recent studies have shown that the high-frequency Lg/P ratio can be an effective discriminant at regional distances. However, this ratio must be recalibrated for each new source region. Our primary goal is to derive regional wave attenuation models for up to ten subnetworks of the International Monitoring System (IMS) primary network and use them to evaluate the transportability of the Lg/P discriminant to uncalibrated regions.

We now have frequency-dependent regional amplitude measurements for more than 7900 station-event pairs using data from the Group of Scientific Experts Third Technical Test, called GSETT-3. These were computed using data at the Prototype International Data Center (PIDC) located in Rosslyn, Virginia. We have completed a preliminary analysis based on data from 66 regional events recorded by IMS stations in Australia.

We measured six types of time-domain amplitudes and spectral amplitudes for each regional phase. The time-domain measures are the root mean-square (*rms*), short-term average (*stav*), and average absolute value (*abs*) amplitudes on coherent and incoherent beams. We estimated the correlation and variance between these different measures. We do not recommend using amplitudes on coherent beams for attenuation studies because the signal loss from the beam forming process contaminates the high-frequency measurements. There is a high degree of correlation among the three amplitude measures on incoherent beams. However, it appears the absolute value has a higher variance. Therefore, we recommend either the *stav* or the *rms* amplitude for attenuation studies. The correlation between the incoherent *rms* and the spectral amplitudes decreases with increasing frequency. We have not yet evaluated the merits of using spectral amplitudes versus time-domain amplitudes, however it is known that the time-domain measures can be biased by leakage from frequencies outside of the intended filter passband [Lay *et al.*, 1997]. In this preliminary study we have used only the *rms* amplitudes on incoherent beams to estimate attenuation.

We developed a new program called AmpInv that inverts frequency-dependent amplitudes for attenuation and source models. After applying AmpInv to our initial data set from Australia, we found Pn attenuation results are similar to those obtained by Sereno [1990] for Fennoscandia but that Sn appears to attenuate more rapidly. We do not yet have enough Pg and Lg data to be confident of our results for these phases.

Keywords: Discrimination, Frequency-Dependent Attenuation, Regional Seismicity, Lg/P Ratios, Transportability, Regionalization

OBJECTIVE

Identification of small events is the most difficult technical problem for seismic verification of a Comprehensive Test Ban Treaty (CTBT). Previous empirical studies have shown that the high-frequency Lg/P ratio is one of the most promising discriminants at regional distances [e.g., Bennett *et al.*, 1989; Baumgardt and Young, 1990; Chan *et al.*, 1990; Dysart and Pulli, 1990; Baumgardt *et al.*, 1992; Wuster, 1993]. However, these studies are based on co-located earthquakes and explosions in limited geographic regions, and their results must be recalibrated for each new source region. Our main objective is to develop and apply distance corrections so we can evaluate the transportability of the Lg/P discriminant to uncalibrated regions.

We have developed software to invert frequency-dependent regional wave amplitudes for source and attenuation parameters. We intend to apply it to data from up to ten stations in the International Monitoring System (IMS) primary network. The attenuation models will be used as path corrections to the Lg/P discriminant. We will evaluate the identification accuracy of this discriminant at each of the ten stations and generalize the results in terms of the geologic and tectonic environment.

RESEARCH ACCOMPLISHED

This report summarizes our work in progress to date. An annual report [Jenkins *et al.*, 1996] summarizes our work during the first year of this project.

We estimated frequency-dependent amplitudes of regional phases using data from the Group of Scientific Experts Third Technical Test, called GSETT-3. These waveforms were obtained from the Prototype International Data Center (PIDC) at the Center for Monitoring Research (CMR) in Rosslyn, Virginia. We now have amplitude measurements for more than 7900 station-event pairs recorded between September 1, 1995 and August 1, 1996 at stations in ten subnetworks defined for this project [Jenkins *et al.*, 1996]. Additional measurements are being computed. We completed development of our software called AmpInv which inverts the amplitude measurements to estimate attenuation and source parameters. We've reviewed the amplitude measurements and estimated attenuation and source parameters using an initial data set from Australia.

Data Set

We plot Pn and Lg ray-paths in Figure 1 for events recorded by IMS stations located in Australia. Most of the Pn phases originate from events in the Java Trench. We also have data from events within Australia including areas of known mining activity. Lg rays are primarily originating from events within Australia although some Lg arrivals are observed from events in the Java Trench. This data set consists of 66 events with the M_L distribution superimposed in Figure 1.

Waveform examples are plotted in Figure 2 for an event from a local mining area and from the Java Trench. Figure 2a shows four regional phases (Pn, Pg, Sn, Lg) from an M_L 3.5 event recorded at Charters Towers approximately 3 degrees away. Figure 2b shows Pn and Sn phases from an M_L 3.8 event near the Java Trench recorded at the Meekathara station which is approximately 18 degrees away. Both of the waveforms shown in Figure 2 have been filtered in the 1-9 Hz band.

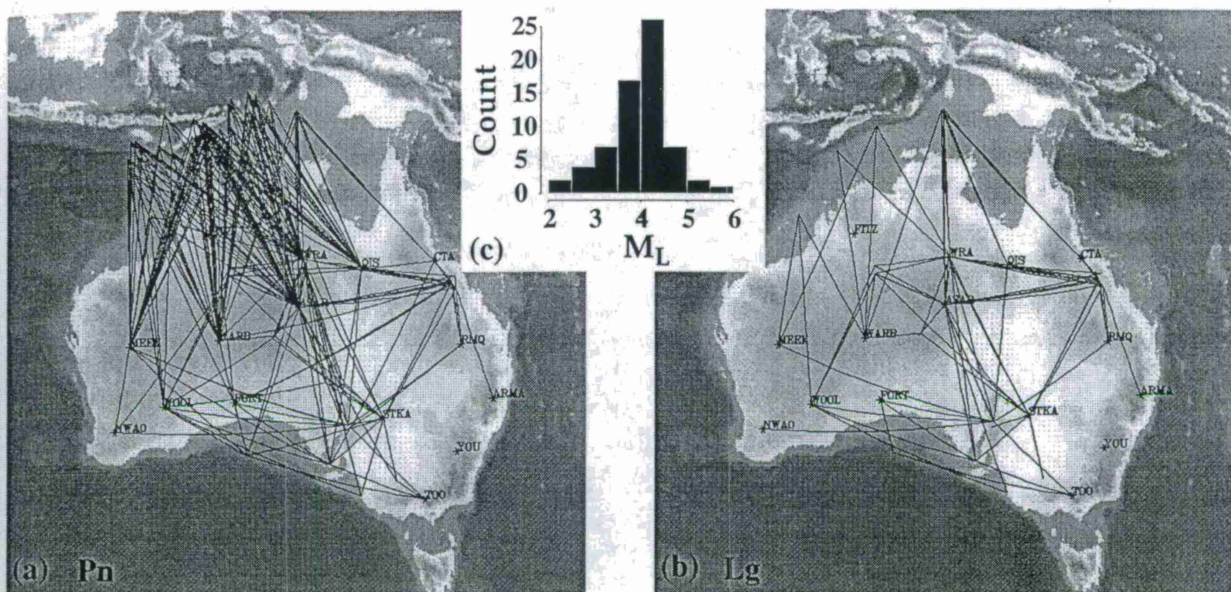


Figure 1. Ray-path maps of regional arrivals used in this study. (a) 288 Pn arrivals, (b) 83 Lg arrivals. (c) Local magnitude, M_L , distribution.

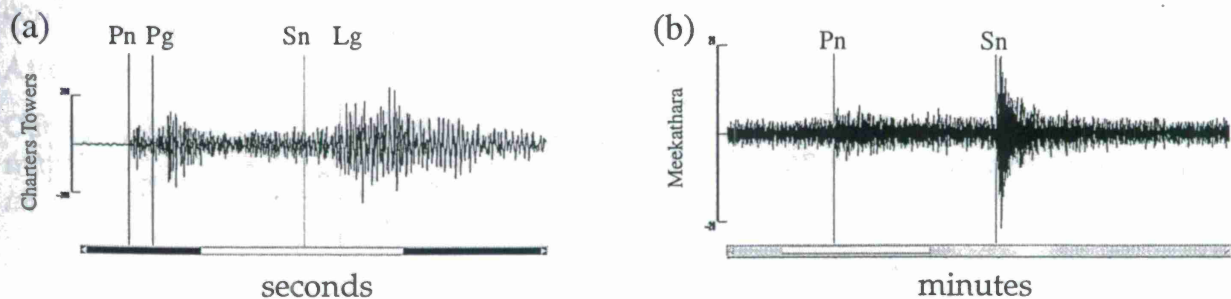


Figure 2. Vertical component waveforms showing regional arrivals from two typical events used in this study. Both waveforms were bandpass filtered, 1-9 Hz. (a) Charter Towers recorded this presumed mining event in northeastern Australia. The event has $M_L=3.5$ and is approximately 3 degrees away. (b) An event near the Java Trench with $M_L=3.8$ recorded by the Meekathara station approximately 18 degrees away.

Amplitude Measures

We measured seven different amplitude types for each regional phase. This will allow us to evaluate which amplitude type produces the lowest variance when estimating attenuation and source parameters. The types of time-domain measurements include root mean-square (*rms*), short-term average (*stav*), and the average absolute amplitude in the time window after removing the *rms* (*abs*). These are made on both coherent (i.e., stack then filter) and incoherent (i.e., filter, rectify then stack) beams. In addition, spectral amplitudes were also measured.

We plot the correlation of log *rms* amplitudes made on coherent and incoherent beams in Figure 3 for Pn arrivals. Figure 3a shows log amplitudes at 3 Hz and Figure 3b at 6 Hz. As expected, the two measures are identical for single stations (pluses). However, the measures are different for array stations (circles), especially at higher frequencies. This is due to a lack of signal coherence across the array. Although a coherent beam tends to increase *snr*, using amplitudes from this beam will corrupt our attenuation estimates at higher frequencies. For this reason, we do not recommend the use of amplitudes made from coherent beams.

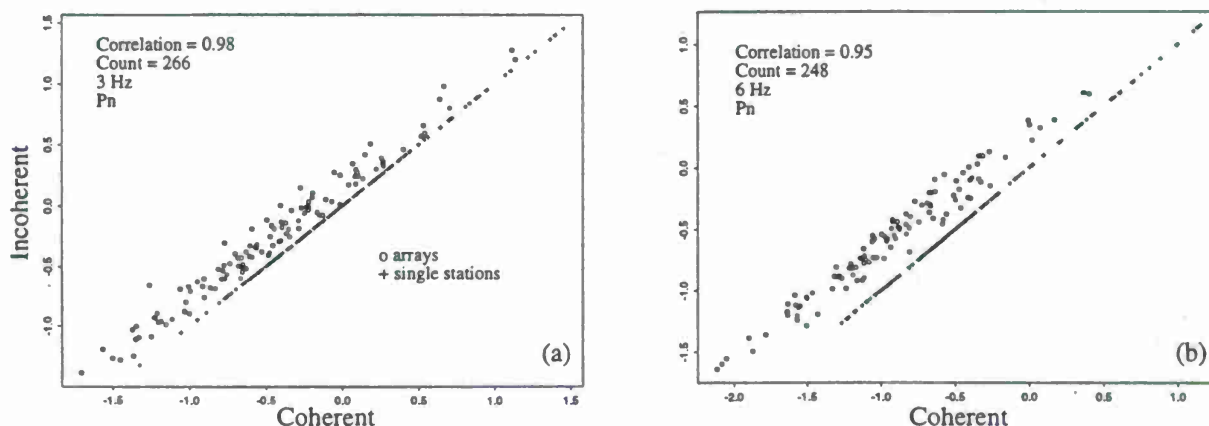


Figure 3. Comparison of log amplitudes measured on both coherent and incoherent beams. A root-mean square amplitude measure was used. (a) Pn at 3 Hz. (b) Pn at 6 Hz. Arrays are denoted by circles and single stations by pluses.

Next, we compare the three different amplitudes for incoherent beams in Figure 4 for Pn arrivals. Figure 4a shows log *rms* amplitudes against log *stav* amplitudes, and Figure 4b shows log *rms* amplitudes against log *abs* amplitudes. Both plots use amplitudes measured in a 4-8 Hz band (i.e., referred to as 6 Hz). As expected, the three amplitude measures on incoherent beams have a high degree of correlation but, *abs* amplitudes appear to have a higher variance. Like coherent beam measurements, *abs* amplitudes produce a separation between arrays and single stations at higher frequencies. In this case, the single station amplitudes are larger than those of the arrays. This is because the incoherent beam from an array averages the amplitudes at individual stations. For this reason, we do not recommend the use of *abs* amplitudes for attenuation studies. Either *rms* or *stav* amplitude measurements could be used since they are nearly the same. The final choice will be based on the variance of the attenuation estimates derived from the inversion.

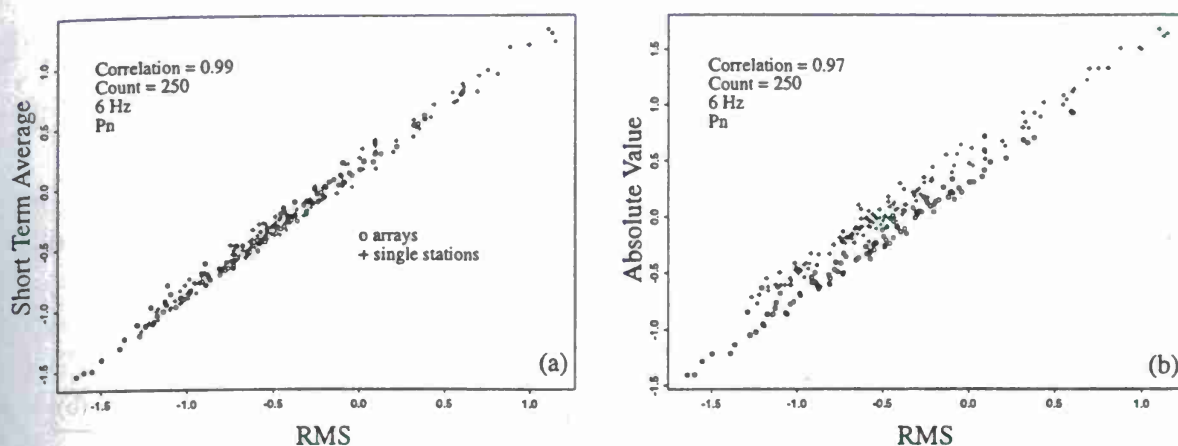


Figure 4. Comparison of three different types of log amplitudes made on 6 Hz Pn arrivals using incoherent beams. (a) root-mean square and short-term average comparison. (b) root-mean square and absolute value comparison. Arrays are denoted by circles and single stations by pluses.

We also computed the spectral amplitude for each signal. We compare log *rms* amplitude and log spectral amplitude in Figure 5 for Pn arrivals. Figure 5a shows log amplitudes at 3 Hz and Figure 5b at 6 Hz. The correlation decreases as frequency increases probably because the time-domain measurements are based on 2-4 Hz and 4-8 Hz filters whereas the spectral amplitudes are measured at 3 Hz and 6 Hz. There is no guarantee that the dominant signal frequency is the center of the passband. Furthermore, leakage outside the intended filter band could reduce the correlation [Lay *et al.*, 1997].

Attenuation

Our parameterization and inversion method are described in detail by Sereno [1990]. Briefly, the frequency-dependent (either time-domain or spectral) amplitude of the k th wave recorded at the i th station from the j th source is parameterized as:

$$\log A_{ijk}(f) = \log A_{jk}^0(f) + B_k(\Delta_{ij}, \Delta_0, f) + \delta_{ik} \quad (1)$$

where $A_{jk}^0(f)$ is the amplitude at a reference distance Δ_0 close to the event, $B_k(\Delta_{ij}, \Delta_0, f)$ is the attenuation from the reference distance to the epicentral distance Δ_{ij} , and δ_{ik} is a station correction. We use either the Mueller and Murphy [1971] or the Brune [1970, 1971] model to parameterize the shape of the source function. Both models feature an f^2 fall off beyond a corner frequency that scales inversely with the cube root of the long-period level.

The attenuation is parameterized in terms of a power-law distance dependence with a frequency-dependent exponent:

$$B_k(\Delta_{ij}, \Delta_0, f) = -\log e \cdot \alpha_k^0 \cdot f + n_k(f) \cdot \log(\Delta_0/\Delta_{jk}) \quad (2)$$

where the first term accounts for anelastic attenuation from the source to the reference distance,

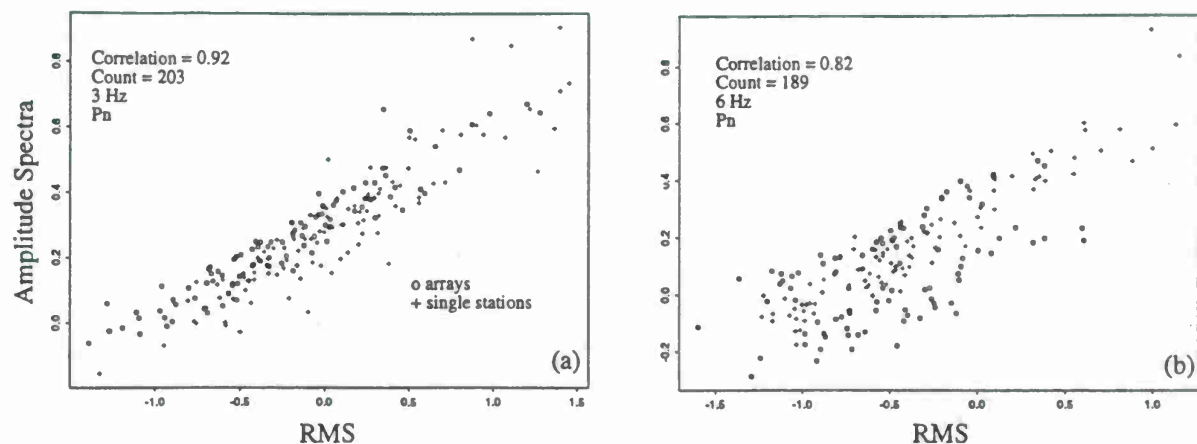


Figure 5. Comparison of root-mean square log amplitudes and log amplitude spectra measurements from Pn arrivals examined in this study. The time domain amplitudes were made on an incoherent beam. (a) Comparison at 3 Hz. (b) Comparison at 6 Hz. Arrays are denoted by circles and single stations by pluses.

and the second term is the total attenuation from the reference distance to the epicentral distance and $n_k(f)$ is parameterized as a linear function of frequency.

The system of equations governing the relationship between the data (log amplitudes) and model parameters is formulated by subtracting theoretical data computed from an assumed starting model from the observed data, and solving iteratively for the model perturbations that minimize the data residuals in the least-squares sense.

We estimated preliminary source and attenuation parameters by applying AmpInv to our Australian data set. We applied a frequency cut-off of 6 Hz for the Lg phase. The standard deviation of the log *rms* amplitudes with respect to our derived models was 0.24-0.26 for all regional phases. The variances are slightly higher (e.g., 0.29) for log *stap* amplitudes. The estimated long-period source level (S_0) is plotted against M_L in Figure 6. The corner frequency scales inversely with the cube root of S_0 . It was determined to be about 20 Hz for an M_L 3.0 event.

We show our estimates of the attenuation, $B(\Delta)$, compared to the log amplitudes in Figures 7 and 8. Figure 7 displays Pn and Pg attenuation, and Figure 8 displays Sn and Lg attenuation. Both figures show $B(\Delta)$ at three frequencies; 1.5 Hz, 3.0 Hz, and 6.0 Hz. The estimated rate of attenuation and one standard deviation are also displayed.

The Pn attenuation results are similar to those obtained by *Sereno* [1990] for Fennoscandia. However, Sn appears to attenuate more rapidly in Australia. Unfortunately, there are only a few Pg and Lg amplitudes in our data set with $snr \geq 3$ db available for the inversion. Therefore, we are not very confident of the results. In fact, it is possible that our Lg attenuation estimates at high frequency are corrupted by Sn coda. We will examine this in more detail in the future.

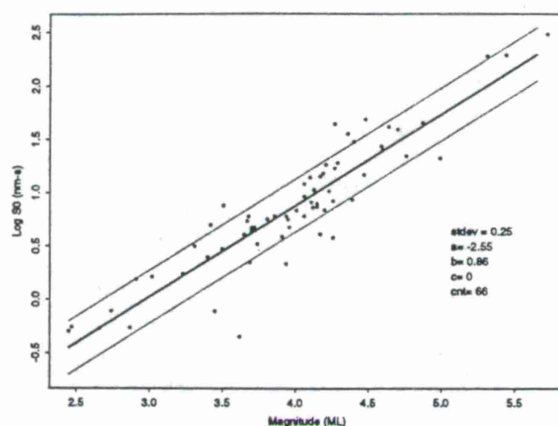


Figure 6. Long-period source level, S_0 , compared to the local magnitude, M_L .

CONCLUSIONS AND RECOMMENDATIONS

We recommend either *rms* or *stap* time-domain amplitude measurements made on incoherent beams for IMS stations. We have not yet evaluated the spectral amplitudes. We will increase the amount of Pg and Lg data for the Australia data set to get stable attenuation estimates at high frequencies for crustal phases. We will also estimate source and attenuation parameters using amplitude spectra and compare the results with those obtained using *rms* time-domain amplitudes measured on incoherent beams. Finally, we will use AmpInv to estimate the attenuation for the other nine IMS subnetworks.

The attenuation estimates will be used to correct regional S/P amplitude ratios as a function of frequency for distance. The ability of the distance-corrected regional S/P amplitude ratio to discriminate between explosions and earthquakes, and its transportability to other source regions, will be evaluated.

REFERENCES

- Baumgardt, D., and G. Young, Regional seismic waveform discriminants and case-based event identification using regional arrays, *Bull. Seismol. Soc. Am.*, 80, 1874-1892, 1990.
- Baumgardt, D., J. Carney, M. Maxson and S. Carter, Evaluation of regional seismic discriminants using the Intelligent Seismic Event Identification System, *Tech. Rep. SAS-TR-93-38*, ENSCO, Inc., Springfield, Virginia, 96 pp., 1992.
- Bennett, J., B. Barker, K. McLaughlin, and J. Murphy, Regional discrimination of quarry blasts, earthquakes, and underground nuclear explosions, *Final Rep. GL-TR-89-0114*, 146 pp., 1989.
- Brune, J., Tectonic stress and the spectra of seismic shear waves from earthquakes, *J. Geophys. Res.*, 75, 4997-5009, 1970.
- Brune, J., Correction to tectonic stress and the spectra of seismic shear waves from earthquakes, *J. Geophys. Res.*, 76, 5002, 1971.

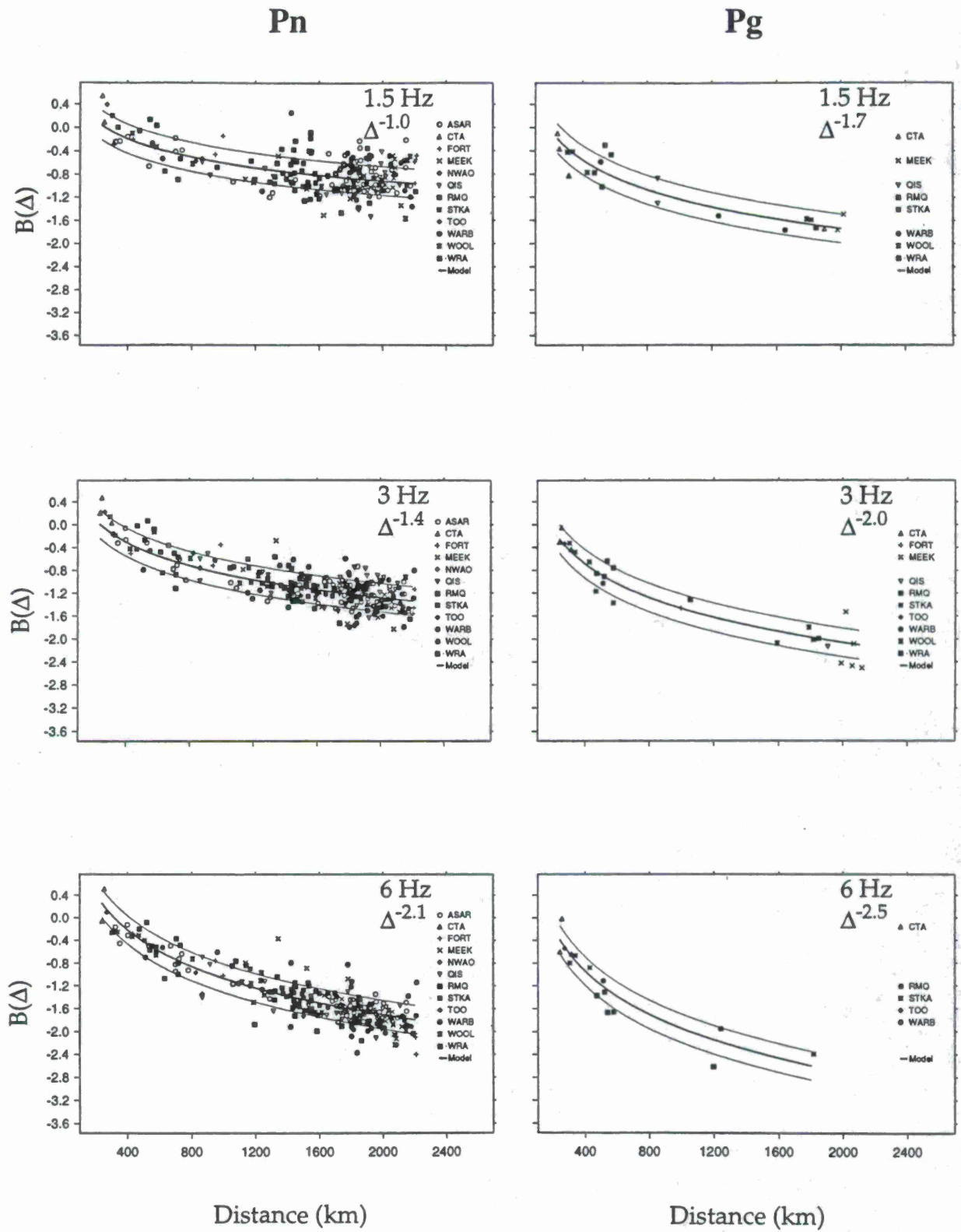


Figure 7. Attenuation of Pn and Pg arrivals at 1.5, 3, 6 Hz.

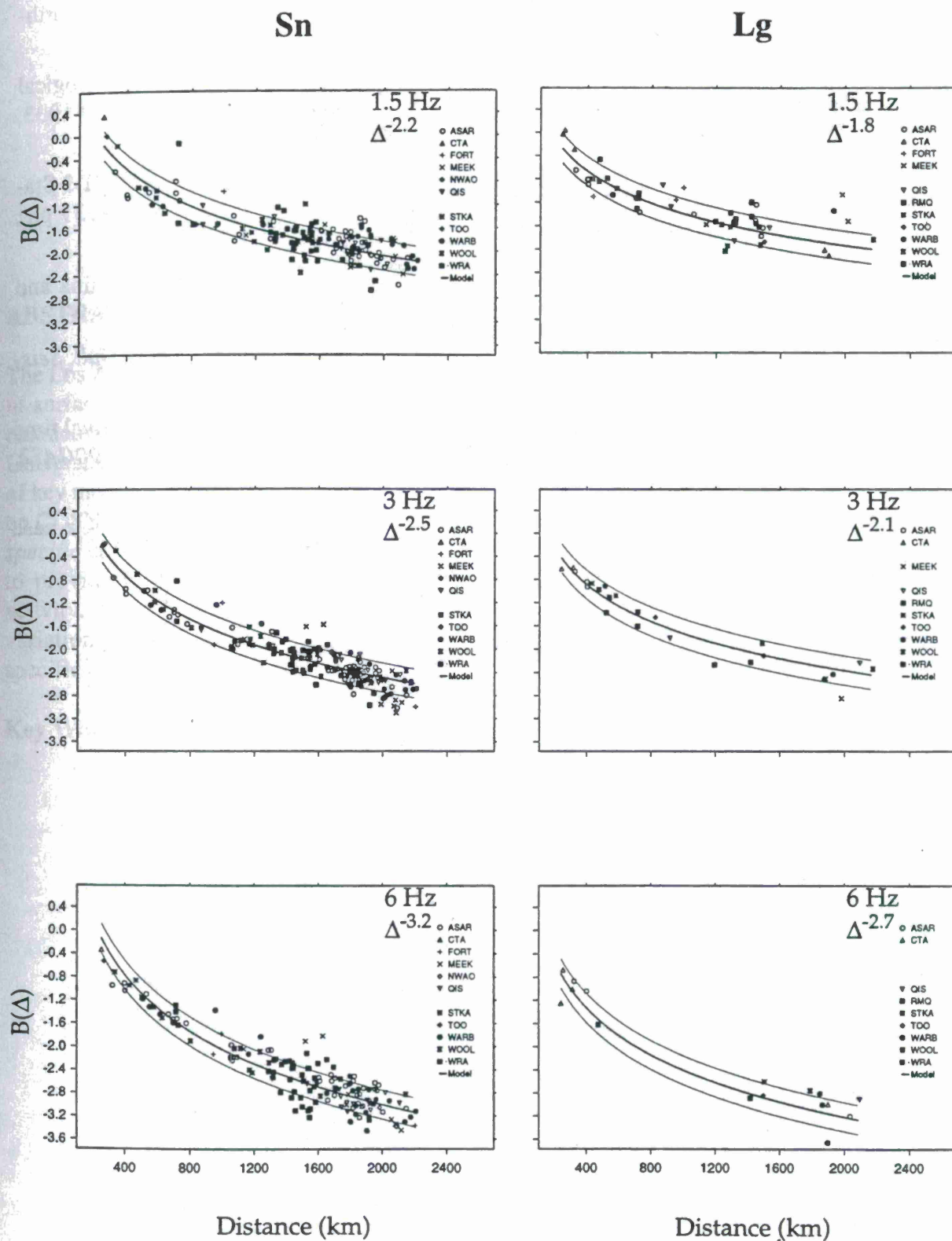


Figure 8. Attenuation of Sn and Lg arrivals at 1.5, 3, 6 Hz

- Chan, W., R. Baumstark, and R. Cessaro, Spectral discrimination between explosions and earthquakes in central Eurasia, *Tech. Rep. GL-TR-90-0217*, 38 pp., 1990.
- Dysart, P., and J. Pulli, Regional seismic event classification at the NORESS array: seismological measurements and the use of trained neural networks, *Bull. Seismol. Soc. Am.*, 80, 1910-1933, 1990.
- Jenkins, R.D., A. Velasco, D.J. Williams, and T.J. Sereno, Regional Attenuation at GSETT-3 Stations and the Transportability of the Lg/P Discriminant, *Tech. Rep. PL-TR-96-2159*, 31 pp., 1996.
- Lay, T., G. Fan, and A. Rodgers, Crustal Waveguide Effects on Regional Phases in China and Southeast Asia, *Tech. Rep. PL-TR-97-2028*, 161 pp., 1997.
- Mueller, R. and J. Murphy, Seismic characteristics of underground nuclear detonations, *Bull. Seismol. Soc. Am.*, 61, 1675-1692, 1971.
- Sereno, T.J., Attenuation of regional seismic phases in Fennoscandia and estimates of arrival time and azimuth uncertainty using data recorded by regional arrays, *Tech. Rep. SAIC-90/1472*, Science Applications International Corporation, 115 pp., 1990.
- Wuster, J., Discrimination of chemical explosions and earthquakes in central Europe - a case study, *Bull. Seismol. Soc. Am.*, 83, 1184-1212, 1993.

HIGH RESOLUTION SURFACE-WAVE DISPERSION STUDIES IN CHINA

Laura E. Jones and Howard J. Patton

Los Alamos National Laboratory, Geophysics EES-3, MS-C335, Los Alamos, New Mexico

Sponsored by U.S. Department of Energy
Office of Nonproliferation and National Security
Office of Research and Development
Contract No. W-7405-ENG-36

ABSTRACT

The Los Alamos National Laboratory regional calibration project is actively assembling a database of surface-wave dispersion information for China and surrounding areas. As part of the effort to characterize surface wave dispersion in China, we integrate prior long period results from the University of Colorado with our shorter period dispersion measurements in a high resolution survey of key monitoring areas. Focusing on western China initially, we employ broadband data recorded on CDSN stations, and regional events (M_s 4 and above). Our approach is twofold, employing *path specific calibration* of key stations and well-recorded reference events, and *tomographic inference* to provide group velocity curves for regions with sparse station distribution and little seismic activity. Initial dispersion studies at Chinese stations WMQ and LZH show substantial azimuthal variation in dispersion, reinforcing the need for careful determination of source regions for path-specific calibration.

Key Words: regional seismic characterization, path effects, China, surface waves, tomography

Objective of Study

We build on prior work done at the University of Colorado, Boulder (JSPC) by Ritzwoller and Levshin [1997] and Ritzwoller *et al.* [1997]. The present study seeks to integrate longer period results from teleseismic data with results from broadband records recorded at regional distances at stations in China and Eurasia. This smaller scale, higher resolution study focuses on western China initially, employing shorter paths, higher frequency data, and events from China and surrounding regions. Our initial objectives are twofold and include:

1. Path specific calibration: We estimate surface-wave dispersion for key stations and source regions, using well-known (CMT) and well-recorded reference events.

Such calibration will result in filters designed to extract surface waves in an automated fashion for use in surface wave detection, M_s estimation, discriminants and further structural or attenuation studies.

2. Tomographic inference: We combine our measurements with long period measurements from the University of Colorado for surface-wave tomography.

We'll use the tomographic results to infer group velocity curves for regions with sparse events and/or station coverage. We then test how effectively the inferred dispersion curves extract surface waves for the purposes outlined above in item 1.

Research Accomplished

Introduction. Regional surface waves carry valuable information for use in the detection, location, and identification of small seismic sources. In principal, techniques for locating and identifying sources developed for teleseismic surface-wave applications might easily be extended to regional problems. One example of high interest is the regional extension of $M_s:m_b$, one of the most powerful teleseismic discriminants. However, major challenges confront the effective implementation of long-period to short-period discriminants as source size decreases: observations must be made at progressively shorter ranges and degrading signal-to-noise conditions for the long period energy.

With these issues in mind, detection of surface waves is presently an important research topic in CTBT monitoring. Emphasis on small magnitudes and regional observations motivates investigation on the effective extraction of Rayleigh- and Love-wave signals from complex regional waveforms, where phases have not significantly dispersed, where there is potentially significant overlap (in frequency and time) between higher-mode surface-waves and lower frequency body-wave arrivals, and where there may be high levels of ambient background noise.

Regional calibration of key monitoring areas provides information necessary to assess capabilities at small magnitudes and to determine propagation characteristics for signal extraction.

We employ two strategies for building a knowledge base of information for use in extracting fundamental-mode energy from regional waveforms. Both strategies are based on empiricism and both involve designing a match filter with some knowledge of the true surface-wave dispersion on a source-receiver path of interest.

The *path specific* approach uses historic events and waveforms to develop dispersion curves from specific source regions. The second strategy, a *tomographic inference* approach, uses historic data from inside and outside the monitoring region to measure dispersion on many criss-crossing paths, and subsequently images the spatial variations of surface-wave velocities for the key areas.

To some extent these approaches are complementary. While the former will supply highly accurate information for active source regions, the latter will provide adequate information for surface-wave extraction when an unknown source occurs in a new source region. We expand on these issues and our approach below.

Data Collection. We have assembled and continue to process broadband waveform data from IRIS and CDSN stations within and around China. Of special interest to us are the short-path (3° to 15°) surface wave data compiled for western China. Further details and a table summarizing the data are found in this volume (Phillips *et al.*, 1997).

Software. We have ported the Ritzwoller and Levshin *Frequency-time analysis* (FTAN) code to our machines, to further ensure the compatibility and smooth integration of our short-path broadband results with existing longer path results from University of Colorado. In addition, this code has the attractive feature that it allows easy selection of the appropriate surface wave mode branch for analysis, helping to separate out fundamental modes on our shorter paths. This processing scheme also allows simultaneous determination of spectral amplitudes and phase and group dispersion.

Preliminary Regionalization Results. Preliminary results are presented in this paper for paths involving two stations of the Chinese Digital Seismic network (CDSN), WMQ and LZH, and events shown as circles or diamonds for earthquakes, and a star for East Kazakh explosions [Figure 1].

One pressing issue in our study concerns the detection of surface waves as a function of magnitude and distance. In areas of the western United States, regional surface waves with periods between 8 - 50 sec are recorded well enough to be used in moment tensor inversions of earthquakes as small as m_b 3.5 (Patton and Zandt, 1991; Romanowicz *et al.*, 1993). Despite the relative complexity of structures in western China, surface waves appear to be cleanly recorded on some far-regional paths to small magnitudes. To illustrate this, we show a Rayleigh-wave record section using the events plotted as diamonds on Figure 1 [Figure 2, right-hand panel]. Broadband records have been filtered to enhance the surface waves. These results show that events with m_b in the mid-4 range are well recorded across the Tibetan Plateau out to at least 1500 km. The record section also shows the evolution of wave-trains with distance, illustrating compact waveforms at short distances and better-separated, more easily identifiable fundamental-mode surface waves at far distances.

Definition of distinct source regions for the *path specific* approach is a major consideration in our work. This is driven by the scale of heterogeneity the extent to which dispersion curves vary laterally. We illustrate this on the left-hand side of Figure 2 with waveform data from LZH. Again, broadband data have been filtered to show the surface-wave arrivals for five events in source region A, a compact source site about 25 km across. At a distance of about 800 m, we find that surface waves are well-recorded for the m_b range 4.1 - 6.2. All waveforms display very similar "inverse" dispersion characteristics for the 15 - 40 sec period

range visible after filtering. Waveforms are presented for two other source regions at about the same range as A, but different backazimuths. The dispersion characteristics for these events may be different enough to define two more source regions distinct from region A. Tests need to be devised to evaluate criteria for source region definition.

Similarly, preliminary dispersion results for station WMQ underscore the need for path-specific calibration, and also for limiting the size of a specific source area in path calibration. We have collected and processed three-component broadband data for 26 CMT events recorded at station WMQ. Group velocities for Love and Rayleigh waves were measured at periods of 10 to 50 seconds. Resulting dispersion curves for paths around WMQ are generally consistent with a modified Eastern Tien Shan earth model (Figure 3ab, bold curve) but nonetheless show significant azimuthal variation. Curves for paths through the Jungarrian basin (fine dashed line; Figure 1, Figure 3) show the effects of slow basin structure at higher frequencies. Note that prior long-period studies do not resolve the Jungarrian basin, but our higher resolution work clearly will.

Recommendations for Future Work

Along with the ongoing measurement of dispersion curves for specific source sites and stations, we'll devise tests to determine the lateral extent of such source regions to increase the reliability and robustness of our *path specific* approach. Dispersion curves inferred from our tomographic maps will be tested for their effectiveness in signal extraction, and the maps may be modified accordingly. We plan analysis of spectral amplitudes and the eventual construction of an attenuation map for western China and later, Asia. Finally, the accumulated broadband data allows the possible use of body waves and higher modes for source parameter studies, including accurate determination of depth.

References

- Patton, H. J., and G. Zandt, Seismic Moment Tensors of Western U. S. Earthquakes and Implications for the Tectonic Stress Field, *J. Geophys. Res.*, Vol. 86, B11, 18245-18259, 1991.
- Phillips, W. S., G. E. Randall, H. E. Hartse, S. R. Taylor and H. J. Patton, Source and Path Effects on Regional Phases in China, *19th Ann. Seismic Research Symp. on Monitoring a Comprehensive Test Ban Treaty*, (this volume), 1997.
- Ritzwoller, M. H., and A. L. Levshin, Eurasian Surface Wave Tomography: Group Velocities, *J. Geophys. Res.*, submitted, March 1997.
- Ritzwoller, M. H., A. L. Levshin, L. I. Ratnikova, and A. A. Egorkin, Intermediate Period Group Velocity Maps Across Central Asia, Western China, and Parts of the Middle East, *J. Geophys. Res.*, submitted, May 1997.
- Romanowicz, B., D. Dreger, M. Pasyanos and R. Uhrhammer, Monitoring of Strain Release in Central and Northern California Using Broadband Data, *Geophys. Res. Lett.*, Vol. 20, No. 15, 1643-1646, 1993.

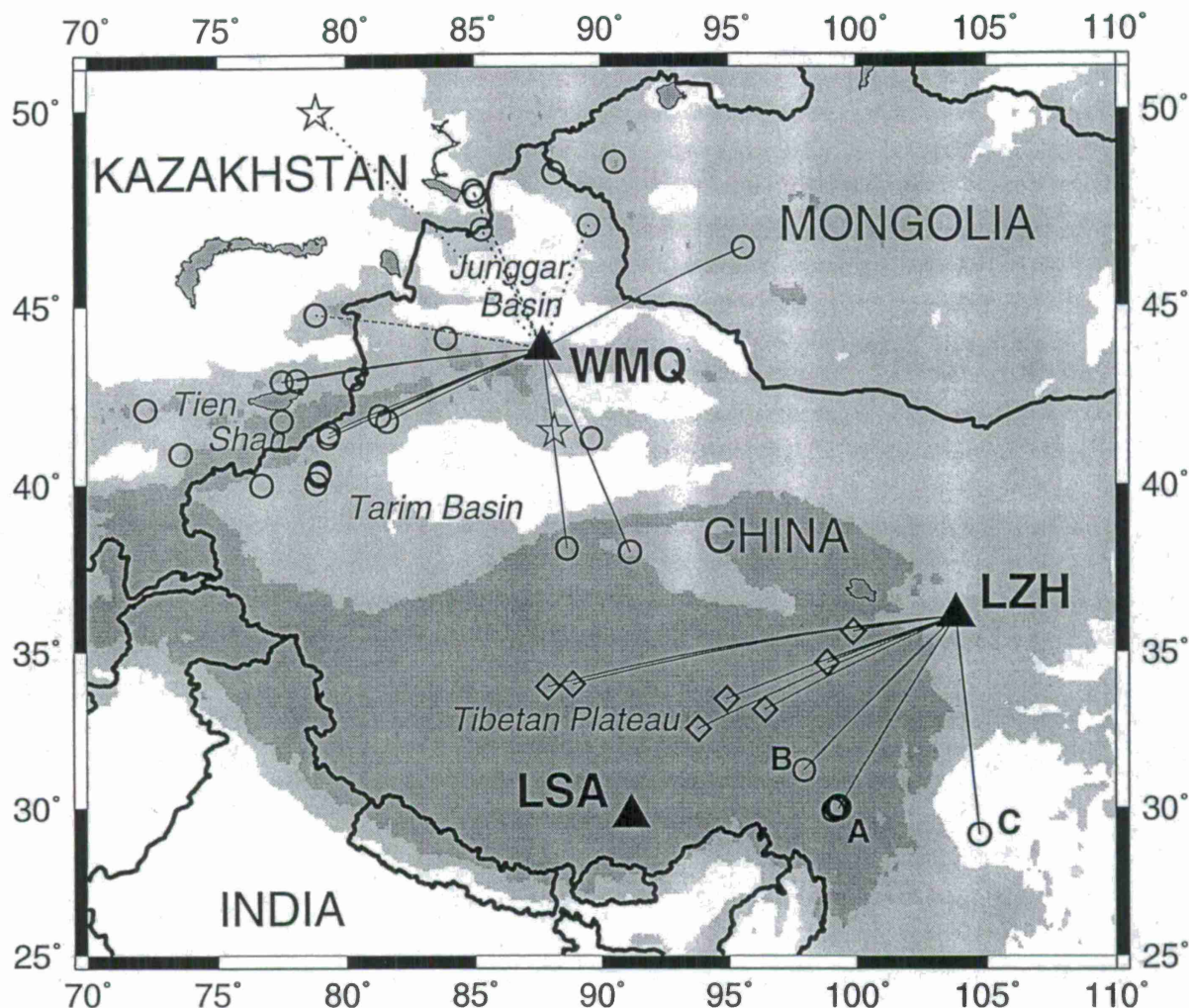


Figure 1. Map of study area showing locations of stations, events, and paths discussed in this paper. Elevations are shown as shades of grey in three intervals: -100 to 1000 m above sea level, no shading; 1000 to 3000 m, light grey; and above 3000 m, darker grey. Large bodies of water are shown by the darkest grey areas. Source regions A, B, and C, discussed in the text, are identified on the map. Earthquakes used in making the Rayleigh-wave profile in Fig. 2 are plotted as diamonds. Other earthquakes are plotted as open circles, and the East Kazakh and Lop Nor test sites as open stars. Great circle paths are shown as lines. Dotted lines are those paths through the Junggarian Basin with slow group velocities at short periods in Fig. 3ab.

Rayleigh waves, LZH

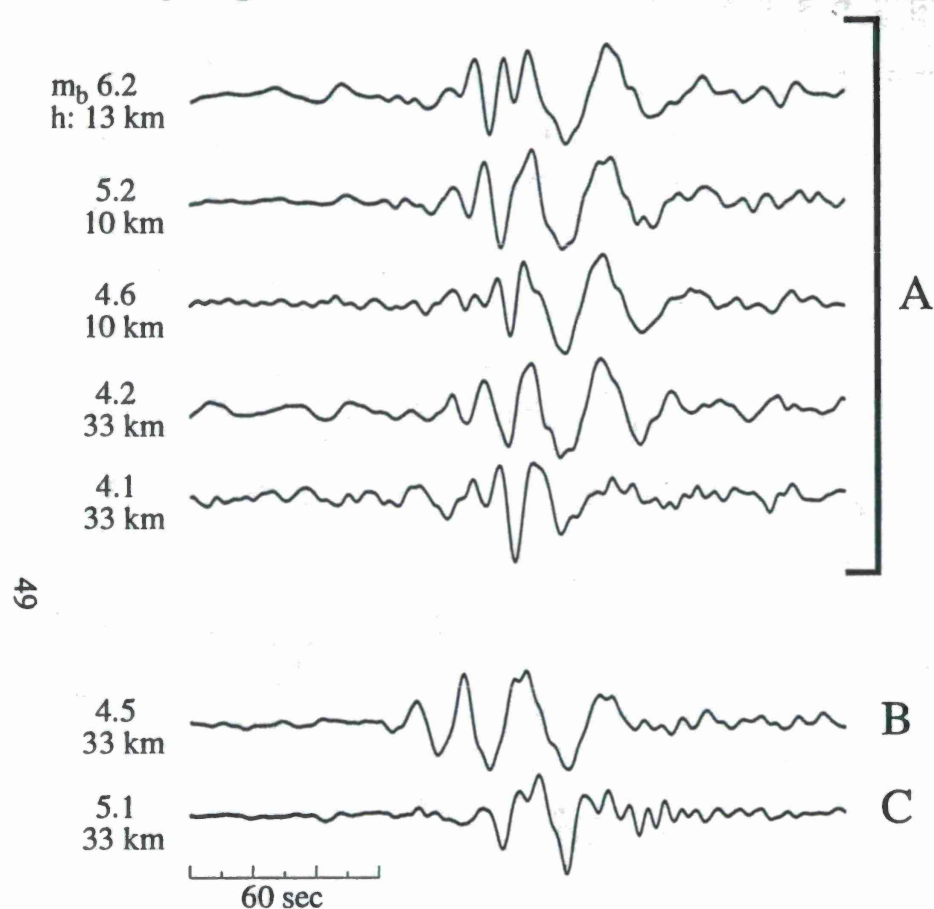
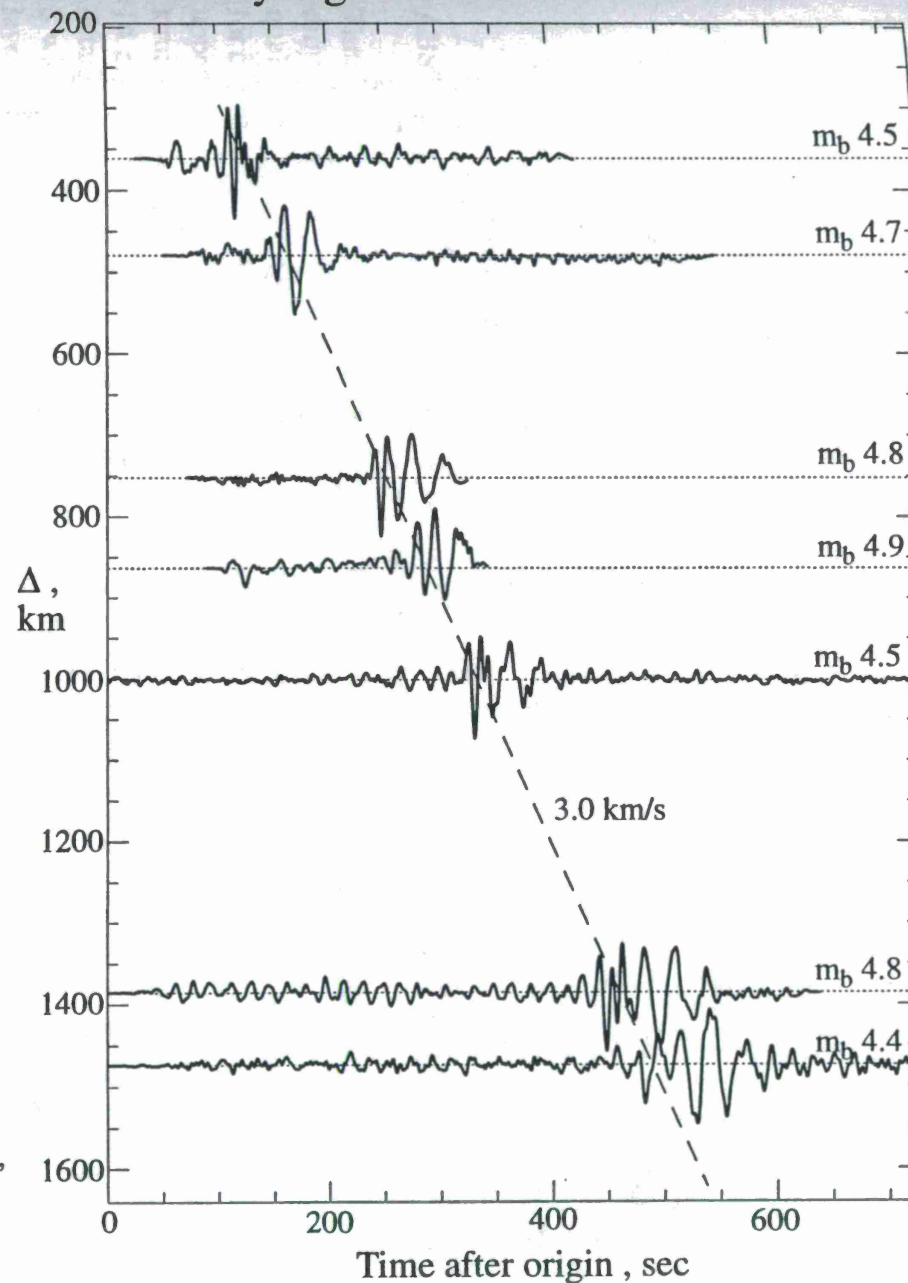


Figure 2. Vertical component recordings at station LZH low-pass filtered at 0.03 Hz. The traces on the left have been phase equalized by simply time aligning on the largest downswing. Three source regions are shown: **A** at an average distance of 803 km and back-azimuth of 214° ; **B** 767 km, 227° ; and **C** 779 km, 174° . On the right, a record section is plotted for earthquakes located on the Tibetan Plateau for backazimuths between 246° and 265° . See the map in Figure 1 for reference.

Rayleigh-wave Record Section



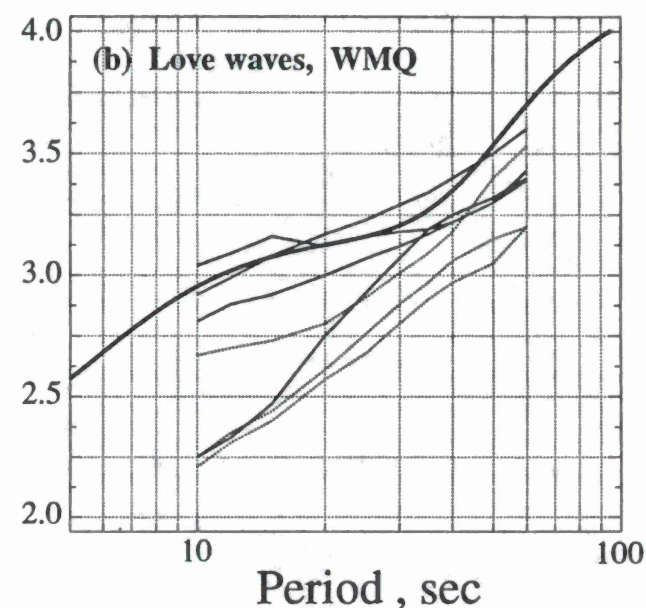
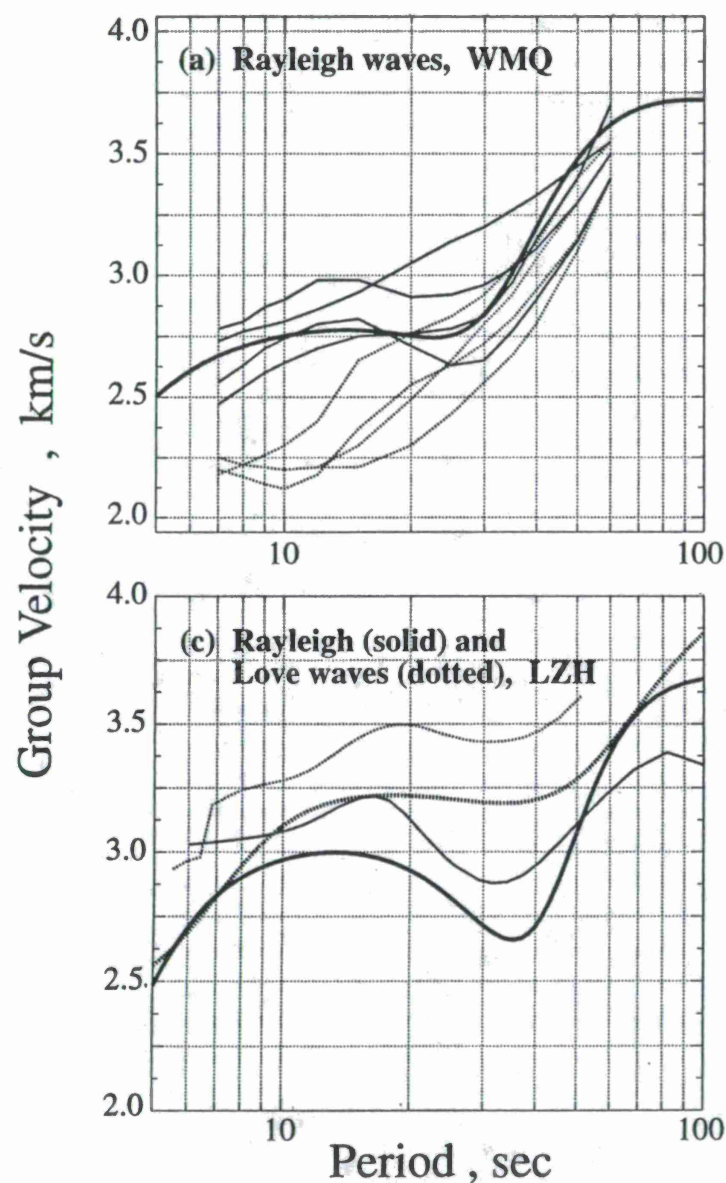


Figure 3. Group velocity dispersion curves for selected paths in western China. (a) Rayleigh-wave dispersion curves are broken down into two groups: paths that pass through the Junggarian Basin (dotted) and those paths that sample mainly crystalline basement paths (solid). See Figure 1. (b) Same as (b) but for Love waves. In both (a) and (b), a model group velocity curve is shown, which is based on a modified crustal structure from Kosarev et al., (1993; JGR, 98, p.4437) with a PREM upper mantle. (c) Thin lines are observed dispersion curves between source region A and LZH on the Tibetan Plateau. For comparison, we show model dispersion curves predicted by crustal model 45 of Romanowicz (1982; JGR, 87, p.6865) with a PREM upper mantle. Model dispersion curves generally agree in shape with the observed, but some significant differences exist probably due to lateral heterogeneity.

3-D STRUCTURE FROM SEISMIC TOMOGRAPHY - IMPLICATIONS FOR EVENT LOCATION

B.L.N. Kennett

Research School of Earth Sciences, The Australian National University,
Canberra, ACT 0200, Australia

Grants from Air Force Office of Scientific Research
AFOSR F49620-94-1-0022
AFOSR F49620-94-1-0110

ABSTRACT

Time corrections for seismic travel tables are an effective way of summarizing information on three dimensional structure in the Earth in the context of event location. In many parts of the earth the quality of information on 3-D structure available from seismic tomography provides a good basis for calculating corrections for far-regional and teleseismic waves based on the transit time through upper-mantle structure. In regions with high densities of sources and/or stations resolution of P wave structure to $1^\circ \times 1^\circ$ horizontally and about 50 km vertically is possible, and this is now available for 14 zones across the globe; the consistency between overlapping zones is very encouraging. The detailed results are complemented by medium resolution studies for the whole mantle for both P and S waves with now a $2^\circ \times 2^\circ$ set of cells and 18 layers extending through the mantle (100 km thick layers near surface). The lower resolution information extends geographic coverage from the main seismicity zones into continental regions such as Northern Asia, the Arctic and parts of Africa. However, the distribution of stations means that many parts of the world are not well sampled. An alternative approach in which 1-D models are developed down to 660 km between nine different classes of surface tectonic features provides information on structures beneath oceanic areas and a predictive power for an initial approximation to mantle structure even where no other information is available such as most of Antarctica.

Keywords: Event Location, Time Corrections, Seismic Tomography

OBJECTIVE:

The verification of the Comprehensive Test Ban Treaty requires the accurate location of seismic events wherever they may occur on the globe. The current class of basic tools for event location are based on the use of one-dimensional reference models (e.g. model *ak135*, Kennett, Engdahl & Buland 1995) with the inclusion of corrections to compensate for regional variations in structure.

Seismic tomography has now progressed to the point where, for much of the upper mantle, it is possible to extract resolution of upper mantle structure on $2^\circ \times 2^\circ$ scales and in some parts down to $1^\circ \times 1^\circ$. However, there are still significant areas e.g. much of the oceans where such tomographic results are not available. This work links the detailed tomography with an alternative approach using a tectonic regionalisation to predict structure in otherwise unsampled zones.

RESEARCH ACCOMPLISHED:

The global datasets for the arrival times of seismic phases provide a rich source of information on both the location of seismic sources and the structure within the Earth. The major component of the variation of seismic structure can be captured in a one-dimensional model, and we employ the *ak135* model of Kennett, Engdahl & Buland (1995) which has been constructed to match empirical travel-times for a broad range of seismic phases.

The arrival times for both P and S waves used in regional and global tomography, and the event hypocentres have been taken from the global data set assembled by Engdahl, van der Hilst & Buland (1997). The entire data catalogue of the International Seismological Centre, supplemented by more recent observations, has been relocated using a nonlinear scheme with the inclusion of the depth phases pP, pwP and the *ak135* model as a reference. At each stage, the reported arrival times are re-associated with seismic phases using the improved locations to provide a set of travel times whose variance is significantly reduced compared with the original data catalogues. Over 35,000 events have been used, recorded at one or more of over 3000 seismological stations around the globe to give a set of over 7 million P phase times and about 1.5 million S and SKS times.

This global dataset is sufficient to allow relatively detailed seismic tomography of regions with a high density of sources and/or stations. For the region of interest a high resolution grid ($1^\circ \times 1^\circ$ horizontally, 50-75 km in depth) can be employed, and to avoid mapping structure from the rest of the Earth into the region the inversion includes $5^\circ \times 5^\circ$ parameterisation of the whole of the rest of the mantle. As demonstrated by Widiyantoro & van der Hilst (1996) for Indonesia, this approach can provide good resolution of the details of subduction zones but also gives an effective coverage of the three-dimensional structure of the entire region. Data quality is somewhat higher for P waves, but it is still possible to obtain useful results using S in many areas.

By moving the region of interest and performing separate inversions it is possible to provide detailed cover of the main seismicity zones on the Earth. Figure 1, taken from Widiyantoro (1997) displays the composite results achieved with 14 such inversions. Where regions overlap care has been taken to use the results with the highest reliability but no smoothing has been applied. As can be seen the results of the different inversions fit together very well and this information on 3D structure can provide an excellent basis for constructing correction schemes for far-regional and teleseismic arrivals. The information available on the crust and uppermost mantle in such models is derived mainly from steep paths and as such is not necessarily a good predictor of the properties of regional phases where the propagation paths are much nearer horizontal.

Layer: 4
112. 162. km

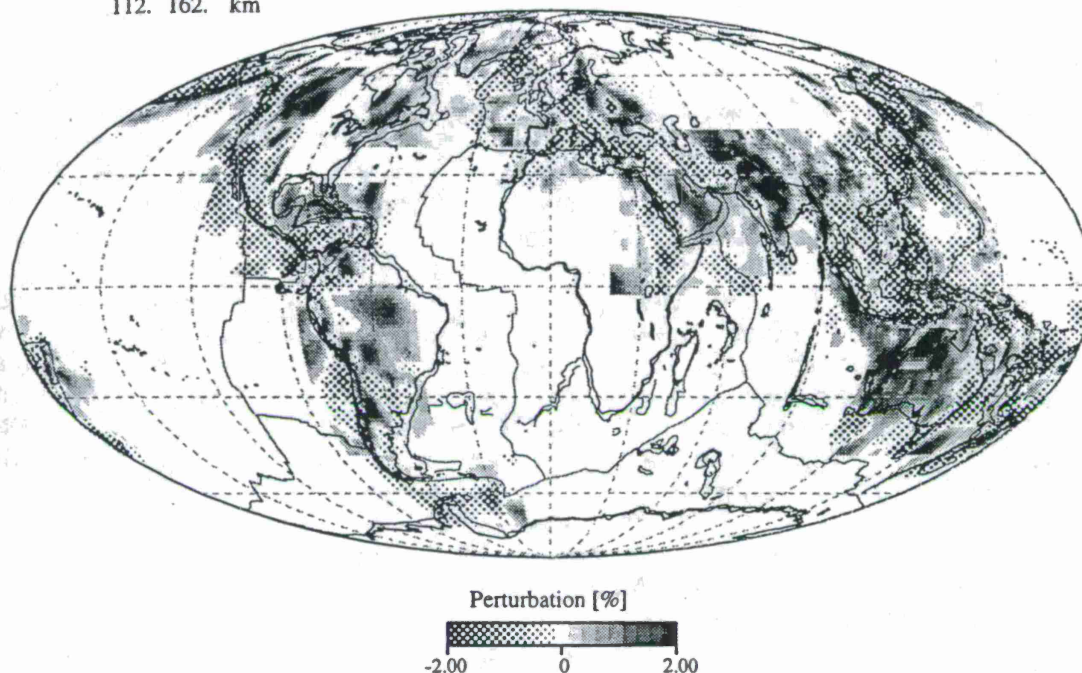


Fig 1: Variations of P wavespeed from the *ak135* reference model in a layer from 112-162 km depth, derived from the combination of 14 separate high resolution ($1^\circ \times 1^\circ$) studies (Widiyantoro 1997).

Layer: 2
100. 200. km

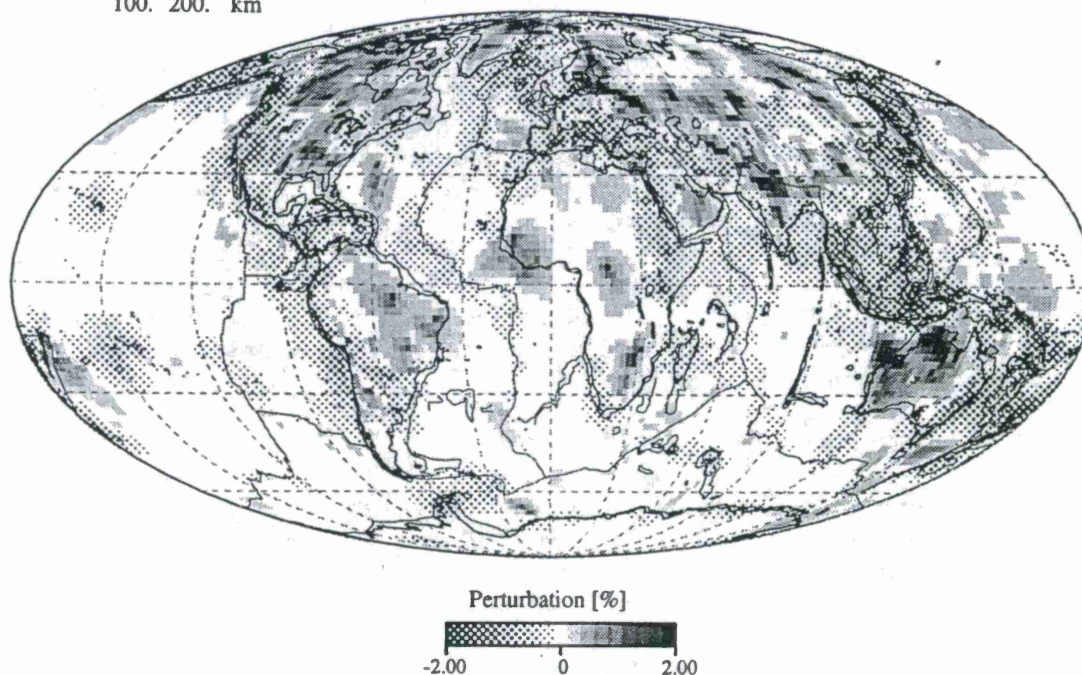


Fig 2: Variations of P wavespeed from the *ak135* reference model in a layer from 100-200 km depth from a medium resolution model ($2^\circ \times 2^\circ$) for the whole mantle (van der Hilst, Widiyantoro & Engdahl, 1997).

Although the high resolution tomography in Figure 1 confers a significant fraction of the Earth's surface, important regions are not covered. The gap in the eastern USA could be covered using available stations, but there would not be any justification for extending the fine grid to the rest of Africa.

If we are prepared to accept somewhat lower resolution, we can make use of seismic tomography for the entire mantle in which results are stabilised by using summary rays combining information between nearby groups of sources and receivers. In this way it is possible to achieve $2^\circ \times 2^\circ$ resolution with 18 layers in depth and to determine 3-D structure for a broader zone in the upper mantle than in the high resolution work. Figure 2 displays the variation in P wavespeed in the second layer of the model developed by van der Hilst, Widiyantoro & Engdahl (1997). There is a good general concordance with the high resolution results in Figure 1, though the amplitude variation is a little lower. The model now extends to northern Asia and the Arctic as well extending cover in South America. Resolution of structure in Africa is difficult because of the limited number of permanent stations. This is also true for the interior of Australia but we have augmented the international datasets with readings from the ANU SKIPPY project in which 65 sites across the continent have been occupied using portable broad-band equipment in the period 1993-1996.

A comparable picture to Figure 2 can also be created for S waves with a similar geographic coverage. Such medium resolution 3-D models can provide the starting point for station specific correction schemes.

Even with the best available global data coverage there is limited information on the structure in many areas e.g. Antarctica, parts of Africa and the oceans. As a supplement to conventional tomographic methods, an alternative procedure has been devised which exploits a tectonic regionalisation of the surface (Gudmundsson & Sambridge, 1997). The geometries of the major subduction zones have been delineated by their seismicity patterns, and the travel-times of observed phases are partitioned into their contributions from the slabs and eight other tectonic zones based on the age of continents and oceans. The zones are taken to extend from the surface to 660 km depth and one-dimensional models for each zone are extracted using a representation in terms of irregular cells. The velocity pattern at a depth of 100 km using this RUM (regionalised upper mantle) model is displayed in Figure 3. The perturbation scale is shifted by 1% compared to Figure 1 and 2, to allow for the component absorbed in slab structure. The RUM model explains about 15% of the variance in the data used in its construction which is about one-third of what can be achieved in full tomography. However, RUM has a predictive capacity in regions unsampled in any other way. The 1-D velocity models for the different regions are displayed for both P and S waves in figure 4 as deviations from the *ak135* reference model together with their uncertainties. A particular benefit of RUM is that it provides some resolution of structure beneath oceanic zones which is difficult to achieve by other methods.

CONCLUSIONS AND RECOMMENDATIONS:

Tomographic models provide a good basis for constructing corrections for travel-times for teleseismic and far-regional arrivals and can provide a useful check on empirical determinations. The scale of variation in 3-D structure is quite rapid (200-400 km) so that relatively specific corrections are likely to be needed for accurate event locations to be produced.

In zones where tomographic studies are not available, the use of tectonic regionalisations can provide a useful starting point for refining corrections, and extend information to depths not covered in other treatments such as that by Nataf & Ricard (1995).

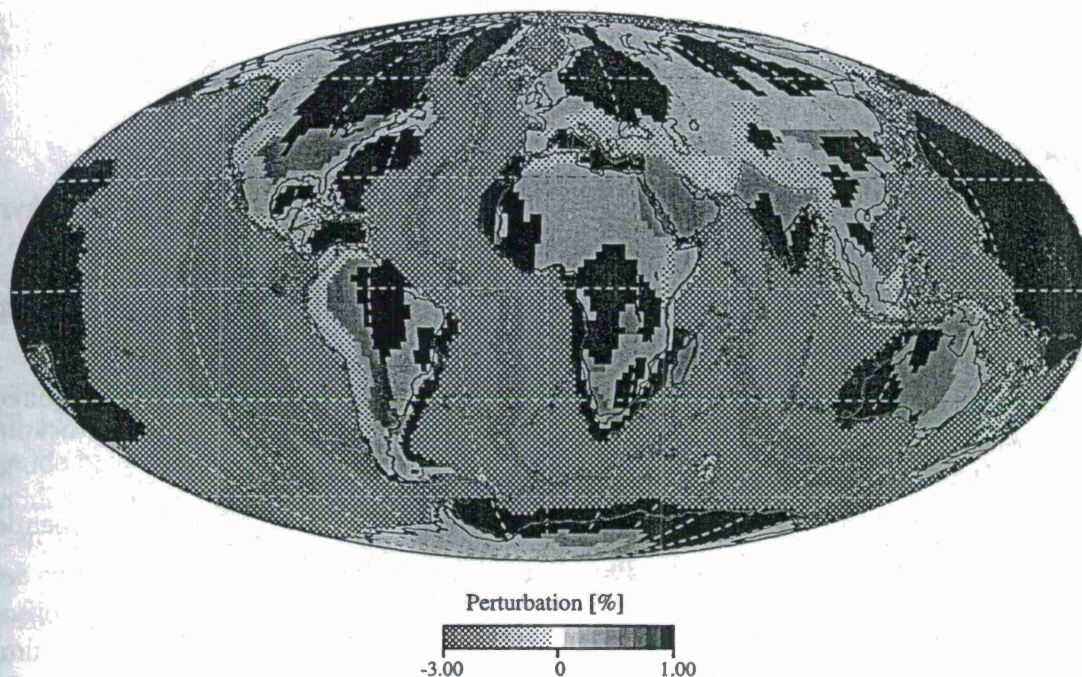


Fig 3: Velocity perturbations from *ak135* model for the layer from 66-122 km in the RUM model (Gudmundsson & Sambridge 1997) based on tectonic regionalisation.

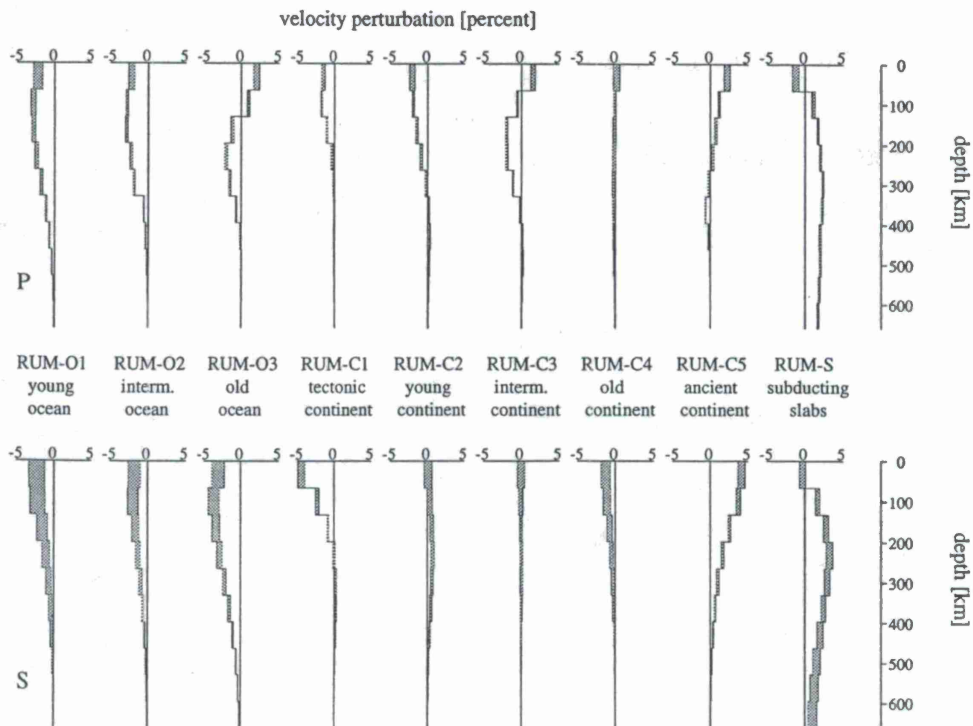


Fig 4: 1-D velocity profiles for nine surface tectonic regions for both P and S waves from the RUM model

Acknowledgement:

The research reported here builds on the work of many members of the RSES group particularly O. Gudmundsson, M. Sambridge and S. Widiyantoro and continuing cooperation with R. van der Hilst (MIT).

References:

- Gudmundsson O. & Sambridge M., 1997. A regionalized upper mantle model, *J. Geophys. Res.* submitted.
- Kennett B.L.N. , Engdahl E.R. & Buland R., 1995. Constraints on seismic velocities in the Earth from traveltimes, *Geophys. J. Int.*, **122**, 108-124.
- Engdahl E.R.; van der Hilst, R.D. & Buland R., 1997. Global teleseismic earthquake relocation with improved travel times and procedures for depth determination, *Bull. Seism. Soc. Am.*, submitted.
- Nataf, H-C & Ricard Y., 1996. 3SMAC: an a priori tomographic model of the upper mantle based on geophysical modelling, *Phys. Earth. Planet. Inter.*, **95**, 101-122.
- Sambridge M. & Gudmundsson O., 1997. Tomography with irregular cells, *J. Geophys. Res.* submitted.
- van der Hilst R.D., Widiyantoro S. & Engdahl E.R., 1997. Evidence for deep mantle circulation from global tomography, *Nature*, **286**, 578-584.
- Widiyantoro S. & van der Hilst R.D., 1996, Structure and evolution of lithospheric slab beneath the Sunda Arc, Indonesia, *Science*, **271**, 1566-1570.
- Widiyantoro S., Kennett B.L.N. & van der Hilst R.D., 1997, Improving shear-wave tomography from travel-time data, *Phys. Earth. Planet. Inter.*, submitted.
- Widiyantoro S., 1977. Studies of seismic tomography on regional and global scale, *Ph.D. Thesis, Australian National University*.

CRUSTAL WAVEGUIDE EFFECTS ON REGIONAL PHASES IN CHINA AND SOUTHEAST ASIA

Thorne Lay and Guangwei Fan
University of California, Santa Cruz

Sponsored by U.S. Department of Energy
Office of Nonproliferation and National Security
Office of Research and Development
Contract FI9628-95-K-0014

ABSTRACT

This research is intended to enhance seismic discrimination capabilities in China and Southeast Asia, as well as in the Middle East, by assessing the influence of large- and intermediate-scale crustal waveguide heterogeneity on regional waveforms. Short-period regional phases play an important role in identifying low magnitude seismic events in the context of monitoring the Comprehensive Test Ban Treaty. Amplitude ratios of regional phases comprised mainly of P wave energy (P_n , P_g) to those comprised mainly of S wave energy (S_n , L_g) effectively discriminate between explosions and earthquakes in many regions, particularly at frequencies higher than 3 Hz. At lower frequencies, discrimination is usually poor due to large scatter that causes overlapping of event populations, and possibly diminished source type sensitivity. Scatter in regional discriminant measures such as P_g/L_g ratios is caused by both source and propagation effects, and reducing the scatter imparted by the latter is essential to improving the discriminant performance when events do not share identical paths. Regional phases experience distance-dependent amplitude variations due to effects such as critical angle amplification, geometric spreading, and attenuation. Discriminant measures are usually corrected for empirically determined distance trends for a given region, but large scatter persists after such corrections. This study seeks to develop more sophisticated empirical corrections for path properties in order to further reduce the scatter in regional discriminant measures caused by propagation effects. Broadband seismic waveforms recorded at station WMQ, in western China, demonstrate that regional phase ratios such as P_n/L_g , P_g/L_g , P_n/S_n , P_g/S_n , and S_n/L_g , all show significant distance dependence for frequencies less than 6 Hz. However, variations in crustal structure cause additional path-specific amplitude fluctuations that are not accounted for by regionally averaged distance corrections. Blockage of L_g phases on paths traversing the margins of the Tibetan Plateau is one such effect. Regression analysis demonstrates that regional discriminants measured at WMQ display significant correlations with path-specific properties such as mean elevation, topographic roughness, basement depth and crustal thickness. Multiple regressions using optimal combinations of parameters yield corrections that reduce variance in P_g/L_g measurements for frequencies less than 3 Hz by a factor of two or more relative to standard distance corrections. This should systematically enhance the performance of the P_g/L_g discriminant at low frequencies. The method presented here can be used for all regions and all short-period regional discriminants. It is likely that the extraordinary crustal heterogeneity in western China represents an extreme case of path dependent effects.

Keywords: Regional Seismic Phases, China, Middle East, Seismic Discriminants

OBJECTIVE This research is directed at enhancing the confidence in regional seismic wave discriminants used in monitoring a Comprehensive Test Ban Treaty. Our approach involves analysis of large numbers of signals, emphasizing common seismic discriminant measures, seeking empirical relationships with independently observed properties of the crustal structure on each path. The intent is to develop empirical relationships when possible that will reduce the scatter in discriminant measures for a given region, and will provide predictive capabilities for assessing the likely energy partitioning on a new path which has not been previously calibrated.

RESEARCH ACCOMPLISHED There are two main research efforts supported by this contract. Regional phase analysis and assessment of effects of crustal waveguide properties are being conducted separately for China and Southeast Asia (Guangwei Fan) and for the Middle East (Arthur Rodgers). As the Middle East results are described elsewhere, we will focus on the results for China in this paper. The motivation for this work is the previous analysis of energy partitioning in the regional signals for nuclear explosions in Eurasia (Zhang and Lay, 1994 a,b), for earthquake and explosion signals in Eurasia (Zhang et al., 1994) and for earthquakes in the western U.S. (Zhang et al., 1996). These studies demonstrated that scatter in regional phase amplitude ratios may be reduced by developing empirical corrections for waveguide structure variations from path to path, extending conventional distance-correction approaches. The value of this is that any reduction in the variance of regional discriminant measures associated with propagation effects should allow intrinsic source distinctions to be more clearly observed, enhancing seismic discrimination.

In the first year of this effort, a large data set of short-period and broadband recordings by stations in China was assembled. In addition, we collected available information about the crustal properties on each path. Our data collection involved events with magnitudes greater than 5.0, which correspond to those with relatively good source locations (although not necessarily good depths). The resulting path coverage of high quality observations for station WMQ is shown in Figure 1. For each path, we used topographic relief data from the GLOBE project with a spatial resolution of 30-arc-seconds, along with the Cornell database for Eurasian crustal thickness and basement depth to determine path-specific waveguide parameters such as mean elevation, average variance of topography, mean and minimum crustal thickness, gradients of these parameters, and other summary measures. Figure 2 illustrates waveguide variations along one of the paths to WMQ.

After carefully measuring phase amplitudes in different windows and frequency bands (details are given in Fan and Lay, 1997a), logarithmic amplitude ratios for the phase combinations Pg/Lg, Pg/Sn, Pn/Lg, and Pn/Sn were formed and regressed against individual parameters. This defined both distance dependence and correlation with other waveguide variables. Figure 3 illustrates correlations for Pg/Lg as a function of mean crustal thickness variations for different frequency bands. Note that the correlations are strongest in the two lower frequency bands, as is true of all correlations with path properties, including distance. The data in the highest frequency band are rather low signal-to-noise in our data set due to relatively long average propagation paths. Based on a large suite of such correlations, we identified more influential parametric measurements, and then performed multivariate regressions for the purpose of developing models that account for scatter in the associated frequency-dependent discriminant measure. Mean crustal elevation, rms surface roughness, rms surface slope, mean crustal thickness and mean sediment thickness were included, along with distance.

The multiple regressions identified the optimal parameter combinations (see Fan and Lay, 1997b) and associated numerical models were used to correct the data for the propagation

effects. The reduction of the scatter in discriminant measures below 6.0 Hz are illustrated in Figures 4, 5, 6, and 7 for Pg/Lg, Pn/Sn, Pn/Lg, and Pg/Sn, respectively. In every case, it is possible to reduce the variance relative to corrections based on distance alone, but the magnitude of the variance reduction tends to decrease with increasing frequency and is most pronounced for Pg/Lg and Pn/Lg. Significant reductions are also seen for Pn/Sn. The variation in controlling parameters presumably reflects the specific mode of propagation of each phase combination in the waveguide.

The variance reduction in Pg/Lg measurements for frequencies less than 3 Hz is a factor of two or more relative to standard distance corrections. This is significant, and may improve the performance of low frequency discriminants that generally perform poorly due to subtle source differences and/or large propagation induced scatter.

CONCLUSIONS AND RECOMMENDATIONS

Multivariate regression analysis has been introduced into path calibration for regional seismic discriminants using data recorded by station WMQ in Western China. The goal is to empirically reduce the scatter in short-period phase observations using independently known gross attributes of the crustal waveguide. Empirical calibration is the only currently viable approach as detailed knowledge of crustal structure and ability to synthesize realistic propagation corrections are lacking. While path length is a dominant parameter influencing short period discriminant ratio observations for frequencies less than 6 Hz, other path specific parameters extracted from crude crustal models prove to be significant in the regression analysis. In particular, mean path elevation proves to be statistically correlated with Pg/Lg, Pg/Sn, Pn/Lg and Pn/Sn variations in frequency bands of 0.75-1.5, 1.5-3.0, and 3.0-6.0 Hz in Western China. Mean crustal thickness, based on lower resolution models than those available for topography has importance for all phase combinations, while RMS surface roughness is important for ratios involving Lg phases. Mean sediment thickness contributes to variance in low frequency ratios (<3 Hz) involving Pg phases. While deterministic understanding of these observations is yet to be developed, it appears that inclusion of path specific variables other than pathlength can result in significant reduction in discriminant scatter for frequencies below 6.0 Hz. Whether this should be applied on a station-by-station analysis, or whether regional calibration is viable is being addressed in the final stage of this study using observations for multiple stations in China.

REFERENCES

- Fan, G., and T. Lay (1997a). Statistical analysis of irregular waveguide influences on regional seismic discriminants in China, *Bull. Seism. Soc. Am.*, submitted.
- Fan, G., and T. Lay (1997b). Multivariate analysis of waveguide effects on regional seismic phases in Western China, *Seism. Res. Lett.*, submitted.
- Zhang, T., and T. Lay (1994a). Analysis of short-period regional phase path effects associated with topography in Eurasia, *Bull. Seism. Soc. Am.*, **84**, 119-132.
- Zhang, T., and T. Lay (1994b). Effects of crustal structure under the Barents and Kara Seas on short-period regional wave propagation for Novaya Zemlya explosions: Empirical relations, *Bull. Seism. Soc. Am.*, **84**, 1132-1147.
- Zhang, T., S. Y. Schwartz, and T. Lay (1994). Multivariate analysis of waveguide effects on short-period regional wave propagation in Eurasia and its application in seismic discrimination, *J. Geophys. Res.*, **99**, 21929-21945.
- Zhang, T., T. Lay, S. Schwartz, and W. R. Walter (1996). Variation of regional seismic discriminants with surface topographic roughness in the Western United States, *Bull. Seism. Soc. Am.*, **86**, 714-725.

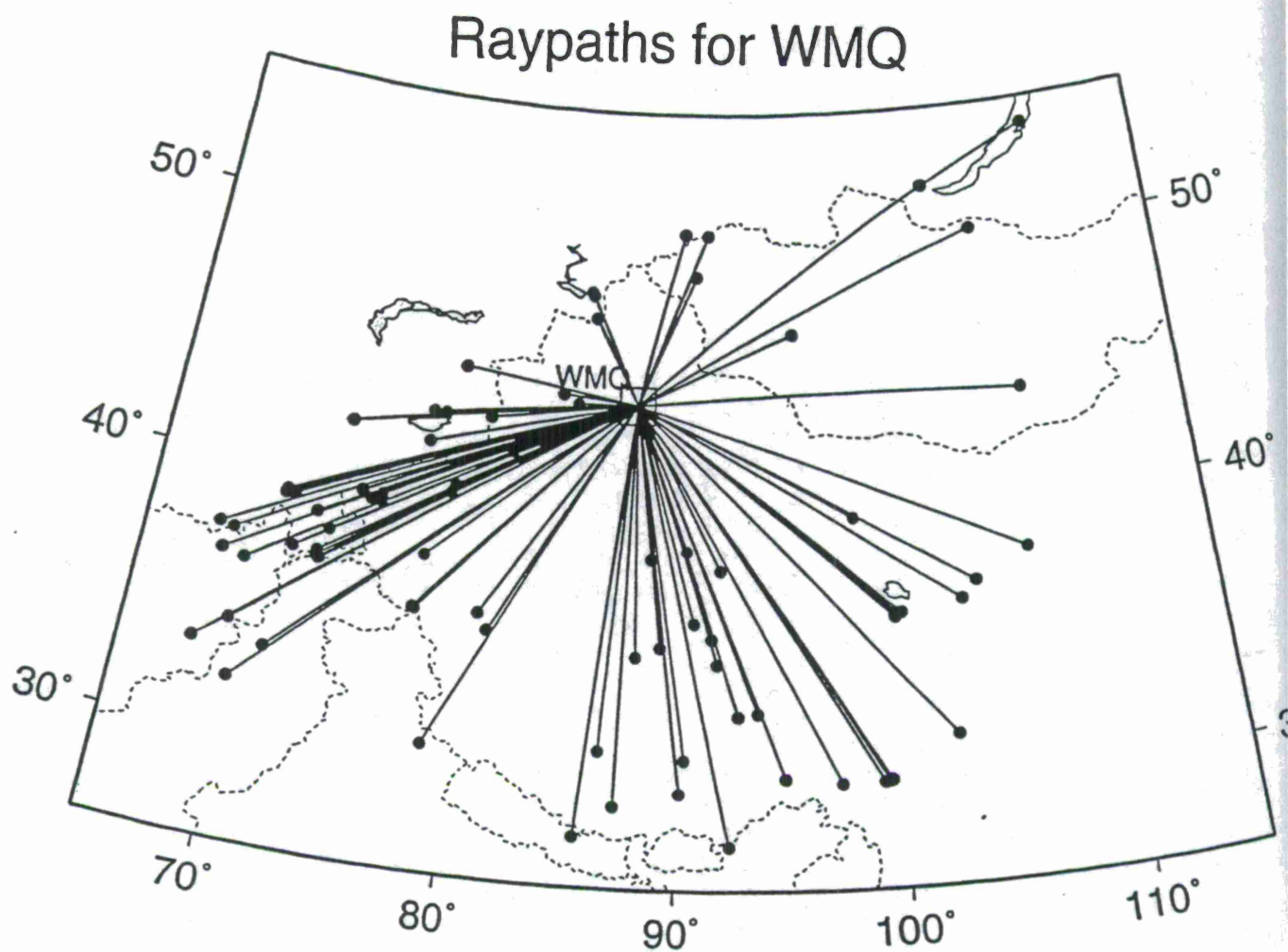


Figure 1. Raypaths for 87 events used in the regional phase analysis for station WMQ in Western China.

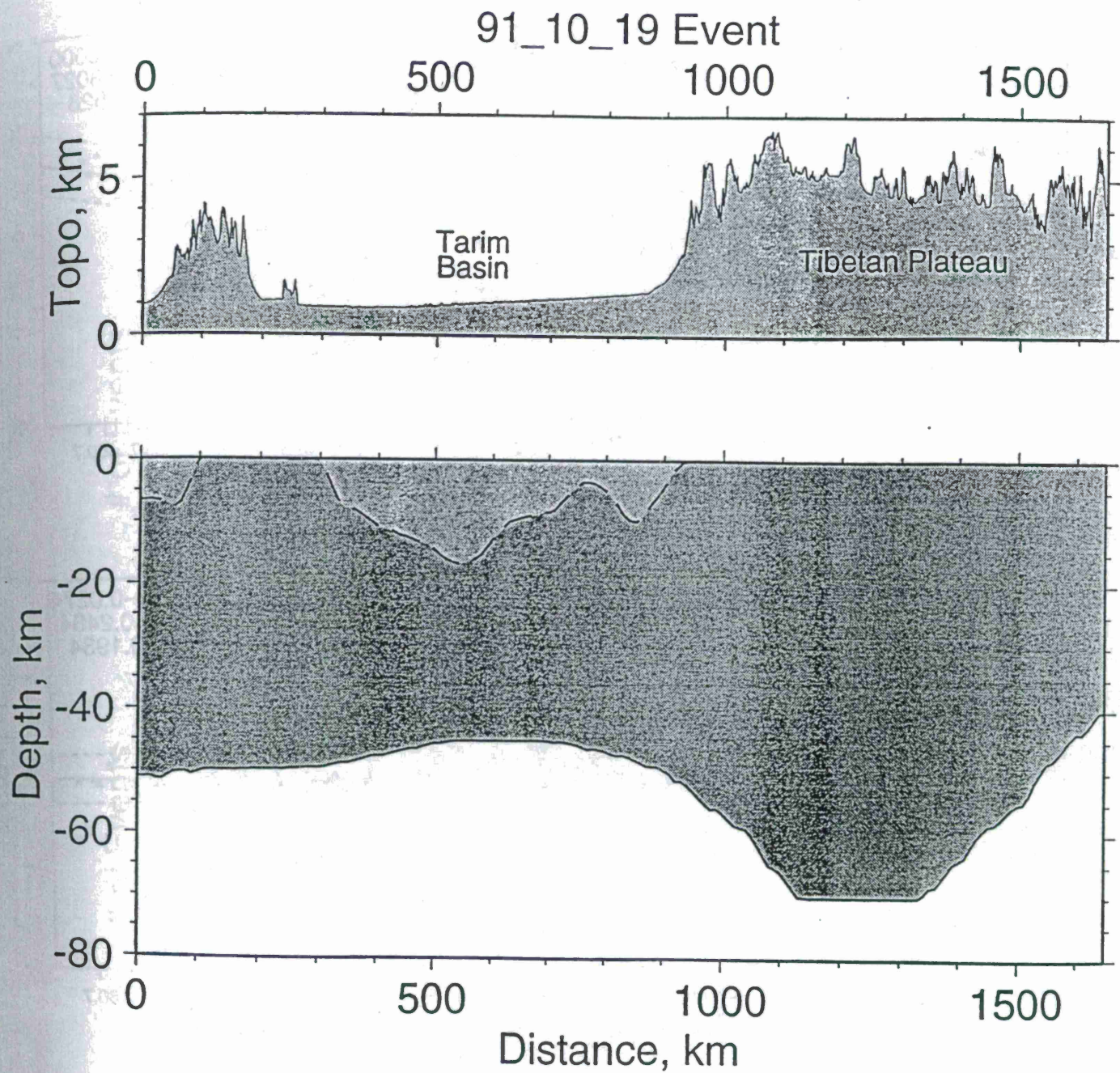


Figure 2. Waveguide information for a path from WMQ to the epicenter of the October 19, 1991 event located in the southern margin of the Tibetan Plateau. The scale for the topography is exaggerated by 5 times relative to the scale in depth. (Fan and Lay, 1997b).

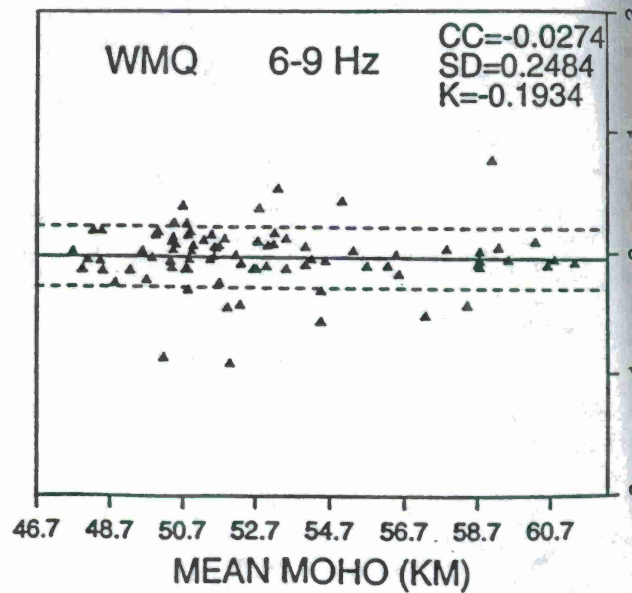
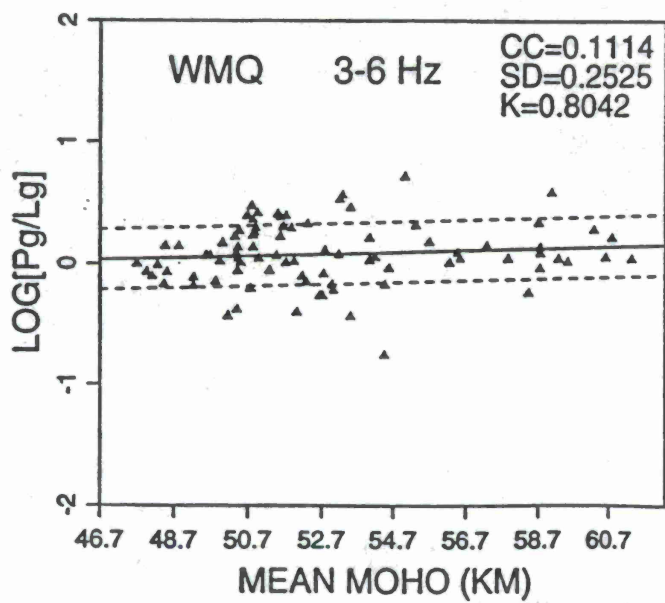
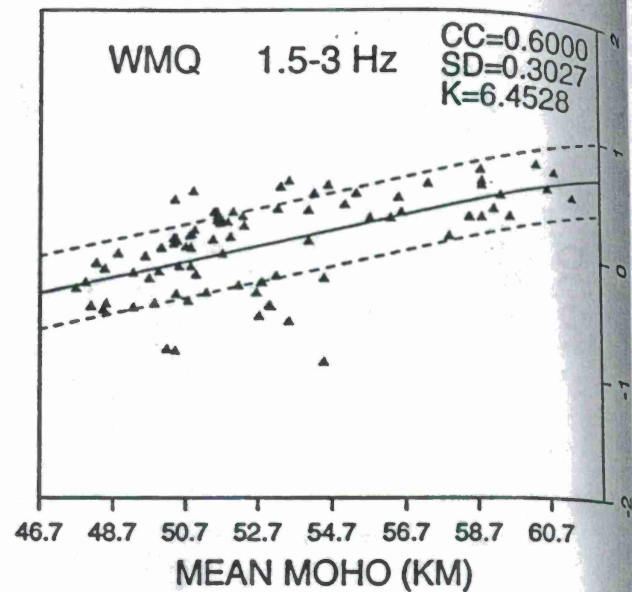
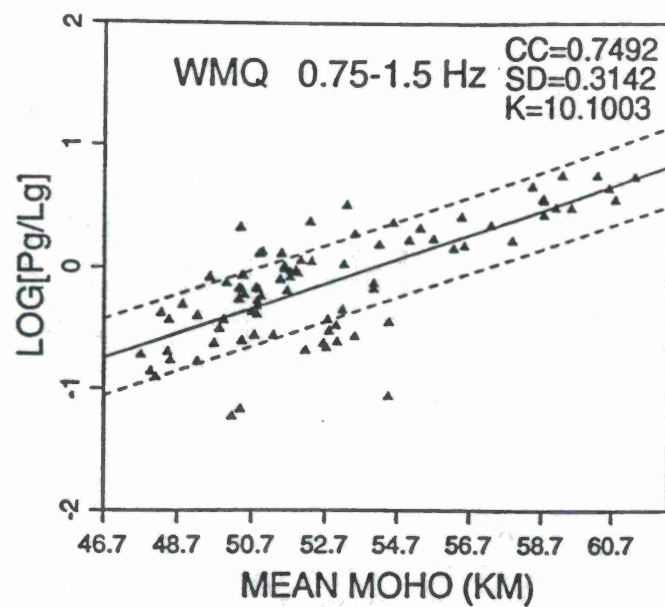


Figure 3. Log (Pg/Lg) as a function of mean crustal thickness in various frequency bands. CC, linear correlation coefficient; SD, standard deviation of the linear regression; K, slope of the regression line. The dotted lines indicate ± 1 standard deviation about the regression line. (From Fan and Lay, 1997a).

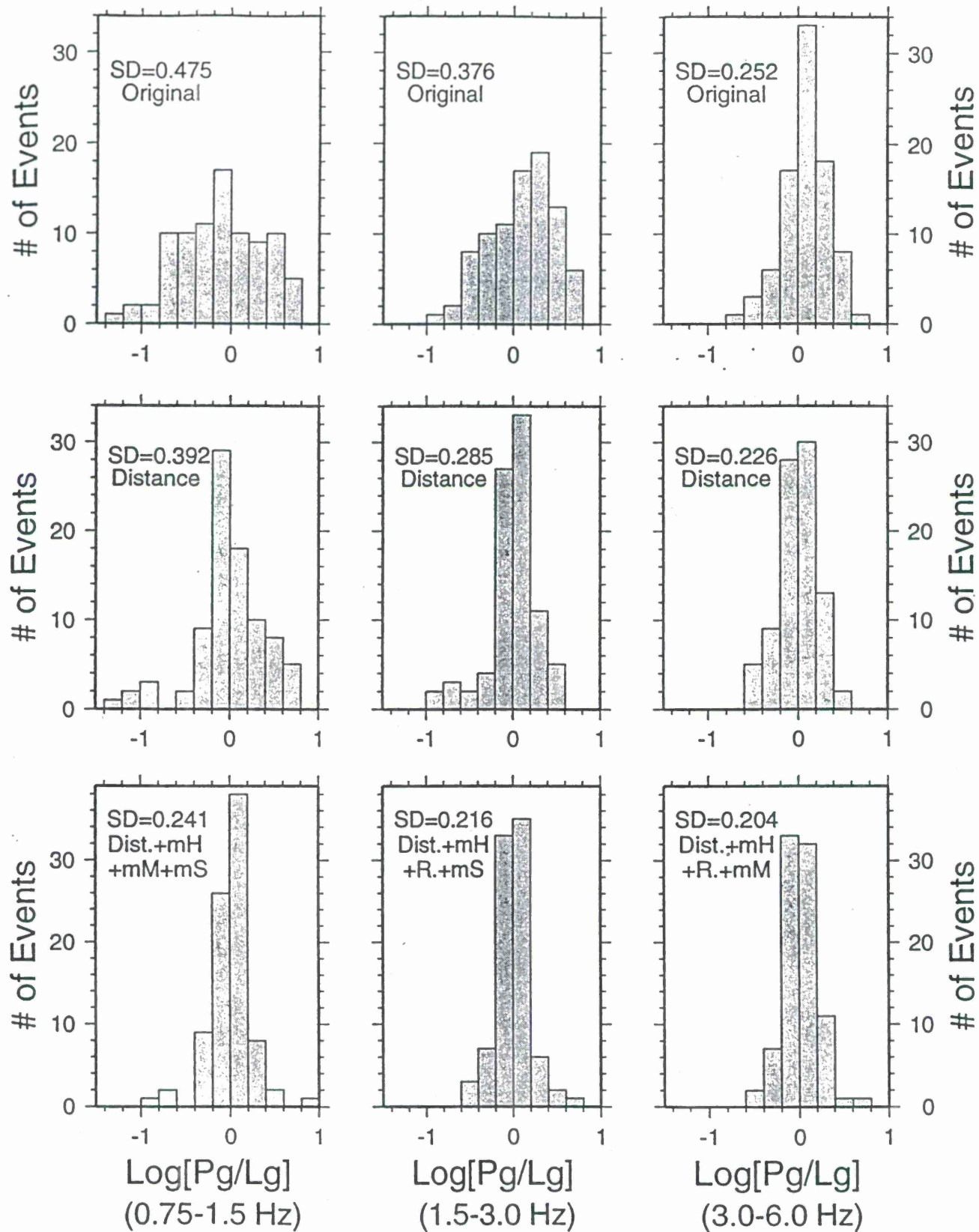


Figure 4. Histograms showing sample distributions for the $\text{Log}(\text{Pg}/\text{Lg})$ measurements. Top figures, for the raw data; middle figures, corrected for distance; bottom figures, corrected for the best models in the three frequency bands. Dist.+mH+mM+mS, corrected for a 4-parameter model involving distance, mean elevation, mean crustal thickness, and mean sediment thickness; Dist.+mH+R+mS, corrected for a 4-parameter model involving distance, mean elevation, surface roughness, and mean sediment thickness; Dist.+mH+R+mM, corrected for a 4-parameter model involving distance, mean elevation, surface roughness, and mean crustal thickness. The standard deviation of each population is given by SD.

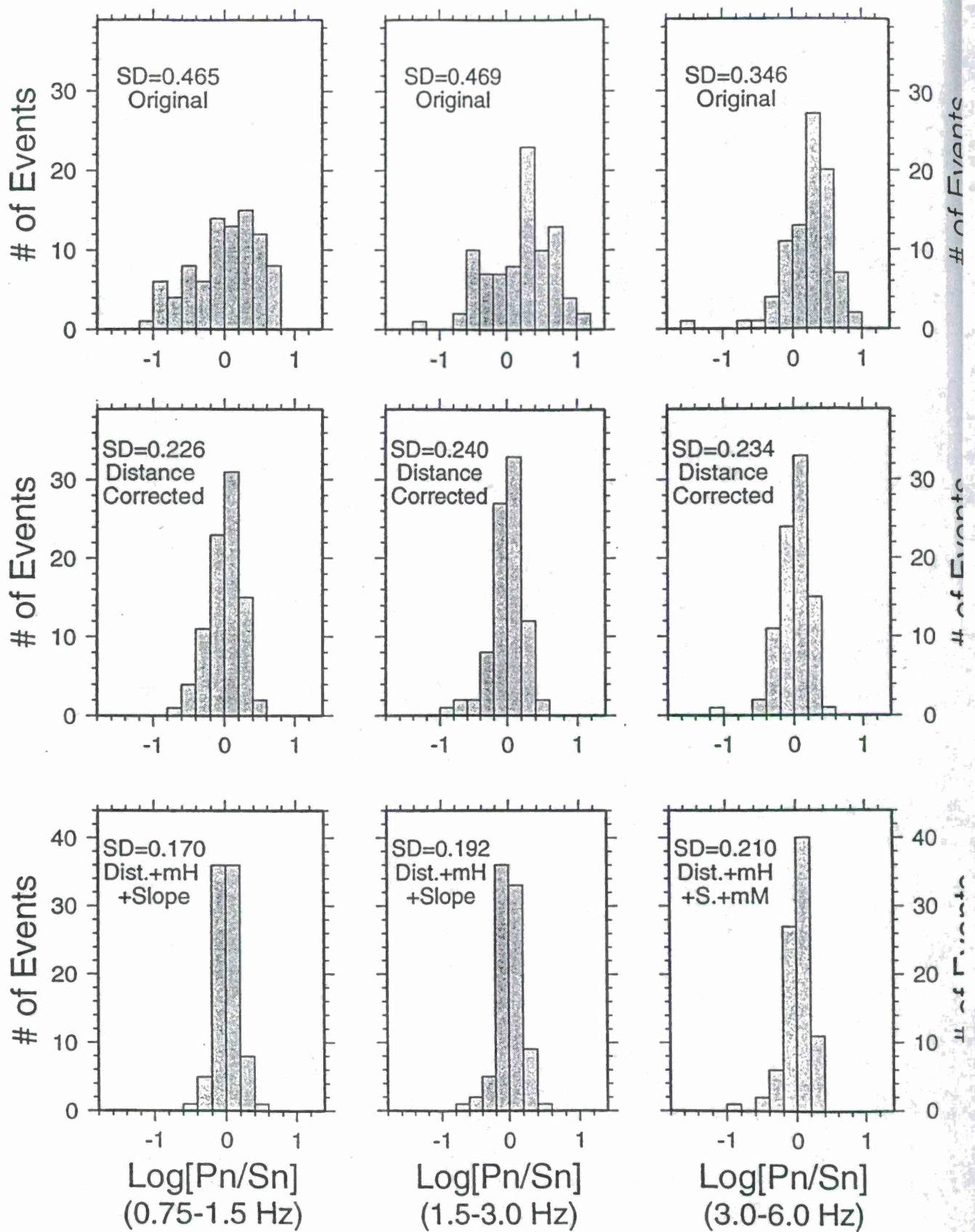


Figure 5. Same histograms showing sample distributions for the $\text{Log}(\text{Pn}/\text{Sn})$ measurements. All illustrations are the same as in Figure 4. Dist.+mH+Slope, corrected for a 3-parameter model involving distance, mean elevation, and rms slope; Dist.+mH+S.+mM, corrected for a 4-parameter model involving distance, mean elevation, rms slope, and mean crustal thickness.

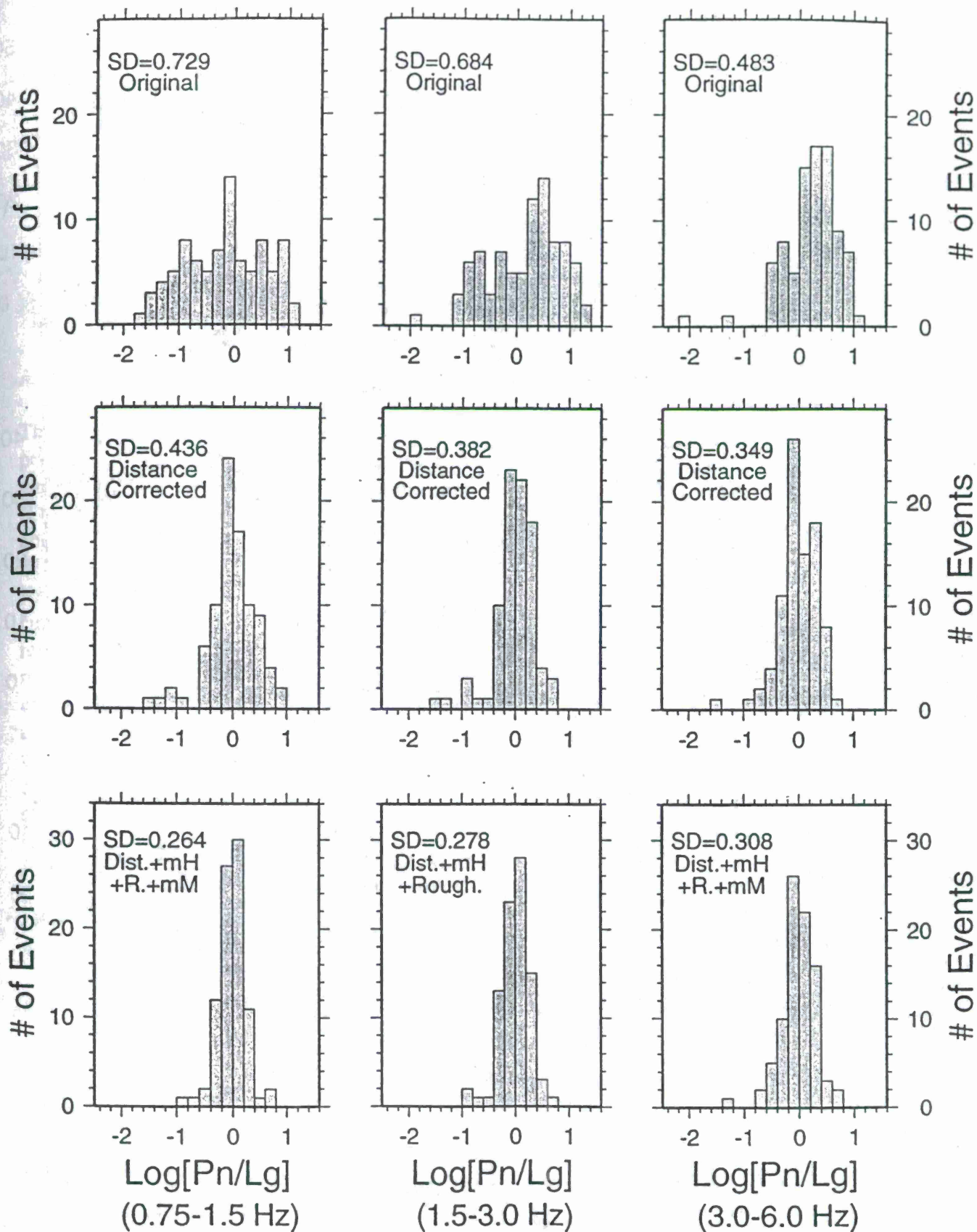


Figure 6. Same histograms showing sample distributions for the $\text{Log}(\text{Pn}/\text{Lg})$ measurements. All illustrations are the same as in Figure 4. Dist.+mH+Rough., corrected for a 3-parameter model involving distance, mean elevation, and surface roughness; Dist.+mH+R.+mM, corrected for a 4-parameter model involving distance, mean elevation, surface roughness, and mean crustal thickness.

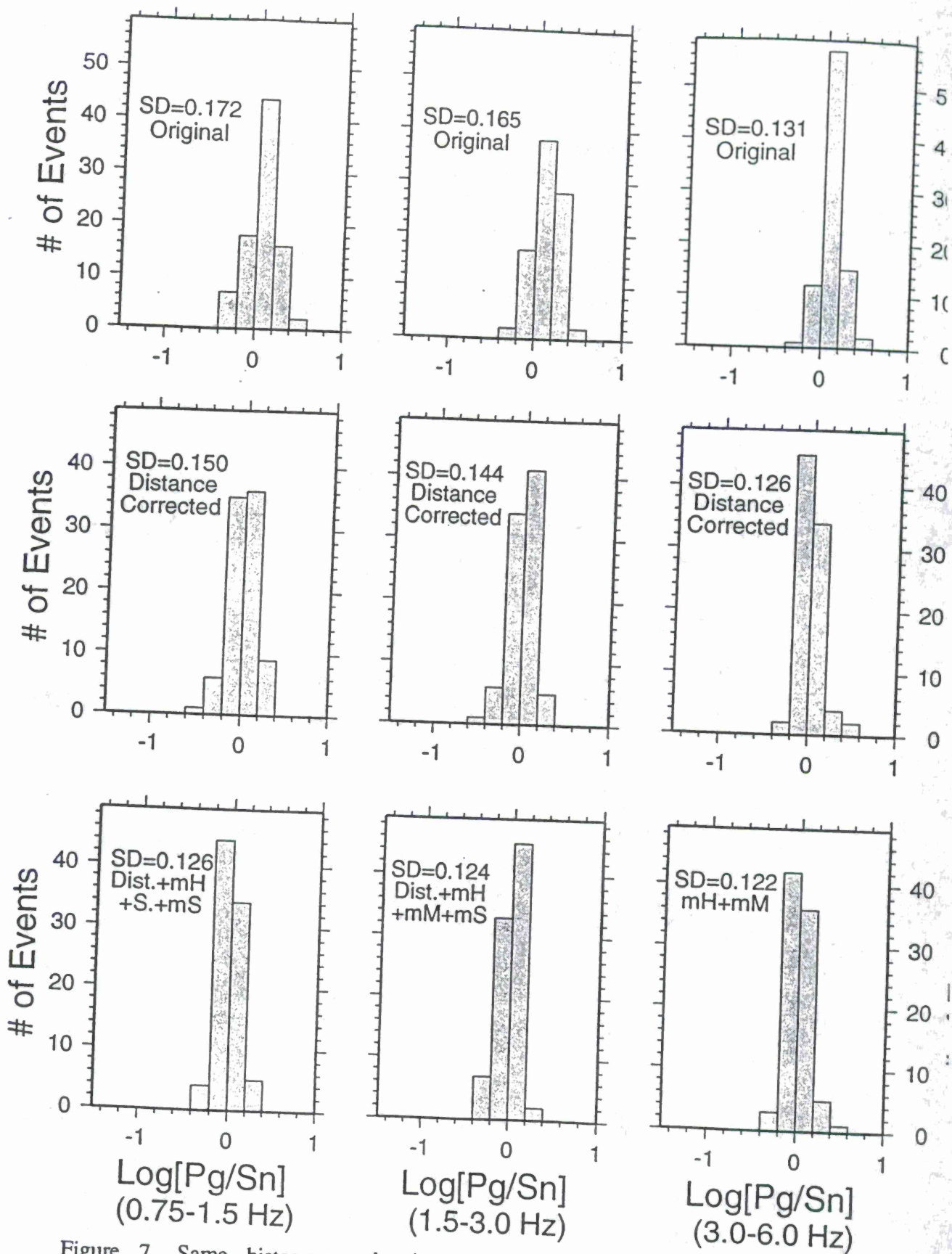


Figure 7. Same histograms showing sample distributions for the $\text{Log}[\text{Pg}/\text{Sn}]$ measurements. All illustrations are the same as in Figure 4. mH+mM, corrected for a 2-parameter model involving mean elevation and mean crustal thickness; Dist.+mH+S.+mS, corrected for a 4-parameter model involving distance, mean elevation, rms slope, and mean sediment thickness; Dist.+mH+mM+mS, corrected for a 4-parameter model involving distance, mean elevation, mean crustal thickness, and mean sediment thickness.

**INTERMEDIATE PERIOD GROUP VELOCITY MAPS
(15 - 30 s) ACROSS CENTRAL ASIA, WESTERN CHINA,
AND PARTS OF THE MIDDLE EAST**

A.L. Levshin, M.H. Ritzwoller, L.I. Ratnikova, M.P. Silitch, R.C. Kelly, and B. O'Sullivan

Department of Physics, University of Colorado, Boulder 80309-0390
<http://phys-geophys.colorado.edu/geophysics/eurasia.dir/eurasia.html>

Sponsored by Air Force Technology Applications Center
Contract Number F19628-95-C-0099

ABSTRACT

This paper presents a report on the status of a study of the dispersion characteristics of intermediate period broad-band fundamental surface waves propagating across Central Asia, Western China, and parts of the Middle East. We present Rayleigh wave group velocity maps from 15 s to 30 s period. (Love wave and longer period maps have also been constructed.) Broad-band waveform data from about 770 events from 1988 - 1995 recorded at 103 individual stations from 'global' (GDSN, IRIS/GSN, GEOSCOPE, CDSN) and 'regional' networks (MEDNET, KNET, KAZNET, Saudi Network) have been processed and produce about 11,000 paths for which individual dispersion curves have been estimated. Resolution is estimated from 'checker-board' tests and we report which regions at each period appear to have resolutions better than 5°. More than 80% of the studied region is resolved at 20 s and above, but resolution degrades at shorter periods so that we have little confidence in the 10 s group velocity maps and do not show them here. Resolution is far from uniform spatially, and is generally worst in NW Iran, India, the Arabian Sea, Egypt, and parts of Central and W. China. The misfit to the data from the estimated maps is about half the misfit from the crustal model CRUST-5.1 (Mooney, *et al.*, 1997). Many known geological and tectonic structures are observed in the group velocity maps. Of particular note are the signatures of sedimentary basins and crustal thickness variations due to mountain roots and deformation resulting from continental collisions. Work is proceeding to further improve the resolution and accuracy of the estimated group velocity maps in this and other parts of Eurasia. All of the measurements and group velocity maps are available at our web site. Shear velocity models that result from the dispersion maps are also at our web site and at Cornell University's Geophysical Database Server.

Keywords: Central Asia, Western China, Middle East, Tarim Basin, Lop Nor, Tibet, Iran, Saudi Arabia, Afghanistan, Pakistan, Kirgizstan, Kazakstan, surface wave dispersion, Rayleigh waves, Love waves, group velocity, M_s ; m_b discriminant

OBJECTIVE

The objective of this research is to produce high resolution ($\sim 3^\circ - 4^\circ$) intermediate period (10 - 40 s) group velocity maps across Central Asia, W. China, and parts of the Middle East. These maps are designed to help identify Rayleigh wave packets in noisy seismic recordings so that more accurate amplitude measurements can be obtained for increasingly smaller events to be used as part of the $M_s : m_b$ method of discriminating explosions from earthquakes (e.g., Stevens and Day, 1985).

RESEARCH ACCOMPLISHED

Data Set

To date, Rayleigh and Love wave group velocity curves have been obtained from 770 events across Eurasia measured at 103 broad-band stations from the following networks: CNSN, CDSN, GEOCOPE, GSN, KAZNET, KNET, MEDNET, Saudi Network (Vernon *et al.*, 1996). Figure 1 summarizes the distribution of sources and receivers. Table 1 presents the number of Rayleigh wave measurements as a function of period for three subset of our data set: rays intersecting Eurasia, rays intersecting the region of study (shown in Figure 1), and rays contained within the region of study. The measurements come from a total of more than 11,000 paths across the continent. The method of measurement has been summarized at some length by Ritzwoller *et al.* (1995) and Ritzwoller and Levshin (1997). Ritzwoller *et al.* (1996a) and Ritzwoller *et al.* (1997) argued that in order to optimize resolution in a region, the azimuthal distribution of rays at each point in the region should be as uniform as possible. The use of measurements made for events which occur outside the region of study is important in optimizing the azimuthal distribution of rays in the region, and is the reason we have in the past and will continue to analyze data from large numbers of events outside the studied region. Our measurements are being used by other researchers in addition to ourselves (e.g., Stevens and McLaughlin, 1997).

Table 1. Number of Rayleigh Wave Measurements

period	Eurasia	Intersecting Studied Region	Within Studied Region
10 s	522	503	451
15 s	1388	1061	451
20 s	3486	2160	812
30 s	7866	4828	948
40 s	8523	5471	837

We have shown intermediate period (10 - 40 s) and broad-band (20 s - 200 s) group velocity maps in several recent papers (e.g., Levshin *et al.*, 1996; Ritzwoller and Levshin, 1997, Ritzwoller *et al.*, 1997). We have begun to add more data designed to improve the resolution of these maps across Central Asia, W. China, and the Middle East. New data processed in the summer of 1997 are of four types: (1) events in the region of study observed at high latitude stations in the Western Hemisphere (e.g., Canadian National Seismic Network); (2) events in and around Eurasia observed at GEOSCOPE stations around Eurasia; (3) events in and around Eurasia observed at GSN, CDSN, MEDNET stations around Eurasia, and (4) events in and around Eurasia observed at the nine-station Saudi Network. The most useful of these are data from the Saudi Network and from the GEOSCOPE station at Hyderabad, India. At the time of writing, about 2,000 new

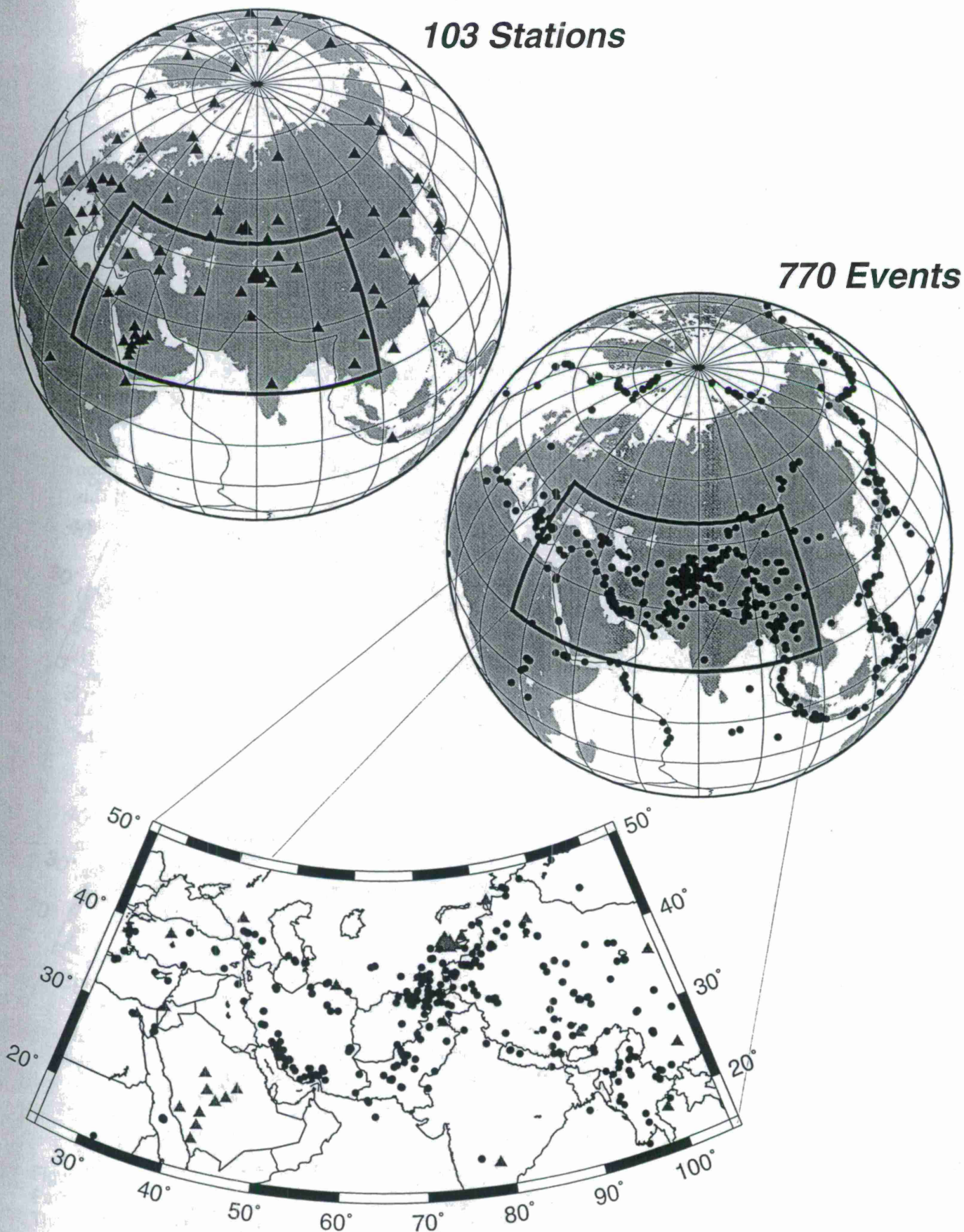


Figure 1. Stations and events used in this study. Stations come from the following networks: CDSN, GEOSCOPE, GSN, KNET, KAZNET, MEDNET, Saudi-Net.

paths have been added in the summer of 1997 and continue to be added. As shown in Figure 2, the addition of these data has significantly improved path density in Iran, Afghanistan, Saudi Arabia, India, and the Arabian Sea.

Analyses of the repeatability of measurements in summary rays or measurement clusters (similar starting and ending points of rays) indicate that measurement uncertainties are about 0.04 km/s at 20 s and 30 s period, and about 0.05 km/s at 15 s.

All of our measurements, sporadically updated, are available through our web site at:

<http://phys-geophys.colorado.edu/geophysics/eurasia.dir/eurasia.html>.

Resolution

To estimate resolution we perform a standard 'checker-board' test. Each model is divided into cells of equal area with each cell possessing a velocity perturbation of $\pm 10\%$ of the average across each map. Travel time perturbations are accumulated along the great circle linking each source and receiver. We estimate resolution as a function of wave type and period by computing synthetic travel times through the checker-board model for the paths and with the inversion method used to construct the group velocity maps. Checker-board plots at the resolutions of this study are difficult to interpret since the cells are very small. To simplify interpretation, we assign a 'Resolution Index', \mathcal{R}_i , to each cell:

$$\mathcal{R}_i = \frac{v_{\max}}{v_{\text{input}}} \quad (\text{in percent}). \quad (1)$$

Here, v_{\max} is the estimated velocity perturbation whose absolute value is maximum in the cell and v_{input} is the input velocity perturbation in the same cell ($\pm 10\%$). Perfect resolution would result in $\mathcal{R}_i = 100\%$, poor resolution results in $\mathcal{R}_i \leq 30\%$. The resolution index can be less than zero if the sign of v_{\max} is opposite from the input value of the cell or greater than 100% if the estimated magnitude is higher than the input.

Figure 3 displays the resolution index for 5° cells at three periods: 15 s, 20 s, and 30 s. The light grey areas indicate that the resolution in the area is estimated to be no worse than 5° . Resolution improves with increasing period. At 15 s, $\sim 60\%$ of the 5° cells that compose the region of study are resolved; at 20 s, 82% are resolved; and at 30 s, 89% are resolved. The Arabian Sea, India, NW Iran, E. Egypt, and parts of Central and NW China are the most difficult areas to resolve and are particularly problematic below 20 s period.

Group Velocity Maps

The method used to estimate group velocity maps is described at some length in Ritzwoller and Levshin (1997). Ritzwoller *et al.* (1997) argue that although many measurements of 10 s Rayleigh and Love waves are made, path distributions are not sufficiently homogeneous to construct useful group velocity maps for most of the region of study at 10 s period. Rayleigh wave group velocity maps are shown in Figure 4 for periods of 15 s, 20 s, and 30 s. Maps are displayed as the percent deviation from the average across each map: 2.856 km/s at 15 s, 2.960 km/s at 20 s, 3.265 km/s at 30 s period. Longer period and Love wave maps have also been constructed. Group velocity maps are also available through our web site.

The geological and tectonic interpretation of group velocity maps is discussed at some length by Ritzwoller and Levshin (1997) and Ritzwoller *et al.* (1997). The 15 s and 20 s Rayleigh waves are most sensitive to crustal velocity variations. In particular, low velocities result from known

Rayleigh Wave Path Density

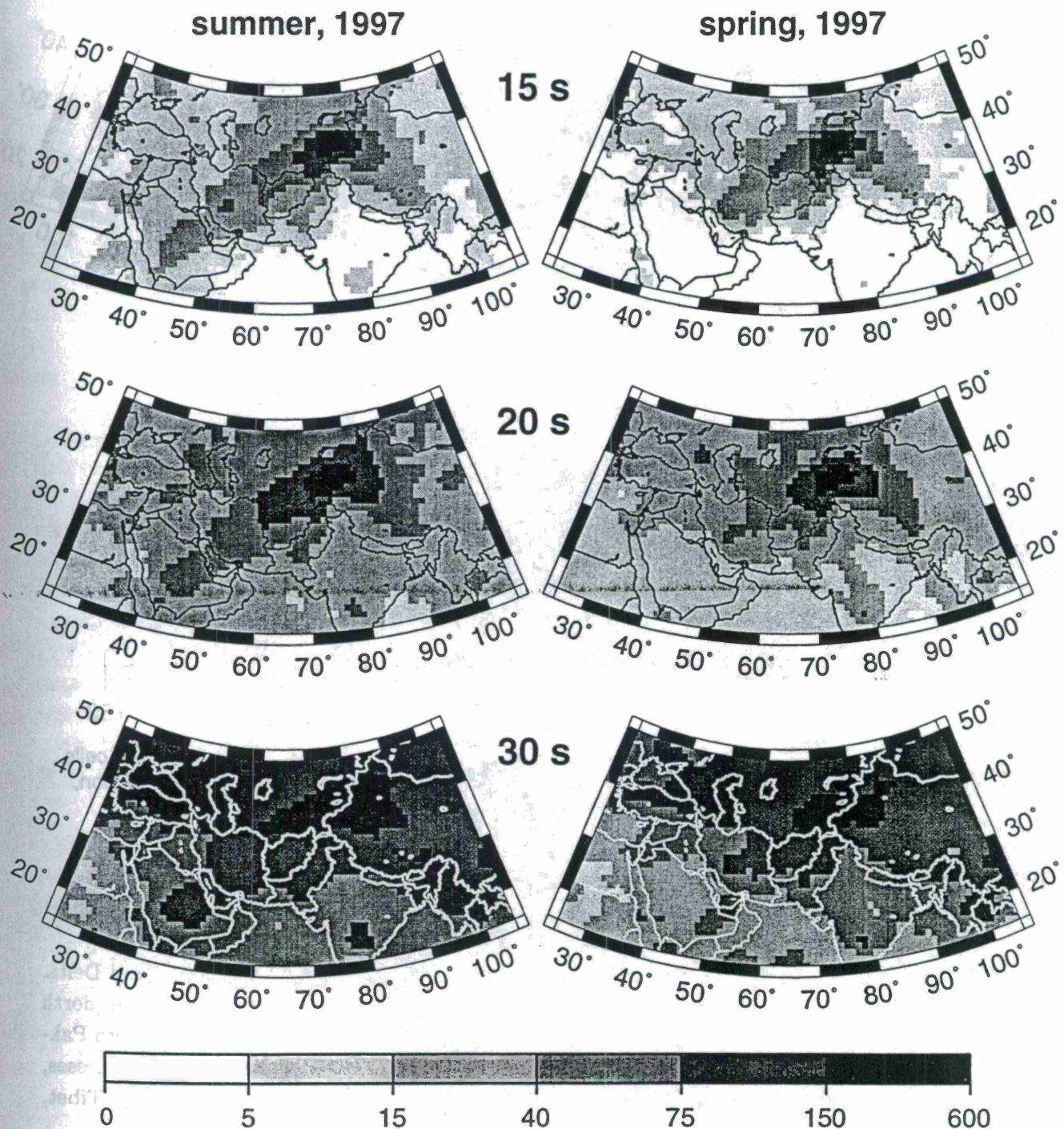


Figure 2. Path density for Rayleigh waves at three periods: (Top) 15 s, (Middle) 20 s, and (Bottom) 30 s. Path density is defined as the number of rays which touch each 2 degree square bin (~50,000 square km). The left column is path density including measurements made in the summer of 1997. These measurements include data from 140 events measured at the Saudi network and a large amount of new data from the GEOCOPE network, most importantly measurements made at Hyderabad, India. The right column displays path densities prior to the summer of 1997.

Rayleigh Wave Resolution Index

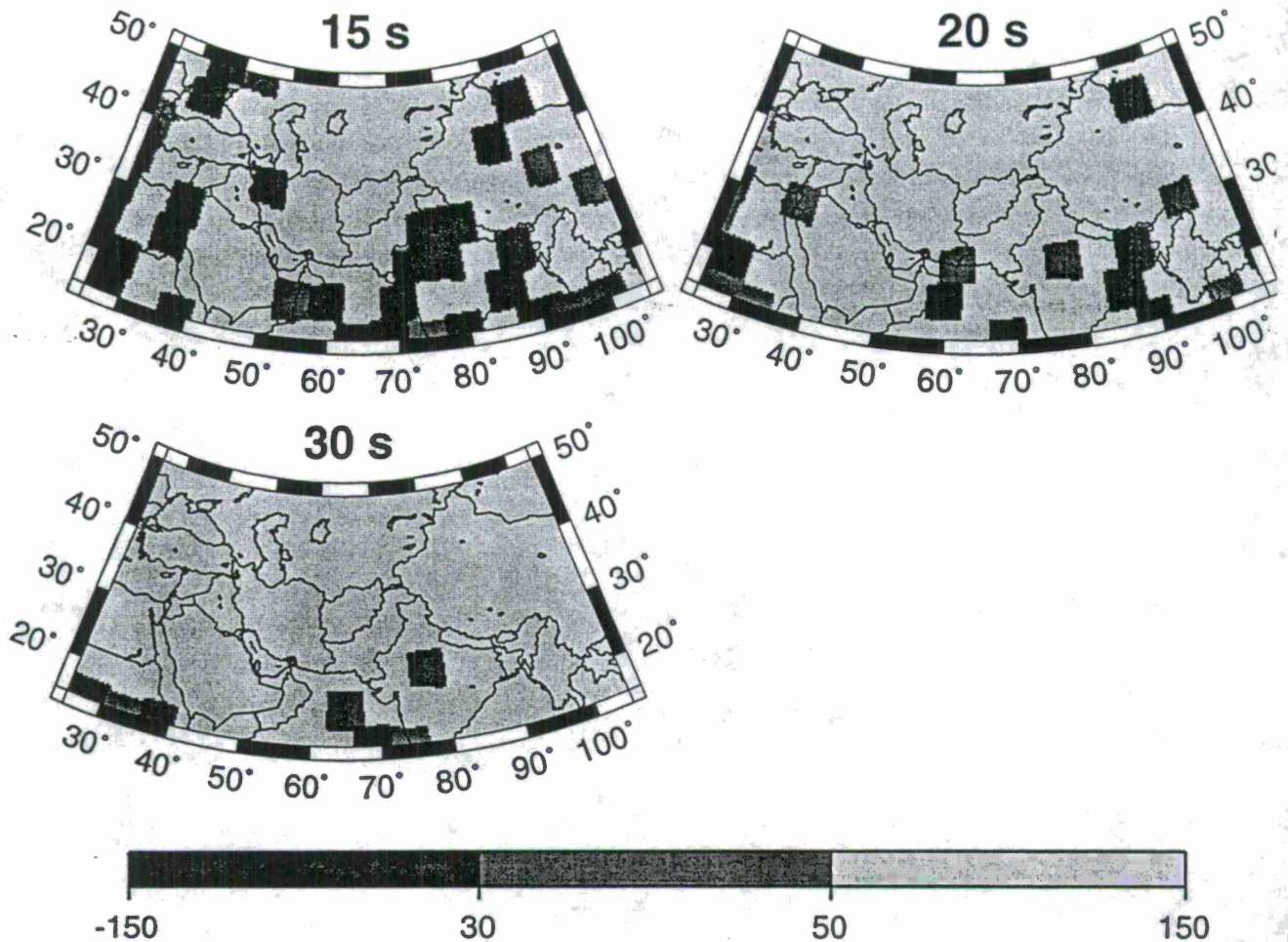


Figure 3. Resolution index (eqn. (1)) for the 15 s, 20 s, and 30 s Rayleigh waves and 5 degree cells. The grey-scale values are presented, the lightest indicates what we consider to be good resolution, increasingly dark cells reveal poorer resolutions.

sedimentary basins; e.g., Black Sea, E. Mediterranean, Tarim Basin, the Ganges Fan and Delta, the Northern and Southern Caspian Depressions, the Persian Gulf, the Tadzhik Depression (north of Afghanistan and Northern Iran), and a basin associated with the Indus River in Southern Pakistan. By 30 s period, group velocities have become increasingly sensitive to crustal thicknesses, and the low velocities result dominantly from thickened crust under mountain ranges; e.g., Tibet, Pamir, Hindu Kush, Tien Shan, Zagros, etc.

Data Misfit: Comparison with CRUST-5.1

Table 2 presents misfit-statistics for three group velocity maps across the studied region. Misfit is defined as the RMS-difference between the group velocities predicted from each map and our group velocity measurements for those ray paths contained entirely within the region of study. The three maps are: (1) the average of our (CU) group velocity maps across the region of

Rayleigh Wave Group Velocity Maps

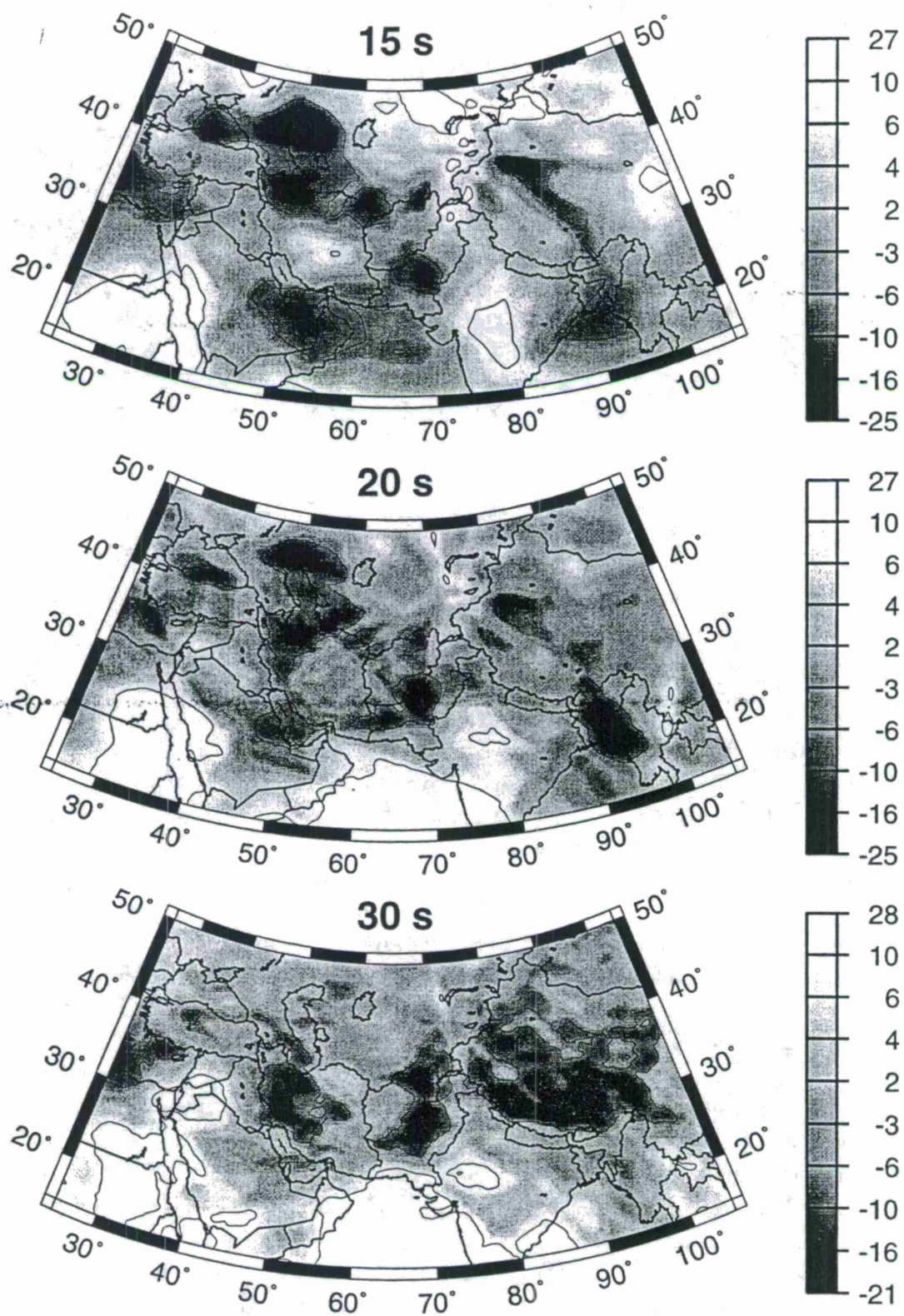


Figure 4. Group velocity variations at the indicated periods expressed in percent deviation from the average across each map (15 s: 2.856 km/s; 20 s: 2.960 km/s; 30 s: 3.268 km/s). The $\pm 10\%$ contours are drawn.

study, (2) our group velocity maps, and (3) the maps derived from the crustal model CRUST-5.1 (Mooney *et al.*, 1997) together with the mantle model S16B30 (Masters *et al.*, 1997). The CU maps provide considerable improvement in the fit to the measurements relative to the reference model (CRUST-5.1/S16B30) and to the average velocity across the region. Our group velocity maps approximately halve the misfit relative to CRUST-5.1/S16B30 and to the average maps. Variance reductions relative to the average across the CU maps are listed in Table 3.

Table 2. RMS-Misfit of Group Velocity Maps to Group Velocity Measurements

<i>period</i>	<i>Average Across CU Maps</i>	<i>CU Maps</i>	<i>CRUST-5.1</i>
15 s	0.180 km/s	0.095 km/s	0.167 km/s
20 s	0.161 km/s	0.082 km/s	0.148 km/s
30 s	0.256 km/s	0.076 km/s	0.137 km/s

Table 3. Variance Reduction Relative to Average Across CU Maps

<i>period</i>	<i>CU Maps</i>	<i>CRUST-5.1</i>
15 s	72%	14%
20 s	74%	15%
30 s	91%	72%

CONCLUSIONS AND RECOMMENDATIONS

Conclusions

We have provided a status report on the study of intermediate period (10 s - 40 s) Rayleigh wave group velocities across Central Asia, Western China, and parts of the Middle East. There are three main reasons why we believe that this study represents a significant improvement in the understanding of intermediate period surface wave dispersion across the studied region. The first has to do with the data used. This study displays denser and more uniform data coverage and demonstrates higher resolution than previous studies that have been performed on this scale and at these periods. Second, the group velocity maps display the signatures of known geological and tectonic features never before revealed in surface wave studies on this scale. In particular, these maps are providing entirely new constraints on sedimentary basins and crustal thicknesses. This both lends credence to the maps and spurs interest in their use to infer information about the features that are observed. Finally, the group velocity maps provide a significant improvement in fit to the observed group velocity curves over other existing models.

For these reasons we believe that the group velocity maps that we are developing should be useful in the future to predict group travel times for the identification and extraction of surface wave packets, to calibrate existing crustal models such as CRUST-5.1, and as data in inversions for crustal models (e.g., Ritzwoller *et al.*, 1996b). Our v_s model of Central Asia is available at our web site and from Cornell University's Geophysical Database Server (Seber *et al.*, 1996): <http://atlas.geo.cornell.edu>.

There are several key elements to estimating group velocity maps at these periods. First, regional earthquakes need to occur and there must be broad-band instrumentation in the region of study. Second, dispersion measurements must be performed carefully to separate the first arrival from coda and other interfering waves. Third, data from smaller earthquakes than those normally studied on continental or global scales need to be processed (i.e., $M_s \leq 5.0$). Finally, the

regional measurements should be combined with measurements made on a larger spatial scale. The inclusion of measurements on paths that propagate more broadly across Eurasia provides greater homogeneity of coverage and azimuthal distribution across the studied region and appreciably improves resolution and accuracy.

Recommendations

The methods described should continue to be applied across the studied region and more generally across Eurasia to new and accumulating data in order to improve resolution and reliability further. In fact, this study is far from complete even across the studied region. For example, we have only analyzed data from small events ($M_s \leq 5.0$) at KNET and KAZNET. The analysis of data from small events recorded at GSN, CDSN, GEOSCOPE, Saudi Network, GEOFON, and PASSCAL installations across the studied region together with historical data before 1988 from the GDSN and ILPA networks, could improve path coverage substantially, particularly below 20 s period where the path coverage is most inhomogeneous. Substantial improvements can still be achieved in the most poorly resolved parts of the studied region; e.g., Northwestern Iran, India, etc.. The methods can also be applied successfully to other areas across Eurasia and to selected regions on other continents.

There remain several shortcomings with the methodology of this study that point the way for future technical enhancements. Most significantly, the use of phase information would help provide tighter constraints on crustal structures. In addition, off-great-circle propagation is significant at the periods studied here. Modeling it by ray tracing through phase velocity maps and potentially using polarization information are also obvious directions to help improve crustal models inferred from the dispersion maps.

The group velocity measurements, maps, and shear-velocity models that are resulting from this research are available at our web site and the models are also at Cornell University's Geophysical Database Server. In the future, research results such as these should be incorporated in data bases that are more commonly accessed by CTBT monitors to be used to help identify surface wave packets as part of, for example, the $M_s : m_b$ method of discrimination.

REFERENCES

- Levshin, A.L., M.H. Ritzwoller, and S.S. Smith, Group velocity variations across Eurasia, *Proceedings of the 18th Seismic Research Symposium on Monitoring a CTBT*, 70 - 79, 1996.
- Masters, G., S. Johnson, G. Laske, and H. Bolton, A shear-velocity model of the mantle, *Phil. Trans. R. Soc. Lond. A*, **354**, 1385-1411, 1996.
- Mooney, W.D., G. Laske, and G. Masters, CRUST 5.1: A global crustal model at 5 degrees by 5 degrees, *J. Geophys. Res.*, in press, 1997.
- Ritzwoller, M. H., A. L. Levshin, S. S. Smith, and C. S. Lee, Making accurate continental broad-band surface wave measurements. *Proceedings of the 17th Seismic Research Symposium on Monitoring a CTBT*, Phillips Laboratory, Scottsdale, AZ, 482-491, PL-TR-95-2108, Sept. 1995.
- Ritzwoller, M.H., A.L. Levshin, L.I. Ratnikova, and D.M. Tremblay, High resolution group velocity variations across Central Asia, *Proceedings of the 18th Seismic Research Symposium on Monitoring a CTBT*, 98 - 107, 1996a.
- Ritzwoller, M.H., A.L. Levshin, and L.I. Ratnikova, Surface wave tomography across Tibet, *EOS Trans. Am. Geophys. Un.*, **77**, F675, 1996b.
- Ritzwoller, M.H. and A.L. Levshin, Eurasian surface wave tomography: Group velocities, *J. Geophys. Res.*, in press, 1997.

- Ritzwoller, M.H., A.L. Levshin, L.I. Ratnikova, and A.A. Egorkin, Intermediate period group velocity maps across Central Asia, Western China, and parts of the Middle East, submitted to *Geophys. J. Int.*, 1997.
- Seber, D., E. Sandvol, M. Vallve, G. Brew, and M. Barazangi, Development of a geological and geophysical information system and seismological studies in the Middle East and North Africa, *Proceedings of the 18th Seismic Research Symposium on Monitoring a CTBT*, 1026 - 1035, 1996.
- Stevens, J.L. and S.M. Day, The physical basis for m_b : M_s and variable frequency magnitude methods for earthquake/explosion discrimination, *J. Geophys. Res.*, **90**, 3009 - 3020, 1985.
- Stevens, J.L. and K.L. McLaughlin, Improved methods for regionalized surface wave analysis, *Proceedings of the 19th Seismic Research Symposium on Monitoring a CTBT*, this volume, 1997.
- Vernon, F., Mellors, R.J., J. Berger, A.M. Al-Amri, J. Zollweg, Initial results from the deployment of broadband seismometers in the Saudi Arabian Shield, *Proceedings of the 18th Seismic Research Symposium on Monitoring a CTBT*, 108 - 117, 1996.

Preliminary Regional Magnitude Results in the Middle East Region Using Narrowband Lg Coda Envelopes

Kevin Mayeda and William R. Walter
Geophysics and Global Security Division Lawrence Livermore National Lab

Sponsored by U.S. Department of Energy
Office of Nonproliferation and National Security
Office of Research and Development
Contract W-7405-ENG-48
Comprehensive Test Ban Treaty Research and Development Program, ST482B

ABSTRACT

We are calibrating a stable magnitude for regional events in the Middle East region using narrowband coda envelopes. This approach produced magnitudes that were 8 times more stable than Pg and Lg-based magnitudes in the western United States. Many regional seismic discriminants are functions of event size, therefore, it is important to obtain a stable measurement especially for smaller events that will likely have very limited station coverage. We have collected and analyzed regional broadband waveforms from stations in the Middle East region for the purpose of calibrating a stable regional magnitude scale that can be applied to events that are too small to detect teleseismically. Our approach is to obtain frequency-dependent empirical Green's function coda envelopes for narrow frequency bands that can be used to correct for gross path effects. We make the assumption that the moment-rate spectra are generally flat below ~2 Hz for these events smaller than $M_w \sim 3.5$. In a least squares sense, we obtain frequency-dependent corrections to the Lg coda measurements to fit the scalar moment estimates. These frequency-dependent corrections remove the effects of the body and surface wave scattering-to-Lg coda transfer function as well as frequency-dependent site effects, thus correcting back to the S-wave source spectra. Due to the averaging nature of Lg coda waves we are then able to obtain a stable single-station estimate of the source spectra. To avoid regional biases we tie our coda envelope amplitude measurements to seismic moments obtained from long period 1-D waveform modeling for moderate sized earthquakes ($M_w \sim 3.5$ -5.5). Most importantly, we can now apply the same corrections to significantly smaller events that cannot be observed teleseismically. Our empirical approach takes into account scattering, absorption, and waveguide losses as well as frequency-dependent site effects. Moreover, the use of the coda envelope mitigates the undesirable effects of source anisotropy, random site interference, path variability, and directivity that plague direct wave measurements. In addition to stable magnitude estimation, the coda-derived source spectra has been successfully used as a discriminant. For example *Walter et al.*, (1995) showed that Lg coda spectral ratios (i.e., 1-2/6-8 Hz ratio) provided the best separation relative to Pn, Pg, and Lg spectral ratios. *Mayeda and Walter* (1996) also showed that unusually shallow sources, such as very shallow earthquakes, NTS explosions, and mining-related collapses exhibited pronounced coda spectral peaking. This approach was successfully applied to other regions where it was observed that the coda-derived M_w estimates showed significantly smaller dependence on lateral path variation and source radiation anisotropy than the more conventional approaches such as $m_b(Pg)$, $m_b(Lg)$, and teleseismic m_b .

Key Words: regional magnitude, Lg coda, discrimination

OBJECTIVE

The goal is to find a method of obtaining a stable magnitude from as few as one station for small-to-moderate sized regional events. Because direct waves are sensitive to geologic structure between source and receiver as well as source radiation pattern, this requires multiple-station averaging to eliminate these undesirable effects. Scattered waves (Coda) average over the lithosphere's small-scale features as well as any source radiation pattern using only one station. In addition, we want to reduce the variability in spectral ratio measurements and use the source spectral shape to identify unusually shallow and deep events.

RESEARCH ACCOMPLISHED

We focused primarily on ABKT recordings of moderate-sized regional events that occurred in the Zagros Range in Iran. The epicentral distances to ABKT were generally around 1000 km. Four of these events were also recorded at station GNI in Armenia, also roughly 1000 km away. All of the events had globally averaged teleseismic m_b values from the USGS NEIC catalog. We first obtained event-averaged empirical Green's function envelopes for the region for narrow frequency bands ranging between 0.05 and 3 Hz (e.g., *Hartse et al.*, 1995). We then corrected for frequency-dependent path and site effects and calibrated against independent moment estimates. (See *Mayeda and Walter*, 1996, for details of the method).

Figure 1 shows coda-derived S -wave source spectra for events recorded at ABKT after all path corrections were performed. Estimates of M_w were obtained from the long-period spectral levels and are compared with teleseismic (CMT) and regional waveform modeling results in Figure 2a. As was found for the western United States (*Mayeda and Walter*, 1996), regional coda magnitudes in this region using a single station are in excellent agreement with network-derived estimates. In addition, inter-station variability is also shown to improve when using the coda spectra. Figure 3 shows that $m_b(P_g)$ measured at ABKT and GNI for common events are considerably more variable than M_w (coda), similar to results from the western United States. With these preliminary path and site calibrations we can now obtain stable estimates of moment and m_b for events that are too small to be recorded teleseismically or at multiple regional stations. This will be essential for low magnitude regional monitoring since a number of regional discriminants are functions of magnitude.

In addition to magnitude estimation, the coda derived source spectra can be used to identify very shallow ($< \sim 2$ km) and deep ($> \sim 60$ km) events. *Mayeda and Walter* (1996) found that NTS explosions, near-surface mine collapses, and very shallow earthquakes exhibited a pronounced spectral peak between ~ 0.2 to 0.8 Hz (Figure 4). This is likely a result of surface excitation that scatters into the coda in this pass band. For deep earthquakes in the Hindu-Kush region we also found peculiar spectral shapes, where the low frequencies are greatly diminished relative to the high frequencies (> 1 Hz). In this case, due to the large depth, surface wave excitation is diminished rather than enhanced as was found for the case of shallow sources.

CONCLUSIONS

The coda methodology for source spectra and magnitude estimation has been successfully applied to the western United States as well the Korea/Yellow Sea region. Our preliminary results for the Middle East region, specifically Iran, shows that the methodology is transportable, providing a means of obtaining stable, single station estimates of small-to-moderate sized regional events. A stable, accurate magnitude is necessary because some regional discriminants are functions of magnitude (e.g., *Walter et al.*, 1995; *Hartse et al.*, 1997). It is clear that subregions such as the Caspian Sea, Makran, Zagros, Hindu-Kush etc. will all require separate path corrections owing to the strong lateral geologic complexities of the Middle East.

References

- Hartse, H., S.R. Taylor, W.S. Phillips, and G.E. Randall, (1997). A preliminary study of regional seismic discrimination in Central Asia with an emphasis on Western China, *Bull. Seism. Soc. Am.* **87**, 551-568.
- Hartse, H., W.S. Phillips, M. C. Fehler, and L.S. House, (1995). Single-station spectral discrimination using coda waves, *Bull. Seism. Soc. Am.* **85**, 1464-1474.
- Mayeda, K., and W. R. Walter, (1996). Moment, energy, stress drop, and source spectra of western United States earthquakes from regional coda envelopes, *J. Geophys. Res.*, **101**, 11195-11208.
- Walter, W. R., K. Mayeda, and H. J. Patton, (1995). Phase and spectral ratio discrimination between NTS earthquakes and explosions, 1, Empirical observations, *Bull. Seismol. Soc. Am.*, **85**, 1050-1067.

**Work performed under the auspices of the U.S. Department of Energy by the Lawrence Livermore National Laboratory under contract W-7405-ENG-48.*

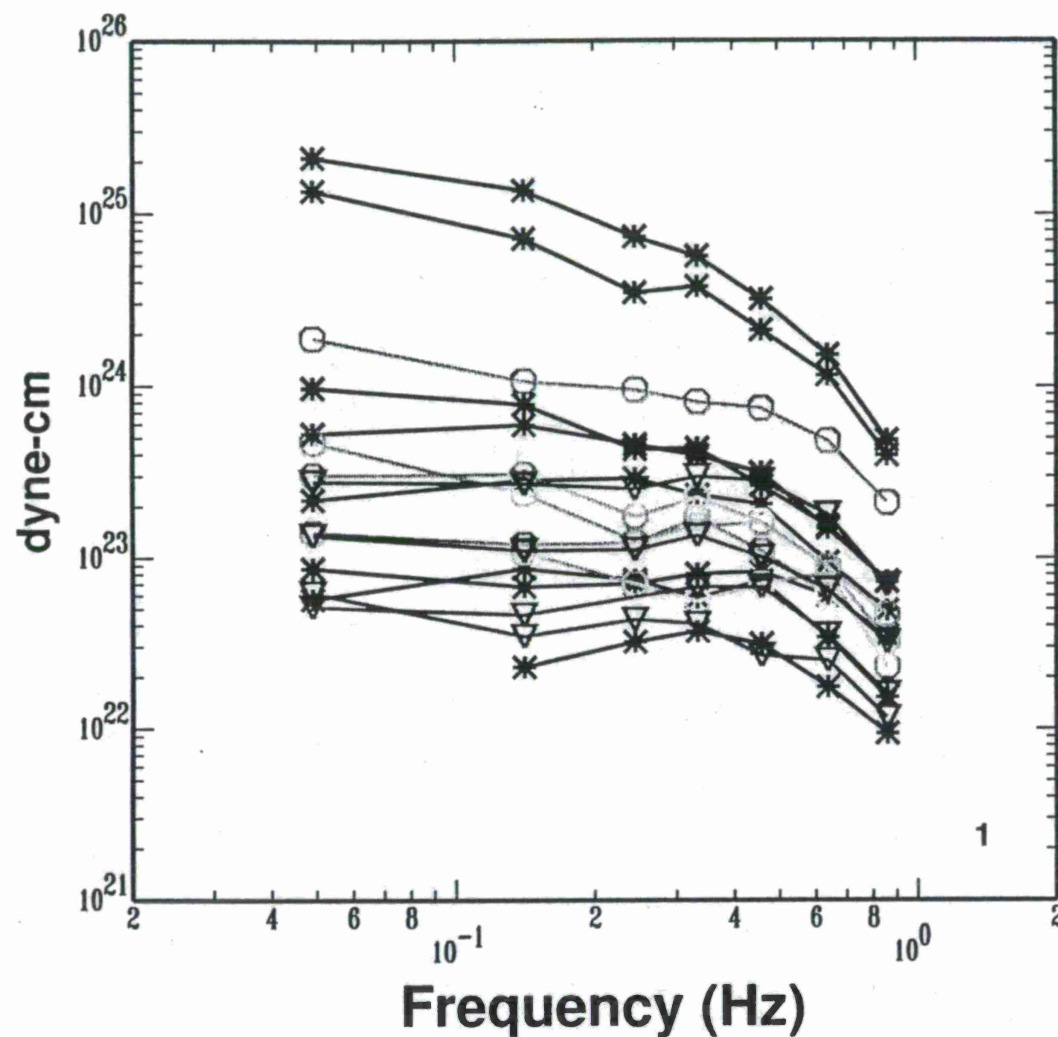


Fig. 1 We have collected regional, moderate-sized earthquakes located by the NEIC that were recorded at stations ABKT and GNI. Moments from the Harvard CMT catalog as well as moments derived from long-period regional waveform modeling were used to calibrate the coda-derived S-wave source spectrum. Our single-station moment estimates from our spectra agree very well with network averaged results. In addition, we used the higher frequencies (0.6-0.9 Hz) to derive a regional m_b scale that agrees well with the globally derived teleseismic USGS NEIC m_b . Above are coda-derived source spectra for events in the central Zagros (stars), north Zagros (circles) and Makran (triangles) regions of Iran ranging between m_b 4.3 and 6.0. All are roughly 1000 km from station ABKT.

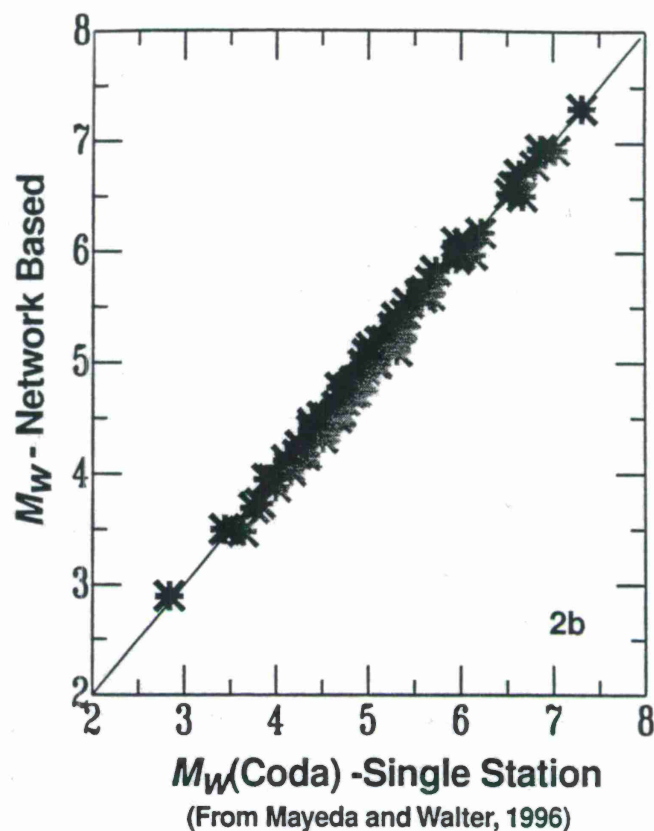
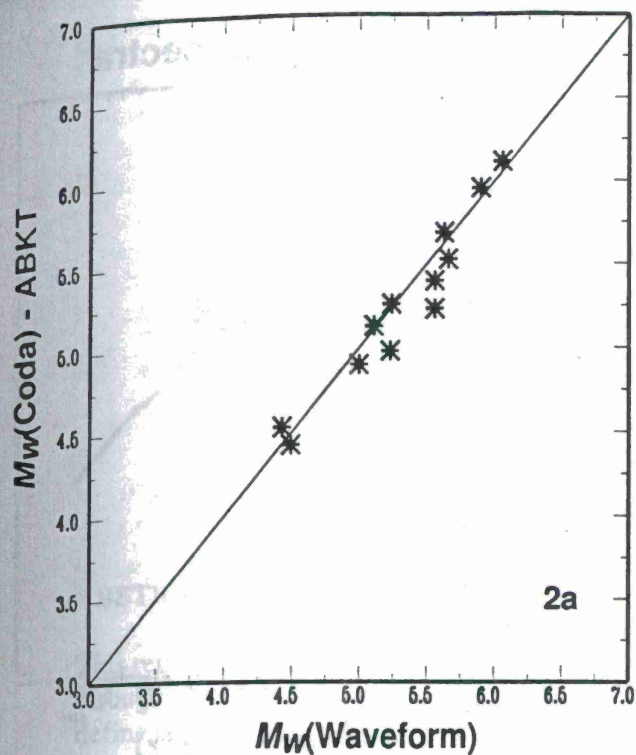


Fig. 2 Single station M_w estimates in Iran (fig. 2a) are comparable to results from the western United States (fig. 2b)

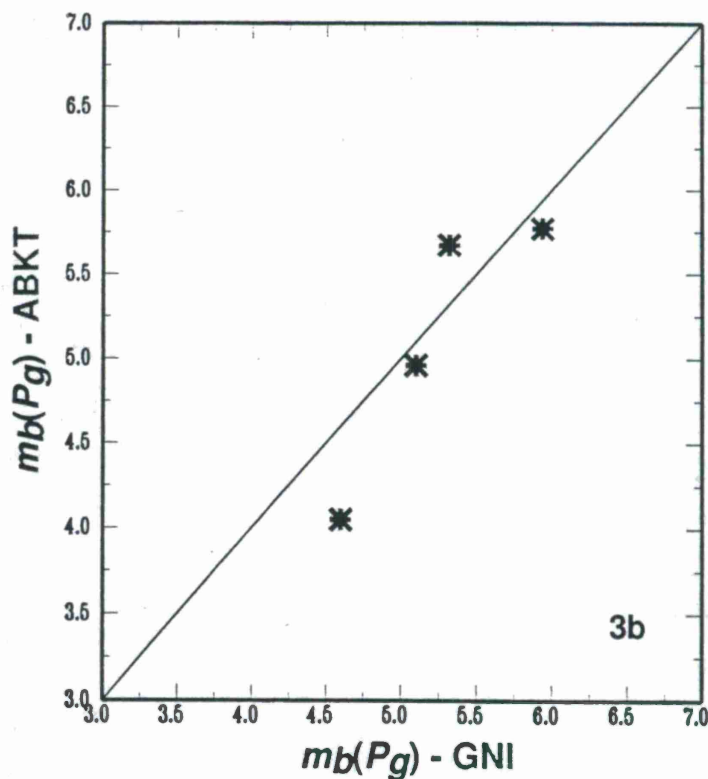
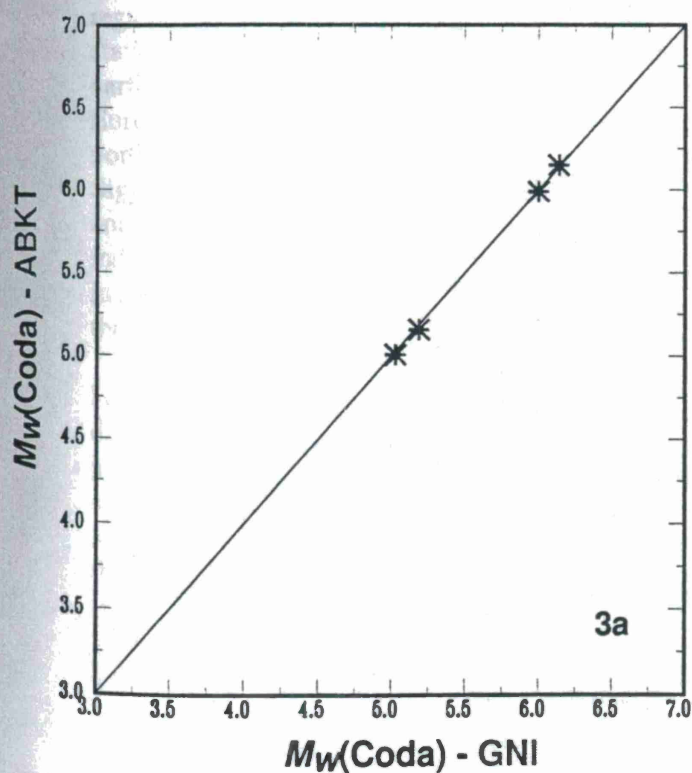


Fig. 3 Interstation variation using the coda (fig. 3a) is much less than magnitudes based on direct phases such as Pg (fig. 3b)

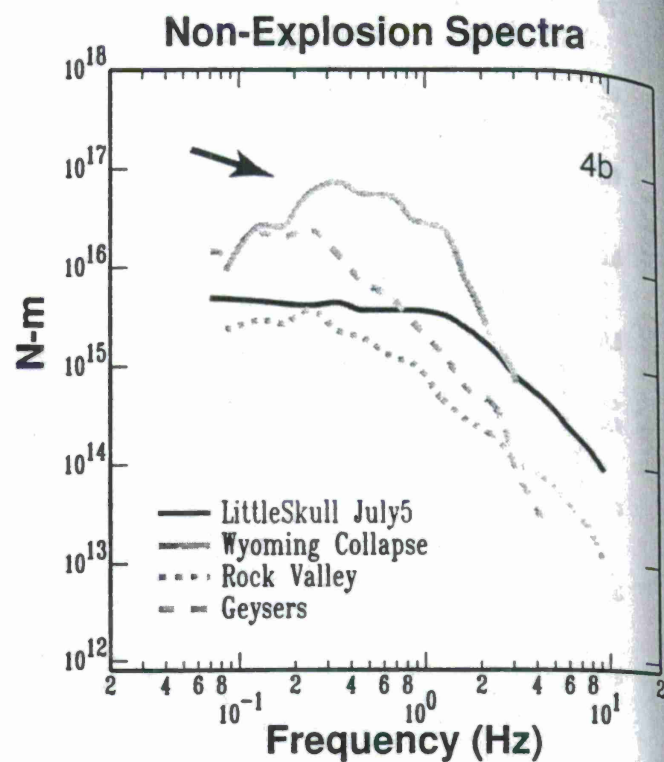
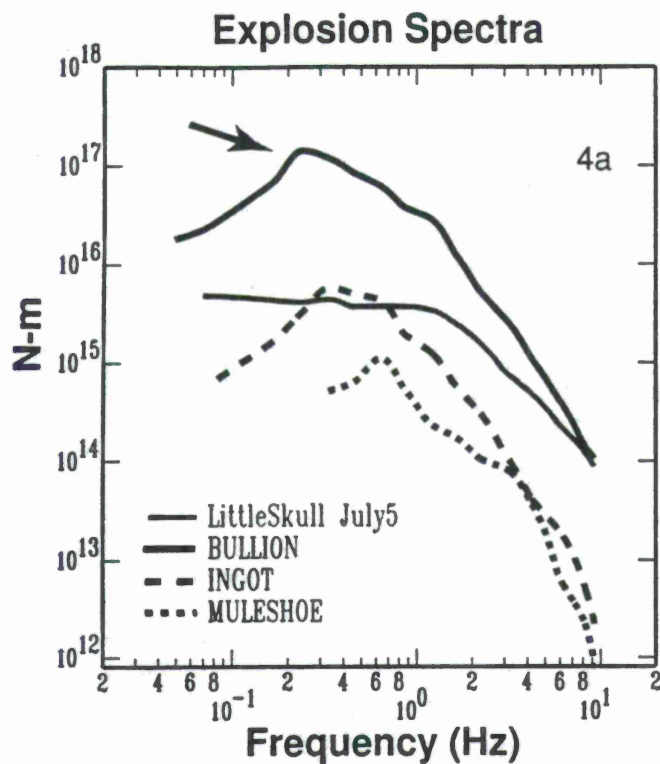


Fig. 4a.
Fig. 4b.

NTS explosions have a pronounced spectra peak relative to an NTS earthquake. Mining collapse events and shallow earthquakes also exhibit peaking.

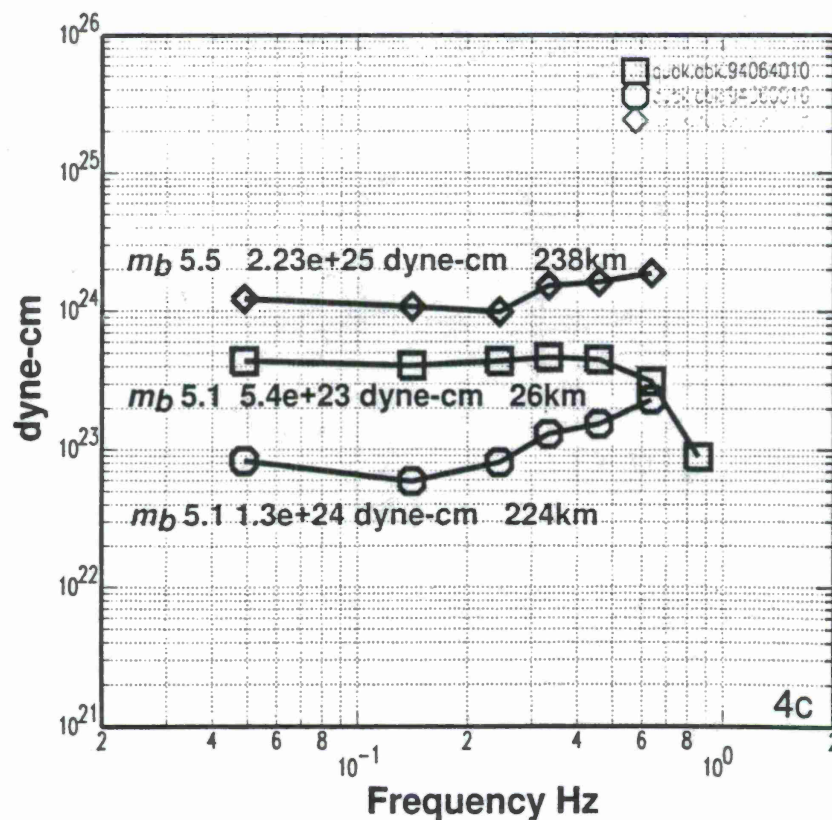


Fig. 4c.

Two deep Hindu-Kush events are compared with a normal depth event from the same region (□). The two deep events are deficient in low-frequency energy.

Surface Wave Group Velocity Dispersion Across Northern Africa, Southern Europe and the Middle East

Daniel E. McNamara, and William R. Walter
Lawrence Livermore National Laboratory

Shannon Hazler
University of Colorado

Sponsored by U.S. Department of Energy
Office of Nonproliferation and National Security
Office of Research and Development
Contract No. W-7405-ENG-48

ABSTRACT

This report presents preliminary results from a large scale study of surface wave group velocity dispersion throughout Northern Africa, the Mediterranean, Southern Europe and the Middle East. Our goal is to better define the 3D lithospheric shear-wave velocity structure within this region by improving the resolution of global surface wave tomographic studies. We hope to accomplish this goal by incorporating regional data, at relatively short periods (< 40 sec), into the regionalization of lateral velocity variation. Due to the sparse distributions of stations and earthquakes throughout the region (Figure 1) we have relied on data recorded at both teleseismic and regional distances. Also, to date we have concentrated on group velocity since valuable measurements can be made without knowledge of the source. The group velocity maps allow phase-match filtering, which can lower the threshold of M_s , an important discriminant measure.

In order to obtain surface wave group velocity throughout the region, vertical component teleseismic and regional seismograms were gathered from broadband, 3-component, digital MEDNET, GEOSCOPE and IRIS stations plus the portable PASSCAL deployment in Saudi Arabia. Figure 1 shows the distribution of earthquakes (black circles) and broadband digital seismic stations (white triangles) throughout southern Europe, the Middle East and northern Africa used in this study. The most seismicity active regions of northern Africa are the Atlas mountains of Morocco and Algeria as well as the Red Sea region to the east. Significant seismicity also occurs in the Mediterranean, southern Europe and throughout the high mountains and plateaus of the Middle East. To date, over 1300 seismograms have been analyzed to determine the individual group velocities of 7-150 second Rayleigh waves. Travel times, for each period, are then inverted in a back projection tomographic method in order to determine the lateral group velocity variation throughout the region.

Here we present preliminary Rayleigh wave group velocity maps for a range of periods (10-95 sec) and discuss initial interpretations. Significant lateral group velocity variation is apparent at all periods. In general, shorter periods (10-45 sec) are sensitive to crustal structure as seen by the relatively low velocities associated with large sedimentary features (eastern Arabian shield, Mesopotamian Foredeep, Eastern Mediterranean, Caspian Sea). At longer periods (50-95 sec), Rayleigh waves are most sensitive to crustal thickness and upper mantle shear-wave velocity structure. This is observed in the group velocity maps as low velocities associated with features as the Zagros Mountains, Iranian Plateau and the Red Sea. Analysis will eventually be expanded to include Love wave group velocities as well as Rayleigh and Love wave phase velocity. Knowledge of the lateral variation of group velocity and phase velocity will allow us to invert for shear velocity at each grid point. A detailed regionalization of shear-wave velocity will improve M_s estimates and event location capabilities throughout the region. Better M_s estimates and locations will improve our ability to reliably monitor the Comprehensive Test Ban Treaty (CTBT).

Key Words: Middle East, North Africa, Rayleigh waves, group velocity, dispersion

OBJECTIVE

The purpose of this research is to develop surface wave group velocity maps and to improve lithospheric shear wave velocity models for northern Africa and the Middle East. Rayleigh group velocity maps allow phase-match filtering, which has the potential to lower Ms thresholds. Ms is an important discriminant measure and could help identify smaller magnitude events. Improved shear velocity should improve event location capabilities throughout the region. Both improved identification and location capabilities are important to monitoring a CTBT. In order to obtain our objective we first estimate the lateral variation of Rayleigh and Love wave group and phase velocity using a backprojection tomography technique. Second, we invert the group and phase velocities at each grid point within the tomogram for shear-velocity structure. This work is on-going and to date, we have concentrated on the Rayleigh wave group velocity component of this study.

RESEARCH ACCOMPLISHED

Our procedure to accomplish the stated objectives has include the following steps: (1) waveform acquisition and dispersion measurement (2) backprojection data selection (3) backprojection and group velocity map construction (4) resolution analysis and (5) preliminary interpretations. Brief discussions of our procedural steps are presented below.

Obtaining Rayleigh Wave Group Velocity Dispersion Curves

To obtain the Rayleigh Wave dispersion curve a narrow-band-Gaussian filter is applied to the broadband vertical component, displacement seismogram over many different periods (Herrmann, 1973; Taylor and Patton, 1986) (Figure 2). The maximum amplitude at each period is picked on the envelope function and the arrival time corresponding to this maximum amplitude is used to compute the Rayleigh wave group velocity (Figure 3).

Backprojection of Travel Times for Lateral Group Velocity Variation

The Rayleigh wave travel time, for a given period, is expressed simply by:

$$(1) \quad t = Ds$$

t is the total travel time, D is source to receiver distance, s is slowness profile as a function of depth, $(1/v)$. For estimating lateral group velocity variations, the sampling region is gridded into a single layer and the slowness for each grid cell is determined.

The travel time equation then becomes:

$$(2) \quad t = \sum d_i s_i$$

where d_i is the distance the ray travels in cell i and s_i is the slowness in cell i .

The individual cell group velocity is calculated using a backprojection algorithm in the following sequence of actions. First, residuals are calculated from the mean fit to the travel time data for a given period. Secondly, using (2), slownesses are estimated as the weighted

mean of the apparent slownesses, t/D , of all rays traversing each cell. The factor used to weight the individual slownesses is the total ray path length within a particular cell. Between iterations, the model is smoothed in order to minimize extreme slowness estimates, due to poor sampling. Smoothing done by averaging each cell value with the surrounding eight cells. Using this new smoothed group velocity model, new residuals are calculated and the process is repeated until convergence is reached. Usually about 40-50 iterations were required for convergence. Convergence is declared when the rms residual improvement is less than 1% between iterations.

Data Selection

Waveforms used in this study were obtained from numerous network sources (IRIS, MEDNET, GEOSCOPE, AFTAC, PASSCAL) in many different tectonic environments. Earthquake mislocation is likely to be the largest source of error since station coverage is sparse throughout large portions of the region. For this reason we have applied strict selection criteria to the earthquakes used in this study order to assure that only high-quality Rayleigh wave travel times are used in the back-projection. Only PDE events with $m_b > 4.0$ (most >4.5) were included. To eliminate potential errors in the group velocity measurement process, such as cycle skipping, only travel times from high-quality (relatively continuous) dispersion curves were used. Qualitative assessments were made at the time of calculation and were used to eliminate spurious travel times. Also, initially travel time residuals resulting in a velocity deviation greater than 20% from the data set mean were eliminated (Figure 4).

After Applying the data selection criteria above, the remaining travel time residuals are likely due to lateral shear velocity variations within the lithosphere. The remaining residuals are then inverted in a backprojection tomography to determine the lateral variation of Rayleigh wave group velocity. Figure 5 shows one example 1019 travel times for 20 second Raleigh waves that met the criteria discussed above.

Resolution

A first-order, qualitative, measure of data set resolution can be obtained by inspecting the ray path distribution throughout the sampling region (Figure 5). Though ray path density is important, azimuthal sampling is most significant. For a more quantitative assessment, resolution is best investigated with synthetic travel times computed through laterally varying "checkerboard" test velocity models. Using the 20 second period as an example we compute the Rayleigh wave travel time for each path (Figure 5) through a model with $10^\circ \times 10^\circ$ checkers that vary in velocity by 5% about a mean of 2.95 km/s. The synthetic travel times are then inverted using the backprojection scheme described above. Our ability to reproduce the input model determines the resolution of the data set. As demonstrated in Figure 6, we are able to resolve the amplitude (5%) of the 10° anomalies throughout much of the Middle East, Mediterranean, Saudi Arabia and the northern most Africa, Resolution is significantly diminished throughout central Africa due to a lack of crossing ray paths (Figure 5).

Preliminary Results

Before interpretation of Rayleigh wave group velocity it is useful to understand how well the backprojection models explain the lateral variation of travel times. Travel time

residual reduction for the 20 second period data set is shown in Figure 7 as a series of histograms. With each successive iteration, residuals are reduced as the spike around 0 increases. This suggests that the resulting laterally varying velocity model sufficiently explains the residuals in the 20 second period data set. Iterations were allowed to continue until the rms residual improvement, between iterations, was less than 1%. Generally 40-50 iterations were required to satisfy this criterion.

Our results are preliminary and we are adding much additional data. Here we show preliminary Rayleigh wave group velocity maps for a range of periods (10-95 sec) and discuss initial interpretations. We observe significant lateral group velocity variation at all periods. In general, shorter periods (10-45 sec) are sensitive to crustal structure as seen by the relatively low velocities associated with large sedimentary features (Eastern Arabian shield, Persian Gulf, Eastern Mediterranean, Caspian Sea) (Figure 8). At the middle periods presented (~50 sec), Rayleigh waves are most sensitive to crustal thickness and topography on the Moho. This is observed in the group velocity maps as low velocities associated with features such as the Zagros Mountains and Iranian Plateau. At the longest periods presented (85-95 sec) sensitivity is greatest to lateral variations of the upper mantle shear velocity. Low group velocity is seen associated with the warm upper mantle beneath the Red Sea (Figure 8e).

CONCLUSION AND RECOMMENDATIONS

We find that Rayleigh wave group velocity models, for periods ranging from 10-100 sec, vary laterally across the region and diverge from global models obtained using longer periods. For this reason it is important to continue utilizing regional data to more accurately determine the lateral variation of shear-wave velocity across the region. We intend to do this by including additional raypaths in the backprojection procedure and expanding our analysis to Rayleigh phase and Love wave group and phase velocity.

References

- Herrmann, R. B., Some aspects of band-pass filtering of surface waves, *Bull. Seism. Soc. Am.*, 63, 663-671, 1973.
- Taylor, S. R., and H. J. Patton, Shear-velocity structure from regionalized surface-wave dispersion in the Basin and Range, *Geophys. Res. Lett.*, 13, 30-33, 1986.

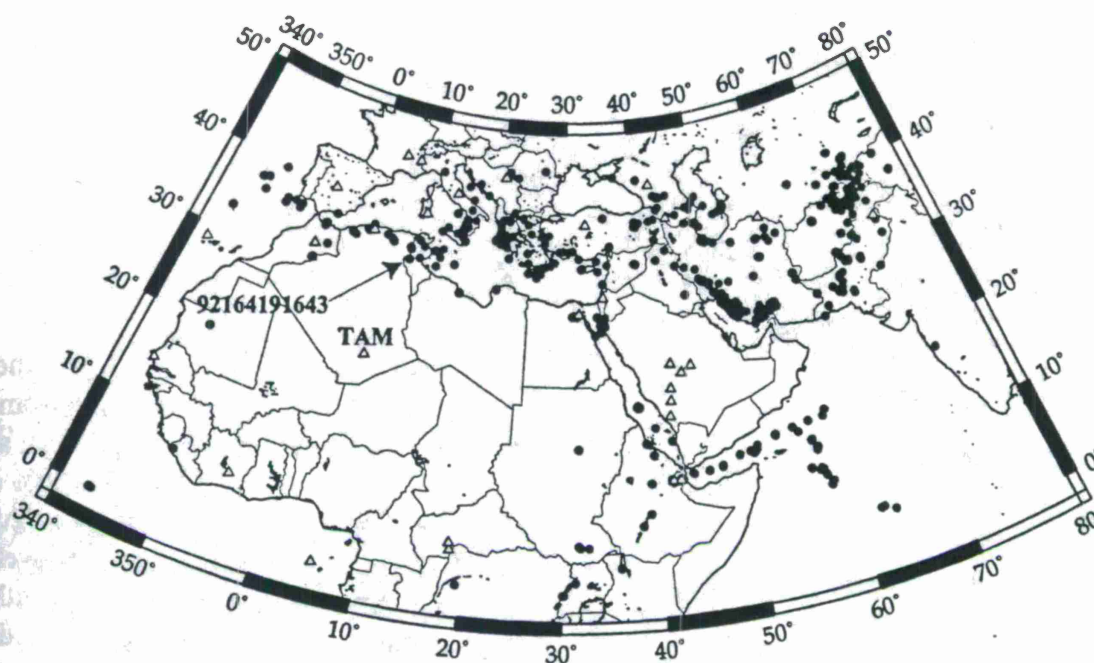


Figure 1: Map of Northern Africa, the Mediterranean, Southern Europe, the middle East and the Arabian Peninsula. Also shown are the recording stations (triangles) and the distribution of earthquakes used in the Rayleigh wave group velocity backprojection tomography. Tunisian earthquake, 92164191643 ($m_b=5.3$) and the GEOSCOPE station TAM are shown to illustrate Rayleigh wave group velocity measurement examples in Figures 2 and 3..

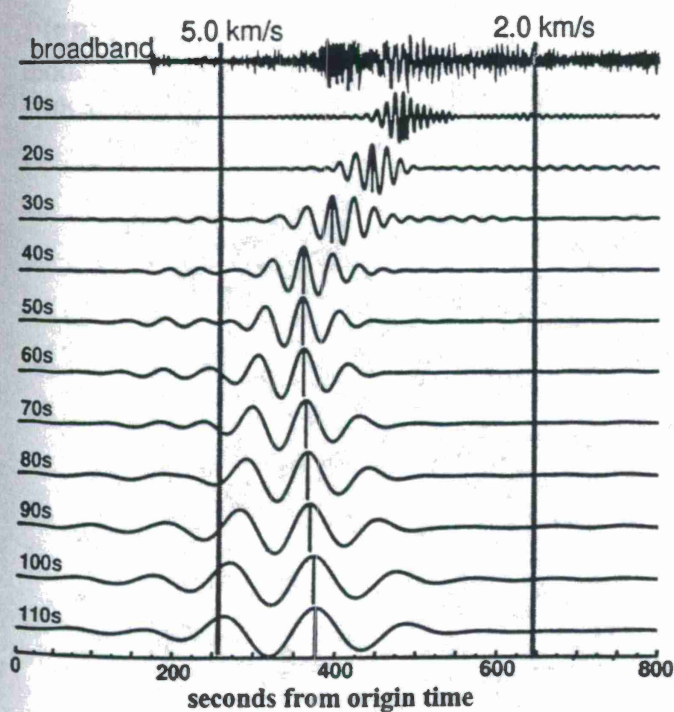


Figure 2: Rayleigh wave from earthquake 92164191643 ($m_b=5.3$) recorded at TAM narrow band filtered for a range of periods (10-110 sec). The Rayleigh wave travel time is taken as the maximum amplitude with the group velocity window of 2.0-5.0 km/s.

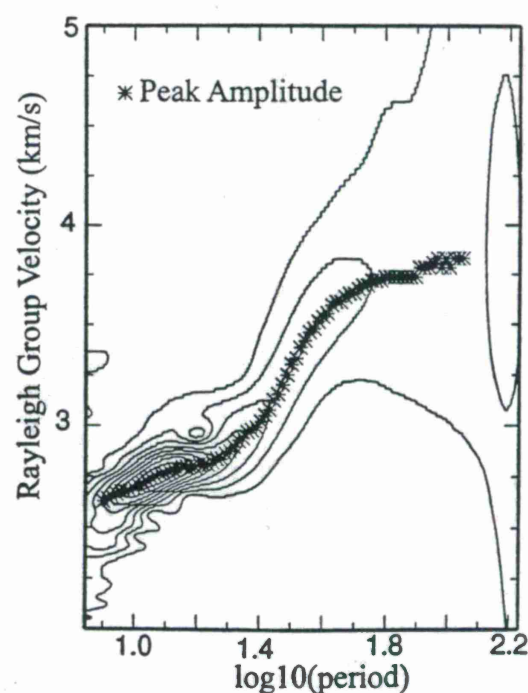


Figure 3: Contoured peak amplitudes for event 92164191643 at station TAM.

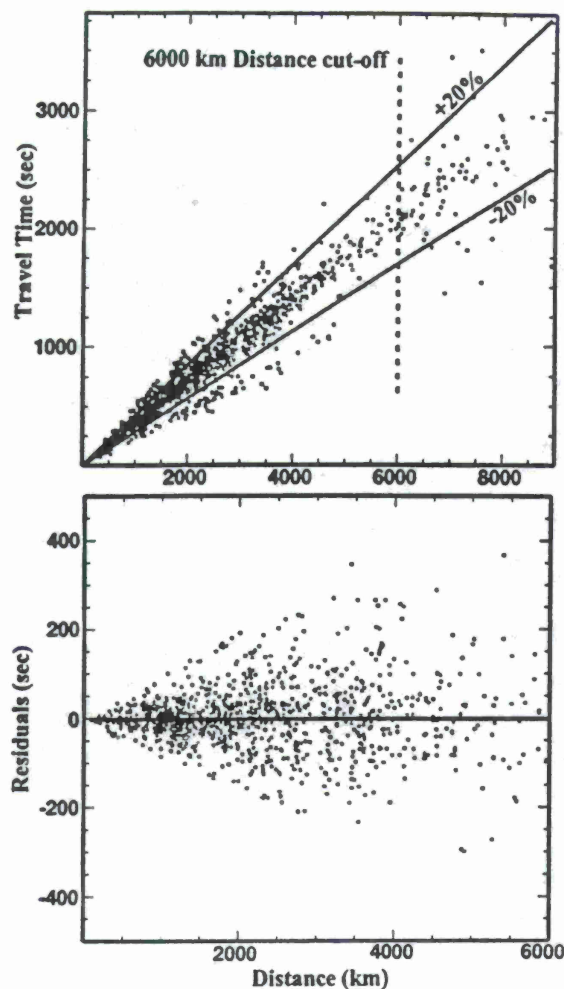


Figure 4: (A) Maximum amplitude travel time pick for 1317 20 second period Rayleigh waves from 572 earthquakes recorded at 31 stations. Individual apparent velocities were constrained to be less than 20% of the average group velocity for the entire data set (2.95 km/s). (B) 1019 20 second period Rayleigh wave travel time that passed the data selection criteria shown with a reducing velocity of 2.95 km/s. Remaining residuals due to lateral velocity variation.

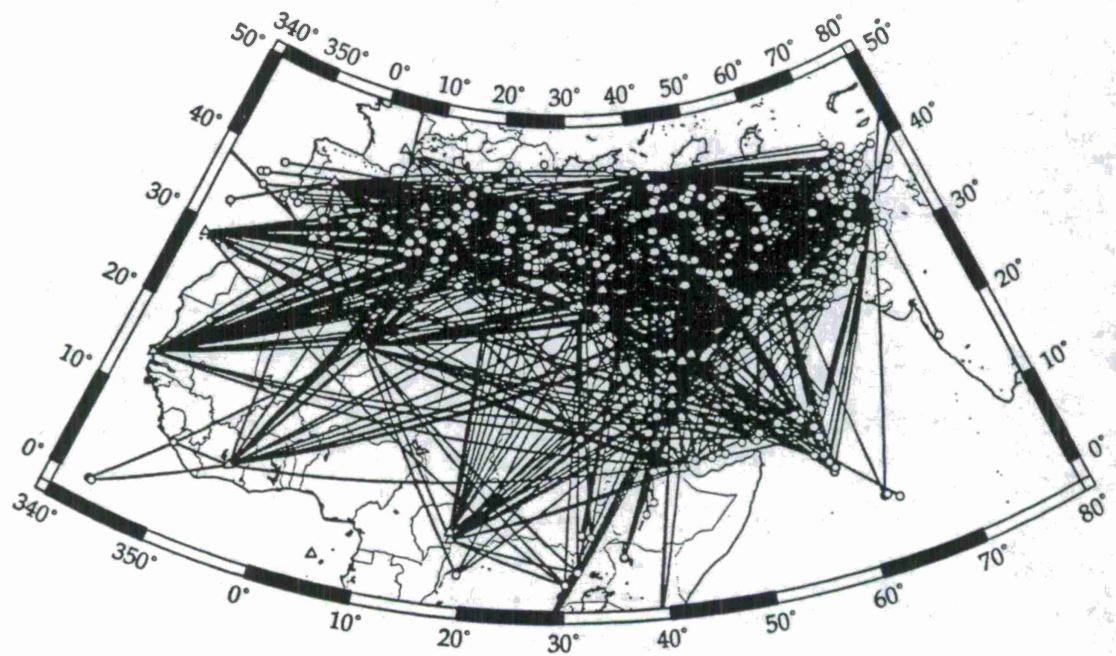


Figure 5: Ray paths for 1019 20 second Rayleigh waves that met the travel time selection criteria and used in the backprojection procedure to determine the lateral distribution of 20 Rayleigh wave group velocity. Triangles are the recording stations and circles are earthquakes.

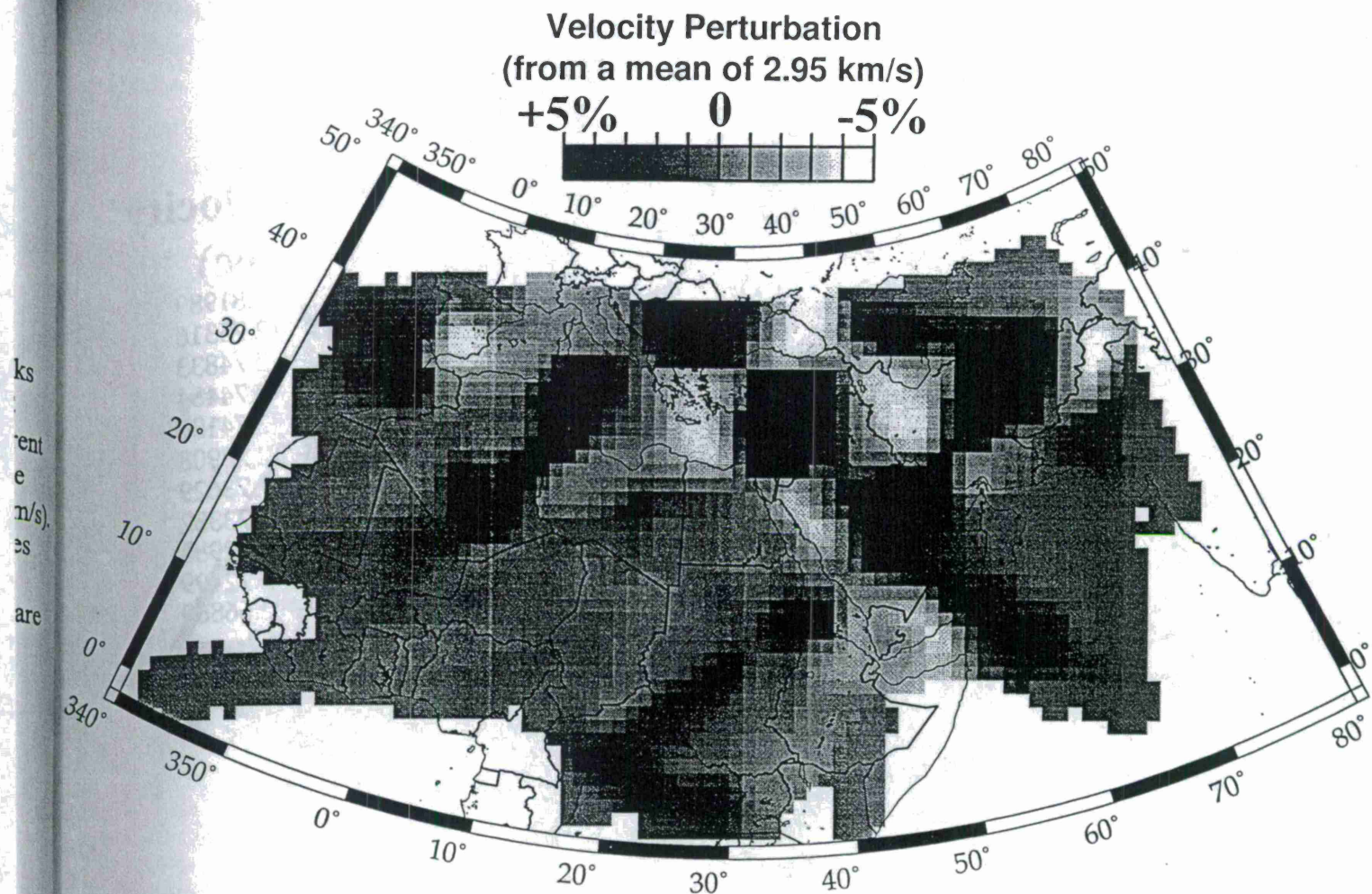


Figure 6: Inversion results from input velocity models used to investigate data set resolution. Input model velocity anomalies alternate in a checkerboard pattern. Each checker is a $10^\circ \times 10^\circ$ square with a velocity perturbation of 5% from the mean. This is an example of the 20 second period data set.

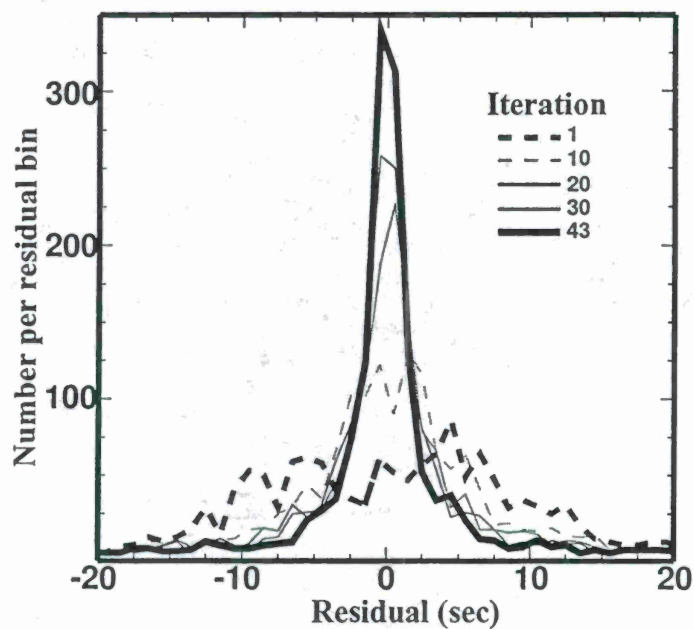


Figure 7: Histograms of residuals for several iterations. Convergence is reached at iteration 43 and residuals are significantly reduced as shown by the spike around zero. This is an example of the 20 second period data set.

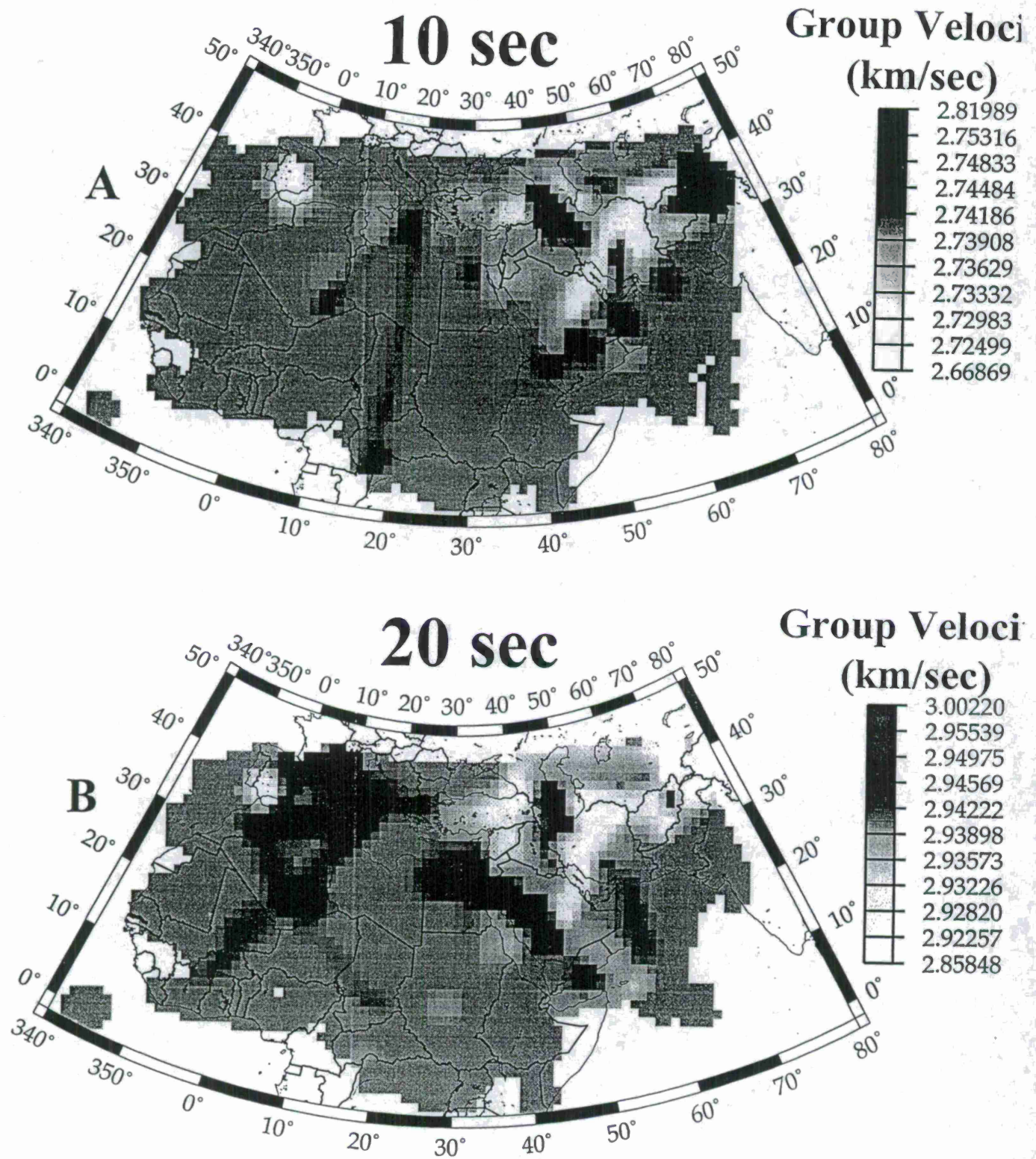


Figure 8: Rayleigh wave group velocity maps (A) 10 second period (B) 20 second period.

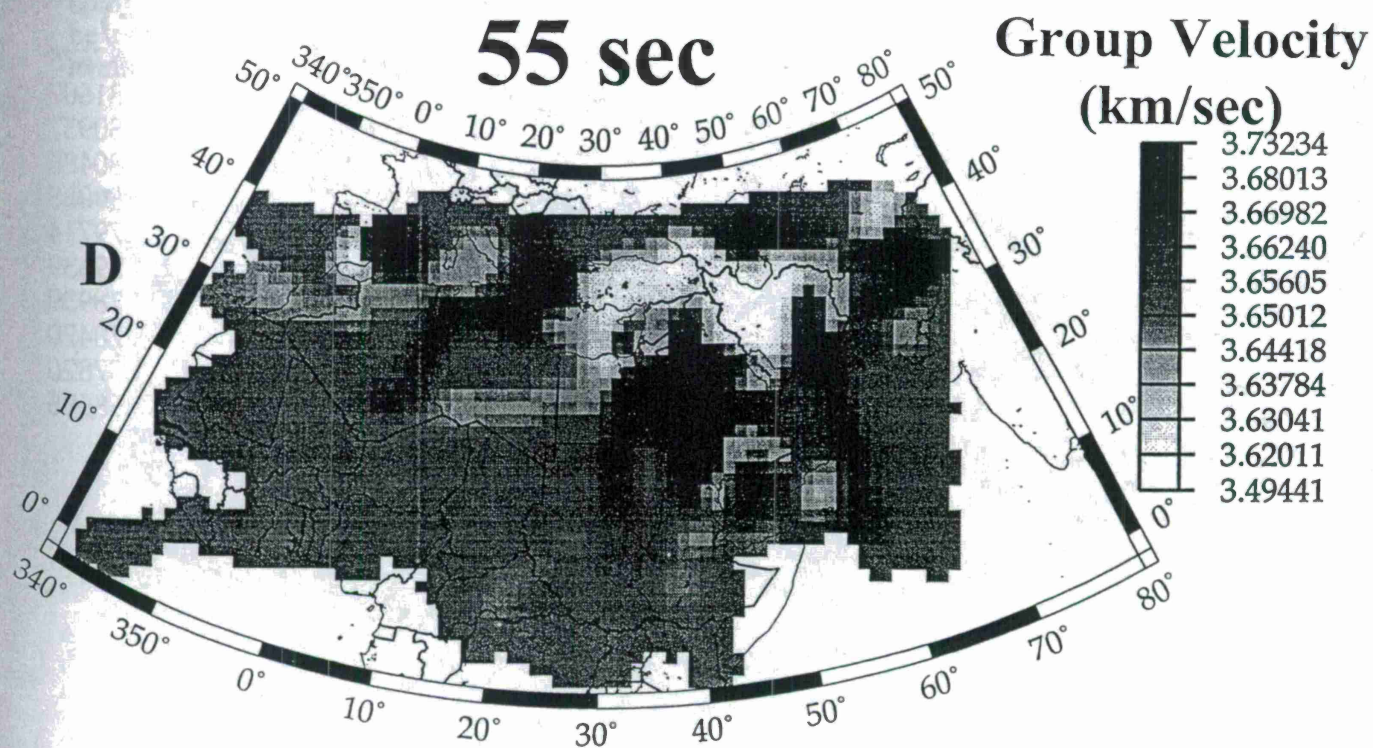
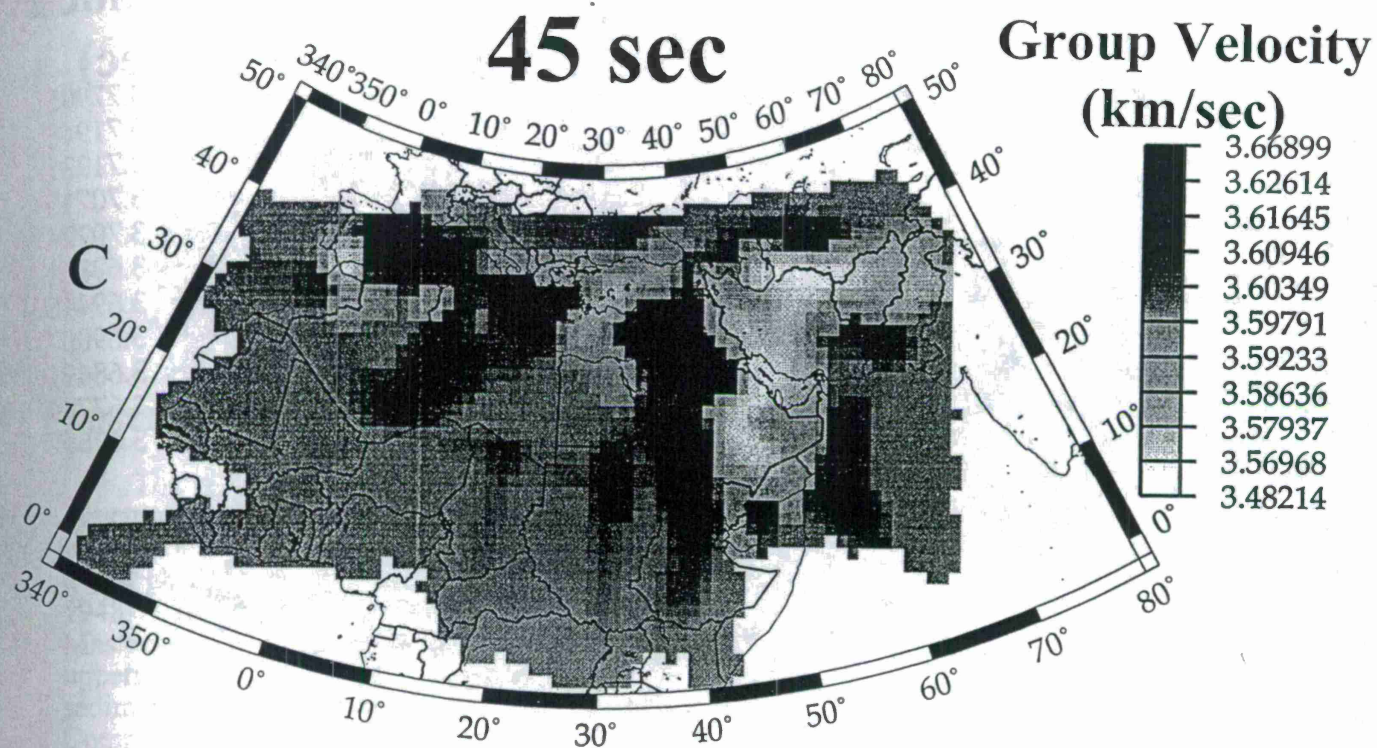


Figure 8: Rayleigh wave group velocity maps (C) 45 second period (D) 55 second period.

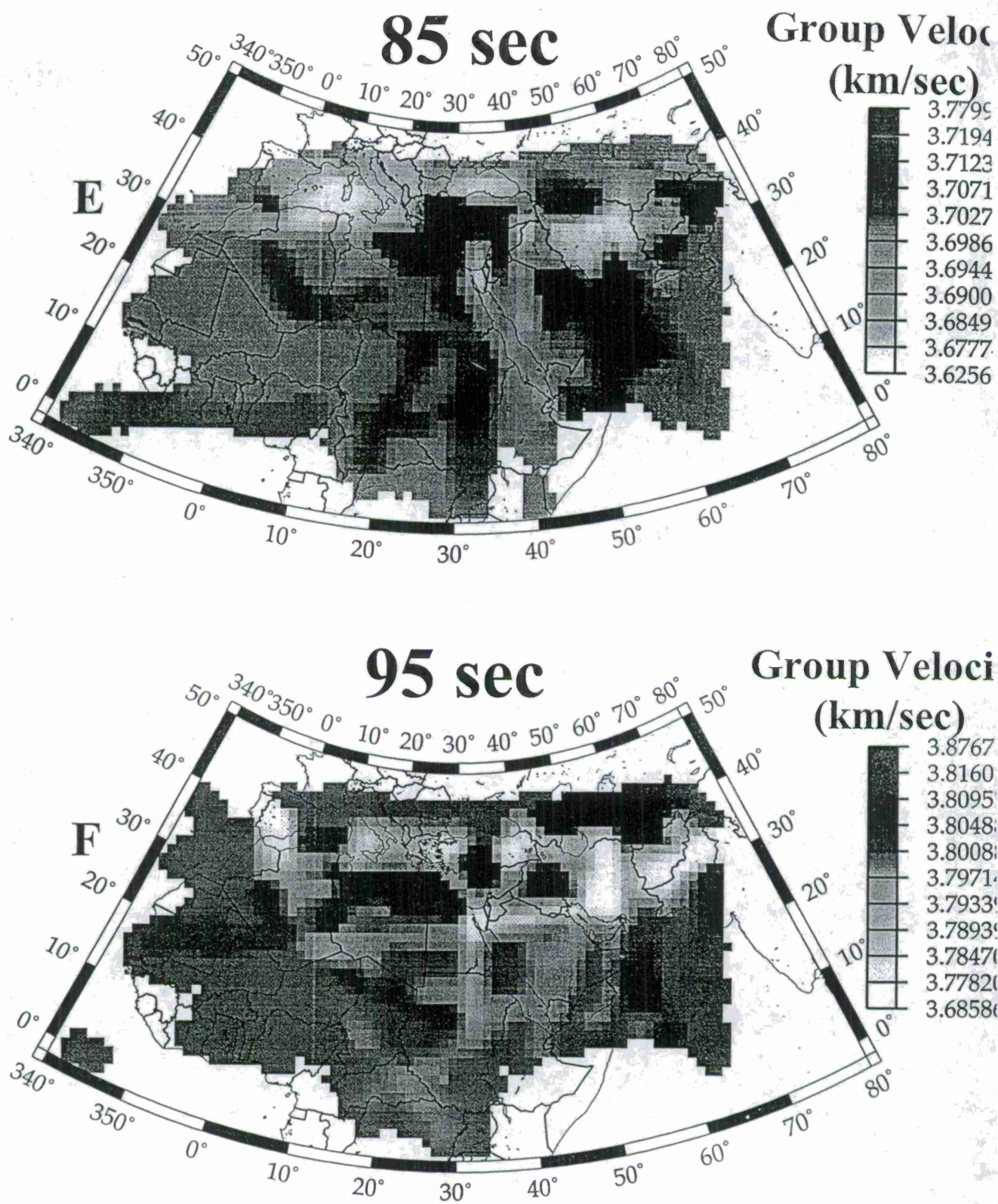


Figure 8: Rayleigh wave group velocity maps (E) 85 second period (F) 95 second period.

A GLOBAL CRUSTAL MODEL FOR CTBT MONITORING: CRUST 5.1

Walter D. Mooney (1), Gabi Laske (2), and T. Guy Masters (2)

**(1) U.S. Geological Survey, 345 Middlefield Road, MS 977,
Menlo Park, CA 94025 USA**

FAX: 415-329-5163, email: mooney@andreas.wr.usgs.gov

**(2) IGPP, Scripps Institution of Oceanography,
University of California San Diego
La Jolla, CA 92093-0225 USA**

FAX: 619-534-5332, email: glaske@ucsd.edu; gmasters@ucsd.edu

Sponsored solely by the U.S. Geological Survey

ABSTRACT

There are numerous applications for a global model of the seismic velocity and density structure of the Earth's crust and uppermost mantle. One application is to the monitoring of regional and global seismicity, as required by the Comprehensive Test Ban Treaty. We describe a new global model for the Earth's crust based on seismic refraction data published in the period 1948-1995 and a detailed compilation of ice and sediment thickness (Mooney, Laske, and Masters, 1997). Our model (CRUST 5.1) consists of 2,592 $5^\circ \times 5^\circ$ tiles in which the crust and uppermost mantle are described by eight layers: (1) ice, (2) water, (3) soft sediments, (4) hard sediments, (5) crystalline upper, (6) middle, and (7) lower crust, and (8) uppermost mantle. Compressional wave velocity in each layer is based on field measurements, and shear wave velocity and density are estimated using recently published empirical V_p - V_s and V_p -density relationships. This global crustal model is based on substantially more data than previous models and differs from them in many important respects. The model CRUST 5.1 provides a complete description of the physical properties of the Earth's crust at a scale of $5^\circ \times 5^\circ$, and can be used for a wide range of seismological and non-seismological problems. This model is available by anonymous ftp through the authors. It is already in widespread use.

Keywords: crustal structure, global, even location, refraction, P-wave, S-wave, density

OBJECTIVE

Monitoring under the CTBT requires strict locations of questionable events. In order to constrain the area in which an event has occurred, it is necessary to have a good model of the crustal structure. The work summarized in this paper provides one of the most accurate and complete models of the crustal structure of the world.

RESEARCH ACCOMPLISHED

Introduction

Previous global crustal models have provided various levels of detail. Soller et al. (1982) presented a crustal thickness map but did not specify seismic velocities or densities. Hahn et al. (1984) presented a model wherein the crustal structure was described in terms of irregularly shaped regions, each with a uniform structure. More recently, Tanimoto (1995) reviewed the crustal structure of the Earth using a wide range of seismic data, and Nataf and Ricard (1996) presented a model for the crust and upper mantle on a $2^\circ \times 2^\circ$ scale (3SMAC). This latter model was derived using both seismological data and non-seismological constraints such as chemical composition, heat flow and hotspot distribution, from which estimates of seismic velocities and the density in each layer were made.

We describe a new global crustal model (Mooney, Laske, and Masters, 1997) that is based on significantly more data than previous models. Compiling a new global crustal model is timely because of the availability of a large body of new data. Our new global model for the Earth's crust (CRUST 5.1) is based on an extensive compilation of information through the year 1995 (Fig. 1). Published interpretations of the seismic velocity structure of the crust are now numerous enough and cover sufficiently diverse geological settings that it is possible to calculate statistical averages for various geological settings such as Precambrian shields, extended continental crust, and passive margins. These statistical averages define a set of standard crustal sections (referred to here as crustal types). For the vast continental regions where, as yet, no seismic measurements are available, such as large portions of Africa, South America, and Greenland, we predict the crustal structure. Our global crustal model can be used for a wide range of geophysical calculations of Earth structure, including monitoring of the Comprehensive Test Ban Treaty.

The Global Crustal Model

Our purpose is to create a model for the seismic velocity (V_p and V_s) and density structure of the crust and uppermost mantle that is at a large enough scale to be commensurate with the (non-uniform) global distribution of seismic field observations but that is also at a small enough scale to resolve significant lateral variations in crustal properties. To meet these competing goals, we have constructed our model using $5^\circ \times 5^\circ$ tiles that measure 550 km by 550 km at the Equator. In each tile, crustal properties are described by seven layers: (1) ice, (2) water, (3) soft sediments, (4) hard sediments, (5) crystalline upper, (6) middle, and (7) lower crust. An eighth layer is included to describe the elastic properties and density immediately below the Moho since this information is readily obtained from the seismic refraction profiles compiled here. Topography and bathymetry are provided as a separate file. Compressional wave velocity in each layer is based on field measurements, and shear wave velocity and density are estimated using empirical V_p - V_s and V_p -density relationships.

Since there are 2592 tiles in our $5^\circ \times 5^\circ$ model and more than 2000 available field measurements of oceanic and continental crustal structure, a reasonable approach is to generalize the field measurements into a limited number (14) of primary crustal types. These are: (1) Archean; (2) Early/middle Proterozoic; (3) Late Proterozoic; (4) Phanerozoic undivided; (5) Platforms; (6) Highly Extended Crust; (7) Orogens; (8) Forearc; (9) Continental magmatic arc; (10) Submarine plateau; (11) Shelf; (12) Continental Margin; (13) Oceanic island (e.g., Hawaii, Iceland); (14) ocean crust. As is evident, the Precambrian shields were divided into three age groups: Archean, Early-Middle Proterozoic, and Late Proterozoic. Precambrian platforms are a

separate crustal type because of the highly variable thickness of sediments. Where possible, Phanerozoic crust was divided into tectonic setting (extended crust, orogen, forearc, continental arc, etc.). Continental shelves, oceanic plateaus and ocean-continent transitions are primary crustal types. The crustal structure used for the ocean basins is a simple 4-layer approximation of published average crustal model. On continents, the average crustal structure for each primary type was statistically determined (Fig. 2) from the field measurements indicated on Fig. 1.

The Sedimentary Layers

An accurate description of the global distribution of sediments and the determination of their physical properties was a major aspect of this study. This was deemed necessary in view of the low elastic velocities and densities of some sedimentary basins that results in these basins having a major effect on all geophysical measurements. This information was compiled on a $5^\circ \times 5^\circ$ grid from the published literature. The densities of the continental sediments were estimated using the velocity/density relationship of Ludwig et al. (1970).

The sedimentary layers in the oceans were compiled from digital data files, maps and atlases. The mean velocity in a sedimentary layer is easily recovered from the sediment thickness using regression formulae. Vast portions of the oceanic crust are covered with 150 m or less of soft sediments. Young oceanic crust has little or no sedimentary cover, and older crust, particularly at low latitudes, has the greatest sedimentary thickness (500 m).

Some of the thickest sedimentary accumulations occur at continental margins and inland seas. For example, sediment thickness in the Bay of Bengal and Arctic Ocean is greater than 10 km locally, and the Red Sea and Mediterranean are underlain by thick sequences of evaporates. Much of the Gulf of Mexico is also covered by thick sequences of sediments and salt deposits. Fortunately, most of these regions have been extensively studied in the course of hydrocarbon exploration, and much information is available regarding the seismic structure of the sedimentary basins at continental margins.

The Crystalline Crust of the Continents and their Margins

The crystalline continental crust has been parameterized in terms of three layers, in agreement with recent summaries of continental crustal structure (Meissner, 1986; Mooney and Braile, 1989; Mooney, 1989; Holbrook et al., 1992; Christensen and Mooney, 1995; Pavlenkova, 1996). The upper crust is defined as the portion of the crust with a P-wave velocity of 5.7-6.3 km/s, and the middle and lower crust by the P-wave velocity of 6.4-6.7 km/s and 6.8-7.4 km/s, respectively. The distribution of continental seismic refraction profiles compiled for this study is shown in Figure 1. Data were compiled from the published literature and from a limited number of unpublished reports. The published literature appears in the years 1948-1995 (Christensen and Mooney, 1995), and includes journal articles, monographs, and special publications such as meeting proceedings, governmental open-file reports, and annual reports of research institutions. Unpublished literature primarily consists of high-quality technical reports of recent field measurements that have been issued prior to journal publication. The shear-wave velocity within the crust has been determined from (1) seismic refraction measurements, where available, and (2) by converting the compressional wave model into a shear wave model using estimated V_p/V_s ratios for each crustal layer determined from field and laboratory measurements (Christensen, 1996). The estimation of crustal density from compressional-wave velocity is non-unique, as attested by the numerous studies that have attempted to estimate crustal density from combined modeling of seismic and gravity data. However, since we are describing $5^\circ \times 5^\circ$ cells, small-scale density inhomogeneities are less important. For the estimation of density at depth, we use the linear regression lines of Christensen and Mooney (1995).

The Crystalline Oceanic Crust

Seismic refraction studies show that the oceanic crust is 6-7 km thick. The crystalline portion of our average oceanic model is a simple 3-layer approximation of previously published standard models. The first layer of the 3-layer crystalline crust (oceanic layer 2) includes pillow

basalts and sheeted dikes. This layer has an average V_p velocity of 5.0 km/s. The lower two layers represent the gabbroic layer with a slightly positive velocity gradient (known as oceanic layer 3). Oceanic layer 3 was subdivided into two layers to conform with the three-layer description of the continental crystalline crust. The P-wave velocities of these layers are 6.6 km/s and 7.1 km/s.

Global Crustal Thickness

The crustal thickness of our model is shown in Fig. 3. In areas with good data coverage crustal thickness is very similar to existing continental-scale models (e.g., compare Eurasia with Meissner, 1986, and North America with Mooney and Braile, 1989). In the oceans, tiles with unusually thick crust correspond to the locations of the largest plateaus. Most of these areas have not been accounted for in previous models. There is also generally good agreement with the crustal thickness of model 3SMAC of Nataf and Ricard (1996), who used different data sources for their compilation. The largest differences between their model and ours occur where constraints from seismic refraction data are sparse (e.g. Africa, Greenland, and Antarctica).

The Moho in our model is located at greater depth in some areas than previous models; especially those with poor data coverage such as Africa and South America (Fig. 3). Our crustal thickness (40 km) for the vast shield areas of Africa and South America is in excellent agreement with the global average for shield areas (Fig. 2), whereas the thin (30 km) crust in the model of Soller et al. (1982) is clearly inconsistent with these statistics. The data coverage in Australia has increased tremendously since the publication of Soller et al. (1982), and our model displays a slightly deeper (by approx. 5 km) Moho. In northeastern Eurasia, the Moho lies substantially deeper in CRUST 5.1 (as it does in 3SMAC of Nataf and Ricard, 1996) than in the model of Soller et al. (1982). In this part of the continent, the Moho depth is constrained quite well by recently released data so that, again, we have more confidence in our model.

The Uppermost Mantle

The P-wave velocity of the uppermost mantle (P_n) has been well determined beneath the continents and oceans from seismic refraction measurements. For the uppermost mantle, we assign a mean seismic velocity to each tile. The average P_n velocity beneath continentals is 8.09 ± 0.20 km/s (Christensen and Mooney, 1995), and the average oceanic P_n velocity is 8.15 ± 0.31 km/s (Christensen and Salisbury, 1975). In our model, the P_n velocity ranges from 7.8 km/s for regions of high heat flow up to 8.2 km/s under shields and platforms. This variation (7.8-8.2 km/s) represents less than half the range in seismic velocity reported for individual seismic refraction profiles (7.6-8.6 km/s). Reliable S-wave velocity determinations for the uppermost mantle (S_n) are less common but are generally consistent with a Poisson's ratio of approximately 0.26. This value, which we have adopted, agrees with that derived from the assumed upper mantle composition of olivine and pyroxene (Christensen, 1996).

The Crustal Model and Mantle Tomography

For continental paths, Love waves with a period of 40 s are dominantly sensitive to crustal structure. In fact, Love wave phase velocities at shorter periods (e.g., Ekström et al., 1997) could be used in the future to further refine crustal models where no refraction seismic data are available.

We have evaluated the seismological effects of CRUST 5.1 by comparing observed short period (40s) Love wave phase velocities with those predicted by the crustal model. This comparison indicates that our model provides a good match to the amplitude and areal extent of phase velocity anomalies that are associated with variations in the thickness of the continental crust and large sedimentary basins.

The signal in the map (Fig. 4a) is greatly decreased (by a factor of 1.7) by the crustal correction (Fig. 4c). The remaining signal is primarily produced by an age-dependent cooling of the oceanic lithosphere, which is not included in the crustal model. For comparison, we also

show the crustal correction for a model (Smith, 1989) used in earlier studies (Fig. 4d). This model includes the Moho variation of Soller et al. (1982) and estimated average seismic velocities and densities for continents and oceans (Smith, 1989) (referred to as the "Soller model" hereafter). It is important to note that the resulting map (Fig. 4d) does not display the pronounced high velocity regions beneath the shields that CRUST 5.1 produces, and there are many other regional differences. Since 40 s Love waves are sensitive to upper mantle structure below 60 km, it is to be expected that the high-velocity mantle beneath shields will be clearly evident in the corrected maps. Based on this comparison, we are confident that the crustal corrections from CRUST 5.1 are more accurate than the corrections derived from the Soller model.

CONCLUSIONS AND RECOMMENDATIONS

The monitoring of regional and global seismicity requires a robust seismic velocity model for the global crust and uppermost mantle. We have developed such a model for the seismic velocities (V_p and V_s) and density structure of the crust and uppermost mantle that may be used for a wide range of geophysical investigations (Mooney, Laske, and Masters, 1997). We have chosen a scale of $5^\circ \times 5^\circ$ for the model because this scale provides a reasonable compromise between the desire for resolution and the geographical distribution of data. The model (CRUST 5.1) is based on more complete information than previous models. Specifically, we have included: (1) the thickness and physical properties of all ice and sedimentary accumulations; (2) the physical properties of normal and anomalous oceanic crust as reported in recently published syntheses of marine seismic measurements; (3) a detailed compilation of continental seismic refraction profiles; (4) statistical estimates of the crustal structure in regions without field measurements based on the average crustal structure determined for 14 standard crustal types; (5) reliable estimates of shear wave velocity and density based on recently published empirical V_p - V_s and V_p -density relationships.

We have evaluated the seismological effects of this model by comparing observed short period (40s) Love and Rayleigh wave phase velocities with those predicted by the crustal model. This comparison indicates that our model provides a good match to the amplitude and areal extent of phase velocity anomalies that are associated with variations in the thickness of the continental crust and large sedimentary basins. We have applied the crustal correction to observed surface wave phase velocity maps to isolate those features that are due to variations in upper mantle structure (Mooney, Laske, and Masters, 1997). The most obvious features in these corrected maps is the enhanced high velocity anomalies under shields. An important factor in mapping these features (especially at long periods) is an accurate knowledge of the contrast between continental and oceanic crustal structure.

There are two primary limitations to this model. The first is the cell size ($5^\circ \times 5^\circ$), which measures 550 km by 550 km at the Equator. This cell size is too coarse to permit an accurate model of many important crustal features (e.g., narrow mountain belts or rifts) other than by using a weighted average to account for lateral variations within a cell. It is possible to further refine this map to a $2^\circ \times 2^\circ$ scale, but significantly more extrapolation of crustal properties would be involved. As global datasets become more complete and processing techniques evolve, it will be possible to better constrain a crustal model by using observations of short period surface wave dispersion (Ekström et al., 1997). For the present, our new model, CRUST 5.1, provides the most accurate mapping of the physical properties of the crust and uppermost mantle available at a $5^\circ \times 5^\circ$ scale. This model is available via ftp through the authors, and is already in widespread use.

Acknowledgments: Many people at the US Geological Survey assisted with compiling seismic refraction data: G. Chulick provided continental refraction data ("Seisprof"). We thank G. Ekström, J. Tromp and E. Larson for making available their global surface wave dispersion maps, and A.M. Dziewonski and J.R. Filson for encouragement and advice. This research was

financed by the USGS Continental Surveys Program and National Science Foundation grants EAR-94-18063 and EAR-94-05948.

REFERENCES

- Christensen, N.I., Seismic velocities, in *Handbook of Physical Properties of Rocks*, vol. 2, edited by R.S. Carmichael, pp. 1-228, CRC Press, Boca Raton, Fla., 1982.
- Christensen, N.I., Poisson's ratio and crustal seismology, *J. Geophys. Res.*, **101**, 3139-3156, 1996.
- Christensen, N.I., and W.D. Mooney, Seismic velocity structure and the composition of the continental crust: a global view, *J. Geophys. Res.*, **100**, 9761-9788, 1995.
- Christensen, N.I., and M.H. Salisbury, Structure and composition of the lower oceanic crust, *Rev. Geophys. Space Phys.*, **13**, 57-86, 1975.
- Ekström, G., J. Tromp, and E.W. Larson, Measurements and global models of surface wave propagation, *J. Geophys. Res.*, 8137-8157, 1997.
- Hahn, A., H. Ahrendt, J. Meyer, and J.-H. Hufen, A model of magnetic sources within the earth's crust compatible with the field measured by the satellite magsat, *Geologisches Jahrbuch*, **A75**, 125-156, 1984.
- Holbrook, W.S., W.D. Mooney, and N.I. Christensen, The seismic velocity structure of the lower continental crust, in *The lower continental crust*, edited by D.M. Fountain, R. Arculus and R. Kay, Elsevier, New York, 1-43, 1992.
- Laske, G., and G. Masters, Constraints on global phase velocity maps by long-period polarization data, *J. Geophys. Res.*, **101**, 16,059-16,075, 1996.
- Meissner, R., *The Continental Crust; A Geophysical Approach*, 426 pp., Academic Press, San Diego, 1986.
- Mooney, W.D., Seismic methods for determining earthquake source parameters and lithospheric structure, in *Geophysical Framework of the Continental United States*, edited by L.C. Pakiser and W.D. Mooney, pp. 11-34, Geol. Soc. Am. Memoir 172, Boulder, Colo., 1989.
- Mooney, W.D., and L.W. Braile, The seismic structure of the continental crust and upper mantle of North America, in *The Geology of North America, Vol. A, Overview*, edited by A.W. Bally, and A.R. Palmer, pp. 39-52, Decade of North Am. Geol. Project, Geol. Soc. Am., Boulder, Colo., 1989.
- Mooney, W.D., G. Laske, T. G. Masters, CRUST 5.1: A global crustal model at 5 X 5, *J. Geophys. Res.*, in press, 1996.
- Mooney, W.D. and R. Meissner, Multi-genetic origin of crustal reflectivity: a review of seismic reflection profiling of the continental lower crust and Moho, in *The Continental Lower Crust*, edited by D.M. Fountain, R. Arculus, and R. Kay, pp. 39-52, Elsevier, New York, 1992.
- Nataf, H.-C., and Y. Ricard, 3SMAC: An a priori tomographic model of the upper mantle based on geophysical modeling, *Phys. Earth Planet. Int.*, **95**, 101-122, 1996.
- National Geophysical Data Center, *ETOPO-5, Bathymetry/Topography data*, Data announcement 88-MGG-02: National Oceanic and Atmospheric Administration, US Department of Commerce, Washington, D.C., 1988.
- Pakiser, L.C., and W.D. Mooney, editors, *Geophysical Framework of the Continental United States*, Geological Soc. Amer. Memoir 172, Boulder, CO, 826 pp., 1989.

- Pavlenkova, N.I., Crustal and upper mantle structure in northern Eurasia from seismic data, *Advances in Geophys.*, 37, 1-133, 1996.
- Prodehl, C., Structure of the Earth's crust and upper mantle, in *Encyclopedia of Geophysics*, Landoldt Boernstein, 11A, 97-206, 1984.
- Smith, M.F., *Imaging the Earth's aspherical structure with free oscillation frequency and attenuation measurements*, Ph.D Thesis, Univ. Cal. San Diego, La Jolla, CA, 97 pp., 1989.
- Soller, D.R., R.D. Ray, and R.D. Brown, A new global crustal thickness model, *Tectonics*, 1, 125-149, 1982.
- Tanimoto, T., Crustal structure of the Earth, *A Handbook of Physical Constants, Global Earth Physics*, edited by T.J. Ahrens, pp. 214-224, AGU, Washington, D.C., 1995.

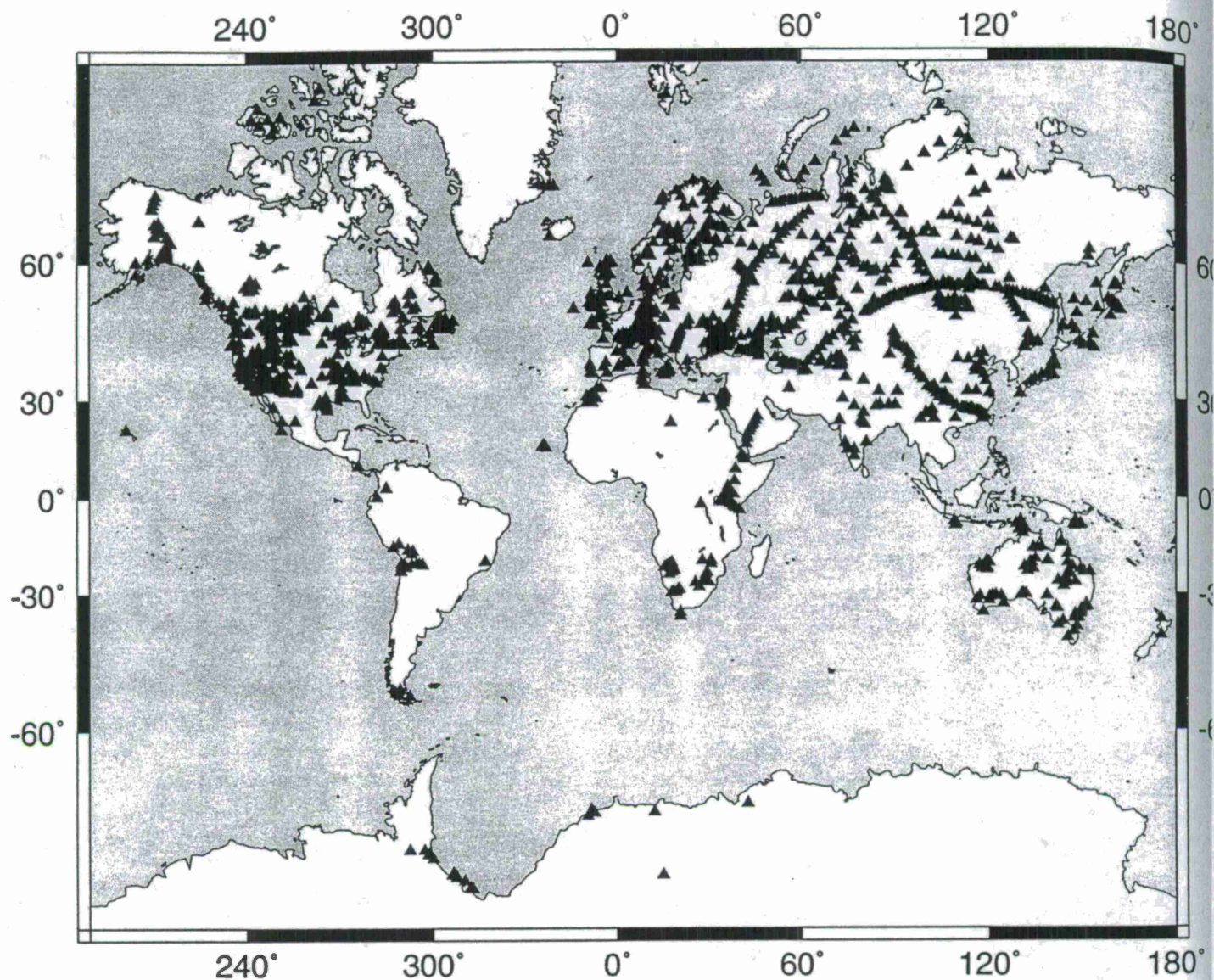


Figure 1. Location of seismic refraction profiles used in this study. Triangles correspond to locations within continents and on margins where a velocity-depth function has been extracted from a published crustal interpretation. These locations are generally at the midpoint between shot points along each profile. These data provide details on the compressional-wave seismic velocity structure and, in about 10% of the cases, also the shear-wave structure of the crust in a wide range of tectonic settings. Sources are cited in Christensen and Mooney (1995). A standard crustal model is used for normal oceanic crust, and appropriate models are used for oceanic plateaus and other features.

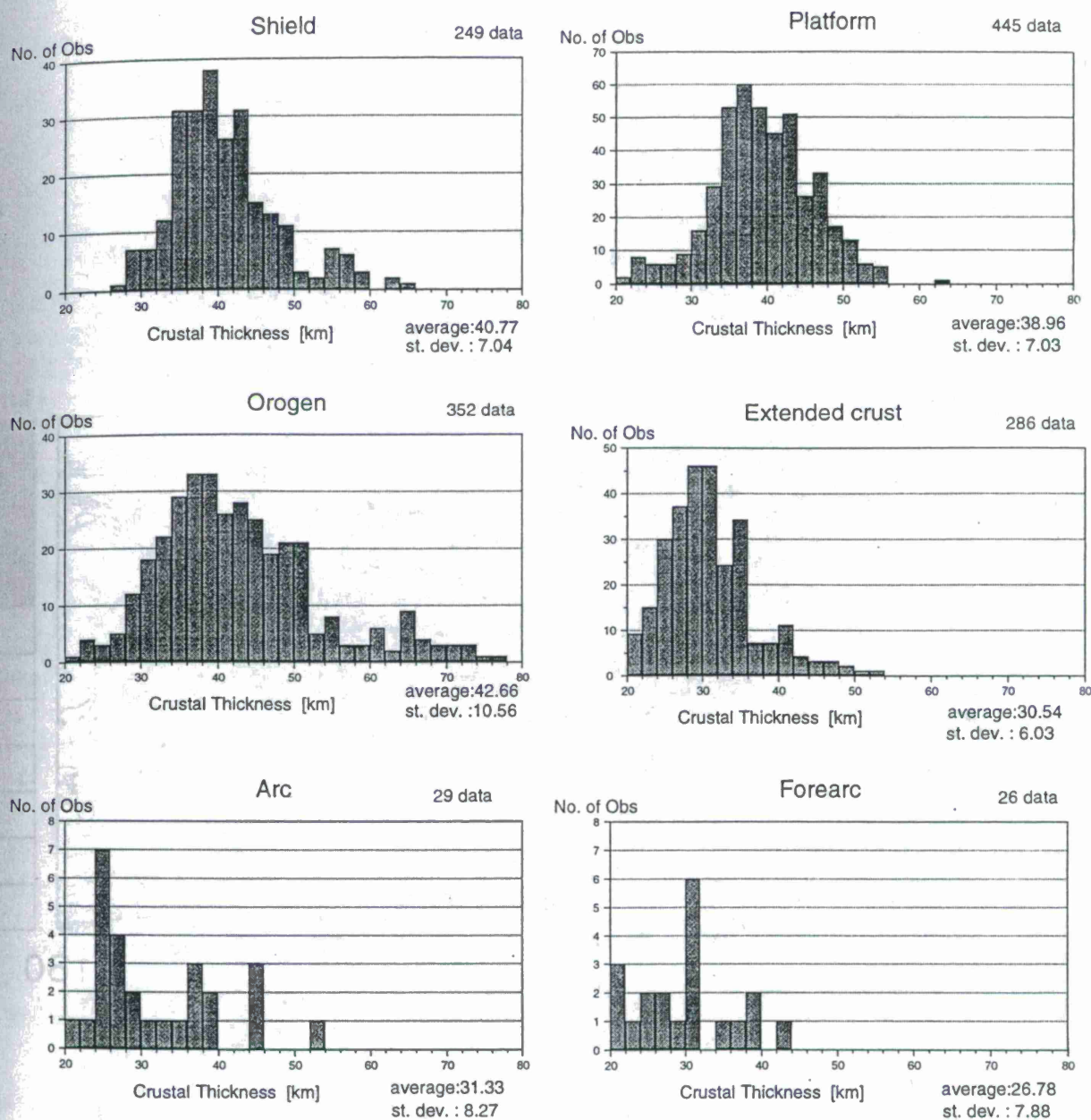


Figure 2. (a) Histograms of crustal thickness for six continental tectonic provinces from the individual point measurements (triangles) of Fig. 1. Average and standard deviation are indicated. These and additional statistics for other tectonic provinces were used to construct the 14 primary crustal types (see text) From Mooney et al., 1997.

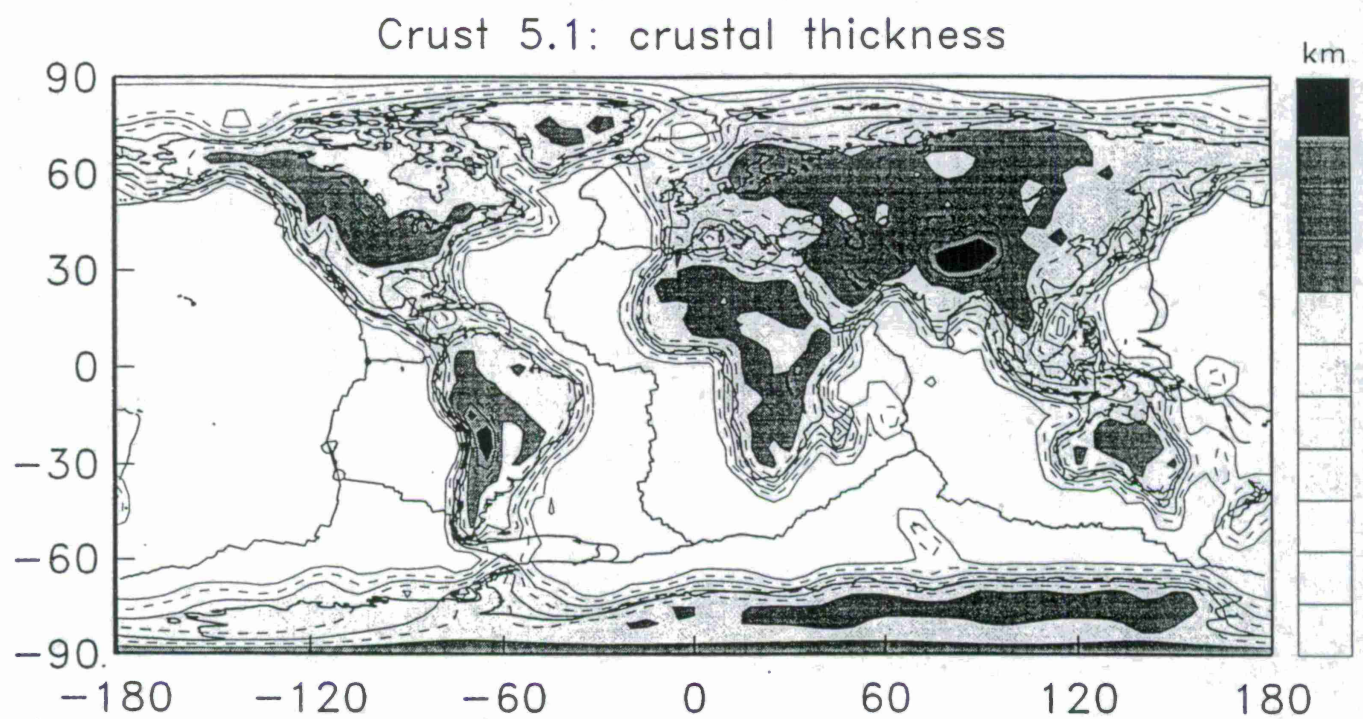
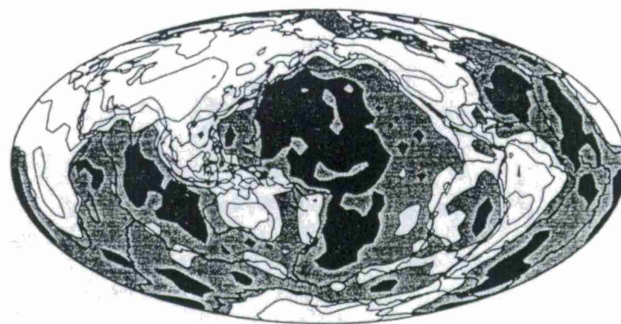
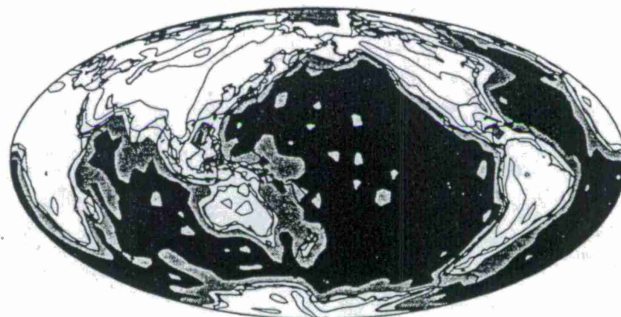


Figure 3. Spherical harmonic expansion of the crustal thickness of CRUST 5.1. The expansion was truncated at harmonic degree 50. The solid contour lines are in steps of 10 km, while the dashed lines indicate 5 km steps. From Mooney et al., 1997

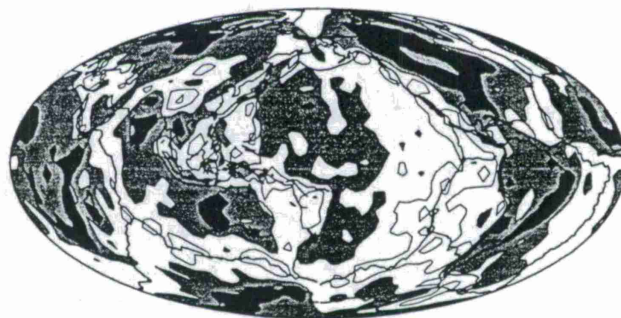
a) ET&L Love 40sec



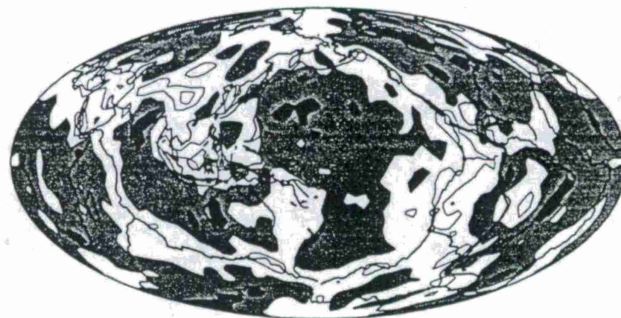
b) CRUST 5.1



c) corrected (CRUST 5.1)



d) corr. (Soller)



$\delta c/c_0$ [%]

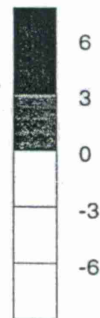


Figure 4. a) Observed phase velocity map for Love waves at 40 s (Ekström et al., 1997). b) Calculated crustal signal in the phase velocity map as predicted by our crustal model CRUST 5.1. c) Observed phase velocity map (a) corrected for crustal signal for the model CRUST 5.1 (b). d) Observed phase velocity map (a) corrected for the crustal signal using Soller's et al. (1982) crustal thickness (see text for details). Note that, while map (c) displays pronounced high velocity anomalies under shields, these anomalies are much smaller in (d). From Mooney et al., 1997.

CRUSTAL STRUCTURE OF CHINA FROM DEEP SEISMIC SOUNDING PROFILES

Walter D. Mooney ⁽¹⁾ and Songlin Li ^(1,2)

(1) U.S. Geological Survey; 345 Middlefield Road, MS 977; Menlo Park, CA 94025

Fax: 415-329-5163, e-mail: mooney@andreas.wr.usgs.gov

(2) Geophysical Prospecting Brigade; State Seismological Bureau;
Zhengzhou, Henan Province, China

Sponsored solely by the U.S. Geological Survey

ABSTRACT

More than 36,000 km of Deep Seismic Sounding (DSS) profiles have been collected in China since 1958. However, the results of these profiles are not well known in the West due to the language barrier. In this paper, we summarize the crustal structure of China in view of applying it to better event locations within the CTBT with a new contour map of crustal thickness, nine representative crustal columns, and maps showing profile locations, and P_n velocity. The most remarkable aspect of the crustal structure of China is the well known 70 + km thickness of the crust of the Tibetan Plateau. The thick (45-70 km) crust of western China is separated from the thinner (30-45 km) crust of eastern China by a north-south trending belt of high seismicity (105° E). The average crustal velocity of China ranges from 6.15 to 6.45 km/s, indicating a felsic-to-intermediate bulk crustal composition. Upper mantle (P_n) velocities are 8.0 +/- 0.2 km/s, equal to the global continental average. These results provide an improved knowledge of the velocity structure of the crust and upper mantle of China, which will improve our ability to monitor and locate seismic activity in this region.

Keywords: crustal structure, China, event location, P_n velocity, average P-wave velocity

OBJECTIVE

Monitoring under the CTBT requires strict locations of questionable events. In order to constrain the area in which an event has occurred, it is necessary to have a good model of the regional crustal structure. The work summarized in this paper provides one of the most accurate and complete models of the crustal structure in China.

RESEARCH ACCOMPLISHED

Profile Locations, Data Acquisition and Interpretation

Approximately 36,000 km of deep seismic sounding (DSS) profiles have been recorded by several institutions in continental China since 1958, primarily by the State Seismological Bureau (SSB) of China, the country's main DSS research group (Fig. 1). Table 1 provides a summary of 22 published profiles; in addition, we have used the results from 19 profiles that are not yet published (dotted lines on Fig. 1). Data quality, in terms of signal-to-noise ratio, is generally very good.

A variety of methods have been used to interpret the DSS data reported here. By far the most common method is the interpretation of seismic travel times (but not amplitudes) using either one- or two-dimensional (1D and 2D) modeling methods. Since about 1980, most interpretations have involved the application of 2D raytracing to compare observed and modeled travel times. The modeling of seismic amplitudes became routinely possible in the past ten years with the development of efficient computers and computer codes for both 1D and 2D models.

In DSS profiles, seismic velocities are directly measured (for reversed profiles), while depths of refraction (or reflection) horizons are successively calculated from the uppermost layer to the deepest measured horizon (usually the Moho). Thus, seismic velocity determinations generally have lower errors than depth determinations. For the seismic profile data compiled here, seismic velocities are accurate to within 3%, or about ± 0.2 km/s. All boundary depths (including the Moho) are accurate to within 10% of the depth. Thus, a reported crustal thickness of 40 km typically has an uncertainty of ± 4 km.

Maps of Crustal Parameters

Crustal thickness is a parameter that is well determined by DSS profiles, since both refracted and reflected arrivals are usually observed from the Moho. However, the map of crustal thickness we present (Fig. 2) is the first complete contour map of the crustal thickness of China based primarily on DSS data. Previous maps have been largely based on surface wave, gravity, topography, and geoelectrical data. The contour map clearly divides China into an eastern portion with a crustal thickness of 30-45 km, and a western portion with a thickness of 45-70 km. In western China, crustal thickness is positively correlated with topography. The 70-km-thick crust beneath the Tibetan Plateau constitutes some of the thickest crust in the world, along with the central Andes of South America. The strong gradient in crustal thickness in central China (visible in gravity as well as seismic data) is coincident with a north-south trending belt of high seismic activity (105° E). In addition, the east-west trending fold belts of western China either end at or abruptly change direction when crossing this seismic belt.

Worldwide, P_n velocities for continental mantle range from 7.6 km/s to 8.4 km/s (higher values are occasionally reported). Low P_n velocities (7.6-7.8 km/s) are usually restricted to

regions of thin (<35 km) crust with moderate to high heat flow, and high P_n velocities correlate with thicker crust (> 40 km) with low heat flow (i.e., stable continental interiors).

Figure 3 shows P_n velocities determined from refraction profiles in China. There is a weak tendency for northeast-southwest refraction profiles to show higher P-wave velocity values (8.1-8.2 km/s), and for northwest-southeast profiles to show lower values (7.7-8.0 km/s). This indicates possible seismic anisotropy in the uppermost mantle of about 4%.

Crustal Columns

Crustal velocity columns (Fig. 4) provide insights into the evolution of the crust of China. The five crustal columns for eastern China all indicate relatively thin (29-33 km) crust, close to the continental global average for extended crust (30.5 km), but significantly thinner than the global average of 39 km. This observation, along with geologic evidence, is consistent with Cenozoic crustal extension in eastern China. The low average crustal velocity (Fig. 7) and uppermost mantle velocity (7.8-8.2) are consistent with this inference, as are global tomographic models that indicate low shear-wave velocities in the upper mantle of eastern China south of 42° N. Northeastern China (above 42° N) has no crustal refraction data, but global tomographic models provide evidence for a thick lithospheric root, and geologic evidence does not indicate significant Cenozoic crustal extension.

The crustal columns for western China (Fig. 4) show thick crust that is characteristic of young orogenic belts. Three of the four columns differ from the thick crust of shields in that they lack a high-velocity (7.0-7.6 km/s) lower crustal layer. These three crustal columns are best considered in light of recent seismological studies in western China that define crustal and upper mantle properties on both a regional scale and locally for the southern Tibetan Plateau. These data are consistent with a model for the evolution of western China that is based on the concepts proposed by Zhao and Morgan (1987) and Nelson et al. (1996). The key concept of this model is that the middle and lower crust of the Tibetan Plateau is a fluid-like layer, and the crust of India is injected into the Tibetan crust as an initially cold slab, but is heated and partially melted after moving 200 - 300 km northward. Thus, the crust of India is assimilated into the crust of Tibet, and the surface of the Plateau is raised by the increasing crustal volume.

CONCLUSIONS AND RECOMMENDATIONS

A great deal of seismic refraction data have been collected in China over the past two decades. A major challenge for Western scientists is to gain access to this information, and to assess its accuracy. This paper summarizes models derived from Chinese seismic refraction profiles recorded through 1990.

Foreign investigators have participated in several seismic reflection and broadband experiments in China over the past ten years. These experiments provide information which complements the refraction data summarized here. In addition, global and regional short period (35 s) Love and Rayleigh wave phase velocity maps provide important constraints on the shear wave structure of the crustal upper mantle.

In order to obtain the best possible crustal and upper mantle model to be used for monitoring of seismic activity in China and the surrounding regions, all of these data should be

synthesized as completely as possible. This work has only recently begun, and improved models can be expected in the near future.

ACKNOWLEDGMENTS

We are grateful to many people for sharing the information that is summarized in this paper. Zhang Xian-Kang, Zeng Rong-Sheng, Wang Chun-Yung, Wang You-Xue, and Yuan Xue-Chung provided data from China, and Katharine Favret and Regina Patzwahl provided helpful comments. Support from the USGS Earthquake Hazards Reduction Program and the Deep Continental Studies Program are gratefully acknowledged.

REFERENCES

- 8301 Program Cooperation Group, 1988. Velocity structure of crust and upper mantle at the east margin of the Tarim Basin and the east part of Qinghai-Tibet Plateau: Developments in the Research of Deep Structures of China's Continent. Geological Publishing House, Beijing, 89-96.
- Chen, B. and W. Gao, 1988. Crustal structure along the Tiajiwen-Shayuan DSS profile: Developments in the Research of Deep Structures of China's Continent. Geological Publishing House, Beijing, 152-168.
- Chen, X., Y. Wu, P. Du, J. Li, Y. Wu, G. Jiang and J. Zhao, 1988. Crustal velocity structure at the two sides of Longmenshan Tectonic Belt: Developments in the Research of Deep Structures of China's Continent. Geological Publishing House, Beijing, 97-113.
- Ding, W., C. Huang, J. Cao and G. Jiang, 1988. Crustal structures along Suixian-Xian DSS profile: Developments in the Research of Deep Structures of China's Continent. Geological Publishing House, Beijing, 38-47.
- Hu, H., X. Chen, B. Zhang, W. Song, Z. Xiao and Z. He, 1988. Crustal structures along Suixian-Anyang DSS profile, Developments in the Research of Deep Structures of China's Continent. Geological Publishing House, Beijing, 48-60.
- Institute of Geophysics, Acad. Sci., 1981. Explosion seismic study for velocity distribution and structure of the crust and upper mantle, from Danxung to Yadong of the Xizang Plateau. ACTA Geophysica Sinica, 24: 155-170.
- Kan, R., H. Hu, R. Zeng, W.D. Mooney and T.V. McEvelly, 1988. Crustal structure and evolution of the Yunnan prov., China from seismic refraction profile: Developments in the Research of Deep Structures of China's Continent. Geological Publishing House, Beijing, 267-276.
- Li, Y. and Z. Xu, 1988. Seismological observation of Qiziqiao Explosion: Developments in the Research of Deep Structures of China's Continent. Geological Publishing House, Beijing, 180-191.
- Liao, Q., Z. Wang, Z. Zhu and X. Wu, 1988. Crust and upper-mantle structure in the Quanzhou-Shantou region of China: Developments in the Research of Deep Structures of China's Continent. Geological Publishing House, Beijing, 227-235.
- Liuzhou Explosion Research Group, 1988. Observation of Liuzhou explosion and the crustal structure in eastern Guangxi: Developments in the Research of Deep Structures of China's Continent. Geological Publishing House, Beijing, 246-252.

- Lu, Z., G. Zhang, J. Li, L. Wang and J. Zhao, 1988. An explosion-seismology study on the structure of crust and upper mantle in South Liaoning Prov., *Developments in the Research of Deep Structures of China's Continent*. Geological Publishing House, Beijing, 114-128.
- McNamara, D.E., Owens, T.J., and Walter, W.R., 1995(a). Observations of regional phase propagation across the Tibetan Plateau. *J. Geophys. Res.*, 100: 22,215-22,229.
- McNamara, D.E., Owens, T.J., and Walter, W.R., 1996. Propagation characteristics of Lg across the Tibetan Plateau. *Bull. Seismol. Soc. Am.*, 86: 457-469.
- McNamara, D.E., Owens, T.J., Silver, P.G., and Wu, F.T., 1994. Shear wave anisotropy beneath the Tibetan Plateau. *J. Geophys. Res.*, 99: 13,655-13,665.
- McNamara, D.E., W.R. Walter, T.J. Owens, and C.J. Ammon, 1997. Upper mantle velocity structure beneath the Tibetan Plateau from Pn travel time tomography. *J. Geophys. Res.*, 102, 493-505.
- Mooney, W.D., 1989. Seismic methods for determining earthquake source parameters and lithospheric structure, in Pakiser, L.C., and Mooney, W.D., *Geophysical framework of the continental United States: Boulder, Colorado*. Geological Society of America Memoir 172.
- Nelson, K.D., and twenty-seven others, 1996. Partially molten middle crust beneath southern Tibet: synthesis of project INDEPTH results. *Science*, 274:, 1684-1688.
- Ni, J. and M. Barazangi, 1983. High-frequency seismic-wave propagation beneath the Indian shield, Himalayan arc, Tibetan Plateau and surrounding regions – high uppermost mantle velocities and efficient Sn propagation beneath Tibet. *J. Geophys. Res.*, 72, 665-689.
- Randall, G.E., C.J. Ammon, and T.J. Owens, 1995. Moment-tensor estimation using regional seismograms from a Tibetan plateau portable network deployment. *Geophys. Res. Lett.*, 22, 1665-1668.
- Sipkin, S.A. and J. Revenaugh, 1994. Regional variation of attenuation and travel time in China from analysis of multiple-ScS phases. *J. Geophys. Res.*, 99(B2), 2687-2699.
- Song, Z., C. An, L. Zhang and Z. Qiu, 1988. P-wave velocity structures of the upper mantle in the mainland and adjacent seas of China: *Developments in the Research of Deep Structures of China's Continent*. Geological Publishing House, Beijing, 205-215.
- Sun, W., Z. Zhu, L. Zhang, S. Song, C. Zhang and Y. Zheng, 1988. Exploration of the crust and upper mantle in North China: *Developments in the Research of Deep Structures of China's Continent*. Geological Publishing House, Beijing, 19-37.
- Teng, J.-W., 1987. Explosion study of the structure and seismic velocity distribution of the crust and upper mantle under the Xizang (Tibet) Plateau. *Geophys. J. R. Astr. Soc.*, 89: 405-414.
- Teng, J.-W., 1979. Geophysical investigations of the Earth's crust and upper mantle in China. *ACTA Geophysica Sinica*, 22: 346-350.
- Teng, J.-W., S. Xiong, Z. Yin, Z. Xu, X. Wang and D. Lu, 1983. Structures of the crust and upper mantle pattern and velocity distributional characteristics at the northern region of the Himalayan Mountains. *ACTA Geophysica Sinica*, 26: 525-540.
- United Observing Group of the Yongping Explosion, SSB, 1988. Yongping explosion and deep structure in Southeast China: *Developments in the Research of Deep Structures of China's Continent*. Geological Publishing House, Beijing, 140-153.

- Xiu, J., 1992. A review of seismic monitoring and earthquake prediction in China. *Tectonophysics*, 209(1-4), 325-329.
- Zhang, S. et al., 1988. Interpretation of the Menyuan-Pingliang-Weinan DSS profile in West China: Developments in the Research of Deep Structures of China's Continent. Geological Publishing House, Beijing, 61-88.
- Zhao, L.-S. and J. Xie, 1993. Lateral variations in compressional velocities beneath the Tibetan Plateau from Pn travelttime tomography. *Geophys. J. Int.*, 115, 1070.
- Zhao, L.-S., et al., 1996. Application of very fast annealing to the determination of the crustal structure beneath Tibet. *Geophys. J. Int.*, 125(2), 355.
- Zhao, L.-S., et al., 1991. Shear-velocity structure of the crust and upper mantle beneath the Tibetan Plateau and Southeastern China. *Geophys. J. Int.*, 105, 713-730.
- Zhao, W.L. and W.J. Morgan, 1987. Injection of Indian into Tibetan lower crust: a two-dimensional finite element viscous model. *Tectonics*, 6: 489-504.
- Zhu, L. and D.V. Helmberger, 1995. High frequency S-wave attenuation on the Tibet Plateau (abstract). *Seism. Res. Lett.*, 66, 53.
- Zhu, L.-P., Owens, T.J., and Randall, G.E., 1995. Lateral variation in crustal structure of the northern Tibetan Plateau inferred from teleseismic receiver functions. *Bull. Seismol. Soc. Am.*, 85: 1531-1540.

Table 1. Brief description of the DSS profiles.

Profile Number	Region	Reference	Source Type*	Crustal Thickness
1**	North China Plain and adjacent regions	Sun et al., 1988	A	30-34
2	Lower Liao River Plain	Lu et al., 1988	A	32-35
3	North China Plain and Qinling Folded Region	Hu et al., 1988	B	30-34
4	Qinling Folded Region	Ding et al., 1988	B	34
5	Qinling Folded Region and Yangtze Quasi-Platform	Chen and Gao, 1988	B	34
6	Yangtze Quasi-Platform and South China Folded Region	United Observing Group, 1988	B	33
7	South China Folded Region	United Observing Group, 1988	B	32
8	Hengyang Basin, Youxian Basin and Chaling-Yongxing Basin	Li et al., 1988	B	29
9	Southeast Coastal Fold belt	Liao et al., 1988	A	29
10	Guilin Uplift and Yishan Uplift	Liuzhou Explosion Research Group, 1988	B	33
11	South China Folded Region	Liuzhou Explosion Research Group, 1988	B	32
12	Ordos Platform	--	A	--
13	Ordos Platform	--	A	--
14	Qilian, Liupian and Qinling Mts.	Zhang et al., 1988	A	38-60
15	Sichuan Basin and Tibet Plateau	Chen et al., 1988	A	40-51
16	Yunnan-Guizhou Plateau	Kan et al., 1988	A	41-46
17	Yunnan-Guizhou Plateau	Kan et al., 1988	A	39-46
18	Qaidam Basin	Tseng, 1979; Teng, 1979	A	51
19	Tarim Basin	8301 Program Cooperation Group, 1988	B	51
20	Qinghai-Tibet Plateau	Teng, 1987	C	70
21	Qinghai-Tibet Plateau	Inst. Geoph. Acad. Sci., 1981	C	45-73
22		Teng et al., 1983	A&C	73-76

- * A. Bore-hole explosion.
 B. Industrial blast.
 C. Explosion in water.

** Including 31 DSS profiles.

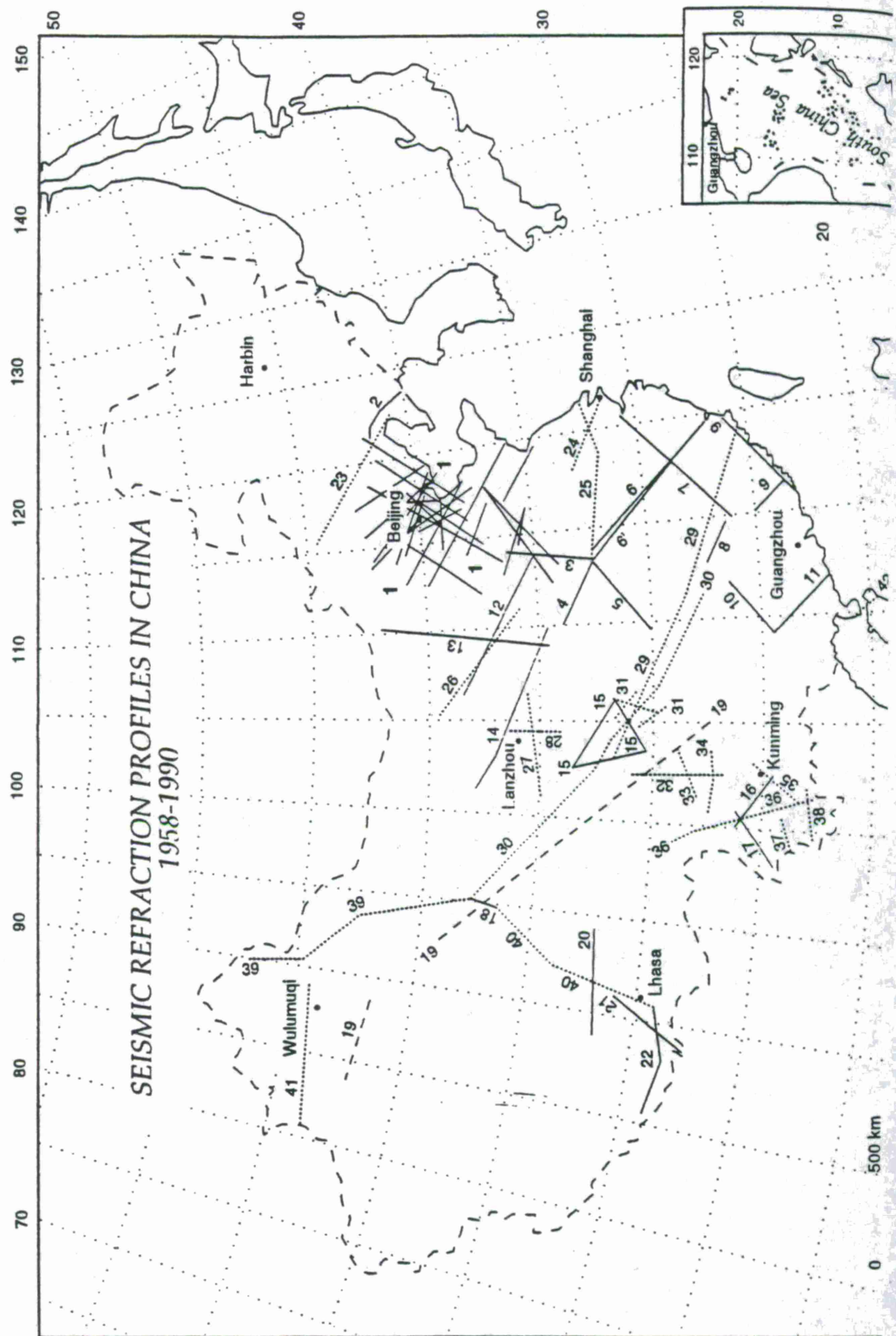


Fig. 1

Position map of the seismic refraction/wide angle reflection profiles in China (1958-1990). The numbers of profiles are same as those used in Table 1.

Solid lines: profiles completed from 1958 to 1986

Dotted lines: profiles completed from 1987 to 1990 (not yet published)

Dashed lines: profiles with sparse observational points

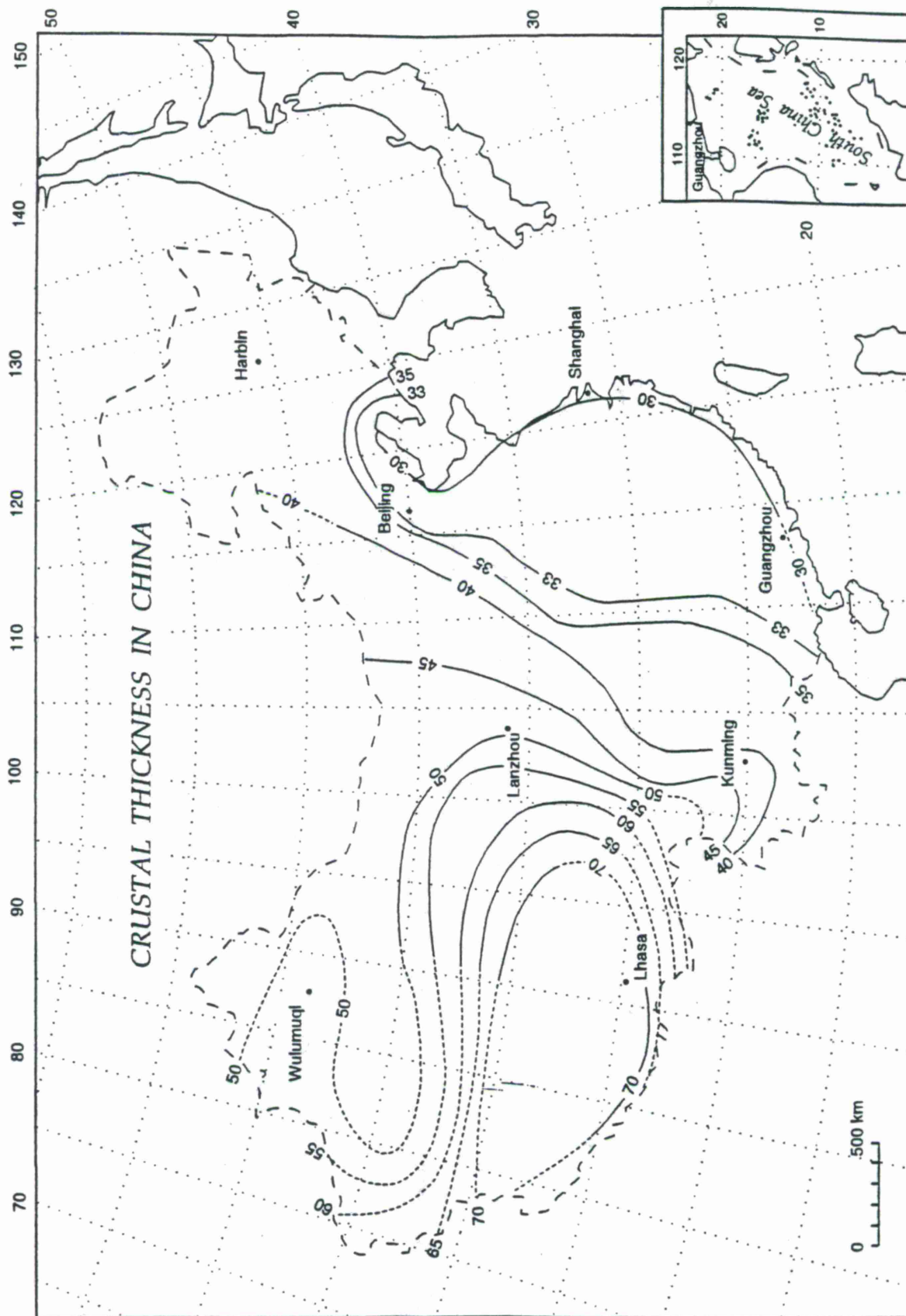
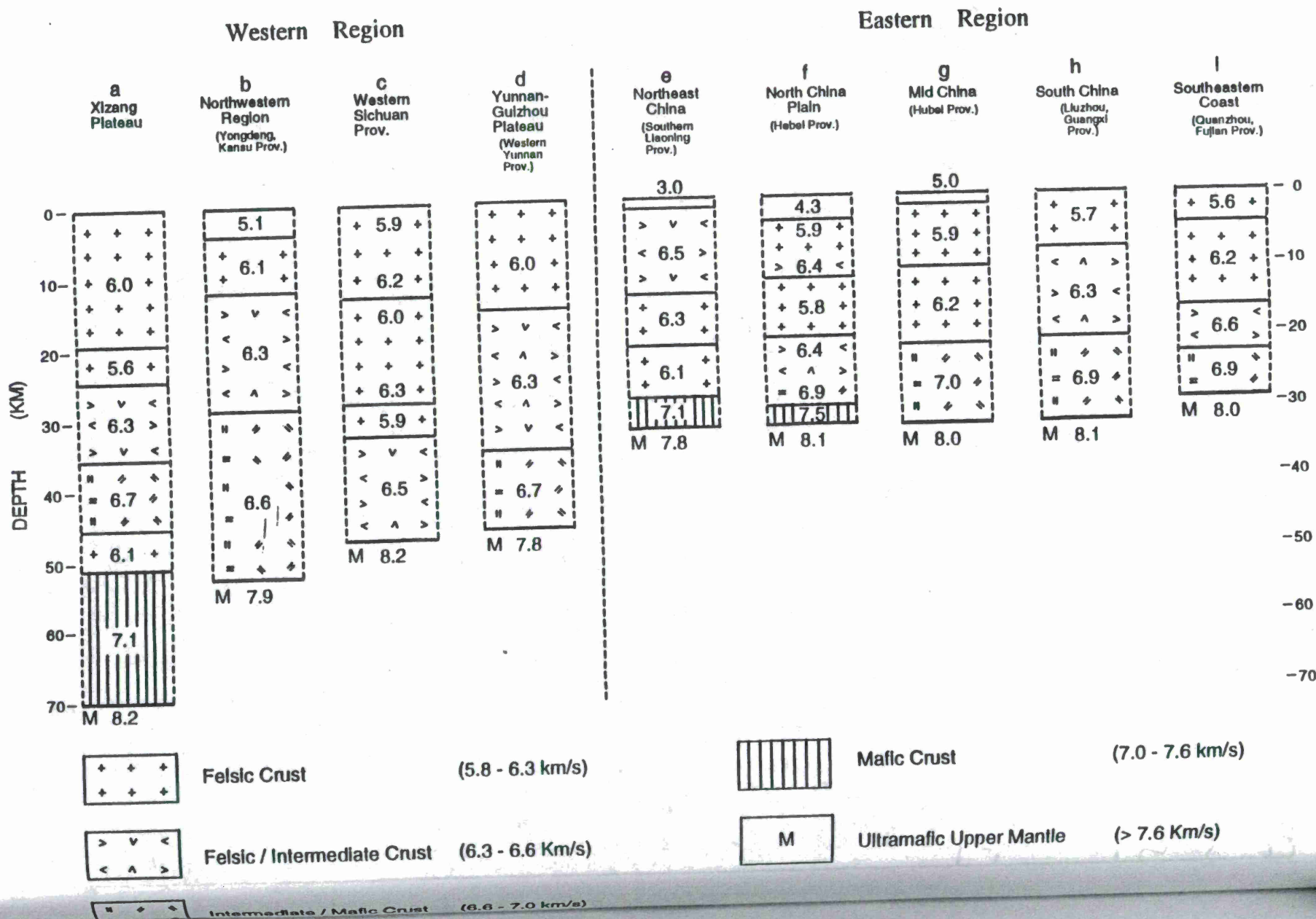


Fig. 2

Crustal thickness obtained primarily from seismic refraction/ wide angle reflection experiments. Solid isolines represent more reliable results. Dashed lines were obtained by considering gravity data. The 45 km contour coincides with the western boundary of the Sino-Korean platform and the Yangtze platform, as well as with the north-south seismic belt.

Fig. 4
Representative seismic velocity-depth functions for nine regions of China which can be divided into two parts by the north-south seismic belt: western region (a-d) and eastern region (e-i). For western region, the crustal thickness is greater than 45 km, while it is less than 35 km for eastern region.



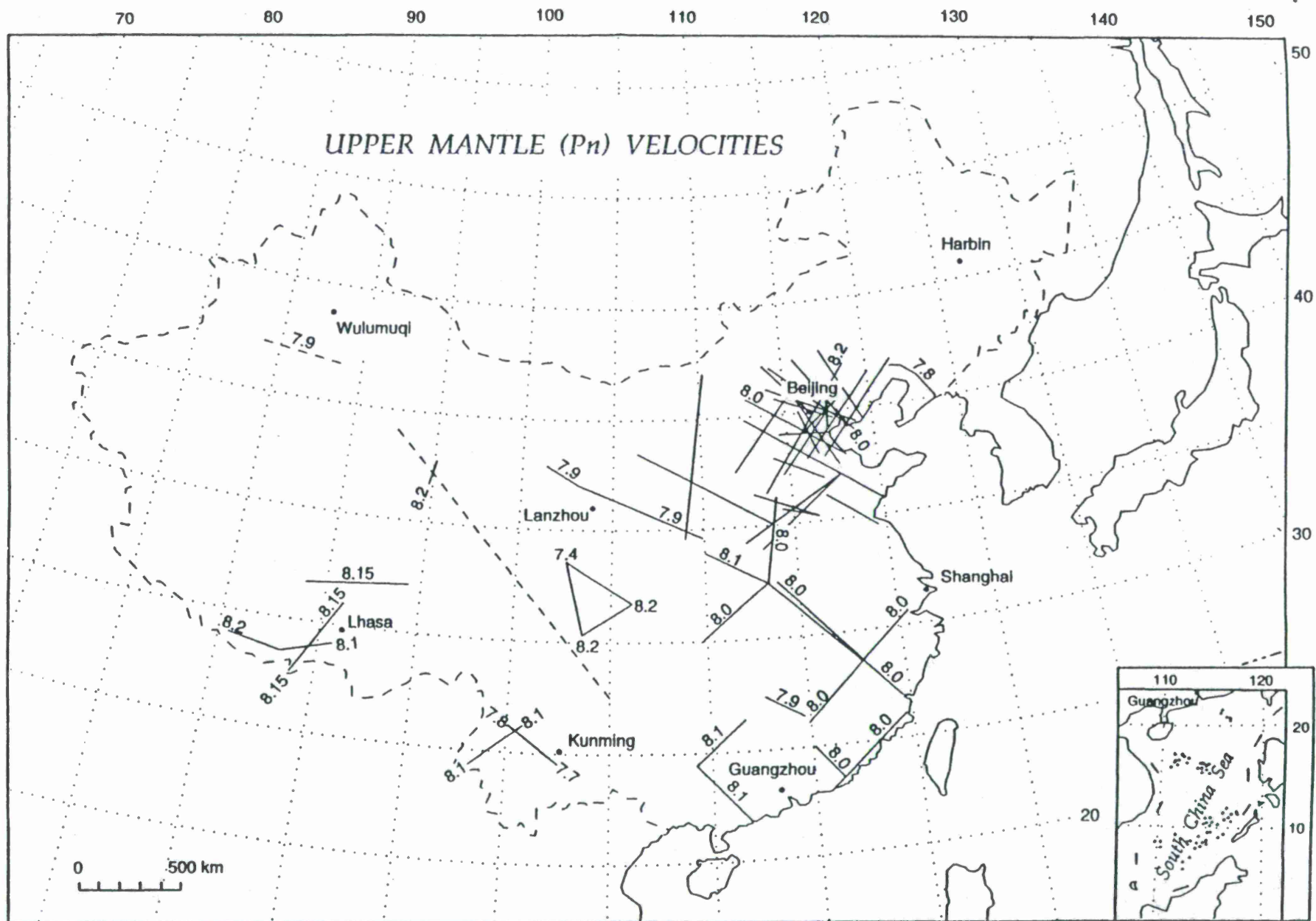


Fig. 3
 P_n wave velocities obtained from seismic refraction profiles in China. Velocities are well within the global average of 8.0 ± 0.2 km/s.

NEW REGIONAL TRAVEL-TIME TABLES FOR THE BALTIC SHIELD INFERRED FROM DSS OBSERVATIONS FOR CALIBRATION OF THE INTERNATIONAL MONITORING SYSTEM (IMS)

Robert G. North, Istvan Bondar, and Vladislav Ryaboy

Center for Monitoring Research
1300 N. 17th Street, Suite 1450, Arlington, VA 22209

Sponsored by Nuclear Treaty Programs Office, Department of Defense
Advanced Research Projects Agency

ABSTRACT

Different one-dimensional (1-D) global reference velocity models were inferred from various observational data (Jeffreys and Bullen, 1940; Herrin, 1968; Dziewonski and Anderson, 1981; et al.) to improve seismic event locations. The IASPEI 1991 Seismological Tables (Kennett and Engdahl, 1991; Kennett, 1991) are now being used by the prototype International Data Center (PIDC) to locate seismic events. Refinements in those globally averaged travel-time curves and underlying 1-D global velocity models cannot improve the locations of regional seismic events.

Accurate travel-time curves derived from explosions with controlled sources reveal major differences between Pn waves propagating in tectonically active regions and Pre-Cambrian platforms. Studies completed at the Center for Monitoring Research (CMR) show that Pn travel-times for tectonically active regions are up to 5 seconds later than the IASPEI-91 tables while those for Pre-Cambrian platforms are 3-6 seconds earlier, in the 1000-1500 km distance range. Regional velocity models are required for the calibration of the IMS network.

This paper illustrates calibration of the Baltic shield area using deep seismic sounding (DSS) data. DSS profile observations for the Baltic shield have been used to derive average Pn-wave travel times to a distance of 1,400 km, and to construct an average 1-D crustal and upper mantle velocity model. Sn travel-times are derived from the Pn velocity distribution by assuming a depth-dependent Vp/Vs ratio, while the Pg and Lg travel-time curves were obtained from relocations of ground truth events. Comparison of the IMS locations for regional seismic events with well known location, mainly mine blasts, based on IASP91 global velocity model with those determined using the Baltic shield model showed clear improvements with the latter. Systematic mislocations of regional seismic events in the Fennoscandia region are significantly reduced.

Keywords: Baltic shield, deep seismic sounding (DSS), mine blasts, earth's crust, upper mantle.

OBJECTIVE

The effectiveness of the IMS for global monitoring will be critically dependent on the accuracy of seismic event locations. For epicentral locations using just a few stations with poor azimuthal coverage, as will be the case for many low magnitude events, accurate travel-time tables, phase timing, and azimuth estimation as well as the correct identification of phases, are all crucial. The objective of this paper is to demonstrate that the use of regional travel-time curves derived from DSS profiles can improve seismic events locations in the Baltic shield and surrounding areas.

Event locations in general have two sources of errors, random and systematic. One source of random errors is measurement error, which is usually a function of signal-to-noise ratio (SNR). Systematic errors, however, are caused by misidentification of phases, inaccurate travel-time tables, and biased azimuth estimates. The most direct application of DSS observations as a tool for improving event locations is to reduce the systematic errors due to inaccurate travel-time tables.

RESEARCH ACCOMPLISHED

Scandinavia and northwestern Russia have been covered with a dense network of DSS profile observations crossing this region in different directions (Figure 1). The results of these studies have been published in numerous papers, monographs, and dissertations. An extensive list of publications on the results of these studies is given by Romney and Ryaboy (1994). Because DSS data are observed from controlled sources and sampled at numerous fairly regular distance intervals, and on reversed and overlapping profiles, the entire wave pattern of initial and secondary arrivals becomes visible and regional phases can be identified more reliably and travel-time measurements can be made with high precision.

We collected and analyzed the available P-wave record sections and travel-time curves inferred from DSS profile observations, and from recordings of large chemical explosions with well known location and origin time for the Baltic shield. The available Pn-wave record sections and travel-time curves constructed for DSS profiles described above were collected to correlate and measure travel-times of Pn first arrivals. Observations for the FENNOLORA DSS profile extended to a distance of 2000 km, but first arrivals could only be reliably picked up to distances of 1300-1400 km because of poor signal to noise ratio.

Travel-time measurements were made from the Pn record sections (measured at ten km spacing). These data were used to produce the composite Pn travel-time plot shown in Figure 2. This figure is based on the analysis of approximately 10,000 km of DSS profiles and consists of 1420 measurements. The observations have a scatter ranging up to about three seconds for a given distance. This scatter is much larger than the observational error and thus is likely caused by factors such as lateral structural variations of the earth crust and upper mantle. Also evident in the data is a discontinuity near 850 km, indicative of a low-velocity zone.

Three travel-time curves are superimposed on the travel-time data shown in Figure 2. Two of these, Fenno and Helsinki (HEL), are the curves used to locate events at the prototype IDC

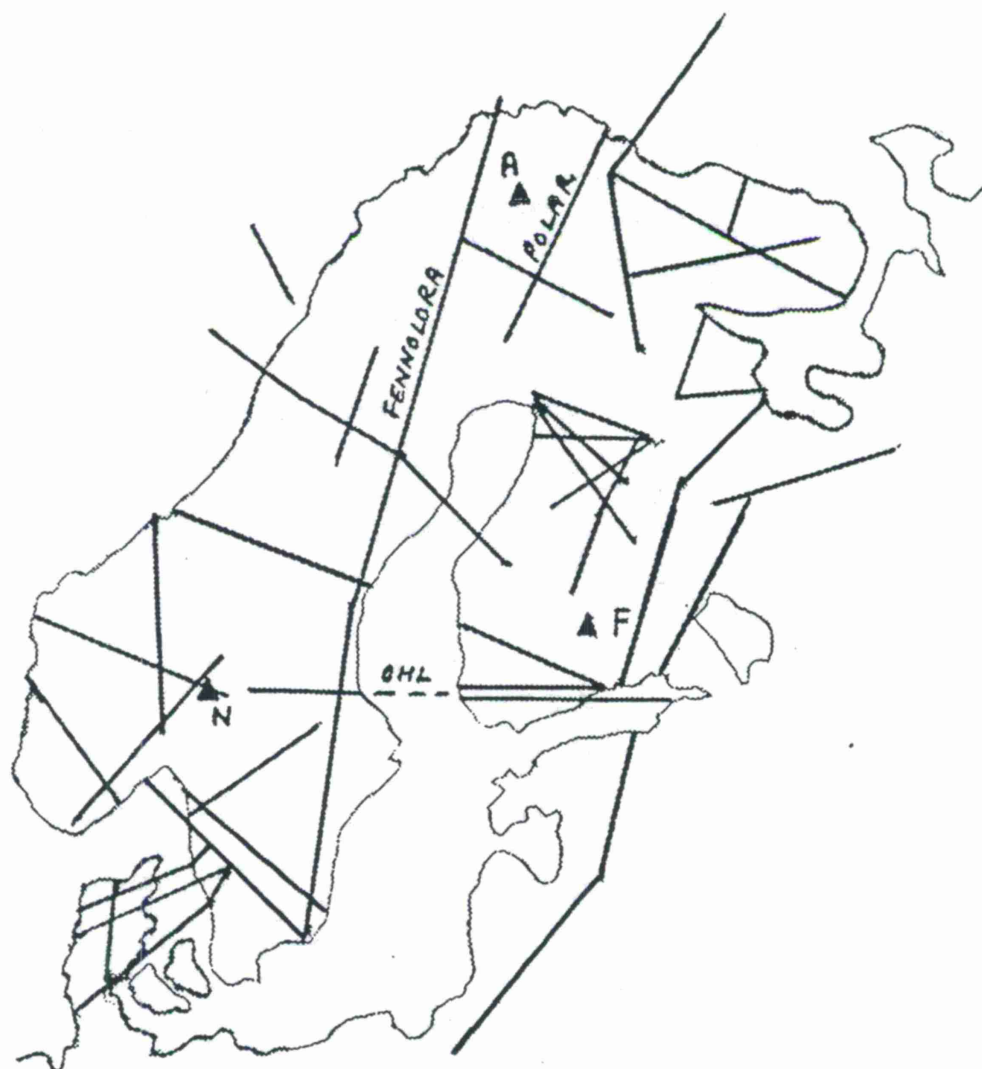


Figure 1: Map of DSS profiles and NORES (N), FINES (F) and ARCES (A) regional array locations. FENNOLORA and POLAR are long-range DSS profiles. OHL is the Oslo-Helsinki-Leningrad profile.

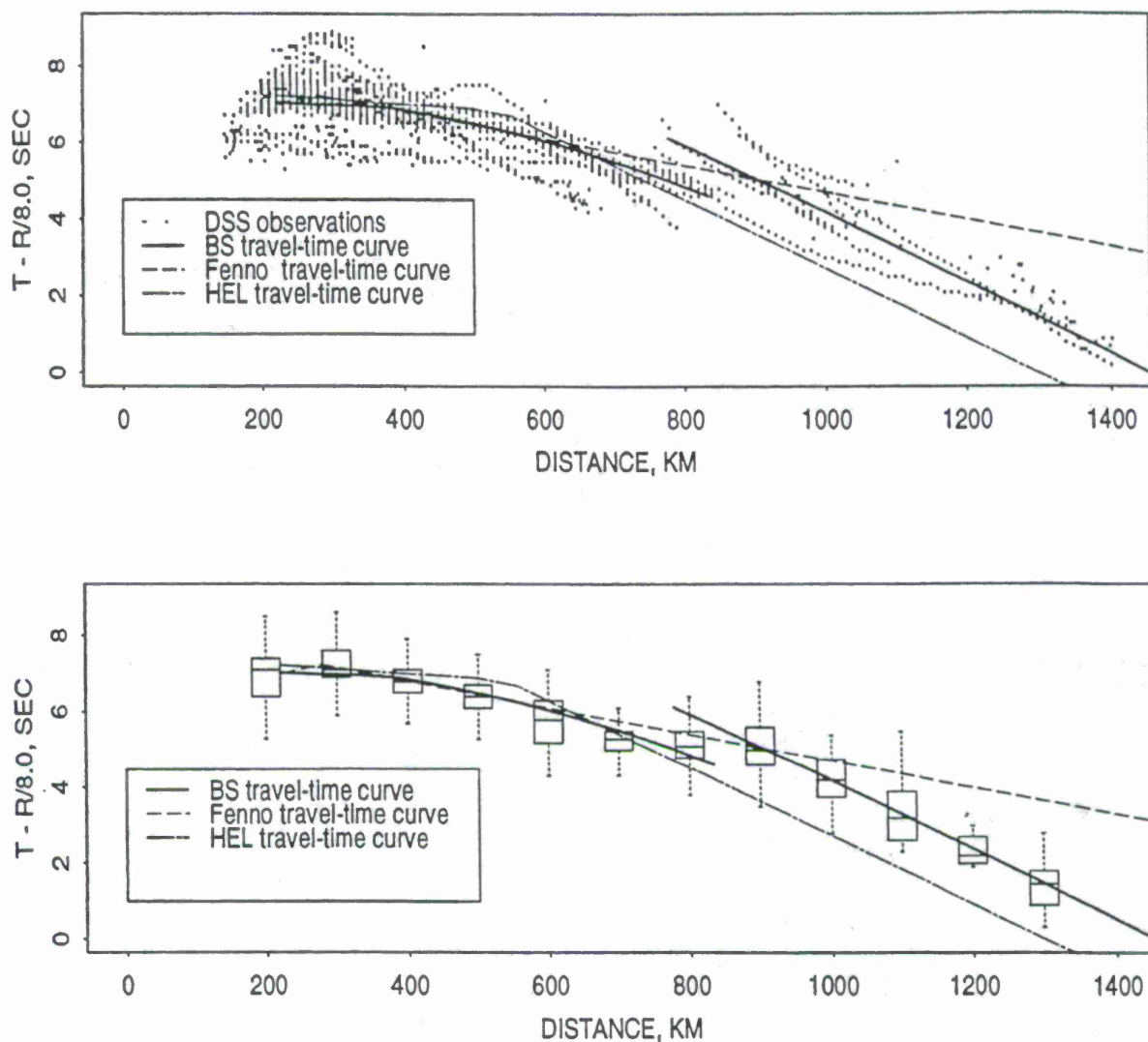


Figure 2: Top: comparison of *Pn*-wave travel-time observations for the Baltic shield measured from explosions with controlled sources (dots), with *Pn* travel-time curves used for event locations in the GSETT-2 experiment (Fenno model) and in the Helsinki (HEL) seismological bulletins. Note that neither the Fenno nor the HEL curves are a good fit to the observed DSS data beyond about 600 km. Bottom: box plots of *Pn* travel-times (dots) shown in the top. Boxes were calculated for 100 km distance windows. The horizontal line in the interior of each box is located at the median of the data. The height of each box is the difference between the third quartile of the data and the first quartile. The dotted vertical lines extend to the extreme values of the data. The solid line is the proposed new regional reference travel-time curve (BS).

during the GSETT-2 experiment and before, and for the Helsinki bulletins, respectively. All of the Pn travel-time curves are fairly good fits to the DSS data for distances less than 500-600 km; large discrepancies, however, are apparent for distances greater than 600 to 800 km. Beyond about 600 km, DSS observations are generally early with respect to the Fenno Pn travel-time curve for the Baltic shield. On the other hand, DSS observations at these longer ranges are generally late with respect to the Pn travel-time curve currently in use to locate events for the Helsinki bulletin (HEL). The third travel-time curve on Figure 2, labeled as Baltic shield (BS), represents our best estimate of a generalized Pn travel time curve for the entire region.

Our preferred model to fit the observed DSS Pn travel-times is based on a one-dimensional (1-D) spherical earth model with two crustal layers and a low velocity zone in the upper mantle. The BS travel time curve shown on Figure 2 is calculated from this model. Because of the non-uniqueness of the inversion problem our preferred model is one representative of a family of velocity models consistent with the observed Pn travel-times. However, it does have the merit of providing a better fit to the DSS Pn observations than do the other two models.

To construct a reference velocity model for the Baltic shield the velocity model inferred from DSS observations was combined with the IASP91 velocity model for greater depths. To do so it was assumed that for a distance range of approximately from 23 to 30 degrees the Baltic shield travel-time table should have travel times for the Pn(P) and Sn(S) waves similar to those predicted by the IASP91 tables for first arrivals. This assumption is based on the observed phenomenon that P and S wave travel-time variations are drastically decreased at distances greater than 23-30 degrees, as compared to regional distances. With the minimization of the discrepancies between travel-times predicted by the Baltic shield and IASP91 model in the 23-30 degree distance range, a smooth transition from the regional model to the global Earth is ensured.

The velocity model for S-waves was calculated from the model for P-waves assuming that the V_p/V_s ratios for the crust and uppermost mantle are 1.732 and 1.760, respectively. The V_p/V_s ratio was increased for greater depths from 1.79 to 1.85, in accordance with the IASP91 model. Figure 3 shows the Baltic shield velocity models for P- and S-waves. In comparison with the IASP91 model, the new velocity model for the Baltic shield has greater velocities up to depths of approximately 300 km, and smaller velocities for larger depths (Figure 3).

For the evaluation of the Baltic shield crustal and upper mantle velocity model a ground truth data set (GT) was selected. The data set contained mine blasts from Sweden, Finland and Poland, with mine dimensions of 3 km or less, known explosions with confirmed locations by the Swedish National Data Center (NDC), the carefully analyzed events by Grant and Coyne (1993) from the pre-GSETT-3 period, and a chemical explosion with well known location and origin time detonated in the Kola peninsula (Russian Federation) and a mine collapse in Germany from the calibration event database.

In order to evaluate the performance of the Baltic shield model, seismic events included in the ground truth data set were relocated - at first with the IASP91 model, then using the Baltic shield model at the IMS Scandinavian stations ARCES, FINES, HFS, KAF, NORES and VAF and the IASP91 model at the non-Scandinavian stations. In the locations only the P, Pn, Pg and

COMPARISON OF THE BALTIC SHIELD (BS) AND IASP91 VELOCITY MODELS

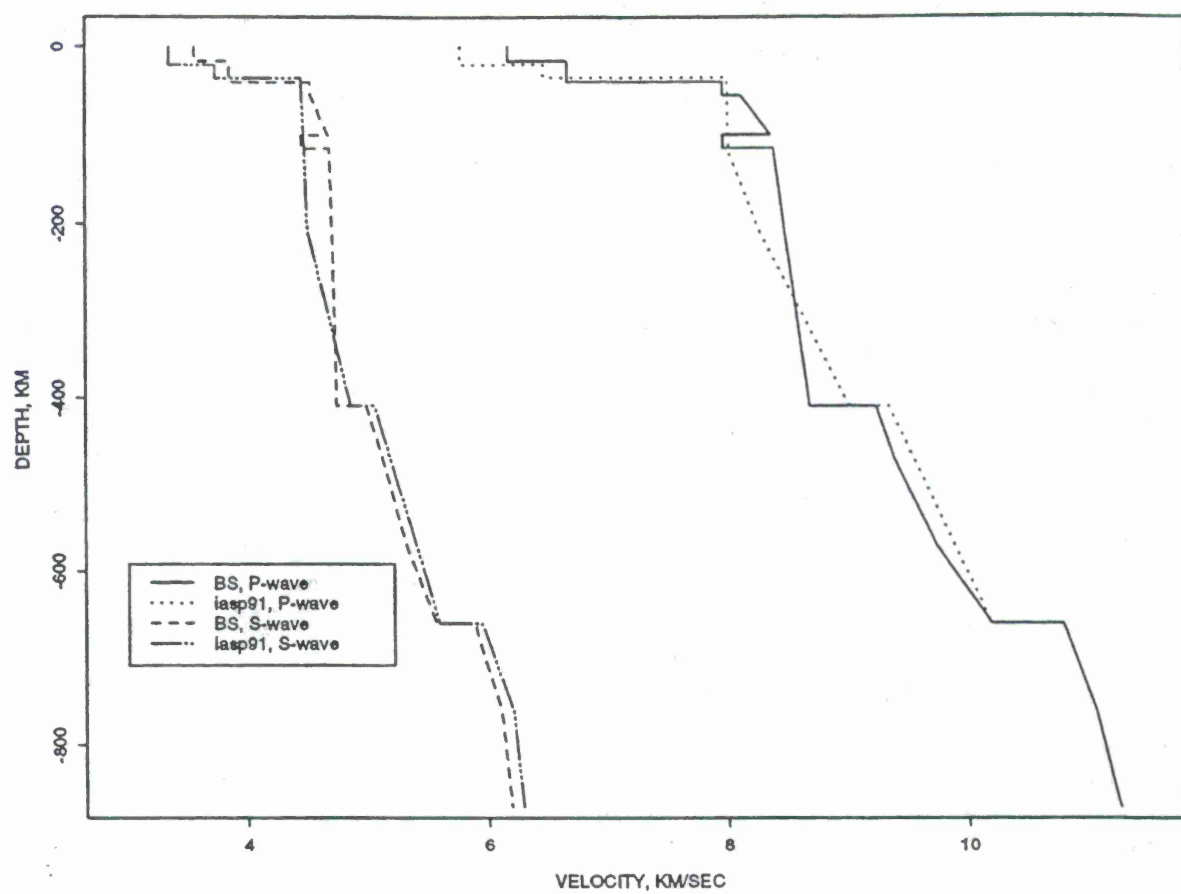


Figure 3: Comparison of the Baltic shield (BS) and IASP91 velocity models.

Sn phases were allowed to constrain the solution, while the Lg phase, being less reliable, was made non-defining. The slowness and azimuth readings were also made non-defining. With these restrictions we were able to locate 425 events out of 622.

The solutions with the Baltic shield model may not necessarily hit the ground truth locations, but they move toward them, as compared to the IASP91 solutions. The more spectacular improvements are experienced in the fringe of the Baltic shield (Kola peninsula, Norway, Poland) where they can move as much as 40-50 km toward the ground truth. As an example, Figure 4 shows comparisons of IASP91 (points) and Baltic shield (open triangles) model solutions to ground truth locations (black squares) for the Kola peninsula, Russia.

The error ellipses with the Baltic shield model are almost without exception smaller than those of the IASP91 model, the median reduction in area being 3000-3600 square km and the linear dimensions of the ellipses being 4-6 times smaller. The distributions of time residuals and the misfit of solutions do not exhibit profound changes, actually, they seem to be relatively independent of the applied velocity model. The reason for this is probably that the location algorithm minimizes the misfits of the solutions (i.e. the rms time residual) and by mislocating an event using a wrong velocity model they may achieve similar misfits and time residuals as with a more appropriate model.

Fig. 5 shows a case study for the calibration event in the GSETT-3 period (chemical explosion in the Kola peninsula, 29 September 1996, 06:05:46, latitude: 67.67deg., longitude: 33.73deg.), labelled as GT, with its location indicated by a black triangle. Besides the ground truth location four other solutions are shown, together with their error ellipse. REB denotes the original Reviewed Event Bulletin (REB) solution published by the prototype IDC; and IASP91 is the solution provided by the IASP91 velocity model using the REB arrivals but with the new measuring and modeling errors recently implemented in prototype IDC routine operations. BALTIC indicates the solution obtained using the Baltic shield model, using the REB arrivals with the corresponding measurement and modeling errors (Bondár and Ryaboy, 1997); Calibration Event Bulletin (CEB) is the same as BALTIC but using also the arrivals provided by the Finnish and Norwegian NDCs from their regional networks.

One can see that the new measurement and modeling errors produce larger coverage ellipses for both the IASP91 and Baltic shield models than that for the REB solution, but unlike the REB location, their error ellipses contain the true location. The IASP91 solution does not differ very much from the original REB location. The solution using the Baltic shield model moves the location toward the ground truth one by some 40 km, and adding extra arrivals (CEB location) further decreases the size of the error ellipse while still containing the true location. The shift in location for this particular event is typical of those for this region as shown in Fig. 4.

CONCLUSIONS AND RECOMMENDATIONS

A new Pn travel-time model and corresponding 1-D velocity model drastically improve the accuracy of PIDC locations in Fennoscandia. However, there are limitations to the refinement of regional seismic event locations based on 1-D crustal and upper mantle velocity models. The

Kola events (vectors point from IASP91 to Baltic solutions)

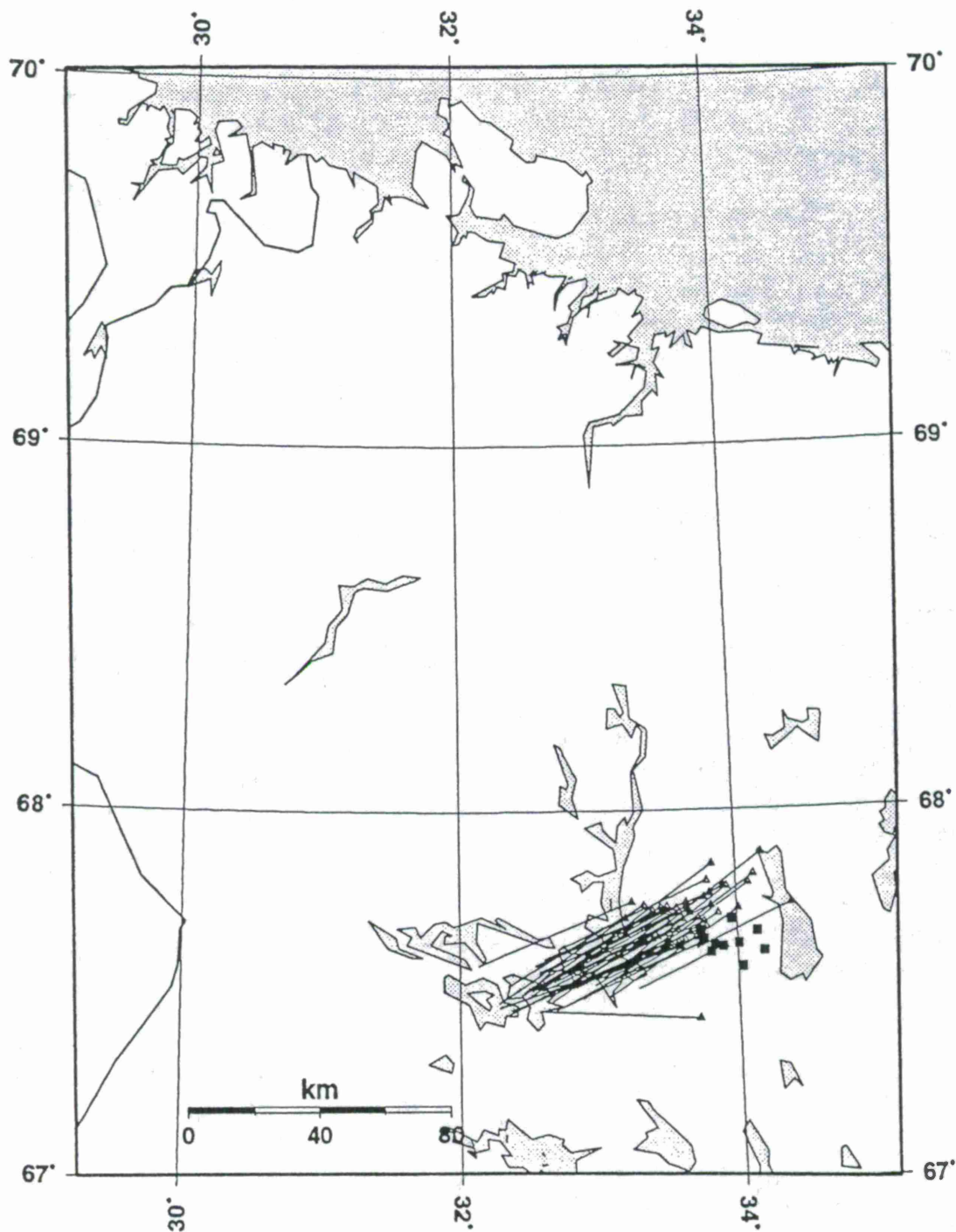


Figure 4: Comparison of Baltic shield model (triangles) and IASP91 model (other end of line) solutions to ground truth locations (black squares), in the Kola peninsula region of Russia.

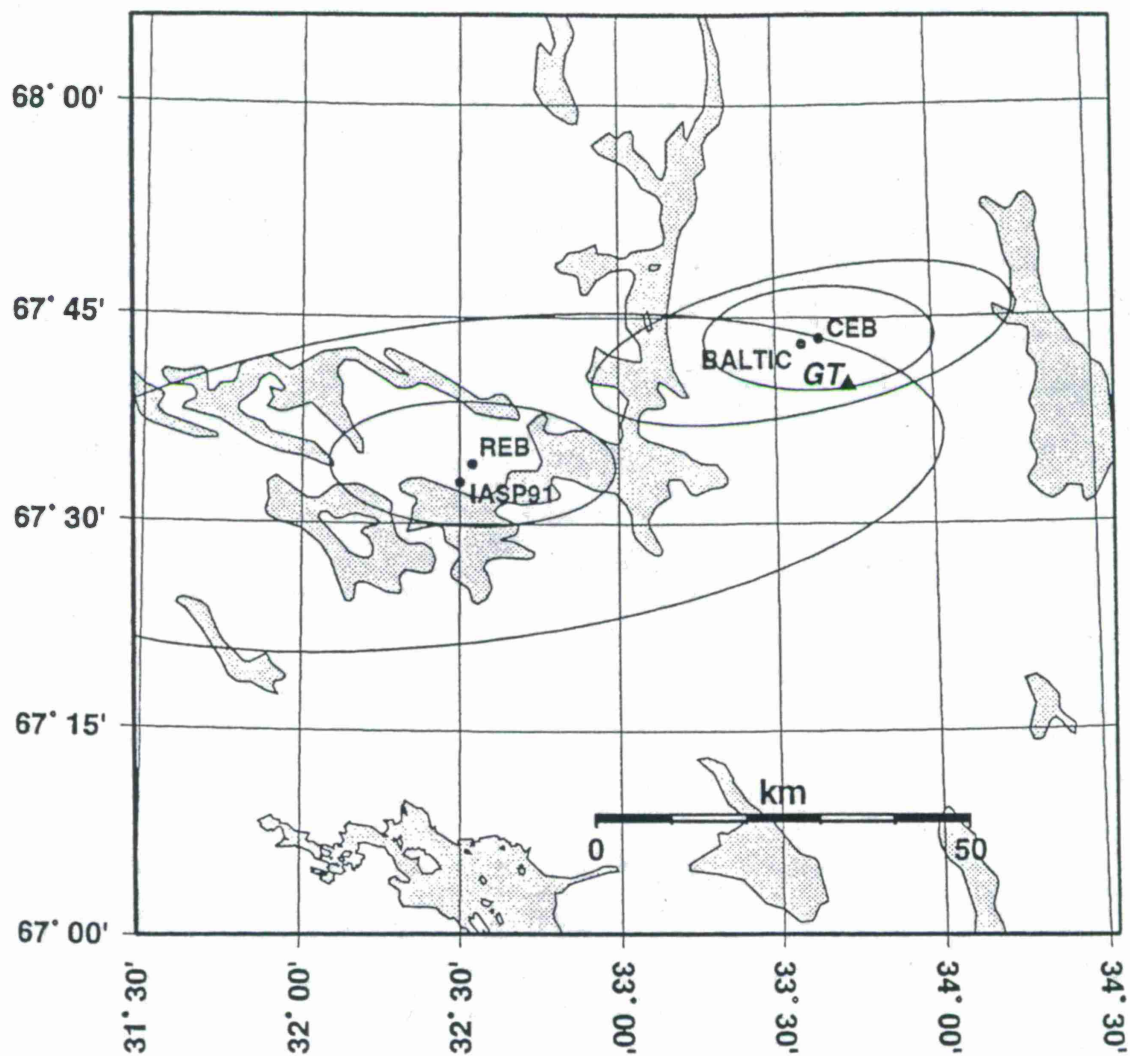


Figure 5: Comparison of locations and error ellipses for the announced chemical explosion in the Kola peninsula (96/09/29 06:05:46, 67.670N, 33.730E, shown as black triangle) provided by the IASP91 and Baltic shield model. REB denotes the original REB location, CEB is the location with the Baltic shield model using arrivals from both the IMS and national (Finland, Norway) networks.

limitations are caused by travel-time variations within major tectonic provinces and paths traversing different tectonic provinces. Seismic event locations based on 3-D velocity models should overcome these limitations.

The Pn travel-time curve for the Baltic shield proposed in this paper is a fit to the available long-range profile data. There is, however, considerable scatter in the observations that is mainly the result of regional variations in the Moho depth and uppermost mantle velocity structure. While this work is primarily focused on the Baltic shield region, the same methodology could be applied to data from other regions.

REFERENCES

- Bondár, I. and Ryaboy, V., 1997: Regional travel-time tables for the Baltic shield region, *Technical Report CMR-97/24*.
- Dziewonski, A.M. and D.L. Anderson, Preliminary reference earth model, *Phys. Earth Planet. Interiors* 25, 297-356, 1981.
- Grant, L. and Coyne, J., 1993: A Ground Truth Database for Seismic Discrimination Research, *Technical Report CMR-92/04*.
- Herrin, E., 1968 seismological tables for P-phases, *Bull. Seism. Soc. Am.* 60, 461-489, 1968
- Jeffreys, H. and K. Bullen. Seismological Tables, *British Association for the Advancement of Science*, London, 1940.
- Kennett B.L.N and E.R. Engdahl, Traveltimes for global earthquake location and phase identification, *Geophys. J. Int.* 105, 429-465, 1991.
- Kennett B.L.N (ed.), IASPEI 1991 Seismological Tables, *Australian National University*, p. 167, 1991.
- Romney, C.F. and V. Ryaboy. Improvement of Regional Seismic Event Locations for Global Monitoring, *Center for Seismic Studies, Technical Report C94-01*, 39, 1994

SOURCE AND PATH EFFECTS ON REGIONAL PHASES IN CHINA

W.S. Phillips, G.E. Randall, H.E. Hartse, S.R. Taylor and H.J. Patton
Geophysics Group EES-3, Los Alamos National Laboratory

Sponsored by U.S. Department of Energy
Office of Nonproliferation and National Security
Office of Research and Development
Contract W-7405-ENG-36
CTBT Research and Development Program, ST482A

ABSTRACT

As part of the CTBT Research and Development regional characterization effort, we are assembling, organizing and analyzing geological, geophysical, and seismic data for inclusion in a knowledge base for the U.S. National Data Center. Guided by the USGS Preliminary Determination of Epicenters (PDE) and Chinese State Seismological Bureau event catalogs, we have collected seismic data from 11 Chinese Digital Seismic Network (CDSN) stations as well as 8 IRIS and Lamont stations from adjoining regions. These include sites at or near proposed primary and secondary seismic stations as designated by the treaty. Using the published event locations and origin times, we identify *Pn*, *Pg*, *Sn*, and *Lg* phases, construct travel time curves, and estimate apparent velocities from broadband and short-period seismograms. Following this, we collect amplitudes of regional seismic phases and associated noise levels using bandpassed waveforms. Studies of path-specific propagation of the seismic phases have mapped blockages and have generated corrections useful in reducing scatter in magnitude estimates and in discriminant ratios. Such path corrections reduce RMS distance- and m_b -corrected *Lg* amplitude to as much as 60% of its original level (\log_{10} domain). Path corrections are less effective with *Pn* data. We also study source scaling effects on these data which will allow us to refine path corrections further.

Key Words: regional seismic characterization, China, path effects, source scaling

OBJECTIVE

We continue to characterize the regional excitation and propagation of seismic waves in China with sufficient accuracy to explain observed seismic data, and to detect, locate, and discriminate seismic events for the verification of a Comprehensive Test Ban Treaty (CTBT). Our primary source of seismic data has been the stations of the Chinese Digital Seismic Network (CDSN), augmented by nearby IRIS and Lamont stations. Using seismic waveforms and event locations from the USGS PDE and Chinese seismicity catalogs, we have identified P_n , P_g , S_n , L_g , Love and Rayleigh phases and picked arrival times and amplitudes for the body waves. Analysis of these arrival times will provide travel time and travel time corrections for large, well-located events to improve regional location. Amplitudes are analyzed to calibrate magnitude scales and for use in discrimination research.

RESEARCH ACCOMPLISHED

Past Regionalization Efforts. Randall et al. (1995) and Randall et al. (1996) have reported on initial data gathering and analysis efforts, including digital geology and cultural data (through USGS, Flagstaff), compilation of mine locations and practices, seismic event cluster analysis to further identify mining regions, magnitude scale calibration and detection threshold studies. Details can also be found in Hartse et al. (1996), Hartse et al. (1997abc) and Taylor and Hartse (1996, 1997).

Data Collection and Processing. We have collected and continue to process data from 11 CDSN and 8 IRIS and Lamont stations in and around China (Table 1, Figure 1). We began working with data from western China (stations WMQ and AAK) and now include data from central and eastern regions. Data consist of short-period, long-period and broadband recordings. We use PDE and SSB catalogs to identify and request data for events out to 2500 km, magnitudes 3.8 and up (PDE) and 2.0 and up (SSB).

Surface Wave Dispersion. We are compiling short-path (under 1000 km) surface wave dispersion results for western China. For areas of interest, we hope to improve on the 5° resolution available from longer path studies (Ritzwoller and Levshin, 1997). Initial results from WMQ clearly show effects of the Junggar basin for periods less than 20 s. Further details may be found in this volume (Jones and Patton, 1997).

Empirical Path Correction Using Topographic Data. We have evaluated empirical path correction methods of Zhang et al. (1996) using correlations with topography as well as basin and crustal thickness to reduce the scatter of discriminant ratios in western China. Physical data have been taken from the Cornell database (Fielding et al., 1993). We find distance-weighted topography and basin thickness corrections improve the separation between earthquake and nuclear test P_g/L_g discriminants in 1.5-3 and 2-4 Hz bands at WMQ. We find no improvement

for data recorded at AAK. Details of this study may also be found in this volume (Hartse et al. 1997b, also see Hartse et al. 1997c).

Empirical Path Corrections Based on Regional Seismic Data. Taking a different approach from Zhang et al. (1996), we have examined spatial distributions of amplitudes of regional phases to find coherent patterns that can be used as path-effect corrections. For example, a well-known path effect is the blockage of Lg across the edge of the Tibetan Plateau (e.g., Rapine et al. 1997). Seismograms recorded at LZH for events in eastern Tibet and the Baikal Rift illustrate this effect (Figure 2). We discuss the path-correction method and initial results further in the following.

To estimate path-correction factors for a given station, we first regress \log_{10} amplitude minus m_b versus \log_{10} distance, obtaining a set of amplitude residuals. As shown by Baker and Minster (1996) for discriminant ratios, patterns often emerge when such residuals are plotted on a map. These values are then smoothed spatially by averaging results for all events that fall within a 250 km circle that moves around a geographical grid (Figure 3). The smoothing is only allowed when there are more than a threshold number of crustal events (currently 5) inside the circle. Event depths are limited to under 50 km. Our assumption is that the smoothing averages out source and depth effects, leaving an estimate of the path effect that can be used for correcting magnitude estimates and discriminants.

We have applied this method to 1-2 Hz, Lg and Pn data from 6 stations in and near China (LZH, XAN, ENH, WMQ, AAK and NIL) using PDE catalog events recorded from 1986 to the present, available from the IRIS database. Spatial patterns are most apparent for the Lg phase. Results for LZH are plotted in Figure 4. The standard deviation of the \log_{10} -domain amplitude residuals is reduced from 0.53 to 0.37 after applying the path correction to LZH data. Scatter reduction quantified by the ratio of standard deviations, before and after path correction, is summarized in Table 2. We also include results for the Pn/Lg ratio, formed after correcting each phase independently.

Our amplitude correction patterns resemble the variation in coda Q throughout China found by Jin and Aki (1988). However, correcting LZH, 1-2 Hz, Lg minus m_b data using these Q values only reduced the RMS scatter to 90% of the original value. The coda Q correction worked well for paths to the southwest (E. Tibet) but poorly for paths to the northeast.

We have successfully applied the path correction technique to 3-6 Hz Pg/Lg discriminant ratios including Lop Nor events using data from AAK (see Hartse et al., 1997b, this volume). In contrast, empirical topographic techniques performed poorly with data from this station. The path correction technique could not be applied to Soviet test discrimination using WMQ data because no earthquakes occurred near the test site that could be used to calibrate those paths.

Source Scaling Corrections. The empirical path correction method outlined above does not account for the effect of source scaling. We evaluate this effect by inverting WMQ data for regional Q and source scaling terms as a function of frequency, assuming standard source models.

We plan to combine results of the source and path studies to refine correction values. Details of the source scaling study can be found in this volume (Hartse et al., 1997b, also see Taylor and Hartse, 1997).

RECOMMENDATIONS AND FUTURE PLANS

We will continue the assembly and analysis of regional information, and refine models by comparing synthetics with real data. Waveform modeling will be employed to characterize seismic sources and attempt to constrain event depths. We will continue to identify propagation issues and details relevant to discrimination and to identify mining events using waveform correlation and clustering techniques. We will begin to collect and process data from additional regions of interest. We will also begin to use data from portable deployments and temporary arrays. Results will be organized in a form suitable for use by AFTAC in their routine processing and special event studies.

ACKNOWLEDGMENTS

We thank the staff of the IRIS Data Management Center for help with our data requests. Maps were created using Global Mapping Tool (GMT) software (Wessel and Smith, 1991). Thanks also to Laura Jones for reviewing this manuscript. This work is in support of the DOE Comprehensive Test Ban Treaty Research and Development Program, ST482A and was performed at the Los Alamos National Laboratory under the auspices of the United States DOE, Contract Number W-7405-ENG-36.

REFERENCES

- Baker, G.E., and J.B. Minster, Quantifying the attenuation and blockage of Lg and robust statistical estimates of site amplifications at SCSN stations, *18th Ann. Seismic Research Symp. on Monitoring a Comprehensive Test Ban Treaty*, 1996.
- Fielding, E.J., M. Barazangi and B.L. Isacks, A geological and geophysical data base for Eurasia, *Final Technical Report, ARPA NMRO F29601-91-K-DB08*, 1993.
- Hartse, H.E., S.R. Taylor, W.S. Phillips and G.E. Randall, Regional seismic discrimination in central Asia with emphasis on western China, *18th Ann. Seismic Research Symp. on Monitoring a Comprehensive Test Ban Treaty*, 1996.
- Hartse, H.E., S.R. Taylor, W.S. Phillips, and G.E. Randall, A preliminary study of regional seismic discrimination in central Asia with emphasis on western China, *Bull. Seism. Soc. Am.*, **87**, 551-568, 1997a.
- Hartse, H.E., S.R. Taylor, W.S. Phillips and G.E. Randall, Applying source and path corrections to improve discrimination in China, *19th Ann. Seismic Research Symp. on Monitoring a Comprehensive Test Ban Treaty*, (this volume), 1997b.
- Hartse, H.E., R.C. Flores and P.A. Johnson, Correcting regional seismic discriminants for path effects in western China, *Bull. Seism. Soc. Am.*, submitted June, 1997c.

- Jones, L.E. and H.J. Patton, High resolution surface wave dispersion studies in China, *19th Ann. Seismic Research Symp. on Monitoring a Comprehensive Test Ban Treaty*, (this volume), 1997.
- Jin, A. and K. Aki, Spatial and temporal correlation between coda Q and seismicity in China, *Bull. Seism. Soc. Am.*, **78**, 741-769, 1988.
- Randall, G.E., T.A. Weaver, H.E. Hartse, S.R. Taylor, R.G. Warren and A.H. Cogbill, Regional characterization of western China, *Proc. 17th Ann. Seismic Research Symp. on Monitoring a Comprehensive Test Ban Treaty*, 1995.
- Randall, G.E., H.E. Hartse, W.S. Phillips and S.R. Taylor, Regional characterization of western China II, *18th Ann. Seismic Research Symp. on Monitoring a Comprehensive Test Ban Treaty*, 1996.
- Rapine, R, T. Hearn, J. Wu and J. Ni, Sn and Lg propagation characteristics beneath China, *18th Ann. Seismic Research Symp. on Monitoring a Comprehensive Test Ban Treaty*, 1996.
- Ritzwoller, M.H. and A.L. Levshin, Eurasian surface wave tomography: Group velocities, *J. Geophys. Res.*, submitted, March 1997.
- Taylor, S.R. and H.E. Hartse, Regional phase seismic detection thresholds at WMQ, *Los Alamos National Laboratory, Los Alamos, NM*, LAUR-96-395, 7pp, 1996.
- Taylor, S.R. and H.E. Hartse, A procedure for estimation of source and propagation amplitude corrections for regional seismic discriminants, *J. Geophys. Res.*, submitted, June 1997.
- Wessel P. and W.H.F. Smith, Free software helps map and display data, *EOS Trans AGU*, **72**, 441, 1991.
- Zhang, T., T. Lay, S. Schwartz and W.R. Walter, Variation of regional seismic discriminants with surface topographic roughness in the western United States, *Bull. Seis. Soc. Am.*, **86**, 714-725, 1996.

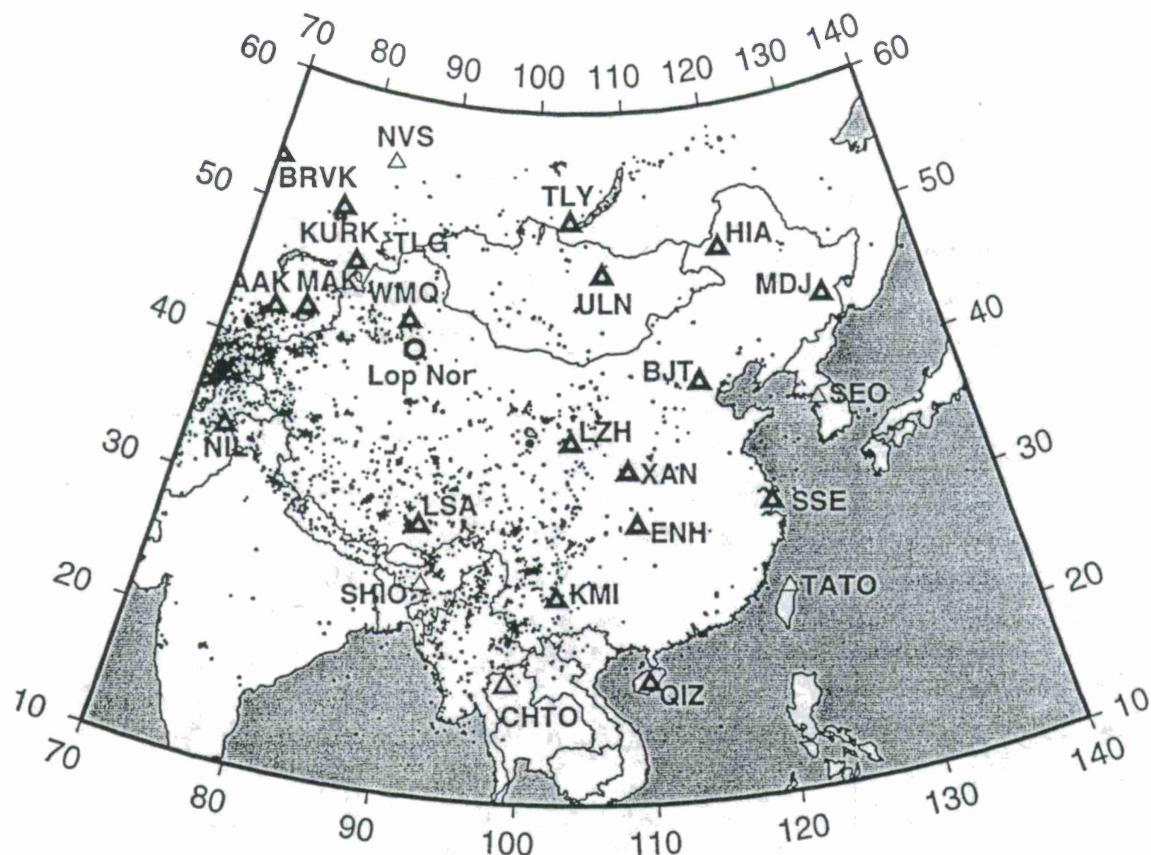


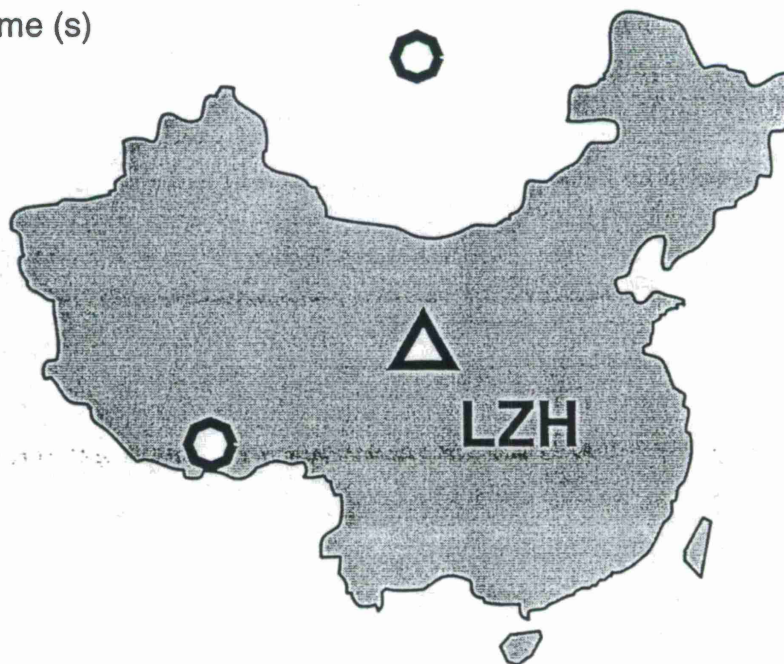
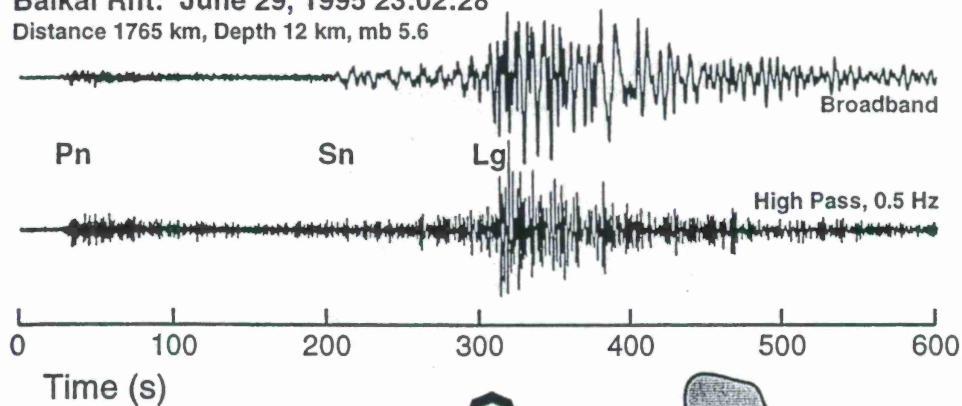
Figure 1. Stations in China and surrounding areas. Bold triangles represent stations for which data have been collected. PDE seismicity, 1986-1996, depth less than 50 km is also included.

Table 1. Data collected from the IRIS DMC.

Station	Location	Years Collected	Total Years
AAK	Kyrgyzstan	1990-1996	7
BJI/T	Beijing	1986-1996	11
BRVK	Borovoye	1994-1996	3
ENH	Enshi	1992-1996	5
HIA	Hailar	1988-1995	8
KMI	Kunming	1987-1996	10
KURK	Kurchatov	1994-1996	3
LSA	Lhasa	1992-1996	5
LZH	Lanzhou	1986-1996	11
MAK	Makanchi	1994-1995	2
MDJ	Mudanjiang	1989-1995	7
NIL	Nilore	1995-1996	2
QIZ	Qiongzong	1992-1996	5
SSE	Shanghai	1992-1996	5
TLG	Talgar	1994-1995	2
TLY	Talaya	1990-1996	7
ULN	Ulaanbaatar	1994-1996	3
WMQ	Urumqi	1986-1996	11
XAN	Xi'an	1993-1996	4

Baikal Rift: June 29, 1995 23:02:28

Distance 1765 km, Depth 12 km, mb 5.6



Eastern Tibet: July 30, 1992 8:24:46

Distance 1470 km, Depth 14 km, mb 5.9

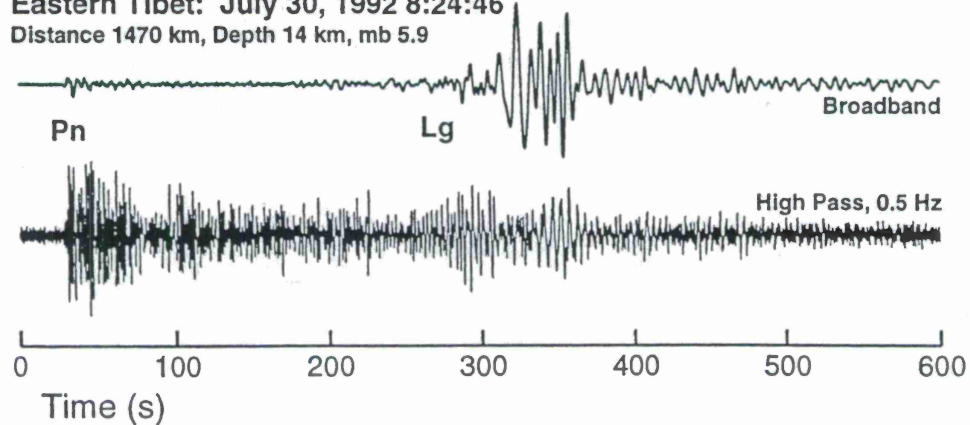


Figure 2. Broadband, vertical-component seismograms for events from the Baikal Rift (top) and eastern Tibet (bottom) recorded at LZH. In both cases, the lower trace has been high-pass filtered at 0.5 Hz. Traces are aligned with respect to the Pn arrivals.

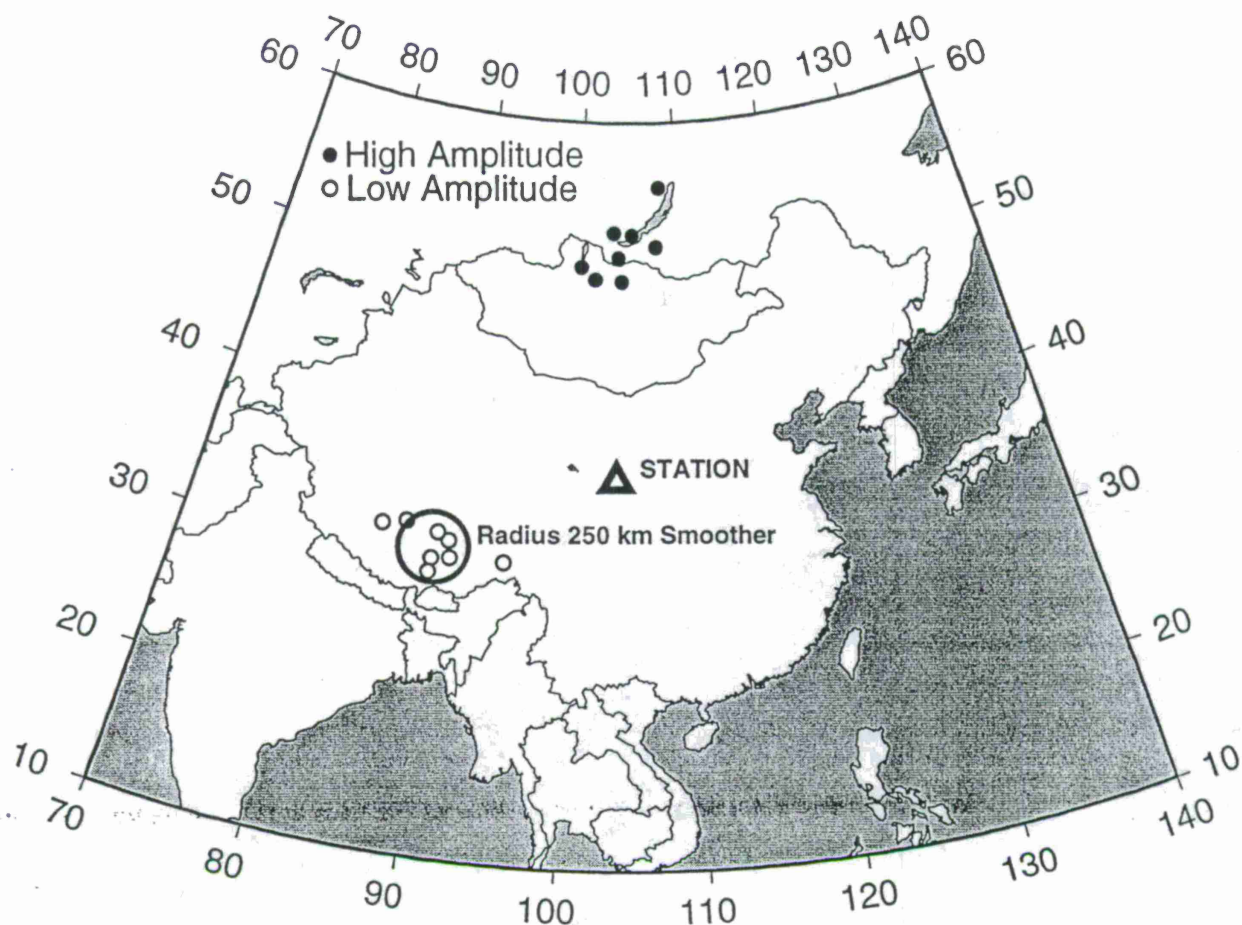


Figure 3. Illustration of the method used to create path corrections. Open and filled circles represent locations of events that generated relatively low and high amplitudes (distance-corrected log amplitude minus m_b), respectively. We require a minimum of five events within the smoothing circle to obtain a usable correction value.

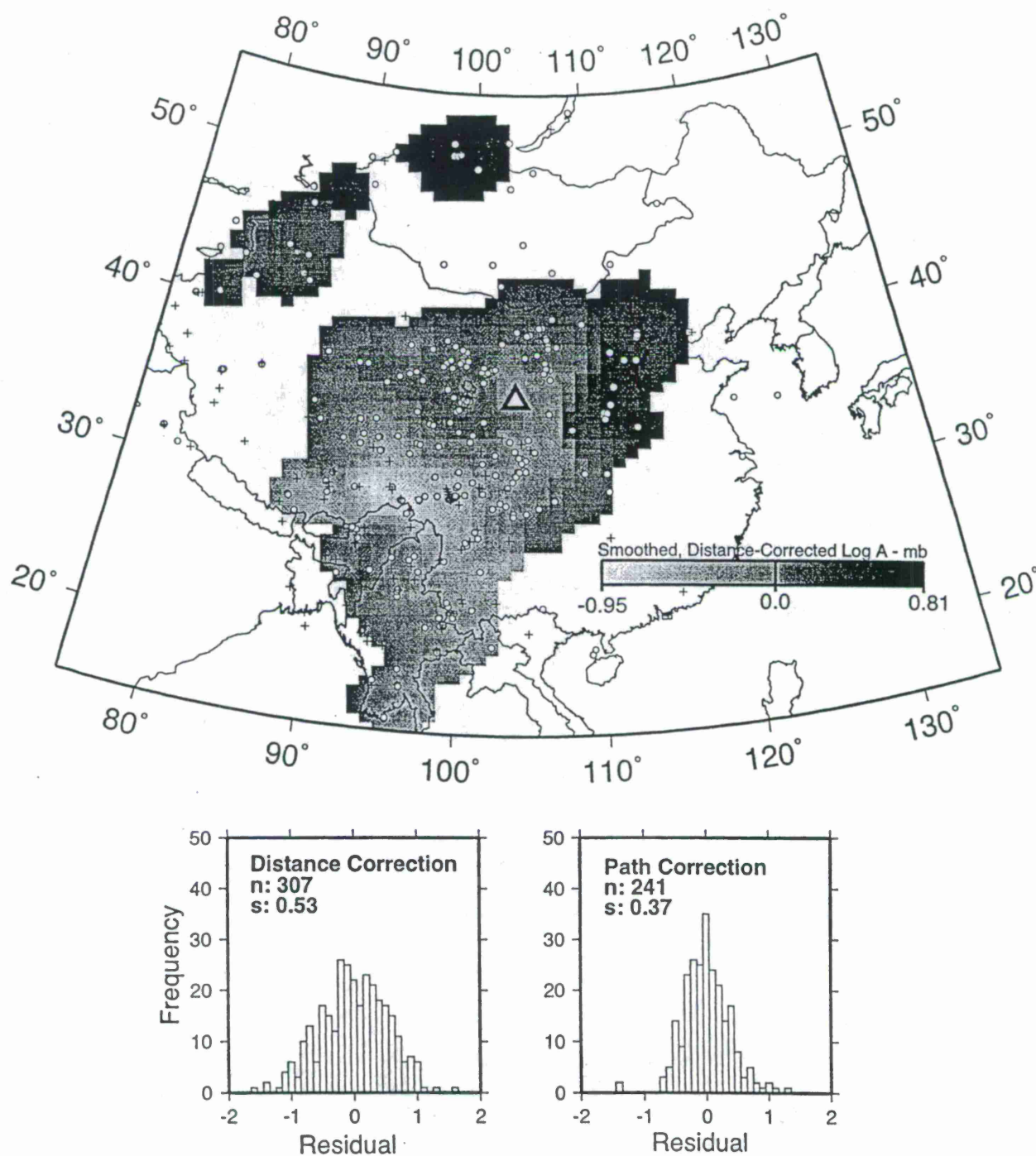


Figure 4. 1.5 Hz L_g path corrections (top) and log amplitude minus m_b residuals after correcting for distance (bottom left) and path (bottom right), for the station LZH, broadband vertical component. Corrections are plotted as a gray-scale image while events used in the analysis are plotted as open circles. Crosses represent events that were eliminated based on poor signal to noise. Histogram plots include the number of events (n) and the standard deviation of the residual (s). Similar results from other stations are summarized in Table 2.

Table 2. Ratio of standard deviations of distance-corrected, \log_{10} amplitude - m_b residuals and similarly calculated P_n/L_g discriminant ratio residuals, after / before path correction for the 1-2 Hz band , broadband vertical component.

Station	L_g	P_n	P_n/L_g
LZH	0.70	0.98	0.87
XAN	0.79	0.73	0.74
ENH	0.60	0.94	0.73
WMQ	0.87	0.88	0.81
AAK	0.89	0.86	0.81
NIL	0.73	0.86	0.87

REGIONAL WAVE PROPAGATION IN CHINA AND ITS SURROUNDING REGIONS

Richard R. Rapine, James F. Ni, and Thomas M. Hearn
Department of Physics, New Mexico State University, Las Cruces, NM 88003

Sponsored by U.S. Department of Energy
Office of Nonproliferation and National Security
Office of Research and Development
Contract No. F19628-95-K-0009

ABSTRACT

A comprehensive study of the gross characteristics of high frequency seismic wave propagation in China and its surrounding regions was accomplished to learn more about how regional geology affects high-frequency phases. Amplitudes of the regional seismic waves Sn and Lg relative to P coda were used to map lateral variations of shear wave attenuation in the crust and upper mantle. Over 7000 digital seismograms from 13 broadband stations of the Chinese Digital Seismic Network and Global Seismic Network in the frequency range 0.5 - 5.0 Hz were visually examined. Propagation efficiencies of Sn and Lg were qualitatively analyzed by ranking their amplitudes relative to the P-wave coda. Efficient Sn propagation is observed in the Tien Shan, Tarim Platform, southern Tibet, Yangzi Paraplatform and Sino-Korean Platform. We have confirmed results of previous studies by finding a lack of Sn transmission in north-central Tibet, the Ryukyu and Japan Arcs, Burma and the Baikal Rift. An important observation, which has not been previously reported, is that Sn does not propagate across Mongolia. The elimination of Sn and the occurrence of recent volcanism in north-central Tibet and Mongolia suggest that there is partial melt in the uppermost mantle beneath those regions. High-frequency Lg waves propagate efficiently for most of China, Indochina and Mongolia. Lg signals are attenuated within central Tibet as well as along its southern boundary. Crustal structure variations along with an anomalously low-Q crust are primarily responsible for weakened Lg amplitudes in Tibet. Propagation paths across oceanic crust in the Sea of Japan and the Andaman Sea show blockage of the Lg phase as well. This investigation has relevance to Comprehensive Test Ban Treaty monitoring by showing where certain regional phases will or will not propagate efficiently.

Keywords: China, Burma, Tibet, Pn, Sn, Pg, Lg, attenuation, discrimination.

OBJECTIVE

We are continuing characterization of the regional propagation of seismic waves in China and surrounding regions to explain observed seismic data, and to detect and discriminate seismic events for the verification of a Comprehensive Test Ban Treaty (CTBT). In particular we map the propagation characteristics of Sn and Lg waves in China through the examination of thousands of seismograms recorded on the Chinese Digital Seismic Network (CDSN) (Figure 1).

RESEARCH ACCOMPLISHED

The propagation characteristics of Pn, Sn and Lg have been used to constrain structure and provide insights into the tectonic processes in China and its adjacent regions. Previous studies (e.g., Kadinsky-Cade et al., 1981; Ni and Barazangi, 1983) analyzed short-period analog seismograms to qualitatively characterize broad tectonic provinces and subprovinces in terms of either efficient or inefficient Pn, Sn and Lg propagation. We have used a similar empirical approach for documenting the efficiencies of observed regional phases. Over 7000 broadband seismograms were examined. The average observed frequency content of Sn and Lg signals was between 0.5-3.0 Hz for all the stations so we used a bandpass filter set between 0.5 and 5.0 Hz. The instrument responses were not removed from the data so all data were analyzed as raw velocity seismograms. P-wave arrivals were manually picked only on the vertical component. We used an 8.2-6.0 km/s group velocity window to pick Pn and Pg. Sn and Lg were picked manually on the horizontal components that displayed the highest amplitudes for these phases. A group velocity window of 4.7-4.3 km/s was used for picking Sn and a 3.7-3.2 km/s velocity window was used for picking Lg. The propagation efficiencies of Sn and Lg were ranked according to their amplitudes relative to the P-wave coda amplitude. The P-wave coda amplitude is defined as the maximum amplitude within the 8.2-6.0 km/s velocity window. Sn and Lg amplitudes greater than the maximum amplitude of the P coda were classified as efficient. Sn and Lg amplitudes approximately one-half the amplitude of the P coda or less were classified as inefficient. No Sn or Lg is specified when neither Sn nor Lg is observed above the noise level of the seismogram. At times for short epicentral distances ($< 6^\circ$), the presence of a Pg wavetrain with frequencies comparable to Sn made it difficult to determine the presence or absence of Sn. Therefore, when Pg obscured the seismogram at the expected arrival time of Sn and no obvious Sn energy existed on the seismogram, we classified Sn as not observed.

The geological environment of China varies from stable continental shields to active/reactivated mountain belts, rifts and plateaus (Figure 2). As a result of the diversity of the regional geology, the high-frequency phases Sn and Lg show great lateral variability. Summary maps of Sn and Lg propagation efficiencies have provided insight into the crustal and mantle properties of the region and, when combined with existing geological information, into the reason why these phases are attenuated. Figure 3 is a summary map showing the major regions of efficient, inefficient and no Sn propagation. Figure 4 is a similar summary map of Lg propagation. Strong Sn waves are observed in the Tien Shan, Tarim Platform, southern Tibet, Yangzi Paraplatform and the Sino-Korean Platform. Efficient transmission is the expected result when propagation paths traverse stable shield regions. Inefficient Sn propagation is found in Western Tien Shan, southwest China and South China Sea. Sn attenuation or blockage occurs in north-central Tibet, the Japan and Ryukyu Arcs, Mongolia, the Baikal Rift and Burma. The strong Sn attenuation we observe on seismograms can be explained by a low-Q upper mantle due to partial melt. Partial melt may result from an enriched or metasomatized mantle caused by past

subduction events as well as high temperatures. Water and sediments contained within the subducted lithosphere increase the amount of crustal material in the mantle of the back-arc region. When this subducted material is subjected to the right pressure-temperature conditions, water will be released into the mantle. This process will enhance partial melt by effectively lowering the solidus temperature. This interpretation, which was applied to the Iranian Plateau by Hearn and Ni (1994) may explain the uppermost mantle in Burma, the Ryukyu and Japan Arcs, and Mongolia. The presence of Neogene alkali basaltic volcanism suggests that the upper mantle beneath Mongolia was hot in the recent past (Tapponnier and Molnar, 1979). In terms of island arc subduction, some studies have shown that Sn does not propagate on the concave side of island arcs due to a discontinuous high-Q upper mantle layer (e.g., Molnar and Oliver, 1969). We have confirmed this result by our observation of Sn attenuation near island arc subduction in Burma and the Ryukyu and Japan Arcs. The spatial relationship between attenuation and volcanism in these island arc regions is consistent with the presence of partial melt in the uppermost mantle, which would account for the Sn attenuation. In the Baikal Rift region, evidence suggests there is a doming of the lithosphere on top of hot upwelling asthenospheric material (e.g., Gao et al., 1994). This asthenospheric material in the lithospheric mantle would severely attenuate Sn phases. In north-central Tibet, Ni and Barazangi (1983) argue that partial melt in the uppermost mantle explains why there is inefficient Sn but no comparable Pn attenuation. Previous studies in Tibet attributed elevated temperatures and low-Q values to Quaternary to Recent basaltic volcanism from an upper mantle source (Turner et al., 1993).

Efficient Lg signals are observed throughout most of China (Figure 4). More specifically, strong Lg energy is recorded for propagation paths crossing the Tien Shan, Tarim Platform, Yangzi Paraplatform, Burma, Mongolia and Sino-Korean Platform. Regions where some inefficient Lg propagation can be seen are in northern Burma, central Tibet and the Pamirs. Lg blockage or partial blockage occurred for paths originating from the Japan Arc and Andaman Sea and for the southern boundary of the Tibetan Plateau (Figure 4). Lg is not expected to propagate along paths traversing oceanic crust in regions such as the Sea of Japan and Andaman Sea. This study could not resolve to what extent the islands of Japan themselves affected Lg propagation. Crustal structure and thickness variations on the boundaries of Tibet partially block Lg energy. The crustal thickness in western China and Tibet can change from 40 to 70 km depth over distances spanning less than a few hundred kilometers. Lg propagates efficiently within Tibet for distances less than 6° away from station LSA, but for longer distances within the plateau, Lg is weakened or extinct. In northern Tibet, Owens and Zandt (1997) found evidence for partial melt in the crust based on the low average S-wave velocity and high Poisson's ratio found there. The attenuation characteristics of southern Tibet were quantified by Reese and Ni (1996). They found a Q_c of approximately 150 at 1 Hz which is consistent with the existence of a low velocity zone in the mid-crust beneath the plateau. This suggests that high intrinsic attenuation in the crust is an important factor in the elimination of Lg as well as changes in the crustal structure.

CONCLUSIONS AND RECOMMENDATIONS

This investigation has increased our knowledge of the crust and uppermost mantle beneath China. It is evident that the complex geological and tectonic history of China has played a major role in the propagation characteristics of regional, high-frequency seismic phases. Partial melt in the upper mantle beneath island arc regions and locations of previous subduction events attenuates Sn signals. In this respect, the mantle in some regions of China may be analogous to the mantle beneath the Turkish-Iranian Plateau. Volcanism in north-central Tibet and in the

Mongolian Plateau provides evidence that the upper mantle beneath them is hot and partially melted and explains why Sn does not propagate through the regions. Another observation is that Lg is blocked when it travels across oceanic crust for more than a few hundred kilometers. It is also completely eliminated by abrupt crustal thickness changes and a partially melted, low-Q crust in Tibet. This study has shown that high Sn attenuation makes this phase difficult to use for nuclear discrimination in most of the region examined; however, Lg could be used as a short-period nuclear discriminant in most of China.

REFERENCES

- Gao, S., P. M. Davis, H. Liu, P. Slack, Y. A. Zorin, N. A. Logatchev, M. Kogan, P. Burkholder, and R. P. Meyer, Asymmetric upwarp of the Asthenosphere beneath the Baikal rift zone, Siberia, *J. Geophys. Res.*, **99**, 15319-15330, 1994.
- Hearn, T. and J. Ni, Pn velocities beneath continental collision zones: the Turkish-Iranian Plateau, *Geophys. J. Int.*, **117**, 273-283, 1994.
- Kadinsky-Cade, K., M. Barazangi, J. Oliver, and B. Isacks, Lateral Variations of high frequency seismic wave propagation at regional distances across the Turkish and Iranian Plateaus, *J. Geophys. Res.*, **86**, 9377-9396, 1981.
- Molnar, P. and J. Oliver, Lateral variations of attenuation in the upper mantle and discontinuities in the lithosphere, *J. Geophys. Res.*, **74**, 2648-2682, 1969.
- Ni, J. and M. Barazangi, Velocities and propagation characteristics of Pn, Pg, Sn and Lg seismic waves beneath the Indian Shield, Himalayan Arc, Tibetan Plateau, and surrounding regions: High uppermost mantle velocities and efficient Sn propagation beneath Tibet, *Geophys. J. R. Astr. Soc.*, **72**, 665-689, 1983.
- Owens, T. J., and G. Zandt, Implications of Crustal Property Variations for Models of Tibetan Plateau Evolution, *Nature*, **387**, 37-43, 1997.
- Reese, C., and J. Ni, Attenuation of Coda Waves in Southern Tibet, *Geophys. Res. Lett.*, **23**, 3015-3018, 1996.
- Rodgers, A., J. Ni, and T. Hearn, Pn, Sn, and Lg propagation in the Middle East, *Bull. Seism. Soc. Am.*, **87**, 396-413, 1997.
- Tapponnier, P. and P. Molnar, Active faulting and Cenezoic tectonics of the Tien Shan, Mongolia, and Baykal regions, *J. Geophys. Res.*, **84**, 3425-3459, 1979.
- Turner, S., C. Hawkesworth, J. Liu, N. Rodgers, S. Kelley, and P. VanCalsteren, Timing of Tibetan uplift constrained by analysis of volcanic rocks, *Nature*, **364**, 50-54, 1993.

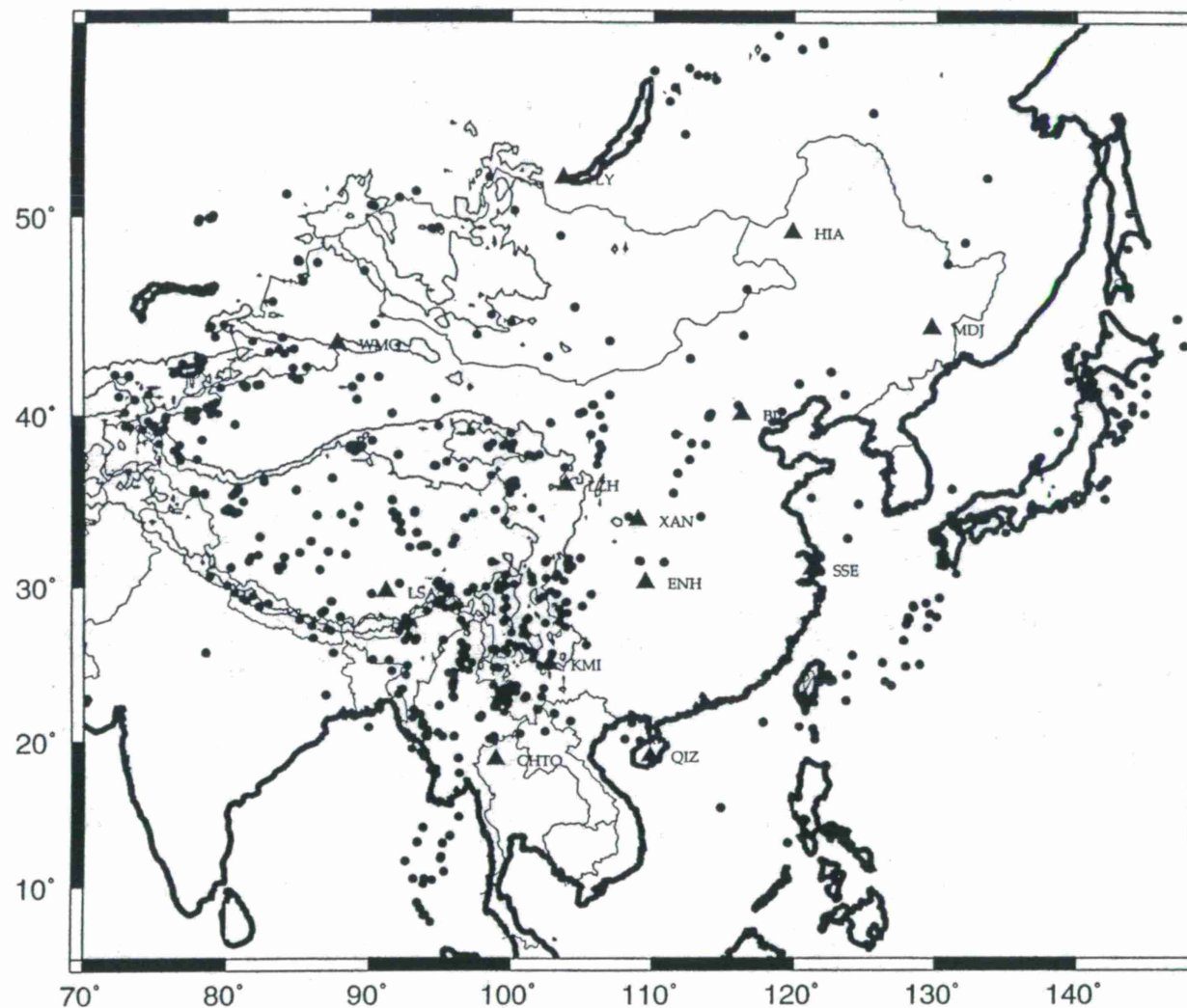


Figure 1. A map showing CDSN station locations. Black triangles represent station locations. Black circles are seismic event locations and gray lines are 2000 and 4000 m elevation contours.

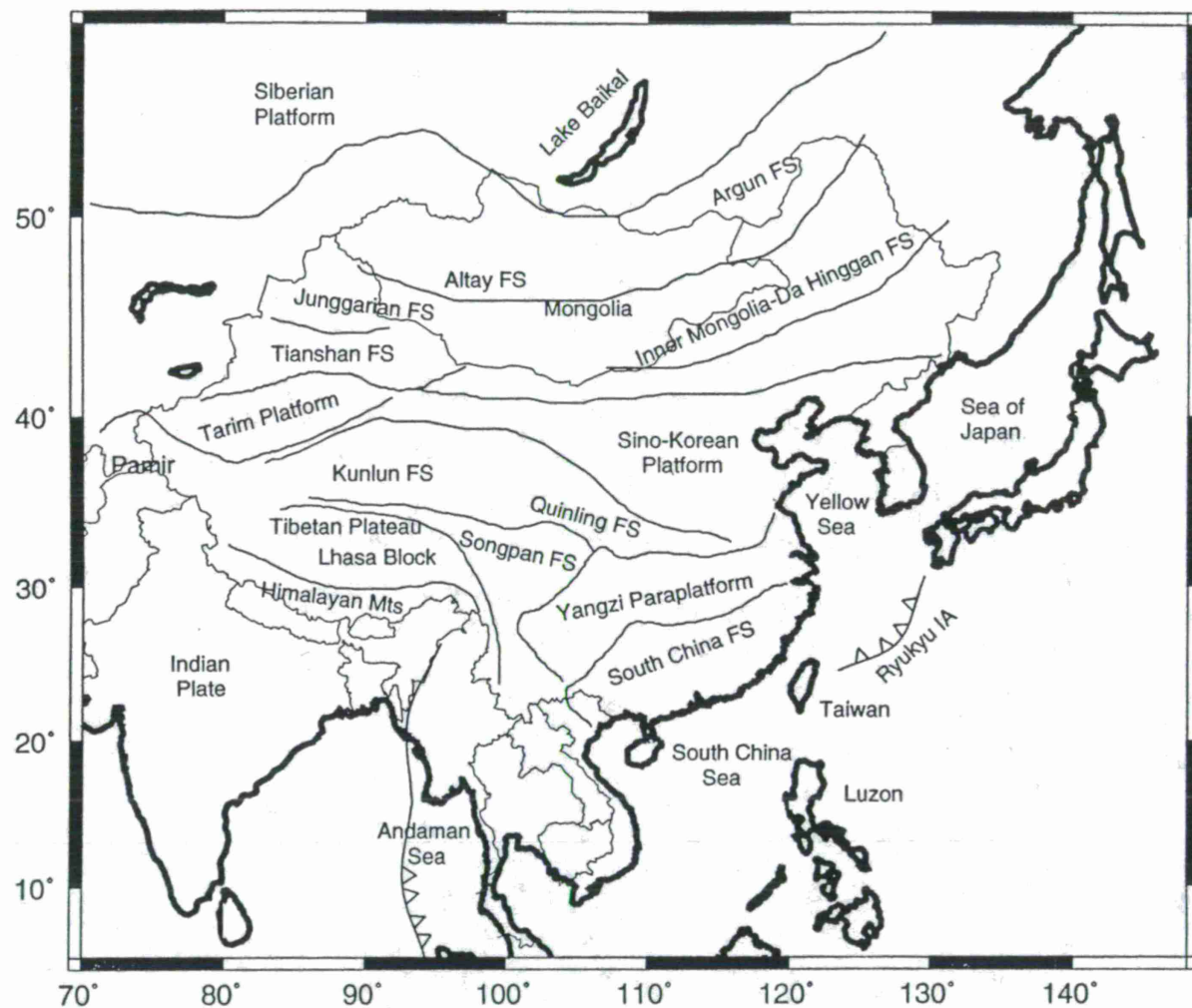


Figure 2. A simplified tectonic map of China and its surrounding regions. Dark lines separate the major tectonic provinces in the region. Open triangles point in the direction of oceanic subduction.

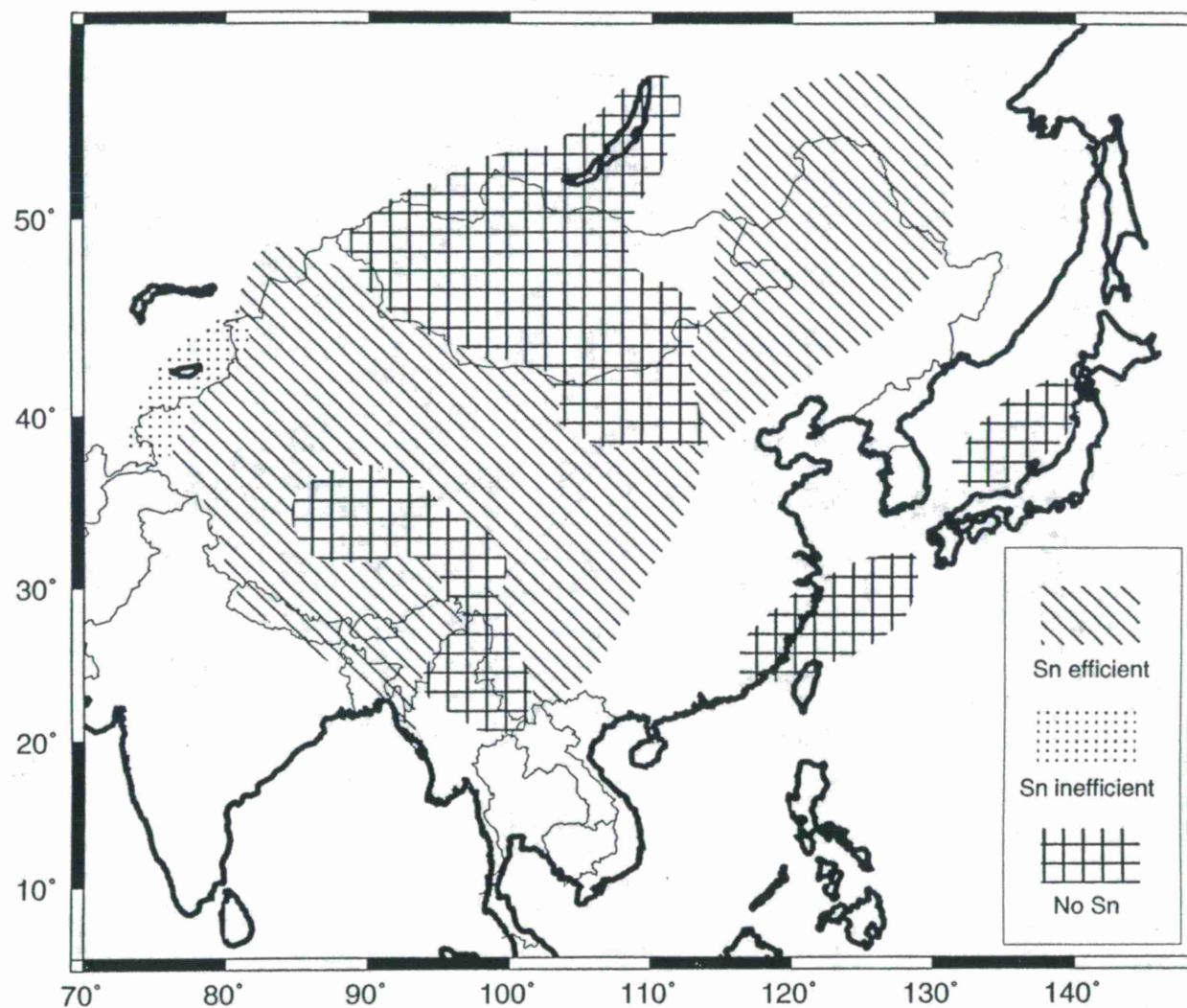


Figure 3. This summary map shows the approximate regions of efficient, inefficient and no Sn propagation in China.

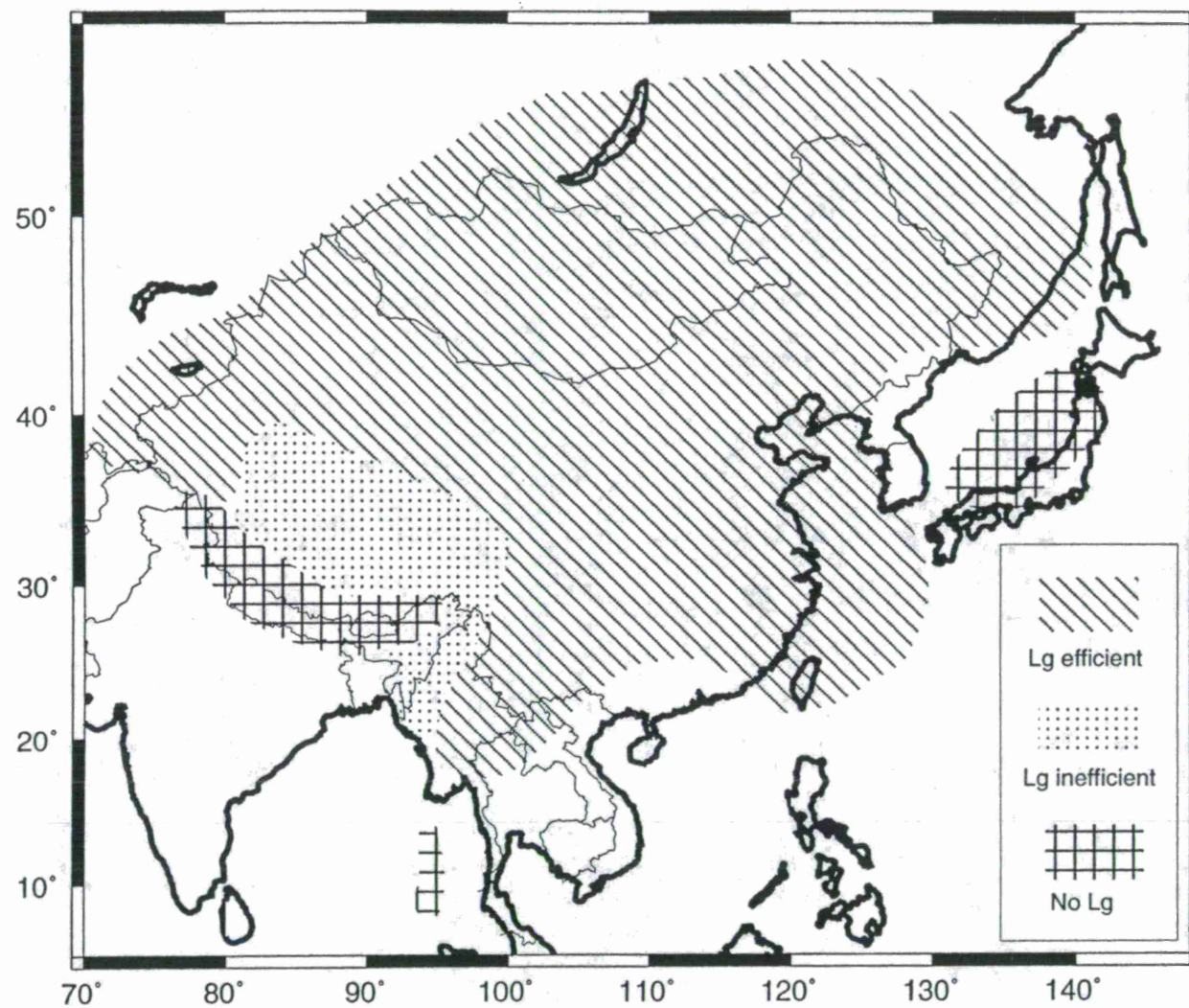


Figure 4. This summary map shows the approximate regions of efficient, inefficient and no Lg propagation in China.

**REGIONALIZATION AND CALIBRATION OF SEISMIC DISCRIMINANTS, PATH
EFFECTS AND SIGNAL-TO-NOISE FOR STATION ABKT
(ALIBEK, TURKMENISTAN)**

Arthur Rodgers and William Walter

*Lawrence Livermore National Laboratory, Earth Sciences Division, Livermore, CA 94551
e-mail.- rodgers@s34.es.llnl.gov,-phone: 510-423-5018*

Sponsored by U.S. Department of Energy
Office of Nonproliferation and National Security
Office of Research and Development
Contract No. W-7405-ENG-48

ABSTRACT

We report measurements and analysis of regional seismic phase amplitude ratios and signal-to-noise for earthquakes observed at the International Monitoring System primary station ABKT (Alibek, Turkmenistan). We measured noise and phase amplitudes of the regional phases Pn, Pg, Sn and Lg in four frequency bands between 0.75-9.0 Hz. Measurements were made in both the time and frequency domains. The spatial variation of amplitude ratios (e.g. Pn/Lg, Pg/Lg, Pn/Sn, Pg/Sn) and signal-to-noise (phase/noise) reveal significant path effect differences between the Hindu Kush, Kazakh Platform, Iranian Plateau and Caspian Sea. In order to represent this behavior, we have investigated several techniques for characterizing the data. These techniques are: 1) correlation with along-path distance and waveguide properties; 2) sector analysis; and 3) spatial averaging.

Along-path waveguide properties, such as mean elevation and rms topographic slope are found to be the strongest factors related to Pg/Lg amplitude ratios at the lowest frequencies (< 3.0 Hz). Other path properties such as mean crustal thickness and basement depth are not strongly correlated with Pg/Lg ratios. For sector analysis we divided the data into four (4) azimuthal sectors and characterized the data within each sector by a distance trend. Sectors were chosen based on the behavior of Pn/Lg, Pg/Lg and Pn/Sn amplitude ratios as well as topographic and tectonic character. Results reveal significant reduction (up to a factor of two) in the scatter of the Pn/Lg and Pg/Lg amplitude ratios for the sectorized data compared to the entire data set from all azimuths. Spatial averaging involves smoothing and interpolation of the ratios projected at the event location. Methods such as cap averaging and kriging will be presented at the meeting.

Key words: CTBT Monitoring, Regional Discriminants, Path Effects, Station ABKT, Middle East

OBJECTIVE

As ratification of the Comprehensive Test Ban Treaty (CTBT) and entry into force approaches, research efforts need to focus on calibration of the International Monitoring System (IMS). In particular, seismic discriminants need to be measured for the earthquake population so that meaningful identification and analysis of outliers can be performed. It is now well accepted that regional seismic P/S ratios can discriminate earthquake and explosion sources, particularly at frequencies above 3.0 Hz (e.g. Walter et al., 1995; Taylor, 1996; Hartse et al., 1997). Station ABKT (Alibek, Turkmenistan) is an IMS primary seismic station and is located within regional distances of Iran, Afghanistan and many Former Soviet Republics. This region has abundant, but unevenly distributed seismicity. However, great variability in earthquake Sn and Lg amplitudes has been reported for this station (Rodgers et al., 1997a). The regional phases Pn and Sn mostly sample the mantle, while Pg and Lg sample the crust. The variability in earthquake generated Pn/Lg, Pg/Lg and Pn/Sn ratios (up to two orders of magnitude) is greater than the typical separation of earthquake and explosion populations. Thus, the spatial variation of earthquake P/S ratios needs to be determined in order to map out discriminant behavior.

The objective of this research is to measure, map and characterize regional P/S discriminants (e.g. Pn/Lg, Pg/Lg, Pn/Sn, Pg/Sn) for station ABKT. In addition we measured the signal-to-noise for each regional phase (Pn, Pg, Sn and Lg). Results of this study are maps of P/S discriminant behavior and individual phase signal-to-noise ratios. We have also attempted to represent the observed spatial variation of discriminant behavior by correlation with along-path distance and crustal waveguide properties, sector analysis and spatial averaging. We have processed and analyzed data at all broadband stations in the Middle East and southern Eurasia (AAK, ANTO, BGIO, KEG, KIV and NIL), but because of the large data set available for ABKT and its importance as an IMS primary station we are focusing on ABKT. Because of the large variability observed at ABKT, this station provides a good data set to test techniques for spatial averaging regional P/S discriminants.

RESEARCH ACCOMPLISHED

Data Processing

Three-component waveform data was requested from the Incorporated Research Institutions for Seismology-Data Management Center (IRIS-DMC) for station ABKT for regional events spanning the period 1993-1995. Event locations and origin times were taken from the National Earthquake Information Center-Preliminary Determination of Epicenters (NEIC-PDE) catalog. We restricted data to depths less than 50 km and body-wave magnitudes greater than or equal to 4.0. All waveforms were previewed and a first-arriving P-wave was picked when possible. Noisy data were immediately discarded. Regional phases were isolated with the following group velocity windows: Pn 8.0-6.2 km/s; Pg 6.2-5.0 km/s; Sn 4.6-4.0 km/s; Lg 3.6-3.0 km/s. In order to account for event mislocations and timing errors, the origin time was shifted so that the Pn phase arrives at 7.9 km/s. This is an appropriate average value for the region (Hearn and Ni, 1994). Normally, this shift was less than about five seconds. Noise was taken as a 35 second window ending 5 seconds before the P-wave. Regional phase and noise amplitude measurements were made on vertical component waveforms in both the time and frequency domains following the procedures outlined in Rodgers et al. (1997b). Time domain measurements were made on bandpass filtered waveforms using the rms amplitude in the phase window. Frequency domain measurements were made on broadband waveforms as the log10-mean amplitude of the phase window spectrum for the given pass band. Differences between these and other regional phase amplitude ratio measurement techniques are described in Rodgers et al. (1997b). P/S amplitude ratios were found in four frequency bands (0.75-1.5, 1.5-3.0, 3.0-6.0 and 6.0-9.0 Hz). The resulting data set contained over 300 earthquakes.

Spatial Variation of Pg/Lg and Pn/Sn

Figure 1 shows the event locations, ABKT location and the major topographic/tectonic provinces of the region. Seismicity is dominated by the Hindu Kush and Zagros Mountains. The spatial variation in the individual Pg/Lg and Pn/Sn amplitude ratios are shown in Figures 2 and 3, respectively. For these maps amplitudes were measured in the time domain using the rms and only data for which the Pn/pre-Pn noise ratio was greater than 2.0 were plotted. Pg/Lg and Pn/Sn amplitude ratios span nearly two orders of magnitude. Two points are immediately notable from these maps. Firstly, as the frequency pass band increases (> 3.0 Hz) most of the paths from the Zagros fail the signal-to-noise criteria, whereas paths from the Hindu Kush survive the signal-to-noise criteria. Note that the signal-to-noise criteria is based only on the Pn/pre-Pn ratio. Signal-to-noise for other regional phases behaves similarly and will be shown at the meeting. Secondly, the Pg/Lg and Pn/Sn amplitude ratios show good spatial coherence with the Hindu Kush showing low Pg/Lg and Pn/Sn and the Zagros showing high Pg/Lg and Pn/Sn. It is important to note, however, that these two regions are at roughly the same distance (about 1100 km) from ABKT. This indicates that there exist different path effects between these two regions. In order to reduce the variability of these amplitude ratios, it is appealing to group paths together on the basis of their topographic and tectonic character as well as their Pg/Lg and Pn/Sn behavior.

Variability of Sn and Lg amplitudes in the Middle East (including observations at ABKT) was reported by Rodgers et al. (1997a). Weak Sn energy corresponds to the high elevations of Iranian Plateau, recent volcanism and low Pn velocities (Hearn and Ni, 1994). The simultaneous occurrence of these observations probably results from partial melt in the shallow mantle. Lg amplitudes are reduced for paths crossing the Zagros relative to paths from the Hindu Kush. Paths crossing the southern Caspian Sea show very little Lg energy, probably due to the remnants of oceanic crust.

Distance Corrections, Along-Path Waveguide Effects and Sector Analysis

Recent discrimination studies have illustrated the importance of correcting amplitude ratios for distance effects before constructing discrimination plots (Taylor, 1996; Hartse et al., 1997). Distance corrections can remove the effects of attenuation and geometric spreading as well as possibly account for other path effects. A recent study of path effects on regional discriminants in China by Fan and Lay (1997) found that distance is an important path parameter along with mean path elevation, topographic roughness, mean crustal thickness and mean basement depth.

Figure 4 shows the \log_{10} Pg/Lg amplitude ratios for the four frequency bands versus distance along with a linear regression fit to a straight line. The symbols are coded by the sectors shown in Figure 1. The linear correlations (r) are rather weak ($< |0.4|$) and the data are very scattered. The standard error about the regression fits (sd) are 0.16-0.27 \log_{10} Pg/Lg amplitude. We investigated the relationship between Pg/Lg ratios and other along-path parameters. These included: mean elevation, surface roughness (rms elevation), rms slope, elevation skewness, mean basement depth and mean crustal thickness. Topography was taken from ETOPO5; basement and Moho depths were taken from the (Soviet) Institute of Physics of the Earth compiled maps.

For ABKT we found that rms slope is well correlated with the Pg/Lg ratios, but only for frequencies less than 3.0 Hz. Figure 5 shows the Pg/Lg ratios vs. rms slope. Note that the linear correlations are stronger for rms slope than for distance, but the standard error about the regression fits (sd) are only slightly smaller. For this plot the data are symbol-coded by sector as in Figure 4. Grouping of the ratios by sector is also seen: Hindu Kush paths (circles) have lower rms slope than Zagros paths (triangles). Pn/Lg showed more scatter, but slightly stronger distance dependence.

When the data is subdivided by azimuthal sector, as shown in Figure 1, the Pg/Lg ratios are strongly correlated with distance. Figure 6 shows the distance trends for each sector. The data demonstrate less scatter and have stronger linear correlations (up to 0.7) than the data set for all azimuths. The largest reduction in scatter is seen for the Hindu Kush and Zagros at frequencies less than 3.0 Hz. But for these sectors the data sampling is not evenly distributed over distance. Slightly smaller scatter reduction was obtained by sector subdivision of the Pn/Lg ratios.

CONCLUSIONS AND RECOMMENDATIONS

Regional seismic P/S discriminants observed at station ABKT for a large earthquake population show great variability. However, this variability results from regional (azimuthal) variations in path effects. We have shown that reduction in the scatter of regional discriminants can be achieved by subdividing the data into azimuthal sectors and characterizing the data within each sector by a simple distance correction. We are currently investigating the relationship of regional discriminants with along-path topographic and waveguide properties (similar to Fan and Lay, 1997) and spatial averaging (such as cap-averaging and kriging). Hopefully by the meeting we will be able to compare the performance of these three techniques for characterizing the spatial variation of regional discriminants. Performance will be judged by the predictive capabilities of each technique.

Although the reduction of regional discriminant scatter obtained by sector analysis for low frequencies (< 3.0 Hz) is encouraging, the scatter remains and signal-to-noise is low for higher frequencies (> 3.0 Hz). Large reduction in discriminant scatter for low frequencies was obtained by correlating amplitude ratios with along-path crustal waveguide properties (Fan and Lay, 1997). Regional discrimination studies typically find better discriminant performance for higher frequencies (e.g. Walter et al., 1995; Taylor, 1996; Hartse et al., 1997). The low signal-to-noise we report for the Iranian Plateau is probably due to higher lithospheric attenuation and may lead to higher detection thresholds for this region.

REFERENCES

- Fan, G. and Lay, T. (1997). Statistical analysis of irregular waveguide influences on regional seismic discriminants in China, (submitted to *Bull. Seismo. Soc. Am.*).
- Hartse, H., Taylor, S., Phillips, S., and Randall, G. (1997). A preliminary study of regional seismic discrimination in Central Asia with emphasis on western China, *Bull. Seismo. Soc. Am.*, **87**, 396-413.
- Hearn, T. and Ni, J. (1994). Pn velocities beneath continental collision zones: the Turkish-Iranian Plateau, *Geophys. J. Int.*, **117**, 273-283.
- Rodgers, A., Ni, J. and Hearn, T. (1997a). Propagation characteristics of short-period Sn and Lg in the Middle East, *Bull. Seismo. Soc. Am.*, **87**, 396-413.
- Rodgers, A., Lay, T., Walter, W. and Mayeda, K. (1997b). Comparison of regional phase amplitude ratio measurement techniques, UCLR-JC-127080 (submitted to *Bull. Seismo. Soc. Am.*).
- Taylor, S. (1997). Analysis of high-frequency Pg/Lg ratios from NTS explosions and western U.S. earthquakes, *Bull. Seismo. Soc. Am.*, **86**, 1042-1053.
- Walter, W., Mayeda, K. and Patton, H. (1995). Phase and spectral ratio discrimination between NTS earthquakes and explosions. Part 1: empirical observations, *Bull. Seismo. Soc. Am.*, **85**, 1050-1067.

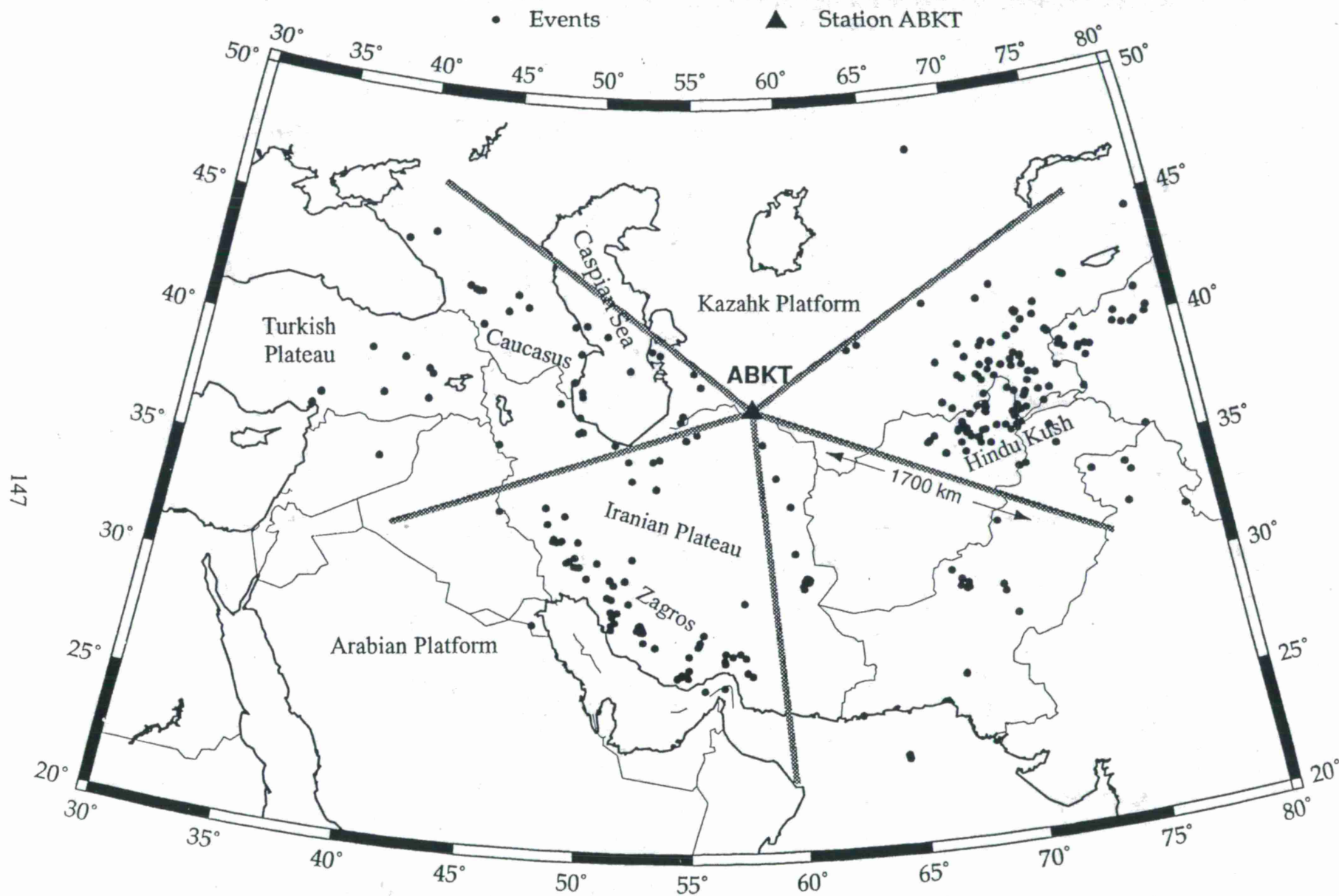
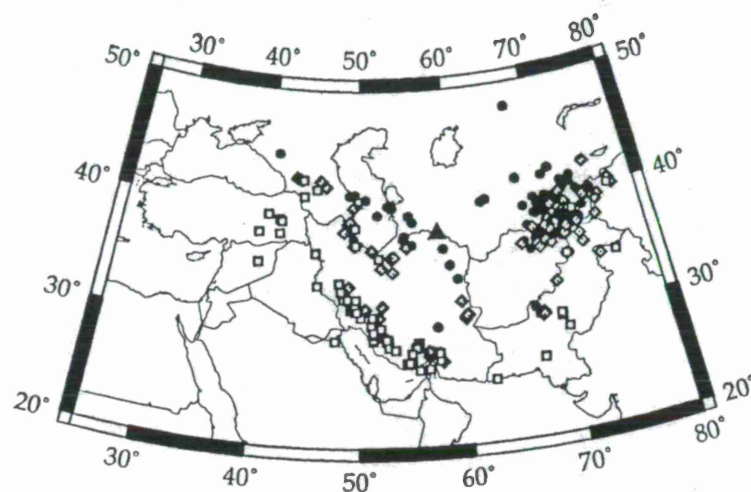


Figure 1. Locations of station ABKT and the regional events studied. Major topographic/tectonic units are labeled. Heavy grey lines mark the azimuthal boundaries of the sectors described in the text.

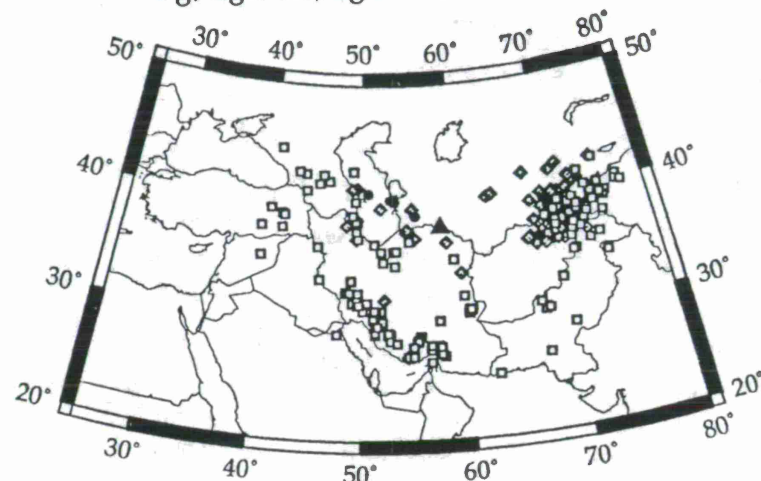
ABKT Pg/Lg

Amplitude Ratio
Time domain: Rms
Pn/noise > 2.0

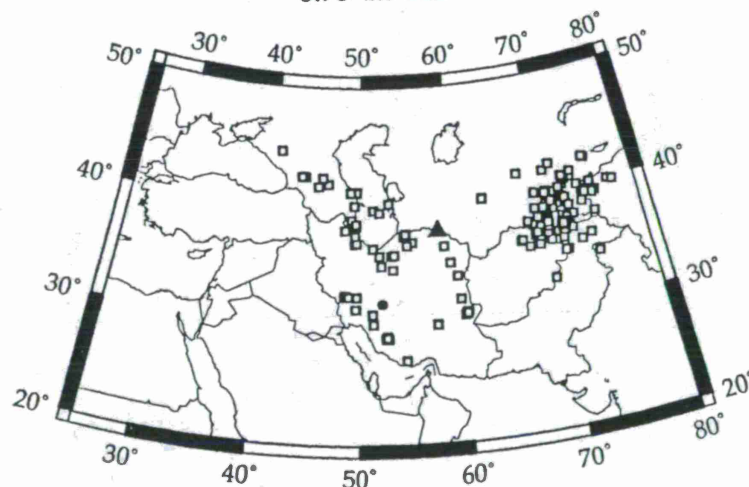
- $Pg/Lg < 0.5$, Lg efficient
- ◆ $0.5 \leq Pg/Lg \leq 1.0$, Lg intermediate
- ▣ $Pg/Lg > 1.0$, Lg weak



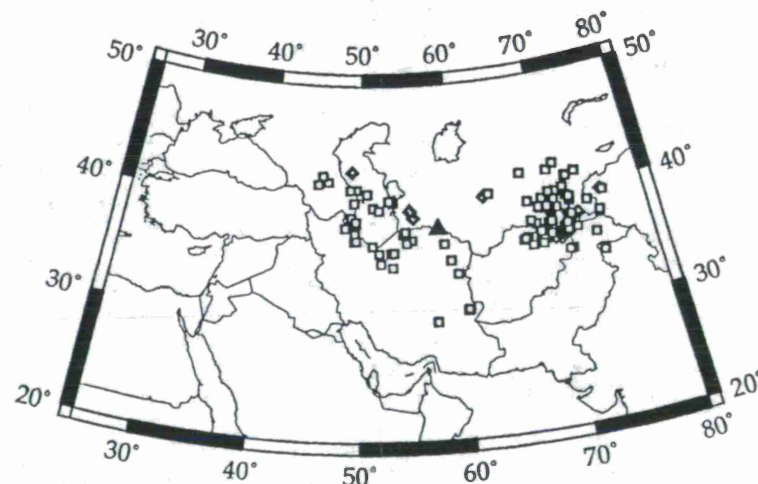
0.75-1.5 Hz



1.5-3.0 Hz



3.0-6.0 Hz



6.0-9.0 Hz

Figure 2. Map of Pg/Lg amplitude ratios observed at ABKT for the four frequency bands considered.

ABKT Pn/Sn

Amplitude Ratio
Time domain: Rms
Pn/noise > 2.0

- Pn/Sn < 0.5, Sn efficient
- ◆ 0.5 ≤ Pn/Sn ≤ 1.0, Sn intermediate
- ◻ Pn/Sn > 1.0, Sn weak

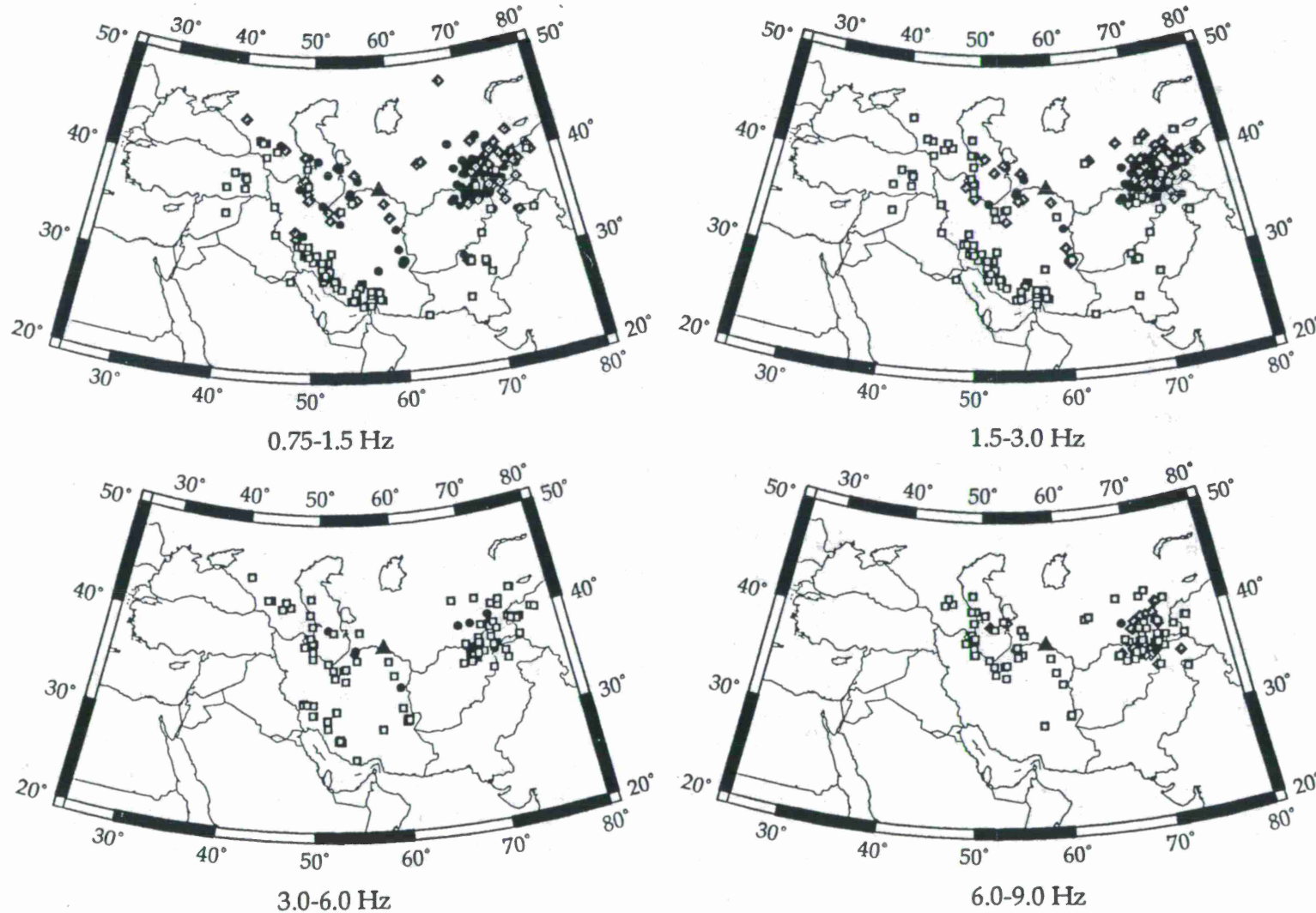
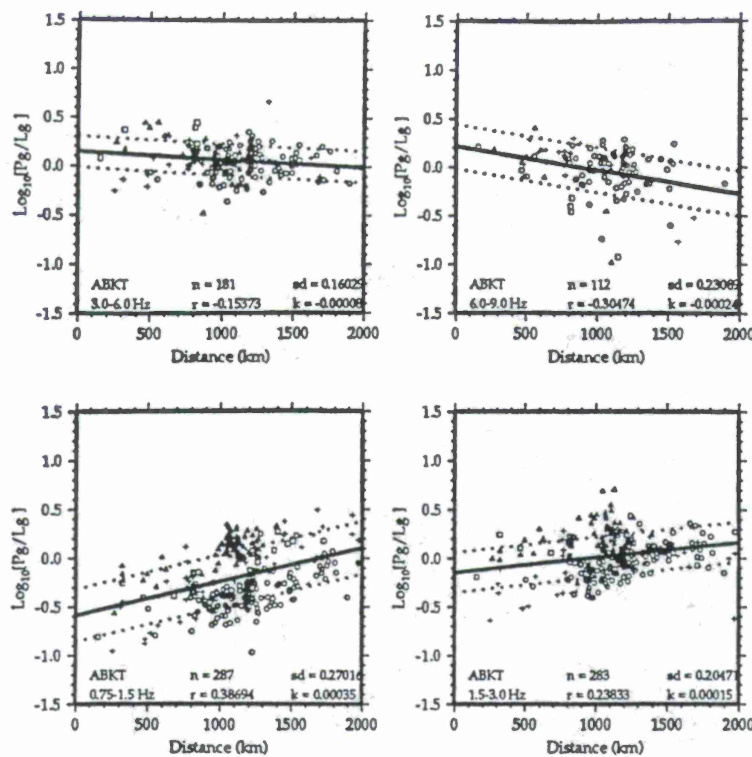


Figure 3. Map of Pn/Sn amplitude ratios observed at ABKT for the four frequency bands considered.

ABKT Pg/Lg vs. Distance



Symbols coded by sector

- Hindu Kush
- Southeast
- Zagros
- Caspian

Figure 4. Correlations of Pg/Lg ratios observed at ABKT (0.75-9.0 Hz) versus distance. Symbols are coded by the sectors shown in Figure 1. The number of data (n), linear correlation (r) and the standard error about the fit (sd) are shown. Note that the Pg/Lg ratios tend to group by sector.

ABKT Pg/Lg vs. Rms Topographic Slope

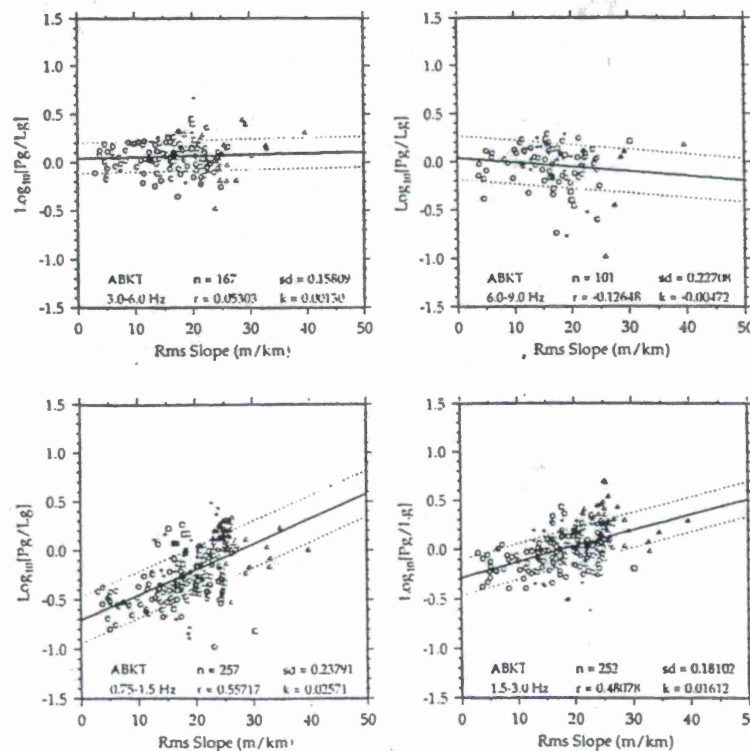
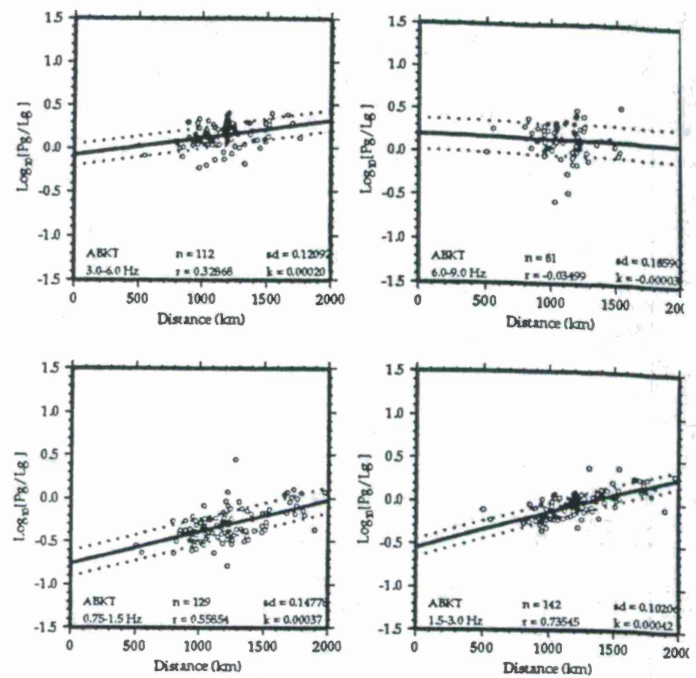
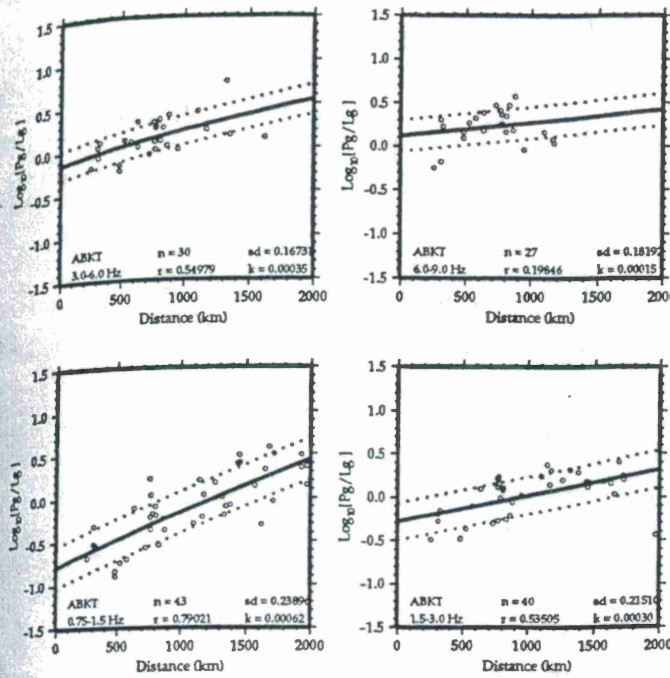


Figure 5. Correlations of Pg/Lg ratios observed at ABKT (0.75-9.0 Hz) versus along path distance. Symbols are coded by the sectors as shown above. The number of data (n), linear correlation (r) and the standard error about the fit (sd) are shown. Note that the Pg/Lg ratios tend to group by sector.

ABKT Pg/Lg Distance Trends for the four Sectors

Caspian

Hindu Kush



Zagros

Southeast (Makran, Afganistan)

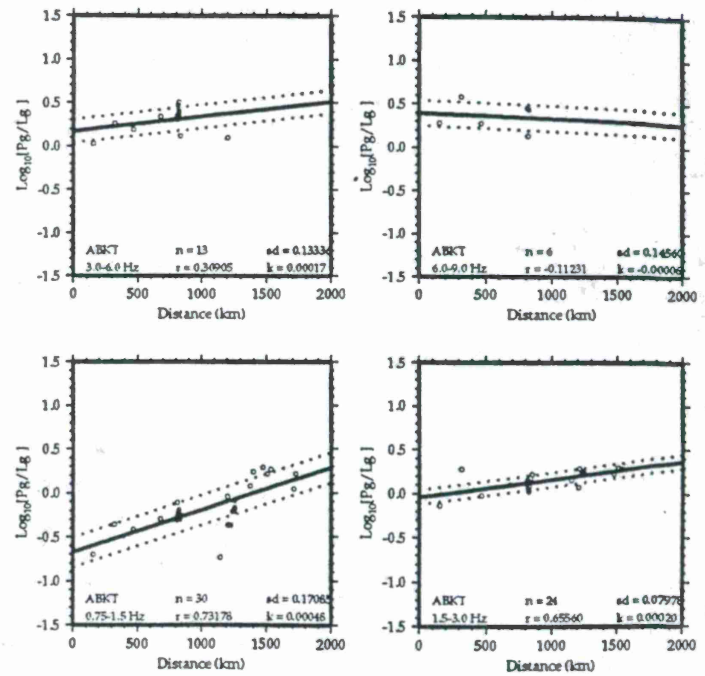
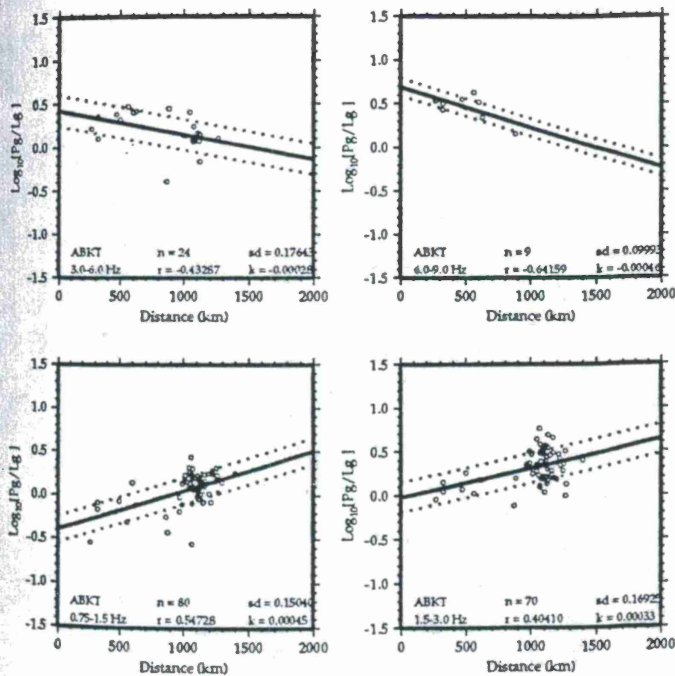


Figure 6. Correlations of Pg/Lg observed at ABKT (0.75-9.0 Hz) for the four sectors shown in Figure 1. The number of data (n), linear correlation (r), slope of the regression fit (k) and the standard error about the fit (sd) are shown. Note that the scatter in the data are reduced and the linear correlations are increased relative to those shown in Figure 4.

**JOINT RF/US RESEARCH PROGRAM OF SEISMIC CALIBRATION
OF THE INTERNATIONAL MONITORING SYSTEM
IN NORTHERN EURASIA AND NORTH AMERICA**
First Steps

US WORKING GROUP (Contact Person: Vladislav Ryaboy)
Center for Monitoring Research
1300 N. 17th Street, Suite 1450, Arlington, VA 22209

Sponsored by Defense Special Weapons Agency
Contract No. DSWA001-93-C-0173

ABSTRACT

Joint Research Program of Seismic Calibration of the International Monitoring System (IMS) in Northern Eurasia and North America was signed by Nuclear Treaty Programs Office (NTPO) DOD USA and Special Monitoring Service (SMS) RF MOD on 18 March 1997. The two-year joint research is aimed at seismic calibration of some regions of Northern Eurasia and North America through the development, verification and application of a three-dimensional (3-D) velocity model of the earth's crust and upper mantle, for a substantial improvement in seismic event location accuracy. The main objective of the Joint Program is collection, interpretation and application for calibration purposes of data from the extensive deep seismic studies, carried out during the past 25-30 years in both countries, and based on recordings of earthquakes, recorded with dense networks, and large chemical and nuclear explosions with well known location and origin time. As a result, an accurate travel-times database will be developed which will provide a substantial improvement in seismic event location accuracy. The RF/US working group was established to coordinate the joint research program. The US members of the working group are: A. Dainty (chair), D. Baumgardt, J. Murphy, R. North, and V. Ryaboy. Responsibility for the work rests with the Center for Monitoring Research (CMR) and the Special Monitoring Service RF MOD.

RF and US both have started inventory, collection travel-times and preliminary analysis of seismic data available for the IMS calibration. This paper shows some preliminary results of Pn travel-time collection and analysis for North America. Completed analyses of travel-time curves and maps of travel-time deviations from the global IASPEI-91 tables which are being used now by the prototype International Data Center (IDC) for seismic event locations, dramatically illustrates that Pn travel-times for tectonically active western regions of North America are up to 5 seconds slow compared to IASPEI-91 tables. On the other hand, Pn travel-times for Canadian Shield and North American Precambrian platform plate are 3-6 seconds faster at the distances 1000 - 1500 km when compared to IASPEI-91. Pronounced variations of the Pn travel-time deviations from the IASP-91 tables vs. distance and azimuth have been found. The Pn travel time variations are caused by lateral inhomogeneities of the earth's crust and upper mantle velocity structure, which we observed on large and small scales, and should be taken into account for precise locations of the seismic events. Similar data for Northern Eurasia will be provided by the SMS, RF MOD.

Keywords: earth's crust, upper mantle, travel-times, three-dimensional (3-D) velocity model, nuclear explosions, large chemical explosions, earthquakes.

OBJECTIVE

The global monitoring under the Comprehensive Test Ban Treaty (CTBT) requires precise and unbiased event locations. The problem of obtaining accurate locations is especially serious for sparse networks such as the monitoring system specified by the CTBT. At the present time, location of seismic events by global monitoring systems is typically based on globally averaged travel-time curves. These are, in turn, calculated from averaged one-dimensional (1-D) reference velocity models. The IASPEI-91 Seismological Tables (Kennett and Engdahl, 1991; Kennett, 1991) were adopted for the Group of Scientific Experts Technical Test (GSETT-3), and continue to be used by the prototype IDC for seismic event locations.

However, it is a well known fact that globally averaged travel-time curves and underlying 1-D models are of limited use for regional event locations because of large variations of travel-times of regional phases due to lateral velocity variations in the crust and upper mantle. To achieve the CTBT goal of attaining 1000 sqkm location accuracy the IMS has to be calibrated, i.e. travel-times of seismic waves used in the location must be corrected for the laterally heterogeneous 3-D structure of the Earth (Romney and Ryaboy, 1994; Firbas and North, 1997; Firbas et al., 1997). The most precise data which can be used to calibrate the IMS are large explosions with well known locations and origin times. Long-range seismic profiles can also make important contribution to IMS calibration. These data can be complemented by earthquakes located with dense networks. In accordance with the Joint RF/US research program, the first task of the work is to collect, evaluate, and analyze travel times of major regional seismic phases from events with accurately known location and origin time recorded within different geological provinces of Northern Eurasia and North America along long-range profiles and by permanent and temporary seismological networks. The main objective of this paper is to provide information on the first steps undertaken to calibrate the IMS within North America. In accordance with the Joint Research Program, RF and US will exchange collected observational data.

RESEARCH ACCOMPLISHED

An inventory of available data was performed to select for the IMS calibration nuclear and large chemical explosions with well known locations and origin times and to create a list of permanent and temporary seismic stations used for recording these explosions. This work consisted of analysis of published data, data stored in the CMR database and data available through other organizations (Cornell University, USGS etc.). As a result, we selected a number of explosions for the IMS calibration located in different geological provinces of North America and developed an extended list of seismic stations consisting of approximately 2,500 permanent and temporary stations.

A generalized digital tectonic map of North America was developed with the aim of using this map for interpolation, extrapolation and comparison of seismic data (travel times of seismic waves, crustal and upper mantle velocity models, location of seismic station and seismic events) for different geological provinces. Figures 1 and 2 show the locations of the CTBT network and nuclear and large chemical explosions with well known locations and origin times, respectively.

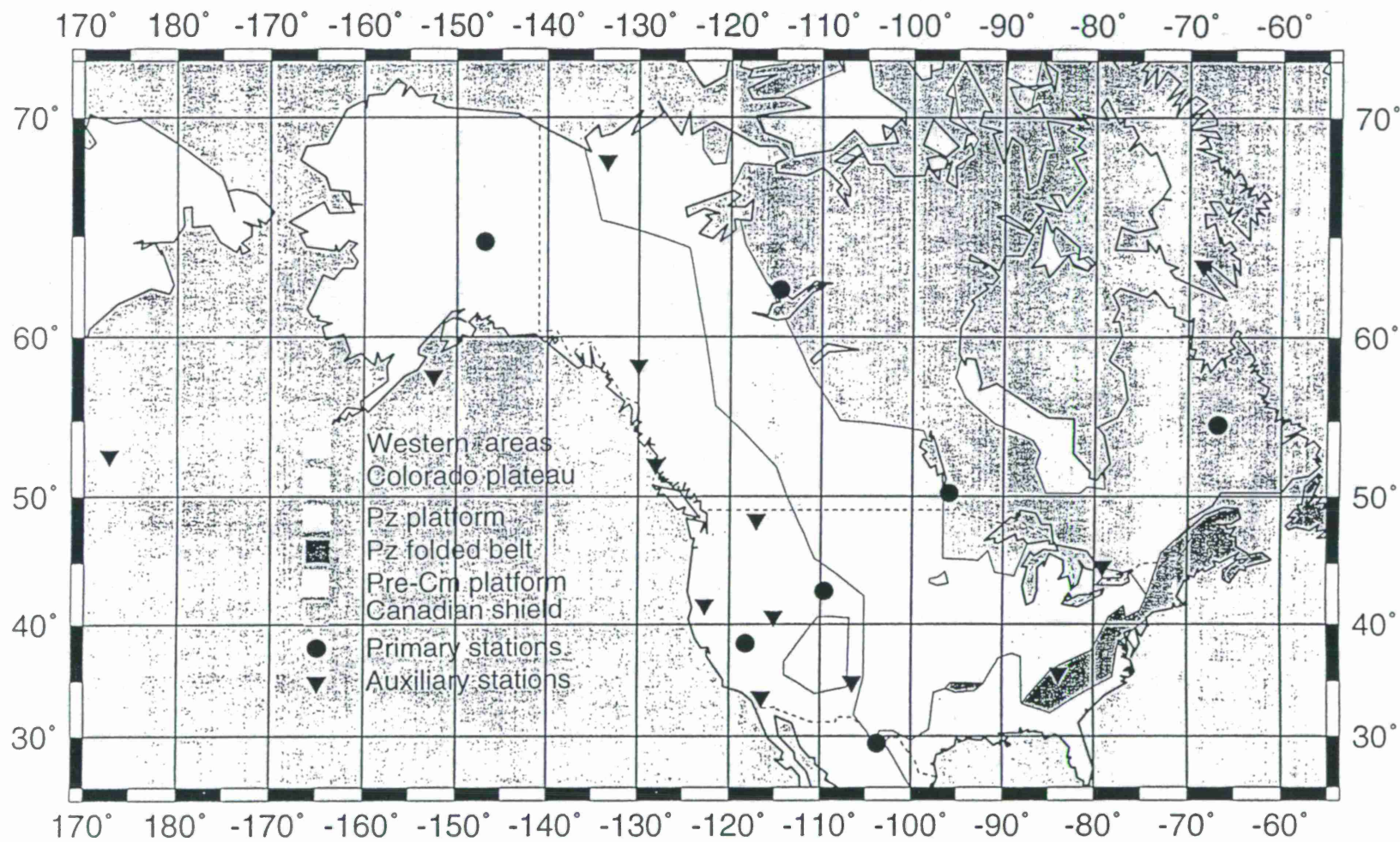


Figure 1. North America. Locations of CTBT monitoring seismological stations

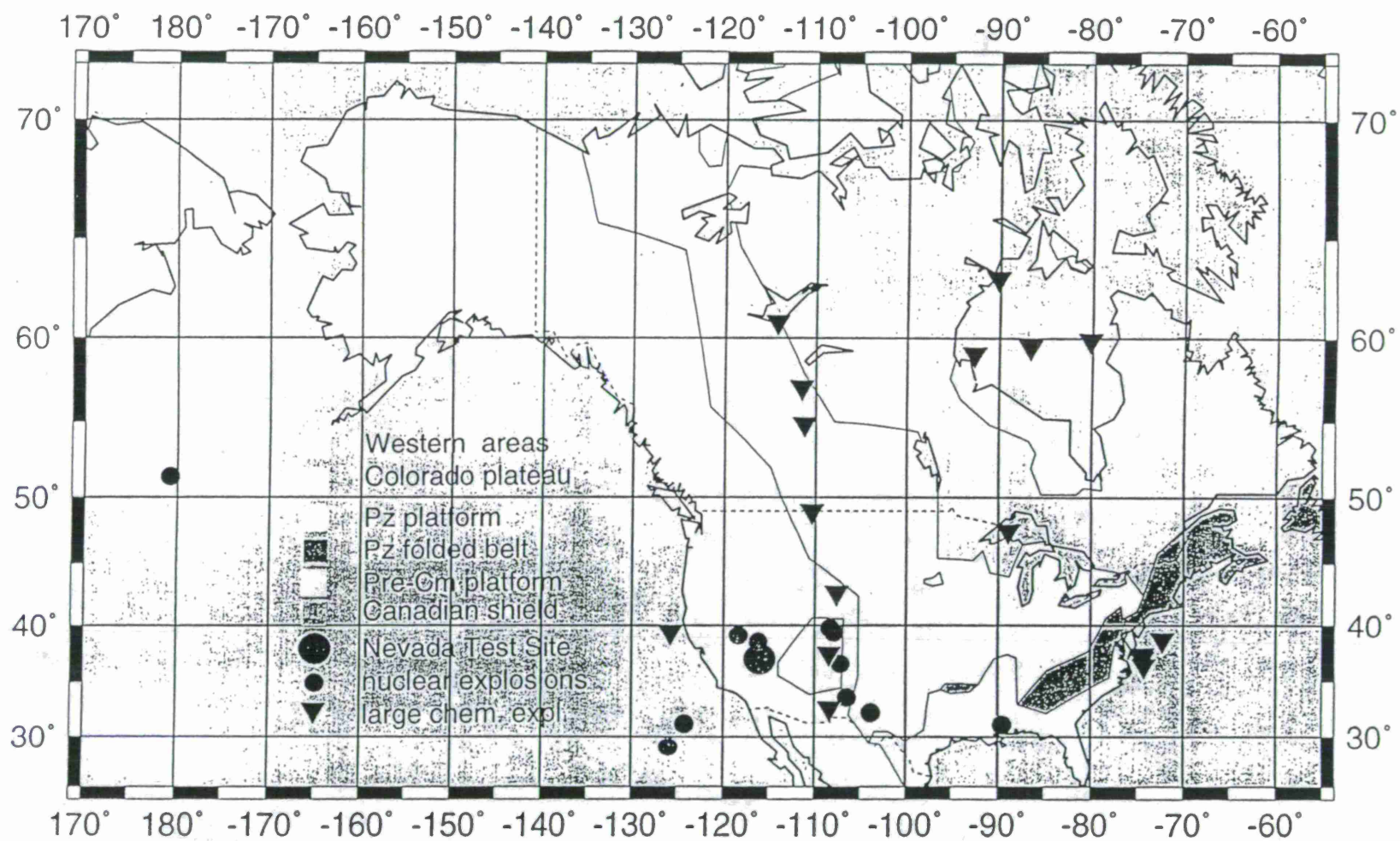


Figure 2. North America. Locations of calibration explosions

One can see that the primary and auxiliary CTBT seismic stations are located within a variety of tectonic regions including the tectonically active western areas of North America, the Canadian shield and Precambrian platform of central U.S. and Canada, and the Paleozoic folded belt of the eastern U.S. (Figure 1). Raypaths of seismic waves from regional events will cross boundaries of substantially different geological provinces. Large chemical and nuclear explosions are also located within different geological provinces of North America (Figure 2).

We collected, evaluated and analyzed Pn (P) travel times for the following events selected for the IMS calibration nuclear and chemical explosions:

Table 1: List of analyzed explosions

EVNAME	LAT.	LONG.
1. Gnome (nuclear)	33.6752	-106.4747
2. Shoal (nuclear)	39.2002	-118.3803
3. Salmon (nuclear)	31.1421	-89.5699
4. Rulison (nuclear)	39.4058	-107.9481
5. Rio- blanco (nuclear)	39.7930	-108.3666
6. Long shot (nuclear)	51.43805	179.1825
7. NTS (nuclear)	37.10	-116.04
8. Chase 3 (large chemical)	37.1967	-74.3517
9. Chase 5 (large chemical)	39.4667	-125.48
10. Early rise (large chemical)	59.1065	-92.6548

For explosions included in Table 1, we constructed and analyzed travel-time curves and maps of variations of travel-time residuals from the IASPEI-91 tables. Several hundreds nuclear explosions were detonated within Nevada Test Site (NTS). We selected 40 explosions located within area one square km and performed Pn(P) travel time analysis jointly for all these events. The latitude and longitude of center of this NTS area are given in Table 1. The same approach was used in the analysis of all chemical explosions detonated during the Early rise experiment. Figure 3 shows the travel times of Pn-waves from chemical and nuclear explosions with accurately known sources and with raypaths within the Precambrian North American platform. Pronounced variations of the Pn travel times are apparent caused different scale lateral inhomogeneities in the earth's crust and upper mantle. The travel-time observations have scatter ranging up to about three to four seconds for a fixed distance (when plotting the travel times regardless of the azimuth from the source). This scatter is much larger than the P wave onset reading error, and thus it is likely caused by factors such as relatively smaller scale lateral structural variations (of spatial extent of 100 - 500 km or less) in the earth's crust and uppermost mantle beneath the North American platform.

To take into consideration the influence of regional structural variations for seismic event locations we compared the regional Pn travel-time curve for the North American platform (Figure 3) with the similar curves constructed for other regions. We collected and analyzed with this aim results of the most accurate Pn travel-time measurements for large geological provinces of the world (Romney and Ryaboy, 1994). Figure 4 shows a comparison of the standard global Pn travel-time curves from the Jeffreys and Bullen, Herrin et al., and IASPEI-91 seismological tables with the most accurate observed regional curves inferred from explosion seismology observations when source location and origin time were known accurately. Analysis of the curves on the Figure 4 clearly shows major differences in travel times of Pn-waves propagating in tectonically active regions as compared with propagation within the Precambrian platforms. The Pn travel-time curve for a tectonically active region of the western USA is characterized by substantially larger travel-times (up to 10 sec within the distance range from 500 to 2000 km) in comparison with Precambrian geological provinces. Pn travel-time curves for the Precambrian platforms and shields are characterized as having the fastest values for Pn travel-times in the world and agree in general within one to two seconds. These Pn travel-time variations manifest an influence of large scale lateral velocity inhomogeneities of the earth's crust and upper mantle with linear size of approximately 1000-2000 km.

Maps of Pn travel-time deviations from the IASPEI-91 tables were developed and used for study of Pn travel-time variations vs. distance and azimuth within different geological provinces of North America. As example, Figure 5 shows a map of interpolated/extrapolated travel-time anomalies (in isolines and color coded) for the Salmon nuclear explosion. The black crosses show the locations of the stations used. The technique developed for calculation and plotting of the travel-time deviation maps is based on the GMT software package (Wessel, Smith, 1995). One can see at regional distances for the Salmon explosion variations of Pn travel-time residuals from approximately 3 s for western areas of North America to -4 s for North American platform. Similar maps will be used for verification and improvement of 3-D velocity models by comparisons with results of travel-time calculations. The 3-D velocity models will be used to derive maps of Source-Station Specific Corrections (SSSC).

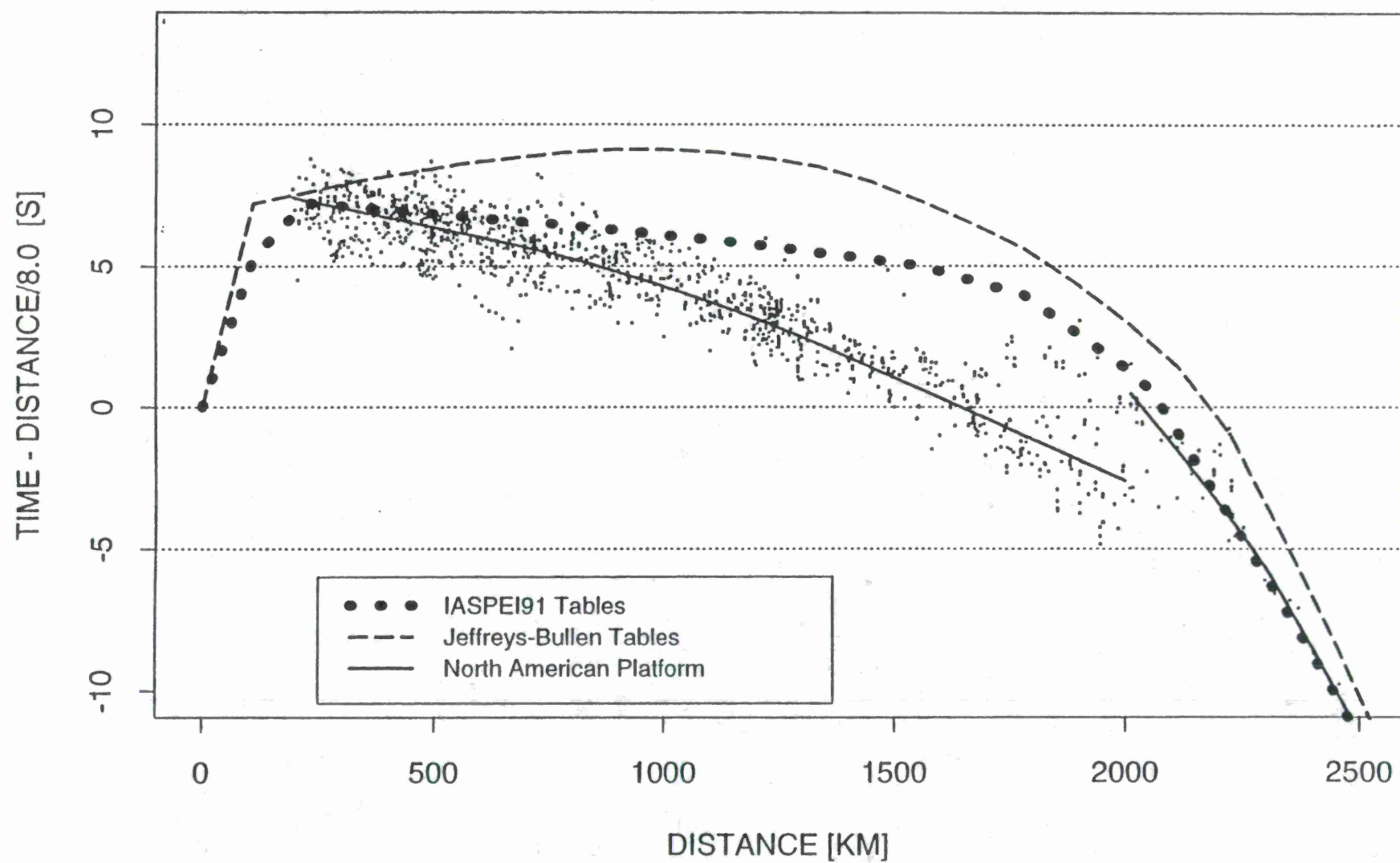


Figure 3. North American Platform. Pn travel times based on explosion seismology observations

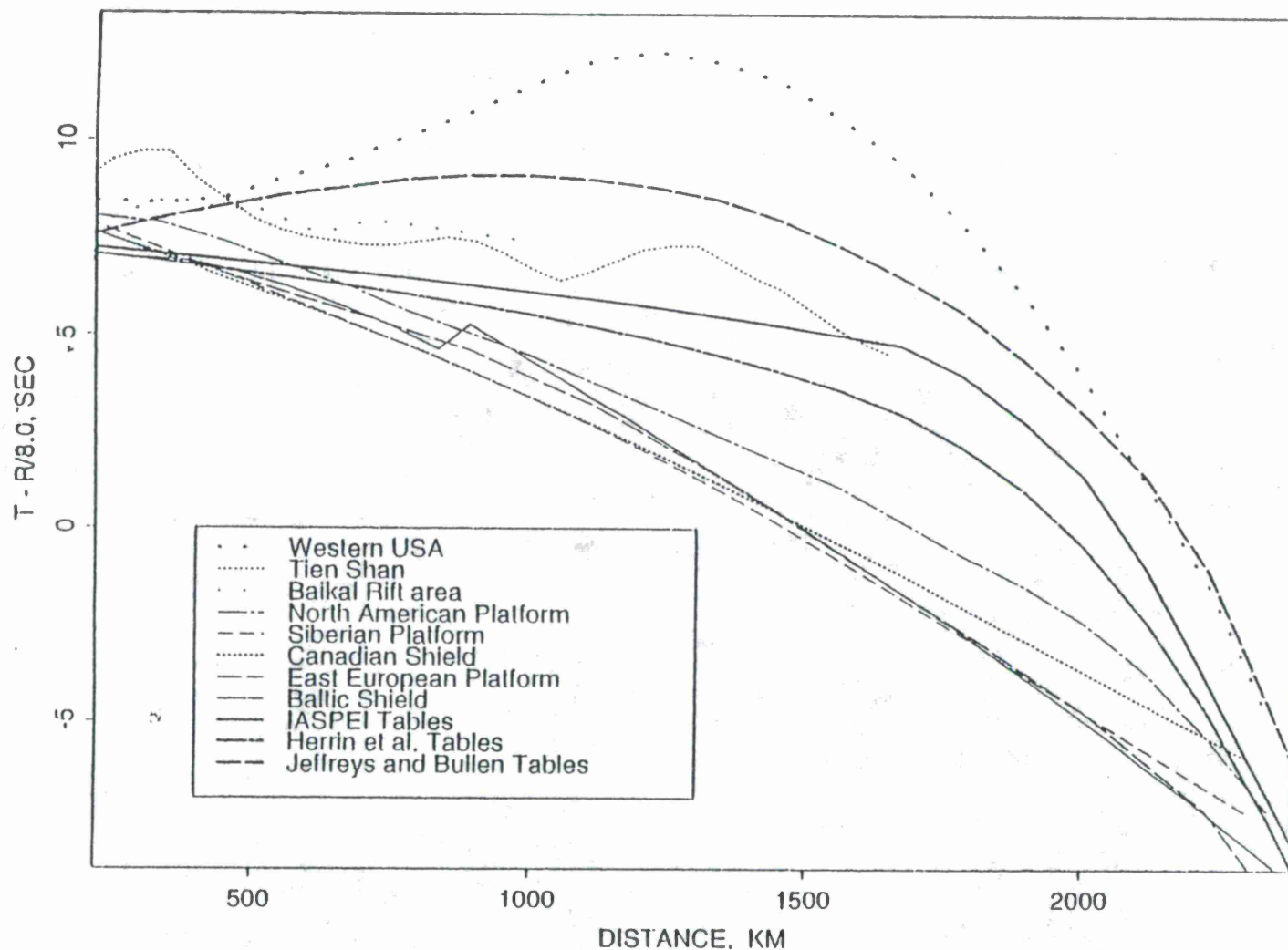


Figure 4. Comparison of regional P_n travel-time curves for different geological provinces with the reference P_n travel-time curves from the Jeffreys and Bullen, Herrin *et al.*, and IASPEI 1991 Seismological Tables used as global average. Ancient platforms and shields have the fastest P_n travel-times, and tectonically active regions are substantially slower (up to 10 sec).

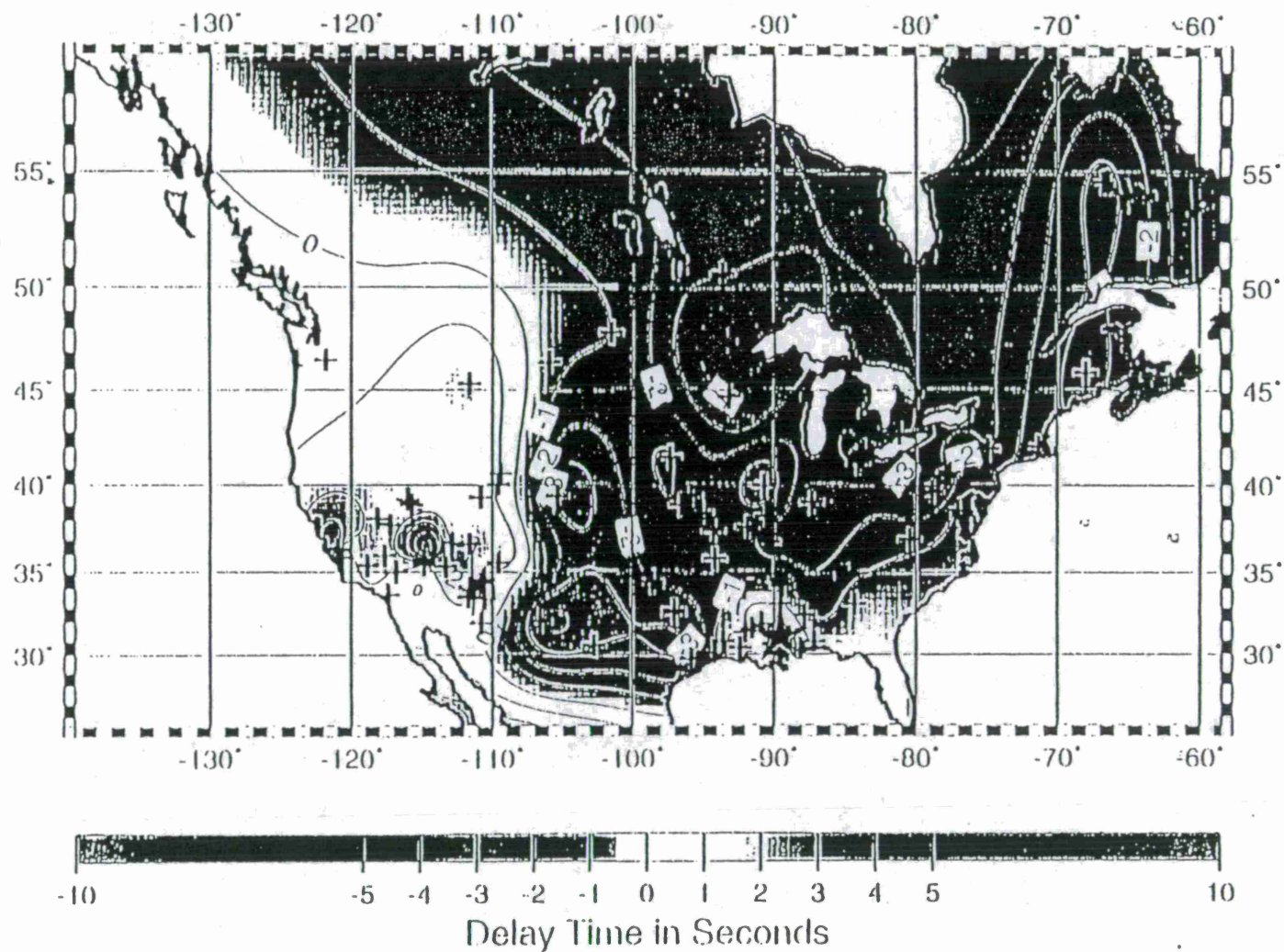


Figure 5. Salmon nuclear explosion. Map of Pn/P travel-time deviations from IASPEI-91 tables. The black crosses show the locations of the used stations. The shot point is shown as a star.

CONCLUSIONS AND RECOMENDATIONS

A number of large chemical and nuclear explosions with controlled sources have been selected for the IMS calibration within the central and southern regions of North America; only a few similar events were found for the territory of Canada and Alaska. Maps of contoured Pn travel-time deviations are useful for examining how these deviations differ.

As now completed for different tectonic regions, analyses of travel-time curves and maps of travel-time deviations from the global IASPEI-91 tables (now used by the prototype IDC for seismic event locations) illustrate the well-known difference across North America. Pn travel-times for the tectonically active western regions of North America are up to 5 seconds slower compared to IASPEI-91 tables, while those for the Canadian Shield and North American Precambrian platform plate are 3-6 seconds faster at the distances 1000 - 1500 km.

In accordance with the Joint US/RF research program of the IMS seismic calibration, our main recommendations include: continuation of accurate travel-time data collection for major regional phases including data from well located earthquakes, collection of data to develop 3-D crustal and upper mantle velocity model for North America, and joint analysis and comparison of seismic data for North America and Northern Eurasia.

REFERENCES

- Firbas, P. and R.G. North, 1997. Development of calibration techniques for potential use by the CTBT International Monitoring System. *Proceedings of NATO advanced research workshop: "Upper mantle heterogeneities from active and passive seismology"*, Moscow 13 to 16 April 1997 (in press).
- Firbas, P., A.B. Peshkov, and V. Ryaboy, 1997. From IASP-91 global model to a 3-D model for CTBT monitoring. *Proceedings of NATO advanced research workshop: "Upper mantle heterogeneities from active and passive seismology"*, Moscow 13 to 16 April 1997 (in press).
- Kennett, B.L.N. and E.R. Engdahl, 1991. Travel times for global earthquake location and phase association. *Geophys. J. Int.*, 105, 429-466.
- Kennett, B.L.N. (editor), 1991. IASPEI 1991 Seismological Tables. *Research School of Earth Sciences, Australian National University*.
- Romney, C.F. and V. Ryaboy. Improvement of regional seismic event locations for global monitoring, *Center for Seismic Studies, Technical Report C94-01, 1994*.
- Wessel, P. and W.H.F. Smith, 1995. The Generic Mapping Tools (GMT). Version 3. *Technical Reference and Cookbook. Geodynamics Branch, Geosciences Laboratory NOAA, NOAA, N/OES12*.

IMPROVEMENTS IN MONITORING THE CTBT IN THE MIDDLE EAST WITH THE ISRAEL SEISMIC NETWORK

Avi Shapira, Vladimir Pinsky, Yefim Gitterman and Alona Malitzky
Seismology Division, Geophysical Institute of Israel, P.O. Box 2286, Holon 58122, Israel

Sponsored by U.S. Department of Energy
Office of Nonproliferation and National Security
Office of Research and Development
Contract F19628-95-K-0006

ABSTRACT

Monitoring of the CTBT requires reliable detection, accurate location determination and identification of low magnitude seismic events. According to the latest evaluations of the prototype of the international Monitoring System (IMS), the performance of the existing global seismic network of primary and auxiliary stations is significantly far from meeting these requirements in the Middle East (ME).

Over the past decade the Israel Seismic Network (ISN) has recorded thousands of small seismic events occurring in Israel, Jordan, Lebanon, Syria, Egypt, Iraq, Saudi Arabia, Iran and the East Mediterranean. Much of these data have not been fully analyzed and most (mainly explosions) cannot be traced in any publication. The ISN has recently been upgraded to meet IMS standards and is already acquiring high quality seismic data from the Middle East.

A basic requirement for studying monitoring capabilities in the Middle East and improving on monitoring the CTBT in this region is the availability of high quality data. Thus, the main objective of this study is to prepare a validated data set of waveforms and source information of low magnitude ($M_L < 4.0$) earthquakes and man-made sources (quarry blasts, underwater explosions, etc.) which occurred in the Middle East; this data set will be used to estimate performance/capability of the upgraded ISN and other IMS stations in adjacent areas. To reach this objective we plan to implement innovative methods and algorithms such as the Statistically Optimal Technique, Maximum Likelihood Onset and Polarization Analysis, Master Images Processing, Velogram Analysis, Spectral Energy Ratio and Semblance techniques, Auto Regressive Processing and more. These will be applied to determine the basic source parameters of the events in the data set and identify their type. In turn, the new data set will be used to evaluate source-site propagation path effects on different seismic phases with respect to their influencing the ability to detect, locate and identify low magnitude seismic events occurring in the Middle East.

It is anticipated that much of the analysis to be performed throughout these studies can be automated. Consequently, we plan to test and evaluate the applicability of some of the algorithms in automatic processing.

Seismic monitoring of the CTBT in the Middle East is evidently complicated owing to the large variety of geological conditions, sparsity of high-quality stations and lack of available calibration explosions. This proposed project will provide data, information and tools to significantly improve the monitoring of the CTBT in the Middle East.

Keywords: scientific monitoring, Middle East, low magnitude seismic events, validation of waveforms dataset

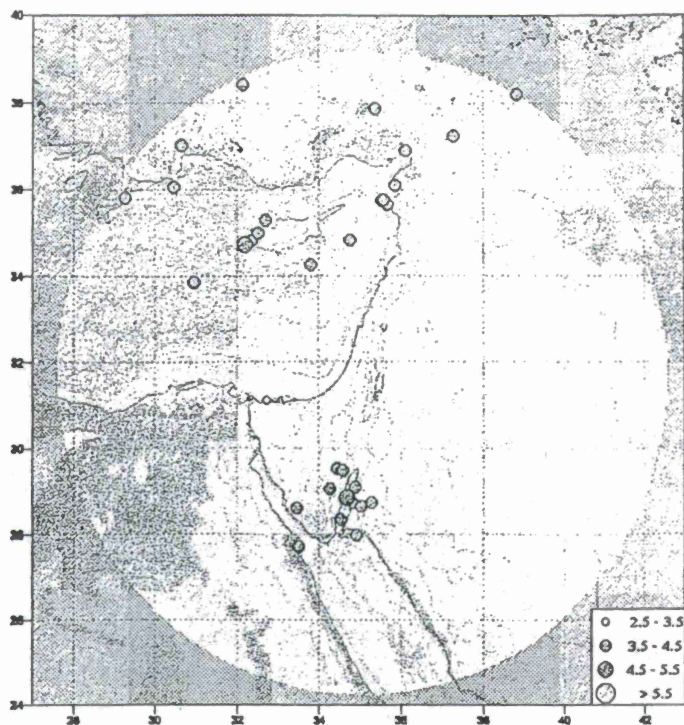
OBJECTIVES:

- To prepare a validated data set of waveforms and source information of low magnitude ($M_L < 4.0$) earthquakes and man-made seismic events to be used for evaluating and improving the monitoring of the CTBT in the Middle East.
- Evaluate current capabilities of the ISN to monitor the CTBT and its potential contribution for improving the performance of the International Data Center for monitoring the CTBT.
- Implement innovative methods and algorithms such as Statistically Optimal Technique, Maximum Likelihood Onset and Polarization Analysis, Master Images Processing, Velogram analysis, Spectral Modulation Technique, Auto Regressive processing, Semblance and other correlation techniques for automated seismic monitoring.

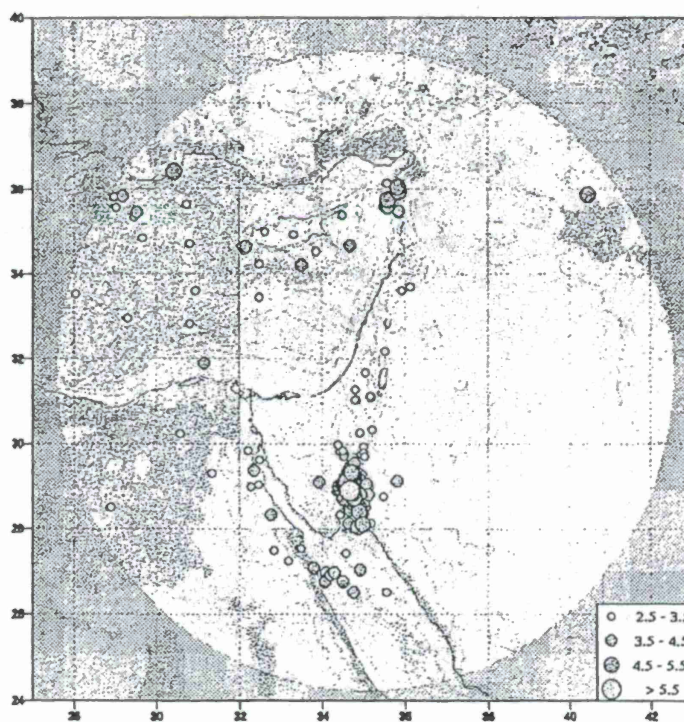
CURRENT STATUS

The paper presented is based on the project selected for negotiation in the framework of the DSWA CTBT program. The project research will be, to some extent, a natural continuation of methods and procedures developed in the former DOE project and will use obtained results.

- There are over 100 seismic stations monitoring the seismic activity in the Middle East (Fig. 1) nevertheless, most of them operate within a low dynamic range, do not provide ground truth information on quarry blasts and other explosions and their waveform data are difficult to obtain. During the recent Joint Seismological Observing Program (JSOP) experiments, it was observed that:
 - a) Although the magnitude determinations made by the different seismological centers monitoring the Middle East are consistent within local operations, there is a significant discrepancy between the reported event magnitudes. In many cases there is a high uncertainty regarding the magnitude of the reported seismic event.
 - b) There are often significant differences in the hypocenter location determinations which are probably a result of the existing heterogeneities in the propagation paths to the various stations and the spatial distribution of station with respect to the epicenter.
- Based on the most recent evaluations of the capabilities of the Experimental International Monitoring System to detect seismic events in and around Israel (Malitzky and Shapira, 1996) it became evident that most of the events with magnitudes lower than 4.5 are not detected (Fig. 2). A portable BB network was recently deployed in Saudi Arabia at sites which are very quiet. It was expected that these stations would have a relatively high detection performance. However, it was observed that many aftershocks of the Gulf of Aqaba earthquake of November 22, 1995, in the magnitude range $3.0 < m_b < 5.0$ at distances about 10° are not presented in the network bulletin (Dr. M. Hedlin, personal communication), possibly due to very weak P and S waves and the automated picking program used (Vernon et al., 1996). The most complete seismic source parameter information for the Middle East currently available is provided by the Seismology Division of the Geophysical Institute of Israel through the operation of the ISN (see Fig. 1). These, however, can be much improved by combining advanced analysis techniques. As an example



Events reported by IDC



Events reported by ISN

Fig. 2. Performance of IDC during January, 1 to June, 30, 1996.
(from Malitzky and Shapira, 1997)

we can see in Fig. 3 the results of the OGF technique implemented on a set of 13 stations of the ISN where the obtained SNR is higher than that observed at the quietest station, PRNI.

- A rather striking observation, made while evaluating the performance of the IMS, is the fact that in many cases the locations of the events reported in the IMS Review Bulletin are far outside the area (90% confidence) of the determined error ellipse (Fig. 4). In actual fact, this phenomenon was reported before (Shapira and Du Plessis, 1988). Accurate hypocenter locations and mislocation estimations require better knowledge of the characteristics of the crust and upper mantle across the Middle East and a good data base of events with ground truth information.
- Classification of seismic events in the Middle East, even those with large magnitudes, is problematic. For most of the stations monitoring the Middle East region, seismic paths from the ME cross the Mediterranean subduction zone and are subjected to strong attenuation of Lg and Sn waves, thus preventing efficient events classification, e.g., implementation of the conventional Pg/Lg ratios (Dowla, et al., 1996). In a discrimination study based on KEG (Kottamya, Egypt) station, Baumgardt (1996) refers to difficulties associated with Lg blockage along paths crossing the Levantine basin and has emphasized on the lack of calibration explosions and mining blasts for areas along the Dead Sea transform.

Under DoE contract F19628-95-K-0006, Gitterman, Pinsky and Shapira (1996) tested different discriminants and developed new network based discriminants to identify seismic events in and around Israel, i.e.:

1. Subnet average of the seismic energy spectral ratio (R_E) between the low frequency and the high frequency bands;
2. Group velocity statistics based on "velogram analysis", characterizing kinematic properties of the S and surface wave phases;
3. Spectral "semblance" and "cross-correlation" statistics measuring the coherency of smoothed spectra at different ISN stations.

The algorithms were tested on 212 events: earthquakes, quarry ripple-fired and single blasts and underwater explosions from some areas of the Middle East region with a 97-100% success rate. The study of these physically approved algorithms was complimented by testing the multivariate procedures based on the formal Integrative Approach: King's clustering procedure, Linear Discrimination Function and Artificial Neural Networks. When applied to a vector of spectral parameters derived from the database including 145 quarry blasts and earthquakes from the Galilee, southern Dead Sea and the Negev desert and Gilad, Jordan, they provided 99% of true classification in a cross-validation test.

Following these investigations it is possible to identify with great confidence (presently, through interactive off-line analysis) the type of seismic event recorded by the ISN. In this respect, it will be of great importance to analyze many of the earthquakes and explosions which, according to preliminary evaluations, are associated with seismic activity in the low-seismicity or aseismic areas in Eastern Jordan, South-Western Iraq, Syria and the Arabian Shield (see map in Fig. 5). These unclassified events are roughly located and, for most of them, even the magnitude is undetermined.

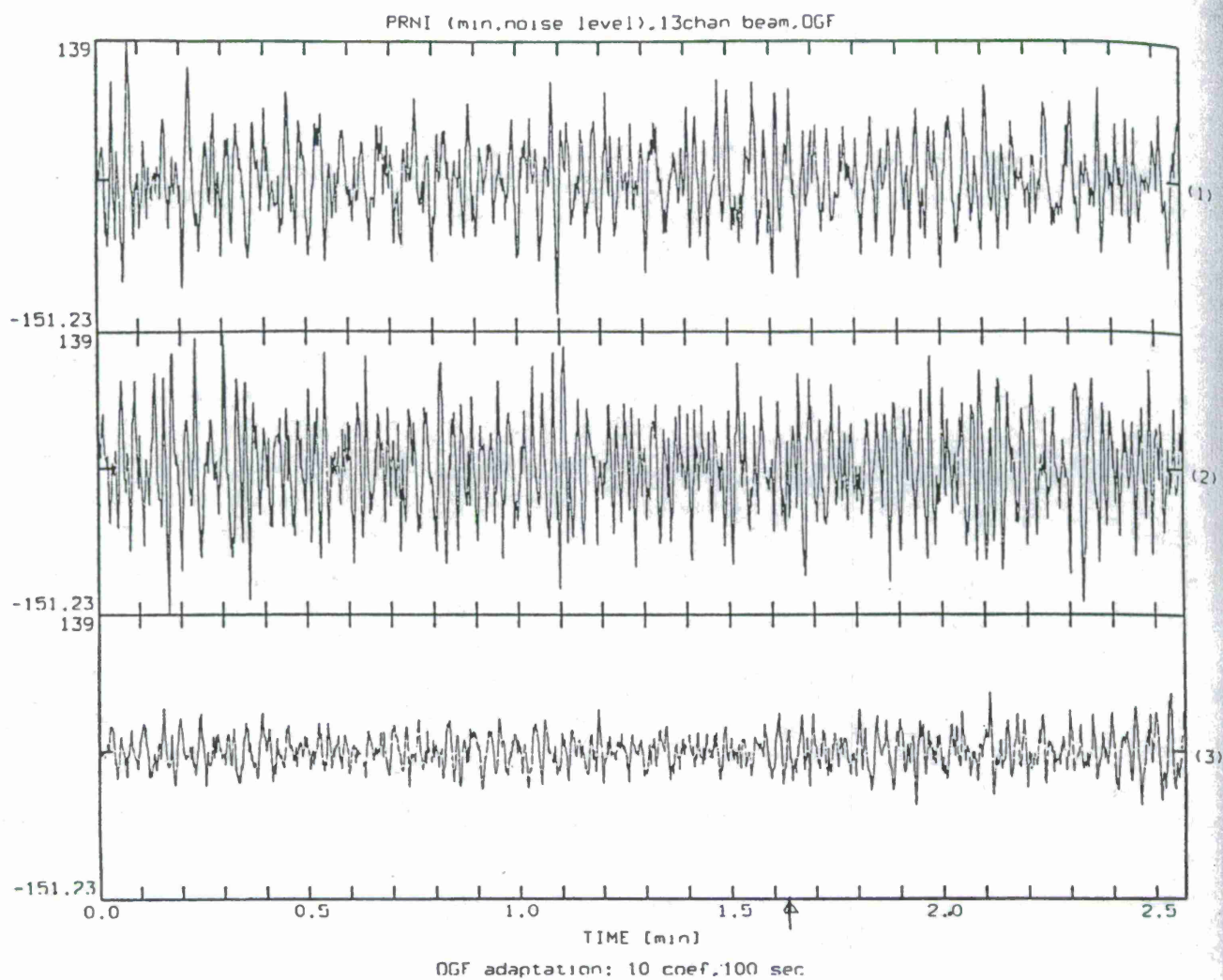
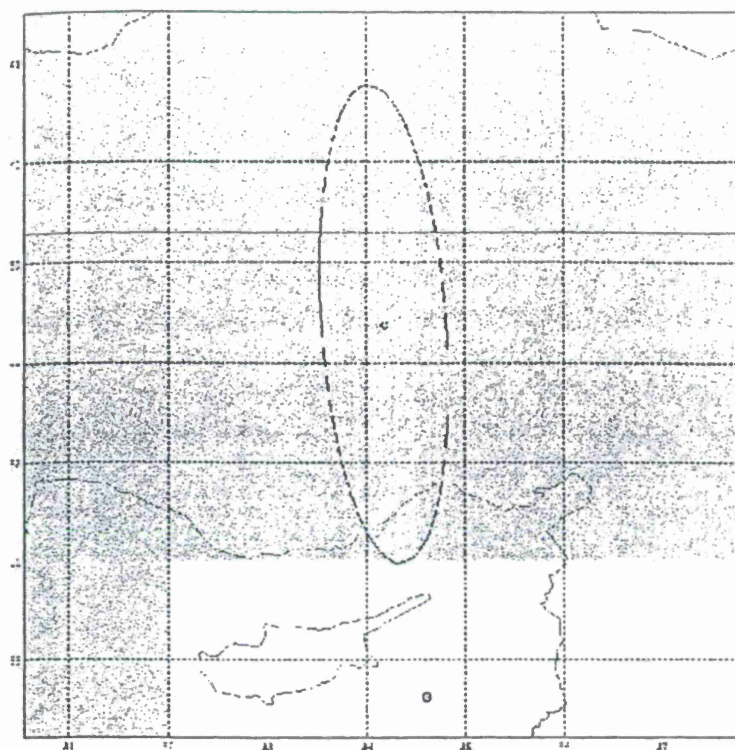


Fig.3. Results of the OGF technique implemented on a set of 13 ISN stations where the obtained SNR is higher than that observed at the quietest station, PRNI.



18-01-1995

IDC:

O.T. 01:43:46.1

$m_b=4.1$

38.37°N 34.18°E

ISN:

O.T. 01:43:24.6

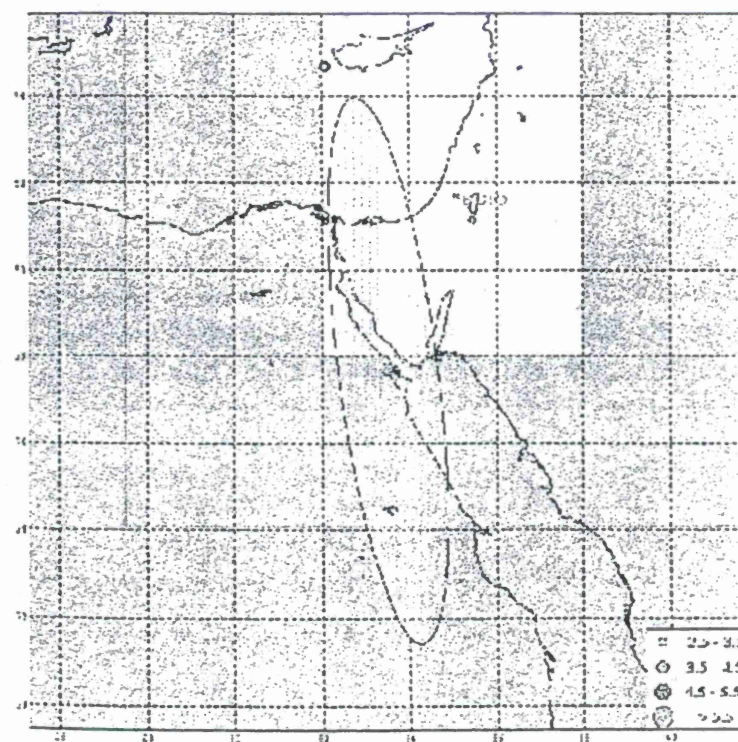
$m_b=4.3$

$M_L=4.1$

34.60°N 34.60°E

$D_{RES} = 420 \text{ km}$

$T_{RES} = 22 \text{ sec}$



09-02-1996

IDC:

O.T. 08:15:32.8

$m_b=3.9$

27.70°N 33.51°E

ISN:

O.T. 08:16:39.8

$M_L=3.1$

34.64°N 32.13°E

$D_{RES} = 780 \text{ km}$

$T_{RES} = -67 \text{ sec}$

Fig. 4. Examples of events mislocated by IDC.
(from Malitzky and Shapira, 1997)

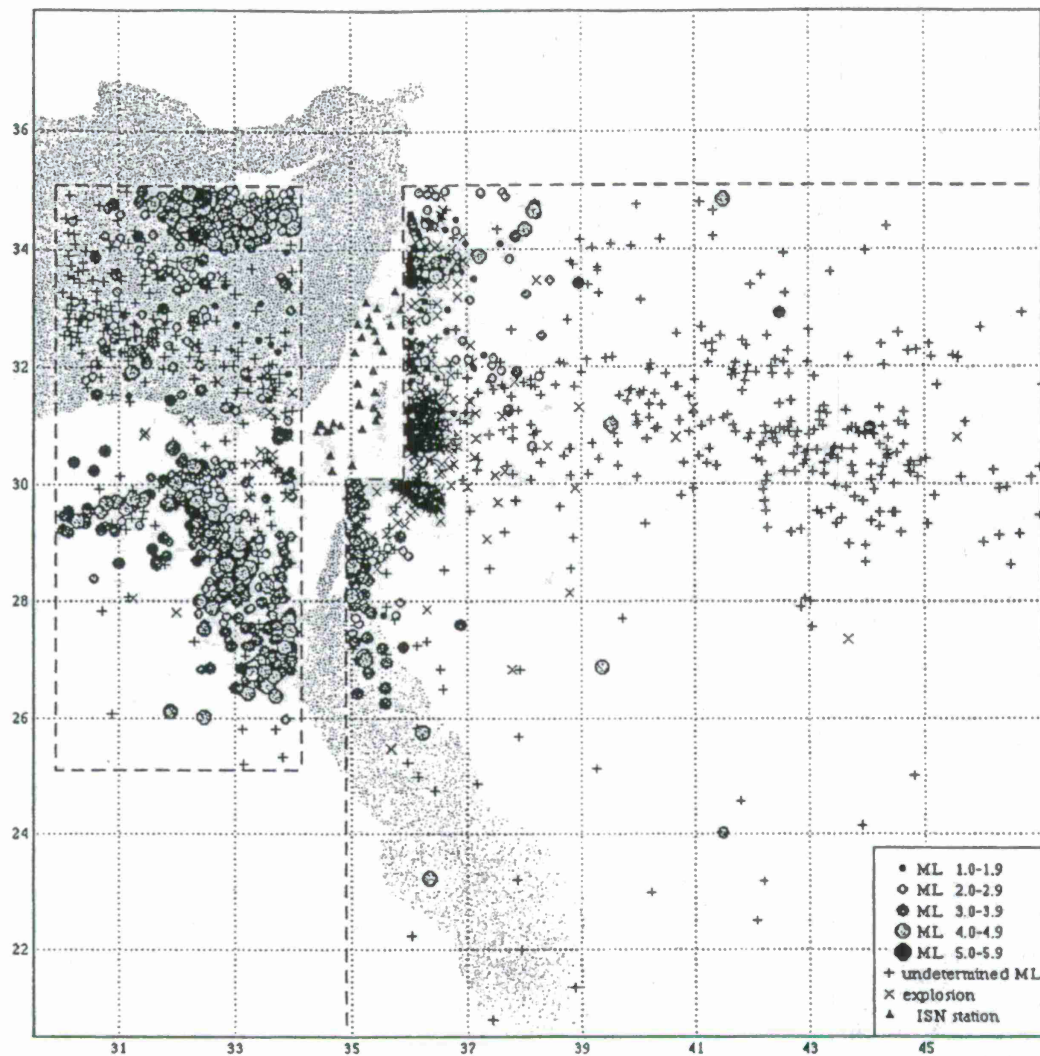


Figure 5. Map showing seismic events in the low-seismicity and aseismic areas of the Middle East, recorded digitally by the short-period ISN stations between 1985-1996 and stored in the GII data bank (thousands of recorded events in Israel and some nearby locations are not shown to avoid overcrowding of the map).

RESEARCH PLANS

1. Preparation of a validated data set of low magnitude seismic events occurring in the Middle East. Within the framework of this task we intend to focus on:
 - a) Implementation of modern location procedures to improve accuracy in locating detected events in the Middle East.
 - b) Extending the range for determining magnitudes by the ISN (currently limited to 700 km) and correlating it with standard scales (m_b , M_w , etc.) using both SP and BB data.
 - c) Investigation of source - station propagation path effects on travel times, excitation of surface waves and attenuation of different seismic phases to improve event location and identification.
 - d) Collection of Ground Truth Information.
 - e) Testing and application of discrimination methods and algorithms to identify events located outside of the borders of Israel.
2. The validated data, together with new data of the current ISN, additional ground truth information and seismograms of controlled sources, will be used to improve the monitoring of the CTBT in the Middle East. In this framework we intend to target:
 - a) Analysis of the detection capabilities of Middle East events and the development of new procedures to improve the detection of single BB stations and regional networks.
 - b) Evaluation of the success rate of the discriminants applicable to the Middle East and tune discrimination parameters.
 - c) Simulation of evasion scenarios and implement the developed procedures to identify and locate the "source".
 - d) Formulation and testing of algorithms for automated data processing and analysis.

REFERENCES

- Baumgardt, D.R., 1996. Characterization of Regional-Phase Propagation Seismic Discriminants for the Middle East. Proceedings of the 18th Annual Seismic Research Symposium on Monitoring a CTBT, 4-6 September 1996, PL-TR-96-2153, 474-483.
- Dowla, F., Goldstein, P., Harben, P., (17 authors), 1996. Seismic Regionalization in the Middle East and North Africa. Proceedings of the 18th Annual Seismic Research Symposium on Monitoring a CTBT, 4-6 September 1996, PL-TR-96-2153, 55-64.
- Gitterman, Y., Pinsky, V. and Shapira, A., 1996, Discrimination of seismic sources using the Israel Seismic Network, PL-TR-96-2207, Phillips Lab., 98pp.
- Malitzky, A. and Shapira, A., 1997. On the performance of the International Data Center as compared with the ISN, for monitoring the CTBT, Abstracts of Annual Meeting of the Israel Geological Society, Kefar Giladi, 15-17 April, 1997.
- Shapira, A. and Du Plessis, A., 1989. A semi-empirical analysis of hypocenter mislocations, Tectonophysics, 157, 301-313.
- Vernon, F.L., Mellors, R.J., Berger, J., Al-Amri, A.M. and Zollweg, J., 1996. Initial Results From the Deployment of the Saudi Arabian Shield. Proceedings of the 18th Annual Seismic Research Symposium on Monitoring a CTBT, 4-6 Sept. 1996, PL-TR-96-2153, 108-117.

IMPROVED METHODS FOR REGIONALIZED SURFACE WAVE ANALYSIS

Jeffrey L. Stevens and K. L. McLaughlin

Maxwell Technologies

8888 Balboa Ave, San Diego, CA 92123-1506

Contract No. F19628-95-C-0110

Sponsored by U. S. Air Force

ABSTRACT

Surface waves are of primary importance for CTBT monitoring because the $M_s:m_b$ discriminant and its regional variants are among the most reliable means of determining whether an event is an earthquake or an explosion. In this project, we have developed improved methods for measuring surface wave amplitudes in order to reduce the threshold for which surface waves can be reliably measured, and to develop a consistent way of measuring surface waves that is valid at regional and teleseismic distances. The basic elements of the procedure are: development of a regionalized earth model for determining surface wave phase velocity, amplitude, dispersion, and attenuation; phase-matched filtering to improve signal/noise ratio with phase-matched filters derived from the regionalized earth model; a unified surface wave magnitude, the scalar moment, which has a consistent value over different frequency bands and distance ranges; and maximum likelihood magnitudes which correct for censoring and allow an upper bound on the magnitude to be determined for events with no measurable surface waves.

A regionalized earth model was developed by starting with the earth models developed by Mooney et al (1997) with some additional regionalization of the oceans and then varying the shear velocities in each model to obtain a better fit to observed dispersion curves. Dispersion information from the University of Colorado, Harvard, and St. Louis University were combined with dispersion curves from historic explosion data and PIDC data to perform a tomographic inversion of about 90,000 data points to determine the shear velocity structure of 149 earth models on a 5 degree grid. Dispersion curves derived from the final earth models are sufficient to predict dispersion and to generate phase-matched filters for most regions of the world.

The detection threshold of the automatic surface wave processor at the PIDC is about one magnitude unit lower than NEIS bulletins, and there is a bias of about 0.24 magnitude units between the two bulletins. Maximum likelihood scalar moments and M_s were calculated for a data set of 700 events using 10,000 PIDC seismograms and historical explosion seismograms. The reliability of maximum likelihood magnitudes has been greatly improved through improved methods for automatic identification of surface waves, although problems can still occur due to low amplitude noise measurements from malfunctioning stations. Maximum likelihood magnitudes combined with maximum likelihood upper bounds allow reliable discrimination down to at least m_b 4.0. The discrimination line between earthquakes and explosions has a slope of 1.4, rather than the expected 1.0 at low magnitudes.

Keywords: surface wave, discrimination, M_s , moment, dispersion, CTBT, phase-matched filter.

OBJECTIVE

Surface waves are of primary importance for CTBT monitoring because the $M_s:m_b$ discriminant and its regional variants are among the most reliable means of determining whether an event is an earthquake or an explosion. With the International Data Center identifying approximately 20,000 events per year, it is particularly important to be able to unambiguously identify as many of these events as possible. The primary objective of this research program is to develop improved methods for measuring surface waves in order to reduce the magnitude threshold for which surface waves can be reliably measured, minimize the number of events that require more detailed analysis, decrease the number of unidentified events, avoid unnecessary on-site inspections, and allow identification of underground nuclear tests.

RESEARCH ACCOMPLISHED

The research accomplished under this project, which is discussed in the following sections, includes development of the theoretical basis for improved surface wave measurements; development of regionalized earth models; use of regionalized models for surface wave identification, phase-matched filtering, and moment estimation; tests of the procedures on Prototype International Data Center (PIDC) and other data; application of maximum likelihood procedures to M_s and log moment; comparison with traditional M_s measurements; estimation of the surface wave detection threshold; and evaluation of the discrimination capability of the $M_s:m_b$ and $M_0:m_b$ methods.

1. Spectral magnitudes and scalar moment: Theory

The key to developing a surface wave magnitude that is regionalizeable, and gives consistent values at regional and teleseismic distances and in different frequency bands, is to use the equation for surface waves in a plane-layered structure to correct the spectrum. This equation can be factored into functions that depend on the source and receiver earth structure and the phase velocity and attenuation integrated over the path. The displacement spectrum for a Rayleigh wave at distance r from an *explosion* is given by:

$$U(\omega, r) = M_0' \frac{S_1^x(\omega, h_s) S_2(\omega) \exp[-\gamma_p(\omega)r + i(\varphi_0 - \omega r / c_p(\omega))]}{\sqrt{a_e \sin(r/a_e)}} \quad (1.1)$$

S_1^x depends on the source region elastic structure and the explosion source depth. S_2 depends on the receiver region elastic structure, γ_p is the attenuation coefficient that depends on the attenuation integrated over the path between the source and receiver. c_p is the phase velocity integrated over the source to receiver path. φ_0 is the initial phase of the source. a_e is the radius of the earth. $M_0' = \frac{3\beta^2}{\alpha^2} M_0$ where M_0 is the explosion isotropic moment. This definition is introduced so that the function S_1^x does not depend explicitly on the material properties at the source depth.

We can use equation 1.1 to define a spectral magnitude corrected for distance and spectral shape. We define, for any event, earthquake or explosion, the estimated scalar moment:

$$M'_0 = \left| U(\omega, r, \theta) \frac{S_1^x(\omega, h_x) S_2(\omega) \exp[-\gamma_p(\omega)r + i(\varphi_0 - \omega r / c_p(\omega))]}{\sqrt{a_e \sin(r/a_e)}} \right| \quad (1.2)$$

This is similar to the approach taken by Okal and Talandier (1987) in defining a mantle magnitude M_m , except that they used an averaged earthquake source spectrum that they referred to as the Rayleigh Wave "Excitability" instead of the explosion excitation function S_1^x . Although the imaginary part of the exponential is removed by the absolute value, it is shown here explicitly because in practice the phase is used to generate a phase-matched filter to compress the signal and improve signal/noise ratio prior to taking the spectrum. The spectrum is then averaged over a frequency band to smooth the spectrum and get a stable measurement.

For an isotropic explosion source at depth h_x , M'_0 is independent of frequency. Equation 1.2 therefore corrects completely for all frequency dependent and distance dependent factors in the observed spectrum. In general M'_0 for an earthquake is not completely frequency independent, but it is partially corrected for frequency dependence by removal of the path attenuation and receiver structure and similarities in the explosion and earthquake excitation functions in the same source region. The remaining differences mean that the earthquake magnitude will vary somewhat when measured over different frequency bands while the explosion will not. In particular the spectra of deeper earthquakes will decline more rapidly with increasing frequency, while the path corrected spectra of shallow earthquakes is approximately flat over the frequency band of about 0.01-0.08 Hz. Figure 1 shows the scalar moment calculated with equation 1.2 of an explosion and a typical earthquake with strike 0, dip 80, rake 15, observed at an azimuth of 45 degrees for several depths in a Eurasian earth structure. The explosion has unit scalar moment, and the earthquake has unit double couple moment.

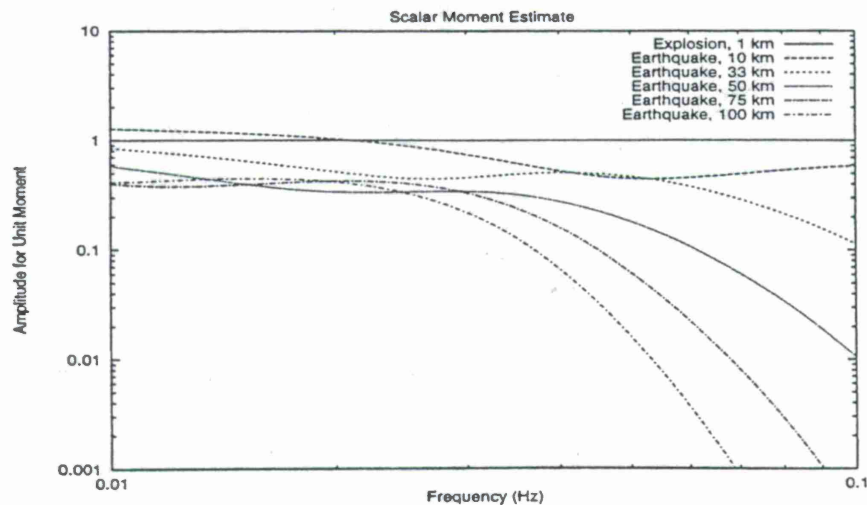


Figure 1. Scalar moment for an explosion and earthquake (Equation 1.2) calculated for several earthquake depths. The spectral amplitude decays more rapidly with increasing frequency for deeper sources.

By defining the scalar moment with equation 1.2, we obtain a measure of surface wave magnitude that is independent of range, nearly independent of frequency, and regionalizeable. The functions S_1^x and S_2 depend only on the source and receiver points and can be stored in a simple lookup table. The functions γ_p and c_p depend on the source to receiver path and can be found by integrating along a great circle path between the source and receiver in a regionalized earth model.

2. Development of regionalized earth models

The Crust 5.1 model of Mooney et al. (1997) provides an excellent starting point for development of regionalized surface wave parameters. The Crust 5.1 model divides the earth into 139 distinct plane-layered earth models on a 5 degree by 5 degree grid. However, comparisons with surface wave dispersion data showed that although group velocities predicted by Crust 5.1 were quite good on continental paths at periods close to 20 seconds, they were not as good as models currently in use at the IDC for oceanic paths, particularly at periods < 25 seconds, and for continental paths at periods > 30 seconds. In order to make the models more useful for surface wave analysis, we made a first order improvement to the models using the following procedure:

1. We assume that the 139 models in Crust 5.1 are an adequate classification of the earth's structure in continental regions, but that the constraints on the shear velocity in each model are weak and that a first order improvement can be made by varying the shear velocity in each model. In oceanic regions, we created some additional models corresponding to different ocean ages, using the Crust 5.1 model as a starting model, but then allowing the models in these distinct regions to vary independently. We also removed 5 models with very thick low velocity sediments that led to unrealistic dispersion curves. The final model has 149 distinct earth structures.

2. We used the following data sets to improve the models:

1. Global surface wave group velocities from earthquakes derived using IDC data (Stevens and McLaughlin, 1996), augmented with more recent measurements derived from PIDC data.
2. Surface wave phase and group velocity dispersion curves from underground nuclear test sites (Stevens, 1986; Stevens and McLaughlin, 1988).
3. Phase and group velocity measurements for western Asia and Saudi Arabia from Mitchell et al (1996).
4. Global phase velocity model of Ekstrom et al. (1996) for periods > 35 seconds.
5. Group velocity measurements for Eurasia from Ritzwoller et al (1996) and Levshin et al (1996).

3. The complete data set of approximately 90,000 data points were used to invert for shear velocity structure in each model. This was accomplished using a tomographic inversion of the entire data set for all models at the same time. That is, we solve the equation $\mathbf{A}\mathbf{m}=\mathbf{d}$ where \mathbf{m} is

the change in the shear velocity of each model (limited to depths of 3-200 km, excluding water layers, where Crust 5.1 was extended to greater depths using PREM), d is the difference between the observed and predicted slowness of each data point, and A is a matrix constructed from the partial derivatives of phase or group velocity with respect to shear velocity in each layer, and the fraction of each model crossed by each data point. The calculations were performed on a DEC Alpha 2100 dual-processor computer using the LSQR algorithm as described by Nolet (1987). The group velocities calculated from the models at 50 seconds are shown in Figure 2.

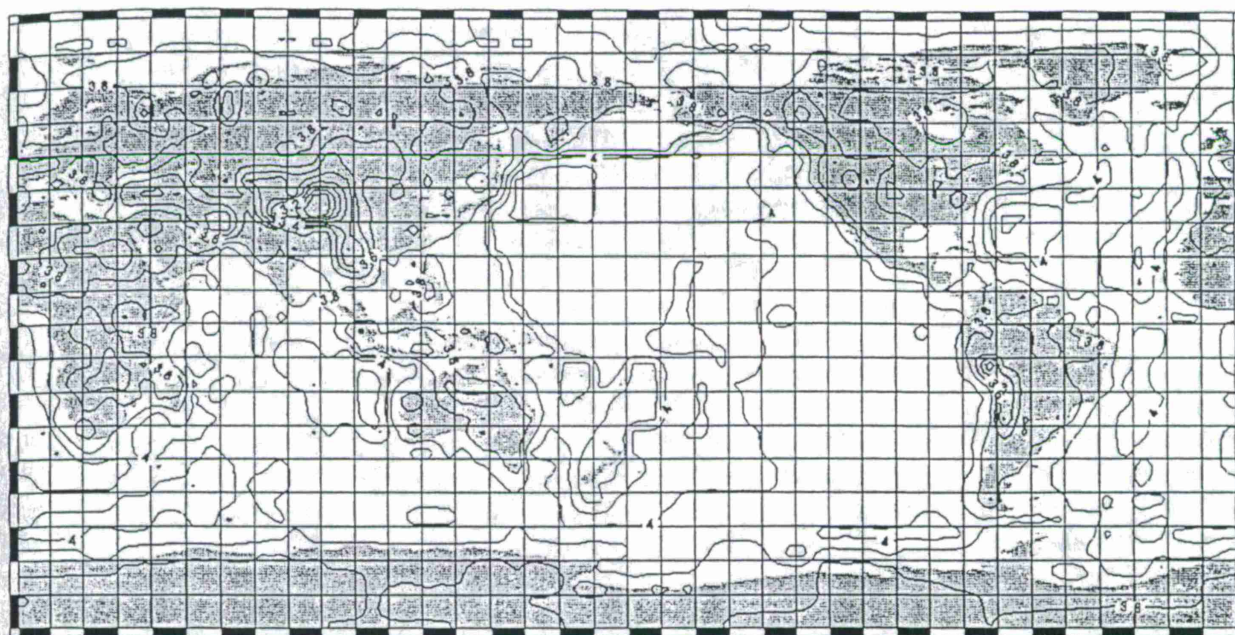


Figure 2. Group velocity contours of the inversion model at 50 seconds period.

The results show some significant improvements over both the model currently being used at the IDC and the Crust 5.1 model. The following tables show group velocity residuals (and standard deviations) in percent for the three models for data from nuclear test sites and for the global travel times derived from IDC data. The three models below are the group velocity model currently used at the IDC (Stevens and McLaughlin, 1996), as modified by Harkrider (personal communication) to a 5 degree grid; the original Crust 5.1 model, and the inversion results described above.

40 Second Group Velocity % Average Residuals (Standard Deviations)

Source	PIDC	Crust 5.1	Inversion
NTS (59)	0.93 (1.80)	2.08 (2.46)	0.15 (1.40)
East Kazakh (40)	1.20 (3.53)	5.00 (3.47)	0.80 (2.21)
Mururoa (13)	-0.80 (1.74)	-2.45 (1.73)	-0.78 (1.43)
Novaya Zemlya (99)	2.01 (2.39)	2.00 (2.28)	-0.06 (2.06)
Amchitka (55)	1.68 (1.58)	0.51 (2.54)	0.25 (1.39)
Earthquakes (1572)	1.44 (4.98)	1.68 (5.32)	0.46 (3.48)

20 Second Group Velocity % Average Residuals (Standard Deviations)

Source	PIDC	Crust 5.1	Inversion
NTS (58)	-1.83 (4.85)	-1.17 (2.48)	-0.47 (2.25)
East Kazakh (40)	-2.61 (3.23)	-0.31 (2.46)	-0.75 (1.96)
Mururoa (11)	-1.43 (2.30)	-1.47 (1.84)	0.41 (1.43)
Novaya Zemlya (99)	2.44 (6.15)	0.35 (4.68)	-0.26 (3.61)
Amchitka (54)	-1.23 (4.43)	1.42 (4.33)	0.83 (3.76)
Earthquakes (1673)	0.31 (5.82)	2.17 (6.31)	2.00 (5.46)

The average shear velocity change was -0.16 (2.57) %, with extreme values of -11% and 15%. Additional improvements can be made in these models, particularly in the western Pacific, where many rays follow grazing paths along continental boundaries, and in areas such as the south Pacific where coverage is limited. There is more variation and more error at periods less than 25 seconds than at longer periods. Nevertheless, the models work quite well for predicting group velocity dispersion and generating phase-matched filters over a frequency band of .01-.06 hz.

3. Automated surface wave identification, phase-matched filtering, and moment estimation using regionalized models at the Prototype International Data Center

All of the surface wave magnitudes currently being measured at the PIDC are identified and measured automatically with no operator intervention using the program Maxsurf, which has been developed and maintained by Maxwell Technologies. Surface waves are only measured using primary stations; for economic reasons the PIDC does not request data in the surface wave arrival time window from auxiliary stations. Surface waves are identified in the following way: a set of narrow band filters are applied to the data over a set of 8 frequencies from 0.02 to 0.06 hz. The arrival times at each frequency are then compared with predicted arrival times generated from the regionalized group velocity model described earlier. A few spurious or misassociated arrivals will pass the dispersion test, and these are removed with a set of queries designed to identify them. Such misassociated arrivals occur, for example, for an aftershock immediately following a large earthquake, or two aftershocks closely spaced in time and location. Until recently, the PIDC also applied a test based on azimuth estimated by 3-component polarization filtering, however this test proved to be unreliable because of high noise levels on the horizontal components, frequent polarity errors and other problems. Consequently, this test was discontinued, although the azimuth is still estimated and stored in the database.

Figure 3 shows a cumulative distribution of about one month of PIDC data, and about a year of NEIS data reported in the EDR's. The surface wave detection threshold of the PIDC is approximately one magnitude unit lower than the NEIS detection threshold. As shown in figure 4, there is also a bias of about 0.24 magnitude units between the NEIS and PIDC magnitudes. The reason for this has not been conclusively determined, but it appears to be due to censoring of the NEIS data: the preferential reporting of higher amplitude arrivals.

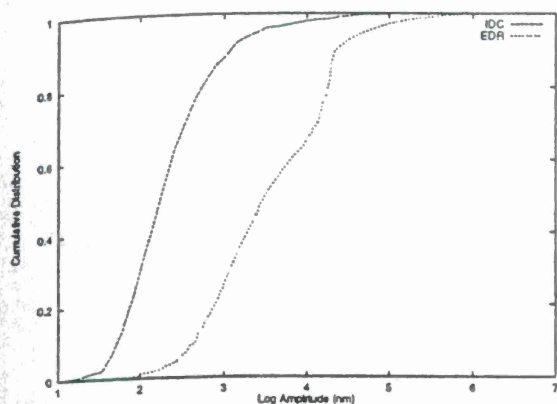


Figure 3. Cumulative Distribution of PIDC and NEIS M_s values.

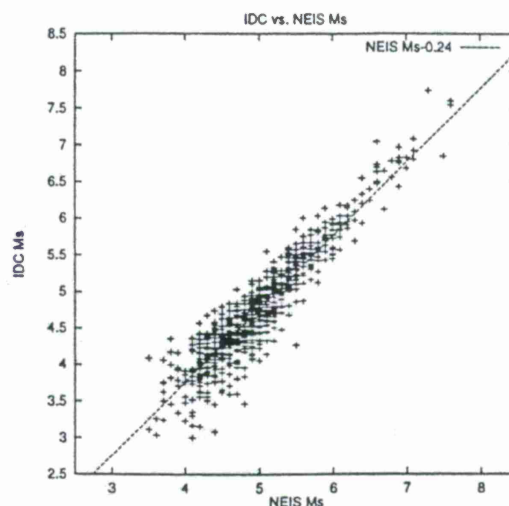


Figure 4. PIDC vs. NEIS M_s shows a bias of about 0.24 magnitude units.

Spectral magnitudes can also be measured automatically, and the program Maxpmf was designed for this purpose. It performs all of the functions of Maxsurf, including measuring a time domain magnitude where possible, and adds a phase matched filtering and path correction module which integrates a regionalized phase velocity model to generate a phase-matched filter and applies amplitude corrections as discussed above to generate a spectral magnitude (scalar moment). Maxpmf works in essentially the same manner as Maxsurf, with the exception that Maxsurf will reject a seismogram if it can't find a 20 second (time domain) arrival within the predicted arrival time window. This often occurs at regional distances and there is no reason for such a restriction for spectral magnitudes. Consequently, moments will be measured for regional seismograms in many cases where standard M_s measurements cannot be made.

4. Maximum likelihood Moment and M_s

Maximum likelihood magnitudes were originally developed to correct for censoring. For small events, it is common for larger arrivals to be measurable while smaller arrivals are lost in noise, causing the average magnitude of the observed arrivals to be biased high. Similarly, for very large events, the largest arrivals may be clipped and therefore discarded, causing the average magnitude of the remaining arrivals to be biased low. Maximum likelihood magnitudes correct for the censoring effect by including the measured noise level as an upper bound on the observed amplitude at a station. This correction, together with station corrections that are derived as part of the processing, lead to more consistent and reliable network magnitudes. Figures 5 and 6 below show the effect of the censoring correction on M_s and log moment for about 700 events, derived using about 10 days of PIDC continuous data and historical explosion data.

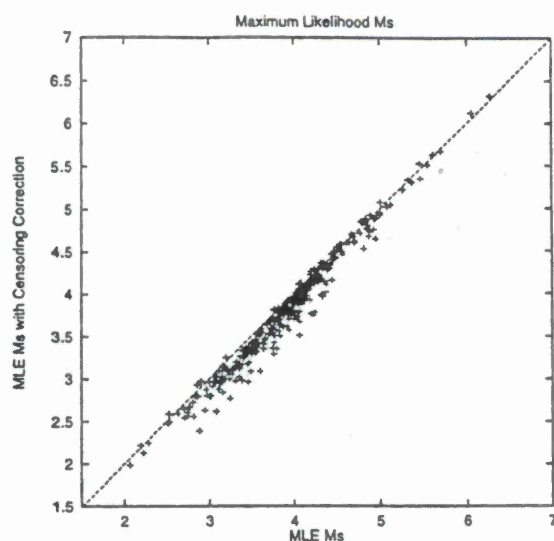


Figure 5. Maximum likelihood M_s with and without censoring correction.

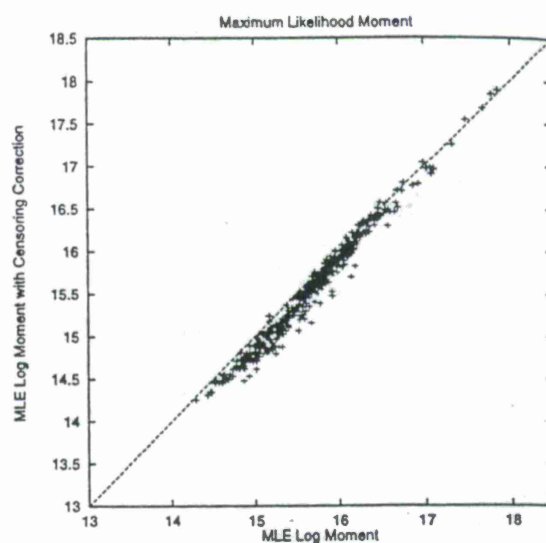


Figure 6. Maximum likelihood log moment with and without censoring correction.

In a CTBT context the most important result of maximum likelihood magnitudes is the ability to determine an upper bound on a magnitude when there is no measurable data. Because m_b - M_s may be as large as 2 magnitude units for an underground nuclear test, surface waves will rarely be observable for explosions with m_b less than 4, and may be difficult to observe up to m_b 5. A large earthquake may obscure surface waves from even larger explosions. However, it is possible to determine an upper bound on M_s for these events and in many cases this will be sufficient to identify the event as an explosion.

5. Earthquake/explosion discrimination using the M_s : m_b and M_0 : m_b methods.

Figures 7 and 8 show M_s and log moment plotted vs. m_b for the data set of PIDC data and historical explosion data described above. Open symbols indicate upper bounds on moment and M_s , while solid symbols indicate events with at least one measured surface wave. Also shown is an approximate discrimination line between the earthquake and explosion populations. Note that most of the explosions with no observations clearly fall into the explosion population based on the upper bound of either moment or M_s for the event. The best separation line has a slope of 1.4, which differs from the 1.0 slope that is expected at low magnitudes (e.g. Stevens and Day, 1985). There are several possible reasons for this. First, although only events with depths less than 75 km are plotted here, many small earthquakes have constrained depths or inaccurate depths. Small events with large m_b - M_s may therefore be deep in many cases. Second, the m_b values are not maximum likelihood values, and therefore are subject to censoring, causing m_b to be biased high for small events. Consequently, we can expect that discrimination will be improved, and the slope of the discrimination line reduced, if maximum likelihood m_b 's are used, and deep events are removed. The explosion m_b values should also be systematically reevaluated since the PIDC measurements are biased low relative to current NEIS m_b values (Murphy and Barker, 1996) due to differences in the way instrument response corrections are implemented, and the bias compared to historical m_b values has not been assessed.

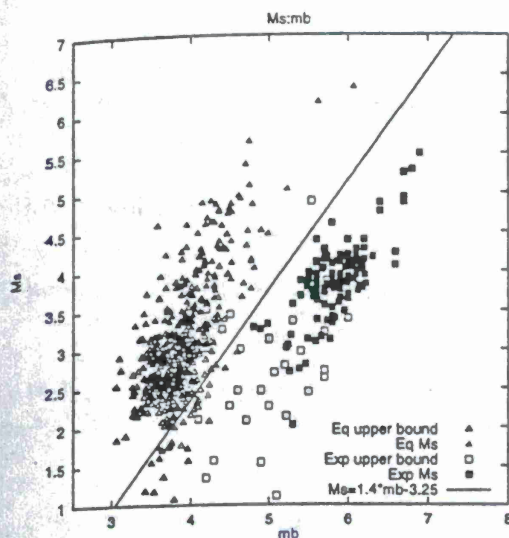


Figure 7. Maximum likelihood M_s and M_s upper bounds plotted vs. m_b for PIDC earthquakes and historical explosion data.

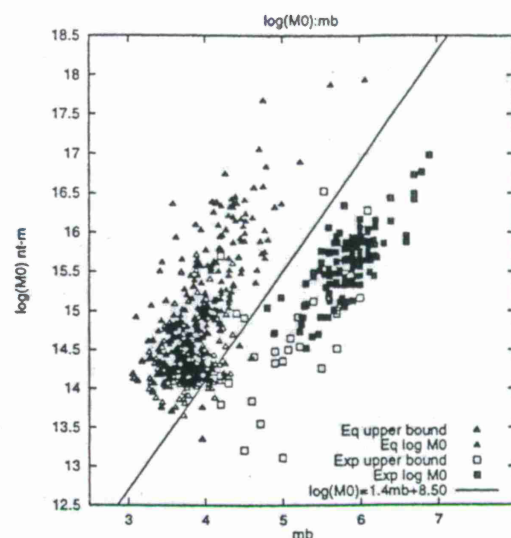


Figure 8. Maximum likelihood scalar moment and moment upper bounds plotted vs. m_b for PIDC earthquakes and historical explosion data.

CONCLUSIONS AND RECOMMENDATIONS

Improved surface wave analysis methods can reduce the surface wave magnitude threshold, improve identification capability, and reduce the likelihood of unnecessary on-site inspections under a CTBT. Recommended techniques include the use of: regionalized earth models and surface wave parameters, phase-matched filtering to improve signal/noise ratio, path corrected spectral magnitudes (scalar moment) in place of or in addition to M_s , and maximum likelihood magnitudes and maximum likelihood upper bounds on magnitudes.

The regionalized models developed in this project can be used to calculate surface wave parameters, generate phase-matched filters, and predict dispersive arrival times. In addition, the techniques used here to develop these models can be used on a continuing basis to improve the models. With the large amount of data now coming into the PIDC and the NDC on a continuous basis, it is possible to maintain a rapidly increasing database of dispersion curves, adding to the database used in this study and improving the results by filling in regions with poor coverage and extending the frequency range.

The analysis performed in this project used data from the IMS primary stations because data is not collected in the long period arrival time window from secondary stations. Since surface wave measurements are best at closer distances, particularly when spectral magnitudes are used, we can expect the surface wave threshold to be reduced by using a larger network. Additional low amplitude, regional explosion data should be acquired and processed in order to better assess the discrimination threshold of the methods described here.

REFERENCES

- Ekstrom, G., A. M. Dziewonski, G. P. Smith, and W. Su (1996), "Elastic and inelastic structure beneath Eurasia," in Proceedings of the 18th annual seismic research symposium on monitoring a comprehensive test ban treaty, 4-6 September, 1996, Phillips Laboratory report PL-TR-96-2153, July, pp. 309-318.

- Levshin, A. L., M. H. Ritzwoller, and S. S. Smith (1996), "Group Velocity Variations Across Eurasia," in Proceedings of the 18th annual seismic research symposium on monitoring a comprehensive test ban treaty, 4-6 September, 1996, Phillips Laboratory report PL-TR-96-2153, July, pp. 70-79.
- Mitchell, B. J., L. Cong and J. Xie, (1996), "Seismic attenuation studies in the middle east and southern Asia", St. Louis University scientific report No. 1 submitted to Phillips Laboratory, July.
- Mooney, W., G. Laske, and G. Masters (1997), "Crust 5.1: a global crustal model at 5x5 degrees," *Journal of Geophysical Research*, submitted.
- Murphy, J. R. and B. W. Barker (1996), "A preliminary evaluation of seismic magnitude determination at the International Data Center (IDC)," EOS Transactions of the American Geophysical Union, November, P. F7.
- Nolet, G. (1987), "Seismic wave propagation and seismic tomography," in *Seismic Tomography with applications in global seismology and exploration geophysics*, G. Nolet, ed., D. Reidel Publishing, Dordrecht, Holland.
- Okal, E. A. and J. Talandier (1987), " M_m : Theory of a variable-period mantle magnitude," *Geophysical Research Letters*, v. 14, pp. 836-839.
- Ritzwoller, M. H., A. L. Levshin, L. I. Ratnikova, and D. M. Tremblay (1996), "High Resolution Group Velocity Variations across Central Asia," in Proceedings of the 18th annual seismic research symposium on monitoring a comprehensive test ban treaty, 4-6 September, 1996, Phillips Laboratory report PL-TR-96-2153, July, pp. 98-107.
- Stevens, J. L. (1986), "Estimation of scalar moments from explosion-generated surface waves," *Bull. Seism. Soc. Am.*, v. 76, pp. 123-151.
- Stevens, J. L. and S. M. Day (1985), "The physical basis of the m_b : M_s and variable frequency magnitude methods for earthquake/explosion discrimination," *Journal of Geophysical Research*, v. 90, pp. 3009-3020.
- Stevens, J. L. and K. L. McLaughlin (1996), "Regionalized Maximum Likelihood Surface Wave Analysis," Maxwell Technologies Technical Report submitted to Phillips Laboratory, SSS-DTR-96-15562, September.
- Stevens, J. L., and K. L. McLaughlin (1988), "Analysis of surface waves from the Novaya Zemlya, Mururoa, and Amchitka test sites, and maximum likelihood estimation of scalar moments from earthquakes and explosions," S-CUBED technical report submitted to Air Force Technical Applications Center, SSS-TR-89-9953, September.

ACKNOWLEDGEMENTS

I would like to thank Gabi Laske of the University of California at San Diego for providing the Crust 5.1 earth models, and Mike Ritzwoller of the University of Colorado, Brian Mitchell of St. Louis University, Goran Ekstrom of Harvard University, and their coworkers for the use of their data and models in this project.

ACCURATE DEPTH DETERMINATIONS AND OTHER DIAGNOSTIC EVENT CHARACTERISTICS IN NEAR-REAL TIME FROM REGIONAL SIGNALS

Shelton S. Alexander and Chih-Chieh Yang
The Pennsylvania State University

Sponsored by the Air Force Office of Scientific Research
Grant No. F49620-94-1-0179

ABSTRACT

Further tests of the Cepstral Stacking Method (CSM) developed in earlier phases of this study have been conducted for crustal events in different geologic settings recorded at regional distances. CSM can be used to obtain accurate focal depth from only one regional station as well as from arrays and combinations of arrays and individual stations when they are available. The procedure is to stack the cepstra of a set of overlapping sub-windows in the (S - P) signal window for each station or array element; for the multi-station or array case the individual stacked cepstra for each station/array element are stacked. Depth-phase delay times are enhanced by this process while delay times between various crustal arrivals are suppressed. Product stacking is shown to be superior to sum stacking.

Software developed to implement the CSM allows depth determinations to be made in near-real time. Various pre-processing options to enhance the effectiveness of the method are also available; they include band-pass filtering, envelope normalization, spectral smoothing, and noise power subtraction.

Based on results for events with independently-known focal depths, accuracies of about 1 km or better can be achieved when signal bandwidths are greater than approximately 5 Hz.

Other diagnostic event characteristics can also be derived from the same data sets in near-real time. For example, band-pass filtering can be used to look for Rg. The presence of Rg indicates that the event is shallow and can be used to confirm a shallow depth obtained by the CSM. When an event is shallower than about 5 km, other information must be used to distinguish earthquakes from explosions; pattern recognition or artificial neural network techniques, among others, can be used to identify regional events in near-real time.

Examples are given to illustrate these methods for different types of regional events.

OBJECTIVE

The overall objective of this research is to develop regional discriminants that can be obtained in near-real time to facilitate automated or mostly-automated regional event identification. Recent efforts have been focused on obtaining accurate focal depths from regional observations in different source regions using the Cepstral Stacking Method developed in this project; investigating improvements in the effectiveness of the CSM; and configuring software for near-real-time depth determinations. Pattern recognition and artificial neural network (ANN) methods developed earlier in this work also can be used in conjunction with the CSM for automated or mostly-automated event discrimination. The relevance of this research to a CTBT is that the CSM provides accurate focal depths from regional observations, unlike other methods which commonly give biased depth estimates; near-real-time CSM depths can then be used to reduce the number of events that require detailed analysis by culling out events that are deeper than 5 km (earthquakes). The pattern recognition and ANN methods developed earlier provide additional capability for rapid regional event identification.

RESEARCH ACCOMPLISHED

The research reported here is an extension of earlier work under this Grant to develop and test the CSM for accurate depth determinations for regional events from single stations and from arrays or networks of regional stations. The CSM and previous results are described in Alexander et al. (1995), Karl (1995), Alexander (1996), and Alexander and Yang (1996). Yang (1996) and subsequent recent work have developed modifications to the basic CSM to enhance its effectiveness; in addition CSM analyses of events from Iran, Korea, western Turkey, and the western United States have been carried out. The CSM software has also been reconfigured to facilitate near-real-time analysis of regional events.

Results to date on crustal events (earthquakes and explosions) with independently-known source depths, indicate that, with signal band-widths of approximately 5 Hz or greater and reasonable signal-to-noise levels, accuracies in source depth of about 1 km or better can be achieved using the CSM.

Figures 1 and 2 show examples of single-station CSM results for two, small regional events in Iran recorded at the SRO station MAJO. Also shown are narrow-band-filtered signals for these events; it is clear that there is a good signal to noise ratio in the frequency band from 0.5 to 7 Hz in the S - P window for both events. The 2/23/77 event (Figure 1) has a strong cepstral peak at a delay time of 2.6 seconds, whereas the 6/04/77 event (Figure 2) has a strong cepstral peak at 0.8 seconds, indicating it is very shallow and significantly shallower than the 2/23/77 event. If the observed cepstral peaks correspond to pP - P delays, the depth of the 2/23/77 event is approximately 7.8 km and the 6/04/77 event is approximately 2.4 km deep, assuming an average crustal P-velocity of 6 km/sec; the depths would be 5.85 and 1.8 km respectively, assuming an average crustal P-velocity of 4.5 km/sec. If the peaks correspond to sP - P, the depths would be 5.85 and 1.8 km, respectively, for a 6 km/sec crustal P-velocity compared to 4.3 and 1.3 km, respectively, for a 4.5 km/sec crustal P-velocity. Therefore, the 2/23/77 event would be identified as an earthquake, whereas the 6/04/77 event cannot be identified based on focal depth alone (if the average shallow crustal

velocity is higher than 4.5 km/sec). The 0.1-0.3 band-pass-filtered signals for both events show the presence of a prominent Rg arrival, indicating that both events are relatively shallow but not indicating which one is shallower. However, the presence of Rg helps corroborate the CSM results that give relatively shallow source depths for both events.

In an operational mode the CSM would cull out the 2/23/77 event and keep the 6/04/77 event for further evaluation using other discriminants. The relatively large Lg/P ratios for the higher frequencies in the band-pass-filtered signals suggest that the 6/04/77 event is also an earthquake..

Other examples of single-station CSM depths are shown in Figures 3 for a magnitude 5 mainshock and two large aftershocks located in western Turkey (Figure 4) that were recorded at the broad-band station DPC at a distance of approximately 1515 km. These events were widely recorded globally, so both the absolute and relative locations are very well-constrained and a normal-fault focal mechanism of the main shock has been determined (Figure 4). If the focal depths of the three events, which occurred only a few hours apart, can be determined accurately, the actual fault plane and its projection to the surface can be found. The table included in Figure 6 compares the focal depths for these three events determined from the ISC stations, the ISC using pP - P, and the CSM for DPC. The ISC (pP - P) and CSM depths agree within 1 km for the mainshock but disagree for the aftershocks. The standard ISC depths are very different, even though a large number of stations were used in the hypocenter determinations. Only a few pP observations were available for ISC's pP - P depth determinations for the two aftershocks and they are not all consistent, whereas the station, propagation path, and processing were identical for the CSM analysis. Therefore, the CSM depths are inferred to be the most accurate. From the mainshock's focal mechanism and the CSM depths (Figure 4), one can infer that the actual fault plane is the one dipping to the southwest; it projects to the surface as shown in Figure 4. The relevance of this example to CTBT monitoring is that similar analyses can be done for areas of interest that are seismically active, such as Iran, to define active faults spatially in three dimensions. This would provide a valuable addition to the knowledge base needed to distinguish earthquakes from explosions in active seismic areas.

An example of combined array and individual station CSM depth determination is shown in Figure 5 for a regional event in north-central Iran recorded at the ILPA array and the SRO station MAIO. In this case the cepstrum for each sub-window was product stacked across the ILPA array and then a final product stack of these composite sub-window stacks and the MAIO cepstral stack was generated (bottom trace). The single, large peak in the final product cepstrum is at 1.5 seconds, corresponding to a source depth of approximately 4.5 km if the peak is pP - P, or 3.3 km if it is sP - P (assuming an average crustal P-velocity of 6 km/sec). If the average crustal P-velocity is less, say 4.5 km/sec, then these estimated depths would be less by a factor of 4.5/6. If this event were encountered during CTBT monitoring, it would be kept for further analysis, because its depth is less than 5 km.

The CSM method has also been applied to regional events recorded at Alpha arrays (e.g. TXAR, the KS Korean array, and NORESS) and to combined KS and individual stations in mainland China. Array stacking and combined array and individual station stacking generally

enhance the depth phase cepstral peak(s) compared to individual station or array-element cepstral peaks and should be used when such data are available.

Further analyses on the same data sets can also be carried out using the pattern recognition and artificial neural network approaches developed earlier in this project (e.g. Hsu, 1995), as well as other discriminant measures, to identify regional events. These CSM and pattern recognition or ANN methods can be applied in near-real-time in automated or mostly-automated operational systems.

CONCLUSIONS AND RECOMMENDATIONS

1. It has been demonstrated that the CSM gives accurate estimates of depth phase delay times using only single regional stations, individual arrays, or combined arrays and distributed regional stations. Tests on calibration events in different source regions indicate that CSM focal depth estimates typically are accurate to 1 km or better.
2. The CSM, as now implemented, allows accurate source depths to be determined in near-real time. In CTBT monitoring, this will permit events deeper than 5 km to be immediately identified as earthquakes requiring no further analysis, thereby significantly reducing the number of events that require more-extensive evaluation.
3. CSM can be used in conjunction with algorithms that give very accurate epicenters and focal mechanisms to determine the 3-dimensional geometry of active faults in source regions of interest for CTBT monitoring (e.g. Iran). Incorporating this information in the ground-truth data base will help identify unknown events located in such active regions.
4. Certain preprocessing steps, such as band-pass filtering, spectral smoothing, and envelope normalization can enhance the effectiveness of the CSM, and product stacking gives significantly better results than sum-stacking.

It is recommended that the CSM be routinely applied to a large number of regional events in different settings to gain further experience with the method and gain confidence in the accuracy of the source depth estimates obtained. In particular the CSM should be applied at all the new Alpha arrays and Beta stations that will be used for CTBT monitoring, to verify that CSM works as expected.

REFERENCES

- Alexander, S. S. and C-C Yang, 1996, Use of the Cepstral Stacking Method (CSM) for Improved Source Depth Determinations from Combined Single-Station and Array or Network Observations at Regional Distances, Proc. of the 18th Annual Seismic Research Symposium on Monitoring a Comprehensive Test Ban Treaty, 4-6 Sept. 1996, PL-TR-96-2153, Env. Res. Papers, No. 1195, 647-656.
- Alexander, S. S., 1996, A New Method for Determining Source Depth From a Single Regional Station, Seis. Res. Ltrs., Vol. 67, No. 1, p. 63.

Alexander, S. S., R. C. Hsu, S. L. Karl, I. N. Gupta, and D. H. Salzberg, 1995, New Techniques for Estimating Source Depth and Other Diagnostic Source Characteristics of Shallow Events From Regional Observations of P. Lg and Rg signals, Proc. 17th Seis. Res. Symposium on Monitoring a Comprehensive Test Ban Treaty, PL-TR-95-2108, Env. Res. Paper, No. 1173, 821-830.

Hsu, C. 1995, Seismic Signal Pattern Recognition, Ph.D. Thesis, EE, The Pennsylvania State University, 185 pp.

Karl, S. L., 1995, Magnitude and Source Depth Estimates for Earthquakes and Explosions in Iran--Regional Observations, B.S. Thesis in Geosciences, The Pennsylvania State University, 185 pp.

Yang, C. C., 1996, Investigation of Cepstral Stacking Methods for Time Delay Extraction, M.S. Thesis (EE), The Pennsylvania State University, 113 pp.

Feb. 23, 1977

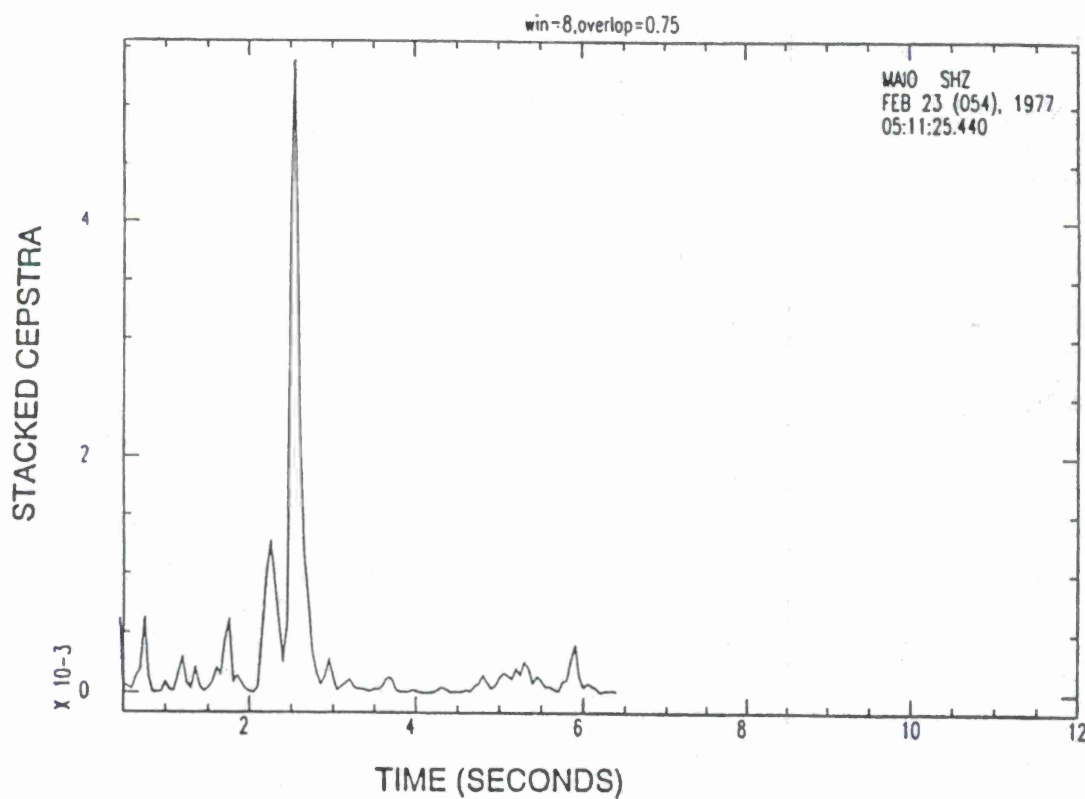
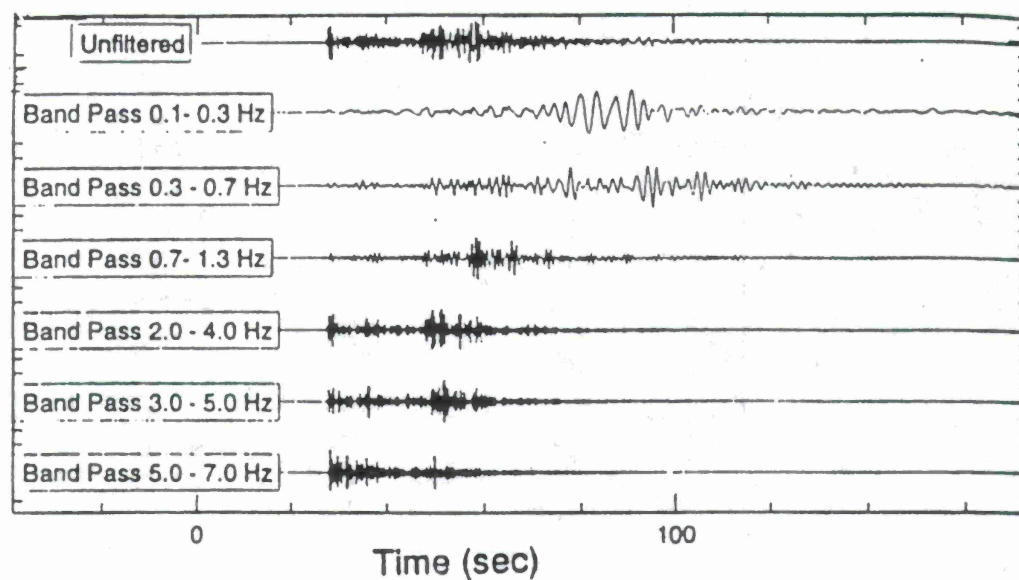


Figure 1. Original and band-pass filtered signals for a regional event on 2/23/77 in Iran recorded at station MAIO (top panel); product-stacked cepstra of sub-windows (bottom).

June 4 1977

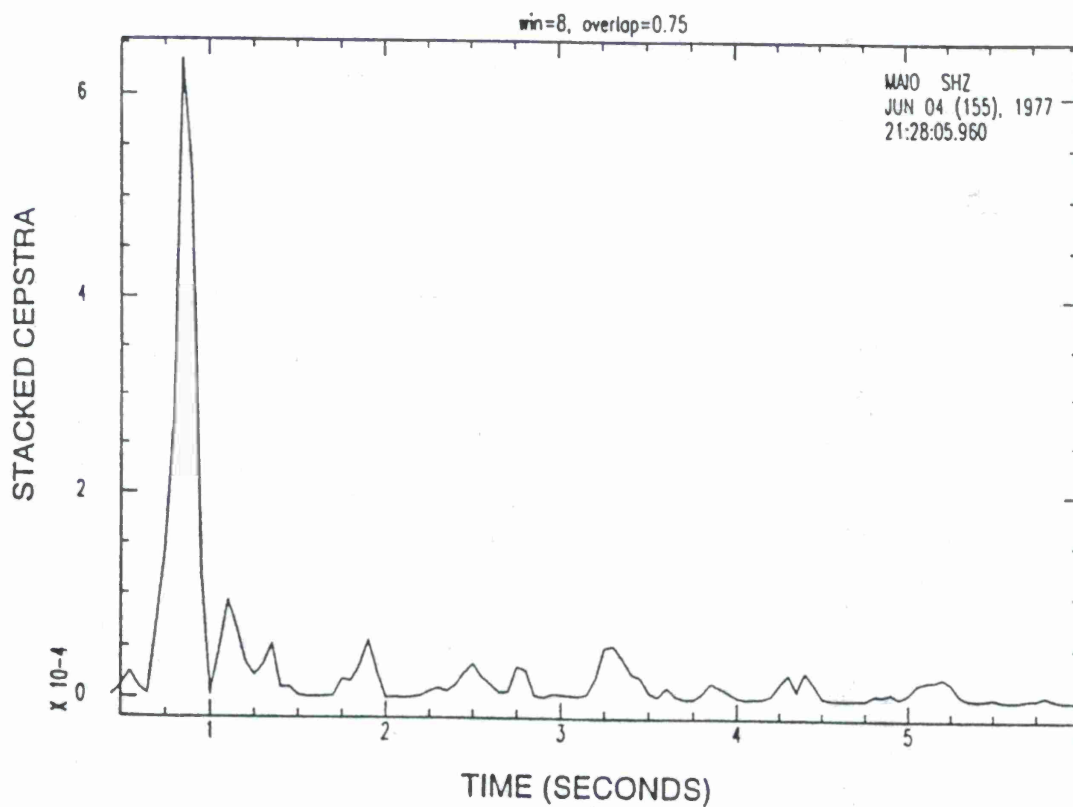
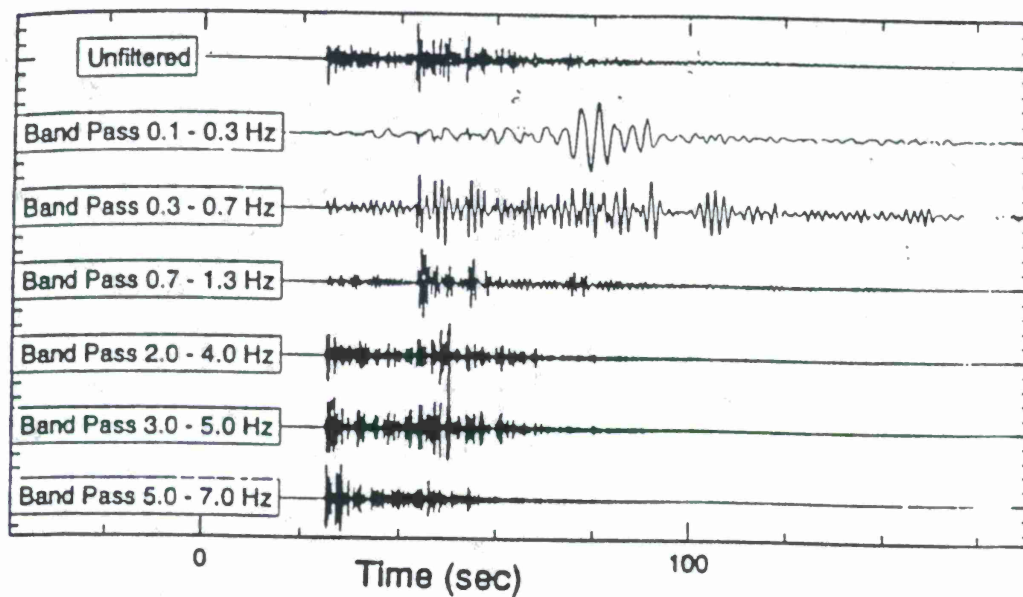
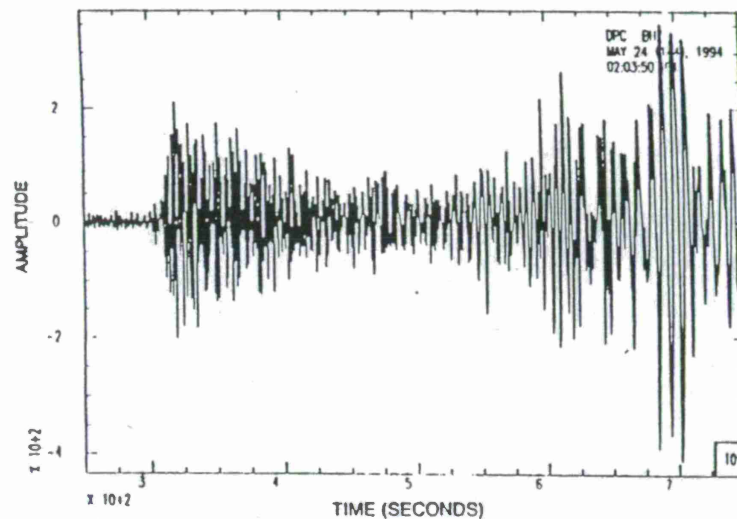
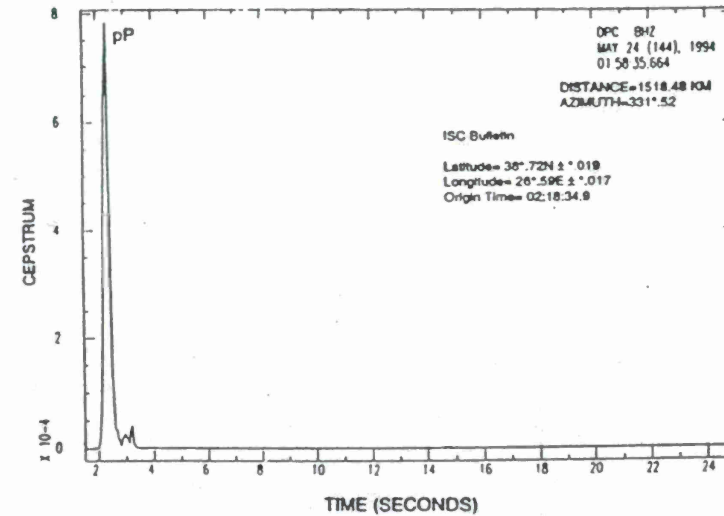


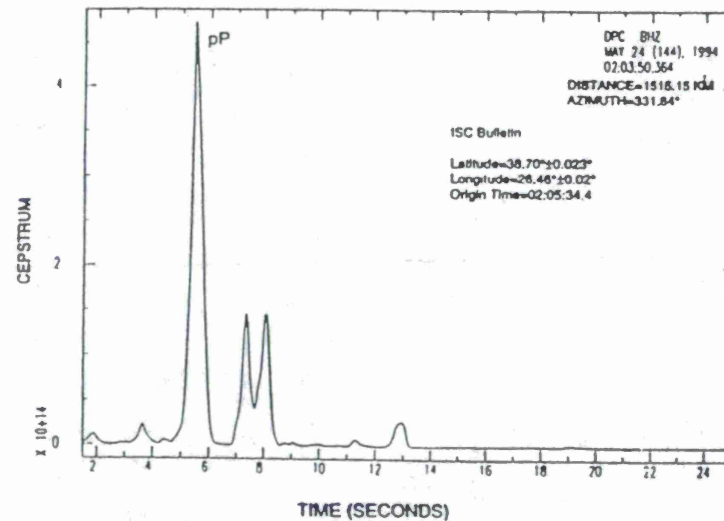
Figure 2. Original and band-pass filtered signals for a regional event on 6/04/77 in Iran recorded at station MAIO (top panel); product-stacked cepstra of sub-windows (bottom).



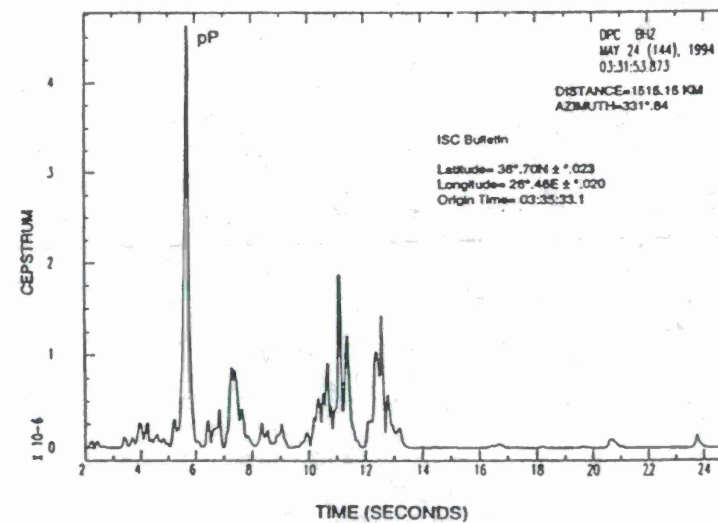
24 May 1994 event signal recorded by DPC station
Bandpass filtering 0.5 Hz - 5 Hz, origin time: 02:05:34.4



Product cepstrum of 24 May 1994 event recorded by DPC station
window length=40 sec., overlap=80% through envelope normalization

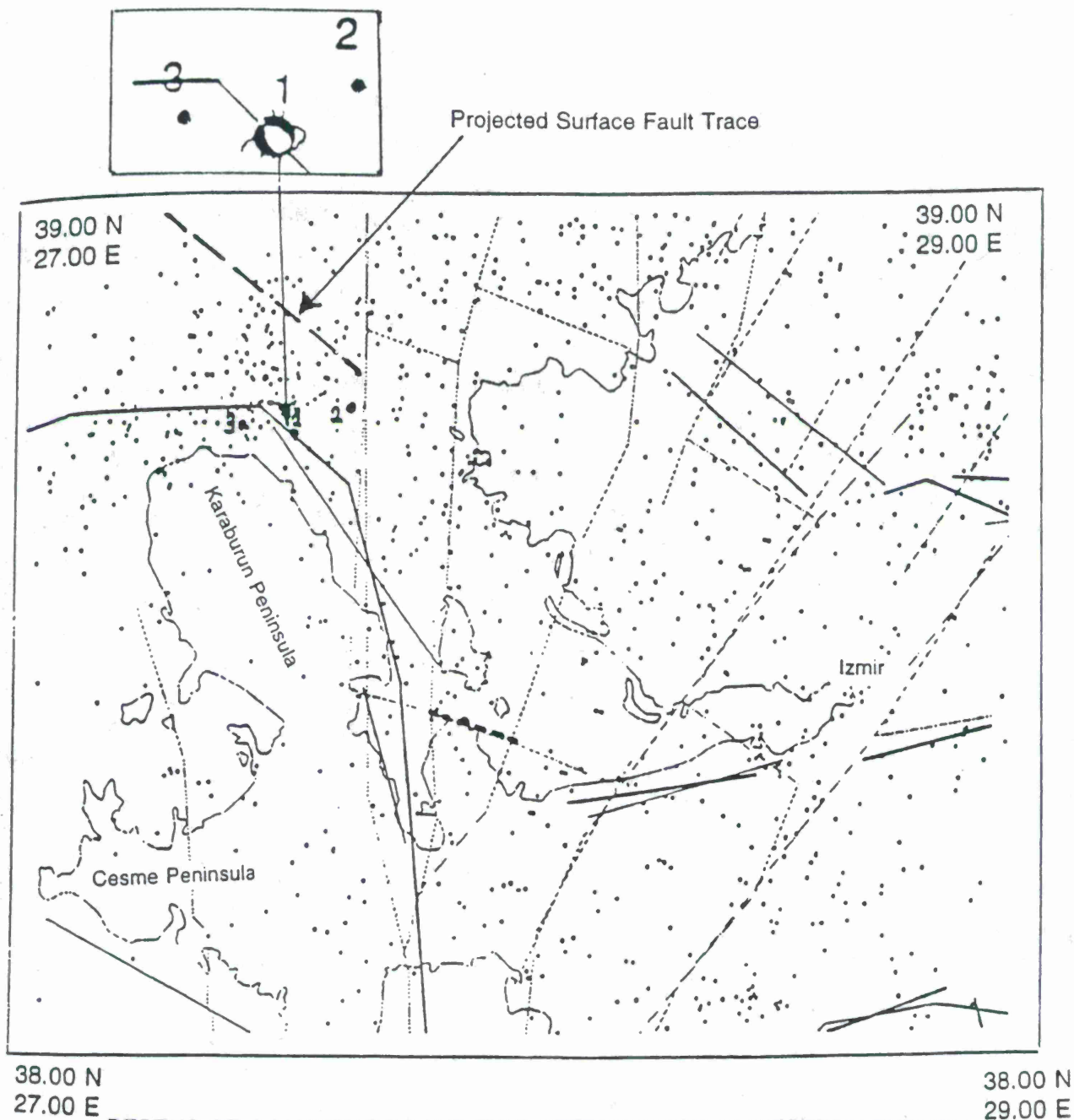


Product cepstrum of 24 May 1994 event recorded by DPC station
window length= 40 sec., overlap=80%



Product cepstrum of 24 May 1994 event recorded by DPC station
window length=40 sec., overlap=80% through envelope normalization

Figure 3. Mainshock signal and product-stacked cepstra for the mainshock and two aftershocks in western Turkey (Figure 4) recorded at regional station DPC.



DEPTHS OF A MAINSHOCK AND TWO AFTERSHOCKS IN WESTERN TURKEY
FROM CEPSTRAL STACKING

Event	Depth(Km)ISC	ISC (pP-P) (Km)	(pP-P) Cepst. Stack (Km)
1	10	16	17.0
2	10	13	7.5
3	0	11	16.0

Figure 4. Map showing location of the mainshock and two aftershocks in western Turkey and the projected surface fault trace. The table (bottom) shows a comparison of depth estimates for these events.

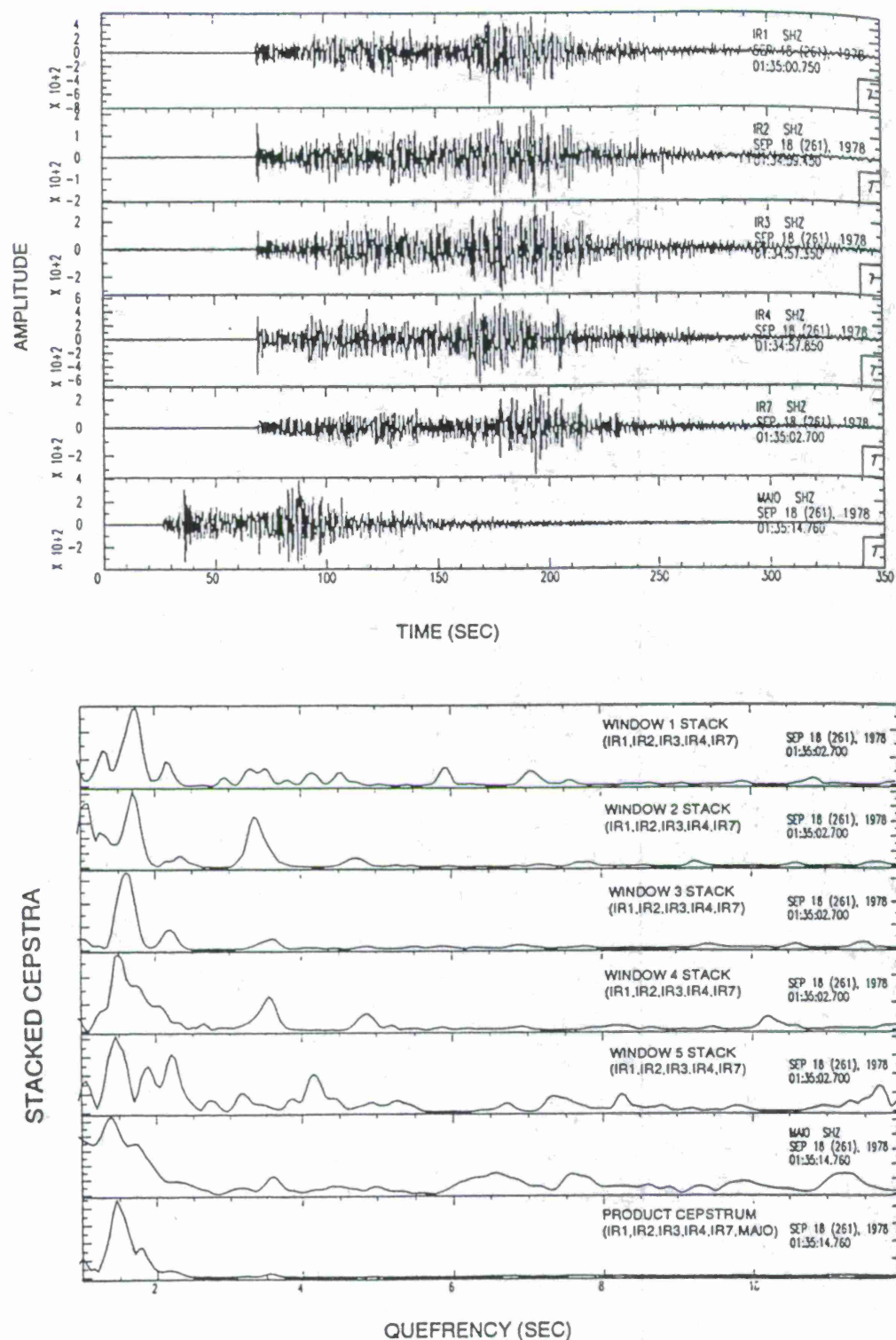


Figure 5. This example illustrates the combined cepstral stacking over the ILPA array and the SRO station MAIO for a regional event in Iran. The signals are shown in the top panel and the normalized, stacked cepstra are shown in the bottom panel. The last trace shows the composite product cepstrum for the ILPA array and MAIO; it has a prominent peak at a delay time of about 1.5 sec representing either the pP - P or sP - P time.

EARTHQUAKE LOCATION WITH A 3-D VELOCITY MODEL FOR THE REGION OF THE BOLIVIAN ANDES

Rodolfo Ayala and Lawrence A. Drake
Observatorio San Calixto
Casilla 12656, La Paz, BOLIVIA
Tel. 591 2 356 098 Fax 376 805
adrake@osc.bo

Sponsored by the Air Force Office of Scientific Research
Grant No. F49620-97-1-0214-POO001

ABSTRACT

The region of the Bolivian Andes has a complex structure and the seismic velocities there are not well known. Geiger-type location methods use only flat-layered velocity models and do not allow the introduction of 3-D heterogeneous velocity models. The Bolivian Andes do not contain good seismograph station coverage and much of the seismicity is outside the seismic net. We have used a new method of earthquake location (3DGRIDLOC): it uses the Tarantol-Valette non-linear algorithm for the earthquake location and the Podvin-Lecomte method for the calculation of the theoretical traveltimes of first arrivals in a 3-D velocity mesh. The new method allows the introduction of 3-D heterogeneous velocity models for the Bolivian Andes that model more realistically the strong lateral variations of the crustal structure and the shape of the Nazca plate beneath the Bolivian Andes. The seismicity recorded by the permanent Bolivian network from June 1988 to November 1994 has been located with the use of the 3DGRIDLOC method and a preliminary 3-D heterogeneous velocity model. The P and S residuals of the 3DGRIDLOC locations are much smaller than those of the National Earthquake Information Center locations for moderate and large events. Important crustal seismicity recorded by the Bolivian seismograph network, but not reported by the international bulletins, is located in the Western Cordillera, in the north of the Eastern Cordillera and near the "Santa Cruz bend". Deeper seismicity is located below the Western Cordillera in the southern Peru-Chile-Bolivia region at depths from 70 to 150 km. Sparser seismicity is located in the region of the Bolivian Andes at depths of from 150 to 325 km; then there appears to be a gap and deeper seismicity is located from 550 to 650 km (including the very large unusual event of 9 June 1994). The 3DGRIDLOC method and the 3-D velocity model have allowed us to obtain a more accurate location of more of the seismicity in the region of the Bolivian Andes.

Keywords: event location, 3-D velocity model, Bolivian Andes.

OBJECTIVES

The objectives of this study were: (1) to propose a 3-D P- and S-wave velocity model for the region of the Bolivian Andes that made use of the available geophysical, geological and tectonic information; (2) to test whether the new location method has sufficient accuracy in a region with sparse seismograph coverage; (3) to locate events recorded by the Bolivian network, but not reported by the international bulletins.

RESEARCH ACCOMPLISHED

Introduction

The region of the Central Andes located above the segment of the subduction zone dipping normally about 30°ENE (Barazangi and Isacks, 1976; Sacks, 1977; Grange et al., 1984; Cahill and Isacks, 1992) is known as the region of the Bolivian Andes. The five main features of the Bolivian Andes are: 1) a high plateau, the Altiplano, and high topography (some summits reach 7000 m); 2) a thick crust (between 60 and 70 km); 3) a change of the structural trend of the Andean Cordillera from NW-SE to N-S, which corresponds to the "Santa Cruz bend"; 4) extensive calc-alkaline Cenozoic to Recent volcanism; and 5) the thin-skinned deformation in the Subandean zone.

The region of the Bolivian Andes has a morphostructural zonation. This zonation comprises three morphostructural zones (Lavenue and Mercier, 1991): 1) the low Pacific lands (altitudes up to 2500 m) comprising, in Chile, the Coastal Cordillera, the Longitudinal Valley and the Chilean Precordillera; 2) the high Andes (altitudes between 2500 and 7000 m) comprising the Western Cordillera, the Altiplano and the Eastern Cordillera; and 3) the Amazonian lands (altitude below 2500 m) comprising the Subandean zone, the Chaco-Beni plains, the Sierras Chiquitanas and the Brazilian Shield.

Most earthquake location methods are derived from Geiger's method (1912). These popular methods, like HYPO71 (Lee and Lahr, 1975) and HYPOINVERSE (Klein, 1978), use only flat-layered velocity models. The direct methods based on a hypocenter searching in a 3-D mesh allow the introduction of complex velocity models (Nelson and Vidale, 1990; Moser et al., 1992; Wittlinger et al., 1993) to represent strong lateral variations, like those of the crust and upper mantle structure in the region of Bolivian Andes (Wigger, 1988; Schmitz, 1993; Comte et al., 1994; Dorbath and Granet, 1996). By these methods, if the velocity models are well known, earthquakes outside the network, where there is sparse coverage of seismograph stations, can be located (Nelson and Vidale, 1990). The direct methods are more robust to time and other errors in the data and are not very sensitive to weak velocity perturbations in the model (Wittlinger et al., 1993; Ayala, 1997).

Data and seismic network

The data used were recorded by the permanent Bolivian seismic net and cover the period from June 1988 to November 1994 (Figure 1). The stations of Arequipa (ARE) in southern Peru, Antofagasta (ANT) in northern Chile and Humahuaca (HJA) and Yavi (YJA) in northern Argentina were also used when data were available.

The uncertainties in picking P and S arrival times were less than or equal to 0.05-0.10 for digital stations and 0.2-0.5 s for analogue stations. The V_p/V_s ratio was equal to 1.78.

Table 1. Station coordinates

CODE	NAME	LATITUDE	LONGITUDE	ALTITUDE
		°S	°W	m
BOA	Zongo	16.2694	68.1240	4397
BOB	Banderani	16.1443	68.1319	3960
BOC	Huaylipaya	16.0508	68.0042	1670
BOD	Gloria	16.6374	68.5981	4230
BOE	Chanca	16.8127	67.9821	4325
BOF	Collana	16.9540	68.3380	4480
MOC	Mochara	21.2500	65.6380	3580
SIV	San Ignacio	15.9913	61.0722	520
LPB	La Paz	16.5327	68.0984	3292
LPAZ	La Paz	16.2879	68.1307	4474
CCH	Cochabamba	17.3842	66.1342	2650
ANT	Antofagasta	23.7050	70.4153	80
ARE	Arequipa	15.4621	71.4913	2452
HJA	Humahuaca	23.2144	65.4056	3000
YJA	Yavi	22.1700	65.5025	3535

Hypocenter location method

The hypocenters are located with the 3DGRIDLOC method (Wittlinger et al., 1993; Ayala and Wittlinger, 1996; Ayala, 1997). This new method is a combination of two tools: 1) for solving the forward problem, the PL method (Podvin and Lecomte, 1991) is used to calculate the first traveltimes, based on the principle of Huygens, similar to the method of Vidale (1988, 1990), for solving the eikonal equation by the finite difference method; and 2) for solving the inverse problem, a non-linear algorithm from Tarantola and Valette (1982) uses a probability density function. The velocity model is described by a 3-D mesh of regular cubic cells. In each cell the P wave velocity is specified. The PL method computes the first theoretical arrival time grids for each of the recording stations, by the use of the reciprocity principle, by placing a fictitious source at the station and computing the traveltimes of the first arrival to each of the cells. The S-wave grids can be deduced from the P-wave grids by the use of a value of V_p/V_s : a constant value of Poisson's ratio is assumed for the whole medium.

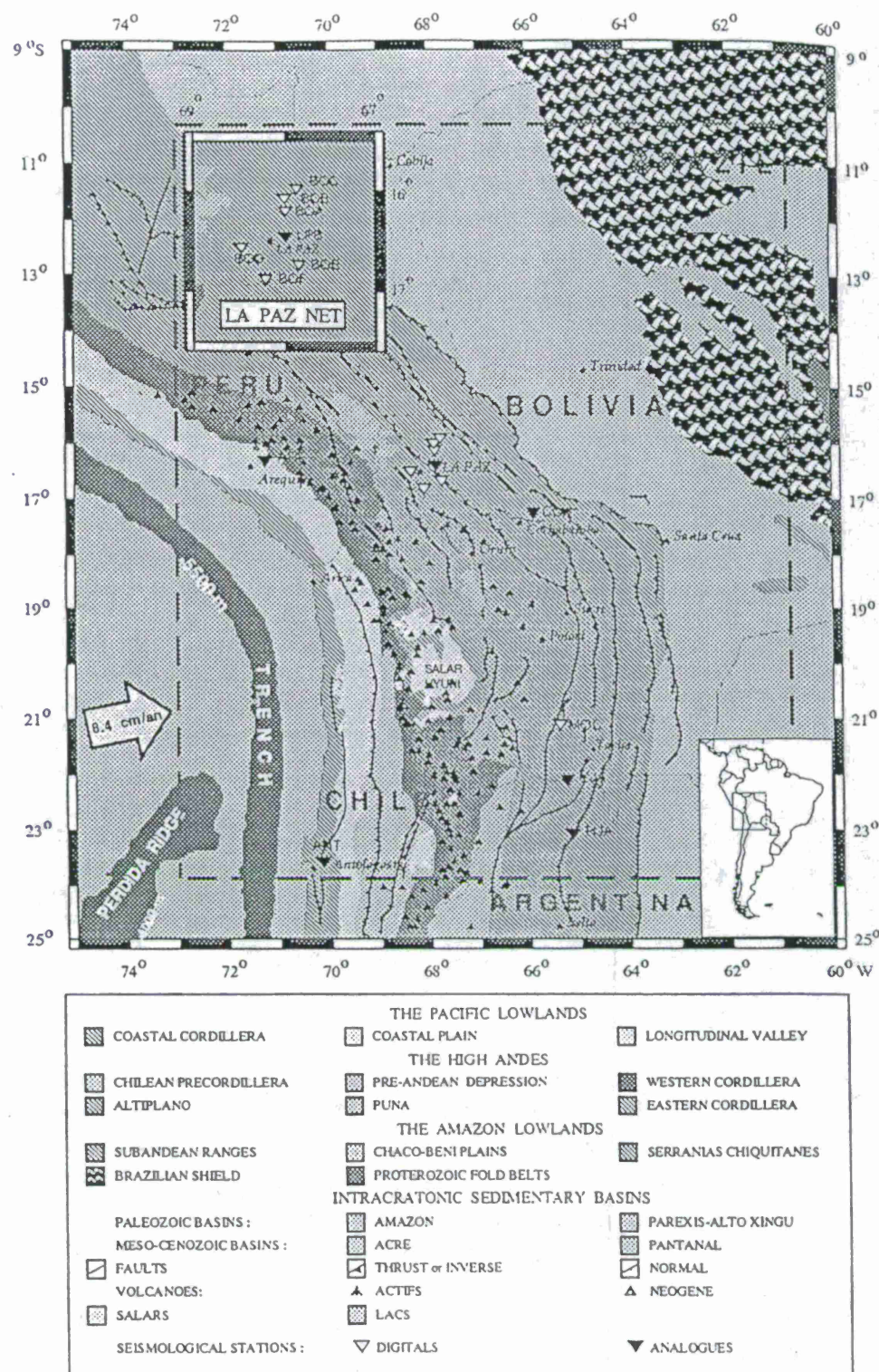


Figure 1. Map of the seismographic stations and morphostructural zones. The dotted line shows the region of the 3-D velocity model. The positions of the stations around La Paz city and the recording center (San Calixto Observatory) are also shown in the upper-left side. The arrow shows the convergence rate between the Nazca and South American plates (DeMetz et al., 1990).

After the computation of the traveltimes grids, to obtain the solution of the inverse problem, it is necessary to decide which cell among the grid cells contains the hypocenter. The Tarantola and Valette formulation, using a probability density function, is applied to obtain the hypocenter. The basic relationship used to evaluate the probability density function (PDF) of the hypocenter is:

$$w(x,y,z) = Kp(x,y,z) \cdot \exp(-1/2[t_o - h(x,y,z)]^T (C_i + C_T)^{-1} [t_o - h(x,y,z)])$$

where K is a normalization factor; $p(x,y,z)$ is an arbitrary *a priori* PDF containing all the *a priori* information that we have on the parameters; t_o is the vector of the observed arrival times minus the mean of the observed arrival times at the recording stations; $h(x,y,z)$ is the vector of the theoretical traveltimes minus the mean of the theoretical traveltimes; C_i is the covariance matrix that expresses the standard deviation of the P and S readings; C_T is the covariance matrix that expresses the velocity model misfit errors. The location process is performed in two steps (following the scheme of Nelson and Vidale, 1990): 1) the searching is in whole medium until the cell of the grid with the maximum probability is found; 2) a finer grid is defined by linear interpolation around the first location and the location process is repeated with the use of the finer grid. In practice, a grid of 10 km is used, with a finer grid of 1 km spacing.

3-D velocity model

A problem of achieving a good velocity structure for the whole region of the Bolivian Andes is the sparse seismograph station coverage. A joint inversion of the whole region to obtain reliable velocity models and event locations, as has been done by Dorbath and Granet (1996) for northern Bolivia, cannot be performed. The region for the 3-D velocity model was between 10.31° and 23.86°S and between 60.74° and 73.00°W. To introduce the altitude of stations, level 1 corresponded to an altitude of 10 km. We also introduced the sphericity of the Earth. The final model comprised 150 x 132 x 69 cubic cells of approximately 10 km size, defining a cubic volume of 1500 km in latitude, 1280 km in longitude, and 650 km in depth (Figure 2).

The 3-D velocity model used was based on the different geophysical, geological and structural information in the literature. We took a different velocity structure for each of the morphostructural zones: 1) from inversion of P- and S-wave residuals of local events: for southern Peru, from Cunningham et al. (1986); Lindo (1993); Dorbath (1996); for the northern Altiplano and Eastern Cordillera, from Dorbath and Granet (1996); south of 18°S, for the fore-arc and Western Cordillera, from Comte et al. (1994); 2) from seismic refraction: for the Western Cordillera and Subandean zones, from Wigger (1988); Schmitz (1993). The Moho depth was taken from the Airy compensation model: for central and eastern Bolivia, from Ussami et al. (1993); for southern Bolivia, from Schmitz (1993). We took a velocity below the Brazilian Shield 3% faster than the asthenospheric velocity (Dorbath et al., 1993). The shape of the slab beneath the Bolivian Andes was taken from the geometry of Wadati-Benioff zone from Cahill and Isacks (1992), with a thickness of 80 km and a velocity 2.7% faster than the surrounding mantle velocity (Engdahl et al., 1995; Dorbath et al., 1996). For the mantle between 200 to 650 km around the slab we took the velocity of the *iasp91* model (Kennett and Engdahl, 1991).

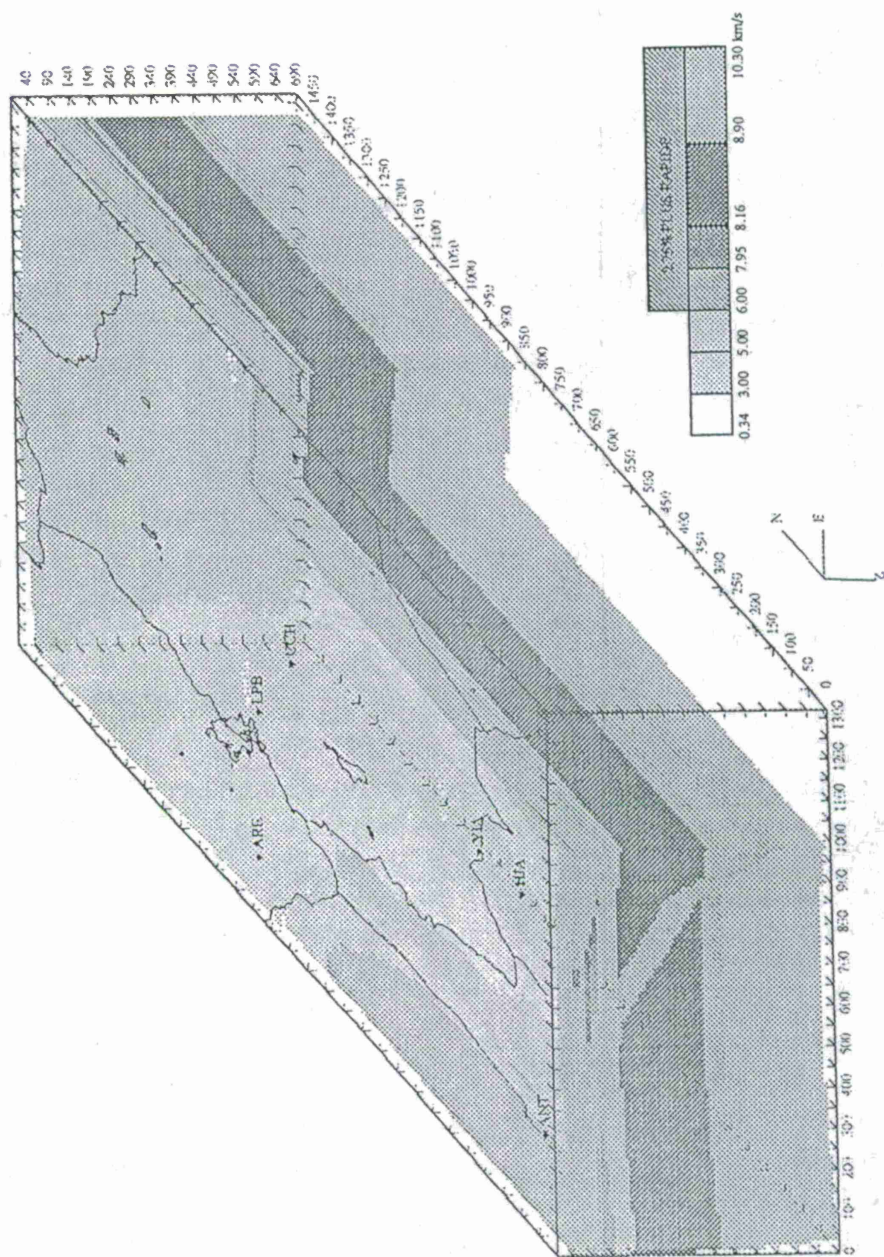


Figure 2. 3-D view inside the heterogeneous velocity model for the Bolivian Andes: the model is composed of 150 x 132 x 69 cubic cells and it takes account the sphericity of the earth: geographic boundaries and some stations are also shown.

Results

We selected 600 events reported by the National Earthquake Information Center (NEIC) with magnitudes $m_b \geq 4.0$ and with various azimuths and depths. The differences of location of NEIC and 3DGRIDLOC are all less than 40 km. Similar differences of location were found between the NEIC locations and those of temporary local arrays in northern Chile (Comte, 1993). The P and S residuals of the 3DGRIDLOC locations are much smaller than those of the NEIC locations (Figure 3).

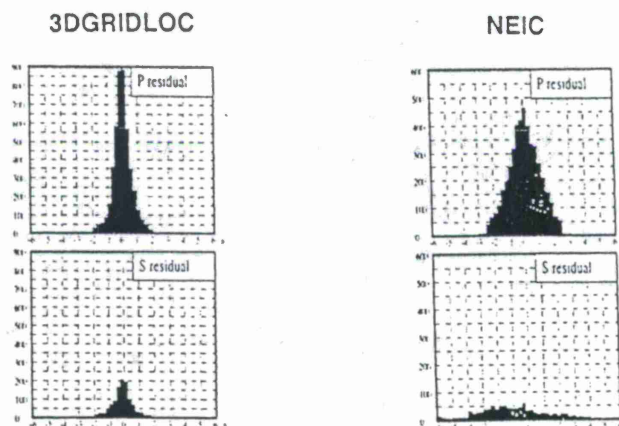


Figure 3. Histograms of P and S residuals from 3DGRIDLOC and NEIC locations.

The recorded crustal seismicity is located in northern Bolivia in the Eastern Cordillera and in the northern Altiplano. A higher concentration of crustal seismicity is located in the Western Cordillera and in the Subandean Ranges near the "Santa Cruz bend" (see Figure 4a). An important part of this seismicity is recorded by the Bolivian seismograph network, but not reported by the international bulletins. Deeper seismicity located below the Western Cordillera in the southern Peru-Chile-Bolivia region at depths from 70 to 150 km is related to subduction zone. Sparser seismicity is located in the region of the Bolivian Andes at depths of from 150 to 325 km; deeper seismicity is located from 550 to 650 km (see Figure 4b).

CONCLUSIONS AND FUTURE PLANS

The preliminary 3-D velocity model seems to be a more realistic approximation to the complex velocity structure of the region of the Bolivian Andes. This model and the 3DGRIDLOC method have allowed us to obtain a more accurate location of more of the seismicity in the region of the Bolivian Andes. Future work will be: 1) to test the 3-D model with more data from Chilean and Peruvian stations; 2) to compare the locations found by the 3DGRIDLOC method with those of the International Data Center; 3) to locate the small events ($M_L < 3$); and 4) to locate quarry blasts in Bolivia.

Acknowledgements

The work in this report has been accomplished with the collaboration of the Laboratoire de Géophysique (LDG) of Paris and of the Institut du Physique du Globe (IPGS) of Strasbourg, France.

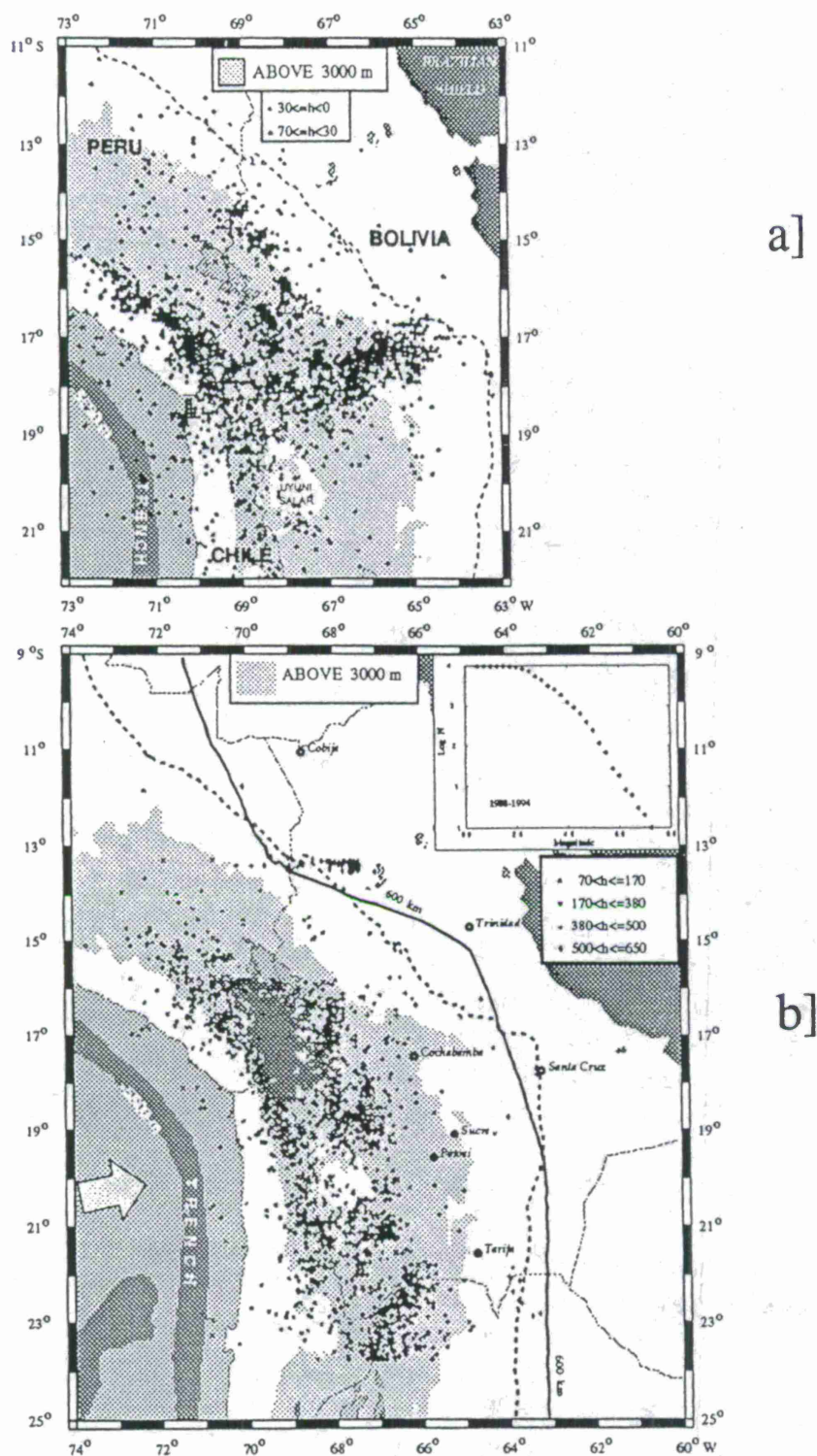


Figure 4. Seismicity map of events recorded by the permanent Bolivian network from June 1988 to November 1994: a) seismicity map for shallow events (less than or equal to 70 km depth); b) seismicity map for deeper events (from 71 to 650 km depth). The magnitude-frequency relationship for all of the recorded events is shown in the upper-right side. The dotted line shows the Andean Cordillera border and the solid line shows the 600 km depth contour of Nazca plate.

REFERENCES

- Ayala, R. and G. Wittlinger, 1996. Seismicity and state of stress in the Central Andes: Bolivian orocline region, in Third ISAG (extended abstracts), St. Malo, France, ORSTOM, pp. 141-144.
- Ayala, R., 1997. Seismotectonique des Andes de Bolivie et rôle de l'Orocline bolivien, *PhD thesis*, Université Louis Pasteur, Strasbourg, France.
- Barazangi, M. and B.L. Isacks, 1976. Spatial distribution of earthquakes and subduction of the Nazca plate beneath South America, *Geology*, **4**, 686-692.
- Cahill, T. and B.L. Isacks, 1992. Seismicity and shape of the subducted Nazca plate, *J. Geophys. Res.*, **97**, 17503-17529.
- Comte, D., 1993. Morfología de la subducción en el Norte de Chile, *PhD thesis*, Universidad Nacional Autónoma de México, México.
- Comte, D., S.W. Roecker and G. Suárez, 1994. Velocity structure in northern Chile: evidence of subducted oceanic crust in the Nazca plate, *Geophys. J. Int.*, **117**, 625-639.
- Cunningham, P.S., S.W. Roecker and D. Hatzfeld, 1986. Three-dimensional P and S wave velocity structures of Southern Peru and their tectonic implications, *J. Geophys. Res.*, **91**, 9517-9532.
- DeMetz, C., R.G. Gordon, D.E. Argus and S. Stein, 1990. Current plate motions, *Geophys. J. Int.*, **101**, 425-478.
- Dorbath, C., 1996. Velocity structure of the Andes of central Peru from locally recorded earthquakes, *Geophys. Res. Lett.*, **23**, 205-208.
- Dorbath, C. and M. Granet, 1996. Local earthquake tomography of the Altiplano and the Eastern Cordillera of northern Bolivia, *Tectonophys.*, **259**, 117-136.
- Dorbath, C., M. Granet, G. Poupinet and C. Martinez, 1993. A teleseismic study of the Altiplano and the Eastern Cordillera in northern Bolivia: new constraints on a lithospheric model, *J. Geophys. Res.*, **98**, 9825-9844.
- Dorbath, C., A. Paul and Lithoscope Andean Group, 1996. Tomography of the Andean Lithosphere at 20°S: Preliminary results of the Lithoscope experiment, *Phys. Earth. planet. Inter.*, (in press).
- Engdahl, E.R., R.D. van der Hilst and J. Berrocal, 1995. Imaging of subducted lithosphere beneath South America, *Geophys. Res. Lett.*, **22**, 2317-2320.
- Geiger, L., 1912. Probability method for the determination of earthquake epicenters from the arrival time only, *Bull. St Louis Univ.*, **8**, 61-71.
- Grange, F., P. Cunningham, J. Gagnepain, D. Hatzfeld, P. Molnar, L. Ocola, A. Rodriguez, S.W. Roecker, J.M. Stock and G. Suarez, 1984. The configuration of the seismic zone and the downgoing slab in southern Peru, *Geophys. Res. Lett.*, **11**, 38-41.
- Kennett, B.L.N. and E.R. Engdahl, 1991. Travel times for global earthquake location and phase association, *Geophys. J. Int.*, **105**, 429-465.
- Klein, F. W., 1978. Hypocenter Location Program - HYPOINVERSE: Users Guide to Versions 1, 2, 3, and 4, *US Geol. Surv. Open File Rep.* **78-694**, 1-113.
- Lavenue, A. and J.L. Mercier, 1991. Evolution du régime tectonique de l'Altiplano et la Cordillère Orientale des Andes de Bolivie du Miocène Supérieur à l'Actuel, un effet des forces de gravité et de forces aux limites, *Geodynamique*, **6**, 21-55.

- Lee, W.H.K. and J.C. Lahr, 1975. HYPO71 (revised): a computer program for determining hypocenter, magnitude and first pattern of local earthquakes, *US Geol. Surv. Open-File Rep.*, **75-311**, 1-116.
- Lindo, R, 1993. Sismotectonique des Andes du Perou Central; Appord des Données Sismologiques de haute precision. PhD thesis, Louis Pasteur University, Strasbourg, France.
- Moser, T.J., T. Van Eck and G. Nolet, 1992. Hypocenter determination in strongly heterogeneous earth models using the shortest path method, *J. Geophys. Res.*, **97**, 6563-6572.
- Nelson, G.D. and J.E. Vidale, 1990. Earthquake locations by 3-D finite difference travel times, *Bull. Seismol. Soc. Am.*, **80**, 395-410.
- Podvin P. and I. Lecomte, 1991. Finite difference computation of travel times in very contrasted velocity models: a massively parallel aproach and its associated tools, *Geophys. J. Int.*, **105**, 271-284.
- Sacks, I. S., 1977. Interrelationships between volcanism, seismicity and anelasticity in western South America, *Tectonophys.*, **37**, 131-139.
- Schmitz, M., 1993. Kollisionsstrukturen in den Zentralen Anden: Ergebnisse refraktionsseismischer Messungen und Modellierung krustaler Deformationen, dissertation, Freie Universität Berlin.
- Tarantola, A. and B. Valette, 1982. Inverse problems = quest for information, *J. Geophys.*, **50**, 159-170.
- Ussami, N., N. Cogo de Sa and E. Cassola, 1993. Gravity map of Brazil. 2. Regional and residual isostatic anomalies and their correlation with major tectonic provinces, *J. Geophys. Res.*, **98**, 2199-2208.
- Vidale, J., 1988. Finite-difference calculation of traveltimes, *Bull. Seism. Soc. Am.*, **78**, 2062-2076.
- Vidale, J., 1990. Finite-difference calculation of traveltimes in three dimensions, *Geophys.*, **55**, 521-526.
- Wigger, P., 1988. Seismicity and crustal structure of the Central Andes, in The Southern Central Andes, H. Bahlburg, C. Breitzkreuz and P. Giese (Editors), *Lecture Notes in Earth Sciences*, **17**, Springer Verlag, 209-229.
- Wittlinger, G., G. Herquel and T. Nakache, 1993. Earthquake location in strongly heterogeneous media, *Geophys. J. Int.*, **115**, 759-777.

SOURCE AND PROPAGATION CHARACTERIZATION FOR NETWORK PERFORMANCE SIMULATIONS IN THE MIDDLE EAST

G. Eli Baker and Terry Barker

Maxwell Technologies, 8888 Balboa Ave, San Diego CA, 92123
(619) 576-7722, FAX (619) 576-7710, eli@maxwell.com

Sponsored by U.S. Department of Energy
Office of Nonproliferation and National Security
Office of Research and Development
Contract no. F19628-95-C-0111

ABSTRACT

Accurate network performance simulation is dependent on accurate characterization of regionalized source and propagation parameters. To improve network performance simulation in the Middle East, we incorporate new and previously determined Middle East seismic propagation and source parameters into the XNICE simulation software (Barker, 1996). The simulations are discussed in Barker and Baker (1997, this volume). This paper concentrates on the determination of source excitations, and on crustal and upper mantle attenuation characteristics. Source excitations predict the \log_{10} (amplitude) that will be observed in a signal from a particular region for a given event magnitude (assuming the propagation parameters are also known.)

We analyze regional phases from eight distinct source areas in and around the Saudi shield, utilizing temporary and permanent IRIS and GEOSCOPE broadband stations, which provide recordings for a range of distances and paths. Wherever possible, the source excitation for each of Pn, Pg, Sn, and Lg, is estimated for each region. A conservative estimate of variations between regional source excitations indicates an expected factor of 15 variation regionally in Lg amplitudes for events of the same magnitude, independent of propagation effects. Where high signal to noise ratio recordings are available for a wide range of frequencies, we determine the frequency dependence of the source excitations. For events in the Zagros, Pn and Sn excitations are frequency independent from 0.6 to 15 Hz. That contrasts with excitations, variously of Pn, Pg, and/or Lg, from the Gulf of Aqaba, the Arabian shield, the Arabian Sea, and eastern Turkey, which decrease with frequency.

Source excitations trade-off with attenuation, which must be determined independently. For the crust we use Q_0 and η values determined from Lg coda (Mitchell, et. al., 1997), with adjustments where indicated by our increased data coverage. Where no other information is available, we use mantle Q_0 values twice those of the overlying crust.

A cluster of events along a transform fault that crosses the Red Sea, along with events on the African side of the Red Sea, present us with an interesting and gradual transition, that we interpret as leakage of shear-wave energy into the mantle from the oceanic crust. The shear-wave energy from events nearest the Saudi shield appears to remain trapped in the crust, arriving at Saudi stations in the Lg phase. For events somewhat further from the Saudi shield, with paths crossing more of the Red Sea, the Lg phase is still observed, but some shear-wave energy arrives as Sn. Recordings at Saudi stations of Red Sea events farthest from the Saudi shield have no Lg, only Sn.

Keywords: Network Identification, Middle East, Source Characterization, Propagation, Lg Blockage, Attenuation

OBJECTIVE:

Network simulation performance is a critical tool for analysis of detection and discrimination capabilities, permitting optimal utilization of resources in support of CTBT monitoring. The precision and accuracy of such simulations depends on the precision and accuracy of the program inputs, namely regional source and propagation characteristics. In support of CTBT monitoring in the Middle East, our objective is to collect and employ the best parameters available, synthesized from previous research results and new analysis presented here.

RESEARCH ACCOMPLISHED:

We have collected, from previous research, and determined, in analysis presented here, seismic source and propagation characteristics for the Middle East. We have incorporated these parameters into Xnice network simulations for the region, results of which are presented in this volume (Barker and Baker, 1997).

We incorporate attenuation information from Mitchell et al (1997) and Xie and Mitchell (1990). Mitchell has provided us with their most up to date estimates of frequency dependent Q in Africa and Eurasia. We have augmented and refined these models where additional data permit.

Our data consist of recordings of events from nine distinct regions on temporary IRIS stations on the Saudi shield (Vernon et. al, 1996) and permanent IRIS and GEOSCOPE stations (figure1).

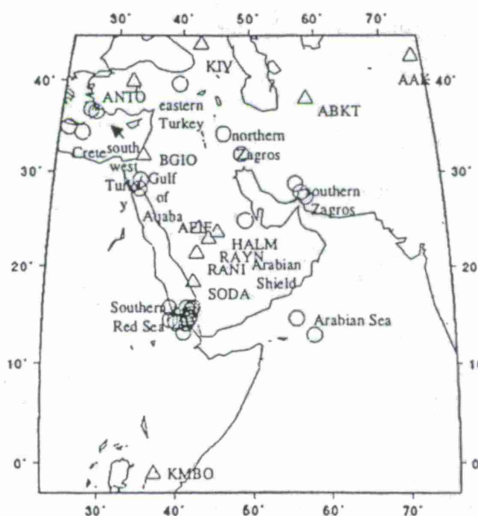


Figure 1: Events (circles) and stations (triangles) used to estimate source and propagation parameters. Distinct source regions are labeled.

Propagation: Lg blockage and Lg vs. Sn propagation

The primary contribution of this work is the determination of source parameters, but we first present observations related to propagation. We compare observations of Lg blockage from this data set with those compiled by previous authors. Figures 2 and 3 indicate paths for which Lg and Sn are, and are not, observed.

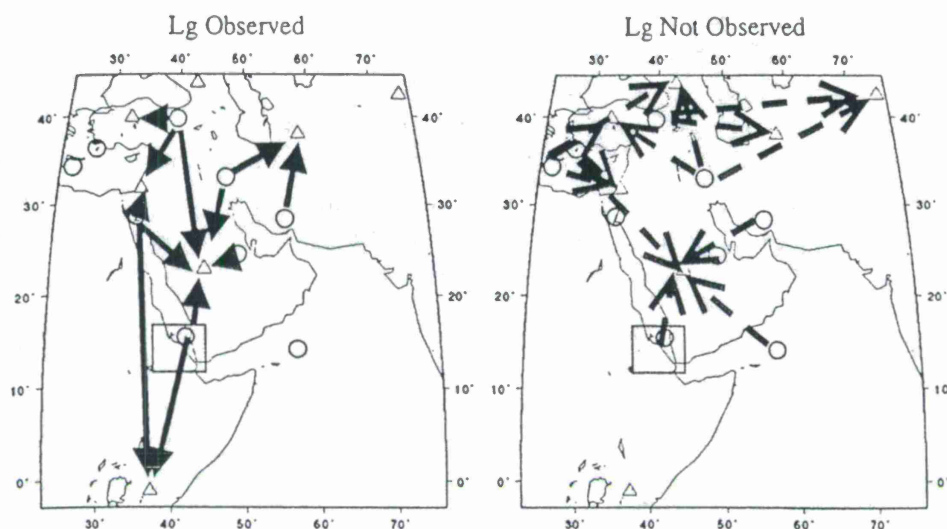


Figure 2: Paths for which Lg is clearly observed (solid lines, left) and paths for which Lg is not observed (dashed lines, right). For clarity a single circle is drawn for each source region. Similarly, one triangle represents the five stations within the Saudi shield. Paths for which we list "Lg not observed" do have clear P arrivals and low noise levels. Even so, blockage is not necessarily implied for each path on the right. Some paths, particularly in the northern part of the map may indicate low crustal Q throughout the entire path lengths. Events from the southern Red Sea region (in box) are drawn with both "Lg observed" and "Lg not observed" for paths to the Saudi shield. A consistent and interesting pattern in this region, which is too fine scale for the maps above, is detailed in figure 4.

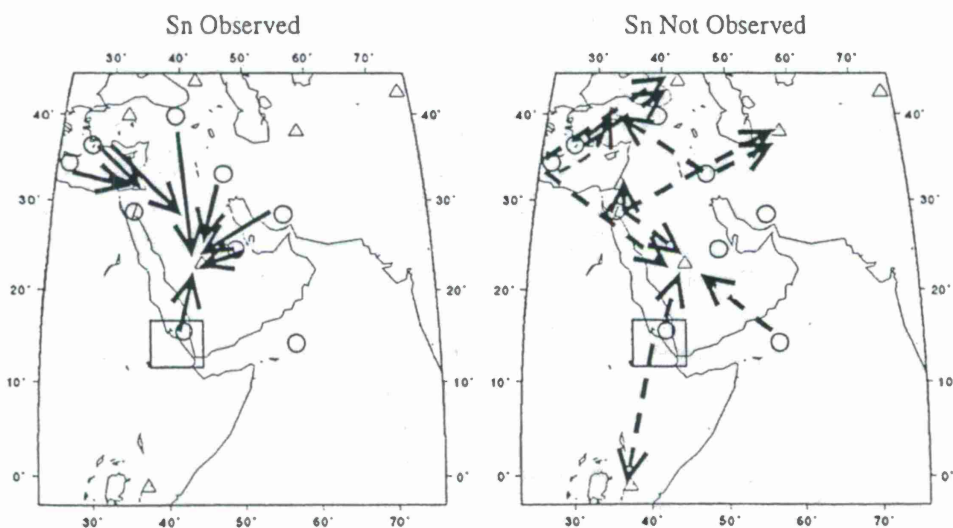


Figure 3: Paths for which Sn is clearly observed (solid lines, left) and paths for which Sn is not observed (dashed lines, right). Again, for details of the southern Red Sea region, see figure 4.

In many regions Lg and Sn are mutually exclusive phases for particular paths. That is the most common case here, although both phases are observed for some paths. In the southern Red Sea (boxed area in figures 2 and 3), we see that whether Lg, Sn, or both, are observed depends on the distance of the event from the shield (figure 4). This highlights the difficulty of parameterizing structurally and tectonically complex regions on the coarse scale necessary for complete global coverage.

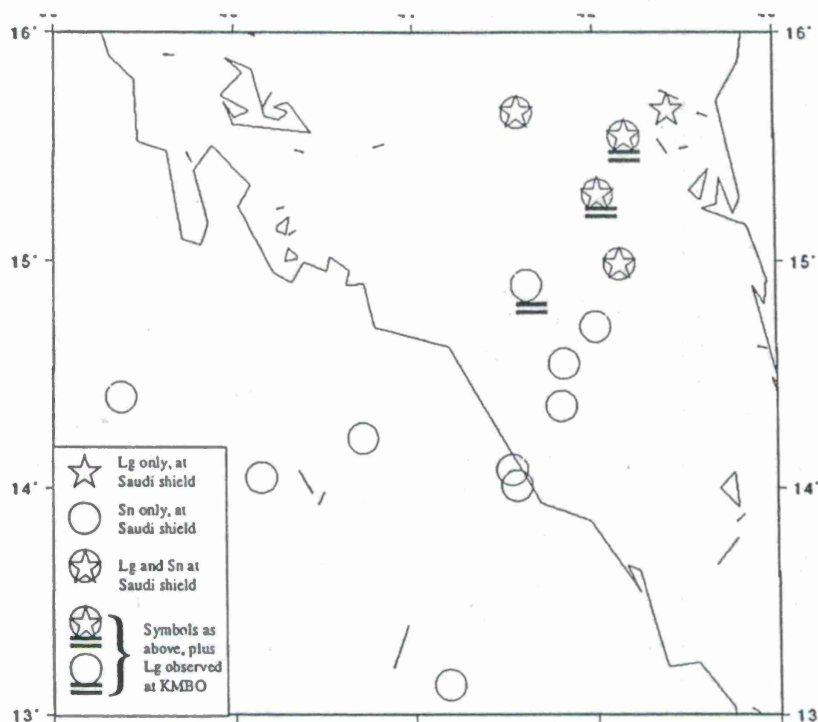


Figure 4: Events occurring within and on the African side of the Red Sea. Lg is observed at Saudi shield stations for those shown as stars, and Sn is observed for those shown as circles. Both phases are observed on the Saudi shield for those shown as stars within a circle. The three doubly underlined events also had Lg phases observed at KMBO, on the African continent. The appearance of Lg vs. Sn on the Saudi shield appears to be a function of distance the shear wave energy must traverse across the oceanic crust of the Red Sea, to stable continental crust. An important future enhancement to Xnice should be the ability to parameterize regions on a variable scale, to enable us to utilize this sort of information.

Both Lg and Sn are observed from events with paths entirely within the Saudi shield, although the passbands in which Lg and Pg are observed have practically no overlap with the passbands in which Sn and Pn are observed (figure 5). This underscores a point that is important to event identification under a CTBT. *Which P-phase and which S-phase are being used for discrimination must be considered.* Simply using whichever phase is observed or largest (i.e. Pn vs. Pg and Sn vs. Lg) can lead to errors in discrimination, particularly with spectral discriminants. For example, for recordings at

approximately 10^0 we commonly observe either Pn and Lg, which have very different spectra, or Pn and Sn, which usually have similar spectra, as illustrated in figure 5.

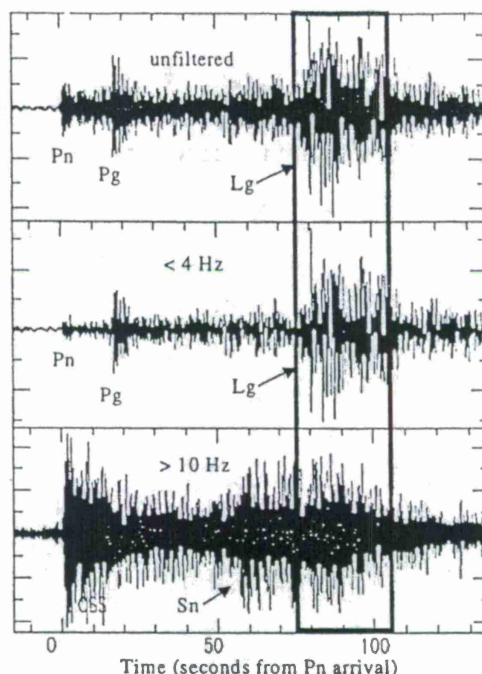


Figure 5: Seismogram of an event on the Saudi shield recorded at HALM (a Saudi shield station). Pn, Pg, and Lg (group velocity window is delineated by vertical lines) are clear in the top (unfiltered) and middle (lowpass filtered below 4 Hz) traces. The bottom trace (highpass filtered above 10 Hz) show Pn and Sn dominating at higher frequencies.

Rodgers et al (1997) examined Lg and Sn propagation for paths in the northern part of the maps in figures 1-3. Their extensive study, particularly in Iran, but also in propagation to ANTO and KIV, confirms and augments our observations, and better constrains propagation effects so that we can effectively estimate source excitations.

Source Excitations for Pn, Pg, Sn, and Lg:

We have used the concept of source excitations (Barker, 1996) to parameterize source regions in a manner useful for network performance evaluation. A source excitation is the factor that relates magnitude to amplitude, relative to some reference location. That is, the amplitude of a given phase should simply equal $\log_{10}(m_b)$ plus a constant, given appropriate corrections for geometric spreading, attenuation, and source spectral shape. Amplitudes of any particular phase, however, vary depending on the source region. Likely causes for this include variations in focal mechanism and depth, and in near source scattering and attenuation characteristics. The source excitation thus becomes a catchall factor for describing amplitude variations. Because they cover such a

multitude of causes for amplitude variation, which are not likely to be well characterized globally in the near future, physical characteristics of the source and source region cannot be directly inferred from the source excitations. On the other hand, this concept permits a very practical statistical characterization of each source region, permitting predictions of amplitude at each station for each phase, given the IMS m_b . We present next the details of the source excitation estimation, the assumptions made, and the results obtained.

We use IMS body wave magnitudes, which have been determined from maximum P-wave amplitudes recorded at greater than 20 degrees, with the peak typically between 1 and 2 Hz. We assume these magnitudes accurately reflect the amount of energy released from the source.

First we define a reference Lg amplitude that is tied to the IMS m_b . The path for the magnitude 3.68 event on January 7, 1996 is entirely within the Arabian Shield, and has a maximum Lg displacement of 117 nm at RAYN, the permanent IRIS station at a distance of 3.62 degrees. For comparison of amplitudes we scale all observations to 10^0 distance and m_b of 5.0. This scaling is done according to

$$\log_{10}(A_{mb=5.0}(10^0)) = 5.0 - mb + \log_{10}(A_{obs}(\Delta^0)) + \frac{5}{6} \log_{10}\left(A_{obs}\left(\frac{\Delta^0}{10^0}\right)\right) + 0.4343 \left(\frac{\pi f^{1-\eta}}{U_g Q}\right) 11.19(\Delta^0 - 10^0).$$

Δ^0 is distance, U_g is group velocity (3.5 km/sec for Lg), Q_0 is the quality factor for attenuation, and η describes the frequency dependence of attenuation. We use $Q_0=400$ and $\eta = 0.5$ for the Saudi Shield. For this calculation we use $f=1.4$ Hz, as this is the center of the measurement passband used. We employ the same filter and passband for this reference Lg amplitude measurement as is used for IMS amplitude measurements for m_b estimation. The fourth term on the right represents geometric spreading. The 5/6 comes from a value of 1/2 for any regional phase which propagates in 2 dimensions (along a surface) plus an additional 1/3 for Lg, due to the definition of its peak amplitude as an Airy phase (Nuttli, 1973). The reference event so scaled should have a \log_{10} amplitude of $\log_{10}(A(10^0))=2.20$, and source excitations for all other passbands and phases are relative to this value.

To estimate the predicted amplitude at the source, we must also correct for the shape of the source spectra. Because the m_b is based on amplitude at approximately 1.4 Hz, the amplitude predicted in the equation above is also valid for approximately 1.4 Hz. To estimate source excitation at other frequencies, we must account for the relative source spectral amplitudes at 1.4 Hz to the amplitudes at other frequencies of interest. Due to the source finiteness, high frequencies have lower amplitude in the far field. The Brune model (Brune, 1970) predicts decay in spectral amplitudes above the corner frequency, f_c , proportional to $\frac{1}{\omega^2}$, as follows: $\Omega(\omega) \propto \frac{f_c^2}{f_c^2 + \omega^2}$. We predict corner frequencies using the

dynamic modeling results of Madariaga (1976), i.e. $f_c = 0.21 \frac{\beta}{a}$ (or $f_c = 0.32 \frac{\beta}{a}$ for P-waves), as this is consistent with the most accurate observational studies of the relationship between magnitude and corner frequency (e.g. Abercrombie, 1996). β is the

shear wave velocity, and a is the characteristic dimension of the fault, defined by $a = \left(0.44 \frac{M_0}{\sigma} \right)^{1/3}$, where M_0 is seismic moment, and σ is stress drop.

We assume $\sigma=100$ bars throughout. Although some studies have indicated a dependence of stress drop on moment for events smaller than $m_b=4.0$, observations made at 2.5 km depth in crystalline granite conclusively demonstrate a constant stress drop down to $M_L=-1.0$ (Abercrombie, 1996). To estimate the moment, we use the equation $\log(M_0)=1.5M_w+16.1$ of Hanks and Kanamori (1979), where M_w may be M_L , m_b , or M_s , depending on event size. This choice is consistent with the moment magnitude relation obtained for Israeli earthquakes by Shapira and Hofstetter (1993), of $\log(M_0)=(1.5\pm 0.1)M_L+(16.0\pm 0.4)$.

For each phase we estimate source excitations for the passbands measured by the IDC, which are 0.8-2 Hz, 2-4 Hz, 6-8 Hz, and 8-10 Hz. For greater accuracy we also estimate phase amplitudes at 0.3-0.6 Hz, 1-3 Hz, 3-5 Hz, 5-7 Hz, 7-9 Hz, 10-12 Hz, 11-13 Hz, 12-14 Hz, 13-15 Hz, and 14-16 Hz. The measurements are of maximum amplitude for each phase and for noise windows before each phase, with windows defined according to the IDC protocol. We were able to make the following minor modifications to the IDC definitions for this study, as individual inspection of records permits us to avoid misassociation errors. We use longer pre-phase windows (10 seconds rather than 3), ending earlier than the predicted phase arrival time. This provides more stable and conservative noise measurements and avoids erroneously large noise measurements due to early arriving phases. The IDC Pg window appears to end very early relative to observed Pg in the Middle East, so we use a Pg window ending at 5.6 km/s group velocity (the IDC definition is 5.8 km/sec). Further, the Sn window is taken to extend from the predicted arrival time until 3.7 km/s group velocity, as largest Sn amplitudes often occur more than 20 seconds after the predicted arrival time (which is the IDC definition of the Sn end time). Only measurements with a signal to noise ratio (S/N) greater than 3 were used. Because the behavior of the spectra is complicated near the corner frequency, we use source excitation estimates from passbands as far above and below the corner frequency as possible to define an empirical source excitation function, $S(f)=S_0+S_1\cdot f$, for each region. $S(f)$ is the \log_{10} of the excitation of energy for each phase relative to the reference value.

Regions:

In this section we describe the results of source excitation estimation for each region.

Saudi Shield: The excitations here are determined from the reference event, which by design will have an Lg excitation of $\log_{10}(1)=0.0$ at 1.4 Hz. That is, the multiplicative correction factor for m_b -based predicted amplitudes will be 1.0. Sn was not observed for this event at sufficiently high S/N to permit source excitation estimation. For Pn, the upper mantle attenuation parameters were set to set $Q_0=1000$ and $\eta=0.9$, as described in the southern Zagros discussion.

Arabian Sea: Despite low noise levels, no Sn was observed from these events, so Sn excitation, S_{Sn} , was set to $S_{Pn}-0.7$, where S_{Pn} is the Pn source excitation. This provides that the Sn amplitude will be 1/5 of the Pn amplitude, assuming similar attenuation.

Southern Zagros: These events have large Pn and Sn phases out to very high frequency. Paths to the Saudi shield cross the sedimentary basin of the Persian Gulf, which appears to block both Lg and Pg, as neither phase is observed in the passbands examined. As was done for Sn from the Arabian Sea, we assume the Pg source excitation is equal to $S_{Pn}-0.7$. This could be an underestimate, but we note that Pg is also not observed for paths northward from this area or the northern Zagros, whereas Lg is. For the frequency bands of interest, we use the same Lg excitation as found for the northern Zagros, because of the similarities between the regions, including comparable Pn and Sn excitations.

Using $\eta=0.5$ for the mantle, even with $Q_0=1000$, would result in a factor of 20 increase in Pn and Sn source excitations from 1.0 to 15 Hz for these events. Although a precise physical interpretation of source excitations is unsettled, we can see no simple explanation that explains such an increase with frequency. Thus we choose a high upper mantle Q_0 of 1000, and $\eta=0.9$, comparable to values in eastern North America (Nuttli, 1973).

The variance of Pn and Sn source excitations increases at the lowest frequencies, presumably because these are large events with predicted corner frequencies (where the source spectral shape becomes complicated) ranging from 0.34 to 1.17 Hz. The median source excitations however are nearly flat across all frequencies. For purposes of prediction, we therefore assume a flat source excitation (i.e. $S_1=0$).

A low frequency Lg phase begins to emerge from the noise at ~ 3.2 km/s at 4 seconds period and becomes more prominent at longer period. We use this observation, and assume most attenuation takes place in the Persian Gulf, to infer an approximate Lg Q_0 of 30 in the Persian Gulf.

Northern Zagros (Iran-Iraq border): Pn for these events is well recorded out to 15 Hz (the highest frequency measured), with no indication of frequency dependence of excitation, and we calculate the same excitation of -0.55 for this region as we found for the southern Zagros. Also, as in the southern Zagros, we find an Sn excitation slightly higher than that of Pn.

The Pg and Lg paths for these events to the Saudi stations cross a deep sedimentary basin west of the Zagros, which may significantly diminish crustal phase amplitudes and bias the source excitation estimates downward. Pg is not even observed for these events. We do use a lower Q_0 of 250, as an average of values along the path, as Mitchell (1997) found an average Q_0 of 200 north of the Arabian shield, and Lg Q is likely much lower still in the sedimentary basin. The low S/N of the measurements, and the low frequency content, which coincides with the events' corner frequencies, makes Lg excitation difficult to measure. The Lg observed is quite late, so we use a group velocity of 3.2 km/sec, rather than the typical value of 3.5 km/sec. Only the lowest frequencies of Lg were observed, so no estimate of frequency dependence could be made. We do find an excitation of 0.2 at 0.6 Hz, corresponding to amplitudes approximately 1.6 times larger than the reference value. This is consistent with the observation of Rodgers et al (1997) of reasonable Lg amplitudes at the Iranian Long Period Array and at ABKT.

Eastern Turkey: Pn and Lg are observed from this event. There appears to be some decrease in Pn source excitation with frequency, although interpretation is difficult due to the low corner frequency of this $m_b=4.9$ event ($f_c=1.1$). Lg is very prominent at lower frequencies. Pn, Sn, and Lg amplitudes, corrected for propagation, are much greater in the Saudi shield than elsewhere. This could be due to a number of causes, and more events with paths crossing this region will be analyzed.

Southwest Turkish Coast: Only the mantle phases are observed from these events, and those only at lower frequencies. These provide a tentative indication of frequency dependence of excitation, but cover too small of a range to be conclusive. These events appear to occur just offshore, but could be on the shelf. As we have no information about Lg, except that it is not observed, we will for now assume a somewhat smaller Lg excitation, as is done for Pg (as described in the southern Zagros section above).

Crete: Although there is a hint of frequency dependence in the Pn measurements, it is not strong enough to use, and we use a constant Pn excitation of -0.4 . Sn is only well recorded at BGIO. No Lg or Pg phases are observed.

Gulf of Aqaba: All phases but the rarely observed S_N for these 3 events indicate some frequency dependence. The variance of Pn excitations is high, but a moderate slope of excitation with frequency is apparent. As the data at higher frequencies are fewer, and lower signal to noise level, we purposely underestimate the slope, thus splitting the difference between choosing a constant vs. choosing frequency dependence. This is the case with much of the data, and we take the conservative approach in all regions, of moderating the slope, to avoid predicting erroneous extreme values.

Southern Red Sea: These events present an interesting set of observations, as illustrated in figure 4. Events within the Red Sea appear to be located on a transform fault, such as discussed in El-Isa and Shanti (1989). As the source excitation is currently determined for each $5^\circ \times 5^\circ$ region, we use an average of all the values.

Region	Pn excitation	Pg excitation	Sn excitation	Lg excitation
SW Turkey Coast	0.0	-0.7*	0.0	-0.7*
Crete	-0.40	-1.1*	0.08	-1.1*
Gulf of Aqaba	$-0.50-0.05 \cdot f$	$0.53-0.17 \cdot f$	0.0	$1.6-0.36 \cdot f$
southern Red Sea	-0.8	-1.5*	-0.3	0.2
Arabian Sea	$-0.29-0.10 \cdot f$	-1.09*	-1.09*	-2.0*
Saudi Shield	-0.64	$-0.11-0.13 \cdot f$	-1.34*	$0.38-0.27 \cdot f$
southern Zagros	-0.55	-1.25*	-0.31	0.2*
northern Zagros	-0.55	-1.25*	-0.46	0.2
eastern Turkey	$0.09-0.17 \cdot f$	$-0.78 \cdot f^*$	$0.11-0.17 \cdot f^*$	1.3

Table 1: Regionalized source excitations. Asterisks identify values assumed for phases not observed. These are assumed to be $S_{Pn}-0.7$, unless otherwise constrained, as discussed in the text.

CONCLUSIONS AND RECOMMENDATIONS:

We have assembled attenuation and Lg blockage parameters for the Middle East. For the purpose of network simulation we have extended and refined estimates from previous work using available data from IRIS and GEOSCOPE stations. Using them, we have determined a self-consistent parameterization of source characteristics. Use of these results in the Xnice network performance simulation software improves the accuracy of network detection and discrimination assessment in the Middle East.

Future work should include:

- 1) the incorporation of results of regional crustal and upper mantle velocity modeling studies,
- 2) similar analyses of new data sets in order to expand the region characterized (both into northern Africa and further north and east) and to improve estimates of variance within each region, and
- 3) characterization of a completely new region of interest.

BIBLIOGRAPHY:

- Abercrombie, Rachel E., 1995, Earthquake source scaling relationships from -1 to 5 ML using seismograms recorded at 2.5-km depth, *JGR*, **100**, pp. 24,015-24,036
- Barker, T.G., 1996, Xnice: A system for assessing network identification performance, *Phillips Laboratory Technical Report* PL-TR-96-2087
- Brune, James N., 1970, Tectonic stress and the spectra of seismic shear waves from earthquakes, *J. Geophys. Res.*, **75**, pp. 4997-5009
- El-Isa, Z.H. and A. Al Shanti, 1989, Seismicity and tectonics of the Red Sea and western Arabia, *Geophys. J. Intl.*, **97**, pp. 449-457
- Hanks, T. C. and Kanamori, H., 1979, A moment magnitude scale, *J. Geophys. Res.*, **84**, pp. 2348-2350
- Madariaga, R., 1976, Dynamics of an expanding circular fault, *B.S.S.A.*, **66**, pp. 639-666
- Mitchell, Brian, Y. Pan, and J. Xie, 1997, Lg coda Q variation across Eurasia and its relation to continental evolution, *manuscript submitted for publication*
- Nuttli, O., 1973, Seismic wave attenuation and magnitude relations for eastern North America, *J. Geophys. Res.*, **78**, pp. 876-885
- Rodgers, Arthur, J. Ni, and T. Hearn, 1997, Propagation characteristics of short-period Sn and Lg in the Middle East, *B.S.S.A.*, **87**, pp. 396-413
- Shapira, A., and A. Hofstetter, 1993, Source parameters and scaling relationships of earthquakes in Israel, *Tectonophysics*, **217**, pp. 217-226
- Vernon, F., R. Mellors, J. Berger, A. M. Al-Amri, and J. Zollweg, 1996, Initial results from the deployment of broadband seismometers in the Saudi Arabian shield, *Proceedings of the 18th Annual Seismic Research Symposium on Monitoring a Comprehensive Test Ban Treaty*, pp. 108-117
- Xie, Jiakang, and B. Mitchell, 1990, A back-projection method for imaging large-scale lateral variations of Lg coda Q with application to continental Africa, *Geophys. J. Intl.*, **100**, pp. 161-181

CAPABILITY MODELING OF THE PROPOSED INTERNATIONAL MONITORING SYSTEM 60-STATION INFRASONIC NETWORK

Dr. Dean Clauter and Dr. Robert Blandford
Air Force Technical Applications Center (AFTAC)

sponsored by Air Force Technical Applications Center

ABSTRACT

We have modeled the detection and location capability of the International Monitoring System (IMS) proposed 60-station infrasonic network using a statistical model which assumes a log normal distribution of signal and noise. Model inputs were determined empirically from infrasonic data of US nuclear tests. Amplitude as a function of source distance was determined after normalizing the amplitude by the square root of the yield. An empirical relationship was derived for the background noise as a function of wind speed. Modeling results indicate that the proposed 60-station international network with 4-element arrays will achieve detection capabilities for two stations at the 90% confidence level between 0.1 kt over land areas and 0.7 kt over ocean areas. Location uncertainties are based on empirically determined azimuth and arrival time errors. The location radius of uncertainty circle at the 90% confidence level ranges from 50 km over land to 150 km over the southern ocean areas.

Keywords: Infrasonic, Infrasound, detection and location modeling

Objective

AFTAC had an infrasonic nuclear monitoring mission until 1974. Currently, the mission is being reestablished by the international community. For support to the United States delegation at the Comprehensive Test Ban Treaty (CTBT) talks in Geneva, we modeled the detection thresholds and the location uncertainty of the proposed 60-station international infrasonic network consisting of 4-element arrays. We used actual data from nuclear tests of known yields, origin times, and locations recorded at historical infrasonic stations and included these as empirical inputs to the modeling program. We have three objectives for this presentation. Our first objective is to describe our method and show our modeled detection and location capability for the 60-station infrasonic network. Our second objective is to demonstrate that both azimuth and arrival times can be used to reduce the area of the location uncertainty ellipse. Our third objective is to convey to the research community the additional work that we anticipate is needed to improve location methods in order to meet international expectations.

Research Accomplished

The model for signal detection thresholds model was first developed for the determination of seismic detection and location capabilities (Serenio, 1990). The model assumes a log normal distribution of signals and noise amplitudes. The probability of detection is given by the expression:

$$P_{ijk} = R_i \times \Phi \left[\frac{\log S_{ijk} - \log N_{ijk} - \log SNR_{ijk}}{(\sigma_{S_{ijk}}^2 + \sigma_{N_{ijk}}^2)^{1/2}} \right]$$

where

P_{ijk} is the probability of detection at the i th station for the j th epicenter and the k th event.

R_i is the reliability of the station i , assumed to be 95%.

S_{ijk} is the signal amplitude. This number is a function of distance and was empirically determined and will be shown in the first figure.

N_{ijk} is the station noise amplitude, for which we developed an empirical relationship between station noise and wind speed. We assumed that for 4-element arrays, we can also reduce the wind noise for a single sensor by a factor of 2.

SNR_{ijk} refers to the signal-to-noise ratio expected for a detection. This number is 1.5, based on empirical experience.

$\sigma_{S_{ijk}}$ refers to the log standard deviation of the signal. This number was empirically determined to be 0.3 log units. We used this number for all station-event pairs.

σ_{Nijk} to the log standard deviation of the noise background. This number was empirically determined to be about 0.4 log units for a number of our stations. We used this number for all stations.

Φ is the probability density function.

In Figure 1, we show our empirically determined amplitude distance relationship. The horizontal axis is in kilometers, and the vertical axis is in microbars. The black crosses are nuclear events from Nevada Test Site (NTS) shots, and the Dominick series of tests in the Pacific. The X's are ammonia nitrate and fuel oil (ANFO) explosions, which had their size corrected for the equivalent nuclear energy. The amplitudes observed were scaled to 1 kt by square root scaling of the yield. Shots at the surface were multiplied by a factor of 2 in yield to account for the surface reflection. In addition, amplitude corrections were made for the wind direction for the ANFO shots, but not the others. A least squares scaling was done on the events which give the relationship between pressure and range given at the bottom of the slide. From the scatter, a log signal deviation of 0.28 was determined of the individual points from the best fitting straight line. This is thought to be due in large part to the variation in the upper level winds.

We determined the mean wind speed in meters per second on an annual and monthly basis from meteorological stations adjacent to our old infrasonic stations. There was a period of 36 months for which we have data of background noise measurements made four times per day at each sensor. The arrays had Daniels pipes to suppress noise. We took those noise levels and plotted them versus mean annual wind speed in meters per second, taken at the standard meteorological height of 10 meters. The empirical relationship obtained is plotted in Figure 2. The circles represent yearly averages. In order to obtain the extremes, we looked at particularly calm or windy months and plotted the noise values versus the monthly means. One observation from this graph is that the noise rarely goes below about 0.3 microbars. This level must represent the zero-wind background noise levels which are presumably usually due to propagating infrasound signals from distant storms. Note also that the noise varies quadratically with speed. High wind speeds along with few land areas contribute to the problem in the southern ocean areas of finding suitably spaced sites. In these areas the arrays may have to be expanded to 16 elements to achieve the required detection and location thresholds. In the modeling, meteorological stations near proposed sites or other data were used to estimate the typical wind speed at a site and the derived empirical relationship between wind speed and noise was used to model the noise. Other effects besides wind speed contribute to wind noise. These included the vegetation and topography of the sites. These differences contribute to the scatter of the data points along the best fitting empirical relationship.

Based on the model and empirical data described above, we show our detection capability for the proposed international 60-station network in Figure 3. The detection capability is modeled for detection by two stations at the 90% confidence level. The detection contours are in Kilotons (KT). Over land areas the network will have a detection threshold considerably below 1 KT, and only approaching 1 KT in the remote ocean areas. The objective of the international community is to be at or below 1 KT worldwide.

In addition to modeling the detection thresholds, the location uncertainty was modeled. Inputs required for determining the location uncertainty in addition to the probability of detection are the standard deviation in the velocity and azimuth. Figure 4 shows the azimuth uncertainty for Dominic and NTS events as a function of distance. From these data, a standard deviation of 1.8 degrees was used in the modeling for events less than 27 degrees distant from the event. For events between 27 and 35 degrees, linear interpolation was used to a value of 7 at 35 degrees; between 35 and 91 degrees, 12.2 was used; and 27.5 was used for stations at greater distances from the event. These values could be reduced if the conditions of the upper level winds are known.

Figure 5 is a graph of the mean wind speed as a function of distance from the Novaya Zemlya test site to our infrasonic stations at the distances indicated. The average standard deviation from this test site is 5.17 meters per second which represents a velocity error of 1.7%. This is probably the best one can do for a calibrated test site where station bias has been removed without independent meteorological information.

In Figure 6 shown is the radius of uncertainty circle for the 60-station network where arrival time is not considered in the solution. The errors over land range from 50 - 150 kilometers, whereas over water they exceed 1000 kilometers.

In Figure 7 we have assumed a 5% uncertainty in the arrival time and factored it into the uncertainty estimate for the uncertainty circle. Note that we have reduced our error considerably for location.

If we assume a 2% uncertainty in velocity, we get an uncertainty radius of around 100 kilometers over most ocean areas and, in the worst case, 225 kilometers as shown in Figure 8.

We have taken the worst case in the southern ocean areas and shown in Figure 9 that when the velocity uncertainty falls beneath 10%, there is a significant drop in the radius of uncertainty circle. The international community's goal is 100 kilometers or less for location uncertainty everywhere. Some array sites may be supplemented by more than 4-element arrays to help meet this goal.

Conclusions and Recommendations

1. The detection threshold for the 60-station, 4-element array international infrasonic network at the 90% level for two stations to detect a signal is below 1 KT.
2. Location uncertainty can be reduced considerably using both arrival times and azimuth of incoming signals.
3. Location uncertainties with a 5% velocity uncertainty vary from approximately 50 - 100 kilometers over land areas and from 200 - 300 kilometers over ocean areas for 1 KT events. With satellite observations, both azimuth and velocity errors may be significantly reduced, giving a more precise event location.

4. Future research will be necessary to meet the goals for location accuracy of events required by the international community. Since there are several infrasonic phases that all travel at different velocities, one must identify the detected phase arrival times before they can be used to constrain location. This is not a simple procedure since not all phases are identified with a particular event. The event may have to be located first with azimuth information, and this information used to identify the phase in a second iteration. In addition, corrections for azimuth and velocity bias may be possible by knowing the velocity of the upper level winds with the Upper Atmospheric Research Satellite and other satellites. These winds have large standard deviations so that a dynamic model will have to be developed.

References

Sereno, Thomas J. Jr., *Simulation of the Detection and Location Capability of Regional Seismic Networks in the Soviet Union*, SAIC technical report 91/1061, March 1, 1991.

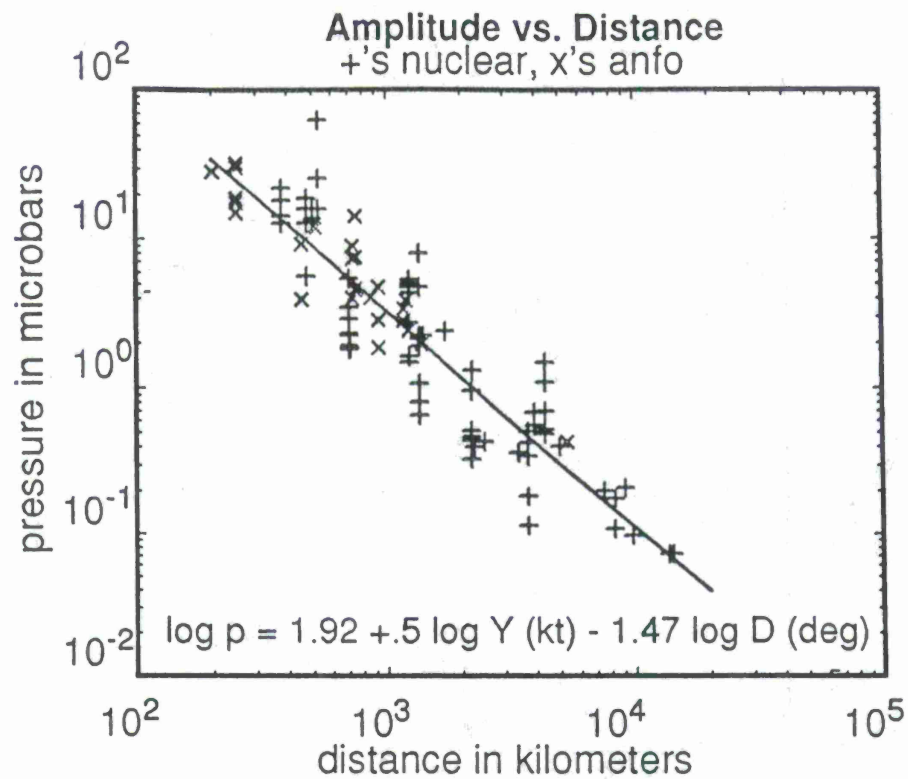


Figure 1. Amplitude versus distance relationship for infrasonic waves based on nuclear tests and ANFO data.

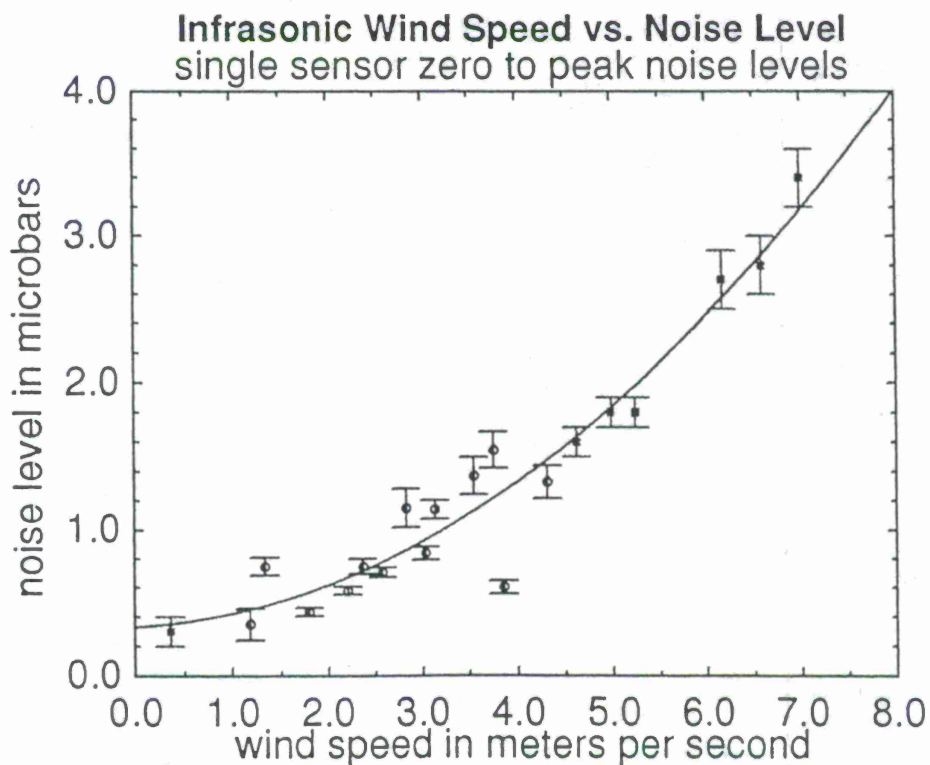


Figure 2. Model for wind speed versus noise level based on infrasonic and meteorological data; circles yearly, squares monthly averages

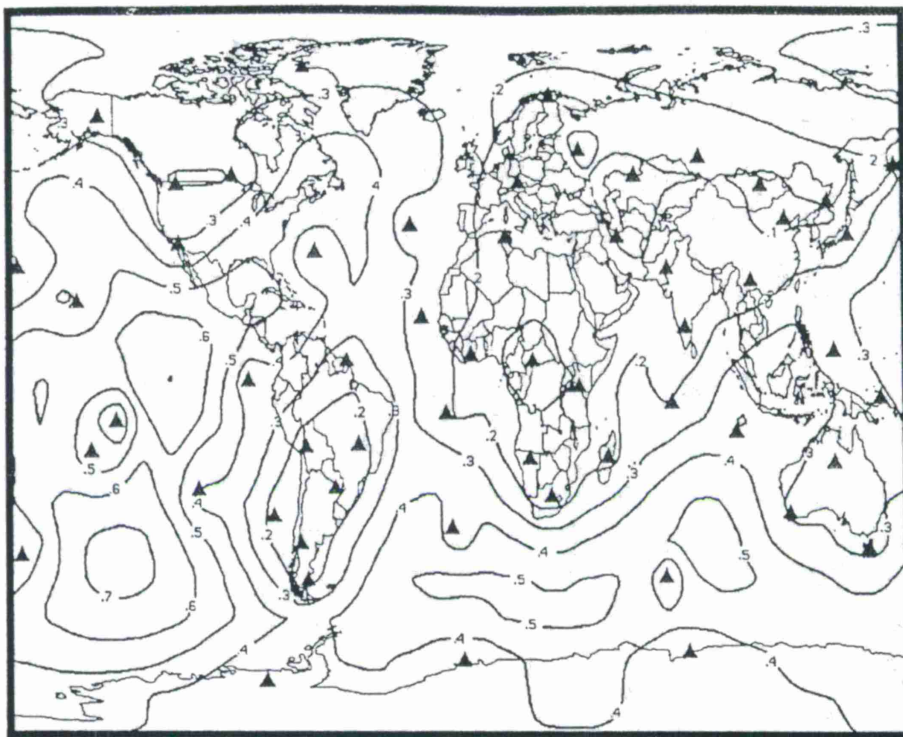


Figure 3. Detection capability at the 90% confidence level for two stations for the 60-station infrasonic network with 0.1 KT contours.

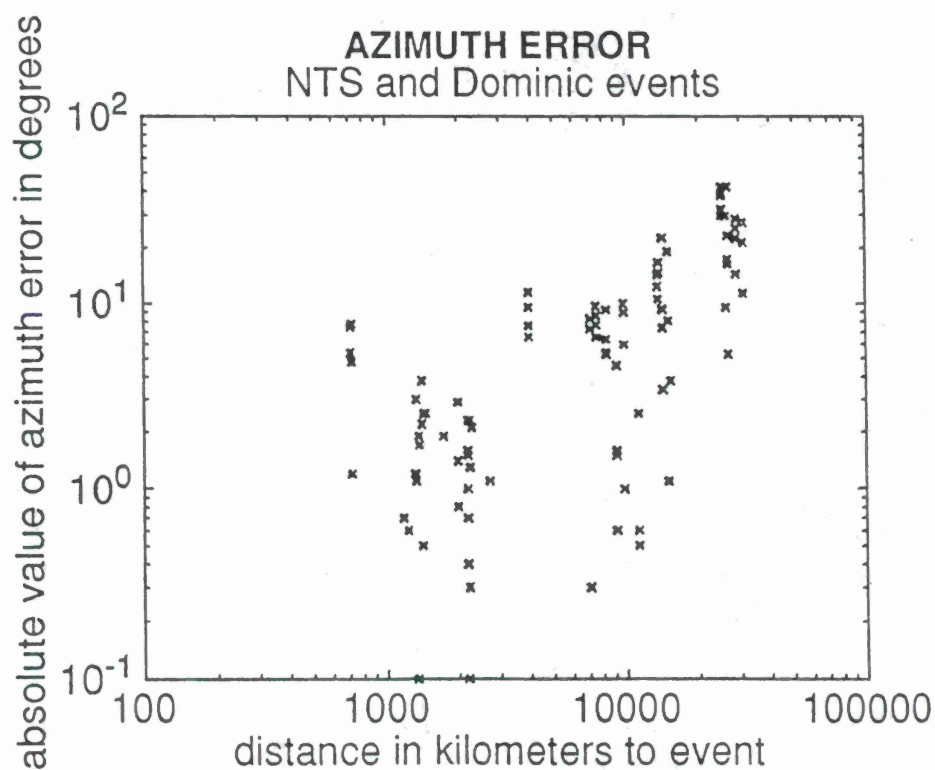


Figure 4. Azimuth error as a function of distance from the events

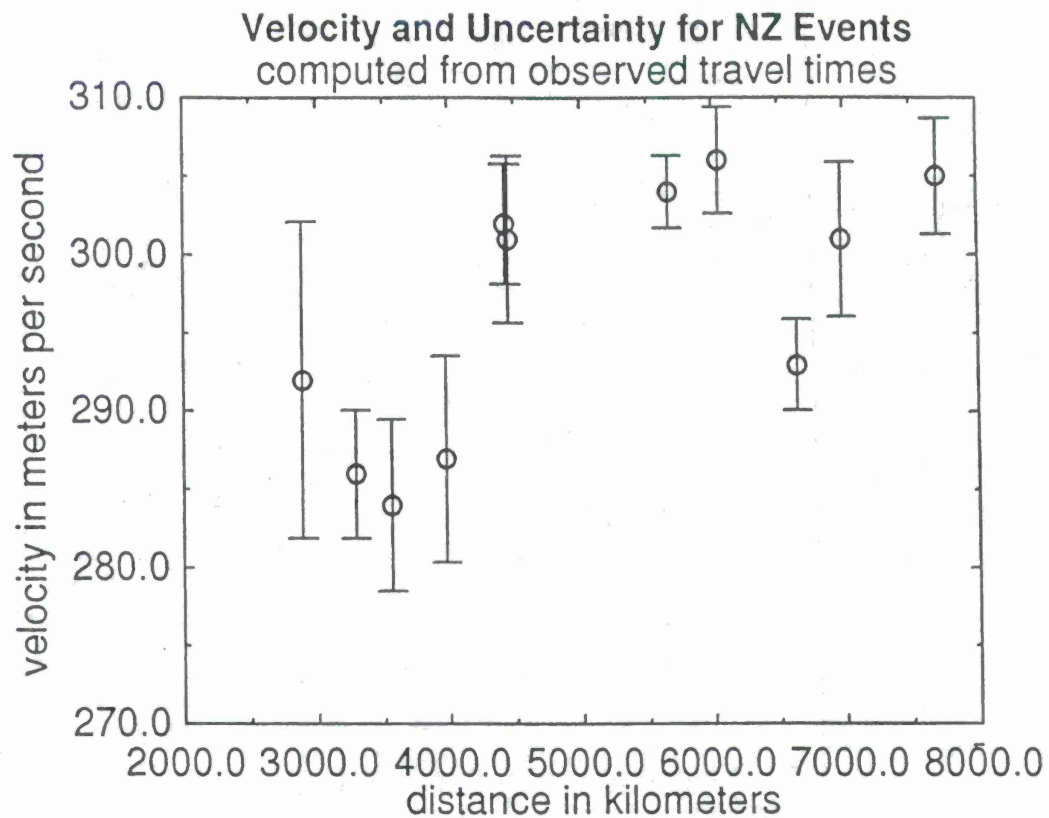


Figure 5. Velocity and velocity uncertainty for events from the Novaya Zemlya test site recorded by the Dawn Star (AFTAC) infrasonic network.

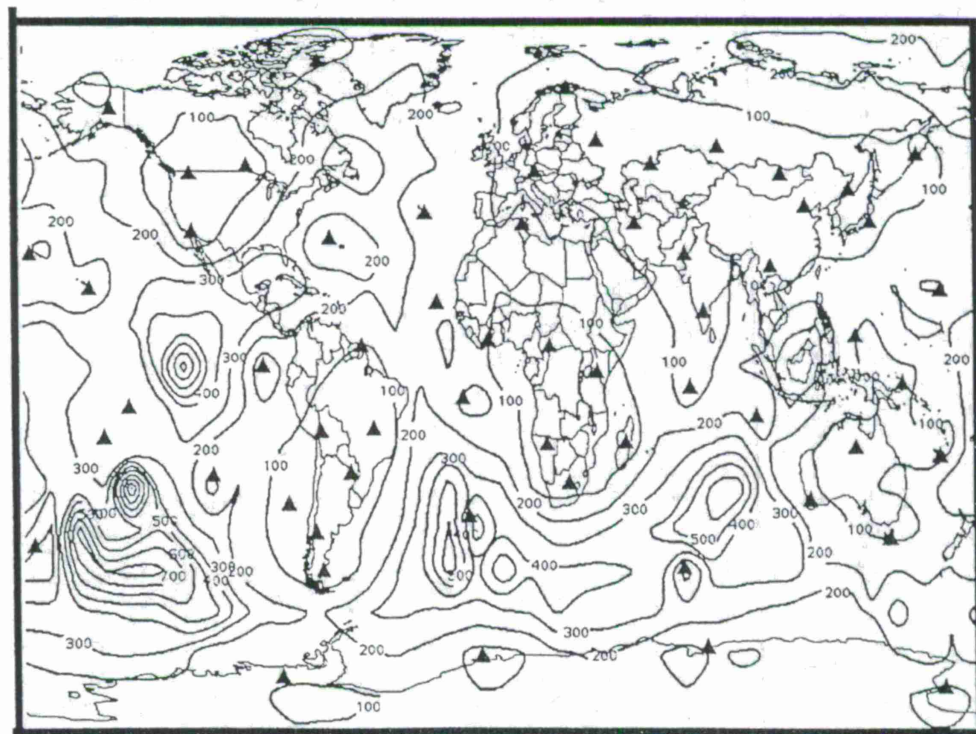


Figure 6. Contours of radius of uncertainty circle (kilometers) for 100% velocity uncertainty, 1 Kiloton sources.

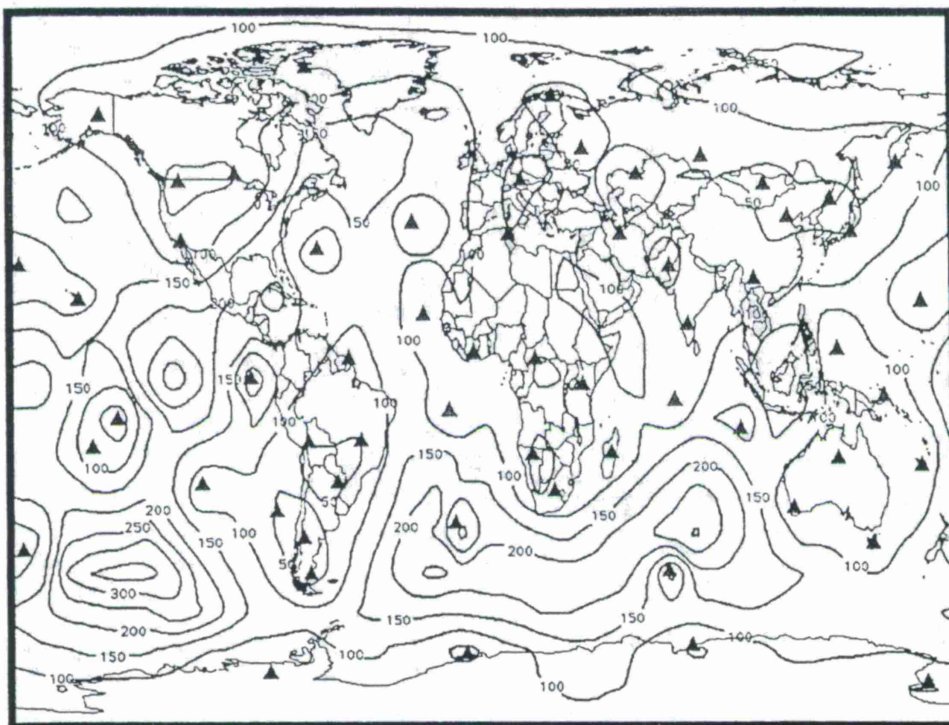


Figure 7. Contours of radius of uncertainty circle (kilometers) for 5% velocity uncertainty, 1 Kiloton sources.

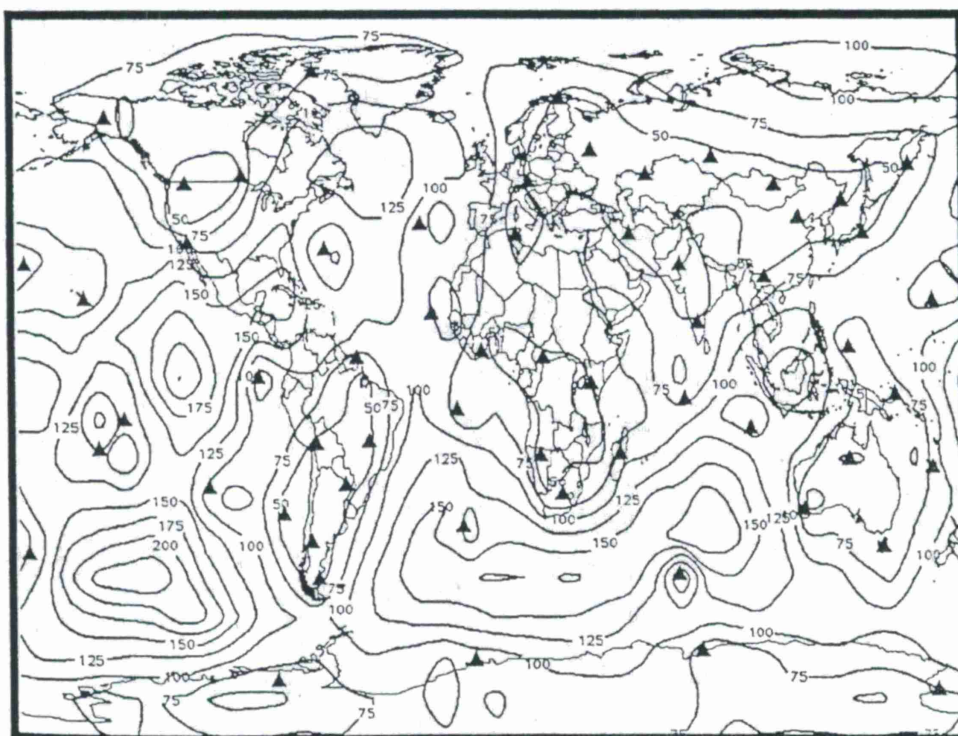


Figure 8. Contours of radius of uncertainty circle (kilometers) for 2% velocity uncertainty, 1 Kiloton sources.

Location Uncertainty as a Function of Velocity Uncertainty

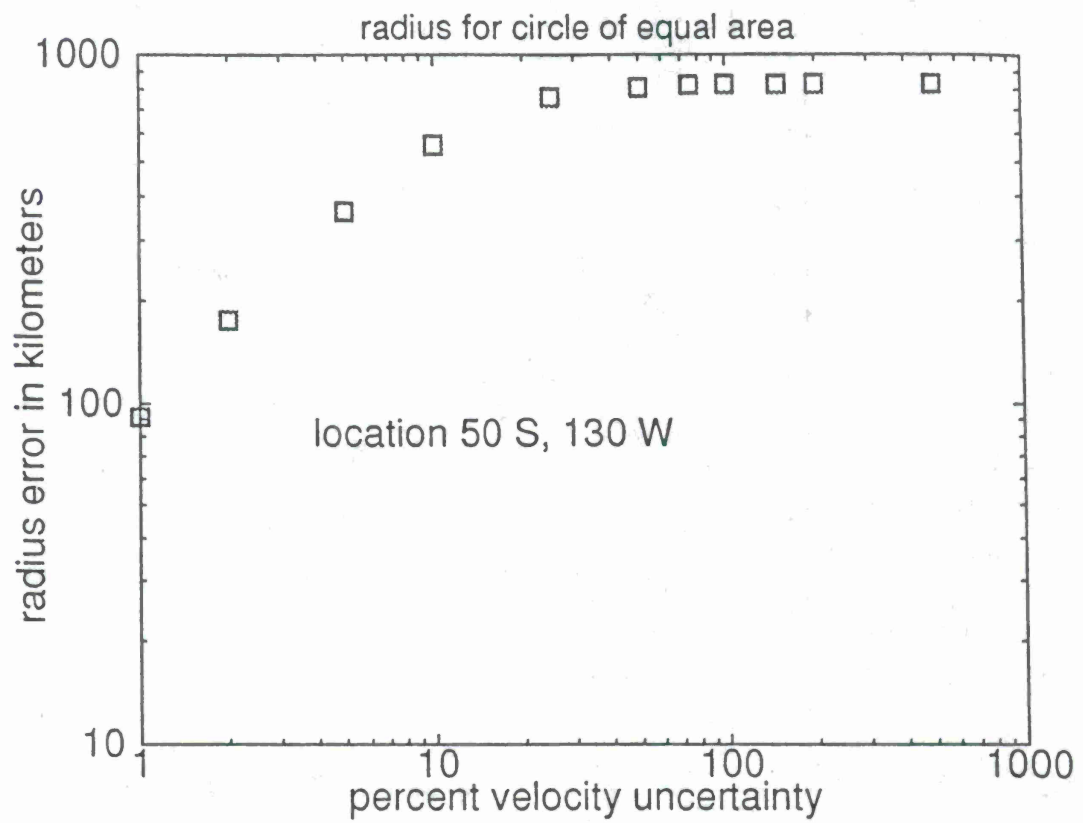


Figure 9. Location uncertainty improves considerably if the velocity uncertainty is known to 10% or better.

STRATEGIES FOR IMPROVING SEISMIC EVENT LOCATION AT REGIONAL AND TELESEISMIC DISTANCES

Göran Ekström, Adam M. Dziewonski and Gideon P. Smith

Department of Earth and Planetary Sciences
Harvard University
Cambridge, MA 02138

Contract pending
Sponsored by Defense Special Weapons Agency

ABSTRACT

We are engaged in a program of basic and applied research to address the problem of accurately locating seismic events at teleseismic and regional distances. Our research builds on our NSF-funded research effort of mapping the seismic propagation characteristics of the Earth's interior, and the demonstrated improvement in seismic event location that can be achieved when Earth's 3-D heterogeneous seismic velocity structure is accounted for in travel time calculations. Recognizing that a majority of the data which have been utilized in earlier tomographic models have primary sensitivity to variations in S-velocity, and that P-waves are of greater importance in the location of events, we are developing new datasets and new models emphasizing P-wave structure. P-wave propagation at regional distances is of particular importance, and we have collected datasets of Pn and other upper mantle P-phases for improved shallow mantle imaging. Crustal corrections and additional station and/or region corrections are being developed in conjunction with the velocity models to provide a consistent set of model based and empirical corrections to be used in an event location algorithm. We are collecting an expanded set of natural and explosion calibration events to be used for developing and/or testing our models and algorithms for seismic event location.

Keywords: Event location; seismic tomography; mantle heterogeneity

Objective

We are engaged in a research program aimed at improving the location of natural and artificial events at regional and teleseismic distances using seismological data. Progress towards this goal is being accomplished in six steps:

1. development of techniques to improve current tomographic Earth models, including multi-resolution techniques and incorporation of new data, in particular regional seismic phases;
2. construction of higher resolution three-dimensional Earth models, with an emphasis on *P*-wave structure;
3. evaluation of the new models using independent data;
4. incorporation of the models into location algorithms, including the development of additional station and/or path corrections;
5. compilation of a high quality dataset of well located master events; and
6. use of master events in assessing achieved improvements in location capability.

The CTBT technical goal of locating events with an area of uncertainty less than 1000 km² is ambitious, and this accuracy is currently achieved only in a few areas of the world. The research described here should lead to improved locations, in particular for events in uncalibrated regions, and is therefore relevant to the successful monitoring of the CTBT.

Research Accomplished

Our research program aimed at improving seismic event detection was initiated under a previous contract with AFOSR, and also builds on our NSF-funded research effort of mapping the seismic propagation characteristics of the Earth's interior (e.g., Su *et al.*, 1994; Dziewonski *et al.*, 1996; Ekström *et al.*, 1997; Ekström and Dziewonski, 1997). DSWA support for our research program is currently pending. The following sections provide a discussion of the merits of our research strategy, and some examples of our previous findings.

Relevance of the Research Strategy

It has been argued that the technical challenges associated with a successful monitoring of a CTBT using a relatively small number of IMS stations is best addressed by focussing on empirical location calibration using data collected at these stations. Our approach instead rests on the assertion that much of the calibration information (travel time corrections) can be predicted by incorporation of our improving knowledge of Earth's seismic velocity structure, determined by analysis of all available (including historical) seismic data. This is our primary justification for the efforts that we devote to analysis of the 30 years' worth of phase data from the several thousand observatories reporting to the ISC. At new stations, knowledge of site specific anomalies accumulate slowly with time, at a rate determined by the occurrence of relevant calibration events. We intend to incorporate data from the designated monitoring stations as they become available.

The quality of seismic event locations is critically dependent on the accuracy of predicted travel-times. Traditionally, travel-times are calculated from 1-Dimensional (1-D) models of seismic velocities. However, departures from the spherically symmetric Earth are evident on many length scales, resulting in significant, systematic errors in location.

Two ways around this are possible: (1) use of station corrections, and (2) use of a laterally varying Earth model. Whereas use of a laterally varying Earth model requires calculation of a travel-time correction for each ray, station corrections are only calculated once and then stored, therefore allowing rapid application. However, station corrections, on their own, have two major disadvantages. First, station corrections which are regionally invariant give very small improvements in location, and in under-sampled regions can reduce the quality of location. This is because they average very different source regions and are thus frequently appropriate to none (or, at best, are dominated by one).

Second, source-region dependent station corrections can only be derived if events have previously been recorded at that particular station from the particular region in question. This leaves the problem of what to do about unusual or suspicious events, which may occur far from any previously active seismic region, and for which no calibration is therefore possible. In this case calculating a correction based on a 3-D Earth model is helpful, because the structure along the path is sampled by rays that cross the path; no ray need ever have followed the exact path previously.

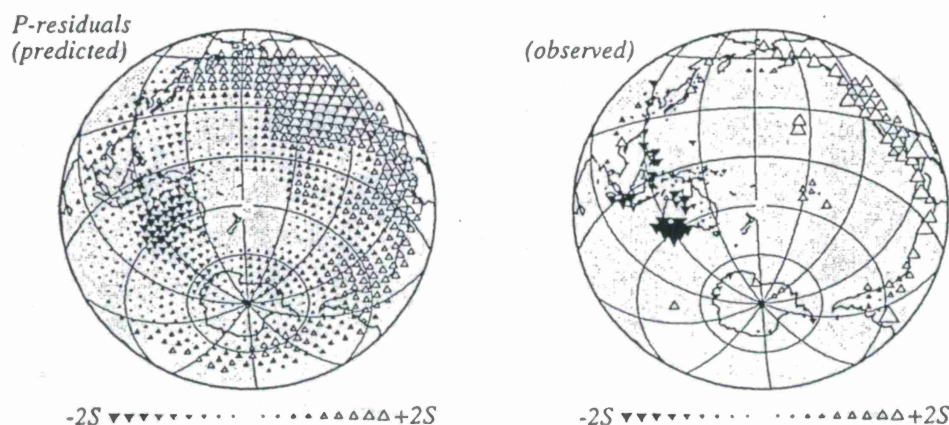


Figure 1: Predicted and observed P wave residuals for an event in Kermadec.

A justification for our approach can be seen in Figure 1, which shows average P residuals for events in Kermadec as observed at observatories reporting to the ISC. Both earthquakes and stations have been geographically averaged, to derive region-to-region residuals or corrections. It is clear that the pattern of observed residuals varies quite smoothly. Also shown in Figure 1 are the predictions of these anomalies, calculated for our 'best' P wave model S&P12/WM13, derived from a wide variety of traveltimes and waveform data. The model clearly captures a very significant portion of the observed variations in anomalies, suggesting also that it could be used to predict the anomalies that would be seen at a new station.

In our earlier work we have shown that 3-D Earth models are now of sufficient quality to be useful in improving event location (Smith and Ekström, 1996). We inverted P -wave arrival times for event locations using a 3-D mantle model (S&P12/WM13; Su and Dziewonski,

1993) and several 1-D Earth models (JB, PREM, IASP91) and found that not only are location and origin time estimates improved when using the 3-D mantle model, but that systematic location biases due to large scale heterogeneities are also reduced.

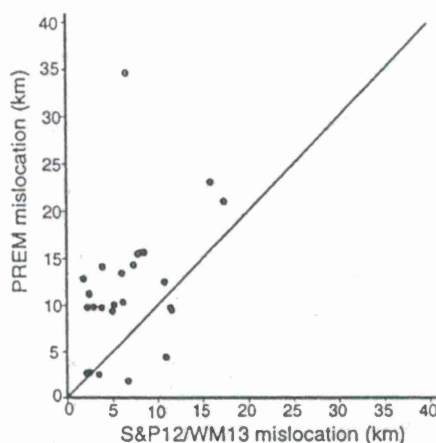


Figure 2: Mislocation of 26 explosion events with known hypocentral coordinates using the S&P12/WM13 3-D mantle model versus the 1-D PREM (Dziewonski and Anderson, 1981) model.

LOCATION FROM	RESIDUALS WITH RESPECT TO			
	PREM	IASP91	JB	S&P12/WM13
PREM	1.35			
IASP91		1.35		
JB			1.38	
S&P12/WM13				1.10
Ground Truth	1.79	1.87	3.48	1.60

Table 1: Residual travel time rms in seconds for four Earth models calculated at the locations obtained after inversion using each model. Sources are explosions with known locations. The lowest rms is obtained using S&P12/WM13 at the location derived using this model. At the ground truth location S&P12/WM13 is again the best model.

For events which occurred in geologically stable areas, away from plate boundaries, the average mislocation distance was reduced by approximately 40% using the 3-D mantle model — a 64% reduction in the area of the error ellipse; for events in geologically complex areas, the improvements were smaller. The greater improvement for tectonically simple regions suggests that potential for future improvements exist in the development of higher resolution mantle models to adequately account for smaller scale structure. The key result of the earlier study is demonstrated in Figure 2 and Table 1, which show that the derived locations are better, and the residual misfit is lowest when when a 3-D Earth model is used in the location.

The model S&P12/WM13 was not developed with the particular application of improved event location in mind. No set of station corrections consistent with this model was de-

veloped, nor was anything but a crude correction for the crust applied. In addition, since its development, new datasets with high sensitivity to the top few hundred kilometers of the mantle have been collected and are available for incorporation in the development of tomographic models. We therefore expect that new models of *P*-wave mantle structure will provide additional improvements in routine event location, in particular when combined with corresponding station and path corrections.

Improving Seismic Event Locations

The frequently stated goal of the International Monitoring System (IMS) is to locate events such that the area of uncertainty is less than 1000 km². To any seismologist with experience in earthquake location work, this constitutes a significant challenge. It is well known that different agencies commonly disagree on the locations of earthquakes by tens of kilometers (cf. GSETT evaluations) in particular when a comparison is made between local or regional locations vs. teleseismic ones. Similarly, it is well known that in some areas, in particular near subduction zones, propagation effects (Earth structure) can systematically bias teleseismic locations by as much as 50 km.

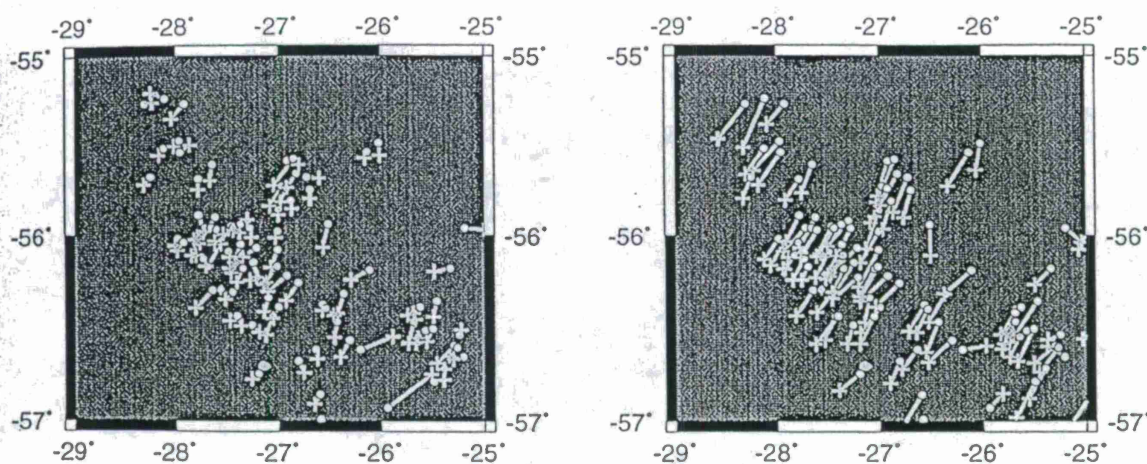


Figure 3: Relocation vectors in the South Sandwich Islands. Dots are the original ISC locations. Lines and plusses indicate the new location. Left — results from Engdahl et al.; right — our analysis.

Figure 3 illustrates the disagreement that can remain after careful relocation of $m_b \geq 5.0$ earthquakes in the South Sandwich Islands using ISC phase data using two different approaches: (1) work by Engdahl and van der Hilst which relies solely on the application of station corrections, and (2), our study which incorporates the effect of 3-D mantle structure, but no additional station corrections. Differences in the new locations are of the order of tens of kilometers, and while we believe our locations, which show a systematic movement of epicenters towards the SW, are better, this still needs to be verified by additional experiments.

Improved Focal Depth Estimates

We have demonstrated that use of current 3-D mantle models in event location can lead to reduction in mislocation. We have begun to relocate the events reported in the CMT

catalogue, using reassociated travel-times from the ISC bulletin and a 3-D mantle model. In this work we are investigating the importance of multiple phases (P , S , pP , sP , $PKIKP$, $PKPAB$, $PKPBC$, SKS) for constraining event location and focal depth. Introduction of PKP phases, which are accurately picked, often help to constrain event location due to the improvement in azimuthal coverage, and the sensitivity of the differential travel times of these phases to distance. However, as with direct P , it is largely insensitive to the trade off between origin time and depth, and therefore rarely helps to constrain depth. In contrast, introduction of S -waves, which often have larger picking errors associated with them, does not appear to improve location but, due to the difference in velocity of P and S waves, greatly enhances depth resolution.

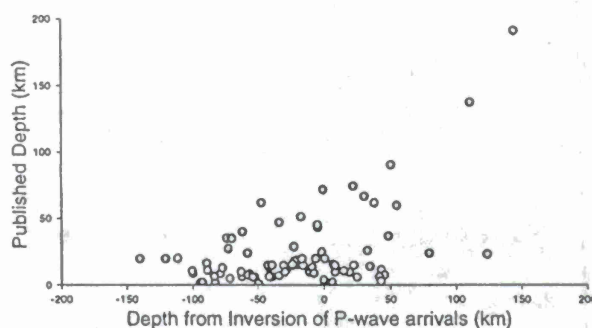


Figure 4: Depths from P waves only. Note negative depths.

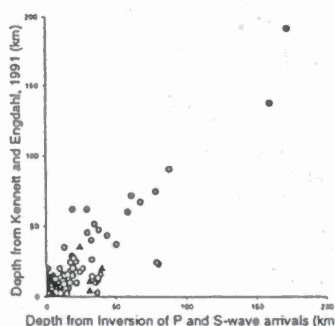


Figure 5: Depths from P and S waves.

Figure 4 shows the result of inverting ISC phase data for a set of events with known hypocenters for location and depth using only teleseismic direct P arrivals. Many of these inversions result in significantly different depths to those published. Negative depths (Figure 4) are clearly unrealistic but result from the inability to constrain depth with this data set alone. Figure 5 shows the result following inversion using both P and S arrivals. To avoid degrading our location due to the larger picking errors in S these arrivals were down-weighted. Our epicenters were almost identical to those obtained using P arrivals alone, however, our ability to resolve depth was much improved. In Figure 5, we show our preferred P and S results, for which the events were also constrained to have positive depths.

The results of experiments such as these will help us in designing an optimal location algorithm which maximizes our ability to effectively use all the available phase data. Such optimization will be vital in application of seismic techniques to events which have few

observations. Our continued research in this area will help us understand the different sensitivity of individual phases, and combinations of phases, to different parameters, as well as their expected variances. We can then aim at determining the most appropriate way to combine and weight these different data-sets.

The Role of Station Corrections

It is clear that there is a limit to the resolution of smaller scale heterogeneities in the Earth that can be attained by seismic tomography. We are therefore faced with two questions: Is smaller scale structure than has already been modelled significant? If so, what is the best method to deal with this structure in event location?

The answer to the first question is straightforward: numerous studies, including our own, have established that small scale, but strong and localized, heterogeneity can produce large, and systematic errors in location (Engdahl *et al.*, 1977; Engdahl *et al.*, 1982; Engdahl and Billington, 1986; Smith and Ekström, 1996). The strength of the signal from smaller scale structure can also be seen by examining the residuals that remain after correction for large scale 3-D structure. Poor pick times may account for some of these, but consistency in the residual pattern between events indicates structure that is not accounted for in the 3-D mantle model.

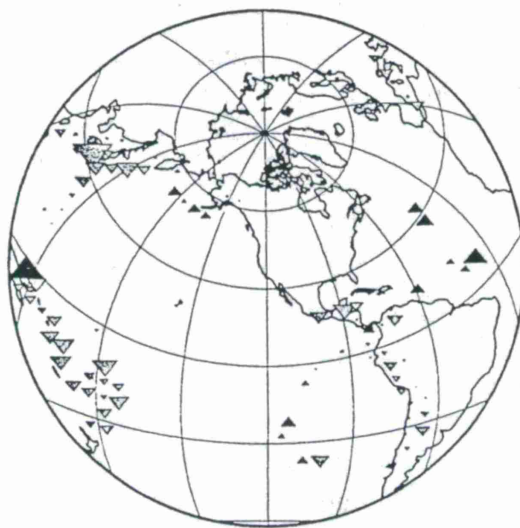


Figure 6: Figure shows empirically derived source-region dependent station corrections for station JAS after the effect of 3-D mantle structure (S&P12/WM13) has been removed. The range of variation is ± 1.5 s, and darker triangles show positive station corrections. Although the range of variation is large it is spatially consistent.

Two solutions for dealing with this unmodelled, presumably smaller scale, structure are possible: production of higher resolution models, or calculation of station corrections which complement our existing 3-D models. Although the former approach in the long term will lead to the desired improvements, the latter solution would appear to be the best way to maximize the utility of current 3-D models in event location. We therefore suggest a process of progressive refinement, with the more empirical station corrections being calculated after each improvement in Earth model is obtained. However, station corrections can themselves

be of varying complexity and we have been performing preliminary experiments to determine what type of station correction, static or regionally varying, may prove most useful. Although regionally varying corrections would seem preferable, it is unclear whether, for a majority of stations, there is adequate data coverage to constrain them.

Figure 6 shows a preliminary calculation of additional path corrections for the station JAS. We divided the Earth into 1654 source region caps spaced at 5 degrees, with radii of 2.5 degrees. We then use a 3-D Earth model to relocate all the K events in the i th source region, and derive a station correction S for the j th station by combining all the individual travel-time residuals δt_{ijk} , calculated after subtraction of the 3-D Earth model correction:

$$S_{ij} = \sum_k^K \delta t_{ijk} / K$$

Residuals for this particular station vary from -1.5 s to +1.5 s depending on the source region. It is clear, therefore, that a single static station correction could not be derived which would be appropriate for events in all regions. However, despite the caps having no overlap there is a surprising level of spatial coherence between neighboring source regions. It would therefore be possible to estimate source-station corrections using some smooth function dependent on the value at, and the distance from, the center of neighboring caps. In this way we could avoid the artificial roughness of poorly determined corrections, and the problem of discontinuities across source-region boundaries. This then is our proposed approach for developing source-station corrections to complement our 3-D Earth models in an event location algorithm.

Collection and Use of Calibration Events

Master events (alternatively called calibration or ground truth events) are events for which both the location and/or origin time are known with some small uncertainty. They are useful both for the development of station calibrations and in evaluating the performance of different location algorithms.

Explosions make ideal master events as both origin time and location are frequently accurately known by non-seismic means. However, to be useful for far-regional or teleseismic applications, master events must be detectable at great distances and thus only the largest explosions are usable for this purpose. Nuclear Weapons Tests and Peaceful Nuclear Explosions (PNEs) have been very valuable in this respect, however, they have the disadvantage that their locations are quite limited (except for the extensive PNE program in the FSU), and their exact hypocentral parameters are not always easily available. To obtain a more even global distribution it is possible to use well located earthquakes. Reliable locations for earthquakes can be obtained if the earthquakes are shallow and occur within a dense local network of seismometers. In addition, the particular linear geology and corresponding seismicity of the ocean floor, with near perpendicular ridges and transform faults, can be utilized to develop accurate locations for clusters of events, by imposing the constraint that the events lie on the plate boundaries.

Figure 7 shows the distribution of events used in our earlier study (Smith and Ekström, 1996). The earthquakes are from the compilation of Kennett and Engdahl (1991). Although the objective of Kennett and Engdahl's compilation was to obtain a more even global distribution, lines drawn at the equator, 30° and 60° North, highlight the uneven distribution:

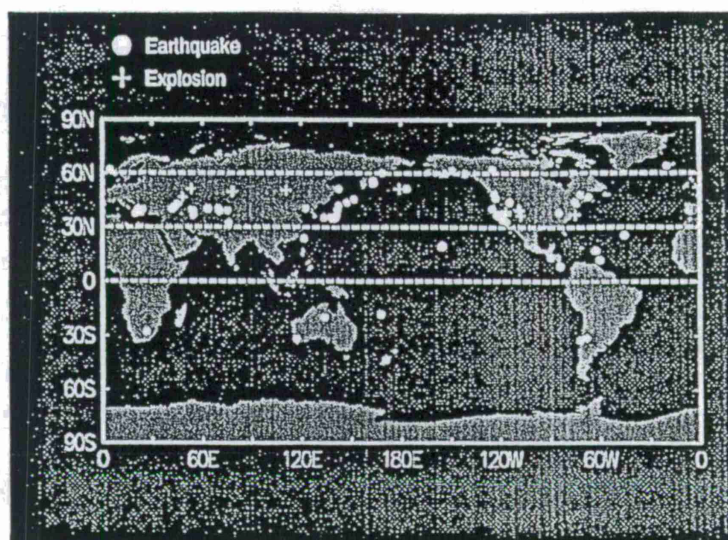


Figure 7: Figure shows the calibration events collected by Kennett and Engdahl (1991) (dots), and the additional explosions (plusses) used by Smith and Ekström (1996).

almost 80% of the events occur between 30° and 60° North, only seven of 104 events are in the southern hemisphere and almost all are on or close to land. We are adding to this database, and developing a set of high quality event locations distributed more evenly across latitudes and between continents and oceans.

Conclusions and Recommendations

By combining large numbers of diverse seismological observations, we continue to make progress towards obtaining higher resolution tomographic images of the Earth's internal elastic structure. A strategy for incorporating the growing knowledge of Earth's internal velocity structure in seismic event location has been outlined, including the derivation of station corrections to account for remaining patterns of travel time residuals, once mantle and crustal effects have been removed. Master events are extremely important for ascertaining the performance of location algorithms, and the collection of a geographically well-distributed set of high-quality event locations would be of great value.

References

- Dziewonski, A. M., and D. L. Anderson, Preliminary Reference Earth Model (PREM), *Phys. Earth Planet. Inter.*, 25, 289-325, 1981.
- Dziewonski, A. M., G. Ekström, and X.-F. Liu, Structure at the top and bottom of the mantle, in E. S. Husebye and A. M. Dainty (eds.), *Monitoring a Comprehensive Test Ban Treaty*, pp. 521-550, Kluwer Academic Publishers, Dordrecht, 1996.
- Ekström G. and A. M. Dziewonski, Improved models of upper mantle *S* velocity structure, *EOS, Trans. Am. Geophys. Soc.*, 75, 471, 1995.
- Ekström, G., J. Tromp, and E. W. F. Larson, Measurements and global models of surface wave propagation, *J. Geophys. Res.*, 102, 8137-8157, 1997.
- Ekström G., and A. M. Dziewonski, Imaging upper mantle *S* velocity structure: compatibility of different data sets, *EOS, Trans. Am. Geophys. Soc.*, 77, 483, 1996.
- Ekström, G., and A. M. Dziewonski, The unique anisotropy of the Pacific upper mantle, *Nature*, , submitted, 1997.
- Engdahl E. R., and S. Billington, Focal depth determination of Central Aleutian earthquakes, *Bull. Seism. Soc. Am.*, 76, 77-93, 1986.
- Engdahl E. R., J. W. Dewey, and K. Fujita, Earthquake location in island arcs, *Phys. Earth Planet. Inter.*, 30, 145-156, 1982.
- Engdahl E. R., N. H. Sleep, and M.-T. Lin, Plate effects in North Pacific subduction zones, *Tectonophysics*, 37, 95-116, 1977.
- Kennett, B. L. N., and E. R. Engdahl, Traveltimes for global earthquake location and phase identification, *Geophys. J. Int.*, 105, 429-465, 1991.
- Smith, G. P., and G. Ekström, Improving teleseismic event locations using a three-dimensional Earth model, *Bull. Seism. Soc. Am.*, 86, 788-796, 1996.
- Su, W., and A. M. Dziewonski, Joint 3-D inversion for P- and S-velocity in the mantle, *EOS, Trans. Am. Geophys. Soc.*, 74, 557, 1993.
- Su, W.-J., R. L. Woodward, and A. M. Dziewonski, Degree-12 model of shear velocity heterogeneity in the mantle, *J. Geophys. Res.*, 99, 4945-4980, 1994.

TRAVEL-TIME CORRECTION SURFACE GENERATION FOR THE DOE KNOWLEDGE BASE

Jim Hipp, Chris Young, Ralph Keyser
Sandia National Laboratories

Sponsored by U.S. Department of Energy
Office of Nonproliferation and National Security
Office of Research and Development
Contract No. DE-AC04-94AL85000
Comprehensive Test Ban Treaty Research and Development Program

ABSTRACT

The DOE Knowledge Base data storage and access model consists of three parts: raw data processing, intermediate surface generation, and final output surface interpolation. The paper concentrates on the second step, surface generation, specifically applied to travel-time correction data. The surface generation for the intermediate step is accomplished using a modified kriging solution that provides robust error estimates for each interpolated point and satisfies many important physical requirements including differing quality data points, user-definable range of influence for each point, blend to background values for both interpolated values and error estimates beyond the ranges, and the ability to account for the effects of geologic region boundaries. These requirements are outlined and discussed and are linked to requirements specified for the final output model in the DOE Knowledge Base. Future work will focus on testing the entire Knowledge Base model using the regional calibration data sets which are being gathered by researchers at Los Alamos and Lawrence Livermore National Laboratories.

Keywords: Knowledge Base, kriging, interpolation, deluanay tessalations, natural neighbors

OBJECTIVE

The purpose of travel-time correction data in the DOE Knowledge Base is to provide to a client the best estimate possible of the travel-time correction and associated error for any arbitrary point at or near the Earth's surface as quickly as possible. In order to accomplish this, we have developed a three-part model for the storage and access of travel-time correction information in the Knowledge Base, comprised of raw data input (including various validity and consistency checks), conversion to a complete and internally consistent storage representation, and fast output of interpolated data to the clients. The portion of that research discussed in this paper focuses on the intermediate step: the conversion of raw data to the data which will be the basis for the on-the-fly interpolation in the final step. The intermediate step is necessary because the raw data points themselves are not expected to provide a sufficient basis for the final interpolation due to inadequate sampling and a lack of a means to account for other important factors which are expected to influence the interpolated travel-time correction values (e.g. nearby geologic province boundaries).

In our research we have investigated methods of gridding or tessellating data as well as interpolation methods that provide accurate results, including surface error estimates, given the constraints of sparse data and smoothly varying and continuously differentiable surfaces. Our major objectives are to provide a comprehensive set of data representation and interpolation schemes capable of meeting the requirements for providing travel time corrections from the Knowledge Base. Although our discussion here will be limited to travel time correction data, it is expected that the techniques developed will apply to many of the other Knowledge Base data sets as well, such as corrections for amplitude, azimuth, and slowness.

RESEARCH ACCOMPLISHED

Introduction

As stated above, this paper will focus on the intermediate data representation portion of the three-part Knowledge Base model. The technique that we have chosen to use to convert raw data to the data to be stored in the Knowledge Base, is a modification of the interpolation method known as kriging. Kriging can be used to calculate travel-time corrections and also provides associated error estimates, which most other interpolation schemes do not. We can use the modified kriging technique to create a dense grid of interpolated data and errors which will then serve as the basis for the fast interpolation techniques in the final part of the Knowledge Base data storage and access model.

Our technique was modified from ordinary kriging in order to meet certain constraints. In order to fully understand the reasoning behind these constraints imposed on the method used to generate the intermediate data, we must briefly describe the requirements of the final corrections presented to the user. From the perspective of the Knowledge Base, the processed surface data representations presented to any user, either human or an Automated Data Processing (ADP) code, will have to satisfy several basic criteria. These criteria include:

- 1) The representation should support a sparse unstructured data distribution, as is typically associated with seismic data,

- 2) The representation should be based on a local interpolation scheme to minimize error propagation,
- 3) The representation should provide accurate results within a specified tolerance,
- 4) The representation should possess first and second order continuity to support data processing algorithms, and finally
- 5) The representation should minimize the amount of data required to represent the surface and provide for rapid searching techniques to maintain reasonable performance margins.

The first criteria is simply a statement that the final surface should not be constrained to a regular grid. Regular grids, in regions of high surface complexity (curvature), are, of course, efficient representations and lend themselves to rapid searching techniques (direct indexing) which are required by the 5th criteria. However, regular grids do not allow thinning of data in regions of simple surface curvature (flat) and are difficult to refine to the surface of a sphere, especially near the poles. If an ADP code constantly accesses a database during data processing, it follows that having more data in the database will result in slower processing times. For these reasons, smooth irregular tessellations such as the Delaunay triangular tessellation (Delaunay, 1934 and Fortune, 1992) are generally thought to be better representations. The mesh density can easily be refined as a function of surface curvature and the surface can be rapidly searched with $n \log(n)$ speeds using algorithms such as the "walking triangle" searcher (Lawson, 1977 and Sambridge, 1995).

The second and third criteria are simply a statement that the final representation be an accurate one. By accuracy we mean that the interpolation must yield values at certain known locations which are within a specified range of tolerance; that is, we must have an error specification that accompanies the result. In fact, some ADP codes require an error estimate to function properly. Additionally, if the travel-time correction surface representation is especially erroneous at some arbitrary location, we wish to localize that error and not allow it to propagate to other locations in the surface. These criteria can be satisfied in both the intermediate and final stages of the DOE Knowledge Base model. We shall soon describe the methods for the intermediate stage. In the final stage we simply require that the interpolation scheme that returns results from the intermediate surface to the user be local in nature. That is, that it only uses information near the interpolation point to estimate a result. Many fast interpolation schemes satisfy this result such as linear interpolation or natural-neighbor interpolation (Watson, 1992), to mention just two.

The fourth criteria is necessary because some ADP codes require it. A good example is the event location algorithm used at the USNDC. This algorithm requires continuous first and second derivatives from the interpolation to allow proper convergent behavior. Although discontinuities are readily observed in the real Earth, compliance with the derivative continuity requirement is essential to ensure proper performance from the location algorithm.

The last requirement is a performance requirement. Simply stated, with the massive amounts of data that are transferred over the computational data bus from the server to a client we have little time to spend searching for data points and we must minimize the amounts of data transferred over the bus to reduce the total data access times. This criteria also suggests that a moldable unstructured grid that can be tailored to regions of high surface curvature while

maintaining only a few points in regions that are relatively flat is highly desirable. To reiterate, this function is easily accomplished with smoothed triangular grids.

All of the requirements stated above for the final surface representation provided to user ADP codes drive the requirements for the generation of the surface in the intermediate representation. The process whereby the intermediate representation is calculated for a data set is the subject of the rest of this paper. The discussion is divided into three main sections including a synopsis of the requirements for the development of the intermediate surface and how they relate to the criteria defined for the final output surface described above; a brief overview of the modified kriging model including those modifications that satisfy the intermediate surface requirements; and lastly, an example of the results of the modified kriging algorithm that illustrates the behavior of the kriged residual and error surfaces for a real data set.

Travel-Time Correction Surface Requirements

Any developed travel-time correction surface (i.e. mesh of points) must satisfy several key constraints before the surface can be considered acceptable for the Knowledge Base. These constraints include the following:

- 1) The surface must be first and second order continuous and be well behaved to properly support ADP codes that require continuity and non-oscillatory behavior,
- 2) The surface must include associated error estimates,
- 3) The variance and associated residual at each data point must provide an analyst sufficient capability for modeling the data points range of influence, magnitude, and shape and rate of fall-off (or increase for variance) for each group of data points,
- 4) The residual surfaces must go to zero, and error surfaces to a specified background, at the extreme range of influence of each data point,
- 5) The surface must be capable of supporting groups of data with different error estimates that can coexist spatially in neighborhoods whose data density can vary from a single point to hundreds or thousands.
- 6) At any arbitrary interpolation point, the influence of low variance data (reliable) must be greater than the influence of high variance data (unreliable).
- 7) At any arbitrary interpolation point, the interpolated value must reflect the influence of known boundaries across which travel-time corrections are expected to change (e.g. geologic provinces).

The first and second constraints above are necessary primarily to satisfy ADP codes such as event locators where continuity and an estimate of error are required to locate an event within a calculated error ellipse. These two requirements translate directly from the 2nd, 3rd and 4th criteria specified in the previous section.

The third constraint is to provide sufficient modeling flexibility so that a seismologist can properly represent the expected physical behavior of a set of data points. Each interpolation may involve different factors such as differing quality of data points (e.g. earthquake versus calibration), or proximity to a tectonic province boundary. This requirement is purely a data modeling constraint and has no equivalent in the output model criteria specifications.

The fourth constraint is also a modeling constraint and is necessary to allow interpolated data from different regions to blend together uniformly and continuously. This constraint provides a means to support arbitrary and different error models and yet insure consistency between different regions. It also provides a means to blend to a default model for uncalibrated regions,

The fifth and sixth constraints are necessary to support real world data acquisition including quality and quantity of data, and to take advantage of higher quality data whenever possible.

Since requirements 4 through 7 all result in a continuous surface everywhere they all contribute to satisfying the continuity criteria for the output model data. In addition to providing an accurate physical picture of the travel-time correction surface. In the next section we will briefly outline the changes imposed on an ordinary kriging model that allow surfaces to be generated that satisfy the requirements defined above.

Travel-Time Correction Surface Model

Most surface interpolation schemes can adequately provide accurate, smooth, and continuous surfaces with moderate to high calculational performance margins. However, all but a few are unable to relate any information about error when data error information exists.

One common method of interpolating a surface that will account for error in the raw data is the method of least squares. Least squares interpolation techniques can provide error bounds on the interpolated surface that minimizes the mean squared difference from the regression function chosen to represent the surface. In this sense, the selected function fits the data more closely than any other function of the same type. Unfortunately, least squares techniques have a tendency to over- and under-shoot dramatically near steep slope changes. Additionally, the surface is equally affected by a distant data point, as it is by a near data point which implies that the fit function is not representative of the spatial variation in the data (Watson, 1992). A final undesirable consequence of the method is that even when measurement error on the data is eliminated or inconsequential, the least squares surface still fails to pass through any of the data points any where on the surface. Given the points delineated above one can see that the method of least squares generally fails all of the requirements defined in the previous section with the exception of requirement 2).

Other methods that include error estimates when developing an interpolated surface are termed kriging methods (named after the South African who originally developed the methods) or are strongly related to kriging methods in that the interpolated point is determined as a linearly weighted combination of the data where the weights are evaluated as a best linear unbiased estimate (blue) such that the error of the predicted surface is minimized. Only a modified version of the ordinary kriging method that satisfies the constraints prescribed in the previous section will be described here. The interested reader should consult Wackernagel, 1995, Cressie, 1993, or Isaaks, 1989, for further information concerning kriging and associated derivative methods.

Ordinary kriging methods in and of themselves are unappealing for our problem in that many of the surface constraints specified in the previous section are not met. First, ordinary kriging assumes equal variances for all data points. This assumption violates constraints 5) and 6). Secondly, ordinary kriging does not guarantee that the residual surface will fall away to zero at some range beyond the data or that the variance surface will move to a specified back-

ground value. This fact violates constraint 4). Finally, ordinary kriging has no way to account for regional boundaries in the data which violates constraint 7). Boundaries are either completely smooth (ignored) or discontinuous which violates constraint 1).

Since ordinary kriging methods do not completely satisfy the necessary requirements a modified methodology is required. The first major modification of ordinary kriging is to remove the requirement that all data possess the same variance. This means that the traditional variogram approach to kriging is replaced by the covariance definition that includes a correlation coefficient and the variances between data points or a data point and an interpolation point. This reformulation is written as

$$C_{ij} = \rho_{ij} \sigma_i \sigma_j$$

We can now assign different values of variance to each data point which removes the aforementioned restriction. This allows one to incorporate data points that possess variances of varying quality (e.g. explosions vs. earthquakes) such that constraint 5) is now satisfied.

Constraint 4) can be satisfied by allowing the value and variance to transition as a function of distance from the data point. Figure 1) shows a typical transition kernel. Notice that the value (a correction relative to a base model) transitions from its value, Z_i , at range = 0, to 0, at the data point's specified range of influence; while the variance transitions from its value, σ_i , at range = 0, to the background variance, σ_{bg} , at the specified range of influence.

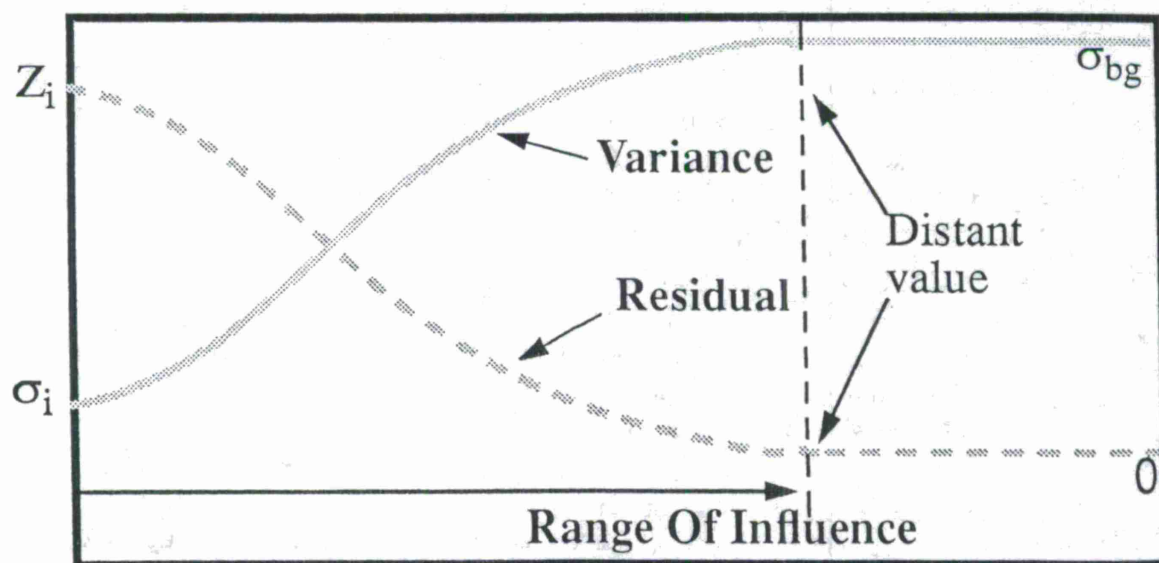


Figure 1). Typical Transition Kernels for Residuals and Variances

Constraint 6) can be satisfied by specifying the interpolation point variance prior to estimating the surface at that point. By forcing the interpolation point variance σ_p to be equal to the minimum of all other variances evaluated at the interpolation point, we can always force the solu-

tion to utilize the best available error in the local neighborhood about the interpolation point. We can write the above statement mathematically as

$$\sigma_p = \min(\sigma_i(h_{ip}); i=1, N)$$

where h_{ip} is the range between the i th data point and the interpolation point and the minimization is carried out over all N data points.

Finally, if the distance between a data point and the interpolation point is intersected by a region boundary we can correct the interpolated value to reflect this by forcing the transition function of a data point to move to zero (for the residual or σ_{bg} for the variance) earlier than it would normally. Figure 2) shows how the transition is patched in the influence region of a boundary for a residual blending kernel.

Every boundary can have a different width for the transition zone and can be arranged in arbitrary open or closed segment groupings. This provides a wealth of flexibility while making transitions smooth and continuous.

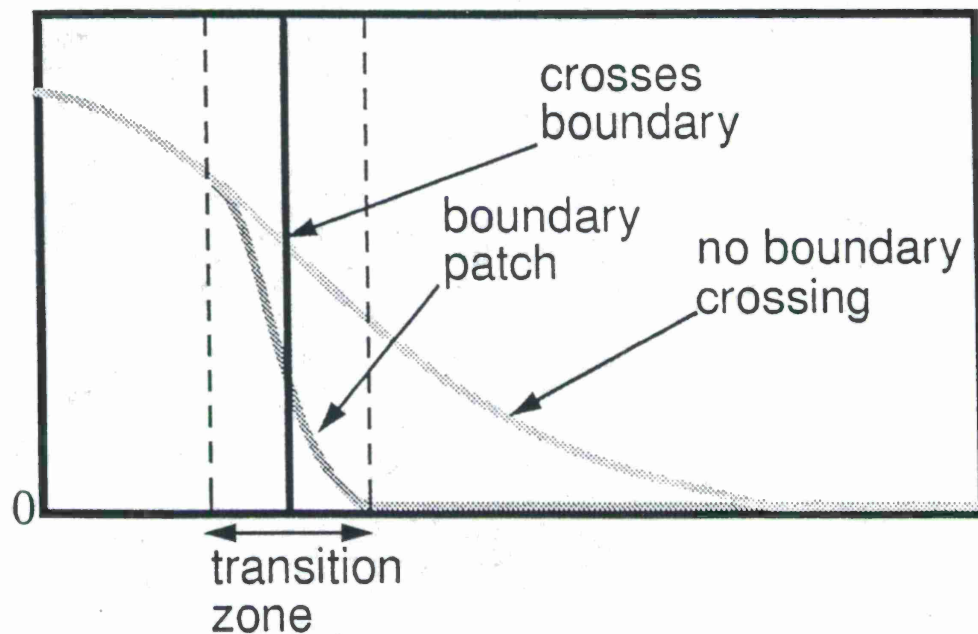


Figure 2). Typical Transition Patch of a Residual Kernel as it Crosses a Region Boundary.

In the next section we shall give an example problem that utilizes the modified kriging method defined above. The resulting solution shows that surface continuity exists everywhere and that both the residual and error surfaces migrate to their respective background values as the interpolation point leaves the influence range of the data.

Example of a Modified-Kriged Surface

The following illustrations depict travel time residual and error surfaces taken from regional travel time correction data calculated for seismic station LZH from a set of events located in China. The data was provided by Allen Cogbill of Los Alamos National Laboratories.

The surfaces are calculated using the residual and error blending kernels depicted in Figure 3). The range selected for this example is 10 degrees and the variance for all the data was set to zero. The background variance was arbitrarily chosen to be 2 sec^2 . The error blending kernel is the y-axis flip of the residual blending kernel as shown in Figure 1) above.

Figure 4) shows the residual surface using the modified kriging solution described in the previous section. Notice the smooth behavior throughout the region and the way that the residual surface falls back to zero outside the range of the data. Figure 5) shows a top down view of Figure 4) with the input data points indicated by small circles.

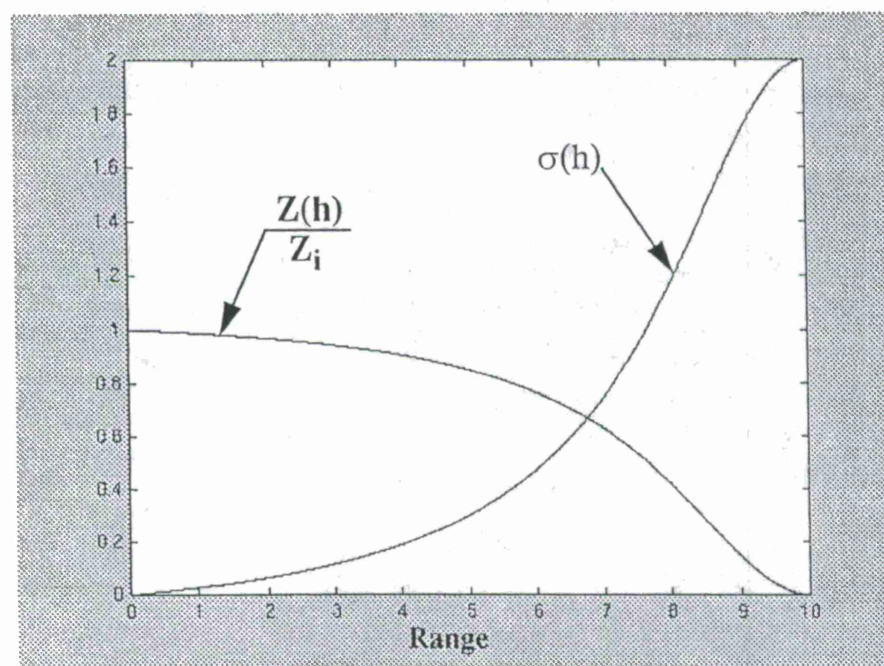


Figure 3). Residual and Error Transition Kernels Used by the Example Problem in this Section.

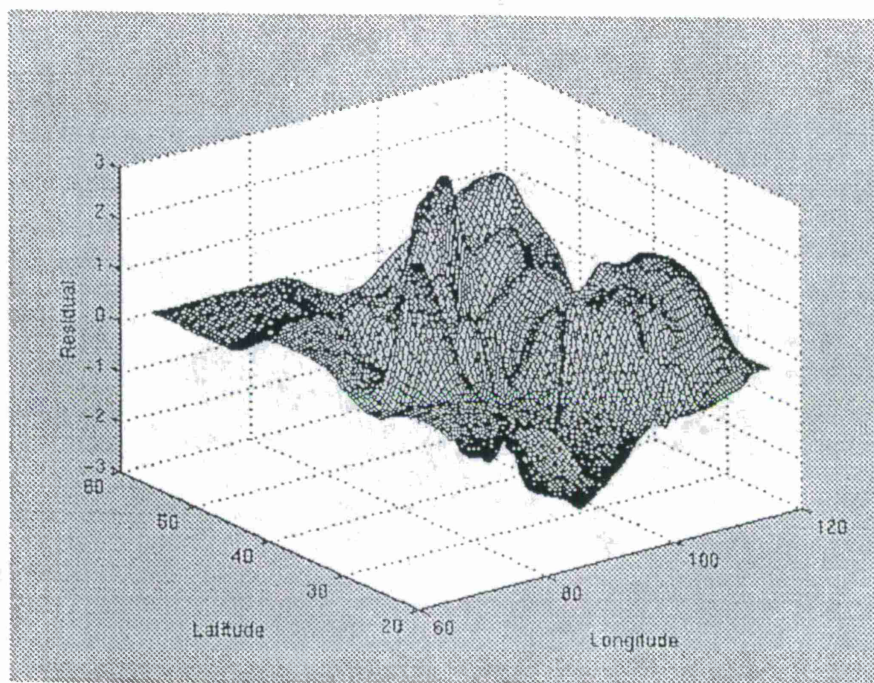


Figure 4). Resulting Residual Surface for the Example Problem in this Section.

Figure 6) illustrates the accompanying error surface to the residual surface shown in Figure 4). Notice that the error drops to essentially zero throughout the region of influence of the data and rises sharply to the background variance outside of the data points influence region.

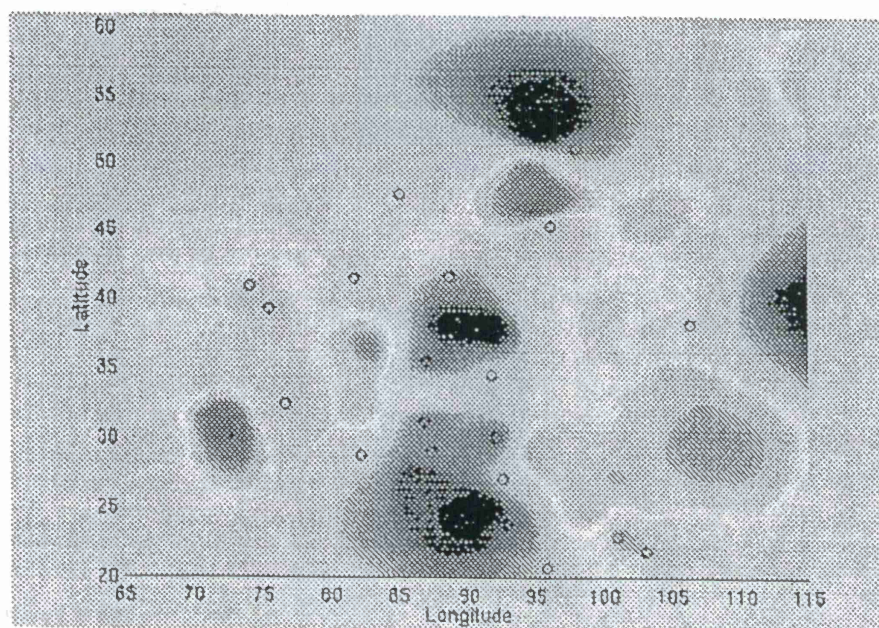


Figure 5). Top View of the Residual Surface. Data points are indicated by the small circles.

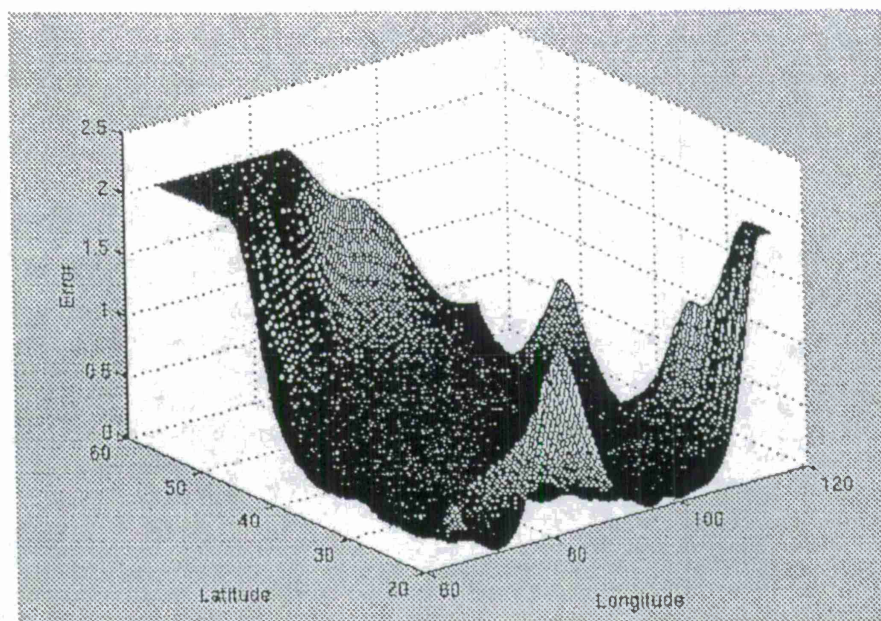


Figure 6). Resulting Error Surface for the Example Problem in this Section.

CONCLUSIONS AND RECOMMENDATIONS

The research described here has focused on the intermediate portion of the three part DOE Knowledge Base data storage and access model. We defined the requirements of the intermediate surface representation and used them to develop a modified kriging approach to generate the surface. We have shown that the modified-kriging approach satisfies all of the requirements of the intermediate surface representation which in turn solves all of the requirements specified for the final data product provided to Knowledge Base clients. These requirements provide for smooth continuous residual and error surfaces that mold easily to background values. Additionally, they allow for data of differing quality to exist simultaneously while forcing the highest quality data in the interpolation neighborhood to control the resulting interpolated surface values. Regional boundaries are also accounted for by forcing the solution to background values when boundaries are intercepted between data points and interpolation points.

Future work will include using data from the regionalization efforts under way at Los Alamos and Lawrence Livermore Laboratories to begin testing the entire Knowledge Base model, from input of raw data to output of travel-time corrections for clients. A major part of this testing will involve connecting the current event location algorithm to the Knowledge Base to demonstrate both the accuracy of the collected data and the speed of the final interpolation step. Our work with the example data set described in the previous section represents a first step in this process. Performance issues will also become increasingly important as we attempt to demonstrate that the overall performance of the final output step is acceptable from the perspective of the ADP codes which are expected to request travel-time correction data from the Knowledge Base.

REFERENCES

- Delaunay, B.N., 1934. "Sur la sphere vide," Bull. Acad. Science USSR VII: Class. Sci. Math., 793-800.
- Cressie, N. A. C., 1993. "Statistics for Spatial Data," John Wiley & Sons.
- Fortune, S., 1992. "Voronoi diagrams and Delaunay triangulations," Computing in Euclidean Geometry, eds. Du, D.Z., and Hwang, F., World Scientific.
- Isaaks, E. H., Srivastava, R. M., 1989, "An Introduction to Applied Geostatistics," Oxford University Press, New York.
- Lawson C. L., 1977, "Software for C1 surface interpolation," Mathematical Software III, ed. Rice. J., Academic Press, New York.
- Sambridge, M., Braun, J., and McQueen, H., 1995, "Geophysical parameterization and interpolation of irregular data using natural neighbors," Geophys. J. Int.
- Wackernagel, H., 1995, "Multivariate Geostatistics: An Introduction With Applications," Springer-Verlag, Berlin.
- Watson, D. F., 1992, "Contouring: A Guide to the Analysis and Display of Spatial Data," Pergamon, Oxford.

SEISMIC WAVE PROPAGATION IN THE CRUST - EVENT LOCATION IN A SEMIAUTOMATIC MANNER

Eystein S. Husebye and Bent O. Ruud
Institute of Solid Earth Physics, University of Bergen, Norway

Sponsored by Air Force Office of Scientific Research
Grant No. F49620-94-1-0278

ABSTRACT

A major CTBT monitoring issue is that of detecting and locating seismic events precisely at local and regional distance ranges. If the epicenter error significantly exceed 20 km OSI would not be much of a deterrent for treaty violations. An instructive controversy here was the 13 Jan 1996 event on Novaya Zemlya which location in the Barents Sea (van der Vink and Wallace, 1997) also was controversial. Using elaborated envelope analysis we were able to extract with confidence Sn times from Norilsk (NRI) and thus restrict the event epicenter to NZ (75.38N, 56.55E).

The very many seismograph networks in operation globally are not of much interest in a CTBT monitoring context partly because of long delays in analysis of recorded events. This adverse situation is rectifiable by introducing reliable and robust analysis schemes for accurate epicenter locations. We have experimented with envelope transforms of prefiltered (3 - 6 Hz) waveforms producing records dominated by only 2 phases; Pn/Pg and the prominent Lg. To avoid ambiguities in picking onset times we used computer read P- and Lg-peak arrival times. The ensuing epicenter determinations had the same accuracy as the analyst epicenter solutions. The envelope scheme is transportable since Lg propagation is remarkable consistent (group velocity 3.50 ± 0.10 km/sec) largely irrespective of tectonic regimes.

In many industrialised countries a real nuisance in seismic network operation is the very many (chemical) explosions recorded on working days. Recording of such signals are unavoidable, but do we really need to waste analysis resources on such events? The answer is NO in view of our recent results in training the computer to recognize events from a priori known explosion sites like Titania and underwater construction in Geiranger Fjord, both Norway. In doing so we used a multistation interpolation and approximation neural network (IANN) scheme in analysis of envelope records from the local network. The IANN is user friendly; the output is a single number between 0 and 1 and with an acceptance threshold of 0.4 we obtained 100% separation between 'site explosions' and hundreds of 'non-site' events.

Our work on synthetic seismogram analysis in 2D and 3D is steadily progressing. Even 3D topography effects can be handle in a realistic manner; viscoelastic regime (intrinsic attenuation) is in near completion and is now being tested on a parallel machine simulating secondary Rg-scattering from hills adjacent to NORESS.

Keywords: CTBT monitoring, automatic event location, explosion site recognition, 2D and 3D FD synthetics.

OBJECTIVES

- Principal objective: contribute to more efficient CTBT monitoring capabilities at local and regional distance ranges.
- Refine envelope epicenter determination in analysis of seismic network records in a semi-automatic manner.
- Enhanced network operational efficiency by learning the computer to recognize subsequent signals from *a priori* known explosion sites.
- Adapt 'recognition' procedures for establishing 'ground truth' learning sets for subsequent establishing explosion site recognition routines.
- Foster a better understanding of seismic wave propagation in complex media like the crust through wavefield synthetics in 2D and 3D.
- Extend synthetics to visco-elastic media for incorporating attenuation effects and even 3D topography.
- Modify finite difference software to parallel processing schemes for flexible wavefield simulations for large crustal models.

RESEARCH ACCOMPLISHED

In the following summaries are given for different research tasks accomplished.

The puzzling 13 Jan 1996 event on Novaya Zemlya

The political sensitivity of certain seismic event locations was amply demonstrated by this particular event. Data at hand stemmed only from the 2 arrays ARCESS and Spitsbergen since the event magnitude was about 2.4 units only and initial epicenter determinations differed by more than 100 km (Van der Vink and Wallace, 1997). Obviously, access to more station recordings would be an advantage for better constraining source location but in view of its $m_b \sim 2.4$ other station data could apparently be ruled out. Not being discouraged by this conventional wisdom we looked for other 3-component recordings and the obvious candidate was Norilsk (NRI) in Siberia. Albeit very weak signals and many spikes in the records we were able to extract reliable S_n arrival times with confidence and likewise obtaining a reliable epicenter location at 75.38 N and 56.55 E using P- and S-arrival time information from the 2 arrays and NRI but Bergen University travel time tables (details in Henger et al., 1997). In retrospect, hopefully we have contributed to resolving the 'seismopolitical' controversy of the 13 January 1996 event on Novaya Zemlya. Particularly gratifying is that by using the novel envelope analysis technique we could extract useful traveltime information from the Norilsk 3C station, despite the poor quality of the NRI records for an event of magnitude 2.4 at an epicenter distance of about 1200 km. However, we confess that such low magnitude events can neither be accurately located nor clearly identified with seismological means

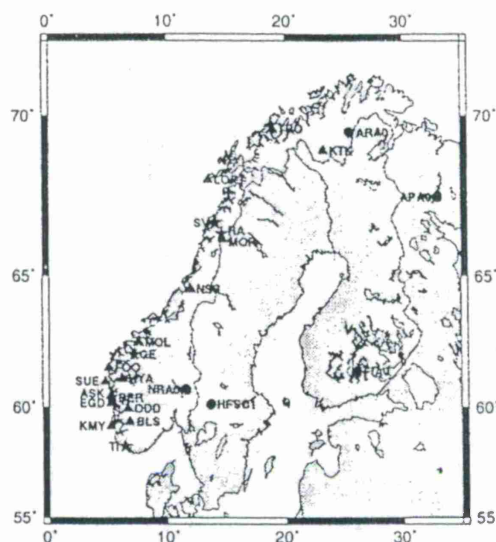


Figure 1: The Norwegian Seismograph Network and Scandinavian array stations used in analysis. Explosion sites for which envelope location accuracy were tested, are also shown.

only. In particular, the IASPEI travel time tables are not well suited for accurate event locations in the Novaya Zemlya area for regional epicenter distances.

Envelope Processing of Local Network Data

Local event recordings are complex in the sense that relevant P- and S-phases vary in an unpredictable manner even between closely spaced stations; thus, manual analysis of such records is still commonplace. Our approach to solving this long standing problem of observational seismology is to bandpass filter (3–6 Hz) to ensure good SNR and then form envelopes to ensure simple signals across a seismograph network (Fig. 1). The physical basis is that Pg and Lg are crustal waveguide phases reflecting P- and S-energy propagation. Extensive tests on envelope analysis of local records from different areas found that arrival times of the maxima of Pg and Lg envelopes increase very consistently with distance even in different tectonic regimes. Typical velocities being 6.1 and 3.5 km/sec respectively. These arrival time parameters are easy to extract in a semi-automatic manner and besides are highly suitable for local epicenter determinations. Extensive tests on locating mining explosions were conducted and on average the ‘envelope’ solutions were similar or even closer to ‘true’ locations than those in bulletins which are based on conventional phase pickings (Fig. 2). Occasionally, the Pg/Pn envelope may be very weak but can be replaced by the easily pickable (non-envelope) Pn-phase. An additional advantage with envelope locations are transportability since Lg remains a consistent (group velocity about 3.5 ± 0.1 km/s) and prominent phase even for travel paths across adverse tectonic regions. We have confirmed this result theoretically (Mendi et al., 1997) and observationally through envelope analysis of network data from diverse areas like Fennoscandia, New England, Germany and Italy. Note that envelope amplitudes can be directly converted to ground motion and hence provide near instantaneous event magnitude estimates. In case of noise envelopes the corresponding ground motion conversion enable us to compute station

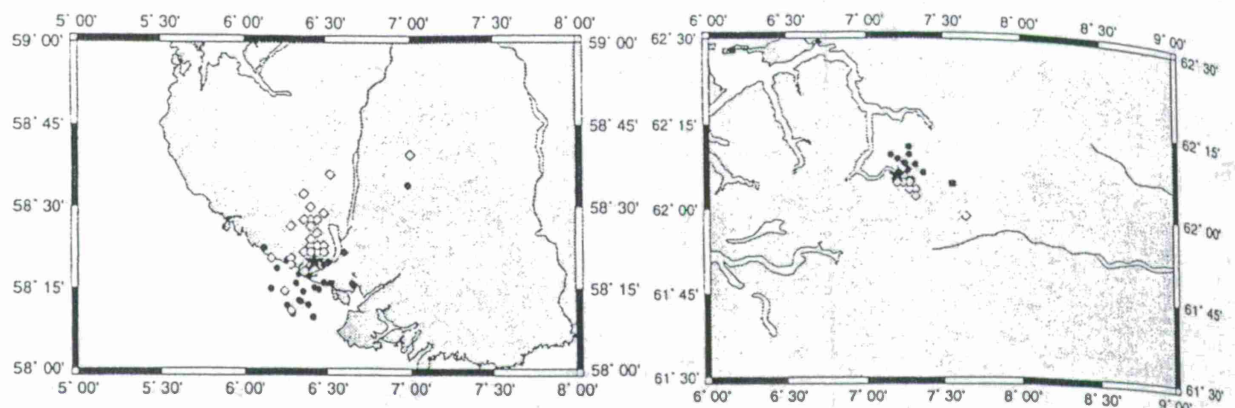


Figure 2: Envelope location experiment using Titania mining explosions (to the left) and Geiranger quay construction explosions (to the right), S. Norway. PG and LG peak amplitude arrival times were read automatically from segmented detector output files and epicenter coordinates were obtained by a grid search procedure. Star is the mine site, diamonds envelope locations, and dots analyst-derived bulletin solutions. Almost all locations are within 10 km of the sites.

detectabilities (Mendi and Husebye, 1995). For a more comprehensive description of our novel envelope analysis scheme for reliable and robust epicenter determination, reference is made to a forthcoming paper by Husebye, Ruud and Dainty (1997).

Recognizing explosion sites without seismogram readings: neural network analysis of envelope transformed multistation SP recordings 3–6 Hz

An experienced analyst is often capable to locate an earthquake simply by a brief visual inspection of a single station recording. With easy access to digital recording the ability to recognize specific explosion sites at least in a semi-automatic manner has been explored by several investigators like Israelsson (1990), Harris (1991), and Riviere-Barbier and Grant (1993) among others. The basic idea is that explosion sources are spatially stationary for a given site and hence individual sites should be recognizable through combined paired and cluster correlation analysis of waveform records. Data used in such studies are mainly single station or array short-period vertical component records including envelopes. Research focus has been mainly on separating closely spaced explosions of various kind for which accurate 'ground truth' information is lacking. Here we describe a neural network scheme for recognizing specific *a priori* known explosion sites using envelope transformed (short period Z-component) network recordings of local events.

Typical of classification problems is an abundance of observational data but a somewhat poor understanding of the corresponding wavefield differences. Various kinds of neural network schemes have proved to be efficient tools in discrimination analysis (Dowla, 1996). In case of our site recognition problem the so-called interpolation and approximation neural nets (IANN; Winston, 1993) appears to be ideally suited for our purpose. It has the virtue that training (or learning) can be tied to solving a set of linear equations hence it is not necessary to involve any optimization method in order to obtain the weights.

The starting point is a neural net with an input vector x and a single output Y as illustrated

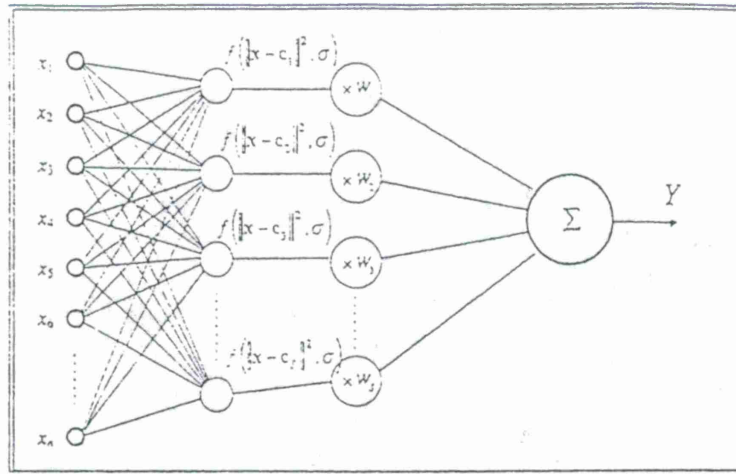


Figure 3: The Interpolation and Approximation Neural Net (IANN)

in Fig. 3. The physical basis is that Pg and Lg The input vector \mathbf{x} consists of sub-vectors, $\mathbf{x} = (\mathbf{x}_1, \mathbf{x}_2, \dots, \mathbf{x}_K)^T$ where K is the total number of stations used in analysis. Each sub-vector \mathbf{x}_m , $m = 1, 2, \dots, K$ is the envelop record for station m . The number of samples in each sub-vector is different because it is determined using the distance from each station to site when calculating time windows. Since signal amplitudes decay with the inverse of square root of distance, the different stations traces are weighted accordingly. The output Y may be a single number (the score) and preferably $Y \in [0, 1]$ for facilitating performance comparisons. The aim is to predict future Y -values for new (and unknown epicenters) given a proper data set (or learning set) of input-output combinations.

Let the output function $Y(\mathbf{x})$ have the following properties; (i) the value of Y is exactly equal to 1 whenever the inputs are drawn from one of the input-output combinations of the learning set. (ii) The value of Y should be close to 1 for future events stemming from sites subject to recognition analysis and close to 0 for all other events. The output Y is denoted the 'interpolation' function by Winston (1993) and may be expanded into a weighted sum of other functions $f_i(\mathbf{x})$, $Y(\mathbf{x}) = \sum_{i=1}^S W_i f_i(\mathbf{x})$, where S is the number of events in learning set. Using vector notation this might also be written as

$$Y(\mathbf{x}) = \mathbf{W}^T \mathbf{f} \quad (1)$$

where $\mathbf{W} = (W_1, W_2, \dots, W_S)^T$ is a vector of weights.

According to Winston, the convenient choice for $f_i(\mathbf{x})$ is a Gaussian function that may be written in the form $f_i(\mathbf{x}) = \exp(-\frac{1}{2\sigma^2} \|\mathbf{x} - \mathbf{c}_i\|^2)$, where the norm $\|\mathbf{x} - \mathbf{c}_i\|^2 = \sum_{j=1}^N (x_j - c_{ij})^2$ and N is number of observation points (total number of samples) in input. The shape of $f_i(\mathbf{x}) = f_i(\|\mathbf{x} - \mathbf{c}_i\|^2, \sigma)$ is controlled by given values of σ and \mathbf{c}_i . The latter is a reference vector obtained from the i -th event in the learning set. Because each $f_i(\mathbf{x})$ -value depends on only one \mathbf{c}_i -value the $f_i(\mathbf{x})$ -function clearly is tailoring the influence of the i -th learning sample on future predictions of Y . To summarize, the function Y is computed by a 2-layer net by which the single node in the second layer (see Fig. 3) computes a weighted sum of the outputs of the first layer nodes. In turn, each of the first layer nodes 'computes' a Gaussian function centered on the 'sample' input.

For a given σ -value of f_i a set of linear equations can be written for calculating the vector \mathbf{W} in eq. (1). In our IANN approach the output Y is 1 for samples drawn from the learning set, so

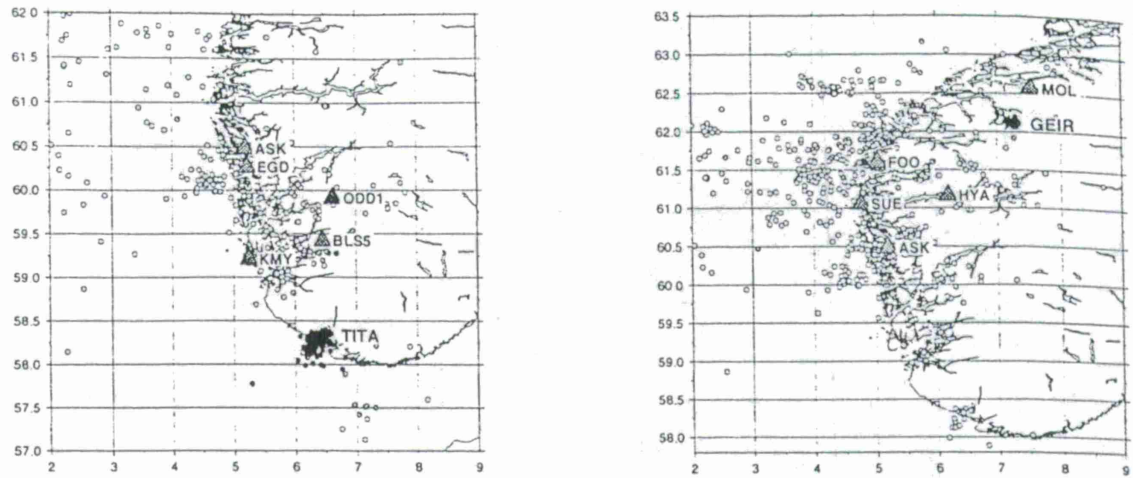


Figure 4: The stations of the Norwegian Seismograph Network (NSN) used in our site recognition analysis for the open pit mine at Titania (TITA; left figure) and underwater construction in Geiranger (GEIR; right figure). Rings are event epicenter locations taken from the NSN-bulletins while ring grey shading indicate recognition score: white is zero and dark-to-black for scores exceeding 0.6.

substituting the input x by the c_i we rewrite eq. (1).

$$\sum_{j=1}^S f_i(\|x_j - c_{ij}\|^2, \sigma) \cdot W_i = 1, \text{ for } i = 1, \dots, S \quad (2)$$

or, in matrix notation $AW = 1$ where $1 = (1, \dots, 1)^T$, $A_{ij} = f_i(\|x_j - c_{ij}\|^2, \sigma)$ and $W = (W_1, W_2, \dots, W_S)^T$. The linear system of equations in (2) comprises S unknowns but also S -equations. The A -matrix is positive definite and symmetric. However it may be ill-posed due to the arbitrary choice of events for learning set (some very small eigenvalues may appear if chosen envelopes are quite similar) so the SVD approach (singular value decomposition) was preferred for solving eq. (2). The record lengths are varying for individual stations and preferably both the P and LG envelopes should be included for all stations in a learning set. This in turn should comprises the largest number of recording stations available because this 'master' learning set then can easily be adjusted to any sub configuration of the network. This option is important since quite often one or more stations in a network are in a non-recording mode and corresponding new weights are fast to compute from eq (2). Using network envelopes have two advantages, (i) signal similarity is high so few events needed in learning set and (ii) good spatial resolution relative to single station/small array analysis like that of Israelsson (1990) and Harris (1991).

The data used in analysis are local event recordings from the Norwegian Seismograph Network (NSN) as shown in Fig. 4 for the time period September 1992 to May 1997. It is operated in a trigger mode implying that original waveforms from individual detecting stations are merged into so-called event files being easily accessible from disc. An essential element in our site recognition analysis is that of establishing with confidence appropriate event learning sets. In this regard, only

2 explosion sites proved convenient, namely the open pit mine Titania (TITA) and an underwater harbor construction site in Geiranger Fjord (GEIR). For both of these sites written notifications were received on individual shots fired. The NSN events used in analysis are not identical for TITA and GEIR reflecting varying station detectabilities for these 2 sites as shown in Fig. 4a and 4b. The first steps in analysis were to bandpass filter (3–6 Hz) the original waveform records and then compute the envelope transforms. Then the envelope files were screened for appropriate candidates for the TITA and GEIR learning sets conditioned on; (i) events with relatively large number of reporting stations and (ii) a minimum of 3 events (but more than 10 events is redundancy). In case (i) the point is that in average the TITA and GEIR explosions are recorded at 3 to 6 stations only so there is an obvious need to adjust the learning set to the specific event recordings at hand as discussed above. Even in the extreme case of only 2 recording stations site recognition was feasible. In Fig. 5 TITA and GEIR learning set envelopes are shown. The site recognition performance depends on the variance (σ parameter) in the presumed Gaussian distribution, see eq. 1; Extensive testing gave that the best population separation was obtained for a σ value around 0.04 which was used in subsequent analysis.

The outcomes of the site selection analysis are displayed in Fig. 4a and 4b and for GEIR also in Figs. 6 and 7. The performance for the Geiranger site was better which partly is attributed to a better site and station configuration (see also Fig. 2). Occasionally, 'true' Titania events had scores below the threshold of 0.4. To our surprise this was due to problems in calibration of the PC recording clock by the 'external' GPS clock. This is well known to the analyst but not in cases of small errors of a few seconds

Our site recognition scheme does not incorporate specific earthquake/explosion source selection criteria but essentially discriminate on spatial locations for presumed identical sources. However, for this type of problems we may for envelope generation use several bandpass filters reflecting those Pn and Lg-signal frequencies for which the best earthquake/explosion source separation has been obtained (Dowla, 1996). The main potential of our flexible explosion site recognition approach is to reduce significantly the analyst work in many industrial countries. For detail on the work reported here, we refer to Federenko et al. (1997).

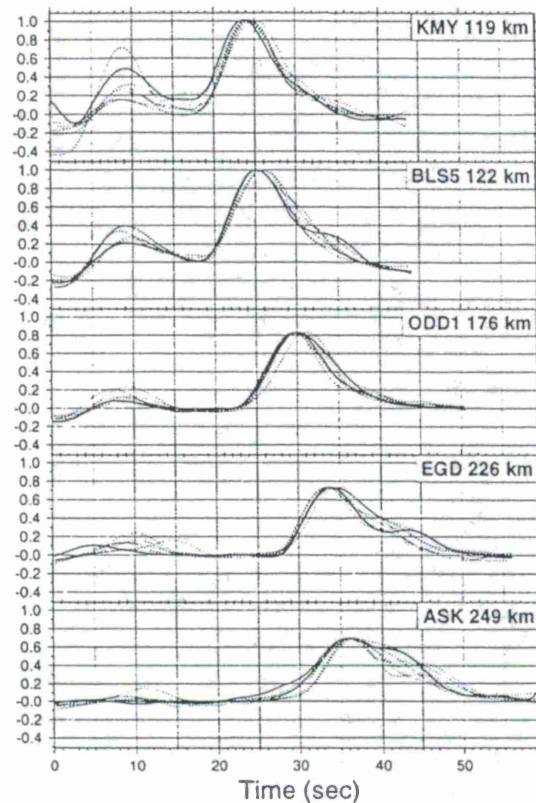
Synthetic wavefield simulation in 2D and 3D

On the theoretical level the work challenge is to incorporate 3D topography effects and adapting software codes to parallel machine computing so realistic crustal model can be used. The importance of incorporating anelastic effects is clear from the Lg-blockage study of Mendi et al. (1997). We are now developing a viscoelastic wave equation code for investigating this kind of problems in a more realistic manner. Our observational efforts aim at a better physical understanding of observed wavefield phenomena like prominent Rg-waves in the NORESS teleseismic P-coda.

CONCLUSIONS AND RECOMMENDATIONS

The great challenge for efficient CTBT monitoring is fast and reliable epicenter locations for local and regional events. Our experience here, based on extensive analysis of local network recordings, is that working with envelope transformed records significantly facilitate analysis work including

TITA Q=0.838 P=0.040 1993-351:14:17:19.375



TITA Q=1.000 P=0.040 1996-299:10:55:08.296

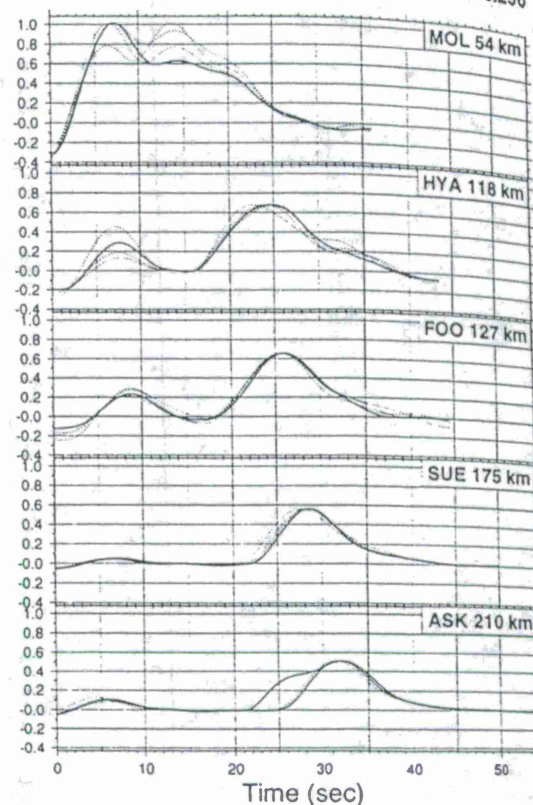


Figure 5: Envelope traces for individual station recordings for known (confirmed) Titania (left) and Geiranger (right) explosions used as learning sets in the site recognition analysis. These learning sets, typically comprising 3–10 events, are flexible in the sense that no of stations used can be reduced to 3 or even 2 if some of the station recordings are lacking or defect. Notice the consistent dominance of LG-phase and the often weak, first arriving PG-phase. The latter are occasionally lost in the noise and a safeguard against noise contamination is to eliminate the smallest envelope values that is 10% of total. All individual records are normalized and signal distance decay (inverse of square root of distance) are used as inverse station weights.

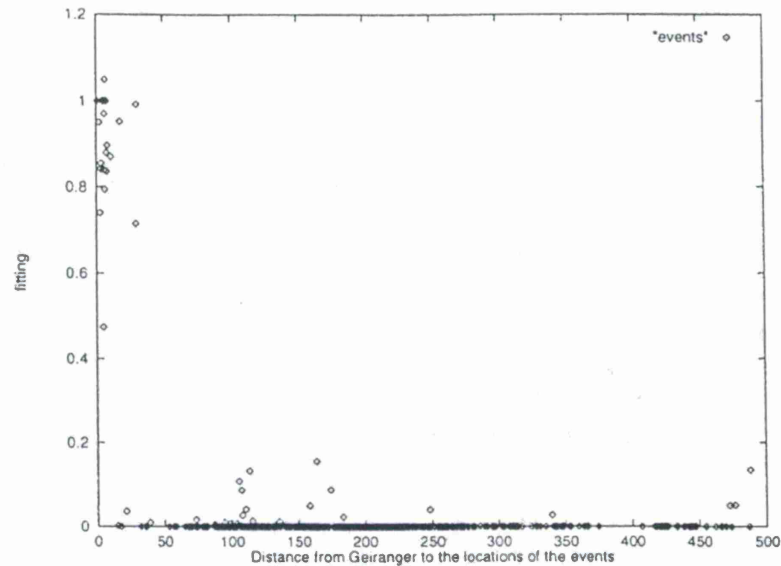


Figure 6: Site recognition scores for Geiranger for all events used in analysis and max. score for 'non-site' explosions was only 0.2. The 'distance' (horizontal axis) is the difference between the epicenter as reported in local bulletins (located from manual arrival time readings) and the site location.

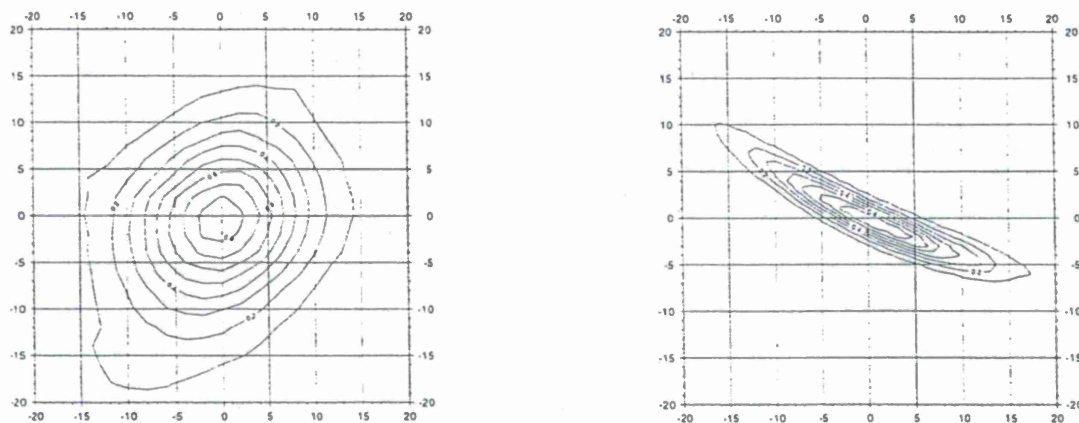


Figure 7: Simulating spatial score performance for Titania (left) and Geiranger (right) under idealized condition i.e., retaining optimum waveforms while time shifts corresponds to moving epicenter away from site. The near circular and prolonged shapes for TITA and GEIR respectively reflect corresponding differences in network geometries (Fig. 4). Max axis length is approximately 5 km for both sites for score contour of 0.6. This implies that for alien events to 'pass' IANN recognition their epicenters must at be within 5 km of site!

picking phases and their identification. Envelopes have only 2 prominent phases, Pg/Pn and Lg, and peak amplitude arrival times are easily pickable by computer. Testing this set of phase timing parameters our epicenter locations were slightly better than those of analyst based on manual readings. Also, envelope P and Lg reflect P- and S-energy transport in the crustal waveguide so their travel times are far less sensitive to crustal structures regimes than their counterparts Pn and Lg. In other words, envelope location schemes are transportable. A paradox in monitoring is that explosion signals from known mining sites are analysed as no knowledge of their source were available. We have trained the computer to literally recognize such sites in a most reliable manner thus significantly reducing analyst workload. This so-called IANN scheme is very flexible and can be adapted to envelope recordings from single station, array, 3-component, network or combinations hereof and different prefilter frequency bands as well. We strongly recommend that the operational efficiency of this approach to be fully explored both at EIDC and NDCs. Synthetics aimed at mimicing seismic wavefield observations is most instructive in fostering a better physical understanding of earthquake and explosion source differences contained in the seismic records but not easily extracted at local distances. We recommend that such studies are undertaken in 3D - the way the real Earth is.

References

- Dowla, F. U. (1996). Neural networks in seismic discrimination. In E.S. Husebye and A.M. Dainty (eds), *Monitoring a Comprehensive Test Ban Treaty*. NATO ASI Series, Kluwer Academic Publ., Dordrecht, The Netherlands, 777 - 789.
- Fedorenko, Y.V., E.S. Husebye, B. Heincke and B.O. Ruud (1997). Recognizing explosion sites without seismogram readings: Neural Network analysis of envelope transformed multistation SP recordings in the 3 - 6 Hz band. M/s in preparation
- Harris, D.B. (1991). A waveform correlation method for identifying quarry explosions. *Bull. Seism. Soc. Am.*, 81, 2395 - 2418.
- Henger, M., K. Koch, B.O. Ruud and E.S. Husebye (1997). The political sensitivity of seismic event location. *IRIS Newsletter*, in press.
- Hestholm, S. and B.O. Ruud (1997). 3-D finite difference elastic wave modeling including surface topography. M/s accepted for publication.
- Husebye, E.S., B.O. Ruud and A.M. Dainty (1997). Fast, robust and reliable epicenter determinations: Envelope processing of local network data. M/s submitted for publication.
- Israelsson, H. (1990). Correlation of waveforms from closely spaced regional events. *Bull. Seism. Soc. Am.*, 80, 2177 - 2193.
- Mendi, C.D. and E.S. Husebye (1995). Near real time estimation of seismic magnitude and moment via P and Lg phases. In: R. Console and A. Nikolaev (eds.), *Earthquakes induced by underground explosions*. NATO ASI Series 2, Springer-Verlag, Berlin, Germany.
- Mendi, C.D., Ruud, B.O., and Husebye, E.S. (1997). The North Sea Lg-blockage puzzle. *Geophys. J. Int.*, 130, in press.
- Riviere-Barbier, F., and L.T. Grant (1993). Identification and location of closely spaced mining events. *Bull. Seism. Soc. Am.*, 1527 - 1546.
- Winston, P.H. (1993). *Artificial Intelligence*. 3rd ed. Addison-Wesley Publ. Co., 491 - 504.
- van der Vink, G.E., and T. Wallace (1996). The political sensitivity of earthquake locations. *IRIS Newsletter*, Vol XV, No 3, 20 - 23.

Epicenter Estimation Using Erroneous Crustal Model(s) and Skew Regional Networks

Rong-Song Jih

HQ Defense Special Weapons Agency / PMP
6801 Telegraph Road, Alexandria, VA 22310

Abstract

A simple, hybrid procedure is proposed for seismic location at regional distances when [1] the crustal model is not known, [2] the seismic network is not calibrated, and [3] the azimuthal coverage of recording stations is poor. Among all parameters related to event location, the backazimuth estimated with a skew network (array) appears to be the least sensitive to the model error. This observation leads to a hypothesis that epicenters could be better constrained through triangulation using backazimuths derived from two skew, large-aperture subnetworks or arrays. If two subnetworks can be found such that the corresponding backazimuths are sufficiently apart (say, they intersect at an angle of 20° or larger), the resulting absolute mislocation associated with the intersection point is often less than 18 km, which is the permissible location accuracy as quoted in the Comprehensive Test Ban Treaty (CTBT). The origin time and source depth can then be obtained from a standard location procedure with the approximate epicenter held fixed. If the network can not be partitioned to provide two "good" backazimuths, then the conventional location procedure (which feeds on the phase picks altogether) can still be used. The proposed algorithm is tested with U.S. explosion Salmon of Oct 22, 1964. While the absolute location error associated with this hybrid method is typically comparable to that of the conventional method, this new approach offers a measurable quantity which positively flags when the location is more likely to be good - even for regions that are not calibrated. This could have important implications for the CTBT implementation as the proposed algorithm can readily be used as an *ad hoc* procedure on problem events while the International Monitoring System (IMS) stations are being deployed and calibrated gradually.

I. Objective

To develop algorithms which can effectively tackle the seismic location problem under the following difficult yet realistic situations to be encountered in a CTBT era: [1] the crustal model is not known, and hence an arbitrary global model (such as IASP91) will be used; [2] the seismic network is not calibrated, and hence the phase arrivals will be used as they are - without any correction; and [3] the azimuthal coverage of recording stations is poor.

II. Research Accomplished

II.1 Introduction

Seismic event location remains as one of the most important discriminants for separating natural tectonic and explosive events. Positive determination of a seismic event as deep suffices to classify it as an earthquake, while if it can be established that the event is shallow and if M_s -mb is small, then one may classify the event as an explosion with a small probability of error. Approximately 80% of known global earthquakes have focal depths greater than 50 km or are located more than 25 km at sea. Thus the vast majority of earthquakes can potentially be identified on the basis of location alone.

If the ground-truth location of a nearby seismic event is known, the arrival readings at seismic stations can be individually "calibrated" to match the predicted travel-time curves of some postulated velocity model. It has been long established that, with the station corrections, locations of other seismic events in the vicinity around the ground-truth event can be significantly improved. This is the standard approach of "calibration". In a special application of this technique, travel-time residuals are obtained from a least-square location program which is run with the depth constrained to the known "true" value. When these residuals are used as travel-time corrections in the same program run depth-free, nearby events can be located with smaller errors in depth. An elaboration of this specific application has been denoted the SRST (Source-Region-Station-Time) technique by Veith (1975) (see also Blandford, 1975). Alternatively, a postulated crustal velocity model can be adjusted so that the estimated hypocenter would perfectly match the ground-truth event. Thus, the fine-tuned velocity model can be used to determine the location of nearby events without the need of establishing residual corrections for individual stations. Both the SRST and the model-tuning procedures require at least one ground-truth event.

There are cases where no nearby event of known location is available. Furthermore, there are cases where not only the crustal model is not well known, the seismic stations could be sparse or even spread in a very skew geometry. This paper presents a procedure which could be particularly suitable for these disadvantageous situations. The basic idea is to decompose the recording network into (at least) two subnetworks so that each subnetwork is comprised of stations spread over only one side of the postulated epicenter. That is, each subnetwork should have a very large azimuthal gap and preferably a large aperture as well. The locations determined with these skew networks have huge uncertainty ellipses and hence these would be situations to avoid in traditional location procedures. However, the proposed algorithm somehow turns these situations to advantages in location. This procedure is illustrated with Salmon explosion, for which the true location is known. A globally-averaged continental model, IASP91 (Kennett, 1991), is arbitrarily chosen to mimic the situation where the true crustal structure of a region of interest may not be available, and seismic analysts would have to use a possibly erroneous crustal model to start with.

II.2 Proposed Location Algorithm

1. Group the recording seismic stations into at least two networks such that each network is on one side of the preliminary location and has a lateral aperture as large as possible.
2. Re-locate the event with each individual network. Since all stations are spread on one side, the error ellipse is inevitably elongated. The major axis of the ellipse points to the same direction of the most probable backazimuth as observed from that hypothetical array.
3. If the two major axes intersect at an angle larger than 20° , accept the intersection point as the location.
4. Otherwise go back to Step 1 and re-group the stations. Usually this can be easily done by simply looking at the map of all stations. If no two subnetworks can co-exist fulfilling the requirement of Step 3, then use the conventional location algorithms with all phase arrivals lumped into one group in the inversion. Alternatively, use the mean location of the two epicenters determined in Step 3.

This algorithm calls for a few steps that may not be regarded as favorite or appropriate in typical seismic location procedures. It is generally desirable to have a network with an azimuthal gap as small as possible - ideally the network should encircle the epicenter. In the proposed algorithm, however, stations on only one side are deliberately sought. This skew geometry, in conjunction with travel-time tables derived with a possibly erroneous crustal model, will inevitably lead to an incorrect epicenter. Nevertheless, the major axis of the prolonged error ellipse, not the epicenter itself, represents the best backazimuth one can get. This is true only if the stations are on one side and have a large aperture. Under these conditions, the proposed algorithm turns the disadvantages of skew network and erroneous crustal model into advantages in deriving the best estimate of backazimuth. Other pieces of information (such as the location itself and the size of error ellipse) are tossed out, as they are not well constrained under these same conditions. When two rays (or backazimuths) are available for triangulation, it is well known in geodesy that the ideal situation is when the two rays are perpendicular to each other. This may be difficult to achieve in reality, depending on the actual network configuration. Experience indicates that if the intersection angle is larger than 20° , then the result would generally be acceptable. If the intersection angle is too small, that means the two networks are virtually leading to backazimuths close to each other, *i.e.*, the two arrays are not providing additional or independent information. Thus the new algorithm will not offer a location result any better than what the conventional algorithm would do. Consequently, all stations should be lumped together in the location exercise in this case. Alternatively, one can use the mean location of the two epicenters determined with the two subnetworks. This is the procedure used in the following test ing case.

II.3 Example: Relocation of Salmon Explosion

Salmon, an underground nuclear explosion in Mississippi, was seismically recorded throughout North America and at some teleseismic stations. The 5-kt explosion was detonated at 16h 00m 00.0s UT on October 22, 1964, at a depth of 828.1 meters. The epicenter is $31^\circ 08' 31.57''\text{N}$, $89^\circ 34' 11.8''\text{W}$, in the Taut salt dome in Hattiesburg, Southern Mississippi. Extensive studies have been conducted for this event to validate crustal profiles toward different directions (Jordan *et al.*, 1966; Springer, 1966; Warren *et al.*, 1966). In the following discussion, IASP91 model (Kennett, 1991) will be deliberately used to test the robustness of the proposed algorithm. No station correction will be applied to this crustal model, which is basically a world-wide average.

Jordan *et al.* (1966) published phase picks recorded at 143 stations for Salmon explosion. Thirty arrivals from stations within 10° are used in the following tests. The stations are partitioned into nine groups which are labeled "a" through "i". Selecting two subnetworks at one time, there are 36 possible combinations in total. Table 1 below summarizes the results of 36 tests of using individual subnetworks (columns 1 and 2), standard method with two subnetworks combined (column 3), as well as the triangulation result using two backazimuths (column 4). Columns 1 and 2 have three entities: the network identification, number of stations in the network, and the mislocation (in km) associated with this network. Column 3 is self-explanatory: the number represents the mislocation measured in km associated with the corresponding combined network. Column 4 has two numbers. The first number is the mislocation of the proposed location method based on the triangulation. The second number is the mislocation corresponding to the mean location of two epicenters estimated with two subnetworks listed in columns 1 and 2. The intersection angle of the two corresponding major axes is labeled as the diagnostic (measured in degrees; column 5). An asterisk in columns 4 and 5 indicates that the diagnostic is less than 20° , and the mean location is used. It is clear that whenever the intersection angle is larger than 20° or so, the resulting epicenter has an absolute error less than 18 km, a radius corresponding to the 1000 km^2 confidence region as specified in the CTBT. If the intersection angle is less than 20° , the two backazimuths are close to each other, and the location would be off (see lines marked with an asterisk). In these cases, the epicenters derived from the standard location algorithm should be used. Some of the subnetworks could give very good epicenter without the need of using triangulation. However, the triangulation step provides a quantitative measure as when the location could be reliable, using the intersection angle as a diagnostic. Out of the 36 tests listed in Table 1, 32 have a location error within 18 km when this hybrid method is used.

Figure 1 illustrates several major features that constitute the corner stones of this proposed algorithm. The testing network, labeled "h", comprises of four stations (WMO, FAY, GRV, and FLO) spread on the northwestern quadrant of the event, with a maximum azimuthal gap of 305° . When the first P arrivals of these four stations are fed into the standard location routine, six different continental models (labeled "I", "J", "B", "D", "L", and "K" in Figure 1) lead to locations that are off from 31.6 km to 53.9 km. Obviously these locations are very poor, due to the sparse, skew geometry of the network plus the erroneous crustal model. Nevertheless, the uncertainty ellipses associated with these six crustal models consistently aligned along a backazimuth between 147.67° and 148.95° .

Figure 2 shows the testing result using the IASP91 model as well as networks "h" and "i". The configuration of the networks and the location of Salmon are shown in the top frame of Figure 2. Both networks "h" and "i" have essentially a linear configuration. The ground-truth location of Salmon event is shown in a plus sign. The two epicenters estimated with networks "h" and "i" are shown as open circles, respectively, which are outside the 18 km permissible location accuracy as specified in the CTBT (the dashed circle). The two major axes as determined by the two networks intersect at an angle of 43.94° , and the resulting intersection point (blue star) is only 1.8 km away from the ground-truth location. If the conventional method is applied to the network with all seven stations combined, the location (unfilled star) is 5.0 km off. In this case, certainly the result of conventional approach is not bad either. What the adaptive method would offer is a measurable quantity, namely the intersection angle, which tells us whether we should use the triangulation result or use the mean location (without triangulation).

Table 1. Relocation Results Using IASP91 Model and Various Networks

Network 1	Network 2	Conventional	Adaptive Method	Diagnostic
a 5 6.1	b 6 8.9	a+b 11.1	a#b 28.3 7.0*	14.66*
a 5 6.1	c 9 12.4	a+c 7.4	a#c 4292 3.6*	0.12*
a 5 6.1	d 7 7.3	a+d 11.9	a#d 13.6 3.3	50.08
a 5 6.1	e 6 8.2	a+e 2.8	a#e 22.3 3.3*	12.45*
a 5 6.1	f 7 16.6	a+f 4.2	a#f 39.6 6.1*	17.44*
a 5 6.1	g 8 41.4	a+g 7.8	a#g 11.2 21.7	33.71
a 5 6.1	h 4 48.5	a+h 9.1	a#h 7.8 22.9	20.48
a 5 6.1	i 4 24.5	a+i 9.5	a#i 7.9 15.2	23.46
b 6 8.9	c 9 12.4	b+c 4.6	b#c 7.9 2.5*	14.54*
b 6 8.9	d 7 7.3	b+d 5.4	b#d 8.5 6.5	35.42
b 6 8.9	e 6 8.2	b+e 2.6	b#e 4.9 0.7	27.11
b 6 8.9	f 7 16.6	b+f 6.4	b#f 10.2 3.9	32.1
b 6 8.9	g 8 41.4	b+g 9.4	b#g 2.2 24.6	48.37
b 6 8.9	h 4 48.5	b+h 3.4	b#h 7.4 20.1	35.14
b 6 8.9	i 4 24.5	b+i 8.3	b#i 27.6 16.3*	8.80*
c 9 12.4	d 7 7.3	c+d 5.5	c#d 6.3 7.6	49.96
c 9 12.4	e 6 8.2	c+e 2.0	c#e 18.7 10.0*	12.57*
c 9 12.4	f 7 16.6	c+f 13.3	c#f 11.7 14.4*	17.56*
c 9 12.4	g 8 41.4	c+g 2.7	c#g 4.6 17.5	33.83
c 9 12.4	h 4 48.5	c+h 7.6	c#h 17.4 29.3	20.6
c 9 12.4	i 4 24.5	c+i 5.2	c#i 15.1 6.1	23.34
d 7 7.3	e 6 8.2	d+e 5.6	d#e 7.4 4.4	62.53
d 7 7.3	f 7 16.6	d+f 5.9	d#f 7.3 8.9	67.52
d 7 7.3	g 8 41.4	d+g 6.7	d#g 6.2 23.4	83.79
d 7 7.3	h 4 48.5	d+h 4.0	d#h 8.0 22.5	70.56
d 7 7.3	i 4 24.5	d+i 12.4	d#i 18.5 12.0	26.62
e 6 8.2	f 7 16.6	e+f 3.5	e#f 81.4 12.3*	4.99*
e 6 8.2	g 8 41.4	e+g 1.5	e#g 4.9 17.0	21.26
e 6 8.2	h 4 48.5	e+h 1.2	e#h 15.4 28.3*	8.03*
e 6 8.2	i 4 24.5	e+i 2.7	e#i 3.1 9.1	35.91
f 7 16.6	g 8 41.4	f+g 13.9	f#g 18.2 15.5*	16.27*
f 7 16.6	h 4 48.5	f+h 11.0	f#h 171.3 31.8*	3.04*
f 7 16.6	i 4 24.5	f+i 10.3	f#i 13.4 4.8	40.9
g 8 41.4	h 4 48.5	g+h 7.0	g#h 16.4 6.2*	13.23*
g 8 41.4	i 4 24.5	g+i 6.3	g#i 3.9 29.2	57.17
h 4 48.5	i 4 24.5	h+i 5.0	h#i 1.8 17.7	43.94

Several earlier location studies have experimented with the Salmon data with various conditions. To make the comparison meaningful, only those without station corrections are quoted here. Based on 45 stations at distances between 1.5° and 17°, Herrin and Taggart (1966) derived a location 13.2 km off. Rivers *et al.* (1981) used arrival times and backazimuths measured at 12 LRSM stations, and their locations had an absolute error ranging from 37.6 km to a few hundred kilometers. Comparing to these earlier results, it is true that using the conventional location algorithm,

all 36 configurations of seismic network as shown in Table 1 already give very good results, with the largest mislocation being 13.9 km only (Case "f+g" in Table 1). The problem with the conventional location procedure is that the user usually does not have any clue as when the mislocation would be small. The so-called uncertainty error ellipse does not account for the location bias due to model error. The proposed hybrid method does not always offer a location better than that derived from the standard method. It does provide, however, a measurable quantity which tells the user if the triangulation can be used (for a location within 18 km), or the mean location should be used (with a location accuracy comparable to that of standard approach).

III. Discussion, Conclusion, and Recommendation

Quite a few investigators have examined the utility of including azimuth measurements as constraints on location. Early studies by Shilen and Toksöz (1973), Julian (1973), Gjoystdal *et al.* (1973) considered the use of azimuth estimates from arrays in locating primarily teleseismic events. Smart (1978) used Lg azimuth estimates to locate regional events. Rivers *et al.* (1981) extends Smart's (1978) study to incorporate the azimuths in a linearized inversion procedure. However, their azimuth estimates were obtained from three component stations and were less accurate than those deduced from frequency-wavenumber (f-k) processing of NORESS-type array data. Thus Rivers *et al.* (1981) concluded that their azimuth estimates were not very useful, while Bratt and Bache (1988) illustrate that adding azimuth measurements obtained from array data do better constrain the location. The adaptive procedure tested here appears to work exceptionally well because the two azimuth estimates required in locating the event are accurately deduced from networks which can also be considered as two arrays with large apertures. For an array like this, the conventional frequency-wavenumber processing scheme can not be applied because the short-period waveforms would be highly incoherent across the vast area, whereas the long-period signals are not precise enough. Furthermore, in many cases only the arrival readings are available and the f-k technique can not be applied without waveform data.

The proposed new hybrid location procedure consists of a step of azimuth estimation, followed by a simple triangulation step using the optimal azimuth estimates. This procedure is "adaptive" in several senses:

- [1] the technique used in estimating the azimuth overcomes the difficulties in applying the f-k processing to large-aperture array and in the case of lacking waveform data,
- [2] the original network geometry may be severely skew, yet the procedure can turn this disadvantage into advantage to better constrain the azimuth, and
- [3] a good initial crustal model is not required, thus the calibration information may become less critical. In the case the network has too few stations to warrant an adequate partition of the network, the conventional location procedure can still be applied.

Note that in this staged location procedure, different velocity models can be assigned to the two subnetworks so as to best represent the underlying geology and geophysics along different paths, if necessary. In fact, in most cases the resulting final location is relatively less sensitive to the choice of initial velocity model. Thus an advantage of this adaptive location procedure is that perhaps the calibration can be deferred to a later stage. This could have a major implication for both the monitoring and implementation of the CTBT as the calibration may sometimes be delayed to a later stage after more seismic stations are deployed.

Chang *et al.* (1983) (and Chang, 1985) correctly pointed out that station residuals are highly correlated when an erroneous crustal model is used (see also discussion in Blandford, 1995). The assumption that all phase arrivals are uncorrelated as used in many inversion routines is simply

wrong. Chang and his colleagues suggested to establish a covariance matrix of the residuals and to incorporate the covariance matrix into the location inversion. However, the correlation among station residuals is not just a function of the inter-station distances, it is also a function of the earth model. Even if we assume that the crust is truly one dimensional, the larger the discrepancy between the true and the postulated crustal models, the stronger the correlation among stations on the same side from the epicenter. The residual covariance structure also depends on the geometry (relative to the source) of each pair of stations. For instance, assuming the crust of interest is truly one dimensional (yet unknown), stations around the epicenter with the same epicentral distance but different azimuths will have extremely high correlation in the residuals. These make the residual covariance structure very difficult to be represented as a function of the inter-station distance alone. This could be the reason why Chang's approach only provides a marginal improvement in locating NTS events. The proposed hybrid approach appears to be able to get around this difficulty.

Only the absolute location error is addressed in this paper. If seismologists are confident that an epicenter estimate is within 18 km to the true location of a suspicious event, then the area to be inspected by the OSI team is about 1000 km^2 , which is acceptable according to the CTBT. As for other potential applications of this procedure (such as routine generation of seismic bulletins), this procedure offers a quantifiable measure as whether the location derived with conventional location algorithms would be reliable. Location precision associated with this new procedure can be quantified in a straightforward manner with resampling techniques, such as Monte-Carlo iterations or bootstrapping.

IV. Disclaimer

A historical U.S. explosion has been used in this study solely to validate and illustrate the proposed location algorithm. This should not be interpreted, either expressed or implied, as any change, or indication of change, in U.S. Defense Department's strong interest in monitoring nuclear explosions outside U.S. territory.

V. References

- Blandford, R. R. (1975). *Use of Source-Region-Station Time corrections at NTS for depth estimation*, Report SDAC-TR-75-4, Teledyne Geotech, Alexandria, VA.
- Blandford, R. R. (1995). Regional seismic event discrimination, in "Monitoring a Comprehensive Test Ban Treaty" (E. S. Husebye and A. M. Dainty (eds), NATO ASI Series E: Applied Sciences, Vol. 303, pp. 689-719, Kluwer Academic Press, Dordrecht, The Netherlands.
- Bratt, S. R. and T. C. Bache (1988). Locating events with a sparse network of regional arrays, *Bull. Seism. Soc. Am.*, **78**, 780-798.
- Chang, A. C. (1985). *Seismic event locations using multiple phases*, Final Report TGAL-85-10, Teledyne Geotech Alexandria Laboratory, Alexandria, VA.
- Chang, A. C., R. H. Shumway, R. R. Blandford, and B. W. Barker (1983). Two methods to improve location estimates - preliminary results, *Bull. Seism. Soc. Am.*, **73**, 281-295.
- Herrin, E., and J. Taggart (1966). Epicenter determination for the Salmon event, *J. Geophys. Res.*, **71-14**, 3503-3506.
- Jordan, J. N., W. V. Mickey, W. Helterbran, and D. M. Clark (1966). Travel times and amplitudes from the Salmon explosion, *J. Geophys. Res.*, **71-14**, 3469-3482.
- Jordan, T. and K. A. Sverdrup (1981). Teleseismic location techniques and their application to

19th CTBT Research Symposium

- earthquake clusters in the South-central Pacific, *Bull. Seism. Soc. Am.*, **71**, 1105-1130.
- Julian, B. R. (1973). Extension of standard event location procedures, in "Seismic Discrimination SATS", Lincoln Laboratory, Massachusetts Institute of Technology, DDC AD-766559, Cambridge, Massachusetts.
- Kennett, B. (editor) (1991). *IASPEI 1991 Seismological Tables*, Research School of Earth Sciences, Australian National University, 167 pp.
- Rivers, D. W., J. A. Burnetti, and A. C. Chang (1981). *Use of back azimuth measurements in seismic event location with regional data*, Report VSC-81-17, Vela Seismological Center, Alexandria, Virginia.
- Shilen, S., and M. N. Toksöz (1973). Automatic event detection and location capabilities of large aperture seismic arrays, *Bull. Seism. Soc. Am.*, **63**, 1275-1288.
- Smart, E. (1978). *A three-component, single-station, maximum-likelihood surface wave processor*, Report SDAC-TR-77-14, Teledyne Geotech, Alexandria, Virginia.
- Springer, D. L. (1966). Calculation of first-zone P wave amplitudes for Salmon event and for decoupled sources, *J. Geophys. Res.*, **71-14**, 3459-3467.
- Veith, K. F. (1975). Refined hypocenters and accurate reliability estimates, *Bull. Seism. Soc. Am.*, **75**, 1199-1222.
- Warren, D., J. H. Healy, and W. H. Jackson (1966). Crustal seismic measurements in southern Mississippi, *J. Geophys. Res.*, **71-14**, 3437-3458.

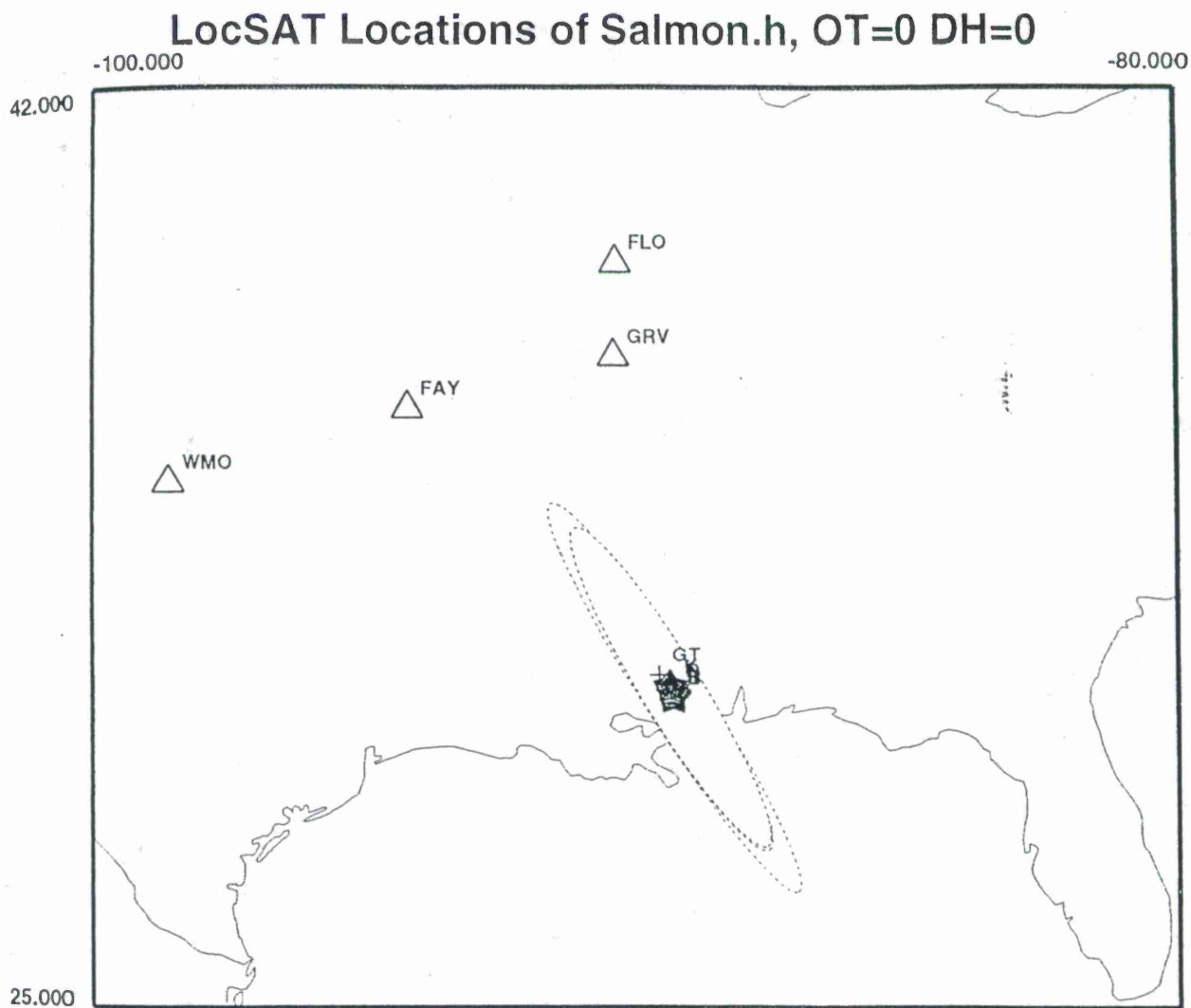


Figure 1. Epicenters of Salmon explosion as determined with the first arrivals reported at four regional stations: WMO, FAY, FLO, and GRV, using travel-time tables of several one-dimensional continental models. The resulting epicenters are shown in blue stars, and the plus sign represents the true location of Salmon explosion. Due to the poor azimuthal coverage of the stations, with a maximum gap of 305° , the mislocations corresponding to six typical continental models vary from 31 to 54 km, which are not impressive at all. Nevertheless, all the elongated error ellipses point to almost the same direction. Two skew, large-aperture networks like the one tested here would suffice to provide a "good" epicenter estimate, provided the two rays used in triangulation are sufficiently apart.

LocSAT Location of Salmon, OT=0 DH=0

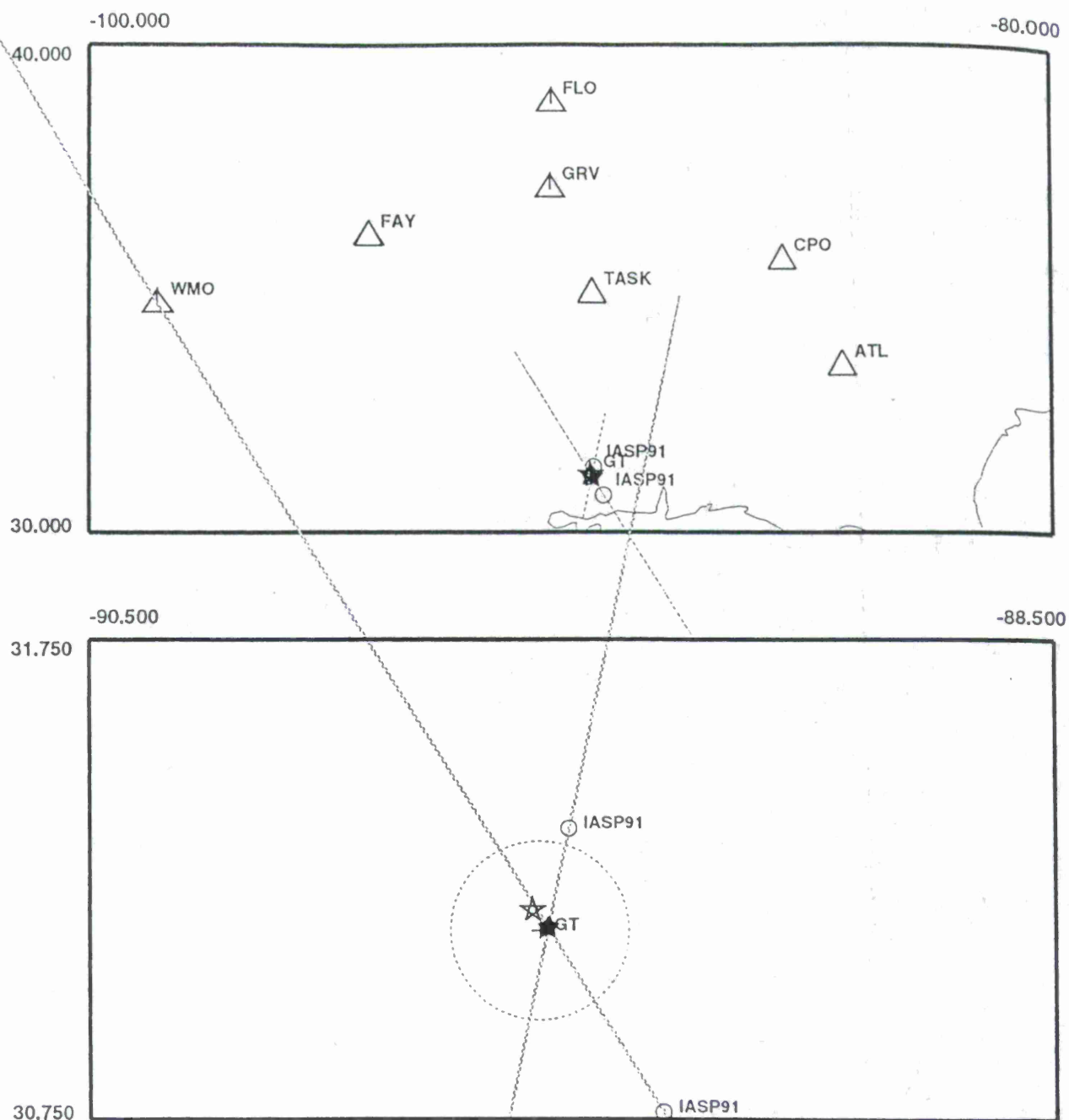


Figure 2. An illustration of the proposed location procedure. Shown on the top frame are the 7 stations which are grouped into 2 networks, "h" and "i". Network "h" consists of WMO, FAY, GRV, and FLO (see Figure 1), whereas network "i" consists of ATL, CPO, TASK, and FAY. The bottom frame shows the locations of Salmon using various networks and methods. Open circles are epicenters estimated with networks "h" and "i", which have offsets of 48 and 25 km, respectively. The dashed circle corresponds to the 1000 km² uncertainty area as specified in the CTBT. If the two networks are combined, the standard location routine gives a location which is 5 km away (unfilled star). Applying the proposed location procedure to these two networks lead to an epicenter (blue star) which is 1.8 km from the ground truth location.

EVENT MAGNITUDES, CAPABILITY MAPS AND MAGNITUDE THRESHOLDS

Tormod Kvaerna and Frode Ringdal
NORSAR
RO. Box 51
N-2007 Kjeller, Norway

Sponsored by Department of Defense
Nuclear Treaty Programs Office
Contract No. F08650-96-C-0001

ABSTRACT

We have developed an algorithm for obtaining short-term average (STA) based magnitude estimates for all primary stations in the current PIDC network. This has been done through analysis of a large event data base, where individual relations between A/T and STA were found for each station.

Preliminary results show that the STA based event magnitudes are in close agreement with the event magnitudes provided by the PIDC, and that the STA based station magnitudes have a lower standard deviation than the A/T based PIDC station magnitudes.

By calculating continuous station magnitudes (noise magnitudes), we have developed a simplified algorithm for assessing network detection capability. During noise conditions these results are in excellent agreement with the detection capability of the PIDC primary network as estimated using the conventional statistical approach (SNAP/D). But unlike the conventional approach, our approach is able to immediately accommodate variations in detection capability caused by "unusual" conditions like station outages, large earthquakes and aftershock sequences, which may cause the network detection capability to deteriorate for hours.

We have made a comparison between these continuous capability maps and the so-called magnitude threshold maps (threshold monitoring, TM). The TM maps include no assumptions on the SNR required for detection or the minimum number of stations required to generate an event hypothesis, but instead use the observed seismic field to place an upper limit to the magnitude of possibly hidden events.

As an example, during background noise conditions the capability maps shows that the PIDC primary network will generally be unable to detect events below mb 3.5 for the region north of 30 degrees N. On the other hand, the TM map tells us that if there was an event in this region it could not have a magnitude above 3.0. In somewhat simplified terms, we could say that during noise conditions the TM approach is able to "monitor" an area at an mb level about 1.0 unit lower than the conventional "detection based" approach. During the occurrence of large earthquakes, we will show that this difference in monitoring capability can become even larger.

Keywords: Body-wave magnitudes, detection capability, threshold monitoring

OBJECTIVE

The objective of the research conducted under this contract has been to investigate the potential and usage of the threshold magnitude calculations when used as a part of a CTBT verification system. In particular, we have studied the relation between magnitudes calculated from short-term averages (STAs) and traditional A/T measurements. Furthermore, we have emphasized research on the usage of continuously updated detection capability maps and maps of upper magnitude limits, both calculated from STA-based magnitude estimates.

RESEARCH ACCOMPLISHED

Definition of station and network magnitude thresholds

Several studies have confirmed that global observations of body-wave magnitude m_b are normally distributed with a standard deviation of about 0.4 m_b units when station corrections are not employed (a.o., Veith and Clawson, 1972; Ringdal, 1976). This is one of the basic assumptions behind the calculation of m_b magnitude thresholds.

If we look for a hypothetical event at a given location and origin time, and consider a "noise situation" at a given station i , i.e., that there are no phase detections at the predicted phase arrival time of the hypothetical event, we can calculate a so-called "noise magnitude" a_i .

If a hypothetical event of magnitude m really was present, it would have phase magnitudes m_i normally distributed around m , and for station i we would know that $m_i \leq a_i$. This is used in the statistical derivation of the single station and network magnitude thresholds, and for details we refer to Ringdal and Kværna (1989, 1992).

Using the formulas developed for calculation of network magnitude thresholds we find that if we e.g., have one single station observation with a "noise magnitude" of m_b 4.0 for a hypothetical event at a given location and origin time, we can say (with 90 per cent confidence) that a hypothetical event would need to have an m_b less than 4.52. If we, on the other hand, had two independent station observations each with a "noise magnitude" of m_b 4.0, we can say (with 90 per cent confidence) that a hypothetical event would need to have an m_b less than 4.20. In a similar way, all network station observations of "noise magnitude" can be combined to place an upper m_b limit on a hypothetical event occurring at a given location and origin time.

It is important to employ a certain degree of conservatism in these statistical threshold calculations, so as to avoid using values too far out in the "tail" of the probability distribution.

By repeating the calculation of network magnitude thresholds in origin time steps, we obtain a so-called threshold trace for a given geographical location. It has been shown in several NOR-SAR reports and papers that such a threshold trace can be effectively used to conduct a site-specific threshold monitoring of interesting areas like the Novaya Zemlya and Lop Nor nuclear test sites.

By gridding the Earth into discrete target areas, we can compute threshold traces for each separate target area, and then interpolate to create global or regional maps of magnitude thresholds. From inspecting these maps we can get an instant picture of the monitoring capability of the

network, as well as being able to identify regions and time intervals with particularly high magnitude thresholds. The primary causes of such increases would be signals and coda from large events and/or station outages.

What happens to the magnitude thresholds when an event occurs?

In cases when signals are observed from an event occurring in the target area, it would be appropriate for the detecting stations to use $m_i = a_i$ and not the weaker constraint $m_i \leq a_i$, which is one of the basic assumptions behind the statistics of the network threshold calculations. In practice, the use of $m_i \leq a_i$ instead of $m_i = a_i$ will cause the calculated magnitude threshold to be biased low. This bias is small for events detected by few stations, but will generally increase with the magnitude of the event. In such a situation, the correct approach would be to use the maximum-likelihood formalism of Ringdal (1976), taking into account both the detecting and non-detecting stations of the network. But this will require that we have available both the event locations from the standard network processing, as well as knowledge of which stations had detections on the beams used for threshold calculations.

As a preliminary solution to this problem, we have chosen to provide information on the detected events (from the AELs or the REBs) together with the threshold maps and threshold traces, such that the user can be aware that the calculated threshold magnitudes could be biased low around the origin time and location of the events.

Strictly speaking, the magnitude threshold calculations should also handle situations when an event occurred in the target area, without being detected by the processing algorithms. The reason for this could be SNRs below the detection thresholds or too few stations detecting the event. In this case the bias in threshold magnitudes will be negligible, and the conservativeness used in our parametrization should be able to accommodate such situations.

As an example, a 3 station event in Finland with a maximum-likelihood m_b of 2.71 resulted in a 90% magnitude threshold of 2.66 using data from the full primary network. This event was detected by the processing algorithms, and illustrate that the bias effect resulting from ignoring the detection information is very small for such low-magnitude events.

Tuning of the PIDC primary network

In order to obtain useful and reliable estimates of the magnitude thresholds, we have tuned the stations in the primary network. From analysis of a fairly extensive event database of 20-60 events per station, we have for each of the stations derived the following parameters:

- The frequency bands for filtering of the beams used to monitor targets in the different distance regimes (local, regional or teleseismic).
- The relations between the manual A/T measurements in the 0.8-4.5 Hz band and the STA values of the filtered beams. This filter band has been chosen to ensure compatibility between the PIDC magnitude measurements and the magnitude thresholds provided by the Threshold Monitoring (TM) system.

- For the arrays, we have derived beam sets that ensure complete coverage of the entire Earth, using the constraint that the maximum allowable beamloss caused by mis-steering of the beams was 3 dB. In addition, we have derived expected values for the signal loss by beam-forming.

The derivation of frequency bands for filtering of the beams was a quite difficult task, as it often involved balancing of two conflicting demands. The first was to ensure that there was a good correspondence between the STA values of the filtered beams and the manual A/T measurements in the 0.8-4.5 Hz band. On the other hand, we also wanted to obtain low magnitude thresholds during regular noise conditions.

In order to verify the quality of our tuning, we have for about 15 events compared the PIDC station magnitudes with the station magnitudes derived from the STA traces. The agreement seems to be remarkably good, but because of the small raw data set available at NORSAR, we have not been able to compile any comprehensive statistics.

An example is given in Table 1, for an event located southwest of Africa. For all primary stations outside the distance interval 97-125 degrees, we have computed station magnitudes from the STA traces of the TM system. Except for the station LPAZ, we find a very close agreement between the PIDC station magnitudes and the STA magnitudes. We suspect that the PIDC station magnitude at LPAZ actually is a measurement of the strong noise field leaking into the 0.8-4.5 Hz filter band. The dominant period of 1.6 seconds indicates this. For LPAZ, we have in the teleseismic regime decided to use a bandpass filter between 1.0 and 4.5 Hz for calculation of STA station magnitudes. In this particular case, this filter ensured that we actually measured the signal. At the bottom of Table 1 we show a comparison between the PIDC network magnitude, the PIDC network magnitude of the primary stations within 97 degrees, the STA based network magnitude of the primary stations within 97 degrees, and the STA based network magnitude of all primary stations outside the distance interval 97-125 degrees. A significant feature is the lower standard deviation of the STA based station magnitudes, compared to the magnitudes calculated at the PIDC.

When the tuned TM system is installed on the PIDC testbed, we will investigate whether the PIDC and the TM system provide on the average the same station and network magnitudes, and determine to which extent TM magnitudes are useful to supplement PIDC magnitudes.

Network capability and magnitude thresholds

As another indirect test of the quality of the tuned TM parameters we have computed a simplified three-station detection capability map of the primary network using data from a time interval without any reported events. Our TM capability map has been computed by choosing the third lowest of the station "noise magnitudes", and then adding $0.7 m_b$ units to accommodate an SNR of 5.0 required for phase detection. The TM capability for 1997-058:20.08 is shown in Fig. 1, where the filled circles symbolize operating primary stations and the open circles symbolize primary stations without available data. This capability map show striking similarities with the simulated 90% detection threshold for the GSETT-3 network presented in Fig. 5.2.a of CD report no. 1423 (4 September 1996), although there are a few minor differences between the configurations of the GSETT-3 network and the operating primary network of February 27,

1997. Thus, the very simple "third lowest TM magnitude" approach provides an excellent approximation to the standard 3-station 90% capability maps.

It should also be emphasized that the capability map of the GSETT-3 network is derived from statistical models of signal and noise characteristics, whereas the TM capability is derived from actually observed noise data. In this way, the TM approach is able to immediately accommodate variations in detection capability caused by "unusual" conditions like station outages, large earthquakes or aftershock sequences, which may cause the network capability to deteriorate for hours.

In contrast to the "capability maps" discussed above, the standard TM maps include no assumptions on the SNR threshold required for detection or the minimum number of stations required to generate an event hypothesis. Instead, the observed "seismic field" is used to place an upper limit to the magnitude of possibly hidden events. Fig. 2 shows the 90% magnitude threshold for the same origin time instant as used in the capability map of Fig. 1. While the capability map of Fig. 1 tells us that for most of the region north of 30° N our processing algorithms will be unable to detect events below m_b 3.5, the threshold map of Fig. 2 tells us that if there was an event in this region it could not have a magnitude above 3.0. For the areas close to some of the stations, the magnitude thresholds are even below 2.5.

In somewhat simplified terms, we could say that the TM approach is able to "monitor" an area at an m_b level about 1.0 unit lower than the conventional "detection based" approach.

In order to illustrate the effect of the occurrence of a large earthquake, we have estimated the three-station detection capability and the magnitude thresholds for a time instant 9 minutes after the origin time of a M_S 7.2 earthquake located in Pakistan. The capability map of Fig. 3 tells us that except for parts of Australia and parts of north and south America, the detection threshold is above 4.5 for the entire Earth. For parts of Asia and Africa, the threshold even exceeds 5.0.

When turning to the magnitude thresholds of Fig. 4, we find significantly smaller numbers. The usefulness of the threshold map is illustrated by the fact that while we could not be certain to detect a magnitude 5 event in parts of Asia and Africa, the threshold map tells us that a hypothetical event in these regions could not have had a magnitude significantly above 4. For most parts of the world, we find the upper magnitude limits to be more than 1.0 m_b unit lower than the three-station detection capability in this case. So the "gain" by applying the TM technique is even greater than during noise conditions.

CONCLUSIONS AND RECOMMENDATIONS

Usage of magnitude thresholds and capability maps in CTBT monitoring

It should be evident from the discussions above that both the magnitude threshold maps and the detection capability maps could be useful supplements in the monitoring of a CTBT. While the capability maps provide the lowest event magnitude the processing system is likely to detect, the magnitude threshold maps put an upper limit to the size of a possibly hidden event.

An application of the capability maps and the threshold maps would be to provide continuous confirmation and quantification of the monitoring capability of regions of interest to the international community. In addition, these maps would also provide an instantaneous warning and quantification of a reduced monitoring capability during station outages or high-noise intervals.

Another scenarios for the use of the results from the TM system would be investigation of time intervals for which questions have been raised regarding possible non-compliance with the treaty. By going back to the magnitude threshold maps for a given region and time interval, we could by selecting the pointwise maxima of the magnitude threshold maps for the given time period, get a useful overview of the maximum size of a hypothetical event in the region during this time period. This could be helpful to decide if further investigation would be needed. Along the same lines we could display the threshold trace for given target areas. If this trace shows an increase that is not caused by any known event, and at the same time exceed a magnitude threshold of interest, it might be meaningful to continue the investigation. E.g., our one-month monitoring experiment of the Novaya Zemlya test site (Kværna, 1992) showed that from inspection of the threshold traces, we were able to exclude 99.7% of the total time from search for signals from possible events of $m_b > 2.6$ at the test site. The remaining 0.3% of the time contained threshold increases that could be explained by signals from detected interfering events.

If the magnitude thresholds for a given region show increased values during a particular time interval, we would like to know the reason why so happened. Signals from events located outside the region, station outages or increased noise levels at some stations are usually the main causes. By looking into the event bulletins and the station performance reports it should be possible to explain the majority of the threshold increases. But if threshold peaks remain unexplained, we should start to look more closely for events in the target region. This could be done by optimized manual data analysis of the stations known to have the best capability for the given target region, and/or by requesting and analyzing additional data.

Future applications

For the future, we have in mind several interesting applications of data from the TM system that could be useful in the CTBT context.

E.g., we showed in the previous chapters that there seems to be a very good agreement between the PIDC magnitudes and the STA based magnitudes from the TM system. It would therefore be interesting to investigate if the usage of STA based magnitudes will provide any improvement to the network m_b estimates. By combining the STA traces with a detector, it will also be quite straightforward to implement procedures for automatic maximum likelihood m_b estimation, which again will help to reduce the m_b bias problem for smaller events.

Another interesting application is threshold monitoring of surface waves. In principle, such processing should be feasible using the already existing processing modules, but some studies on filter settings, STA lengths and the usage of surface magnitude correction tables would be needed. The upper limit M_s calculation could be applied to extend the functionality of discriminants like M_s/m_b . For small explosions, surface waves frequently are too weak to be observed at any station of the recording network. Obtaining reliable upper bound on M_s in such cases

would expand the range of usefulness of this discriminant. In practice, an "upper bound" for single station measurements has often been given as the "noise magnitude" at that station, i.e., the M_s value that corresponds to the actually observed noise level at the expected time of the Rayleigh arrival. The threshold monitoring procedure will include this as a special case of a more general network formulation.

As a final comment, we still believe that the best monitoring performance is achieved through an optimized site-specific monitoring, incorporating region-specific calibration information like travel time, slowness and magnitude anomalies, and optimal bandpass filters for assessment of magnitude thresholds. Such high-quality monitoring has already been demonstrated for the Novaya Zemlya and the Lop Nor test sites, using data from the Scandinavian arrays. By integrating the output from the optimized site-specific threshold monitoring with the results from "traditional" data analysis of detected signals we would utilize the resources of the monitoring network in a new tool that might enable a very high continuous automatic monitoring capability.

References

- CD/1423 (1996): Report of the Ad Hoc Group of Scientific Experts to the Conference of Disarmament on the GSETT-3 experiment and its relevance to the seismic component of the Comprehensive Nuclear Test-Ban Treaty International Monitoring System
- Kværna, T. (1992): Continuous seismic threshold of the northern Novaya Zemlya test site; long-term operational characteristics, *PL-TR-92-2118, Phillips Laboratory, Hanscom Air Force Base, Mass., USA*.
- Ringdal, F. (1976): Maximum-likelihood estimation of seismic magnitude, *Bull. Seism. Soc. Am.*, 66, 789-802.
- Ringdal, F. and T. Kværna (1989): A multi-channel approach to real time network detection, location, threshold monitoring. *Bull. Seism. Soc. Am.*, 79, 1927-1940.
- Ringdal, F. and T. Kværna (1992): Continuous seismic threshold monitoring, *Geophys. J. Int.*, 111, 505-514.
- Veith, K. F. and G. E. Clawson (1972). Magnitude from short-period P-wave data, *Bull. Seism. Soc. Am.*, 62, 435-452.

EVENT 963562

Date	Time	Latitude	Longitude	Depth	Ndef	Nsta	Gap	Mag1	N
rms	OT_Error	Smajor	Sminor	Az	Err	mdist	Mdist	Err	
1997/02/27	20:22:54.6	-52.3900	16.7500	0.0 f	22	19	114	mb 4.6	12
1.03	+ 0.65	31.2	25.4	44		20.21	165.00	+0.4	

SOUTHWEST OF AFRICA

Sta	Dist	EvAz	Phase	Time	Def	SNR	Amp	Per	Mag1	MagTM
SUR	20.21	10.0	P	20:27:31.4	T	6.4	51.3	1.08 mb	4.8	
TSUM	33.12	1.4	P	20:29:32.6	T	5.4	7.3	1.08 mb	4.5	
VNDA	48.56	170.4	P	20:31:39.3	T	4.2	11.8	1.00 mb	4.7	4.57
BGCA	57.36	2.0	P	20:32:44.5	T	11.9	3.4	0.97 mb	4.3	4.16
PLCA	57.62	244.0	P	20:32:47.1	T	3.1	2.3	0.90 mb	4.1	4.29
PLCA	57.62	244.0	PcP	20:33:40.7	T	3.2	2.2	0.83		
CPUP	60.03	265.0	P	20:33:04.0	T	4.6	2.2	0.40 mb	4.5	4.56
DBIC	61.65	335.4	P	20:33:14.2	T	4.3	5.0	0.83 mb	4.5	4.41
BDFB	62.39	280.4	P	20:33:20.0	T	13.0	14.2	0.98 mb	4.9	4.86
LPZ	74.17	263.8	P	20:34:34.5	T	13.1	50.8	1.60 mb	5.3	4.47
LPZ	74.17	263.8	PcP	20:34:47.0	T	5.9	5.4	1.10		
STKA	83.26	135.3	P	20:35:23.5	T	10.0	8.1	0.95 mb	4.8	4.49
ASAR	86.62	125.2	P	20:35:40.3	T	34.5	12.3	1.10 mb	5.0	4.85
WRA	89.95	123.5	P	20:35:55.7	T	8.4	1.1	0.80 mb	4.2	3.95
SCHQ	127.22	313.8	PKP	20:42:00.7	T	7.2	4.0	0.73		4.77
TXAR	131.00	266.2	PKP	20:42:08.4	T	10.9	2.1	1.00		4.39
PDAR	143.30	276.7	PKP	20:42:27.4	T	22.6	2.3	0.65		4.55
MNV	145.99	264.0	PKPbc	20:42:35.0	T	23.1	21.9	1.00		4.84
MBC	150.80	340.1	PKPbc	20:42:46.7	T	15.2	7.4	0.98		
YKA	152.60	310.8	PKP	20:42:43.8		9.5	0.9	1.04		
YKA	152.60	310.8	PKPbc	20:42:52.0	T	4.7	2.1	0.57		4.12
YKA	152.60	310.8	PKPab	20:43:01.2	T	4.9	0.7	0.72		
ILAR	165.00	332.2	PKPab	20:43:58.0	T	10.1	1.5	1.05		4.41

Average PIDC magnitude : 4.63, St.dev. 0.35

Average PIDC magnitude (primary network < 97 deg): 4.63, St.dev. 0.38

Average TM magnitude (primary network < 97 deg): 4.46, St.dev. 0.28

Average TM magnitude (primary network) : 4.49, St.dev. 0.27

Table 1. REB bulletin information for an event southwest of Africa. The PIDC magnitudes are given in the Mag1 column, whereas the STA-based TM magnitudes are given in the MagTM column. The average network m_b values and the corresponding standard deviations are given at the bottom of the table.

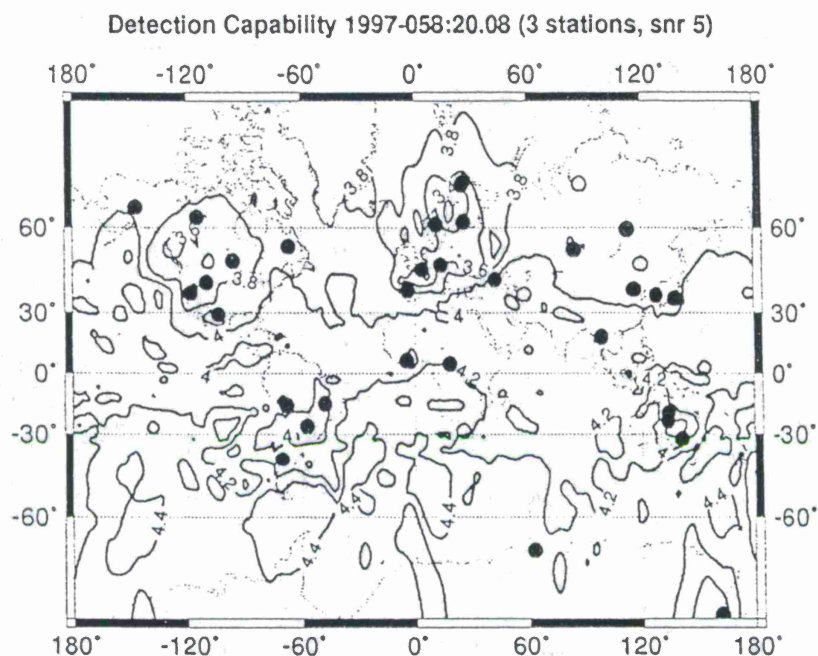


Fig. 1. Three-station detection capability map during noise conditions for the primary network for the time instant 1997-058:20.08. The capability map has been computed by choosing the **third lowest** of the station "noise magnitudes", and then adding $0.7 m_b$ units to accommodate an SNR of 5.0 required for phase detection. The filled circles symbolize operating primary stations and the open circles symbolize primary stations without available data.

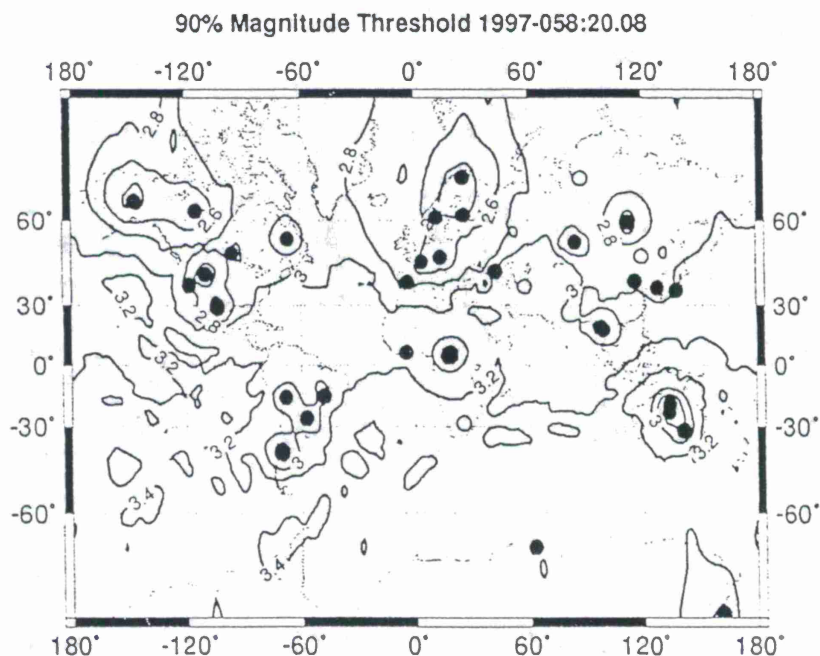


Fig. 2. 90% magnitude threshold for the same origin time instant as used in the capability map of Fig. 1.

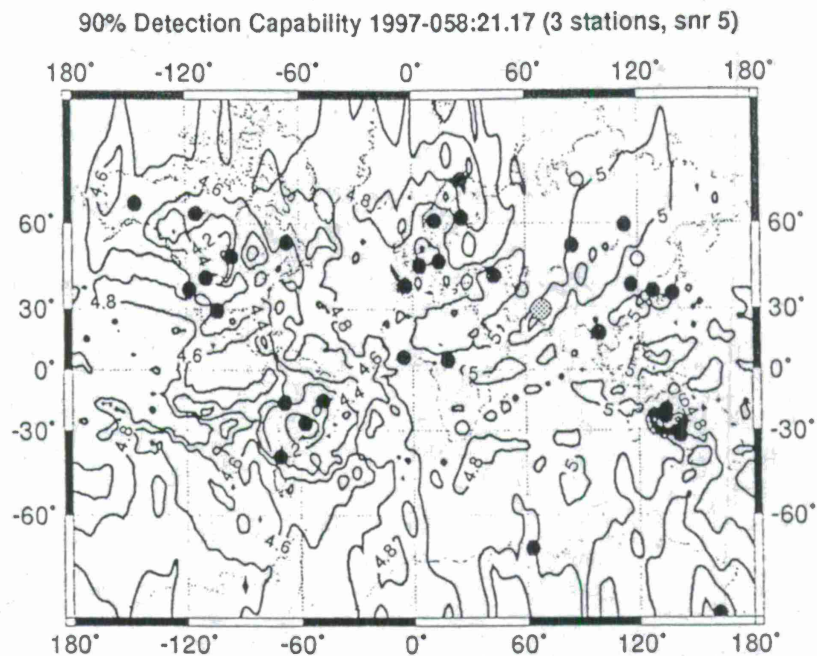


Fig. 3. Three-station detection capability 9 minutes into the coda of a M_s 7.2 earthquake located in Pakistan (shaded symbol). Again, the filled circles symbolize operating primary stations and the open circles symbolize primary stations without available data

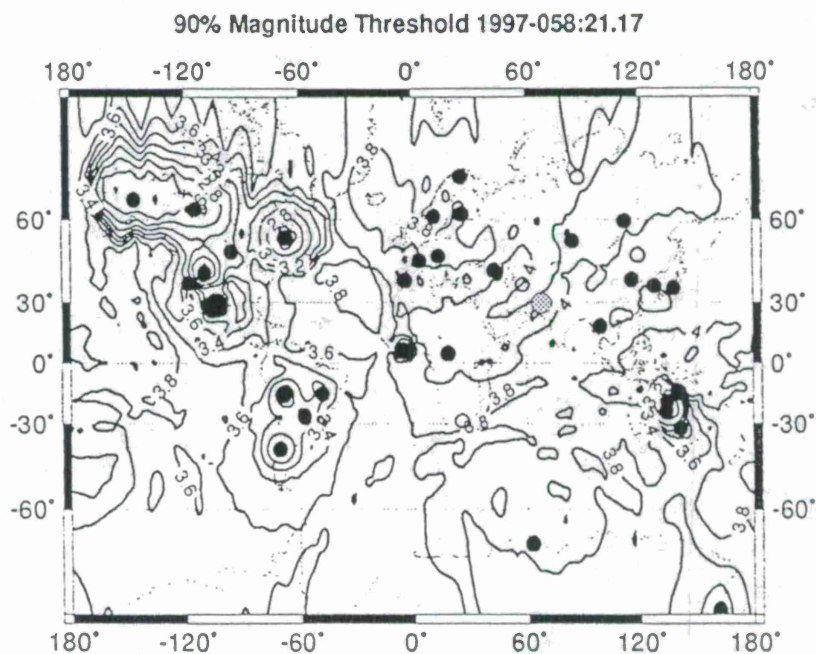


Fig. 4. 90% magnitude threshold for the same origin time instant as used in the capability map of Fig. 3.

FACTORS CONTROLLING SINGLE-STATION LOCATION

Jay Pulliam¹, Cliff Frohlich¹ and Stephen P. Grand²

¹Institute for Geophysics

²Department of Geological Sciences

University of Texas at Austin

Sponsored by the Air Force Office of Scientific Research
and the Defense Special Weapons Agency
Contract F49620-94-0287

ABSTRACT

The increasing availability of digital, broadband, three-component data ultimately will make it feasible to routinely locate regional seismic events using only a single station. The most sensitive single-station location methods utilize comparison of observed and synthetic seismograms. Our previous research suggests that it is necessary to determine a reasonable three- or four-layer crustal model in order to obtain good matches; receiver-function methods provide an adequate method for determining the appropriate crustal structure. Our current research program focuses on ways to make waveform matching and the construction of synthetics more efficient. We are continuing to evaluate polarization methods for assessing event-station azimuth; this involves an empirical assessment of errors in azimuth determination for numerous small (M-3-4) seismic events, and evaluating the sources of systematic errors.

For the Comprehensive Test Ban Treaty (CTBT) it is especially critical to be able to accurately determine focal depth. The portion of a signal most sensitive to focal depth generally arises from near-surface reflections. We have synthesized the up- and down-going waveforms separately, and find that the shape of each is largely insensitive to focal depth; however, the focal depth is strongly correlated with their relative offset. We hope that exploiting this may allow us to significantly decrease the number of synthetics needed for matching to determine focal depth.

It now seems that important features of practical single-station location probably may need to be different in different geographic regions. Thus, our future plan is to focus attention on one or two geographic regions and develop demonstration software that will allow the CTBT community to assess the limits of the methodology.

Keywords: single-station location, depth determination, synthetic seismograms

Objectives

An essential element for monitoring the Comprehensive Test Ban Treaty (CTBT) concerns how to most effectively use seismic network data to identify and locate small magnitude ($M \sim 2.0$ to 4.5) seismic events. An overall difficulty is that, except in a few geographic areas, such small events are usually recorded by very few seismic stations. This is both an immediate (1-3 years) and a long-term (5-10 year) problem. The immediate problem is that many of the in-place methods for locating seismic signals rely heavily on travel-time based methods; these methods are notoriously poor at obtaining reliable focal depths. Moreover, in geographic regions where there is regular activity and many stations, there may be so many signals recorded that it is difficult to sort out which signals belong to which events. The longer-term problem is that travel-time based methods require reliable phase information from several stations; thus, to monitor smaller-magnitude events one must cover the entire Earth with a very dense seismic network. A more economical and attractive alternative is to develop reliable methods which accurately locate events using waveforms recorded at only a single station.

Our program objective is to utilize recent progress in several areas so as to make single-station location methods a practical alternative to multi-station methods. In situations where data are sparse single-station methods may provide the only effective alternative. Our particular research focus concerns the accurate determination of focal depth, since knowledge of focal depth is often sufficient to discriminate between earthquakes and explosions.

Completed Research

Previous research suggests that a reasonable knowledge of near-station crustal structure is critical for identifying which body-wave phases constrain focal depth. However, when crustal structure is known and is reasonably heterogeneous, one can construct synthetics which contain the essential features of observed seismograms at regional distances (< 1000 km). A significant component of our past investigations has concerned practical ways to determine crustal structure at typical broadband seismic stations; in several different regions we have been able to obtain apparently reliable crustal models (e. g., Figure 1) using receiver-function analysis of teleseismic signals [Zhao and Frohlich, 1996]. Basically, these methods invert vertical- and radial-component signals to determine flat-layered crustal models, generally consisting of three or four layers over a halfspace. In addition, we have focused some attention on ways to make these methods practical and efficient by using very fast simulated annealing to speed the search over the range of candidate crustal models [Zhao *et al.*, 1996]. We have also developed ray-selection schemes to calculate synthetics more quickly for comparison with the teleseismic observations.

When we then use these three- and four-layer crustal models and construct synthetics seismograms at regional distances, our experience has been that they often match observations adequately. That is, we do not obtain significantly better waveform matches when we increase the number of layers. The highest-energy parts of the signal may be explained with three or four layers, and the unexplained signal energy is not attributable to flat-layered structures.

Ongoing Research

Focal depth. Even when near-station crustal structure is known, the most time-consuming aspect of determining accurate focal depths by waveform matching is calculating synthetics. We are presently investigating ways to make depth determination more efficient. For a particular crustal structure, we use a reflectivity method to synthesize two seismograms, S_u and S_d , that correspond to wave fields that leave the source in upgoing and downgoing directions, respectively. The sum of S_u and S_d equals S , the signal expected for the traditional, simultaneous computation for all energy leaving the source (Figure 2). Our analysis shows that in many cases the S_u and S_d

synthetics are only weakly dependent on focal depth, except for a time shift; both are clearly less depth-dependent than the full synthetics S . This suggests that one can determine focal depth by matching observations with time-shifted linear combinations of the S_u and S_d synthetics, with the focal depth coming essentially from the time shift. Because of the weaker depth-dependence of S_u and S_d synthetics, one needs to perform significantly fewer calculations than when using synthetics generated for both upgoing and downgoing wave fields simultaneously.

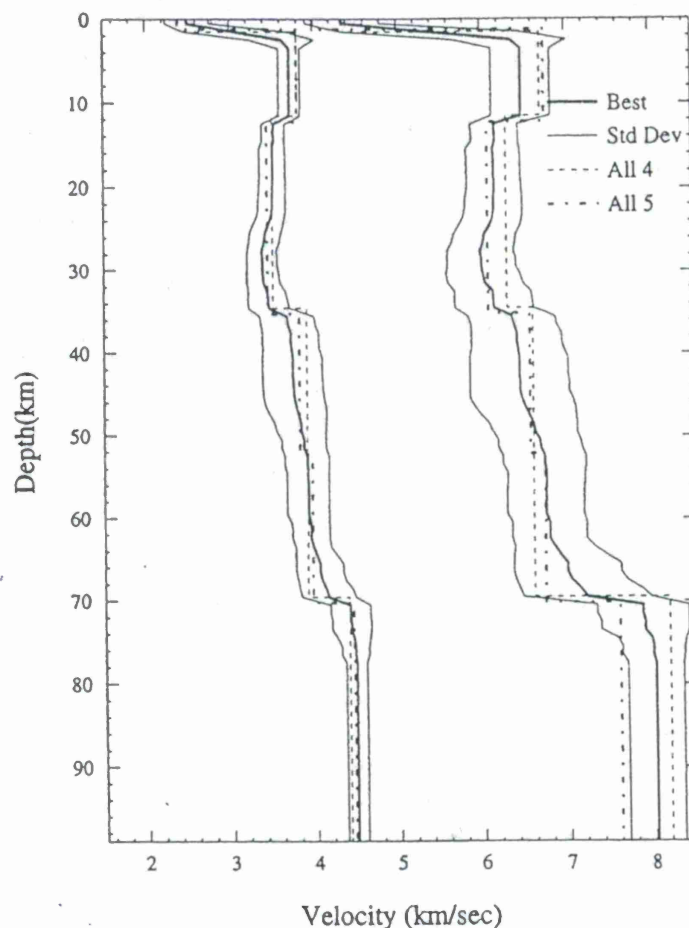


Figure 1. P and S velocity structure determined by receiver-function methods at station BUDO in north central Tibet [Zhao *et al.*, 1996]. 'Best' and 'Std Dev' indicate the mean and standard deviation of all models found from a very fast simulated inversion of about 50 teleseisms; 'All 4' and 'All 5' are the best-fitting four- and five-layer models determined from a simultaneous inversion of all available waveforms. Note that the four- and five-layer models are not significantly different above a depth of 70 km.

A related problem concerns the fact that, because moment tensors have six independent components, actual seismic sources are not all alike. Thus, a full matching calculation requires synthesizing all six source components and determining the best fit to observations; for single-station observations this fit is nearly always non-unique. However, our preliminary analysis suggests that we most often obtain the correct focal depth even when we use the wrong source to synthesize up- and downgoing synthetics. Our hypothesis is that this works when ray theory confirms that the S_u synthetics have significant upgoing S_v and P energy; i. e., when the energy leaving the source doesn't fall along a nodal line. Again, this robustness provides a potential means for making the focal depth calculation significantly more practical and efficient.

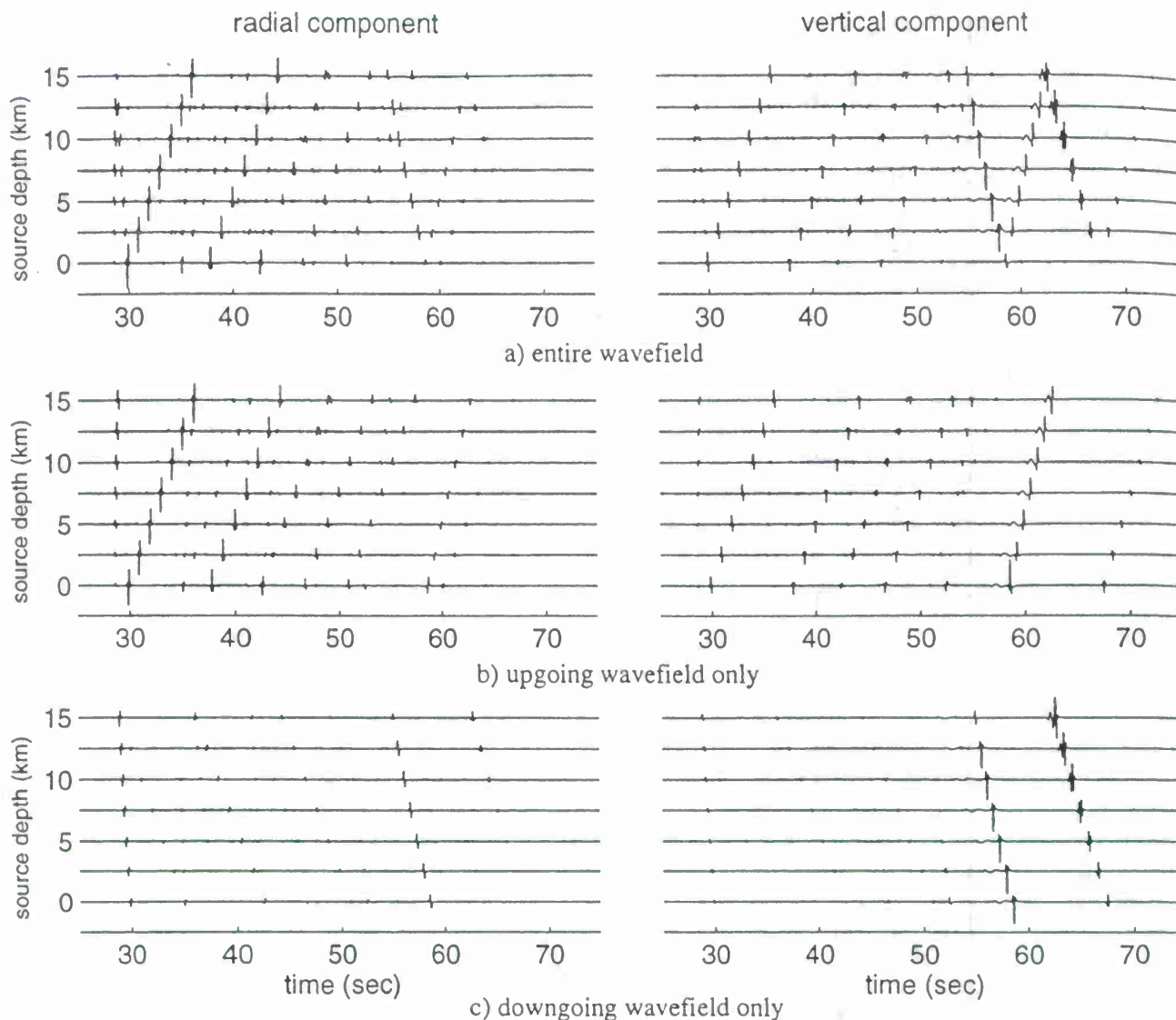


Figure 2. Comparison of the entire wavefield (a) vs. wavefield components that leave the source in the upward (b) and downward (c) directions, as computed with a reflectivity method for a single distance of 100 km and a suite of source depths from 0 to 15 km. The model for which these synthetics were computed is a solid layer over a solid halfspace, with the V_p/V_s ratio fixed at 1.7. Energy reflected from the near-surface layers is the most useful for constraining source depths; the separation of the wavefield components shown here indicates that upgoing phases may be expected to dominate the energy content of recorded seismograms. This observation suggests that methods for determining focal depths based on correlations between observed seismograms and suites of synthetics computed only for energy leaving the source in the upward direction (as in (b)), may be fruitful.

Event-station azimuth. For single-station location, in most cases signal polarization provides the only information available to constrain event-station azimuth. The generally accepted strategy [e. g., *Magotra et al.*, 1987; *Jurkevics*, 1988; *Thurber et al.*, 1989] is to use the three signal components $x_N(t)$, $x_E(t)$, and $x_Z(t)$ and form the covariance matrix

$$\mathbf{C} = \begin{bmatrix} c_{ZZ} & c_{ZN} & c_{ZE} \\ c_{ZN} & c_{NN} & c_{NE} \\ c_{ZE} & c_{NE} & c_{EE} \end{bmatrix}$$

where each matrix element is of the form

$$c_{ij} = \sum_t x_i(t) x_j(t)$$

Then, the azimuth and incident angle are determined from the eigenvalues and eigenvectors of \mathbf{C} , (e. g., Figures 3 and 4) with details depending on whether the sums are for P-SV, S, or surface wave arrivals [*Roberts et al.*, 1989; *Kim and Gao*, 1997]. However, there are essential differences among published methods concerning several features of the analysis—how to filter the data to obtain optimum results, how to properly evaluate errors [*Kim and Wu*, 1997], and whether to perform the analysis in the frequency or the time domain [e. g., see *Roberts and Christoffersson*, 1990; *Christoffersson et al.*, 1988].

Instead of developing new methods, we are currently assembling a fairly general polarization-assessment package which can be used to investigate the arrival direction problem for data from any particular station of interest. Previous researchers have already demonstrated [*Walck et al.*, 1991; *Suteau-Henson*, 1991] that at some stations—particularly those along boundaries between different geologic regimes—there can be large discrepancies between observed and actual azimuths. This problem can be particularly troublesome for small seismic events in regions where seismic activity is rare. For example, for a magnitude 3.8 earthquake in Texas (Figures 3 and 4), the discrepancy between actual and polarization-determined azimuth was only 2°. In a related effort, we are currently considering ways to assess how much anisotropic velocity structures in the crust and upper mantle may contribute to these errors.

Planned Research

Strategy: focus on individual regions. Our working hypothesis--supported by both our previous and ongoing research--is that single-station determination of epicenter and focal depths is realizable for small ($M \sim 3$) seismic events at regional distances (~ 100 -500 km) IF one attacks the problem on a region-by-region basis. Yet, regional differences in crustal structure and in origins of ambient noise are large enough that it is NOT possible to design a single scheme that is effective at all stations.

Thus, our plan is to coordinate with other members of the CTBT-monitoring community to identify one or two geographic areas and there develop workable single-station location packages. We will determine a three-layer crustal structure at individual target stations using our previously-developed methods [*Zhao and Frohlich*, 1996; *Zhao et al.*, 1996]. Synthetic seismograms constructed using this crustal structure will be used to determine focal depth and event-distance, using a waveform matching scheme which may well differ at different stations.

Demonstration software. Our basic research products will be demonstration software packages and a library containing both synthetic and actual seismogram for the regions chosen for study. These products will be fully documented, and available for assessment or comparison by all in the CTBT community. If we can demonstrate, at least in a few geographic locations, that single-station location can compete favorably with array and multi-station methods, then this suggests that future research on the problem is best attacked on a region-by-region basis.

Alice Texas Earthquake

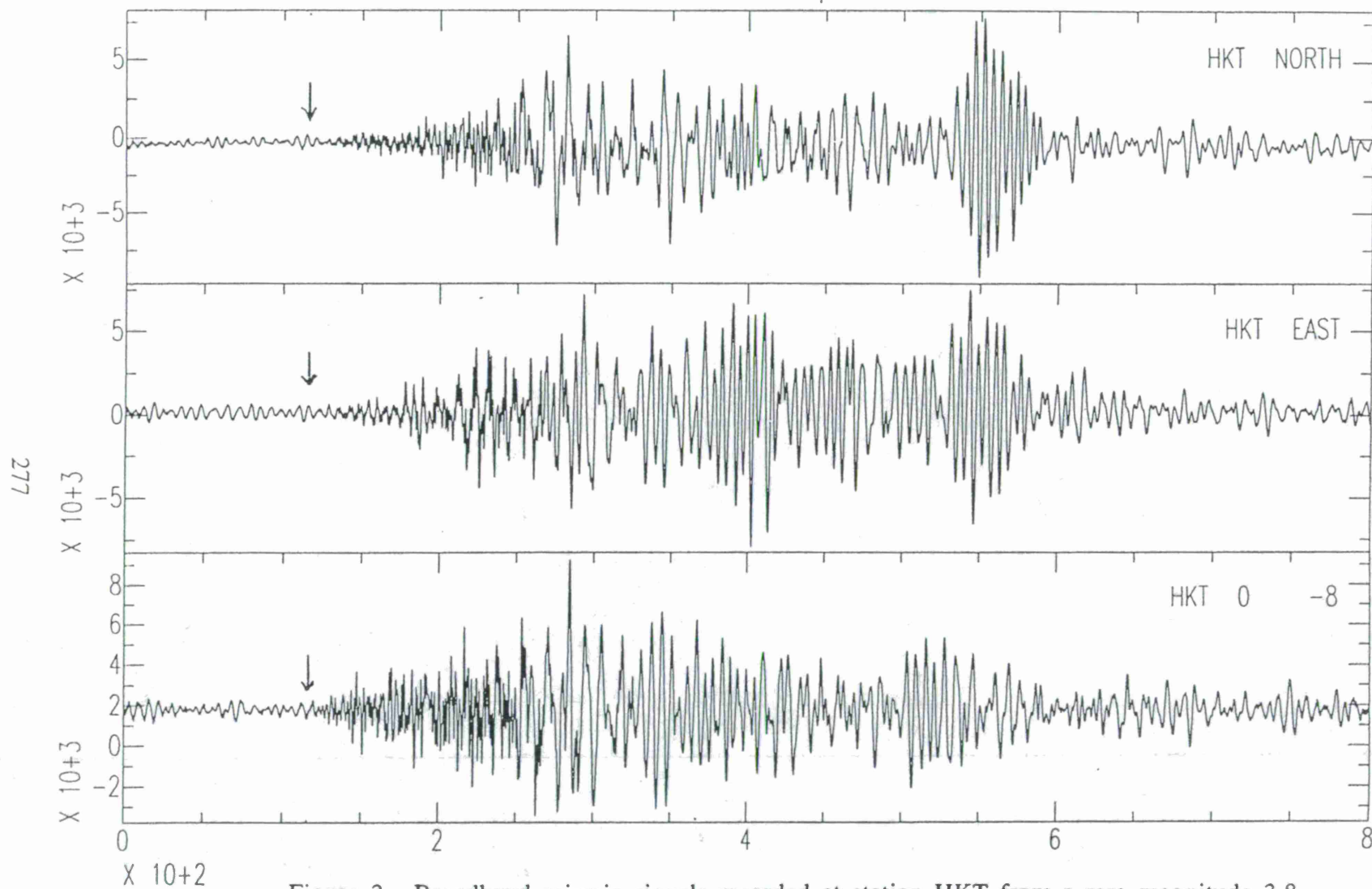


Figure 3. Broadband seismic signals recorded at station HKT from a rare magnitude 3.8 earthquake which occurred on 24 March 1997 near Alice, Texas (station-event distance - 324 km; azimuth - 218.1° E of N). Arrow indicates the predicted time of the P arrivals.

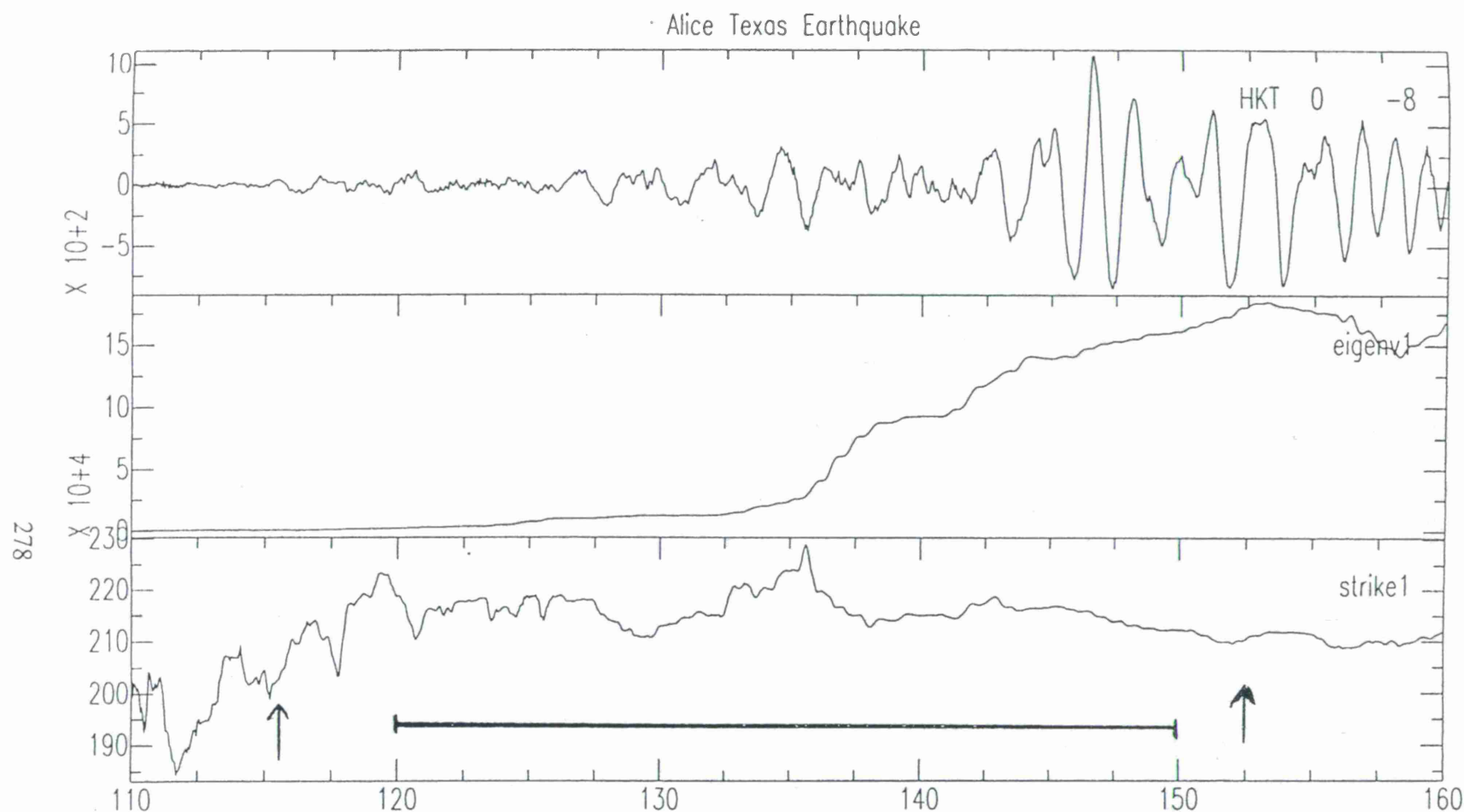


Figure 4. Apparent station-event azimuth for the Alice, Texas earthquake (vertical component signal, top), determined from analysis of the signal covariance matrix (see text). For the indicated time period between P and S (horizontal bar, and arrows) the strike (bottom) of the eigenvector of the largest eigenvalue (center) indicates an azimuth of $216^{\circ} \pm 3^{\circ}$, in agreement with the correct value of 218.1° . The value and uncertainty depend strongly on subjectively chosen filter parameters. For this figure the data were highpass filtered with a 0.5 Hz corner and smoothed over a 20-sec interval before plotting the azimuth. With no highpass filtering applied the polarization azimuth determined is $332^{\circ} \pm 6^{\circ}$, or more than 100° from the correct value.

Our proposed research is a three-year program; during this period we hope to develop demonstration packages which address the following questions relevant to CTBT monitoring:

- 1) *focal depth* - can comparison of observed and synthetic waveforms provide accurate focal depths for seismic events with known epicenters?;
- 2) *phase association* - when network observations provide phase arrival times for numerous events of unknown location, can single-station location methods determine a large enough fraction of event locations to significantly simplify the problem of assigning signals to specific events?;
- 3) *single-station location* - how can we best utilize data from auxiliary seismic stations which are remote from other network stations?—can we determine near-station crustal structure well enough to develop single-station location algorithms which identify and locate regional events, and which operate without regular human interaction?;
- 4) *future events in 'quiet' areas* - can we develop a credible strategy for predicting the characteristics of seismograms in regions where we have no past record of activity?; thus, do we have a reasonable likelihood of quickly identifying and locating potential future events in geographic regions that may be quiet tectonically but politically uncertain?

Conclusions and Recommendations

In many geographic regions, single-station methods to determine epicenter and focal depth may provide a more effective means of discriminating small ($M \sim 3$) natural and man-made sources than conventional methods relying on spectral ratios, such as comparison of surface- and body-wave magnitudes. In many geographic regions events can be located efficiently by comparing synthetic seismograms and observations, even though this approach may not work in laterally heterogeneous or structurally complex regions.

Our current strategy is to focus attention on a few regions and determine the crustal structure and the associated geographic extent over which we can reasonably compare observations and synthetics. An important unresolved question concerns the typical size extent of such regions, and whether there is a legitimate hope that a 'regionalized' single-station approach to seismic event location can be effective.

References

- Christoffersson, A., E. Husebye and S. Ingate. Wavefield decomposition using ML-probabilities in modeling single-site 3-component records, *Geophys. J.*, 93, 197-213, 1988.
- Jerkevics, A. Polarization analysis of three-component array data, *Bull. Seismol. Soc. Amer.*, 78, 1725-1743, 1988.
- Kim, S. G. and Gao. Study on some characteristics of earthquakes and explosions using the polarization method, *J. Phys. Earth*, 45, 13-27, 1997.
- Kim, S. G. and Z. Wu. Uncertainties of seismic source determination using a 3-component single station, *J. Phys. Earth*, 45, 1-11, 1997.
- Magotra, N., N. Ahmed and E. Chael. Seismic event detection and source location using single-station (three-component) data, *Bull. Seismol. Soc. Amer.*, 77, 958-971, 1987.
- Roberts, R. G. and A. Christoffersson. Decomposition of complex single-station three-component seismograms, *Geophys. J. Int.*, 103, 1990.

Roberts, R. G., A. Christoffersson and F. Cassidy. Real-time event detection, phase identification and source location estimation using single-station three-component seismic data, *Geophys. J.*, 97, 471-480, 1989.

Suteau-Henson, A. Three-component analysis of regional phases at NORESS and ARCESS: Polarization and phase identification, *Bull. Seismol. Soc. Amer.*, 81, 2419-2440, 1991.

Thurber, C., H. Given and J. Berger. Regional seismic event location with a sparse network: Application to eastern Kazakhstan, USSR, *J. Geophys. Res.*, 94, 17767-17780, 1989.

Walck, M. C. and E. P. Chael. Optimal backazimuth estimation for three-component recordings of regional seismic events, *Bull. Seismol. Soc. Amer.*, 81, 643-666, 1991.

Zhao, L.-S. and C. Frohlich. Teleseismic body waveforms and receiver structures beneath seismic stations, *Geophys. J. Int.*, 124, 525-540, 1996.

Zhao, L.-S., M. K. Sen, P. Stoffa and C. Frohlich. Application of very fast simulated annealing to the determination of the crustal structure beneath Tibet, *Geophys. J. Int.*, 125, 355-370, 1996.

WAVEFORM COMPLEXITY AS A POSSIBLE DEPTH DISCRIMINANT FOR THE AUTOMATED IDC SYSTEM

C. K. Saikia, H-K Thio, B. B. Woods and D. V. Helmberger*

Woodward-Clyde Federal Services, 566 El Dorado St., Pasadena, CA 91101

*Seismological Laboratory, CIT, Pasadena, CA 91125

Sponsored by Advanced Research Projects Agency
Contract No F19628-95-C-0093

ABSTRACT

For monitoring a comprehensive test ban treaty (CTBT) in a region, where earthquakes are plentiful and explosions are very few, at the kiloton level requires locating and identifying seismic events down to magnitude 4 and lower, if decoupling scenarios are possible. Unlike large magnitude earthquakes ($M_w > 4.5$), small earthquakes lack long-period waves at regional distances. Using short-period waves makes the task of small magnitude event identification difficult because they are strongly influenced by heterogeneities along the propagation path. In general, the seismic phases of small earthquakes correlate well with those of large events occurring in the same neighborhood. This correlation is highly relevant to the IDC, because by correlating an event to known events, it is possible to characterize its source type. Hence, establishing source mechanisms and focal depths for a large number of known earthquakes spanning many magnitudes and depths becomes essential in a new area. In this paper, we demonstrate the potential of a new algorithm based on the Lg wave complexity that can help to locate small magnitude events, particularly their depth, down to $M_L \approx 3.5$, using regional broadband seismograms. This method will be especially helpful to the automated IDC system, because the Lg wave complexity of deep earthquakes is characteristically different from the Lg wave complexity of the shallow earthquakes. By quantifying these differences, it is possible for the IDC system to screen out many deep mantle earthquakes in the region of intermediate and deep seismicity. Another issue can be the difficulty in locating small events due to sparse station coverage as in the middle-east region. Although, teleseismic and far-regional arrays can lower the detection threshold by enhancing signals, many small events are recorded by only two IMS stations, rendering location more difficult. We are optimistic that Lg wave complexity will take the load off the IDC system by permitting initial screening of many deep and intermediate depth earthquakes.

OBJECTIVE:

Monitoring a comprehensive test ban treaty (CTBT) at the kiloton level requires locating and identifying seismic events down to magnitude 4 and lower, if decoupling scenarios are possible. Characterizing source types down to a low magnitude ($M_L \approx 3$) is a difficult task. Unlike large magnitude earthquakes ($M_w > 4.5$), small earthquakes lack long-period waves. Using short-period waves makes the task of event identification difficult because they are strongly influenced by heterogeneities along the propagation path. In general, the seismic phases of small earthquakes correlate well with those of large events occurring in the same neighborhood. This correlation is highly relevant to the IDC, because by correlating an event to known events, it is possible to characterize its source type. Hence, establishing source mechanisms and focal depths for a large number of known earthquakes spanning many magnitudes and depths becomes essential in a new area. Another issue can be the difficulty in locating small events due to sparse station coverage as in the middle-east region. Although, arrays can lower the detection threshold by enhancing signals, many small events are recorded by only two IMS stations, rendering location more difficult. In this paper, we demonstrate the potential of a new algorithm based on the Lg wave complexity that can help to locate small magnitude events, particularly their depth, down to $M_L \approx 3.5$, using regional broadband seismograms. This method will be especially helpful to the automated IDC system, because the Lg wave complexity of deep earthquakes is characteristically different from the Lg wave complexity of the shallow earthquakes. By quantifying these differences, it is possible for the IDC system to screen out many deep mantle earthquakes in the region of intermediate and deep seismicity.

RESEARCH ACCOMPLISHED

To date, our focus has been on the estimation of source parameters and depths using local and regional seismograms ($\Delta < 600\text{km}$) and the relationship of these parameters to our energy-based $E_{sp-Pz}:E_{lp-3}$ seismic discriminant (Woods and Helmberger, 1997). We have found that depth has a significant influence on the $E_{sp-Pz}:E_{lp-3}$ ratio, with deep earthquakes generating little or no long-period surface wave energy and thus appearing explosion-like by the discriminant's criterion (Saikia *et al.*, 1996a). Figure 1b shows the $E_{sp-Pz}:E_{lp-3}$ ratios vs. distance for PAKN-recorded events (a temporary PASSCAL array, Sandvol *et al.*, 1994); the deep events (pluses) plot higher than other crustal (circles) and near-moho (triangles) depths. In southwestern United States, the $E_{sp-Pz}:E_{lp-3}$ ratios for the NTS explosions also plot higher than the crustal earthquakes (Woods and Helmberger, 1997) and the separation of the two population is comparable to the separation of the deep events from crustal earthquakes in Figure 1b, thus rendering the applicability of this discriminant somewhat difficult without accurate depth estimates. Thus, establishing of methods to constrain relatively deep events ($h < 33\text{km}$) becomes a key part of this discrimination procedure. This discriminant recently has been implemented at CMR (Center for Monitoring Research) and usable regional data are routinely processed with respect to this discriminant. Figure 1a shows a world-wide population of $E_{sp-Pz}:E_{lp-3}$ ratios vs. distance. The large scatter in these data is primarily due to the mixing of events from different tectonic regions and many data points are from deep seismicity, especially those high values.

In a region of deep seismicity, it is quite possible that an explosion may fall into the zone of deep events with respect to the $E_{sp-Pz}:E_{lp-3}$ discriminant. To solve this problem, Saikia *et al.* (1996b) developed a new diagnostic tool to identify deep earthquakes in conjunction with the $E_{sp-Pz}:E_{lp-3}$ discriminant using the Lg wave complexity. In their study, they constructed a

characteristic time series $g(t)$ using

$$g(t) = f^2(t) + c^2 [df(t)/dt]^2$$

from the recorded time series $f(t)$, where the weighting constant " c " varies the relative weight assigned to the first derivative and its value is based on the digital sample rate and noise characteristic of the station (Allen, 1978). By examining broadband time series of 10 master events from the PAKN array for which both source mechanisms and source depths were determined using regional waveform modeling technique (Zhu *et al.*, 1997), they noted that the duration of Lg wave complexity in a time series of short-term average of $g(t)$ is short in duration for the deep events relative to the shallow earthquakes at similar depths. This duration measurement was quantified to identify many deep small earthquakes from the shallow events.

In this paper, we proceed further to demonstrate that the short duration of Lg wave complexity for deep events is a commonly observed phenomenon and so it can probably be applied to isolate deep earthquakes from shallow events elsewhere. In a new region, this complexity functions needs to be calibrated relative to known events of larger magnitude ($M_w \approx 4.0$). In Figure 2, we show locations and source mechanisms of 17 regional earthquakes whose depths were determined by fitting regional waveform data recorded at NIL and AAK stations; both are β stations. We have applied the same procedure discussed in our earlier reports (Saikia, *et al.*, 1996a,b; Zhu *et al.*, 1997). In our previous studies, we did not have regional data from NIL station and we used regional waveforms from the PASSCAL station "sbra" as surrogates for NIL. Figure 3 shows an example of agreement between data and synthetic seismograms for one shallow and one deep earthquakes at NIL and AAK stations. Compared to the deep event, the shallow event has elongated long-period surface waves. Figure 4a shows a comparison of complexity functions for a pair of shallow and deep events at NIL stations, the upper panel showing the shallow earthquake. The upper two traces correspond to the complexity time series processed from the radial and tangential components shown in the bottom two traces. The lower panel is for an event of 200 km depth. Both the events are recorded at similar epicentral distances.

We have also collected regional waveforms from the Indian subcontinent recorded at Chinese digital station KMI to examine the nature of Lg wave characteristics. Figure 5a shows an example in which the top panel shows one event which occurred in the northeast part of India and has a depth of 10 km (ISC depth). The event is recorded at distance of 1370 km from the source. The duration of the Lg wave complexity is long, almost in the order of 200 seconds. In the bottom panel, we show another event at similar distance, its depth reported as 33 km. This event has a small duration for the Lg wave complexity. This event is probably deep, certainly deeper than 10 km, as it does not have long-period waves that are generated by the shallow event. Although, at present we do not have any calibration for these events, it is likely that Lg wave complexity may be applicable to discriminant deep events from very shallow earthquakes even at large distances. Figure 5b shows another example of deep vs. shallow earthquakes recorded at College station in Alaska, the shallow event having much longer duration than the deep event.

Figure 4b shows examples deep and shallow North African earthquakes recorded at MDT station. The depths of these two events were determined using regional waveform modeling scheme. The deep event has a simple waveform complexity, further strengthening its potential as a depth discriminant. In Figure 6, we present more examples of waveform complexity for deep vs. shallow earthquakes from different tectonic regions recorded at VSL and PAB stations.

In Figure 7, we present another example of waveform complexity for south American earthquakes recorded at station NNA. While many of the deep earthquakes have simple waveform complexity, one that we show in this figure looks complex. This is apparently caused by the strength of the short-period sSmS. The two pulses in this deep event are direct S and sSmS (also shown schematically in the bottom). Automated software to recognize this feature can probably be accomplished identifying the periodicity.

CONCLUSIONS AND RECOMMENDATIONS

All the examples presented above on the Lg wave complexity suggest that the measure of waveform complexity is a viable approach to discriminate deep earthquakes from shallow events. To monitor a new region and to screen deep events with respect to the Lg wave complexity, it is necessary to develop a catalog of master events constraining depths fairly well. Master events are large in magnitude ($M_w \approx 4$) and their high frequencies correlate well with lower magnitude events. By quantifying the Lg wave complexity of the master events in terms of duration, it may be possible to develop an algorithm that will help IDC automated system to screen out the deep events. It is also further possible to develop a semi-empirical approach to quickly model the recorded complexity function and constrain depth of small events. Presently, we are pursuing this effort by generating scattering functions using recorded data and convolving this empirical scattering function with simplified path effect. Our success is in a preliminary stage and we shall be able to present results from this effort in the meeting.

In addition, for a single region the $E_{sp-P_z}:E_{lp-3}$ ratios vs. distance discriminant show reduced scatter. Hence, it is recommended that the $E_{sp-P_z}:E_{lp-3}$ vs. distance population should be examined separately for each individual tectonic area, not as shown in Figure 1 by assembling all global data together.

We are currently working on making the $E_{sp-P_z}:E_{lp-3}$ discriminant compatible with m_b-M_s measurements. This will make it possible to examine smaller events with the latter discriminant, as $E_{sp-P_z}:E_{lp-3}$ energy measurements are made primarily on records at less than 1500 km. At these distances surface waves can be observed from smaller events for which is not possible to see at teleseismic distances.

Distance corrections for the energy measurements are determined from waveform modeling. Once a regional crustal model is established, synthetic seismograms are generated for a suite of distances and their short-period and long-period energy levels are determined for the P_n and surface wave trains, respectively. The distance dependence so established is then applied to the data, which are corrected to 500 km, which should be past critical distance for any region. Scaling relationships are then determined between the distance-corrected short-period P_n energy E_{sp} and m_b , and the long-period surface wave energy E_{lp} and M_s . Thus an equivalent m_b-M_s differential can be obtained from the regional E_{sp-P_z} and E_{lp-3} energy measurements.

REFERENCES

- Saikia, C. K., B. B. Woods, L. Zhu, H-K Thio, and D. V. Helmberger (1996a). Path calibration, source estimation and regional discrimination for the Middle East: Application to the Hindu Kush Region, Scientific Report 1, PL-TR-96-2069, HAB, MA 01731-3010
- Saikia, C. K., H-K. Thio, B. B. Woods, X. Song, L. Zhu and D. V. Helmberger (1996b). Path calibration, source estimation and regional discrimination for the Middle East and Western Mediterranean, Scientific Report 2, PL-TR-96-2307, HAB, MA 01731-3010.
- Sandvol, E., J. Ni and T. Hearn (1994). Seismic azimuthal anisotropy beneath the Pakistan Himalaya, *Geophys. Res. Lett.*, 21, 1635-1638.
- Zhu, L., D. V. Helmberger, C. K. Saikia and B. B. Woods (1997). Regional waveform calibration in the Pamir-Hindu Kush Region, *J. Geophys. Res.*, (accepted on May 29, 1997).

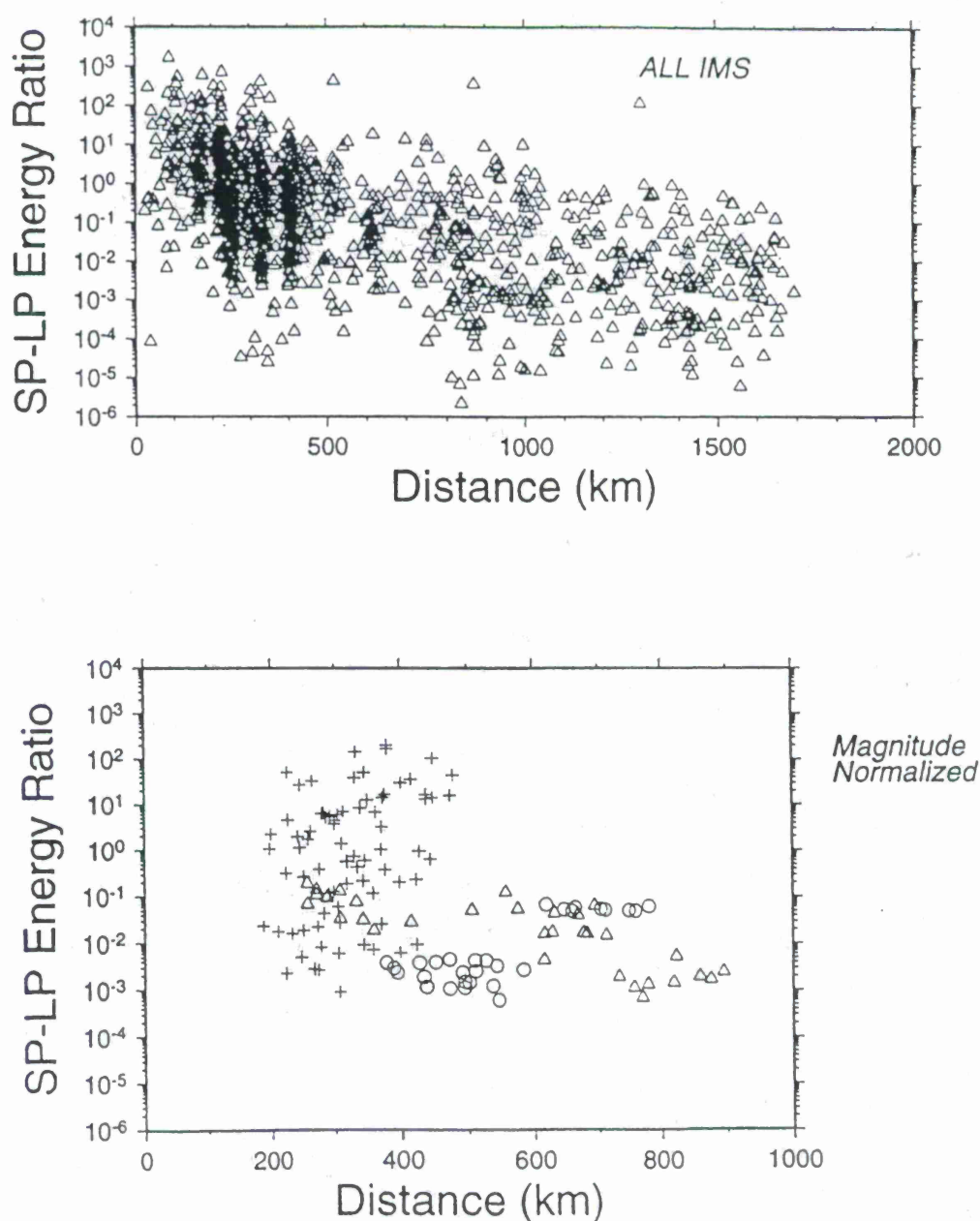


Figure 1. Display of SP:LP energy ratios as a function regional distance for the IMS (top panel) and PAKN (bottom panel) stations. The PAKN data points are magnitude normalized. "+" correspond to deep events, Δ to crustal and \circ to intermediate depth earthquakes.

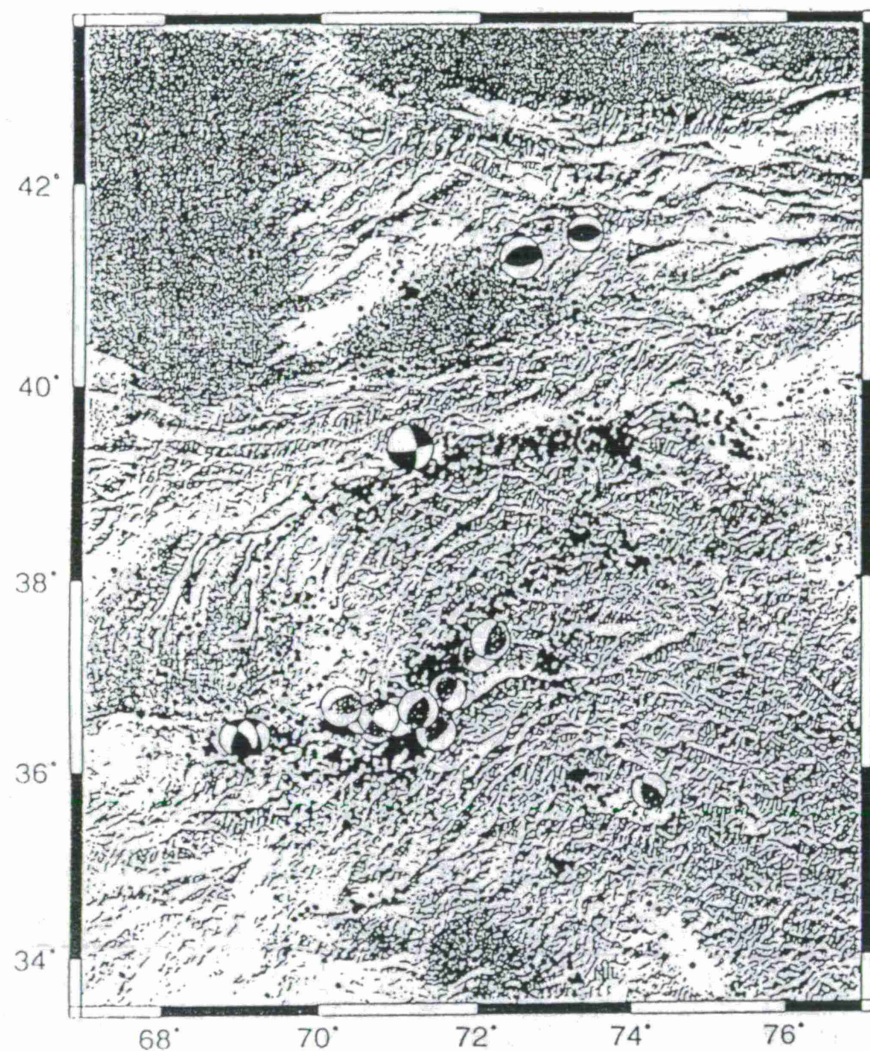


Figure 2. Focal mechanisms of 17 events determined using two-station waveform modeling technique (Zhu *et al.*, 1997; Saikia *et al.*, 1996a,b). Regional seismograms recorded at AAK and NIL stations (both are β stations) were used.

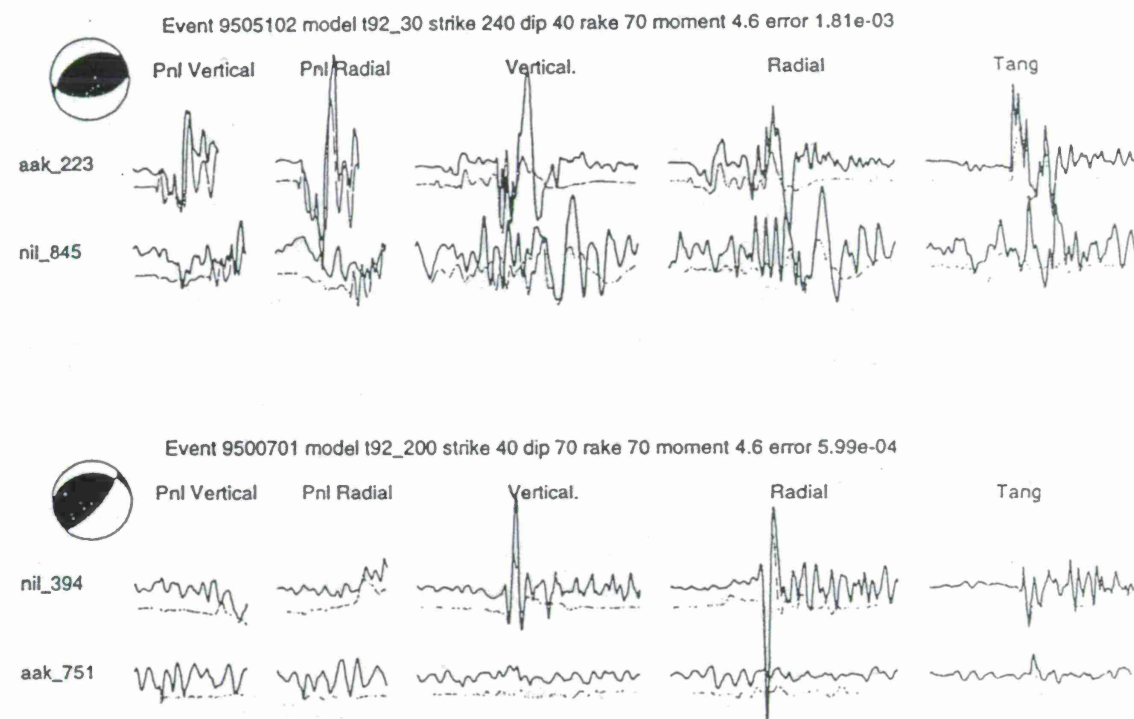


Figure 3. Comparison of data vs. synthetic seismograms at NIL and AAK stations for one shallow (top) and one deep (bottom) earthquakes.

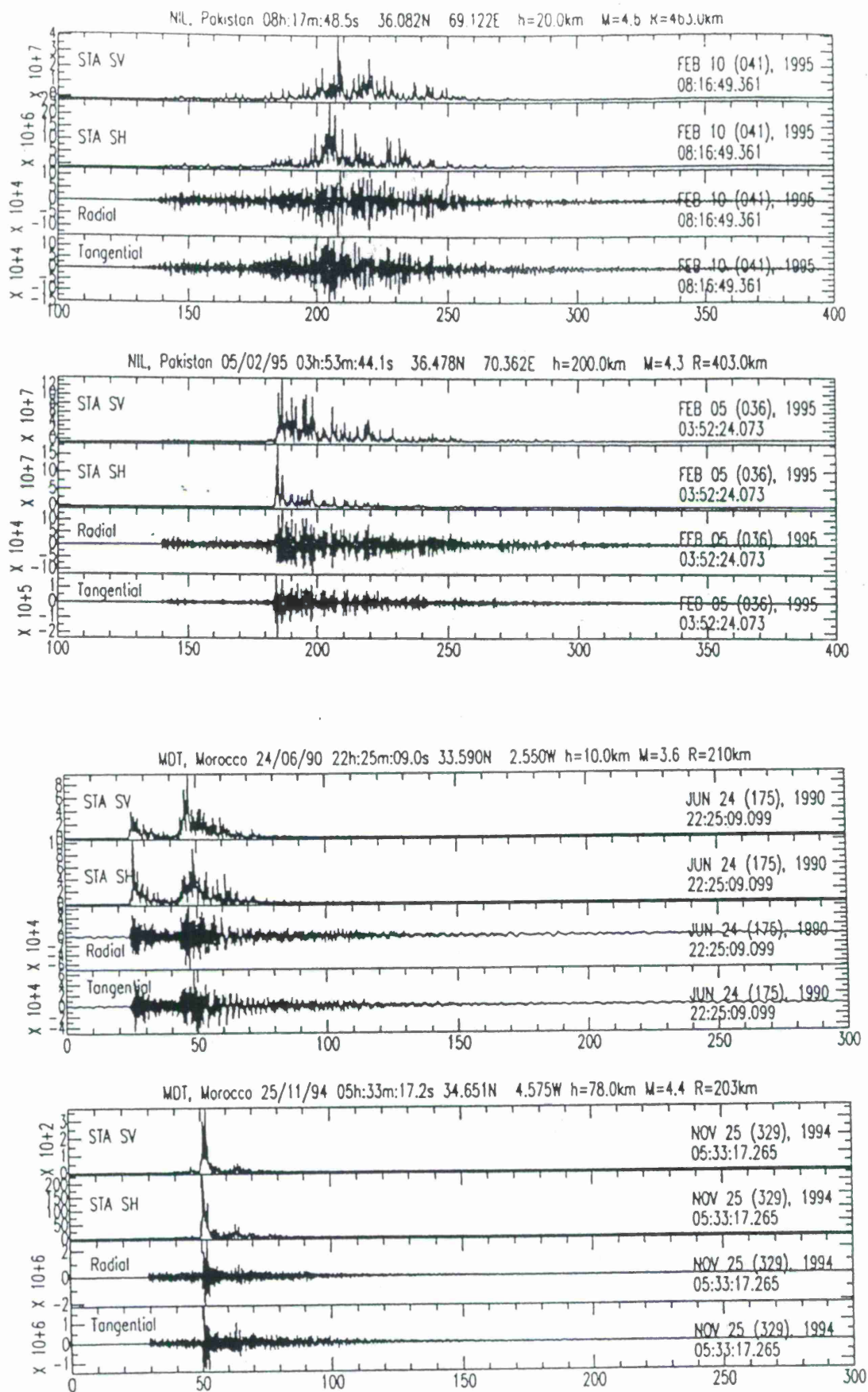


Figure 4. Examples of waveform complexity for a deep and a shallow earthquake. Time series are plotted in the same time scale. Clearly, the deep events have simple looking waveform complexity presented in the upper two traces of each panel (top trace correspond to the radial motion and bottom trace correspond to the tangential component). (a) NIL station and Pakistani event, and (b) MDT station and African event.

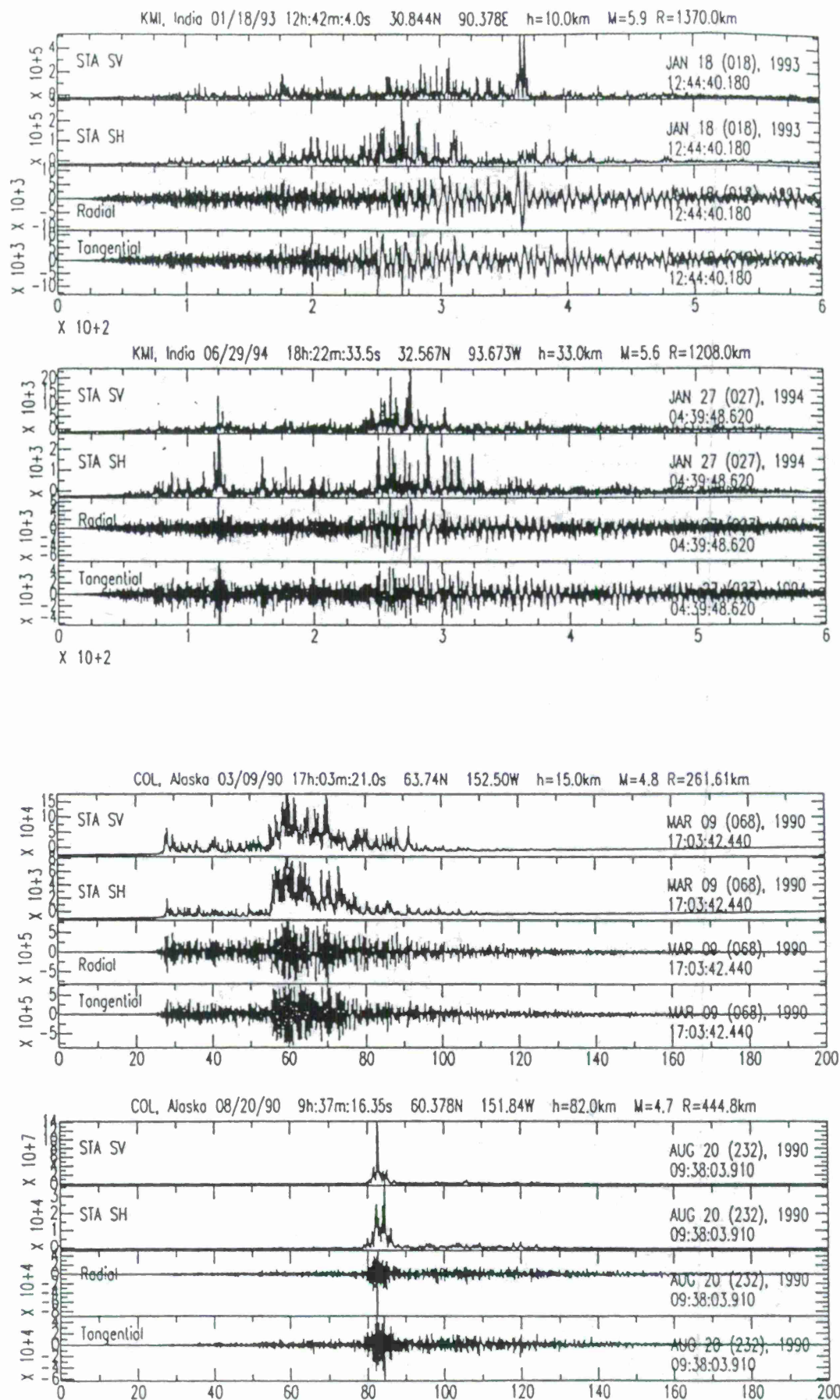


Figure 5. Same as Figure 4 showing waveform complexity for a deep and a shallow earthquake. (a) KMI station ($\Delta \approx 1300$ km) and Northeast India event, and (b) COL station and Alaskan event.

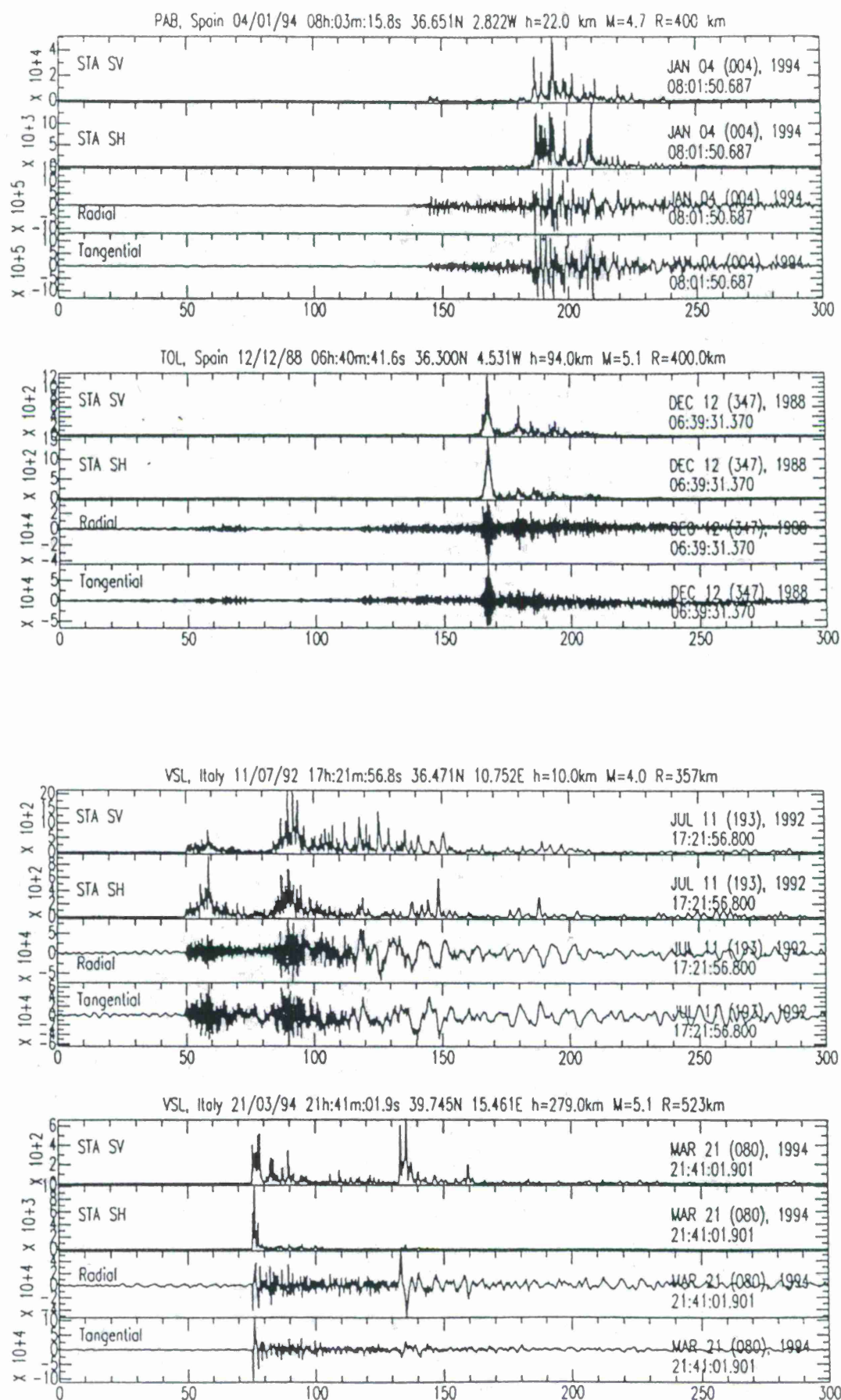


Figure 6. Same as Figure 5 showing waveform complexity for a deep and a shallow earthquake. (a) PAB station and Spanish event, and (b) VSL station and Italy event.

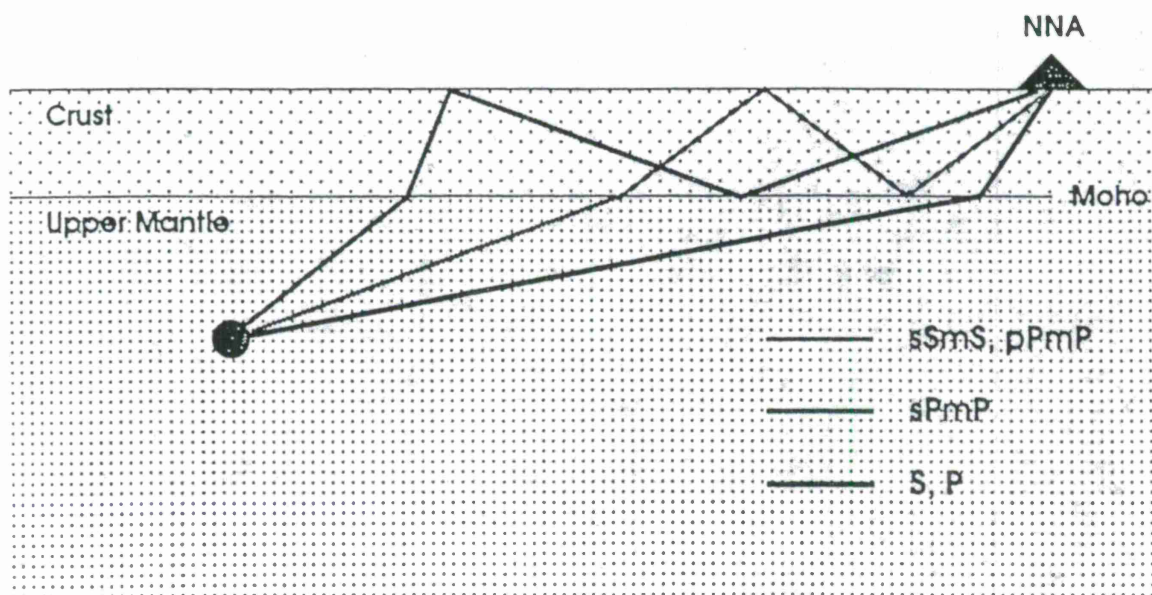
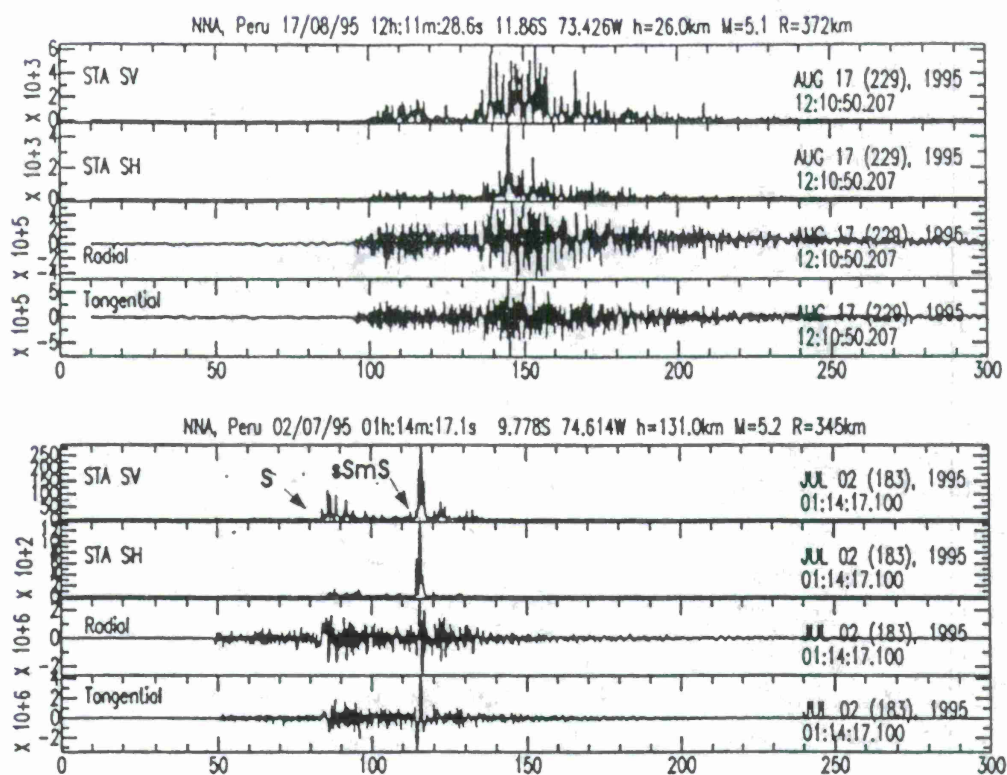


Figure 7. Same as Figure 4 showing waveform complexity for a deep and a shallow earthquake. (Top) NNA station and Peruvian event, and (bottom) schematic diagram of the direct S and sSmS phases for explaining the complex looking complexity for deep event shown in the top panel.

Event Location in the Middle East and North Africa

Craig A. Schultz, Stephen C. Myers, Stanley D. Ruppert

*Geophysics and Global Security, Lawrence Livermore National Laboratory
University of California*

Sponsored by U.S. Department of Energy
Office of Nonproliferation and National Security
Office of Research and Development
Contract W-7405-ENG-48

ABSTRACT

The Lawrence Livermore National Laboratory (LLNL) CTBT R&D program has made significant progress towards improving the ability of the IMS seismic network to locate small-magnitude events in the Middle East and North Africa (ME/NA). Given that high-grade ground truth (such as known explosions) has been difficult to obtain in these regions, we have placed a significant effort towards the development of a teleseismically constrained seismic database that provides event locations good to within 20 km. This data set is used to make an initial evaluation of the effectiveness of calibration on the proposed seismic IMS network in the ME/NA. Utilizing a surrogate IMS regional network in the Middle East, we find that when a seismic event lies within the footprint of the recording network, the uncalibrated event locations are good to within about 25 km of the teleseismically constrained (TC) location. Using region specific static station corrections further reduces this difference to about 20 km. To obtain further improvement in location accuracy we have used the modified kriging technique developed by SNL to interpolate new travel-time corrections. We compare this technique with other robust linear interpolation techniques with the goal of enhancing the estimation of travel-time corrections. This is important for TS constrained events which we find can have large uncorrelated uncertainties. Finally, we are making a large effort to incorporate LLNL analyst picks on primary and secondary phases and develop azimuth and slowness estimates from current IMS arrays to improve/supplement the NEIC picks.

Key Words: seismic, regional location, kriging

Objectives

The primary objective of this study is to improve our ability to locate seismic events in the Middle East and North Africa (ME/NA) by generating travel-time corrections for the IMS seismic station network. These corrections should reduce both the bias and variance error in the location estimate. In order to assess the effectiveness of our corrections and location techniques, accurate locations of seismic events must be obtained. To avoid circularity there must be enough events so that the events tested are independent of the events used to generate the original corrections. For large areas of the ME/NA this poses an immediate difficulty, since good recordings of explosions in the region are scarce. Thus, to calculate preliminary corrections for travel-times we utilize the best constrained data set of locations currently available. This data consists of well-recorded large (teleseismic) events that have occurred at relatively shallow depths (Cogbill and Steck, 1996). By restricting this data set to only those events having very good, worldwide station coverage we can generate a higher-grade ground truth set of event locations that are known with a measurable level of uncertainty.

In the first section, we focus on the development of this teleseismically constrained data set, demonstrating that these seismic event locations have an uncertainty of about 20 km. We then make a preliminary evaluation of the effectiveness of the proposed IMS network by designing and testing a surrogate network that has a similar geometry. Finally, we demonstrate the need for better 1-D velocity models and more detailed source-specific station corrections in the ME/NA.

Research Accomplished

Teleseismically constrained database. Generating travel-time corrections for improved location requires well-located events in terms of origin time, epicenter, and hypocentral depth. In the Middle East and North Africa, there is a hierarchy of ground truth that can be obtained. This hierarchy ranges from explosions with exact locations to carefully studied aftershock sequences, events located by dense local networks, and teleseismically constrained events such as CMT and EDR bulletin events. Although the location accuracy goes from better to worse as we work through this list, the ease of obtaining these locations and the abundance of data increases greatly. Given that there are many thousands of TC events in the ME/NA and only a scarce number of higher-grade events, we begin with the development of the TC data set. LLNL has an active effort in obtaining new ground truth and this information is being incorporated continuously as it becomes available.

The work of Sweeney (1996) shows that teleseismic events can give event locations with a known uncertainty. His work focused on four different regions of the Middle East and North Africa. In this study accurate locations based on aftershock and dense array studies were compared with the corresponding teleseismic locations for those same events, as reported by the ISC and NEIC. Figure 1 shows the location error as a function of the number of defining P phases used in the location. Also shown is the location error as a function of the maximum azimuthal gap. This work shows that if one uses an acceptance criterion of $ndef > 50$ and $azgap < 90$ (50-90 criterion), the teleseismic event locations are good to within 20 km. In addition, Sweeney's work shows that even though fewer picks are used by the NEIC for their final location their picks give more accurate locations than the ISC picks. For this reason, we restrict this study to teleseismic events located using only the NEIC EDR picks and our own supplemental analyst picks.

The NEIC bulletin locations are referenced to the Jeffreys-Bullen velocity model. To be consistent with the International Data Center (IDC), whose standard is the AK135 velocity model, we have relocated all EDR events that fit the 50-90 criterion using the this velocity model. Relocation was done using EvLoc which operates on the LLNL Oracle database. Figure 2 shows all of the teleseismically constrained events relocated in one portion of the Middle East, while Figure 3 shows the difference in epicentral location and origin time resulting from the use of this new velocity model. These plots show a convergence of the two teleseismic locations as the number of stations increases and a shift of about 2 s in the origin time. These horizontal differences all lie well within the uncertainty of the initial teleseismic location suggesting consistent TC locations. All of the AK135 relocations shown in Figure 2 have been incorporated into the LLNL hierarchical ground truth database with a 20 km uncertainty assigned to the location.

Surrogate IMS network. The TC data set developed above can allow for an initial evaluation of the effectiveness of the IMS seismic network in the ME/NA. Unfortunately, many of the stations have not been installed and the poor geometry of currently installed IMS stations makes it difficult to obtain an initial estimate of the proposed networks ability to locate events accurately. Thus, a preliminary evaluation of the network is made by designing a surrogate network. This surrogate network is close, but not identical, to the proposed IMS network. Such a network may perform either better or worse than the proposed IMS system. Figure 4 illustrates the surrogate IMS network as utilized in this study. Stations were chosen such that the actual IMS stations was used if it exists. If an IMS station does not yet exist then the nearest station is used. For reference, the map also shows those stations that are within 50 km from a proposed IMS station and those that are greater than 50 km away.

Evaluating the effectiveness of this surrogate network can give a preliminary estimate of how the actual IMS may perform for regional events. We assume here that the TC events are recorded only at the corresponding regional and near teleseismic stations making it a regional event. These regional events are then separated into two sets. The first set consists of those events recorded with good regional station coverage. In this case the maximum azimuthal gap was required to be less than 180° . In other words, the event lies within the footprint of the locating stations. The first plot in Figure 5 shows the predicted location assuming no station calibration. The second plot shows the location given an optimal set of static station corrections that were estimated and applied using a leave-one-out robust statistical approach. Without any calibration the surrogate network locates to within 25 km. Static station corrections generate only a mild improvement, reducing the maximum horizontal error to about 20 km which is within the uncertainty of the known location of the TC event locations. The second set consists of those events that are outside the footprint of the recording regional stations, so that station coverage is poor. This is the case where the maximum azimuthal gap is greater than 180° . Figure 6, showing the resulting regional locations, demonstrates that this poorer station coverage results in much larger location errors. Horizontal differences reach values greater than 100 km, showing that large mislocations can occur when station coverage is poor. We are currently developing more robust nonlinear location techniques that can help to improve these regional locations.

A summary of the surrogate networks effectiveness is given in Figure 7. This plot shows that the locations appear to be good to within 20 km of the TC location when the azimuthal gap is less than 200°. Once the gap exceeds this value large mislocations can result. Clearly, static station corrections account for only a mild improvement in the regional locations.

Source specific travel-time correction surfaces. The station corrections utilized in the surrogate study were static station corrections, meaning that only a single correction was applied at each station. Given that such corrections appear to lead to only a mild improvement in location, we are currently working with SNL to evaluate the effectiveness of kriging and other geostatistical techniques as a means of estimating site-specific, travel-time corrections. Examination of travel-times from seismic sources to a particular station reveals that spatially clustered sources tend to have similar residuals, and the distance to which residuals are correlated can be quantified. Such spatial statistics of sampled data can be used to extrapolate residuals (and uncertainty) of sampled points to unsampled regions. Figure 8 is an example of using a modified kriging technique developed at SNL to estimate travel-time residuals for the station SHI in Iran. This example shows that (to first order) corrections to travel times based on event location produces a spatially coherent pattern. However, kriging and other geostatistical techniques often do not account for data characteristics that are common in seismological data sets. Specifically, the variance of travel-time residuals can change for each datum and current techniques do not use this information when estimating unsampled points. Additionally, some regions are sparsely sampled, forcing extrapolation of known data points far beyond average correlation distances. We are currently considering further modifications to the kriging technique that address these issues. Once statistical techniques are tailored to the special considerations of seismological data sets, these techniques will likely be useful for estimating a range of seismological parameters including discriminant corrections (e.g. Pg/Lg spectral ratios).

Conclusions and Recommendations

LLNL is working to develop improved IMS location estimates in the ME/NA through the use of ground truth calibrations. A ground truth hierarchical data base has been developed that includes more than one thousand TC events with event locations accurate to within 20 km. Utilizing this data base, static station corrections, 1-D regionalized velocity corrections, and more elaborate source specific station corrections are being developed and evaluated in this region.

Preliminary tests show that region specific static station corrections lead to only a mild improvement in regional locations. Thus, we are utilizing instead one-dimensional regionalized velocity models and more sophisticated correction surfaces to completely describe the final correction surfaces for each station. Initial estimates of these surfaces have been generated in conjunction with SNL using their modified kriging interpolation algorithm and performance of these correction surfaces is being assessed. We find that given the variable and somewhat large uncertainties associated with our hierarchical ground truth data base, it is clear that additional modifications need to be made to the kriging approach. These modifications need to allow for a better statistical estimate of the final correction surface when variable uncorrelated errors are present. We are currently examining a number of robust interpolation modifications and will present their ability to estimate and predict the uncertainty of source-specific travel-time corrections.

References

Cogbill, A. & Steck, L, 1996, Regional location in Western China, Proceedings of the 18th Annual Seismic Research Symposium on monitoring a CTBT, p. 685-694.

Sweeney, J., 1996, Accuracy of teleseismic event locations in the Middle East and North Africa. Lawrence Livermore National Laboratory, UCRL-ID-125868.

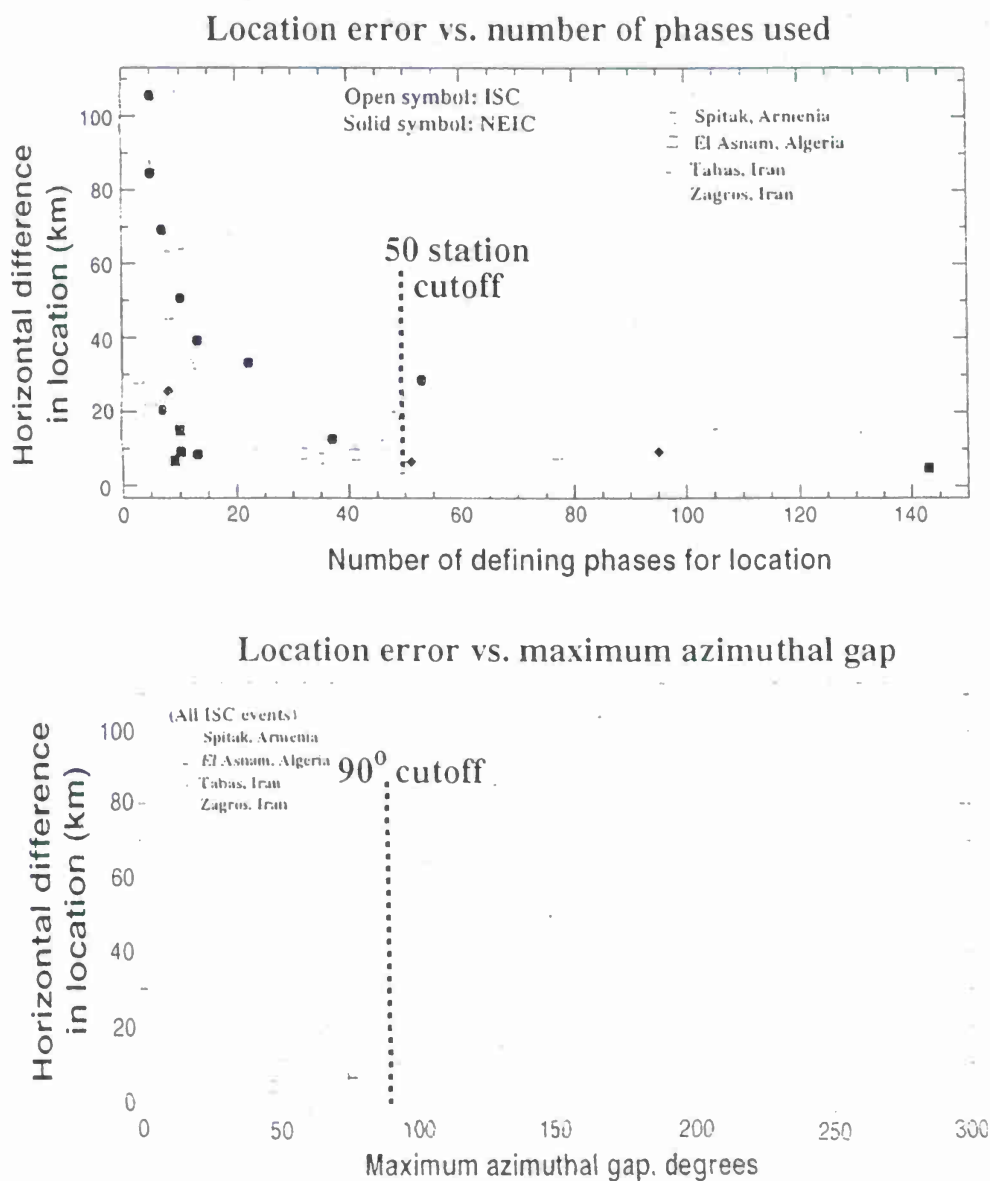


Figure 1. Summary of the results from Sweeney (1996) showing the horizontal difference between teleseismically constrained ISC/EDR event locations and more accurate aftershock/dense network locations. The horizontal difference is shown both as a function of (a) number of defining phases and (b) maximum azimuthal gap.

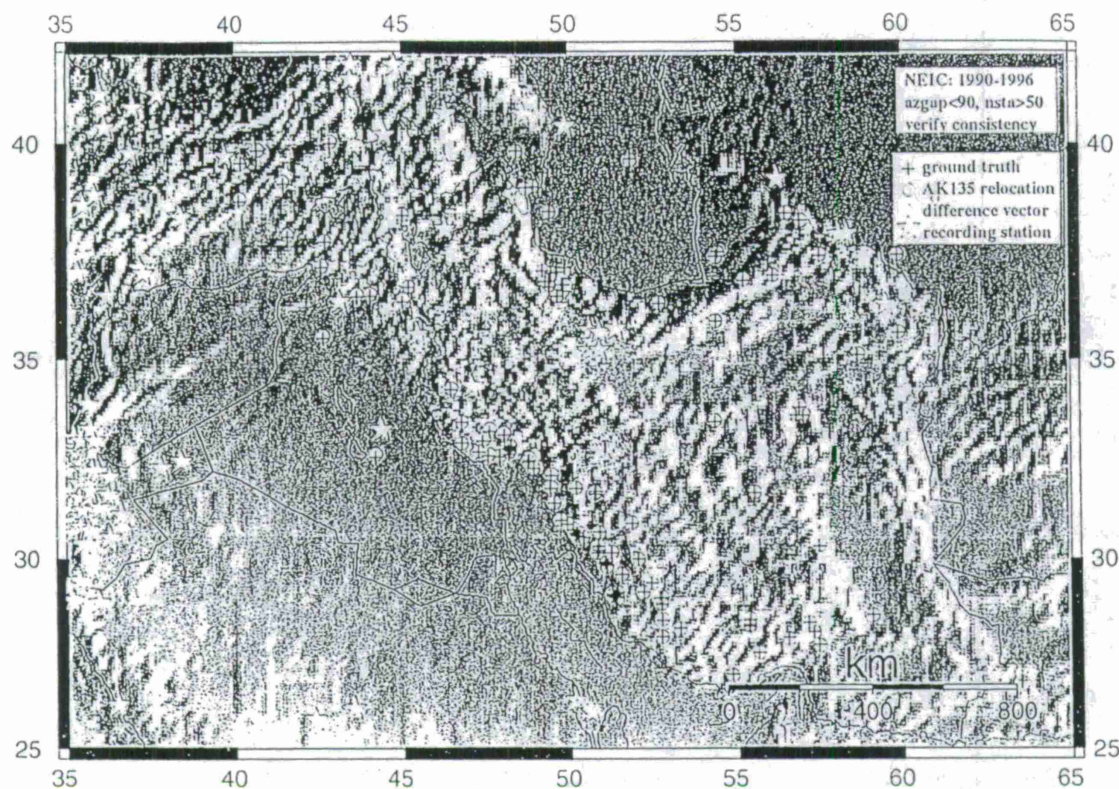


Figure 2. Plot showing teleseismic events relocated in a portion of the Middle East. Each of the events shown matches the 50-90 criterion based on the work of Sweeney (see Figure 1).

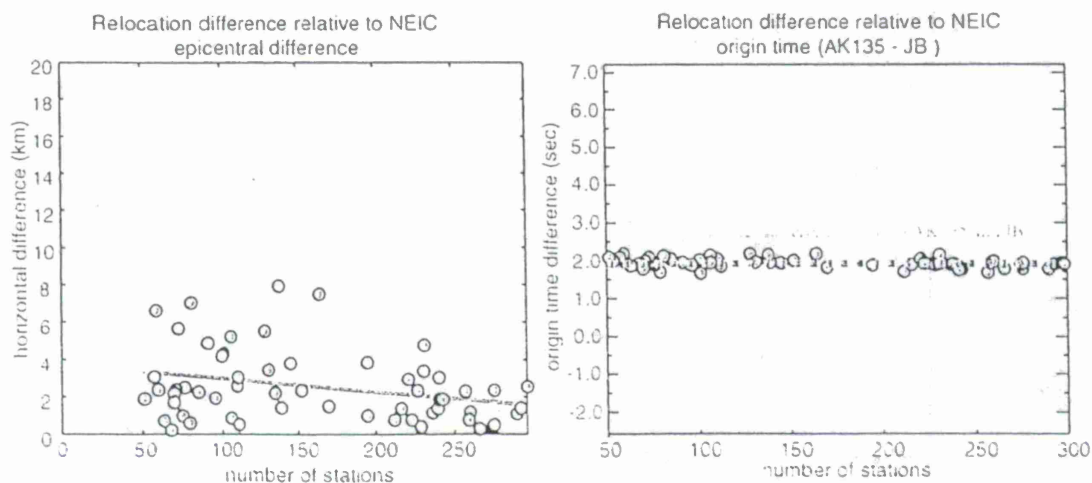


Figure 3. (a) horizontal difference and (2) origin time error for relocation of teleseismic events using AK135 velocity model and EDR travel-time picks.

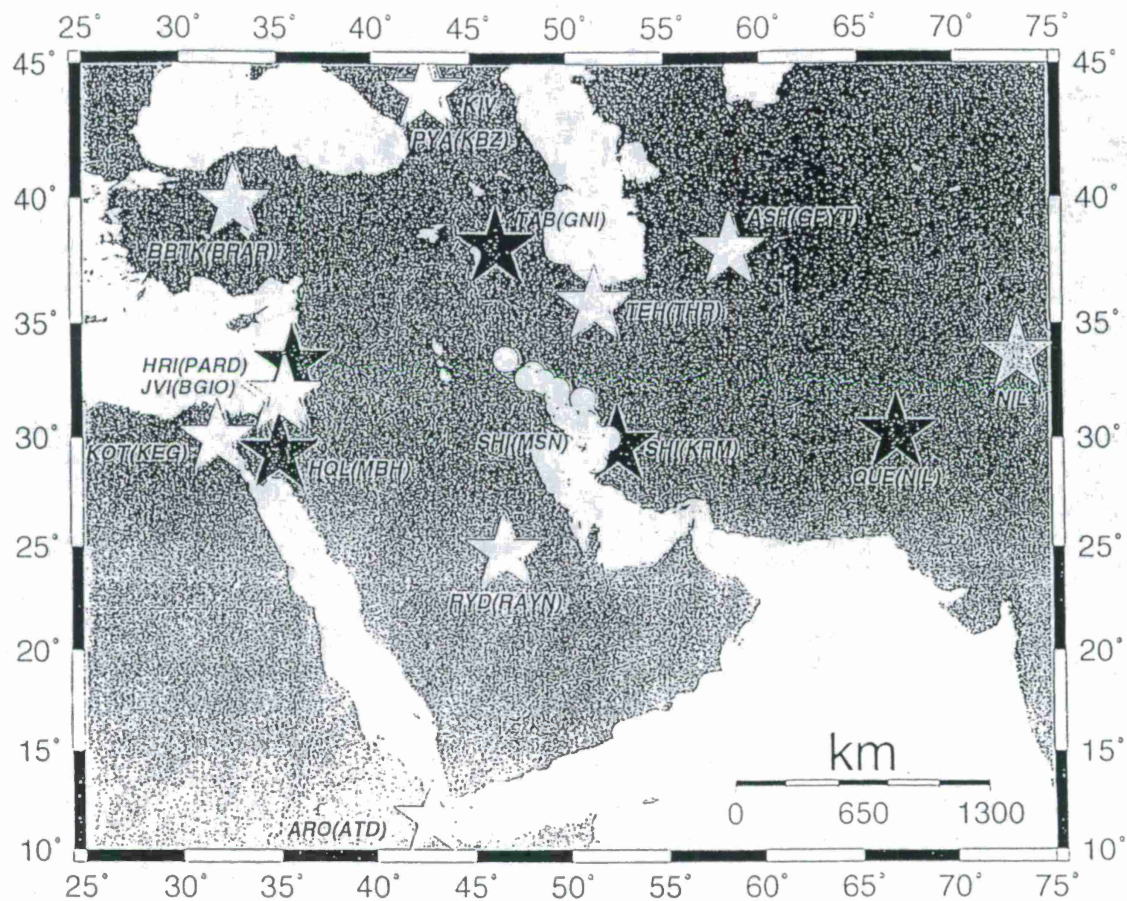


Figure 4. Map view of the surrogate IMS network used to make a first-order estimate of the networks effectiveness. The stars show actual IMS stations (light gray), EDR reporting stations that are within 50 km of a proposed IMS station (white), and EDR reporting stations that are greater than 50 km from a proposed station (dark gray). The circles show the events that to be relocated in the Zagros region.

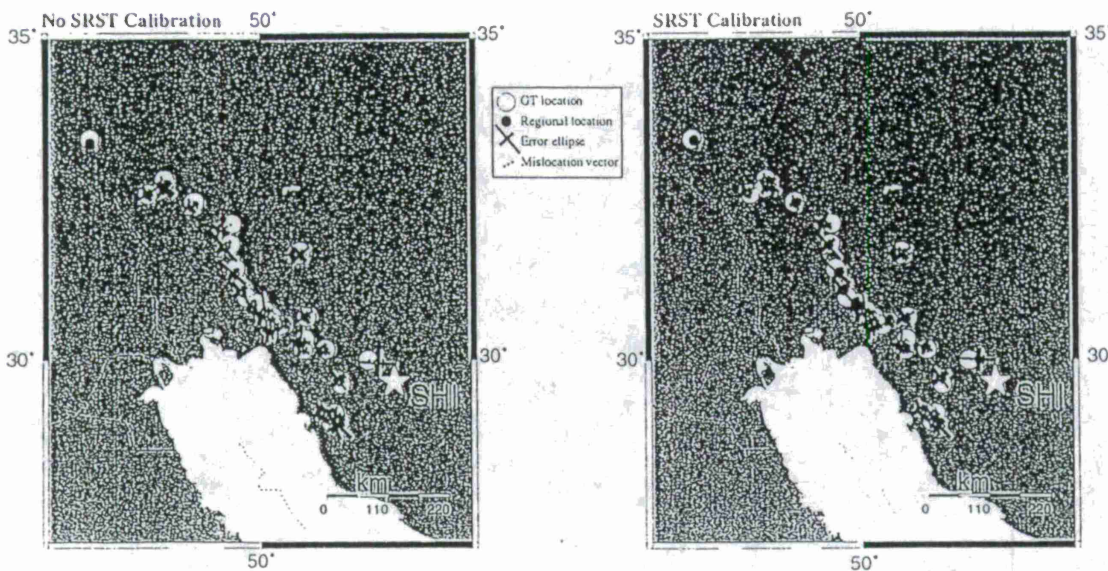


Figure 5. Map view of regional relocations plotted over the teleseismically constrained locations for the case that the event was within the footprint of the recording stations ($AzGap < 180^\circ$). The locations are shown for the case of no station calibration and the case of an optimal static station calibration. At least three regional P recordings were required for a location and station calibrations were applied only if 10 or more independent events were available for the correction.

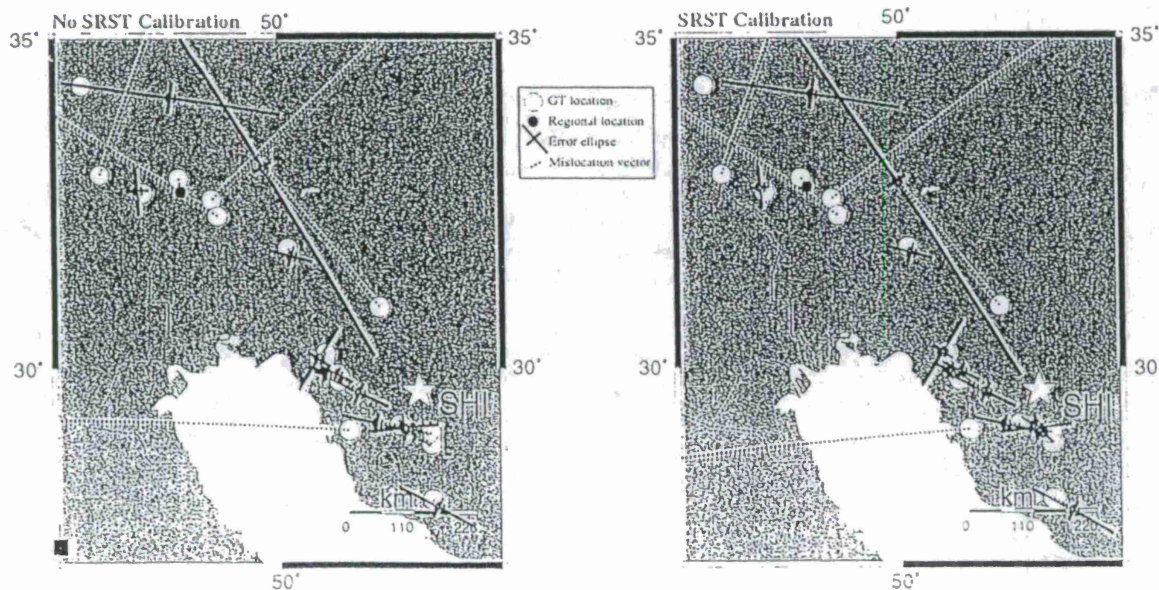


Figure 6. Similar to Figure 5, except that the events lie outside the footprint of the recording stations ($AzGap > 180^\circ$).

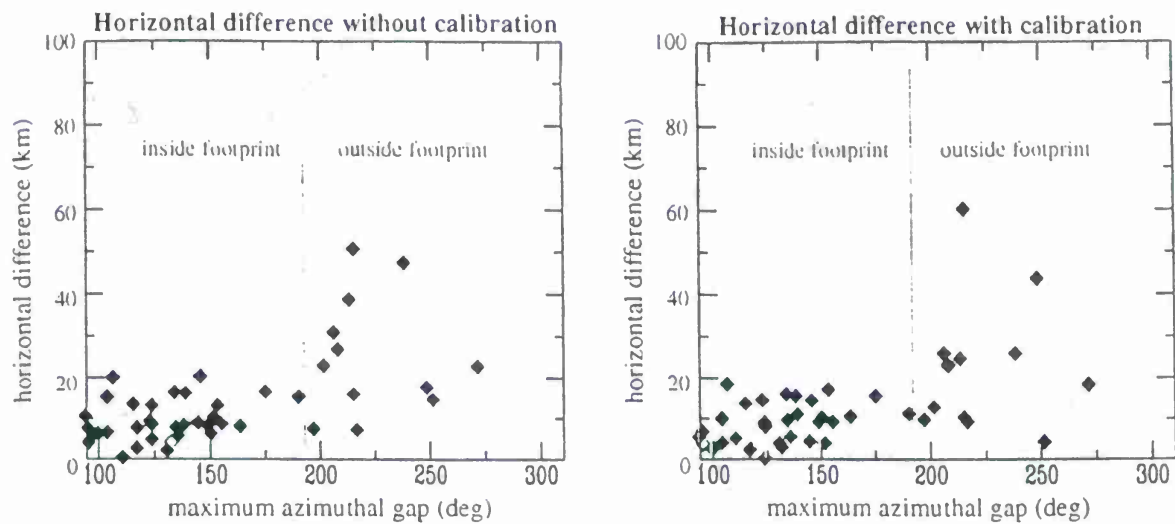


Figure 7. Summary figure showing the horizontal difference between the regional surrogate network and the teleseismically constrained location. Both the case of no calibration and the case of incorporating a static station correction are shown.

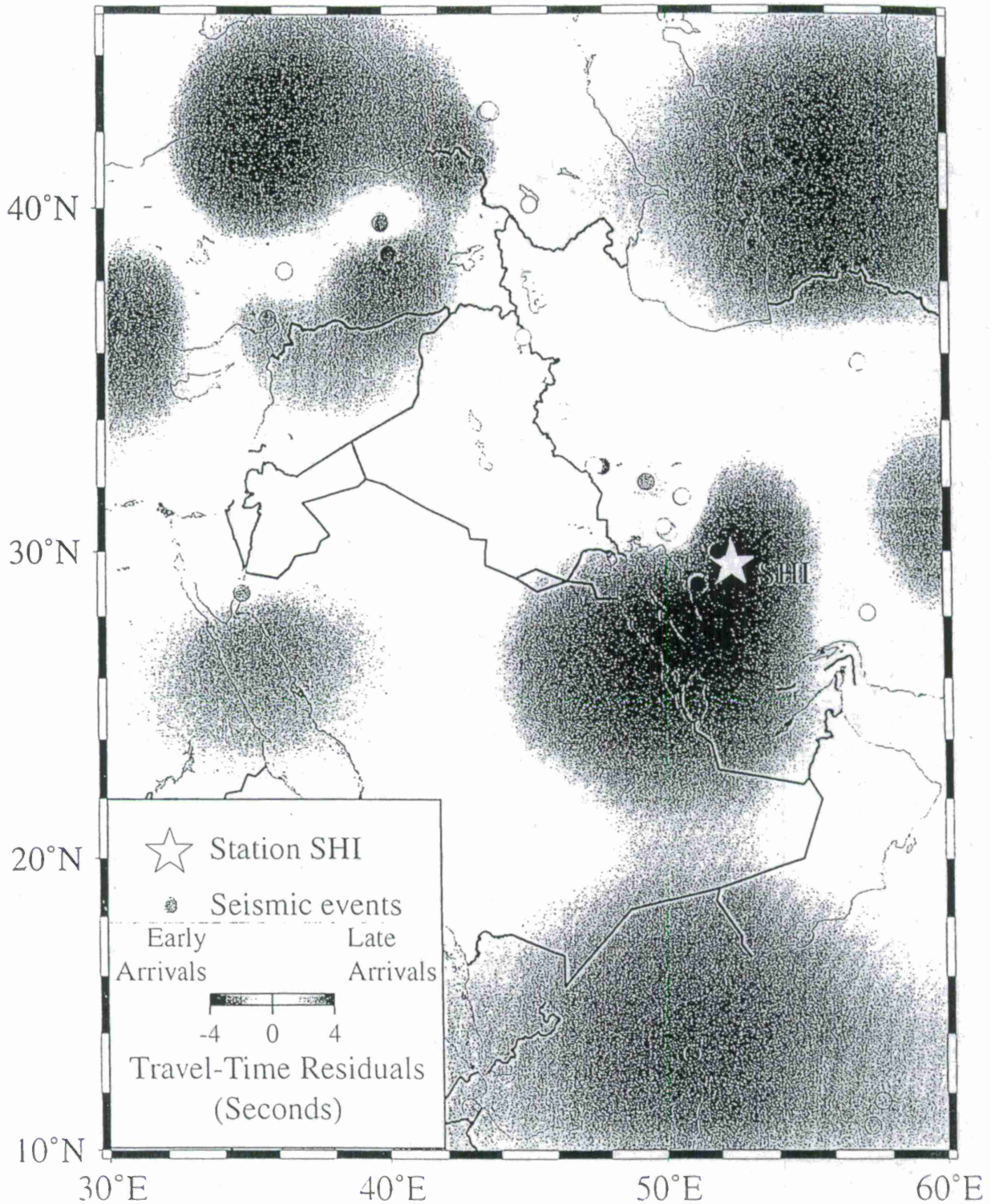


Figure 8: Kriged surface of travel-time residuals calculated using data from the events shown. Residuals of events and kriging results are color coded with red and blue representing late and early arrivals, respectively.

LOCATING NUCLEAR EXPLOSIONS USING WAVEFORM CROSS-CORRELATION

Peter M. Shearer and Luciana Astiz
Institute of Geophysics and Planetary Physics
University of California, San Diego
pshearer@ucsd.edu, lastiz@ucsd.edu

Sponsored by the U.S. Geologic Survey

ABSTRACT

We apply waveform cross-correlation to seismograms from the global seismic networks to measure the differential times between P-wave arrivals from nuclear explosions-at both the Semipalatinsk (Soviet) and Lop Nor (Chinese) test sites. Waveform cross-correlation is ideally suited for this purpose, due to the high degree of waveform similarity observed at individual stations between closely spaced events. The differential times are more precise than could be obtained by picking the P arrival times on the seismograms separately. We use these times to compute relative event locations at both test sites, using a grid-search algorithm based on the LI norm. Our locations show reduced scatter compared to catalog locations for these events and better agreement with satellite observations. This is achieved using only a small number of global stations (8 to 15). However, the accuracy of the final locations is sometimes limited by small timing errors (several tenths of seconds) in the seismic data. The technique should be applicable to other areas of clustered seismicity.

Keywords: event location, nuclear explosions

OBJECTIVE

To test the effectiveness of waveform cross-correlation methods in measuring relative locations between nuclear explosions.

RESEARCH ACCOMPLISHED

Introduction

Locating earthquakes is one of the oldest problems in seismology and remains an area of active research. The problem is complicated by the nonlinear dependence of seismic travel times on location, the often incomplete knowledge of the full three-dimensional velocity structure along the source-receiver paths, and difficulties associated with inadequate station coverage and outliers in the observed travel-time picks. The advent of computers enabled routine event locations for large numbers of events, using one-dimensional reference velocity models and linearized, least-squares techniques [e.g., *Flinn*, 1965]. This made possible the production of both global and local earthquake catalogs listing thousands of events, each located in a standard way.

As computer capabilities improved, researchers began to develop new methods for earthquake location. These include joint-hypocenter-velocity (JHV) inversions to handle the effects of three-dimensional velocity structure [e.g., *Thurber*, 1983; *Dziewonski*, 1984; *Eberhart-Phillips*, 1990; *Lees and Malin*, 1990; *Magistrale et al.*, 1992; *Eberhart-Phillips and Michael*, 1993; *Vasco et al.*, 1994; *Magistrale and Sanders*, 1996], techniques to downweight the effect of data outliers [e.g., *Anderson*, 1982; *Buland*, 1986; *Kennett*, 1992; *Kijko*, 1994], station term and master event methods to improve relative location accuracy in clusters of events [e.g., *Douglas*, 1967; *Evernden*, 1969; *Frohlich*, 1979; *Jordan and Sverdrup*, 1981; *Smith*, 1982; *Pavlis and Booker*, 1983; *Pujol*, 1988], grid search, simulated annealing and evolutionary programming approaches to finding global misfit minima [e.g., *Sambridge and Kennett*, 1986; *Sambridge and Gallagher*, 1993; *Billings*, 1994; *Billings et al.*, 1994; *Minster et al.*, 1995].

When seismic waveforms are available, cross-correlation techniques can be used to achieve precise relative locations between closely spaced events with similar waveforms [e.g., *Poupinet et al.*, 1984; *Ito*, 1985, 1990; *Fremon and Malone*, 1987; *Xie et al.*, 1991; *Deichmann and Garcia-Fernandez*, 1992; *Nadeau et al.*, 1995; *Haase et al.*, 1995; *Dodge et al.*, 1995; *Got et al.*, 1994; *Gillard et al.*, 1996; *Shearer*, 1997]. This approach is illustrated in Figure 1. Two nearby events will often produce nearly identical waveforms at individual stations, despite the fact that the waveforms vary widely between stations. If the waveforms are similar enough, a time shift can be obtained from the cross-correlation function (or from the phase spectra in frequency domain methods). These differential times are typically much more accurate than can be measured by picking individual seismograms, and can be used to compute high-precision relative event locations. For local earthquakes, standard location errors of tens of meters or less have been achieved for closely spaced events.

Despite these successes the waveform cross-correlation approach has generally been used only to relocate small numbers of earthquakes in special areas of interest and has not been applied to large portions of earthquake catalogs. This stems in part from the storage and computational difficulties associated with computing cross-correlation functions for large numbers of events. It is also unclear how similar the earthquakes must be in location and focal mechanism for the method to produce useful results. Cross-correlation methods have most often been applied to local earthquake data and their applicability to teleseismic records from the global seismic networks is uncertain.

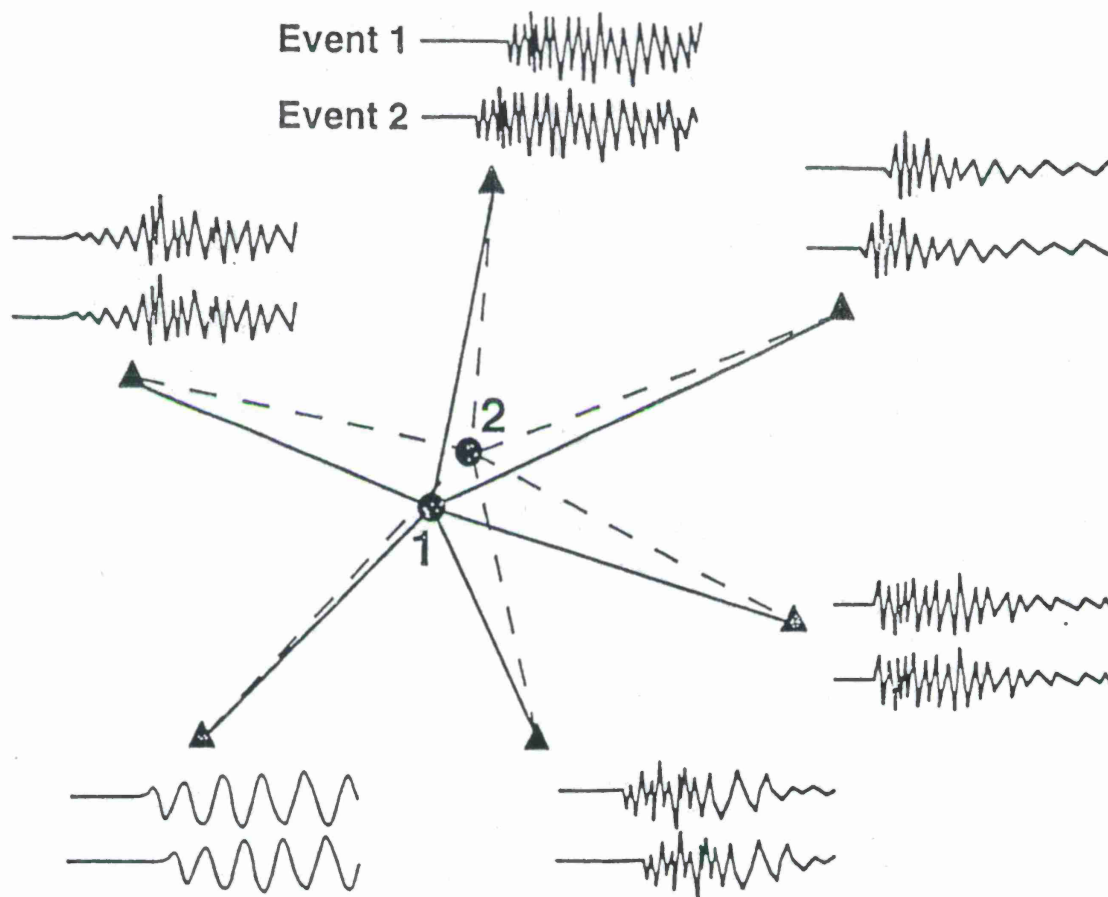


Figure 1. A cartoon showing how waveform cross-correlation has been used to improve relative event location. Two closely spaced earthquakes will often produce similar waveforms at individual seismic stations, even though the traces may vary widely between different stations due to propagation and site effects. If the waveforms are similar enough, cross-correlation can be used to measure differential times between the events; these times are more accurate than individual arrival times can be picked. These times can then be used to constrain the relative location between the two events.

Nuclear explosions at the major test sites are an ideal test case for cross-correlation methods because they provide a series of closely located events with similar source mechanisms. In addition, their locations are often precisely known so that the effectiveness of relocation methods can be directly tested. Here, we examine waveform data from two nuclear test sites—the Soviet Kazakhstan site and the Chinese Lop Nor site.

The Kazakhstan test site

For Kazakhstan, we extracted short-period, vertical component data for 30 events between 1980 and 1987 from GDSN stations as archived by the National Earthquake Information Center (NEIC) on CD-ROM. These data windows do not include the *S* arrivals, so our analysis is limited to *P* data. Figure 2 plots a comparison of seismograms recorded at 8 different stations for a pair of events, a $m_b=6.1$ event on 12 June 1983 and a $m_b=5.9$ event on 20 July 1985. The waveforms are very similar, and the cross-correlation functions show well defined peaks. Other

event pairs exhibited comparable levels of correlation, and 22 events were sufficiently similar that their relative locations could be computed.

Kazakhstan Event Pair

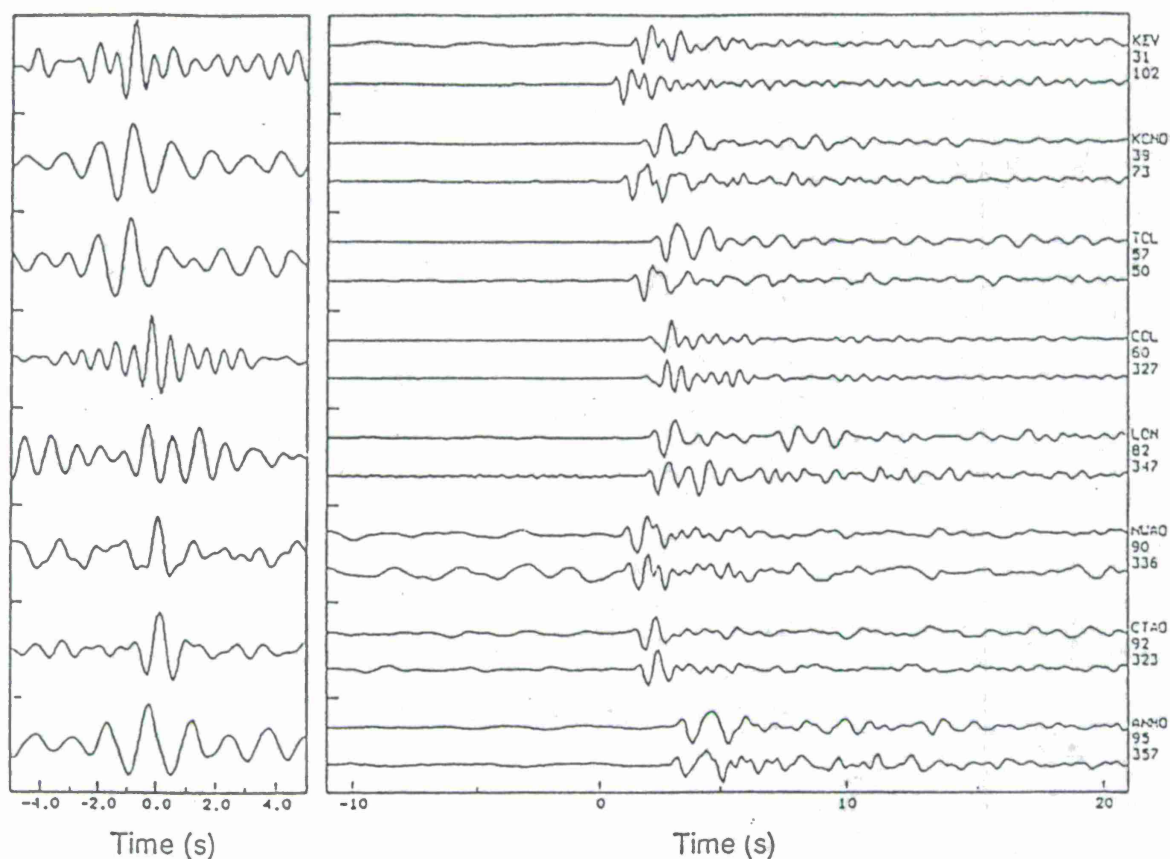


Figure 2. Short period GDSN records of the P wave from a pair of nuclear explosions at the Kazakhstan test site in the former Soviet Union. The top trace in each pair is from a $m_b=6.1$ event on 12 June 1983, the bottom trace is from a $m_b=5.9$ event on 20 July 1985. Station names, ranges, and azimuths are plotted on the right. Note the very similar waveforms produced by the two events. Cross-correlation functions for these traces are plotted on the left; the well-defined peaks can be used to define very accurate differential times at each station.

We compute cross-correlation functions between records for every pair of events. For n events, this results in a total of $n(n-1)/2$ possible pairs. From the peaks in the cross-correlation functions we estimate differential times between the waveforms. We then compute the relative location between the event pair using a grid-search, L1-norm approach [see *Shearer, 1997*, for details] for robustness with respect to data outliers. Finally we reconcile all of the differential locations from the different event pairs into a single best-fitting set of relative locations for all of the events. This is analogous to the method used by *Got et al. [1994]* for the local earthquake location problem, except that, for robustness, we use the L1-norm measure of misfit and we apply a grid-search approach to computing the differential locations, avoiding the need to linearize this step.

The resulting relocations show less scatter than the NEIC locations for the same events

(Figure 3). Estimated standard location errors for most of the events are less than 1 km. For comparison, locations obtained from analysis of satellite images by *Thurber et al.* [1994] are also plotted. These locations agree much more closely to our relocated events than to the original catalog locations. However, there are still some discrepancies, which may be caused by absolute timing errors in the waveform data (see below).

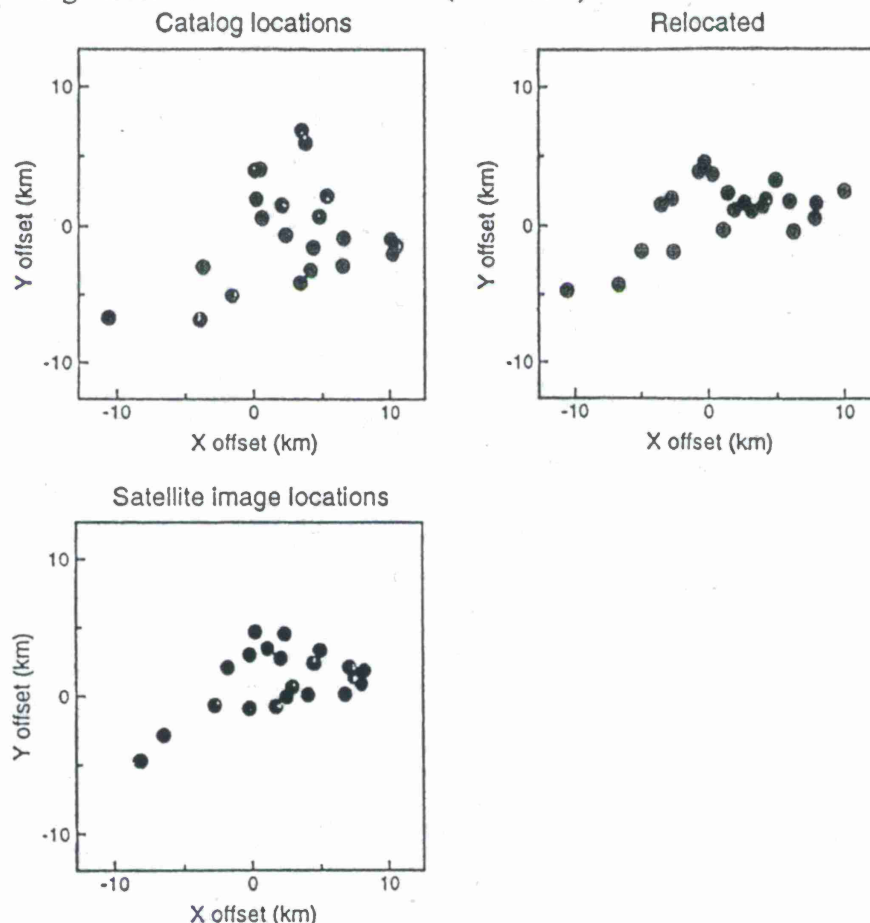


Figure 3. Relative locations for 22 events at the Balapan test site in Kazakhstan as derived from the PDE catalog (top), determined using our waveform cross-correlation procedure (middle), and estimated from satellite images by *Thurber et al.* [1994] (bottom). Note the reduced scatter in the revised locations compared to the PDE locations and the better agreement with the satellite locations.

The Lop Nor test site

For the Chinese test site, we examined data from IRIS stations for 7 events of $m_b > 5.5$ between 1990 and 1995. Figure 4 plots P arrivals at 10 different stations for a pair of events, a $m_b=6.1$ event on 15 May 1995 and a $m_b=6.0$ event on 17 August 1995. The vertical component data have been filtered to between 0.4 and 2 Hz. For this event pair, the waveforms are very similar and the cross-correlation functions show well defined peaks. Six events are similar enough to relocate with our method; our relocations for these events are compared to the PDE locations in Figure 5. The scatter in the location is reduced; the estimated location errors are generally between 1 and 3 km (in these examples, we do not attempt to solve for depth; we assume the sources are at the surface).

Lop Nor Event Pair

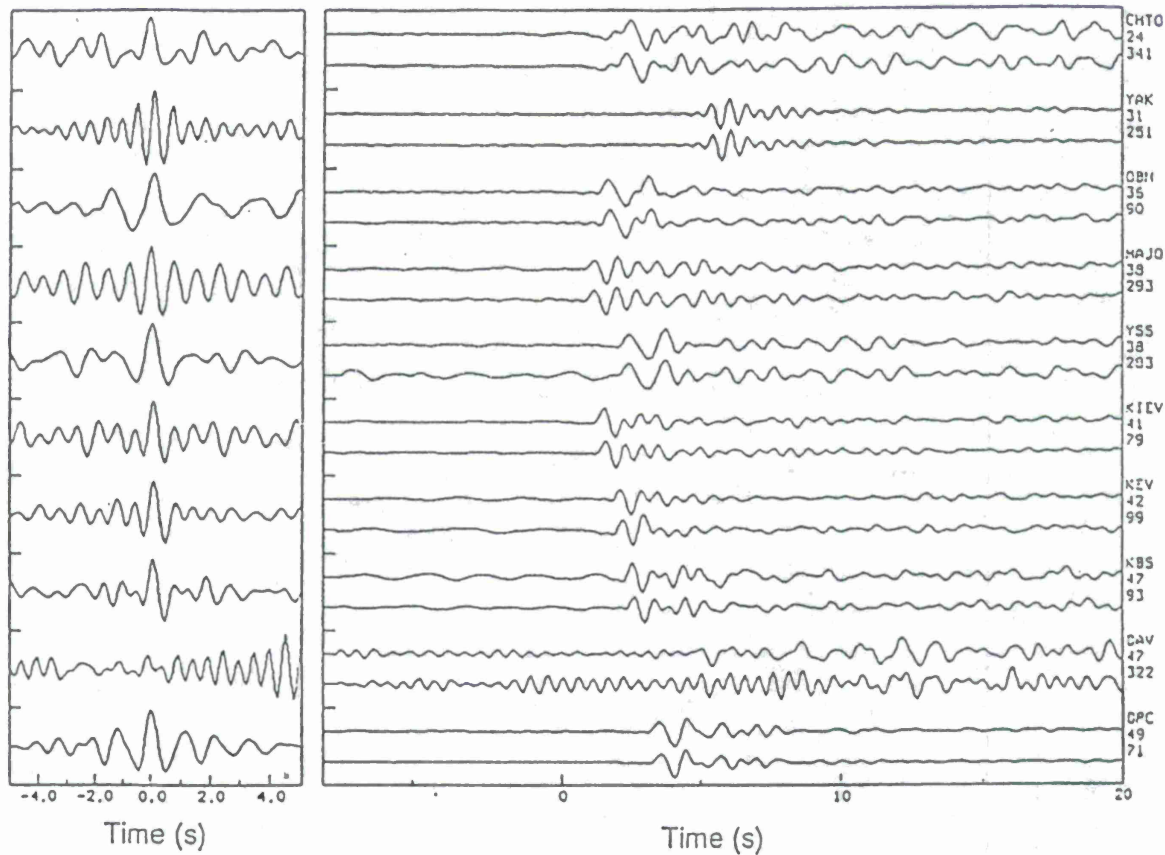


Figure 4. Teleseismic records of the P wave from a pair of nuclear explosions at the Lop Nor test site in China. The top trace in each pair is from a $m_b=6.1$ event on 15 May 1995, the bottom trace is from a $m_b=6.0$ event on 17 August 1995. Station names, ranges, and azimuths are plotted on the right. Note the very similar waveforms produced by the two events. Cross-correlation functions for these traces are plotted on the left; the well-defined peaks for most of the stations can be used to define very accurate differential times.

One source of bias that is not removed through waveform cross-correlation is absolute timing errors for individual seismograms. This is not a problem for network data that are telemetered and recorded with a common time base. Unfortunately, in the global data, it appears that small timing errors of 0.1 to 0.3 s are common in many of the older records. This is apparent in careful examination of the cross-correlation results for the Kazakhstan data and probably is an important factor limiting the accuracy of our final results. Modern seismographs have more accurate clocks and are presumably less prone to such problems. In principle, the uncertainties associated with timing errors could be eliminated through the use of differential times between different phases, such as P and S . We plan to experiment with this approach to see if any improvements to our results are possible, and to begin characterizing the extent of timing problems in the global networks.

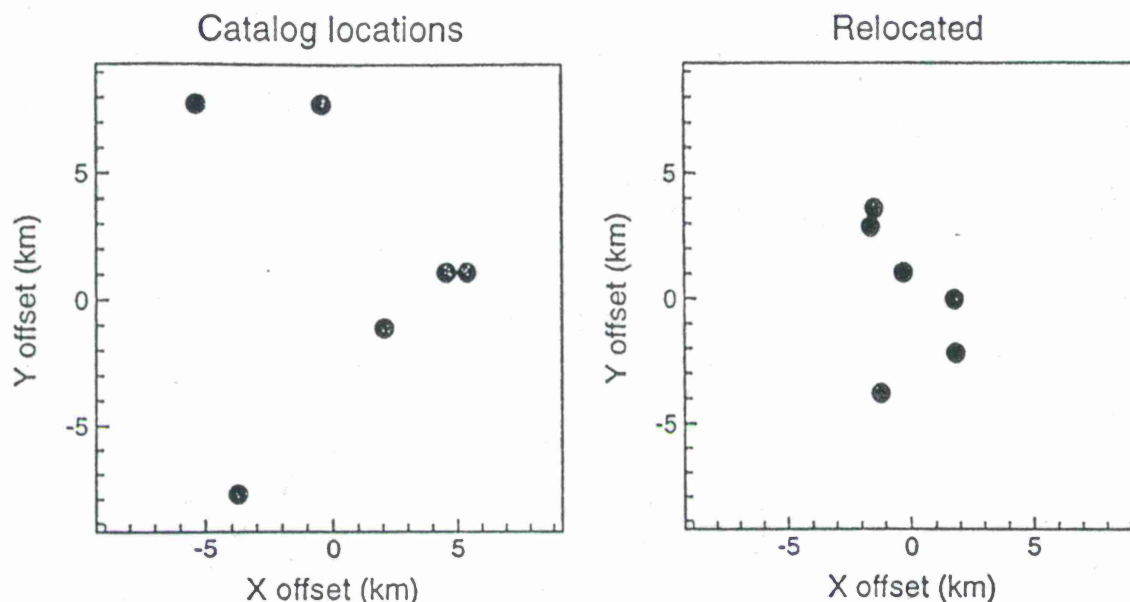


Figure 5. Relative locations for 6 events at the Lop Nor test site as derived from the PDE catalog (left) and determined using waveform cross-correlation (right). Note the reduced scatter in the revised locations.

CONCLUSIONS AND RECOMMENDATIONS

Differential locations provided by waveform cross-correlation methods promise to provide a useful complement to ongoing efforts in seismic tomography and joint-hypocenter-velocity (JHV) inversions, which improve absolute event locations but do not affect relative event locations at 1 to 20 km spacing. Waveform cross-correlation produces information in addition to differential times. For example, the optimal amplitude scaling between traces is provided by the cross-correlation function and could be used to compute differential magnitudes between event pairs. One could then solve for a best fitting magnitude for each event, probably obtaining much greater accuracy than the nominal 0.1 precision with which magnitudes are generally listed in earthquake catalogs. It also would be useful to explore the relationship between event focal mechanism and the degree of waveform similarity. If waveforms remain similar for closely spaced events with different focal mechanisms, differing primarily only in their amplitude and polarity, it might be possible to compute differential focal mechanisms using waveform cross-correlation. This would be analogous to a method used by *Ekström and Richards* [1994] to determine source parameters of closely spaced events using surface wave amplitudes. Finally, waveform cross-correlation might prove useful in detecting anomalous events in regions of known seismicity. For example, if new events were routinely cross-correlated against previous nearby events, this could provide an automated way to identify explosions.

References

- Anderson, K.R., Robust earthquake location using M-estimates, *Phys. Earth Planet. Inter.*, 30, 119-130, 1982.
- Billings, S.D., Simulated annealing for earthquake location, *Geophys. J. Int.*, 118, 680-692, 1994.
- Billings S.D., B.L.N. Kennett and M.S. Sambridge, Hypocentre location: genetic algorithms incorporating problem-specific information, *Geophys. J. Int.*, 118, 693-706, 1994.
- Buland, R., Uniform reduction error analysis, *Bull. Seismol. Soc. Am.*, 76, 217-230, 1986.

- Deichmann, N. and M. Garcia-Fernandez, Rupture geometry from high-precision relative hypocentre locations of microearthquake clusters, *Geophys. J. Int.*, **110**, 501-517, 1992.
- Dodge, D.A., G.C. Beroza and W.L. Ellsworth, Foreshock sequence of the 1992 Landers, California, earthquake and its implications for earthquake nucleation, *J. Geophys. Res.*, **100**, 9865-9880, 1995.
- Douglas, A., Joint epicentre determination, *Nature*, **215**, 47-48, 1967.
- Dziewonski, A.M., Mapping the lower mantle: determination of lateral heterogeneity in P velocity up to degree and order 6, *J. Geophys. Res.*, **89**, 5929-5952, 1984.
- Eberhart-Phillips, D., Three-dimensional P and S velocity structure in the Coalinga region, California, *J. Geophys. Res.*, **95**, 15,343-15,363, 1990.
- Eberhart-Phillips, D. and A.J. Michael, Three-dimensional velocity structure, seismicity, and fault structure in the Parkfield region, central California, *J. Geophys. Res.*, **98**, 15,737-15,758, 1993.
- Ekström, G. and P.G. Richards, Empirical measurements of tectonic moment release in nuclear explosions from teleseismic surface waves and body waves, *Geophys. J. Int.*, **117**, 120-140, 1994.
- Evernden, J.F., Precision of epicentres obtained by small numbers of world-wide stations, *Bull. Seismol. Soc. Am.*, **59**, 1365-1398, 1969.
- Flinn, E.A., Confidence regions and error determinations for seismic event location, *Rev. Geophys.*, **3**, 157-185, 1965.
- Fremont, M.J. and S.D. Malone, High precision relative locations of earthquakes at Mount St. Helens, Washington, *J. Geophys. Res.*, **92**, 10223-10236, 1987.
- Frohlich, C., An efficient method for joint hypocenter determination for large groups of earthquakes, *Comput. Geosci.*, **5**, 387-389, 1979.
- Gillard, D., A.M. Rubin and P. Okubo, Highly concentrated seismicity caused by deformation of Kilauea's deep magma system, *Nature*, **384**, 3433-346, 1996.
- Got, J.-L., J. Fréchet and F.W. Klein, Deep fault plane geometry inferred from multiplet relative relocation beneath the south flank of Kilauea, *J. Geophys. Res.*, **99**, 15,375-15,386, 1994.
- Haase, J.S., P.M. Shearer and R.C. Aster, Constraints on temporal variations in velocity near Anza, California, from analysis of similar event pairs, *Bull. Seismol. Soc. Am.*, **85**, 194-206, 1995.
- Ito, A., High resolution relative hypocenters of similar earthquakes by cross-spectral method, *J. Phys. Earth*, **33**, 279-294, 1985.
- Ito, A., Earthquake swarm activity revealed from high-resolution relative hypocenters—clustering of microearthquakes, *Tectonophysics*, **175**, 47-66, 1990.
- Jordan, T.H. and K.A. Sverdrup, Teleseismic location techniques and their application to earthquake clusters in the south-central Pacific, *Bull. Seismol. Soc. Am.*, **71**, 1105-1130, 1981.
- Kennett, B.L.N., Locating oceanic earthquakes—the influence of regional models and location criteria, *Geophys. J. Int.*, **108**, 848-854, 1992.
- Kijko, A., Seismological outliers: L_1 or adaptive L_P norm application, *Bull. Seismol. Soc. Am.*, **84**, 473-477, 1994.
- Lees, J.M. and P.E. Malin, Tomographic images of P wave velocity variation at Parkfield, California, *J. Geophys. Res.*, **95**, 21,793-21,804, 1990.
- Magistrale, H., H. Kanamori and C. Jones, Forward and inverse three-dimensional P wave velocity models of the southern California crust, *J. Geophys. Res.*, **97**, 14,115-14,135, 1992.
- Magistrale, H. and C. Sanders, Evidence from precise earthquake hypocenters for segmentation of the San Andreas fault in San Geronio Pass, *J. Geophys. Res.*, **101**, 3031-3044, 1996.
- Minster, J.-B. H., N.P. Williams, T.G. Masters, J.F. Gilbert and J.S. Haase, Application of evolutionary programming to earthquake hypocenter determination, in *Evolutionary programming; Proceedings of the fourth annual conference on EP*, Ed. J. McDonnell, pp.3-17, 1995.
- Nadeau, R.M., W. Foxall and T.V. McEvilly, Clustering and periodic recurrence of microearthquakes on the San Andreas Fault at Parkfield, California, *Science*, **267**, 503-507, 1995.
- Pavlis, G.L. and J.R. Booker, Progressive multiple event location (PMEL), *Bull. Seismol. Soc. Am.*, **73**, 1753-1777, 1983.
- Poupinet, G., W.L. Ellsworth and J. Fréchet, Monitoring velocity variations in the crust using earthquake doublets: an application to the Calaveras fault, *J. Geophys. Res.*, **89**, 5719-5731, 1984.
- Pujol, J., Comments of the joint determination of hypocenters and station corrections, *Bull. Seismol. Soc. Am.*, **78**, 1179-1189, 1988.
- Sambridge, M. and K. Gallagher, Earthquake hypocenter location using genetic algorithms, *Bull. Seismol. Soc. Am.*, **83**, 1467-1491, 1993.
- Sambridge, M.S. and B.L.N. Kennett, A novel method of hypocentre location, *Geophys. J. R. Astron. Soc.*, **87**, 679-697, 1986.

- Shearer, P.M., Improving local earthquake locations using the L1-norm and waveform cross-correlation: application to the Whittier Narrows, California, aftershock sequence, *J. Geophys. Res.*, *102*, 8269–8283, 1997.
- Smith, E.G.C., An efficient algorithm for routine joint hypocentre determination, *Phys. Earth Planet. Inter.*, *30*, 135–144, 1982.
- Thurber, C.H., Earthquake locations and three-dimensional crustal structure in the Coyote Lake area, central California, *J. Geophys. Res.*, *88*, 8226–8236, 1983.
- Thurber, C.H., H.R. Quinn and R. Saleh, Catalog of locations of nuclear explosions at Balapan, Kazakhstan, 1965 to 1985, *Bull. Seismol. Soc. Am.*, *84*, 458–461, 1994.
- Vasco, D.W., R.J. Pulliam, L.R. Johnson and P.S. Earle, Robust inversion of IASP91 travel time residuals for mantle P and S velocity structure, earthquake mislocations, and station corrections, *J. Geophys. Res.*, *99*, 13,727–13,755, 1994.
- Xie, J., Z. Liu, R.B. Herrmann and E. Cranswick, Source processes of three aftershocks of the 1983 Goodnow, New York, earthquake: high resolution images of small symmetric ruptures, *Bull. Seismol. Soc. Am.*, *81*, 818–843, 1991.

RELOCATION OF GULF OF AQABA EARTHQUAKES USING THE JSOP BULLETIN

Jerry J. Sweeney, Lawrence Livermore National Laboratory

Sponsored by U.S. Department of Energy
Office of Nonproliferation and National Security
Office of Research and Development
DOE Contract No. W-7405-ENG-48

ABSTRACT

Ground truth information (i.e. precise information about the hypocenter and origin time of a seismic event) is difficult to obtain in the Middle East and North Africa region. One source of ground truth we are attempting to exploit is data from local seismic networks. An electronic bulletin from the second phase of the Joint Seismic Observation Period (JSOP), with participating countries in the eastern Mediterranean region, provides a source of local network data not ordinarily available. I have used JSOP bulletin data for the period January 1996 through June 1996 to relocate over 100 earthquakes occurring in and around the Gulf of Aqaba. Fourteen of these earthquakes have picks in the bulletin for stations surrounding the Gulf (Egypt, Saudi Arabia, Israel, and Jordan). The rest of the data involves picks for stations either in Israel, Jordan, and Saudi Arabia (east side and north of the Gulf) or for stations in Israel, Jordan, and Egypt (west side and north of the Gulf). The VELEST code (Joint Hypocenter Determination method) was used to calculate improved locations (over what can be obtained from single event determinations--SED with poor station configurations) for the all the earthquakes in the data set. Location differences between the JHD solution and SED are discussed, along with determination of the minimum 1-D velocity model. Waveform correlation was used to validate observed event clusters in the VELEST solutions. This provided evidence that some of the VELEST solutions are more accurate than NEIC solutions. The subset of 14 events with good station coverage provides a good set of ground truth (location uncertainty < 5 km). The rest of the events are probably located more accurately with local data than is available from NEIC determinations, but such a conclusion needs to be supported by further study.

OBJECTIVE

Ground truth information (i.e. precise hypocenter and origin time) from regional earthquakes, mine explosions, calibration explosions, or other seismic sources is essential for the development of regional seismic monitoring (detection, location, discrimination) capabilities. The Comprehensive Test Ban Treaty (CTBT) research program at LLNL is currently developing seismic data for a knowledge base for the Middle East and North Africa (MENA) region. The objective of the work reported in this paper is to create ground truth seismic events by analyzing data from a series of recent earthquakes in the Gulf of Aqaba. Local networks operated by Israel-Jordan (IL), the Egyptian Geological Survey (EGS), and King Saud University in Saudi Arabia (KSU) provide a distribution of stations surrounding the area where local earthquake swarms have been occurring in the Gulf of Aqaba since 1993. Picks of P and S phases at stations from these networks are included in the bulletin of phase two of the Joint Seismic Observation Period (JSOP), assembled by the European-Mediterranean Seismic Center (EMSC). In the bulletin, there are three groups of station configurations associated with earthquakes in the Gulf of Aqaba: 1) events with coverage to the north, east, and west (IL+KSU+EGS), 2) events with coverage only from the north and west (IL+EGS), and 3) events with coverage from the north and east (IL+KSU). With full station coverage (IL+EGS+KSU), it is expected that events inside the combination of networks will be located well with standard methods (e.g. HYPO71 - Lee and Lahr, 1975 or HYPOINVERSE - Klein, 1978). However, the station configurations (IL+EGS) and (IL+KSU) are not well suited for reliable locations with standard methods. For this study, we used a combination of the three configurations in a Joint Hypocenter Determination (JHD) mode, incorporating the code VELEST (Kissling et al., 1994) to obtain improved locations and origin times as well as regional station corrections.

RESEARCH ACCOMPLISHED

Data

Because of additional stations and added country participation, data from many more stations were available during round two of the JSOP, which took place during 1995-1996. Figure 1 shows locations of most of the stations (excepting those in Yemen and many in Turkey) providing data to the bulletin assembled by the EMSC. Note that station coverage is most dense in the more populated areas of the region and along the Gulf of Aqaba-Jordan-Dead Sea transform, an area of significant seismic hazard.

We obtained an electronic version of the JSOP bulletin (the most recent version was obtained in mid-April 1997) from the EMSC. In the bulletin format, each event is listed starting with location/origin time/magnitude data as determined by each separate network (e.g. IL and/or EGS and/or KSU and/or SYR [Syria]) followed by a listing of stations from the combined networks with picks of P and S phases. Origin times and locations quoted in the bulletin for each event come from each network separately, with no determinations from combinations of networks. A C++ program was written to scroll the bulletin for identification of individual events and save each one as a separate file in HYPOINVERSE/HYPO71 format. Using this code, events were selected which had preliminary locations identified with the Gulf of Aqaba region and for which there were more than four stations reporting. The events were put into the categories IL+KSU+EGS, IL+KSU, or IL+EGS depending on the station configuration as described above. The files were checked for obvious bad data or format irregularities and location solutions were

obtained for each event using HYPO71. The initial 1-D velocity model for the HYPO71 calculations was based on results of a seismic refraction study along the western side of the Gulf of Aqaba (Ginzburg et al., 1979). See below for further discussion of the velocity model. Travel time data for the P and S phases indicate that the P_g velocity in the region is approximately 6.8 km/s, with a transition to P_n (about 8.0 km/s) at a distance of 150-200 km. Shear wave velocity at distances < 250 km or so is about 3.8 km/s. More detailed study of the travel time residuals from the initial HYPO71 locations revealed that there is a systematic increase in the P residuals of about 2 seconds at distances greater than 150 km for stations to the north in the Israel-Jordan network. Such a difference could be due to systematic clock errors or (more likely) due to a variation in crustal velocities; for this study, I limited station distance to 150 km for location calculations. In addition to the 150 km limit, I also determined 95% confidence limits (two standard deviations from the mean) to the P and S residuals and removed all picks outside of these limits. This refined data set was then used to calculate a new set of locations with HYPO71 using the same 1-D velocity model as before.

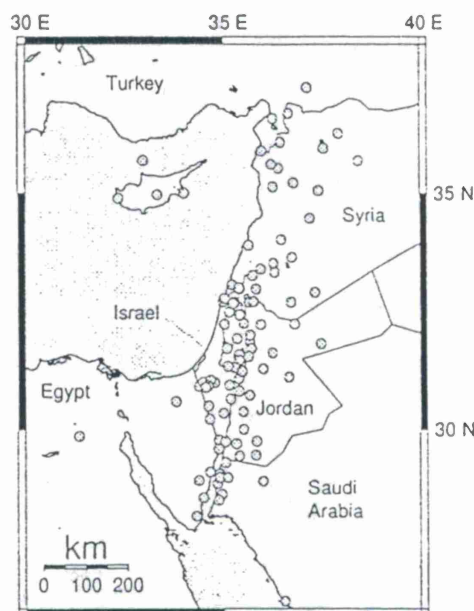


Figure 1. Map showing locations of most of the stations involved in the second phase of JSOP.

The final set of data consisted of 106 events, 14 of which were detected by the IL+KSU+EGS combined stations. Of the rest, about 60% involved the IL+KSU combination and about 40% the IL+EGS combination. There were no KSU stations reported in the catalog for the period March-June 1996; hopefully the next bulletin update will include additional data from the KSU stations and greatly increase the number of events with IL+KSU+EGS station coverage.

VELEST Calculations

The initial locations determined by HYPO71 were used as input for JHD locations with the VELEST code. A UNIX script was used to convert the HYPO71 output file into VELEST input format. VELEST simultaneously inverts the complete set of events for location, 1-D velocity structure, and station corrections for P and S phases. Station YASH, located in Israel at the north-

ern end of the Gulf of Aqaba, had the largest number of events in common from all three station configurations and was thus used as the reference station. Many different initial velocity models were tried in order to define the solution space, as recommended by Kissling et al. (1994). The set of 14 events with good station coverage were run separately prior to running all of the events simultaneously. The optimum velocity model and locations for these two sets of events were very similar (with a lower combined rms residual for the smaller set of events). The range of velocity models used, including the initial HYPO71 model and the final model which yielded the lowest combined rms residual in the VELEST calculation, are shown in Fig. 2. When the extreme low velocity model (which has relatively low velocities in the upper crust) was used the inversion moved toward a velocity model with higher velocities in the shallow crust. When the extreme high model was used (with relatively high velocities in the upper crust and a deeper Moho), the inversion moved toward slightly lower upper crustal velocities and toward a Moho at 30 km depth. All of these VELEST runs were made with no allowance for a low velocity layer. The final velocity model (Fig. 2) also represents consolidation of layers which in the inversion came out with similar velocities.

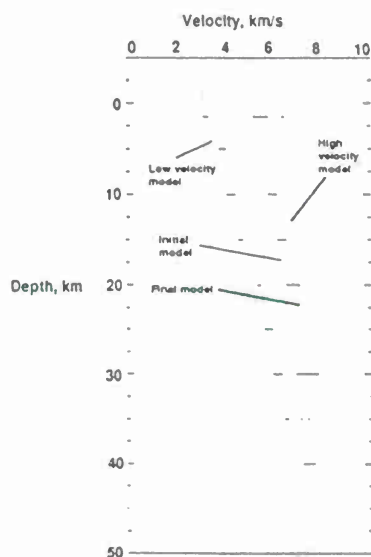


Figure 2. Velocity models used for the SED and JHD calculations. VELEST velocity models start at -3 km depth to allow for elevation differences in stations.

An additional concern in the VELEST inversion is the trade-off between shear wave velocities and station corrections in the inversion. Shear wave velocity in VELEST is not tied to P velocity and cannot be constrained in the inversion by setting a P/S ratio. In the model runs I found that the code had a tendency to invert toward anomalously low P/S ratios with large P and S station corrections. I was able to suppress this tendency by using initial shear velocities with a P/S ratio of 1.75-1.8 and heavily damping them in the inversion. This resulted in much more reasonable shear velocities and station corrections without large changes in the rms residual or the event locations. Figures 3a and 3b show the areal distribution of P and S station corrections. Pujol (1992) suggests that in regions with lateral velocity variations, the pattern of station corrections should correlate with local tectonics and structure. For this study the data involve a comparatively small number of stations and events and it may be possible that the station configuration affects the residual pattern, so the connection with structure may be problematic. Nevertheless, the sta-

tion corrections determined for this data set (Fig. 3a and 3b) do tend to reflect the general tectonics of the region, with lowest corrections in the center of the region, along the Dead Sea transform, with highest corrections along the sides of the transform shear zone to the east and west.

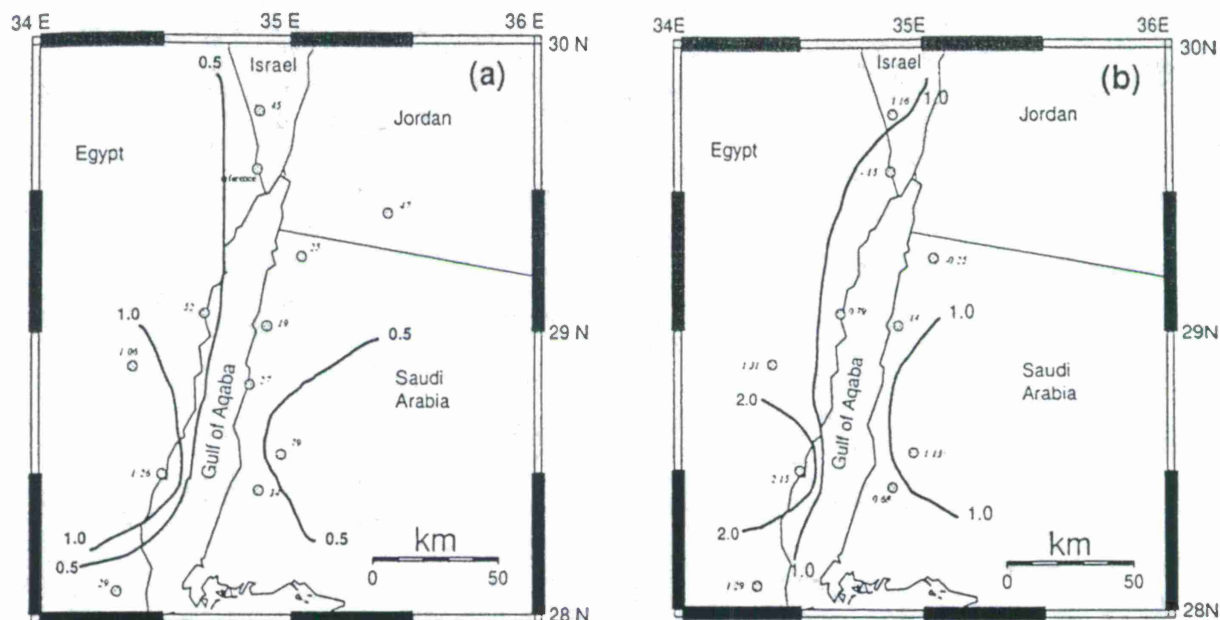


Figure 3. Station corrections, in seconds, determined by the VELEST calculations, (a) is for the P phase and (b) is for the S phase. Contour units are seconds.

Once the initial optimum VELEST JHD solution was determined, the code was run again in single event mode (SED) with the optimal velocity model and resulting station corrections determined in the JHD calculation. Locations of the Gulf of Aqaba earthquakes determined by JHD and SED are compared in Figs. 4, 5, and 6. For the set of events with good station coverage (Fig. 4) the JHD and SED locations show very good agreement. However, the effect of station coverage is readily seen by the differences between the JHD and SED locations shown in Figs. 5 and 6. Earthquakes occurring within the Gulf are associated with two clusters, one located slightly north of 29N and one slightly south of 29N. These are probably related to the boundaries of two pull-apart basins, the Elat deep (north) and Aragonese deep (south) identified by Alamri et al. (1991). Earthquakes flanking the Gulf on the east and west can be associated with NNE trending normal or strike-slip faults. There is a suggestion of a WNW trend of earthquakes just north of station NUA in Fig. 5.

Further assessment of the location determinations

An array of broadband seismometers were in operation in Saudi Arabia (Vernon et al., 1996) during the period when the Gulf of Aqaba earthquakes occurred. Waveform data for a cluster of Aqaba earthquakes, eight of which were used in this study, were obtained from the Multimax internet web site (<http://www.multimax.com/~gtddb/saudi>). Data from station HALM, which is located about 1200 km SE of the Gulf of Aqaba was used to test the relative location accuracy of the NEIC locations compared to the VELEST locations of this study. Locations of the eight events are shown in Fig. 7. One set of events, 361 - 359 - 362, has a close cluster of NEIC deter-

minations and a somewhat looser cluster of VELEST locations. Another set, 386 - 378 - 389 - 355, has a close cluster of VELEST locations, but the NEIC locations are spread out. Event 385 shows the largest difference between the NEIC and VELEST location. NEIC depths for all eight events are listed as 10 km. Magnitudes of these events range from M_b 3.6 (ev359) to M_b 5.1 (ev386) and the number of defining phases (NDEF) used in the location ranging from 6 (ev362) to 143 (ev386). Based on the study of Sweeney (1996), events with $NDEF < 50$ can be expected to have NEIC location errors of > 15 km. Based on this criterion, only ev386 and ev389 should be expected to have reliable NEIC locations. Note in Fig. 7 that the NEIC and VELEST locations for ev386 are less than 10 km apart, although the NEIC and VELEST solutions are about 20 km apart for ev389.

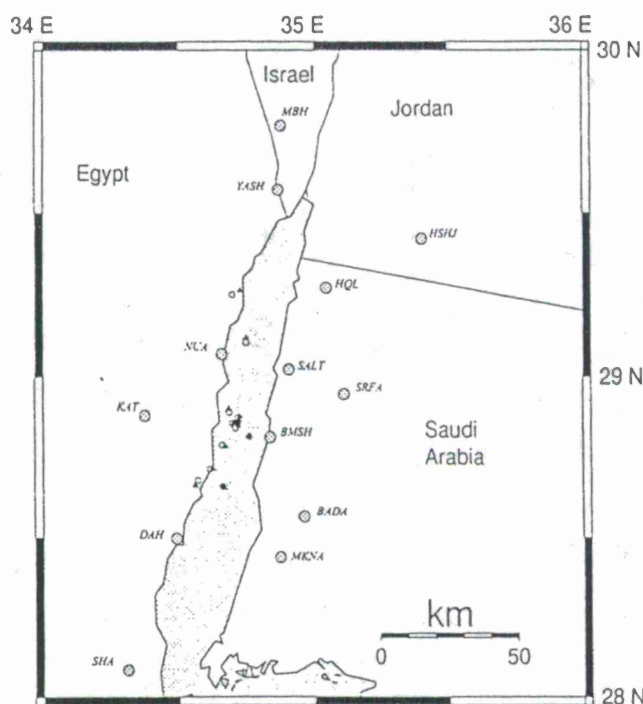


Figure 4. Map comparing JHD (solid diamonds) and SED (open circles) locations for 14 events with IL+EGS+KSU network stations (shown by shaded circles with station name).

Cross correlation functions were computed for the vertical component of the seismic signal recorded at station HALM for all eight events. The data were cut from the VELEST origin time to 380 s to include most of the L_g coda. (The P_n phase is very weak for events in Aqaba recorded on the Arabian shield--see the Multimax web page discussion.) The data were low-pass filtered at 5 Hz and then cross correlation functions were calculated for all eight events. The highest correlations (0.881 and 0.875) were obtained for events 362-361 and 359-361 (Fig. 8). These are the events that are closely located by the NEIC (Fig. 7). Events 361 and 362 are close in the VELEST solution, but ev359 is about 15 km away. The only other events showing a notable waveform correlation, 355 and 386, are close together in the VELEST solution, but the NEIC locations for these events are about 40 km apart. Figure 9 shows the waveform correlation functions for events 386, 355, 378, and 389. The VELEST locations show these events to be clustered, but this is not corroborated by the waveform correlation. Of course, this does not prove that they are not clus-

tered; the poor waveform correlation of events 378 and 389 could be due to source effects.

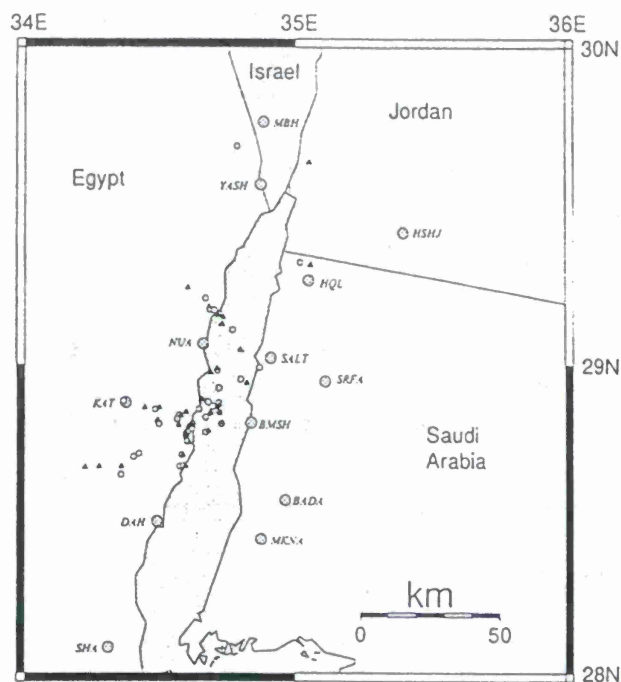


Figure 5. Map comparing JHD (solid triangles) and SED (open circles) locations for events detected by stations with the IL+EGS combination (west side of the gulf). Shaded circles are station locations with station names.

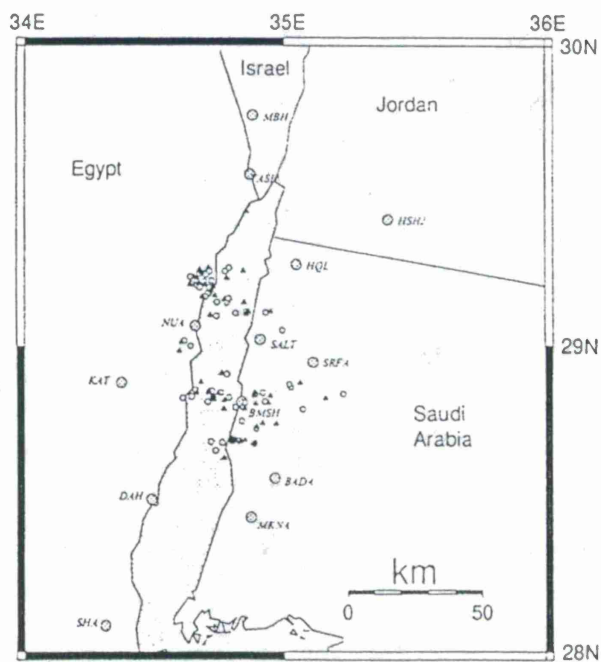


Figure 6. Map comparing JHD (solid triangles) and SED (open circles) locations for events detected by stations with the IL+KSU combination (east side of the gulf). Shaded circles are station locations with station names.

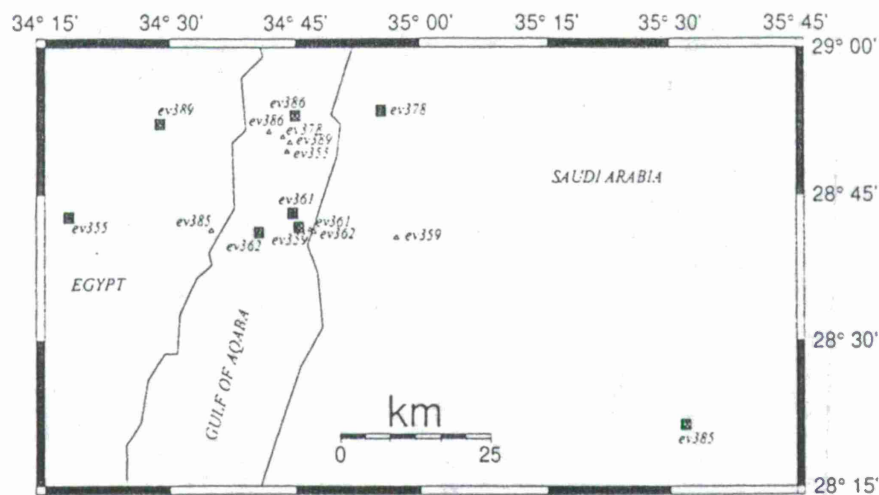


Figure 7. Detailed map of earthquakes with NEIC locations comparing NEIC (gray squares) and JHD (open triangles) locations. Event ev386 is the most reliable NEIC location in the group (see text).

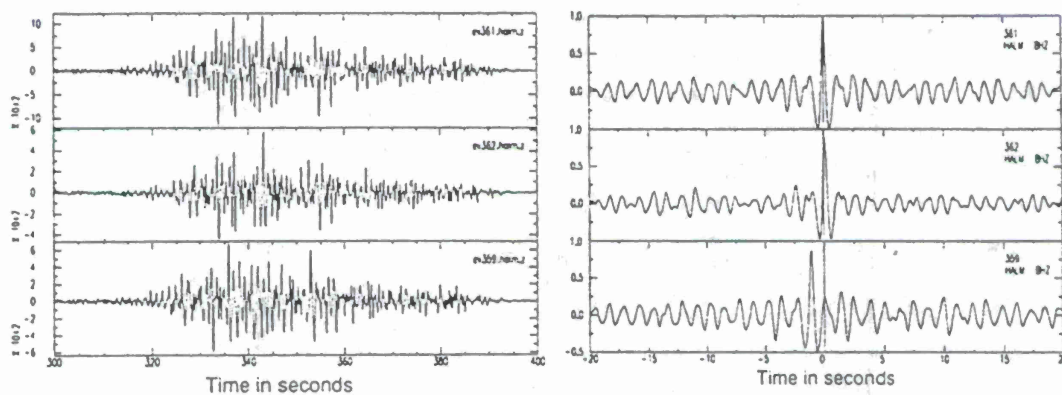


Figure 8. Lg waveforms for events 361, 362, and 359 of Fig. 7 (left) and corresponding correlation functions (right) relative to event 361.

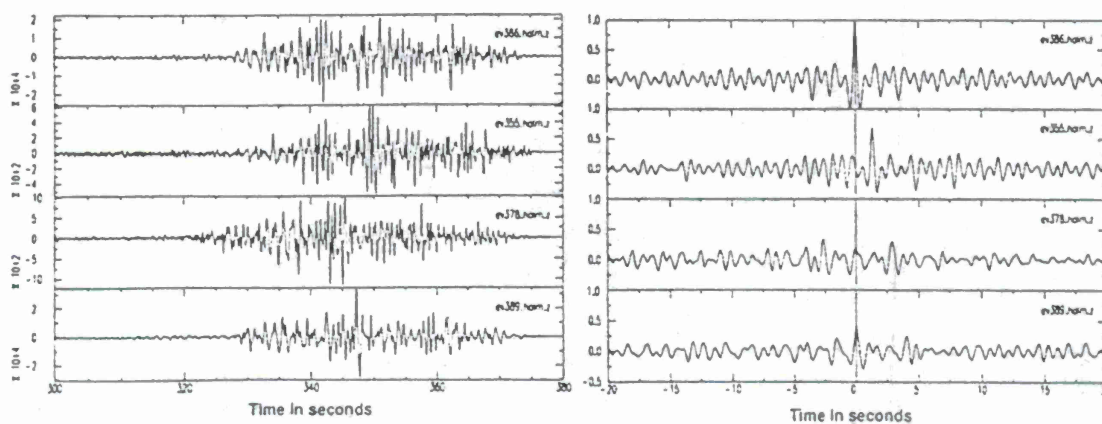


Figure 9. Lg waveforms for events 386, 355, 378, and 389 of Fig. 7 (left) and corresponding correlation functions (right) relative to event 386.

CONCLUSIONS AND RECOMMENDATIONS

Locations of 106 earthquakes, occurring in the Gulf of Aqaba between January 1996 and June 1996, were determined by both SED and JHD methods. Hypocenters determined by the two methods were nearly the same (within 2 km) for 14 events with good azimuthal station coverage. For the remainder of events, for which station coverage was biased toward either the east or west side of the Gulf, significant differences were seen between the JHD and SED locations. Waveform correlation studies help to confirm one cluster of events identified by the JHD locations and by NEIC locations, but another cluster identified by the JHD locations cannot be similarly confirmed, perhaps because of differences in source characteristics. Further study of the event clusters with waveform data from closer stations will help better characterize the accuracy of the JHD locations. Meanwhile, the 14 events with good station coverage have locations with relative uncertainty less than 5 km (based on the solution statistics) and thus serve as good ground truth events with magnitudes ranging from about M_b 3.6 to 5.1.

ACKNOWLEDGEMENTS

Dave Harris wrote the C++ program to extract and convert the JSOP bulletin data. Al Smith wrote the UNIX script to convert HYPO71 output files to VELEST input and provided much help on operation of the VELEST code. Dr. Bruno Feignier and Frederic Ramon of the CSEM/EMSC provided the electronic version of the JSOP bulletin. This work was performed under the auspices of the U.S. Department of Energy by Lawrence Livermore National Laboratory under contract No. W-7405-ENG-48.

REFERENCES

- Alamri, A.M., F. Schult, and C.G. Bufe, 1991, Seismicity and aeromagnetic features of the Gulf of Aqaba (Elat) region, *Journal of Geophysical Research*, v. 96, pp. 20,179-20,185.
- Ginzburg, A., J. Makris, K. Fuchs, B. Perathoner, and C. Prodehl, 1979, Detailed structure of the crust and upper mantle along the Jordan-Dead Sea Rift, *Journal of Geophysical Research*, v. 84, pp. 5605-5612.
- Kissling, E., W.L. Ellsworth, D. Eberhart-Phillips, and U. Kradolfer, 1994, Initial reference models in local earthquake tomography, *Journal of Geophysical Research*, v. 99, pp. 19,635-19,646.
- Klein, R.W., 1978, Hypocenter location program HYPOINVERSE, I, Users guide to versions 1,2,3 and 4, U.S. Geological Survey Open File Report 78-694.
- Lee, W.H.K., and J.C. Lahr, 1975, HYPO71: A computer program for determining hypocenter, magnitude, and first motion pattern of local earthquakes, U.S. Geological Survey Open File Report 75-311.
- Pujol, J., 1992, Joint hypocentral location in media with lateral velocity variations and interpretation of the station corrections, *Physics of the Earth and Planetary Interiors*, v. 75, pp. 7-24.

Sweeney, J.J., 1996, Accuracy of teleseismic event locations in the Middle East and North Africa, Lawrence Livermore National Laboratory report UCRL-ID-125868.

Vernon, F.L., R.J. Mellors, J. Berger, A. M. Al-Amri, and J. Zollweg, 1996, Initial results from the deployment of broadband seismometers in the Saudi Arabian Shield, in Lewkowicz, J.F., J.M. McPhetres, and D.T. Reiter, eds., Proceedings of the 18th Annual Seismic Research Symposium on Monitoring a Comprehensive Test Ban Treaty, Phillips Laboratory report PL-TR-96-2153, pp. 108-118.

Disclaimer

This document was prepared as an account of work sponsored by an agency of the United States Government. Neither the United States Government nor the University of California nor any of their employees, make any warranty, express or implied, or assumes any legal liability or responsibility for the accuracy, completeness, or usefulness of any information, apparatus, product, or process disclosed, or represents that its use would not infringe privately owned rights. Reference herein to any specific commercial products, process, or service by trade name, trademark, manufacturer, or otherwise, does not necessarily constitute or imply its endorsement, recommendation, or favoring by the United States Government or the University of California. The views and opinions of authors expressed herein do not necessarily state or reflect those of the University of California, and shall not be used for advertising or product endorsement purposes.

EPICENTER DETERMINATION WITH SPARSE BROADBAND ARRAYS AT REGIONAL DISTANCES USING ONLY AZIMUTHAL INFORMATION: THE INCORPORATION OF SURFACE WAVES

Mark Andrew Tinker
Terry C. Wallace

Southern Arizona Seismic Observatory
Department of Geosciences
University of Arizona
Tucson, Arizona

Sponsored by Air Force Phillips Laboratory and Defense Special Weapons Agency
Grant No. F 19628-95-K-007

ABSTRACT

One of the most important problems in monitoring a Comprehensive Test Ban Treaty (CTBT) is the detection and location of small seismic events. However, determining location becomes more difficult at smaller magnitudes primarily due to a decrease in the signal to noise. Nonetheless, low magnitude detection and location determination is paramount if a global CTBT is to be truly viable and deter clandestine and evasive nuclear tests. One way to improve traditional travel time location methodologies is to utilize information contained in the "entire" waveform. In some instances, surface waves are not only recorded with the best signal to noise ratio, but are the only usable phase on the seismic wavetrain. Thus, it is this circumstance that motivates this study. We develop methodologies for extracting azimuthal information from Rayleigh waves recorded on a sparse, broadband array and "focusing" the array on the best epicenter.

Mid-period (1-50 seconds) Rayleigh waves are used in a grid search on azimuth to determine where the radial component best correlates with the vertical component. Based primarily on the magnitude and timing of the correlation, the best backazimuth can be determined. We also incorporate backazimuth information from body waves. This information is extracted using the established technique of a polarization filter parameterizing the three component ground motion into an ellipse.

Both the body wave and surface wave backazimuth techniques are sensitive to both the regional structure as well as the receiver structure. Therefore, it is necessary to take advantage of the full benefit of utilizing array data by "focusing" the array on the best location, thereby averaging out any localized effects. We use a standard least squares inversion scheme to iterate upon the backazimuth information from each station to determine the best solution. We test this technique on five earthquakes ($4.9 < m_b < 5.8$) recorded on a broadband array in Bolivia at a range of distances (2° to 13°) and azimuths. The locations are compared to locations posted in the PDE catalog.

Keywords: Rayleigh waves, regional distances, single-station backazimuth, epicenter determination, sparse broadband array.

OBJECTIVE

Seismic arrays have become the central tool for event detection in the context of monitoring a nuclear weapons treaty (Mykkeltveit et al., 1990) and much work has been done developing methodologies for large, dense, short-period arrays (Jurkevics, 1988; Suteau-Henson, 1990). For a low magnitude event, a few broadband stations from a global network may also be used in a single station (Vsevolozhsky and Wallace, 1997) or multi-station location. Somewhere between an array location and a single station detection lies sparse regional networks. Since the seismic coverage of the globe is non-uniform, there will be cases where small (<4.0) events are recorded on several broadband stations. Optimization of this information is essential to high performance of any monitoring effort.

There has been some work on event location with sparse broadband networks. For example, Bratt and Bache (1988), using two short period arrays, and Thurber et al. (1989), using a three station network, incorporated P-wave backazimuth information into a travel time location algorithm. Bratt and Bache (1988) used a frequency-wavenumber analysis to determine backazimuth, and Thurber et al. (1989) estimated the polarization direction using a two-axis principal component method. Other backazimuth estimation techniques have been evaluated by Walck and Chael (1991). However, these methods all utilize P and S waves, hence the full power of the waveform, in particular the surface wave, has not been utilized until recently when Chael (1997) developed an automated Rayleigh wave detection algorithm for a single station. Furthermore, there is still a strong reliance on travel times, which are a function of the assumed velocity structure and the ability to correctly identify seismic phases, to determine distance. Therefore, we use information contained in the surface wavetrains to improve on body wave backazimuth schemes and altogether avoid the dependence on a distance determination by "focusing" the network on the best epicenter. The benefit of this technique is that it is completely transportable and can be automated. The data used in this study consists of small seismic events recorded on a sparse broadband network in Bolivia containing at peak operation up to 23 stations.

In pursuing our objective of developing processing techniques for the full waveform, we have worked on three methodologies. To determine backazimuth we use 1) a polarization filter for body waves, and 2) a correlation grid-search on mid-period Rayleigh waves (1 to 50 sec). The third methodology consists of combining the information from the body and surface wavetrains in a linear least squares inversion to determine location.

RESEARCH ACCOMPLISHED

In a cooperative project, the University of Arizona, the Carnegie Institute of Washington, and Lawrence Livermore National Laboratory deployed a total of 23 broadband stations (10 to .01 Hz) in Bolivia for over one year. The Arizona and Carnegie transect, known as BANJO, consisted of 16 stations forming an east-west transect. The BANJO line traversed extremes in elevation and geology. The stations span from Chile, over the Western Cordillera, Altiplano, Eastern Cordillera, and down into the sub-Andean zone and into the Chaco Plain. The SEDA array deployed by Lawrence Livermore National Laboratory consists of seven stations and strikes north-south along the eastern edge of the Altiplano.

The location of the sparse array in Bolivia resulted in events being recorded which traversed extremes in crustal geology; crustal thickness varies from 40 to 75 km. We test the location algorithm on five earthquakes. The first earthquake (April 3, 1994) occurred during the early stage of the deployment. Thus, it was recorded with good surface waves at only 7 stations (Fig 1). This event has an epicenter located northeast of the array. In Figure 2 the circled star represents the Preliminary Determination of Epicenters catalog location (17.694°S , 64.816°W , depth = 38km, $m_b=5.3$, $M_s=4.4$), and the grey ellipse represents the location determined by a standard body wave travel-time algorithm (dbloc) using data from only the 7 stations in the BANJO array.

Flinn (1965) showed that it is possible to use a three-axis principal component analysis to characterize the polarization of seismic waves. Subsequent techniques have been used by other investigators. Magotra et al. (1987) used only the horizontal components in a two-axis principal

component method. Christoffersson et al. (1988) implemented a maximum-likelihood approach for backazimuth estimation, and Roberts et al. (1989) extended this to near real-time. Kvaerna and Doornbos (1986) developed a frequency-wavenumber algorithm to estimate backazimuth. Walck and Chael (1991) used a distributed network of three-component, short period stations in central and eastern North America to evaluate four of these different computational methods for determining backazimuth as well as the effects of receiver structure on backazimuth determination.

Unlike P-waves, surface waves are confined to travel along the surface of the earth; Rayleigh waves, tied to the P-SV system, have retrograde elliptical particle motion. Thus, coherent energy is defined in two dimensions by a plane that is associated with the backazimuth, instead of in one dimension by a ray, as is the case for the particle motion of P-waves. In the simplest sense, the "best plane" on the basis of particle motion gives the best backazimuth determined from Rayleigh waves.

We prefer the three-axis principal component analysis of Flinn (1965) to determine P-wave backazimuth. Jurkevics (1988) extended Flinn's method to arrays, however, this technique cannot be applied to a sparse network nor can it accommodate our technique of determining backazimuth from surface wave information. Therefore, we modify the method of Bratt and Bache (1988), who extended the travel time residual algorithm of Jordan and Sverdrup (1981) to include azimuthal data. The following sections describe the techniques used to estimate backazimuth from body waves and surface waves and how this information is used in an iterative least-squares inversion scheme to determine the epicenter.

Body Wave Backazimuth

The polarization of three-component P-waves is a function of the backazimuth. A data covariance matrix C is first developed

$$C = \begin{bmatrix} \sigma_{nn} & \sigma_{ne} & \sigma_{nz} \\ \sigma_{ne} & \sigma_{ee} & \sigma_{ez} \\ \sigma_{nz} & \sigma_{ez} & \sigma_{zz} \end{bmatrix} \quad (1)$$

where $\sigma(i,j)$ represents the zero-lag cross power

$$\sigma_{ij} = \frac{1}{N} \sum_{i=1}^N x_i y_j \quad (2)$$

In (2), x and y are equal to the north-south, east-west, or vertical components of the seismic data. The data covariance matrix C is rotated into its principal directions, which lie along the eigenvectors of C . The rotated covariance matrix C' has the form

$$C' = \begin{bmatrix} \lambda_1 & 0 & 0 \\ 0 & \lambda_2 & 0 \\ 0 & 0 & \lambda_3 \end{bmatrix} \quad (3)$$

where the diagonal elements are the real eigenvalues of C , with $\lambda_1 \geq \lambda_2 \geq \lambda_3$. The three eigenvectors associated with the eigenvalues define a polarization ellipsoid that has any arbitrary orientation with respect to the original north, east, and vertical system. P-waves propagate along,

and are contained within, the true radial direction between the source and receiver. Thus, the dominant eigenvector (associated with λ_1) for P-waves is assumed to lie in the radial direction of propagation. The backazimuth is the projection of this eigenvector, or radial direction, onto the horizontal plane at the receiver.

Trade-offs between resolution and estimation variance are a function of both window length and bandwidth. Short windows and narrow bands distinguish between close arrivals and illuminate the frequency varying properties of polarization, whereas longer windows and wider frequency bands yield more stable and reliable estimates. On average, we use a sliding time window of 2 seconds in length that steps at one half the window length for the total duration of the waveform record. Thus, as is the case for most regional events, P_n is sampled followed by the remaining signal. We experienced no adverse effects from potential converted phases or off-azimuth scattered energy with longer window durations consistent with the analysis of Walck and Chael (1991). Stable backazimuths are determined for the time-sampled P energy.

Since we are interested in the most stable estimates, we want to utilize a wide range of frequencies. However, a single wide frequency band will result in the frequency component at the peak amplitude dominating the polarization estimate. Therefore, we incorporate a wide-band frequency estimate following Jurkevics (1988) that provides spectral balancing over a range of frequencies. To achieve high signal to noise in the P-waves, it was necessary to high pass filter the signal at least at 0.5 Hz.

Surface Wave Backazimuth

Regional distance surface waves can be very complex. They are highly dependent on the crust and upper mantle structure and extremely sensitive to source radiation patterns. Furthermore, at regional distances, Love and Rayleigh waves can arrive with little separation in time. Nonetheless, they can provide valuable backazimuth information. To extract this information, we use mid-period (1-50 seconds) Rayleigh waves in a grid search on azimuth to determine where the radial component best correlates with the vertical component. Theoretically, the retrograde elliptical motion implies that the radial and vertical components should correlate well with a 90° phase change. The magnitude of the correlation between the trial radial to vertical is normalized to 10. A statistical analysis is performed on the normalized radial correlation value, the relative timing of the correlation (in an attempt to remove any Love wave contribution), and the kurtosis (third moment of the population) to determine the best backazimuth and the corresponding weighting to be used in the epicenter inversion. Although this technique is redundant every 180° in azimuth, the backazimuth can be uniquely determined by examining both the relative timing across the array and the particle motion. The true backazimuth occurs where the Rayleigh wave particle motion is retrograde elliptical instead of prograde elliptical.

Epicenter Determination

Both the body wave and surface wave backazimuth techniques are sensitive to both the regional structure as well as the receiver structure. Therefore, it is necessary to take advantage of the full benefit of utilizing array data by "focusing" the array on the best location, thereby averaging out any localized effects. We use a standard least squares inversion scheme to iterate upon the backazimuth information from each station to determine the best solution. This technique involves iteratively solving a perturbation vector $\Delta \underline{x}$ that minimizes the residuals \underline{r}_w between the observed azimuths and those azimuths computed from a trial epicenter \underline{x}_c (Aki and Richards, 1980),

$$\Delta \underline{x} = (\underline{A}_w^T \underline{A}_w)^{-1} \underline{A}_w^T \underline{r}_w \quad (5)$$

where \underline{A}_w is the weighted system matrix. The new estimate of epicenter \underline{x} is $\underline{x}_c + \Delta \underline{x}$.

The system matrix \underline{A} has dimensions $2N \times M$. Since we are only solving for epicenter, we have only two model parameters (M). In terms of N , each station providing information adds two rows to the residual (\underline{r}) and system (\underline{A}) matrices. The \underline{A} matrix contains the azimuthal information

of partial derivatives of the data with respect to hypocentral Cartesian coordinates x (easterly) and y (northerly). Backazimuth α is measured clockwise from north. Following Bratt and Bache (1988),

$$\frac{\partial \alpha}{\partial x} = - \frac{\cos(\alpha_e)}{\sin(\Delta)} \frac{0.0090^\circ}{\text{km}} \quad (6)$$

where the station is initially Δ radians distant and α_e radians azimuth from the event. Similarly, the northerly partials are

$$\frac{\partial \alpha}{\partial y} = \frac{\sin(\alpha_e)}{\sin(\Delta)} \frac{0.0090^\circ}{\text{km}} \quad (7)$$

The partials for the P-wave azimuthal information fill one row, and the partials for the surface wave azimuthal information fill a second row for each station used.

A trial epicenter is chosen by inspecting the first motions or the relative arrival time of energy across the array. The trial azimuths are calculated and the data residual vector determined. Subsequently, the \underline{A} matrix is filled and normalized by the appropriate standard deviations before computing the perturbation vector ($\Delta \underline{x}$). Figure 2 shows three separate starting epicenters and the subsequent trial epicenters determined by the inversion before the convergence criteria were met.

Results

The final epicentral solution and confidence bounds on that solution depend on the variance assigned to the data. Therefore, after determining the backazimuth for each technique at each station, it is necessary to quantify standard deviations to the backazimuth solutions. The determined standard deviations are based on measurable attributes of the signal. The 3-component polarization technique yields three eigenvectors that define an ellipsoid. The eigenvectors associated with the medium (λ_2) and minimum (λ_3) eigenvalues are perpendicular to the backazimuth and dictate the shape of the ellipsoid. If these eigenvalues are large, the ellipsoid approaches sphericity, and thus is poorly resolved. If these eigenvalues are small, the ellipsoid becomes elongate, and the backazimuth solution is well resolved. To incorporate this into a weighting scheme, the eigenvalues are normalized to the largest eigenvalue (λ_1) having a value of 10. The average of the remaining eigenvalues (λ_2 and λ_3) is the standard deviation used to weight the backazimuth result and varies between 10 (not resolved) and 0 (perfectly resolved).

It is important that the standard deviation for the surface wave backazimuth determination have the same value for the same resolution of the 3-component polarization technique. Otherwise, one technique will dominate the weighting scheme and drive the location solution even though the two differently determined backazimuth solutions may share the same resolution. Therefore, the values of the surface wave correlation grid search are normalized so that the maximum value is 10. The standard deviation consists of 50% of the normalized correlation value, 25% of the timing, and 25% of the percentage of radial correlation curtos to the vertical correlation curtos.

In the epicenter inversion, the 90% confidence bounds of the final epicenter ellipse is the formal error. Variance in the data due to, for example, structure causing off-azimuth solutions, or scattering causing imperfect particle motions resulting in imperfectly polarized data, has not been accounted for. Furthermore, no confidence bounds have been determined for each backazimuth solution that may propagate through the location inversion. Therefore, with only two model parameters (latitude and longitude) to fit, the magnitude of the residual vector (\underline{r}) can be significantly affected by the number of stations. Unless $N \gg M$, the magnitude of \underline{r} is very small. If all 23 stations in the network contributed to the solution, $N=46$. Even in this case, the magnitude of \underline{r} is still small and results in an unreasonably small confidence ellipse. Thus, for the solutions shown in Figures 2 and 3, each ellipse has been enlarged, but its shape remains unchanged.

CONCLUSION AND RECOMMENDATIONS

Traditional travel time location inversions are dependent on both knowing the velocity structure *a priori*, and, in some cases, not being able to use a laterally varying structure. Azimuth information is also a function of the velocity structure, but only in that the velocity structure determines off-azimuth deflections from the true back-azimuth. In an effort to avoid the dependence on *a priori* information, azimuth data is used to "focus" a sparse network and determine the best location. However, P-waves and surface waves are sensitive to different regions of the earth, because they have very different ray paths. Thus, the information in surface waves is also used to determine back-azimuth, thereby not biasing the location solution towards an off azimuth characteristic of using only one seismic phase.

Using P-wave and Rayleigh wave back-azimuth information recorded on a broadband array in Bolivia, an iterative least-squares inversion is performed to determine the epicenter. In spite of the complex structure the network covers, the inversion converges on a "best" location. The back-azimuth location is located to the east of the locations determined using traditional travel time residuals.

- Aki, K. and P.G. Richards (1980). *Quantitative Seismology*, W.H. Freeman and Company, San Francisco, California, 641-719.
- Bratt, S.R. and T.C. Bache (1988). Locating events with a sparse network of regional arrays, *Bull. Seism. Soc. Am.*, **78**, 780-798.
- Chael, E.P. (1997). An automated Rayleigh-wave detection algorithm, *Bull. Seism. Soc. Am.*, **87**, 157-163.
- Christoffersson, A., E.S. Husebye, and S.F. Ingate (1988). Wavefield decomposition using L-probabilities in modeling single-site 3-component records, *Geophys. J.*, **93**, 197-213.
- Flinn, E.A. (1965). Signal analysis using rectilinearity and direction of particle motion, *Proc. IEEE*, **53**, 1874-1876.
- Jordan, T.H. and K.A. Sverdrup (1981). Teleseismic location techniques and their application to earthquake clusters in the South-Central Pacific, *Bull. Seism. Soc. Am.*, **71**, 1105-1130.
- Jurkevics, A. (1988). Polarization analysis of three-component array data, *Bull. Seism. Soc. Am.*, **78**, 1725-1743.
- Kvaerna, T. and D.J. Doornbos (1986). An integrated approach to slowness analysis with arrays and three-component seismometers, in *NORSAR Scientific Report 2-35/86*, Kjeller, Norway.
- Magotra, N., N. Ahmed, and E.P. Chael (1987). Seismic event detection and source location using single-station (three-component) data, *Bull. Seism. Soc. Am.*, **77**, 958-971.
- Mykkeltveit, S., F. Ringday, T. Kvaerna, and R. Aleurine (1990). Application of regional arrays in seismic verification research, *Bull. Seism. Soc. Am.*, **80**, 1777-1800.
- Roberts, R.G., A. Christoffersson, and F. Cassidy (1989). Real-time event detection, phase identification and source location estimation using single-station three-component seismic data, *Geophys. J.*, **97**, 471-480.
- Suteau-Henson, A. (1990). Estimating azimuth and slowness from three-component and array stations, *Bull. Seism. Soc. Am.*, **80**, 1987-1998.
- Thurber, C., H. Given, and J. Berger (1989). Regional seismic event location with a sparse network: Application to eastern Kazakhstan, USSR, *J. Geophys. Res.*, **94**, 17,767 - 17,780.
- Vsevolozhsky, G. and T.C. Wallace (1997). Seismic source location with a very broad band single station, submitted to *Seism. Res. Lett.*
- Walck, M. and E. Chael (1991). Optimal back azimuth estimation for three component recordings of regional seismic events, *Bull. Seism. Soc. Am.*, **81**, 643-666.

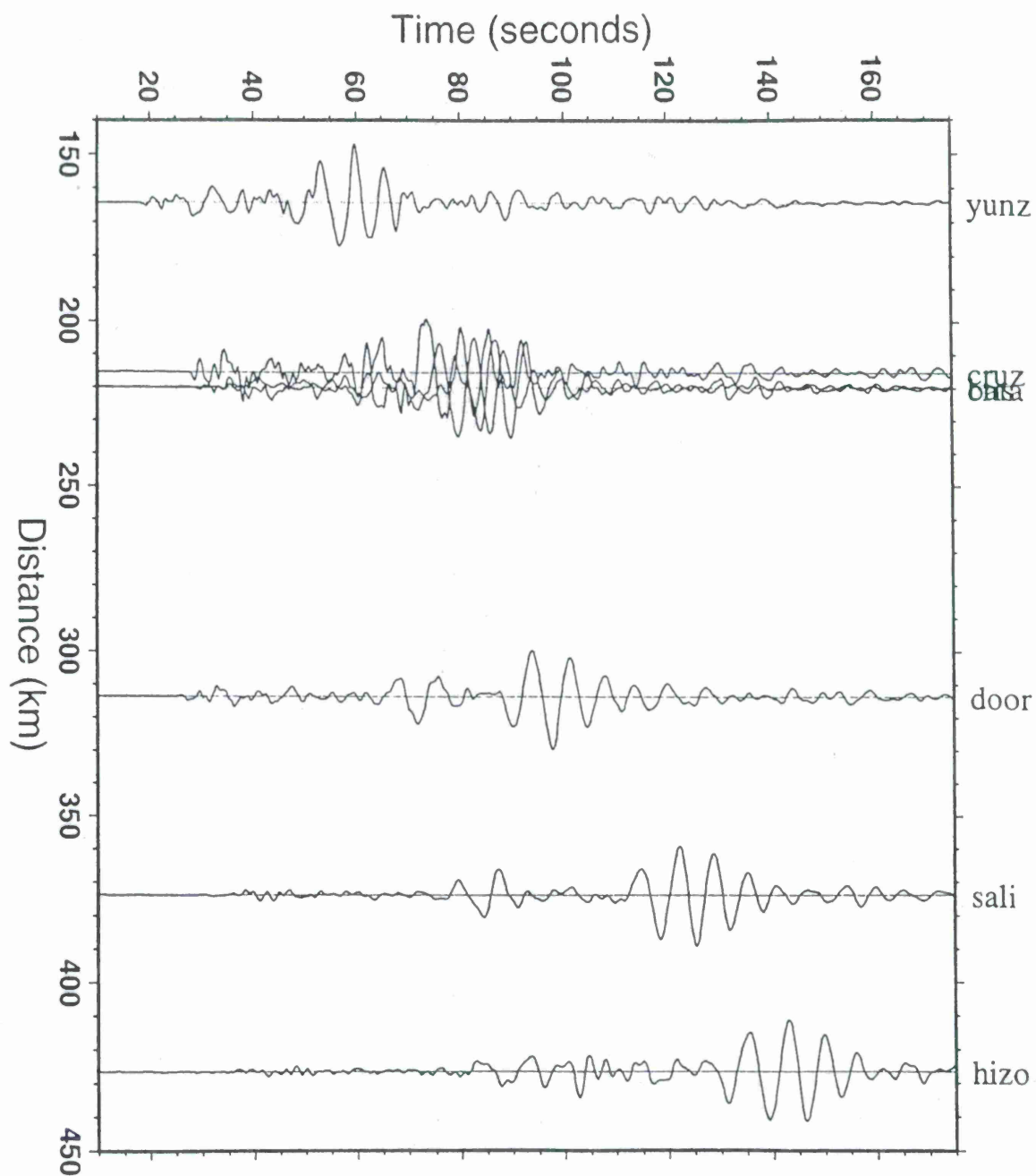


Figure 1 A record section of the long period signal (5 - 20 seconds) for the event on April 3, 1994, recorded on the vertical components of the BANJO stations.

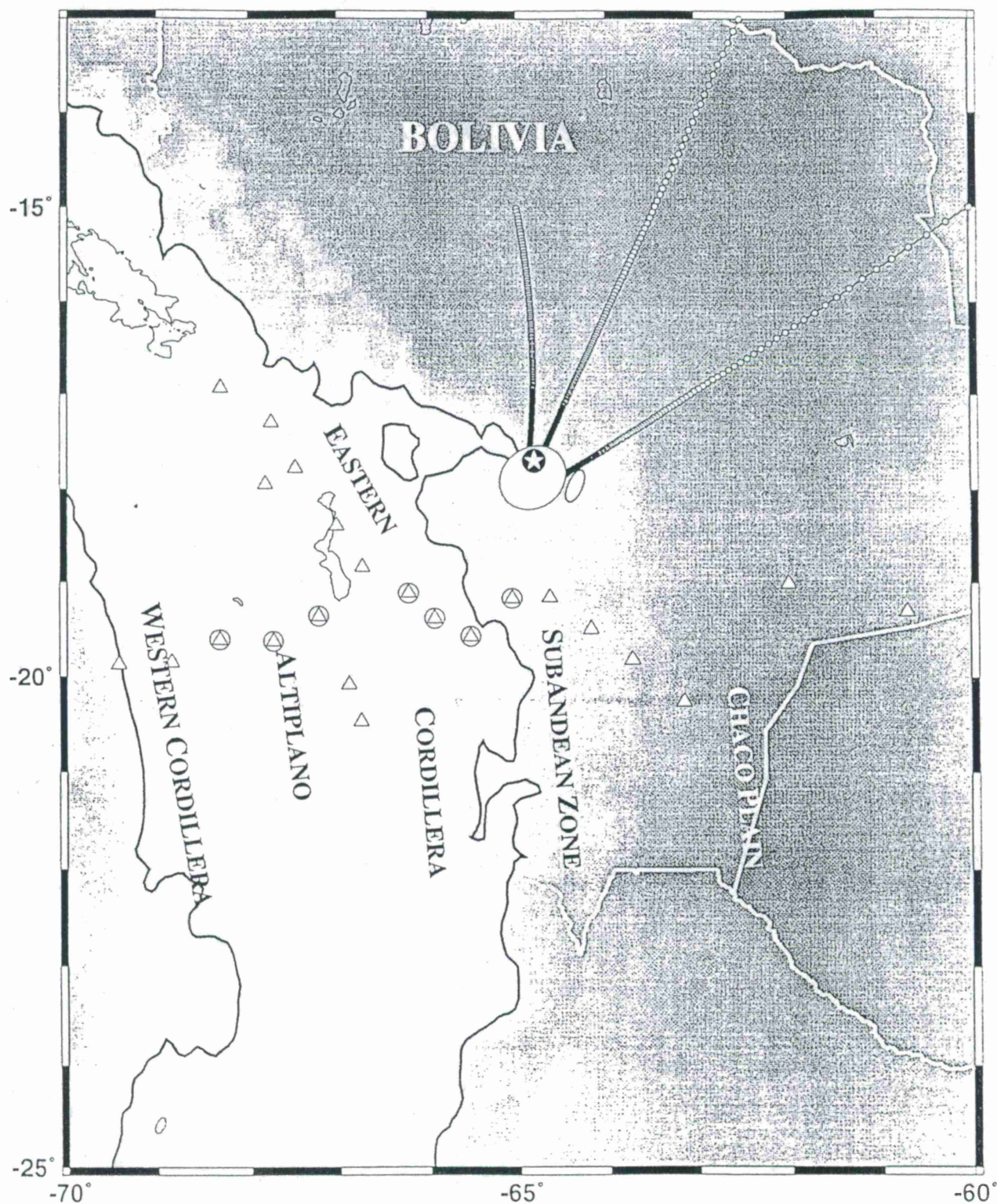


Figure 2. A map of Bolivia showing the BANJO and SEDA stations (white triangles). The PDE location for the April 3, 1994, event is shown as a circled star and was recorded at the seven circled BANJO stations. The epicenter determined by the inversion on backazimuth is shown as the white ellipse and the three "tracks" shown represent three different starting locations. The grey ellipse represents the epicenter determined by body wave travel time picks using the same BANJO data. The 12,000 foot contour line is also shown.

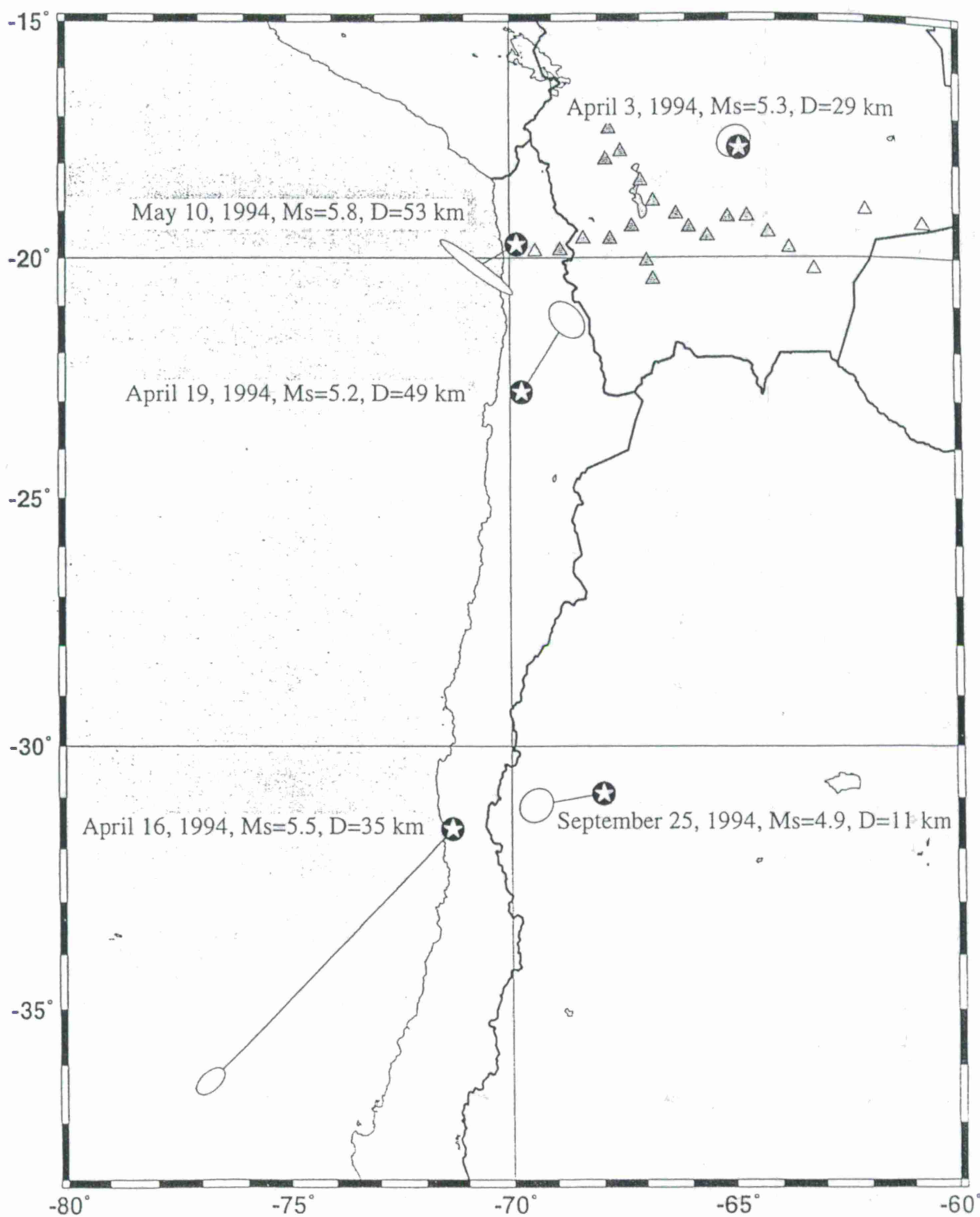


Figure 3. A map of South America showing the PDE locations (circled stars) and corresponding locations determined by the inversion on backazimuth for five earthquakes.

Testing the Waveform Correlation Event Detection System:
Teleseismic, Regional, and Local Distances

Christopher J. Young, Judy I. Beiriger, J. Mark Harris, Susan G. Moore, Julian R. Trujillo
Sandia National Laboratories

Mitchell M. Withers, Richard C. Aster
New Mexico Institute of Mining and Technology

Sponsored by U.S. Department of Energy
Office of Nonproliferation and National Security
Office of Research and Development
Contract DE-AC0494-AL85000
Comprehensive Test Ban Treaty Research and Development Program

ABSTRACT

Waveform Correlation Event Detection System (WCEDS) prototypes have now been developed for both global and regional networks and we have extensively tested them to assess the potential usefulness of this technology for CTBT (Comprehensive Test Ban Treaty) monitoring. In this paper we present the results of tests on data sets from the IDC (International Data Center) Primary Network and the New Mexico Tech Seismic Network. The data sets span a variety of event types and noise conditions. The results are encouraging at both scales but show particular promise for regional networks.

The global system was developed at Sandia Labs and has been tested on data from the IDC Primary Network. We have found that for this network the system does not perform at acceptable levels for either detection or location unless directional information (azimuth and slowness) is used. By incorporating directional information, however, both areas can be improved substantially suggesting that WCEDS may be able to offer a global detection capability which could complement that provided by the GA (Global Association) system in use at the IDC and USNDC (United States National Data Center).

The local version of WCEDS (LWCEDS) has been developed and tested at New Mexico Tech using data from the New Mexico Tech Seismic Network (NMTSN). Results indicate that the WCEDS technology works well at this scale, despite the fact that the present implementation of LWCEDS does not use directional information. The NMTSN data set is a good test bed for the development of LWCEDS because of a typically large number of observed local phases and near network-wide recording of most local and regional events. Detection levels approach those of trained analysts, and locations are within 3 km of manually determined locations for local events.

Keywords: event detection, event location, waveform correlation, CTBT monitoring

Sandia is a multiprogram laboratory operated by Sandia Corporation, a Lockheed Martin Company, for the United States Department of Energy.

OBJECTIVES

The goal of the Waveform Correlation Event Detection System (WCEDS) Project at Sandia has been to assess the potential usefulness for Comprehensive Test Ban Treaty (CTBT) monitoring of a seismic event detection system based on the correlation of waveforms. Shearer (1994) showed that this type of system may have an ability to detect events that traditional event detection systems cannot, but the potential relevance to CTBT verification was not clear due to the type of data used (long-period) and the less-stringent event detection requirements of that study.

We believe that pursuing alternative event detection technologies for CTBT monitoring is warranted for at least two reasons. First, although the current system (Global Association or GA) is highly sophisticated and is a vital part of the current monitoring pipelines at both the IDC (International Data Center) and the USNDC (United States National Data Center), the quality of the bulletins produced still shows significant room for improvement, particularly in reducing the number of false events (i.e. those that are not real and which must be disassociated by an analyst). Second, the USNDC is seeking to develop new methods to "spotlight" certain regions of interest to substantially lower the global threshold achieve in those regions. Many approaches to improving event detection could be investigated, of course, but to create the most sensitive detector possible a full waveform approach is especially attractive. Such an approach has not been practical in the past due to the processing and disk storage requirements, but the ever-increasing rate of technological innovation in computer hardware continues to reduce the severity of these problems.

INTRODUCTION

The WCEDS Project was initiated in the Spring of 1995. We started with the algorithm developed by Shearer to process long-period data, and by May of 1995 a rudimentary prototype was available. Details of the initial prototype development and testing were given in a presentation at the 17th Seismic Research Symposium (Young et al., 1995). The prototype was then refined based on the results of repeated testing with a set of continuous data from the Incorporated Research Institutions for Seismology (IRIS) broadband three-component global network, and the results of that study were presented at the 18th Seismic Research Symposium (Young et al., 1996a). At the same time, a local/regional version of the system was being developed and tested at New Mexico Tech using data from the New Mexico Tech Seismic Network (Withers, 1997).

In the past year, both systems have substantially matured and have undergone extensive testing. The global version has been modified to process array data, allowing us to conduct tests with data from the IDC Primary Network. The local/regional version has been fully-automated and is now routinely used by New Mexico Tech to detect and locate events in New Mexico. In this paper we will briefly review the basic features of the WCEDS system, and then discuss in detail recent modifications and testing results for the global and local/regional versions. The global and local/regional systems are described in detail in Young et al. (1996b) and Withers (1997).

REVIEW

WCEDS is a grid-based automatic system which examines processed continuous seismic data streams for matches with some portion of a master set of waveforms which we refer to as the *Master Image* (MI). The grid covers the area which the user is interested in monitoring, and should have a spacing appropriate for the desired accuracy of the locations and the frequency content of the data. To understand how the detector works, it is useful to think of it as creating a waveform profile for each grid point at a given time and comparing this observed profile with the expected

profile if an event had indeed happened at that point and time. A "good" match would indicate that an event had occurred at the location at that given time. The comparison of observations and the MI is accomplished via simple dot products of the waveforms.

Prior to forming the profiles, the waveforms are processed (e.g. bandpass filtering followed by STA/LTA processing) to enhance phases relative to noise and to generalize the waveforms for correlation with the generalized MI. We refer to this step as *preprocessing* because it occurs prior to execution of the detector itself. The detector is then run on the preprocessed data at some specified time discretization interval.

Detection and location are accomplished by computing the correlation value for each grid point for each time point over some specified period (e.g. an hour), and then finding the grid and time point combination with the maximum value; if this value exceeds a threshold value, an event is declared. Other events in the processed period can be detected by masking the detected event and repeating the search.

To improve the efficiency of the algorithm, at each potential origin time all possible epicentral distance correlations for each processed waveform can be pre-calculated and stored in an array which we call the C matrix:

$$C_{ij} = \sum_{k=1}^{N_t} M_{ik} D_{kj} \quad (\text{EQ 1})$$

Where D is the data matrix whose columns are the observed waveforms at each station, M is the MI matrix whose rows are the expected waveforms at each discrete distance, and N_t is the number of time points. i and j refer to the distance (discrete) and the station, respectively. Note that C has one column for each station and a number of rows equal to the number of discrete distances in the MI.

The detector can be run much more efficiently using C because no further dot products are needed; C contains all of the information necessary to calculate the correlation sum for any grid point. The detector output at each grid point is determined by summing one element from each column of C :

$$O = \sum_{j=1}^{N_s} C_{ij} \quad (\text{EQ 2})$$

Where N_s is the number of stations. Which row index is used for each column is dependent on the epicentral distance between the station and the grid point for which the summation is calculated. This indexing information, which we refer to as the *grid map*, is static and need only be calculated once, prior to running WCEDS, and stored as a look-up table.

RESEARCH ACCOMPLISHED

WCEDS (Global System)

Data Set

For the purposes of this paper we will discuss testing of Primary Network data using a global (surface only) grid with a spacing of 2 degrees. We have had difficulty in getting continuous Primary Network data from either the IDC or the USNDC and so have had to limit our testing to the few short intervals which we were able to obtain. For the purposes of this paper we will discuss 2

hours of data from June 19, 1996 (00:00 - 02:00). Despite the obvious limitations of such a small data set, we feel that this interval offers a number of excellent tests of the WCEDS systems. The events reported by the IDC for the interval are listed in Table 1.:

TABLE 1. IDC REB events for 6/19/96 00:00 to 02:00

origin time	latitude	longitude	depth	mb	region	in AEB?
00:01:31.5	7.36 S	123.22 E	619.7	3.2	Banda Sea	no
00:18:08.9	36.11 N	35.87 E	51.0	4.0	Turkey	yes
00:55:18.9	13.5 S	174.59 W	0.0	4.2	Samoa	yes
01:16:17.7	5.69 N	126.18 E	87.9	4.3	Mindanao	yes
01:38:57.8	6.58 S	132.92 E	0.0	3.4	Tanimbar	yes
01:47:34.9	41.92 N	142.47 E	71.0	3.6	Hokkaido	yes

This is a challenging set of events for any automatic detection system. None of the events is particularly large, most of them are in the southern Pacific region where Primary Network coverage is poor, and one was small enough to have been missed in the AEB (Alpha Event Bulletin). According to the REB (Reviewed Event Bulletin), only Turkey and Mindanao had substantial signal above background at more than a few Primary Network stations.

New Preprocessing

Because the Primary Network includes arrays, to process this data set we had to develop a strategy to pre-process array data. The simplest approach is to treat each channel of an array as a separate station and process in the standard manner, but to do so with such a coarse global grid (we use 2 degrees) would give none of the coherent signal enhancement which arrays are designed to provide. In fact, because our Master Image is smoothed and therefore the data to be correlated must also be smoothed (i.e. run through an STA/LTA filter), it is essential that array noise cancellation be accomplished in the pre-processing prior to the smoothing.

One obvious method to achieve the noise cancellation is to form a beam to each grid point, which is essentially the strategy currently used for array signal detection at the IDC and USNDC (a set of beams is formed which spans azimuths and slownesses and then each is run through a signal detection algorithm). We did not pursue this approach, however, because it requires the calculation and storage of a huge number of beams, which would significantly degrade our system performance.

In fact, given that our full matrix correlation approach uses an azimuth-independent Master Image, we would prefer to use one "best beam" for each array. This could be accomplished by forming some sort of a composite maximum value beam from a beam set, but we found that the spatial coherency analysis technique of Wagner and Owens (1996) provides a much more efficient means to do this. To calculate a spatial coherency stream for an array, we transform all data channels to the frequency domain, form the covariance matrix, and then solve for the principal eigenvalue. This process is repeated for a moving window to generate an output time series. Thus the technique, which can be applied to a station with any number of data channels (we have used for the Primary Network 3-component stations as well), yields one directionally independent stream for each array, as we require. Further, this stream should always have a high response to any spatially coherent signal, regardless of the azimuth, slowness, or even phase delay between channels. In our testing, we found that the technique can yield results quite comparable to, if not superior to, traditional beam-forming but that it is very sensitive to parameter choice. We selected optimal

parameters (10 second window, 3 frequency bands: 0.5-1.5 Hz, 1.5-2.5 Hz, 2.5-3.5 Hz) based on extensive analysis of the smaller, more poorly detected events from segments of our Primary Network test data sets.

Test Results

Despite the excellent signal enhancement provided by the spatial correlation technique, when we ran the original WCEDS prototype on our Primary Network test sets using relative timing only, we found that we had difficulty properly building many of the smaller events due to the sparse coverage provided by the Primary Network. Particularly troublesome are small events (less than mb 4.0) in the South Pacific, where network coverage is especially poor (the closest station can be more than 40 degrees away). These events are difficult for WCEDS to build properly because typically the only observations are P phases at the Australian arrays WRA and ASAR, which are unfortunately quite close together and hence function much like a single array.

Figure 1 compares the REB events with the set of WCEDS events for the 2 hour test set. We used a total of 35 stations: 12 arrays and 23 three-component single site stations.

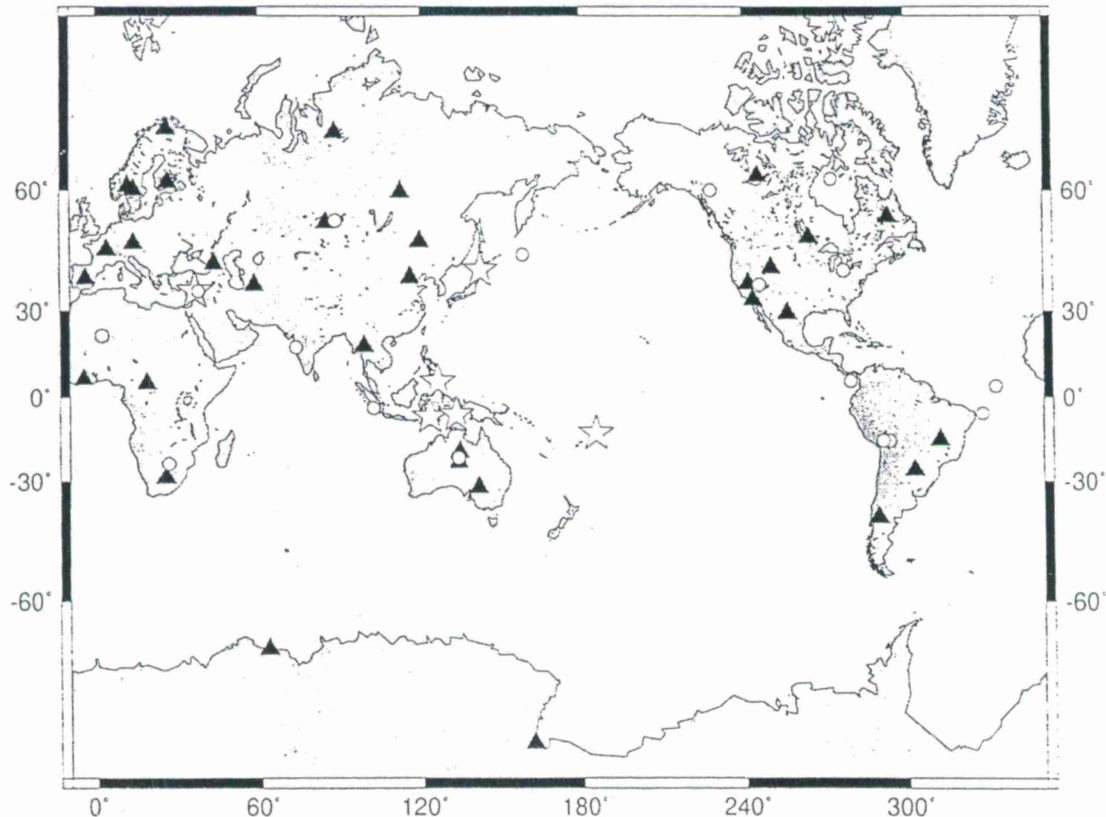


FIGURE 1. WCEDS vs. REB event locations - A comparison of REB events (white stars) and WCEDS events (white circles). The stations in the network used by WCEDS are indicated with black triangles.

The large number of events built by WCEDS is due to the fact that we let the system continue to try to build events in the time interval well down into the noise level to give the system every opportunity to build all of the REB events. In spite of this, very few of those events seem to have been built. There is one excellent agreement (the event in Turkey has a mislocation of 0.80 degrees), but in general we found very little correspondence between the WCEDS events and the

REB events. This is because very few of the REB events are large enough to be seen by more than a few stations, so relative timing does not constrain them well. In our tests with the IRIS network we found that if an event is at all widely recorded, as was the event in Turkey, WCEDS will do an excellent job of locating it because the relative timing information across the network provides a unique constraint on location and origin time. Conversely, when very few stations see an event, the relative timing provides a very non-unique constraint and the event may be very poorly built, perhaps so poorly that it will show almost no resemblance to the true event. In fact, we have found that for several of the REB events the relative timing information could be fit equally well by so many different grid and time point combinations that the wrong combination was often picked in order to falsely correlate an unrelated noise feature at a non-observing station with a predicted phase in the Master Image.

Fortunately, with array data (and perhaps three-component data, as well), we can significantly improve this result by taking advantage of the available directional information. By investigating the events in our sample data set, we found that a simple way to use directional information is to verify directional compatibility with a grid point location. Almost all of the legitimate signals from the REB events seen at the arrays had observed azimuths which were within ± 10 degrees of the predicted azimuths, suggesting that this simple test could be used to prevent non-compatible high-amplitude features from contributing incorrectly to event detection and location. Thus we modified the software to require that the observation fall within these limits, or the correlation for that particular station/phase will not be added to the overall grid point value. This prevents the random inclusion of unrelated signals with the true signals to get a higher correlation (but at the wrong grid and time point).

To implement this test, for each array we require a continuous stream of azimuth as a function of time. We obtain the additional streams by measuring the azimuth of the peak of an FK (frequency-wavenumber) transform of a moving window of the same length as the spatial coherence calculation. In many cases, there is no obvious peak and the azimuth is indeterminate which could lead to erroneous results, but we avoid this problem by only referring to directional information when a sufficiently strong signal is seen on the spatial coherence stream.

The results of processing the same two hour interval using the arrays only and incorporating the azimuthal verification step are shown in Figure 2. The improvement is dramatic. In this case, the first 6 events that WCEDS built were the 6 REB events, including the Banda Sea event which did not appear in the AEB. The sensitivity of the system is excellent, even though we are using only 12 arrays and no 3-component stations. Some of the mislocations are large, up to 44 degrees for the Tonga event, but very understandable when one examines the contributing stations and considers how the technique works. For example, the Tonga event was seen only by ASAR and WRA, hence the azimuth to those stations is well-constrained but the distance is not because of the large azimuthal gap in station coverage. Similarly, the Turkey event, which is mislocated by 17.0 degrees, was seen only by the northern European arrays and so is azimuthally well-constrained to be somewhere along the arc connecting those arrays and the true location, but has very little constraint on distance. The mislocation for this event increased dramatically from that shown in Figure 1 because for this test we did not include that data from 3-component European stations, some of which had good signals for this event. The use of these stations for this event, even without incorporating directional information, dramatically reduces the azimuthal gap and consequently dramatically improves the location estimate.

An obvious way to improve these mislocations is to incorporate slowness information as a verification as we did with azimuth, and we have begun to investigate this. We also generate a

continuous slowness stream from the moving FK window, so the data is readily available. So far, the results have been mixed. In some cases slowness can dramatically improve location while in others it can prevent events from being properly built. It may be that in order to use this information properly, at some stations we will need to account for local heterogeneity which causes observed slownesses to deviate from simple radial Earth model predictions.

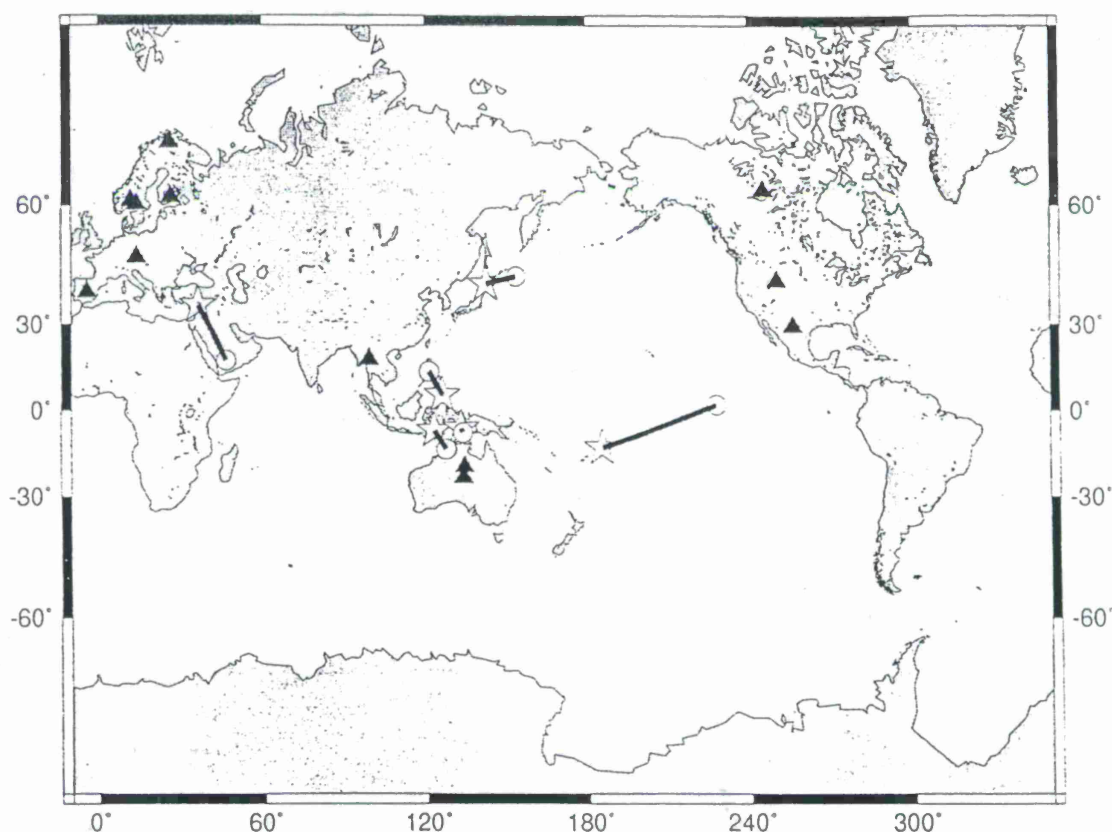


FIGURE 2. WCEDS vs. REB event locations: directional information used - A comparison of REB events (white stars) and the first 6 WCEDS events (white circles). Corresponding events are linked with black lines. The stations (all are arrays) in the network used by WCEDS are indicated with black triangles.

LWCEDS (Local/Regional System)

Data Set

New Mexico Tech operates a short-period digital seismic network consisting of 17 vertical-component seismometers, nine of which are employed in an approximate 60 km aperture centered on the central Rio Grande rift near Socorro, New Mexico. We will present results from testing using data from those nine stations. The grid we used is actually two grids: a 10 km spaced grid which covers the state of New Mexico and 1 km spaced grid which covers the central Rio Grande Rift. The algorithm starts with the coarse grid and then uses the fine grid for location refinement if an event is declared and the coarse grid location falls within the confines of the fine grid.

The test set used for this paper consisted of 10 local events selected to span a reasonable range of location and event quality. The events are listed in Table 2. The events were located by New Mexico Tech personnel who hand-picked the arrivals and then used the program *Seismos* (Hartse, 1991) to invert for location. The magnitudes are duration magnitudes (Ake, 1983).

TABLE 2. New Mexico Tech Seismic Network test events

origin time	latitude (N)	longitude (W)	depth	Md	RMS
09/20/95, 09:10:36.16	34.1158	106.8282	5.89	0.84	0.218
09/22/95, 10:37:57.84	34.3043	106.9240	6.35	0.84	0.362
09/22/95, 22:45:56.25	34.3550	106.7097	8.71	1.35	0.265
09/24/95, 16:04:51.57	34.0333	107.0288	7.56	1.37	0.369
09/24/95, 16:06:44.75	34.0345	107.0328	9.22	0.16	0.242
09/24/95, 16:11:25.43	34.0323	107.0318	8.89	0.33	0.234
09/24/95, 17:58:40.95	34.0297	107.0282	7.81	1.57	0.348
09/24/95, 18:10:55.02	34.0285	107.0283	8.80	0.59	0.202
10/14/95, 04:24:03.87	34.4477	107.0180	4.93	1.43	0.191
09/27/96, 08:35:33.71	34.4275	107.0678	2.08	1.32	0.392

PreProcessing

Unlike the teleseismic problem where often only a P arrival can be clearly identified, at regional or local distances several phases are often readily apparent within observed waveforms even for small events. Thus a full waveform technique should be particularly effective at these distances. Unfortunately, however, local and regional phases span a wide range of frequencies, so it is not possible to choose a single set of STA and LTA windows which will do a good job of emphasizing all phases. For this reason, we developed an adaptive STA/LTA algorithm (Withers et al., 1997) which maintains the same proportion between the window lengths but changes their absolute lengths to adapt to the dominant frequency of the signal. Our testing indicates that this algorithm has an excellent ability to emphasize each phase in a local or regional waveform, from high-frequency Pn to low-frequency Lg.

Test Results

The LWCEDS system is a much simpler system than the global system because it does not contain any of the masking or continuous processing capabilities. Masking is unnecessary because overlapping events are rarely recorded by the network due to the relatively low level of seismic activity in New Mexico and the size of the network (LWCEDS does not try to locate teleseismic or far-regional events, which it identifies by frequency content). Also, true continuous operation is not necessary because the algorithm is launched by a trigger in the acquisition system which is set to "go off" when a significant signal is measured at a user defined number of stations (currently 4) in the network during some specified period of time. For the test set, the trigger was assumed to have occurred (it did occur originally -- hence the presence of these events in the archive) and LWCEDS was launched manually on the archived interval for each of the 10 events.

A comparison of the LWCEDS and Seismos events is shown in Figure 3. The results are very encouraging. The largest mislocation is 3.53 km, and none of the others is more than 2 kms. Despite the fact that we use no directional information, these results are at least as impressive as those of the global system, suggesting that a low threshold ($>\sim 0.1$) and high-quality locations can be achieved using relative timing information only if the event is recorded by several stations in the network, as we discussed above. Tests with an expanded test set including regional events from New Mexico and eastern Arizona show a similar detection sensitivity to those events, though the mislocations increase dramatically (10 to 100 km), depending on the size of the azimuthal gap.

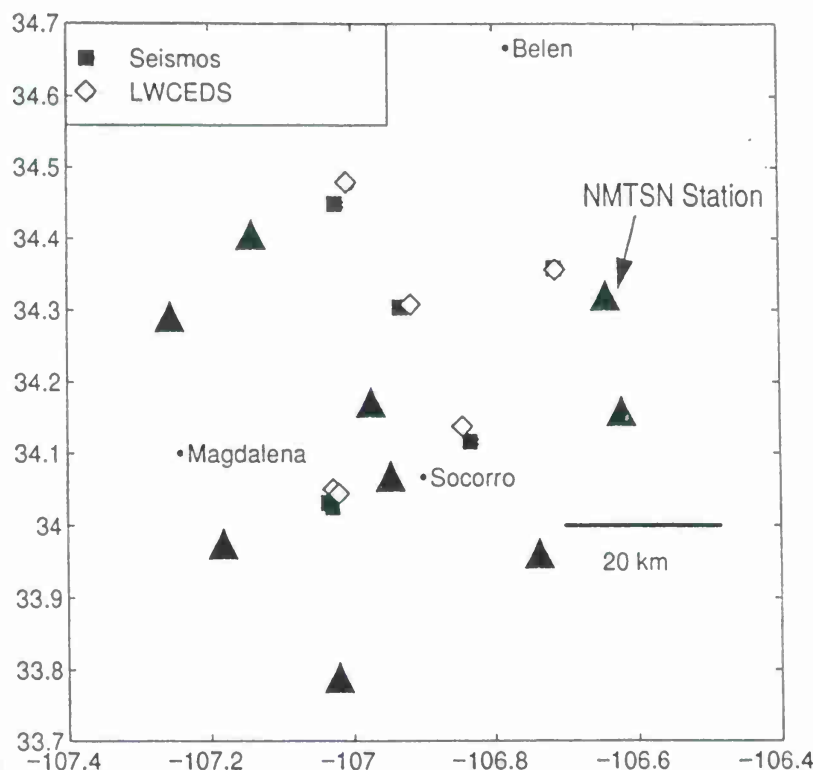


FIGURE 3. LWCEDS vs. Seismos locations - A comparison of LWCEDS locations and analyst locations for the 10 event test set. The shaded triangles show the locations of the elements of the New Mexico Tech Seismic Network (NMTSN).

CONCLUSIONS AND RECOMMENDATIONS

Mature, second-generation WCEDS software has been developed for both global and local/regional networks and tested with data sets from the IDC Primary Network and the New Mexico Tech Seismic Network, respectively. Our results indicate that the technique can work well at both scales but shows particular promise for local/regional networks where multiple phases for a given event are often recorded by many stations. In fact, the local/regional version of WCEDS (LWCEDS) has proven so successful that it is now routinely used at New Mexico Tech to automatically locate events which trigger their acquisition system. In regions of the world where dense single station coverage is available, this technology could be used to develop highly sensitive, highly accurate monitoring systems.

Our results from the global system have been much less clear cut. Testing on IDC Primary Network data with a version of the system which does not use directional information (ala LWCEDS) yielded unsatisfactory results for many events in the IDC REB. However, if directional information is included results improve dramatically. By including a simple azimuthal consistency check we found that WCEDS can achieve a detection threshold comparable to if not superior to GA with a low false alarm rate, though the locations can be off by as much as 30 degrees for events with large azimuthal gaps. We have begun to test schemes using slowness information as well, and have found the results to be mixed: mislocations are generally considerably reduced and the number of misassociated detections decreases dramatically, but in some cases obvious phases are missed because observed slownesses do not match predictions.

Our future work will focus on the use of the WCEDS technology for "spotlighting". We believe that both the global and the local/regional results suggest that WCEDS shows promise for this problem. Which version of the algorithm is most appropriate will depend on the proximity of the monitoring stations to the region of interest. Our testing of both versions suggests that a very low detection threshold could be achieved.

REFERENCES

- Ake, J. (1983). A magnitude scale for central New Mexico based on signal duration, *Geophysics Open-file Report*, 45, 8 pp.
- Hartse, H. (1991). Simultaneous hypocenter and velocity model estimation using direct and reflected phases from microearthquakes within the central Rio Grande Rift, New Mexico, *Ph.D. Dissertation, New Mexico Tech*, 251 pp.
- Shearer, P. M. (1994). Global seismic event detection using a matched filter on long-period seismograms, *J. Geophys. Res.*, 99, 13713-13725.
- Withers, M. M. (1997). An automated local/regional seismic event detection and locations system using waveform correlation, *Ph.D. Dissertation, New Mexico Tech*, 195 pp.
- Withers, M. M., R. C. Aster, C. J. Young, J. I. Beiriger, J. M. Harris, S. G. Moore, J. R. Trujillo (1997). A comparison of select trigger algorithms for automated global seismic phase and event detections, *submitted to Bull. Seismol. Soc. Amer.*
- Young, C. J., J. I. Beiriger, J. M. Harris, S. G. Moore, J. R. Trujillo, M. M. Withers, and R. C. Aster (1996a). The waveform correlation event detection system project: issues in system refinement, tuning, and operation, *Proceedings of the 18th Annual Seismic Research Symposium on Monitoring a CTBT*, p. 789-798.
- Young, C. J., M. Harris, J. I. Beiriger, S. G. Moore, J. M. Trujillo, M. M. Withers, and R. C. Aster (1996b). The waveform correlation event detection system project, phase I: issues in prototype development and testing, *SAND Report #SAND96-1916*.
- Young, C. J., J. I. Beiriger, J. M. Trujillo, M. M. Withers, R. C. Aster, L. Astiz, and P. M. Shearer (1995). WCEDS: a waveform correlation event detection system, *Proceedings of the 17th Seismic Research Symposium on Monitoring a CTBT*.

OPTICAL AND ELF SIGNATURES OF LIGHTNING, SPRITES, ELVES AND JETS
DETECTION AND DISCRIMINATION

Russell A. Armstrong, Trella H. McCartor
Mission Research Corporation, Nashua, NH 03062

Walter A. Lyons
FMA Research, Fort Collins, CO 80524

Earle R. Williams
Massachusetts Institute of Technology, Cambridge, MA 02139

Sponsored in part by the Air Force Phillips Laboratory under contract F19628-93-C-0186 and
NASA Kennedy Space Center under grant NAS10-12113.

ABSTRACT

Both lightning and nuclear airbursts are well established sources of optical and RF emission observed from satellites and ground stations. Global attempts to detect nuclear airbursts using optical and/or RF techniques often encounter lightning and related phenomena as background "clutter". As part of the mission to monitor compliance with the nuclear test-ban and non-proliferation treaties, a number of different techniques for detecting and identifying nuclear detonations (NUDETS) around the world have been developed. Recently, a class of atmospheric phenomena, called "sprites", "elves" and "jets" (Transient Luminous Events, TLEs) and associated RF signatures have been identified above thunderstorms which exhibit certain potential for introducing uncharacterized backgrounds and clutter for treaty monitoring, as well as a broad range of other system missions, such as surveillance, TW/AA and theater combat.

Improved sensors with increased sensitivity and dynamic range will be required for next-generation detection. Such sensors will be significantly more vulnerable to "confusion" from natural cluttered backgrounds. Therefore, new discrimination algorithms will be required to process the signals recorded by the sensor. Such algorithms must be based on a full understanding and characterization of both nuclear and natural clutter backgrounds. That fusion of ground-based data on lightning and the newly-discovered TLE phenomena in the middle atmosphere with data from research and mission satellites on these phenomena and from calculations of NUDETS signatures can form the basis for such algorithms. There are systematic patterns emerging from the data which strongly suggest that we can derive discriminating processing algorithms and models to aid in data analysis and system effects mitigation.

In this paper, we review the relevant characteristics of lightning, TLEs and associated RF signatures. These characteristics will form the basis for developing discrimination algorithms for natural events vs NUDETs for treaty monitoring applications.

Key words: Lighting, Sprites, Elves, Blue Jets, Transient Luminous Events, NUDETS Optical Signatures, Discrimination Algorithms.

OBJECTIVE: We are initiating a research activity to analyze emerging data on lightning, Transient Luminous Events (TLEs) and associated ELF signatures from electrodynamic phenomena above thunderstorms. We will compare these signatures with low-altitude NUDET_s calculations to develop robust models and discrimination algorithms for TLE phenomena based on correlated and integrated satellite-and-ground truth data.

RESEARCH ACCOMPLISHED: This research project has just been initiated, hence there has been no reportable results to-date. We describe below the relevant background information obtained in work sponsored elsewhere which leads to the basis of this research project.

INTRODUCTION: Both lightning and nuclear airbursts are well established sources of optical and RF emission observed from satellites and ground stations. Recently, a class of atmospheric phenomena, called "sprites", "elves" and "jets" (we will refer to them collectively as Transient Luminous Events, TLEs) has been identified above thunderstorms which exhibit certain optical and RF signatures that have potential for introducing uncharacterized backgrounds and clutter for treaty monitoring, as well as a broad range of other system missions, such as surveillance, TW/AA and theater combat.

TLEs are recently-confirmed transient luminous events which are manifestations of electrodynamic activity in the region between the tops of mesoscale convective systems (MCSs) and the ionosphere. Although anecdotal evidence for their existence has been reported for decades, (Corliss, 1983; Wilson, 1956) they have only recently been unambiguously recorded and characterized from ground stations, aircraft and research satellite observations (Boeck, et.al., 1995; Franz et.al., 1990; Hampton, et.al., 1996; Lyons, et.al., 1996; Sentman and Wescott, 1993, Vaughn, et.al., 1992, Winkler, et.al., 1994). Observations from relevant satellite assets have also been reported (Glass, 1997), some of which have been shown to be related to these events. Current data indicates that optical emissions from TLEs are associated with some type of cascade discharge in the region between large thunderstorms and the ionosphere (Boccippio, et.al, 1995, Pasko, et.al., 1995, Roussel-Dupré and Gurevich, 1996).

Various other signatures have been associated with these phenomena. Boccippio et.al. (1995) have obtained Schumann-resonance Q-burst data (ELF signals (3-50 Hz) that resonate with the Earth's electromagnetic cavity) that are highly correlated with sprite observations. Inan (1996) and Dowden (1995) have observed strong VLF signatures associated with sprites. Roussel-Dupré and Blanc (1996) have obtained radar returns above thunderstorms which are consistent with electron densities approaching 10^5cm^{-3} . Blackbeard and Alexis observations of RF signatures (Sub-Ionospheric Pulse Pairs, SIPPS, and Trans-Ionospheric Pulse Pairs, TIPPS) have been reported (Roussel-Dupré, 1995) which may be related to precursor events. The Burst and Transient Source Experiment (BATSE) on the Compton Gamma-Ray Observatory (CGRO) has recorded events in regions associated with thunderstorms (Inan et.al., 1996). Although not all of this data have yet been shown to be *directly* correlated, it certainly confirms that there are highly energetic events of interest occurring in the middle atmosphere above thunderstorms. No single theory or model has yet emerged which *collectively* explains these events.

SIGNATURES OF SPRITES, ELVES AND JETS: Sprites typically extend from 35 kilometers to 90 kilometers in altitude and range from 10 kilometers to 50 kilometers across, occupying volumes of hundreds-to-thousands of km^3 . They have been shown to be highly structured

(Sentman, et.al., 1996, Pasko, et.al., 1996). Estimates of their energy exceed 1 *megajoule* and their optical power exceeds 10^5 W Sr^{-1} . Figure 1 shows an actual image of a simultaneous sprite and elve along with an actual overlay image of a jet. The duration of the optical emissions ranges from sub-milliseconds for "blue" emissions to greater than 100 milliseconds for "red" emissions. Although not yet directly measured, infrared emissions are estimated to last several seconds to several tens-of-seconds (Armstrong, 1995).

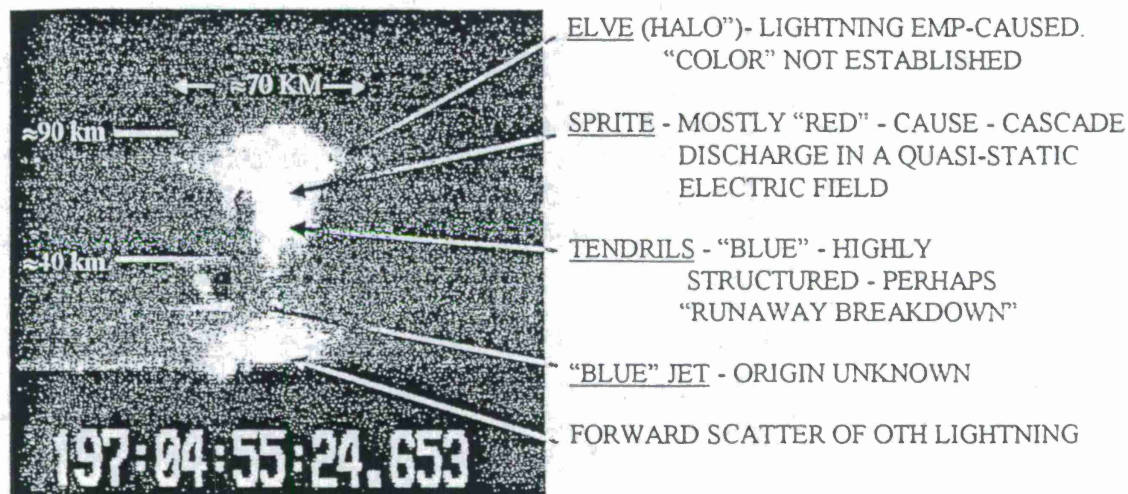


Figure 1. General morphology of a sprite, elve and "blue" jet (the jet image is an overlay).

"Elves" appear as a sudden and short-lived "brightening" at the lower ionospheric ledge. Elves sometimes occur with sprites and sometimes alone. Fukunishi, et.al. (1996) and Inan, et.al. (1997) have collected data which clearly show elves as a fast, high-altitude optical signature that can be hundreds of kilometers in lateral dimension and about 10 kilometers in depth. Their optical power has not been quantified but appears to be greater than sprites and different in spatial and temporal character.

Perhaps related phenomena called "blue jets" appear to be electron-beam-like events propagating from the tops of thunderstorms (Wescott et.al., 1995; Lyons, 1996). These events typically have radii of a few kilometers and extend from about 20 kilometers up to perhaps 40-45 kilometers in altitude. Although we know less about the jets than we do about sprites and elves, they appear to have a much higher concentration of energy than do sprites, and the terminus of the jet appears to spawn an upward-going visible shock wave.

Although there has been significant amounts of monochrome video data collected on TLEs over the last three years, there is limited spectral data. Lyons et.al. (1996) have collected literally *thousands* of images of these events. From the significant data base that exists on sprites, it is very clear that there is no such thing as "a sprite". The spatial structure and temporal persistence of sprites are highly variable. In Figure 2, we show four different types of sprites at different ranges, indicating the variable nature of the events. However, we have found that certain fundamental characteristics exhibit clear "patterns" which can be used as identifying features (location, color, intensity patterns, lifetimes, etc.)

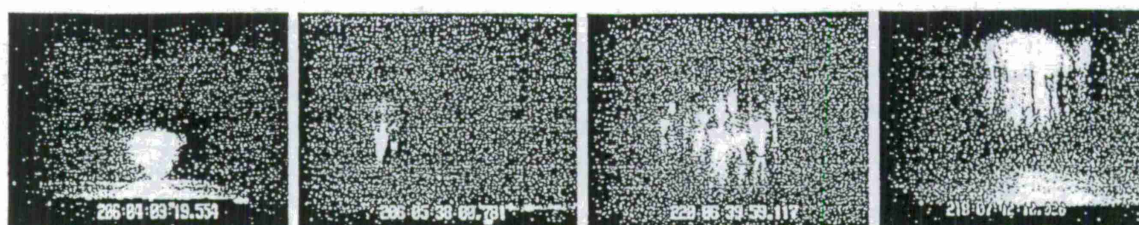


Figure 2. Example of various types of sprites.

In the SPRITES '94 campaign, Sentman and Wescott (1993) collected the first three-channel "color" video which clearly showed the dominant color in sprites to be red, but with blue "tendrils" structure in the lower altitude regions of the phenomenon. In the SPRITES '95 campaign, Mende, et.al. (1995) and Hampton, et.al. (1996) obtained spectral observations of sprites which clearly identified the red emission from sprites as nitrogen first positive emission. The "blue" component(s) of sprites and jets has not yet been spectrally identified. However, photometric data (Armstrong, et.al., 1997, Suszcynsky, et.al., 1997) confirms the presence of both N_2^+ 427.8 nm first negative emission and N_2 399.8 nm second positive emission, both of which are blue. The presence of these emissions is consistent with a combination of the theories that have emerged to-date, although the quantitative details (persistence, relative brightness, spatial structure) have yet to be fully explained.



Figure 3. Isocon 665 nm image of an elfe. (Courtesy of Mike Taylor, Utah State University)

In figure 3, we show a red-filtered isocon image of an elfe. The corresponding 427.8 nm photometer trace is shown in figure 4(d). Inan, et.al. (1997) have suggested the source of elves is the EMP emitted from very strong charge-acceleration events. The EMP will couple to the lower ledge of the ionosphere, accelerating the ambient electrons, resulting in electron impact excitation of the ambient molecular species.

For discrimination purposes, among the more important current information is contained in the 427.8 nm and 399.8 nm photometry data (Armstrong, 1997). In both SPRITES '95 and SPRITES '96 campaigns, we deployed photometers to obtain time-based characterization of sprites, elves and any other related phenomena. The 427.8 nm emission originates with prompt ionization processes which yield the N_2^+ first negative ion transition (which also emits 391.4 nm light - too scattered to observe from the ground). The 399.8 nm emission originates with electron-impact excitation of the N_2 second positive neutral transition. The ratio of these two bands yields evidence on both the energy deposition rate and the ion-to-neutral populations.

Most importantly, our preliminary analysis shows that the ratio of the 399.8 nm neutral emission to the 427.8 nm ion emission appears to be very sensitive to the specific phenomenon. This strongly suggests that two-color analyses may be used to discriminate sprites and elves against normal lightning and nuclear airbursts. In Figure 4, we show four photometer time-traces for the 427.8 nm and 399.8 nm emissions, the first two from normal lightning, the third from a sprite and the fourth from an elfe (399.8 nm emission is plotted "negative" only for convenience of comparison). What is obvious from the traces, is that the ratio $I_{399.8}/I_{427.8}$ appears to be specific to

each phenomena. In fact, this appears to be systematic for all of the data obtained in SPRITES '96. The lightning-only data has a ratio close to unity, consistent with a continuum emission. Sprites appear to have a ratio close to 2 and elves appear to have a ratio close to 3 (or greater).

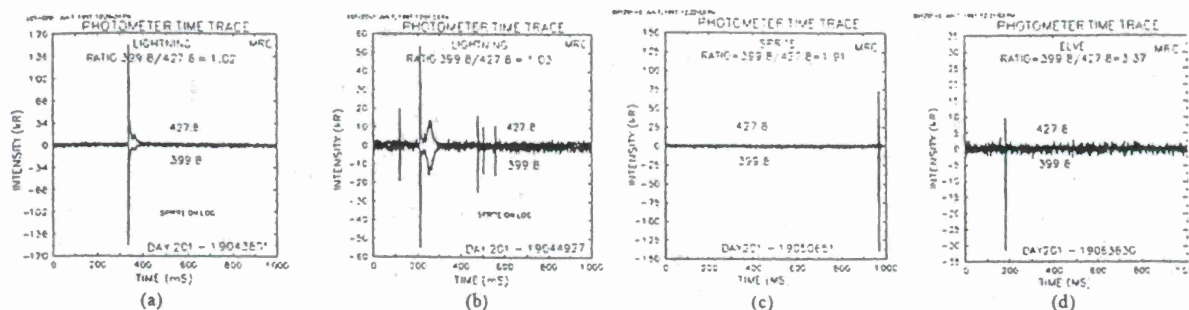


Figure 4. 427.8 nm and 399.8 nm photometer traces for (a,b) lightning, (c) sprite and (d) elve.

Another characteristic of optical signatures of these events is both spatial and temporal multiple-maxima. As discussed above, sprite events can take many forms, including multiple events which are spatially or temporally separated. Elves can occur without sprites but we often find that the two occur together (Figure 1). In all coincident cases investigated to-date, it appears that the elve occurs before the sprite, with varying time delays, from nearly simultaneous, to several milliseconds. In Figure 5, we show a sprite case where there is a 45 millisecond time delay between the first 427.8 nm maximum and the second. In this case, the video signature from the

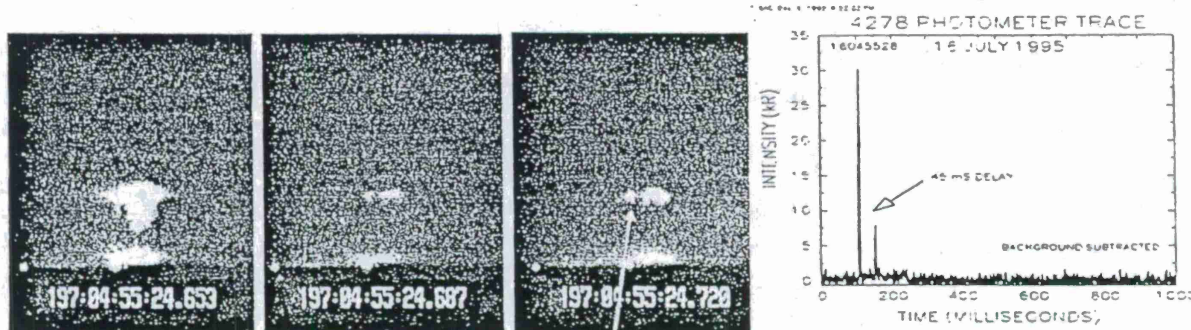


Figure 5. Sprite/Elve sequence showing a "re-brightening" and the corresponding 427.8 nm photometer time trace (field time is 17 ms).

sprite lasted nearly 200 milliseconds and there was a "re-brightening" source event which gave rise to a "second maximum" with a delay of 45 milliseconds in both the 427.8 nm emission and the visible image.

Suszcynsky et.al. (1997) have unquestionably shown that the time-constant of the 427.8 nm emission is typically 0.3 ms or less, consistent with our photometer data which puts an upper limit on the time-constant for both 427.8 nm and 399.8 nm emission of 1.3 ms. An interesting feature of the Suszcynsky, et.al. data is the presence of a "secondary maximum" in the 427.8 nm data at about 1 ms, as shown in figure 6. This feature is not always present and has yet to be explained.

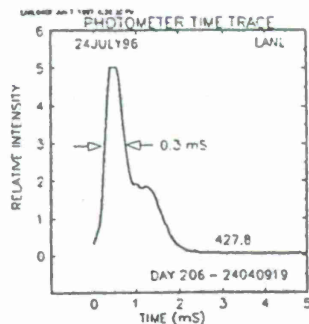


Figure 6. High temporal resolution 427.8 nm photometer time trace (Courtesy of Dave Suszcynsky, Los Alamos National Lab).

Finally, a note about the photometric observations of forward-scattered lightning, as in figure 4 (a&b). First, we have found that in all such data investigated to-date, the ratio of the emission intensities of 399.8 nm to 427.8 nm is very close to unity. This is consistent with observation of lightning continuum. Second, one notes in figure 4 that, in addition to the main lightning intensity peak, there is a secondary emission which sometimes appears as a "tail", as in figure 4(a) or a completely time-separated feature, as in figure 4(b). We have found in the data analyzed to-date that whenever this secondary emission feature is present, it maintains the same intensity ratio as the parent peak. Unfortunately, we do not yet have data which would confirm a direct correlation of this secondary peak and the generation of sprites.

This secondary peak is evidence of a "continuing current" indicative of continuing charge re-distribution within the thundercloud. Sprites may be associated with this re-distribution rather than being a direct result of the parent positive CG. However, it is likely that the two are not separate events but one continuous phenomenon. Given the paucity of data on this phenomena, it is impossible yet to derive a definitive explanation of the importance of the secondary emission observed in the photometer time traces. Given both the 399.8 nm/427.8 nm ratios, and the time constants, we know with certainty that this secondary peak is neither from sprites nor elves.

These combined results indicate the presence of multi-maxima optical signatures with at least three time-periods of importance: (1) the initiating breakdown, occurring on sub-millisecond time scales, (2) the "prompt" emission from the secondary electron impact processes occurring on a few-millisecond time scales, and (3) an "afterglow" caused by relatively cool electrons which can persist for up to several hundred milliseconds. It is most likely that the 427.8 nm and 399.8 nm emissions are a trace of the initiating ionization (e.g., runaway breakdown, Roussel-Dupré and Gurevich., 1996), consistent with the relatively short time constants and the fact that such an initiating process will not be spectroscopically "dark". The broad-band and red-filtered photometer results are likely a trace of the emission from the secondary electron excitation mechanisms in the quasi-static electric field, consistent with the theory of Pasko, et.al (1995).

RF SIGNATURES: ELF methods are particularly well suited for the global detection of lightning, nuclear and TLE-related electrodynamic signals because of two fortuitous circumstances: (1) the attenuation at ELF is minimal in propagation around the globe and (2) ELF is strongly excited because of the 1-100 msec time scales inherent in the phenomena. The long time scale in lightning is associated with continuing currents (Burke and Jones, 1996) that dominate total charge transfer. In nuclear airbursts, the sustained phenomenon is the Compton current resulting from sustained gamma emission (Glasstone, 1977).

The theory for ELF propagation in the earth-ionosphere cavity is well established (Wait, 1970; Ishaq and Jones, 1977; Nickolaenko and Kudintseva, 1994; Sentman, 1995) and has been validated experimentally (Kemp and Jones, 1994; Boccippio et al, 1995; Burke and Jones, 1996).

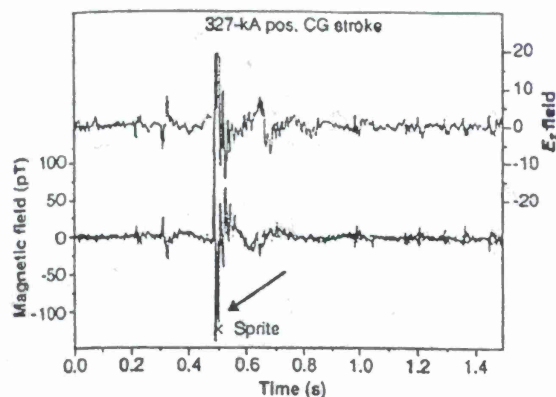


Figure 7. Typical sprite-related ELF transient

term provides an important quantitative characteristic of the event that may enable a distinction between lightning and nuclear airbursts. To locate events, one needs to determine a great circle bearing (based on standard crossed-loop measurements of the horizontal magnetic field) and a great circle distance. The distance is uniquely related to the oscillation rate of the wave impedance (Ishaq and Jones, 1977). The workability of these equations with the observations in locating events on a global scale on a continuous basis from the single ELF station in West Greenwich, Rhode Island is amply demonstrated by the global map of events in Figure 8, showing a predominance of activity in three major zones of tropical convection where lightning activity is well established. The events located in Figure 8 are in the high-energy "tail" of the global popula-

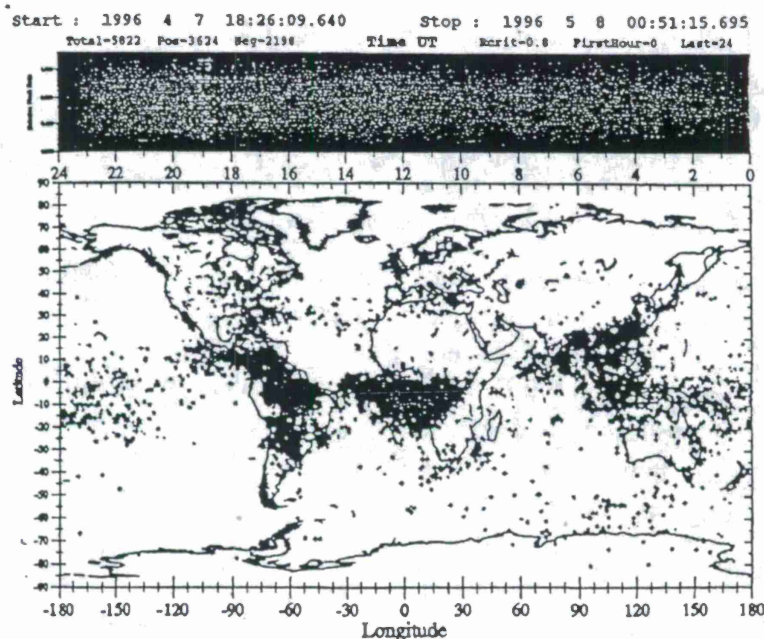


Figure 8. "Q-Burst" event locations 4/7/96 - 5/8/96. Of the total of 5822 events, 3624 were positive. Positive strokes are suggestive of sprites.

Figure 7 shows an example of a sprite-related ELF transient obtained on 7 September 1994. The vertical electric and horizontal magnetic fields are shown. The times of the associated sprite and the positive CG stroke are overlaid. The ELF signature observed, ≈ 25 pT magnetic amplitude, implies a change in total dipole moment greater than 1000 C-km.

The source term for ELF generation is the current moment (ampere-meter) which can be extracted from the measurements from a single station (Burke and Jones, 1996). The source

term provides an important quantitative characteristic of the event that may enable a distinction between lightning and nuclear airbursts. To locate events, one needs to determine a great circle bearing (based on standard crossed-loop measurements of the horizontal magnetic field) and a great circle distance. The distance is uniquely related to the oscillation rate of the wave impedance (Ishaq and Jones, 1977). The workability of these equations with the observations in locating events on a global scale on a continuous basis from the single ELF station in West Greenwich, Rhode Island is amply demonstrated by the global map of events in Figure 8, showing a predominance of activity in three major zones of tropical convection where lightning activity is well established. The events located in Figure 8 are in the high-energy "tail" of the global popula-

tion of lightning flashes. The dominant element of that tail is the positive ground flash which has been shown to exhibit the largest peak currents (>200 kA), the longest continuing currents (>100 msec), the largest charge transfers (hundreds of coulombs), and the brightest optical emissions of any lightning event.

Positive ground flashes have been closely associated with sprites (Boccippio et al, 1995) but their relationship to elves and jets is not yet established. More importantly, positive ground flashes are the leading contributor to ELF Q-bursts (Ogawa et al, 1967; Boccippio et al, 1995; Burke and Jones, 1996) and in a single stroke, excites the earth-ionosphere cavity to an amplitude greater than the integrated amplitude of all the other lightning events on the planet, for periods of hundreds of milliseconds.

The intimate association of sprites with positive ground flashes (and the probable correlation between sprite brightness and the intensity of the positive CG) and the ability to locate the positive CG with the aforementioned ELF method, provides a means for near-real-time mapping of bright events and sprites on a global basis. Comparisons between the optical intensity of lightning events observed by NASA's Optical Transient Detector (OTD) in space and the amplitudes of ELF events in Rhode Island (Boccippio et al, 1996) support the conclusion that, on average, the brightest lightning events are also the most likely to be strong ELF events.

It is well recognized that nuclear air bursts are a potent source for ELF Q-bursts (Fellmann, 1973). The "Starfish" event in the upper atmosphere over Johnston Island in the Pacific Ocean produced a large amplitude ELF transient at a magnetic observatory near Paris, France. Analysis of the calibrated magnetic wave amplitude (60-70 pico-Tesla) suggested a source strength large in comparison with most lightning Q-bursts. Nearly one third of the sprite-associated Q-bursts reported in Boccippio et.al. (1995) exceeded this amplitude, for events at comparatively close range (2,000-3,000 kilometers).

The correlation of sprites and related phenomena with observations of world-wide Q-bursts has yielded a rate of approximately 1 event every 2-5 seconds. In addition, data from recent SPRITES '95 and SPRITES '96 campaigns, have shown that literally *hundreds of events per night* can occur from certain types of MCSs in a given region. For certain types of storms, the predictability is nearly 100%! Therefore, it is likely that these events occur sufficiently often in regions of interest that they are observable with current systems.

CONCLUSIONS AND RECOMMENDATIONS: It is clear from the emerging data on electrodynamic phenomena above thunderstorms that optical and ELF signatures can be generated by these events yielding a considerable source of clutter. This clutter may interfere with NUDETs discrimination programs which support monitoring of the Comprehensive Test Ban Treaty. Given the apparent electrodynamic behavior of the sources of these signatures, e.g., EMP, lightning and charge acceleration, it is likely that NUDETs *themselves* can generate such events.

Both the data on this phenomena, and the various theories purporting to explain the data, suggest highly energetic processes which can yield electromagnetic signatures of interest to processing and interpreting satellite data, as well as forming a basis for model development and validation. There are systematic patterns emerging from the data which strongly suggest that we can derive discriminating processing algorithms and models to aid in data analysis and system effects mitigation. In order to develop robust algorithms to treat this data, we require a knowledge of NUDET signatures to identify differentiating characteristics.

We will perform a two-year research program to develop robust models and algorithms based on analysis of the emerging data along with correlated and integrated satellite-and-ground truth data. We will also compute the expected signatures of low-altitude NUDETs and evaluate the effects of radiative transfer on both these signatures and the TLEs. We will include the expected ELF signatures as a position locator and possible adjunct for developing discrimination rules.

REFERENCES:

- Armstrong, R.A., Shorter, J.A., Taylor, M.J., Suszcynasky, D.M., Lyons, W.A., Jeong, L.S., (1997) Photometric measurements in the SPRITES'95 and SPRITES'96 campaigns - nitrogen second positive (399.8 nm) and first negative (427.8 nm) emission, *Journal of Atmospheric and Solar-Terrestrial Physics*, submitted for review.
- Armstrong, R.A., (1995) A White Paper on Sprites, presented to AFPL, Hanscom AFB
- Boccippio, D.J., Williams, E.R., Lyons, W.A., Baker, I., Boldi, R. (1995) Sprites, ELF transients and positive ground strokes, *Science*, **269**, 1088-1091.
- Boccippio, D. Wong, C., Williams, E.R., Boldi, R., Goodman, S., Christian, H., (1996) Global validation of ELF Q-burst events, *Journal of Atmospheric and Solar-Terrestrial Physics* (in review).
- Boeck, W.L., Vaughn, Jr., O.H., Blakeslee, R.L., Vonnegut, B., Brook, M., McKune, J., (1995) Observations of lightning in the stratosphere, *Journal of Geophysical Research*, **100**, 1465-1475.
- Burke, C.P., Jones, D.L., (1996) On the polarity and continuing current in unusually large lightning flashes deduced from ELF events, *Journal of Atmospheric and Solar-Terrestrial Physics* (in review).
- Corliss, W.R., (1983) *Handbook of Unusual Natural Phenomena*, Anchor Books/ Doubleday, Garden City, NJ
- Dowden, R.L., Brundell, J., Lyons, W.A., (1996) Are VLF rapid-onset, rapid-decay perturbations produced by scattering off sprite plasma?, *Journal of Geophysical Research*, **101**, 19175-19183
- Fellmann, E., (1973) Analysis of Schumann resonances simultaneously recorded at two distant stations, PhD thesis, Saarbrücken
- Franz, R.C., Nemzek, R.J., Winkler, J.R., (1990) Television image of a large upward electrical discharge above a thunderstorm system, *Science*, **249**, 48-51
- Fukunishi, H., Takahashi, Y., Kubota, M., Sakanoi, K., Inan, U.S., Lyons, W.A., (1996) Elves: Lightning-induced transient luminous events in the lower ionosphere, *Geophysical Research Letters*, **23**, 215-216
- Glass, E., (1997) Unpublished results, Sandia National Laboratory
- Glasstone, S., Dolan, P.J., (1977) *The Effects of Nuclear Weapons*, 3rd edition, United States Government Printing Office, Washington, DC
- Hampton, D.L., Heavner, M.J., Wescott, E.M., Sentman, D.D., (1996) Optical Spectral characteristics of Sprites, *Geophysics Research Letters*, **23**, 89-92
- Inan, U.S., Barrington-Leigh, C., Hansen, S., Glukhov, V.S., Bell, T.F., Rairden, R., (1997) Rapid lateral expansion of optical luminosity in lightning-induced ionospheric flashes referred to as "elves", *Geophysical Research Letters*, **24**, 583-586.
- Inan, U.S., Slingeland, A., Pasko, V.P., Rodrigues, J.V., (1996) VLF and LF Signatures of Mesospheric and Lower Ionospheric Response to Lightning Discharges, *Journal of Geophysical Research*, **101**, 5219, 1996.
- Inan, U.S., Reisling, S.C., Fishman, G.J., Horack, J.M., (1996) On the Association of Terrestrial Gamma-Ray Bursts with Lightning and Implication for Sprites, *Geophysical Research Letters*, **23** (9) 1017-1020
- Ishaq, M., Jones, D.L., (1977) Methods of obtaining radiowave propagation parameters for the Earth-ionosphere wave duct at ELF, *Electronics Letters*, **13**, 254-255.
- Kemp, D.T., Jones, L., (1994) A new technique for the analysis of transient ELF magnetic disturbances within the Earth-ionosphere cavity, *Journal of Atmospheric and Solar-Terrestrial Physics*, **56**, 1493-1498,
- Lyons, W.A., (1996) Sprite observations above the U.S. high plains in relation to their parent

- thunderstorm system, *Journal of Geophysical Research*, **101**, 29641-29652
- Mende, S.B., Rairden, R.L., Swenson, G.R., Lyons, W.A., (1995) Sprite spectra: N₂ first positive band identification, *Geophysical Research Letters*, **22**, 2633-2636.
- Nickolaenko, A.P., Kudintseva, I.G., (1994) A modified technique to locate the sources of ELF transient events, *Journal of Atmospheric and Solar-Terrestrial Physics*, **56**, 1493-1498.
- Ogawa, T., Tanaka, Y., Yasuhara, M., Fraser-Smith, A.C., Gendrin, R. (1967) Worldwide simultaneity of occurrence of a Q-type ELF burst, *Journal of Geomagnetism and. Geoelectromagnetics*, **19**, 115.
- Pasko, V.P., Inan, U.S., Bell, T.F., (1996) Mesospheric modifications above thunderstorms and spatial structure of sprites, *EOS Transactions (Supplement)*, **77**, F68
- Pasko, V.P., Inan, U.S., Taranenko, Y.N., Bell, T.F., (1995) Heating, ionization and upward discharges in the mesosphere due to intense quasi-static thundercloud fields, *Geophysical Research Letters*, **22** 365-368
- Roussel-Dupré, R.A., (1995) Los Alamos National Laboratory, unpublished results
- Roussel-Dupré, R.A., Blanc, E., (1997) HF Echoes from ionization potentially produced by high-altitude discharges", *Journal of Geophysical Research*, **102**, 4613-4622
- Roussel-Dupré, R.A., Gurevich, A.V., (1996) On Runaway breakdown and upward-propagating discharges, *Journal of Geophysical Research*, **101**, 2997-2311
- Sentman, D.D., Wescott, E.M., Heavner, M.J., Moudry, D.R., (1996) Observations of Sprites beads and balls, *EOS Transactions (Supplement)*, **77**, F61
- Sentman, D.D., Wescott, E.W., (1993) Observations of upper atmosphere optical flashes recorded from aircraft, *Geophysical Research Letters*, **20**, 2857-2860
- Sentman, D.D., Schumann Resonances, (1995) CRC Handbook on Atmospheric Electrodynamics, Ed., Hans Volland, CRC Press, Boca Raton, Florida, 1995.
- Suszcynsky, D.M., Roussel-Dupré, R.A., Lyons, W.A., Armstrong, R.A., (1997) Blue light imagery and photometry of sprites, *Journal of Atmospheric and Solar-Terrestrial Physics*, *Journal of Atmospheric and Solar-Terrestrial Physics*, submitted for review
- Vaughn, Jr., O.H., Blakeslee, R., Boeck, W.L., Vonnegut, B., Brook, M., McKune, J., (1992) A cloud-to-space lightning as recorded by the space shuttle payload bay TV cameras, *Monthly Weather Reviews*, **120**, 1459-1461
- Wait, J.R., (1970) *Electromagnetic Waves in Stratified Media*, 2nd Ed., Pergamon, New York,
- Wescott, E.M., Sentman, D.D., Hampton, D.L., Heavner, M.J., Osborne, D.L., Williams, J.D., (1995) Preliminary results from the Sprites94 aircraft campaign: 2. Blue Jets", *Geophysical Research Letters*, **22**, 1209-1212
- Wilson, C.T.R., (1956) A theory of thundercloud electricity, *Proceedings of the Royal Meteorological Society, London*, **236**, 32D-37D
- Winkler, J.R., Lyons, W.A., Nelson, T.E., Nemzek, R.J., (1996) New high-resolution ground-based studies of Sprites, *Journal of Geophysical Research*, **101**, 6997-7004

IDENTIFICATION PERFORMANCE OF THE IMS IN THE MIDDLE EAST AND NORTH AFRICA

Terrance G. Barker

G. Eli Baker

Keith L. McLaughlin

Maxwell Technologies, Inc.
8888 Balboa Ave., San Diego, CA 92123-1506

Contract No. F19628-95-C-0111
Sponsored by U.S. Department of Energy
Office of Nonproliferation and National Security
Office of Research and Development

Abstract

We have simulated the detection and identification performance of the current and proposed IMS seismic networks in the Middle East/North Africa. The identification performance of a network is strongly dependent upon regional source and propagation variability. However, knowledge of those variations permits estimation of their impact on the effectiveness of discriminants throughout the region. A comprehensive compilation of source and propagation properties and our own analyses are described in a companion paper for this symposium (Baker and Barker, 1997). The simulations described here include a greater area (northwestern Africa) and use a far more extensive set of source and propagation parameters than our previous work (Barker, 1996).

The identification performance is strongly influenced by the Q distribution. The poor performance of Lg/P in the Saudi peninsula is caused by poor Lg detection and also by propagation which attenuates Lg more than Pn. Each of the stations proposed for this region is very important to identification performance. Due to lack of coverage to the SE of SAUD (in the Arabian Sea), this station is essential for monitoring the Arabian shield and the Sinai peninsula. Without station LXEG, there are no regional detections in NE Africa and stations THR and BEYT are needed for regional detections south of the Caspian Sea.

In another set of simulations, we have investigated the relationship between confidence ellipses estimated by the event location procedure and the distribution of locations found by the procedure. It appears that the confidence ellipses are underestimates of the location variance.

Key Words: seismology, network simulations, Middle East, North Africa

Objective

Monitoring a CTBT requires accurate assessments of how well the monitoring networks detect and identify seismic events. The computer program Xnice, for Network Identification Capability Evaluation running under an X-windows interface, has been written by Maxwell Technologies to assess the ability of a seismic network to identify seismic sources. The program simulates the detection, location and identification of populations of events recorded on regional and teleseismic networks using a Monte Carlo approach. This approach allows isolation of the effects of source type, propagation path, and choice of discriminants on the discrimination process. In addition, discriminant performance and network thresholds of detection, location and identification are assessed. Xnice generates the parameters of a sequence of events and computes the ground motions from the events at the stations of the network. The features of the ground motions used for discrimination are then measured, and discrimination scores are assigned to each event. From a suite of events, the performance of the network and the discriminants can be assessed. The program has the capability to compute signals from earthquakes, quarry blasts and both overburied and normally buried explosions.

Under programs jointly sponsored by DoD and DoE, data on the source and propagation characteristics of the Middle East and North Africa have recently been compiled. These data were used to simulate earthquakes and explosions in this region and then assess the identification performance of existing and proposed IMS Alpha and Beta stations. This is a complicated area with several regions of Lg blockage. We show magnitude levels at which identification can be made and expected success rates.

Research Accomplished

1. Simulations of Detection and Identification Performance

The IMS network proposed by the Conference on Disarmament Experts working Group in August, 1995 is more dense in the Middle East than that which is currently in place. Figure 1 shows a map of Africa and western Eurasia with the proposed IMS alpha stations and the area for which the simulations were done. An image of predicted m_b detection thresholds for the proposed network is shown in Figure 2. Detection is based on the criteria used in GSETT-3 and currently implemented at the pIDC. The rules are based on a weighted sum of travel time, azimuth and slowness measurements (J. Carter, Center of Monitoring Research, personal communication).

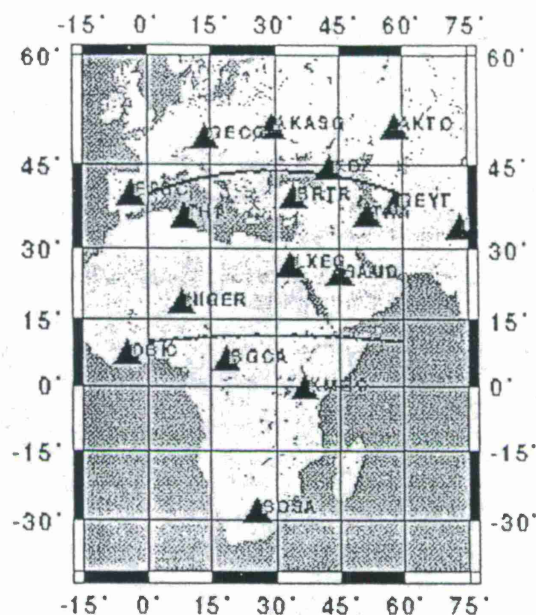


Figure 1. Proposed IMS seismic stations and study area (indicated by box).

The thresholds increase towards the southern part of the Arabian peninsula. This is due to very low Lg Q values surrounding the region which prohibit signals reaching the requisite 3 stations, as exemplified by Lg Q shown in Figure 3. Lg blockage (modeled in Xnice by zones of very low Q) prevents Lg measurements at the stations LXEG and NIGER. Similarly, very low Q in the Persian Gulf and the sediments to the north of the Gulf prevent Lg energy from reaching THR. Even for purely continental paths, the low Lg Q of ~ 200 greatly attenuates Lg signals traveling to BRTR. Variability within the region is also due to station geometry and variations in source strength and propagation parameters.

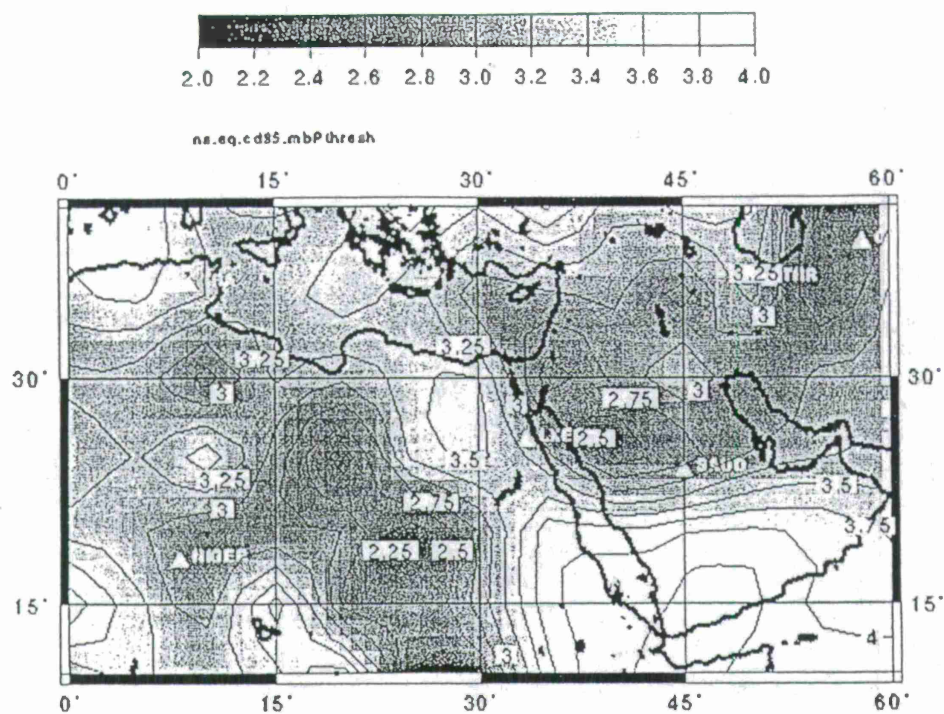


Figure 2. Image of $m_b(P)$ detection thresholds for the proposed IMS network.

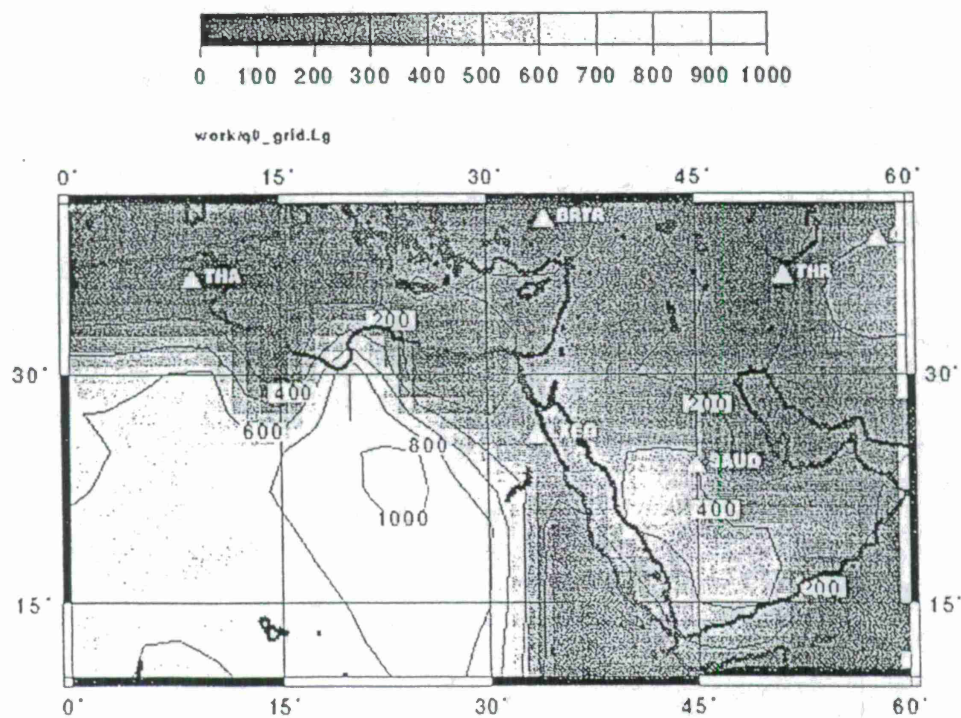


Figure 3. Image of Q at 1 Hz for L_g . Low L_g Q north of the Arabian Shield, very low Q in the Persian Gulf and blockage in the Red Sea prevent detections of L_g by the requisite 3 stations from events in the southern part of the shield.

We turn now to identification performance. We note first that teleseismic discriminants are ineffective because events in the simulation are shallow (<10 km). We did not model the $M_s:m_b$ discriminant because we need accurate estimates of long-period noise for the networks, which we currently do not have. Thus, for events occurring on-shore, we must rely on regional discriminants for identification. Since there are no events detected (in the sense of the GSETT-3 rules) in the simulation by the current IMS network in this region, discrimination cannot be done. On the other hand, the proposed network is capable of regional discrimination. We consider first the Lg/P discriminant. An event is considered identified as an earthquake if (1) the event satisfies the event detection criterion (Table 1), (2) both Lg and Pn or Pg exceed the signal-to-noise ratio at at least 1 station, and (3) the Lg/P ratio exceeds a specified value. The fraction of events identified as earthquakes by the Lg/P discriminant at $m_b=4.0$ is contoured in Figure 4.

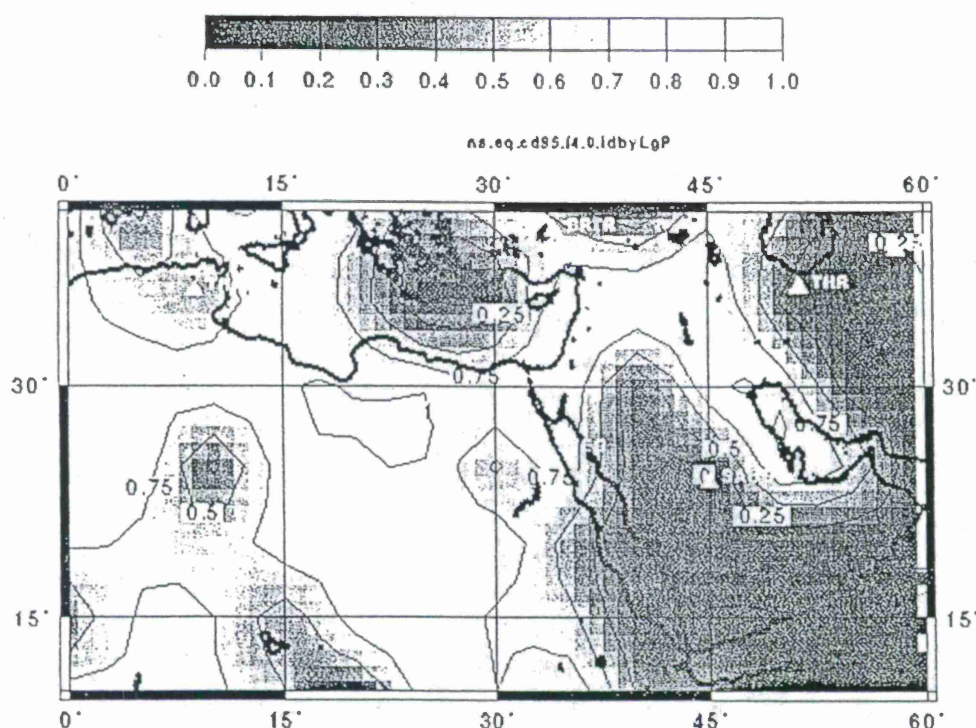


Figure 4. Contours of fraction of events identified as earthquakes by the Lg/P discriminant at $m_b=4.0$ for the proposed IMS network. The decision line is $\log(Lg/P) = 0.0$.

The identification performance is strongly influenced by the Q distribution. The poor performance of Lg/P in the Saudi peninsula is caused by poor Lg detection and also by propagation which attenuates Lg more than Pn.

Each of the stations proposed in this region is very important to identification performance. Due to lack of coverage SE of SAUD (in the Arabian Sea), this station is essential for monitoring the Arabian shield and the Sinai peninsula. Without station LXEG, there are no regional detections in NE Africa and stations THR and BEYT are needed for regional detections south of the Caspian Sea.

2. Monte Carlo Versus Formal Location Uncertainties

An important aspect of event identification is location uncertainty, typically estimated from formal location errors. Network simulations use two methods for estimating network location capability. The first method tabulates estimated location covariances from a Monte Carlo ensemble of event realizations. The second method tabulates formal location errors from a Monte Carlo ensemble of event realizations. In this section, we compare these two methods.

Earthquake epicenter location is normally treated as a non-linear least squares (NLLSQ) estimation procedure. The location is estimated by a step-wise minimization of a linearized least-squares estimator. At each step the location is perturbed to minimize the objective function composed of a weighted sum of the squares of the travel time residuals. The weighted sum of the squared residuals (the objective function) is a non-linear function of the location. In the linearized formulation, the objective function is replaced by a Taylor series expansion at each iteration. The new source location is chosen to minimize the truncated series. The procedure iterates until a minimum in the objective function is found (least squares).

The first derivatives are zero at the minimum of the objective function, and it is assumed that the function is well represented by a quadratic form. Under these assumptions, error estimates for the epicenter location are derived that depend upon the curvature (second derivatives) of the objective function and the data variances. This formulation reduces to an equation for the location covariance matrix, $\Sigma = (A^T A)^{-1} \sigma^2$, where A is a matrix of derivatives of the individual station-phase travel times w.r.t. distance and σ^2 is a normalized data variance. We refer to location error estimates derived from this formal linearization procedure as "formal errors". The formal covariance estimates, Σ , depend only upon the "curvature matrix", $(A^T A)^{-1}$.

Since the objective function is non-linear, the shape of the function near the minimum may depart from a simple quadratic form. Under these conditions the estimated location covariance matrix may be an underestimate of the true location covariance. This assumption may be tested by comparing the ensemble of Monte Carlo locations with the predicted location errors.

Since variations in source and propagation properties in the eastern U.S. are somewhat less than in the Middle East, we performed simulation there to isolate the effects of station geometry and location procedure. Figure 5 a,b,c shows a Monte Carlo ensemble of $m_b(L_g)=3.5 \pm 0.1$ events generated for three locations in the Midwest. The 90% confidence error ellipse derived from the population of Monte Carlo errors is shown on each plot. Each Monte Carlo realization was generated by adding Gaussian random numbers to the predicted travel times and then locating the event. The following full Monte Carlo procedure was used:

1. synthetic events with uniformly distributed log moment from 10 to 15 Nt-m, and a log-normal distributed stress drop of 100 bars and a 50% standard deviation were generated on a grid of locations,
2. spectral amplitudes of P, Pn, Pg, Sn, and Lg phase arrivals were computed at all station for each event,

3. probability of detection of each phase arrival was calculated using a statistical noise model at each station, 95% station reliability, and log-normal phase amplitude variability of 50% standard deviation,
4. realizations of phase detection were selected for each event based on the predicted probabilities,
5. travel times for each detected phase of each event realization were computed and a Gaussian random variable was added with standard deviations of 1.5, 2.5, 3.5, and 5.5 sec for P, Pg, Sn, and Lg respectively,
6. location and location error were estimated for each event using Pn, Pg, Sn, and Lg travel times,
7. network mb(Lg) was computed for each event from the detected Lg phase amplitudes,
8. and finally each detected event was added to the synthetic location bulletin.

Figure 5 a,b,c shows 90% confidence error ellipses based upon analysis of the Monte Carlo errors defined as "synthetic location" - "true location". This analysis assumes errors are Chi-squared distributed with two degrees of freedom, or equivalently as two independent Gaussian random deviates along the semi-major and semi-minor axes of the error ellipse. Under these assumptions, the $X \times 100\%$ confidence error ellipse should contain $N \times X \pm S$ of the N events in the Monte Carlo ensemble, with the variance $S^2 = N \times (X \times (1-X))$. In contrast to confidence ellipses estimated in this manner we can examine location ellipses estimated from each realization.

We expect 90% of the 90% confidence ellipses to contain the true location. In fact we find only 80% to 85% of the ellipses contain the true location. This discrepancy is common for selected locations around the network. Formal 90% confidence ellipses are underestimated at selected locations within the USNSN network. Simple tests of significance verify that these are not due to sample variability. The Monte Carlo populations are large enough to distinguish when formal 90% confidence ellipses differ significantly from the Monte Carlo derived 90% confidence ellipses. No places in the network were found where the converse was true. While in most locations, the formal errors appear to be consistent with the Monte Carlo errors, there are no places where the formal errors bounds are larger than the Monte Carlo error bounds.

If the distribution of errors was different from the assumed Chi-Squared distribution, then we might have tails of the distribution contaminated by a few "bad" locations and hence underestimates of the 90% confidence bounds. However, when we examine the Monte Carlo produced errors and compare them to the best fitting Chi-squared distribution in Figure 6, we find that the cumulative distribution of errors produced by the fully non-linear network simulation are indistinguishable from Chi-squared. Therefore, while the formal procedure assumes the right shape of the error distribution, the formal method underestimates the scaling represented by the "curvature matrix".

This simple result has interesting consequences. Nearly all location programs cite formal confidence ellipses based on linearization of the non-linear estimation problem. It appears the curvature of the objective function is sometimes overestimated. The objective function is often flatter than estimated near the minimum, and therefore formal confidence bounds are often too small.

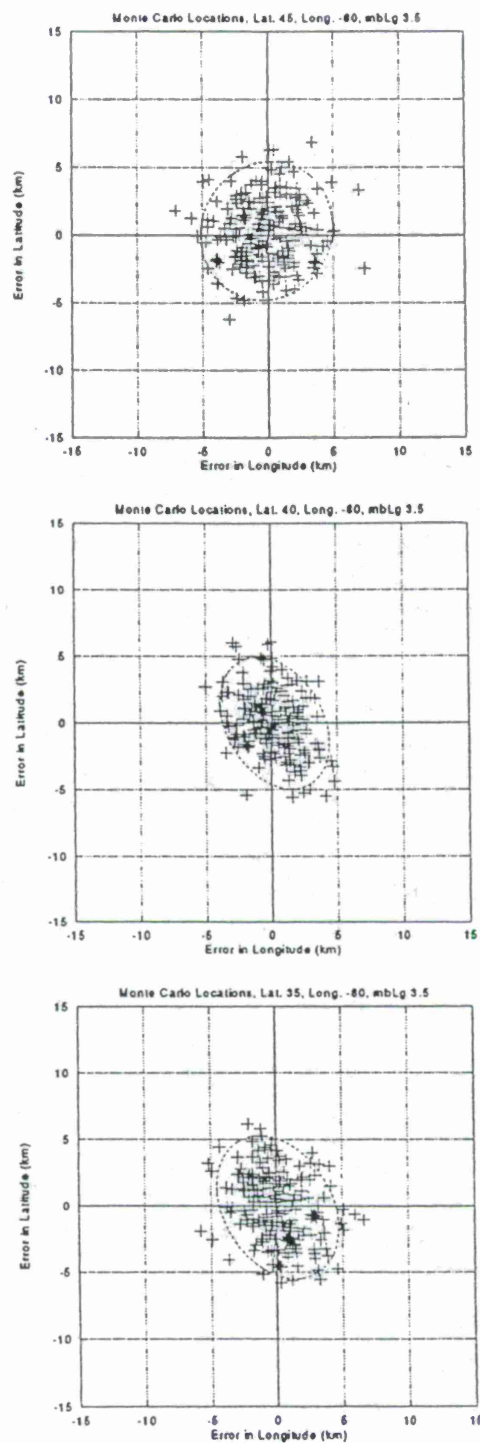


Figure 5 a,b,c Monte Carlo locations for 35N (bottom), 40N (middle), and 45N (top) at 85W for $mb(Lg) = 3.5 \pm 0.1$. The 90% confidence ellipse is drawn for each ensemble of realizations. There are approximately 200 to 300 events on each plot.

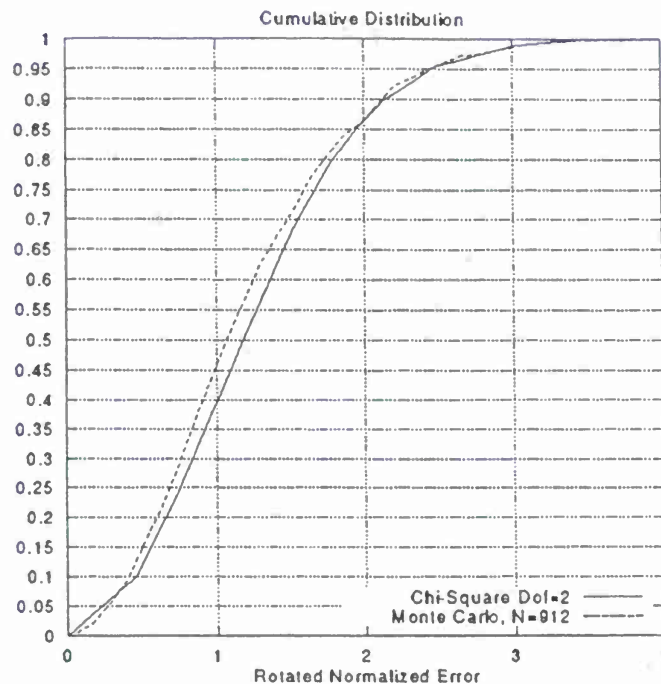


Figure 6. Comparison of the normalized cumulative errors compared to those predicted by a best fitting Chi-squared distribution. The non-linear Monte Carlo distribution did not generate excessive errors in the tails or a skewed distribution of error. While the formal methods underestimate the bounds, they appear to assume the correct shape of the error distribution.

Conclusions and Recommendations

The identification performance is strongly influenced by the Q distribution. The poor performance of Lg/P in the Saudi peninsula is caused by poor Lg detection and also by propagation which attenuates Lg more than Pn. Each of the stations proposed for this region is very important to identification performance. Due to lack of coverage to the SE of SAUD (in the Arabian Sea), this station is essential for monitoring the Arabian shield and the Sinai peninsula. Without station LXEG, there are no regional detections in NE Africa and stations THR and BEYT are needed for regional detections south of the Caspian Sea.

Location programs typically cite formal confidence ellipses based on linearization of the non-linear estimation problem. It appears the curvature of the objective function is sometimes overestimated. The objective function is often flatter than estimated near the minimum, and therefore formal confidence bounds are often too small.

Future plans include extending the study area to include the Caucasus region and investigating location statistics for the current and extended study areas.

References

- Baker, G.E. and T.G. Barker (1997), "Source and Propagation Characteristics for Network Performance Simulations in the Middle East", presented to DSWA symposium on Monitoring a Comprehensive Test Ban Treaty, Orlando, FL.
- Barker, T.G. (1996), "Xnice: A System for Assessing Network Identification Performance", S-CUBED Scientific Report No.2 to Phillips Laboratory, PL-TR-96-2087.
- Barker, T.G (1996), "Advanced Systems for Assessing the Performance of Regional Networks", Proceedings of the 18th Annual Seismic Research Symposium on Monitoring a Comprehensive Test Ban Treaty, edited by J.F. Lewkowicz, J.M. McPhetres and D.T. Reiter, Annapolis MD.

REGIONAL DISCRIMINATION USING L_g/P AND REGIONAL PHASE SPECTRAL RATIOS: STUDIES OF PHYSICAL BASIS AND TRANSPORTABILITY

T.J. Bennett, K. L. McLaughlin, R. W. Cook, and J. A. Carter
Maxwell Technologies, Inc., Federal Division
11800 Sunrise Valley Dr., Suite 1212
Reston, Virginia 20191

Sponsored by Air Force Technical Applications Center
Contract Nos. F19628-95-C-0107 and F19628-95-0108

ABSTRACT

Regional discrimination methods for distinguishing different types of seismic sources, including potential underground nuclear explosions, earthquakes, chemical explosions, and rockbursts, are expected to provide an important tool for monitoring the Comprehensive Test Ban Treaty (CTBT). This paper reports on the results of two nearly completed investigations of regional seismic discrimination. The first study involved analysis of the regional phase spectral ratio as a discriminant and its transportability between regions, and the second study investigated the L_g/P ratio as a function of frequency and possible physical explanations for observed differences in this ratio between underground nuclear explosions and other source types. We experimented with several different spectral analysis techniques for estimating the regional phase spectral ratios and the L_g/P ratios, and we finally settled on a band-pass filtering method which provides spectral estimates which closely match Fourier spectra in the group velocity window corresponding to the regional phase of interest. We have carefully analyzed selected data samples, applying corrections for seismic instrument response, propagation path, and source size to the regional phase spectral ratios and for propagation path to the L_g/P ratios as a function of frequency. The samples analyzed included regional signals from explosions and earthquakes in the western U.S. and Eurasia recorded at high-quality digital stations from near to far regional distances. To correct for propagation path, we have utilized attenuation and spreading models appropriate to the regional phases involved and based on prior published results from analyses of regional phase attenuation in the U.S. and Eurasia. As a test of the propagation models, we applied the propagation corrections to regional phase spectra at stations with different paths from the same source, or sources in the same area, and looked for improved correspondence in the corrected spectral shapes. The corrected spectra generally showed better agreement between stations after all corrections were applied, but some differences persist. To provide additional theoretical understanding of the physical basis for regional seismic discriminants, and in particular for L/P ratios as discriminants, we have used structural models characteristic of different regions of the world to develop synthetic seismograms for source types including explosion, tension crack, CLVD, and double-couple mechanisms. We have found that common source types produced generally similar regional phase excitation behavior in a variety of earth models, while some excitation differences were apparent between different source types.

Keywords: Seismic, Discrimination, Regional, Attenuation, Spectra, Modeling

OBJECTIVE

Several regional discriminants, including regional phase spectral ratios and L_g/P ratios, have previously been identified as promising for identification of possible underground nuclear explosions in the context of a CTBT. To make these potential regional discrimination techniques more generally applicable in distinguishing source types, it is necessary to take account of differences in signal propagation, seismic instrumentation, and source size which could affect the characteristics of the recorded signals between regions and between events. By adjusting for such differences, it should be possible to extend regional identification capabilities from calibrated regions into untested areas. Our investigations have also sought to develop a physical basis for some regional discriminants (e.g. L_g/P ratios), so that the factors which might alter discriminant performance in specific applications may be better understood.

RESEARCH ACCOMPLISHED

Each of the studies noted above combines an empirical element and a theoretical element. For the empirical element we have collected and analyzed the behavior of relatively strong regional phase signals from representative samples of underground nuclear explosions, earthquakes, rockbursts, and mine explosions in several different tectonic regions. These signals have been used to develop regional phase spectral ratio discriminant measures and L_g/P ratios as a function of frequency. In the theoretical element for the spectral ratio measurements, we have developed analytic correction factors to compensate for recording instrument response, regional attenuation with distance, and source size differences as a function of frequency. The corrected regional phase spectral ratios can then be compared between source types to assess discrimination capability and between source and propagation regions to assess transportability of discriminant measures between regions. For the L_g/P ratios as a function of frequency we have applied corrections for regional attenuation of the measured L_g and P phases (adjustments for instrument response and source size are not required) and analyzed what physical factors in the different source types could contribute to differences in the measured ratios using synthetic seismograms developed for the various possible source types and for structural models characteristic of different regions of the world. Throughout these studies we have applied some innovative spectral analyses methods and sought to identify techniques which could be efficiently implemented in realistic nuclear explosion monitoring situations, such as those at the IDC and NDC, and utilized over the wide range of regional tectonic environments likely to be encountered in a worldwide comprehensive monitoring effort.

Database

An important aspect of both of these studies has been identification of an appropriate database of signals recorded at regional stations from the various seismic source types of interest in discrimination monitoring. As we have noted previously (cf. Bennett et al., 1996; Bennett et al., 1997), the amount of high-quality digital data available from regional stations for underground nuclear explosions is extremely limited with respect to both quantity and regional coverage. In our investigations we have sought to establish relevant databases including regional recordings of nuclear explosions from several different tectonic regions. These databases include NTS explosions recorded at near and intermediate regional distances, intermediate and far regional recordings from the former Soviet test site at Balapan in East Kazakhstan, and near

and intermediate regional recordings from selected PNE explosions in the former Soviet Union recorded at the high-quality station at Borovoye. The maps in Figure 1 show the locations of selected nuclear explosion sources and stations used in these studies. In addition, we have used for comparison recordings from other source types, including earthquakes, chemical blasts and rockbursts. In general, these were chosen to minimize potential propagation path differences between source types either by selecting events in the same source region or by comparing events at similar epicentral distances.

Regional Phase Spectral Ratio Discriminants

The original development of spectral ratios as seismic discriminants (cf. Murphy and Bennett, 1982) was based on observations of near-regional signals from NTS underground nuclear explosions and nearby earthquakes. Murphy and Bennett found that the earthquake regional phases, and in particular L_g , appeared relatively enriched in high frequencies compared to the explosions. A spectral ratio discriminant measure based on the ratio of the average L_g spectral level between low and high frequencies was seen to provide excellent distinction between the NTS explosions and surrounding earthquakes measured at VELA stations. Because the recording stations were common and the propagation paths were similar, there was no need to adjust the spectral ratios for these factors in these initial studies. However, it was recognized at the time that some adjustments to the measurements for propagation effects and recording instrument response would probably be required to make the discriminant more effective in areas where the explosion and earthquake sources were separated or recorded by different seismic stations. It has been our goal in the current studies to analyze how prior knowledge of regional phase attenuation and instrument response could be used more effectively to extend capabilities with spectral ratio discriminants from calibrated areas into areas with no prior explosion experience.

To make our discriminant measurement procedures more systematic and easier to implement in a realistic monitoring environment, we have defined a spectral ratio measurement scheme based on band-pass filtering of the recorded signals (cf. Murphy et al., 1996; Bennett et al., 1996). This scheme utilizes fairly narrow Gaussian filters, for which the RMS output amplitudes tend to match Fourier spectral estimates computed for the corresponding regional phase group velocity windows. We then compute spectral ratios for the regional phase, as a function of frequency, by dividing the spectral amplitude, determined from the filter output, by an average of the spectral amplitudes in the bands near 1 Hz (i.e. the spectral amplitudes are normalized at 1 Hz to produce the spectral ratio).

The correction to the spectral ratios for seismic instrument response is straightforward utilizing the reported responses from specific stations. However, transportability of regional spectral ratio discriminants would be expected to be critically dependent on our ability to properly correct for the attenuation and spreading of the signal between source and receiver. We have been experimenting with procedures to apply such corrections. Since the L_g phase is believed to be fairly insensitive to source radiation patterns (especially for explosion sources), we have first attempted to verify our ability to correct L_g spectral ratios for these propagation effects. L_g coda Q models were developed for Eurasia, Africa, and North America (cf. Mitchell et al., 1996; Baqer and Mitchell, 1997) through inversion of L_g coda in a back projection algorithm that produces a tomographic image of $Q(L_g)$ in the form of gridded cells of Q_0 and η where $Q(L_g) = Q_0 f^\eta$. We used these Q models as the basis for the attenuation corrections to the

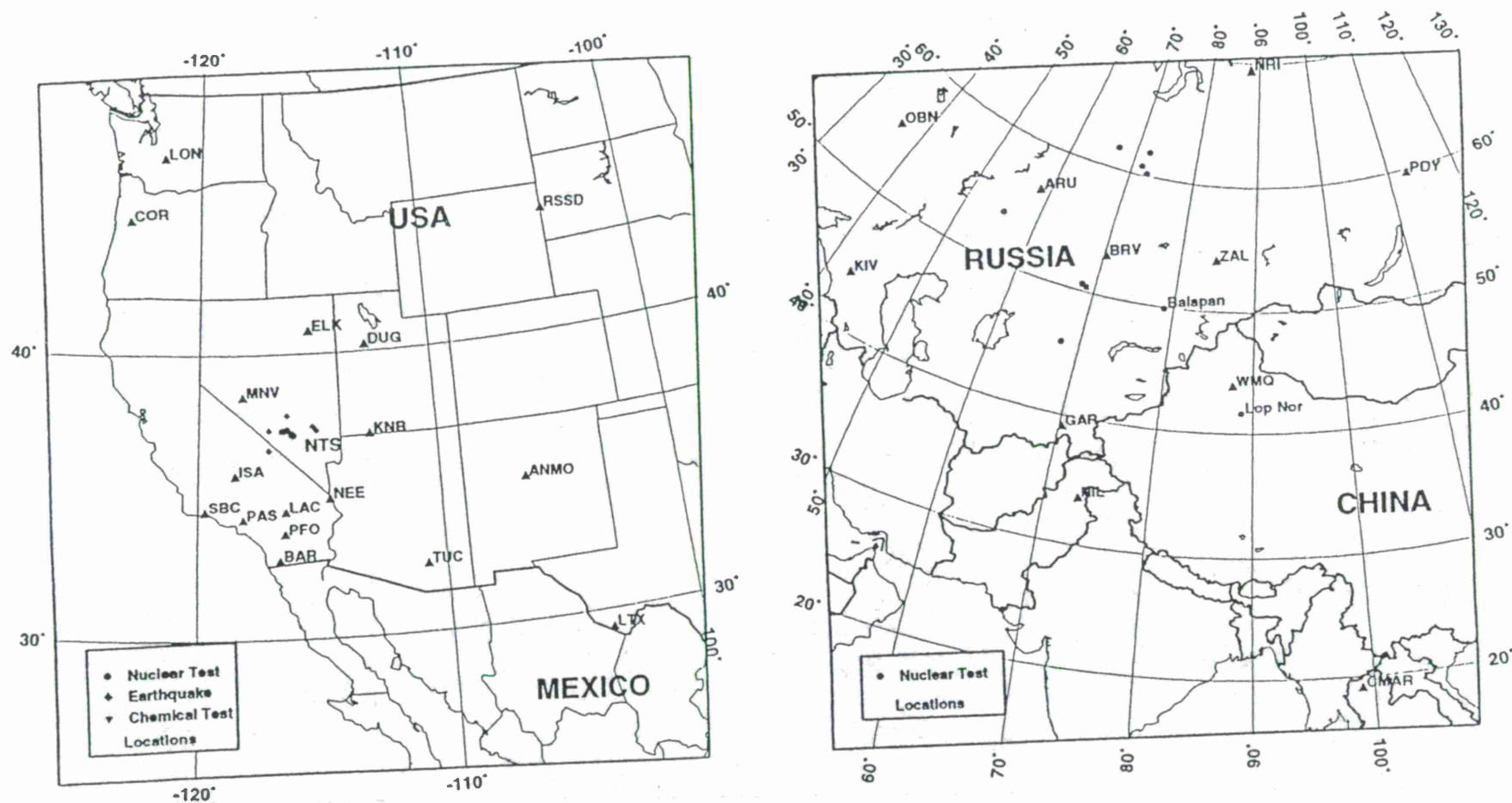


Figure 1. Locations of selected explosions, earthquakes, and stations used in analyzing regional signals from western U.S. events (left) and Eurasian events (right).

L_g spectral ratio measurements. The correction procedure determines the source-to-receiver path through the grid of Q values and sums the attenuation contributions at each frequency from each cell along the path. For the geometrical spreading factor, we assume spherical spreading in the first 100 km, after which spreading is assumed to be cylindrical. A combined correction for attenuation and geometrical spreading is calculated for each source-receiver path and applied to the instrument-corrected spectral ratios.

Figure 2 shows the combined corrections, plotted as a function of frequency, to the L_g spectral ratios for attenuation and geometrical spreading computed using the North American $Q(L_g)$ grid model for nine specific source-station paths from the NTS explosion Junction. As would be expected, the corrections increase with frequency and generally tend to be quite large at more distant stations. For stations at 1000 km and beyond, the correction to the spectral ratio would be more than a factor of 100 at frequencies above about 5 Hz. At nearer stations the corrections can also be quite large, although they are generally less than a factor of 100. It should be noted that attenuation in the western U.S. is strong compared to other areas, so correction factors for other regions are not always so large at intermediate-regional stations. Figure 3 illustrates application of the path corrections to the L_g spectral ratios at the same nine stations for the explosion Junction. The spectral ratios have been corrected for instrument response and attenuation. We first note that several of the ratio estimates appear anomalous and tend to increase with frequency beyond about 2 Hz. This is true for the four stations at 1000 km and beyond and appears to be attributable to artificial inflation of noise for the records which have low signal-to-noise ratios at higher frequencies. The corrected L_g spectral ratios at the nearer stations tend to have consistent shapes, particularly at frequencies out to about 5 Hz. Above 5 Hz the ratios exhibit somewhat greater scatter (as much as a factor of 10), which may be attributable to noise in the signal windows or imprecise modeling for the attenuation correction.

We have applied similar corrections for instrument response and attenuation to selected samples of explosions and earthquakes recorded at near-regional stations in the western U.S. These corrections generally tend to reduce the scatter between stations, but some differences remain. When the corrected spectral ratios for explosions and earthquakes are compared, we still see the same kinds of differences reported previously (i.e. earthquakes showing relative enrichment of high frequencies). However, it should be noted that some of these differences may be reduced when the explosion signals are scaled down to the somewhat smaller earthquake magnitudes, as we reported previously (cf. Bennett et al., 1996). We are continuing to test this methodology and the attenuation models with single events recorded at multiple stations in the U.S. and Eurasia. We have also been developing procedures to apply attenuation corrections to other regional phase spectral ratios (e.g. P_g).

L_g/P Ratio Discriminant

L_g/P ratios have been recognized for many years as a regional seismic discriminant measure which offers great promise for distinguishing underground nuclear explosions from other source types (cf. Blandford, 1981; Pomeroy et al., 1982). For the observational element of the L_g/P ratio discriminant studies, we have been computing L_g/P ratios as a function of frequency for regional recordings of nuclear explosions, earthquakes, non-nuclear blasts, and rockbursts in a variety of propagation environments. In general, we continue to find support for our previous observations (cf. Bennett et al., 1997) that these ratios tend to be larger for

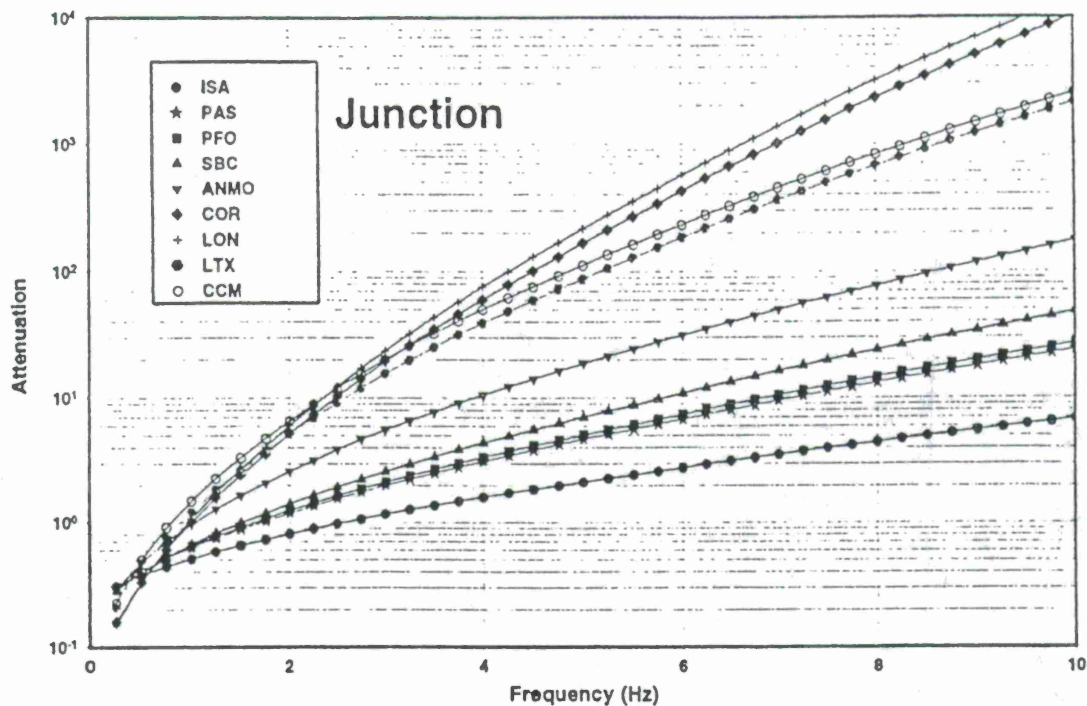


Figure 2. Combined attenuation and geometrical spreading correction factors determined for specific source-station paths from explosion Junction in the western U.S. Q model.

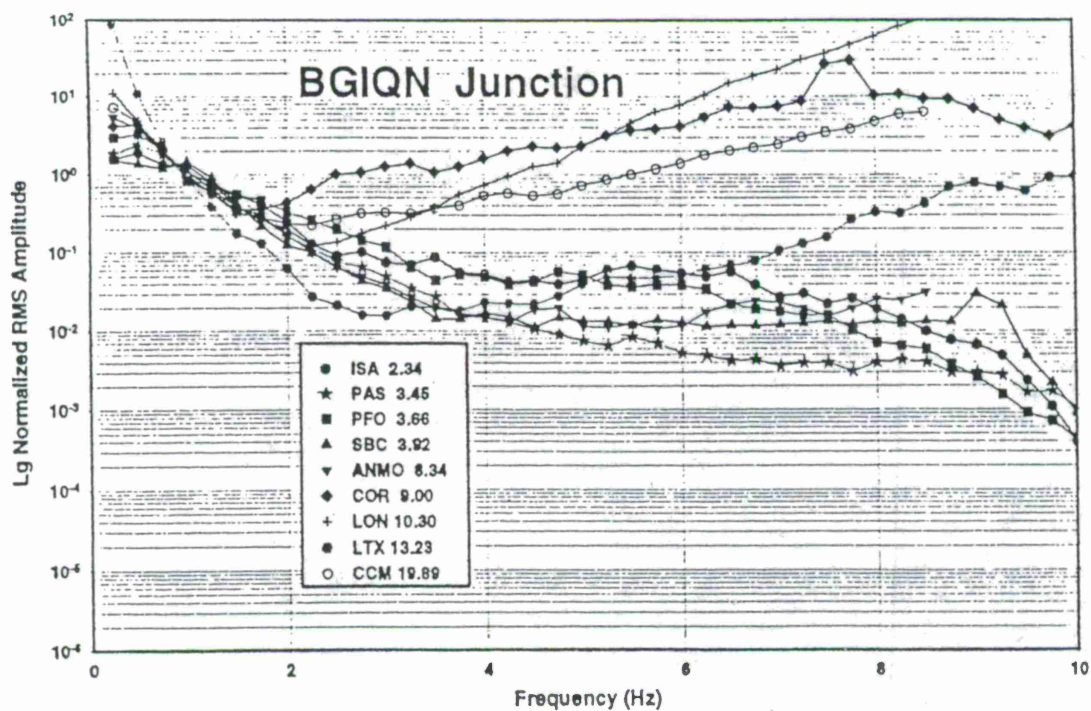


Figure 3. Lg spectral ratios at nine regional stations as a function of frequency for explosion Junction after application of combined propagation corrections from Figure 2.

earthquakes and rockbursts than for explosion sources and that these differences tend to be greater at higher frequencies. One problematic aspect of the observations with respect to discriminant reliability is the amount of scatter seen in the observations between events. We have been working on two aspects of this problem. First, we have been looking into alternative algorithms for determining more consistent spectral estimates from the regional signals. In these studies we have been comparing L_g/P spectra from several band-pass filtering methods and traditional Fourier analyses. Some of the narrower band-pass filtering schemes produce spectra which closely match Fourier spectra, and they may have some operational advantages. The scatter in the ratios between events appears to be reduced at some frequencies using these methods, but the variability between frequencies seems larger than for broader filter passbands. We have also been investigating whether propagation corrections to the regional L_g and P signals can help reduce scatter in the L_g/P ratios between events with somewhat different paths. For this analysis we have been developing regional attenuation corrections for the L_g and regional P phases using procedures similar to those described above.

Observed and synthetic L_g and P_g amplitudes and L_g/P_g ratios exhibit many interesting features as a function of frequency, distance, crustal structure, source type and depth. To help understand this behavior, we have analyzed amplitudes of P_g and L_g from suites of synthetic seismograms for a world-wide collection of crustal models. Mooney et al. (1997) have assigned a representative model for each 5-degree-by-5-degree region covering the whole Earth. We placed 80 continental models over PREM and adjusted shear velocities in a world-wide surface wave inversion (cf. Stevens and McLaughlin, 1997). Models with and without thin (1 km) random layering are considered. Broadband synthetic seismograms were obtained by wavenumber integration at nominal ranges of 200, 400, 600, and 800 km for 6 moment tensor sources (dip-slip, thrust, strike-slip at 15km, explosion, tension crack, and CLVD at 1 km). Figure 4 shows some examples of the synthetic seismograms at 200 km obtained for earthquake and explosion sources in common crustal models with different attenuation. The synthetic records were band-pass filtered for overlapping passbands of 0.5-1.0, 0.75-1.5, 1.0-2.0, 1.5-3.0, 2.0-4.0, 3.0-6.0, 4.0-8.0, and 6.0-8.0 Hz; and the maximum envelope was recorded in each of five group velocity windows corresponding to 100-20, 10-6.8, 6.8-4.6, 4.6-3.8, and 3.8-2.5 km/sec. Several $Q(f)$ models were considered. Based on L_g/P_g ratios versus frequency and distance, we favor a model with $Q(f) = Q_0 f^\eta$ (where $\eta = 0.5$, $Q_0 = 25$ for $z < 1$ km, $Q_0 = 75$ for $1 \text{ km} < z < 2 \text{ km}$, $Q_0 = 150$ for $2 \text{ km} < z < 3 \text{ km}$, $Q_0 = \beta/5$ for $z > 3 \text{ km}$). The resulting 76,800 synthetic amplitudes from 80 models at 4 distances, 8 passbands, 5 group velocity windows, and 6 combinations of depth and mechanism were saved to a small database. The P_g and L_g time-domain amplitudes, $A(f, \Delta)$, were then fit to "empirical" models for each crustal structure and moment tensor source (where

$$\text{Log}(A(f, \Delta)) = A_0 - n \text{Log}(\Delta/100) - \pi \Delta f^{(1-\eta)}/Q_0/U + \epsilon$$

with $n = 5/6$, $U_{Pg} = 6.5 \text{ km/s}$, and $U_{Lg} = 3.5 \text{ km/s}$). While synthetics were generated with $\eta = 0.5$, inversions exhibit an apparent bias between "empirical" and "true" Q models in estimates of both Q_0 and η . Synthetic $Q_{Pg}(f)$ fits do not obey the rule that $Q_{Pg} \equiv 2 Q_{Lg}$. Fits with $Q_{Pg} \equiv Q_{Lg}$ are favored. After attenuation effects have been accounted for, the results of our studies indicate that crustal structures have the most significant effect on the behavior of L_g/P_g ratios. The ratios developed from the synthetic seismograms for the different crustal models fall into three natural clusters (cf. Figure 5) or groups related to the crustal structures (cf. Figure 6). Group #1 corresponds to models with sedimentary layers thicker than 2 km, Group #2 consists of models

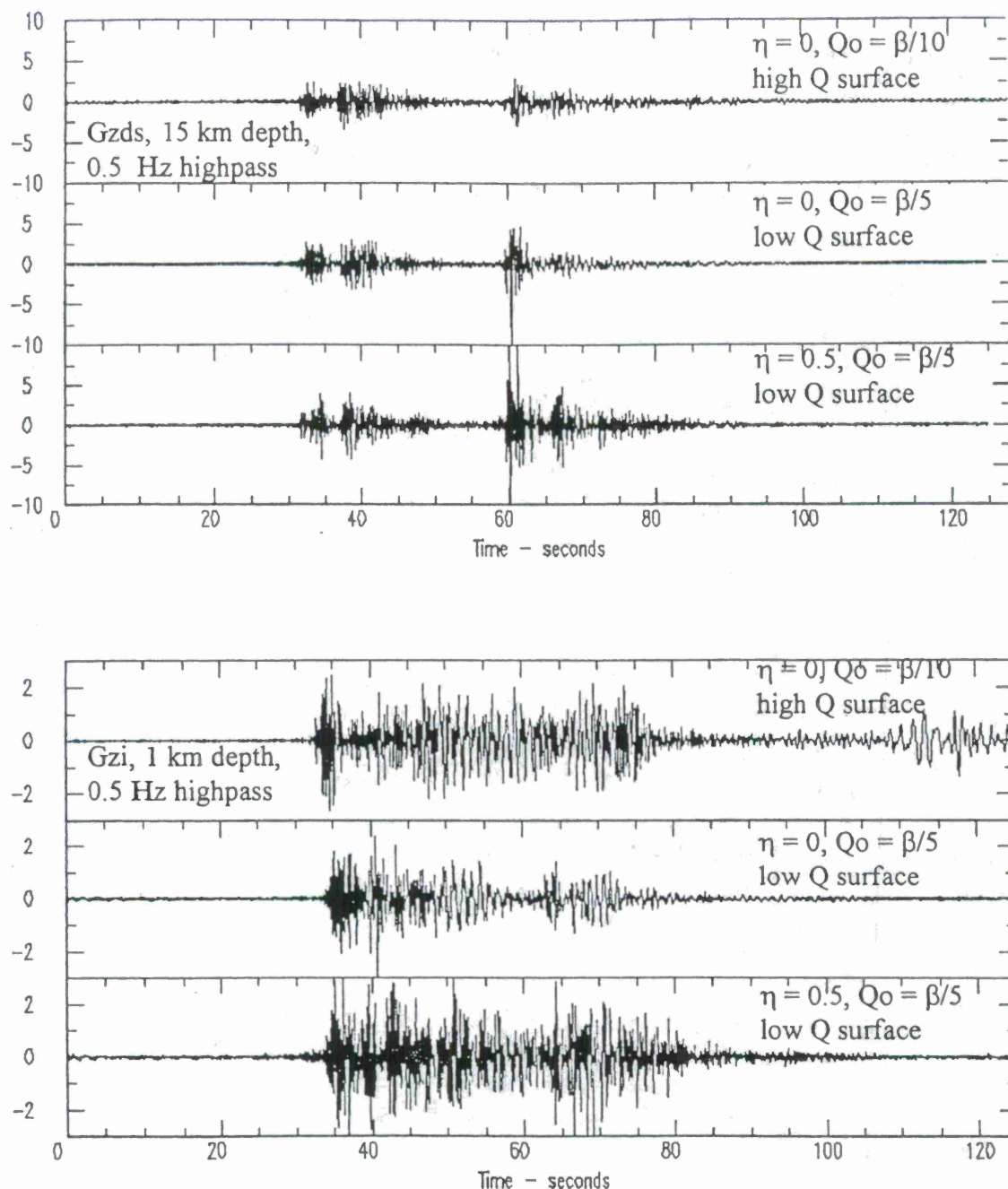


Figure 4. Comparison of vertical component synthetics (high pass at 0.5 Hz) at 200 km for three $Q(f)$ models in a thick stable crust with 10 km of platform deposits. A dip-slip double-couple source (Gzds) at 15 km depth is shown above and an explosive source (Gzi) at 1 km depth is shown below. The earthquake L_g amplitude is significantly increased relative to the P_g amplitude for the $\eta=0.5$, $Q_0=\beta/5$, Q model. The high Q surface layer model does not attenuate the late arriving fundamental surface waves excited by the shallow explosive source. Also, it is clear that the $\eta=0$, $Q_0=\beta/10$, high Q surface layer model contains too much shallow propagating energy in the L_g window that is absent in the low Q surface layer models.

with thin sediment layers, and Group #3 consists of models with high velocities directly at the surface. Figure 7 compares synthetic L_g/P_g ratios in three frequency bands for explosion and earthquake source mechanisms in the different model groups. With few exceptions common source types (viz. explosion, tension crack and CLVD sources at 1 km and the double-couple mechanisms at 15 km) show similar source excitation as a function of frequency for most crustal models, and we see some differences in excitation between the different source types.

CONCLUSIONS AND RECOMMENDATIONS

These investigations have involved some innovative analyses to assess the reliability of two regional discrimination techniques (viz. regional phase spectral ratios and L_g/P ratios) which are expected to be important for CTBT monitoring. We have derived procedures to enable transportability of regional phase spectral ratios and to improve physical understanding of the L_g/P ratios from different source mechanisms and source environments. Additional studies would be useful to test applicability of regional phase propagation corrections for a greater variety of monitoring regions worldwide. In the synthetic modeling of L_g/P ratio behavior, we have found some interesting dependencies which need to be closely linked with observed regional behavior in different source areas.

REFERENCES

- Baquer, S., and B. J. Mitchell (1997). " L_g Coda Q Tomography in the United States," (In Preparation).
- Bennett, T. J., M. E. Marshall, B. W. Barker, and J. R. Murphy (1996). "Investigations of Regional Phase Spectral Ratios: Transportability and Measurement Algorithms," PL-TR-96-2283.
- Bennett, T. J., K. L. McLaughlin, M. E. Marshall, and J. L. Stevens (1997). "The Physical Basis for the L_g/P Discriminant: General Properties and Preliminary Modeling," Maxwell Report No. MFD-FR-97-15727.
- Blandford, R. (1981). "Seismic Discrimination Problems at Regional Distances," in Identification of Seismic Source - Earthquake or Underground Explosion, D. Reidel Publishing Co., pp. 695-740.
- Mitchell, B. J., Y. Pan, and J. K. Xie (1996). "The Variation of L_g Coda Q Across Eurasia and Its Relation to Continental Evolution," PL-TR-96-2154.
- Mooney, W., G. Laske, and G. Masters (1997). "Crust 5.1: A Global Crustal Model at 5x5 Degrees," (Submitted to J. Geophys. Res.).
- Murphy, J. R., and T. J. Bennett (1982). "A Discrimination Analysis of Short-Period Regional Seismic Data Recorded at Tonto Forest Observatory." Bull. Seism. Soc. Am., 72, pp. 1351-1366.
- Murphy, J. R., D. D. Sultanov, B. W. Barker, I. O. Kitov, and M. E. Marshall (1996). "Application of Soviet PNE Data to the Assessment of the Transportability of Regional Discriminants," PL-TR-96-2290.
- Pomeroy, P. W., W. J. Best, and T. V. McEvilly (1982). "Test Ban Treaty Verification with Regional Data - A Review," Bull. Seism. Soc. Am., 72, pp. S89-S129.
- Stevens, J. L., and K. L. McLaughlin (1997). "Improved Methods for Regionalized Surface Wave Analysis," (This Volume).

APPLICATION OF SPECTRAL SEMBLANCE AND RATIO DISCRIMINANTS TO REGIONAL AND TELESEISMIC EVENTS RECORDED BY ISN AND NORESS

Yefim Gitterman, Vladimir Pinsky and Avi Shapira
Seismology Division, Geophysical Institute of Israel, P.O. Box 2286, Holon 58122, Israel

Sponsored by U.S. Department of Energy
Office of Nonproliferation and National Security
Office of Research and Development
Contract F19628-95-K-0006

ABSTRACT

Two new multi-station spectral discriminants were verified on selected regional and teleseismic events recorded by the short-period Israel Seismic Network (ISN) and NORESS. The Spectral Semblance (SS) statistic measuring coherency of smoothed spectra, and averaged Spectral Ratio (SR) of low-to-high frequency energy, were evaluated for a given event at a subnet of 7-10 stations. The regional database includes 212 ripple-fired and single quarry blasts, underwater explosions and earthquakes of local magnitudes $M_L=1.0-2.8$, at distances 5-250 km from various areas in Israel, Jordan and the Mediterranean Sea. Most of the explosions were supplied by ground-truth information. Teleseismic data consist of 58 earthquakes and nuclear tests from Eurasia ($m_b=5.2 \div 6.5$).

Our primary objective was twofold: (1) to evaluate the performance of the statistics on the enlarged database at different frequency ranges and estimate the best parameters and (2) to compare and interpret the obtained results for different event types and seismic systems.

Quarry blasts and underwater explosions showed, as a rule, higher SR and SS values than local earthquakes owing to dominant low-frequency surface waves and source spectral modulation in seismograms. Different frequency bands were tested: the ratio (1-3 Hz)/(6-8 Hz) and semblance (1-12 Hz) provided the best discriminant performance, with a success rate of 97% for the whole database. A characteristic feature of the statistics is that they are calculated from smoothed (0.5 Hz window), instrument-corrected spectra of the whole signal (20-30 sec) on the vertical component, thus accumulating the maximum useful information; they are robust to the accuracy of onset time estimation and duration of analyzed time window and, thus, well suited to automatic event identification.

Applying the same procedures to teleseismic events, with the only evident correction being a shift of spectral analysis bands to lower frequencies, also demonstrated their significant resolving power. Contrary to observations of local data, SS and SR values calculated from ISN seismograms in time windows ~13-15 sec (containing P and P-coda waves), are higher for earthquakes where the analyzed waves are richer in low-frequency energy and have more coherent spectral shapes than nuclear explosions. The best performance is provided in the frequency ranges (0.6-1 Hz)/(1-3 Hz) for SR and (0.6-2 Hz) for the SS. Joint application of the two discriminants showed almost full (95%) separation between the two populations. The NORESS records showed the same (as ISN) relation between SR values, whereas the character of SS was reversed: we obtained very high (>0.94) values for explosions and scattered, in average less values for earthquakes. This observation is attributed to the small size of the array (3 km diameter), where local inhomogeneities and azimuth differences are negligible. Joint application of the both SR and SS statistics provided better discrimination results for the two types of seismic events.

Keywords: dense array/network oriented discriminants, spectra coherency, low-to-high frequency energy ratio

OBJECTIVE

The main objectives of this research are the testing and validation of newly developed spectral semblance and energy ratio discriminants on a variety of data including local and teleseismic events of different types occurring in contrasting geological environments, recorded by the dense regional Israel Seismic Network (ISN) and the NORESS seismic array; performance evaluation of different frequency ranges used for statistics calculations and estimation of the best parameters; comparison and interpretation of the results for different event types and seismic systems.

RESEARCH ACCOMPLISHED

In our previous study (Shapira et al., 1996; Gitterman et al., 1996a) we applied a newly developed spectral semblance (SS) and a modified spectral ratio (SR) of low-to-high frequency seismic energy to earthquakes and quarry blasts in the Galilee, northern Israel, which were successfully separated. In the present research we significantly extended the regional database for comprehensive testing of the procedures and included new types of seismic events: underwater explosions (UWE), single quarry blasts and we also examined Eurasian teleseismic events recorded both at the ISN and NORESS.

Data. Regional data include 212 quarry blasts, underwater explosions and local earthquakes of magnitudes $M_L=1.0-2.8$ from different areas in Israel, Jordan and Mediterranean Sea, recorded at distances of 5-250 km by the ISN with a 0.2-12.5 Hz bandpass filter. Most explosions are supplied by ground-truth information. Basic parameters of the selected events and information about used quarries are presented in Tables 1 and 2, locations are shown on a map (Fig. 1). Complete information regarding earthquake parameters and blast ground-truth information is available from the report by Gitterman et al. (1996b). Spectral computations are made for a time window about 20-30 sec, which is the same for all stations for a fixed event and includes the whole signal to avoid picking out separate wave phases at short distances and accumulate information about source features being kept in all wave forms, thus enhancing the resolving power of the discriminants considered. The spectra were instrument-corrected and smoothed in a fixed 0.5 Hz moving window to provide equivalent spectral resolution for different stations.

A teleseismic database consisting of 29 nuclear tests (Lop Nor, Semipalatinsk, W. Siberia, N.Zemlja) and 29 earthquakes (China, Tajikistan, Afghanistan), of magnitudes $m_b=5.2-6.5$. In parallel with ISN recordings, we collected and processed NORESS seismograms for 20 explosions and 16 earthquakes from this database. (More detailed source information and a location map are presented in the paper by Pinsky et al., 1997, these proceedings). A time window about 13-15 sec comprising P- and P-coda waves, was used for the analysis, the spectra were smoothed in 0.2 Hz window, ISN spectra were instrument-corrected.

Computation of SS and SR statistics is based on vertical short-period seismograms from a set of 7-10 stations, selected for a given event and covering broad spacing range.

Description of Discriminants. ISN seismograms of quarry blasts demonstrate more low-frequency content of seismic waves than local earthquakes (Fig. 2). It has been suggested that spall mechanisms contribute to low frequency seismic energy and the general tendency for quarry blasts to appear deficient in high frequency energy (Barker et al., 1993). We suggest that the phenomenon is mainly due to dominant surface waves (including Rg on the vertical component), generated by quarry blasts and associated with the regional crustal structure of widespread unconsolidated, low velocity and low Q subsurface sediments (e.g. Ginzburg and Folkman, 1980), trapping of low frequency energy and absorbing high frequencies. This explanation is supported by similar observations for New England (Li et al., 1996) and by the reverse situation for quarry blasts in the Scandinavian shield (Baumgardt and Young, 1990).

Table 1. Database used in the study.

#	Region, dataset	Number of earthquakes	Number of explosions	Comments
1	Galilee, Northern Israel	30	39	Earthquake depth $H = 0-21$ km Charge $W = 2000-14000$ kg
2	Southern Dead Sea and Negev desert, Israel	16	26	$H = 0 - 24$ km $W = 1700 - 10500$ kg
3	Gilad region, Jordan	19	15	$H = 2 - 18$ km Quarry blasts - no GTI
4	Tyre region, Mediterranean sea	8	16	$H = 6 - 17$ km UWE - unauthorized fishing, no Ground Truth Information
5	Dead Sea basin, seismic refraction profile	-	28	UWE for seismic prospecting depth $h = 70$ m; $W=16-304$ kg
6	Jordan/Saudi Arabia border	-	5	Jordanian quarry blasts $W = 15000-17000$ kg
7	Quarries Revaya, Mt. Nitzim	-	10	Single quarry blasts (no delays) $W = 900 - 2800$ kg
8	Eurasia: China, Kazakhstan, Russia	27	29	nuclear tests and earthquakes $m_b=5.2\div 6.5$

Table 2. Information about open-pit quarries presented in the study.

#	Name	short	Lat.	Long.	Product
1	Aroar	aror	31.125	35.003	phosphates
2	Carmel	nshr	32.758	35.040	dolomites (construction, roads)
3	Dragot	drgt	31.309	35.078	phosphates
4	Gilad		32.457	35.862	construction materials
5	Golani	goln	32.782	35.397	aggregate, blocks, beton
6	Hanaton	hntn	32.773	35.241	dolomites (construction, roads)
7	Jordan		31.519	35.584	road construction
8	Kadarim	kdar	32.913	35.465	limestone, dolomite (construction, roads)
9	Mt.Nitzim	ntzm	31.184	35.051	calcium carbonates
10	Oceana	oce	31.208	35.385	salt aggregates
11	PhosphArad	arad	31.131	35.210	phosphates
12	PhosphZin	pzin	30.851	35.082	phosphates
13	Poria	pori	32.764	35.553	basalt, aggregate, asphalt, beton
14	Revaya	rvya	32.439	35.480	limestone (construction, roads)
15	Shefaram	shfr	32.797	35.211	aggregate, asphalt, beton
16	Tamra	tmra	32.858	35.220	carbonate, chalk, cement
17	Vered	verd	32.479	35.069	dolomites

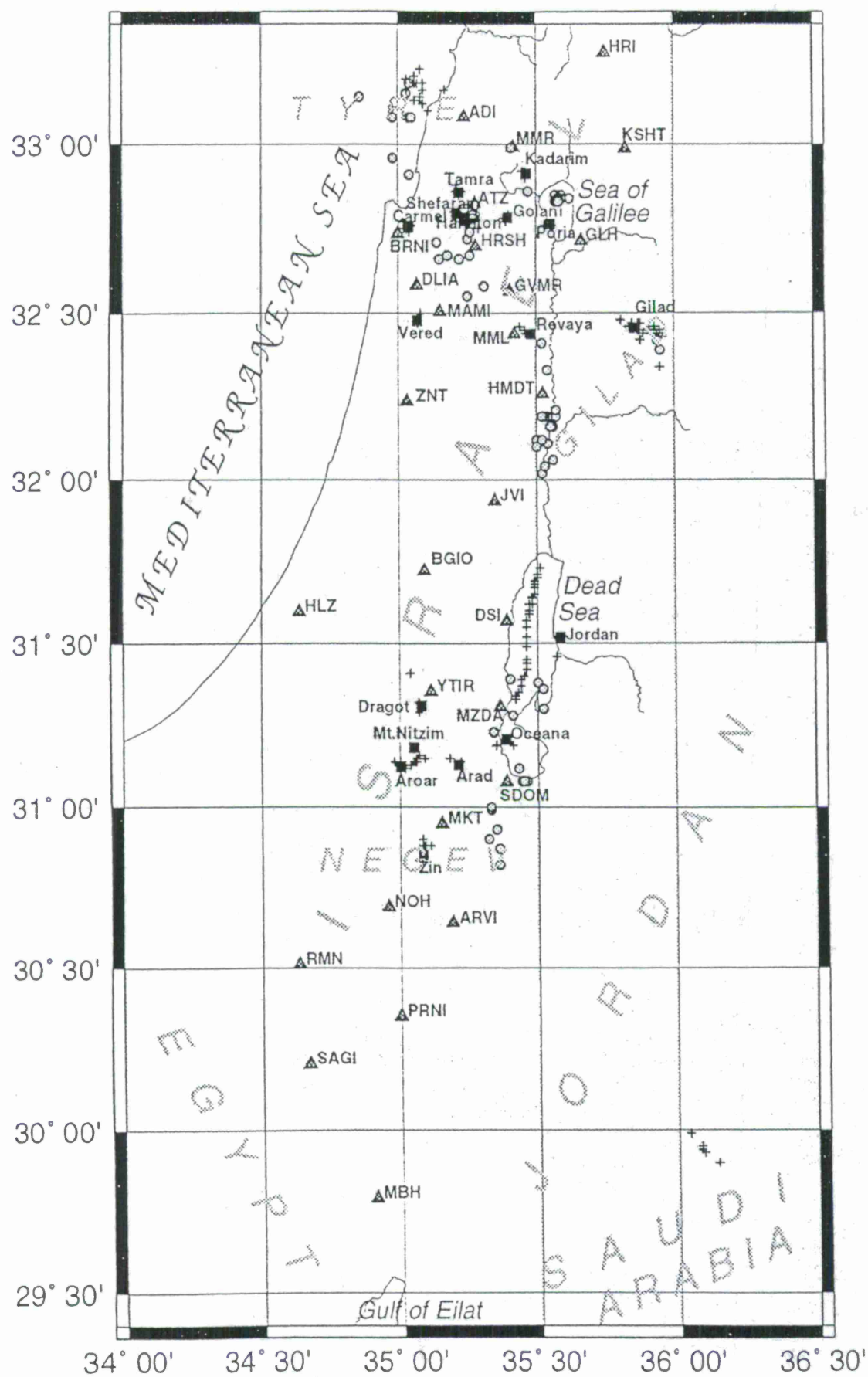


Fig. 1. Database map shows epicenters of earthquakes (O), quarry blasts and underwater explosions (+), location of quarries (■) and ISN stations (Δ). The Dead Sea seismic prospecting explosions are located along a line.

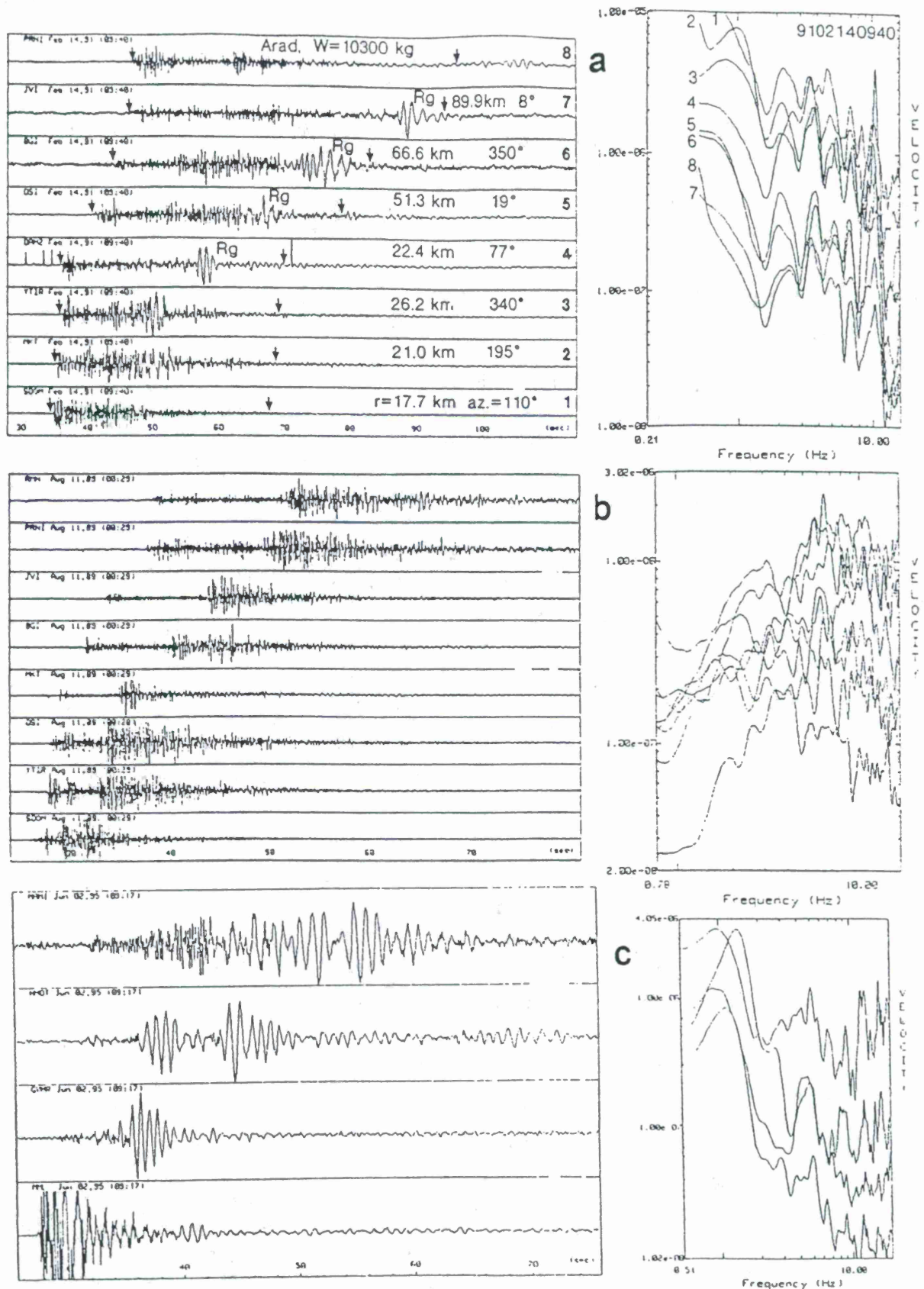


Fig. 2. Examples of recordings at different ISN stations and appropriate spectra: (a) a ripple-fired blast (ES6) from a quarry in the Negev desert, showing distinct azimuth and distance-independent spectral modulation, and low-frequency spectral content due to strong surface (Rg) waves; (b) an earthquake from the Dead Sea (QS3), demonstrating non-coherency of spectral shapes and high-frequency energy. Arrows show analyzed time windows; (c) a single blast at Revaya quarry (SB2, W=2840kg, r=3-28km), with prominent surface waves.

We utilized this effect in the energy spectral ratio R_E of seismic energy in the low-frequency range $[f_1, f_2]$ and the high-frequency range $[f_3, f_4]$ (Gitterman and Shapira, 1993):

$$R_E = \frac{\int_{f_1}^{f_2} |S(f)|^2 df}{\int_{f_3}^{f_4} |S(f)|^2 df} \quad (1)$$

where $|S(f)|$ is the smoothed spectrum of ground velocity for the whole signal. This ratio, implying evident physical meaning, is similar to the ratios of average spectral amplitude (Bennett and Murphy, 1986), or power spectrum (Pulli, 1995), calculated for specific regional phases. For an event, R_E values at different stations show strong scattering; averaging over a subnet is crucial for separation between earthquakes and explosions (Shapira et al., 1996).

Another feature of the blasts and underwater explosions records is clear spectral modulation patterns presented by coherent minima (or nulls) and maxima observed at low frequencies 1-10 Hz even at remote network stations with SNR~1-2 (Fig. 2a). This azimuth-independent modulation is caused by constructive-destructive interference of linearly superimposed waveforms from spaced charges exploded at millisecond delays ("ripple-firing") (Gitterman, 1982; Stump and Reinke, 1988), or from oscillations of gaseous bubbles in water, and indicative of the source-effect. Another approach to reveal spectral modulation involves the time-independent pattern in a sonogram at a single station (e.g. Hedlin et al., 1989), but this kind of modulation can appear also due to a propagation path effect.

In contrast to a ripple-fired blast, the spectral pattern for an earthquake is strongly azimuth-dependent, partly owing to the directivity effect (e.g. Bakun et al., 1978), therefore, for stations with broad azimuthal coverage, we observe an irregular character of spectral shapes and minima for different azimuths (Fig. 2b). The coherency of spectral shapes for different stations was quantitatively assessed by modified "semblance" statistic commonly used in seismic prospecting for phase correlation of seismic traces in the time domain:

$$S_f = \frac{1}{N} \sum_{F_1}^{F_2} \left[\sum_{k=1}^N (S_{ki} - \bar{S}_k) \right]^2 / \sum_{F_1}^{F_2} \sum_{k=1}^N (S_{ki} - \bar{S}_k)^2 \quad (2)$$

where $S_{ki} = \log_{10} S_k(f_i)$ - log spectral amplitude at k station; \bar{S}_k is the average spectral level; N is the number of used stations and $[F_1, F_2]$ is the frequency range for the analysis.

Results: Local Events. Initially we tried for the Galilee region $f_1=1$ Hz, $f_2=f_3=6$ Hz, $f_4=11$ Hz for SR and $F_1=1$ Hz, $F_2=12$ Hz for SS (Gitterman et al., 1996), thus facilitating almost the whole recording frequency band. Application of another ratio (2-4 Hz)/(6-8 Hz), used by Li et al. (1996) for the Lg spectra to separate small events in New England, reduced the resolving power (Fig. 3a). However, after a low-frequency shift, the (1-3 Hz)/(6-8 Hz) ratio enhanced separation between quarry blasts and earthquakes and provided the best discriminant performance (Fig. 3b). As expected, the semblance values are much higher for quarry blasts than for earthquakes and remain practically unchanged when using different windows of spectra smoothing (0.25 Hz and 1 Hz), or analyzed records (± 5 sec).

For the few earthquakes originating on the main fault in the Sea of Galilee, we obtained anomalous high SR and SS values. A different range (1-7 Hz) provided "normal" semblance values for these earthquakes, but for the rest of events we obtained worse separation. The best semblance performance for the Galilee and Gilad regions was obtained for the (1-8 Hz) band (Fig. 3c), nevertheless, due to worse results for quarry blasts and earthquakes from the southern Dead Sea/Negev area (Fig. 3d), UWE and single blasts, the optimal range remained valid as 1-12 Hz. In general, all earthquakes show consistent ratio and semblance values, lower than those for ripple-fired quarry blasts with the thresholds: $R_E = 6.1$, $S_f = 0.7$.

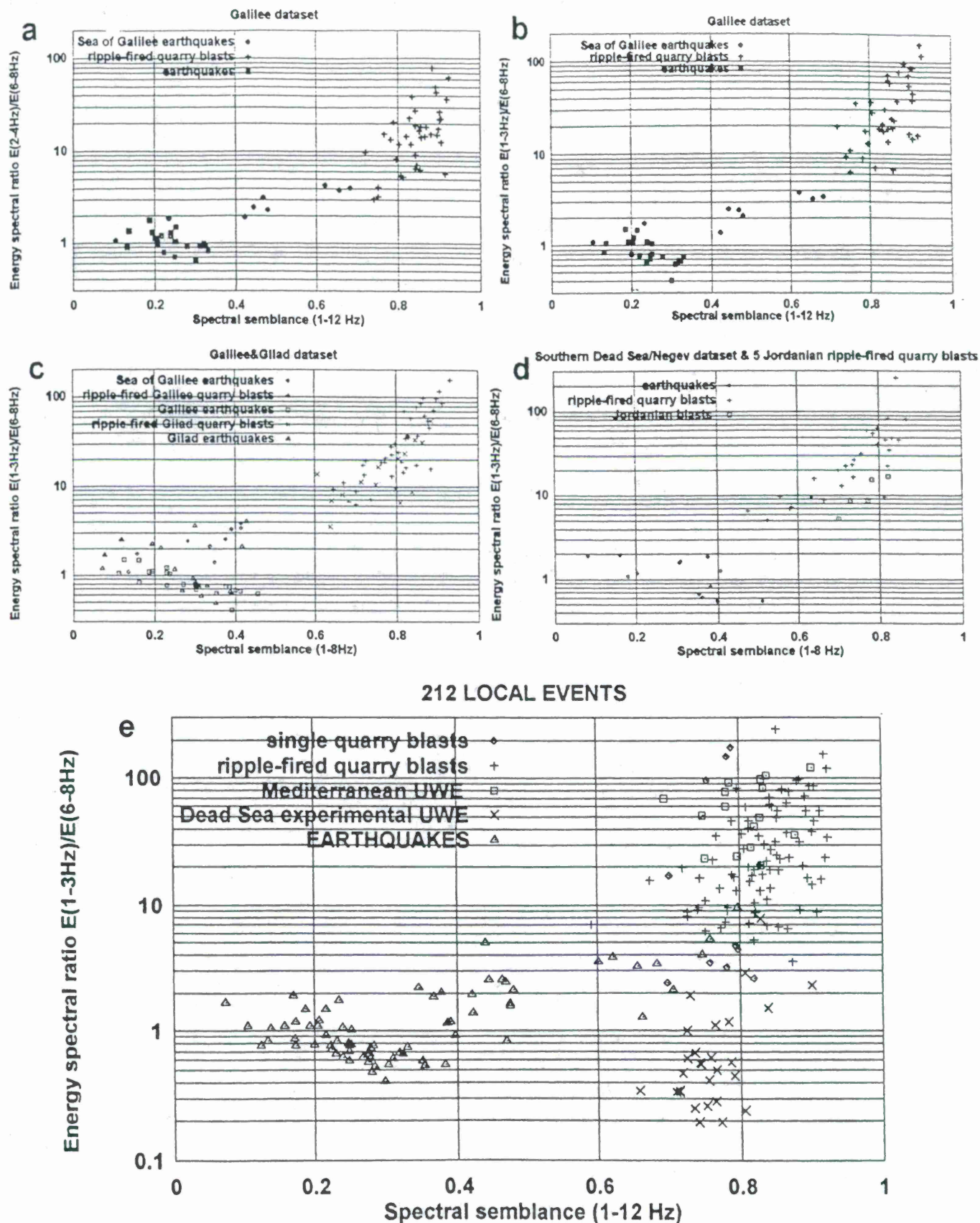


Fig. 3. Discrimination results for local events at different frequency ranges. Separation of earthquakes and quarry blasts in Galilee was improved after a shift of low-frequency band in the energy ratio from (2-4Hz) (a) to (1-3Hz) (b); the semblance range (1-8Hz) provided the best separation of the events from Galilee and Gilad regions (c), but showed a reduced resolving power for the Southern dataset (d). The semblance range (1-12Hz) was found optimal for all 212 events (e).

The discrimination results for all local events are presented in Fig. 3e. Anomalous low ratio values for experimental Dead Sea UWE can be referred to a higher frequency content of radiated seismic waves due to deeper source (70m) than for off-shore Tyre UWE (assumed 10-30m), higher density of water and small charges, mostly 16 and 24 kg. The spectral ratios for seven single blasts in the Mt. Nitzim quarry are low ($R_E=2-5$), unlike those for three single blasts at the Revaya quarry ($R_E>100$) showing strong low frequency surface waves (Fig. 2c). This is possibly caused by the uppermost geology near the quarries located in different regions (see map in Fig. 1). The semblance values for single blasts are lower than for ripple-fired but higher than for earthquakes. A possible reason is that though single shots do not possess the modulation in spectra caused by delays, they are, actually, point sources and radiated waves are azimuth-independent, unlike earthquake line sources which are subjected to the directivity effect. Single blast spectral curves at ISN stations show some coherent gross-structure (or envelope of random small scallops), mainly due to low frequency surface waves, making a significant contribution to the semblance. This effect is inherent also in ripple-fired blasts spectra.

Results: Teleseismic Events. The same procedures were applied to 58 Eurasian teleseismic events, with the only evident correction being a shift of spectral analysis bands to lower frequencies. The semblance and ratio values for ISN records of the earthquakes were found to be higher than those for the nuclear explosions (see Fig. 4a). This relationship is contrary to the results from local events, i.e. that analyzed waves (P and P-coda) from teleseismic earthquakes have more low-frequency energy and more coherent spectral shapes than explosions (Fig. 5a and b). This may be explained by a smaller spatial area of energy release for nuclear tests (the finite elastic radius) and shorter duration of the source function (the time rise), as compared to earthquakes (Savage, 1972) which produces a shorter wave length of P-waves and recorded signals (including scattered waves in P-coda) are more influenced by inhomogeneities in the upper crust beneath the ISN stations spaced by several dozen kilometers. Moreover for teleseismic earthquakes azimuths to the stations are very close (in contrast to local earthquakes), thus significantly increasing coherency of the spectra.

The best SS and SR performance was provided in the frequency ranges (0.6-1 Hz)/(1-3 Hz) for the energy ratio and (0.6-2 Hz) for the semblance. Joint application of the two discriminants provided almost full separation between the earthquake and explosion populations. Some explosions demonstrated pronounced minimum (null) near 1 Hz (Fig. 5c), which could be interpreted in terms of interference of P- and pP-waves from a very shallow source, about several hundreds meters (Kulhanek, 1971). Nevertheless, this feature cannot be utilized here as a discriminant: many explosions revealed strong variability of this null at ISN stations, while several earthquakes distinctly showed this phenomenon, possibly caused by interference of rupture sub-events (Fig. 5d).

In the NORESS data we found a similar high-frequency character of the P-arrivals for explosions relative to earthquakes, consistent with results of Tsvang et al. (1993). Therefore, spectral ratios showed the same as at ISN interrelation between the two populations, whereas the character of the semblance was changed to the opposite: very high (>0.94) close values for explosions and in-average lower dispersed values for earthquakes (Fig. 4b). In this case, due to the small dimensions of the array (diameter 3 km) as compared to the ISN network, local inhomogeneities in the upper crust and azimuth differences are negligible. We suppose that the main factor affecting station spectra coherency is a waveform character in (0-15 sec) window: one predominant P-signal for explosions, and several equal-amplitude signals of different shape for earthquakes. A joint application of the two statistics provided reliable discrimination between the two types of seismic events.

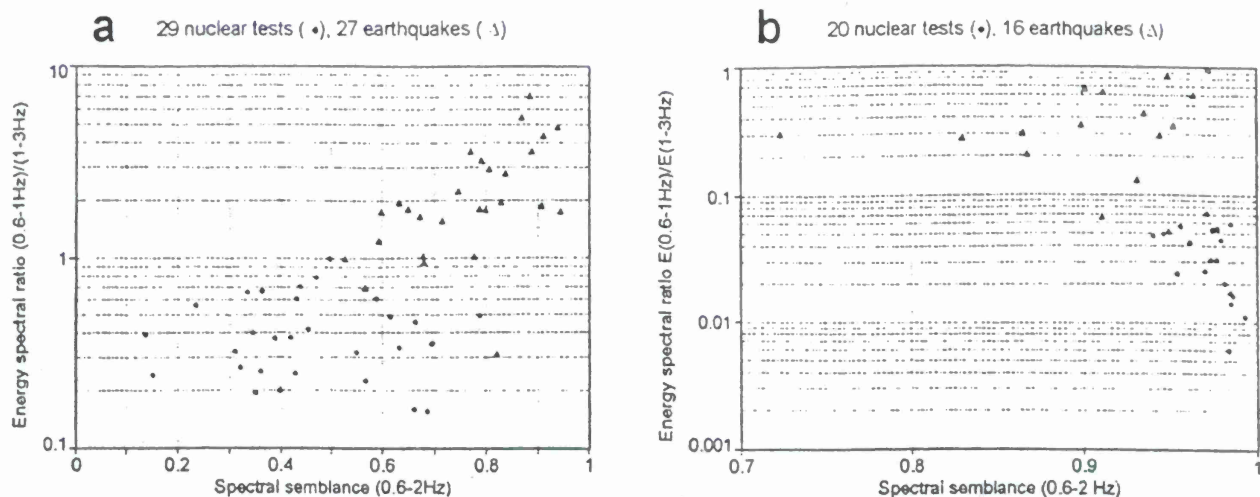


Fig. 4. Discrimination results for teleseismic Eurasian earthquakes (Δ) and nuclear explosions (\bullet), based on ISN recordings (a), and NORESS recordings (b).

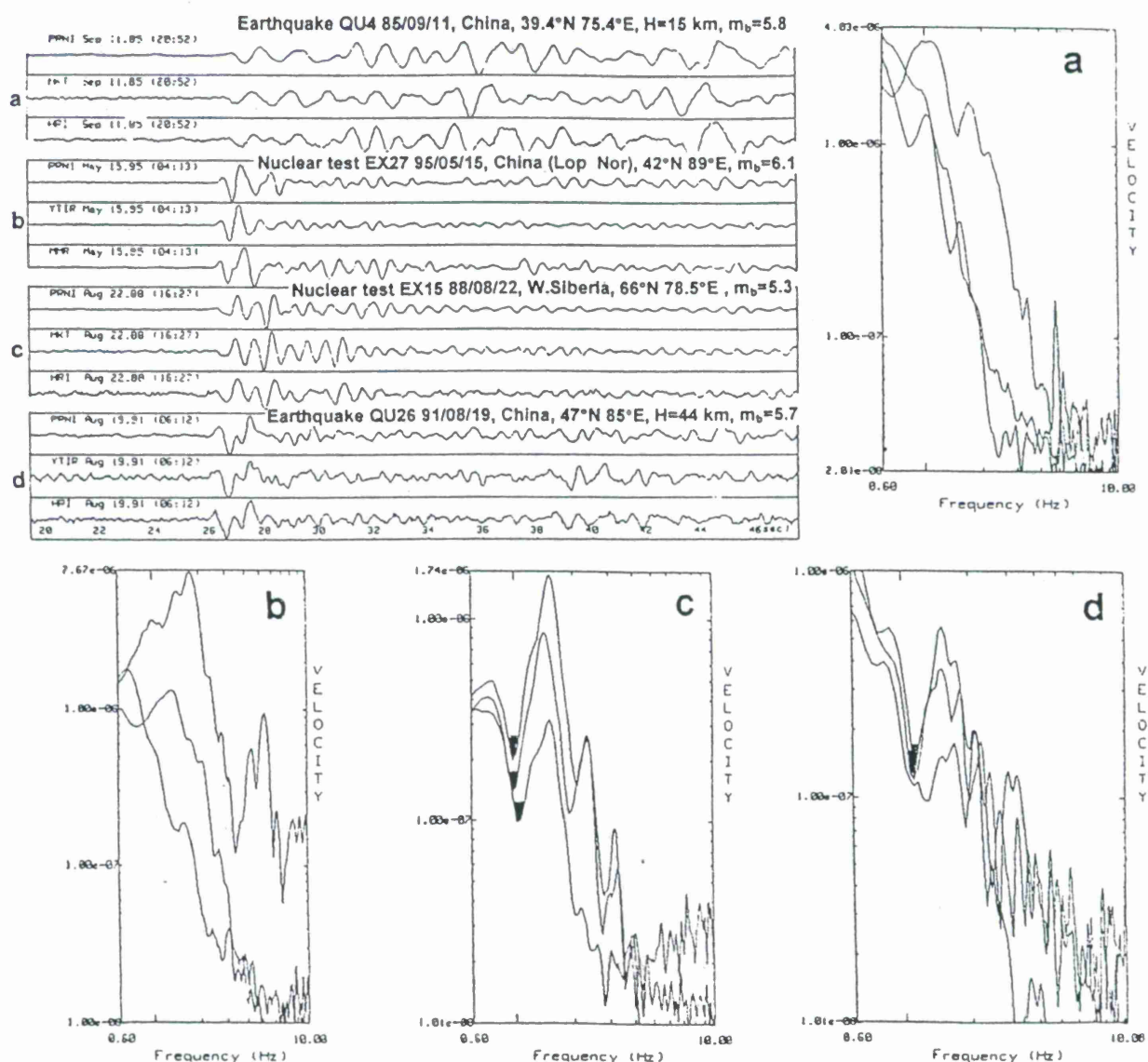


Fig. 5. Examples of teleseismic recordings at different ISN stations and appropriate spectra: (a) an earthquake in China, showing low-frequency spectral content; (b) a nuclear explosion at Lop Nor, demonstrating low coherency of spectral shapes. The prominent spectral modulation with a null near 1 Hz is observed for a nuclear test in W. Siberia (c), and for an earthquake in China (d).

CONCLUSIONS AND RECOMMENDATIONS

Using network-oriented short-period discriminants based on spectral features of seismic waves is an attractive method of effective discrimination of small-magnitude regional events. Our results indicate that application of the modified energy ratio and newly developed spectral semblance statistics to a variety of event types in various Middle East areas (Israel, Jordan, Mediterranean Sea) provide successful separation of earthquakes and man-made events. Rather surprisingly, application of the same procedures to teleseismic Eurasian nuclear tests and earthquakes recorded by a network (ISN) and an array (NORESS), also demonstrated their significant resolving power. The project results suggest that utilization of developed procedures and estimated optimal processing parameters would contribute to discrimination ability in other regions, at least in places with similar geological settings.

REFERENCES

- Bakun, W.H., Stewart, R.M. and Bufe, C.G., 1978, Directivity in the high-frequency radiation of small earthquakes, *Bull. Seism. Soc. Am.*, 68, 1253-1263.
- Barker, T.G., McLaughlin, K.C. and Stevens, J.L., 1993, Numeral simulation of quarry blast sources, SSS-TR-93-13859, S-Cubed, La Jolla, CA.
- Baumgardt, D.R. and Young, G.V., 1990, Regional seismic waveform discriminants and case-based event identification using regional arrays, *Bull. Seism. Soc. Am.*, 80, 1874-1892.
- Bennett, T.J. and Murphy, J.R., 1986, Analysis of seismic discrimination capabilities using regional data from Western United States events, *Bull. Seism. Soc. Am.*, 76, 1069-1086.
- Blandford, R.R., 1995, Regional seismic event discrimination, in Husebye, E.S. and Dainty, A.M. (eds.), *Monitoring a CTBT*, NATO ASI Series, Vol. 303, 689-719.
- Ginzburg, A. and Folkman, Y., 1980, The crustal structure between the Dead Sea rift and the Mediterranean Sea, *Earth Planet. Sci. Lett.*, 41, 181-188.
- Gitterman, Y., Shapira, A. and Pinsky, V., 1996a, Spectral Semblance Statistics as effective Regional Discriminant of Seismic Events in Israel, *Proceedings of the XXV General Assembly of the ESC*, September 9-14, 1996, Reykjavik, Iceland, 587-592.
- Gitterman, Y. and Shapira, A., 1993, Spectral discrimination of underwater explosions, *Isr.J.Earth Sci.*, 42, 37-44.
- Gitterman, Y., 1982, Assessment of dynamic parameters of seismic and air shock waves from multiple shot systems, Ph.D. Thesis, Academy of Sciences of the USSR, Novosibirsk.
- Gitterman, Y., Pinsky, V. and Shapira, A., 1996b, Discrimination of seismic sources using Israel Seismic Network, Scientific Report No.1, PL-TR-96-2207, Phillips Lab., MA, 98pp.
- Hedlin, M., Minster, J.G. and Orcutt, J.A., 1989, The time-frequency characteristics of quarry blasts and calibration explosions recorded in Kazakhstan, USSR, *Geophys. J. Int.*, 99, 109-121.
- Kulhanek, O., 1971, P wave amplitude spectra of Nevada underground nuclear explosions, *Pure Appl. Geophys.*, 88, 121-136.
- Li, Y., Toksöz, M.N. and Rodi, W.L., 1996, Discrimination of small earthquakes and explosions, *Proceedings of the 18th Symposium on CTBT Monitoring*, Annapolis, PL-TR-96-2153, 574-583.
- Pinsky, V., Gitterman, Y. and Shapira, A., 1997, Multiparameter-multistation regional and teleseismic event discrimination using ISN and NORESS recordings (these proceedings).
- Pulli, J.J., 1995, Extracting and processing signal parameters for regional seismic event identification, in: Husebye, E.S. and Dainty, A.S. (eds.), *Monitoring a CTBT*, NATO ASI Series, 303, 741-754.
- Savage, J.C., 1972, Relation of corner frequency to fault dimensions, *JGR*, 77, 577-592.
- Shapira, A., Gitterman, Y. and Pinsky, V., 1996, Discrimination of seismic sources using the Israel Seismic Network, *Proceedings of the 18th CTBT Symposium*, PL-TR-96-2153, 612-621.
- Stump, B.W. and Reinke, R.E., 1988, Experimental confirmation of superposition from small explosions, *Bull. Seism. Soc. Am.*, 78, 1059-1073.
- Tsvang, S.L., Pinsky, V.I. and Husebye, E.S., 1993, Enhanced seismic source discrimination using NORESS recordings from Eurasian events, *GJI*, 112, 1-14.

APPLYING SOURCE AND PATH CORRECTIONS TO IMPROVE DISCRIMINATION IN CHINA

Hans E. Hartse, Steven R. Taylor, W. Scott Phillips, and George E. Randall
Geophysics Group - EES-3, Los Alamos National Lab

Sponsored by U.S. Department of Energy
Office of Nonproliferation and National Security
Office of Research and Development
Contract W-7405-ENG-36

Comprehensive Test Ban Treaty Research and Development Program, ST482A

ABSTRACT

Monitoring the Comprehensive Test Ban Treaty (CTBT) to magnitude levels below 4.0 will require use of regional seismic data recorded at distances of less than 2000 km. To improve regional discriminant performance we tested three different methods of correcting for path effects, and the third method includes a correction for source-scaling. We used regional recordings of broadband from stations in and near China. Our first method removes trends between phase ratios and physical parameters associated with each event-station path. This approach requires knowledge of the physical parameters along an event-station path, such as topography, basin thickness, and crustal thickness. Our second approach is somewhat more empirical. We examine spatial distributions of phase amplitudes after subtracting event magnitude and correcting for path distance. For a given station, phase, and frequency band, we grid and then smooth the magnitude-corrected and distance-corrected amplitudes to create a map representing a correction surface. We reference these maps to correct phase amplitudes prior to forming discrimination ratios. Our third approach is the most complicated, but also the most rigorous. For a given station and phase, we invert the spectra of a number of well-recorded earthquakes for source and path parameters. We then use the values obtained from the inversion to correct phase amplitudes for the effects of source size, distance, and attenuation. Finally, the amplitude residuals are gridded and smoothed to create a correction surface representing secondary path effects.

We find that simple ratio-parameter corrections can improve discrimination performance along some paths (such as Kazakh Test Site (KTS) to WMQ), but for other paths (such as Lop Nor to AAK) the corrections are not beneficial. Our second method, the empirical path correction surfaces, improves discrimination performance for Lop Nor to AAK paths. Our third method, combined source and path corrections, has only been tested at WMQ (primarily using KTS explosions and northwest China earthquakes), but the method successfully corrects for source-scaling and propagation effects. We favor this combined source and path correction technique over the other correction methods, and we plan to test this method at other Asian stations.

Key Words: seismic discrimination, path correction, source correction, China

OBJECTIVE

Monitoring the Comprehensive Test Ban Treaty (CTBT) to magnitude levels below 4.0 will require use of regional seismic data recorded at distances of less than 2000 km. One way to improve discriminant performance is to reduce scatter within ratio or phase amplitude measurements by correcting for the effects of source and path. By reducing scatter, separation between earthquake and explosion populations may be increased. Typically, researchers remove ratio-distance trends before forming discrimination plots (*cf.* Hartse *et al.* (1997a)). A linear distance correction approximately accounts for attenuation and geometrical spreading, but other path effects, such as partial blockage of S_n or L_g , are not accounted for and contribute to scatter on discrimination plots. Furthermore, trends on spectral and cross-spectral discrimination plots are produced by the effect of source-scaling. Figure 1 shows an uncorrected P_g spectral ratio discrimination plot, the distance trend, and the distance-corrected discrimination plot. The remaining trend on the distance-corrected plot is due to source-scaling.

In this paper our objective is to test three different methods of correcting for path effects, and the third method includes a correction for source-scaling. Our first method follows the approach of Zhang *et al.* (1996). We remove ratio-parameter trends to reduce scatter within earthquake and explosion populations. This approach requires knowledge of the physical parameters along an event-station path, such as topography, basin thickness, and crustal thickness. Our second approach is somewhat more empirical. We examine spatial distributions of phase amplitudes after subtracting event magnitude and correcting for path distance. For a given station, phase, and frequency band, we grid and then smooth the magnitude-corrected and distance-corrected amplitudes to create a map representing a correction surface. Our third approach to path corrections is the most complicated, but also the most rigorous. For a given station and phase, we invert the spectra of a number of well-recorded earthquakes for source and path parameters. We then use the values obtained from the inversion to correct phase amplitudes for the effects of source size, distance, and attenuation.

We find that simple path parameter corrections can improve discrimination performance along some paths (such as Kazkh Test Site (KTS) to WMQ), but for other paths (such as Lop Nor to AAK) the path parameter corrections are not beneficial. We find that the empirical path correction surfaces improve discrimination performance for Lop Nor to AAK paths. Our combined source and path correction method has only been tested at WMQ (primarily using KTS explosions and northwest China earthquakes), but the method successfully corrects for source-scaling and propagation effects. We favor this combined source and path correction technique over the other correction methods.

RESEARCH ACCOMPLISHED

Data Used and Region Studied.

Most of the waveforms used in this study were recorded at WMQ in northwest China and AAK in Kyrgyzstan. However, we have also used data recorded at CDSN stations LZH, ENH, and XAN, and NIL in Pakistan recorded at distances of up to 2500 km (Figure 2). Most events studied are regional earthquakes, but WMQ has recorded over 25 KTS explosions (at a distance of about 960 km), and AAK has recorded 7 Lop Nor nuclear explosions (at a distance of about 1190 km). We obtained event locations, magnitudes, and origin times from United States Geological Survey Preliminary Determination of Epicenter (PDE) catalogs for the years 1987-1996, and we obtained event information from regional Chinese catalogs for earthquakes smaller than about magnitude 4.0 for the years 1987-1989 (Gao and Richards, 1994).

Method 1 - Correcting Ratios Using Physical Path Parameters.

Zhang and Lay (1994) showed that statistical trends exist between topography and some phase amplitude ratios for nuclear explosions from the Former Soviet Union's Kazakh Test Site (KTS) recorded at several seismic stations distributed throughout Eurasia. Later, Zhang *et al.* (1996) obtained a reduction in variance of earthquake phase ratios from the western United States by correcting for surface roughness. While these earlier studies have shown that variance reduction within an earthquake-ratio population is possible, they do not address whether separation between earthquakes and explosions can actually be increased by correcting for path effect. Here, we examine the scatter within each event population and we measure the change in separation between earthquake and explosion populations after correcting P_g/L_g ratios for path effects related to topography, basin thickness, and crustal thickness (Figure 3).

For northwest China earthquakes and nuclear explosions from KTS recorded at WMQ, we find that distance-weighted topography and distance-weighted basin thickness corrections do indeed improve the P_g/L_g discriminant for the 1.5-3 and 2-4 Hz bands. We speculate that this increased separation occurs because the explosions from KTS traverse paths with relatively smooth topography and uniform crustal thickness, while most earthquakes we studied have more complicated paths, traversing the topographically rough Tian Shan, the Tarim Basin, and the Junggar Basin (Figure 2). For northwest China earthquakes and nuclear explosions from the Lop Nor test site recorded at AAK, we do not find path corrections that improve the P_g/L_g discriminant. For details concerning this study see Hartse *et al.* (1997b). The primary drawbacks of this method is the required reliance on physical path measurements, which may often be quite coarse, and the fact that we have not accounted for source-scaling effects.

Method 2 - Empirical Path Corrections.

We have examined spatial distributions of amplitudes of regional phases to find coherent patterns that can be used as path corrections (Phillips *et al.*, this volume). For data recorded at a given station, we first correct phase amplitude for source size by subtracting event magnitude (m_b), followed by a linear distance correction. The corrected amplitudes are then smoothed spatially by averaging values over a geographical grid (Figure 4). We smooth only where a threshold number of crustal events (currently 5) fall inside a given bin. Our implicit assumption is that the smoothing averages out source radiation and depth effects, leaving an estimate of the path effect that can be used for correcting phase amplitudes and, therefore, individual discriminants.

After estimating correction surfaces for several phases and frequency bands, we use the correction maps to form amplitude ratios and then discrimination plots. Figure 5 shows results for Lop Nor events recorded at AAK. For the P_g/L_g (3-6 Hz) band, the corrections increase separation between the earthquakes and explosions. There are two drawbacks to this method. First, correction maps can only be estimated when there are abundant earthquakes from a given region. Second, we have still not considered the source-scaling effect that will be present in the spectral and cross-spectral ratios.

Method 3 - Source and Path Amplitude Corrections.

Our third correction technique is a procedure for the estimation of frequency-dependent source and propagation amplitude corrections for regional seismic discriminants (Source Path Amplitude Correction - SPAC; Taylor and Hartse, 1997). For a given station and phase, a number of well-recorded earthquake spectra are inverted for source and path corrections. The method assumes a simple Brune (1970) earthquake-source model and a simple propagation model consisting of a frequency-independent geometrical spreading and

frequency-dependent power-law Q . The inverted low-frequency levels are then regressed against m_b to derive a set of corrections that are a function of m_b and distance. Once a set of corrections are derived, effects of source scaling and distance as a function of frequency are applied to amplitudes from new events prior to forming discrimination ratios. The resulting discriminants are normally distributed and amenable to multivariate feature selection, classification, and outlier techniques.

To date, most discrimination studies have removed distance corrections once a particular amplitude ratio is formed (Distance Corrected Ratio - DCR; Figure 1). DCR generally works well for phase ratios taken in a particular frequency band. However, when different frequency bands are combined (for phase spectral ratios or cross spectral ratios), significant source-scaling effects (e.g. corner-frequency scaling) can remain, causing the discriminants to vary as a function of event size and to be non-normally distributed. It is then often necessary to construct non-physical transformations in an attempt to make the discriminants multivariate normal. The SPAC technique can be used to construct discriminants that are multivariate normal. Moreover, phase amplitude residuals as a function of frequency can be spatially averaged and used as additional path-specific corrections to correct for additional propagation effects, such as phase blockages.

For the frequency-dependent amplitude inversion, we basically follow the technique of Sereno et al., (1988) with minor modifications. The results of the inversion for the source-path corrections for L_g are shown in Figure 6. Once the parameters are obtained, the amplitudes from other events can be corrected for source scaling and propagation using SPAC. To do this, it is first necessary to obtain an estimate of the low-frequency level, S_0 . We have chosen to tie the low-frequency level to magnitude. Note that although the dislocation source model used in correcting the amplitudes is not appropriate for nuclear explosions, we still use it because, in an actual monitoring situation, the source type would be unknown.

As an example application, we corrected P_g amplitudes and plotted P_g (0.75-1.5 / 4-8) Hz spectral ratios versus m_b . The top portion of Figure 7 shows the distance-corrected spectral ratio (this correction is illustrated in Figure 1) and the SPAC-corrected ratio. For the upper left figure, we formed P_g spectral ratios for earthquakes with good signal-to-noise ratio, and then regressed the ratios against the logarithm of distance. We then applied the distance correction factors to all ratios for earthquakes and nuclear explosions having signal-to-noise values greater than 2. The corner frequency scaling is still present as an increase in the spectral ratio with magnitude. The overlap between the two populations is illustrated in the lower left portion of the figure using the estimated normal probability density function. Visually, the P_g ratio with just the distance correction plotted versus m_b appears to show good separation between earthquakes and explosions. However, m_b is never actually used as a discrimination variable and a multivariate discrimination method would see the projection of the spectral ratio on the ordinate. For the SPAC method, the trend with m_b is removed and the separation and variance projected on the ordinate are improved and reduced, respectively (compare Figure 7 lower left with lower right).

CONCLUSIONS AND RECOMMENDATIONS

We tested three path correction methods for regional seismic discriminants. The first method removes the effects of particular physical parameters along a given path, such as topography or crustal thickness. The advantage of this method is that it is easy to apply, and it can be applied where little historical seismicity has been recorded. However, in many regions, some physical parameters are poorly known, such as basin thicknesses. Also, for northwest China we did not find consistent corrections that work for stations

AAK and WMQ, two relatively "close" stations for this region of Asia. Our second method is an empirical path correction, relying solely on the residuals of phase amplitudes. Based on initial results, this method has helped increase P_g/L_g discriminant performance. However, this method relies on abundant data and hence will not be applicable to relatively aseismic regions. Our final method corrects for both source-scaling effect and propagation effects. We have used this method to improve the P_g spectral ratio discriminant using data from WMQ. We favor this correction technique as it removes source-scaling effect and propagation effect. We plan to apply this technique across central Asia.

REFERENCES

- Brune, J. N. (1970). Tectonic stress and spectra of seismic shear waves from earthquakes, *J. Geophys. Res.*, **75**, 4997-5009.
- Fielding, E. J., M. Barazangi, and B. L. Isacks (1993). A geological and geophysical data base for Eurasia, *Final Technical Report, ARPA NMRO F29601-91-K-DB08*.
- Gao, L. and P. G. Richards (1994). Studies of earthquakes on and near the Lop Nor, China, nuclear test site, *Proceedings of the 18th Annual Seismic Research Symposium on Monitoring a Comprehensive Test Ban Treaty*, 106-112.
- Hartse, H. E., S. R. Taylor, W. S. Phillips, and G. E. Randall (1997a). Preliminary study of seismic discrimination in central Asia with emphasis on western China, *Bull. Seis. Soc. Am.*, **87**, 1464-1474.
- Hartse, H. E., R. A. Flores, and P. A. Johnson (1997b). Correcting regional seismic discriminants for path effects in western China, submitted, *Bull. Seis. Soc. Am.*, submitted, June, 1997.
- Phillips, W. S., G. E. Randall, H. E. Hartse, S. R. Taylor, and H. J. Patton (1997). Source and path effects on regional phases in China, *Proceedings of the 19th Annual Seismic Research Symposium on Monitoring a Comprehensive Test Ban Treaty*, (this volume).
- Sereno, T. J., S. R. Bratt, and T. C. Bache (1988). Simultaneous inversion of regional wave spectra for attenuation and seismic moment in Scandinavia, *J. Geophys. Res.*, **93**, 2019-2035.
- Taylor, S. R. and H. E. Hartse (1997). A procedure for estimation of source and propagation amplitude corrections for regional seismic discriminants, submitted, *J. Geophys. Res.*, June, 1997.
- Zhang, T. and T. Lay (1994). Analysis of short-period regional phase path effects associated with topography in Eurasia, *Bull. Seis. Soc. Am.*, **84**, 119-132.
- Zhang, T., T. Lay, S. Schwartz, and W. R. Walter (1996). Variation of regional seismic discriminants with surface topographic roughness in the western United States, *Bull. Seis. Soc. Am.*, **86**, 714-725.
- Wessel, P. and W. H. F. Smith (1991). Free software helps map and display data, *EOS Trans. AGU*, **72**, 441.

Acknowledgements

We thank Howard Patton for a thoughtful review of this paper. We thank the staff at the IRIS Data Management Center for prompt replies to our data requests. Maps were created using the Global Mapping Tool (GMT) (Wessel and Smith, 1991). This work is in support of the DOE Comprehensive Test Ban Treaty Research and Development Program, ST482A, and was performed at Los Alamos National Laboratory under the auspices of the United States Department of Energy, Contract Number W-7405-ENG-36.

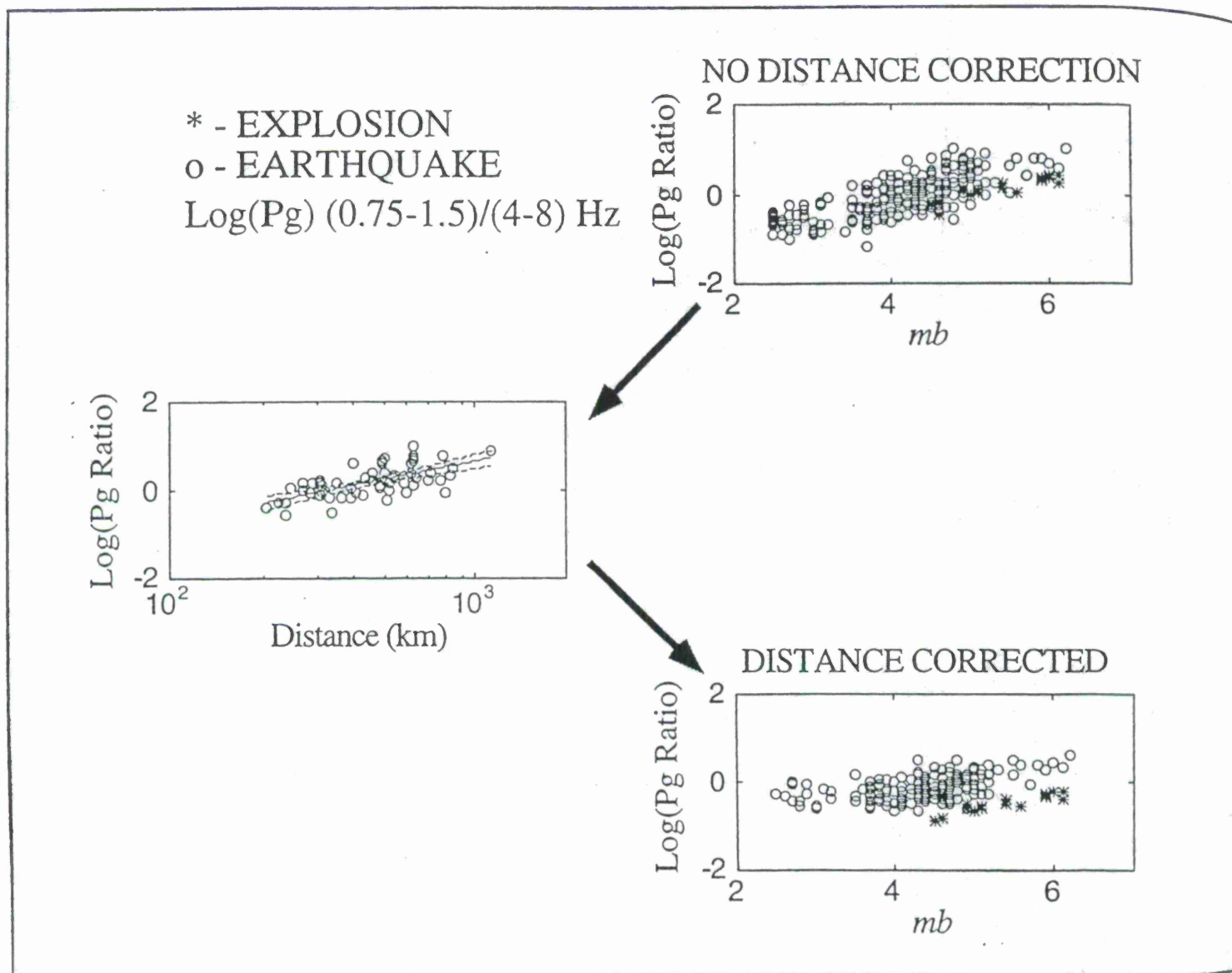


Figure 1. Illustration of the Distance Corrected Ratio (DCR) technique commonly used for applying distance corrections to a Pg spectral ratio discriminant. Upper right panel shows uncorrected spectral ratios for earthquakes and nuclear explosions at WMQ (Hartse et al., 1997a). Left panel shows earthquake P_g spectral ratios for events with a signal-to-noise ratio greater than 10 regressed versus the logarithm of the distance. Lower right panel shows distance-corrected P_g spectral ratio. Notice dependence of the spectral ratio with magnitude remains.

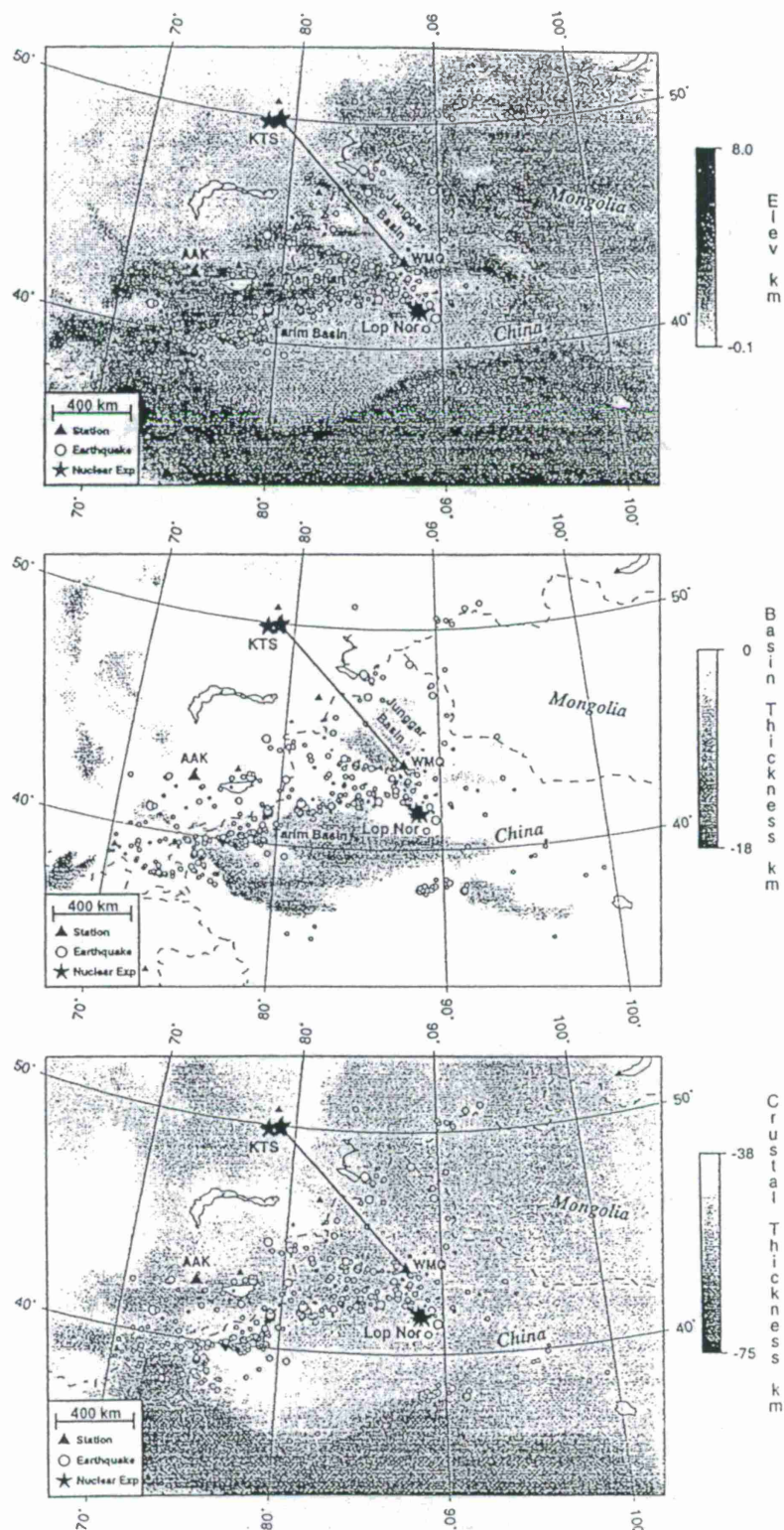


Figure 2. Topography, basin thickness and crustal thickness maps of the northwest China region. Nuclear explosions and earthquakes used in this study were recorded at WMQ and AAK. The heavy line marks the path from the Kazakh Test Site to WMQ. Gridded data obtained from the Cornell Database (Fielding *et al.*, 1993). Parameters displayed and extracted from data grids using the GMT software of Wessel and Smith (1991).

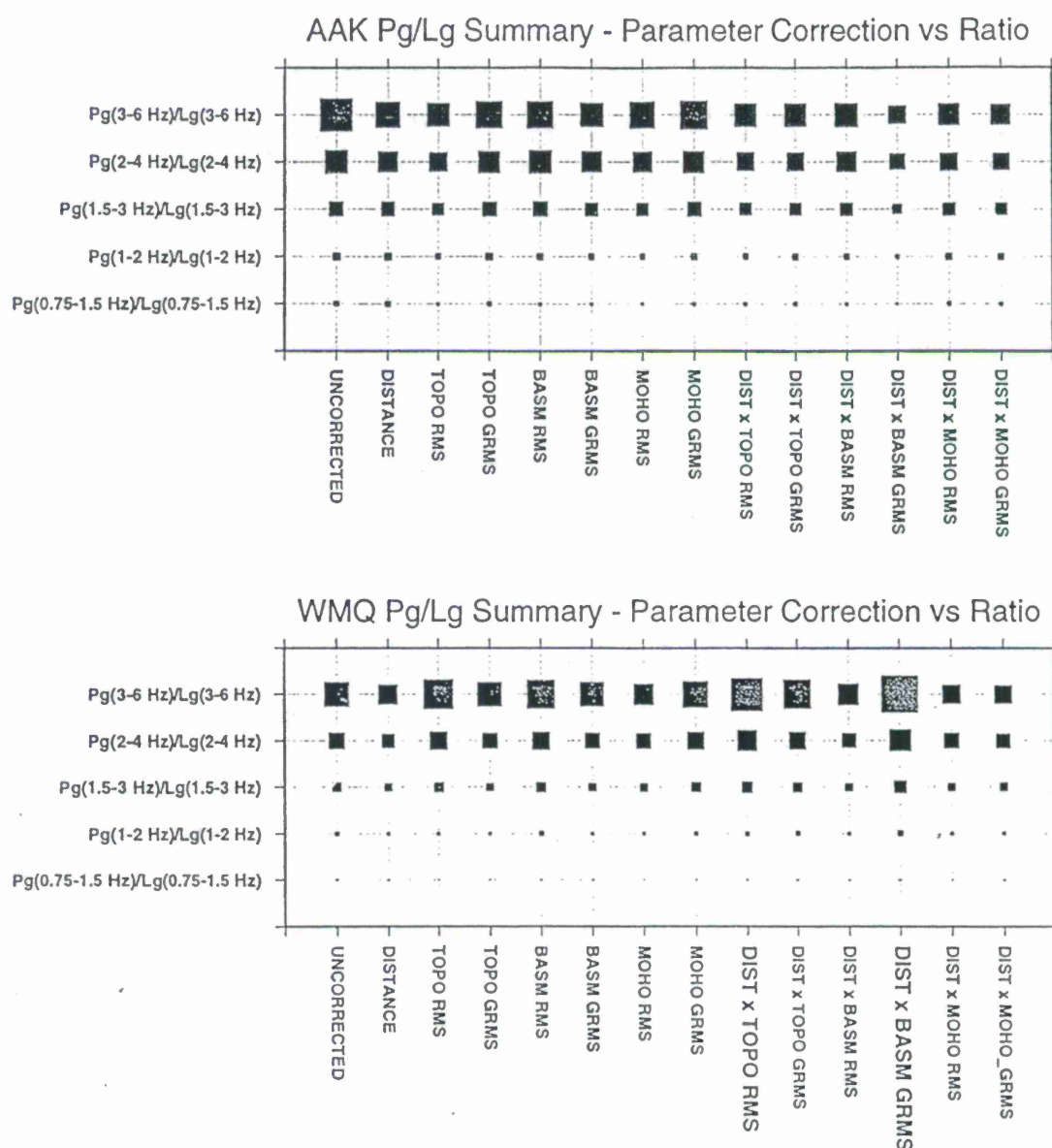


Figure 3. Summary discrimination plots for P_g/L_g ratios at AAK and WMQ for various physical parameter corrections. Bands tested are indicated along the vertical axis. The size of each square is scaled to the Mahalanobis Distance (Δ^2), a function of separation between population means (\bar{v}) and variance within each population (σ^2): $\Delta^2 = (\bar{v}_x - \bar{v}_q)^2 / (\sigma_x^2 + \sigma_q^2)$. Actual values range from 0.03 to 14.6. As has been shown previously, as f increases, the P_g/L_g discriminant performance also increases. The most successful corrections for WMQ are distance-weighted roughness of the basin thickness gradient (DIST x BASM GRMS) and the distance-weighted roughness of the topography (DIST x TOPO RMS). For AAK we found no corrections which increase Mahalanobis Distance relative to the uncorrected case.

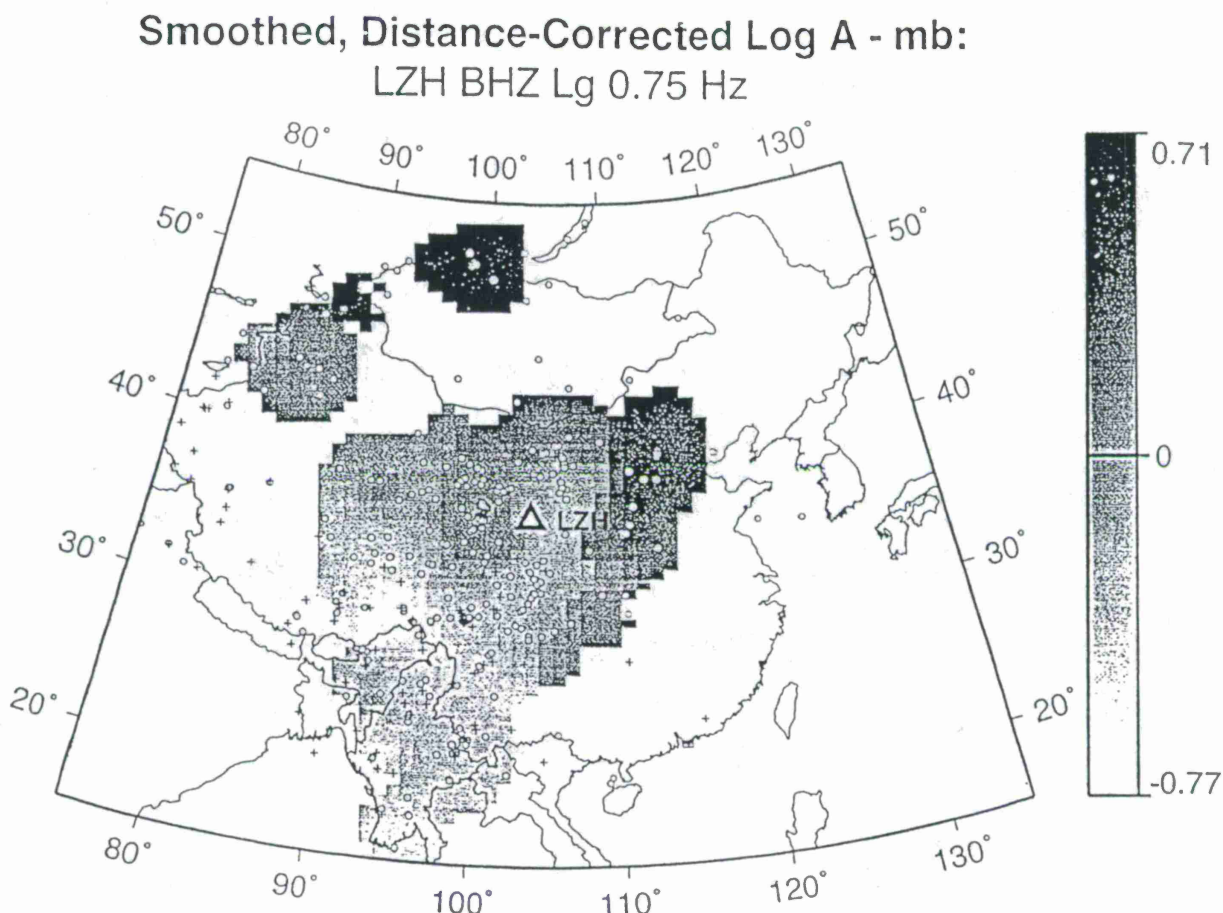


Figure 4. Path correction map of L_g amplitude residuals. See Phillips *et al.* (1997) in this proceedings volume for more details.

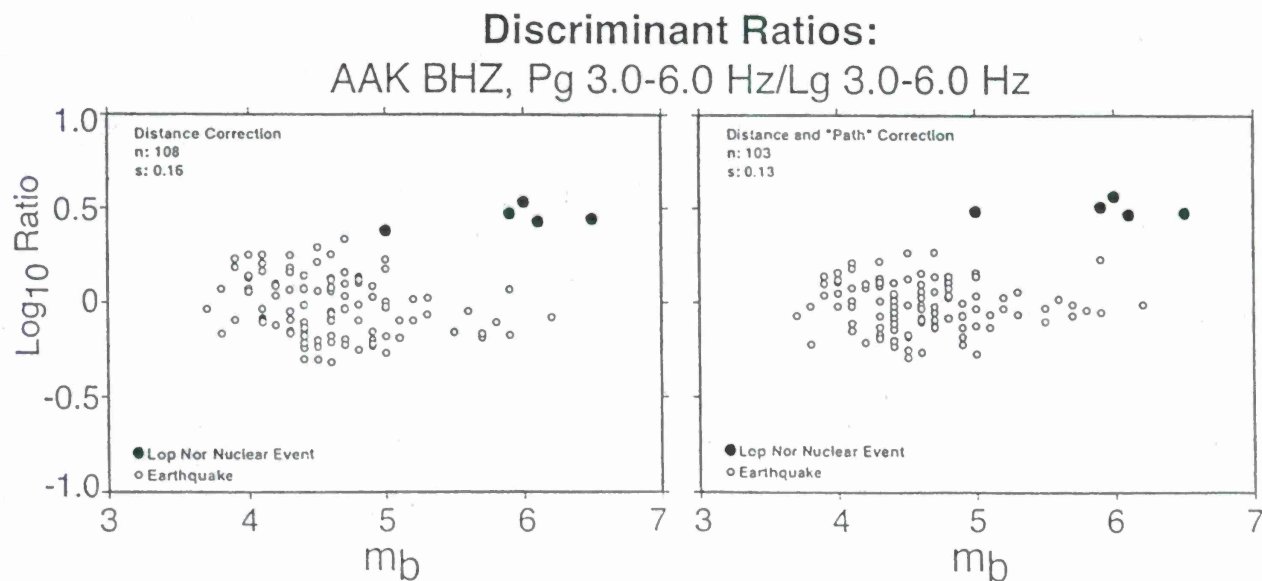


Figure 5. Discrimination plots for the P_g/L_g (3-6 Hz) ratio before (*left*) and after (*right*) empirical path corrections have been applied. The path corrections have increased separation between northwest China earthquakes and Lop Nor explosions.

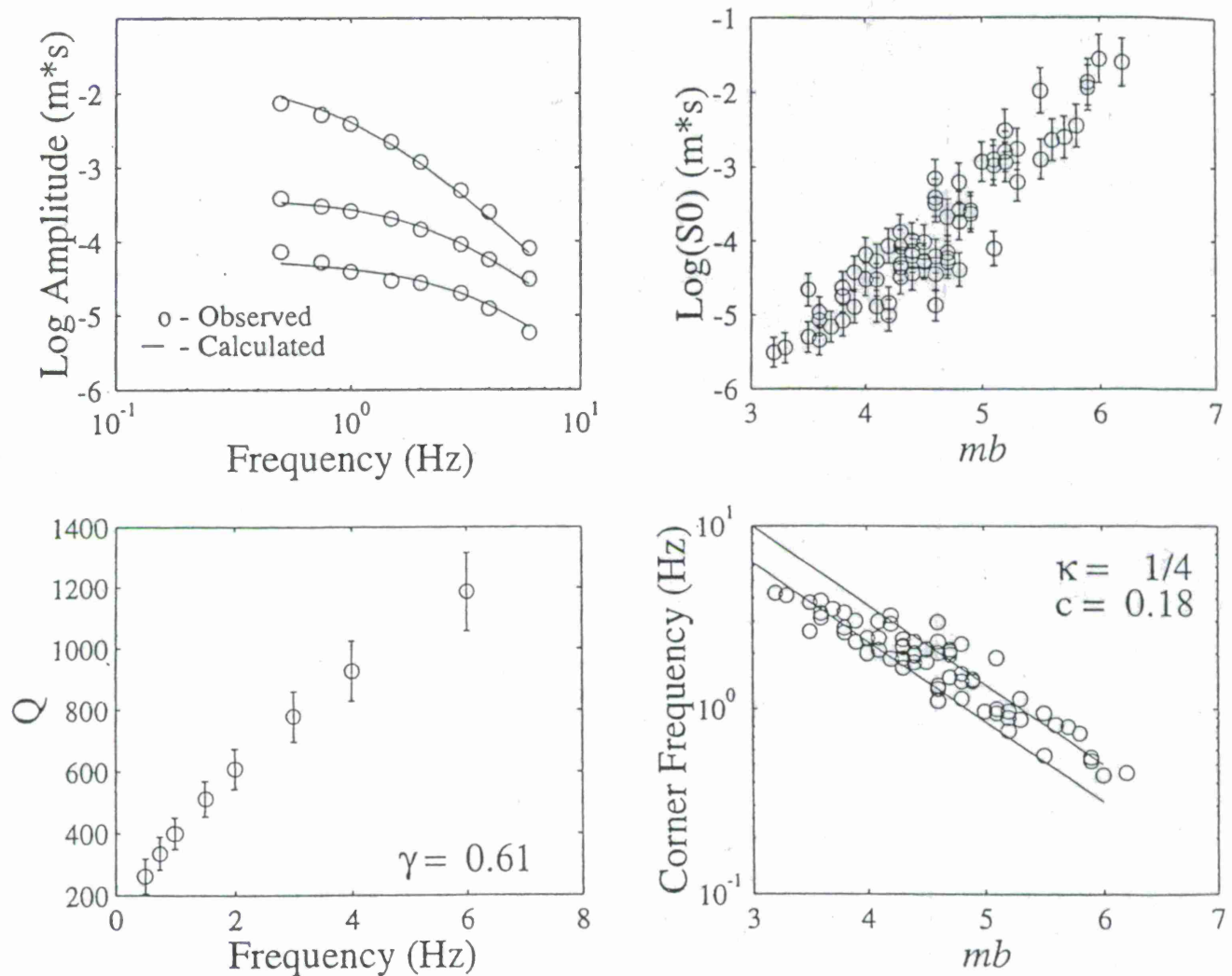


Figure 6. Results from inversion of earthquake L_g pseudo spectrum. Geometrical spreading factor (η) assumed to be 1/2. Upper left; calculated and observed spectra for 3 randomly chosen events. Lower left; frequency-dependent Q values, 95% confidence limits, and γ (Q_0 set to 400). Upper right; logarithm of the low-frequency level, S_0 , versus m_b and 95% confidence limits. Lower right, corner frequency versus m_b . Also shown are theoretical curves for S-wave corner frequency using a Brune (1970) dislocation source model (where $\kappa = 1/3$) for stress drops of 5 and 20 MPa (50 and 200 bars; lower and upper curves, respectively).

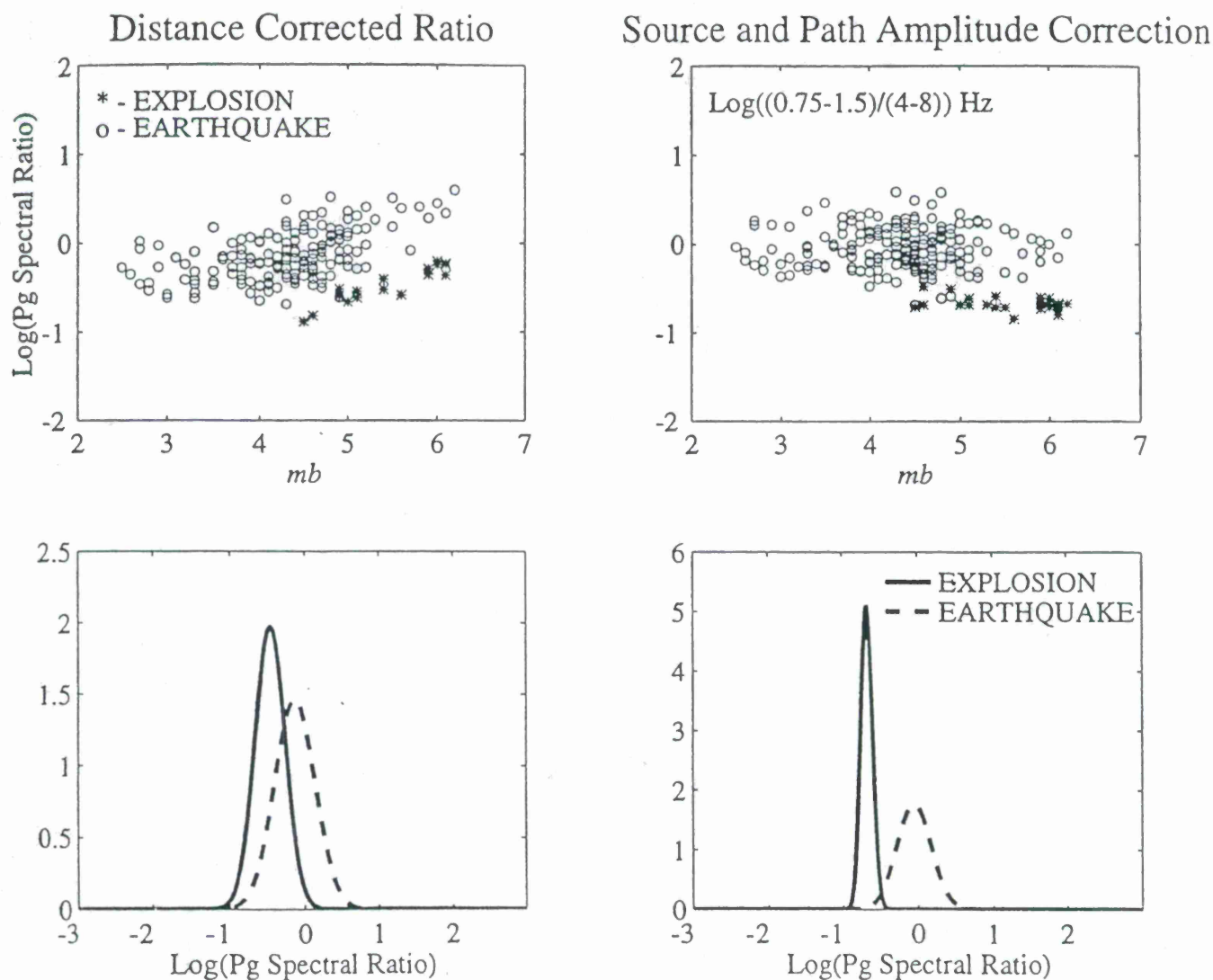


Figure 7. Comparison of DCR (left) and SPAC (right) techniques. P_g spectral ratio of the 0.75 to 1.5 and 4 to 8 Hz bands versus m_b using the distance correction method illustrated in Figure 1 (top left) and using the combined source and path corrections (upper right) for earthquakes and nuclear explosions described in Hartse *et al.*, (1997a). Normal probability density function for P_g spectral ratio of earthquakes and nuclear explosions using just distance correction (lower left) and combined source and path corrections (lower right).

A GLOBAL TEST OF A TIME-FREQUENCY SMALL-EVENT DISCRIMINANT

Michael A.H. Hedlin

IGPP, Scripps Institution of Oceanography, University of California, San Diego

Sponsored by Air Force Technology Applications Center
Contract No. F19628-95-K-0012

ABSTRACT

The comprehensive nuclear test ban treaty, which was recently adopted by the UN General Assembly, has lowered to zero the testing yield limit and raised the profile of the smallest ($m_b \sim 2.5$) events. Given that significant mining operations exist worldwide, and some use several kilotons of explosives in a single delay-fired shot sequence, these complex events must be separated from earthquakes and single explosions. Since relatively small events are very common, there is a strong need for automated algorithms which can be used to screen out the events which are obviously chemical or natural and identify those few curious enough to warrant closer scrutiny.

This paper summarizes a recent global analysis (*Hedlin, 1997*) which found that spectral modulations can be used to routinely discriminate mining blasts from single explosions and earthquakes. This paper also describes preliminary efforts to understand better why expected high-frequency modulations are sometimes absent. A recent regional experiment in Wyoming has given recordings of known millisecond delay-fired events which did not yield high-frequency scallops. Ground truth information suggests that of the many possible explanations the two most likely are shot scatter and waveform variability. These events produced obvious modulations below 10 Hz. These modulations, which appear to be due to source finiteness, are similar to those at high frequencies in other events as they are independent of time, sensor orientation and, to a large extent, source-receiver azimuth. As expected due to recent work by *Anandakrishnan et. al. (1997)* these cast shots also produced significant energy at 10 to 20 s. These low-frequency features might be useful for discrimination at mid- to far-regional ranges but require further study.

Keywords: delay-firing, automated discrimination, sonogram, multitapers, wavelets, multivariate statistics.

OBJECTIVES

We have used spectral characteristics of whole waveforms to discriminate delay-fired mining events from earthquakes and single explosions. We have favored time-frequency displays (commonly known as sonograms or spectrograms) for this purpose. A recent test of this approach on globally distributed datasets (*Hedlin, 1997*) has produced misclassification probabilities ranging from 0.5 to 3.5%. Although these results have been encouraging we hope to improve the method by concentrating on the causes of outliers. The data examined in the previous study have a limited potential as they do not come with sufficient "ground truth" information to allow us to fully explain the failures. The current project will begin with an analysis of seismic recordings made recently in Wyoming in collaboration with Brian Stump (SMU) and Craig Pearson (LANL). The three salient features of these data are that they were collected by broadband STS2's at 4 azimuths and are accompanied by ground truth (in the form of blasting records, near-field seismic and in-mine video data collected by LANL). The seismic records will be modeled using a linear elastic model developed recently by *Anandakrishnan et al (1997)* to dissect the regional waveforms so that we can better understand which source effects make significant contributions. We are doing this to explain both the frequency and time domain features which are routinely present and will likely allow us to separate mining blasts from other events as well as to explain why the expected features are sometimes absent. We are particularly interested in those seismic signals which exist at frequencies below 10 Hz and, ultimately, in the use of these features for discrimination at mid-regional (~ 1000 km) range.

Eventually we would like to explore discrimination which doesn't rely solely on seismic data but on a combination of downward directed seismic energy and upward directed acoustic energy. Toward this end we have collaborated with Rod Whitaker (LANL) and collected recordings of infrasound emissions during the Wyoming experiment.

RESEARCH ACCOMPLISHED

Global Test Under our recent contract with AFTAC we developed and tested a time-frequency discriminant which separates delay-fired mining blasts from other events on the basis of the presence of spectral modulations which are independent of time and recording component. The adaptability of the discriminant was tested using a number of well separated, and dissimilar, datasets. The algorithm was tested using dissimilar styles of seismic deployment (*incl.* a single 3-component station, single- and 3-component networks and arrays) varying seismic instrumentation (*incl.* short period and broadband), located in distinct tectonic regions where mining techniques are likely to be tailored to local needs (*Hedlin, 1997* & Figure 1 in this paper). The misclassification probabilities ranged from 0.5% (GERESS) to 3.5% (KNET) (Figure 2) suggesting that the automated discriminant is robust and easily adapted to a wide range of deployments.

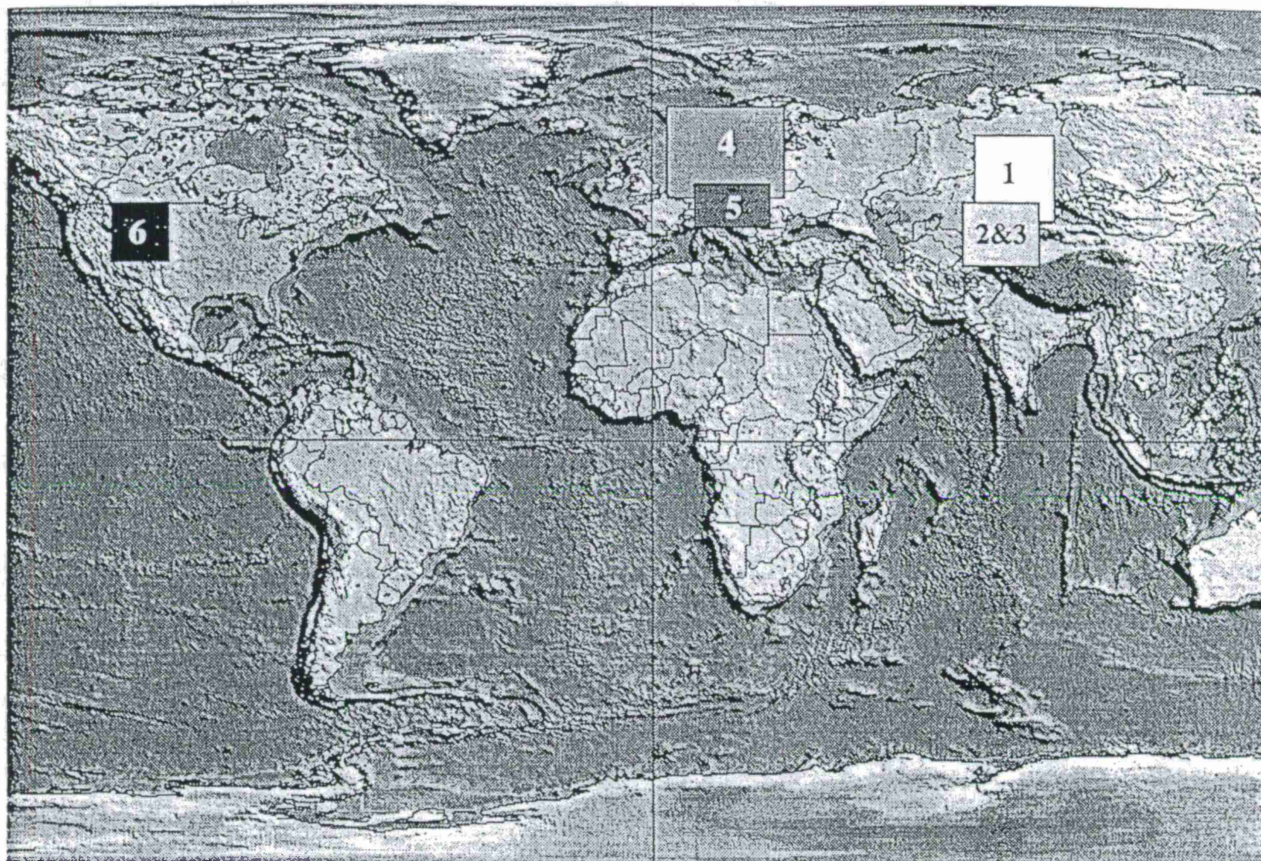


Figure 1: All the datasets used in the global test of the discriminant are highlighted. Three kinds of deployments were considered. Networks (1, 2 & 3), tight arrays (4 & 5) and a single, 3-component, station (6). The basemap was obtained from the Cornell group (http://www.geo.cornell.edu/geology/me_na/dataset_info/new_etopo5.html)

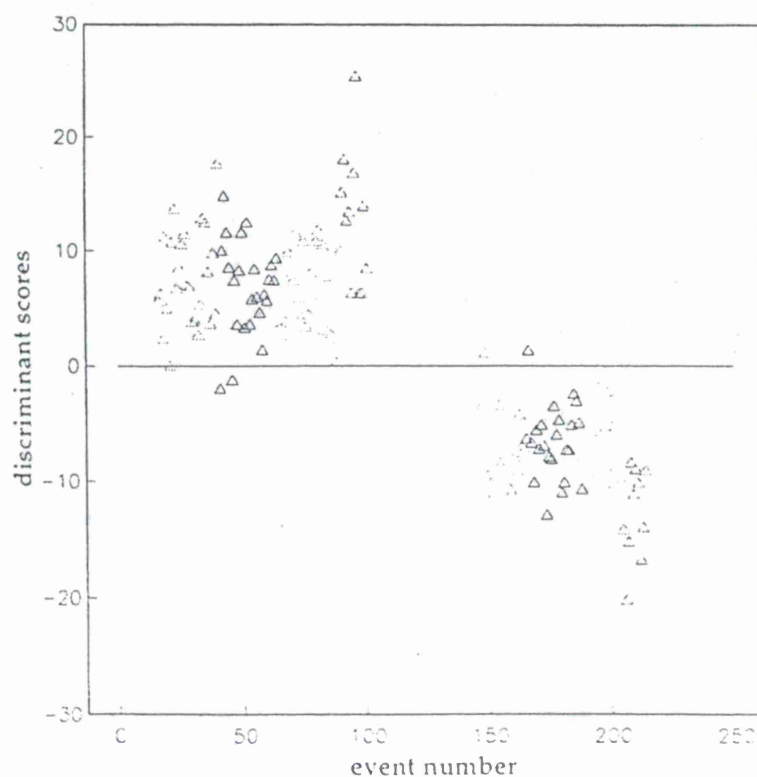


Figure 2: Discriminant scores from datasets 2 through 6. The NRDC scores haven't been included since there were too few explosions (3) to permit a statistical evaluation. Linear discriminant functions were used for all datasets except the sixth (collected by the single station). The raw parameters suggest that 2 of the 15 quarry blasts in the NRDC dataset would be misidentified. Of the 232 events in the other datasets, all but 6 were correctly identified. As expected the scatter increases as averaging becomes less effective (single 3-component station).

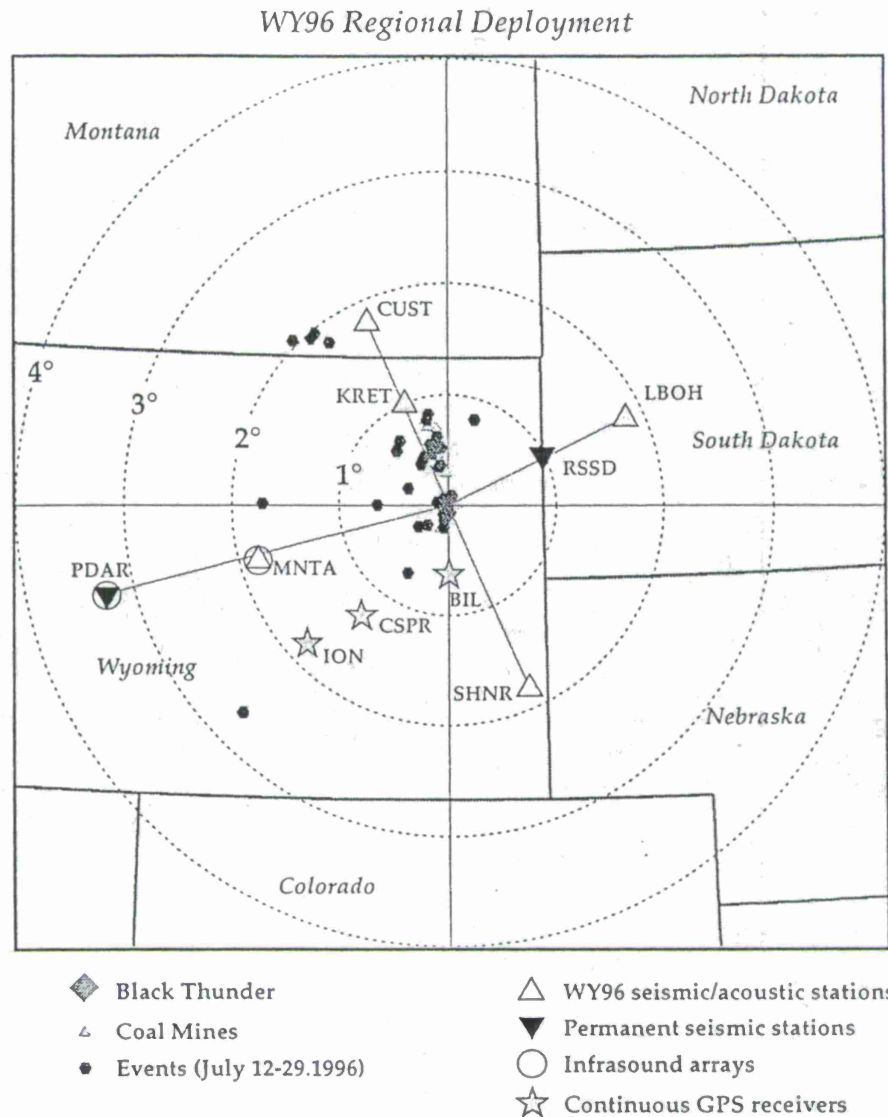
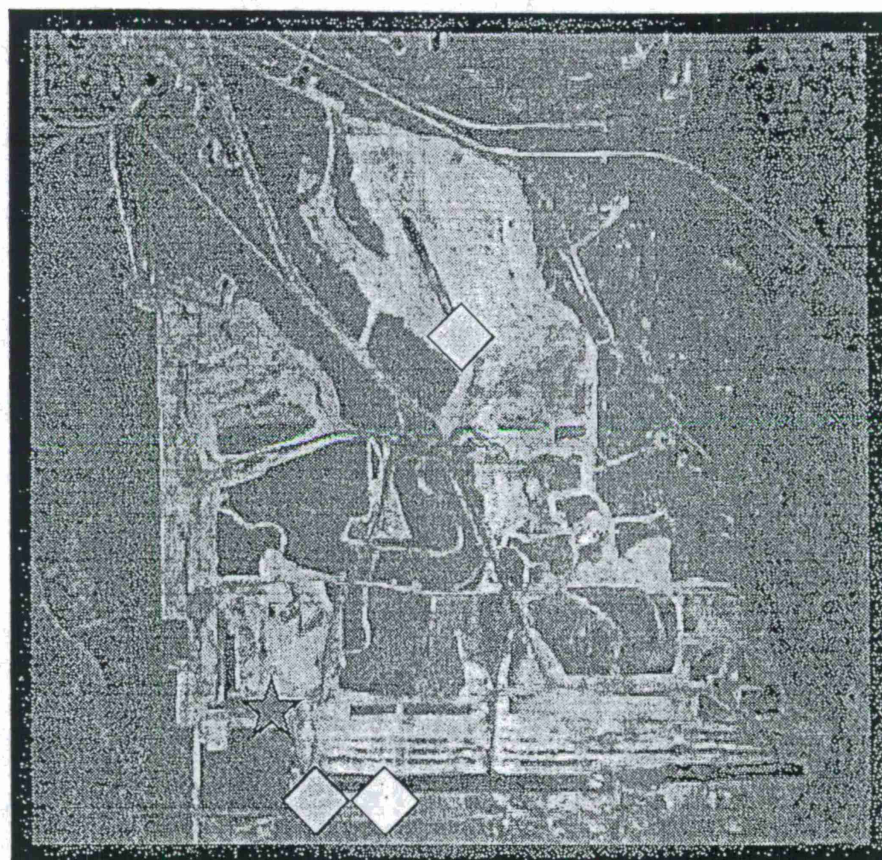


Figure 3: The 1996 Wyoming regional deployment. Although this paper is concerned with seismic results the deployment also consisted of a three station (100 m aperture) infrasound array located at MNTA and continuous GPS receivers placed at 3 sites. The GPS receivers were deployed to scan for ionospheric perturbations caused by the the acoustic pulse rising from mine shots (Calais *et al.*, 1997). Two of the receivers were located within the first quiet zone where infrasound would likely be ineffective.

Outliers Although the misclassification statistics quoted above are promising, the time-frequency discriminant, like any other, is not perfect - it alone is not the antidote for the small event discrimination problem. Some of the events may have been misclassified because they were misidentified in the first place - *i.e.* the algorithm is simply correcting the *apriori* information. Perhaps a few mining events were misidentified because millisecond delays were not used. It seems more likely that the *apriori* identifications are correct, that millisecond delays were used and errors have been made because of some inadequacy of the approach. There is much to be learned from the mistakes - what is the physics underlying the outliers? Although many causes of outliers of this sort have been proposed (see summary

The Black Thunder Mine



◇ July 19.1996 ◇ August 2.1996
 ◆ August 1.1996 ★ Observation pt.

Figure 4: Satellite photo of Black Thunder. The deployment recorded 3 significant cast shots. The first two occurred in the south pit, the third was located in the northeast pit.

in Hedlin, 1997) substantial progress to a better understanding and possible remedies likely lies in careful modeling of well documented anomalous events.

The Wyoming ground truth experiment In the summer of 1996 UCSD and LANL conducted a joint ground truth regional experiment. Five broadband (STS2) seismic stations were placed around the Black Thunder coal mine in eastern Wyoming (Figures 3&4). Four of the stations were at a range of 200 km, the fifth (KRET) was located at a range of 100 km on the same azimuth as one of the outer ring stations. Although the Powder River basin mines are extremely active, and will be discussed more fully in a forthcoming paper, the events of greatest interest to us were the extensive cast shots located in the south pit of the Black Thunder coal mine (Pearson *et al.*, 1995; Stump, 1995). These multi-million pound shots are used to cast overburden to expose the coal seam. A typical cast shot will consist of ~300 shots arranged in 7 rows detonated within 4 s. Intershot delays of 35 ms, interrow delays of 235

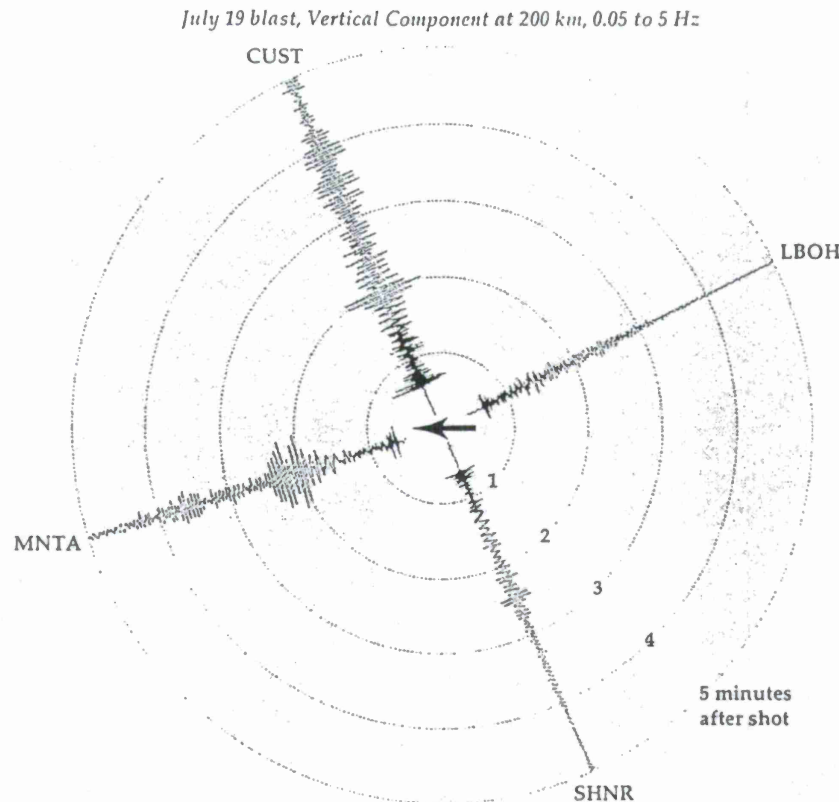


Figure 5: July 19 low (0.05 to 5 Hz) frequency radiation recorded by vertical component sensors at a range of 200 km. The shot grid detonated from East to West - in the general direction of the recordings with the most energetic surface waves. An analysis of radiation at very short ranges can be found in *Pearson et al. (1995)*.

ms (unpublished Black Thunder mine blasting report for cast shot on Aug 1, 1996) suggest modulations at every 4.2 and 30 Hz. Waveforms recorded by stations in the 200 km ring seem to be highly dependent on source-receiver azimuth (Figure 5) with, as expected (due to previous observations by Stump and colleagues at LANL) little, or no, broadband spectral modulations. This loss is easily synthesized by adding random perturbations to the shot times. This large (1.25 kT) event is a solid example of known millisecond delay-firing not yielding the expected modulations. It did not have a sympathetic component and was recorded at near-regional range with high SNR. Only two (of the numerous) explanations for this seem likely - shot scatter and waveform variability. This event also might suggest a remedy to this problem.

Low frequency traits There are numerous sources of modulations. Considering the likely effect of source finiteness on low frequencies, spectra were calculated using long (15 s) windows. Whitened log spectra from the full network (Figure 6) show clear time-independent modulations which do not depend strongly on source-receiver azimuth and recording component. The blast reports can be used to predict spectral modulation although as pointed out by *Stump et al. (1994)* this kind of calculation is only useful as a rough guide since no blast will detonate exactly as planned. Although the planned July 19 shot spanned ~ 3.5 s the bulk of the energy was expended in the middle 2 s. This leads to spectral modulations spaced \sim every 0.5 Hz - very similar to those observed in the spectra (*Hedlin, 1997*).

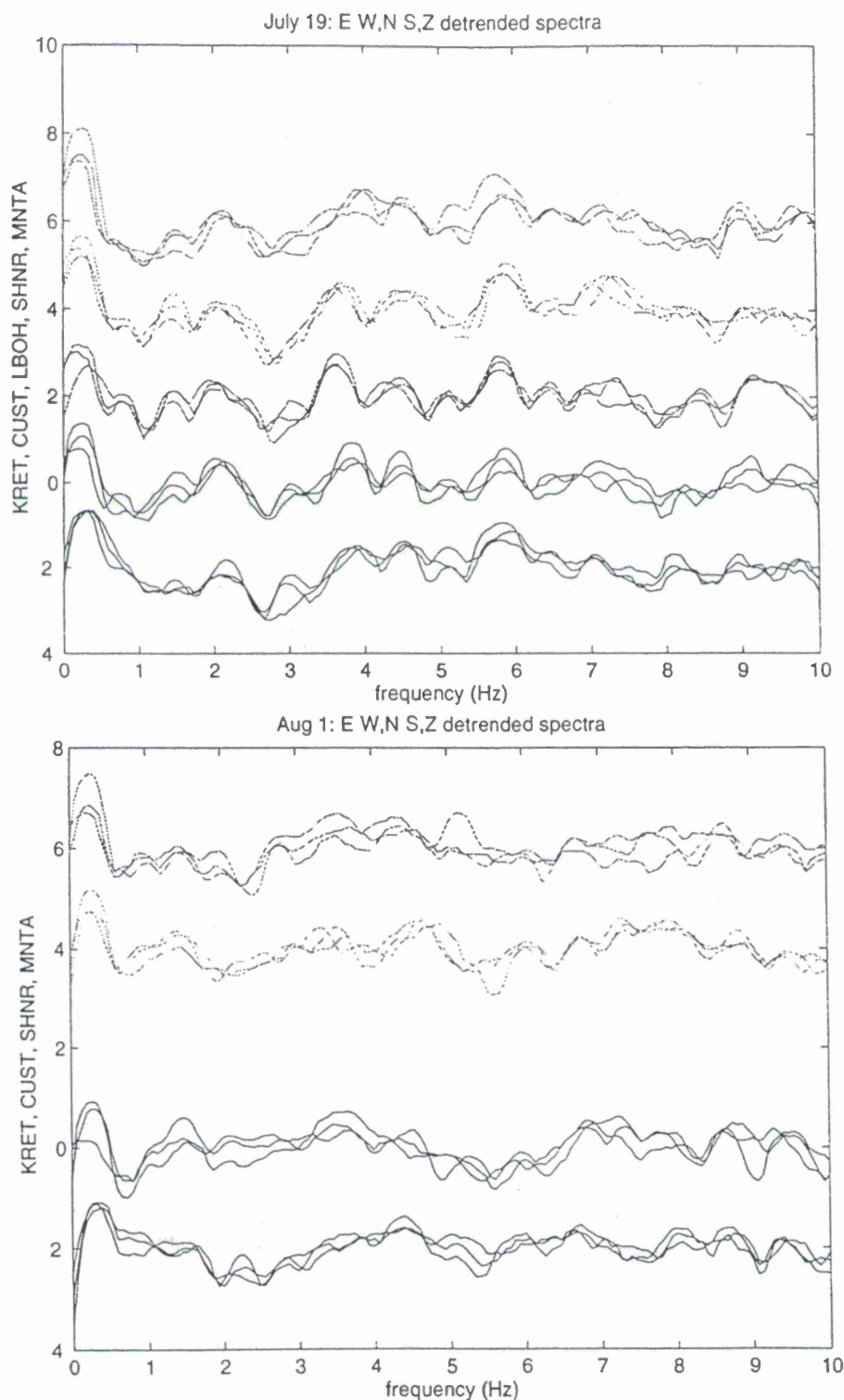


Figure 6: In the upper panel we display whitened spectra computed from the 3-Component broadband recordings of the cast shot which occurred in the Black Thunder mine on July 19, 1996. From bottom to top are spectra from KRET, CUST, LBOH, SHNR and MNTA respectively (see Figure 3). Each station has yielded three spectral estimates taken from each of the components. These spectra contain an obvious modulation which is independent of source-receiver azimuth and recording component. The lower panel shows spectra taken from recordings of the cast shot which occurred on August 1 (LBOH data were unavailable due to a problem with the instrument). These spectra possess scalloping which is more dependent on source-receiver azimuth. Although the discrepancy between the July 19 and Aug 1 spectra is as yet unexplained it likely stems from a sympathetic detonation which occurred with the cast shot on August 1. In other respects the two shots were quite similar and located side by side in the south pit.

Relatively significant modulations are expected every 2 Hz (with the most noticable one at 4 Hz). This prediction is, again, in rough agreement with what is observed in the July 19 spectra. Surprisingly, although the August 1 cast shot occurred in the same (south) mine pit and the shooting arrangement was quite similar to the July 19 shot the spectra are quite dissimilar (Figure 6). Although clear spectral modulations are present below 10 Hz they don't exhibit the same independence from recording azimuth as those in the spectra of the July 19 event. This might be due to the fact that part of the August 1 shot grid is believed to have detonated simultaneously (Brian Stump personal communication). The detonation of a significant percentage of the total explosive might have imparted an azimuthal dependence on the modulations. Although the spectra are somewhat dissimilar, the two events yielded remarkably similar waveforms at very long periods (10 to 20 s; Figure 7). Two of the stations recorded sharp low frequency pulses as expected (due to previous observations by *Anandakrishnan et al., 1997*). While two south pit shots are similar at long periods a later shot in a different pit (see Figure 4) exhibits notable differences (Figure 8).

CONCLUSIONS AND RECOMMENDATIONS

Delay fired mining blasts are extraordinarily complicated events with significant seismic energy resulting directly from the individual explosions, rock fracture and spall. We need to understand which of these source components play an important role in shaping the regional signals in time and frequency to better understand features like those mentioned above and identify which of these should be useful for discrimination. Our recent interest has been in low frequencies but our examination of energy above 10 Hz will continue as it is as yet unclear why high frequency modulations are sometimes absent. Much of the development of the automated discriminant mentioned above has been based on recordings of earthquakes and mining events. We need to do more to contrast single explosions from mining blasts. To meet these needs we have taken two steps.

A calibration experiment / Linear elastic modeling In August of 1997 a calibration experiment will be conducted at the Black Thunder mine in Wyoming in which single shots (~ 50,000 pounds) will be detonated. While the principal motive for the experiment is to study the effect of blasting on structures on the mine property these calibration shots are expected to generate significant regional seismic signals which are particularly prized because of the simplicity of the source. In early August we will reoccupy the four outer ring seismic stations (Figure 3). In collaboration with Pearson, Taylor and Yang (LANL), Stump (SMU) and Hsu (AFTAC) we will use these data and linear elastic modeling (*Anandakrishnan et al., 1997*) in part to better understand the genesis of the frequency and time domain features in the cast shots recorded last year. We intend to separate source and propagation effects and better understand which components of these complex cast shots are providing the features observed in the regional waveforms and to explain the variability like that shown in Figures 7 and 8.

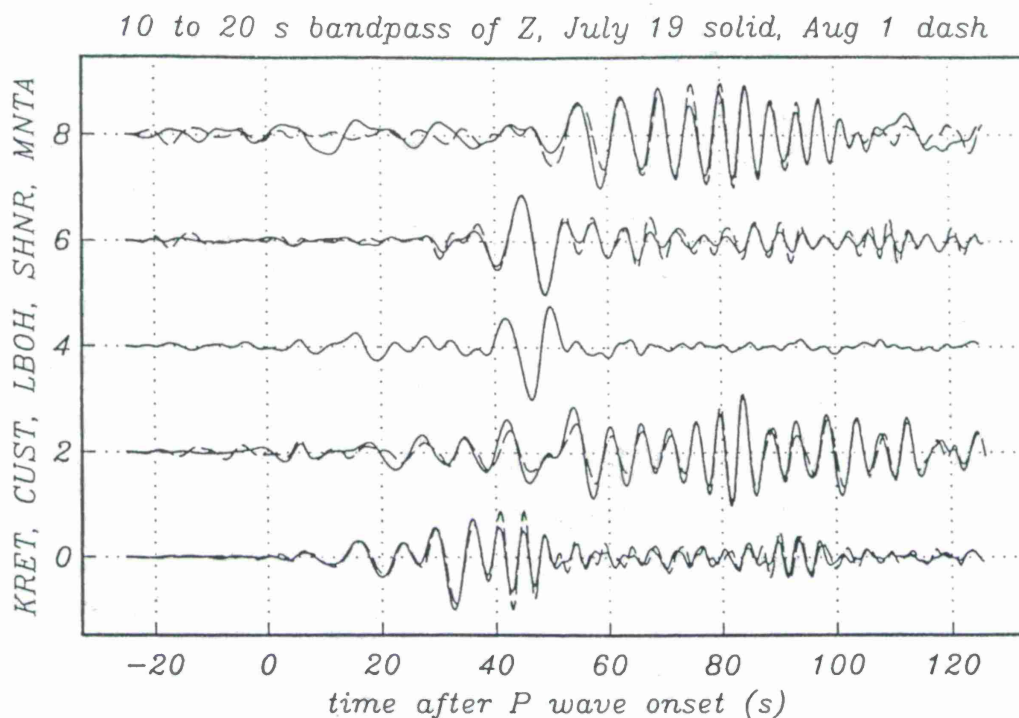


Figure 7 Time domain comparisons of the July 19 and August 1 cast shots. These vertical component timeseries have been bandpassed between 10 and 20 seconds. Despite the sympathetic detonation of part of the August 1 cast shot the two sets of recordings are similar although there is a strong azimuthal dependence. Some of the traces (e.g. LBOH, SHNR) display a sharp pulse previously observed in cast shot recordings made at PDAR (Anandakrishnan *et al.*, 1997). Data from the 1997 calibration experiment should help us determine which aspects of these waveforms are due to the source and which were acquired during propagation.

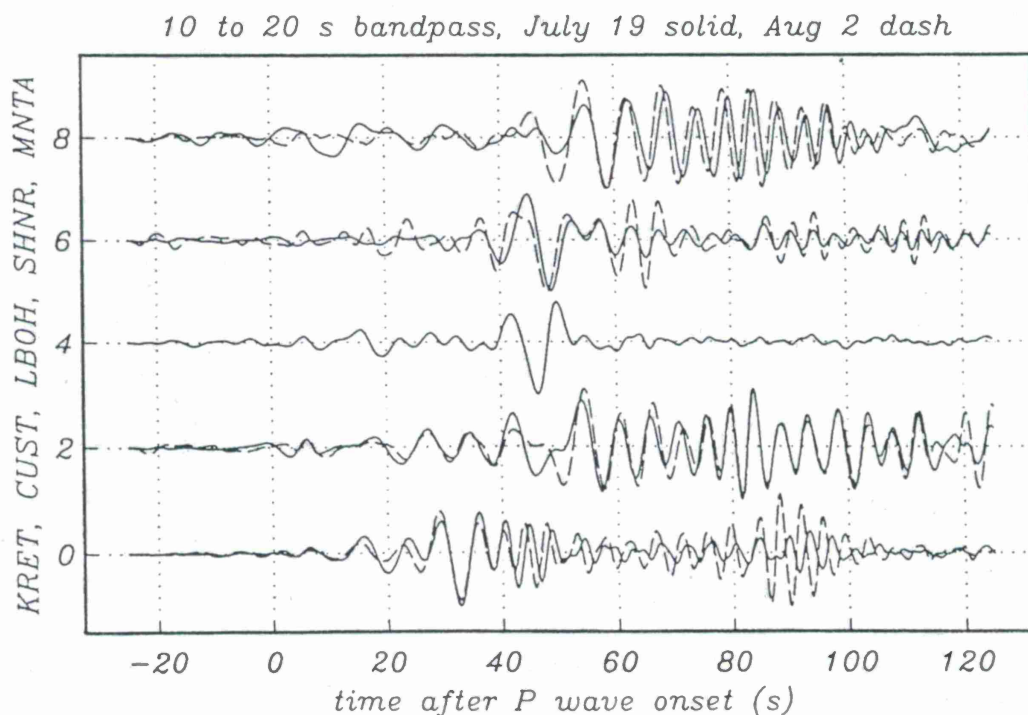


Figure 8 This figure is the same in all respects to Figure 7 except the July 19 south pit event is being compared with an event which occurred in the northeast pit (Figure 4).

Loss of high frequency modulations Our upcoming analysis of the Wyoming data might give us a better understanding of why high frequency modulations are sometimes absent. It seems likely that the dominant factor is shot scatter but waveform variability (Baumgardt, 1996) cannot be ruled out.

Multiple vs single explosions By necessity we have paid the closest attention to the problem of discriminating quarry blasts from earthquakes - single large chemical shots are in short supply. We expect that earthquakes should not yield coda with time- or component-independent spectral qualities and thus have used them to serve as proxies for single explosions. However, the most challenging and interesting problem involves the discrimination of single and multiple explosions. Although we haven't analyzed a large number of single explosions (3 recorded by the NRDC network in Kazakhstan) it appears that the ATFD is effective at separating these event types. To further address this problem we will examine the single explosions recorded during the 1995 Black Thunder experiment (Stump *et al.*, 1995; Pearson *et al.*, 1995) and use recordings of calibration shots made in Wyoming in 1997.

Broaden global test In the coming year we will broaden the scope of our test of the ATFD by analyzing data at greater ranges and in regions not closely studied before. We will examine data collected by the Saudi Network (Vernon *et al.*, 1996). We will consider dual (seismic and acoustic) monitoring technology in our analysis of the data collected in Wyoming during the summer of 1996.

Wavelet expansions We are attempting a fuller analysis of quarry blast coda using wavelets developed by Lilly & Park (1995) which yield time-frequency expansions of the spectral energy and polarization.

REFERENCES

- Anandakrishnan, S., Taylor, S.R. & Stump, B.W., 1997, Quantification and Characterization of Regional Seismic Signals from Cast Blasting in Mines: A Linear Elastic Model, *Geophysical Journal International*, *in press*.
- Baumgardt, D.R., 1996, Case studies of seismic discrimination problems and regional discriminant transportability, PL final report PL-TR-95-2106.
- Calais, E., Minster, J.B., Hofton, M. & Hedlin, M.A.H., 1997, Ionospheric signature of surface mine blasts from Global Positioning System measurements, *manuscript to be submitted to the Geophysical Journal International*.
- Hedlin, M.A.H., 1997, A global test of a time-frequency small-event discriminant, in review with the *Bulletin of the Seismological Society of America*.
- Lilly, J. & Park, J., 1995, Multiwavelet spectral and polarization analyses of seismic records, *Geophysical Journal International*, **122**, 1001-1021.
- Pearson, D.C., Stump, B.W., Baker, D.F. & Edwards, C.L., 1995, The LANL/LLNL/AFTAC Black Thunder Mine regional mining blast experiment, *proceedings of the 17th Seismic Research Symposium on Monitoring a CTBT*, Scottsdale, AZ, Sept, p562-571.
- Stump, B.W., 1995, Practical observations of US mining practices and implications for CTBT monitoring, *Phillips Lab report*, PL-TR-95-2108.
- Stump, B.W., Pearson, D.C., Edwards, C.L. & Baker, D.F., 1995, The LANL Source Geometry Experiment, *proceedings of the 17th Seismic Research Symposium on Monitoring a CTBT*, Scottsdale, AZ, Sept, p684-693, PL-TR-95-2108, ADA310037.
- Vernon, F.L., Mellors, R.J., Berger, J., Al-Amri, A.M. & Zollweg, J., 1996, Initial Results from the Deployment of Broadband Seismometers in the Saudi Arabian Shield, *proceedings of the 18th Seismic Research Symposium*, Annapolis, MD, Sept 4-6, PL-TR-96-2153.

EVALUATION OF INTERMEDIATE-PERIOD RAYLEIGH WAVE GROUP VELOCITY MODELS

David G.Harkrider, Institute of Scientific Research, Boston College
Contract No. F19628-95-C-0116
Sponsored by Phillips Laboratory

ABSTRACT

The evaluation of 11 Rayleigh wave global group velocity dispersion models is presented. The period range of most of the models is from 10 to 100 seconds. The test data base of observed explosion Rayleigh waves consists of arrival time periods from 17 to 67 seconds. The arrival time test of the models was restricted to periods of 40 seconds and less. A description and historical background of the development of each model is given. The global grid sizes range from 1x1 degrees to 10x10 degree models. The majority of the models are 5x5 degrees including the "Stevens May 97" model, which was judged as the best. The test results are given in four tables

OBJECTIVE:

To collect existing intermediate period regional Rayleigh wave group velocity models and incorporate them into a coherent global regionalization grid model for use in association codes for finding the surface wave associated with an event and improving its signal to noise ratio by match phase filtering for better magnitude and source mechanism determinations.

RESEARCH ACCOMPLISHED:

The research accomplished includes a description of the various global models tested, the test data, and the results of the model tests.

HISTORICAL GLOBAL MODELS

In the late 1960's, Kimbal and Kovacs of GEOTECH, developed a 1x1 degree global grid of Rayleigh and Love surface wave group velocities. The grid was used to estimate surface wave arrival times for use in seismic surface wave association codes; in other words, for determining which of many recorded surface waves is associated with a particular seismic event. The emphasis was on surface wave energy in the 17-23 second period band MS, which is used for yield estimation and as a discriminant when compared with the body wave magnitude, mb. There were 16 Rayleigh wave regions of which 9 were oceans or shallow seas. South America, Australia and Antarctica were considered the same group velocity region. The group velocity dispersion curves were from Santo&Saito(1966) and Santo(1968). Outside the 17-23 second period range, the velocities and more important the shape of these regionalized dispersion curves from 10-50 seconds did not agree with observations and were of no use for phase matched filtering, a common technique for finding and extracting surface wave signals from noise.

In 1977, Okal introduced a 15x15 degree global grid for long-period Rayleigh waves. Okal&Talandier(1989), using the 5x5 degree global tectonic regionalization(GTR1) of Jordan(1981) as a guide, presented a 10x10 degree grid of Rayleigh group velocities. They used the seven basic regions of Okal(1977) (four oceanic regions, shield, trench and mountain) with velocities in the period range from 300 to 35 seconds. The ocean velocities were from Yu&Mitchell(1977) and Mitchell&Yu(1980) and the regionalization was based on ocean ages. Mitchell and Yu also determined separate SV and SH velocity profiles to approximate the anisotropy of the oceanic lithosphere and low velocity zone. Shield, mountain, trench and subduction zone velocities were taken from Nakanishi(1981) and Hwang&Mitchell(1987). Since 1989, Okal and students, Mark Woods in particular, have extended the velocities down to 17 seconds. Since the early 90's, this model has been used by AFTAC and is referred to as the "Okal Woods 10x10 degree" model.

Since March of 1996, Jeff Stevens of SCUBE and I have been responsible for modernising AFTAC's long-period global association capabilities. Stevens has concentrated on improving their regional Rayleigh wave group velocity curves in the period range of 10 to 50 seconds for the purpose of match phase filtering. I have spent most of my effort on testing various global regional Rayleigh group velocity models in the period range of 17-23 seconds with group arrival times compiled by Yacoub of AFTAC for various seismic event to station pairs. This period range is used to make the surface wave magnitude measurement. In April of 1997, I included the averaged explosion data of

Stevens at 20, 28.57, and 40 seconds period as part of the data test bed for the models.

Jordan's model GTR1 has 6 regions with 3 ocean regions based on age and was presented mainly as a geographic framework in order to test new tectonic models or velocity structures as more observations and dispersion values became available. The regional dispersion was Rayleigh wave phase velocities from 20 to 120 seconds based on representative curves from Brune&Dorman(1963), Landisman et al.(1969) and the Knopoff UCLA group. Rosa (1986) performed a numerical differentiation of the scanned phase velocities to obtain group velocities. Since the periods of Yacoub's group arrival test data were mostly less than the frequency end-point of 20 seconds(the least reliable of the differenced curves), we were not able to use the majority of Yacoub's test data source-receiver pairs to perform a meaningful test of GTR1. With addition of Stevens data, which restricted the periods for an event or averaged regional event to a particular period and not the period with the largest spectral amplitude, we were able to add GTR1 model to the test.

Using over 4000 source-receiver pairs, Stevens was able to perform a tomographic determination of Rayleigh group velocities from 300 to 12.5 seconds. This allowed him to refine the Okal dispersion values in the shield and sub-divide the mountain region into two. In addition, he obtained vastly improved group velocities for the trench-subduction region for a total of 8 distinct dispersion regions. This 10x10 degree model is implemented at the Prototype International Data Center. The model is referred to as "Stevens 10x10 degree" model in Table A and as the "PIDC 10x10 degree" in TABLES B,C, and D

Again using GTR1 as a guide, I interpolated the Stevens-Okal ocean and trench-subduction regionalization into a 5x5 degree global model. Each shield and mountain region of the the original 10x10 degree grids was sub-divided into four constant velocity 5x5 degree grids. Arbitrarily reducing the grid size for tomographic determined velocities can create problems, but in this case the inversion path lengths across the age boundaries for the oceanic dispersion curves of Yu&Mitchell(1979) and Mitchell&Yu (1980) were based on smooth boundaries. Thus, in the oceans, the smaller the grid, the closer to the actual path lengths used in the original inversions. This model is referred to as the "Stevens with 5x5 degree oceans" model in TABLE A and the "Stevens Hark" model in TABLES C and D.

For the purpose of obtaining a more detailed regionalization for use with regional dispersion and magnitudes, I used Mooney's global crustal structure model for calculating shorter period Rayleigh and Love wave dispersion. Originally Mooney had a 5x5 degree global grid of 52 crustal P-velocity structures down to the crust mantle interface(Moho). The crust was divided into 5-7 layers. In 1995, Mooney, Laske&Masters included S-velocity and density in the crustal models. The result was 89 seismic structures. The 5-6 layer P-velocities and interfacedepths were obtained from refraction and reflection profiles. The structures included Moho velocities and densities. There can be a water or ice layer at the surface. S-velocities and densities were obtained from some surface wave inversions, refraction profiles, observed relations between Poisson ratio, density, and depth and when all else failed, intuition. Thus, the part of the model with the most control is the P-velocity profile. For this preliminary model, Rayleigh and Love waves were calculated for periods between 7 and 50 secs. Because the structures only went to Moho depths, the oceanic group velocities are featureless at periods greater than 17 secs. This resulted from the common observation that the depth of influence in kilometers on the fundamental Rayleigh wave is approximately twice the period in seconds, and that all the ocean structures

in this model were essentially identical below a depth of 20 kms. Because of this it was suggested that at periods near 20 secs., the Mooney et al. models be used for continents and regions of thick crust in conjunction with a 5x5 degree interpolation of the ocean models of Mitchell and Yu and the trench-subduction regions of Stevens. This was accomplished again using GTR1 as a guide and is my composite grid of 94 dispersion regions, the "Mooney-Stevens" model in the TABLES.

NEW MODELS

Mooney, Laske and Masters(1997) have finalised their crust model 5.1 and released it for general use. The new crustal model has 139 distinct dispersion regions. Also released with the crustal model is Laske and Masters spherical harmonic model of the mantle's lateral and radial shear velocity variations, S16B30. The 5.1 crustal model with an earth stretching upper mantle model composed of a linear gradient starting from the "Moho" velocities of 5.1 is referred to as the "Crust 5.1 5x5 degree" in the TABLES. Earth stretching is a common technique used to approximate the effect of the earth's curvature in flat earth dispersion programs. Stevens calculated group velocities for the crustal model 5.1 overlying a laterally homogeneous PREM mantle (Dziewonski & Anderson, 1981) and found as one might expect that the ocean group velocities are much too high. This is because the upper mantle low velocity zone is much nearer to the oceans surface than the continents and the observation that the upper mantle has to be anisotropic beneath oceans (Jordan et al., 1996 and Ekstrom et al., 1996). The ocean models of Mitchell and Yu were inverted for both a low velocity zone and anisotropy and explain the relative success of the models tested above which include their ocean dispersion. Although it must be noted that Jeff used the SV shear velocity structure of the "Transverse Isotropy" PREM model in order to approximately take the effect of anisotropy into his model.

The model composed of Mooney et al.'s continents with earth stretching, Stevens' trench-subduction zones, and Mitchell and Yu's oceans is referred to as "Crust 5.1 Stevens 5x5 degree" in the TABLES. Out of curiosity, I constructed a modification of this model by keeping the Arctic dispersion of crustal model 5.1 and referred to it as "Crust 5.1 Stevens w/o Arctic" in TABLE B. It was not as good and discarded.

In the meantime Jeff Stevens continued to work on an improvement to his Crust 5.1 over PREM model since the dispersion curves derived from the Mooney et al. Crust 5.1 models fit the data pretty well on continental paths at periods near 20 seconds, but were not as good on oceanic paths or at longer periods on continental paths. His new dispersion curves and global grid referred to as the "Stevens Mar 97" model in earlier versions of TABLES C and D and were developed by varying the shear velocity in the Crust 5.1 earth models (over PREM) to obtain a better fit to observed dispersion curves. He used the following dispersion data sets: the dispersion curves derived from IDC data in SCUBES annual report, all of the explosion test site dispersion curves (phase and group velocity), the Harvard global phase velocity model from Goran Ekstrom, the Eurasian group velocities of Ritzwoller and Levshin, and dispersion curves in Western Asia the Arabian shield from Brian Mitchell. Altogether, this amounted to about 90,000 data points. In particular, Jeff allowed the inversion to modify shear velocities in the crust and upper mantle up to a depth of 225 km, so it included part of the PREM model. He also excluded layers in Crust 5.1 with depth less than 3 km and/or shear velocities less than 1.5 km/sec since the data can't resolve the shallowest structure. Jeff noted that there is still room for improvement in these models, notably in the Arctic and the Western Pacific Ocean, but they

appear to be a significant improvement over any of the other dispersion models, particularly for phase-matched filtering which requires accurate dispersion curves over a broad frequency band.

In May 1997, Stevens sent me an improvement on his March model. This set of curves and corresponding global grid is derived in a similar manner by varying the shear velocities in the Mooney/Laske Crust 5.1 earth models. Most of the difference is in the ocean, where he added some additional models to correspond to ocean age, and separated the Arctic region into its own set of models. There are a total of 154 models, 5 of which (models A6-AA with very deep sediments that gave unrealistic dispersion curves) are not used. This model is referred to "Stevens May 97" model in TABLES C and D.

TEST DATA

The models were tested with Yacoub's group arrival times of the narrow band filtered(NBF) period of maximum energy in the range of 17-23 secs. The process involved applying a set of narrow band filters at successive center frequencies corresponding to integer periods in that range and determining the arrival time of the maximum amplitude. The arrival time in the test data was that corresponding to the maximum amplitude of the 7 periods. There were 18 events. The number of recording stations ranged from 13 to 82. The results are given in TABLE's A, B, and C. The number of stations for each event or an averaged test site in the case Mururoa appear in square brackets in column 1. The period of maximum amplitude depended not only on the recording station and instrument but the explosion source and site. Thus in the second column of TABLE C, the station average value of the period of maximum amplitude or group arrival time and its standard deviation are given for each event. These period values apply to TABLES A, B, and C.

Stevens' test data set was composed of the station group travel-times of 17 test sites for the frequencies .015, .02, .025, .03, .035, .04, structures for his 1986 and subsequent studies. This data is similar to the "Event" Mururoa in TABLES A, B, and C in that it is not the NBF arrival times or their event average values at common test-sites but arrival times obtained from the event-site to station structure inverted from the averaged NBF group arrival times. The dispersion data used in the inversion is obtained by first applying a set of NBF at successive center frequencies and computing the arrival times of energy envelopes in order to obtain an initial group velocity curve. The phase velocities are found next by integrating the group delays to find the phase as a function of frequency, forming a phase-matched filter, cross-correlating the filter with the seismograms, windowing the compressed signal and unrapping the residual phase spectrum to correct the initial phase estimate. The residual phase is then differentiated to obtain an improved group velocity estimate. The shear velocity structure is then found by simultaneously inverting the phase and group velocities. Now that Stevens has a decent global regionalized model, he can use the phase velocities derived from them to make phase-matched filters that he can use for further improvements in his test data set. The most representative models, which were tested with Yacoub's data in TABLE C with the exception of the Jordan Rosa model, are tested with this data for frequencies .05, .035, and .025. The results are shown in TABLE D.

The station average and its standard deviation of the relative misfit error for the observed and calculated group velocity(U) or travel time(TT) are given in the model

columns of all the TABLES. The TABLES give the misfit% as $(TT_{obs} - TT_{calc})$ divided by TT_{calc} then times 100. The column headings of the detailed test results for each model(not presented in this paper) show U_{obs} , U_{calc} , misfit%, and TT_{diff} for each station and each event. The misfit column indicates that misfit% is obtained from $(U_{calc} - U_{obs})$ divided by U_{obs} then times 100. A little algebra shows that they are the same. ,ie

$$\frac{(U_{calc} - U_{obs})}{U_{obs}} = \frac{(TT_{obs} - TT_{calc})}{TT_{calc}}$$

The program now uses the latter even though they are equivalent. Since the regionalizations were designed for predicting the arrival time at individual stations of a given event, I feel a reduction in the standard deviation is the better indicator of the success of a given model.

COMMENTS

As one might hope, the average percentage in error of the arrival times or path group velocity was reduced by the addition of the new models. Even the Mooney model with its poor oceanic dispersion was better than the Okal model, which was a major improvement over the Kimbal-Kovacs model. The reduction in arrival time error is essentially in the order of the listed models with some exceptions. Notably the Jordan-Rosa model in TABLE D, which for reasons mentioned above, only the longer periods are a fair test.

The "Stevens May 97" model does a little better on test sites (~5-10% reduction in standard deviation) and considerably better on global earthquake paths (~30% reduction in standard deviation) than the newer models based on Crust 5.1. It also correspond to a more realistic earth model. There is still room for improvement, particularly at higher frequencies, but Jeff thinks this is about as well as can be done with minor variations on the Crust 5.1 structures. Additional improvement would require additional layering and/or additional structure models and probably more and better high frequency data.

Except at the highest frequencies, the average residual is less than one percent, and the standard deviation of test site data is about 2%

CONCLUSIONS AND RECOMMENDATIONS

The 10-50 second period dispersion range of "Stevens May 97" model has also been tested for it's ability to produce phase match filters that are effective in improving signal to noise ratio of observed Rayleigh waves. That work was done by Mark Woods and he has found that it is indeed an improvement over earlier models and feels that it meets the requirements for the "90% modernization" of the NDC global surface wave association model.

There is one obvious weakness in the model and that is the ocean's azimuthally dependent anisotropy especially at the shorter periods. Work will continue in this area. It must be remembered that this model is primarily for teleseismic use in that a 5 degree global grid is too coarse for regional observations. Since the observed absence of Love waves for an event is a discriminant feature, it is also important to develop a global model for the association of Love waves.

REFERENCES

- Brune, J. & Dorman, J., 1963. Seismic waves and Earth structure in the Canadian Shield. *Bull. Seism. Soc. Am.*, 53, 167-210.
- Dziewonski, A.M. & Anderson, D.L., 1981. Preliminary reference Earth model. *Physics of the Earth and Planetary Interiors*, 25, 297-356.
- Ekstrom, G., Dziewonski, A. M., Smith, G. P. & Su, W.-J., 1996. Elastic and anelastic structure beneath Eurasia. *Proceedings of the 18th Annual Seismic Research Symposium on Monitoring a Comprehensive Test Ban Treaty*, PL-TR-96-2153, Phillips Laboratory, Massachusetts, 309-318.
- Hwang, H.-J. & Mitchell, B.J., 1987. Shear velocities, Q_b , and the frequency dependence of Q_b in stable and tectonically active regions from surface wave observations. *Geophys. J. R. astr. Soc.*, 90, 575-613.
- Jordan, T.H., 1981. Global tectonic regionalization for seismological data analysis. *Bull. Seism. Soc. Am.*, 71, 1131-1141.
- Jordan, T.H., Gaherty, J. B., Kato, M., & van Genabeek, O., 1996. Regional upper-mantle structure and their interpretation in terms of small-scale, anisotropic heterogeneities. *Proceedings of the 18th Annual Seismic Research Symposium on Monitoring a Comprehensive Test Ban Treaty*, PL-TR-96-2153, Phillips Laboratory, Massachusetts, 361-370.
- Knopoff, L., (1972). Observation and inversion of surface wave dispersion. *Tectonophysics*, 13, 497-519.
- Landisman, M., Dziewonski, A., & Sato, Y., 1969. Recent improvements in the analysis of surface wave observations. *Geophys. J.*, 17, 369-403.
- Levshin, A.L., Ritzwoller, M.H., & Smith, S.S., 1996. Group velocity variations across Eurasia. *Proceedings of the 18th Annual Seismic Research Symposium on Monitoring a Comprehensive Test Ban Treaty*, PL-TR-96-2153, Phillips Laboratory, Massachusetts, 70-79.
- Masters, T. G., Johnson S., Laske, G., & Bolton, H., 1996. A shear-velocity model of the mantle. *Phil. Trans. R. Soc. A*, 354, 1385-1411.
- Mitchell, B.J. & Yu, G.-K., 1980. Surface wave dispersion, regionalized velocity models, and anisotropy of the Pacific crust and upper-mantle. *Geophys. J. R. astr. Soc.*, 63, 497-514.
- Mooney, W.D., Gabi, L. & Masters, T.G., 1997. Crust 5.1: A global crustal model at 5 deg x 5 deg. *J. Geophys. Res.*, in press.
- Nakanishi, I., 1981. Shear velocity and shear attenuation models inverted from the worldwide and pure-path average data of mantle Rayleigh waves (0S25 to 0S80) and fundamental normal modes (0S2 to 0S24). *Geophys. J. R. astr. Soc.*, 66, 83-130.
- Okal, E.A., 1977. The effect of intrinsic oceanic upper-mantle heterogeneity on the regionalization of long-period Rayleigh wave phase velocities. *Geophys. J. R. astr. Soc.*, 49, 357-370.
- Okal, E.A., 1989. A theoretical discussion of time domain magnitudes: The Prague formula for M_s and the mantle magnitude M_m . *J. Geophys. Res.*, 94, 4194-4204.
- Okal, E.A. & Talandier, J., 1989. M_m : A variable-period mantle magnitude. *J. Geophys. Res.*, 94, 4169-4193.
- Oliver, J., 1962. A summary of observed seismic surface wave dispersion. *Bull. Seism. Soc. Am.*, 52, 81-86.
- Ritzwoller, M.H., Levshin, A.L., Ratnikova, L.I. & Tremblay, D.M., 1996. High resolution group velocity variations across central Asia. *Proceedings of the 18th Annual*

- Seismic Research Symposium on Monitoring a Comprehensive Test Ban Treaty, PL-TR-96-2153, Phillips Laboratory, Massachusetts, 98-107.
- Rosa, J.W.C., 1986. A global study of phase velocity, group velocity, and attenuation of Rayleigh waves in the period range 20 to 100 seconds. Ph.D.thesis, Mass. Inst. Tech., Cambridge.
- Santo, T. & Sato, Y., 1966. World-wide survey of the regional characteristics of group velocity dispersion of Rayleigh waves, Bull. Eq. Res. Inst., 44, 939-964.
- Santo, T., 1968. Lateral variation of Rayleigh wave dispersion character. Part V. North American continent and Arctic Ocean. Bull. Eq. Res. Inst., 46, 431-456.
- Schule, J.W. & Knopoff, L., 1977. Shear-wave polarization anisotropy in the Pacific Basin. Geophys. J., 49, 145-165.
- Stevens, J.L. & McLaughlin, K.L., 1996. A transportable regional discriminant using a maximum likelihood analysis of surface waves. Proceedings of the 18th Annual Seismic Research Symposium on Monitoring a Comprehensive Test Ban Treaty, PL-TR-96-2153, Phillips Laboratory, Massachusetts, 622-630.
- Yu, G.-K. & Mitchell, B.J., 1978. Regionalized shear velocity models of the Pacific upper mantle from observed Love and Rayleigh dispersion. Geophys. J. R. astr. Soc., 57, 311-341.

TABLE A

Surface Wave Regionalization Models Rayleigh Wave Travel Time(TT) Test Results								
Avg. $\langle (TT_{obs} - TT_{calc}) / TT_{calc} \rangle \times 100$ (SD)								
Models Events [#sta.]	Kimbal Kovacs 1°x1°	Okal Woods 10°x10°	Mooney 5°x5°	Stevens 10°x10°	Stevens with 5°x5° oceans	Mooney Stevens 5°x5°	Crust 5.1 5°x5°	Crust 5.1 Stevens 5°x5°
Yucca Flat [23]	-5.94 (5.23)	-3.29 (4.45)	-2.84 (4.92)	-2.57 (5.18)	-2.31 (5.14)	-2.65 (3.41)	-2.15 (4.58)	-1.83 (3.28)
Yucca Flat [41]	-4.94 (5.07)	-2.48 (4.45)	-2.43 (3.40)	-1.96 (5.05)	-1.80 (4.96)	-2.38 (2.75)	-1.87 (2.96)	-1.70 (2.51)
Yucca Flat [27]	-7.84 (3.48)	-4.31 (3.90)	-3.41 (2.17)	-3.19 (4.55)	-3.20 (4.52)	-3.38 (2.20)	-2.15 (2.38)	-2.13 (2.40)
Qinnger [32]	-4.60 (7.01)	-1.73 (3.94)	-1.50 (2.85)	-1.83 (2.57)	-1.81 (2.59)	-0.80 (2.51)	-1.92 (3.25)	-1.29 (2.64)
Shagan River [26]	-3.69 (6.36)	-1.80 (4.80)	-1.57 (3.57)	-1.80 (3.58)	-1.60 (3.65)	-1.24 (3.04)	-0.43 (3.38)	0.06 (2.91)
Pahute Mesa [33]	-4.24 (4.85)	-2.10 (4.40)	-2.18 (3.05)	-1.75 (5.35)	-1.55 (5.44)	-1.92 (3.15)	-1.86 (2.61)	-1.36 (2.95)
Pahute Mesa [18]	-2.99 (5.95)	-1.91 (4.42)	-1.91 (2.93)	-1.59 (5.30)	-1.61 (5.28)	-1.75 (3.08)	-1.65 (2.07)	-1.36 (2.58)
Pahute Mesa [23]	-5.45 (4.54)	-2.79 (5.46)	-2.03 (3.68)	-1.89 (5.86)	-1.82 (5.81)	-2.11 (3.63)	-1.46 (3.32)	-1.36 (3.48)
Pahute Mesa [27]	-6.03 (2.76)	-2.79 (4.42)	-3.23 (2.21)	-2.80 (5.29)	-2.81 (5.52)	-3.06 (2.23)	-2.42 (2.31)	-2.24 (2.31)
Pahute Mesa [28]	-6.34 (3.34)	-3.05 (4.55)	-3.09 (2.25)	-2.78 (5.30)	-2.80 (5.24)	-3.02 (2.32)	-2.07 (2.20)	-1.98 (2.28)
Novaya Zemlya [19]	0.94 (5.07)	5.32 (4.80)	-1.37 (3.11)	3.12 (4.54)	3.14 (4.55)	-0.11 (2.67)	-0.97 (2.76)	0.17 (2.01)
Novaya Zemlya [22]	-2.03 (6.08)	5.53 (7.17)	-0.83 (6.34)	4.14 (7.11)	4.24 (7.23)	0.23 (4.86)	-0.29 (5.67)	0.72 (3.87)
Novaya Zemlya [21]	2.72 (5.79)	7.64 (5.83)	-0.91 (6.47)	5.11 (5.96)	5.13 (5.97)	1.32 (5.43)	-0.89 (5.83)	1.22 (4.90)
Mururoa [13]	-1.48 (2.95)	-2.33 (2.78)	-2.75 (2.14)	-1.99 (2.50)	-1.68 (1.86)	-0.80 (1.99)	-1.62 (2.26)	-0.93 (1.96)
Longshot [33]	2.92 (6.80)	-4.42 (6.10)	1.17 (5.96)	-1.71 (5.68)	-0.53 (6.41)	-0.56 (6.06)	0.02 (6.12)	-0.56 (6.05)
Milrow [55]	3.49 (4.40)	-2.34 (5.63)	1.68 (4.75)	-0.14 (4.76)	0.69 (4.92)	0.43 (4.78)	0.67 (5.03)	0.18 (4.72)
Cannikin [82]	3.52 (4.63)	-2.29 (6.78)	1.70 (4.84)	0.13 (4.98)	1.02 (5.25)	0.62 (4.89)	0.96 (4.64)	0.57 (4.56)

TABLE B

Surface Wave Regionalization Models Rayleigh Wave Travel Time(TT) Test Results							
Avg. $\langle (TT_{obs} - TT_{calc}) / TT_{calc} \rangle \times 100$ (SD)							
Models Events [#sta.]	Kimbal Kovacs 1°x1°	Okal Woods 10°x10°	PIDC 10°x10°	Mooney Stevens 5°x5°	Crust 5.1 5°x5°	Crust 5.1 Stevens 5°x5°	Crust 5.1 Stevens w/o Arctic
Yucca Flat [23]	-5.94 (5.23)	-3.29 (4.45)	-2.57 (5.18)	-2.65 (3.41)	-2.15 (4.58)	-1.83 (3.28)	-2.07 (3.90)
Yucca Flat [41]	-4.94 (5.07)	-2.48 (4.45)	-1.96 (5.05)	-2.38 (2.75)	-1.87 (2.96)	-1.70 (2.51)	-1.80 (2.53)
Yucca Flat [27]	-7.84 (3.48)	-4.31 (3.90)	-3.19 (4.55)	-3.38 (2.20)	-2.15 (2.38)	-2.13 (2.40)	-2.13 (2.40)
Qinnger [32]	-4.60 (7.01)	-1.73 (3.94)	-1.83 (2.57)	-0.80 (2.51)	-1.92 (3.25)	-1.29 (2.64)	-1.98 (3.22)
Shagan River [26]	-3.69 (6.36)	-1.80 (4.80)	-1.80 (3.58)	-1.24 (3.04)	-0.43 (3.38)	0.06 (2.91)	-0.37 (3.43)
Pahute Mesa [33]	-4.24 (4.85)	-2.10 (4.40)	-1.75 (5.35)	-1.92 (3.15)	-1.86 (2.61)	-1.36 (2.95)	-1.39 (2.97)
Pahute Mesa [18]	-2.99 (5.95)	-1.91 (4.42)	-1.59 (5.30)	-1.75 (3.08)	-1.65 (2.07)	-1.36 (2.58)	-1.36 (2.58)
Pahute Mesa [23]	-5.45 (4.54)	-2.79 (5.46)	-1.89 (5.86)	-2.11 (3.63)	-1.46 (3.32)	-1.36 (3.48)	-1.36 (3.48)
Pahute Mesa [27]	-6.03 (2.76)	-2.79 (4.42)	-2.80 (5.29)	-3.06 (2.23)	-2.42 (2.31)	-2.24 (2.31)	-2.37 (2.43)
Pahute Mesa [28]	-6.34 (3.34)	-3.05 (4.55)	-2.78 (5.30)	-3.02 (2.32)	-2.07 (2.20)	-1.98 (2.28)	-2.02 (2.30)
Novaya Zemlya [19]	0.94 (5.07)	5.32 (4.80)	3.12 (4.54)	-0.11 (2.67)	-0.97 (2.76)	0.17 (2.01)	-0.92 (2.73)
Novaya Zemlya [22]	-2.03 (6.08)	5.53 (7.17)	4.14 (7.11)	0.23 (4.86)	-0.29 (5.67)	0.72 (3.87)	-0.30 (5.64)
Novaya Zemlya [21]	2.72 (5.79)	7.64 (5.83)	5.11 (5.96)	1.32 (5.43)	-0.89 (5.83)	1.22 (4.90)	-0.70 (6.00)
Mururoa [13]	-1.48 (2.95)	-2.33 (2.78)	-1.99 (2.50)	-0.80 (1.99)	-1.62 (2.26)	-0.93 (1.96)	-0.93 (1.96)
Longshot [33]	2.92 (6.80)	-4.42 (6.10)	-1.71 (5.68)	-0.56 (6.06)	0.02 (6.12)	-0.56 (6.05)	-1.13 (5.91)
Milrow [55]	3.49 (4.40)	-2.34 (5.63)	-0.14 (4.76)	0.43 (4.78)	0.67 (5.03)	0.18 (4.72)	-0.48 (4.86)
Cannikin [82]	3.52 (4.63)	-2.29 (6.78)	0.13 (4.98)	0.62 (4.89)	0.96 (4.64)	0.57 (4.56)	-0.09 (4.56)

TABLE C

Surface Wave Regionalization Models Rayleigh Wave Travel Time(TT) Test Results									
Avg. $\langle (TT_{obs} - TT_{calc}) / TT_{calc} \rangle \times 100$ (SD)									
Models Events [#sta.]	Period sec	Kimbal Kovacs 1°x1°	Okal Woods 10°x10°	PIDC 10°x10°	Stevens Hark 5°x5°	Mooney Stevens 5°x5°	Crust 5.1 5°x5°	Crust 5.1 Stevens 5°x5°	Stevens May 97
Yucca Flat [23]	17.83 (1.40)	-5.94 (5.23)	-3.29 (4.45)	-2.57 (5.18)	-2.31 (5.14)	-2.65 (3.41)	-2.15 (4.58)	-1.83 (3.28)	-0.30 (3.72)
Yucca Flat [41]	17.83 (1.46)	-4.94 (5.07)	-2.48 (4.45)	-1.96 (5.05)	-1.80 (4.96)	-2.38 (2.75)	-1.87 (2.96)	-1.70 (2.51)	-0.02 (2.61)
Yucca Flat [27]	17.33 (1.27)	-7.84 (3.48)	-4.31 (3.90)	-3.19 (4.55)	-3.20 (4.52)	-3.38 (2.20)	-2.15 (2.38)	-2.13 (2.40)	-0.68 (2.15)
Qinnger [32]	19.62 (1.83)	-4.60 (7.01)	-1.73 (3.94)	-1.83 (2.57)	-1.81 (2.59)	-0.80 (2.51)	-1.92 (3.25)	-1.29 (2.64)	-1.00 (1.41)
Shagan River [26]	18.65 (2.15)	-3.69 (6.36)	-1.80 (4.80)	-1.80 (3.58)	-1.60 (3.65)	-1.24 (3.04)	-0.43 (3.38)	0.06 (2.91)	0.60 (2.18)
Pahute Mesa [33]	17.64 (1.25)	-4.24 (4.85)	-2.10 (4.40)	-1.75 (5.35)	-1.55 (5.44)	-1.92 (3.15)	-1.86 (2.61)	-1.36 (2.95)	0.11 (2.41)
Pahute Mesa [18]	17.94 (1.73)	-2.99 (5.95)	-1.91 (4.42)	-1.59 (5.30)	-1.61 (5.28)	-1.75 (3.08)	-1.65 (2.07)	-1.36 (2.58)	0.45 (2.18)
Pahute Mesa [23]	17.96 (1.46)	-5.45 (4.54)	-2.79 (5.46)	-1.89 (5.86)	-1.82 (5.81)	-2.11 (3.63)	-1.46 (3.32)	-1.36 (3.48)	-0.06 (3.06)
Pahute Mesa [27]	17.33 (0.62)	-6.03 (2.76)	-2.79 (4.42)	-2.80 (5.29)	-2.81 (5.52)	-3.06 (2.23)	-2.42 (2.31)	-2.24 (2.31)	-0.64 (1.16)
Pahute Mesa [28]	17.46 (0.84)	-6.34 (3.34)	-3.05 (4.55)	-2.78 (5.30)	-2.80 (5.24)	-3.02 (2.32)	-2.07 (2.20)	-1.98 (2.28)	-0.42 (1.54)
Novaya Zemlya [19]	18.47 (1.65)	0.94 (5.07)	5.32 (4.80)	3.12 (4.54)	-3.14 (4.55)	-0.11 (2.67)	-0.97 (2.76)	0.17 (2.01)	0.30 (1.81)
Novaya Zemlya [22]	18.36 (1.73)	-2.03 (6.08)	5.53 (7.17)	4.14 (7.11)	4.24 (7.23)	0.23 (4.86)	-0.29 (5.67)	0.72 (3.87)	1.08 (3.46)
Novaya Zemlya [21]	18.24 (1.41)	2.72 (5.79)	7.64 (5.83)	5.11 (5.96)	5.13 (5.97)	1.32 (5.43)	-0.89 (5.83)	1.22 (4.90)	1.03 (3.53)
Mururoa [13]	20.00	-1.48 (2.95)	-2.33 (2.78)	-1.99 (2.50)	-1.68 (1.86)	-0.80 (1.99)	-1.62 (2.26)	-0.93 (1.96)	-0.46 (2.08)
Longshot [33]	20.09 (1.99)	2.92 (6.80)	-4.42 (6.10)	-1.71 (5.68)	-0.53 (6.41)	-0.56 (6.06)	0.02 (6.12)	-0.56 (6.05)	1.42 (5.62)
Milrow [55]	20.45 (2.02)	3.49 (4.40)	-2.34 (5.63)	-0.14 (4.76)	0.69 (4.92)	0.43 (4.78)	0.67 (5.03)	0.18 (4.72)	1.91 (3.86)
Cannikin [82]	20.72 (2.07)	3.52 (4.63)	-2.29 (6.78)	0.13 (4.98)	1.02 (5.25)	0.62 (4.89)	0.96 (4.64)	0.57 (4.56)	1.99 (4.27)

TABLE D

Surface Wave Regionalization Models Rayleigh Wave Travel Time(TT) Test Results									
Avg. $\langle (TT_{obs} - TT_{calc}) / TT_{calc} \rangle \times 100$ (SD)									
Models Events [#sta.]	Period sec	Kimbal Kovacs 1°x1°	Jordan Rosa 5°x5°	Okal Woods 10°x10°	PIDC 10°x10°	Stevens Hark 5°x5°	Crust 5.1 5°x5°	Crust 5.1 Stevens 5°x5°	Stevens May 97
Amchitka [54]	20.00	2.97 (4.48)	4.15 (4.55)	-3.04 (4.94)	-1.23 (4.43)	-0.21 (4.63)	-0.50 (4.71)	-0.54 (4.62)	1.07 (3.72)
Amchitka [56]	28.57	1.24 (2.16)	-0.53 (4.00)	-9.14 (5.05)	0.25 (2.42)	0.37 (2.46)	0.54 (2.38)	1.36 (2.43)	-0.32 (1.91)
Amchitka [55]	40.00	0.92 (1.89)	-1.17 (2.89)	-10.39 (4.74)	1.68 (1.58)	1.56 (1.53)	2.29 (1.78)	2.93 (1.91)	0.14 (1.41)
E.Kazakh [40]	20.00	-3.32 (4.51)	8.20 (3.82)	-2.46 (3.42)	-2.61 (3.24)	-2.58 (3.25)	-1.48 (2.46)	-1.31 (2.48)	-0.88 (2.04)
E.Kazakh [40]	28.57	4.14 (2.44)	10.28 (5.22)	-3.24 (4.49)	-0.26 (3.18)	-0.27 (3.14)	1.27 (2.51)	1.37 (2.51)	0.59 (1.79)
E.Kazakh [40]	40.00	2.24 (3.44)	6.03 (5.59)	-4.87 (4.37)	1.20 (3.53)	1.17 (3.53)	4.63 (3.23)	4.64 (3.24)	0.94 (2.25)
Hoggar [5]	20.00	5.97 (5.42)	8.03 (4.24)	-1.43 (2.86)	-2.33 (4.06)	-2.33 (4.05)	-1.60 (2.23)	-1.60 (2.23)	1.39 (1.62)
Hoggar [5]	28.57	2.19 (3.80)	1.23 (2.60)	-8.14 (1.85)	-3.66 (2.74)	-3.68 (2.71)	-2.81 (2.65)	-2.48 (3.34)	-0.86 (1.85)
Hoggar [5]	40.00	0.62 (2.37)	-0.30 (1.29)	-8.30 (2.47)	-0.94 (1.71)	-0.95 (1.68)	1.55 (1.24)	1.83 (1.81)	-0.21 (0.96)
Mururoa [11]	20.00	-0.87 (2.66)	-3.21 (2.27)	-1.87 (2.74)	-1.43 (2.29)	-1.23 (1.63)	-1.13 (1.88)	-0.30 (1.33)	0.13 (1.59)
Mururoa [13]	28.57	-1.41 (2.15)	-5.08 (2.36)	-3.94 (2.15)	-1.81 (1.37)	-1.69 (1.23)	-1.05 (1.03)	-0.88 (1.03)	-0.40 (0.97)
Mururoa [13]	40.00	-0.17 (1.83)	-3.78 (1.63)	-3.67 (2.54)	-0.81 (1.73)	-0.94 (1.50)	0.61 (1.42)	-0.35 (1.50)	-0.79 (1.42)
NTS [58]	20.00	-0.74 (3.33)	5.76 (5.14)	-2.29 (4.97)	-1.82 (4.85)	-1.42 (4.58)	-2.36 (2.52)	-2.33 (2.48)	-0.55 (2.24)
NTS [59]	28.57	0.94 (2.96)	2.99 (4.52)	-6.81 (5.29)	-1.29 (2.69)	-1.06 (2.61)	-0.23 (2.49)	0.15 (2.66)	-0.09 (1.80)
NTS [59]	40.00	0.25 (2.07)	1.13 (2.28)	-7.57 (5.03)	0.93 (1.79)	1.01 (1.80)	2.79 (2.05)	2.95 (2.06)	0.19 (1.44)
Novaya Zemlya [98]	20.00	2.14 (5.09)	10.04 (6.41)	4.31 (6.87)	2.47 (6.17)	2.69 (6.09)	-1.11 (4.60)	-0.13 (4.84)	-0.31 (3.59)
Novaya Zemlya [98]	28.57	2.37 (2.36)	5.45 (3.90)	0.44 (4.66)	3.16 (3.24)	3.24 (3.22)	0.71 (2.63)	1.28 (2.85)	0.22 (1.84)
Novaya Zemlya [98]	40.00	-0.27 (2.36)	1.39 (2.74)	-2.53 (4.14)	2.04 (2.39)	2.06 (2.37)	2.46 (2.18)	2.66 (2.23)	-0.03 (2.07)

GROUND TRUTH FOR REGIONAL SEISMIC EVENTS RECORDED AT TXAR

Eugene Herrin
Southern Methodist University

Sponsored by Air Force Technical Applications Center
PL Contracts F19628-95-C-0184

ABSTRACT

TXAR is located in far west Texas only a few miles north of the border with Mexico. The seismic sources for regional events recorded at TXAR are scattered throughout northern Mexico, Texas, New Mexico and Arizona. Early analysis indicated that at least 75% of these events were industrial explosions. Whereas the mine operators in the U.S. have been helpful in identifying their explosions, we have not been able to obtain similar information from mines in Mexico. We established a four element infrasonic network within TXAR in the hope that infrasonic signals associated with surface explosions could be combined with the seismic data so as to allow identification of mining shots, particularly in Mexico. This method has proved to be very useful in this regard during periods when TXAR is in the stratospherically downwind direction from the source. Identification of a variety of seismic sources is possible using the seismo-acoustic data. These include mining and construction explosions, local explosions, shuttlequakes and bolidequakes.

Keywords: Seismic, infrasonic, ground truth, discrimination of seismic sources, TXAR.

OBJECTIVE

The objective of this study is to establish a ground truth data base for regional seismic events recorded at TXAR. Because the array is located almost on an international border, the situation is a good analog of situations that will arise when the proposed CTBT primary arrays are established. A ground truth data base for each CTBT array must be established in order to test discrimination algorithms developed elsewhere.

RESEARCH ACCOMPLISHED

An infrasonic array has been established at TXAR and has proved very useful in the identification of sources that produce both seismic and infrasonic signals. The seismo-acoustic analysis process we developed has allowed the construction of a large ground truth data base without direct information regarding the sources.

CONCLUSIONS AND RECOMMENDATIONS

A number of features may be used to group regional seismic events into clusters.

Associated infrasonic signals can be used to identify some of the clusters as commercial explosions.

Seismic events that do not fall into the usual categories - commercial explosions and earthquakes - may be identified using both seismic and acoustic data. Examples are shuttlequakes and bolidequakes.

The establishment of a small infrasonic array at a primary CTBT seismic station greatly increases the discrimination capability of the station.

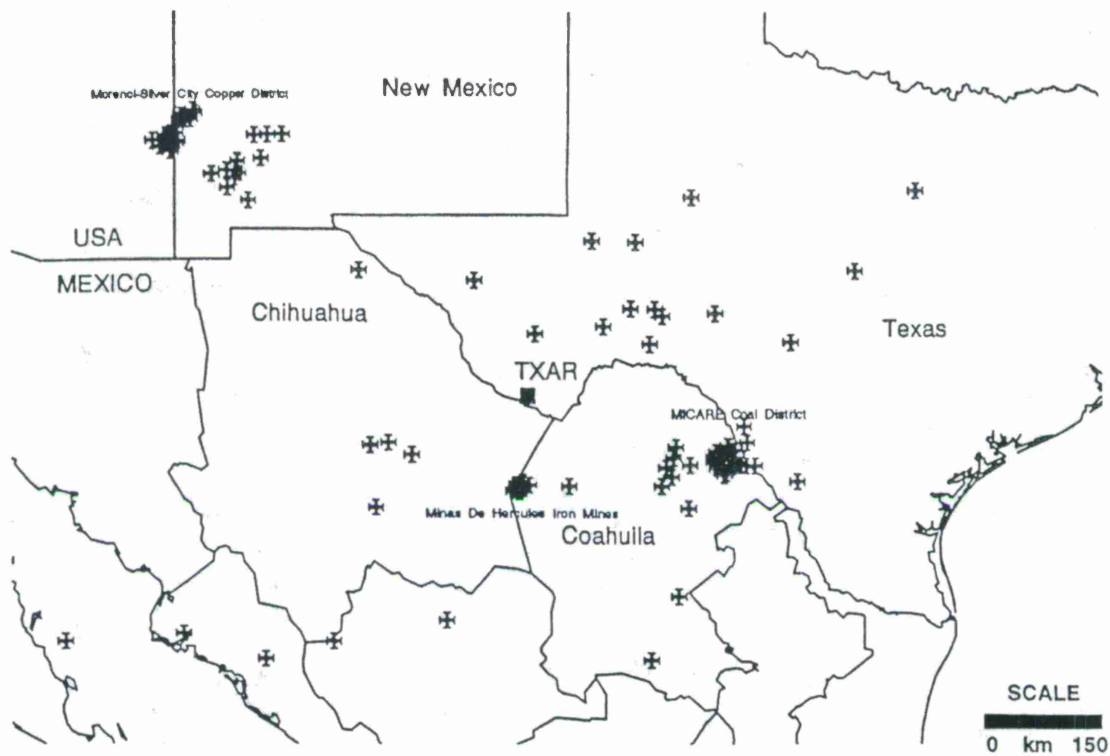


Figure 1. Location of events recorded at TXAR between July 15, 1996 and August 10, 1996.

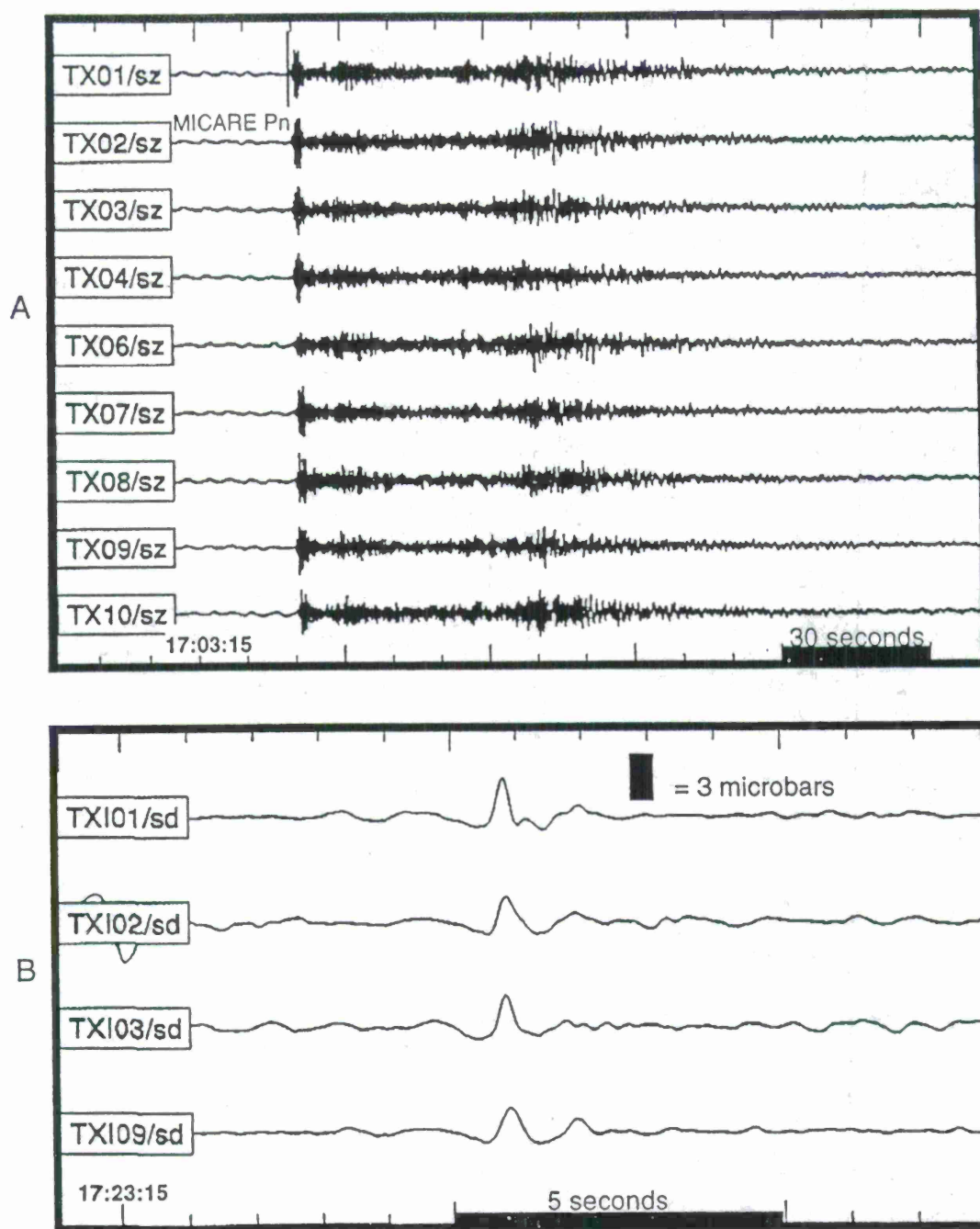
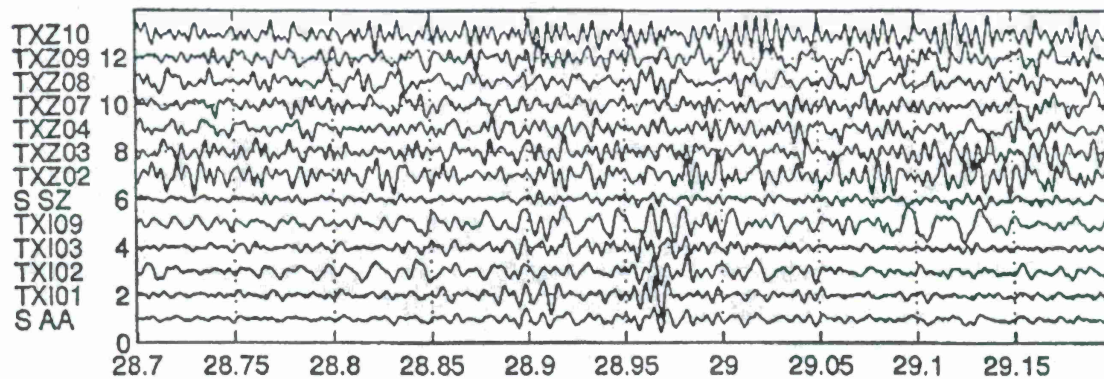


Figure 2. Seismograms (A) and barograms (B) from an explosion in the MICARE mining district of northern Mexico

Tyrone AZ explosion 11 October 1996 546.0 km 0.75-5 Hz shifted: 325 deg 0.35 km/s



1.025 second semblance filtered signal Semblance power 3

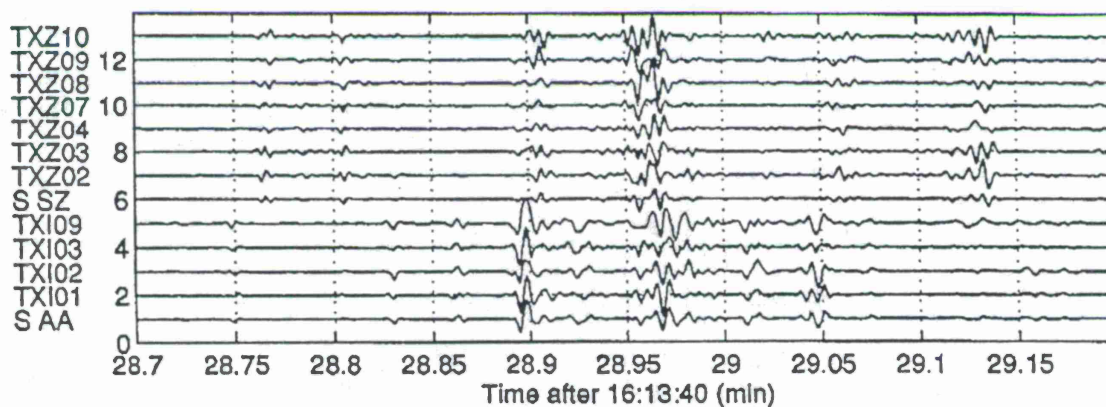


Figure 3. Results of semblance processing on seismo-acoustic data at TXAR.

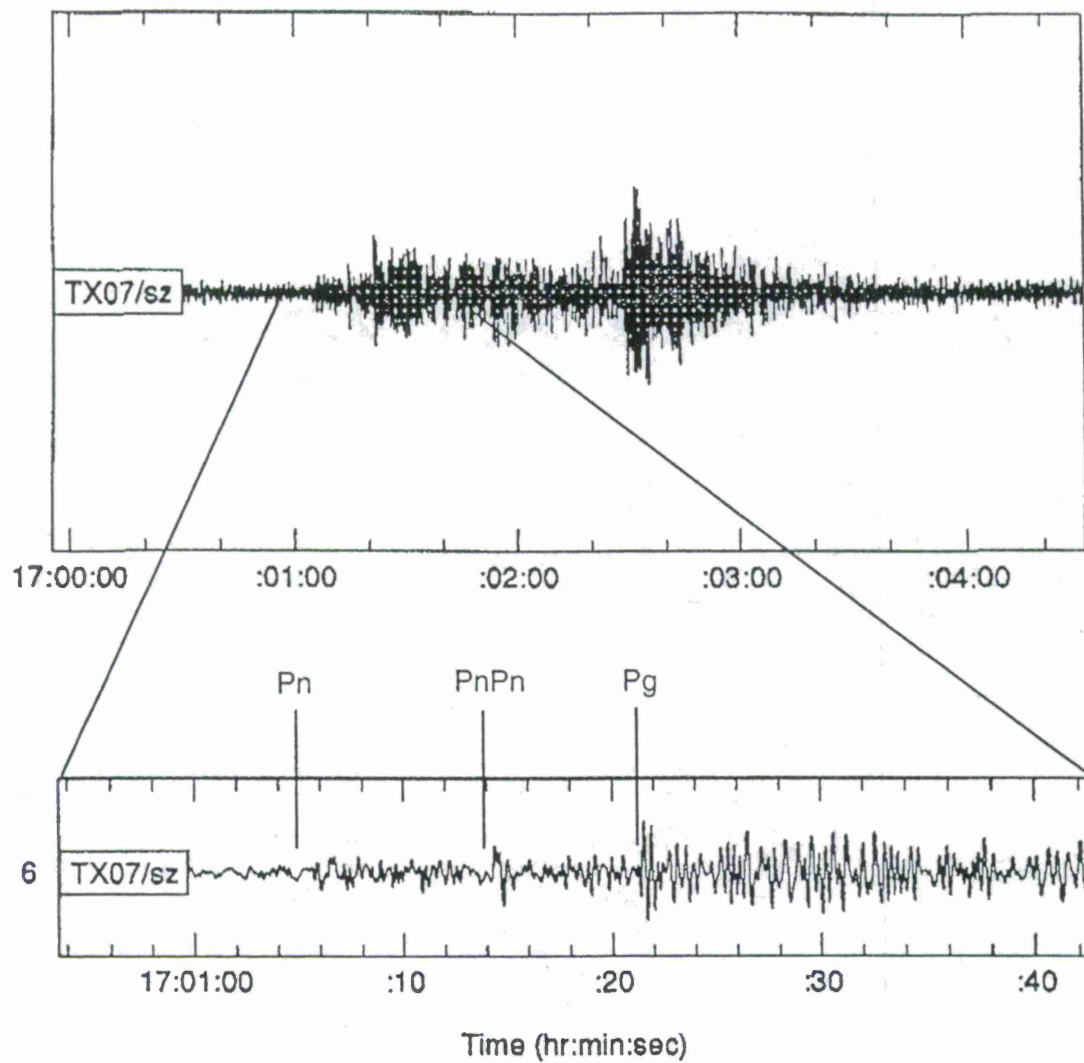


Figure 4. P wave arrivals at TXAR from a Tyrone explosion on Nov. 4, 1996.

Local Explosion-- February 11, 1997

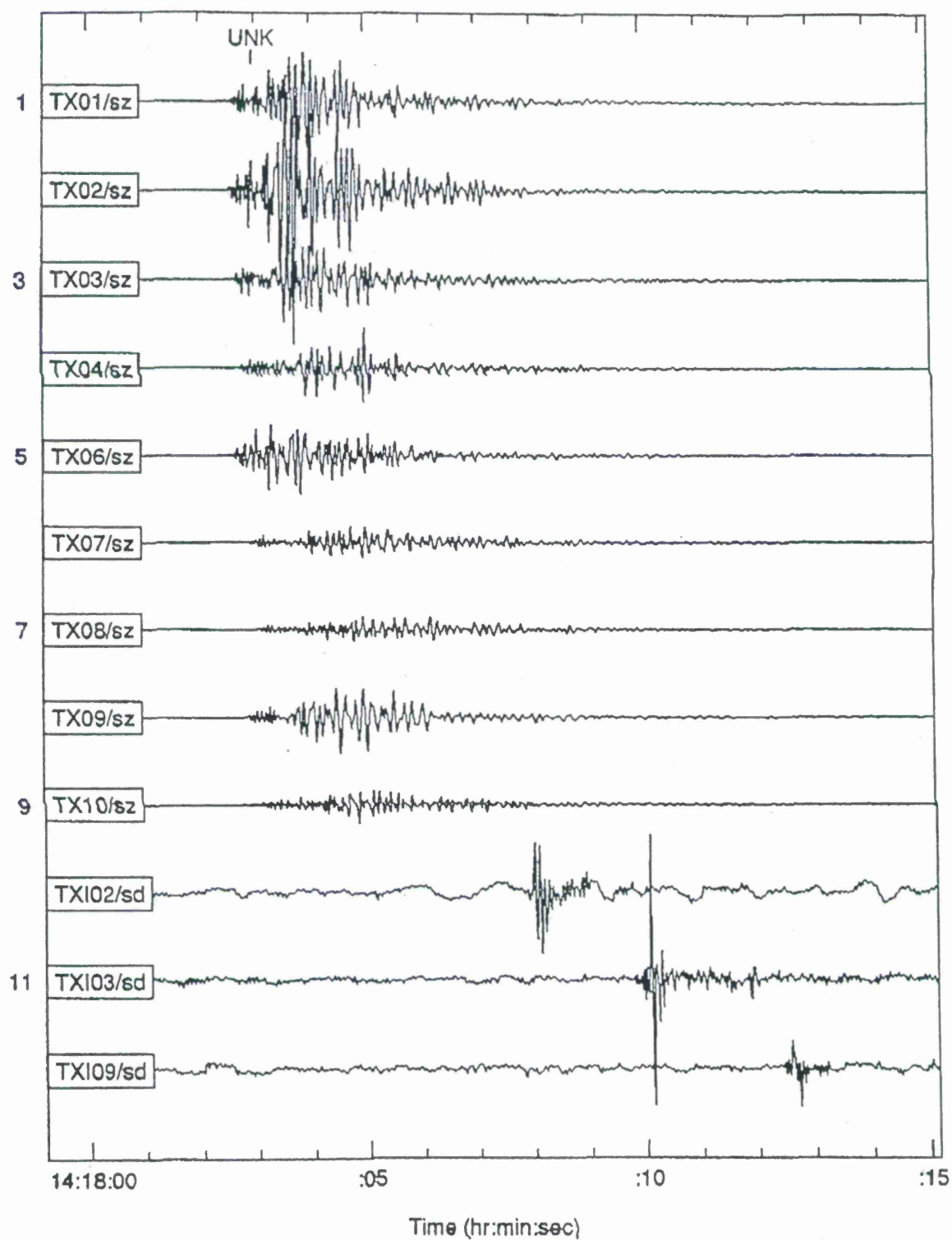


Figure 5. Local seismic event thought to be from an explosive source due to associated infrasonic signals.

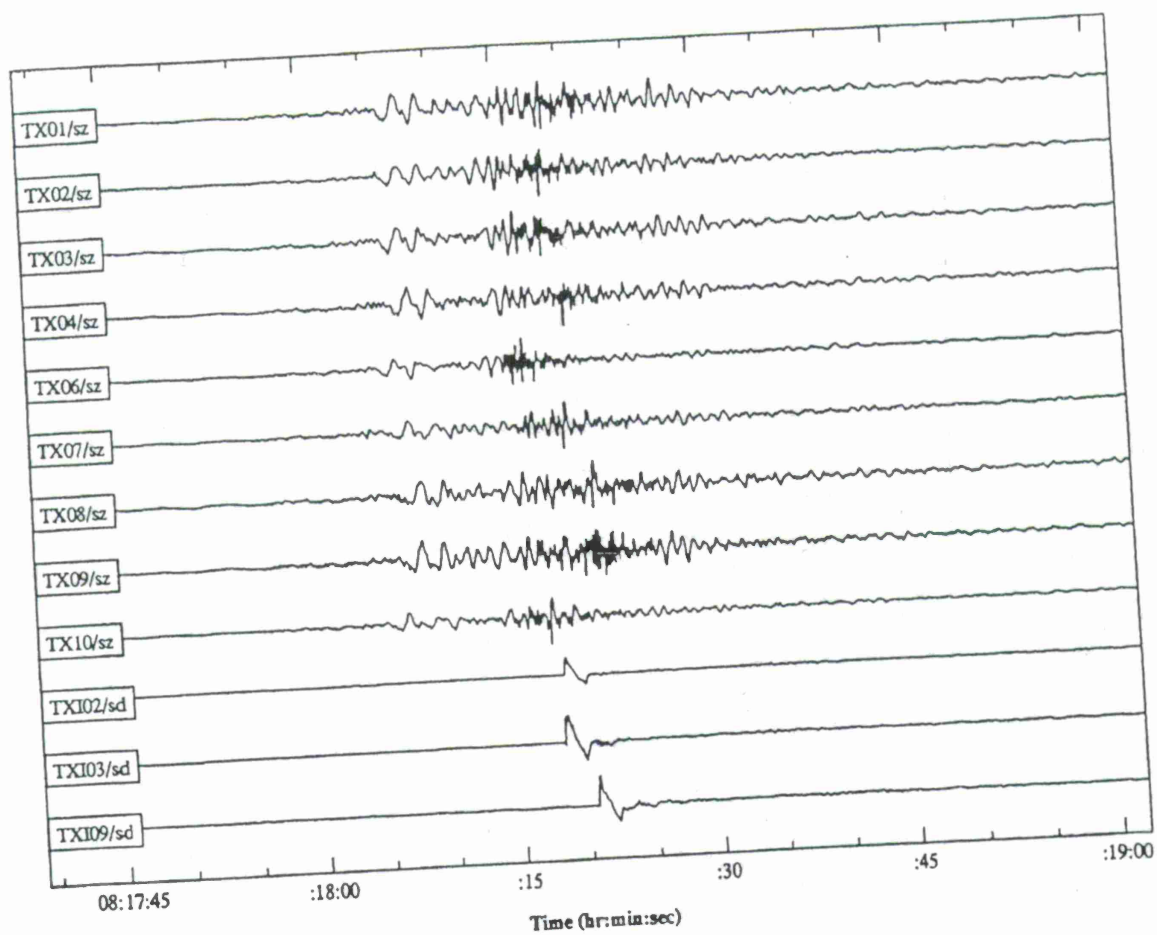


Figure 6. N waves (on sd channels) and shuttle quake (on sz channels) for the STS-82 mission. STS-82 (Shuttle Discovery) passed ~55 km south of TXAR and landed at 08:32:26 UTC on February 21, 1997.

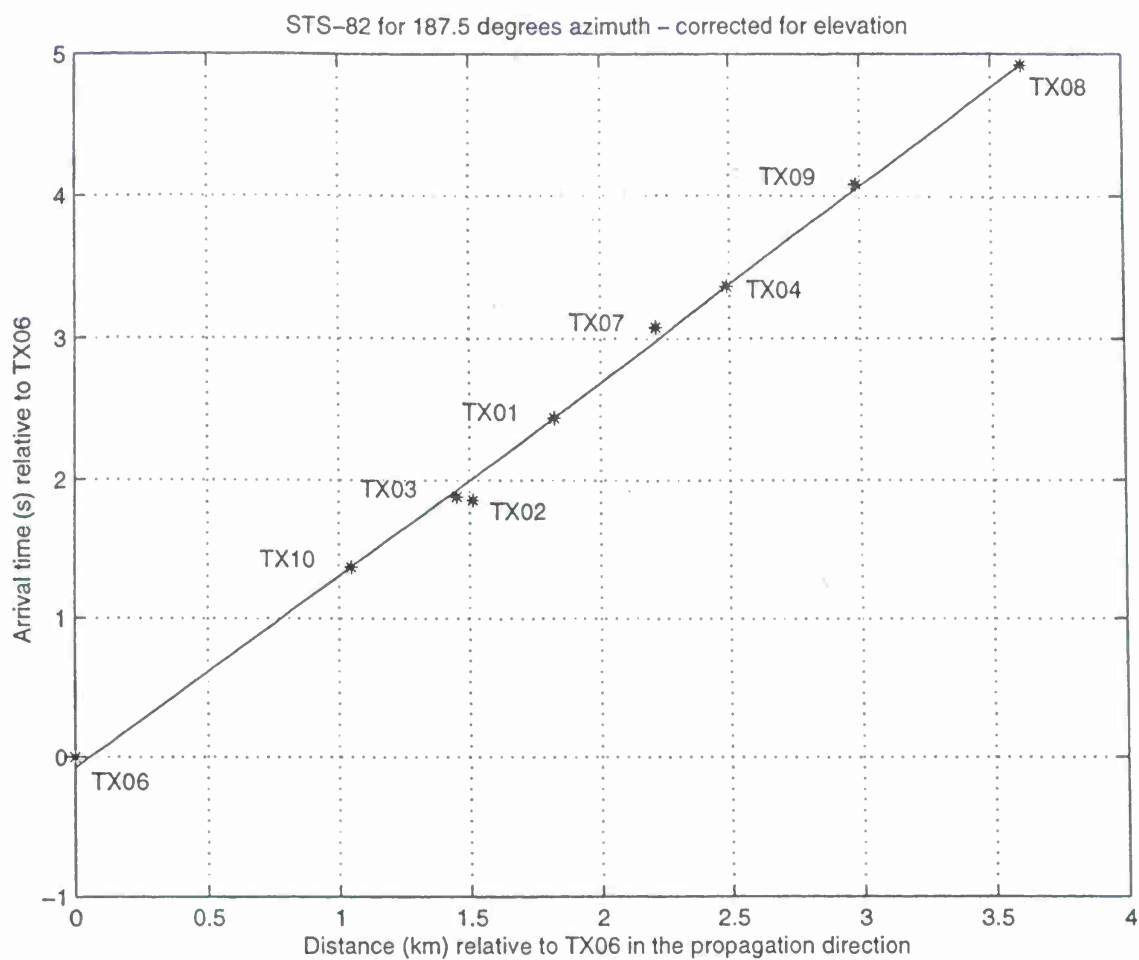


Figure 7. Seismo-acoustic arrival times for Shuttle STS-82 vs. down range distance.

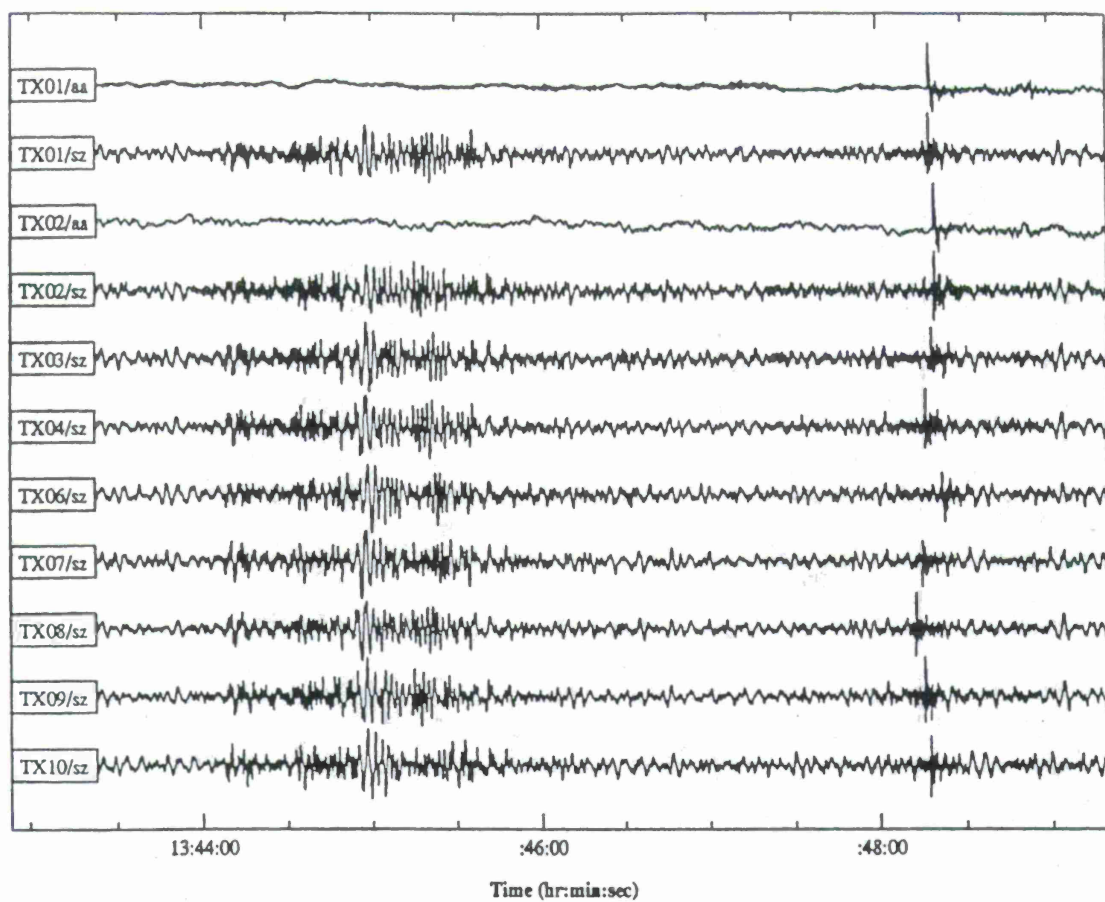


Figure 8. N waves and shuttle quake for the STS-75 mission. The shuttle Columbia passed ~150 km north of TXAR and landed at 08:32:26 UTC on February 21, 1997.

APPLICATION OF SOVIET PNE DATA TO THE ASSESSMENT OF THE TRANSPORTABILITY OF REGIONAL DISCRIMINANTS

J. R. Murphy, D. D. Sultanov*, B. W. Barker, I. O. Kitov*, and M. E. Marshall
Maxwell Technologies, Inc., Federal Division
111800 Sunrise Valley Dr., Suite 1212
Reston, Virginia 20191

Sponsored by Air Force Technology Applications Center
Contract No. F19628-95-C-0109

ABSTRACT

In order to discriminate the regional seismic signals produced by underground nuclear explosions from those produced by earthquakes, rockbursts and conventional mining explosions of comparable magnitude, it is necessary to know the range of nuclear explosion signal variation that can be expected as a function of source and propagation path conditions over the entire ranges of these conditions which may be encountered in global test monitoring of the CTBT. For this reason, Maxwell Technologies and the Russian Institute for Dynamics of the Geospheres (IDG) have been working on a joint research program to improve regional discrimination capability through analyses of seismic data recorded from the Soviet PNE program. This test program sampled wide ranges of source media (i.e. sandstone, clay, salt, limestone/dolomite and other hardrock) and source depth (i.e. 131-2859 m) and consisted primarily of the low-yield, overburied explosions of the type which represent the greatest challenge to seismic monitoring. Broadband seismic data recorded at the Borovoye station in Central Asia from 29 of these PNE tests in the distance range extending from about 7 to 19 degrees have now been processed and analyzed in an attempt to separate and characterize the frequency dependent explosion source and propagation path effects on the observed regional phase spectra. The characteristics of the explosion source coupling inferred from this analysis are consistent with those determined from previous teleseismic analyses in that they indicate systematic variations with source yield and depth which are generally consistent with those predicted by the Mueller/Murphy source model and suggest that, with the exception of clay, the coupling in all the other hardrock media sampled by these PNE is roughly comparable. The associated inferred propagation path functions indicate an amplitude decrease with distance which is significantly stronger than that predicted for the initial P wave used in magnitude determinations, but which shows surprisingly little frequency dependence over the 1.0 to 5.0 Hz frequency band, particularly for the Pg and Lg phases. Moreover, the Lg/P spectral ratios determined from these observed Borovoye PNE data generally decline to average values of 1 or less at frequencies above about 4 Hz and, therefore, typically appear explosion-like at high frequencies over this entire range of source and propagation path conditions.

Keywords: Seismic, Discrimination, Regional, Soviet, PNE

* Institute For Dynamics of the Geospheres, Russian Academy of Sciences

Objective

The principal objective of this research program is to improve regional seismic discrimination capability by deriving improved, quantitative bounds on the ranges of seismic signal characteristics which can be expected from underground nuclear explosions that might be conducted under the wide variety of source and propagation path conditions which must be considered in global monitoring of the CTBT. In order to reach this objective, we are working with scientists from the Russian Institute for Dynamics of the Geospheres (IDG) to conduct detailed analyses of regional seismic data recorded from selected Soviet PNE events which encompass the widest currently available ranges of explosion source conditions and propagation path variables.

Research Accomplishments

Analysis of the Soviet PNE data recorded at the Borovoye station has now been extended to encompass a sample of 29 explosions located at distances ranging from 7.2 to 19.1 degrees from the station. The locations of these events are shown on a map of the region in Figure 1 and are listed in Table 1 together with their associated source parameters. As is indicated in Table 1, these explosions have been separated into subsets identified as Groups I, II, A, B, Azgir and Astrakhan, where the events in each subset are all located in fairly narrow, common distance ranges. Groups I and II are made up of previously analyzed explosions in the distance range extending from 7.2 to 11.0 degrees, here subdivided such that Group II contains the five events in the northern azimuth which have large Pg/Pn ratios, as is illustrated in the waveform plots for these two groups shown in Figure 2. It can also be seen from Table 1 that the Azgir and Astrakhan explosions are located at distances from Borovoye which are very comparable to those for the Group A events. However, they have been analyzed separately as distinct groups in order to assess any propagation path effects which may be related to their locations within the Caspian Basin.

As in our previous analysis (Murphy et al., 1996), the Borovoye data have been bandpass filtered using a Gaussian comb of filters spaced at intervals of 0.25 Hz between 0.5 and 10 Hz. These filter outputs were sorted into six distinct group velocity (V_g) windows (i.e. pre-signal noise, $V_g > 7$ km/sec, $6 < V_g < 7$ km/sec, $5 < V_g < 6$ km/sec, $4 < V_g < 5$ km/sec, $3 < V_g < 4$ km/sec) designated herein as pre-signal noise and the five regional phases Pn, Pcoda, Pg, Sn and Lg. For each phase, the spectral amplitudes at each center frequency were estimated by computing RMS values from the instrument-corrected filter outputs in each of the designated group velocity time windows.

Since the selected data represent a wide range of epicentral distance, the effects of the propagation paths on the individual phase spectra must be estimated and separated from the source effects. This has been accomplished using statistical covariance analysis techniques. In this approach, it is assumed that the explosion seismic source function, $S(\omega)$, can be approximated as a product of simple power law relations of the form

$$S(\omega) \sim W^{n(\omega)} h^{m(\omega)} \quad (1)$$

where W , h are the explosion yield and depth of burial. On the basis of the results of the previous study (Murphy et al., 1996) it is also assumed that $n(\omega)$ and $m(\omega)$ are independent of epicentral distance and phase type. Then, allowing for separate propagation path effects for each phase, our model for describing the variations of the observed spectra for each regional phase p is

$$A_{p,k}(\omega) = \beta_{p,k}(\omega) W^{n(\omega)} h^{m(\omega)} \quad (2)$$

where $k = 1, \dots, K$ denotes the designated event subgroups (e.g. Groups A, B etc.). The $n(\omega)$, $m(\omega)$ and $\beta_{p,k}(\omega)$ have been simultaneously estimated from the observed spectral data using covariance analysis procedures based on the least squares fit criterion.

In order to assess any possible dependence of source coupling on source medium, the covariance analysis results have been used to predict the phase spectra for each event and observed to predicted spectral ratios have been computed, averaged over the frequency band from 0.5 to 5.0 Hz, and the resulting values for the five regional phases have been logarithmically averaged for each event. The results of this analysis are summarized in Table 2, where the events

Table 2
Borovoye PNE Spectral Ratios

Event	Medium	W, kt	h, m	Average: $\frac{\text{Observed}}{\text{Predicted}}$ 0.5 - 5.0 Hz
09/25/82	gabbro	8.5	554	0.48
10/17/78	sandstone	23	593	0.49
09/02/81	limestone	3.2	2088	0.74
07/21/84	salt	13.5	846	0.74
09/04/82	sandstone	16	960	0.79
04/19/87	limestone	3.2	2015	0.81
10/03/87	salt	8.5	1000	0.87
08/20/77	tuff	8.5	592	0.89
07/26/77	salt	13	879	0.94
11/01/80	dolomite	8	720	0.95
04/11/72	argillite	14	1720	0.95
06/18/85	argillite	2.5	2859	0.98
09/06/88	dolomite	7.5	793	1.09
10/22/81	dolomite	8.5	581	1.10
10/26/73	dolomite	10	2026	1.11
12/10/80	sandstone	15	2485	1.12
05/25/81	clay	37.6	1511	1.24
10/04/74	clay	21	827	1.33
08/25/84	clay	8.5	726	1.38
08/11/84	clay	9.5	759	1.74
08/15/73	clay	6.3	600	2.09

are listed in order of increasing observed/predicted ratio and it can be seen that the values of this coupling parameter vary from about 0.5 to about 2.0. Note, for example, that the three explosions in sandstone correspond to low, intermediate and higher than average values, indicating that the coupling in this medium shows no systematic difference from the average. In fact, the only consistent dependence on source medium is observed for the explosions in clay, which correspond to the five highest values in this table. Note also that within this clay subgroup, the offset from average coupling increases with decreasing yield, consistent with the alternate source model for explosions in clay which was proposed by Murphy and Barker (1994) on the basis of their analysis of the corresponding network-averaged, teleseismic P wave spectra.

The yield and depth scaling exponents as a function of frequency obtained from a covariance analysis of the sample of spectra remaining after elimination of the 5 clay events is shown in Figure 3, where they are compared with the corresponding values derived from the Mueller/Murphy source model. We conclude from this comparison that the observed variations in these Soviet PNE regional phase spectra with explosion yield and depth are consistent with the predictions of the Mueller/Murphy explosion seismic source scaling model, at least within the rather large uncertainty bounds on the experimental values.

One of the most robust regional discriminants which has been identified to date is the Lg/P spectral ratio. Although a firm, qualitative understanding of the basis for this discriminant has yet to be demonstrated, available observational data indicate that this ratio is typically less than 1.0 at high frequencies for underground nuclear explosions and greater than 1.0 for natural earthquakes and rockbursts. The observed Lg/Pg spectral ratios corresponding to each of our six subgroups of Soviet PNE events are shown in Figure 4, where it can be seen that these ratios are indeed generally less than 1.0 at high frequencies. Note, however, that the spectral ratios for Groups I and II, which encompass explosions in the same distance range, are quite different, particularly at low frequencies. This reflects the differences in relative Pg excitation between these two groups noted in conjunction with Figure 2, and indicates that propagation path effects can have a significant influence on the spectral composition of the regional phases used for event identification. In any case, these observed Borovoye Lg/Pg spectral ratios generally decline to average values of 1.0 or less at frequencies above about 4 Hz and, therefore, typically appear explosion-like at high frequencies over the entire ranges of source and propagation path conditions represented by this selected sample of Soviet PNE events.

Conclusions and Recommendations

Over the past two years, we have been working with scientists from the Russian IDG on a research program directed toward the derivation of improved, quantitative bounds on the ranges of regional seismic signal characteristics which can be expected from underground nuclear tests that might be conducted under the wide variety of source and propagation path conditions which will need to be considered in global monitoring of the CTBT. This research has centered on analyses of regional seismic data recorded at the Borovoye station in Central Asia from a sample of 29 Soviet PNE events representing a wide variety of source and propagation path conditions. The characteristics of the explosion source coupling inferred from this analysis are consistent with those determined from previous teleseismic analyses in that they indicate systematic

variations with source yield and depth which are generally consistent with those predicted by the Mueller/Murphy source model and suggest that, with the exception of clay, the coupling in all the other hardrock media sampled by these PNE is roughly comparable. Moreover, the L_g/P spectral ratios determined from these observed Borovoye PNE data generally decline to average values of 1 or less at frequencies above about 4 Hz and, therefore, typically appear explosion-like at high frequencies over the entire ranges of source and propagation path conditions represented by this selected sample of Soviet PNE events.

References

Murphy, J. R. and B. W. Barker (1994), "Application of Network-Averaged Teleseismic P Wave Spectra to an Analysis of the Seismic Source Characteristics of Soviet PNE Explosions," S-CUBED, SSS-FR-94-14528.

Murphy, J. R., D. D. Sultanov, B. W. Barker, I. O. Kitov and M. E. Marshall (1996), "Application of Soviet PNE Data to the Assessment of the Transportability of Regional Discriminants," PL-TR-96-2290.

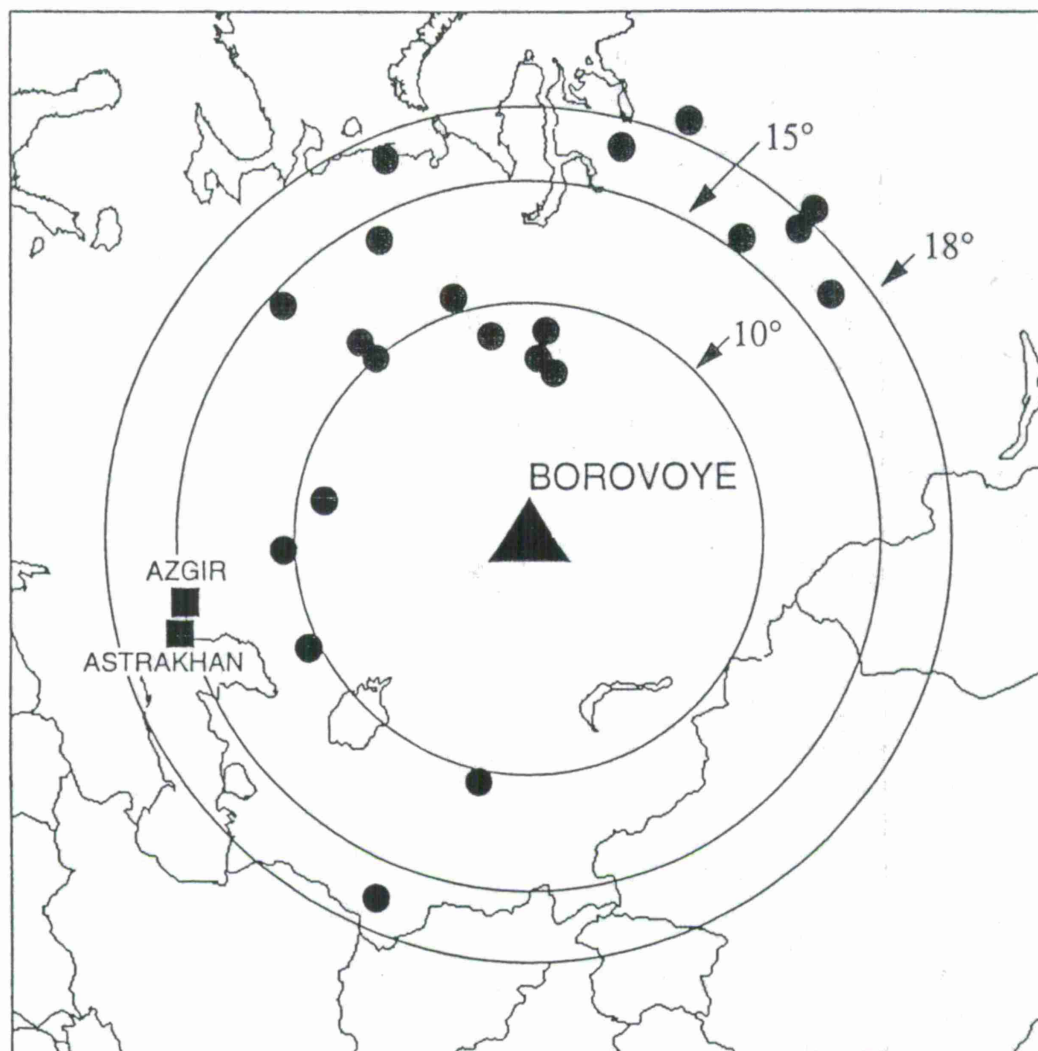


Figure 1. Map locations of selected Soviet PNE tests which were recorded at the Borovoye digital station in Kazakhstan.

Table 1
Borovoye Regional PNE Data Sample

Group I ($\bar{\Delta} = 10.2^\circ$)

Date	W, kt	h, m	Medium	$\Delta, ^\circ$
08/15/73	6.3	600	clay	10.5
10/26/73	10	2026	dolomite	8.3
09/02/81	3.2	2088	limestone	11.0
07/21/84	13.5	846	salt	10.6
04/19/87	3.2	2015	limestone	10.4
10/03/87	8.5	1000	salt	10.5

Group II ($\bar{\Delta} = 8.6^\circ$)

Date	W, kt	h, m	Medium	$\Delta, ^\circ$
10/17/78	23	593	sandstone	10.7
10/04/79	21	837	clay	7.7
12/10/80	15	2485	sandstone	8.8
08/25/84	8.5	726	clay	8.9
06/18/85	2.5	2859	argillite	7.2

Group A ($\bar{\Delta} = 15.6^\circ$)

Date	W, kt	h, m	Medium	$\Delta, ^\circ$
04/11/72	14	1720	argillite	16.7
11/01/80	8.0	720	dolomite	16.7
09/25/82	8.5	554	gabbro	15.8
08/11/84	9.5	759	clay	14.2
09/06/88	7.5	793	dolomite	14.6

Group B ($\bar{\Delta} = 18.0^\circ$)

Date	W, kt	h, m	Medium	$\Delta, ^\circ$
07/26/77	13	879	salt	19.1
08/20/77	8.5	592	tuff	18.9
05/25/81	37.6	1511	clay	17.2
10/22/81	8.5	581	dolomite	17.7
09/04/82	16	960	sandstone	17.0

Astrakhan ($\bar{\Delta} = 15.5^\circ$)

Date	W, kt	h, m	Medium	$\Delta, ^\circ$
10/08/80	8.5	1050	salt	15.5
09/26/81	8.5	1050	salt	15.5
10/16/82	8.5	974	salt	15.5
09/24/83	8.5	1050	salt	15.4
10/27/84	3.2	1000	salt	15.5

Azgir ($\bar{\Delta} = 15.0^\circ$)

Date	W, kt	h, m	Medium	$\Delta, ^\circ$
09/30/77	9.3	1503	salt	15.0
07/14/79	21	982	salt	15.1
10/24/79	33	982	salt	15.0

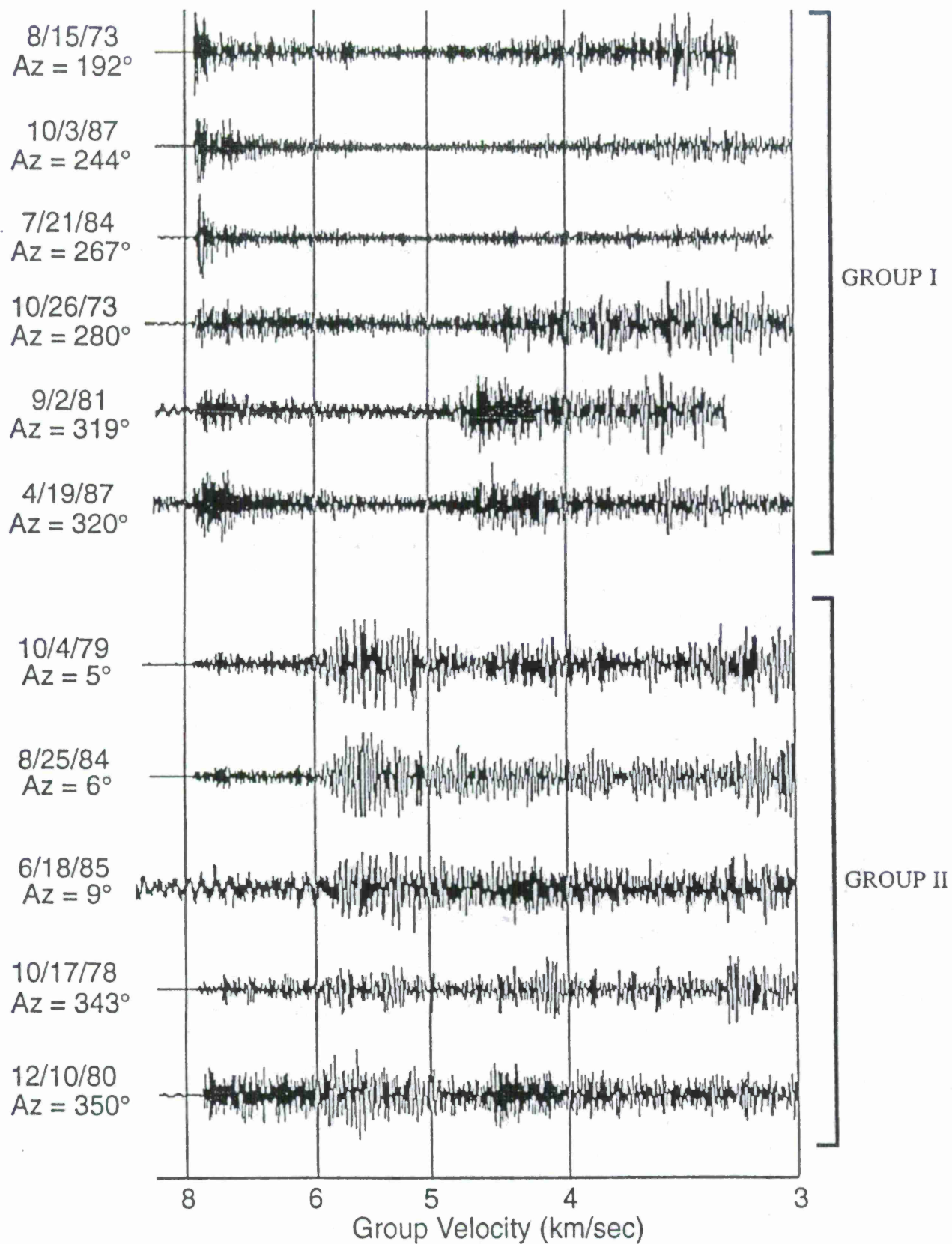


Figure 2. Vertical component regional signals recorded at Borovoye from selected Soviet PNE events in Groups I and II.

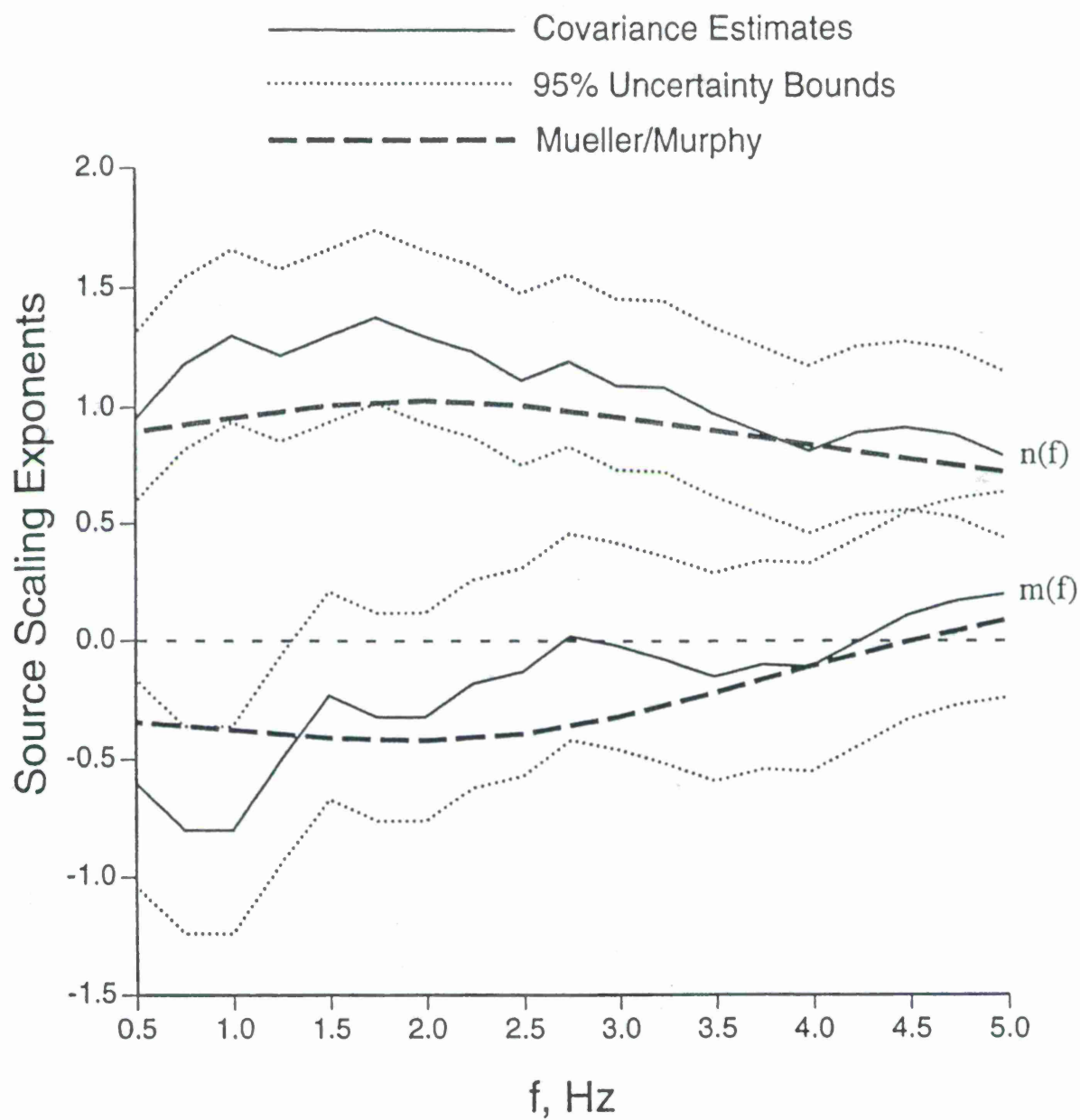


Figure 3. Comparison of yield (n) and depth (m) scaling exponents derived from the covariance analysis of the non-clay Borovoye PNE data with corresponding values predicted by the Mueller/Murphy model.

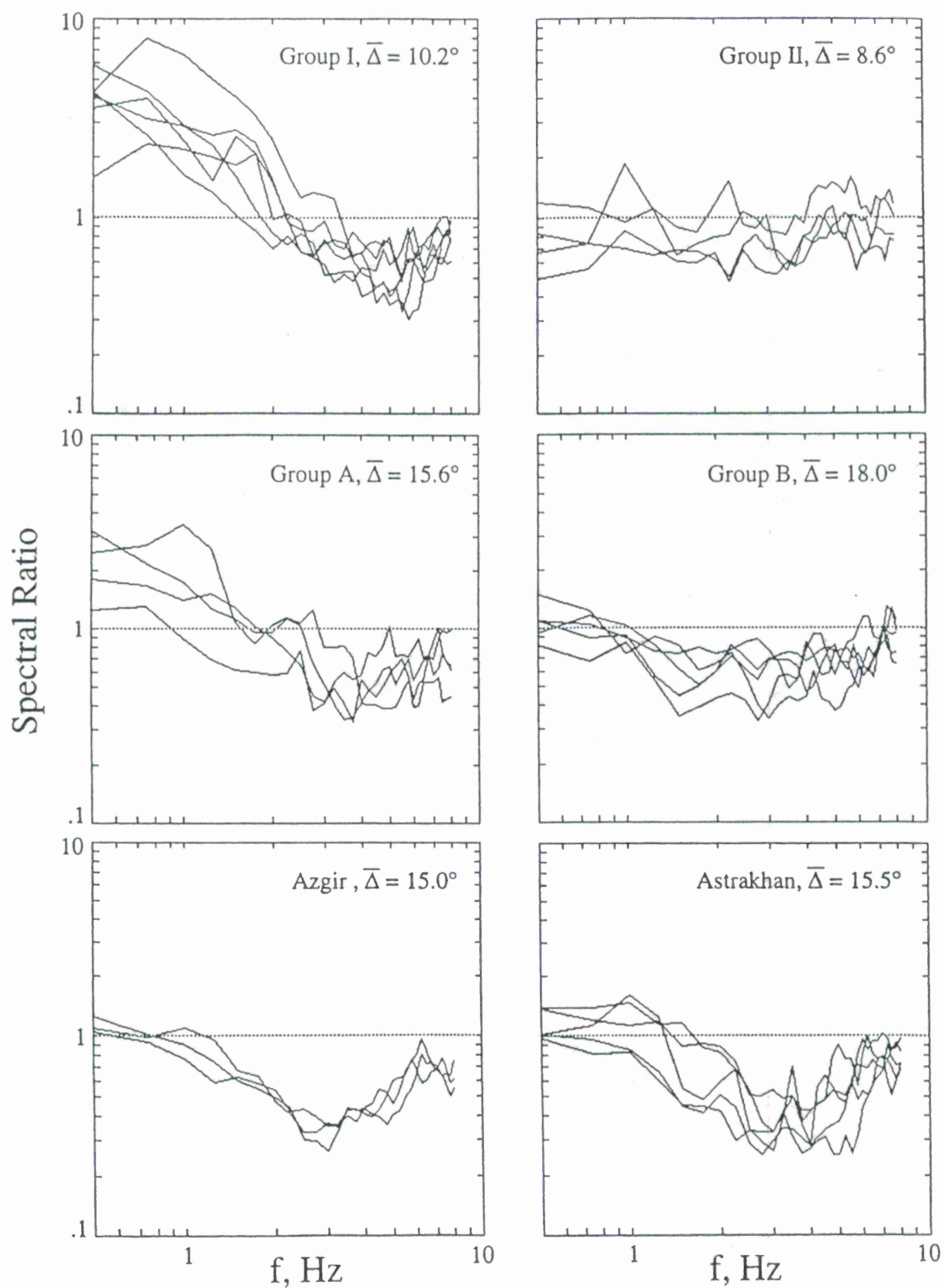


Figure 4. Observed L_g/P_g spectral ratios corresponding to different groups of Soviet PNE events recorded at Borovoye.

MULTIVARIATE DISCRIMINATION OF REGIONAL AND TELESEISMIC EVENTS, USING THE ISRAEL SEISMIC NETWORK RECORDINGS

Vladimir Pinsky, Yefim Gitterman and Avi Shapira
Seismology Division, Geophysical Institute of Israel, P.O. Box 2286, Holon 58122, Israel

Sponsored by U.S. Department of Energy
Office of Nonproliferation and National Security
Office of Research and Development
Contract No. F19628-95-K-0006

ABSTRACT

We investigated combinations of several statistics, oriented to local and teleseismic discrimination of events recorded by a dense network of seismic stations in order to enhance classification performance. The ground-truth local data base comprised 80 quarry blasts and 65 earthquakes from three geologically different regions of Israel recorded by the Israel Seismic Network short period stations. The seismograms of the groups of stations were used to construct several scalar and vector statistics: *spectral semblance*, *velogram parameter C*, *spectral ratio* together with *spectrograms* between 1 and 11 Hz. Majority voting as well as automatic classifiers based on Fisher Linear Discrimination Function (LDF) and non-linear Artificial Neural Network (ANN) were used. The performance of the different classification schemes, determined by the pair classifier and parameter vector, were compared on the basis of error probability estimation using the leave-one-out procedure. The best result, with an error probability equal to 0.006, was achieved when ANN was applied to the *spectrogram*, calculated by averaging the FFT squared amplitudes in the five equal and consecutive frequency bands.

The teleseismic data base was presented by 29 records of Eurasian nuclear tests, ten deep and 17 shallow and normal depth earthquakes recorded by the ISN. The *spectral semblance*, the *spectral ratio* of high and low frequencies energy and ratio of *P/P-coda* spectral maximums, were used for the classification. None of the above statistics resolved nuclear tests and deep earthquakes, but did show good performance on shallow and normal depth events. For the teleseismic data base free of deep earthquakes the leave-one-out cross-validation test provided no errors for both the LDF and the ANN procedures, applied to the vector of the three classification parameters.

Keywords: Automatic discrimination, local and teleseismic sources, integrative approach, Linear Fisher discriminator, Artificial Neural Networks, semblance, spectral ratio, velogram parameter, spectrogram.

OBJECTIVE

Automated Signal Classification (ASC) is a significant challenge in the monitoring of a Comprehensive Nuclear Test Ban Treaty. Our objective is to construct a reliable automatic classifier for regional and teleseismic events identification as a combination of the most promising discriminators, using advantages provided by a dense regional seismic network.

RESEARCH ACCOMPLISHED

Introduction. Pulli (1995), formulated the main steps of the ASC procedure as: signal processing, parameter selection and extraction, parameter evaluation, classifier design and classifier evaluation. At the parameter selection stage, ASC splits into two main branches: parametric and non-parametric. Dysart and Pulli (1990) demonstrated the first approach by using of a *small* set of seismic measurements (mainly P/S and P/Lg ratios in various frequency ranges) to discriminate between regional earthquakes and explosions. Dowla et al. (1995), showed efficiency of the non-parametric scheme using *numerous* signal decomposition coefficients as discriminants. The decision in both cases is provided automatically by the ANN, as a result of training procedure. Both methods have certain advantages and shortcomings, but the best performance is expected from a combined effort, investigating interactions of the different combinations of the signal features with various configurations of classifiers, which we call an *integrative approach*.

Local events data base for the research comprises 80 quarry blasts and 65 earthquakes with a magnitude ML range (1.5-2.5) and a depth H range (0-28 km) from three geologically different regions of Israel and Jordan: the Galilee, southern Dead Sea and Gilad (see map in Fig. 1). This data collection is the part of the larger data base, described in Gitterman et al., 1997. The events are recorded by the vertical short period (50 Hz sampling rate, 0.5-12.5 bandpass filtering) stations of the Israel Seismic Network (~36 stations spread all over the country), which are characterized by enhanced excitation of surface waves for explosions as compared to earthquakes. This is possibly the main reason for the predominant *low frequency* and *coherency* of spectral shapes at different stations, as well as the *lagging behind* of the S wave trains for explosions as compared to earthquakes. These three phenomena we measured by "spectral ratio", "spectral semblance" and "velogram parameter C", respectively, at the Galilee data set only (Shapira et al., 1996).

Here we test the above mentioned statistics on the extended data base and, in addition, utilize a spectrogram, namely, normalized sum of the squared smoothed FFT amplitudes in a series of frequency bands. Depending on the normalization coefficient, two types of spectrogram were considered: "spectrogram N1" - normalization by the maximum of the sums and "spectrogram N2" - by the total sum of squares. Finally, for both cases, the vector statistic was averaged over several (4-20) available stations. So, all the discriminants mentioned, integratively utilize the multistation character of the recordings. Some of their combinations, are listed in Table 1.

Teleseismic data base, comprising 29 nuclear tests and an arbitrary sample of 27 earthquakes from Eurasia (see map in Fig. 2) recorded by the ISN, covers the period from 1984 up to 1996 and a magnitude range from 5.3 to 6.5. The records (2-2.5 minutes in length) are represented by only P wave and P coda owing to the long delay of the following seismic phases which are outside the recording time frame of the acquisition system. The nuclear test seismograms are characterized on average by the relatively higher frequencies of particle motion and pulse (short) waveform of the first P wave arrival. Most of the tests (18) are from the Shagan river (Semipalatinsk) test site, eight from China (Lop Nor), one from West Siberia

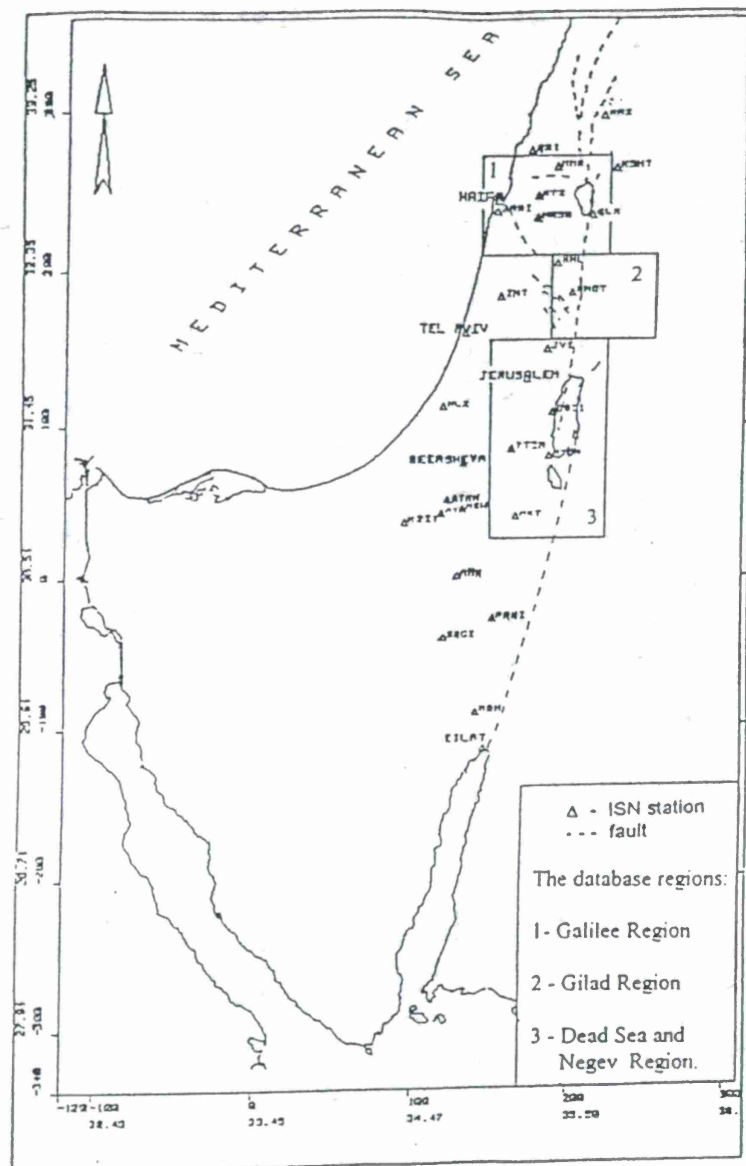


Fig. 1. Locations of the Israel Seismic Network stations and the three investigated seismic regions.

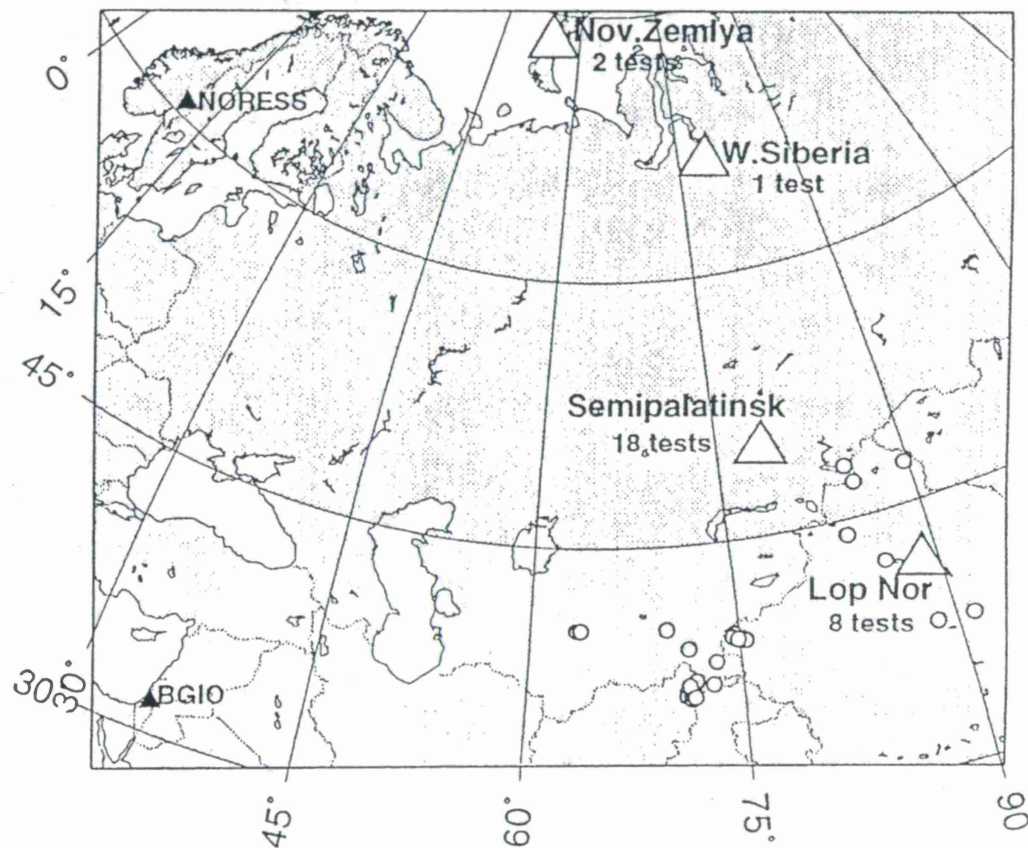


Fig. 2. Location of events from the teleseismic data base.

and two from Novaia Zemlya test sites. The tests are promoted in various geological conditions and show significantly different waveforms.

The earthquake origins of our selection are clustered in different mountain regions: Kunlun, Southern Tien Shan (close to the Lop Nor test site), Altai, Hindukush and Pamir and could be classified according depth as shallow ($h < 50$ km) and deep ($h > 90$ km). The deep events, mostly from northern Afghanistan, exhibit usually impulsive P wave seismograms similar to most of nuclear tests mentioned above (see Fig. 4). The shallow events are less impulsive, showing series of delayed waves (reflected and refracted near the source) just after the first arrival. According to this classification, there are 16 shallow and 11 deep events. The same data base is used by Gitterman et al., (1997) for testing the newly developed *spectral semblance* (0.6 - 2 Hz Hz) and *energy spectral ratio* (0.6-1 Hz)/(1-3 Hz) statistics, with frequency ranges chosen to provide optimal resolving power. We try to investigate these discriminators in combination with the ratio of *P/P-coda* spectral maximums, (resembling classical complexity statistics of Dahlman and Israelson, 1977), which was shown to be efficient for the NORESS teleseismic recordings in Tsvang et al., 1993.

For calculating the *P/P-coda* parameter only the channels with $SNR > 3$ were automatically selected. As a result there were from 3 to 30 ISN channels per event. FFT was computed for the two time intervals: 2 seconds and the following 30 seconds. RMS of spectral amplitudes was calculated for each of them in six equal frequency bands from 0 to 5 Hz. Then the maximum of the RMS was taken in each of the two samples and averaged over the set of stations, reducing randomness. The resulting two statistics were used to calculate the *P/P-coda* discriminator. The above mentioned scalar discriminators and their combinations are presented in Table 2.

Method. We select for the analysis of local and teleseismic events several useful parameters, choose empirical thresholds and evaluate rate of mistakes, integrated by the majority voting scheme. The simple majority voting was shown by Wuster (1993) to be useful for multidimensional classification analysis of local events. It does not, however, account for the mutual dependency (cross-correlation) and different weights of scalar statistics and may be regarded only as the first order approximation of *error probability*. Therefore, we address more sophisticated classifiers such as the linear Fisher discriminator and ANN, applying them to some of the most promising combinations of parameters and evaluate error probability through the leave-one-out cross-validation test (Fukunaga and Hummels, 1989) to create an independent test data base.

Results of the local events classification using the four scalar statistics, specified in Table 1, are presented in Fig. 3 together with depth specification at the top and the results of majority voting at the bottom. The data on Fig. 3 is split according regions of event location. The *Voting* is defined as the sum of units for the "correct vote" and zeroes for the "wrong vote". Hence, "correct" majority decision corresponds to the $Voting > 2$ for the four voters case. The results of the analysis of Fig. 4 are as follows:

- The chosen statistics exhibit from good (4 mistakes for the *semblance* and the *velogram parameter C*) to excellent performance (2 mistakes for the *spectrogram 7-9 Hz* and the *spectral ratio*); 144 events out of 145 are correctly classified using the majority $Voting > 2$ criterion.

- The worst $Voting$ equal to 1 is obtained for the event N 119 - an earthquake from the Dead Sea region with zero depth specification. The only positive voice for it belongs to the *velogram parameter C*.

- 11 events have $Voting = 3$ value, providing their correct classification. Only one of these four earthquakes, event N120, may be specified as shallow.

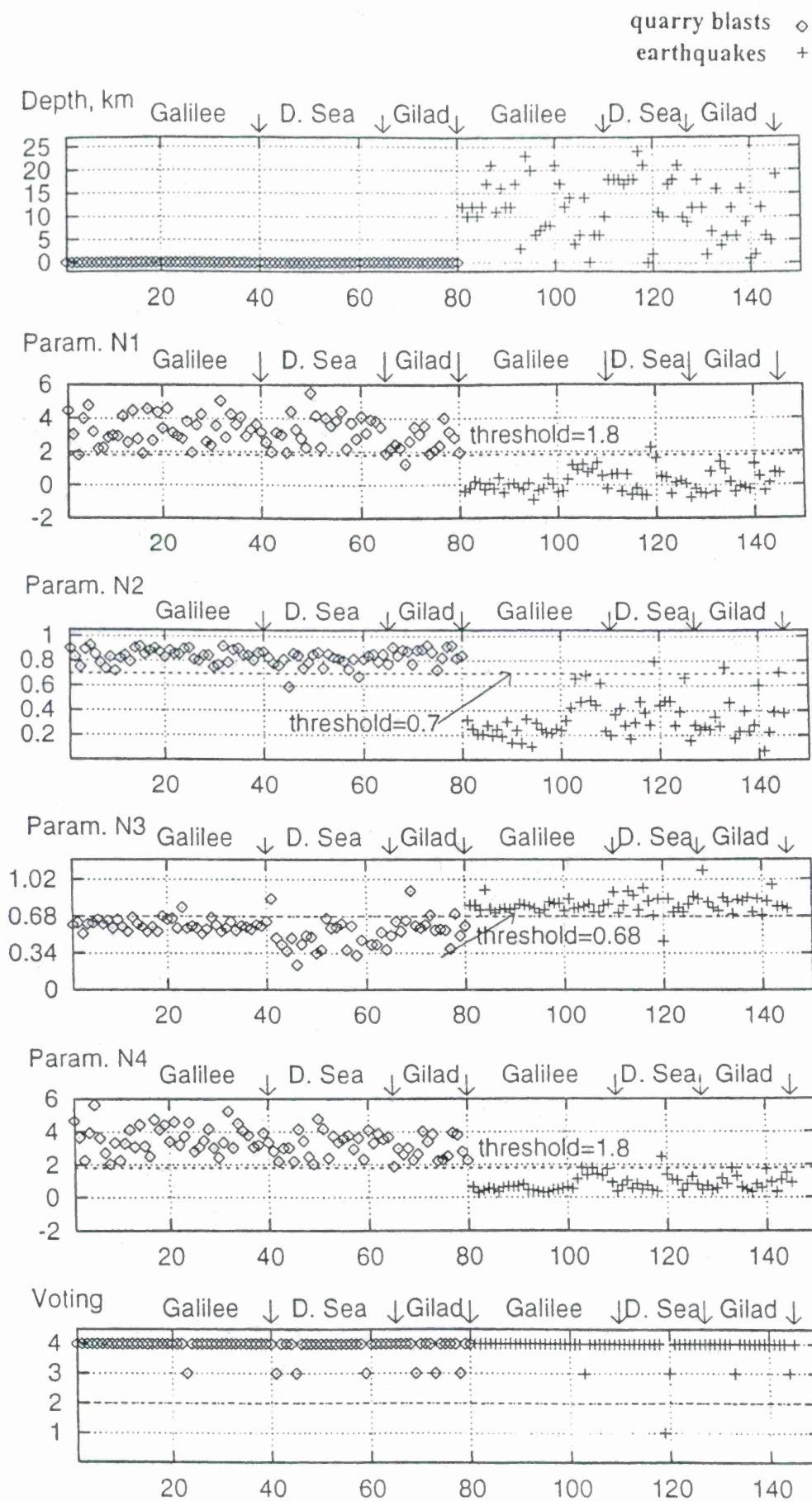


Fig. 3. Empirical thresholding and majority voting for the four main scalar statistics from Table 1 for the 80 quarry blasts and 65 earthquakes from the Galilee, Dead Sea and Gilad regions.

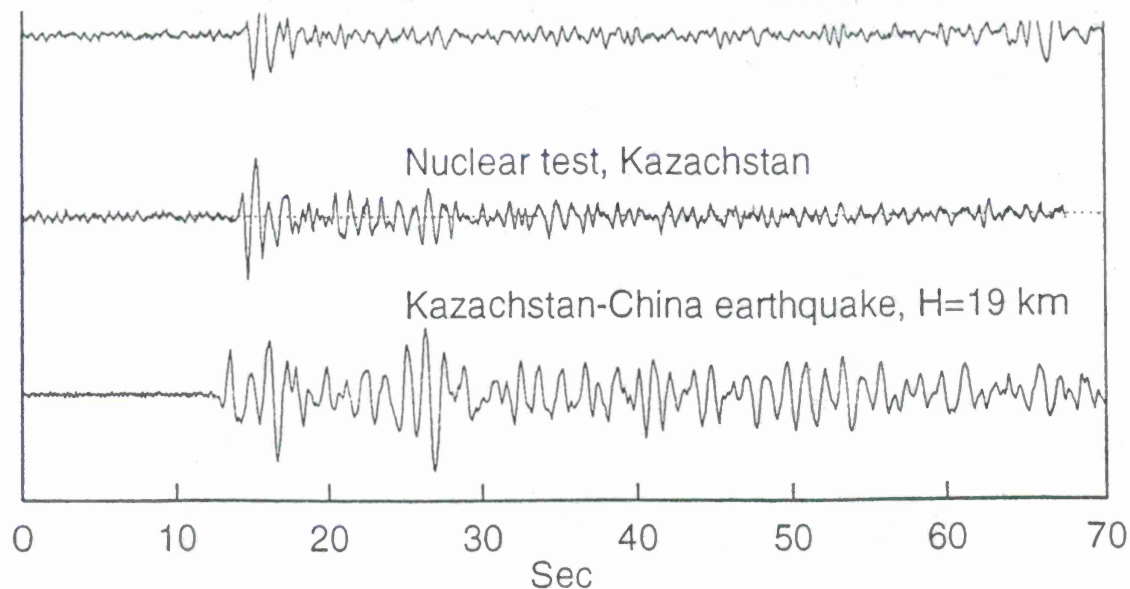


Fig. 4. Examples of records from the DSI station of the ISN: deep earthquake, nuclear test and shallow earthquake.

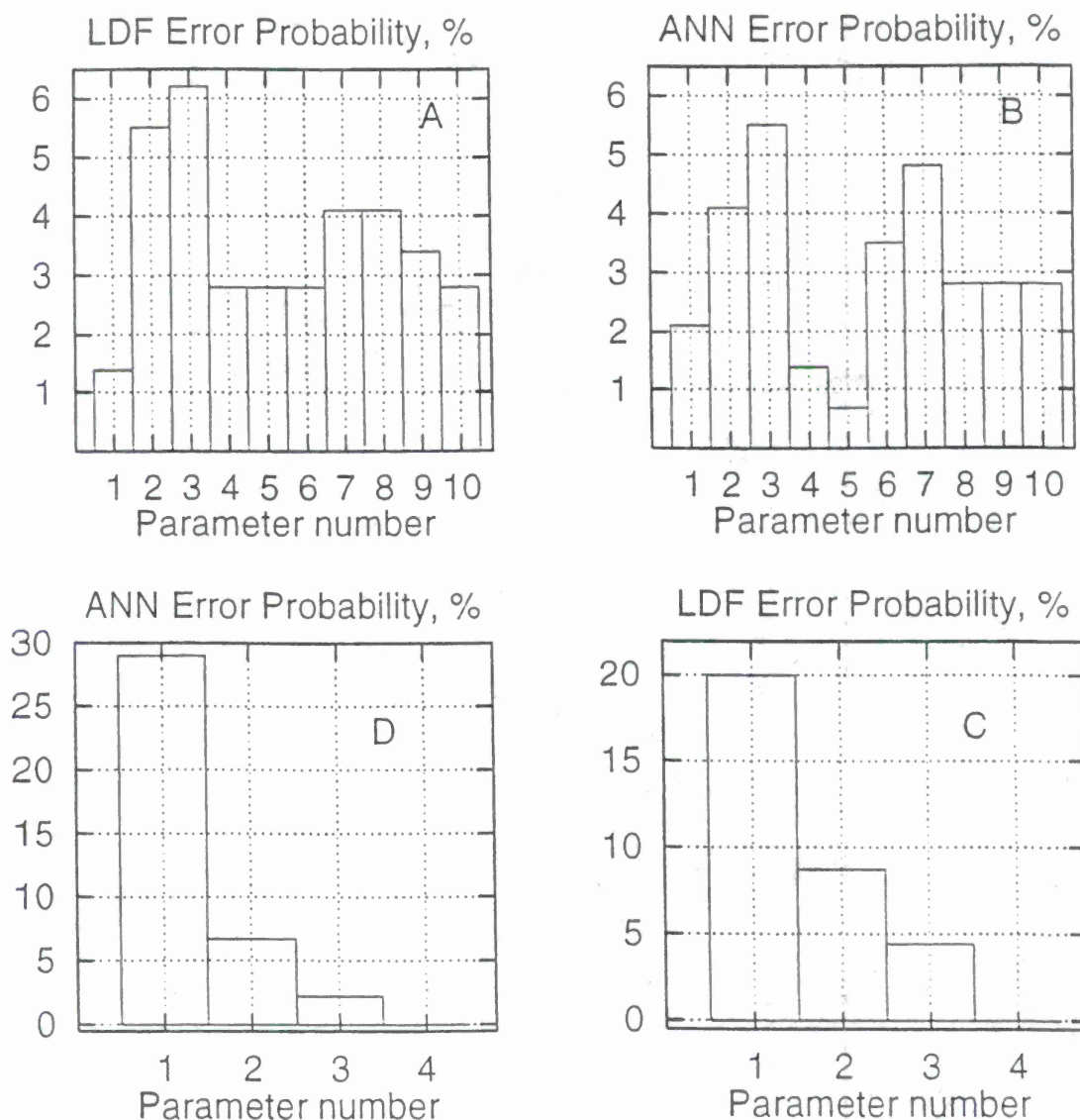


Fig.5 Error probability estimation by the leave-one-out test for the local (A, B) (Parameters from the Table 1) and teleseismic (C,D) (Parameters from the Table 2) events classification, using the LDF and ANN procedures.

Fig. 5 A, B presents the results of the *Error probability* estimation by the leave-one-out test for the LDF and ANN, applied to the statistics described in Table 1. As it follows from Fig. 5, the error probability for the classifiers varies between 0.6% to 6.2% with, on average, better ANN performance than LDF. The best computational scheme is ANN + *spectrogram N1 (5 band case)*, which provided only one mistake (event N 119). The second place with an error probability of 1.4 shares the ANN + *spectrogram N1 (7-9 Hz)* and LDF + *Spectral ratio* - both scalar statistics.

Results of the teleseismic events classification are presented in Table 2, Table 3 and Fig. 5 C, D. The results of the majority voting, including three discriminators: ratio of *P/P-coda* spectral maximums, *Semblance (1-3 Hz)* and *Spectral ratio (0.6-1 Hz)/(1.-3 Hz)*, are shown in Table 3 together with depth specification and empirical thresholds, and in Table 2. From the table it follows that:

- None of the scalar discriminators separates all the data set resulting in six mistakes for *P/P-coda*, 10 mistakes for the *Semblance* and three mistakes for the *Spectral ratio*.
- Voting procedure, applied to all the data set of 29 nuclear tests and 27 earthquakes results in two errors: earthquakes from China N24 and Afghanistan N9 are classified as nuclear tests.
- If only shallow earthquakes are taken for the classification, then only one mistake is encountered in majority voting, earthquake N24, the *Semblance* and *Spectral ratio* show reduced number of mistakes and *P/P-coda* becomes error free.

The LDF and ANN classifiers applied to the three selected scalar discriminators and their combination were tested on the reduced data set, comprising 29 nuclear tests and 17 shallow earthquakes. The results of the leave-one-out cross-validation test, presented in the Table 2 and Fig. 5 C, D are as follows:

- Each of the scalar discriminators provides some misclassifications on the selected data base: *P/P-coda* - one-two mistakes, *Spectral ratio* - three-four mistakes, *Semblance* 9 - 13 mistakes.
- A combination of the three statistics is error free for both the LDF and the ANN, when the leave-one-out test is applied.

CONCLUSIONS AND RECOMMENDATIONS

As a result of the analysis facilitating the *integrative multistation approach*, the Fisher Linear Discriminator Function and the Artificial Neural Network procedure, we selected the following features most informative for classification of man-made and natural seismic events and drew the following conclusions.

For the local data set of 80 quarry blasts and 65 earthquakes, the best classification results with an error probability equal to 0.006 is achieved at the 5 band *Spectrogram N1* with the help of the ANN, which is selected from the several cases with different numbers of frequency bands and different normalization. The scalar statistics of *Spectral ratio (1-3 Hz)/(6-8 Hz)* and the *Spectrogram N1 (7-9 Hz)*, bearing great resemblance to each other, are the closest competitors, all three reflecting the physical phenomenon of the excitation of the long period surface waves by explosions in the region with thick subsurface sediments. The more complicated and interesting *spectral semblance* and *velogram parameter C* discriminators unfortunately lag behind.

- As it was expected, joint parameter vector (1,2,3,5) (Par. N 10 in the Table 1) performs slightly better than parameter vector (1,2,3) alone. (Par. N 9 in the Table 1). However, we were surprised by the fact of decreasing of the performance of the (1,2,3,5) statistic, as compared to the *Spectrogram N1* alone (Par. N 5 in the Table 1), the ANN being applied. This may be due to the limited sample of observations and lacking of the additional information carried by the (1,2,3) discriminant.

- The only event misclassified from 145 events in the best case mentioned above, is the shallow Dead Sea earthquake with an estimated source depth equal to zero. Misclassification occurred due to the excitation of low frequency (near 1 Hz) surface waves energy, observed at some close stations. In the other four shallow cases the earthquakes were correctly classified.

- Although the data belong to the three different geological areas, we handled it without splitting with good classification results, thus showing robustness and transportability of the designed classification procedures.

For the teleseismic events the classification results are different, depending on whether deep events are included or not. The fact is that deep events can be easily recognized due to the presence of the depth *pP*, *sP* phases, always present in the coda of *P* waves. In our opinion, if the deep events are excluded from the data base, reliable classification is available by using the combined vector of the ratio of the *P/P-coda* spectral maximums, *spectral ratio* and *spectral semblance* statistics, which yielded no errors in the leave-one-out cross-validation test of the LDF and ANN procedures on our limited data set of 29 nuclear tests and 16 shallow earthquakes. The best of three appeared to be *P/P-coda* discriminant, measuring complexity of the signal.

For confirmation of the results and implementation of the automated classifiers in routine data processing, we recommend they be tested in large scale experiments comprising hundreds of events from different regions.

ACKNOWLEDGMENT

We are grateful to Farid Dowla, who kindly provided the software of the Artificial Neural Network with detailed explanations and assistance in implementation.

REFERENCES

- Dahlman, O. and Israelson, H., 1977. Monitoring Underground Nuclear Explosions, Elsevier, Amsterdam, 440pp.
- Dowla, F.U., 1995. Neural networks in seismic discrimination, in: E.S. Husebye and A.M. Dainty (Eds.), Monitoring a Comprehensive Test Ban Treaty, NATO ASI Series, Series E: Applied Sciences, 303:741-754.
- Fukunaga, K. and Hummels, D.M., 1989. Leave-one-out procedure for nonparametric error estimates, IEEE Trans. Pattern Anal. and Machine Intel., 11, 421-423.
- Gitterman, Y., Pinsky, V. and Shapira, A., 1997. Application of spectral semblance and ratio discriminants to regional and teleseismic events recorded by ISN and NORESS, Proceedings of the 19th Research Symposium on Monitoring a CTBT (these proceedings).
- Pully, J.J., 1995. Extracting and processing signal parameters for regional seismic event identification, in: E.S. Husebye and A.M. Dainty (Eds.), Monitoring a Comprehensive Test Ban Treaty, NATO ASI Series, Series E: Applied Sciences, 303:741-754.

- Shapira, A., Gitterman, Y. and Pinsky, V., 1996. Discrimination of seismic sources, using Israel Seismic Network, Proceedings of the 18th Research Symposium on Monitoring a CTBT, PL_TR-96-2153, 612-621.
- Tsvang, S.L., Pinsky, V. and Husebye, E.S., 1993. Enhanced seismic source discrimination using NORESS recordings from Eurasian events, J. Geophys. Int., 112, 1-14.
- Wuster, J., 1993. Discrimination of chemical explosions and earthquakes in central Europe - a case study, Bull. Seism. Soc. Am., 83:1184-1212.

Table 1. Parameters for discrimination of the local 65 earthquakes and 80 quarry blasts, the results of empirical thresholding and the leave-one-out test.

Par. N	Name, Spectral bands	Threshold	Number of errors		
			Voting	LDF	ANN
1	log. spectral ratio, (1-3 Hz) /(6-8Hz)	1.8	2	2	3
2	spectral semblance, (1 - 12 Hz)	0.7	4	8	6
3	velogram parameter, C (1 - 10 Hz)	0.68	4	9	8
4	spectrogram N1, (7 - 9 Hz) 1 band	1.8	2	4	2
5	spectrogram N1, (1 - 11 Hz) 5 band	-	-	4	1
6	spectrogram N1, (1 - 11 Hz) 10 band	-	-	4	5
7	spectrogram N1, (1 - 11 Hz) 20 band	-	-	6	7
8	spectrogram N2, (1 - 11 Hz) 5 band	-	-	6	4
9	parameter vector (1, 2, 3)	-	2	4	4
10	parameter vector (1, 2, 3, 5)	-	1	4	3

Table 2. Parameters for discrimination of the teleseismic 17 earthquakes and 29 nuclear tests, the results of empirical thresholding and the leave-one-out test.

Par. N	Name, Spectral bands	Threshold	Number of errors		
			Voting	LDF	ANN
1	spectral semblance, (1 - 3 Hz)	0.65	8	9	13
2	log. spectral ratio, (0.6-1 Hz) /(1-3Hz)	0.9	2	4	3
3	ratio of P/P-coda spectral maximums	2.3	0	2	1
4	parameter vector (1, 2, 3)	-	1	0	0

Table 3. Teleseismic events majority voting discrimination results.

Nuclear tests

No	Location	Depth	P/Pcoda		Semblance		Spec. Ratio		Voting
			value	thr.=2.3	value	thr.=0.65	value	thr.=0.9	
1	Kazakh	0	3.844	+	0.311	+	0.32	+	3:0
2	Kazakh	0	3.639	+	0.139	+	0.395	+	3:0
3	Kazakh	0	3.781	+	0.551	+	0.317	+	3:0
4	Kazakh	0	4.260	+	0.440	+	0.703	+	3:0
5	Kazakh	0	4.400	+	0.665	+	0.455	+	3:0
6	China	0	2.740	+	0.352	+	0.194	+	3:0
7	Kazakh	0	2.563	+	0.391	+	0.376	+	3:0
8	Kazakh	0	4.274	+	0.788	-	0.497	+	2:1
9	Kazakh	0	4.302	+	0.348	+	0.403	+	3:0
10	Kazakh	0	4.808	+	0.237	+	0.561	+	3:0
11	Kazakh	0	4.253	+	0.336	+	0.662	+	3:0
12	Kazakh	0	3.954	+	0.590	+	0.606	+	3:0
13	Kazakh	0	4.499	+	0.456	+	0.419	+	3:0
14	Kazakh	0	4.029	+	0.153	+	0.241	+	3:0
15	W.sib.	0	3.763	+	0.687	-	0.156	+	2:1
16	Kazakh	0	3.317	+	0.696	-	0.349	+	3:0
17	Kazakh	0	4.936	+	0.661	-	0.159	+	2:1
18	N.Zemla	0	2.842	+	0.473	+	0.791	+	3:0
19	Kazakh	0	5.430	+	0.617	-	0.488	+	2:1
20	Kazakh	0	4.280	+	0.433	+	0.607	+	3:0
21	Kazakh	0	4.241	+	0.366	+	0.667	+	3:0
22	N.Zemla	0	3.400	+	0.499	+	0.995	-	2:1
23	China	0	2.430	+	0.420	+	0.378	+	3:0
24	China	0	3.890	+	0.429	+	0.246	+	3:0
25	China	0	4.142	+	0.323	+	0.262	+	3:0
26	China	0	3.726	+	0.568	+	0.223	+	3:0
27	China	0	3.800	+	0.399	+	0.201	+	3:0
28	China	0	3.990	+	0.362	+	0.252	+	3:0
29	China	0	3.611	+	0.635	+	0.336	+	3:0

Earthquakes.

N	Location	Depth	P/Pcoda		Semblance		Spec.ratio		Voting
			value	thr.=2.3	value	thr.=0.65	value	thr.=0.9	
1	Uzbek	15	1.028	+	0.832	+	1.945	+	3:0
2	Tajik	33	1.915	+	0.788	+	1.802	+	3:0
3	China	7	0.802	+	0.717	+	1.560	+	3:0
4	China	15	1.255	+	0.909	+	1.858	+	3:0
5	Tajik	16	1.331	+	0.771	+	3.577	+	3:0
6	Tajik	187	2.42	-	0.942	+	4.819	+	2:1
7	Tajik	235	3.74	-	0.801	+	1.774	+	2:1
8	Tajik	89	1.12	+	0.679	+	1.017	+	3:0
9	Tajik	120	3.85	-	0.595	-	1.227	+	1:2
10	China	33	2.160	+	0.891	+	3.606	+	3:0
11	China	9	1.384	+	0.871	+	5.439	+	3:0
12	China	33	1.307	+	0.808	+	2.927	+	3:0
13	Tajik	95	1.89	+	0.792	+	3.222	+	3:0
14	Tajik	121	4.16	-	0.947	+	1.737	+	2:1
15	Tajik	41	1.352	+	0.840	+	2.759	+	3:0
16	Tajik	195	1.76	+	0.600	-	1.739	+	2:1
17	Tajik	188	3.76	-	0.914	+	4.352	+	2:1
18	China	33	1.733	+	0.777	+	1.001	+	3:0
19	Tajik	107	2.8	-	0.674	+	1.645	+	2:1
20	Tajik	110	1.93	+	0.823	+	0.310	-	2:1
21	China	33	1.304	+	0.886	+	7.050	+	3:0
22	Kazakh	19	1.241	+	0.651	+	1.804	+	2:1
23	China	20	1.330	+	0.681	+	0.938	+	3:0
24	China	22	1.188	+	0.569	-	0.691	-	1:2
25	China	44	1.763	+	0.529	+	0.999	+	3:0
26	Tajik	117	1.66	+	0.748	+	2.233	+	3:0
27	China	16	1.288	+	0.634	-	1.965	+	2:1

TRANSPORTABLE SEISMIC DISCRIMINANTS: STABILIZING SPECTRAL RATIOS USING SOURCE DECONVOLUTION

Jay J. Pulli
jpulli@bbn.com
BBN Systems & Technologies
1300 N. 17th Street, Suite 400, Rosslyn, VA 22209

Sponsored by U.S. Department of Energy
Office of Nonproliferation and National Security
Office of Research and Development
Contract No. F19628-95-C-0175

ABSTRACT

This research addresses the issue of discriminant transportability, that is, the development of discriminants which can be applied to events in a variety of geographic areas. The failure of discriminants to work for events in new areas of study is most often attributed to the effects of changes in the propagation path (Q, phase blockage, scattering, focusing/defocusing, etc.). An additional contributing factor is the instability of spectral ratio measurements. The spectra of P_n and L_g waves for small explosions often exhibit spectral nulls due to the time-delayed multiple source, and this is a useful seismic discriminant in itself. But often these spectral nulls occur at slightly different frequencies, contributing to artificial maxima and minima of the L_g/P_n spectral ratio. Parameterization of the spectral ratios then shows a great deal of scatter. In our approach, we deconvolve the source effects separately for L_g and P_n before the spectral ratio is computed. This is accomplished by first detrending the array averaged log-spectra of L_g and P_n , then computing a source time function based on the spectral nulls. This source time function is then deconvolved from the observed spectra in the frequency domain. The scatter in the resulting spectral ratio parameterizations is then reduced. This procedure has been tested on a number of Ground Truth Databases which include events from Scandinavia, central Europe, Spain, and the Middle East. The next step is to combine the spectral ratios and derived source time functions into a joint discriminant and test whether or not discrimination performance is improved with this additional information.

CTBT RELEVANCE

Transportability of discriminants is an important issue in the monitoring of a global CTBT because the events which generate the most interest will likely be those which occur in geographic areas which have yet to be studied with seismic methods. Additionally, if the scatter in discriminants can be reduced, their reliability for source identification even in areas already studied should improve.

Keywords: Discrimination, mining, explosions, signal processing, discriminant transportability, ground-truth databases

OBJECTIVE

The primary objective of this research is to assess the utility of a variety of methods for computing spectral ratios for the purpose of regional seismic event identification. The goal is to develop a stable, low variability method of spectral comparison for application to the problem of discriminant transportability. Specific objectives are:

- to apply these methods to an existing database of about 200 regional events which have already been studied using parameterizations of the Lg/Pn and Sn/Pn spectral ratios;
- to compare the identification performance of these new methods with that of the older parameterizations;
- to apply these methods to new events in other areas, specifically the Middle East and North Africa, which are being compiled as part of the overall DOE CTBT research effort.

RESEARCH ACCOMPLISHED

For over ten years it has been known that there are observable differences in the regional phases Pn , Sn , and Lg for earthquakes and explosion sources (e.g. Dysart and Pulli (1987), Baumgardt and Ziegler (1988), Hedlin *et al.* (1990)). These differences were noted in the (relatively) high-frequency band of the data, using events recorded at the newly installed NORESS, ARCESS, and FINESA arrays. However, when these discriminants were applied to events in new areas of interest, their ability to identify source types was shown to be inferior when compared to events from the original source area. This has most often been attributed to the area-to-area variation in propagation effects which can change the spectral content of the regional phases. Some of these effects, such as anelastic attenuation, can be independently measured and modeled for application to the observed spectra. Other effects, such as Lg blockage and the focusing/defocusing of regional phases due to velocity perturbations are more difficult to correct. Scattering also contributes to spectral variation (Dainty, 1996), although recent developments in the measurement of scattered waves (coda) show promise for source identification (Mayeda and Walter, 1996).

An additional consideration is the actual comparison of the Pn , Sn , and Lg phase spectra. Spectral ratios are typically used for spectral comparison and these formed the basis of our early studies. To parameterize the spectral ratios, we computed the mean values of Lg/Pn and Sn/Pn over a variety of frequency bands: 0-20 Hz to characterize the broadband spectra as well as 2-5 Hz, 5-10 Hz, and 10-20 Hz. However, the spectra of Pn and Lg waves for small explosions often exhibit spectral nulls due to the time-delayed multiple source, and this is a useful seismic discriminant in itself. But often these spectral nulls occur at slightly different frequencies,

contributing to artificial maxima and minima of the Lg/Pn spectral ratio. Parameterization of the spectral ratios then shows a great deal of scatter. In our approach, we deconvolve the source effects separately for Lg and Pn before the spectral ratio is computed in order to stabilize this calculation.

Figure 1 shows Pn recordings at the ARCESS array of six small explosions at the Apatity mining area. In each case the array data have been steered toward the source to illustrate the correlation of multiple arrivals in the Pn wave train. Note that for Events 2022, 2023, 2024, 2039, and 2046, the Pn wave consists of 2 or 3 distinct arrivals, whereas for Event 2045 the Pn arrival is a single pulse. Since these events are from the same area, this difference in arrival structure is likely a source effect, resulting from different firing patterns for each explosion at the quarry. *Figure 2* shows the corresponding spectra of Pn , Lg , and pre-event noise for these same mining explosions. Note that for event 2039 the spectral nulls for Pn and Lg waves occur at the same frequencies, but for event 2046 the spectral nulls are absent for Lg . *Figure 3* shows the array averaged autocorrelations of Pn and Lg . Note that these autocorrelations indicate a source time function that is different for Pn versus Lg .

The objective of the deconvolution is to remove the effect of the multiple explosions while retaining the information from the individual shot. This can be accomplished in a number of ways. One way is to manually pick the peaks and troughs of the Pn and Lg spectra and sort the delays. The delay pattern is determined from either the inverse of the peak frequency of the inverse, or 2 times the trough frequency. A second way is to pre-whiten the observed spectra with a frequency-squared correction, threshold the spectra, inverse Fourier transform, and compare the results with the autocorrelation. A third way is to precompute the interference spectra for a wide range of possible source time functions (*Figure 4*) and perform a pattern match between the models and the pre-whitened observed spectra. This is followed by an inverse Fourier transform and a comparison with the autocorrelation.

Figure 5 shows the resulting effect on the broadband Pn/Lg spectral ratios for 100 events recorded at the NORESS array. The upper figure shows the spectral ratios calculated without source deconvolution. Note that the scatter in this discriminant is large for explosions, since these events show the largest variation in source time function. Once this source time function is deconvolved from the spectra, the resulting spectral ratios show much less scatter.

CONCLUSIONS AND RECOMMENDATIONS

We have applied a source deconvolution process to the Pn and Lg waves of small mining explosions and earthquakes in order to stabilize the spectral ratio estimates and improve discrimination capability. This procedure has been tested on a number of Ground Truth Databases which include events from Scandinavia, central Europe, Spain, and the Middle East. We have found that the scatter in the spectral ratios and their parameterizations is reduced.

leading to fewer misidentified events. The next step is to combine the spectral ratios and derived source time functions into a joint discriminant and test whether or not discrimination performance is improved with this additional information.

REFERENCES

- Baumgardt, D.R. and K.A. Zeigler (1988), Spectral evidence for source multiplicity in explosions: application to regional discrimination of earthquakes and explosions, *Bull. Seis. Soc. Amer.*, 78, 1773-1795.
- Dainty, A.M. (1996), The influence of seismic scattering on monitoring, in Husebye and Dainty, eds., Monitoring a Comprehensive Test Ban Treaty, NATO ASI Series, Kluwer Academic Press, 836 pp.
- Dysart, P. and J. Pulli (1987), Spectral study of regional earthquakes and chemical explosions recorded at the NORESS array, Center for Seismic Studies Technical Report C87-03.
- Dysart, P. and J. Pulli (1990), Regional seismic event classification at the NORESS array: seismological measurements and the use of trained neural networks, *Bull. Seis. Soc. Amer.*, 80, 1910-1933.
- Grant, L., J. Coyne, and F. Ryall (1993), CSS Ground Truth Database: Version 1 Handbook, Center for Seismic Research Technical Report C93-05.
- Hedlin, M., J.B. Minster, and J.A. Orcutt (1990), An automatic means to discriminate between earthquakes and quarry blasts, *Bull. Seis. Soc. Amer.*, 80, 2143-2160.
- Mayeda, K. and W.R. Walter (1996), Moment, energy, stress drop, and source spectra of western United States earthquakes from regional coda envelopes, *J. Geophys. Res.*, 101, 11,195-11,208.
- Pulli, J. (1996), Extracting and processing seismic signal parameters for regional seismic event identification, in Husebye and Dainty, eds., Monitoring a Comprehensive Test Ban Treaty, NATO ASI Series, Kluwer Academic Press, 836 pp.
- Shumway, R.H. (1996), Statistical approaches to seismic discrimination, in Husebye and Dainty, eds., Monitoring a Comprehensive Test Ban Treaty, NATO ASI Series, Kluwer Academic Press, 836 pp.

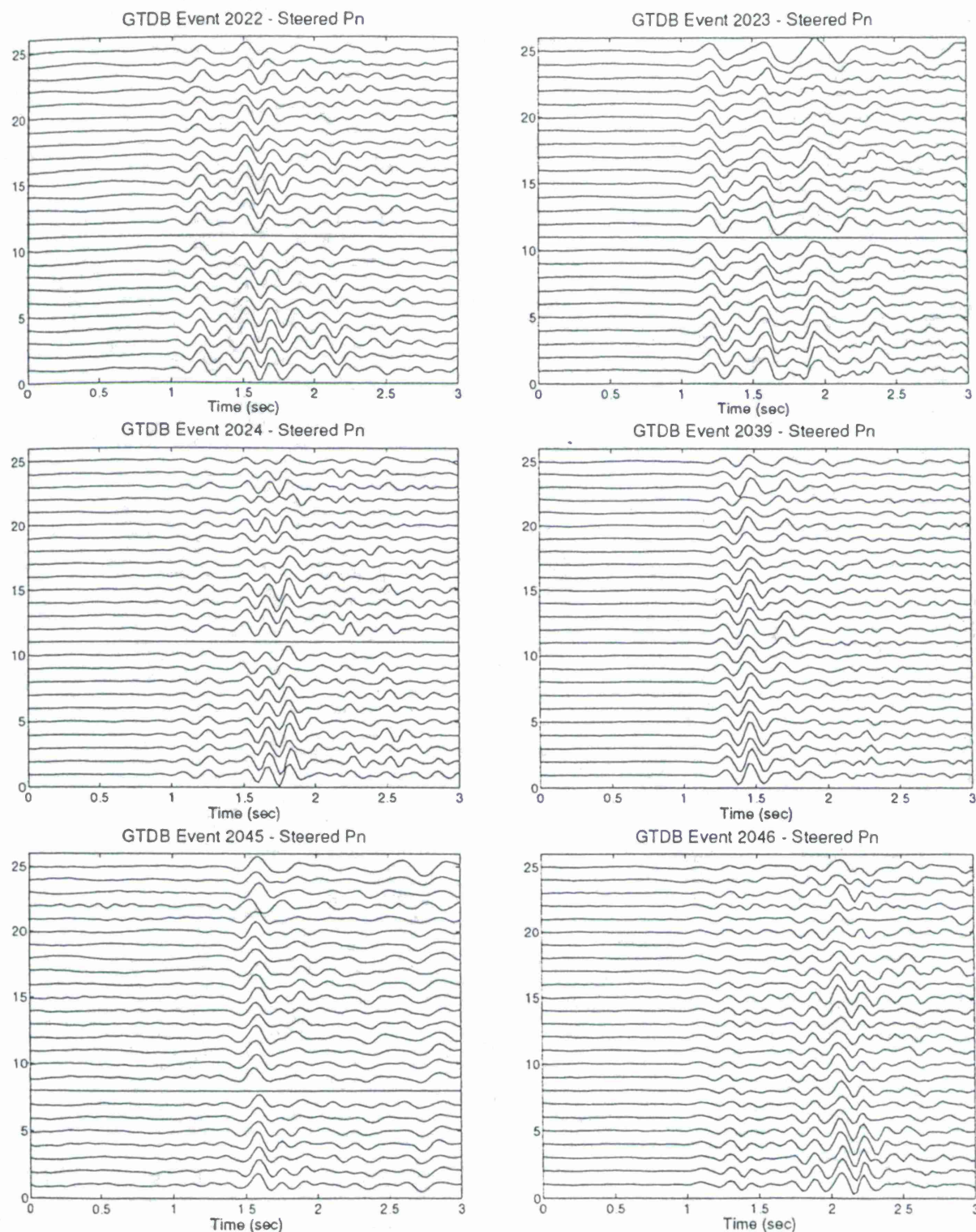


Figure 1. *Pn* record sections for 6 mining explosions at the Apatity mining site, recorded at the ARCESS array. The data have been steered toward the explosion. Note that for Events 2022, 2023, 2024, 2039, and 2046, the *Pn* wave consists of 2 or 3 distinct arrivals, whereas for Event 2045 the *Pn* arrival is a single pulse.

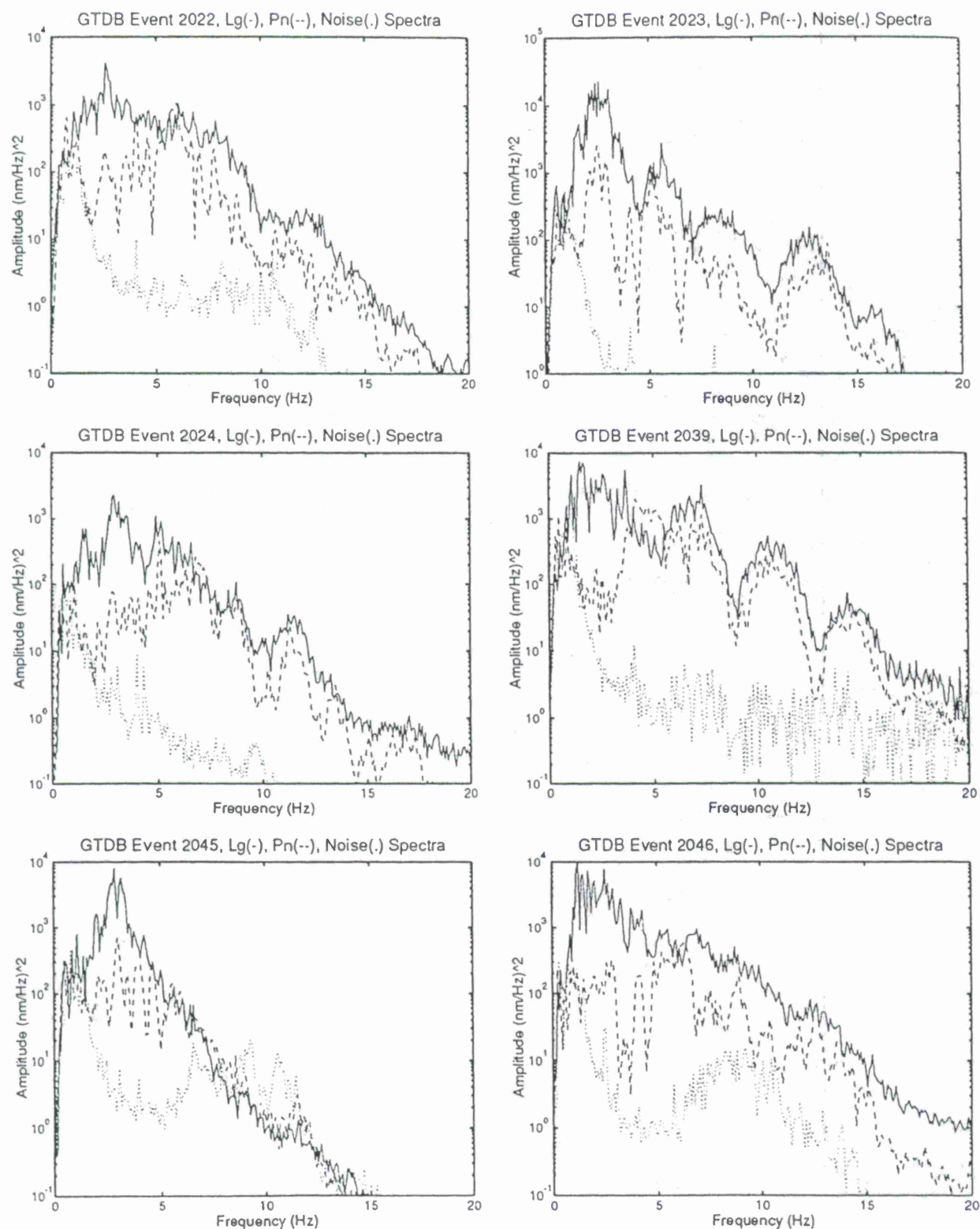


Figure 2. Spectra of *Pn* (dashed line), *Lg* (solid line), and pre-event noise (dotted line) for the 6 Apatity mining explosions cited in Figure 1. Note that for event 2039 the spectral nulls for *Pn* and *Lg* waves occur at the same frequencies, but for event 2046 the spectral nulls are absent for *Lg*.

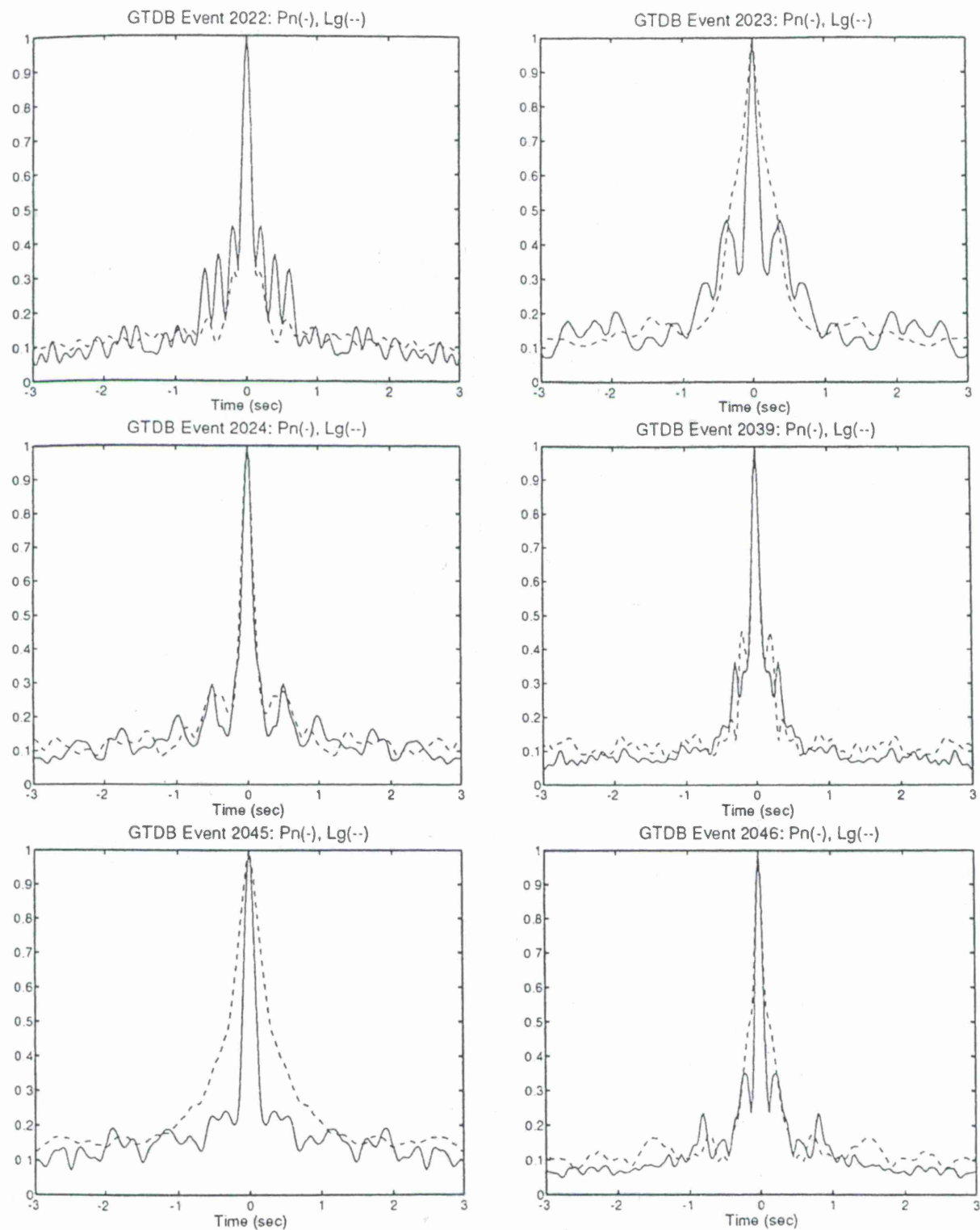


Figure 3. Array-averaged autocorrelations for Pn and Lg waves for the Apatity events cited in Figures 1 and 2. The autocorrelations illustrate the difference in derived source time function from Pn and Lg waves.

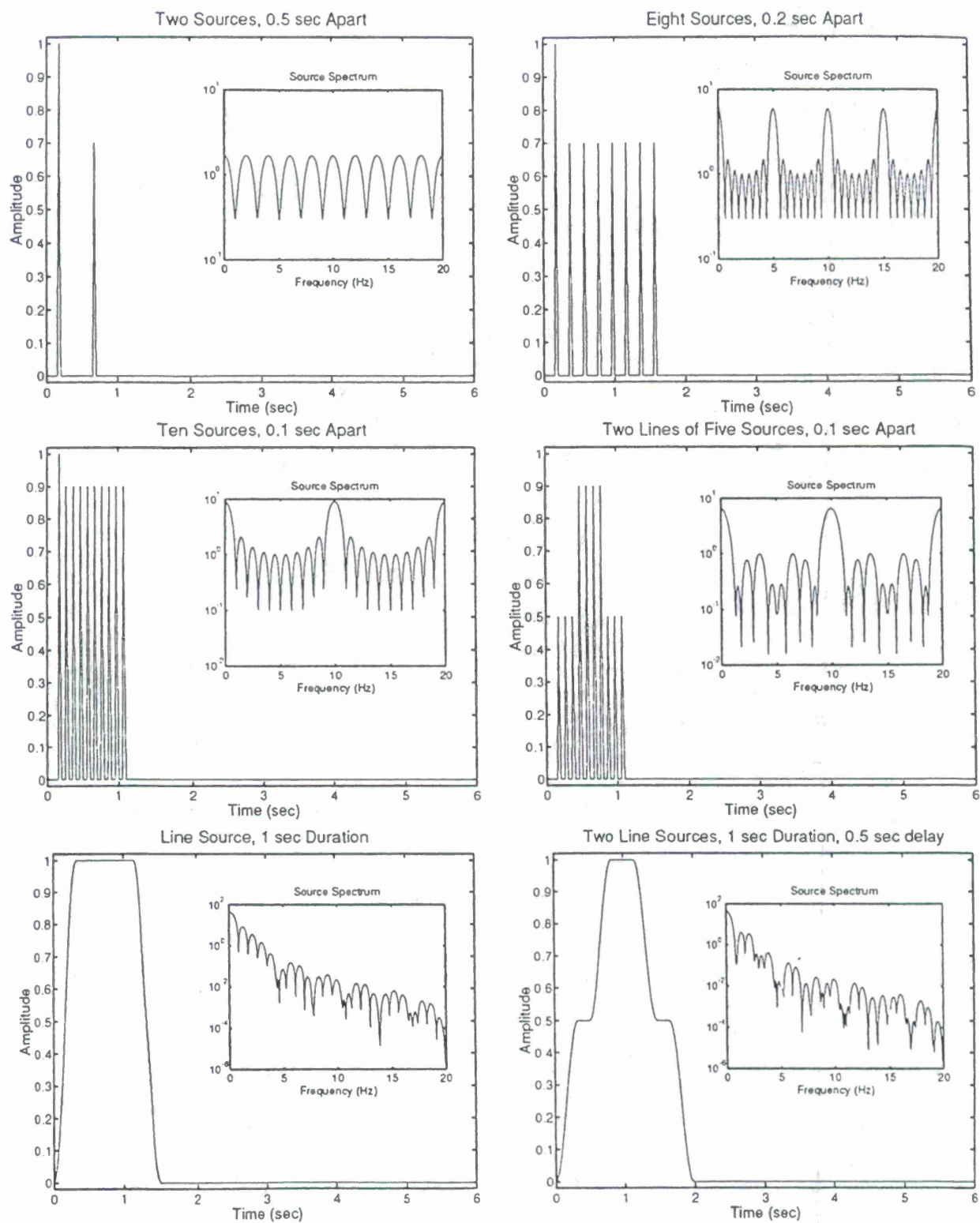


Figure 4. Six models of quarry blast sources and their associated spectra.

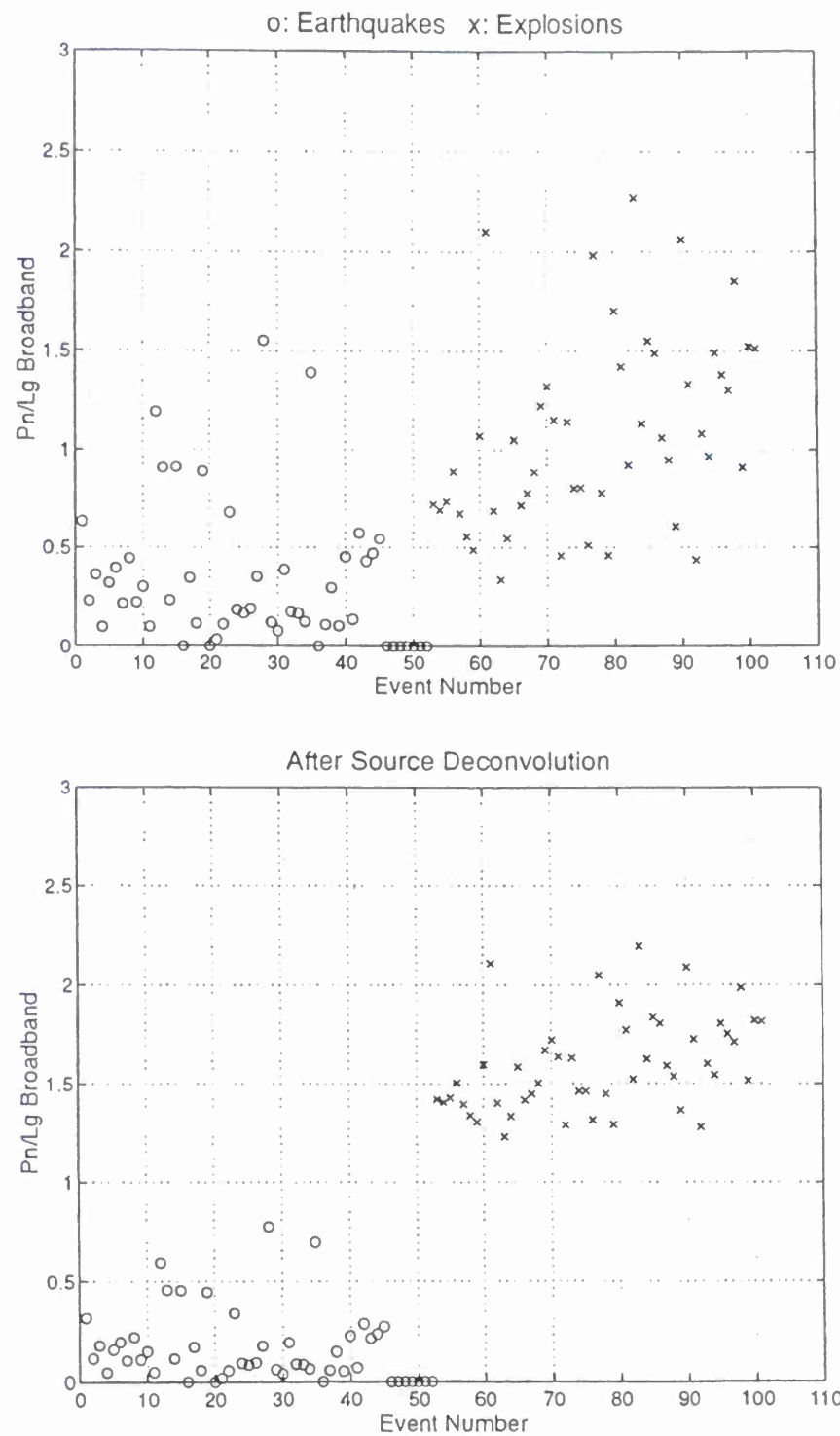


Figure 5. Comparison of broadband Pn/Lg spectral ratios before and after source deconvolution.

DETECTING RIPPLE-FIRING IN TIME AND FREQUENCY

Robert H. Shumway
University of California, Davis

Sponsored by the Air Force Technology Applications Center
Contract F19628-95-K0010

ABSTRACT

Time and frequency domain approaches to detecting a consistent pattern of reflections on an ensemble of seismic recordings are reviewed. Such patterns are characteristic of mining bursts and not of nuclear explosions or earthquakes so that detecting a ripple delay structure can serve as one component for discrimination.

In the nonlinear frequency domain approach, a generalization of cepstral analysis has been used to derive an F-Statistic for detecting delay-fired events observed on an array. Detrended log spectra are considered as realizations of stationary processes whose periodic components are quefrequencies, with periods proportional to delay time differences. An F-Statistic is derived that is proportional to the stacked or summed cepstra and the spectrum of the stacked log spectra.

A linear frequency domain approach is proposed that is based on a time series factor analysis model, where the site and path effects comprise the factor loadings and are convolved with some common factor series that should contain the possible ripple delays. We estimate the factor loadings and the common factor series by maximum likelihood, using a single factor model. The common factor series is to be deconvolved and examined for evidence of ripple-firing.

The frequency domain approaches are compared to a time domain approach that involves searching seasonal autoregressive models with a fixed regular delay structure. Data from a number of mining explosions, measured at an array in northern Norway, are analyzed by the three approaches.

Keywords: Cepstral analysis, Multiplicative Models, ARMA, F-Statistic, Factor Analysis, Deconvolution.

OBJECTIVE

Regional seismic monitoring and discrimination capabilities that are desirable under a potential Comprehensive Test Ban Treaty (CTBT) can be improved by developing algorithms and new procedures for distinguishing between earthquakes, nuclear explosions and mining explosions of various kinds. Much effort in past discrimination studies has concentrated on extracting various features of the spectrum that are characteristic of earthquakes, nuclear explosions or mine blasts.

One particular spectral feature that characterizes some mining explosions is a modulation of the spectrum introduced by a ripple-fired explosion. A ripple-fired event usually involves detonation of a number of explosions that are often regularly grouped in space and time. Such explosions, known as quarry blasts, have low magnitudes that may be close to those of nuclear explosions that one might monitor under the CTBT. As examples of these kinds of mine blasts, we consider using array data from the Arctic Experimental Seismic Station (ARCESS) in northern Norway, previously analyzed by Der et al (1993).

In previous work (see Shumway, 1996), we have examined two approaches to determining a consistent pattern of reflections in N time series, assuming a multiplicative model of the form

$$y_j(t) = a_j(t) \otimes \theta(t) \otimes n_j(t), \quad (1)$$

$j = 1, 2, \dots, N$, where the response of the j^{th} seismometer at time t is regarded as a convolution (\otimes) of a function $a_j(t)$ representing deterministic path and site effects, $n_j(t)$ representing random effects and a common part $\theta(t)$ that presumably contains the reflection sequence. It is assumed to be of the general form

$$\theta(t) = \sum_{j=0}^n \theta_j \delta(t - \tau_j), \quad (2)$$

where $\delta(\cdot)$ denotes the Kronecker delta, $\theta_0 = 1, \tau_0 = 0$, and the reflections occur at time delays $\tau_1, \tau_2, \dots, \tau_n$ with amplitudes $\theta_1, \theta_2, \dots, \theta_n$.

The frequency domain approach expresses the log spectrum of (1) as

$$\log f_j^y(\nu) = \log |A_j(\nu)|^2 + \log |\Theta(\nu)|^2 + \log f_j^n(\nu). \quad (3)$$

where $f_j^y(\nu)$ and $f_j^n(\nu)$ are spectra of the observed series and noise series respectively and

$$|\Theta(\nu)|^2 = \sum_{j=0}^n \sum_{k=0}^n \theta_j \theta_k \cos[2\pi\nu(\tau_j - \tau_k)] \quad (4)$$

shows that ripples will appear at multiples of the possible time delay differences $\tau_j - \tau_k, j \neq k$. In particular, the Fourier transform of the log spectrum, i.e. the cepstrum, will tend to a general shape that has peaks at $(\tau_j - \tau_k)/T$, when the data are sampled at T points in time (see Bogert et al, 1962, Baumgardt and Ziegler, 1968).

In Shumway (1996) and Shumway, Baumgardt and Der (1997), we use an F-Statistic, derived from regarding the detrended log periodograms as realizations of stationary processes. The *detrended* log-periodogram model is of the form

$$\log \frac{|Y_j(\ell)|^2}{|\hat{A}_j(\nu_\ell)|^2} = \log |\theta(\nu_\ell)|^2 + \log |N_j(\ell)|^2, \quad (5)$$

where $Y_j(\ell)$ and $N_j(\ell)$ are Fourier transforms of the observed data and multiplicative noise respectively. The detrended log-periodogram is expressed in terms of a common signal $\log |\theta(\nu_\ell)|^2$ and a noise term $\log |N_j(\ell)|^2$ which differs from site to site and represents local site effects. Based on Shumway (1971), we Fourier transform both sides of (5) and obtain an F-statistic for testing for no signal component as a function of delay. Letting $Q_j(d), j = 1, 2, \dots, N$ be the transforms of the lefthand side of (5), the statistic

$$F_{2,2(N-1)} = (N-1) \frac{N|\bar{Q}(d)|^2}{\sum_j |Q_j(d) - \bar{Q}(d)|^2} \quad (6)$$

has an F distribution with 2 and $2(N-1)$ degrees of freedom, where $\bar{Q}(d)$ is the mean of the cepstral series at delay d .

An example involving the P_n phase from a mining explosion in the Kola Peninsula, observed at 5 channels of the ARCESS array in northern Norway (see Der et al, 1993) is shown in Figure 1. The F-Statistic for this event shows peaks at .18, .35, .68 and .85 seconds (7, 14, 24 and 34 points). One might tentatively hypothesize ripple-firing with delays of about .18-.25 seconds.

RESEARCH ACCOMPLISHED

We have recently investigated an alternative for analyzing data conforming to the multiplicative model, defined in (1) and (2). In this model we regard the time delays as being at multiples of some underlying delay d , so that $\tau_j = jd$ in (2). Then, (1) can be written as

$$y_j(t) = s_j(t) + \sum_{k=1}^n \theta_k B^{kd} s_j(t) \quad (7)$$

where $s_j(t) = a_j(t) \otimes n_j(t)$ is modeled as an autoregressive series of the form

$$(1 - e^{-k_0} B)^3 s_j(t) = w_j(t), \quad (8)$$

where $Bs_j(t) = s_j(t-1)$ is the usual backshift operator and $w_j(t)$ are independent white noise processes. The model (8) has been shown by Dargahi-Noubary (1996) to include a number of earthquake and explosion source functions as special cases and is technically a special case of the Box-Jenkins seasonal ARIMA model, corresponding to $ARIMA(0,0,3) \times (0,0,n)_d$. In the above model, the delay d corresponds to the spacing of the charges in the ripple-fired events and the number of pulses n is proportional to the

Stacked plot of PN110 Signal

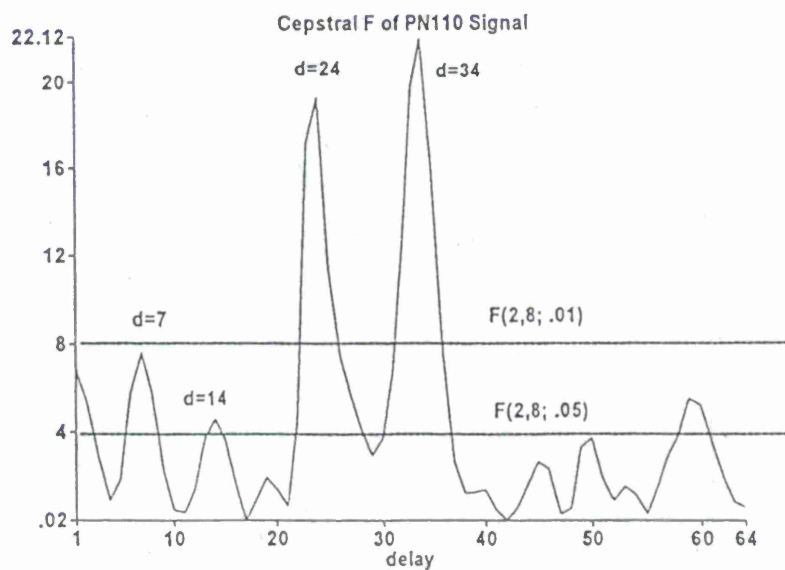
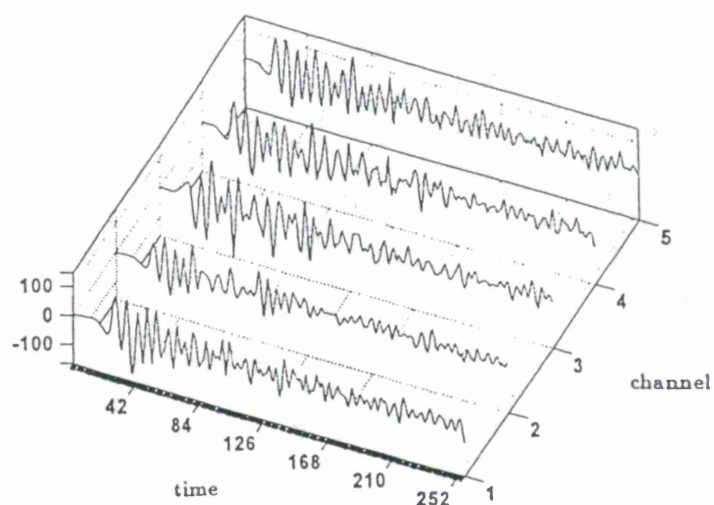


Figure 1 Array recordings of P_n Phases for Event 110 Recorded at ARCESS (Top Panel) and Cepstral F-Statistic (Bottom Panel) Showing Ripple Delays at 7, 14, 24, 34 Points. The sampling rate is 40 points per second.

number of charges. We estimate the parameters $k_0, \theta_1, \theta_2, \dots, \theta_n$ by maximum likelihood and choose the number of pulses n and delay d as the joint minimizers of the *Bayesian Information Criterion (BIC)* of Schwarz, 1978, say

$$BIC(n, d) = \log \hat{\sigma}^2 + \frac{(n+1) \log(NT')}{NT'} \quad (9)$$

where $\hat{\sigma}^2$ is the average residual sum of squares from the fitted model.

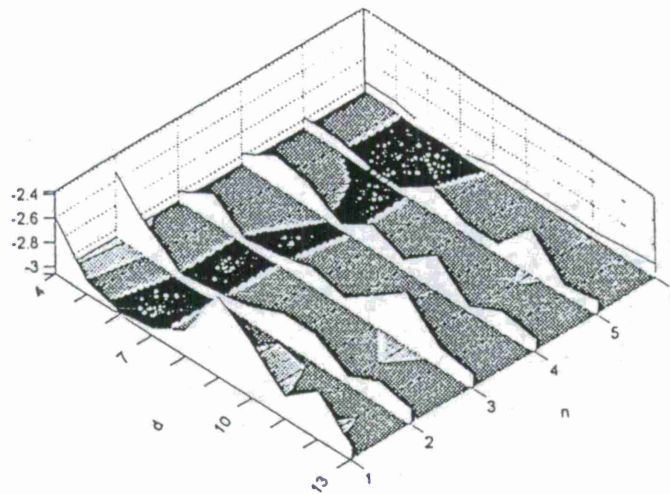
Applying the corresponding time domain approach to the P_n signal in Figure 2 shows possible consistent delays at 6 to 7 points or .15-.18 seconds. The parameter estimates were $\hat{k}_0 = .708$ and $(\hat{\theta}_1, \hat{\theta}_2, \hat{\theta}_3, \hat{\theta}_4, \hat{\theta}_5) = (.33, .02, .14, .22, .18)$ and they are all positive, showing a more reasonable model for $d = 6$ points.

We have also analyzed the P_n phases from eight additional mining explosions and the results are shown in Table 1. Only peaks that are significant at level .01 are quoted in the cepstral analysis of variance. The results are mixed, with the time and frequency domain results not matching in a number of cases. Again, the BIC criteria from the seasonal ARIMA searches had to be averaged to show a consistent pattern. Relatively consistent delay patterns were obtained, except for events 219 and 246. Note that there are cases where the cepstral analysis show peaks at delays longer than those that are searched over in the seasonal ARIMA model. Events 219, 246 and 282 show cepstral peaks at relatively long time intervals, namely those that are greater than .3 seconds. Generally, ripple firing proceeds at relatively closely spaced delays, typically .035 seconds for inter-shot delays, and .2 seconds for delays between symmetrically placed rows of charges. At longer delays, it is possible that we may only be observing spectral modulations acquired from such factors as resonance in the low velocity layers of the crust.

Table 1: Estimated Time Delays for HD9 Explosions (in points)

Event	Cepstral F-Statistic	Seasonal ARMA Search
PN-054	4, 21, 33	4
PN-066	10, 23	5
PN-110	7, 15, 24, 34	7
PN-147	7, 20	4, 6
PN-182	3, 21	4
PN-219	15, 26, 30	4, 6
PN-246	15, 23	10, 11
PN-282	12, 20, 25, 31	6, 10
PN-285	4, 22, 26, 39	5

Stacked plot of PN-110 BIC



Stacked plot of PN-110 BIC ave. over t

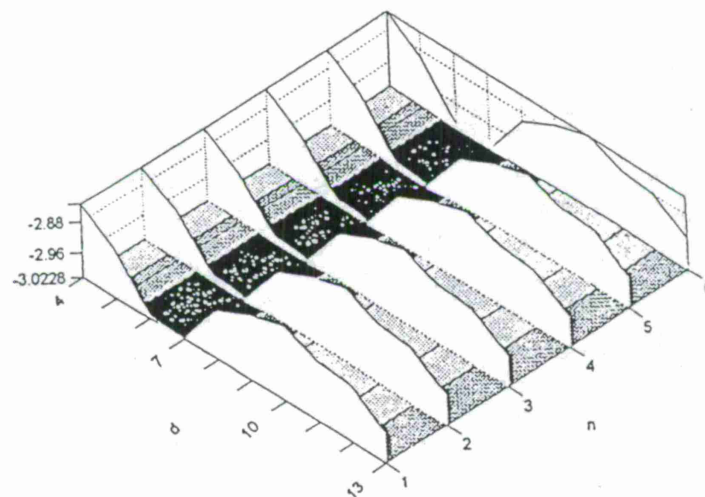


Figure 2: BIC Contours for Event 110 as a Function of Delay d and Number of Reflections n . The darkest value corresponds to the minimum. The three levels shown correspond to the values labeled on the ordinate. The bottom panel averages BIC over the number of reflections and shows consistent delays at $d = 6$ and $d = 7$ points.

CONCLUSIONS AND RECOMMENDATIONS

We have developed frequency and time domain approaches to detecting ripple-firing and have tested these methods, both on simulated data and on very small arrays of real data. In general, the frequency domain method leading to the cepstral F-Statistic, is preferred because the presumed irregularities that will be present in most ripple-fired signals dictate a more nonparametric approach that does not assume a given delay structure. These irregularities are due, in part, to the geometry of the firing pattern and the limitations of sampling at rates comparable to 20 Hz.

We have shown that the cepstral F-Statistic and the time domain ARIMA methodology, to a lesser extent, can be successful in detecting a sequence of reflections in contrived array data. While there are some difficulties in detecting the correct number of reflections and delay in the time domain methodology, the estimation of the delay parameter d seems quite successful when the cepstral F-Statistic is computed. We were not able to identify consistent ripple-firing in all of the observed arrays but there were several cases where reflections that were reasonable were isolated.

In the next phase of the research, we intend to investigate an additive noise model of the form

$$y_j(t) = a_j(t) \otimes \theta_t + n_j(t) \quad (10)$$

where both the convolving function $a_j(t)$ and the ripple signal θ_t are unknown. This model is essentially the factor analysis model with a single common factor series θ_t (see Geweke and Singleton, 1981). In this model, we assume the signal θ_t to be a random white noise process and the noises to be independent with unequal spectra $f_j^n(\nu)$. The fixed function $a_j(t)$, expressing site and path effects and the underlying source function, will be assumed to be smooth enough in frequency so that the model

$$Y_j(\ell) = A_j(\nu)\Theta(\ell) + N_j(\ell) \quad (11)$$

is reasonable over a restricted band of frequencies $\ell = 1, 2, \dots, L$, centered on ν . It is easy enough to derive maximum likelihood estimators for the complex amplitudes $A_j(\nu)$ and the spectral densities $f_j(\nu)$. Using the complex normal distribution as an approximation for the distribution of the vector $\mathbf{Y}(\ell) = (Y_1(\ell), Y_2(\ell), \dots, Y_N(\ell))'$, we may use the EM algorithm to estimate the parameters and to derive an associated estimator for the deconvolved time function θ_t . For multiple sites and multiple events, Shumway and Der (1985) have shown how to simultaneously deconvolve source and site functions (see also Der et al, 1996).

REFERENCES

- Baumgardt, D.R. and K.A. Ziegler (1988). Spectral evidence for source multiplicity in explosions: Application to regional discrimination of earthquakes and explosions. *Bull. Seismolog. Soc. of Amer.*, 78, 1773-1795.
- Bogert, B.P., M.J.R. Healy and J.W. Tukey (1962). The frequency analysis of time series for echoes: cepstrum, pseudo-autocovariance, cross cepstrum and saphe cracking. In *Proceedings of a Symposium on Time Series Analysis*, ed. M. Rosenblatt. New York: John Wiley.
- Dargahi-Noubary, G.R. (1995). Stochastic modeling and identification of seismic records based on established deterministic formulations. *J. Time Series Analysis* 16 201-219.
- Der, Z.A., D.R. Baumgardt and R.H. Shumway (1993). The nature of particle motion in regional seismograms and its utilization for phase identification. *Geophy. J. Int.* 115 1012-1024.
- Der, Z.A., A.C. Lees, K.L. McLaughlin and R.H. Shumway (1992). Multichannel deconvolution of short period teleseismic and regional time series. Chapter 9 in *Statistics in the Environmental and Earth Sciences*, A.T. Walden and P. Guttorp (eds.), 156-188. London: Edward Arnold (New York: Halsted Press).
- Geweke, J.F. and K.J. Singleton (1981). Maximum likelihood confirmatory factor analysis of economic time series. *Int. Econ. Rev.* 22 37-54.
- Schwarz, G. (1978). Estimating the dimension of a model. *Ann. Statist.* 6 461-464.
- Shumway, R.H.(1971). On detecting a signal in N stationarily correlated noise series. *Technometrics*, 13, 499-519.
- Shumway, R.H. and Der, Z.A.(1985). Deconvolution of multiple time series. *Technometrics*, 27, 385-393.
- Shumway, R.H. (1996). Array detection of ripple-fired signals: The cepstral F-Statistic. Scientific Report 1. PL-TR-96-2253, Phillips Laboratory, Directorate of Geophysics, Air Force Materiel Command, Hanscom AFB, MA 01731-3010.
- Shumway, R.H., D. R. Baumgardt and Z.A. Der (1997). A cepstral F-Statistic for detecting delay-fired seismic signals. Submitted to *Technometrics*.

Seismic Discrimination Between Earthquakes and Explosions in the Middle East and North Africa

William R. Walter, David B. Harris, and Steven C. Myers
Geophysics and Global Security Division, Lawrence Livermore National Lab

Sponsored by U.S. Department of Energy
Office of Nonproliferation and National Security
Office of Research and Development
Contract W-7405-ENG-48

Comprehensive Test Ban Treaty Research and Development Program, ST482B

ABSTRACT

The recently signed Comprehensive Test Ban Treaty provides for an international network of primary and auxiliary seismic monitoring stations (IMS) to verify its compliance. Calibration is required to confidently use these stations to identify and discriminate between earthquakes, mine-related events and clandestine nuclear explosion, particularly for small to moderate seismic events recorded regionally at only a few stations. Given the lack of regional recordings of underground nuclear tests in most of the world, we are making use of mining and industrial explosions to test discriminants. For example, we use the Multimax compiled dataset of small earthquakes and quarry explosions in Israel to test regional discriminants at local distances with mixed results.

Further complicating calibration is the fact that many IMS sites have not yet been installed and others have very short operating histories. When IMS data are available, there is often a lack of independent information ("ground truth") on the seismic sources. Here we describe a procedure for calibrating stations with limited data and apply it to the IMS auxiliary station MDT in Morocco. Data were initially available for three months in 1990 when MDT was operated as part of MEDNET. An event detector was run over the continuous data and regional events identified and roughly located using S-P time and back azimuth. The procedure uses spatial and temporal clustering to identify "known" mine blasts. The spatial clustering is done using the waveform correlation technique of Harris (1991) to find events with similar sources and locations. Temporal clustering looks at the time of day and repetition in time of events with the mine blasts occurring during working hours and days repeatedly over a period of time. A set of "known" earthquakes is also determined using location, time of day, distribution in time and size criteria. With these independent libraries of identified seismic events, we evaluate promising regional discriminants such as high frequency P/L_g . We also examine distance and path effects on the discriminants. Preliminary results indicate high frequency P/L_g provides some separation between mine blasts and earthquakes at MDT.

Key Words: seismic, discrimination, identification, mine-blast, Middle East, North Africa

OBJECTIVES

Monitoring of the Comprehensive Test Ban Treaty requires seismically discriminating between earthquakes, mining activities and any potential clandestine nuclear test. LLNL is evaluating regional discriminants in the uncalibrated Middle East and North Africa (ME&NA) and other regions of interest to improve the CTBT monitoring capability.

RESEARCH ACCOMPLISHED

As part of the overall Department of Energy CTBT Research and Development program, LLNL is pursuing a comprehensive identification research effort to improve our capabilities to seismically characterize and discriminate potential underground nuclear tests from other natural and man-made sources of seismicity. Here we present preliminary results in two parts. First, we present a methodology for obtaining ground truth from time and spatial clustering of seismically recorded events. We apply this methodology to three months of data available from MEDNET for the IMS auxiliary station MDT in Morocco. We then use the results to evaluate regional discriminants at MDT. Second, when ground truth is available, as in the Multimax dataset from Israel, we evaluate regional discriminant performance directly.

Calibration of CTBT Monitoring Stations for Event Identification: MDT, Morocco

Regional discriminants such as high frequency (>4 Hz) P/S ratios and high/low frequency ratios show great promise to discriminate events based on studies near the major test sites (e.g. Walter et al. 1995; Hartse et al. 1997). However, the physical basis of these discriminants is not firmly established, and regional phases can be strongly affected by the heterogeneous structure of the lithosphere. Therefore it is important to calibrate these discriminants in new regions like ME&NA at each of monitoring stations. Unfortunately many of these stations are not yet installed or have limited data. Further complicating calibration is the lack of ground truth data, particularly explosion data for evaluating the discriminants. Here we present techniques to obtain ground truth using correlation, and spatial and temporal clustering techniques. We apply this data the IMS auxiliary station MDT in Morocco which has limited data available. Morocco is a region of low-to moderate natural seismicity and is known to have active mines. We believe we can follow-up this initial "blind" study by working with our university partners at Cornell to connect the seismically identified events to actual active mine provided ground truth. For all these reasons, MDT in Morocco is an ideal place to test these techniques.

We began the analysis procedure by running an STA/LTA detector over the three months of continuous data available from June-August 1990 from MEDNET via the IRIS DMC. We found 195 regional events with reasonable signal-to-noise ratios. Of these events, nine correspond to earthquakes in the NEIC catalog. We used these nine events with known locations to check regional phase propagation in the region (see figure 1). We found that events west of Gibraltar showed strong Sn phases and a notable absence of Lg. In contrast events east of Gibraltar and within Morocco itself show little Sn but a strong Lg phase. We also used these events with known locations to check the feasibility of estimating back azimuth from initial P-wave polarization. This process and other indications (long period noise) led us to discover the vertical and east components were switched and the north component had reversed polarity. We were subsequently able to confirm this with the MEDNET operators for the 1990 data. After correcting the channels we found back azimuth calculations at the broadband three component stations were generally accurate to 10 degrees or so provided the signal-to-noise ratio was good.

The 195 events were then analyzed using a waveform correlation technique (Harris, 1991; for more details please see Harris this volume). The three-component seismograms of each of the 195 events was cross correlated with all other events. Events with high correlation values must have similar mechanisms and locations and are grouped into "clusters". Using a fairly high threshold correlation value (0.7) we found twelve clusters containing three or more events, but two of these were discarded as too noisy for our discrimination study. An example of three such clusters at MDT is shown at the top of figure 2. We then applied spatial and temporal clustering analyses to the clusters. Eight clusters were found to have patterns consistent with mine blasts: they occurred only during working hours and were repeated over a period of days to weeks. Earthquakes are expected to have more random distribution in time and if aftershocks, have timing more consistent with Omori's law (exponential decay). Time of day and day of week histograms for the 43 events in these eight clusters are shown at the bottom of figure 2. Note the working hour distribution and the lack of events on Sunday.

Two of the clusters were identified as earthquakes since in each case there was a larger event in the PDE or ISC catalog and the other events occurred within 24 hours, not necessarily during working hours. One cluster remains unidentified. For known earthquakes we made use of the 4 PDE events in the Alboran sea. Given the daylight-only distribution of the blasts we decided to use a 10PM-5AM time window to find more earthquakes, discovering an additional 10 events, some of which appeared in the ISC or PDE catalogs. (We never found a blast in the PDE or ISC catalogs). With the PDE events, earthquake clusters and nighttime events, we have 16 independently identified earthquakes.

We estimated distance away from MDT in kilometers using eight times the hand picked S-P times. Because clusters should have nearly identical S-P times were able to estimate our picking accuracy as about within one second by examining the variability within the clusters. Back azimuths were determined using a polarization analysis of the initial P onset. The approximate locations determined this way are shown in Figure 3. The eight mining clusters fall into 4 different mining areas. The earthquakes show a distribution throughout Morocco. Note all events outside of Morocco and west of Gibraltar were discarded due to lack of Lg.

We used the 43 mine blasts and 16 earthquakes shown in Figure 3 to test the regional discriminants. The Moroccan crustal thickness is 30-35 km (e.g. Calvert et al., 1997) with a Pn-Pg cross-over distance near 150 km. Since our distances ranged from 100-400 km we did not attempt to separate Pn and Pg but used a P window that included both, from the hand-picked onset time to a group velocity of about 5 km/s for P and 3.6 to 3.0 km/s for Lg. We also averaged the results from all three components to improve stability (e.g. Kim et al. 1997). The results are shown for four frequency bands in Figure 4. Note the mean value of the earthquakes and explosions shows increasing separation with frequency though there remains substantial overlap even at 6-8 Hz. While several studies show better discrimination for P/Lg at even higher frequencies (e.g. Kim et al. 1997, Plafcan et al., 1997 pre-print.), 6-8 Hz was the highest achievable frequency using this 20 sps data. We are currently in the process of evaluating other regional discriminants using this data.

Evaluation of Regional Discriminants Using Israeli Ground Truth Dataset

Ground truth explosion and earthquake data is very limited in the Middle East. One such dataset was put together by Multimax Inc. (Grant et al., 1996) based on data provided by Shapiria (1996 et al.). This dataset consists of 30 earthquakes and 20 quarry blasts in northern Israel recorded by the Israeli Seismic Network. A discrimination study was done on these events by Gitterman and van Eck (1993) using a variety of measures but not relative P/S amplitude ratios. Shapira et al. (1996) looked at P/S in Israel using a 1-10 Hz band with mixed results and

suggested a strong dependence on path effects in this heterogeneous region. As noted previously, higher frequency (>4 Hz) regional P/S measures show much promise in discriminating explosions from earthquakes. We tested the higher frequency regional P/S discriminant on this ground truth data at a number of the Israeli network stations as shown in Figure 5. Unfortunately at any given station only a fraction of the 50 events are available with good signal to noise and without glitches in the regional phases. We examined 6-8 Hz regional P/S at four of the stations with the most explosion data and show the results in Figure 6. While there appears to be reasonable discrimination at stations ADI and JVI the picture at DSI and MML is more mixed, although the mean values of the explosions are still higher than that of the earthquakes. One might consider averaging over stations, but using data with stations in common restricts the number of events even further, and averaging over not common stations mixes site effects together with discriminant separation clouding the evaluation of discriminant performance.

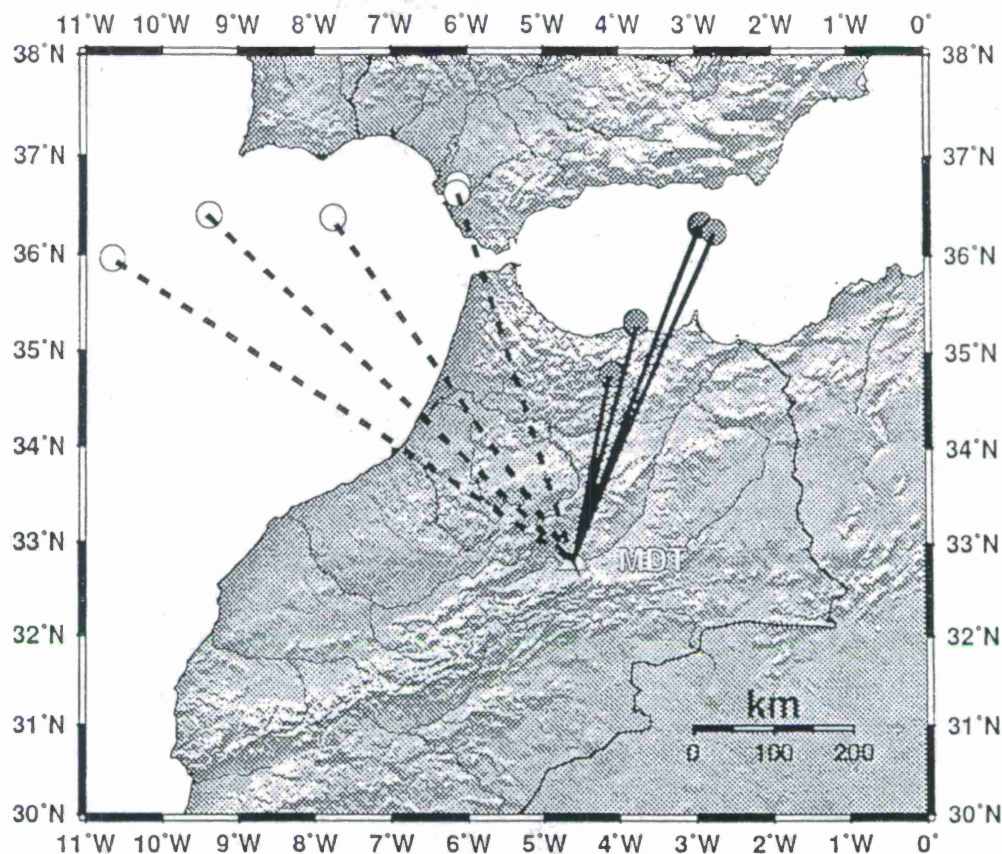
Northern Israel is the site of a future IMS auxiliary station PARD, but data is not yet available for it. We are examining a nearby station BGIO run by the GEOPHONE network for which data is presently available. We are currently exploring the same type of analysis for BGIO as was done for MDT in the hopes of increasing the number of ground truth explosions and earthquakes available and will present preliminary results at the meeting.

CONCLUSIONS AND RECOMMENDATIONS

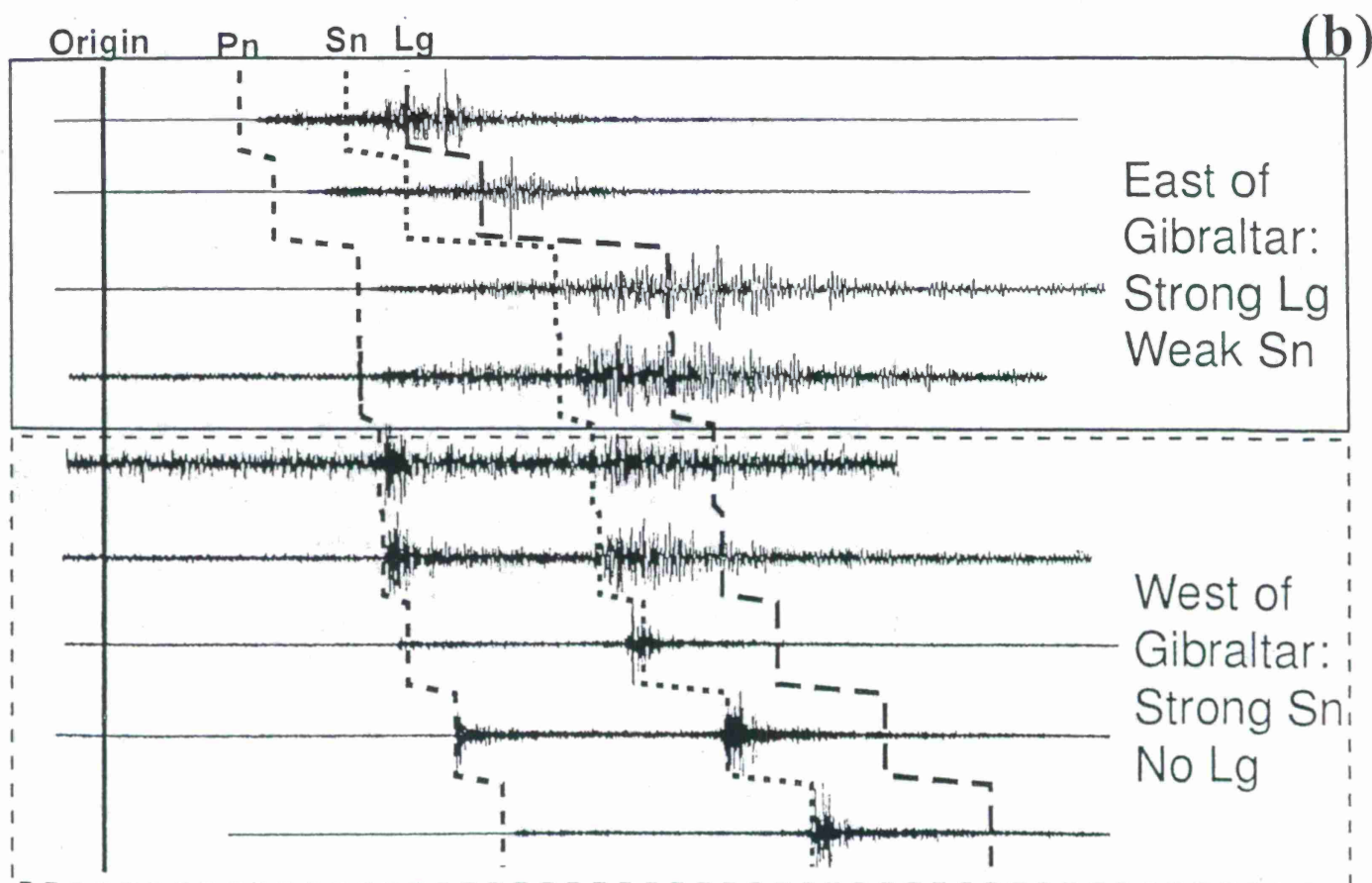
The ME&NA is a challenging and tectonically complex area, requiring calibration in each of many geophysically distinct subregions. Calibration is severely limited by a lack ground truth explosion data. When available, we are evaluating discriminants on such data. When ground truth is lacking, LLNL has developed and tested an empirical procedure using correlation and clustering (see also Harris this volume) to independently identify groups of events to use in evaluating regional discriminants. Using this technique we are calibrating MDT, Morocco, and other IMS stations or their surrogates in the ME&NA. For regions without sufficient empirical data, we are improving our physically based discriminant models using the best available data worldwide.

References

- Calvert A., F. Gomez, D. Seber, M. Barazangi, N. Jabour, A. Ibenbrahim and A. Demnati. (1997) An integrated geophysical investigation of recent seismicity in the Al-Hoceima region of north Morocco, *Bull. Seism. Soc. Am.*, **87**, 637-651.
- Gittermann, Y., and T. van Eck, (1993). Spectra of quarry blasts and micro-earthquakes recorded at local distances in Israel, *Bull. Seism. Soc. Am.* **83**, 1799-1812.
- Grant, L., F. Ryall, I Hensen, and W. Rivers (1996). Ground truth database for seismic discrimination research, *Proceedings of the 18th annual seismic research symposium on a monitoring a comprehensive test ban treaty*, Phillips Lab., PL-TR-96-2153, 997-1006.
- Harris, D. B. (1991). A waveform correlation method for identifying quarry explosions, *Bull. Seism. Soc. Am.*, **81**, 2395-2418.
- Hartse, H., S. R. Taylor, W. S. Phillips, and G. E. Randall, (1997). A preliminary study of regional seismic discrimination in Central Asia with an emphasis on Western China. *Bull. Seism. Soc. Am.* **87**, 551-568.
- Shapira, A., Y. Gitterman and V. Pinsky, (1996). Discrimination of seismic sources using the Israeli seismic network, *Proceedings of the 18th annual seismic research symposium on a monitoring a comprehensive test ban treaty*, Phillips Lab., PL-TR-96-2153, 612-621.
- Walter, W. R., K. Mayeda, and H. J. Patton (1995). Phase and spectral ratio discrimination between NTS earthquakes and explosions Part 1: Empirical observations, *Bull. Seism. Soc. Am.*, **85**, 1050-1067



(a)



(b)

Fig. 1. (a) Map of MDT region and NEIC located events recorded at MDT. These events were used to confirm back-azimuth calculations and test regional S phase propagation (solid lines show Lg, dashed lines do not). (b) High-pass filtered seismograms. Group velocity onset times shown by dashed lines: Pn (8 km/s), Sn (4.5 km/s) and Lg (3.5 km/s). Note events west of Gibraltar show Sn but not Lg.

Example Mine Blasts Identified at MDT

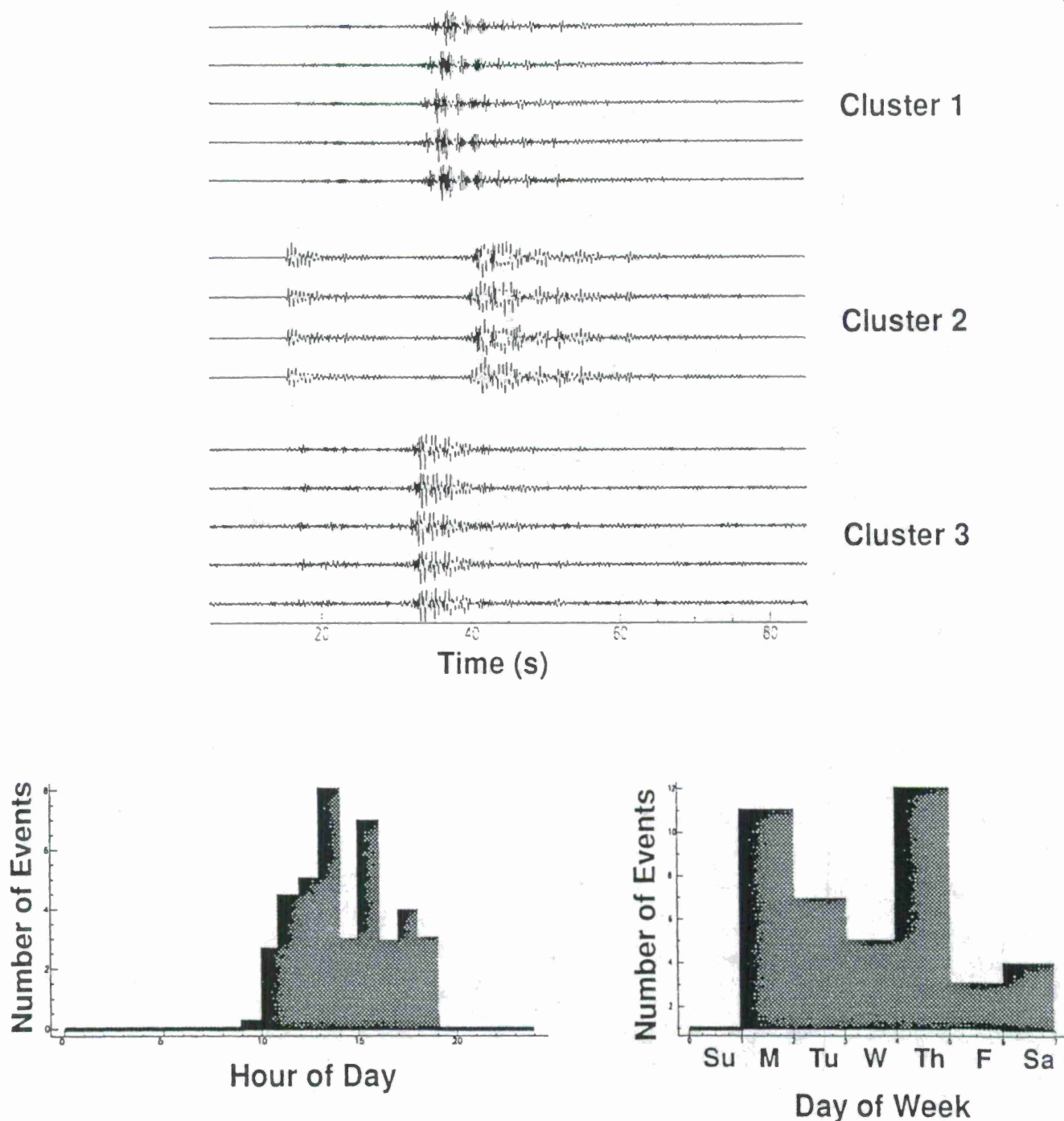


Fig. 2. Example of clustering results at MDT. Using the technique of Harris (1991) we found 12 clusters with three or more events each. Using temporal and spatial information we determined 8 clusters to be mine blasts, 2 to be earthquakes, 2 others were too noisy to use and 1 cluster remains unidentified. Shown here are 3 examples of mine blast clustered seismograms and temporal histograms made for all 8 mine blast clusters. Clustered events have high correlations indicating similar locations and mechanisms. We expect mine explosions to have different temporal behavior than earthquakes. For example mine blasts should occur during working hours and on working days and regularly over a long period of time. Earthquakes should have more random distributions in time of day and week and in the case of aftershocks show exponential decay with time.

Locations of Discrimination Study Events

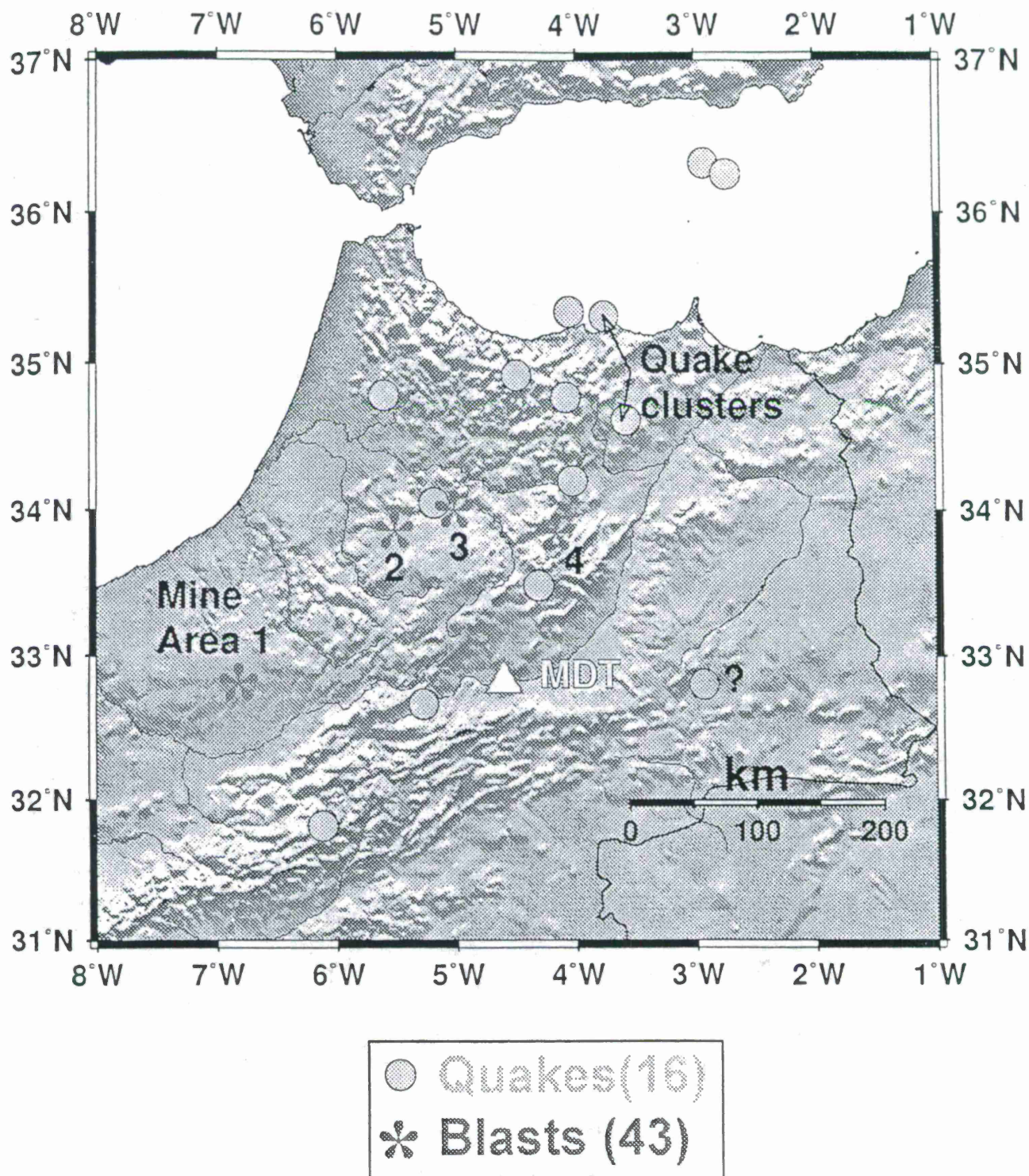


Fig. 3. Map showing approximate locations of discrimination study events estimated from S-P times and back-azimuths calculated from initial P-wave polarization using 3-component particle motion. The 43 mine-blasts are from 8 separate clusters that appear to be from 4 distinct mining regions. The eastern most mine area appears to be the phosphate mines near Khouribga. The 16 earthquakes include 10 events between 10 PM and 5 AM presumed to be earthquakes. All these events fall in the region where we expect efficient Lg propagation.

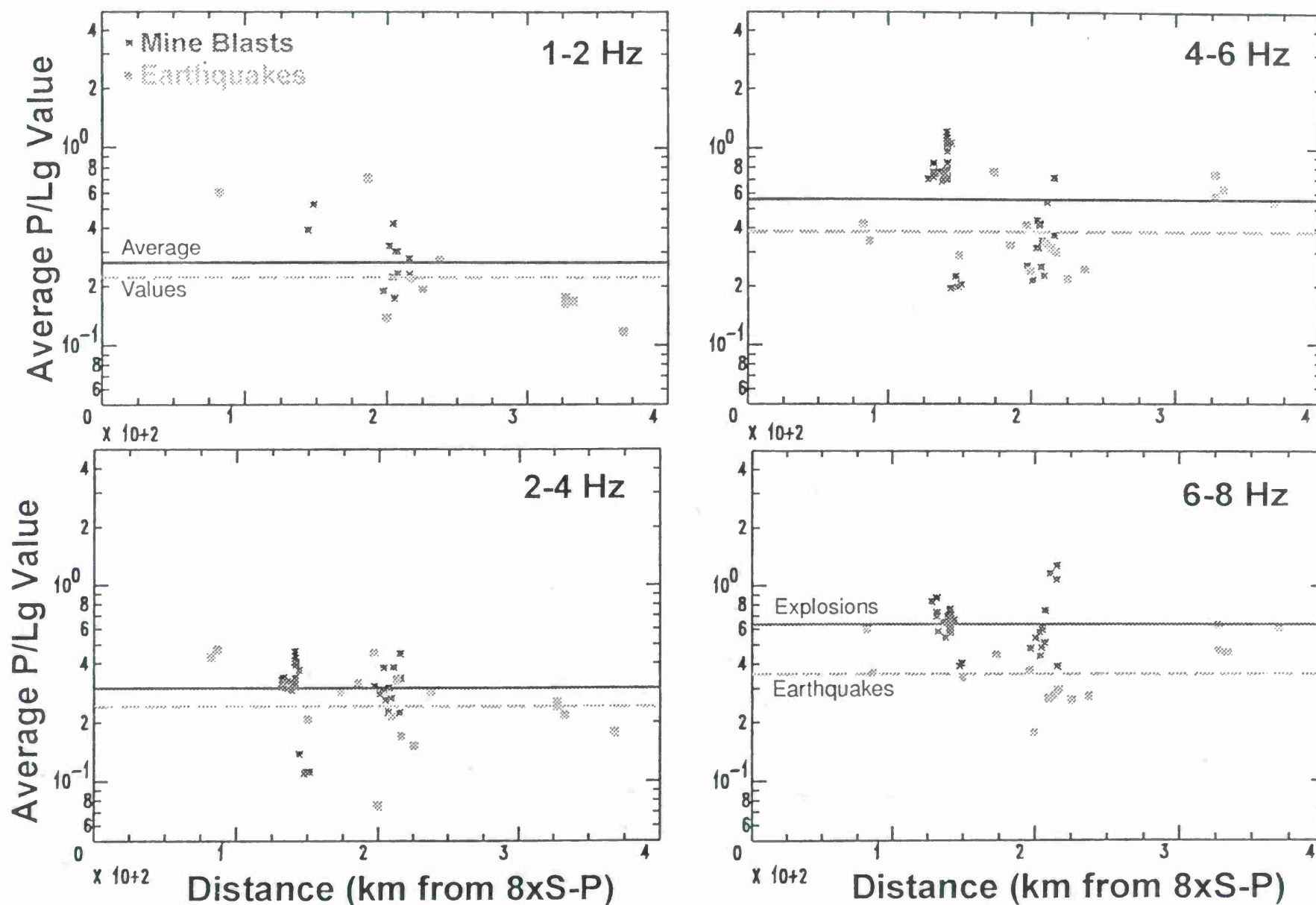


Fig. 4. Evaluating the P/Lg discriminant in four different frequency bands as a function of distance. Distance is approximated by eight times the S-P time interval. Note the separation between event population increases with frequency up to 6-8 Hz the maximum achievable with this 20 sps data. While the average value for the explosion group (solid line) is larger than the earthquake group (dashed line), there remains substantial overlap of events even at 6-8 Hz.

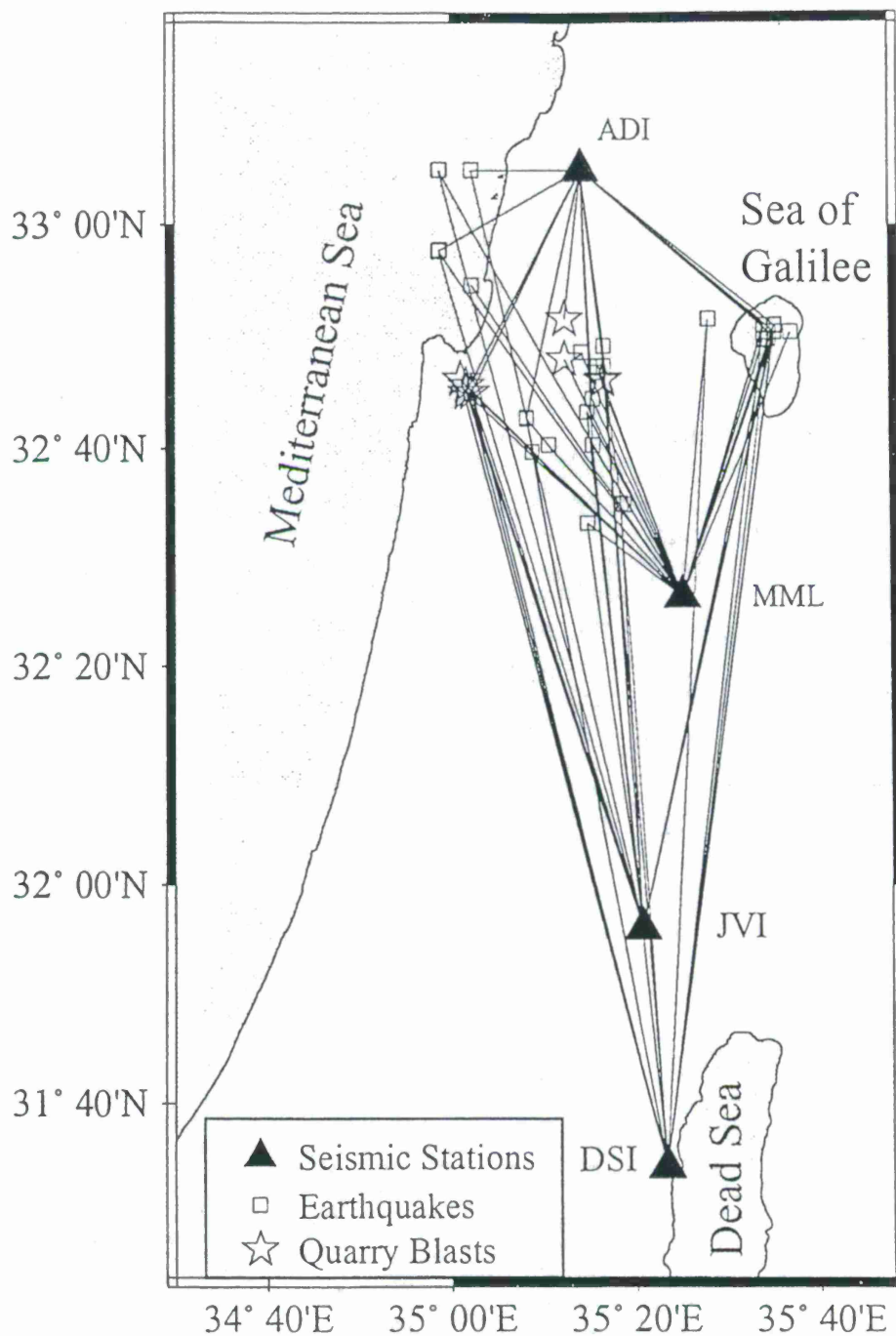


Fig. 5. Earthquakes and Quarry Blasts Recorded at select stations in the Israeli Seismic Network. Selection criteria are Pg and Lg spectra in the 6 to 8 hz frequency band with S/N greater than twenty db. The noise spectra is taken from a pre-arrival window immediately before each phase arrival.

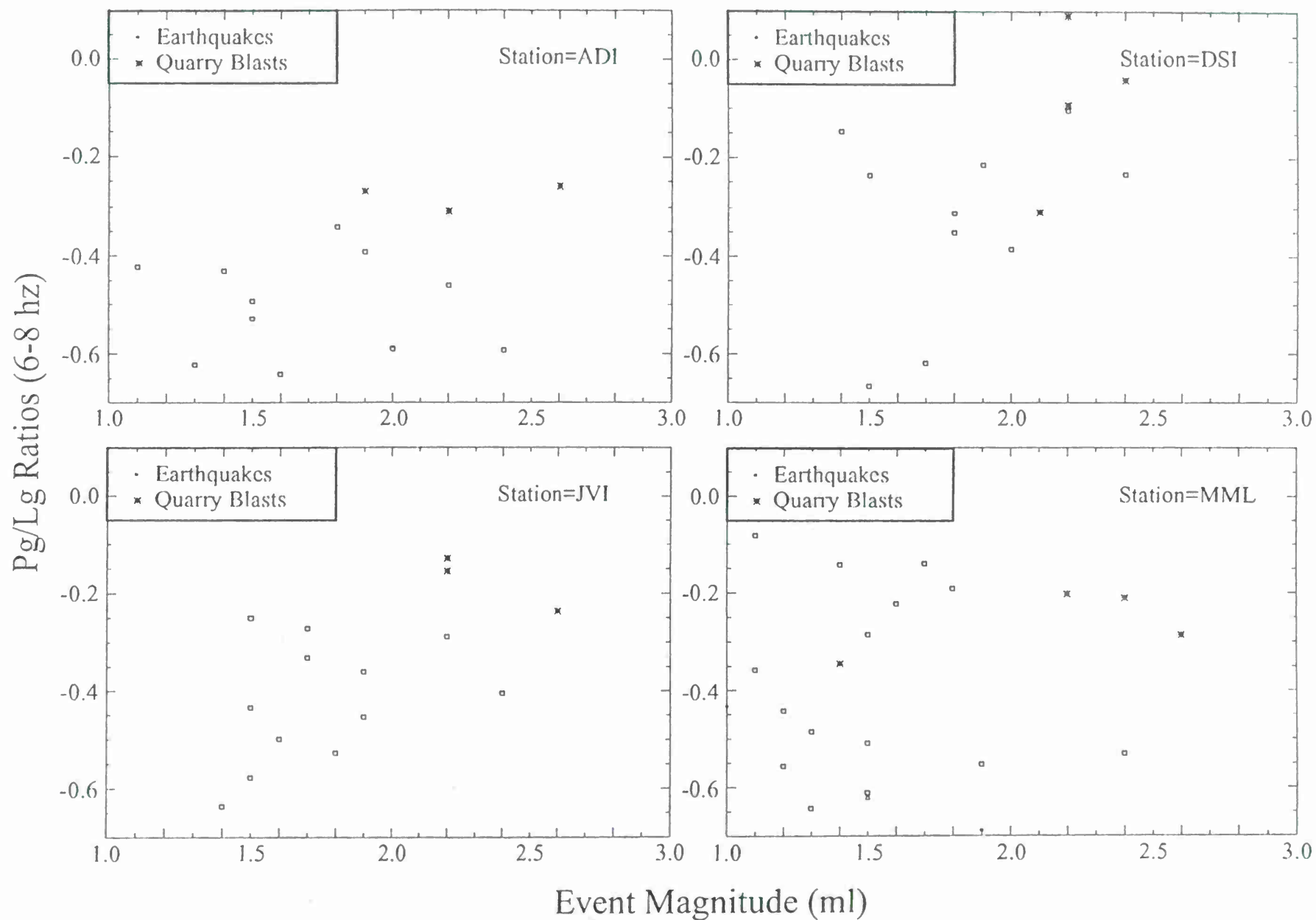


Fig. 6. Pg/Lg ratios for select earthquakes and quarry blasts recorded on four stations of the Israeli seismic network. Event/station ray paths are shown in Figure 5.

AN ALTERNATIVE SHORT-PERIOD P/S DISCRIMINANT USING PHASE-WEIGHTED RATIOS

Bradley B. Woods and C. K. Saikia
Woodward-Clyde Federal Services,
Pasadena, CA

Sponsored by the Air Force Office of Scientific Research
Contract No. F49620-94-C-0046

ABSTRACT

The short-period P/Lg ratio, in its various time-domain and spectral forms, is one of the primary regional discriminants as it has a low magnitude threshold and because of its successful performance throughout Eurasia. However, Lg amplitudes are known to be strongly effected by blockage and scattering. Such propagation effects must be accounted for in order to produce transportable discrimination parameters and considerable progress has been made to this end by various researchers. In the southwest U.S. the performance of this discriminant has been less successful with significant overlap of earthquake and explosion populations. Although part of such results can be explained by propagation effects, source-related effects such as earthquake mechanism and near-source scattering for shallow events (particularly explosions) are believed to be the primary such contributors, although emplacement medium may play a role as well. We examine the P and Lg phases for sequences of earthquakes and NTS explosions recorded by TERRAscope, looking in particular detail at records for events which are misclassified by their P/Lg ratio. Anomalous (high) P/Lg ratio earthquake records are for observations at P-wave maxima and low P/Lg ratios tend to be ubiquitous for a particular explosion. Such explosions are nearly all from Yucca Flat. It is believed that near-source scattering of Rg to S/Lg along the basin edge is primarily responsible for this. Further, explosions which have a large amplitude Lg wavetrain also have a diminished Pg phase relative to Pn. This observation supports results from other studies which find that Pn/Lg is a more effective discriminant than Pg/Lg. From these observations we have developed a modified short-period P/S discriminant, the P_g^*/L_g^* ratio where the two phases are weighted by the ratio of P_n/P_c (the average P-coda envelope level) and the ratio of P_n/P_g , respectively. This measure successfully distinguishes earthquakes from explosions for events which are misclassified by other P/S ratio methods.

Keywords: discrimination and seismic sources

OBJECTIVE

This work regards near-source scattering effects on the character of S/Lg waves observed from NTS explosions and earthquakes throughout California and Nevada. To better understand these effects and what causes events to be misclassified *vis-a-viz* short-period P/S discriminants, We looked at the character of short-period P and S waveforms of these events, *i.e.* explosion-like earthquakes and *visa versa*, to determine if there were still some distinguishing features between them. Any improvements that can be made to current regional short-period P/S ratio analysis efforts are of great importance to seismic monitoring of events below $M=4$ for which long-period surface wave measurements are not usually observed, thus rendering more effective short-period:long-period discriminants infeasible.

RESEARCH ACCOMPLISHED

The events analyzed and the stations on which they were recorded are shown on the map in Figure 1. The waveforms were examined in terms of their ground-velocity envelopes. The records were first high-pass filtered at 2 Hz. The envelope function, $e(t)$, is given by:

$$e(t)=\sqrt{x(t)^2+y(t)^2},$$

where $x(t)$ is the time series and $y(t)$ is its Hilbert transform. We then compared peak envelope amplitudes for the P_n , Pg, and Lg phases, and the average energy level of the P-wave coda (hereafter referred to as Pc). To get more reliable measurements, the envelope function was smoothed over a 10-point (0.5 secs) sampling interval. This interval was effective at making emergent, low-amplitude P_n first-arrivals discernible for noisy records. A wider sampling interval (2 secs) was first used to more clearly examine gross waveform features, in particular the Pc envelope level, however it did smear-out the initial P_n onset for several events. For display purposes, the energy envelopes have been smoothed over the longer interval in order to see the general character of the envelope amplitudes, and in particular the average energy level of Pc, however the initial P_n phase is measured from the unsmoothed envelope.

Figure 2 displays vertical-component velocity records and envelopes for a Skull Mountain aftershock (upper box) and the Pahute Mesa NTS explosion Montello (lower box); both are observed at PFO. The arrival times of the regional phases of interest are marked by vertical dashed lines. These two events both exhibit waveforms "typical" of their respective source types. For the earthquake, the S/Lg phase is much larger than either the P_n or Pg phases. Also note that the average coda level is larger than P_n . Whereas for the explosion P_n is as large as any phase in the Lg wavetrain, as well as being larger than the average Pc level, and Pg is larger still. These two events would in all likelihood separate using any short-period P:S discriminant, as they did with respect to our short-period P:S energy ratio (Woods and Helmberger, 1997).

In contrast, Figure 3 displays the vertical-component velocity records and envelopes for two misclassified events. The earthquake in the upper figure is the Desert Hot Springs

foreshock ($M_L=4.7$) recorded at ISA. Again, pertinent phases are marked. P_g is quite large relative to L_g , however, note the low amplitude, emergent nature of P_n and that it is considerably smaller than that of the P coda level too. The lower figure is of the NTS Yucca Flat explosion Divider recorded at PFO. Yucca Flat shots, particularly at PFO, exhibit large L_g or S waves (Woods and Helmberger, 1997). In fact, this is the very worst-case explosion record (*i.e.*, it looks most like an earthquake vis-a-viz the short-period P:S discriminant) in the TERRAscope data set. Note that both P_n and P_g , which are of comparable size to each other, are small compared to L_g , however both are still a factor of two larger than the P coda level. In examining other explosion records I have found that the explosions which exhibit large S/ L_g wavetrains have roughly equivalent-sized P_n and P_g arrivals, which suggests a mechanism whereby P_g is converted to S.

The observations that the ratio of P_n to P_c for explosions tends to be greater than unity and significantly less for earthquakes, and that explosions with large L_g wavetrains appear depleted in P_g (relative to P_n) are ubiquitous for the TERRAscope data set. We use these features to develop weighting factors for the P_g and L_g strengths. P_g^* is defined as:

$$P_g^* = P_g \times \frac{P_n}{P_c},$$

the rationale being that the larger P_n/P_c ratios associated with explosions will then increase their P_g^* value. L_g is defined similarly as:

$$L_g^* = L_g \times \frac{P_g}{P_n}.$$

The reasoning for this weighting scheme is that P_g/P_n tends to be significantly larger for earthquakes than for explosions. Another way of thinking of it is as minimizing the contribution of L_g for those explosion records which appear depleted in P_g , *i.e.* P_g is comparable in strength to P_n , and are consequently augmented in L_g .

A direct consequence of this weighted P_g/L_g ratio is that the ratio actually becomes:

$$\frac{P_g^*}{L_g^*} = \frac{P_n^2}{P_c \times L_g},$$

which is curious in that the P_g term is cancelled-out. Since P_g has no direct effect then in this discriminant suggests that perhaps a weighted P_n/L_g ratio may be a more specious discriminant criterion.

We have applied the P_g^*/L_g^* ratio to a subset of our TERRAscope data sets which primarily consists of previously misclassified events, although the more typical events in Figure 2 were also included. Thus we can see how this short-period P:S variant performs for both "ideal" events (those with easily identifiable waveforms) and otherwise misclassified ones. These results are given in Figure 4a. The weighted P_g^*/L_g^* ratios are plotted vs. magnitude. No distance corrections were incorporated into these measurements.

Little or no distance dependence for these short-period P:S energy ratios was found previously (Woods and Helmberger, 1997). Also, all data examined fell within the distance range of 375 to 475 km. Further, the idea behind this discriminant -- that is weighting the pertinent phase measurements, is meant to be applicable to any short-period P:S discriminant -- including those with distance corrections.

Figure 5 displays two more examples of earthquakes. The top one, from the Rock Valley sequence, is thought to be a shallow source ($d=2$ km; Smith and Brune, 1993). Earthquakes from this sequence appeared explosion-like with respect to the phase and spectral ratio discriminants of Walter *et al.* (1995). In Figure 4 this particular record plots fairly high, near the range of the worst-case explosion.

The bottom figure is for the 2nd Los Gatos (or San Juan Bautista) earthquake. Note the apparent lack of Lg on the vertical component. On closer inspection there is a slight upsurge on the vertical component at the Lg window. It is, however, just that the P-coda is fairly large relative to Lg. But none the less the ratio of P to Lg is quite large for an earthquake and the relative size of P_n is apparently large, although there is a hint of a smaller, emergent onset. Both of these characteristics would classify this record as an explosion by the weighted P:S discriminant. In fact its value is 4.06, which is higher than many of the explosions. Thus this event poses a problem for this method as it stands.

In fact a number of events from the Loma Prieta and Watsonville sequences also had similar characteristic waveform envelopes. All of these quakes are predominantly strike-slip events, generally on strike with, and within the San Andreas fault zone, which also happens to be on azimuth with PAS, the receiver. This suggests a mechanism effect in the Lg radiation pattern as the azimuth is near a P-SV node and a SH maximum. A later Parkfield event shows similar behavior at this azimuth, while other observations do exhibit well-developed Lg wavetrains, supporting this hypothesis. There is, however, the possibility that the path along the fault zone and through the coastal ranges may possibly cause some strong propagational effect. Obviously other regional data from other azimuths, particularly CMB, would help to answer this question.

To account for such mechanism effects in terms of the discriminant, it would seem that taking the maximum Lg of the three components would be a better measure of the Lg source strength. For the case of the Los Gatos event, we see that there is a relatively large tangential-component Lg (Figure 6a). If it were used instead of the vertical, the envelope-amplitude ratio then would be reduced to 1.78

This value is still somewhat high due to relatively large amplitude P_n . This apparently large P_n for an earthquake needs to be explained, particularly for this P-node observation, for which P_n should be emergent and complex. If one looks at its unsmoothed envelope of the onset in detail, however, this earthquake record does look distinctly different from an explosion. Figure 6b is a blow-up of the initial portion of the unsmoothed vertical-component envelopes for the Los Gatos II quake (recorded at PAS) and the explosion Divider recorded at PFO. For the earthquake the initial pulse is quite small relative to Pg or Pc (a factor of 6 smaller than the smoothed peak P_n , hence yielding a weighted P_g/Lg ratio of 0.296), whereas in the case of Divider (once again an archetypal worst-case

explosion with a fairly complex P onset) the very first P arrival is still significantly sharper and more step-like than the more ramp-like earthquake onset, and its amplitude is relatively large in comparison to the other relevant phases (the unsmoothed P_n onset is within a factor of one (92%) of the smoothed onset). Thus without smoothing the envelope function, the relative $P_n / P_g / P_c$ amplitudes are still indicative of an earthquake and thus their weighting effects would still enhance the $P_g^*:Lg^*$'s identification performance. These unsmoothed P_n values were used in the calculation of ratios displayed in Figure 4a. For comparison, previous short-period P/S energy ratio results of Woods and Helmberger (1997) for the same records are shown in Figure 4b. Note the overlap and greater scatter in those results.

CONCLUSIONS AND RECOMMENDATIONS

There are several possible contributing factors which produce the observations on which this phase-weighting discrimination scheme is based. For the P_n/P_c term, there are two complimentary processes, one of which is related to P-wave complexity.

The complexity of teleseismic signals is known to be fairly indicative of source type (Blandford, 1993; Bowers, 1996), with explosions typically having a fairly strong step-like initial onset and few secondary phases within the initial 5 secs giving it a simple appearance, whereas earthquakes tend to have a much more emergent signal with a number of ensuing pulses (which are thought to be due to S to P scattering) which tend to grow with time, thus giving the onset a more ramp-like character. These characteristics are borne-out for the records in Figure 6b as discussed above. Thus it appears that the difference in source character is able to be discerned using the P_n through Pg wavetrains.

As earthquakes will generate S to P scattered phases, such energy, along with directly-scattered P waves, should produce a higher level of P-coda than explosions which primarily generate only directly scattered P-wave energy.

It is suspected that not only S to P scattering is responsible for the more complex nature of earthquake waveforms, but that asperities and directivity also may be responsible for the complex onset of P_n for earthquakes. In this case the very initial onset may reflect a small nucleation event rather than the primary rupture and thus be small relative to the other phases of interest. In particular, the P-coda is primarily generated by the main rupture, so it should be considerably larger than the onset due to the nucleation phase. The nucleation phase tends to be very small relative to the main waveform both in amplitude and duration. Evidence of such behavior for earthquakes is detailed in Ellsworth and Beroza (1995) wherein they report that for 30 events between magnitude (M_w) 8.1 and 2.6 show evidence of a small nucleation event phase which is on the order of 0.5% of the moment of the main event. As such, it would seem that time-domain measurements would best extract this feature.

As for the P_g/P_n term, there are again several complimentary process which help to differentiate source types. For earthquakes the nucleation phase, or onset of P_n , again plays a significant role in yielding a high P_g/P_n ratio. While the P_n onset is produced by the

small nucleation event, the peak P wave, which is usually taken to be P_g , is, no doubt, due to the main rupture, whereas for explosions the initial P_n onset and P_g are both products of the primary source-time function.

Further, the fact that earthquakes generally produce small P_n relative to P_g (this is apart from the nucleation phase) in comparison to explosions means that this ratio should always be somewhat greater than unity, thus increasing the weighting factor for the Lg wave. This effect is, of course, mechanism dependent.

Explosion observations clearly demonstrate that low P_g/P_n (near unity) ratios are indicative of relatively large Lg waves. Thus this factor minimizes such Lg amplitude values. As the angle of incidence for P_g is somewhat less than P_n , it is more likely to couple into SV shear waves and/or scatter should there be significant near-source structure such as a basin (as in the case of Yucca Flat), or severe topography (as in the case of Rainier Mesa). Thus, as other studies have found and we have heuristically derived, P_n is a more stable measure of P-wave source generation. This discriminant needs regional calibration, as in regions with strong lower crustal gradients P_n may not be observable and an alternative weighting scheme would be needed.

References

- Blandford, R. R., 1993. Discrimination of Earthquakes and Explosions at Regional Distances Using Complexity, *Scientific Report, AFTAC-TR-93-044*, Air Force Technical Applications Center, Patrick AFB, FL.
- Bowers, D., 1996. On the Probability of Mistaking an Earthquake for an Explosion Using the Simplicity of P, *Bull. Seism. Soc. Am.*, **86**, 1925-1932.
- Ellsworth, W. L. and G. C. Beroza, 1995. Seismic Evidence for an Earthquake Nucleation Phase, *Science*, **286**, 851-856.
- Smith, K. D. and J. N. Brune, 1993. A Sequence of Very Shallow Earthquakes in the Rock Valley Fault Zone; Southern Nevada Test Site (abstract), *EOS Suppl.* **74**, 417.
- Walter, W. R., K. M. Mayeda, and H. J. Patton, 1995. Phase and Spectral Ratio Discrimination between NTS Earthquakes and Explosions. Part I: Empirical Observations, *Bull. Seism. Soc. Am.*, **85**, 1050-1067.
- Woods, B. B. and D. V. Helmberger, 1997. Regional Seismic Discriminants Using Wavetrain Energy Ratios, *Bull. Seism. Soc. Am.* **87**, 589-605.

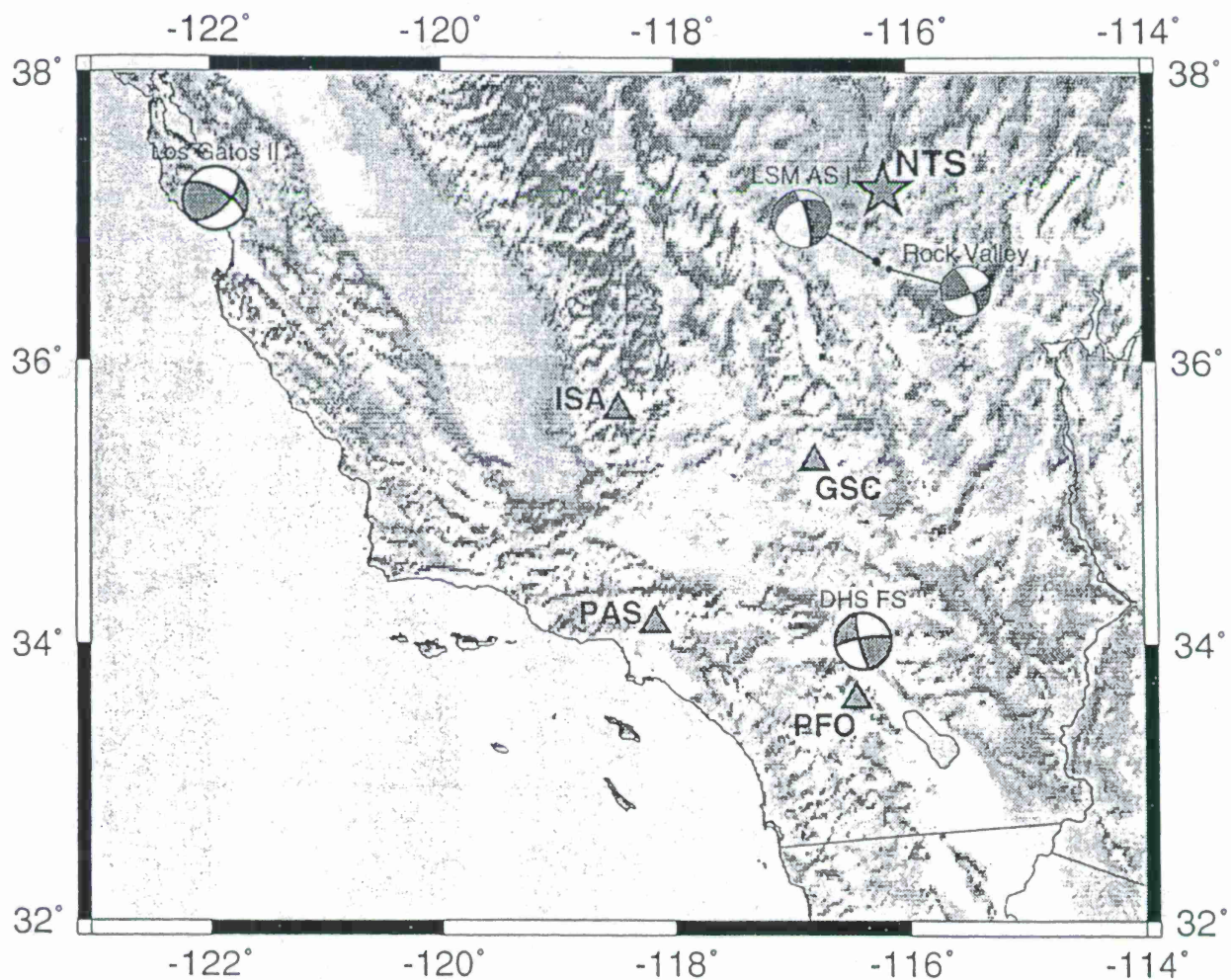
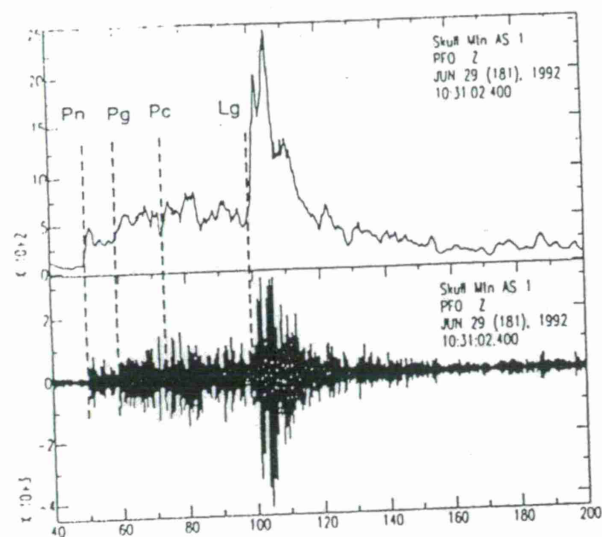
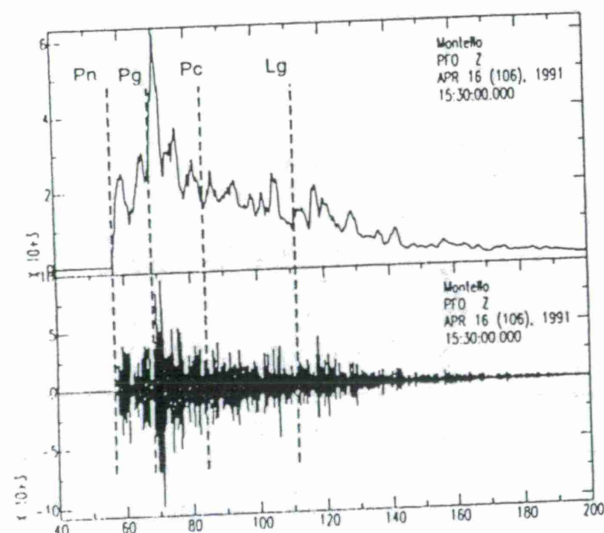


Figure 1. Map of the study area. Triangles denote stations used. NTS's location is denoted by a star. Earthquake mechanisms are provided for events used.

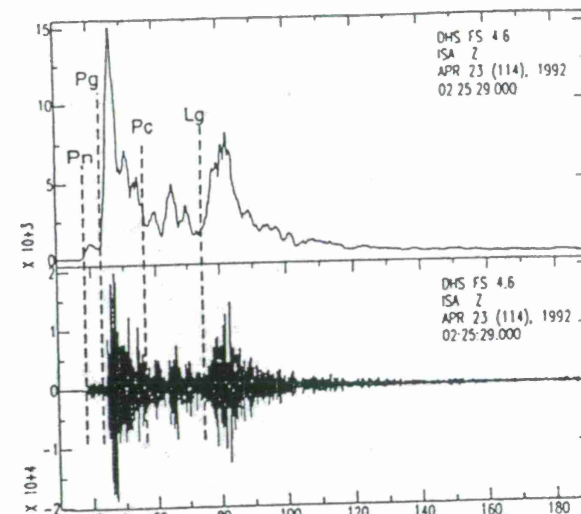


(a)

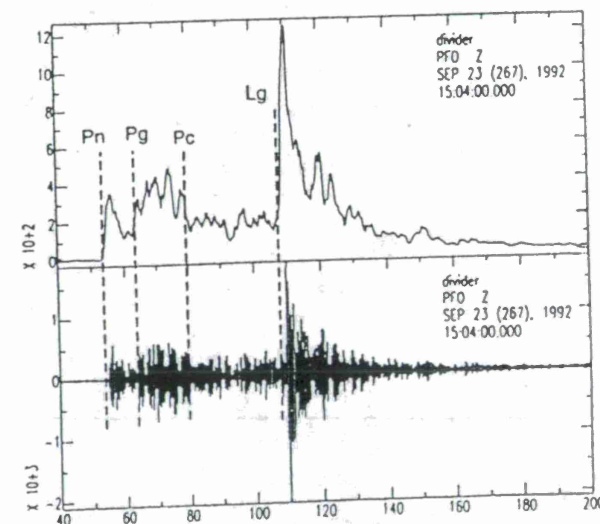


(b)

Figure 2. Short-period, vertical component, velocity (lower trace) and smoothed velocity envelope (upper trace) for (a) a Little Skull Mountain aftershock and (b) the Pahute Mesa shot Montello recorded at PFO. The onsets of pertinent phases are marked by vertical dashed lines.



(a)



(b)

Figure 3. Short-period, vertical component, velocity and smoothed velocity envelope for (a) the Desert Hot Springs foreshock recorded at ISA and (b) the Yucca Flat shot Divider recorded at PFO.

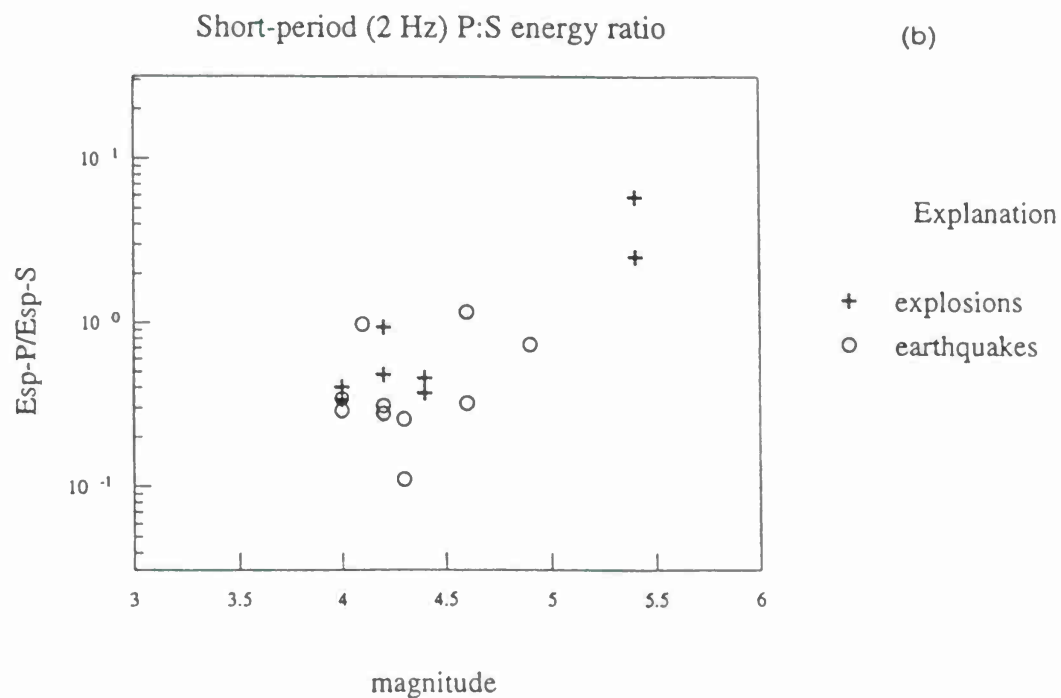
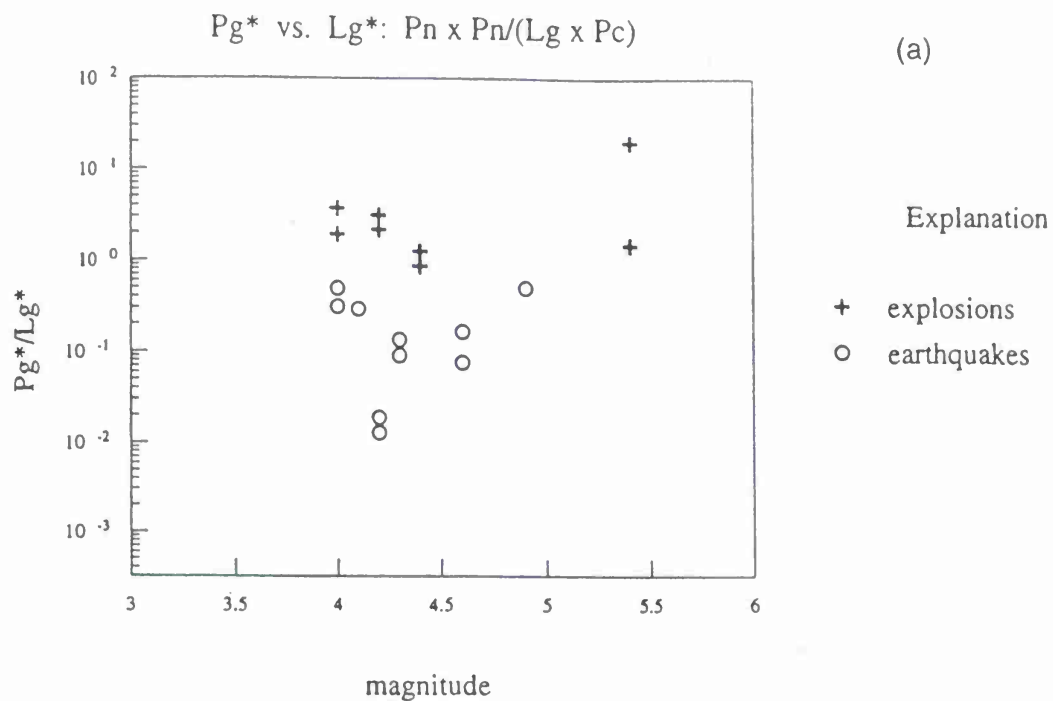
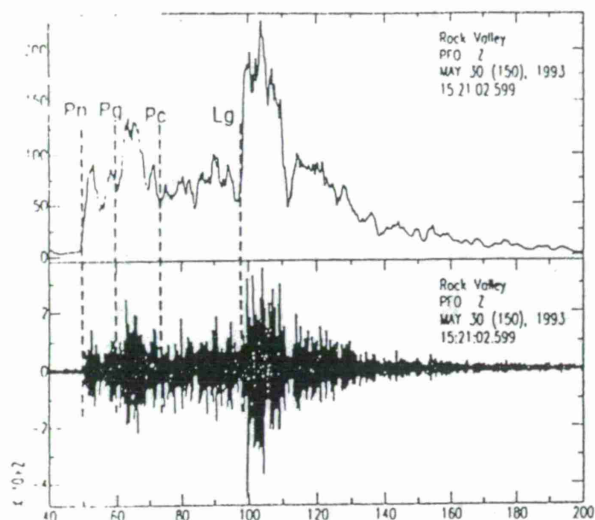
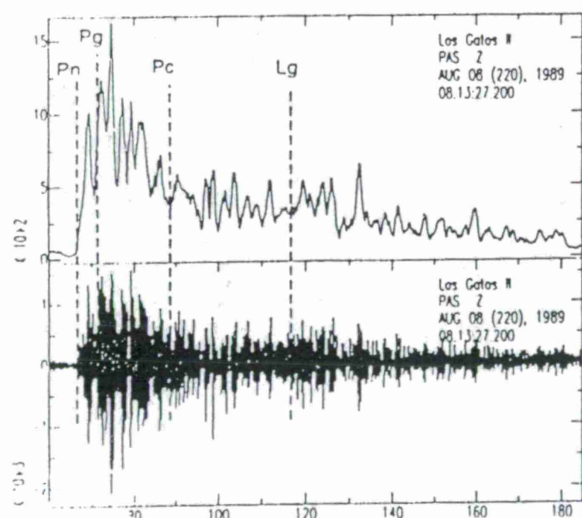


Figure 4. (a) The weighted Pg^*/Lg^* ratio vs. magnitude. Earthquakes are denoted by circles and explosions by crosses. (b) The short-period P:S energy ratio for the same records.

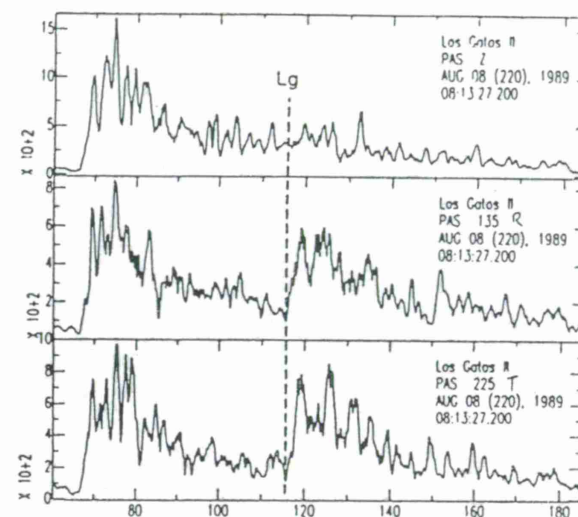


(a)

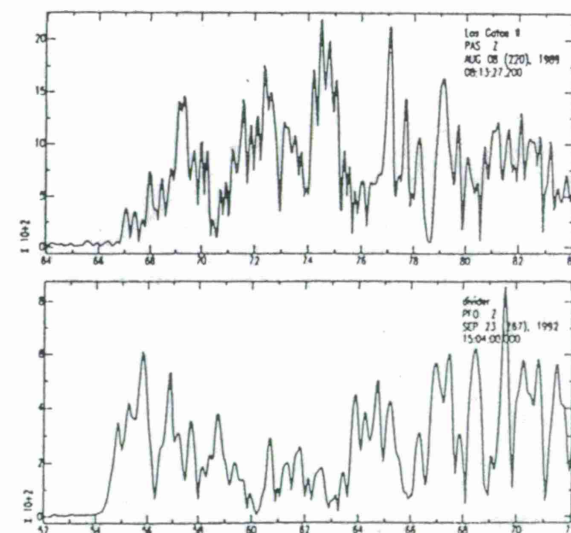


(b)

Figure 5. Short-period, vertical component, velocity (lower trace) and smoothed velocity envelope (upper trace) for (a) a Rock Valley earthquake recorded at PFO and (b) the 2nd Los Gatos earthquake recorded at PAS.



(a)



(b)

Figure 6. (a) Velocity envelopes for the Z, R, T components of the 2nd Los Gatos EQ. The onset of Lg is denoted by the dashed line. (b) A comparison of the unsmoothed velocity envelopes for the Los Gatos PAS and Divider PFO vertical records.

Lg BLOCKAGE AND SCATTERING AT CENTRAL EURASIAN ARRAYS CNET AND ILPA

Vernon F. Cormier and Thomas Anderson
Department of Geology and Geophysics
University of Connecticut
Storrs, CT 06269-2045

Sponsored by Air Force Office of Scientific Research
Contract No. F49620-94-1-0059

ABSTRACT

The effects of 3-D heterogeneity on Lg is investigated using both deterministic and statistical models of crustal structure. Variations in the efficiency of Lg propagation to the CNET and ILPA arrays agree well with predictions deduced from ray trajectories of multiple SmS computed in deterministic models of crustal and basin thickness. Complete regional seismograms are synthesized by the locked-mode method in plane layered models with the effects of scattering small scale heterogeneities included by the Born approximation. Experiments with varying distributions of small scale scatterers have demonstrated that scattering close to the source and receiver is more important than scattering mid-way along the crustal waveguide in lengthening Lg coda and equalizing energy on all components of motion.

Keywords: Seismic wave propagation, Lg, scattering, Moho, basins

OBJECTIVE

There ability to predict the effects of heterogeneous crustal structure on regional phase propagation in regions where little or no seismic recording has occurred must be achieved for a high confidence level in nuclear treaty monitoring. The computational expense of a numerical solution of the wave equation in an arbitrarily heterogeneous model have limited such predictions to primarily 2-D structure and low frequency bands. Ray based techniques of forward modeling, however, are sufficiently fast to allow predictions of regional phase propagation in detailed 3-D structures. The effects of scattering by Moho and basin thickness variations can be efficiently incorporated in the ray summation method in large scale 3-D models to investigate the effects of large scale (greater than 10 km scale length) on the efficiency of regional phase propagation and coda complexity. Small scale crustal structure (less than 10 km scale length) is examined in mode summation for laterally homogeneous models. Faults are modeled as a matrix of inclusions to predict complexity of Lg coda. Goals include (a) an understanding of what crustal structures are most important in determining the efficiency of regional phase propagation, (b) determining what type of non-seismic data (topography, surficially mapped geology, gravity, magnetics) are most useful in inferring 3-D crustal structure, and (c) where and what kind of statistics of small scale structure are important to the description of regional phases.

RESEARCH ACCOMPLISHED

Large Scale Structure. Variations in crustal thickness given in the database of Moho topography compiled by Fielding et al. (1993) are used to construct simple 3-D models of the crust in the vicinity of the CNET and ILPA arrays. Figure 1 shows the topography of Central Eurasian and the regional array region studied. Figure 2 shows crustal thickness variations in the vicinity of CNET and ILPA. Note that CNET lies near a strong gradient in Moho thickness associated with the Caucasus and several other strong gradients lie to the southwest. Events located to east of CNET all exhibit strong Lg excitation; data from events to the southwest of CNET have relatively weak or unidentifiable Lg coda relative to Pg. In ray tracing experiments, the Moho and basin boundaries are modeled as an Epstein transition zone. This introduces a hyperbolic tangent jump in velocity between a crust and upper mantle resulting linear velocity gradients with depth. These models simplify the description of multiple SmS rays comprising Lg coda, which are computed by integrating kinematic and dynamic ray tracing (Cerveny, 1985). The effects of lateral variations in crustal thickness on Lg efficiency are predicted by analyzing SmS ray turning and bounce points, which are plotted for rays shot from a source 1 km deep, at constant vertical and azimuthal take-off angles. Figure 3a shows an example of such a plot of SmS rays shot from station KIV near the center of CNET at constant vertical take-off angle and variable azimuthal angle. The crustal thickness is relatively uniform in the northern sector (see Figure 2), and varies from about 43 to 27 km under the Black Sea. Note that strong defocusing is seen to the west and southwest, with some blockage under the Black sea. All events showing weak or unidentifiable Lg in the group velocity band associated with Lg lie to the west and southwest. Similar strong correlations with Moho gradients and Lg efficiency have been described by us in experiments with Moho topography at the KNET array. Figure 3b illustrates what ray tracing predicts when basins are included in the regional model. The basin effect is very strong and emphasize scattering due to Moho gradients. In Figure 3b, the basin appears to trap Lg to the north-west and south-west, under the Black Sea. While there are too few events to the north-

west to test the prediction, this correlates well with low Lg/P ratios seen in data from events to the south-west. Figures 3c-d show ray bounce points for a source 1km deep centered on the ILPA array in Iran. Figure 3c is generated from a model with only crustal thickness variations. The general blockage or scattering to the north is in good agreement with recent Lg/P studies. The inclusion of the basin in figure 3d predicts strong scattering to the north and north-west as well as trapped and scattered Lg to the south and south-east. We conclude that Moho topography and basin structure are dominant factors in the efficiency of Lg propagation at both the CNET and ILPA arrays.

Small Scale Structure. Although ray models of Lg are useful in qualitatively predicting gross features of blockage by large scale crustal transitions, the effects of smaller scale heterogeneity are more difficult to include. The assumptions of the ray method break down when the scale length of the medium (measured by quantities like the ratio of velocity to magnitude of the spatial gradient of velocity) approaches the scale length of heterogeneity (measured by the a linear spatial dimension of the heterogeneity or radius of curvature of a rough boundary). Paradoxically, the most important effects of small scale heterogeneity can still be accurately included in the ray method by the Rayleigh-Born approximation to scattering when the scale length of the heterogeneity is much smaller than the wavelength (e.g., Wu and Aki, 1985).

Since realistic phase complexity is difficult to achieve in a ray method without either or both fine scale layering and large numbers of scatterers, we have initially investigated the effects of fine scale heterogeneity in plane-layered, laterally homogeneous structures, using the locked mode method (Cormier et al, 1991) and the Rayleigh-Born approximation. A fundamental problem on which we are first focusing is an answer to the question: where in crust and upper mantle is it important to have an accurate statistical description of small scale heterogeneity to describe the complexity of various regional phases. To answer this question we have begun some experiments on the effects of different distributions of scatterers. The dimensions of the scatterers (2.5 km radius) were chosen under the usual assumptions of Rayleigh scattering to insure large effects. The errors associated with wavelength approaching the dimensions of the scatterers, however, are expected to be on the order of 10-30% in amplitude (e.g., Cormier, 1995). In future experiments, we plan to investigate the effects of heterogeneities well within the Rayleigh scattering domain.

For scatterers in the crustal waveguide, prior results have indicated that near source and near receiver scattering is most important in lengthening the Lg coda and equalizing the energy on components of motion. Thus, to simulate these characteristics of a seismogram, it is less important to accurately describe the statistics of scatterers mid-way along the crustal waveguide between source and receiver. Near the source and receiver however, it is important to understand and describe the small scale effects. Figure 4 shows the effects of scatterers on complete regional seismograms generated by Mode-Born method. The model included two near source faults running perpendicular to the wave paths similar to the fault geometries seen in the Caucasus region. Faults were modeled as a matrix of single scatterers, perturbations in λ , μ , and ρ are 9%, 9%, and 6% , respectively. Radius of scatterers is 2.5 km.. Preliminary results are encouraging as the Lg envelope on all three components has realistic shape and decay.

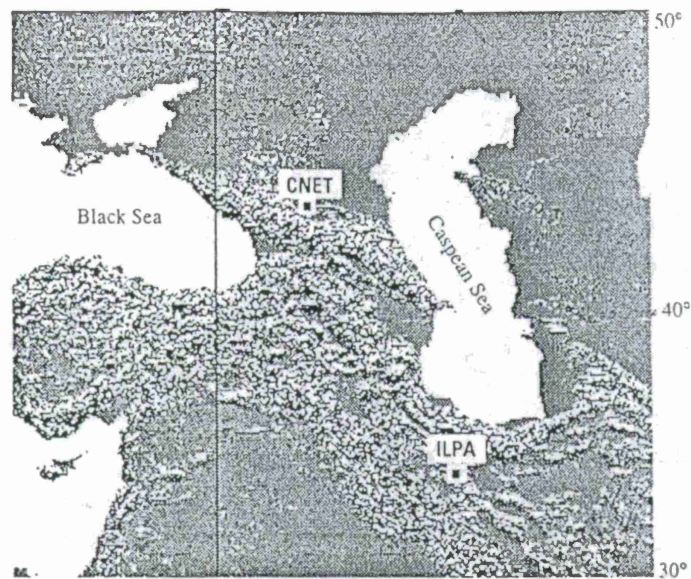


Figure 1. Topography in the vicinity of the CNET and ILPA arrays in Central Eurasia.

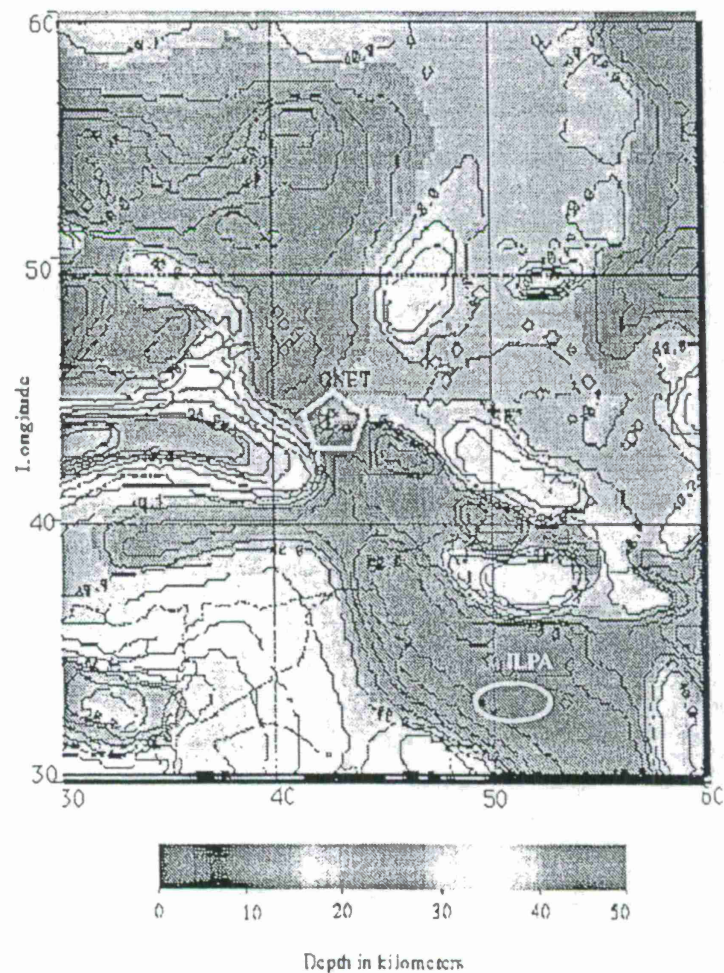
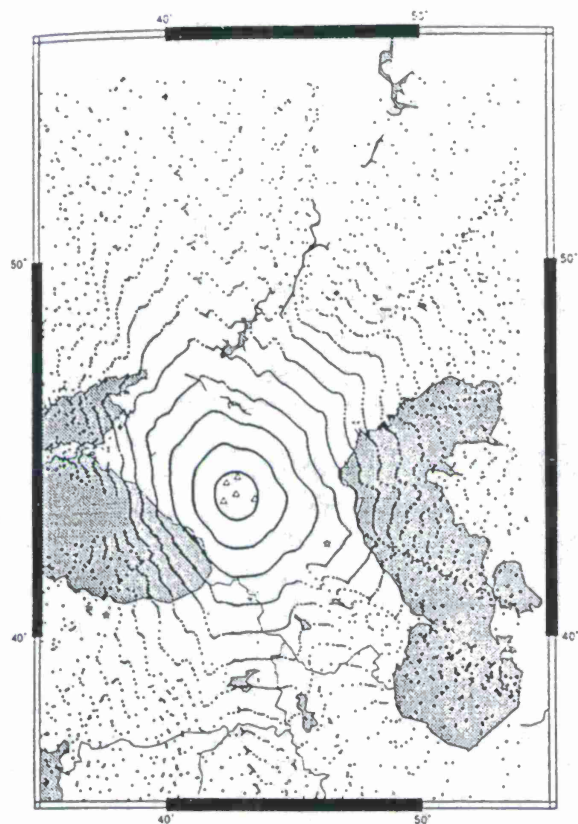
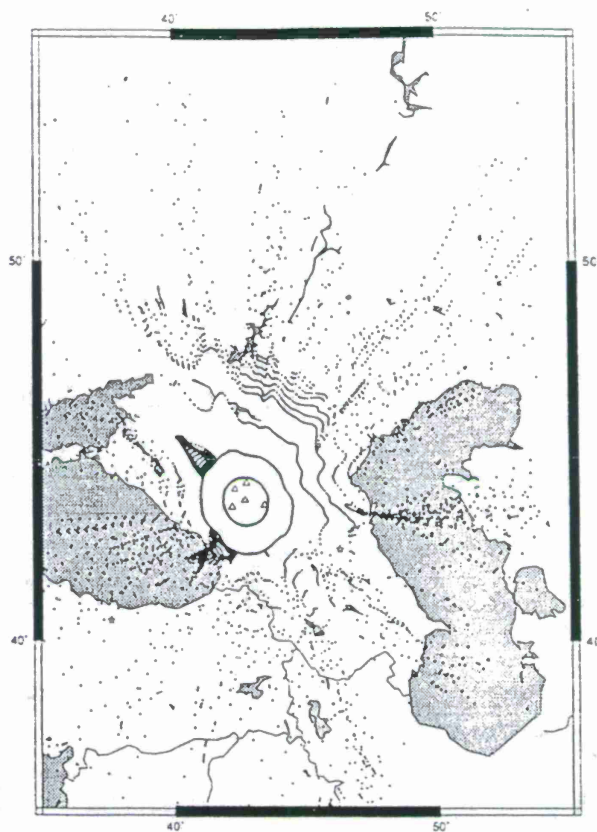


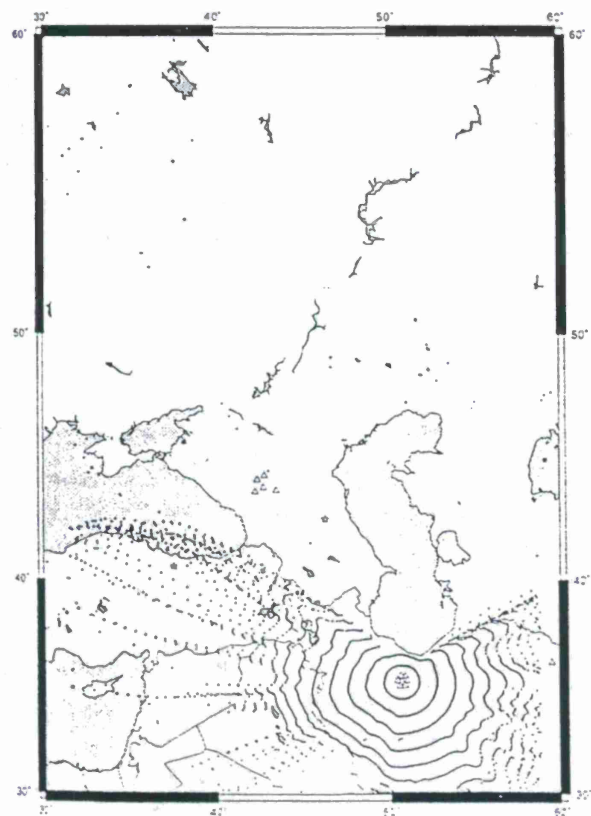
Figure 2. Moho topography based on the Fielding data set in the vicinity of the CNET and ILPA arrays in Central Eurasia.



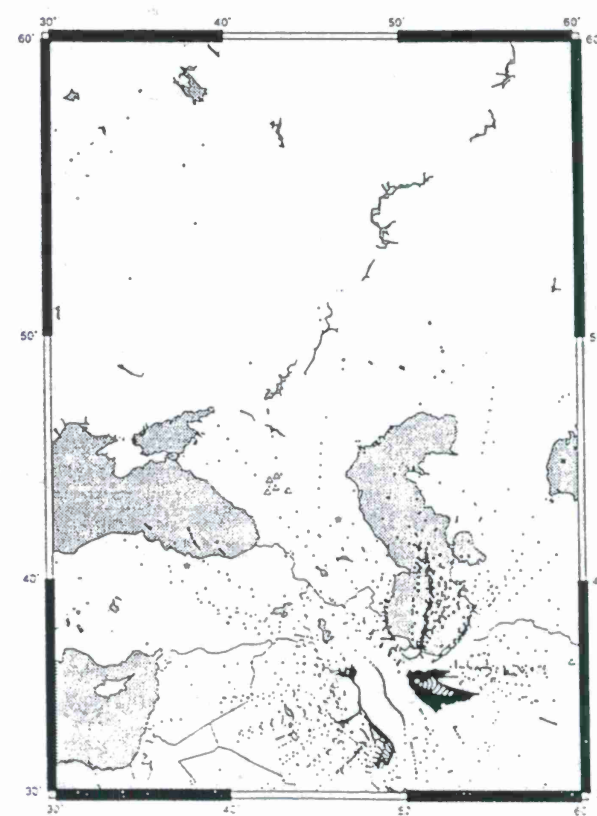
3a: CNET ray bounce points with Moho.



3b: CNET ray bounce points - added basin.



3c: ILPA ray bounce points with Moho.



3d: ILPA ray bounce points - added basin.

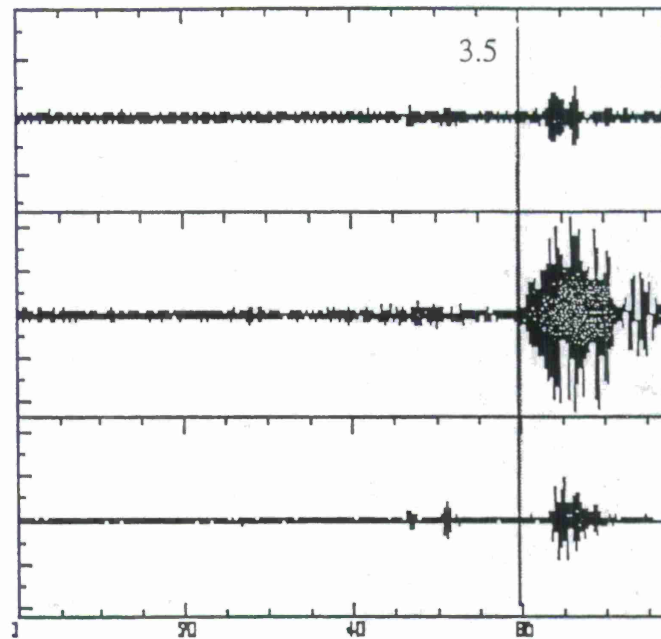


Figure 4. Synthetic seismograms generated from Mode-Born program. Model included two near source faults running perpendicular to the wave paths similar to the fault geometries seen in the caucasus region. Faults were modeled as a matrix of single scatterers, perturbations in λ , μ , and ρ are 9%, 9%, and 6% , respectively. Radius of scatterers is 2.5 km.. The Lg envelope on all three components has realistic shape and decay.

CONCLUSIONS AND RECOMMENDATIONS

A viewpoint is taken that the effects crustal heterogeneity can be best predicted by separating the effects of large scale (10 km and greater) from those of small scale (less than 10 km heterogeneity). The most important effects of large scale structure, including strong Lg attenuation and blockage, can be estimated from deterministic crustal models determined from regional refraction and deep seismic reflection surveys, surficial topography, and gravity. Strong lateral gradients in crustal thickness and basin structure, for example, have been shown to be associated with Lg blockage at CNET and ILPA, and previously with KNET.

Although it is impossible to ever accurately know the smaller scale structure in a given region, the effect of the statistics of the smaller scale structure on regional phases can be easily investigated using simple single scattering approximations and, eventually, numerical solutions of the elastic equation of motion in 3-D heterogeneous media. Scattering statistics close to the source and receiver have been shown to be much more important in controlling Lg complexity than detailed knowledge of scattering statistics all along the crustal waveguide. An understanding of the effects of near source crustal structure and tectonics , such as known faults, on scattering statistics together with an understanding of the gross effects of phase blockage of large scale structure, will form an important knowledge base for the transportability of seismic methods of detection, discrimination and yield estimation.

REFERENCES

- Cerveny, V., The application of ray tracing to the propagation of shear waves in complex media, in *Seismic Exploration* pp. 1-124, Treitel and Helbig, Vol. on Seismic Shear Waves, G. Dohr, ed., Geophysical Press, 1985.
- Cormier, V.F., B. Mandal and D. Harvey, Incorporation of velocity gradients in the synthesis of complete seismograms by the locked mode method, *Bull. Seism. Soc. Am.*, 81, 897-930, 1991.
- Cormier, V.F., and T. Anderson, Regional variations in Lg observed and synthesized at the CNET and KNET arrays, (abstract), *Seismological Research Letters*, 66, 28, 1995.
- Cormier, V.F., (1995). Time domain modeling of PKIKP precursors for constraints on the heterogeneity in the lowermost mantle, *Geophys. J. Int.*, 121, 725-736.
- Fielding, E., M. Barazangi, and B. Isacks, A network-accessible geological and geophysical database for Eurasia, North Africa, and the Middle East, *Proceedings 15th Annual Seismic Research Symposium*, AFOSR/DARPA, 1993.
- Wu, R.S., and K. Aki, Scattering characteristics of elastic waves by an elastic heterogeneity, *Geophysics*, 50, 582-595, 1985.

The Influence of Deep Sedimentary Basins, Crustal Thinning, Attenuation, and Topography on Regional Phases: Selected Examples from the Eastern Mediterranean and the Caspian Sea Regions

Peter Goldstein, Craig Schultz, and Shawn Larsen

Geophysics and Global Security Division, Lawrence Livermore National Laboratory

Sponsored by U.S. Department of Energy, Office of Nonproliferation and National Security

Office of Research and Development

CTBT R&D Program ST482B, Contract No. W-7405-ENG-48

Monitoring of a Comprehensive Test Ban Treaty (CTBT) will require transportable seismic identification techniques, especially in regions where there is limited data. Unfortunately, most existing techniques are empirical and cannot be used reliably in new regions. Our goal is to help develop transportable regional identification techniques by improving our ability to predict the behavior of regional phases and discriminants in diverse geologic regions and in regions with little or no data. Our approach is to use numerical modeling to understand the physical basis for regional wave propagation phenomena and to use this understanding to help explain observed behavior of regional phases and discriminants. In this paper, we focus on results from simulations of data in selected regions and investigate the sensitivity of these regional simulations to various features of the crustal structure. Our initial models use teleseismically estimated source locations, mechanisms, and durations and seismological structures determined by others. We model the Mb-5.9 October 1992 Cairo, Egypt, earthquake at a station at Ankara, Turkey (ANTO), using a two-dimensional crustal model consisting of a water layer over a deep sedimentary basin with a thinning, crust beneath the basin. Despite the complex tectonics of the Eastern Mediterranean region, we find surprisingly good agreement between the observed data and synthetics based on this simple two-dimensional model.

We investigated the sensitivity of the Cairo earthquake synthetics to a number of features including: 1) the thickness and velocity of the sedimentary basin, 2) the amount of crustal thinning, beneath the basin, 3) the amount of attenuation, and 4) the presence of a water layer. We find that, for this region, the presence of a thick sedimentary basin has the most dramatic effects on the regional phases. For example, Pg and Sn are effectively extinguished and the surface waves are dramatically dispersed by the presence of the basin. Crustal thinning, beneath the basin also reduces the amplitudes of Pg and Sri, but its effects are less significant. The effects of attenuation are well approximated by a low-pass filter. The effects of the water layer were small but most noticeable in the later-arriving surface waves. We investigated the effects of free-surface topography for paths in the vicinity of the Caspian Sea. Preliminary results indicate that topography acts as a significant source of scattering and mode conversion. One of the most noticeable effects was a significant increase in the duration of Lg on the vertical component. This result suggests that free-surface topography may be an important contributor to the development of Lg and coda waves. It may also explain the relatively homogeneous nature of three-component regional waveforms.

These results show how we can use simulations to understand observed regional wave propagation phenomena and suggest that it may be possible to predict the behavior of regional phases and discriminants when we have a reasonably accurate model for the regional seismic structure.

Key Words: Seismic, Wave Propagation Modeling, Identification, Regionalization, Middle East, Mediterranean, Caspian, Topography

Objectives

We have been developing the capabilities needed to model regional seismic signals in complex media (e.g., Larsen, 1995; Schultz et al., 1995; Goldstein, et al., 1996; Schultz, 1997) so that we can help understand the physical basis for and performance of existing discriminants, develop transportable seismic identification techniques, and predict the behavior of regional phases and discriminants in regions where there is limited data. In this study, we investigate the sensitivity of regional phases in complex media to features such as deep sedimentary basins, crustal thinning, attenuation, and free-surface topography. Our goal is to understand how these features affect regional signals and to identify those features that have the greatest impact from a monitoring standpoint.

Research Accomplished

Software Development

Our effort to model the propagation of regional phases in complex media to distances and frequencies of monitoring interest has required significant development of our finite-difference wave propagation modeling capabilities (Larsen, 1995). Important enhancements include: hybridization (the ability to input signals from other seismic modeling techniques), two-dimensional topography (Schultz, 1997), and a number of techniques to improve computational speed and efficiency. This software development and the increased speed and efficiency of available computers has brought us to the point where we can begin to model regional phases in realistic structures and at frequencies and distances of monitoring interest.

The October 1992 Cairo, Egypt, Earthquake

We simulated the October 1992 Cairo, Egypt, earthquake, Figure 1, in order to test our predictive modeling capabilities and to investigate the sensitivity of regional phases to complex regional structure. We began by simulating recordings of this earthquake at Ankara, Turkey (ANTO) using the location determined by the National Earthquake Information Center and the Centroid Moment Tensor (CMT) mechanism and source duration (Dziewonski et al., 1981). Based on the depth to basement and crustal thickness given in Cornell University Digital Database for the Middle East and North Africa (Barazangi et al., 1996), we used a two-dimensional earth structure consisting of three crustal layers, the Mediterranean Sea, a thick sedimentary basin, and deeper crust that thins beneath the sedimentary basin (Figure 2). The upper mantle consists of a uniform velocity gradient extending to a depth of 100 km. This structure is deep enough to model Pn and Sn but will not include the effects of any upper mantle discontinuities. In Figure 3, we compare the observed data with the simulation based on the model in Figure 2 and a flat layered approximation of this model. We find excellent agreement between the observed data and the synthetic generated using the two-dimensional structure. In contrast, there are dramatic differences between the flat-layered approximation and the observed data. The excellent agreement between observed data and synthetic based on the two-dimensional model suggest that it may be possible to predict regional waveforms in regions where we have reasonably accurate estimates of the seismic velocity structure.

Sensitivity of Regional Phases to Two-Dimensional Crustal Structures:

In this section, we describe our investigation of the sensitivity of our simulations of the Cairo, Egypt, earthquake to a number of features of the two-dimensional crustal model including: 1) the thickness and velocity of the sedimentary basin, 2) the amount of crustal thinning beneath the basin, 3) the amount of attenuation, and 4) the presence of a water layer. The effects of many of these features are indicated by the synthetic seismograms in Figure 4.

We began our sensitivity analysis by replacing the Mediterranean Sea with sediments. Not surprisingly, the effects of this layer were relatively minor since only P-waves can propagate within it. The most noticeable difference was a lack of high-frequency energy riding on top of the late-arriving, dispersed surface waves. Since the effects of this change on the regional phases was relatively minor, we left out the Mediterranean Sea in many of our simulations.

The deep sedimentary basin was found to have the most significant effects on the regional phases. When the maximum basin thickness was reduced to approximately 5 km, Pg and Sn amplitudes were increased dramatically and the amount of surface wave dispersion was decreased dramatically. Reducing the amount of crustal thinning decreased Pn and increased Pg and Sn, but not nearly as dramatically as the sedimentary basin. Based on differences between a model with and without attenuation, the effects of attenuation can be accurately approximated by a low-pass filter.

These results show how we can use simulations to understand observed regional wave propagation phenomena and suggest that it may be possible to predict the behaviour of regional phases and discriminants when we have a reasonably accurate model for the regional seismic structure.

The Influence of Two-Dimensional Topography on Regional Phases

Recent studies by Zhang and Lay (1994), Rodgers et al., (1997), and Hartse et al., (1997) have found significant correlations between the variability of regional discriminants and free-surface topography. However, it is not clear whether the observed correlations are due to topography or some highly correlated parameter of the underlying geologic structure. We have developed and begun implementing the capability to test the hypothesis that a significant portion of the variability of regional discriminants is due to free surface topography. Our initial simulations are for profiles of the highly variable topography to the west of the Caspian Sea (Figure 5). The topography we used is based on the approximately 1-km sampling, African digital elevation map from USGS, EROS data center. We accounted for potential effects of short-wavelength variation in topography by interpolating to a higher spatial sample rate using fractal statistics. The underlying velocity structure is based on a one-dimensional model from Campillo (1990). This model is undoubtedly inappropriate for these profiles but we considered it useful for preliminary hypothesis testing. The resulting synthetics for models with and without topography are shown in Figure 6. The most noticeable result is the difference in the amplitude and duration of Lg and the Pg and Lg coda on the vertical components. When topography is present, the Lg and coda amplitudes and durations are enhanced significantly by the effects of scattering and mode conversion at the free-surface. These observations suggest that

topography is a plausible mechanism for significant Lg generation and may be responsible for the relatively homogeneous nature of three-component regional waveforms.

Conclusions

We have developed and are utilizing state-of-the-art, elastic, finite-difference wave propagation modeling capabilities to understand the physical basis of regional wave propagation phenomena. Understanding the physical basis of these phenomena is essential for developing transportable seismic identification techniques and for predicting the behavior of regional phases in relatively aseismic regions. Based on modeling of data in the vicinity of the Eastern Mediterranean, we find that regional phases (body waves, guided waves, and surface waves) are very sensitive to the existence of deep sedimentary basins. Crustal thinning also affects the regional body and guided waves but to a much lesser degree. The effects of attenuation are well approximated by a low-pass filter. The effects of the water layer were small but most noticeable in the later-arriving surface waves.

We investigated the effects of topography for profiles to the west of the Caspian Sea. These simulations show that topography can increase the amplitude and duration of Lg and Pg and Lg coda via significant scattering and mode conversions at the free surface. These results suggest that free-surface topography may be responsible for significant generation of Lg and coda waves and may also explain the relatively homogeneous nature of three-component regional waveforms.

References

- Barazangi, M., D. Seber, E. Sandvol, M. Vallve, 1996, "Digital database development and seismic characterization and calibration for the Middle East and North Africa", PL-TR-96-2222, Phillips Lab., Hanscom AFB, Massachusetts, pp. 63.
- Campillo, M., 1990, Propagation and attenuation characteristics of the crustal phase Lg, *Pure Appl. Geophys.*, 13, 1-19.
- Dziewonski, A.M., T.A. Chou, and J.H. Woodhouse, 1981, "Determination of earthquake source parameters from waveform data for studies of global and regional seismicity", *J. Geophys. Res.*, 86, 2825-2852.
- Goldstein, P., C. Schultz, S. Larsen, and L. Minner, 1996, "Modeling of regional wave propagation phenomena in the Middle-East and North-Africa and new analysis capabilities in SAC2000", Proceedings of the 18th annual seismic research symposium on monitoring a CTBT, Annapolis, MD, September 4-6, 1995
- Hartse, H., R.A. Flores, and P.A. Johnson, 1997, "Correcting regional seismic discriminants for path effects in western China", LAUR-97-1978.
- Larsen, S.C., 1995, 3D MPP simulations in the earth sciences: seismic applications, LLNL Symposium on Distributed Computing and Massively Parallel Processing.
- Rodgers, A., and W.R. Walter, 1997, Regionalization and calibration of seismic discriminants, path effects and signal-to-noise for station ABKT (Alibek).

Turkmenistan), submitted to the 19th annual seismic research symposium on monitoring a CTBT, Orlando, FL, September 23-25, 1997.

Schultz, C. A., S. C. Larsen, P. Goldstein, S. D. Ruppert (1995), "Wave propagation modeling capabilities at LLNL: applications to regional discrimination", Lawrence Livermore National Laboratory, Livermore, CA, UCRL-JC-121748. also submitted to the 17th annual seismic research symposium on monitoring a CTBT, Scottsdale, AZ, September 11-15, 1995.

Schultz, C. A., 1997, "A modified density tapering approach for modeling the seismic response of free-surface topography", accepted for publication in Geophysical Research Letters.

Zhang, T. and T. Lay, 1994, Analysis of short-period regional phase path effects associated with topography in Eurasia, Bull. Seis. Soc. Am., 84, 119-132.

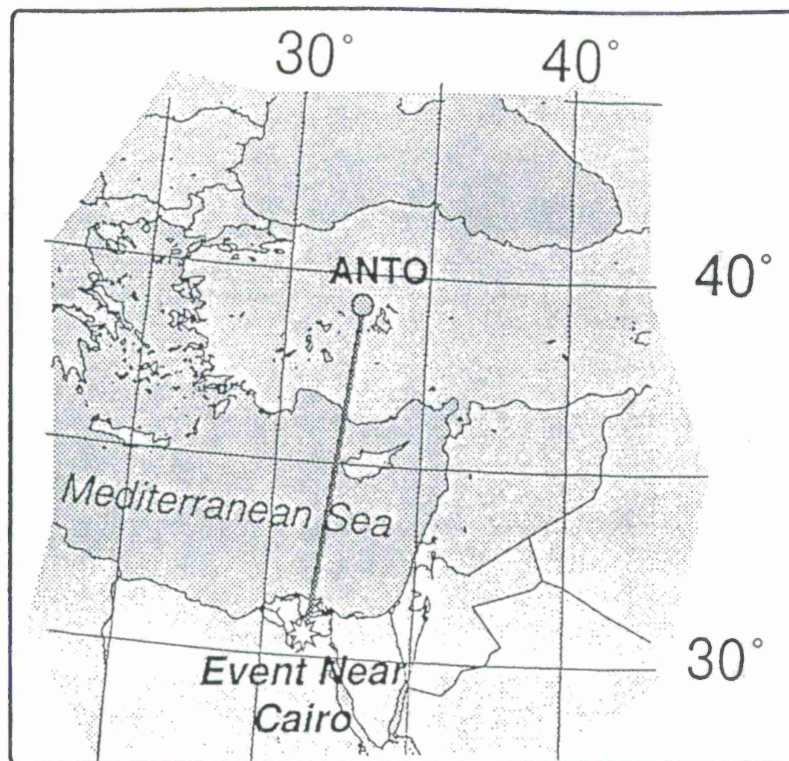


Figure 1. Map showing locations of the Mb-5.9 Cairo, Egypt, earthquake on October 12, 1992, and the seismic station at Ankara, Turkey (ANTO).

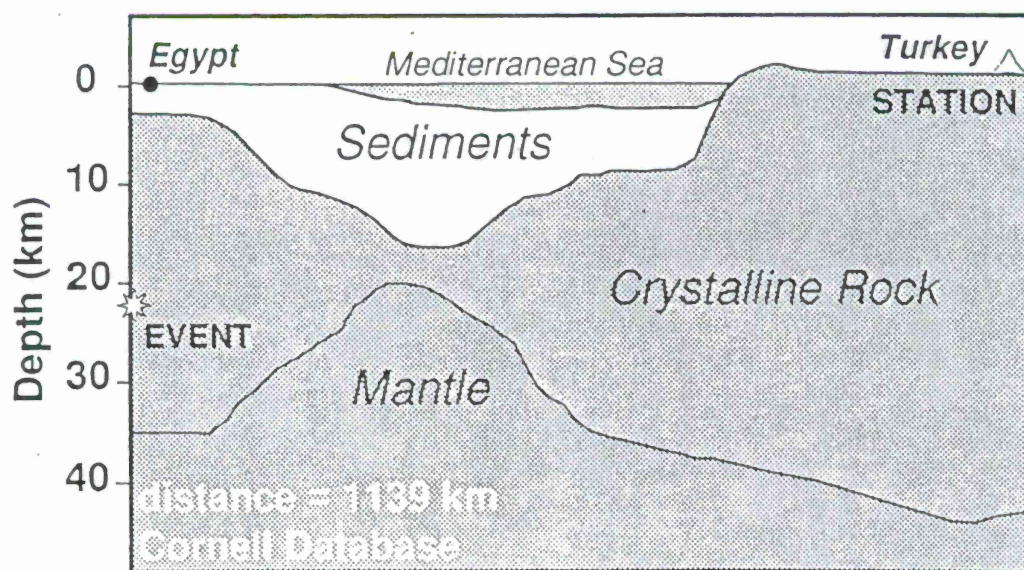


Figure 2. Cross section of crustal structure used to simulate wave propagation between Cairo, Egypt and Ankara, Turkey. The earthquake location is indicated by the star along the left boundary. The seismic station ANTO is indicated by the triangle near the upper right corner.

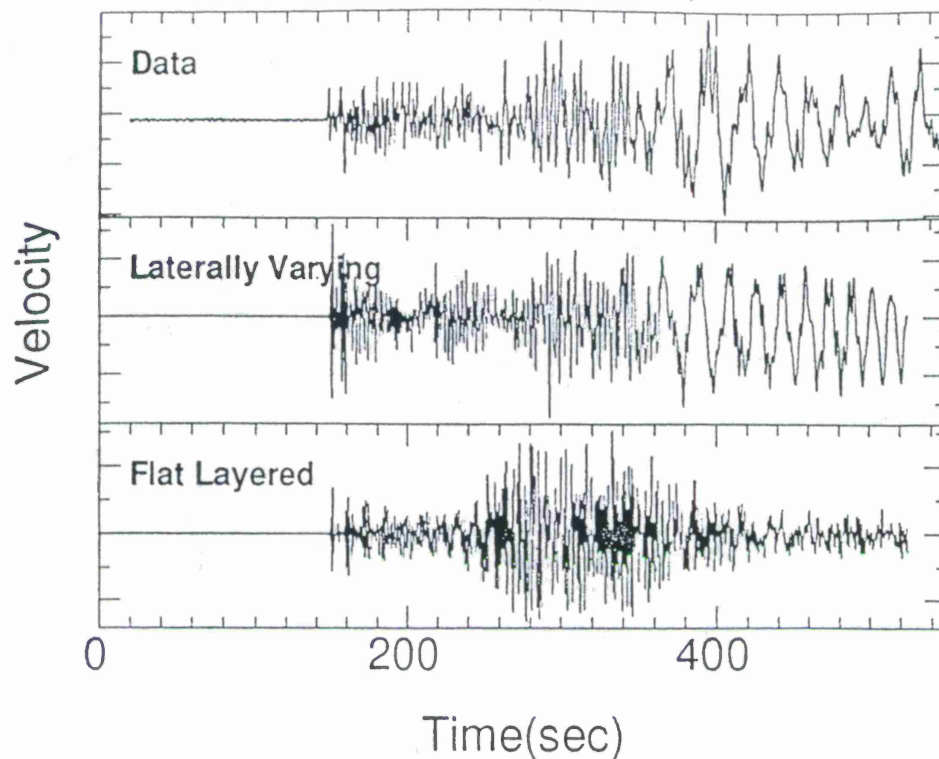


Figure 3. Comparison of vertical component data and synthetics for the Mb-5.9 October 1992 Cairo, Egypt, earthquake. The synthetic seismogram based on the laterally varying earth model provides a much better fit to the data.

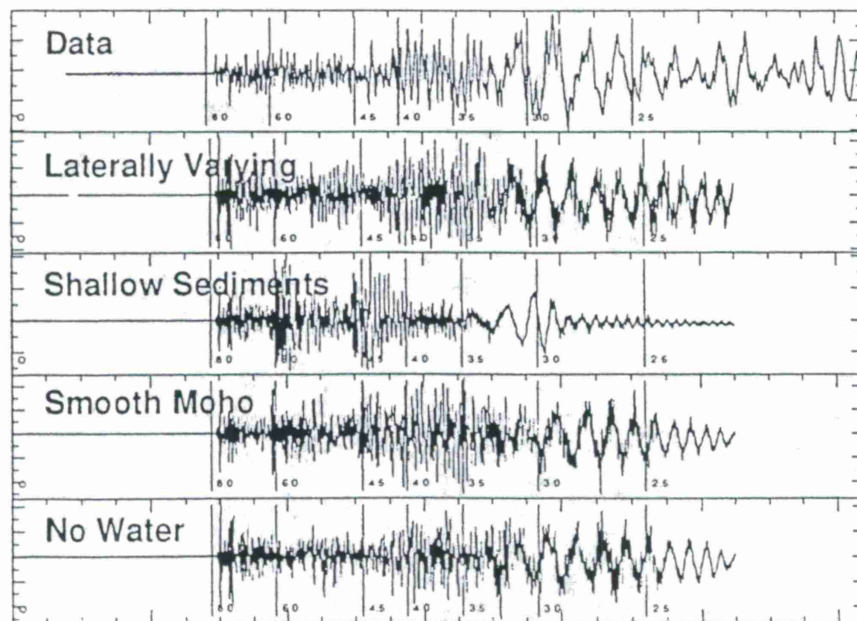


Figure 4. Comparison of vertical component data with synthetics for our preferred model, and models with shallow sediments, a smooth moho, and no water layer. Removing the shallow sediments from the preferred model has a dramatic effect on the agreement with the observed data.

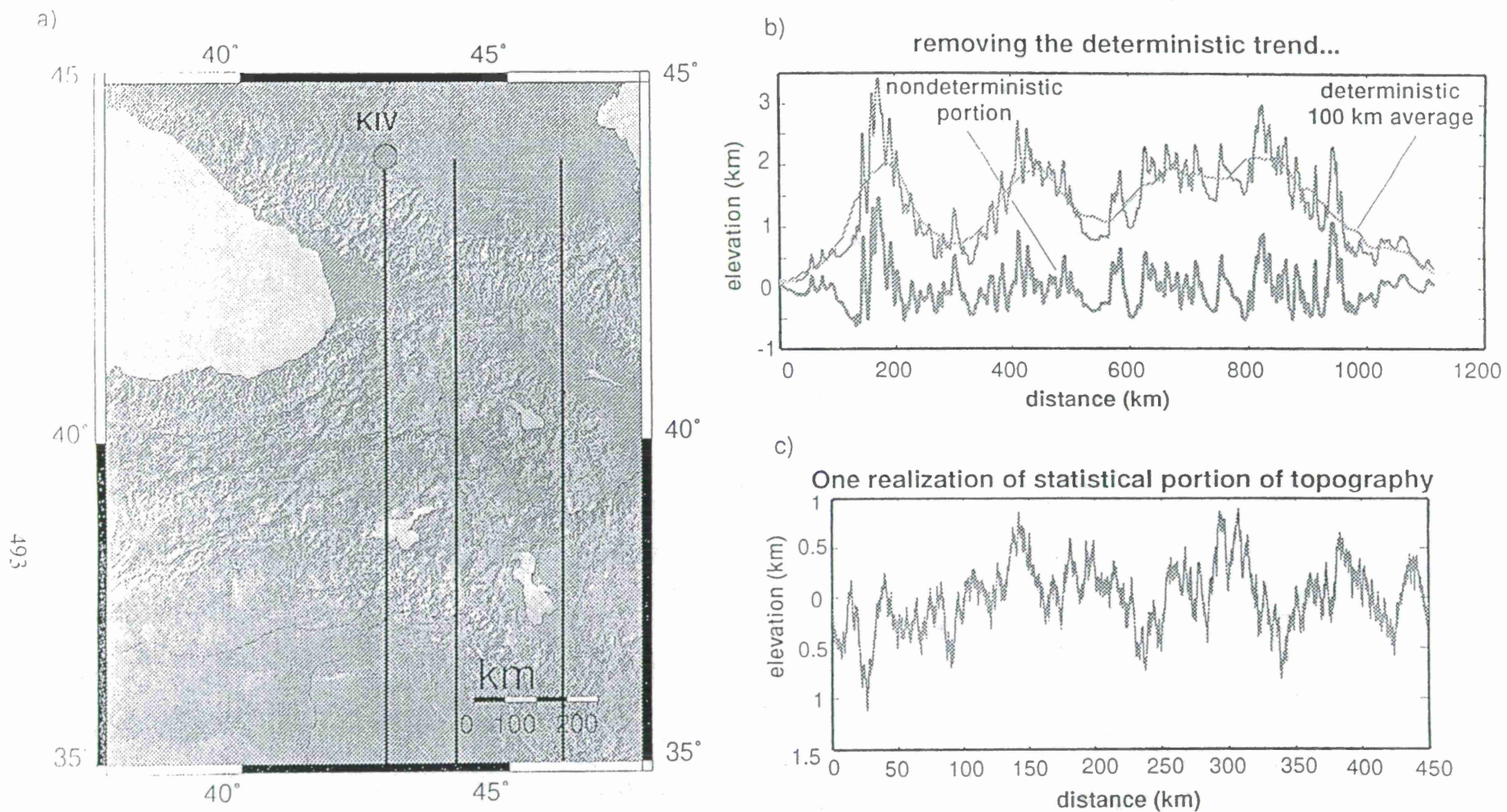
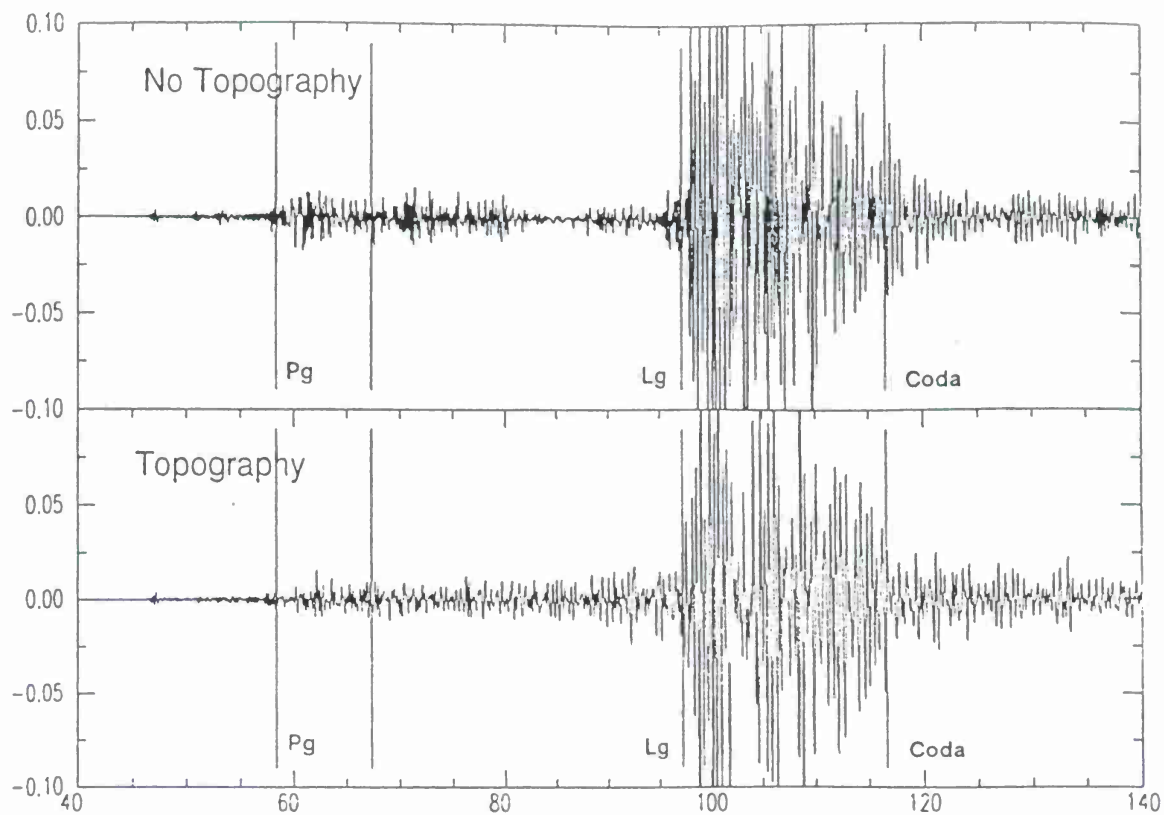


Figure 5. Locations and profiles of topography in the Caspian Sea region. a) Map showing location of the topographic profiles. b) Deterministic and statistical portions of observed topography. c) One realization of the statistical portion of topography, interpolated to a finer scale using fractals.

a)



b)

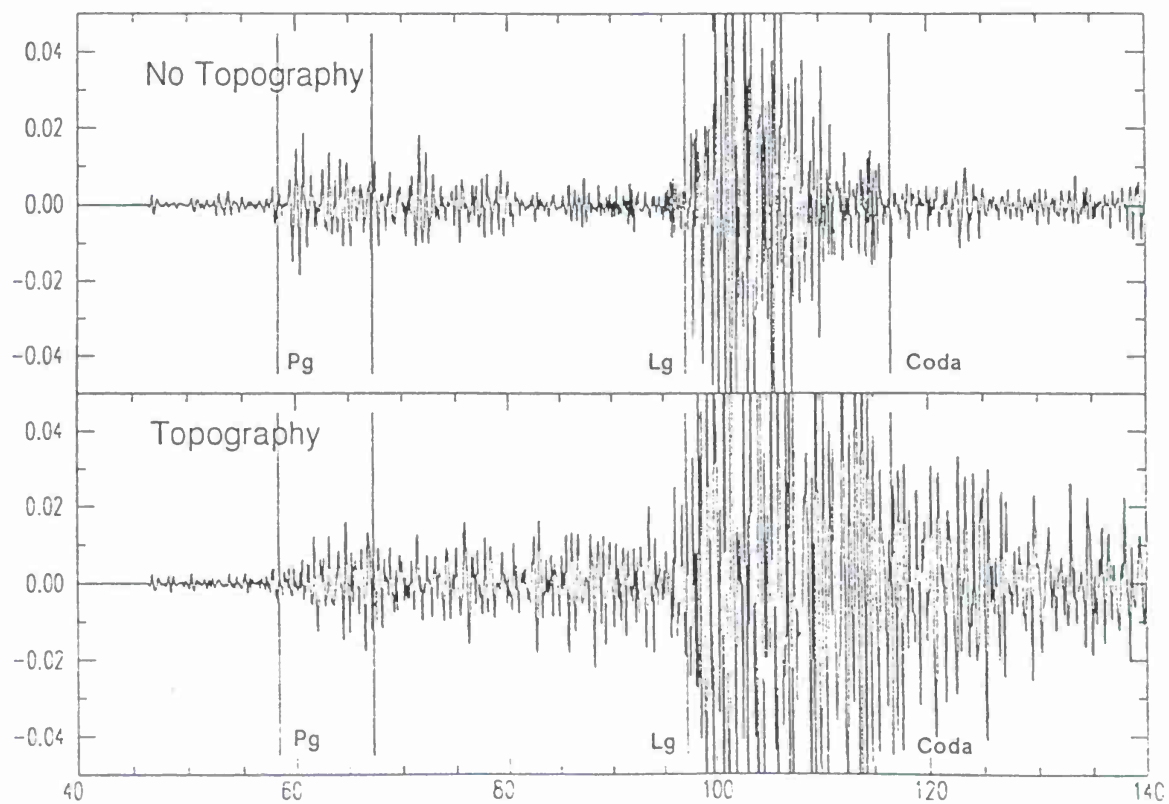


Figure 6. Comparison of simulations with and without topography. a) Radial components. b) Vertical components. The vertical component of the simulation with topography has much larger Lg than the vertical component of the simulation without topography because of scattering and mode conversions at the free-surface

WAVE PROPAGATION - 16 Hz TO 60 sec

R.B. Herrmann, T. A. Mokhtar, M. Raoof and C. Ammon
Saint Louis University

Sponsored by U.S. Department of Energy
Office of Nonproliferation and National Security
Office of Research and Development
Contracts F19628-95-K-0005 and F19628-95-K-0019

ABSTRACT

Wave propagation is investigated in the 0.16 - 16 Hz frequency band by examining the propagation of Lg with distance at high frequencies and the regional variation of surface-wave dispersion in the Arabian Plate. Lg propagation is characterized in terms of anelastic attenuation, geometrical spreading and signal duration. Although regional differences in anelastic attenuation were expected, differences in spreading and signal duration were not. These parameters are a property of crust and upper mantle structure, which control the Lg wave guide. The structure normally used for location is not sufficient to describe the dynamic properties of the crust.

The surface wave studies for the Arabian Plate provide tomographic images of fundamental mode Love and Rayleigh wave group velocity dispersion in the 5 - 60 second period range. These data will be used to infer crustal structure and will form a nucleus of a test of the value of such data for constraining crustal structure adequately for location and source quantification.

Keywords: Lg, Wave Propagation, Surface Waves, Arabian Plate

OBJECTIVE

These two research projects, F19628-95-K-0005 *Seismic Wavefield Calibration* and F19628-95-K-0019 *Wave Propagation in the Arabian Plate*, examine crustal wave propagation in two frequency ranges: 1 - 16 Hz for Lg and crustal S and 0.016 - 0.2 Hz for surface wave. The first study strives for a better understanding of Lg, and the other represents the opportunity to characterize surface wave propagation for some regions of interest.

RESEARCH ACCOMPLISHED

1. Lg and S-wave Propagation

The paper entitled "Variability in M_L , ψ_∞ versus Y from regional surface waves." The co-authors are R. B. Herrmann, G. I. Al-Eqabi, K. D. Hutchensen and M. Denny was submitted to Bulletin, Seismological Society of America - essentially unchanged from the version published in Technical Report 1.

Our studies of actual Lg wave propagation continues by investigating the variation of the maximum amplitude in the Lg or S window to 500 km. This is done by using regional seismic network recordings of small earthquakes. Typically 2000 waveforms are used per region studied. The distinguishing feature of these studies is that we entertain no preconception about the distance dependence of amplitude scaling -- the data themselves define the scaling which is then characterized by simple parameters.

The attenuation of Lg can be characterized by three factors: geometrical spreading, anelastic attenuation and signal duration. The first two affect Fourier amplitude spectra, while all three control peak time domain measurements. For purposes of the DOE program, the data sets are limited in that data are not available beyond 500 km. This means that there are still tradeoffs between geometrical spreading and $Q(f)$, and thus extrapolation to larger distances is a bit touchy. Regional variability changes the relation between Lg excitation by the source and observations at large distance both in level and in proportional frequency content. We are working toward characterizing these variations.

Figures 1.1 and 1.2 compare the Fourier amplitude spectra and peak time domain amplitudes as a function of bandpass filter frequency for four regions of the U. S. Since the curves are normalized at 40 km, they cannot be used directly for comparison of high-frequency/low-frequency levels for the time domain because of the effects of bandpass filters used.

For each region we have tabulated values of $Q(f)$, a $G(r)$ and a $T(r)$ that characterize the anelastic attenuation, geometrical spreading of Fourier amplitude spectra and the signal duration. The distance beyond which $G(r)$ varies as $r^{-1/2}$ varies regionally. This implies that the relation of distant observation to the excitation of Lg or S also varies regionally. Other research efforts are gathering data for the Pacific Northwest of the U.S. and in central Europe.

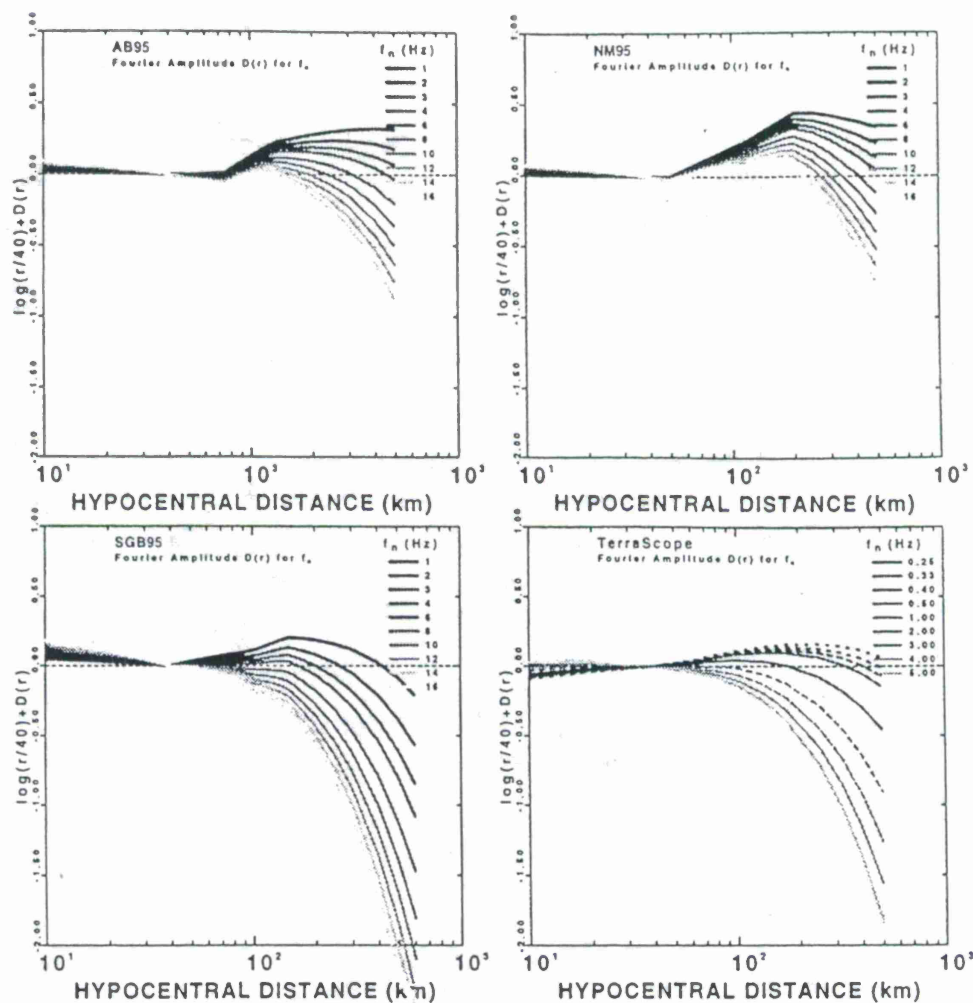


Fig. 1.1. Comparison of normalized Fourier Amplitude Spectra for four regions: AB95 - southeastern Canada, most vertical data ; SGB95 - southern Great Basin, vertical; NM95 - New Madrid, vertical and horizontal; TERRAScope, vertical . Shading indicates filter frequency. For comparison, all spreading has been adjusted for r^{-1} . Note that the TERRAScope frequencies vary from 0.25 - 5 Hz, while the others vary from 1 - 15 Hz.

2. Surface Waves in the Arabian Plate

The purpose of this effort is to use broadband digital data to characterize seismic wave propagation across the Arabian plate as observed by instruments within the plate. This is a cooperative effort between Saint Louis University and King Abdulaziz University in Jeddah, Saudi Arabia, for surface wave analysis and determination of crustal structure, and the University of California San Diego, who deployed instruments and acquired data.

The unique aspect of this effort is the direct involvement with Dr. Talal A. Mokhtar of King Abdulaziz University. Dr. Mokhtar will perform significant portions of the data analysis.

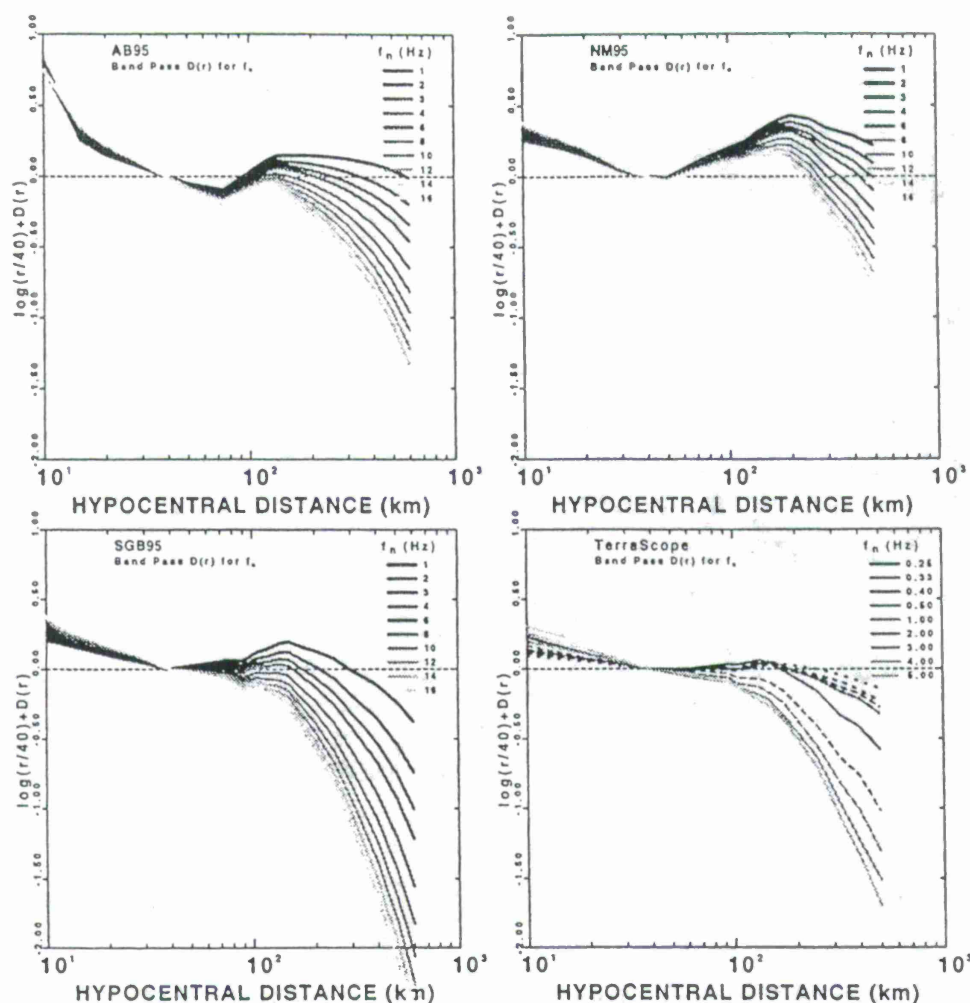


Fig. 1.2. Comparison of normalized peak bandpass filtered velocity for four regions: AB95 - southeastern Canada, most vertical data; SGB95 - southern Great Basin, vertical; NM95 - New Madrid, vertical and horizontal; TERRAScope, vertical. Shading indicates filter frequency. For comparison, all spreading has been adjusted for r^{-1} . Note that the TERRAScope frequencies vary from 0.25 - 5 Hz, while the others vary from 1 - 15 Hz.

The joint data set is comprised of dispersion measurements by Dr. Mokhtar and Dr. Ghalib using analog WWSSN data, digital GEOSCOPE and IRIS data as well as DIGITAL data from the Saudi PASSCAL experiment. A regionalization for dispersion on a 111.195 km x 111.195 km grid has been completed for the region covered by 10°N to 45°N and 30°E to 65°E. We used C. Ammon's tomography program for this purpose.

The data set has been processed using multiple filter analysis only. Later processing may involve use of phase match filter techniques to clean up traces prior to multiple filter analysis. Dispersion was measured at periods of 5, 6, 7, 8, 9, 10, 11, 12, 13, 14, 15, 16, 17, 18, 19, 20, 22, 24, 26, 28, 30, 32, 34, 36, 38, 40, 42, 46, 48, 50, 52, 54, 56, 58 and 60 seconds. The present Love and Rayleigh wave data sets consist

of 178 to 670 and 359 - 1000 paths, respectively, with the least observations at 60 seconds and the most at 10 seconds. This is due to the event sizes and well as to the relatively short travel paths. Figure 2.1 shows representative ray paths for Rayleigh waves as well as the stations providing data. The stations deployed in Saudi Arabia provided significant coverage of the Arabian shield. There is also significant coverage of the western part of Pakistan and all of Iraq.

11-13 S $V = 2.77$ KM/S 916 Rays used

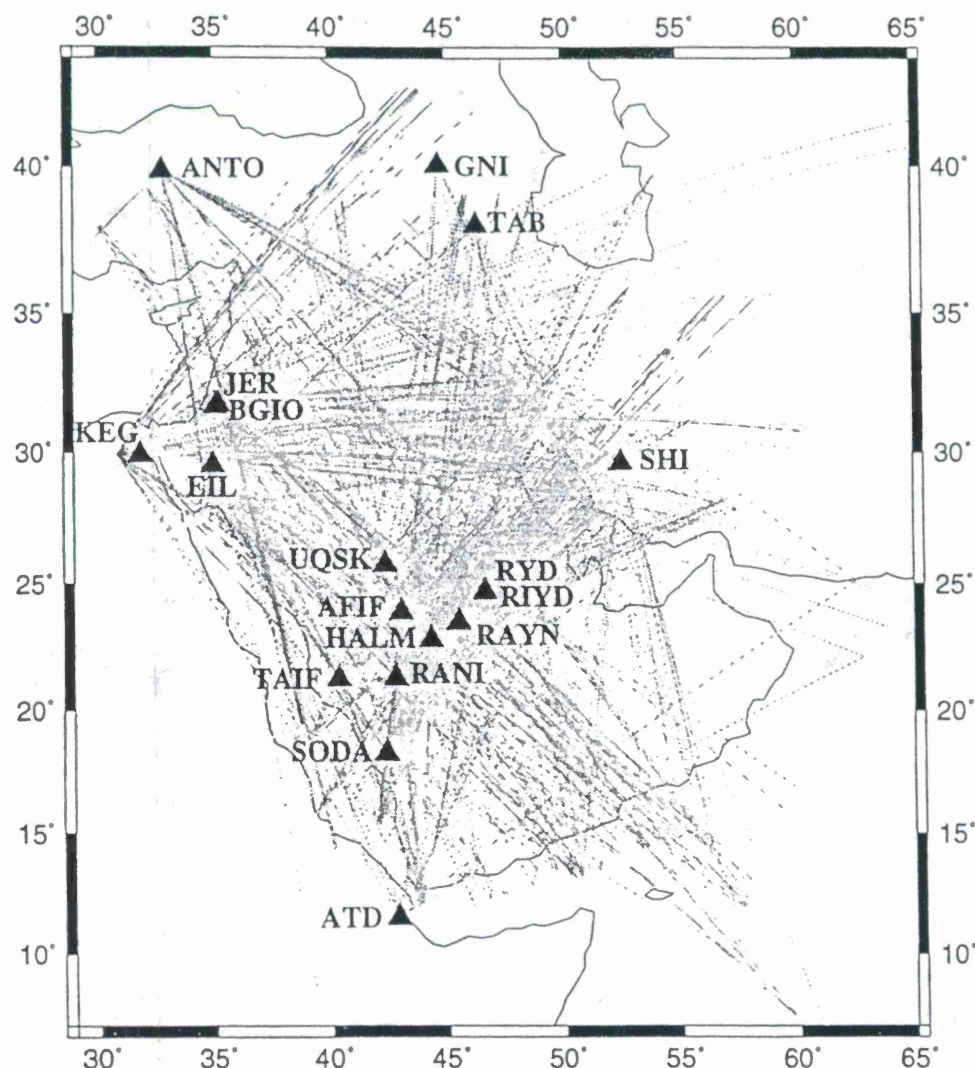
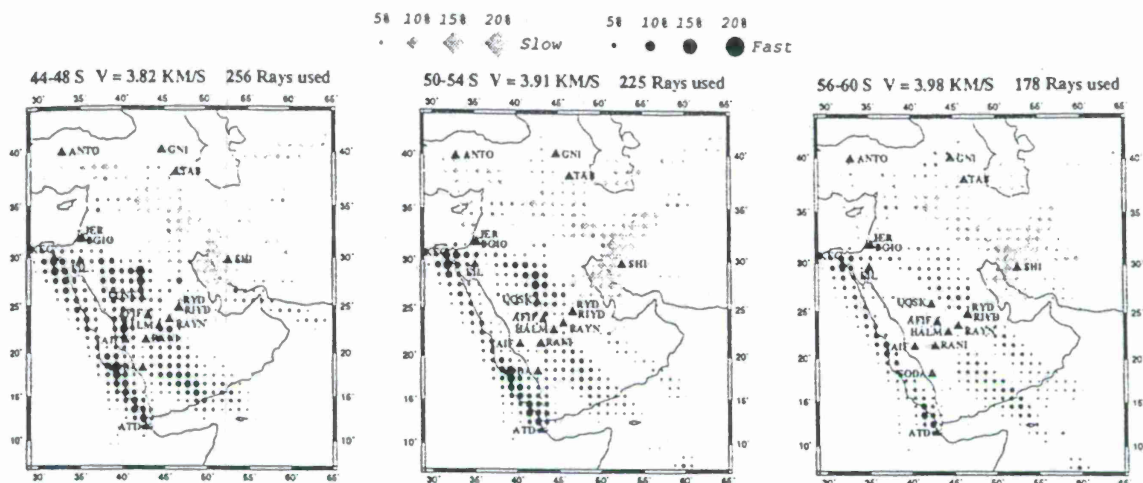


Fig. 2.1. Distribution of great circle paths for data with a periods from 11-13 sec. The solid triangles show the station locations. The shaded lines show the path coverage.

Figures 2.2 - 2.4 show the results of tomographic back projection to obtain dispersion for the entire data set. For this display, data at three adjoining periods were aggregated. The shield region of western Saudi Arabia is characterized by high velocities, while the Arabian or Persian Gulf is characterized by lower velocities.

Love Waves



Rayleigh Waves

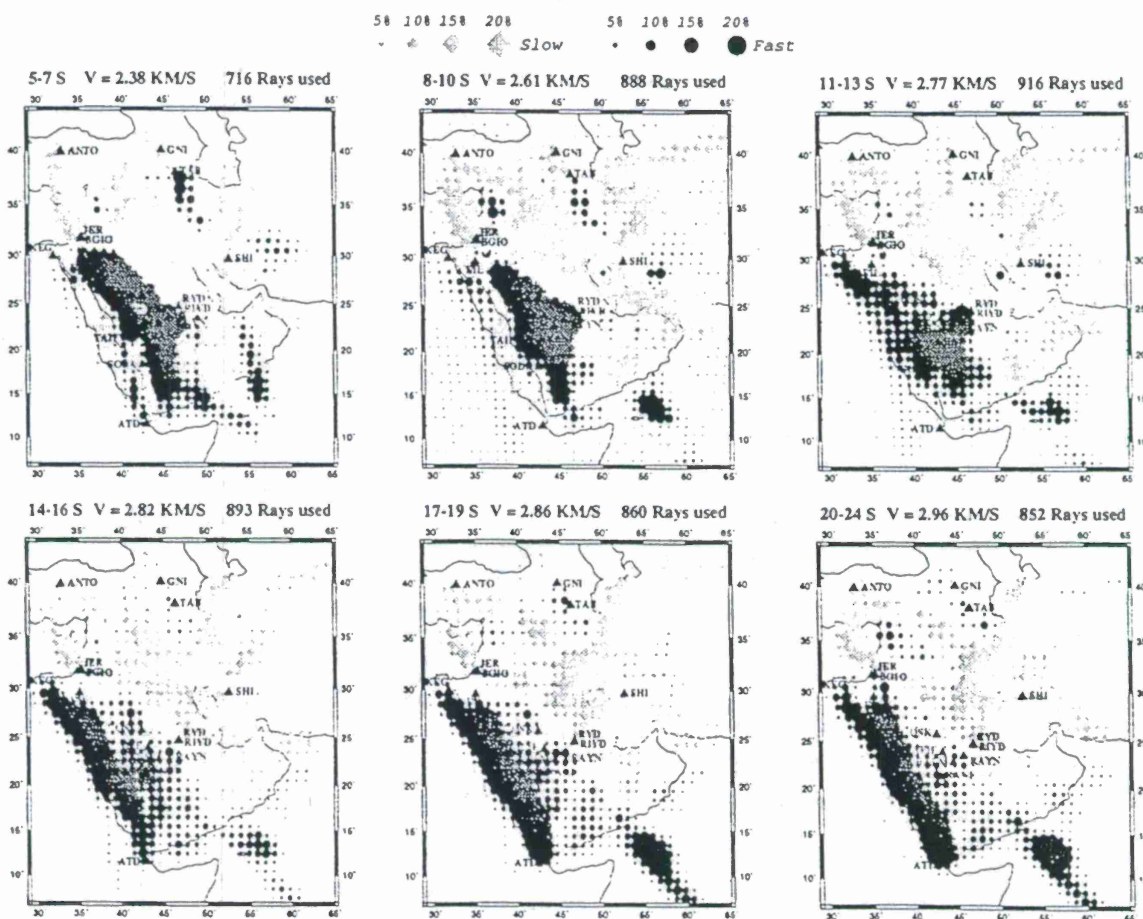


Fig. 2.3. Results of tomographic back projection for the Love wave data set from 44-48 sec to 56-60 sec and the Rayleigh wave data set from 5-7 sec to 20-24 sec.

structure. This work compared genetic algorithm generalized seismological data functional and linear least squares inversion techniques for broadband waveform

Rayleigh Waves

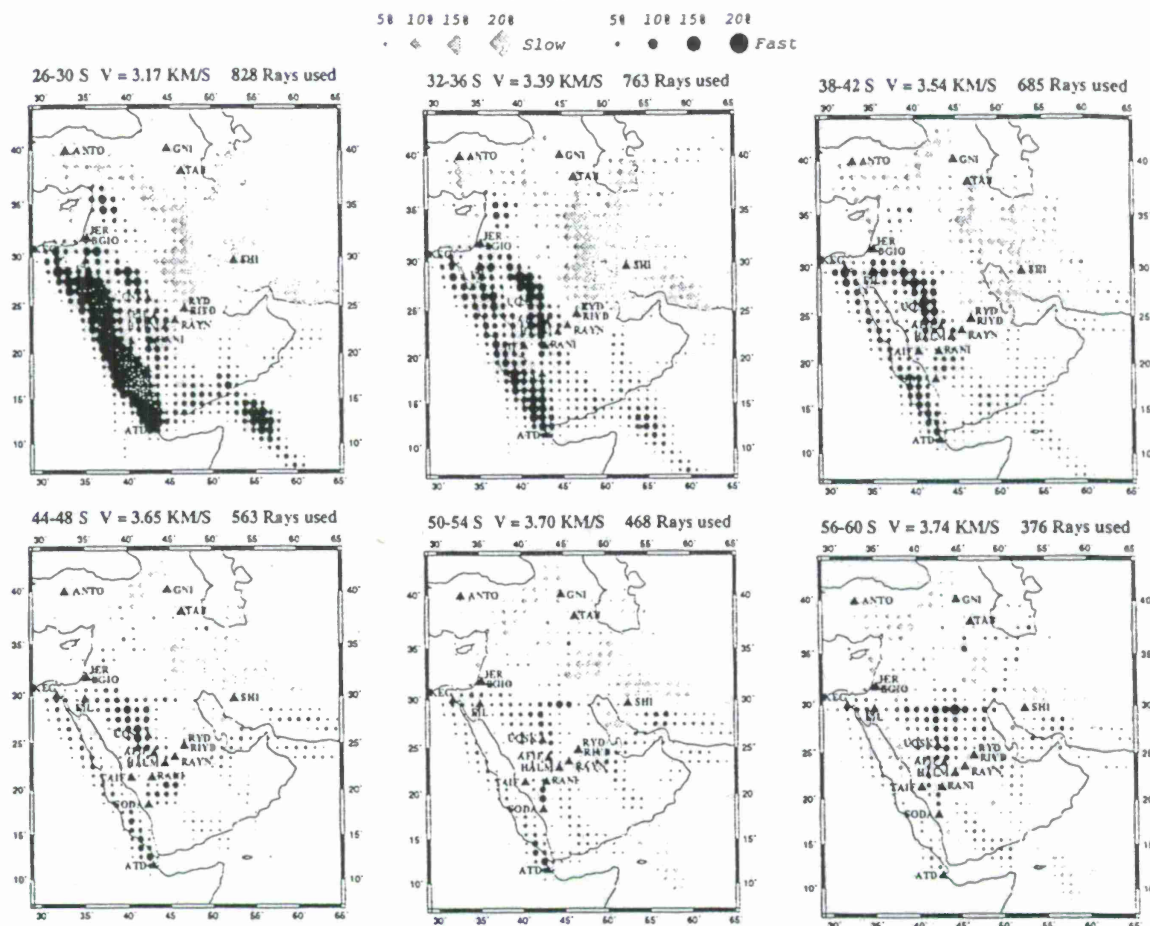


Fig. 2.4. Results of tomographic back projection for the Rayleigh wave data set from 26-30 sec to 56-60 sec.

inversion for earth structure.

These color versions of the Figures 2.1-2.4 in this report are available at
<http://www.eas.slu.edu/People/RBHerrmann/Arabia/q08.html>

Continuing efforts will be directed toward quantifying the confidence in the tomographic inversion, in inverting for earth structure, and in combining the surface wave dispersion with receiver function information to constrain crustal velocity models.

CONCLUSIONS AND RECOMMENDATIONS

Both the low and high frequency wave propagation investigations point out the spatial variability of wave propagation, on scales of 5° for the surface waves and of 1° for the Lg waves. Each frequency band indicates its own class of continued investigation.

The high frequency studies require a large number of waveforms and a very fine spatial sampling. This is only possible where there are both a good distribution

of digital stations and also a uniform pattern of seismicity. These seismicity conditions are met in Pakistan and Iran. The installation of broadband digital seismograph stations in these countries may permit a continuation of these studies, especially since the ground motion versus distance relation is of importance to earthquake engineering.

The surface wave study of the Arabian plate has significant information at short periods. Much of the current surface wave regionalization has been focused at the 20 second period for purposes of automating M_S determination. The shorter period data here will permit source parameter estimation at regional distances and perhaps enhanced detection.

The question of crustal structure is intimately tied to both studies, since structure is causing these observations. The crustal structure required to model broadband waveforms requires much more detail than that needed to locate events, which is a much easier problem. We hope to continue to use the Arabian Plate data set to see how surface wave dispersion can be combined with receiver functions and refraction surveys to yield a self-consistent crustal model for both location, quantification and source characterization.

It is now time to acquire large data sets for regions of interest.

THE EFFECTS OF MAJOR STRUCTURAL FEATURES IN WESTERN CHINA ON EXPLOSION SEISMOGRAMS

Eric M. Jones, Fred N. App, Randy J. Bos
Earth and Environmental Sciences Division
Los Alamos National Laboratory
Los Alamos NM 87545

Sponsored by U.S. Department of Energy
Office of Nonproliferation and National Security
Office of Research and Development

ABSTRACT

Synthetic explosion seismograms have been calculated on paths from Lop Nor to the NIL station in northern Pakistan and from Lop Nor to the TLY station in the Baikal Rift. Computational studies were done of the influence on the character of the seismograms of major structural features such as sedimentary basins, topography associated with the Himalayas and the Tibetan Plateau, roughness of the Moho, and the presence of a deep Moho depression under the Tibetan Plateau. The simulations were done with a 1-Hz Kelly wave source and 500-m resolution. Uniform elastic constants and frequency-independent quality factors, Q_p and Q_s , were used in each of three materials: basin sediments, crust, and mantle. The deep-basins which straddle both paths were found to have the dominant influence due to the generation of large-amplitude Rayleigh waves at the transition from crustal material to basin sediment at the source-ward basin edges. In simulations done with the effects of anelastic attenuation included, the amplitude of the Rayleigh-wave train was reduced to insignificance during passage across the 800-km-wide Tarim Basin on the Lop Nor \rightarrow NIL path but not on the 200-km path across the basin that straddles the Lop Nor \rightarrow TLY path.

Keywords: explosions, seismic wave propagation, synthetic seismograms, discrimination, sedimentary basins, attenuation, Rayleigh waves

Introduction

In simple geologic settings, seismograms recorded at regional distance from earthquakes and from explosions exhibit significant differences in character. Explosions produce strong, early arrivals of compressive-wave (P) energy while earthquakes produce primarily strong, later-time arrivals of shear-wave (S) energy. For simple settings, the gross features of a recorded seismogram can be used to characterize the source. In complex geologic settings, seismic waves traversing regional paths are modified by interactions with the free surface and structures like low-velocity basins and the Moho. Multiple reflections and interconversions of P- and S-wave energy can change the character of regional seismograms and complicate the source characterization process.

Generally, the best guide to source characterization is a comparison between seismograms from a source being analyzed and seismograms recorded with the same instruments for sources of known types that previously occurred at approximately the same location. Necessarily, the seismograms from the uncharacterized source and the known sources will contain similar path effects and, to the extent that the known earthquake and explosion seismograms show differences, characterization of the unknown source is possible. If suitable comparison seismograms are not available, numerical simulations can be used to (1) identify structural features along the source-receiver paths that are likely to produce significant signal modifications, (2) identify similar paths for which suitable comparison spectra are available and/or (3) produce synthetic seismograms for use in the characterization process. Toward these ends, we present the results of a parametric study of the effects of major structural features on seismic waves in Western China.

In a prior study (App, Bos, and Kamm 1996), we discussed variations in waveforms recorded for a 15 May 1995 explosion at Lop Nor and for a 2 May 1995 earthquake that occurred about 400 km northwest of Lop Nor. Generally, there were pronounced variations in the character of the waveforms from station to station and, in the previous study, we were able to reproduce the general character of most of the waveforms with finite-difference, elastic-wave-propagation simulations. Of particular interest were the recorded and simulated waveforms for the paths from Lop Nor to the seismic stations at NIL in Pakistan and TLY in the Baikal Rift. These two stations are separated by about 180 degrees in azimuth and are both about 1700 km from Lop Nor. In a simple geologic setting would show similar seismograms for any centrally-located source. However, as can be seen in bottom part of Figure 1, the explosion seismograms recorded at the two stations show significant differences. In particular, TLY shows a much reduced ratio of P-wave to S-wave amplitudes.

The geologic structure along each of the paths is shown in the top part of Figure 1 and was extracted from the Cornell Middle East/North Africa Project's on-line Profile Maker (Barazangi *et al* 1996). In both cases, Lop Nor is 50 km from the left edge. Along the Lop Nor -> NIL path, the major features are the Tarim Basin, an undulating Moho surface at roughly 50-km depth, the Tibetan Plateau, the Himalayas, and, a Moho depression beneath the Plateau. Along the Lop Nor -> TLY path, the major features are an undulating Moho and two relatively small basins. Readers should note that the topographic features shown in Figure 1 were not used in simulations reported in the prior study.

In this paper, we examine the effects on synthetic waveforms of the various structural features along the two paths. The simulations used in this study were performed with the elastic wave propagation code, AFD (Kamm, Bos, and Jones 1996), which was also used in the prior study. The simulations were all performed in Cartesian (x-z) geometry. Approximate values of the elastic constants (Warren 1996) were assigned to each of three

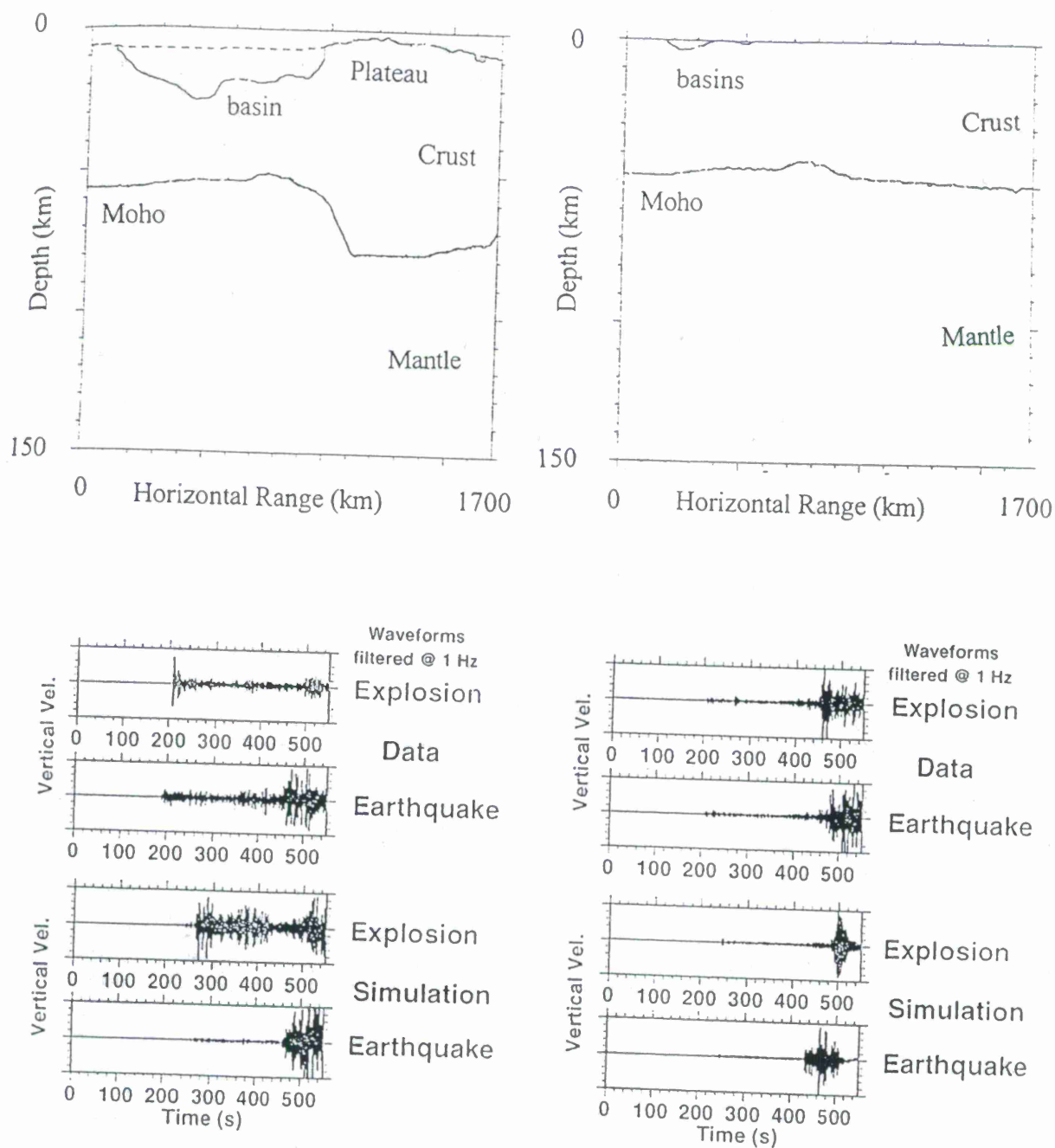


Figure 1 - Comparison of data and simulations for May 1995 earthquake and explosion in western China. the top panel shows the assumed structure along the Lop Nor -> NIL path (top left) and the Lop Nor -> TLY path (top right). In each case, Lop Nor is 50 km from the left boundary. The bottom panels show data and synthetic seismograms at NIL (lower left) and TLY (lower) right. Adapted from App, Bos, and Kamm (1996).

homogeneous materials which represent (1) basin sediments, (2) the crust, and (3) the mantle. The chosen densities were 2.8, 2.8, and 3.3 g/cm³, respectively, while the P-wave speeds were 5.6, 6.1, and 8.2 km/s and the S-wave speeds were 2.5, 3.5 and 4.7 km/s. Some of the simulations included the effects of anelastic attenuation and the chosen values of the frequency-independent compressive quality factors, Q_p , were 200, 500, and 1000 for compressive waves in the basin sediment, crust, and mantle, respectively, while the shear quality factors, Q_s , were 53, 219, and 439 (Minster 1979). The anelastic description used in AFD is based on the method of Emmrich and Korn (1987).

Each of the calculations was performed on a 1700 km by 150 km mesh with 500-m cells. In each of the simulations, a 1-Hz, explosive, Kelly-wave source (Kelly *et al* 1976) was placed 50 km from the left lateral boundary at a depth of 10 km below the free surface. Although this burial depth is far greater than that of any plausible nuclear test, it avoids numerical problems that can result when there are too few cells between the source and the surface. Each of the simulations was run to 600 seconds and vertical-velocity seismograms were calculated at the free-surface at range intervals from the left boundary of 150 kilometers. The seismograms presented below were bandpass filtered between 0.1 and 1.0 Hz. The low-frequency cutoff eliminates numerical resonances due to the finite size of the mesh and the high-frequency cutoff eliminates numerical noise produced by 500m cells.

Readers should note that the simulations were designed for the study of the relative influences of the various structural features and do not capture more than the general character of seismograms recorded for real events. Limiting assumptions include: (1) use of simplified cross-sections; (2) use of uniform properties in the crust rather than realistic gradients; (3) source placement at 10 kilometers depth instead of a more plausible 1 to 2 km; (4) use of two-dimensional Cartesian (x-z) geometry which ignores the effects of geometric spreading and is equivalent to use of a line source; (5) neglect of the effects of attenuation in some of the simulations; and (6) use of 500-m cells, which provide only marginally adequate resolution for a 1-Hz source. In general, these simplifications were adopted so that simulations could be carried out to 1700 kilometers in no more than 36 hours of CPU time on an HP workstation.

Single-Feature Simulations

Figure 2 shows synthetic seismograms for a set of simulations which each included only one of the major structural features on the Lop Nor -> NIL path. The following summaries highlight only the dominant features in the synthetic seismograms calculated at 1350-km range. A more detailed discussion of these features is presented in a later section.

The Flat Moho simulation (top) had a 48-km crust overlying a flat Moho and, therefore, was the simplest possible case other than a homogeneous half space. The first arrival at 1350-km range is a compressive head wave (P_n), which travels primarily in the mantle and arrives at about 170 seconds. The next arrival is the direct compressive wave (P_g) which travels in the crust and arrives at 1350-km range at about 215 seconds. This is followed by a series of signals produced by reflections at the Moho and at the free surface with attendant P -> S conversions. The last notable arrival is a low-amplitude Rayleigh wave which is produced at the source as a result of interactions with the free-surface (see, for example, App, Jones and Bos 1997). The Rayleigh wave arrives at 1350 km at about 400 seconds.

The Rough Moho simulation (second panel) had a roughened Moho. The left half of the Moho profile was taken from the Lop Nor -> NIL path while the right half of the profile was adapted from the Lop Nor -> TLY path. As can be seen in the synthetic seismogram

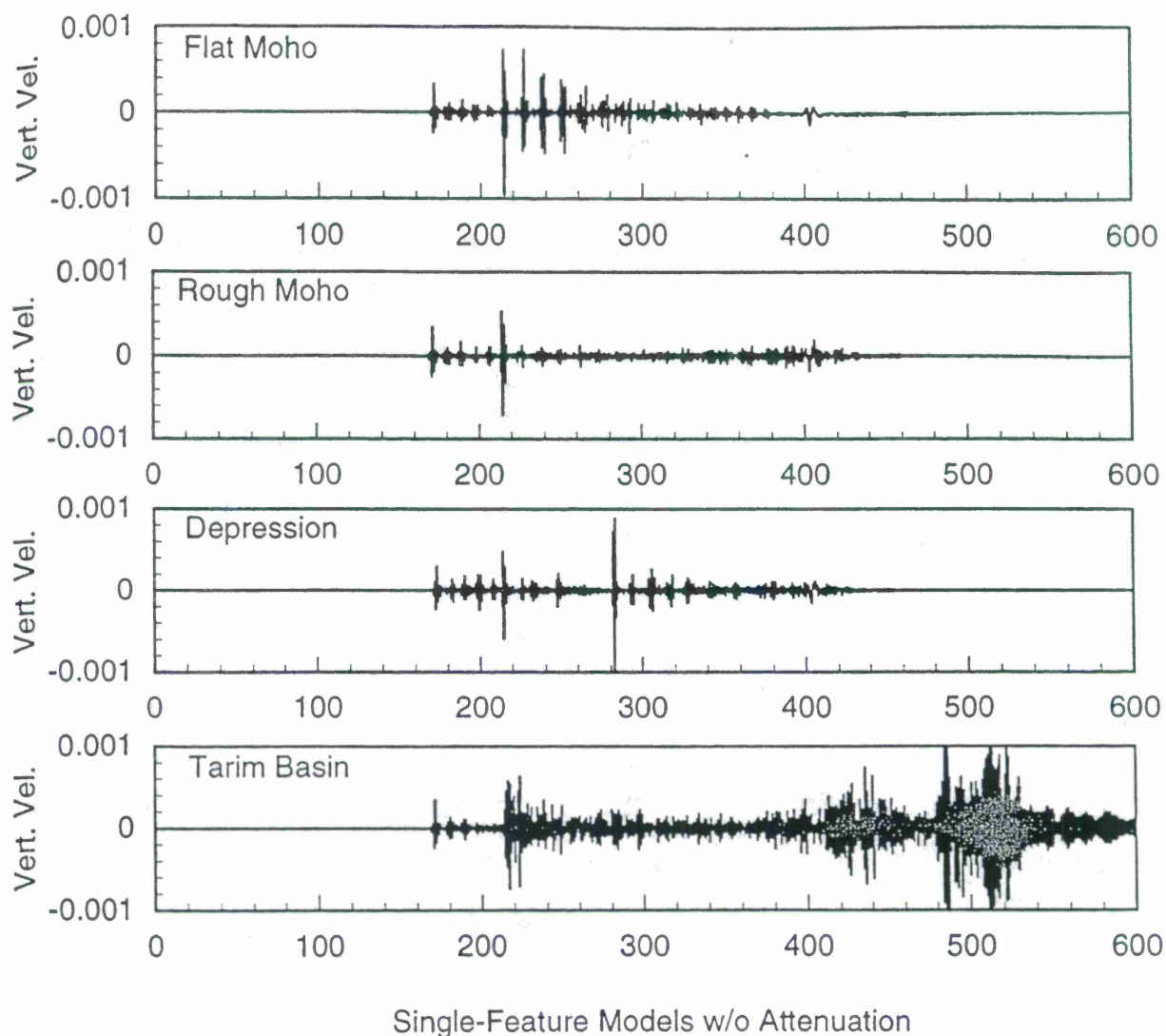


Figure 2 - Synthetic vertical velocity seismograms for simulations with a single structural feature: a Flat Moho at 48-km depth (top panel), a Rough Moho with an average depth of about 48 km (second panel), the full Lop Nor \rightarrow NIL Moho profile including the depression underlying the Tibetan Plateau (third panel), the Tarim Basin (fourth panel), and the full Lop Nor \rightarrow NIL topographic profile. All the sources were placed at 10-km depth.

calculated at 1350-km range, the roughened Moho disrupted the regular pattern of reflections that dominated the Flat Moho seismogram. The roughened Moho also enhanced P \rightarrow S conversion and, consequently, produced relatively large S-wave amplitudes at 1350-km range at times between 320 and 430 seconds.

The Moho Depression simulation (third panel) incorporated the full Lop Nor \rightarrow NIL Moho profile. The main difference from the Rough Moho case was the large amplitude signal which arrives at 1350-km range just after 280 seconds and, in addition, a train of reverberations which follows. Examination of seismograms calculated at other ranges (not shown) indicated that the depression-related signals occurred intermittently.

The Tarim Basin simulation (fourth panel) showed a very different seismic character, due primarily to P \rightarrow S conversions and, as well, the creation of Rayleigh waves at the source-ward edge of the basin. The dominant feature in the seismogram at 1350-km range was the Rayleigh-wave train which arrived just after 480 seconds. The later arrival in comparison to the Flat Moho case is due to the slower propagation speed through the basin material. In higher-resolution simulations (not shown) that covered a portion of the path, the Rayleigh waves in the basin had a period of 2 seconds and a wavelength of about 5 km. As was expected from standard analysis of Rayleigh waves (for example, Kolsky 1963), the vertical extent of the Rayleigh waves was about one-quarter wavelength, or about 1.25 km. Surprisingly, the Rayleigh wave amplitudes were not altered significantly by the change in resolution.

The Topography simulation (not shown) was dominated by a Rayleigh wave that was generated by interactions with near-source topographic features. Because these features were poorly resolved by 500-m cells, an auxiliary run (also not shown) was made with 200-m cells and the main result was a reduction in the Rayleigh-wave amplitude to a level well below that of the basin-related Rayleigh waves. The results of these simulations led us to conclude that, although topographic signals probably will be present in well-resolved simulations of seismic waves traversing the Lop Nor \rightarrow NIL path, they will not be as important as the basin-related signals. A definitive assessment of the role of topography will require simulations run at adequate resolution over the entire path and that is beyond our present capability. In the following models, topography is not included, in part to simplify a comparison of runs made with and without anelastic attenuation.

All-Feature Lop Nor \rightarrow NIL Simulation

The top portion of Figure 3 shows synthetic seismograms calculated at 150-km intervals in a simulation which incorporated all of the Lop Nor \rightarrow NIL structural features other than topography. The major features in the seismogram at 1650-km range are labeled. These are the compressive mantle head wave (P_n), the compressive crustal wave (P_g), a shear-wave packet (S_1 to S_2) and the basin-related Rayleigh wave (R). As can be deduced from the successive seismograms, the labeled shear-wave packet originates at the basin edge between ranges 900-km and 1050-km.

The bottom portion of Figure 3 shows synthetic seismograms for a simulation done with the same structure but with anelastic attenuation included. Readers should note that the vertical scale was changed more frequently in this series of seismograms than in the series shown in the upper panels of the figure. As mentioned previously, the quality factors, Q , were adapted from Minster (1979). The most important effect of attenuation in the Lop Nor \rightarrow NIL case was the near-total elimination of the basin-related Rayleigh wave due to the low value of Q_s in the basin. In essence, although the transition from crustal material to basin sediments at the source-ward edge of the basin was effective in producing Rayleigh waves, the long traverse across the basin was equally effective in attenuating them. Note the near equality of the P_n , P_g , and S_1/S_2 amplitudes at 1650-km range.

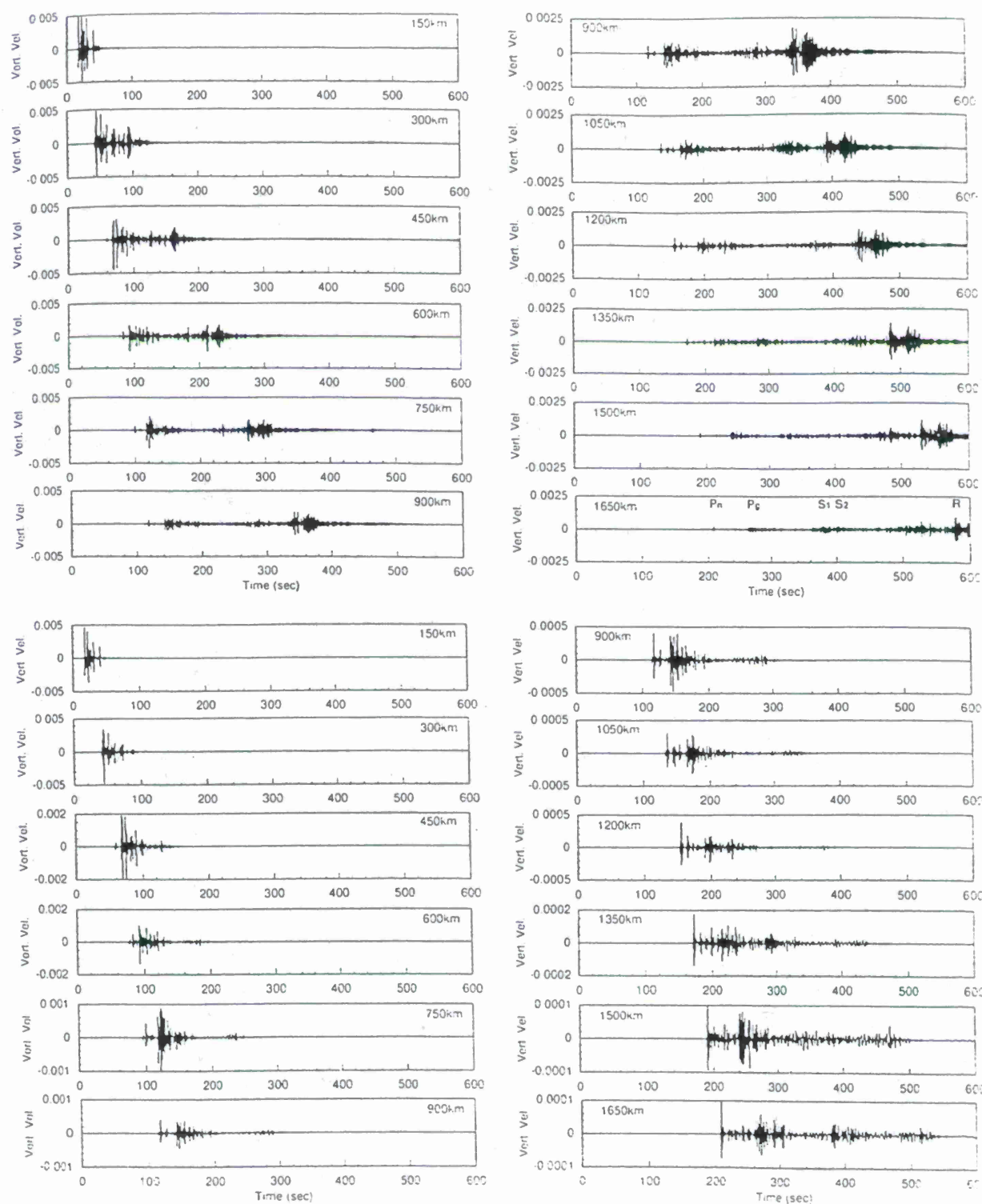


Figure 3 - Synthetic vertical velocity seismograms for simulations including all the Lop Nor -> NIL structural features except topography. The top two frames show results for a run done without anelastic attenuation. The bottom two frames show results from a run done with anelastic attenuation and frequency-independent quality factors discussed in the text. Note the changes in vertical scale between and within the various panels.

Lop Nor -> TLY Simulations

As mentioned previously and as shown in Figure 1, data recorded at the TLY station in the Baikal Rift for the May 1995 Lop Nor explosion was dominated by a very large amplitude S-wave arrival at about 480 seconds. The explosion simulation done by App, Bos, and Kamm (1996) showed similar behavior. The upper portion of Figure 4 shows a series of synthetic seismograms calculated in a Lop Nor simulation that did not include anelastic attenuation. The dominant feature at all ranges is a Rayleigh wave which arrives at 1650-km range at about 500 seconds. The bottom portion of Figure 4 shows the results of a similar simulation that included anelastic attenuation. Here, although the ratio of the Rayleigh wave amplitude to the Pg amplitude is reduced from about 16/1 to about 7/1 at 1650-km range, the Rayleigh wave is still dominant. The main reason for this is the small lateral extent of the main basin, which is deep enough to generate Rayleigh waves but not wide enough to significantly attenuate them.

Summary and Conclusions

In numerical simulations of seismic wave propagation along the paths from Lop Nor to the NIL and TLY seismic stations, we find that large amplitude Rayleigh waves are produced as seismic energy passes from crustal materials into the basin sediments. These Rayleigh waves are the dominant features in seismograms calculated without the effects of anelastic attenuation. When anelastic attenuation is included, a wide basin such as the Tarim Basin, which straddles more than 800 km of the Lop Nor -> NIL path, can reduce the Rayleigh wave amplitudes to insignificant levels. A narrower basin, such as the 200-km-wide basin which straddles the Lop Nor -> TLY path, can produce high amplitude Rayleigh waves, but the path length through highly-attenuating material is too short to reduce the Rayleigh wave amplitudes significantly. Clearly, a resolution of 0.5 km is barely adequate for the simulation of 1-Hz Kelly wave sources on these paths and a resolution of 0.1 to 0.2 km would be much more desirable.

One significant result of this study is that the important structural features which control the character of seismograms recorded at regional distances seem to be the near surface features. Because it should be possible to secure data on the distribution of sedimentary basins and to estimate elastic constants and quality factors for those basins, it appears likely that there will be no major impediments to the production of qualitatively accurate, synthetic explosion seismograms for use in the characterization of sources for the CTBT program. Further work will be required to (1) incorporate realistic crustal velocity gradients, (2) provide adequate resolution for study the effects of topography; and (3) make use of three-dimensional code capabilities to allow use of point sources and to study the effects of out-of-plane structures.

Acknowledgements

We thanks Scott Phillips for comments on a mature draft of the paper and Jim Kamm for his work that made AFD a fruitful research tool.

References

- F. N. App, R. J. Bos, and J. R. Kamm 1996, *Synthetic Seismograms at Regional Distances for May 1995 Earthquake and Explosion Sources in Western China*, unpublished Los Alamos National Laboratory document LA-UR-96-1600.
- F. N. App, E. M. Jones, and R. J. Bos 1997, R&D-Seismic Report on the Influence of the Source Region on Regional Seismic Waveforms as Interred from Modeling, unpublished Los Alamos National Laboratory document (in preparation).

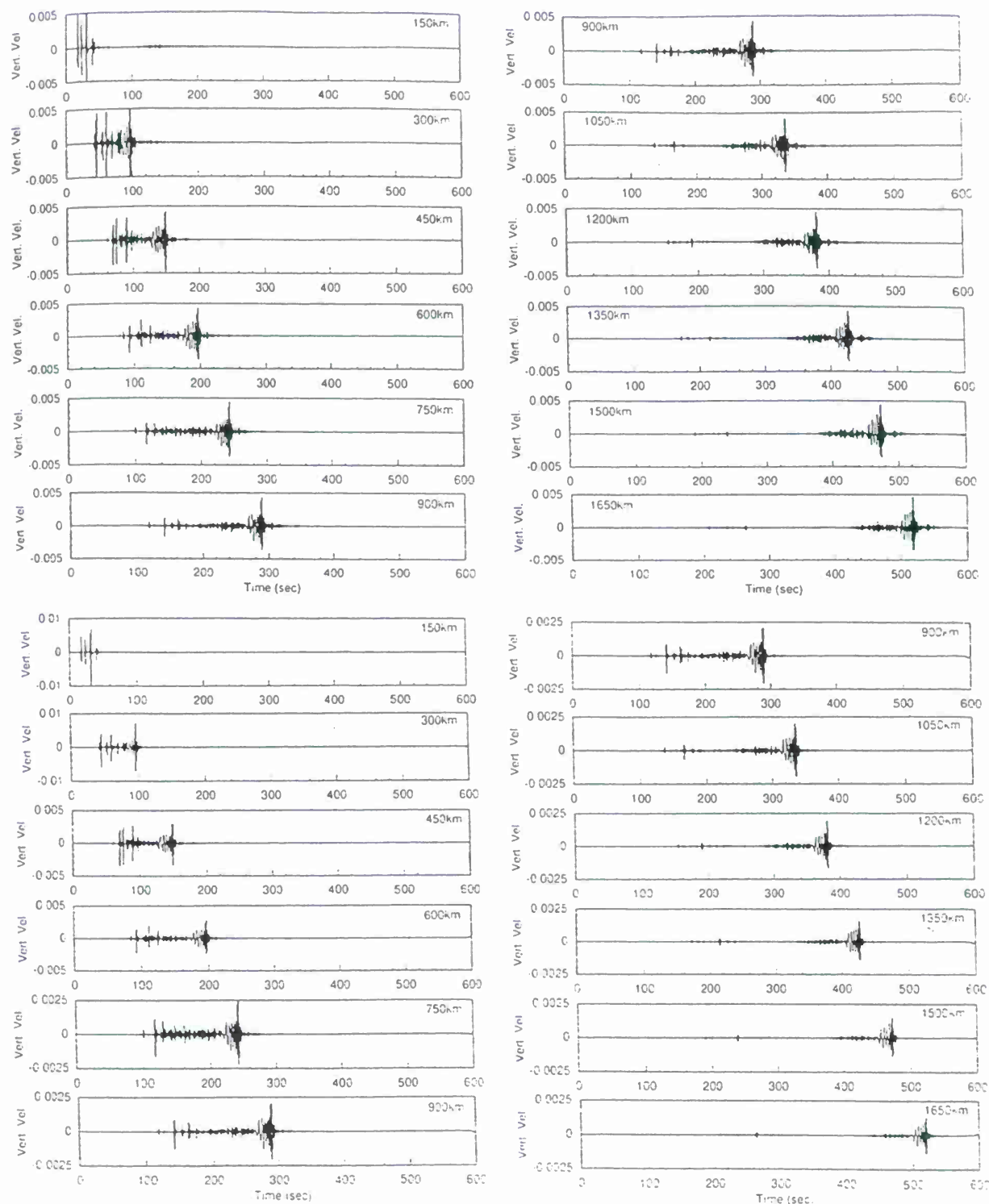


Figure 4 - Synthetic seismograms for a simulation on the Lop Nor -> TLY path. The top panels show a run made without anelastic attenuation. The dominant signal is a Rayleigh wave which originates at the source-ward edge of the near-source basin. The lower panels show a run made with attenuation included. The source depth in both runs was 4 km.

M. Barazangi et al, *Cornell Geological and Geophysical Databases, Information, and GIS Map Server*, <http://atlas.geo.cornell.edu/>, 1996.

H. Emmrich and M. Korn 1987, *Incorporation of attenuation into Time-Domain Computations of Seismic Wave Fields*, *Geophysics*, **52**(9), pp. 1252-1264.

J. R. Kamm, R. J. Bos, and E. M. Jones 1996, *User's Guide to AFD v. 1.0*, unpublished Los Alamos National Laboratory document LA-UR-96-853.

K. R. Kelly, R. W. Ward, S. Treitel, and R. M. Alford 1976, *Synthetic Seismograms: a Finite-Difference Approach*, *Geophysics*, **41**, pp. 2-27.

H. Kolsky 1963, *Stress Waves in Solids*, (Dover Publications: New York), pp. 16-25.

J. B. Minster 1979, *Anelasticity and Attenuation*, in *Physics of the Earth's Interior*, Proc. Enrico Fermi Int. School Physics, (Dziewonski and Boschi, eds.), 551.1 v295s, North Holland.

R. G. Warren 1996, private communication.

PROGRESS IN NUMERICAL METHODS FOR WAVE PROPAGATION

Keith L. McLaughlin (scatter@maxwell.com) and Darin Wilkins (wilkins@maxwell.com) Maxwell Technologies, 8888 Balboa Ave. San Diego, CA 92123, 619-576-7763, Fax 576-7710

Sponsored by U.S. Department of Energy
Office of Nonproliferation and National Security
Office of Research and Development
Contract F19628-95-C-0207

ABSTRACT

Work over the last two years has focused on a diverse set of topics related to numerical simulation of seismic, hydroacoustic, and infrasound signals. 1) A wavenumber integration synthetic wave propagation code for layered Earth structures has been ported to the *Parallel Virtual Machine* (PVM) and has demonstrated parallel computing on heterogeneous networks of workstations. 2) This synthetic code has been extended to admit seismic attenuation parameterized as a function of frequency and 3) to allow an arbitrary number of surface fluid layers. 4) A library of synthetic seismograms has been computed for the Mooney *et al.* (1997) Crust 5.1 continental models placed over a PEM mantle model with frequency dependent attenuation in order to study regional Lg, Pg, and Lg/Pg ratios as a function of distance, frequency, mechanism, depth, and crustal model. This database of synthetic Pg and Lg phase amplitudes is being studied as part of another contract. 5) Scattering calculations have been made using a 3D elastic finite difference code to study the interaction of P and S waves in the crustal waveguide. 6) A finite difference hydrodynamic code, *Maxhose*, has been developed to simulate the response of permeable hose and manifold systems used for infrasound noise reduction. This paper focuses on one specific recent accomplishment and describes numerical analysis of permeable hose responses used for infrasound noise reduction.

Useful detection thresholds for infrasound stations will be directly related to the effectiveness of the hose arrays used for noise reduction. We present numerical analysis of differential equations that describe acoustics of infrasound recording with a permeable hose as opposed to the discrete set of coupled equations that have traditionally been used to describe a Daniels pipe. It is shown that a hose may be characterized by a characteristic time constant, τ_0 , and a characteristic length, k_0 . The time constant is related to permeability of the hose and the characteristic length is related to both flow resistance and permeability of the hose. Signal to noise improvement is directly proportional to the characteristic length of the hose. The low pass filter corner frequency of the system is determined by the characteristic time. Wavelengths of the pressure field shorter than characteristic length are averaged over the length of the hose. A finite difference code, *Maxhose*, is described that computes response of a simple linear permeable hose. The finite difference code is used to model both operational hose designs as well as calibration configurations. Simulations of a single hose to atmospheric pressure fluctuations are presented for a white noise and a fractal noise model. Simulation of an experimental to measure characteristic times of hoses calibration is described and calibration results are shown for commercially available soaker hose. Typical measured characteristic times are between 10 to 20 milliseconds, while characteristic lengths are inferred between 100 and 300 meters. Of particular note are the effects of hose degradation during a typical San Diego winter as demonstrated by a reduction in characteristic length of the hose by a factor of 2. An operational system would have experienced a comparable degradation of signal - to - noise over time. Experiments and numerical analysis combined should provide the tools required to predict noise reduction from wind noise.

Keywords: synthetic seismograms, attenuation, scattering, infrasound, finite differences, CTBT

OBJECTIVE

The principal objectives of this work are to provide more accurate, and efficient means to compute, store, and retrieve synthetic waveforms for reference layered Earth structures and examine limitations of using layered Earth structures to model principal features of regional waveforms in the presence of lateral heterogeneity.

RESEARCH ACCOMPLISHED

Work over the last two years has focussed on a diverse set of topics related to numerical simulation of seismic, hydroacoustic, and infrasound signals. 1) A wavenumber integration synthetic seismogram code for layered Earth structures has been ported to the Parallel Virtual Machine (PVM) and demonstrated to work on a heterogeneous network of UNIX platforms. A version of the code is available upon request. 2) The wavenumber integration synthetics code has been extended to admit seismic attenuation parameterized as $Q_\mu(f)$ and $Q_\kappa(f)$ proportional frequency to an arbitrary power, f^η , where η is an input parameter. This has permitted synthesis of more realistic short-period regional seismograms. 3) The wavenumber integration program has been extended to allow an arbitrary number of surface fluid layers in order to study propagation of hydroacoustic phases in a layered oceanic crustal structure. 4) A library of synthetic seismograms has been computed for the Mooney *et al.* (1997) Crust 5.1 continental models placed over a PEM mantle model with frequency dependent attenuation in order to study regional Lg, Pg, and Lg/Pg ratios as a function of distance, frequency, mechanism, depth, and crustal model. This database of synthetic Pg and Lg phase amplitudes is being studied as part of another contract. 5) Scattering calculations have been made using a 3D elastic finite difference code to study the interaction of P and S waves in the crustal waveguide. The scattered wavefield is decomposed using frequency-wavenumber (FK) transforms on reference phase planes and modal expansions. 6) A finite difference hydrodynamic code, Maxhose, has been developed to simulate the response of permeable hose and manifold systems used for infrasound noise reduction. While each of the listed accomplishments has produced interesting and useful results, we have chosen to highlight recent results from development of a finite difference code to simulate permeable hoses used for infrasound noise reduction.

Permeable Hose Noise Reduction For Infrasound Monitoring - Introduction

The proposed IMS infrasound monitoring system will contain approximately 50 to 60 primary infrasonic arrays scattered around the globe. The arrays will be designed to provide arrival time and azimuth of arrival of low-frequency 0.01 to 10 Hz sound waves propagating in the atmosphere. The final design of sensors and operational procedures for detection, location, and identification of infrasonic events are as yet still in flux. Uncertainties still exist in the areas of 1) excitation as a function of source size and type (explosion, quarry blast, meteor, volcanic explosion) 2) propagation attenuation as function of distance and frequency, and 3) noise reduction through use of hose arrays. Critical to the ability of the proposed networks to monitor near the 1 Kt threshold are the permeable hose noise reduction systems. The concept behind the use of a noise reduction hose relies on the fact that wind generated turbulent eddies have shorter apparent wavelengths than an infrasound signal arriving from great distance (Cook, 1971; Mack and Flinn, 1971; McDonald *et al.* 1971). The hose "averages" the local atmospheric pressure along its length and the incoherent eddies are "averaged" out (Figure 1).

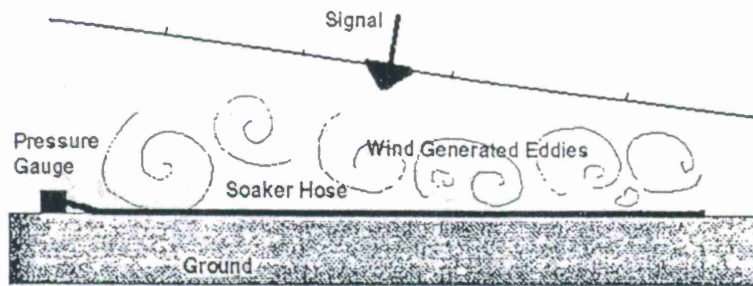


Figure 1. Wind generated eddies create pressure fluctuations and hence noise. The permeable hose acts to spatially "average" the pressure fluctuations.

The original Daniels pipe (Daniels 1959) was conceived as a discrete set of inlet ports along a length of pipe. Grover (1971) presents results for pipe arrays with hypodermic inlet ports while Burrige (1971) presents a numerical solution to this discrete system of inlet ports with a propagator method (a system of coupled equations). However with the advent of soaker hose, the system is analogous to a transmission line or antennae problem and requires the solution of coupled partial differential equation. The following partial differential equation describes the pressure along the hose in terms of the external atmospheric pressure,

$$2\pi a e(p_a(x,t) - p(x,t)) - (1/\nu) \frac{\partial^2 p(x,t)}{\partial x^2} - \dot{p}(x,t) A / (RT) = 0,$$

where x is the position along the hose, t is time, $p_a(x,t)$ is the atmospheric pressure along the hose, $p(x,t)$ is the pressure inside the hose as a function of location and time, a is the hose inner radius, A is the hose inner cross sectional area, R is the gas constant, T is the temperature, and ν is flow resistance. This equation describes the hose system driven by the atmospheric pressure along its length. We can transform from the time-space domain, (t,x) , to the frequency and wavenumber domain, (ω, κ) ,

$$p(x,t) = \iint \hat{p}(\omega, \kappa) \exp(-i\omega t) \exp(-i\kappa x) d\omega d\kappa.$$

We can write the solution in the frequency domain,

$$\tilde{p}(\omega, x) = \int \frac{1}{(1 + i\omega / \omega_0 + (\frac{\kappa}{\kappa_0})^2)} \hat{p}_a(\omega, \kappa) \exp(-i\kappa x) d\kappa.$$

Now we observe that a far-field signal has the form $\hat{p}_a(\omega, \kappa) = \delta(\kappa) \tilde{p}_s(\omega)$ so the signal pressure in the hose is simply

$$\tilde{p}_{signal}(\omega) = \frac{1}{(1 + i\omega / \omega_0)} \tilde{p}_s(\omega).$$

The typical soaker hose has a characteristic time constant, $\tau_0 = 2\pi/\omega_0 = 2\pi a/(2R\tau e) < 0.2$ seconds, so the pressure signal inside the hose is a faithful representation of the signal outside the hose for frequencies of interest. This characteristic time is determined by the permeability of the hose. If we write the atmospheric noise as $\hat{p}_a(\omega, \kappa) = \hat{p}_n(\omega, \kappa)$ then the observed noise signal is given by a Fourier integral over the wavenumber spectrum of the observed atmospheric noise signal,

$$\bar{p}_{noise}(\omega, x) = \int \frac{1}{(1 + i\omega/\omega_0 + (\frac{\kappa}{\kappa_0})^2)} \hat{p}_n(\omega, \kappa) \exp(-i\kappa x) d\kappa,$$

This integral in general can not be evaluated in closed analytic form, however by inspection we can note several interesting features. The incoherent atmospheric wavenumbers are attenuated proportional to $(\frac{\kappa}{\kappa_0})^2$ where $\kappa_0^2 = 2\pi a e \nu = 4\pi A \nu / (RT) / \tau_0 = (2\pi / \lambda_0)^2$ is the square of the characteristic wavenumber for the hose. The smaller the characteristic wavenumber, the more attenuated will be the incoherent wavenumbers of the noise field. The characteristic wave length for the hose is proportional to the square root of the characteristic time constant divided by the flow resistance. Typical soaker hoses have characteristic lengths, λ_0 , of about 100 - 500 meters, but we have found that time constants and hence characteristic lengths and the potential noise reduction change with time as the hose ages.

Figure 2 (left) shows an inexpensive experimental set up for measuring time constants of a soaker hose. The soaker hose is placed in the 44 Liter volume test chamber. The test chamber volume is then altered with a 12 cc step function volume decrease producing a change in pressure of about 300 microbars. Pressure transients measured with this set up are shown in Figure 2 (right) for a virgin soaker hose and the same brand of hose left outside for six months during a typical San Diego winter. The time constant for this aged hose has decreased by nearly a factor of two. Hence noise reduction will have decreased by nearly the same amount.

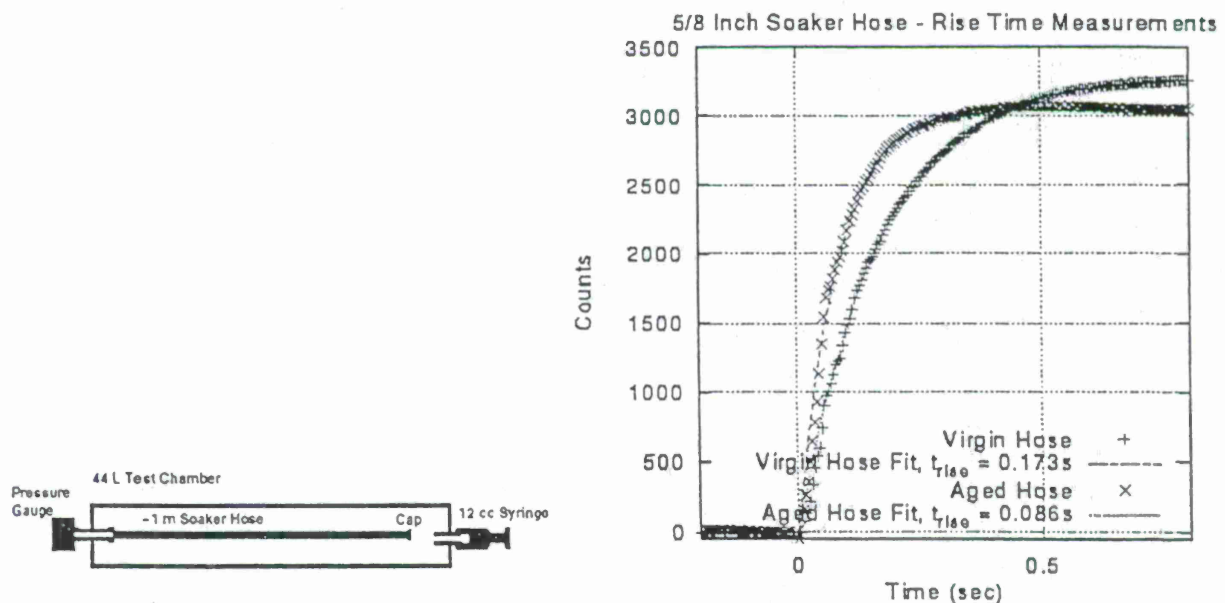


Figure 2. Simple inexpensive test configuration for measuring hose time constants. Rise time calibration (left) of two 2.082 m long hoses. The "aged" hose had been exposed to the elements for about 6 months during a typical San Diego winter. The rise time of the aged hose is about 50% that of the virgin hose.

Analysis of a Helmholtz Oscillator

If a manifold is connected to a short non-permeable hose and a step function in pressure is applied to the manifold, it is possible that a Helmholtz oscillator may be set up. This condition occurs when the slug of air within the hose protrudes into the reservoir without immediate mixing and the reservoir acts like a spring. The slug of air acts as a mass connected to the spring and a damped simple harmonic oscillator is set in motion. The viscous flow of air back and forth in the hose causes damping proportional to the flow velocity and the damped simple harmonic oscillator can be modeled to "measure" the damping constants used in the previous analysis.

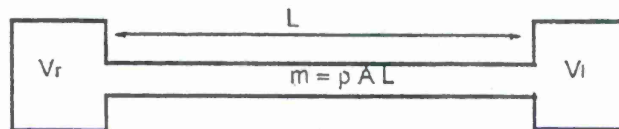


Figure 3. Simple diagram of the principle part of a two ended Helmholtz oscillator.

The geometry of the oscillator is shown above. The mass in the length of hose is given by, $m = \rho A L$. The displacement of the mass in the x direction is $u(t)$, P_r , and P_l are the right and left manifold pressures. If the slug of air protrudes into the manifold with displacement, u , and does not mix with the air in the manifold, then effective volume of the right and left manifolds are $V_r = V_{0r} - Au$ and $V_l = V_{0l} + Au$, where V_{0r} and V_{0l} are the original right and left manifold volumes and isothermal pressure changes in the two manifolds effect restoring forces. We can write the equation for this simple harmonic oscillator,

$$\ddot{u} = -\frac{\zeta}{A\rho}\dot{u} - \frac{AP_0}{L\rho}\left(\frac{1}{V_{0r}} + \frac{1}{V_{0l}}\right)u = -\nu A\dot{u} - \frac{ART}{L}\left(\frac{1}{V_{0r}} + \frac{1}{V_{0l}}\right)u,$$

with natural frequency, $\omega_0 = \sqrt{ART(1/V_{0r} + 1/V_{0l})/L} = \sqrt{(A^2 P_0(1/V_{0r} + 1/V_{0l}))/m}$ and damping constant, $\beta = \nu A/2 = \zeta/(2A\rho)$. The natural period is proportional to the square root of the manifold volumes and square root of the hose length. If we assume Pouisselle flow in the hose then the damping constant only depends upon air viscosity, η , air density, and hose radius,

$$\beta = \frac{4\eta}{\rho a^2}.$$

The damping constant does not depend upon the length of the hose. These relations

can be used to determine damping characteristics and hence drag terms as shown in Figure 4 below. Tests may be made with various lengths of hose and step function amplitudes to test for linearity.

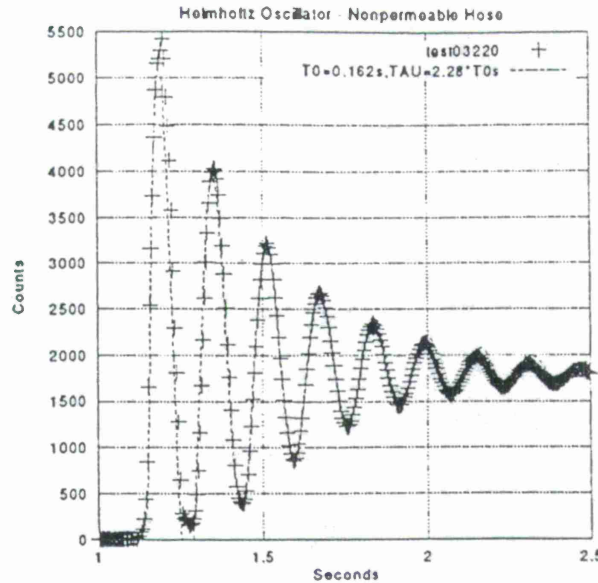


Figure 4. A 0.32 m section of 5/8" non-permeable hose was set up as a Helmholtz oscillator and subjected to a 0.5 millibar step function change in pressure of one manifold. Crosses are data, the dotted line is a damped sinusoidal fit to the data. The damping constant, $\tau = 1/\beta = 0.37 \pm 0.01$ sec, is a direct measure of flow resistance in the hose.

Finite Difference Code, Maxhose

We have developed an implicit finite difference code, *Maxhose*, to simulate the response of a permeable hose and manifold system. Our goal was to model calibration configurations as well as the response of a system to an arbitrary atmospheric pressure field specified as a function of position and time. We start with the partial differential equation for pressure in the hose as derived above,

$$\dot{p}(x,t) = \left(\frac{RT}{A} \right) 2\pi a e (p_a(x,t) - p(x,t)) - \left(\frac{RT}{Av} \right) \frac{\partial^2 p(x,t)}{\partial x^2}.$$

We discretize the space and time variables, $x_j = x_{j-1} + dx_j$ and $t_n = t_{n-1} + dt_n$, and define a pressure vector of j 'th hose elements, $p_j^{(n)}$ for time t_n and $p_j^{(n+1)}$ for time t_{n+1} . Pressure, p_j , is the pressure of the volume between $x_j = x_{j-1} + dx_j$ with cross sectional area $A_j = \pi a_j^2$ and volume $V_j = A_j dx_j$. We follow the Crank-Nicolson implicit scheme (Smith 1978; Davis 1986) to derive a set of second order finite difference equations for the pressure updates at time step $n+1$ from the pressures at time step n . It promotes stability of the finite difference equations to include velocity, v , (momentum) in the set of equations. We must assume that $\dot{m}v \ll m\dot{v}$ for each element or cell or nonlinear terms (velocity times pressure) will appear in the response equations. We derive a difference equation for flow velocity within the hose $\dot{v} = -v Av - \left(\frac{1}{\rho dx} \right) (p(x+dx) - p(x))$. If

this corresponds to simple Poiseuille flow, then flow resistance constants may be computed from the air viscosity, η ; $v = 8\eta / \pi / \rho / a^4$. We require two sets of boundary conditions at the ends of the hose at $x_1 = 0$ and $x_N = L$. The first useful boundary condition is a no flow condition where the spatial pressure derivative and velocities are zero. The second set of boundary conditions assumes isothermal manifolds (volumes) connected to the hose. At each $(n+1)$ time

step, linear equations are solved, $Au^{(n+1)} = Bu^{(n)} + C(w^{(n)} - u^{(n)}) = b^{(n)}$, for the new vector, $u^{(n+1)}$, of pressures and velocities. We construct the pressure-velocity vector components; $u_{2j} = p_j$, $u_{2j-1} = v_j$, and $w_{2j} = p_{aj}$, $w_{2j-1} = 0$, for $j = 1$ to N . $C_{(2j-1),(2j-1)} = 0$ and $C_{2j,2j} = 1$ for $j = 1, N$. The A and B matrices are very sparse but not necessarily banded when multiple coupled hoses are considered, therefore a general sparse matrix linear equation solver is used rather than a solver that assumes a strictly banded system.

Hose Calibration Simulation

Figure 5 shows three *Maxhose* simulations of the calibration test configuration diagramed in Figure 2. Proper analysis of the calibration data requires that the pressure gauge manifold be included in the response. When the manifolds are included in the simulation, the value of $\tau_0 = 0.10$ sec. fits the data very well.

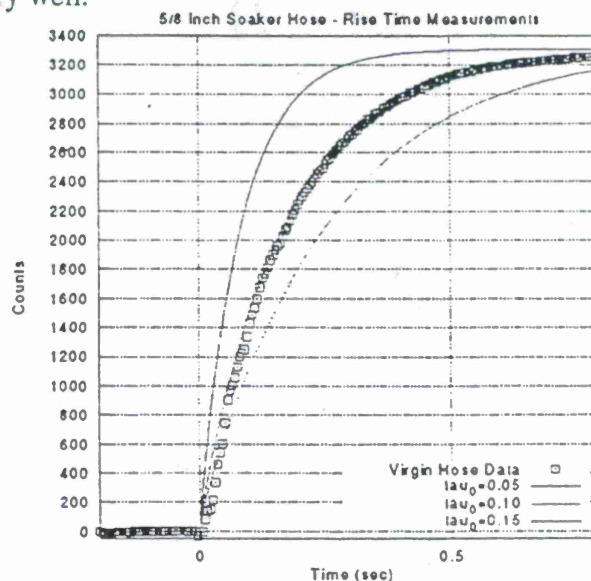


Figure 5. Comparison of data and *Maxhose* finite difference simulations of the calibration test configuration of Figure 2.

Finite Difference Simulations of Wind Noise Response

We demonstrate the use of the finite difference code, *Maxhose*, to model the hose response to atmospheric wind noise. An atmospheric pressure history is specified as a function of time and position along the hose, $p_a(t,x)$, and the pressure inside the hose is computed. Figure 6 shows the results for $p_a(t,x)$ specified as white noise on a 50 m hose with a characteristic time of 0.1 second and a characteristic length of 100 m. While this is not a realistic wind noise situation, it illustrates several aspects of the permeable hose response. The numerical experiment was repeated for several hose lengths and the predicted noise reductions are summarized in Figure 7. RMS noise levels are reduced by nearly a factor of 40 in the middle of a hose that is longer than 1/2 the characteristic length. Noise reduction saturates at about 1/2 the characteristic length. For such a hose under white noise conditions, noise levels at the end of the hose are roughly 30% higher than the levels in the center of the hose.

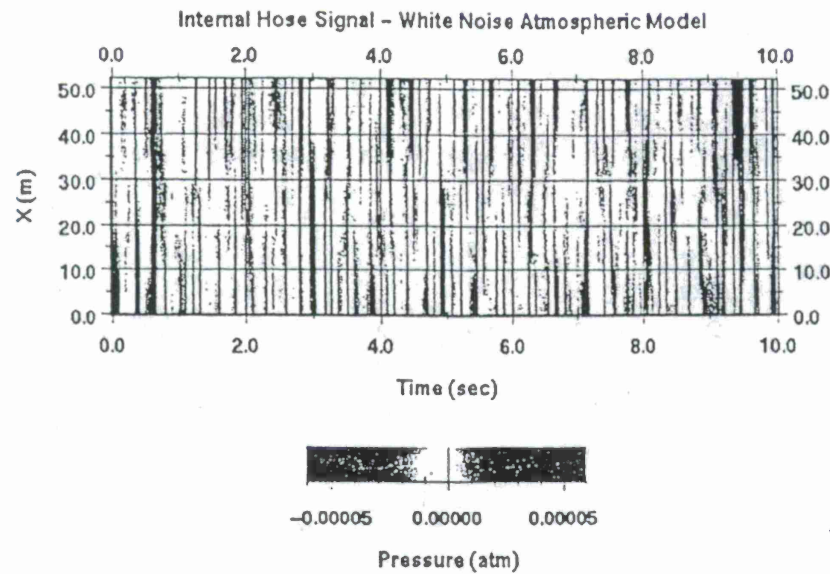


Figure 6. Pressure variation in the hose as a function of time (seconds) and position (X in meters) for random white noise pressure fluctuations in the atmosphere. Note that the hose smooths out the pressures differences along the hose.

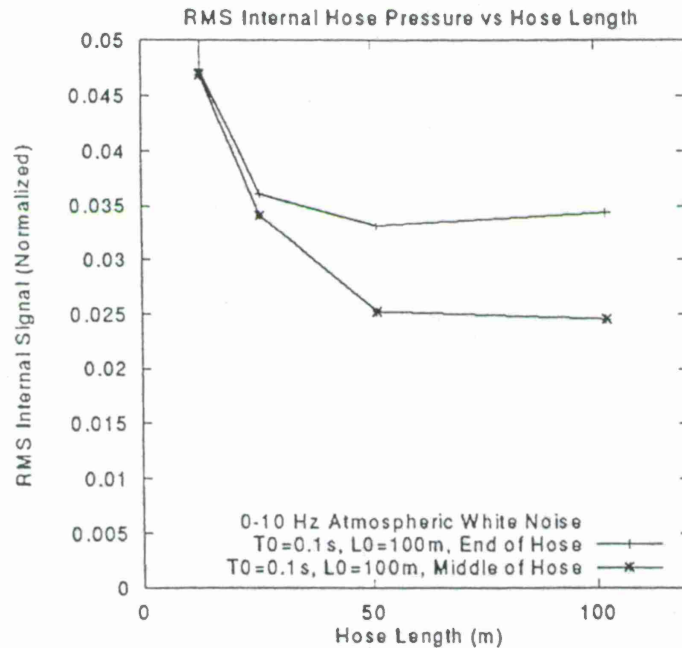


Figure 7. RMS pressure fluctuations normalized to external atmospheric RMS fluctuations at the end of the hose and in the middle of the hose versus different hose lengths for a fixed characteristic length hose. Note that noise reduction is best in the middle of the hose.

Under more realistic wind conditions, atmospheric pressure fluctuations exhibit spatial correlation. Given an arbitrary correlation function or power spectrum we can synthesize a realization of the atmospheric noise. In the absence of a deterministic wind model we have postulated that $p_a(t, x)$ appears as Brownian or fractal noise with a power spectrum that is inversely proportional to frequency and wavenumber, f^{-a} and k^{-b} , where a and b are specified

constants. Figure 8 shows the results of such a Monte Carlo simulation with $a = b = 2$. The same hose characteristics were used as in previous simulations. An atmospheric pressure noise source with a power spectrum approximately proportional to k^{-2} and f^2 is shown on the left and the internal hose pressure fluctuations are shown on the right. Note that the hose has spatially averaged the pressure field. High frequencies and spatial wavenumbers have been reduced. However, low spatial wavenumbers are still evident in the internal hose signal.

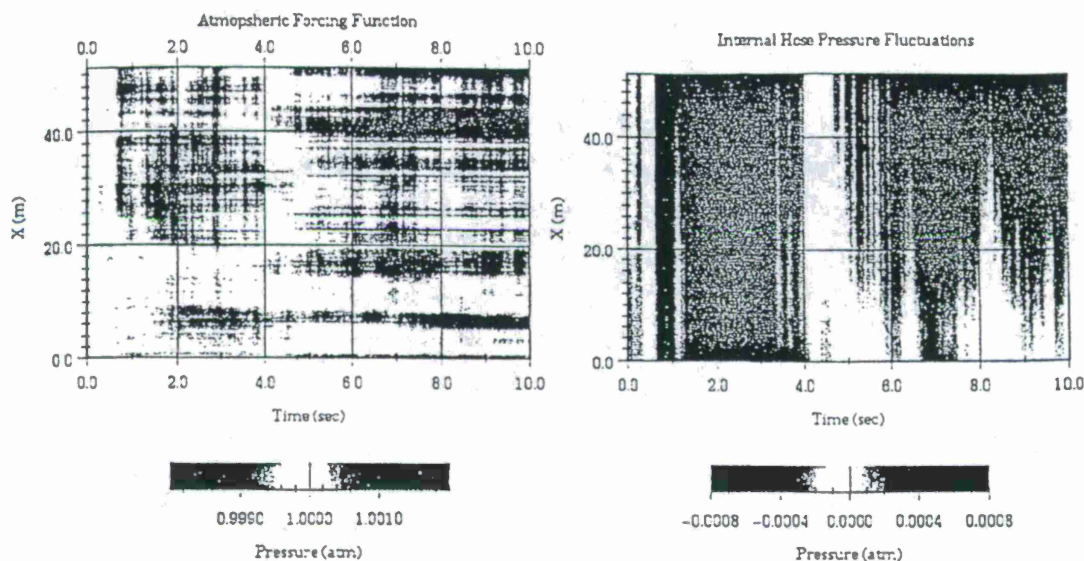


Figure 8. An atmospheric pressure history as a function of space and time on the left and the resulting pressure fluctuation signal in the hose on the right. The 50 m hose reduces the atmospheric noise by averaging it over the length of the hose with characteristic length of 100 m.

CONCLUSIONS AND RECOMMENDATIONS

Wind noise reduction is critical for successful utilization of microbarograph arrays in a future CTBT system. Current plans for the IMS anticipate signal to noise increases from multiple hose arrays on the order of 100 for noisy wind conditions. We present analysis of the partial differential equations that govern the response of pressure within a permeable hose to external atmospheric pressures. We show that a hose may be characterized by a time constant and characteristic length. The characteristic time constant is determined by the permeability of the hose. The characteristic length is determined by the permeability of the hose and flow resistance along the hose. Methods for measurement of the time constant are proposed.

Noise signals in the hose will be attenuated for pressure fluctuations in the atmosphere with wavelengths shorter than the characteristic length. Infrasound signals with apparent wavelengths longer than the hose will not be so attenuated and the hose affords a net signal to noise ratio gain. Control of permeability of the hose is critical to the signal to noise ratio gains that can be realized. Measurements of the time constants of hoses has shown that the permeability can change by a factor of two due to natural weathering of a hose.

Conversion of the partial differential equations to a finite difference program, *Maxhose*, is described. *Maxhose* simulates hose pressure response to an arbitrary atmospheric pressure defined as a function of time and position along the hose. This second order implicit Crank-

Nicholson code runs on UNIX workstations and Windows 95 computers. Results are shown for simple calibration configurations and for two Monte Carlo realizations of wind noise. If wind noise is uncorrelated in space and time, then noise reduction for a single hose is predicted to be about a factor of 40 and maximized in the center of a hose at least as long as $1/2$ the characteristic length. Noise reduction for a single hose in the case of fractal noise is somewhat less. *Maxhose* can be extended to simulate multiple hose arrays and wind noise with arbitrary correlation structures in space and time. Analysis of this kind coupled with an understanding of wind noise correlation structures will prove useful in understanding the potential for permeable hose wind-noise reduction.

Acknowledgments

We wish to thank David Harkrider, Robert Blandford, Dean Clauter, Chris Hayward, Mike Sorrels, Gene Herrin, and Steven Peyton for their helpful discussions on infrasound propagation and hose physics.

References

- Blandford, R. R. and D. A. Clauter (1995). Capability estimation of infrasound networks, AFTAC Technical Report.
- Burridge, R. (1971). The acoustics of pipe arrays, *GJRS* 26, 53-69.
- Cook, R. K., Bedard, A. J. (1971). On the measurement of infrasound, *GJRS* 26, pp 5-11.
- Daniels, F. B. (1959). Noise reducing line microphone for frequencies below 1 c/s. *J. Acoust. Soc. Am.*, 31, 529.
- Davis, J. L. (1986). Finite Difference Methods in Dynamics of Continuous Media, MacMillan Publishing Co., 238 pp.
- Grover, F. H. (1971). Experimental noise reducers for an active microbarograph, *GJRS* 26, 41-52.
- Mack, H. and E. A. Flinn (1971). Analysis of the spatial coherence of short-period acoustic-gravity waves in the atmosphere, *GJRS* 26, pp 255-269.
- McDonald, J. A., E. J. Douze, and E. Herrin (1971). Structure of atmospheric turbulence and its application to the design of pipe arrays, *GJRS* 26, pp 99-109.
- Mooney, Laske and Masters (1997). Crust 5.1: A Global Crustal Model at 5x5 Degrees, submitted to *JGR*.
- Smith, D. D. (1978). Numerical Solution of Partial Differential Equations: Finite Difference Methods 2nd ed., Oxford University Press, 304 pp.

L_g PROPAGATION, UPPER MANTLE STRUCTURE AND ATTENUATION ALONG THE PROFILE "QUARTZ", RUSSIAN EURASIA

I. B. Morozov, E. A. Morozova, and S. B. Smithson

Department of Geology and Geophysics,
University of Wyoming, Laramie,
WY 82071-3006

Sponsored by Air Force Office of Scientific Research
Grant F49620-94-1-0134

ABSTRACT

Understanding of the propagation of regional seismic phases is of a primary importance for the calibration of seismic nuclear test discriminants. Deep Seismic Sounding (DSS) data provide an unparalleled source of information about the propagation of P_n , S_n , L_g , crustal and mantle reflections, and whispering-gallery phases generated by nuclear explosions (PNEs). Based on the analysis of all these phases recorded by DSS profile "Quartz", we demonstrate that the uppermost mantle is significantly heterogeneous, exhibiting vertical and horizontal velocity contrasts and reflecting boundaries. Seismic attenuation of the uppermost mantle exhibits a strong increase at the depth near 200 km, and it is also most likely spatially heterogeneous in 3-D. Analyzing L_g propagation from "Quartz" PNEs, we show that L_g is strongly attenuated within the crust under the sedimentary basins. One of possible proposed decay mechanisms is L_g leakage into the upper mantle through its strong coupling to upper-mantle P-wave modes. All these factors demonstrate that significantly more detailed models of the uppermost mantle structure are necessary in order to understand propagation of regional phases used for seismic monitoring.

Keywords: Peaceful Nuclear Explosions, Deep Seismic Sounding, regional seismic phases, L_g , upper mantle, heterogeneity, attenuation

OBJECTIVE

Ultra-long, densely spaced Deep Seismic Sounding (DSS) profiles using nuclear and chemical explosions provide unique opportunities to calibrate existing seismic nuclear discrimination techniques by studying regional wave propagation through complex lithospheric structures. In this context, the principal objectives of our analysis of the DSS profile "Quartz" are:

1. assessment of a realistic, 2-D, heterogeneous velocity and attenuation structure of the crust and upper mantle that would enable a quantitative analysis of the amplitudes of regional seismic waves;
2. development of robust amplitude measurement techniques, providing stability of the amplitude ratios and improved attenuation estimates, and taking advantage of dense 3-component recordings;
3. modeling of L_g propagation throughout its entire propagation range and correlation of its amplitude characteristics with the tectonic and geologic environment;
4. ultimately, improvement of regional seismic event discrimination techniques by calibrating them using recorded DSS PNEs.

RESEARCH ACCOMPLISHED

Russian DSS profiles have been recognized as unparalleled sources of detailed information about the propagation of various seismic phases across the northern Eurasia comprising about 1/8-1/7 of the land mass of the world. DSS program provided the only existing source of recordings of L_g propagation from nuclear explosions (PNE) along densely spaced linear profiles of 3-component instruments within 0-4000 km ranges.

In this report, we analyze the data from a 3850-km long DSS profile recorded in 1984-87 and spanning six tectonic provinces from Kola Peninsula to Altay foldbelt (Figure 1). For descriptions of tectonic structures crossed by the profile, we refer the reader to our previous reports (Morozova et al., 1994; Morozov et al., 1995) and to the paper by Schueller et al. (1997).

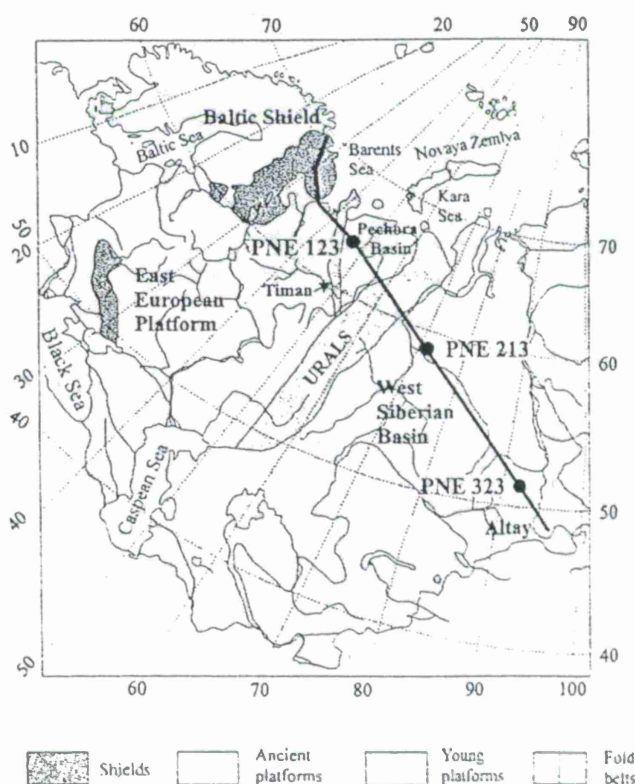


Figure 1. Map of the western part of the former USSR showing the location of profile "Quartz" and its three PNEs. Major tectonic provinces are indicated.

Our analysis of "Quartz" data resulted in two main conclusions directly relevant to the problem of nuclear test discrimination: 1) the uppermost mantle velocity and attenuation structure is significantly heterogeneous, and 2) the propagation of regional phases, including L_g is highly sensitive to this heterogeneity, and to the variations in crustal structure. We summarize these results below, and also describe preliminary results of our analysis of upper mantle attenuation.

Heterogeneity of the uppermost mantle

Inversion of the data from all 3 PNEs and 48 chemical explosions along the profile "Quartz" results in a detailed crustal and uppermost mantle structure shown in Figure 2. The uppermost mantle is significantly heterogeneous, with vertical and horizontal velocity contrasts, high- and low-velocity zones, Moho topography, and two apparently regional reflecting boundaries present at 60-90 and 120-140 km depth. Such a complex structure would cause variations of amplitudes of P_n and S_n phases that cannot be accounted for by using traditional simplified 1-D models of the uppermost mantle.

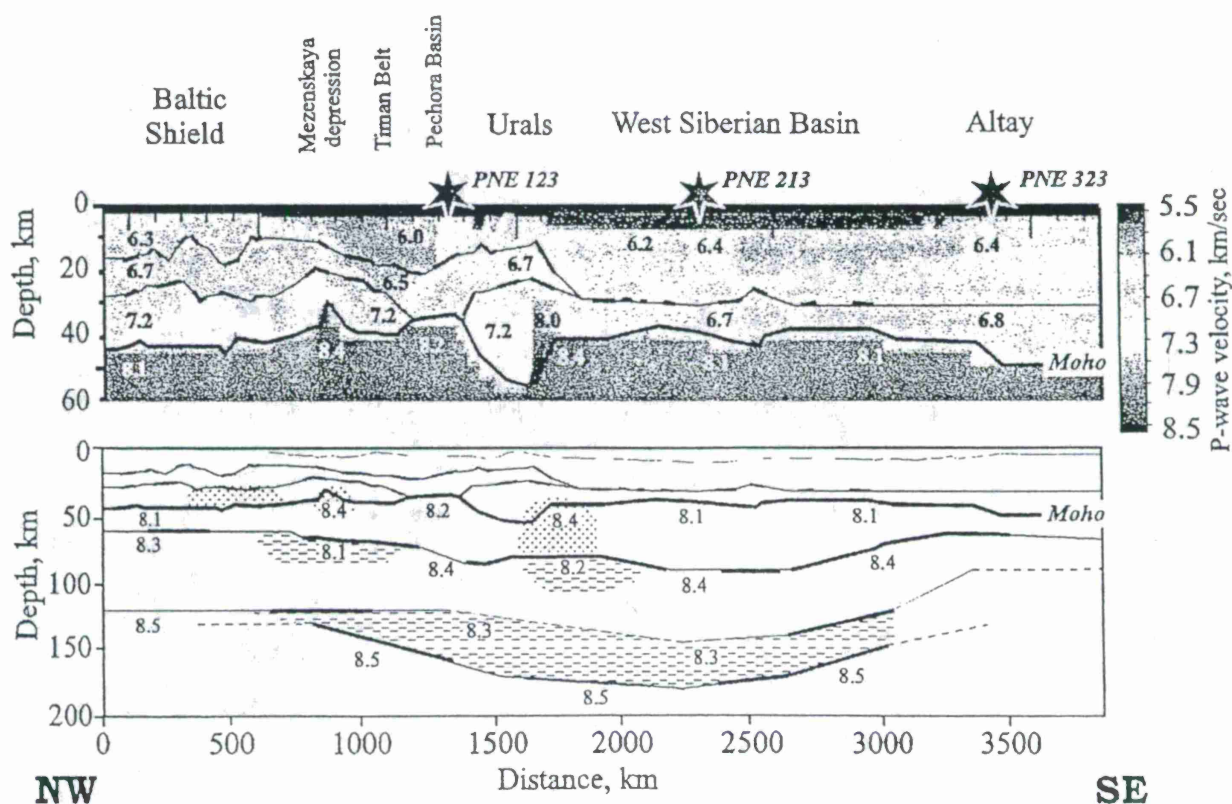


Figure 2. Crustal (top) and uppermost mantle (bottom) velocity-interface structure along the profile "Quartz" obtained using 3 PNEs and all 48 chemical explosions. Locations of the PNEs are indicated. Reflecting boundaries in the crust and mantle are highlighted. P -wave velocity values are given in labels. Note the low-velocity zones (dashed areas), high-velocity regions (dotted), horizontal velocity variations within the mantle, and prominent mantle reflectors at the depths of 60-90 and 120-140 km. Also note the Moho relief, especially the roots under the Ural Mountains and the Moho uplift under the Mezenskaya depression.

L_g propagation across northern Eurasia

Up to 600-sec long "Quartz" records allow us to observe short-period (1-10 Hz) L_g phases propagating from the PNEs (Figure 3, 4). The records show significant differences in L_g amplitude character during its propagation across different geological structures.

The L_g phase from PNE 323 is strong at distances below 500-700 km and at frequencies below 1.5-2 Hz, but is quickly attenuated with distance and nearly disappears between 1200-1400 km from the PNE (Figure 4). Thus in its amplitude-offset dependence, L_g propagation along the West Siberian Basin differs significantly from the propagation within the Baltic Shield where the absolute value of L_g amplitude appears to be substantially stronger, and no indications of its relative attenuation are found, even though the shot point is in a sedimentary basin (Figure 3).

Compared to L_g , the S wave from PNE 323 propagates effectively to regional ranges of about 2000 km, after which it becomes much weaker at teleseismic distances, although it still can be distinguished in the records (Figure 4). The shadow zone that was observed in the P -wave onsets between 1500-2000 km and that is caused by the prominent low-velocity zone (LVZ) below 200 km (Mechie et al., 1993) is recognized in the S wave onsets (Figure 4). Compared to L_g and to the background coda of P -wave arrivals, the S wave has a higher frequency content, and it is strongly attenuated after low-pass filtering below about 2 Hz.

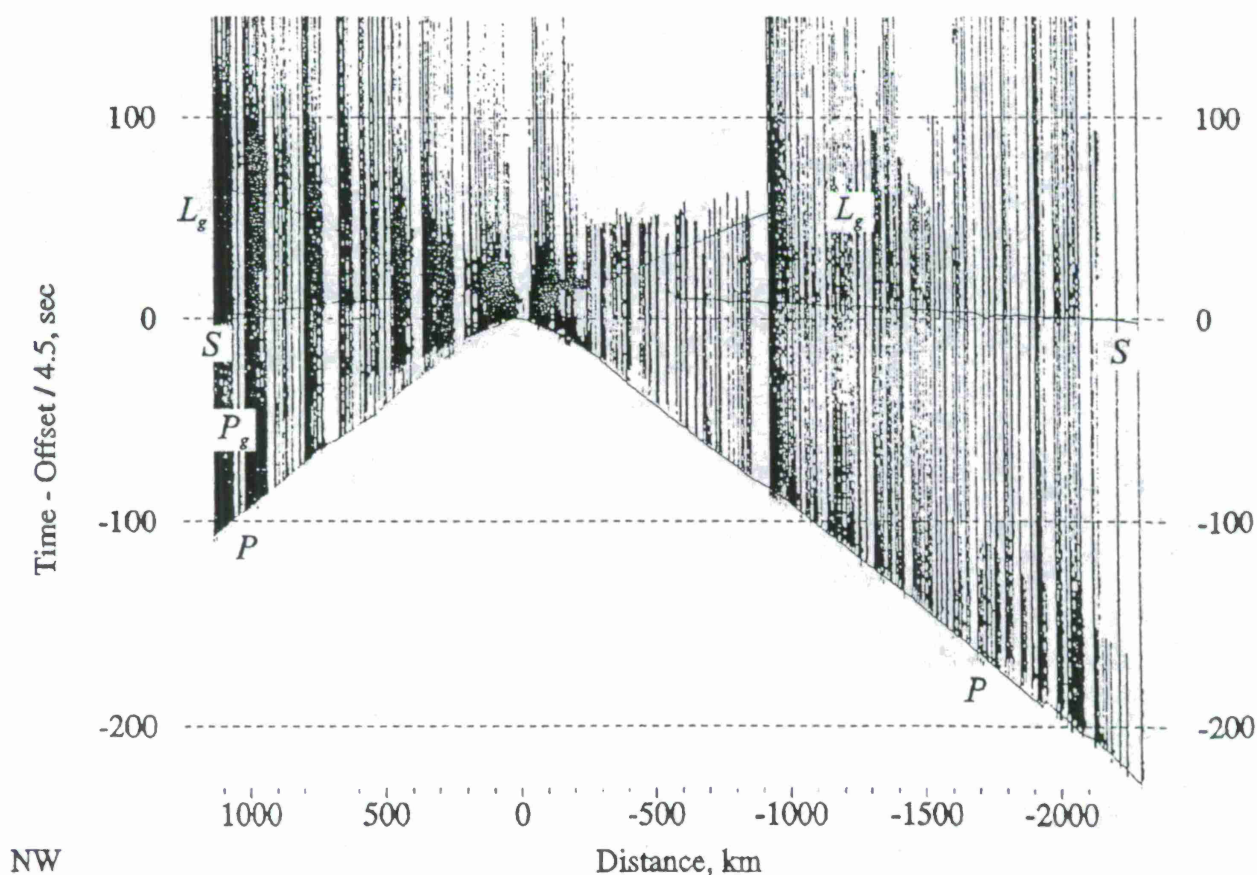


Figure 3. Three-component vector amplitude records from PNE 123, plotted with time reduction velocity of 4.5 km/sec. Note that the L_g is significantly stronger in the Baltic Shield region, NW of PNE 123.

In order to quantify the observed amplitude characteristics of L_g and the regional/teleseismic S waves, we employ an instantaneous 3-component vector amplitude measure (Morozov and Smithson, 1996) that provides more stable estimates (Kennett, 1993). To account for biases in the amplitudes caused by the noise background of the phases of interest, we apply amplitude corrections obtained by measuring signal levels within time windows before the onsets of the corresponding phases. After measuring the amplitudes, we calculate L_g/P and L_g/S amplitude ratios.

Apparently due to low-amplitude L_g and to a complex amplitude pattern of the regional P wave, the L_g/P ratios exhibit poor stability, and are not shown here. Important conclusions, however, can be made from a comparison of L_g and S wave amplitudes (Figure 5). As Figure 5

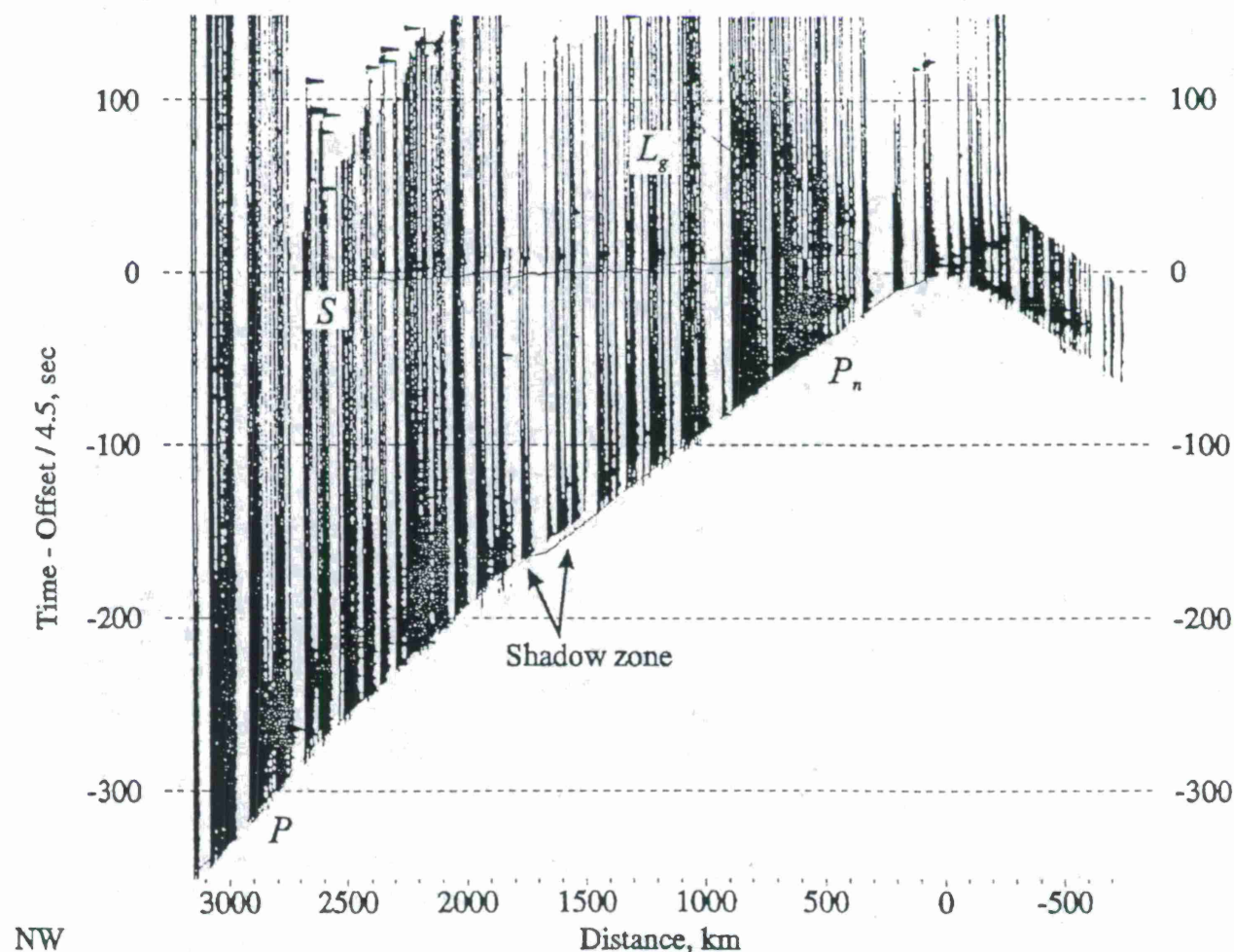


Figure 4. Trace-normalized three-component vector amplitude records from PNE 323. Reduction velocity is 4.5 km/sec. L_g is strong near 500 km offset but rapidly loses its energy with distance and nearly disappears after 1200 km. Note the shadow zone between offsets of 1500 and 1800 km in the first arrivals (indicated by the arrows) and the corresponding gap in the S -wave onset. This shadow zone is caused by a prominent low-velocity zone (LVZ) below a depth of approximately 200 km (Mechie et al., 1993). Also note the sharp attenuation of S wave amplitude at about 2500 km offset, apparently corresponding to its attenuation within the LVZ.

shows, L_g quickly decreases in amplitude (faster than the S wave) during its propagation across the West Siberian Basin, whereas L_g from a PNE in a sedimentary basin effectively propagates in the Baltic Shield region. This observation suggests that the principal cause of the low amplitudes of short-period L_g from "Quartz" is the scattering or attenuation of L_g during its propagation within and below the sedimentary basins, and not the source coupling.

Although one DSS profile still does not provide sufficient data, we speculate that fast dissipation of L_g energy under the West Siberian Basin may be due to its leakage into the mantle through short-scale Moho irregularities and crustal heterogeneities. An indirect support for this mechanism is provided by the observation of a strong coda of the whispering-gallery P wave described in the following section.

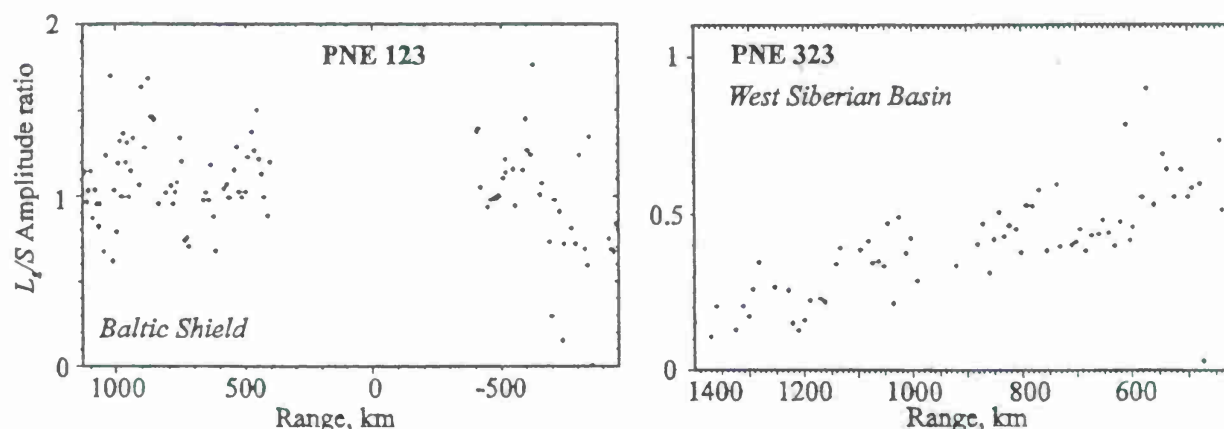


Figure 5. Offset dependence of L_g/S amplitude ratios for PNE 323 and PNE 123. Note the rapid decrease of L_g/S with distance in the West Siberian Basin (PNE 323), and higher L_g/S within the Baltic Shield (PNE 123 to NW).

Mantle attenuation

The understanding of the nature and of the magnitude of upper mantle attenuation is critical for development of seismic discrimination techniques. Heterogeneous uppermost mantle velocity structure shown in Figure 2 suggests a corresponding heterogeneity of the attenuation. Existing Q estimates for the northern Eurasia range from 220 (Yegorkin and Kun, 1978) to 1100 (Der et al. 1986). In their study on the Canadian shield, Evernden et al. (1986) reported values of 5000-9000 for the quality factor Q of short-period P-waves in the uppermost mantle. Therefore, upper mantle Q values are not established reliably, and certainly they exhibit a broad range. Clearly, such wide variations in the values of attenuation would have a profound impact on amplitude ratios between different phases used for nuclear test discrimination.

A unique opportunity for studying contrasts in uppermost mantle attenuation is provided by one of the most remarkable features common to PNE wavefields—a high-frequency teleseismic phase traveling with an apparent group velocity of about 8.1 km/sec, usually called teleseismic P_n (Figure 6; see also Ryberg et al., 1995). Such high-frequency teleseismic P_n phases and corresponding S_n phases propagating within the uppermost mantle to distances of 2000-3000 km were observed by many authors (e.g., Molnar and Oliver, 1969; Heustis et al., 1973; Walker

1977). These phases efficiently propagate through continental shields and deep-ocean basins, but appear to be blocked by major suture zones (Molnar and Oliver, 1969).

A careful examination of the onset of this phase in "Quartz" record sections, which is possible with the dense sampling of DSS records, allows us to distinguish several travel time branches consistent with the interpretation of this phase as two multiple P_n refractions reflected from the Moho down into the mantle (Figure 6, insert). In the following, we refer to this phase as the low-order whispering gallery (WG) mode.

Among the many seismic phases observed in PNE records (Figure 4) this whispering-gallery wave provides one of the best constraints on the vertical attenuation contrast. Its frequency content is very different from that of the first arrivals, and after high-pass filtering this phase dominates the records (Figure 6). Two characteristic features of this phase—its comparatively high-frequency content and the presence of a 20–40 sec long incoherent coda—led Ryberg et al. (1995) to infer a specific "scattering waveguide" propagation mechanism based on strong multiple scattering within the top of the mantle. According to their hypothesis, an about 80-km thick heterogeneous mantle layer filled with scattering lamellae would selectively

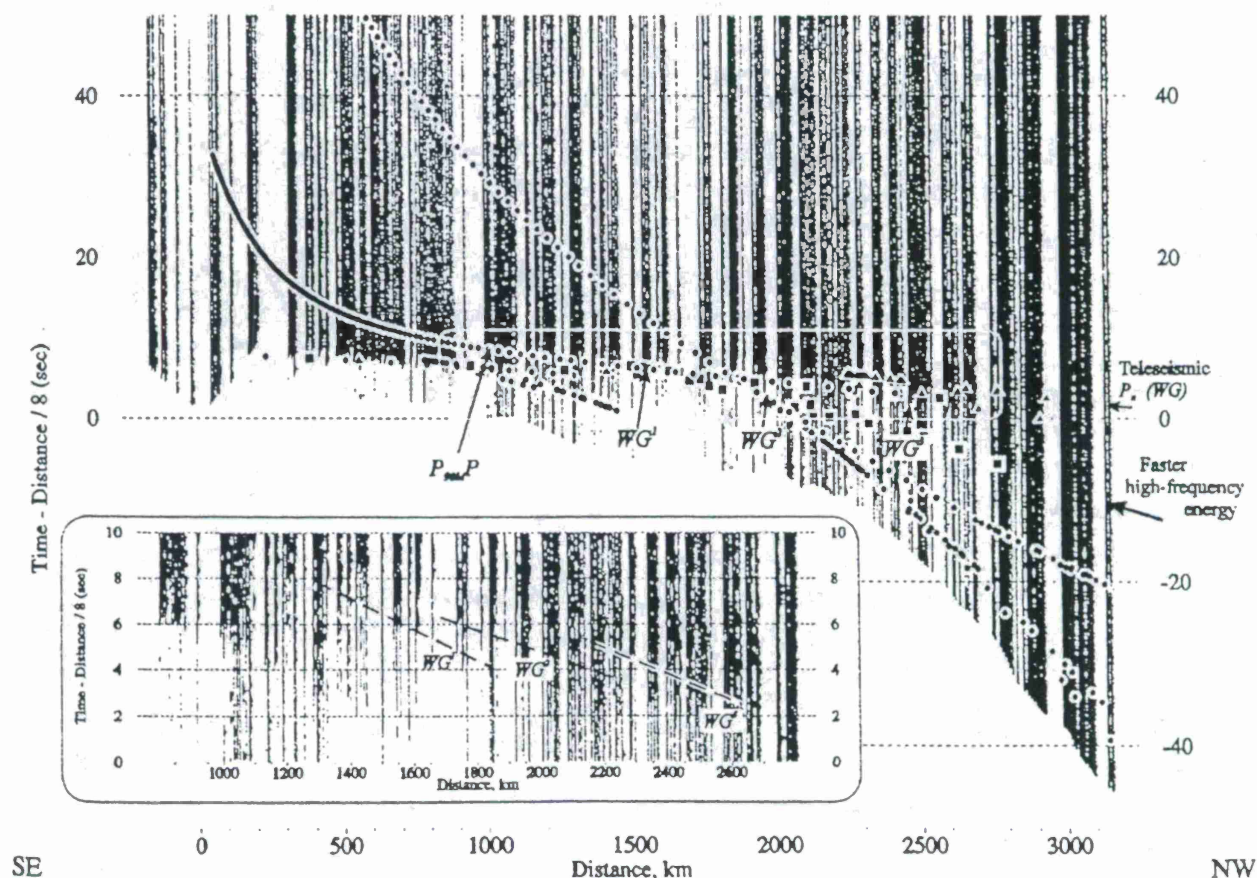


Figure 6. 3-component vector amplitude record section from PNE 323, profile "Quartz" (Figure 4), filtered above 5 Hz. Note how the whispering-gallery phase dominates the high-frequency section. Compared to unfiltered vertical component record, this section is dominated by the teleseismic P_n . The enlarged central part of the gather (insert) shows several travel-time branches in the onset of the teleseismic P_n .

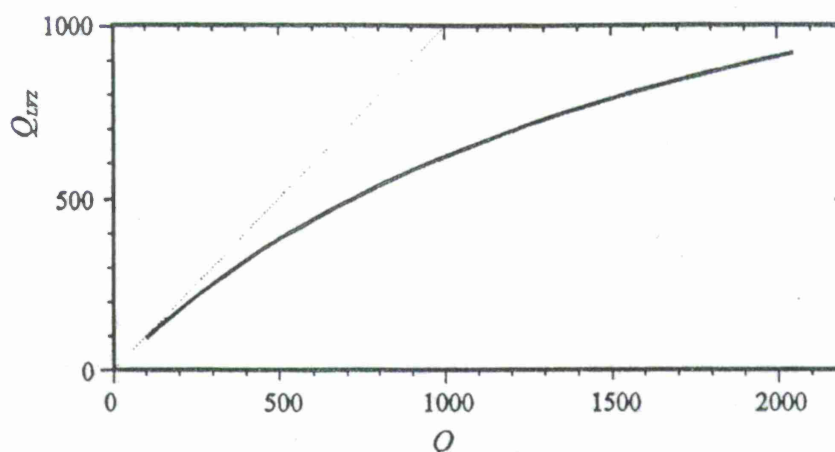


Figure 7. A constraint on the attenuation within the LVZ (Q_{LVZ}) vs. attenuation in the uppermost mantle above the LVZ (Q), inferred from the relative spectral ratios (Morozov et al, submitted to *Bull. Seism. Soc. Am.*). This graph shows values of the quality factor within the LVZ as a function of Q above it. Note that the attenuation contrast increases with increasing Q ; for a value Q above the LVZ of about 1000, a 40% increase of attenuation within the LVZ above the attenuation in the mantle immediately below the Moho is expected. For reference, dotted line correspond to the uniform attenuation model $Q_{LVZ} = Q$.

propagate high-frequency seismic waves horizontally while producing the observed coda. Such a layer would have profound influence on the propagation of seismic phases (especially high-frequency) through the uppermost mantle.

Our amplitude/frequency analysis of the records, however, leads to quite opposite conclusions. The WG phase is broadband, with the high-frequency coda somewhat shorter than the coda at low frequencies due to attenuation within the crust. The apparent frequency contrast between deep refractions and the WG mode is due to the loss of the high frequency energy by the former. This observation allows us to put a sharp constraint on the depth and attenuation contrast at the top of the highly attenuating low-velocity zone (LVZ) beginning at a depth of about 200 km (Mechie et al., 1993).

By observing that all the "high-frequency" phases in Figure 6 do not penetrate into the LVZ, by estimating the relative spectral ratios of the WG mode and deep refractions, and by using a 1-D travel-time simulation, we infer that the attenuation below this depth level should be 30-40% higher than above it, as shown in Figure 7.

The above estimate shows that a sharp vertical attenuation contrast can be directly and reliably observed in DSS PNE records. Moreover, after a further application of spectral ratio methods, we expect to obtain an attenuation image of the upper mantle related to the velocity structure shown in Figure 2. This image will provide valuable information for modeling of the propagation of regional phases and for interpreting their amplitude information.

Finally, the presence of a long incoherent coda of the teleseismic P_n phase (Figure 6) may be related to the fast decay of L_g observed from the same PNE (Figure 5). This coda most likely consists predominantly of postcritical crustal S waves trapped within the crust (Dainty and Schultz, 1995). Therefore, the coda may be an indication of strong coupling between the mantle

P -wave phases incident at the Moho at grazing angles, and S waves within the crust. As a result of such coupling, L_g energy would leak into the mantle, leading to its observed low amplitudes.

CONCLUSIONS AND RECOMMENDATIONS

Understanding of the propagation of seismic regional phases is a principal part of the calibration of seismic nuclear test discriminants. Based on our analysis of the DSS profile "Quartz", we derive the following basic conclusions relevant to the measurement and simulations of L_g , P_n and S_n amplitudes in northern Eurasia:

1. The uppermost mantle is significantly heterogeneous, with vertical and horizontal velocity contrasts and reflecting boundaries present.
2. Seismic attenuation exhibits a strong increase within the LVZ below the level of about 200 km. This depth level, however, varies laterally, and the seismic attenuation in the uppermost mantle is apparently significantly variable in 3-D sense.
3. Measurements of short-period L_g , P_n , and S_n amplitudes show that L_g decays with distance faster than S_n within the sedimentary basins crossed by the profile.
4. Fast decay of L_g amplitudes generated by "Quartz" PNEs may be due to L_g leaking into the mantle. We suggest that this phenomenon might be related to the observed long codas of the whispering-gallery phases from the same PNEs.
5. P/L_g amplitude ratios exhibit poor stability and appears not suitable for calibration purposes using "Quartz" records.

It is important to note that the profile "Quartz" represents only 3 out of nearly 60 PNEs detonated during the fulfillment the DSS program. An analysis of other similar profiles, therefore, would provide a strong basis for verifying these conclusions and for a development of a comprehensive 3-D velocity and attenuation model of the upper mantle of northern Eurasia that is so important for nuclear test discrimination.

REFERENCES

- Dainty, A. M. and C. A. Schultz, 1995, Crustal reflections and the nature of regional P coda, *Bull. Seismol. Soc. Am.*, 85, 851-858.
- Der, Z. A., A. C. Lees, and V. F. Cormier, 1986, Frequency dependence of Q in the mantle underlying the shield areas of Eurasia, Part I: analyses of short and intermediate period data, *Geophys. J. R. Astr. Soc.*, 87, 1057-1084.
- Evernden, J. F., C. B. Archambeau, and E. Cranswick (1986). An evaluation of seismic decoupling and underground nuclear test monitoring using high-frequency seismic data, *Reviews of Geophysics*, 24 (2), 145-215.
- Heustis, S., P. Molnar, and J. Oliver, 1973, Regional S_n velocities and shear velocity in the upper mantle, *Bull. Seismol. Soc. Am.*, 63, 469-475.

- Kennett, B. L. N. 1993, The distance dependence of regional phase discriminants, *Bull. Seismol. Soc. Am.*, **83**, 1155-1166.
- Molnar, P., and J. Oliver, Lateral variations of attenuation in the upper mantle and discontinuities in the lithosphere, 1969, *J. Geophys. Res.*, **74**, 2648-2682.
- Morozov, I. B., and Smithson, S. B. 1996, Instantaneous polarization attributes and directional filtering, *Geophysics*, **61**, 872-881.
- Morozov, I., Morozova, E., Ganchin, Yu., and Smithson, S., 1996, L_g Propagation across Northern Eurasia Recorded by Profile "Quartz", *in: Proceedings of 18 Seismic Research Symposium, PL/DARPA*.
- Morozova, E. A., Morozov, I. B., Smithson, S. B., Schatzman, J., and Solodilov, L. N., 1994, Studies of P_n , S_n and L_g wave propagation across major crustal structures using PNEs, *in: Proceedings of 16 Seismic Research Symposium, PL/DARPA, Thornwood, NY*, 255-261.
- Ryberg, T., K. Fuchs, A. V. Egorkin, and L. Solodilov, 1995, Observations of high-frequency teleseismic P_n on the long-range Quartz profile across northern Eurasia, *J. Geophys. Res.*, **100**, 18151-18163.
- Schueller, W., Morozov, I. B., and Smithson, S. B., 1997, Crustal and Uppermost Mantle Velocity Structure of Northern Eurasia along the Profile *Quartz*, *Bulletin of the Seismological Society of America*, **87**, no. 2, 414-426.
- Yegorkin, A. V., and Kun, V. V., 1978. Absorption of longitudinal waves in the Earth's upper mantle, *Physics of the Solid Earth*, **14** (4), 262-269.

ANOMALOUS WAVE PROPAGATION ACROSS THE SOUTH CASPIAN BASIN

Keith Priestley, University of Cambridge
Howard Patton, Los Alamos National Laboratory¹
Craig Schultz, Lawrence Livermore National Laboratory¹

Sponsored by U.S. Department of Energy
Office of Nonproliferation and National Security
Office of Research and Development
Contract No. F19628-95-K-0017

ABSTRACT

The Caspian basin blocks the propagation of the regional seismic phase Lg and this has importance consequences for seismic discrimination in the Middle East. Intermediate period surface wave propagating across the basin are also severely affected. In a separate study we have developed a crustal model of the south Caspian basin and the surrounding region. The crust of the basin consists of 15-25 km of low velocity, highly attenuating sediments lying on high velocity crystalline crust. The Moho beneath the basin is at a depth of about 30 km as compared to about 50 km in the surrounding region. In this study we used an idealized rendition of this crustal model to compute hybrid normal mode/finite difference synthetic seismograms to identify the features of the Caspian basin which lead to the seismic blockage. Of the various features of the basin, the thickness and attenuation of the sediments appear to be the dominant blocking mechanism.

Keywords: Caspian basin, surface waves, wave propagation, seismic blockage

¹This work was performed under the auspices of the Department of Energy by the Lawrence Livermore National Laboratory under contract W-7405-ENG-48 and by the Los Alamos National Laboratory under contract W-7405-ENG-36.

OBJECTIVES

The Caspian basin blocks the propagation of the regional seismic phase L_g and this has importance consequences for seismic discrimination and a Comprehensive Test Ban Treaty. We have recorded broadband regional and teleseismic distance range seismograms at a number of sites around the south Caspian basin. We find that the south Caspian basin also severely disrupts the propagation of intermediate period surface waves. We are studying these data to understand the cause of the blockage.

RESEARCH ACCOMPLISHED

The crust and upper mantle structure of the south Caspian Basin is enigmatic. Early Soviet studies show that the crust of the basin consists of two layers: a thick sedimentary section (15–25 km) with low P-wave velocity (3.5–4.0 km/s) overlying a 12–18 km thick basaltic lower crust. Mangino and Priestley (1997) used teleseismic receiver function analysis to determine the crustal structure at five sites around the south Caspian basin. These models show that the crust in Turkmenia along the trend of the Apscheron–Balkhan Sill — Kopet Dag Mountains is 50 km thick. In the southwestern part of the Caspian basin the crust is 33 km thick and consists of a 13 km thick sedimentary section lying on a high velocity ($V_p \sim 7.1 \text{ km s}^{-1}$) lower crustal section. In the southeastern part of the basin the crust is 30 km thick and consists of a 10 km thick sedimentary section overlying a 20 km thick low velocity ($V_p \sim 5.8 \text{ km s}^{-1}$) crystalline crust. Mangino and Priestley (1997) combined the receiver function models with velocity models from the previous Russian Deep Seismic Sounding results into a ~ 1800 km long ESE–WNW trending crustal cross-section across the Kura Depression, the south Caspian basin and the Kopet Dag Mountains (Fig. 1). The most significant features of this crustal model are the 20 km variation in thickness of Cenozoic sedimentary basin deposits, the absence of a “granitic” ($V_p \sim 5.8\text{--}6.5 \text{ km s}^{-1}$) crustal layer in the central part of the south Caspian basin, and a 20 km of crustal thinning beneath the central part of the basin. The Moho beneath the south Caspian basin has a broad arch-like structure whose western boundary is a relatively narrow zone across which the crust thins rapidly (~ 20 km thinning over a 100 km zone) and whose eastern boundary has a more gradual change in crustal thickness (~ 20 km thinning over a 400 km zone).

The study of Kadinsky–Cade et al. (1981) demonstrated that the seismic phase L_g is largely blocked for paths crossing the south Caspian Basin. This is clearly demonstrated by the seismograms in Fig. 2 of an earthquake which occurred near the eastern shoreline of the central Caspian Sea. The crust in the vicinity of the epicenter is about 50 km thick (Mangino and Priestley, 1997). The PDE depth for the event is 40 km but because focal depths in this area are not well constrained, it is impossible to tell from this whether the event is in the crust or mantle. Jackson and Priestley (unpublished work) have used waveform modeling to constrain the depth at 45 km placing it in the crust. The seismogram at LNK on the southwestern coastline shows an impulsive S_n phase but little energy in the L_g group velocity window. The crust between KRF near the epicenter and ABKT has nearly a uniform

thickness of 50 km. The seismogram of the event at ABKT show an S_n and L_g phase typical of that seen on stable continental paths. The seismogram at KAT near the southeastern coastline is anomalous. There is a clear S_n phase which is followed by a high amplitude long duration coda. These three seismograms demonstrate the challenge in using regional phases in this region for seismic discrimination.

New seismic data shows that the south Caspian Basin also severely disrupts intermediate frequency (0.017 – 0.10 Hz) fundamental mode surface wave trains (Fig. 3). This effect is observed for surface waves propagating along both east-to-west and west-to-east great circle paths across the south Caspian basin showing that this is not a site or instrumental effect. The top pair of seismograms in this figure show broadband vertical component seismograms, the middle pair show the waveforms low-passed at 22 mHz, and the bottom pair show the waveforms high-passed at 22 mHz. All waveforms are plotted on the same time scale and each of the pairs are plotted on the same amplitude scale. In each case the upper seismogram of each pair is the input to the basin and the lower is the output. There is a well-developed surface wave train for the waveform entering the basin but the intermediate frequency surface waves are largely missing from the surface wave train emerging from the basin only 450 km away. The low frequency surface waves are not significantly affected. This has been observed for both eastward and westward propagating surface waves, which are affected in the same manner.

We have modeled the response of the surface wave to this low-velocity sediment, deep basin structure and crustal thinning using a hybrid normal mode/finite difference approach. In these synthetic test we have used an idealized rendition of the south Caspian basin model shown in Fig. 1. The background model consist of a single layer 38 km thick crust with shear wave velocity 3.7 km s^{-1} overlying a 4.7 km s^{-1} mantle extending to 450.5 km depth. The basin consists of of four layers: a 2.625-km thick water layer, a 14.5-km thick sedimentary layer with shear wave velocity 2.0 km s^{-1} and shear wave Q of 25 in the upper 7 km of sediment and 50 in the lower 7.5 km, an 18-km thick crystalline crust with shear wave velocity 4.3 km s^{-1} and shear wave Q of 500, and a mantle upwarp 3-km thick. The near basin edge is at 381 km from the edge of the input grid and the far edge is at 762 km. The synthetic input is calculated using mode summation and the source is 2000 km outside the input grid. Synthetics seismograms are computed at a 50 km interval across the model at the solid-air or solid-water interface.

The true amplitude synthetic record section in Fig. 4 shows the vertical component seismograms spaced at 50 km intervals across the model. As the wave train passes into the basin [at 380 km distance] there is a significant increase in amplitude due to the impedance mismatch between the high velocity rocks outside the basin and the low velocity sediment within the basin. There are also small amplitude converted body waves in the basin [not seen on this scale] and reflected surface waves back into the crystalline crust on the left. As the wave train propagates through the basin the waveform is spread out in time due to the increased dispersion, and reduced in amplitude due to attenuation. As the wave train passes out of the basin [760 km distance] there is a reduction in amplitude of the waveform and a second surface wave reflected back into the basin. Fig. 5 compares the synthetic seismograms just before entering and just after exiting from the basin. The upper pair

compare the broadband waveforms and the lower pair compare the long period waveforms (< 20 mHz). Each of the pairs have the same amplitude scale but there is a different amplitude scale between the pairs. As in the case of the observed surface wave trains, the synthetic surface wave show a pronounced attenuation of the intermediate period waves and only a small affect on the long period waves. This demonstrates that much of the observed surface wave train degradation can be modeled with the 2-D basin structure.

To gain some insight into the features of the basin which result in the anomalous surface wave propagation we have varied various parameters of the basin model and computed synthetic seismogram record sections for comparison with the seismograms in Fig. 4. We have varied the amount of mantle upwarp, removed the water layer, varied the shape of the boundaries, and varied the thickness and shear wave Q of the sediments. Of these parameters, the intermediate period surface waves are most severely affected by the sediment thickness and shear wave attenuation.

CONCLUSIONS AND RECOMMENDATIONS

The south Caspian basin is known to block L_g waves. We have observed a pronounced degradation of intermediate surface waves propagating across the south Caspian basin. We have begun to model these effects with hybrid normal mode/finite difference synthetics and sediment thickness and shear wave attenuation appear to be the dominate factors affecting the surface wave propagation. We intend to complete the modeling of the intermediate period surface waves, and then extend these calculations to higher frequencies and to the L_g phase.

REFERENCES

- Brune, J.N., J.E. Nafe, and J.E. Oliver, A simplified method for the analysis and synthesis of dispersed wave trains, *J. Geophys. Res.*, 65, 287, 1960.
- Gomberg, J.S., K. Priestley, T.G. Masters, and J.N. Brune, The structure of the crust and upper mantle of northern Mexico. *Geophys. J.* 94, 1-20, 1988.
- Kadinsky-Cade, K., M. Barazangi, J. Oliver, and B. Isacks, Lateral variations of high frequency seismic wave propagation at regional distances across the Turkish and Iranian Plateaus, *J. geophys. Res.*, 86, 9377-9396, 1981
- Mangino, S.G., and K. Priestley, The crust and upper mantle structure of the southern Caspian region, submitted to *Geophys. J. Int.*, 1997.

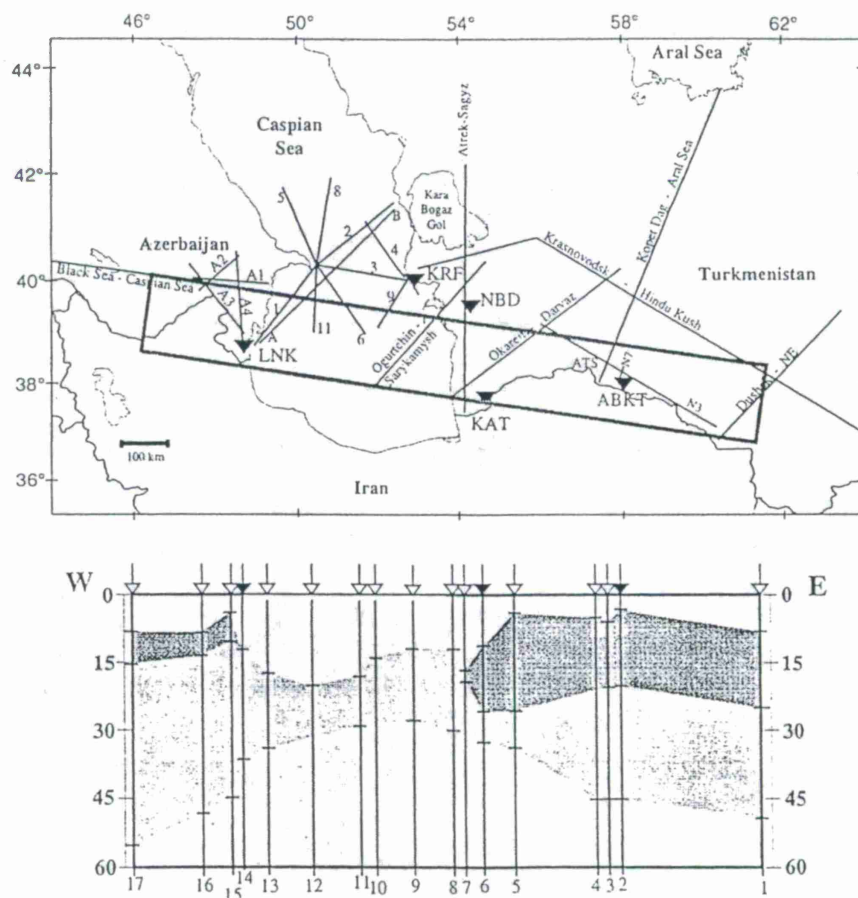


Figure 1: Cross-section of the crust and uppermost mantle (lower panel) beneath the region denoted by the box in the upper panel. Three principal crustal layers are characterized by their P-wave velocities: sediment and consolidated sediment ($V_p < 4.8 \text{ km s}^{-1}$), "granitic" (V_p between $4.8\text{--}6.4 \text{ km s}^{-1}$), and upper mantle ($V_p \geq 8.0 \text{ km s}^{-1}$).

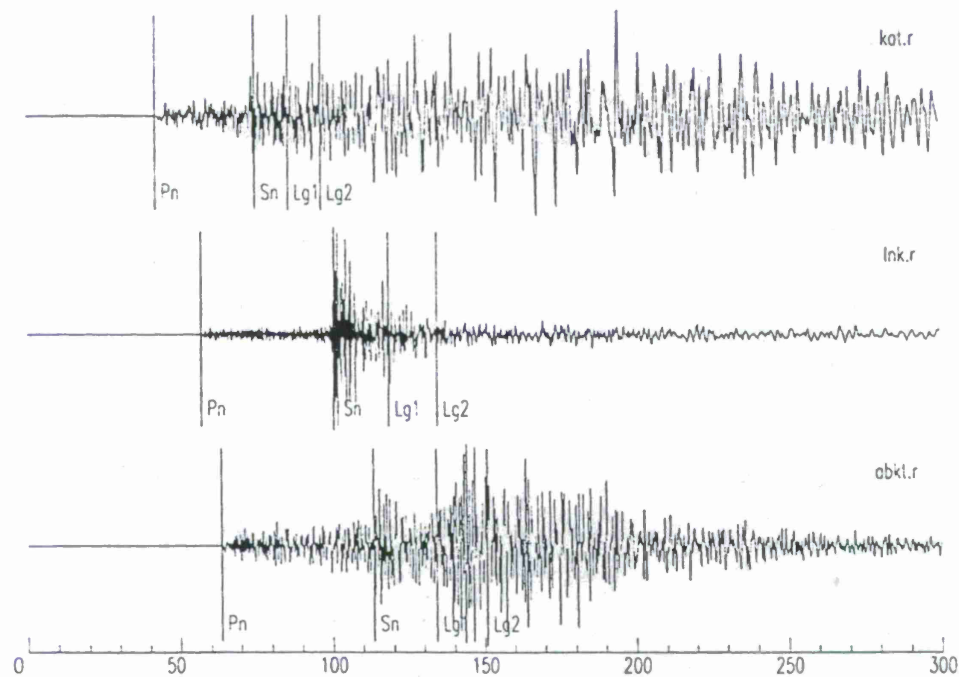


Figure 2: Radial component broadband seismograms for an earthquake occurring near KRF (Fig. 1) and recorded at KAT, LNK, and ABKT. The lines denoted by P_n and S_n indicate the IASPIE91 predicted arrival times for P_n and S_n , and the lines denoted by $Lg1$ and $Lg2$ correspond to group arrival times of 3.6 km s^{-1} and 3.2 km s^{-1} .

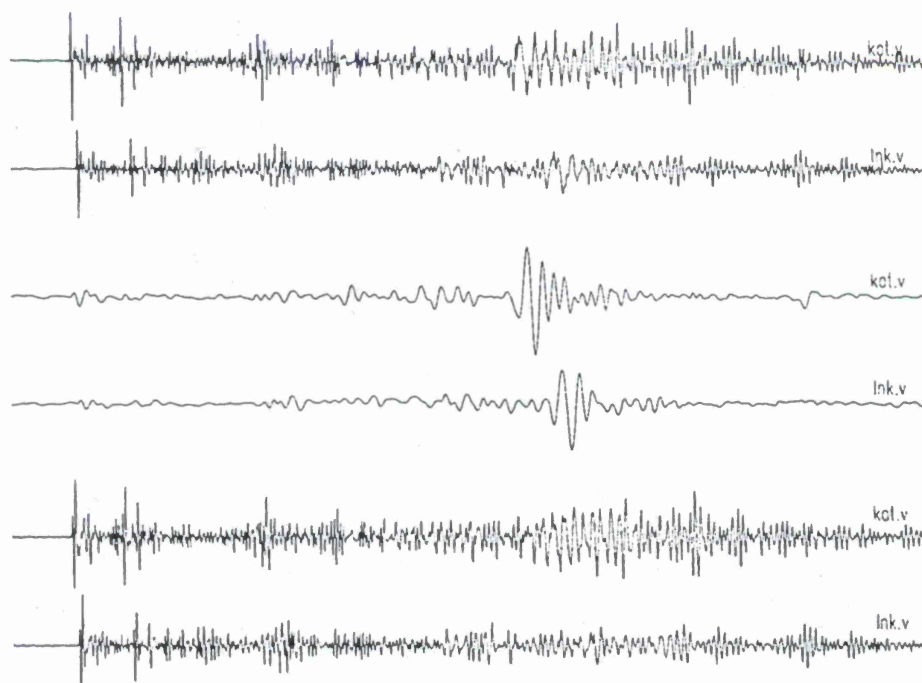


Figure 3: Seismograms from KAT and LNK (Fig. 1) of a teleseism propagating along the great circle path between the stations. The top pair of seismograms are the broadband recordings, the second pair have been lowpass-filtered at 0.022 Hz, and the bottom pair have been highpass-filtered at 0.022 Hz.

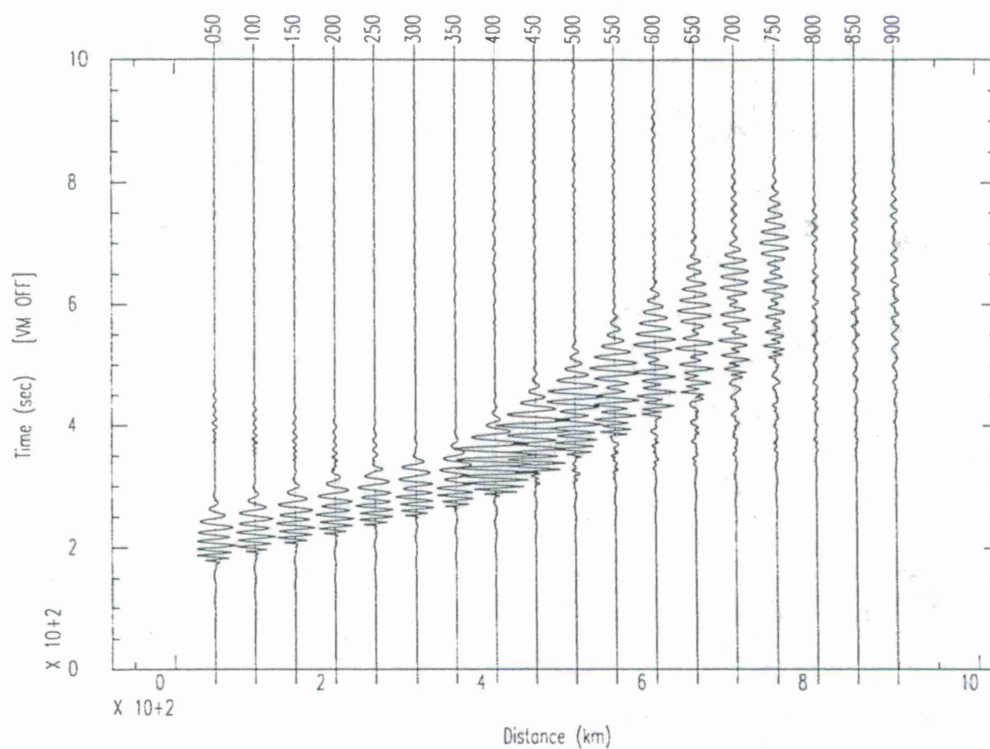


Figure 4: Record section of the finite difference synthetic seismograms across an idealized model of the south Caspian basin. The left edge of the basin is at 381 km and the right edge of the basin is at 762 km.

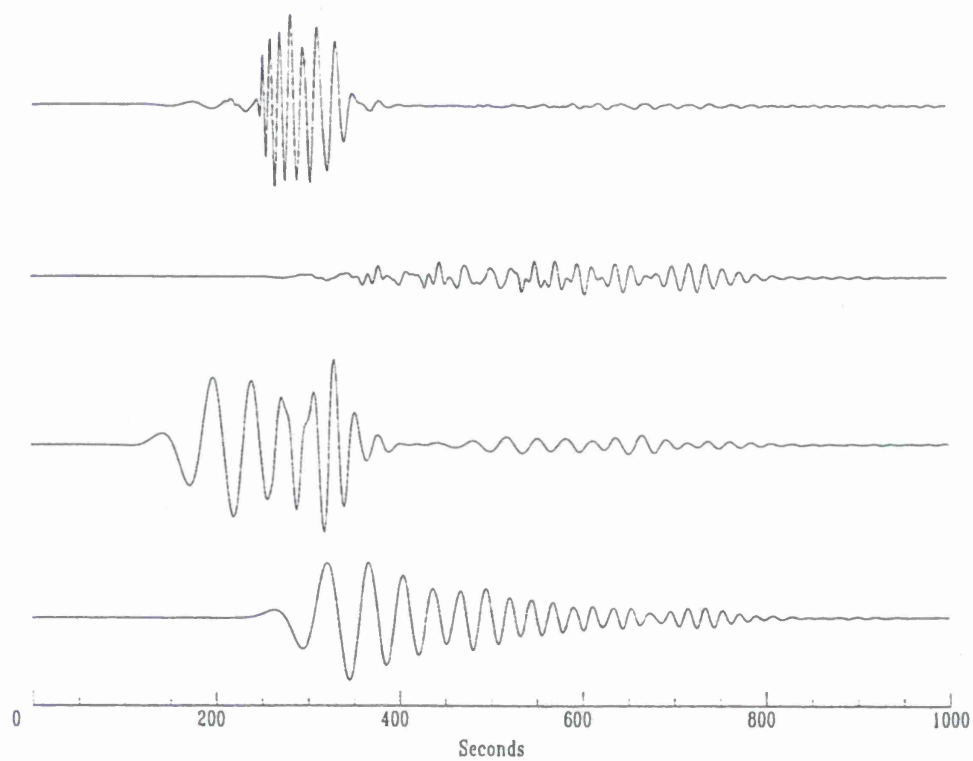


Figure 5: Comparison of broadband (upper pair) and lowpass filtered synthetic seismograms at distances of 300 and 800 km across the model.

SEISMIC ATTENUATION IN THE MINES OF KOLAR GOLD FIELDS

C.Srinivasan
Scientist and Head, Seismology Division
National Institute of Rock Mechanics
Champion Reefs - 563 117
Kolar Gold Fields, India.

ABSTRACT

The loss or absorption of energy in a seismic wave propagating through a rock mass is attributed to many mechanism including geometrical spreading, scattering, dispersion and energy loss due to heat or internal friction. Except for geometrical spreading, each of these mechanism are considered to be attenuating properties of rock mass. Investigation of the quantity of seismic wave attenuation is important for understanding wave-propagation characteristics, computation of energy & local magnitude, source parameters and other related study. The seismic data from the mines of Kolar Gold Fields were used to estimate attenuation coefficient in mining environment and found to be less than 10dB/Km. The attenuation coefficient with respect to depth is found more compared to that along the surface.

Key words : Attenuation coefficient, Seismic wave, rockmass and mining environment.

INTRODUCTION

One of the requirements of modern mine seismic system is the ability to provide accurate and reliable estimates of source parameters and other seismological parameters. Seismic moment estimates are important for quantitative study of mine seismicity and relate to the problem of mining sequences and resulting seismic deformations (Spottiwoode). Stress drops drive the near-field ground velocities and therefore directly relevant to the rockburst problem. Very little work has been done in investigating attenuation in mining environments. Cichowicz and Green (1989) and Cichowicz et.al (1990) have reported the most prominent work in this area. Assuming a single scattering model, they used Q-coda methods for attenuation studies of mining induced seismicity in the South African mines believing this method to give reliable in-situ estimates. The measured values for Q_p ranged from 30 to 100 in a fractured region of an excavation area with an upper limit of 300 outside this area. Although the studies mentioned here likely represent a fraction of the work being done on in-situ attenuation, they help support the fact that the majority of published studies do not address the problem of seismic attenuation in mines. In this study, the seismic data obtained from the seismic network has been analysed to compute the seismic attenuation coefficient of the mining environment of Kolar Gold Fields (KGF).

GEOLOGY

The gold bearing hornblende schist of Kolar Gold Fields belongs to the lower Dharwar age. The gold bearing lodes dip towards west at an angle of $45-50^\circ$ near the surface and gradually become nearly vertical at great depth. Of the many quartz lodes explored on the fields, only two lodes - the Champion lode and the oriental lode - are of economic importance. While the Champion lode has been mined extensively in all the three mining districts of KGF, the oriental lode is being mined on a large scale in the Nundydroog mines only due to economic reasons.

The Champion lode is not a continuous fissure filled with quartz, but is a system of lode made up of individual fissures which taper out both along the strike and the dip, the average width being 1.0-1.2m. In places where the quartz attains a width exceeding 6m, it occurs in a large zig-zag usually called "Folds" which pitch northward (on the champion lode) in the plane of the lode at an angle similar to the angle of dip (Taylor and sons, 1955). While mining in these folded formations, severe rockbursts were encountered in the past leading to the frequent damages to shafts (Krishnamurthy and Gupta, 1983).

The productive working in these lodes have been interrupted by a series of faults, dykes and pegmatite veins, all involving plane of weaknesses. Of them, two major fault planes i.e. the Mysore North Fault (MNF) and the Tennants Fault (TF), attach much significance as they either intercept the lode or run parallel to the main lode in the Northern Folds area of the Champion Reef mine. The TF runs parallel to the main lode in the shallower levels and lies only 30m away in the hanging wall of the lode in the Champion Reef mine. Major rockbursts including area rockbursts have been reported while mining close to these fault planes. In addition, these faults play a dominant role in attenuating the seismic signal also.

ATTENUATION OF SEISMIC WAVES :

Attenuation is defined as the process of decrease of amplitude suffered due to the propagation of seismic wave as it passes through rock medium. The energy of a wave in a given medium is proportional to the square of its amplitude. With spherical propagation the energy is distributed over an area which increases as the square of the radius of the sphere. Hence, the energy per unit area varies inversely as the square of the distance from the source. In other words, the amplitude will be proportional to the square root of the energy per unit area of surface and will be inversely proportional to the distance from the source. As the wave moves away from the source, apart from the decrease in amplitude due to the spherical spreading of the wave, there is also loss due to absorption, i.e., frictional dissipation of elastic energy into heat which increases exponentially with distance from the source (Srinivasan, 1992).

Geologic materials preferentially attenuate the high frequency components of microseismic emissions. This attenuation is caused by internal friction between grain boundaries and along structural discontinuities, (Moroz, 1987). Energy is absorbed from the propagating elastic wave as it travels through the rock mass. The higher the frequency, the greater is the loss in signal amplitude.

The Characteristic pattern of different factors that affect the attenuation of seismic waves in rock masses are listed below :

1. Attenuation of P and S waves is highest in low density, highly porous media.,
2. Weathered and fractured rocks produce higher attenuation.,
3. Fractures and anisotropies at right angles to wave propagation affect shear wave attenuation more than compressional wave attenuation.,
4. Attenuation decreases with increasing differential pressure for both compressional and shear waves.,
5. The decrease in attenuation in saturated and dry rocks as a function of differential pressure is caused primarily by the closing of thin pores cracks as a function of increasing differential pressure.,
6. Attenuation in water saturated rocks is greater than in dry rocks and is usually less for shear waves at both low and high differential pressure.,
7. The attenuation per unit of distance (absorption coefficient) is usually higher for shear waves than compressional waves.,
8. Compressional and shear wave attenuation is lower for waves propagating parallel than perpendicular to anisotropy. Shear waves are usually more sensitive to anisotropy in a given plane than compressional waves.,

The amplitude 'A' at a distance 'r' from the source is given by ,

$$A = A_0 \frac{e^{-qr}}{r} \quad \text{-----} \quad 1$$

where A_0 = Amplitude at source, A = Amplitude at a distance r from the source of an event and q = attenuation coefficient which is directly proportional to the frequency. In order to determine the attenuation coefficient of an area the following method has been adopted.

For a blasting carried out at known distance with known explosive, the amplitude at two different points are measured. Let A_1 and A_2 be the amplitude recorded at a distance ' r_1 ' and ' r_2 ' respectively. Then the relations can be expressed in the following equation.

$$A_1 = A_0 \frac{e^{-qr_1}}{r_1} \quad \text{-----} \quad 2$$

$$A_2 = A_0 \frac{e^{-qr_2}}{r_2} \quad \text{-----} \quad 3$$

Dividing equation 2 by 3, we get ,

$$\frac{A_1}{A_2} = \frac{A_0 \frac{e^{-qr_1}}{r_1}}{A_0 \frac{e^{-qr_2}}{r_2}} \quad \text{-----} \quad 4$$

On rearranging we get the attenuation coefficient 'q',

$$q = \frac{\ln (A_1/A_2 * r_1/r_2)}{(r_2 - r_1)} \quad \text{-----} \quad 5$$

In order to compute the value of 'q' using the rockburst data using the above equation, the sources of the rockbursts data are selected in a location where the two geophones are in the same direction with respect to source. As it is difficult to get two geophones exactly in the same direction, two geophones which are nearly in the same direction have been selected from the network of 14 geophones comprising 8 on the surface and 6 in the underground covering an area 8km. x 3km. x 3km. as shown in the figures 1 and 2. The value of 'q' has been computed for different regions in the Kolar Gold Fields where

the mining activities are being carried out at different different geologic background. The results are tabulated in Table 5.1.,

Table-1 Attenuation Coefficient of Seismic Signal in Kolar Gold Fields

Name of Area (Shaft)	Geophones	A ₁ (mm)	A ₂ (mm)	r ₁ (m)	r ₂ (m)	q db/Km
<u>Champion Reef Mine</u>						
Osborne's Shaft	G7, G6	4.14	3.55	1210	2691	3
	G7, G9	3.44	2.93	1058	2046	4
Aux.Main Winze Shaft	G3, G4	3.78	2.84	3163	3292	6
<u>Nundydroog Mine</u>						
Golconda Shaft	G12,G11	4.16	3.64	1338	2182	3
	G11,G4	3.64	2.39	2182	3291	1
	G12,G4	5.76	4.97	1119	2968	3
Henry's Shaft	G8, G9	4.34	3.60	473	2585	6
	G8,G10	4.82	3.51	743	1189	3
	G8,G11	6.31	4.59	856	1666	4
New Trial Shaft	G11,G12	4.24	3.53	1283	1642	1
	G11,G14	7.22	2.55	1075	1618	11
<u>Mysore Mine</u>						
	G1, G9	4.99	4.21	706	1392	6
	G7, G6	3.43	2.85	1172	1390	1

The data of a set of deep hole blasts carried out in the Nundydroog Mine at shallow depth as explained (Srinivasan,1995) have been used to compute the value 'q' as described above is presented in Table 2.

Figure 1 and 2 show the locations of geophones in X-Y plan and X-Z section of seismic network operating at Kolar Gold Fields since 1980. The coordinates are in feet since all references to mining locations are conventionally referred in feet in the Kolar Gold Fields. The geophones are mainly spread in North - South direction covering the mining working area, whereas in the East-West direction not much geophones are present. The geophones in the

depth cover upto the existing mine workings only. The pair of geophones used for attenuation calculation can be seen in both the figures.

Table-2 Deep Hole Blast in Nundydroog Mine

Date	Geophones	A ₁ (mm)	A ₂ (mm)	r ₁ (m)	r ₂ (m)	q db/Km
15/05/1980	G13, G14	16.5	14.0	688	1048	6
	G13, G12	16.5	10.0	688	2181	3
	G12, G11	10.0	9.0	2181	3243	2
	G11, G4	9.0	5.5	3243	4446	1
	G4, G3	5.5	3.5	4446	5047	5
	G3, G2	3.5	2.75	5047	6035	1
16/05/1980	G13, G12	25.5	23.75	1202	2188	4
	G12, G4	23.75	18.50	2188	4457	1
	G3, G2	20.0	10.0	5059	5875	6

The following observations were made from the attenuation study :

1. The value of the coefficient of attenuation with respect to depth (Z-direction) is more compared to that along surface (X-direction). Attenuation along Y-direction was not carried out for want of two geophones in the same direction.,
2. The value of the coefficient of attenuation of seismic signal using both deep hole blast and rockburst data is found to be less than 10 db/Km.

DISCUSSION

The attenuation characteristics of seismic signal of rockbursts and Deep hole blast in Kolar Gold Fields are obtained from a limited set of data. The gold bearing lodes dip towards west at an angle of 45-50° near the surface and gradually become nearly vertical at great depth. The Champion lode has been mined extensively in all the three mining districts of KGF, the oriental lode is being mined on a large scale in the Nundydroog mines only due to economic reasons. While mining in these folded formations, severe rockbursts were

encountered in the past leading to the frequent damages to shafts. Keeping all the complex situations in the mining environment, further work is required to be carried out to arrive attenuation characteristics in all the directions. This will help in arriving at relations for accurate estimation of the seismic energy released during a rockburst. A detailed evaluation of real time attenuation of body wave along with that of compression velocity holds promise in monitoring precursors and possible prediction of rockbursts. Further this will aid in computing accurate source parameters, know the effect of variations in attenuation coefficient on source parameters with a view to discriminate different sources of events.

ACKNOWLEDGEMENTS

The author is thankful to the Director National Institute of Rock Mechanics, Kolar Gold Fields for permitting to publish this paper. Dr. Anton M. Dainty, Deputy Director, Earth Science Division of Phillip's laboratory is thanked for inviting me to present a poster session during last year Symposium and for the contacts during this year Symposium. The whole hearted support from the colleagues of Seismology section is also thankfully acknowledged.

REFERENCES

1. Spottiswoode, S.M., and McGarr, A. (1975)- Source Parameters of tremors in a deep-level gold mine. Bull. Seism. Soc. Am., 64, Pp. 1295-1317.
2. Cichowicz, A., and Green, W.E., (1989) Changes in the early part of the seismic coda due to localized scatterers: The estimation of Q in a stope environment. Pure and Appl. Geophys. 129: 497-511.
3. Cichowicz, A., Green, W.E., Van Zyl Brink, A., Grobler, P. and Mountfort, P.I. (1990). The space and time variations of micro-event parameters occurring in front of an active stope, in Rockbursts and seismicity in mines, Fairhurst (Ed). 171-175.
4. Srinivasan C. (1995) Seismic monitoring of Rockbursts and underground blastings for assessing the stability of deep mine workings at Kolar Gold Fields. Pro. 17th Seismic Research Symposium on Monitoring a CTBT, 12-15 Sept. 1995 Pp 581-591. PL-TR-95-2108, ADA 310037.
5. Srinivasan C. (1996) Blasting induced seismic events in Kolar Gold Fields, Pro. 18th Seismic Research Symposium on Monitoring a CTBT, held during Sept. 1996 Pp 947-955.
6. Srinivasan C. (1992)- Seismic and Microseismic precursory signals for monitoring and prediction of rockburst in Kolar Gold Fields, Ph.D thesis, Karanataka Regional Engineering college, Mangalore University, (unpublished)
7. Srinivasan C., and Nair G.J.. (1990) Seismic and Microseismic Activity in Glen Ore Shoot region Proc. National Symposium on Recent advances in Seismology and their applications July 16-19, 1990 held at Gauribidanur.

9. Moroz, B.(1987) - Examination of the frequency of acoustic emissions as a method of predicting violent failure and stress conditions in rock - M.Sc., Thesis, Department of Mining Engineering, Queens University, Kingston, Ontario.
10. Subbaramu K.R., Rao B.S.S, Krishnamurthy R. and Srinivasan C.(1989)- Seismic Investigation of Rockbursts in the Kolar Gold Fields, Proc.of the 4th conference on acoustic emission/microseismic activity in geological structures and materials, Pennsylvania State University, Trans. Tech. Publication, Germany, pp. 265-274.
11. Taylor and sons, J.T.M. (1955), Report of the special sub-committee on the occurrence of rockbursts in the mines of Kolar Gold Fields, Mysore State, South India, Pp. 1-30.
12. Krishnamurthy, R. and Gupta, P.D.(1983) - Rock Mechanics studies on the problem of ground control and Rockbursts in the Kolar Gold Fields, Proceeding on Prediction and control, Institute of Mining and Metallurgy, London,Pp 67-80.

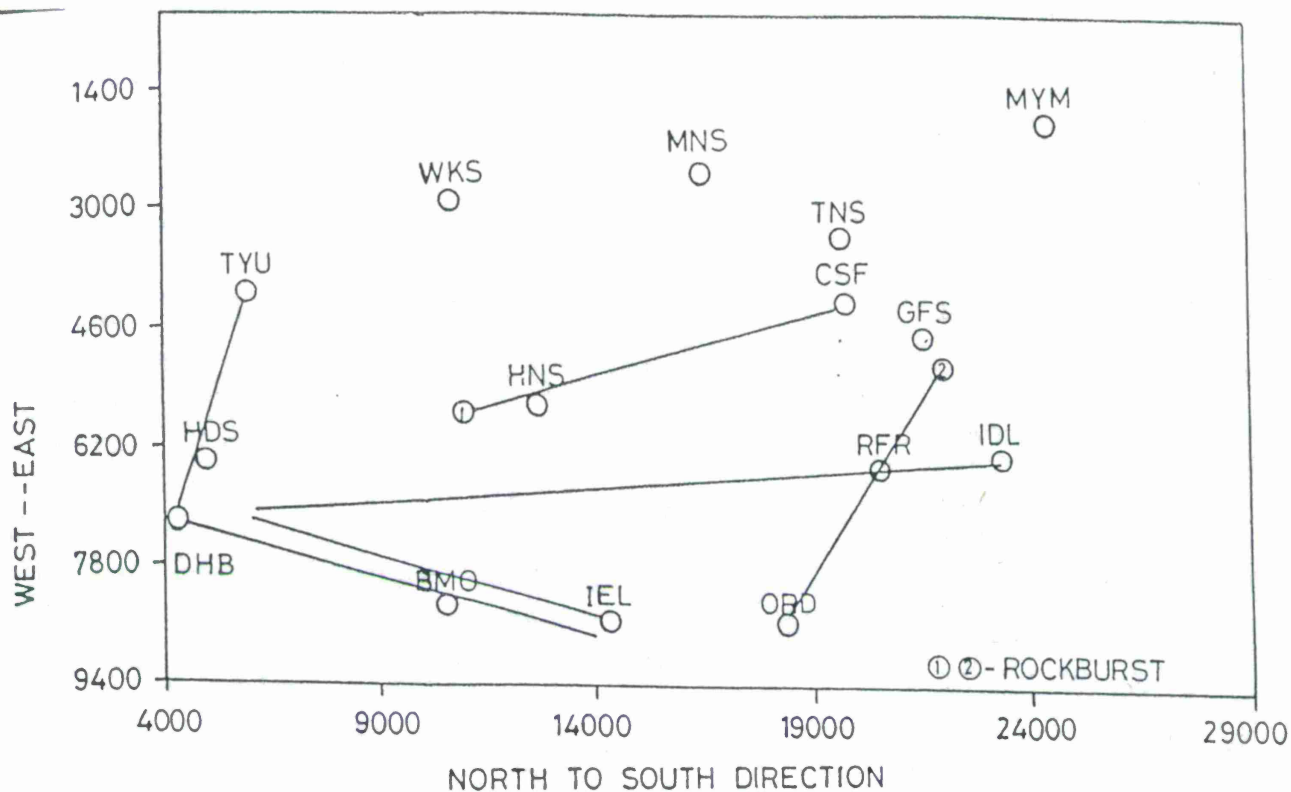


FIGURE-1 X-Y PLAN OF K.G.F SEISMIC NETWORK

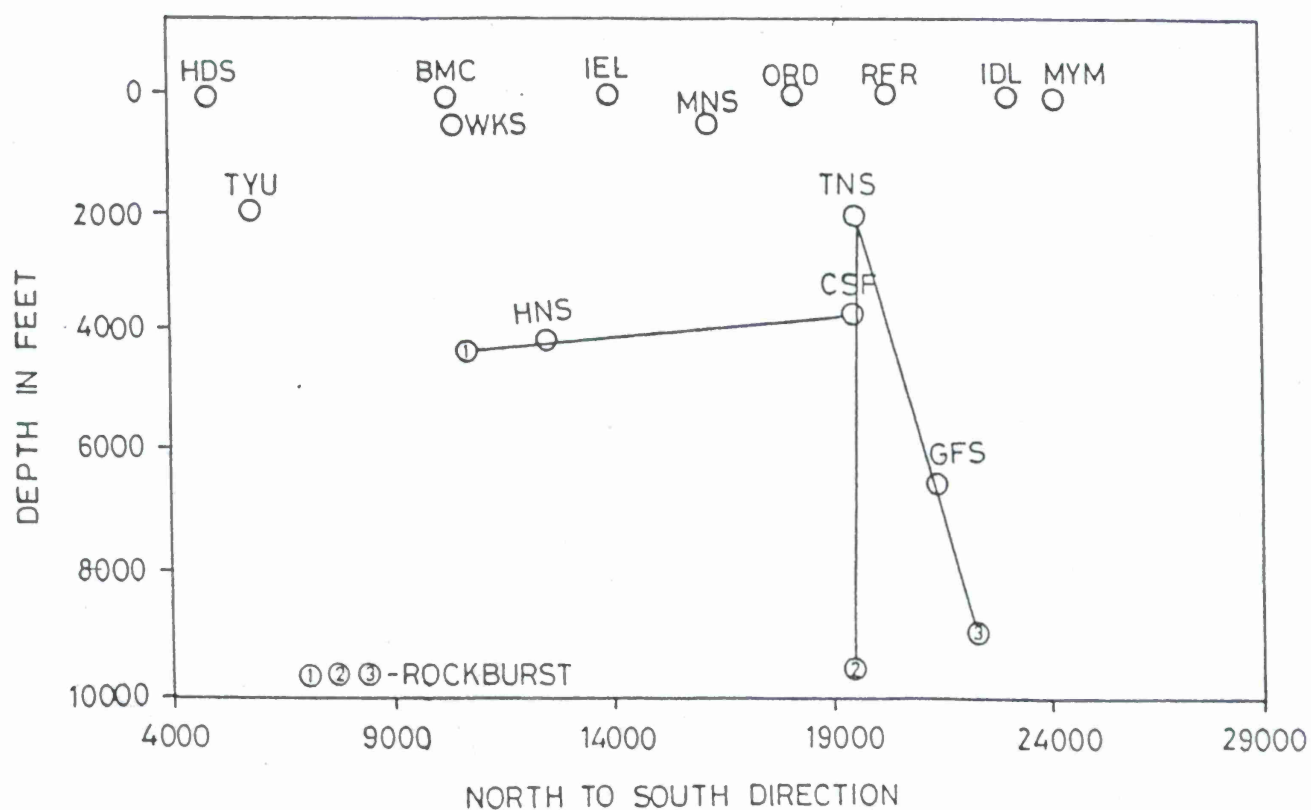


FIGURE-2 X-Z SECTION OF K.G.F SEISMIC NETWORK

VERIFICATION AND APPLICATIONS OF GSP (GENERALIZED SCREEN PROPAGATORS) METHOD FOR REGIONAL WAVE PROPAGATION

Ru-Shan Wu, Shengwen Jin, Xiao-Bi Xie and Thorne Lay
University of California, Santa Cruz

Office of U.S. Department of Energy
Office of Nonproliferation and National Security
Office of Research and Development and
Air Force Office of Scientific Research
Contract No. F49620-95-1-0028 and No. F19628-95-K-0016

ABSTRACT

The object of this project is aimed at development and application of a new 3D wave propagation and modeling method in complex heterogeneous media using one-way wave approximation to study many outstanding problems of regional wave propagation in the context of nuclear test monitoring. Last year we reported the introduction and development of the half-space GSP (Generalized Screen Propagators) method for the 2D SH problem. The theoretical foundation has been laid and numerical tests were conducted. The great advantages of the half-space GSP method are the fast speed of computation, often by several orders of magnitudes faster than finite difference and finite element methods, and the huge saving in internal memory. This year's effort is mainly put on the verification of the method by comparing the results with those from wavenumber integration and finite difference modeling. Comparisons show excellent agreement between these methods for the test models. For a heterogeneous crustal model with propagation distance of 250 km, the GSP method is about 300 times faster than the finite-difference method with a similar accuracy. For high frequency large distance 3D problems, the time saving factor could be much greater. This will make waveform simulation of regional phases realistic for the purpose of CTBT monitoring. We have applied the GSP method to regional wave propagations in different types of complex crustal waveguides including those with small-scale random heterogeneities and random rough interfaces of sedimental layers. We see that random heterogeneities play an important role in the Lg amplitude attenuation and the formation of Lg codas.

Keywords: seismic waves, heterogeneous crustal waveguide, Lg waves, one-way waves, random heterogeneities, rough interfaces, screen propagators.

OBJECTIVES

The new task for monitoring a Comprehensive Test Ban Treaty and the current Nuclear Non-Proliferation Treaty presents a great challenge to the existing modeling methods using regional phases. The study of path effects of complex structure and heterogeneities on the excitation and propagation of regional phases in different areas remains critical for both the discrimination and yield estimation for low-yield nuclear test monitoring. The object of this project is aimed at development and application of a new 3D wave propagation and modeling method in complex heterogeneous crustal waveguides using the one-way wave approximation to study many outstanding problems of regional wave propagation in the context of nuclear test monitoring. The development of the theoretical model will be combined with analysis of the Eurasian regional phase observations to extract quantitative information from regional phases.

RESEARCH ACCOMPLISHED

This is the last year of the project. Our effort was mainly put on the verification of the method by comparing the results with those from wavenumber integration and finite difference modeling. In the process of doing detailed, high-accuracy comparison by wave form matching, many technical difficulties have been overcome and improvements of the method have also been made. Comparisons show excellent agreement between these methods for the test models. For a flat crustal model, for which the wavenumber integration (WI) method (reflectivity method) is considered accurate, our result shows excellent agreement with the WI method. For a heterogeneous crustal model with propagation distance of 250 km, the GSP method is about 300 times faster than the finite-difference method with a similar accuracy. These comparisons demonstrated the accuracy and efficiency of the GSP method.

We have applied the GSP method to regional wave propagations in different types of complex crustal waveguides including those with small-scale random heterogeneities, and random rough interfaces of sedimental layers. The influences of these heterogeneities and rough interfaces to Lg amplitude attenuation and Lg coda formation have been investigated.

It is demonstrated that the half-space generalized-screen propagator is fast and stable, and can be used to calculate synthetic seismograms efficiently for regional distances for complex crustal structures.

In the following, we report the progress in detail.

Introduction

An ideal numerical method for investigating the regional wave propagation should have the capabilities to simulate models that include horizontal variations with scales from geological boundaries to small scatterers with intrinsic attenuation; The frequency range should cover the Lg window between 0.5-8.0 Hz. To discriminate the chemical explosions with other sources, even higher frequencies may be of interest. For the purpose of monitoring the CTBT at regional distances, simulation algorithms are required to be able to generate synthetic waveforms for high frequencies up to 25 Hz at distance greater than 1000 km.

Recently, the generalized screen method has been introduced into seismic wave simulations and has gained growing popularity among both exploration and theoretical seismologists. The generalized screen method is based on one-way wave equation that neglects backscattered waves, but correctly handles all the forward multiple-scattering effects, e.g., focusing/defocusing, diffraction, interference, and conversion between different wave types. Under the AFOSR support we have made two major breakthroughs on the screen method. One is the development of an Elastic Complex Screen (ECS) method for modeling one-way elastic wave propagation in arbitrarily complicated structures (Wu, 1994, 1996). The method is two to three orders of magnitude faster than elastic finite-difference method for medium size 3D problem. The other is the introduction of half-space Generalized Screen Propagators (GSP) to model regional wave propagation in complicated crustal waveguides (Wu et al., 1996). The screen method has been successfully used in forward modeling (Wu, 1994; Xie and Wu 1995, 1996; Wu and Huang, 1995) and as backpropagators for seismic wave migration in both acoustic and elastic media (e.g. Wu and Xie 1994; Huang and Wu 1996). In the crustal waveguide environment, major wave energy is carried by forward propagating waves, including forward scattered waves, and therefore the neglect of backscattered waves in the modeling will not change the main features of regional waves in most cases. In the GSP algorithm, The heterogeneous half-space is replaced by a series of half-screens embedded in the background half-space. The wave propagates between screens in the wavenumber domain and interacts with the generalized screens (representing heterogeneities) in the space domain. The method uses a dual-domain technique, shuttling between the wavenumber and space domains through FFT. For the detailed formulation and treatment of the Moho discontinuity the reader is referred to last year's report (Wu et al., 1996).

Numerical Verification and Tests

To test the validity of the half-space GSP method (or simply call it the screen method), we have conducted extensive numerical tests and check the results with various well known numerical methods, such as the wavenumber integration and finite difference methods.

First, in Figure 1 we show the accuracy of the method by comparing the synthetic seismograms generated by the screen method (thick lines) with those calculated by a reflectivity method (thin lines) for a flat crustal model. The crust has a thickness of 32 km and a shear wave velocity of 3.5 km/s. The mantle beneath the crust has a shear velocity of 4.5 km/s. The source function is a Ricker wavelet with a dominant frequency of 1.0 Hz. Our results agree very well with the reflectivity method which is considered very accurate for flat layered media. The only exceptions are those of near vertical reflections at very small epicenter distances where the screen method has low accuracy for extremely large scattering angles with respect to the propagation direction. However, since regional seismograms are usually recorded at large distances, this limitation does not pose any real problem for its application. Next, we show the accuracy of the method by comparing synthetic seismograms generated by this method with those generated by a finite difference algorithm (Xie and Lay, 1994). For the finite-difference method, a fourth-order elastic SH-wave code is used to calculate the synthetic seismograms. The spatial sampling interval is 0.125 km and the time interval is 0.015 second. For the screen method, the spatial sampling interval is 0.25 km in vertical direction and the screen interval is 1.0 km. A Gaussian derivative is used as the source time function for

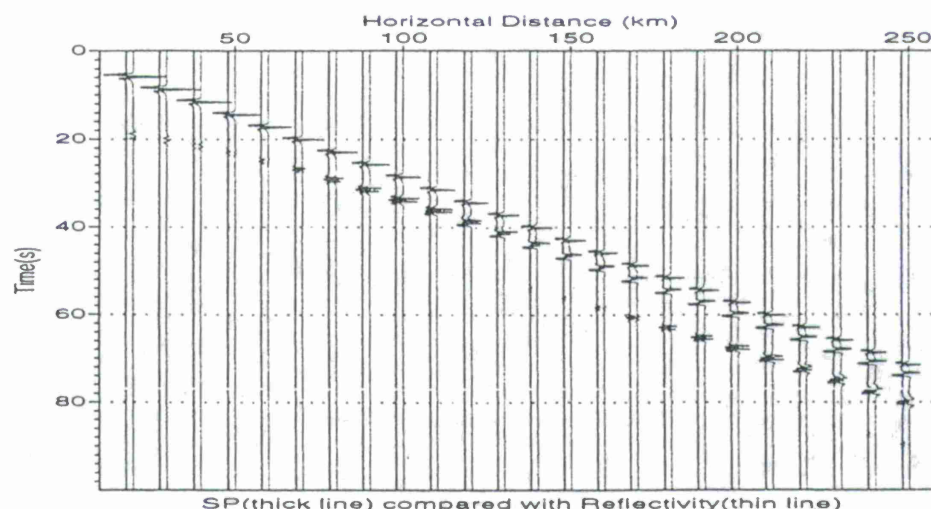


Figure 1: Comparison of synthetic seismograms along the surface calculated by the screen method (thick lines) and reflectivity method (thin lines) for a flat crustal model (32 km thick). The source function is a Ricker wavelet with dominant frequency of 1.0 Hz.

both methods. Because of the computational intensity of the finite difference method, we did the comparison at short propagation distances. Shown on the top of Figure 2 is the crust model with a narrow passage ("neck" type) used to calculate synthetic seismograms; on the bottom, synthetic seismograms along a vertical profile at an epicenter distance of 250 km. The thin lines are from the finite difference method and the thick lines are from the screen method. The source is located at a depth of 2 km. Excellent agreement can be seen. For this example, the GSP method took 20 minutes CPU on SPARC-4. To obtain a similar accuracy, the FD calculation took 3000 minutes CPU on SPARC-20. The speed factor is about 300.

Figure 3 shows the snap shots from the Screen method at 50 sec. for flat, narrowing and broadening crustal waveguides (from top to bottom, respectively). The source is located at the top-left corner at depth 2 km. The development of mantle wave and head wave, and the formation of crust guided wave as multiple reflections between the free surface and Moho discontinuity can be clearly seen. For the inhomogeneous models, wave diffraction, leakage to the mantle, wavefront distortion and increase of wavefield complexity can be also seen clearly. From the comparison it is seen that the passage of narrow crustal waveguide ("neck" type) has greater effect on Lg leakage than the broad passage ("belly" type). In the latter case although the wavefronts are complicated due to scattering at the edges, most of the energy is still trapped in the crust, different from the case of narrow passage in which a large percentage of energy leaks into the mantle. This example demonstrates the potential of the method as a tool for investigating the path effects of different crustal structures.

The following example shows the potential capability of this method for long distance high-frequency synthetic seismograms in a laterally varying structure. Figure 4 shows the laterally varying crust model used in the calculation. Figure 5 shows the high-frequency synthetic seismo-

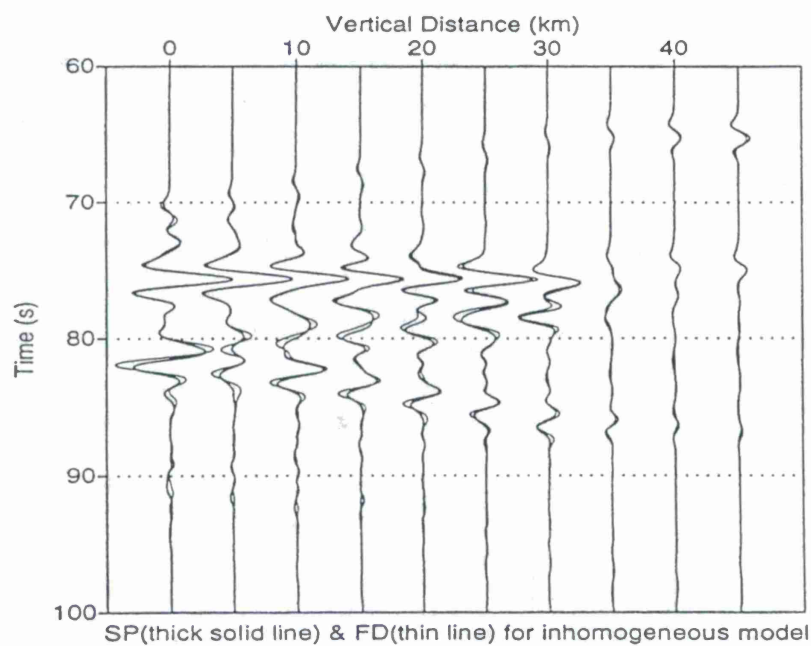
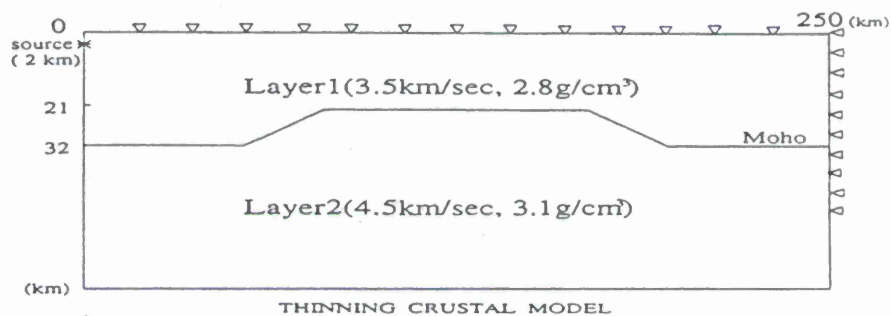
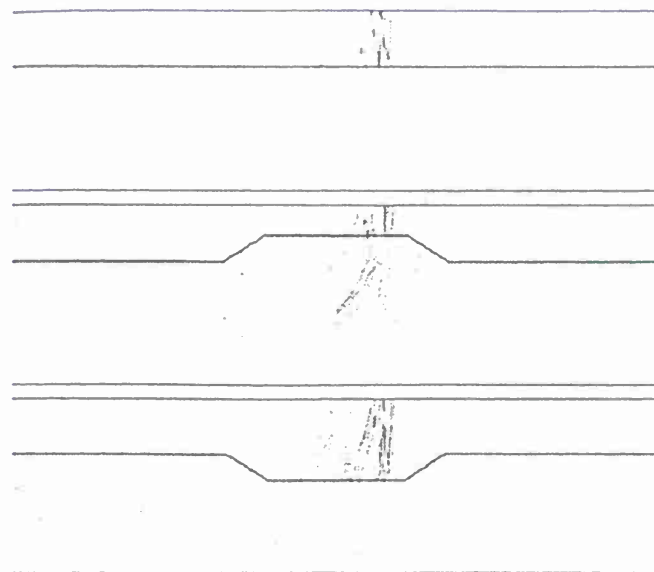


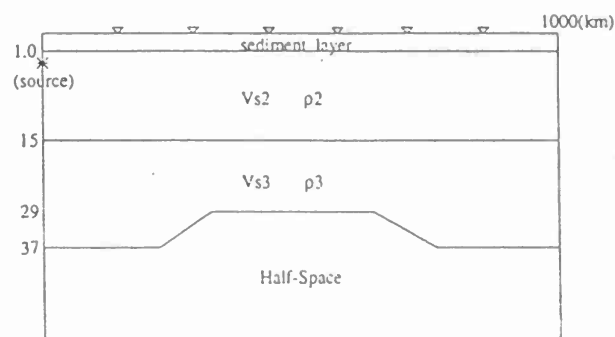
Figure 2: Comparison of synthetic seismograms along a vertical profile at the distance of 250 km calculated by the screen method (thick lines) and a finite-difference method (thin lines) for a laterally varying crustal model shown on the top panel.



Comparison of Wave Propagation in Various Crustal Wave Guides

Figure 3: Snap shots at 50 sec. The development of mantle waves and head waves, and the influence of crust thinning and thickening can be seen clearly.

Parameters of Crustal Model			
Layer	Vs(km/sec)	Density(g/cm)	Thickness(km)
1	3.00	2.60	1.00
2	3.46	2.80	14.00
3	3.76	3.00	22.00
4	4.65	3.30	Half-Space



Crustal Model

Figure 4: An inhomogeneous crustal model used in the calculation of h-f synthetic seismograms. Shown in the upper panel are model parameters and the lower panel gives the geometry of the model. The receivers are on the surface and shown by triangles.

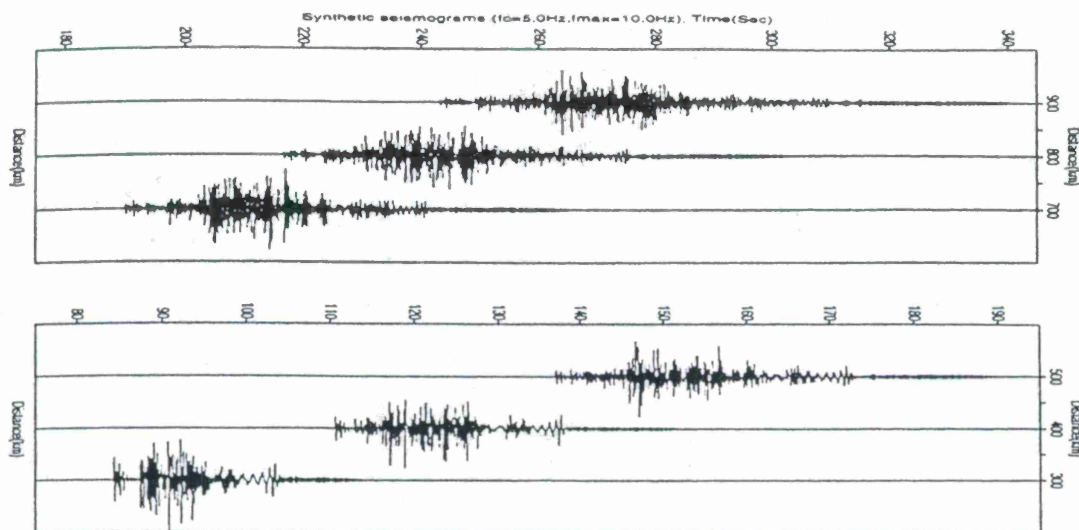


Figure 5: High-frequency ($f_c = 5$ Hz, $f_{max} = 10$ Hz) synthetic seismograms on the surface at distances up to 1000 km for an inhomogeneous crustal waveguide

grams on the surface at distances up to 1000 km. The center frequency is 5 Hz with the maximum frequency of 10 Hz. In comparison, the low-frequency ($f_c = 1$ Hz, $f_{max} = 2$ Hz) synthetic seismograms are shown in Figure 6. It is clear that without high-frequency content, many of the distinctive features associated with Lg measurements can not be adequately modeled. In other words, a proper simulation method with the capability to generate accurate high-frequency signals is a necessity for the purpose of investigating regional phases.

Study the Influences of Random Heterogeneities and Rough Interfaces

The importance of small-scale random heterogeneities to seismic wave propagation is well known. There are extensive publications on this subject in seismology. However, the role of random heterogeneities in Lg excitation, propagation, attenuation and blockage, is still unclear due to the complexity of the problem. The theory of wave propagation in unbounded random media has been well developed. However, for waves in complex crustal waveguides with random heterogeneities, the theoretical difficulties are overwhelming, and no analytical tools are available for performing realistic calculations. Numerical simulation is an attractive alternative to the theory. Some finite difference simulations have been conducted (e.g. Frankel and Clayton, 1986; Frankel, 1987; Jih, 1996). Limited by the computation power, however, the propagation distances of the FD simulations are relatively short. Liu and Wu (1994) has done some numerical simulation using the phase-screen method, but the media simulated are limited to unbounded media. The development of the half-space GSP method, enables us to simulate h-f waves propagating in complex

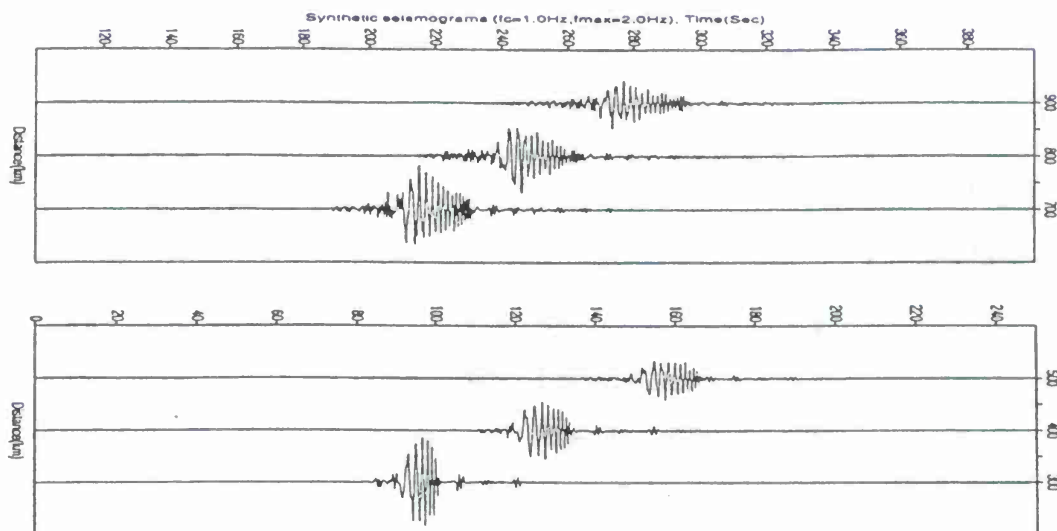


Figure 6: low-frequency ($f_c = 1 \text{ Hz}$, $f_{max} = 2 \text{ Hz}$) synthetic seismograms on the surface at distances up to 1000 km for an inhomogeneous crustal waveguide

crustal waveguides to long distances. In the following, we will show an example demonstrating the capability of the method.

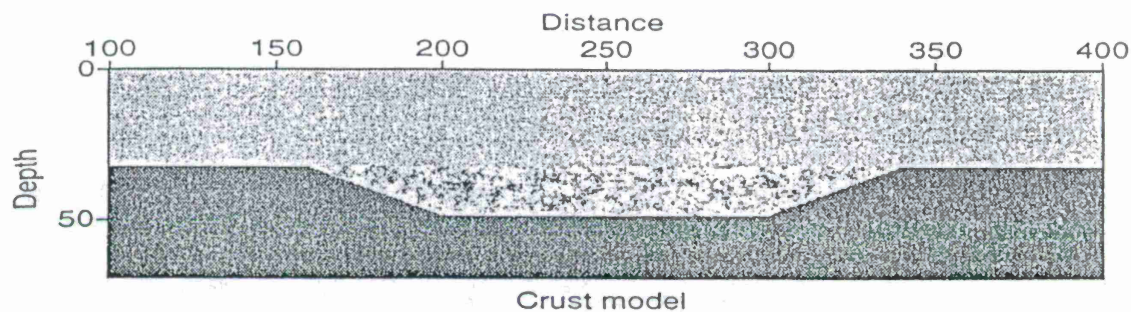
The top panel of Figure 7 shows a heterogeneous crustal model representing a "mountain root" with small-scale random heterogeneities. The heterogeneities have an exponential correlation function, with the scale length $a_x = a_z = 1.6 \text{ km}$ (in horizontal and vertical directions, respectively). The velocity perturbation is 5%. The dominant frequency of the source function is 2 Hz . The bottom two panels of Figure 7 shows the comparison between snapshots for waves passing through the "mountain root" with or without random heterogeneities, shown on B and C, respectively. We see that random heterogeneities drastically increase the leakage of waves to the mantle and the complexity of the waveforms. Extensive numerical experiments will be conducted to study the different influences of various kinds of random heterogeneities.

We have done numerical simulations on the influence of rough interface of sedimentary layers on Lg propagation. It is seen that the rough random interface can also increase the mantle leakage and waveform complexity of regional waves.

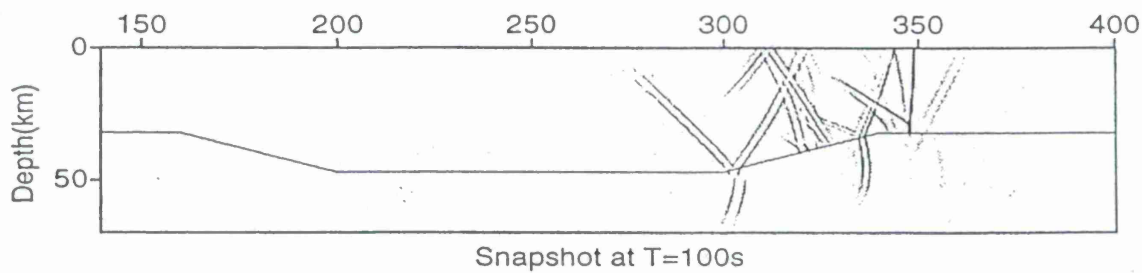
CONCLUSIONS AND RECOMMENDATIONS

The advantages of the GSP method can be summarized as follows.

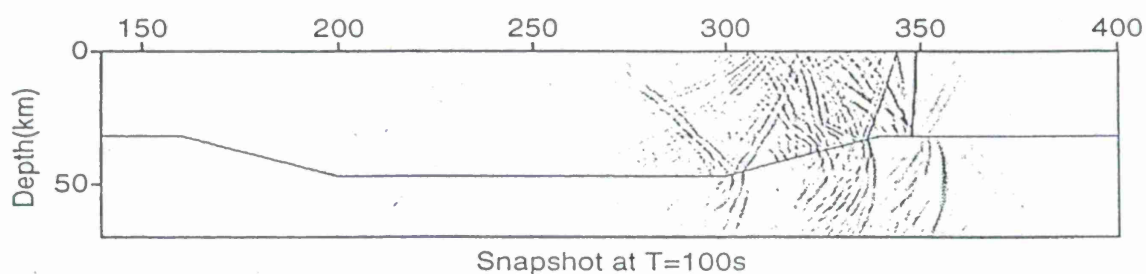
1. Fast speed: For medium size Lg problems, it is 2-3 orders of magnitude faster than the FD methods. For large distance, high frequency 3D problems, the time saving factor could



A. A heterogeneous crustal model representing a "mountain root" with small-scale random heterogeneities



B. Snapshot for waves passing the mountain root without random heterogeneities



B. Snapshot for waves passing the mountain root with random heterogeneities

Figure 7: Comparison between snapshots for waves passing through a 'mountain root' with or without random heterogeneities, shown on B and C, respectively.

be much greater. 2. Memory saving: The GSP needs only to store 2D data arrays for each step instead of 3D volume data, leading to huge memory savings. 3. Stability: The transversal Laplacian is calculated by the Fourier method, therefore no numerical dispersion occurs for high frequency waves. 4. Intrinsic attenuation: Being a frequency domain method, it is easy to incorporate various Q models into the simulation. Therefore, the method can study the effects of scattering and anelasticity to Lg wave blockage and attenuation. 5. Random heterogeneities: Random heterogeneities can be also easily incorporated into the model. The effects of small scale heterogeneities and their statistical characteristics can be studied by numerical simulations using this method.

In order to further explore and take the full advantage of the method, we recommend the following:

1. Further develop the half-space screen propagators for the case of P-SV and full 3D elastic waves.
2. Incorporate the smoothly irregular surface topography into the theory and method so that the fast method can simulate guided wave propagation with irregular surface and interface topographies.

REFERENCES

- Frankel, A. and Clayton, R.W., 1986, Finite difference simulations of seismic scattering: Implications for propagation of short-period seismic waves in the crust and models of crustal heterogeneity, *J. Geophys. Res.*, **91**, 6465-6489.
- Frankel, A., 1987, A review of numerical experiments on seismic wave scattering, "Scattering and Attenuation of Seismic Waves", II, ed. by Wu and Aki, 639-686.
- Huang, L.J. and R.S. Wu, 1996, 3D prestack depth migration with acoustic pseudo-screen propagators, *Mathematical methods in geophysical imaging IV, SPIE*, **2822**, 40-51.
- Jih, R.S., 1996, Waveguide Effects of large-scale structural variation, anelastic attenuation, and random heterogeneity on SV Lg propagation: a finite-difference modeling study, 182-194, *Proceedings of the 18th Annual Seismic Research Symposium on Monitoring a Comprehensive Test Ban Treaty*, 4-6 September 1996.
- Liu, Y.B. and R.S. Wu, 1994, A comparison between phase-screen, finite difference and eigenfunction expansion calculations for scalar waves in inhomogeneous media, *Bull. Seis. Soc. Am.*, **84**, 1154-1168.
- Wu, R. S., 1994, Wide-angle elastic wave one-way propagation in heterogeneous media and an elastic wave complex-screen method, *J. Geophys. Res.*, **99**, 751-766.
- Wu, R.S., 1996, Synthetic seismograms in heterogeneous media by one-return approximation, *Pure and Applied Geophys.*, in press.
- Wu, R.S., Jin, S. and Xie, X.B., 1996, Seismic wave propagation and scattering in heterogeneous crustal waveguides using screen propagators: I SH-waves, 291-300, *Proceedings of the 18th Annual Seismic Research Symposium on Monitoring a Comprehensive Test Ban Treaty*, 4-6 September 1996.
- Xie, X.B. and Lay, T., 1994, The excitation of Lg waves by explosions: A finite-difference investigation, *Bull. Seism. Soc. Am.*, Vol 84, 324-342.

NONLINEAR WAVE PROPAGATION IN THE HALF SPACE

Heming Xu¹, Steven M. Day², and Jean-Bernard H. Minster¹

¹Institute of Geophysics and Planetary Physics
Scripps Institution of Oceanography
University of California, San Diego
La Jolla, CA 92093-0225

²San Diego State University
Department of Geological Sciences
5178 College Avenue
San Diego, CA 92182

Sponsored by Air Force Office of Scientific Research
Contracts No. F49620-94-0204 and F49620-94-0205

ABSTRACT

We have developed a constitutive model applicable to rock in the intermediate strain regime, i.e., approximately 10^{-6} to 10^{-3} where nonlinear losses, pulse distortion, and harmonic distortions have been documented in the laboratory. This model has been fit to a set of laboratory data on Berea sandstone, obtained by Dr. G. Boitnott of New England Research, Inc. The main generalizations we report are (1) the inclusion of nonlinear hysteresis for both hydrostatic compression and for shear deformation and (2) the development of a capability to study nonlinear wave propagation in two-dimensional half space. We find that nonlinear wave propagation from a monochromatic source excites odd harmonics of the source frequency, and there is energy transfer from lower frequencies to a higher frequency band when the medium is excited from a broadband pressure source.

Keywords: Endochronic constitutive, half-space, broadband, harmonic generation

Research accomplished

1. Endochronic constitutive formalism

The endochronic formalism incorporates the fact that the behavior of materials depends not only on the current state but on the entire strain history as well. The formalism requires specification of the kernel functions and evaluation of the intrinsic time scale z . As well defined by Valanis and Read (1982), the equations include:

$$S = \int_0^t \rho(z-z') \frac{\partial e^p}{\partial z'} dz' \quad \text{and} \quad dS = \mu(de - de^p)$$

for deviatoric stress tensor S , strain tensor e and plastic strain tensor e^p . Here μ is the shear modulus. Also

$$\sigma_{kk} = \int_0^t K(z-z') \frac{\partial \epsilon_{kk}^p}{\partial z'} dz' \quad \text{and} \quad d\sigma_{kk} = k(d\epsilon_{kk} - d\epsilon_{kk}^p)$$

for volumetric stress σ_{kk} , volumetric strain ϵ_{kk} , and volumetric plastic strain ϵ_{kk}^p . k is the bulk modulus.

If the kernel functions are given, then given the increment of the strain tensor the corresponding increment of stress tensor can be calculated from the above equations. If the kernel functions are weakly singular, of the form $z^{-\alpha}$, then the constitutive functionals imply that the initial loading/unloading will occur along the elastic slope in the stress-strain plane (Valanis and Read, 1982). The kernel functions are usually expanded into a Dirichlet series to circumvent the integral in the constitutive equations, i.e.

$$\rho(z) = \sum_{i=1}^n A_i e^{-\alpha_i z}; \quad K(z) = \sum_{i=1}^n B_i e^{-\beta_i z}$$

Enough terms should be used to provide an adequate approximation to the weakly singular kernels. Then we get

$$dS = \rho(0)de^p + h(z)dz \quad \text{where} \quad h(z) = \int_0^z \hat{\rho}(z-z') \frac{\partial e^p}{\partial z'} dz'; \quad \hat{\rho}(z) = d\rho/dz$$

$$d\sigma_{kk} = K(0)d\epsilon_{kk}^p + g(z)dz; \quad \text{where} \quad g(z) = \int_0^z \hat{K}(z-z') \frac{\partial \epsilon_{kk}^p}{\partial z'} dz'; \quad \hat{K}(z) = dK/dz$$

Here dz is defined as the length of the plastic strain path increment, which provides a representation of coupling between the deviatoric and volumetric strain tensors:

$$|dz|^2 = c_1 \|de^p\|^2 + c_2 \|d\epsilon_{kk}^p\|^2$$

where c_1 and c_2 are constants.

Given the increment of strain tensor, through a little algebra, we get

$$(dz)^2 [A \|h\|^2 + B g^2 - 1] - 2(dz) [A \mu \|hde\| + B k d\epsilon_{kk} g] + A \mu^2 \|de\|^2 + B k^2 (d\epsilon_{kk})^2 = 0$$

where

$$A = \frac{c_1}{(\mu + \rho(0))^2}; \quad B = \frac{c_2}{(k + K(0))^2}$$

Then h and g will be updated as follows

$$h = \sum_{i=1}^n h_i; \quad h_i(z + \Delta z) = h_i(z) e^{-\alpha_i \Delta z} - A_i [1 - e^{-\alpha_i \Delta z}] \frac{\partial e^p}{\partial z};$$

$$g = \sum_{i=1}^n g_i; \quad g_i(z + \Delta z) = g_i(z) e^{-\beta_i \Delta z} - B_i [1 - e^{-\beta_i \Delta z}] \frac{\partial \epsilon_{kk}^p}{\partial z}$$

2. Experimental data and numerical endochronic simulations

The experiments used in this study were performed at New England Research, Inc. by Dr. Boitnott et al.. Cylindrical Berea sandstone samples were subjected to axial and confining stress histories using a servo-controlled apparatus. In this way, the samples were cycled through a series of loading and unloading histories at predefined loading rates. The resulting hysteresis loops are typically plotted with axial and radial strains versus axial stress and confining pressure, respectively. For example, Figure 1a shows the axial stress versus axial strain and radial strain at constant confining pressure. Volumetric stress versus strain is shown in Fig. 1b in the case where the axial stress and confining pressure were varied to as to provide a hydrostatic load. These loops illustrate the fact that Berea sandstone is not a perfectly linear elastic medium and that its behavior at large strain amplitude levels is in fact dominated by some nonlinear mechanisms.

The hysteresis loops are modeled by the endochronic constitutive law. The parameters k and μ are derived independently from analyzing the hysteresis loops under hydrostatic stress loads and shear stress loads, respectively. The resulting parameters and coefficients are then applied to simulate the hysteresis loops for different loading paths. This provides the means to verify that possible nonlinear interactions between moduli can be ignored at this level of approximation. We then use Prony expansions to approximate the power law kernel functions (We have shown in the past that the selection of $z^{-1/2}$ yields a linear relationship of Q^{-1} with strain amplitude, a common observation for rocks under low confining pressure). Figures 1a-b also show calculated hysteresis loops superimposed on the observed ones. For the one dimensional case the simulations are shown in Figure 2. The match is quite satisfactory. In addition in Fig.3, shown are the phenomenon of cyclic creep, also termed "ratcheting" and the simulations with the endochronic constitutive by using the power law kernel. The simulations duplicate the common features of the ratcheting.

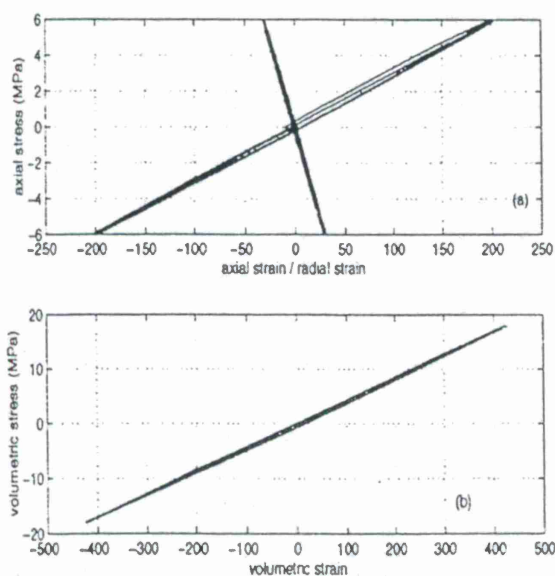


Figure 1 The simulations are represented by dashed lines, solid lines indicate data. (a) axial stress versus axial strain and radial strain at constant confining pressure. (b) confining pressure versus volumetric strain for hydrostatic loading conditions. Strains are in "microstrain".

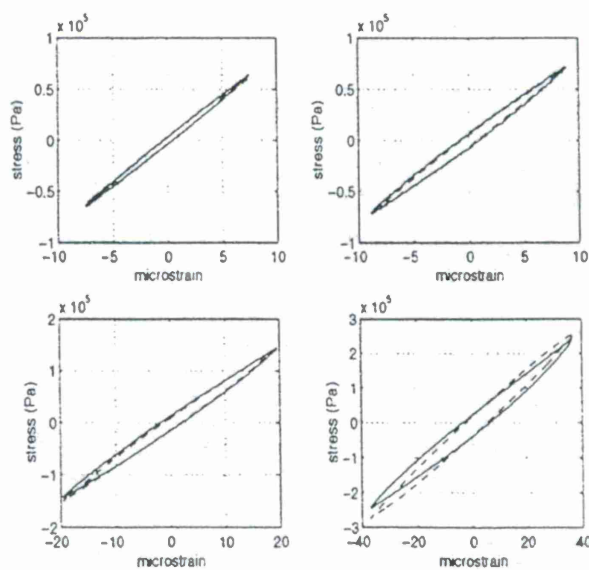


Figure 2 One-dimensional simulations of the hysteresis loops at different strain levels. The simulations are plotted in dashed lines.

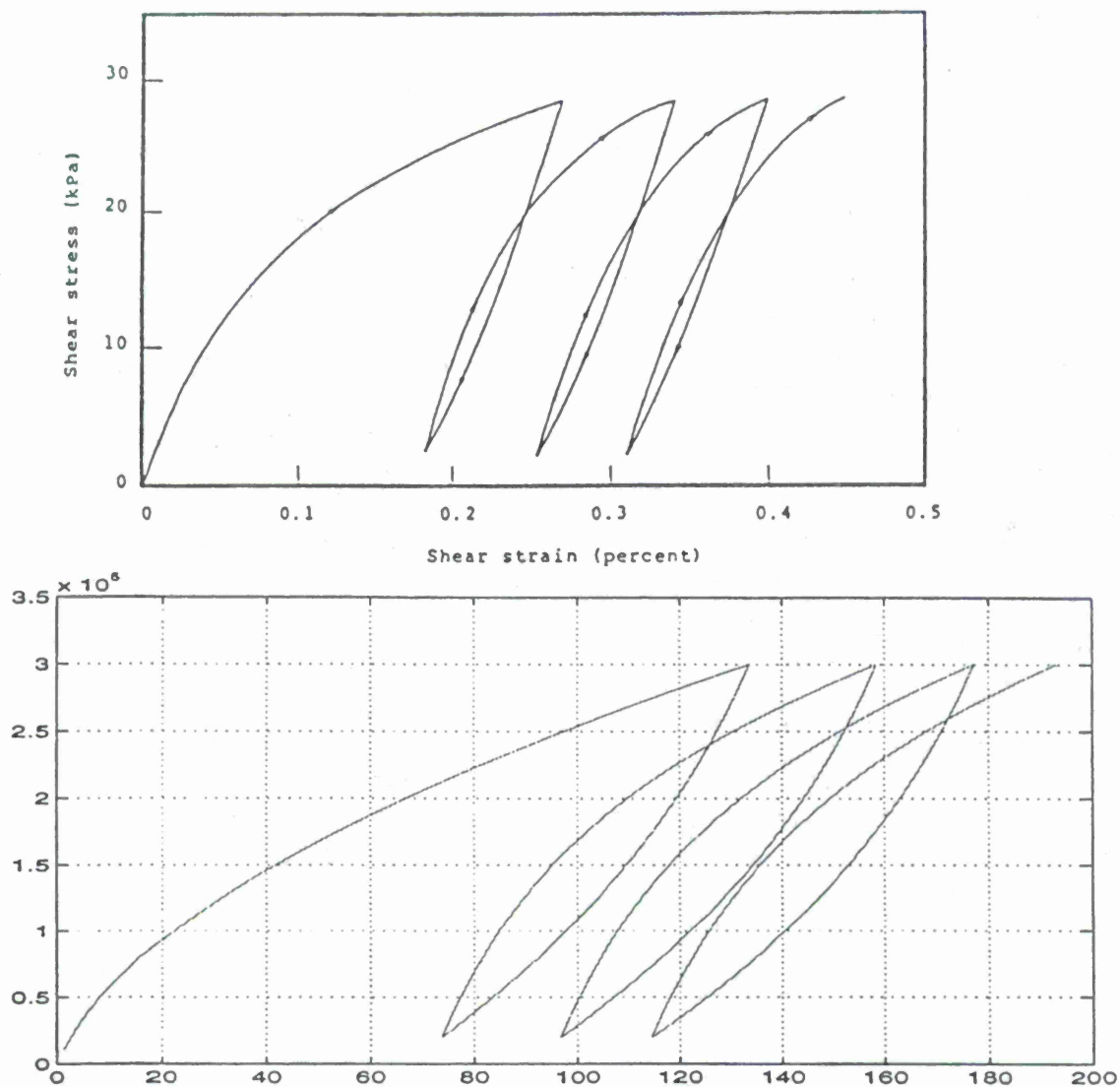


Figure 3 Cyclic deformation of a soil sample (from Valanis and Read (1982)) is shown in the top frame, and the endochronic modeling of this kind of ratcheting in the bottom one (using a power law kernel). The horizontal axis is strain in "microstrain", and the vertical stress in "Pa".

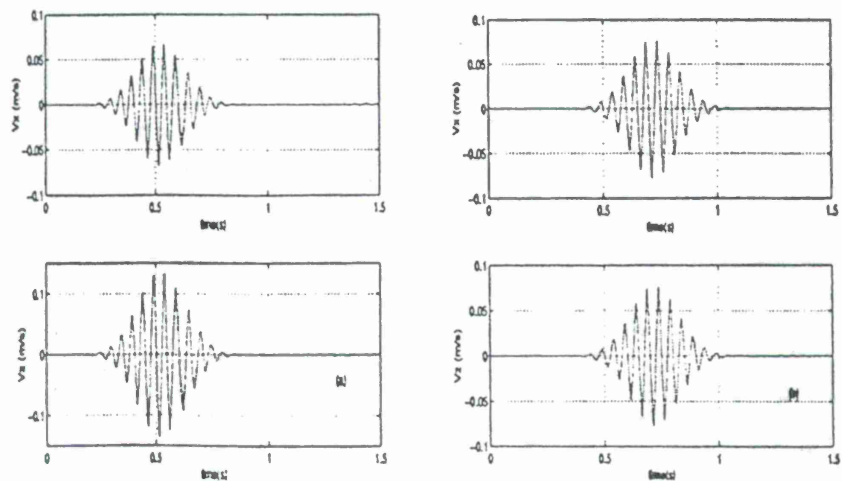


Figure 4 Comparison between pseudo-spectral (dashed lines) and the analytical (solid lines) solutions. (a) x component of velocity and z component of velocity at 4 wavelengths. (b) same as (a) at 8 wavelengths. Numerical solutions by pseudospectral method are consistent with the analytical solutions.

3. Numerical wave propagation simulations

Nonlinearity will distort a propagating wave, more significantly at the larger strain amplitudes. Such distortions will be examined through the following numerical simulations.

2-D wave propagation in purely linear elastic materials in unbounded media

The 2-D elastic wave propagation in linear elastic materials is calculated with the Fourier method. The approximation of spatial derivatives in the Fourier method is infinitely accurate for band-limited periodic functions with cutoff spatial wavenumbers which are smaller than the cutoff wavenumbers of the mesh (Kosloff et al, 1984; Daudt et al, 1989). A larger computational domain (256x256 grids) is used to avoid the unphysical wave interaction that result from the use of periodic boundary conditions. The Courant number $V_p dt/dx$ is set to a value well below the stability limit in order to minimize the numerical dispersion, where V_p is P wave velocity and dt , dx are temporal, spatial steps, respectively.

In the calculations shown here, the homogeneous medium has a P velocity of 4 km/s and S velocity of 2.6 km/s. The time step is 1 ms, and the spatial step is 20 m. The source is a center of dilatation. The solutions are validated in the elastic case by comparison with the analytical solution in Figure 4a-b in the near field and far field and proved to be fully consistent and accurate.

2-D wave propagation simulations in half space

The wave propagation problem for endochronic materials is posed using the same elastic moduli as above, with the added feature that the endochronic plastic strain tensor is introduced. For the lower excitation amplitude (at a strain level as low as 10^{-7}) the elastic wave and endochronic wave are found to propagate at exactly the same speed and with the same radiation pattern. This constitutes further validation of our implementation, since the rheology should be quasi-elastic in the limit of low strain.

But at higher strain levels the linear elastic and nonlinear endochronic solutions become distinctly different in the two following cases.

(a) Narrow-band pressure source excitation

A narrow band pressure source with frequency of 20Hz is used to show the nonlinear harmonic generation. The source is located at a depth of $z=1120$ m beneath the free surface and has a Gaussian tapered sinusoidal function. Figures 5a-b illustrate the resulting simulations for horizontal and vertical velocity components, respectively. Comparing with the linear elastic wave propagation with the same source function at the free surface ($z=0$) and the subsurface ($z=120$ m), as shown in Figure 5a, we find:

1) Linear elastic waves propagate with a slower amplitude decay (due to geometrical spreading) than the endochronic waves at higher strain level (10^{-4}) because of the energy loss due to hysteresis loops in the latter case.

2) Monochromatic elastic waves (20Hz) emanate from the source and remain monochromatic, but endochronic waves from such a monochromatic source propagate as multichromatic waves with harmonic components which evolve with distance. Harmonic generation has been observed in numerous laboratory experiments. This is diagnostic of a nonlinear rheology.

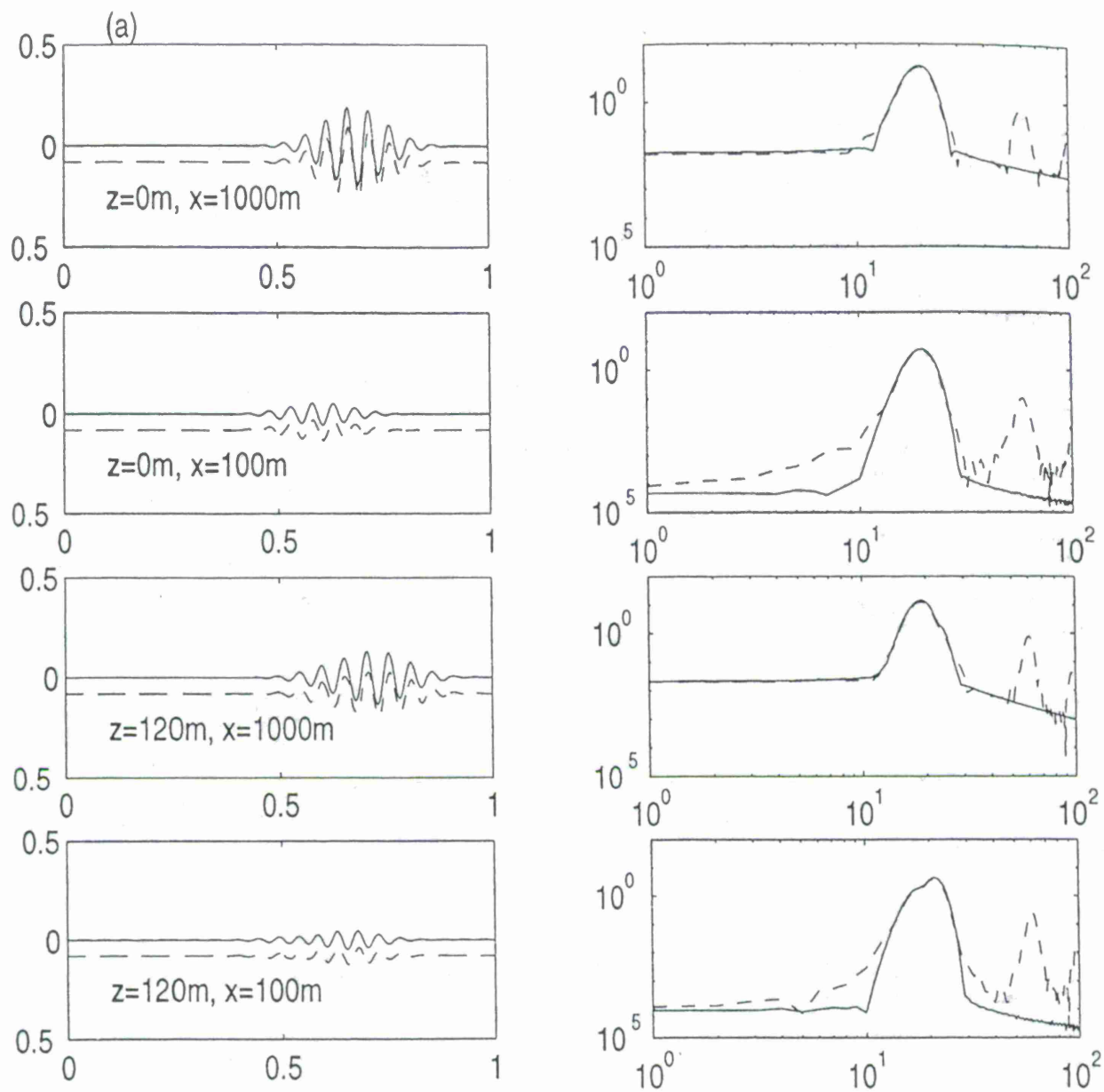


Figure 5 Simulations of wave propagation in the half space from a monochromatic seismic source. (a) the horizontal velocities at different locations indicated on the left plots. The left plots are the waves in the time domain where the horizontal axis is time in second and the vertical axis is velocity (m/s). The endochronic waveforms are shifted down to facilitate comparisons. The right plots are the spectra corresponding to the left ones in which the horizontal axis is frequency (Hz). Linear Elastic waves are plotted with solid lines while the endochronic waves are plotted with dashed lines. Note the third harmonic generation from the monochromatic source. (b) vertical velocities at same locations as in (a).

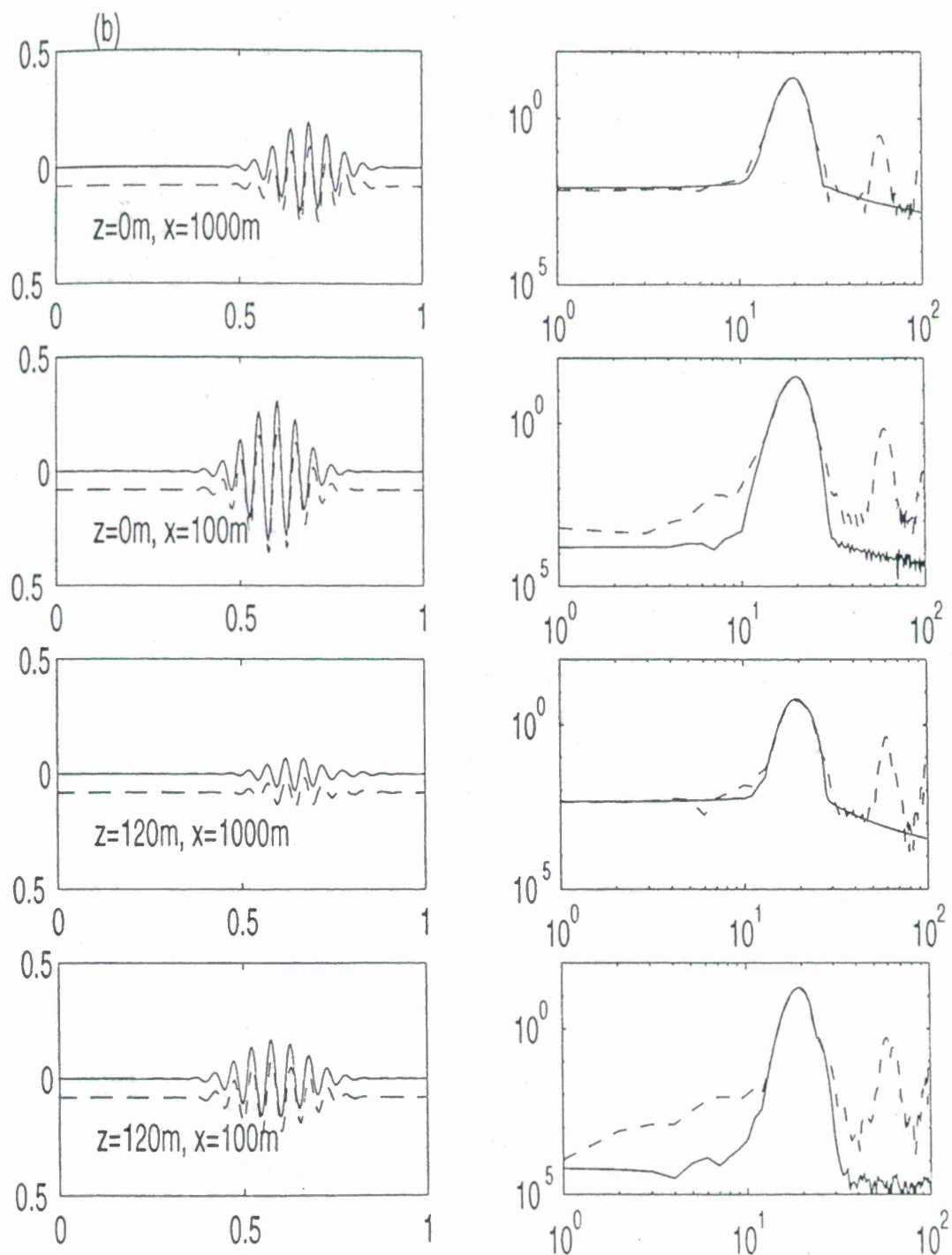
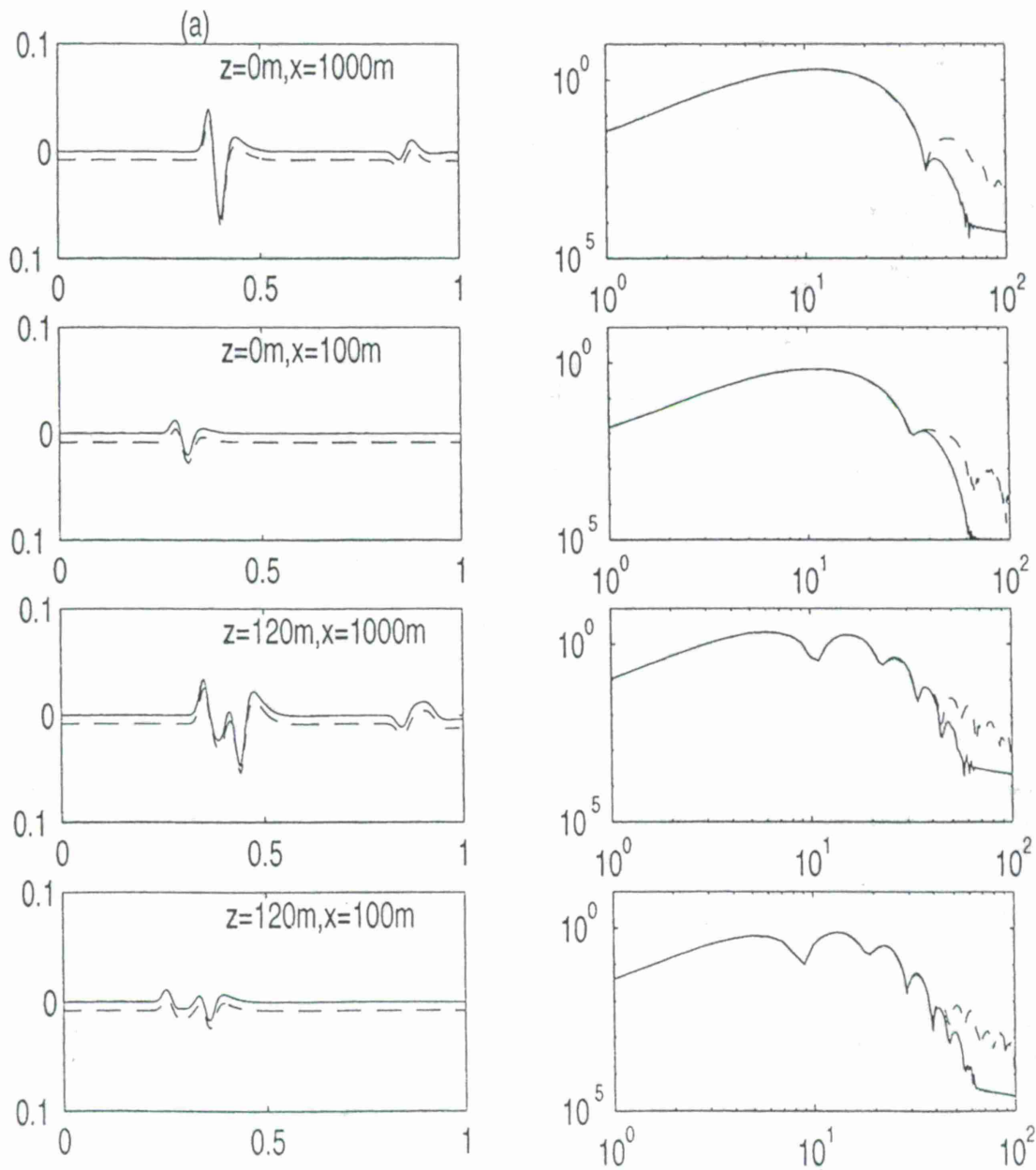


Figure 5 continued

(b) Broadband pressure source excitation

A broadband source function is used to illustrate the energy transfer from lower frequencies to higher frequencies. The strain levels are 10^{-4} . The pressure spectrum is flat at low frequencies and falls as f^{-2} at higher frequencies. Figs 6a-b show the horizontal and vertical velocities at different locations and demonstrate the following points: (1) the amplitudes of the endochronic waves at the surface and subsurface are a little lower than those of the linear elastic waves. (2) higher frequency components are created in the nonlinear interaction as a function of propagation distance (McCall, 1994), which is significantly different from the linear elastic case. (3) the spectra show little change at the low frequencies but the amplitude decrease at the intermediate frequencies as a result of the energy transfer to the higher frequencies.



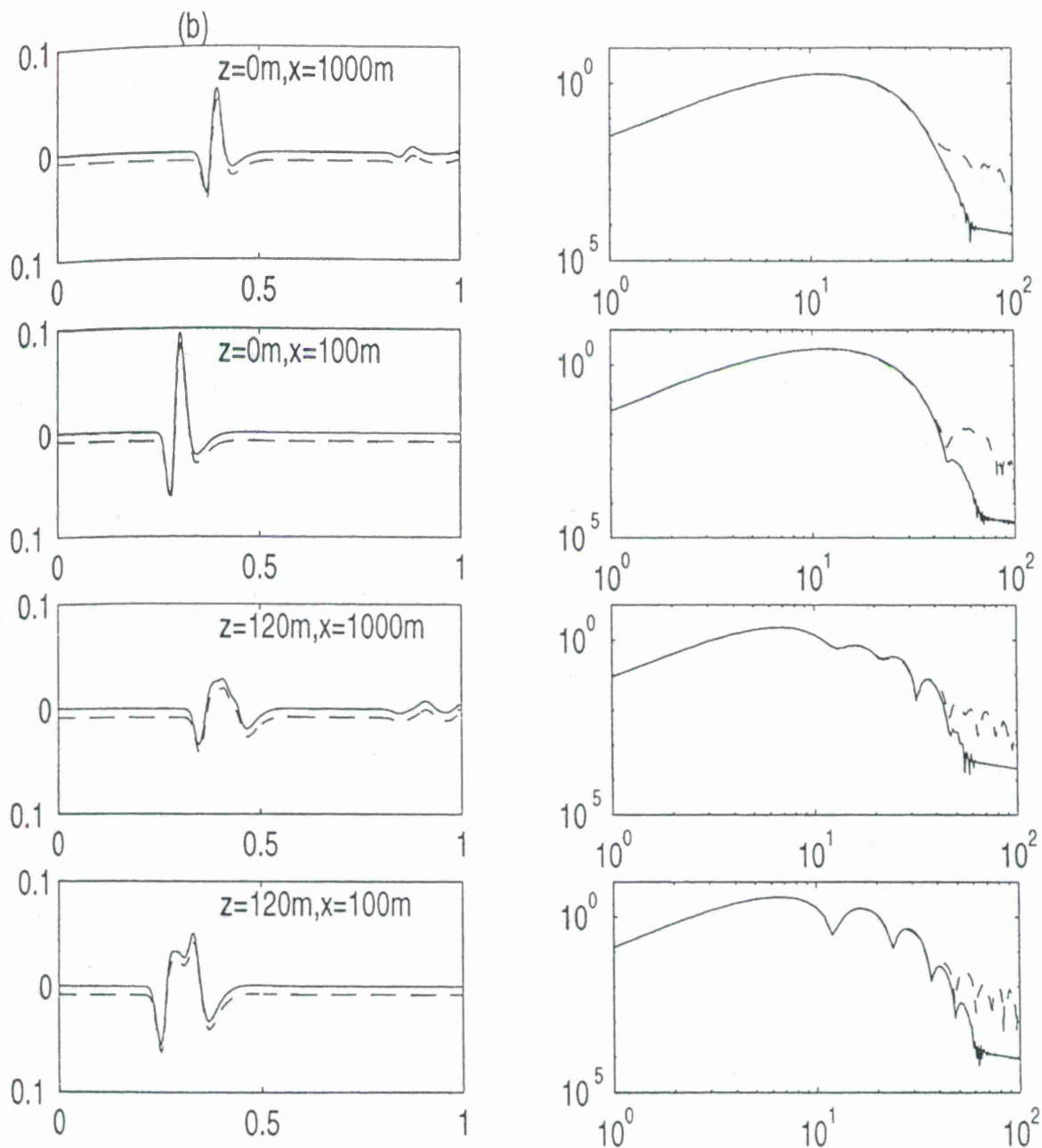


Figure 6 Wave propagation from a wideband seismic source. A wideband pressure source is applied beneath the free surface. The layout is the same as in Figure 5 . (a) the horizontal velocities at different locations. The left plots are the waveforms in the time domain. The horizontal axis is time (s) and the vertical axis is particle velocity (m/s). The right plots are the corresponding spectra where horizontal axis is frequency (Hz). Endochronic waves are also shown, with a slight offset for legibility. In the frequency domain, it is obvious that power is transferred across the band from intermediate frequencies to higher frequencies.

(b) the vertical velocities.

Conclusions

We draw the following conclusions from the above calculations:

- 1) We have generalized our analysis of nonlinear wave propagation in an endochronic solid to permit simulations of wave propagation in two dimensions including the free surface. The results show (1) that the wave spectra have little change with distance while the intermediate frequency spectra decrease with distance as a result of energy transfer to higher frequencies. (2) higher harmonics are generated, and increase with distance, which has been observed in a variety of experiments. This indicates that the endochronic constitutive could reproduce the general characteristics of commonly observed nonlinear behavior.
- 2) The endochronic model has been shown to be able to produce a close match to static laboratory data for nonlinear hysteresis in rock. Simple singular kernel functions and their approximation by Prony series have proved to be adequate to fit the data collected in hysteretic cycling experiments on Berea sandstone.
- 3) This endochronic model is convenient to use in practice because i) it is formulated in terms of a set of equations which may be easily converted into a set of simple differential equations. ii) it does not require specification of the attenuation factor. It intrinsically includes the attenuation which matches the laboratory observations.

Acknowledgments

We would like to thank Dr. G. Boitcott of New England Research, Inc., for providing his pseudo-triaxial experimental data.

References

- Daudt, C.R., Braile, L.W., Nowack, R. L. and Chiang, C.S., A comparison of finite difference and Fourier method calculations of synthetic seismograms, *Bull. Seismol. Soc. Amer.*, **79**, 1210-1239, 1989
- Kosloff, D., Reshef, M. and Loewenthal, D., Elastic wave calculations by the Fourier method, *Bull. Seismol. Soc. Amer.*, **74**, 3, 875-891, 1984
- McCall, K.R., Theoretical studies of nonlinear elastic wave propagation, *Journal of Geophysical Research*, **99**, 2591-2600, 1994
- Valanis, K and Read, H., A new endochronic plasticity model for soils, *S-CUBED report*, SSS-R-80-4292, San Diego, Calif, 1982

Shear Wave Generation from Rock Cracking Induced by Explosions in Spherical Cavities

T. J. Ahrens and C. Liu

Seismological Laboratory, California Institute of Technology, Pasadena, CA 91125

Abstract

We have conducted the first laboratory experiments in which spherical charges are detonated at the center of spherical cavities in rock and the crack-generated shear wave radiation is recorded in the near field. We have conducted preliminary analysis of the P-waves produced by explosions and also shear waves produced by the P-wave-induced radial cracks in limestone. Using the measured displacement decay relation and the dynamic tensile strength, a simple dynamical tensional strength model and the dynamic crack propagation model (Freund, 1990) are used to estimate the S-wave duration and particle displacements. The magnitudes of the S-wave particle displacements and S-wave duration estimated from the theoretical models are in good agreement with experimental results. The present results demonstrated the important role of rock cracking in shear wave generation in slightly overdriven spherical rock cavities.

Research Accomplished

During the last year, we have gone from measuring SV-wave radiation in samples with cylindrical cavities between two rock blocks to a spherical explosion source drilled into a nearly perfect sphere within limestone rocks. This geometry eliminates the possible P- to SV-wave conversion at the block interface. The drilling device (Fig.1) has been used to machine several spherical cavities in Bedford limestone.

We have fired two decoupled explosion tests in spherical cavities. In test #1, the explosives did not detonate. After we redesigned the explosive assembly, test #2 worked well. The experimental method and setup are sketched in Fig.2 and Fig.3. The following summarizes our results.

1. Experimental data

Du Pont sheet explosive was formed into a spherical shape using a hollow spherical glass (the outside diameter and shell thickness of the glass are 13.5 mm and 0.85 mm, respectively.). The explosive mass is 1.9 gram. The diameter of the explosive sphere is 11.8 mm. The explosive assembly is shown in figure 4. The locations of the strain gauges are indicated in figure 3. The spherical cavity is 30 mm in diameter. The depth of the cavity center from the nearest rock interface is 45 mm. The two rock blocks are cemented together. The whole assembly is confined under 10 bars.

2. Experimental records

Recorded strains along the two directions are shown in figure 5.

3. Analysis of the P-waves

From the experimental records, the P-wave velocity is determined to be 4.22 km/s under the experimental conditions as shown in figure 6. The P-wave velocity determined here is somewhat lower than 4.9 km/s measured ultrasonically by Rubin and Ahrens (1991) on a different sample. However, this velocity is still much higher than the bulk velocity (3.68 km/s). This means that the deformation induced by the P-wave is still in the elastic deformation regime over most of its propagation path. The lower P-wave velocity could also be the result of the nonlinear elastic behavior of the rock.

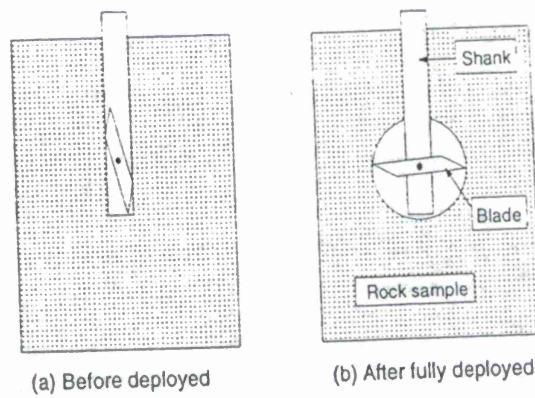


Figure 1: Schematic of spherical cavity drill.

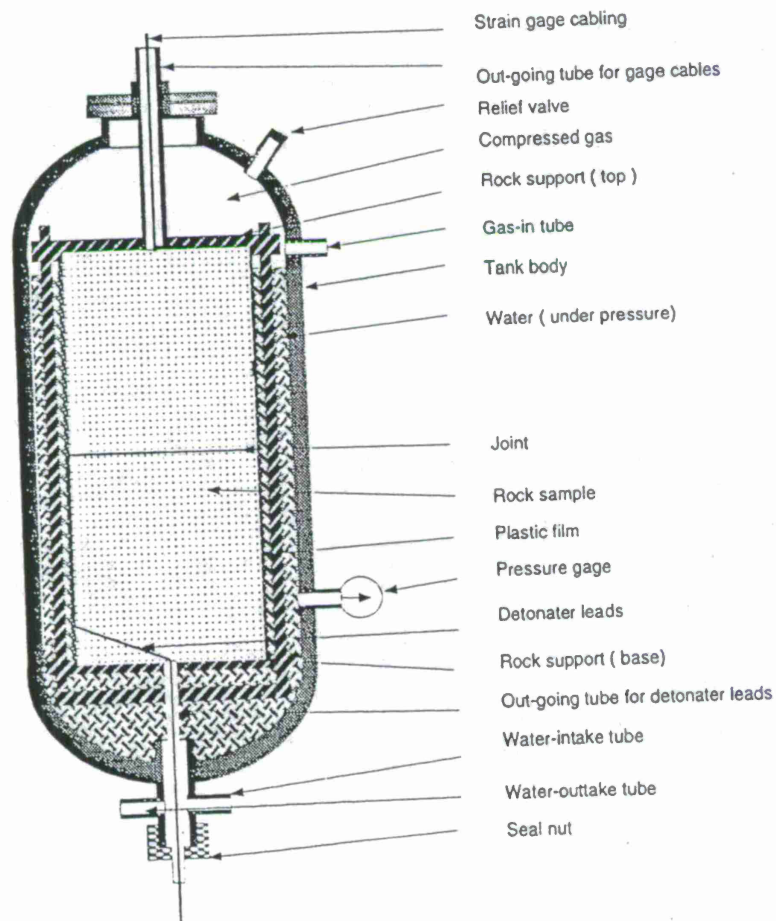


Figure 2: Mechanical configuration of the test chamber.

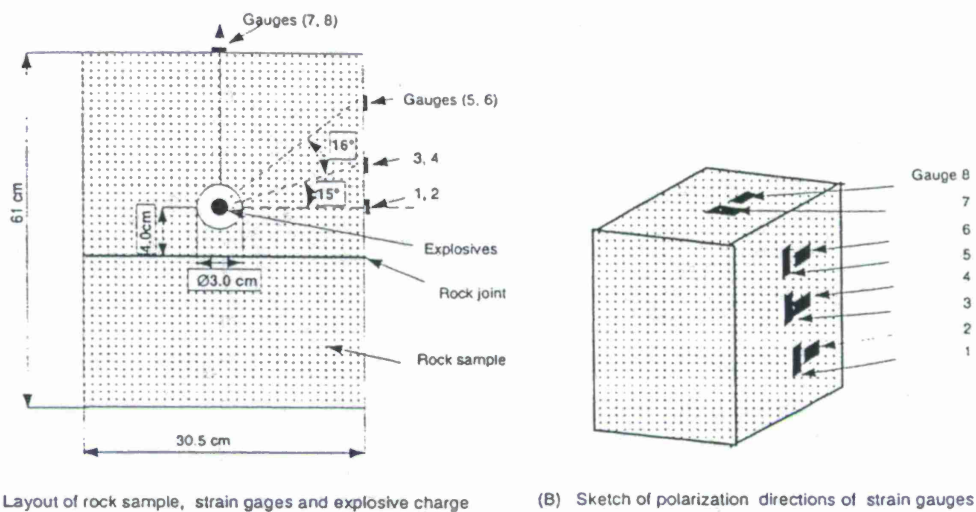


Figure 3: Sample and strain gauge layout.

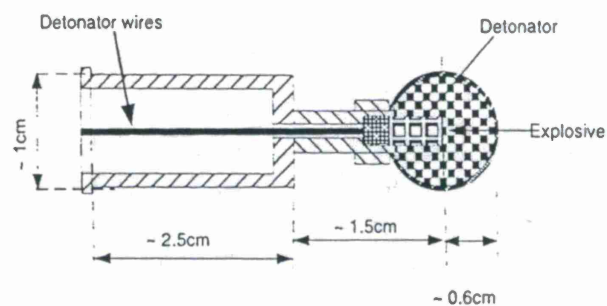


Figure 4: Explosion source arrangement.

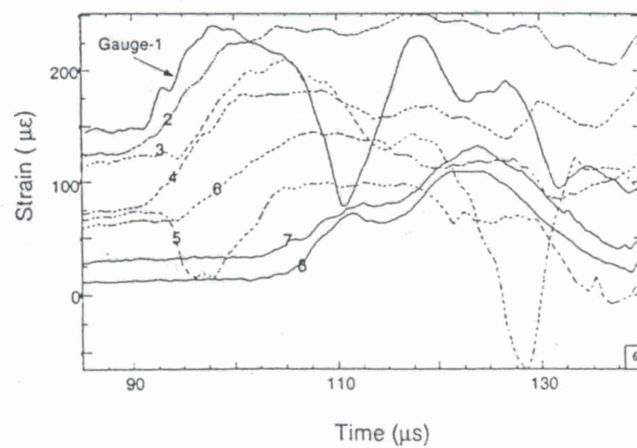


Figure 5: Strain signals from all the gauges.

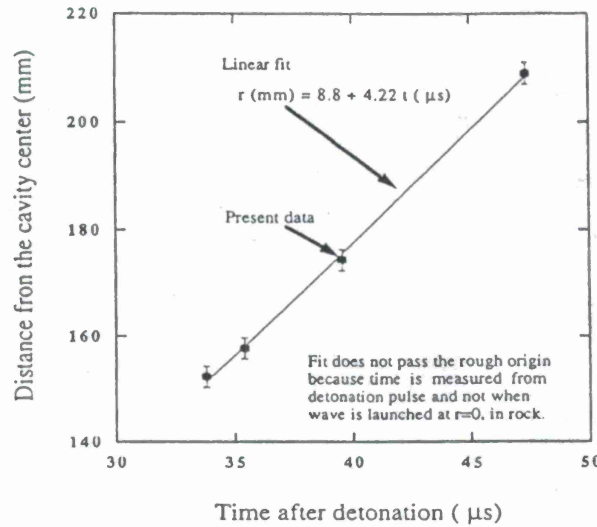


Figure 6: P-wave arrival versus radius.

Using the relations between strains and displacements given by Liu and Ahrens(1997), the P-wave particle displacements are calculated and shown in figure 7. From figure 7, the maximum P-wave particle displacements, $u_{max.}$, at different distances from the cavity center can be obtained and are shown in figure 8 in which Cowboy data (Murphey, 1961) also are plotted. A fit to the experimental data is

$$u_{max.} = 1.32 \times 10^4 r^{-1.46}, \quad (1)$$

where $u_{max.}$ is in μm , r in mm is the distance from the cavity center. In Murphey's(1961) paper, he found that the field results have a dependence of the peak P-wave particle displacement on the distance from the cavity center that is proportional to $r^{-1.5}$. Thus, the previous study is very comparable with the results from this work.

Based on the relation between maximum P-wave particle displacement and the propagation distance, the maximum radial strain, ϵ_r , and tangential strain, ϵ_t , in the present experiments are

$$\epsilon_r = \frac{\partial u_{max.}}{\partial r} = -19.27 r^{-2.46}, \quad (2)$$

$$\epsilon_t = \frac{u_{max.}}{r} = 13.2 r^{-2.46}. \quad (3)$$

From Hooke's law, we have

$$\sigma_r = \frac{E}{(1+\nu)(1-2\nu)} ((1-\nu)\epsilon_r + 2\nu\epsilon_t) \quad (4)$$

$$\sigma_t = \frac{E}{(1+\nu)(1-2\nu)} (\epsilon_t + \nu\epsilon_r), \quad (5)$$

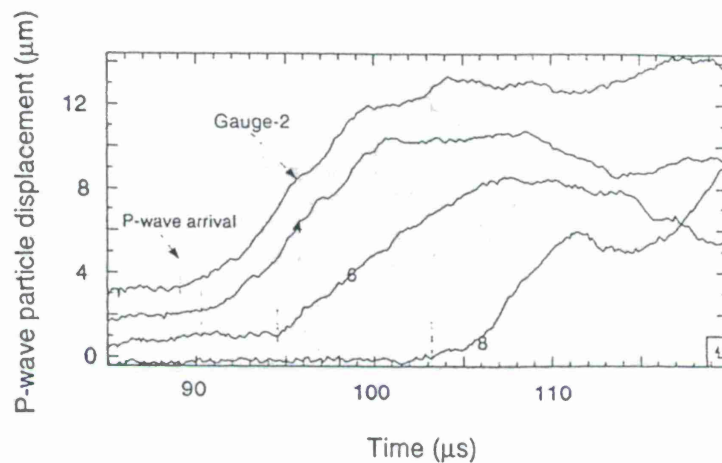


Figure 7: P-wave particle displacement versus time.

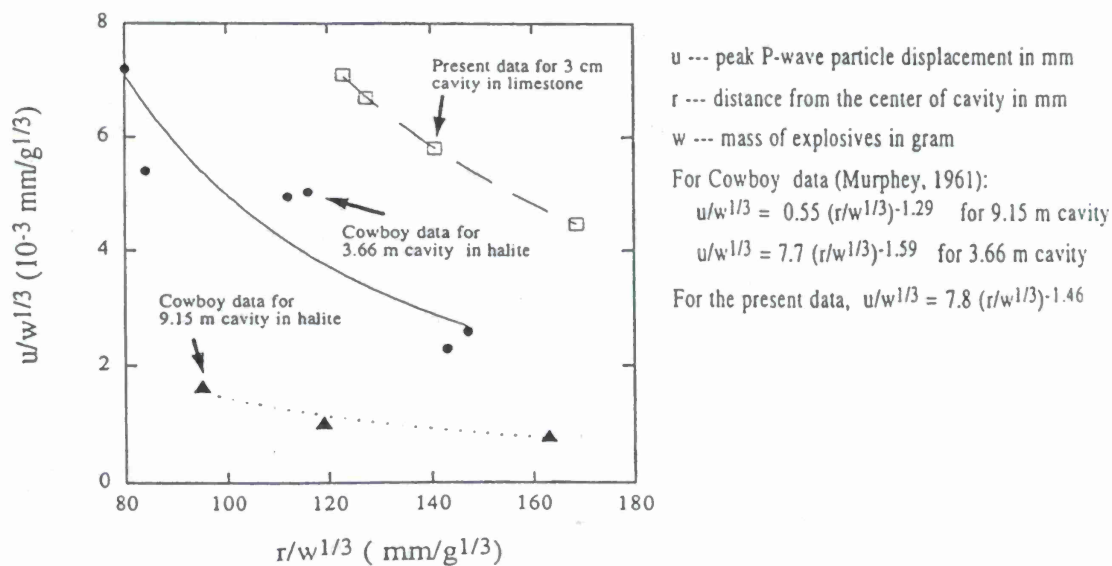


Figure 8: Scaled maximum P-wave particle displacement versus propagation distance.

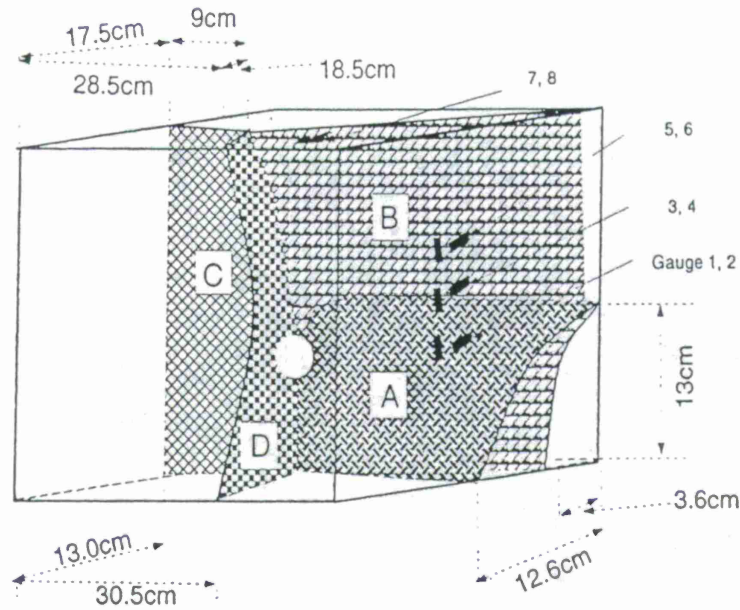


Figure 9: Schematic of the large cracks in relation to the spherical cavity.

where σ_r and σ_t are radial and tangential stresses, respectively. Here, ν is Poisson's ratio. Based on the experimental data, ν is 0.258 for the limestone and E is 47.7 GPa. Substituting Eqs.(2) and (3) into Eqs.(4) and (5), we have

$$\sigma_r = -587.0r^{-2.46}, \quad (6)$$

$$\sigma_t = 646.5r^{-2.46}, \quad (7)$$

where σ_r and σ_t are in GPa, and r is in mm.

4. Analysis of the S-waves

Because the explosion product particle motion in cavities is radial and the shock wave in rocks is assumed to be spherical, these should not generate S-waves when no cracks are induced. The recovered experimental sample, however, shows that there are four large cracks (sin 10 cm) and many small cracks (sin 5 mm) induced by the explosion (Fig.9). From the strain records, we found that S-waves are generated as shown in Fig.(10). These S-waves must have been induced through cracking. We infer that the S-waves given by gauge 1 and 3 mainly are induced by crack "A" (Fig.9) basing on the relative positions of strain gauges and cracks and also the S-wave arrival time (the expected S-wave arrival is labeled in Fig.10).

Based on Eq.(7), the length of the radial tensional cracks can be estimated if the tensional strength of rocks under the appropriate strain rate is known. Rubin and Ahrens' (1991) experimental data on the dynamic tensional strength of Bedford limestone showed that the tensional strength of Bedford limestone was very sensitive to pulse duration ($\sigma_f = 135$ MPa when the pulse duration is 0.3 μ s and 58 MPa when the duration is 1.3 μ s). In order to simply estimate the tensional strength under different wave durations, we assumed that the product of the tensional strength with the square root of the pulse duration, Δt , is a constant. From the experimental results (Rubin and

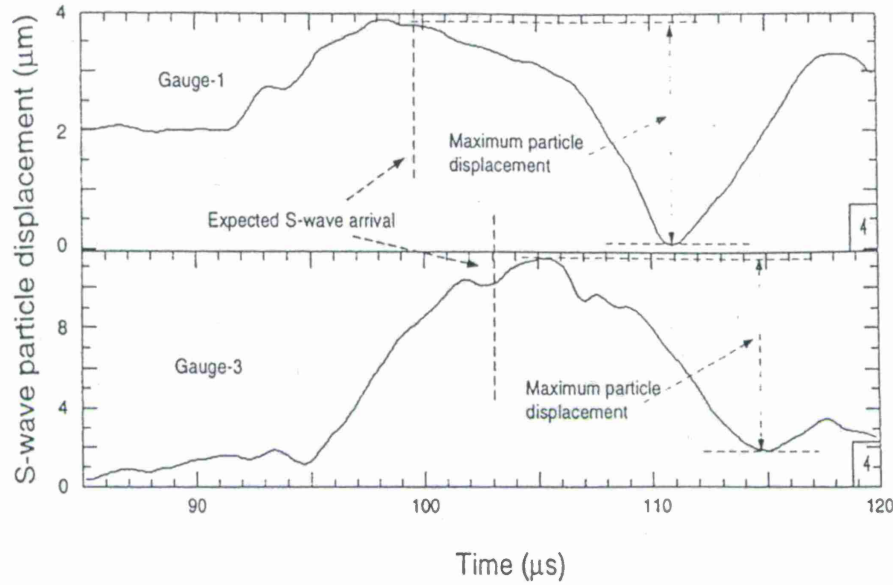


Figure 10: S-wave particle displacement versus time.

Ahrens, 1991), the average $\sigma_f \sqrt{(\Delta t)}$ is $70 \text{ MPa}(\mu\text{s})^{\frac{1}{2}}$. From the P-wave particle displacement profile as shown in Fig.(6), the rise-time of the P-wave particle displacement is approximately $10 \mu\text{s}$. The tensional strength of Bedford limestone for $10 \mu\text{s}$ -duration P-wave pulse is, therefore $\sigma_f \approx 22 \text{ MPa}$. From Eq.(7), the radius at which the tangential stress induced by P-wave is equal to the tensional stress is

$$R_0 = 65.5 \text{ mm.} \quad (8)$$

From the recovered sample, the radius of the explosion product deposition on tensional crack surfaces ranges from sin 100 to sin 180 mm. The difference in the crack radius between the above estimate and the data from the recovered sample may be due to the slower dynamic and quasi-static crack propagation which occurred during and after the experiment.

In general, cracks were not uniformly distributed around the cavity due to the non-uniform pre-existed microcracks. This non-uniformity will result in the aspherical S-wave generation. In order to approximately estimate the S-wave amplitude, we assume that cracks are penny-shaped with final radius, R_0 . The S-wave particle velocity, v_s , near crack surfaces can be estimated using

$$v_s = \frac{\sigma_f}{\rho C_s}, \quad (9)$$

where $\rho = 2.42 \text{ g/cm}^3$ and $C_s = 2.8 \text{ km/s}$ (Rubin and Ahrens, 1991) are the density and shear wave velocity of Bedford limestone, respectively. Then $v_s \approx 3.3 \text{ m/s}$.

If we assume that cracks are immediately generated just behind P-wave when the tangential stress induced by P-wave is greater than the rock tensional strength, the rise-time

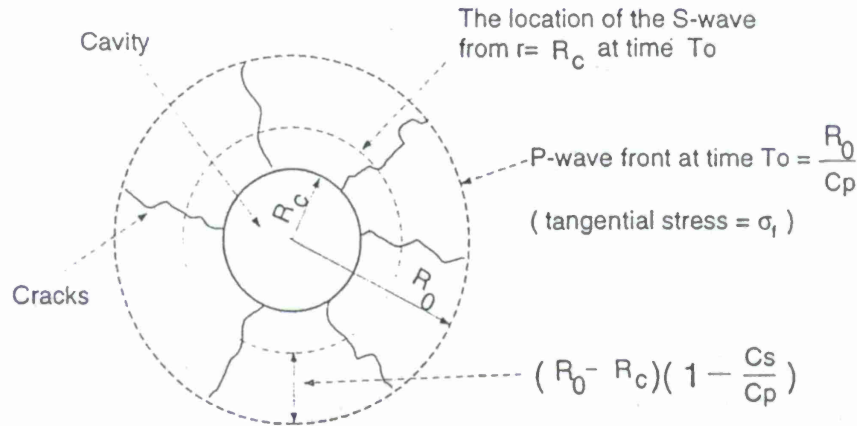


Figure 11: Schematic of the S-wave duration derivation.

of S-wave particle displacement profiles induced by cracks can be estimated as

$$\Delta t = \frac{R_0 - R_c}{C_s} \left(1 - \frac{C_s}{C_p}\right), \quad (10)$$

where R_c is cavity radius. The expression is schematically explained in Fig.(11). Because $R_0 \approx 65.5$ mm, $R_c = 15$ mm, $C_p = 4.22$ km/s and $C_s = 2.8$ km/s, we find that $\Delta t \approx 6$ μ s. Therefore, the maximum S-wave particle displacement near crack surfaces is about $v_s \Delta t \approx 20$ μ m. If it is assumed that S-wave particle displacement decays linearly with distance, the maximum S-wave particle displacement at distance r in the present geometry is

$$u_s(\mu m) = \frac{20R_0}{r}, \quad (11)$$

then $u_s \approx 9$ μ m at $r = 150$ mm.

The other way to estimate the maximum S-wave particle displacements on crack surfaces is to use the crack dynamic propagation solutions given by Kostrov (Freund, 1990) that is expressed as

$$u_s^c(r_c, t) = \frac{\sigma_f B}{G} (R^2 - r_c^2)^{0.5}, \quad (12)$$

where u_s^c is the particle displacement normal to the crack surfaces induced by penny-shaped crack propagation. B is a parameter that varies from 0.1 to 0.8. r_c is the distance from the crack initiation point and R is crack radius. Shear modulus, G , is 19.0 GPa. In the expression, the undetermined parameter, B , is dependent on crack propagation velocity. Because we are only doing an order-of-magnitude estimate, we actually assume that $B = 0.5$. From Eq.(12), the maximum displacement ($r_c=0$) on the crack surface is

$$u_s^c = \frac{\sigma_f B}{G} R. \quad (13)$$

Using $R \approx 50$ mm, $\sigma_f \approx 22$ MPa, $G = 19.0$ GPa, we find that $u_s^c \approx 29$ μ m, which is almost same maximum shear-wave induced displacement value (sin 20 μ m) as that estimated above using only a simple tensional strength theory.

From Fig.(10), we measured that the maximum S-wave particle displacement is about 4 μ m at gauge 1 and 7 μ m at gauge 3. The rise-time of the S-wave particle displacement

is about $10\mu\text{s}$. The magnitudes of all the experimental results are in agreement with the theoretical estimates of the two models (calculated from Eqs.(7), (10), (11) and (12)).

Acknowledgment

We thank Dr. R. Blandford for his critical and helpful comments and Jeff Batten, E. Gelle, M. Long, and V. Nenow for their technical support. We also thank Prof. G. Ravichandran for his advice on crack theory. Contribution number 6216, Division of Geological and Planetary Science, California Institute of Technology.

References

- [1] Freund, L. B., *Dynamic Fracture Mechanics*, Cambridge University Press, 336-340, 1990.
- [2] Klopp, R. W., A. L. Florence and J. K. Gran, Spherical wave interaction with cylindrical holes in large limestone specimens, in *International Conference on Mechanical and Physical Behavior of Materials under Dynamic Loading*, edited by Harding J., Les Editions de Physique, Les Ulis, 735-740, 1994.
- [3] Liu, C. and T. J. Ahrens, Shear wave generation from confined explosions in rocks, in *Proc. of Topical Conference on Shock compression of Condensed Matter*, in press, edited by S. C. Schmidt, American Institute of Physics, 1997.
- [4] Murphey, B. F., Particle motions near explosions in halite, *Journal of Geophysical Research*, 66, 947-958, 1961.
- [5] Rubin, A. M. and T. J. Ahrens, Dynamic tensile-fracture-induced velocity deficits in rock, *Geophysical Research Letters*, 18, 219-222, 1991.

PHYSICAL MECHANISMS OF QUARRY BLAST SOURCES

Terrance G. Barker
Keith L. McLaughlin

Maxwell Technologies, Inc.
8888 Balboa Ave, San Diego, CA 92123-1506

Contract No. F19628-95-C-0112
Sponsored by U.S. Department of Energy
Office of Nonproliferation and National Security
Office of Research and Development

ABSTRACT

Quarry blasts are a common cause of seismic signals in most parts of the world. Monitoring a Comprehensive Test ban Treaty requires routine identification of quarry blasts in a variety of settings where mining practices and local geology may vary. Kinematic models of quarry blasts can be used as source models for transportable discrimination methods. In this paper, we present results of modeling quarry blasts at the Black Thunder mine in the Powder River Basin of Wyoming. These studies have focused on the features of quarry blasts that are unique to that type of source and how these features can be used as discriminants. These features include the large amounts of vertical and horizontal mass movement during blasting, ripple firing which produces long duration sources, the fact that the source is at or near the surface and the quarry and bench geometry.

Inspection of the seismograms recorded at the Black Thunder mine shows that the ground motions are strongly influenced by local earth structure. Signals at 11 km have duration exceeding 25 seconds. Since structure is so important, and we have no independent measurements of seismic velocity, we have inferred a velocity model from the blast data. We began with kinematic models of the quarry blasts based on blast design. We computed synthetic seismograms from plane-layered earth models which were modified to match essential features of the observed seismograms. Having no absolute timing information, the features were the shape and duration of the signals. Comparison of the derived earth structure with recent borehole measurements give us confidence in the results. Having done this, we find that our next step is to modify the source model to include P to S conversion at the source and to increase the explosive coupling efficiency.

Key Words: seismology, quarry blasts, source identification

OBJECTIVE

Models of quarry blasts can be used to develop efficient and robust methods that discriminate quarry blasts from other sources. In this report, we present progress on modeling quarry blasts at the Black Thunder mine in the Powder River Basin of Wyoming.

RESEARCH ACCOMPLISHED

Data for three shots in the South Pit, described in Stump, et al. (1996), were made available to us by Dr. Craig Pearson at LANL. Data from several other shots in the south and West Pits were also provided. In the following, we focus on the three South Pit shots. The shots are two large ripple-fired cast shots, and a simultaneously detonated, contained coal shot (not cast). In Figure 1, we show the locations of the near-field recording sites relative to the cast shots done on Julian days 167 and 174 of 1996. Descriptions of the sensors can be found in Stump, et al. (1996). The plot shows the location of the pit (stippled area) at the time of these shots. Mining operations have proceeded from north to south, and the land is reclaimed after coal is removed. Thus, the highwall is on the south side of the pit. The cast blasts originated at the same location, with shot 167 (4.7 million lbs.) propagating to the right, ending at the edge of the pit, and shot 174 (2.3million lbs.) propagating to the left. The material was thrown to the NE by shot 167 and to the NW by shot 174. The coal shot (day 236) is west of shot 167 near the western end of the South Pit.

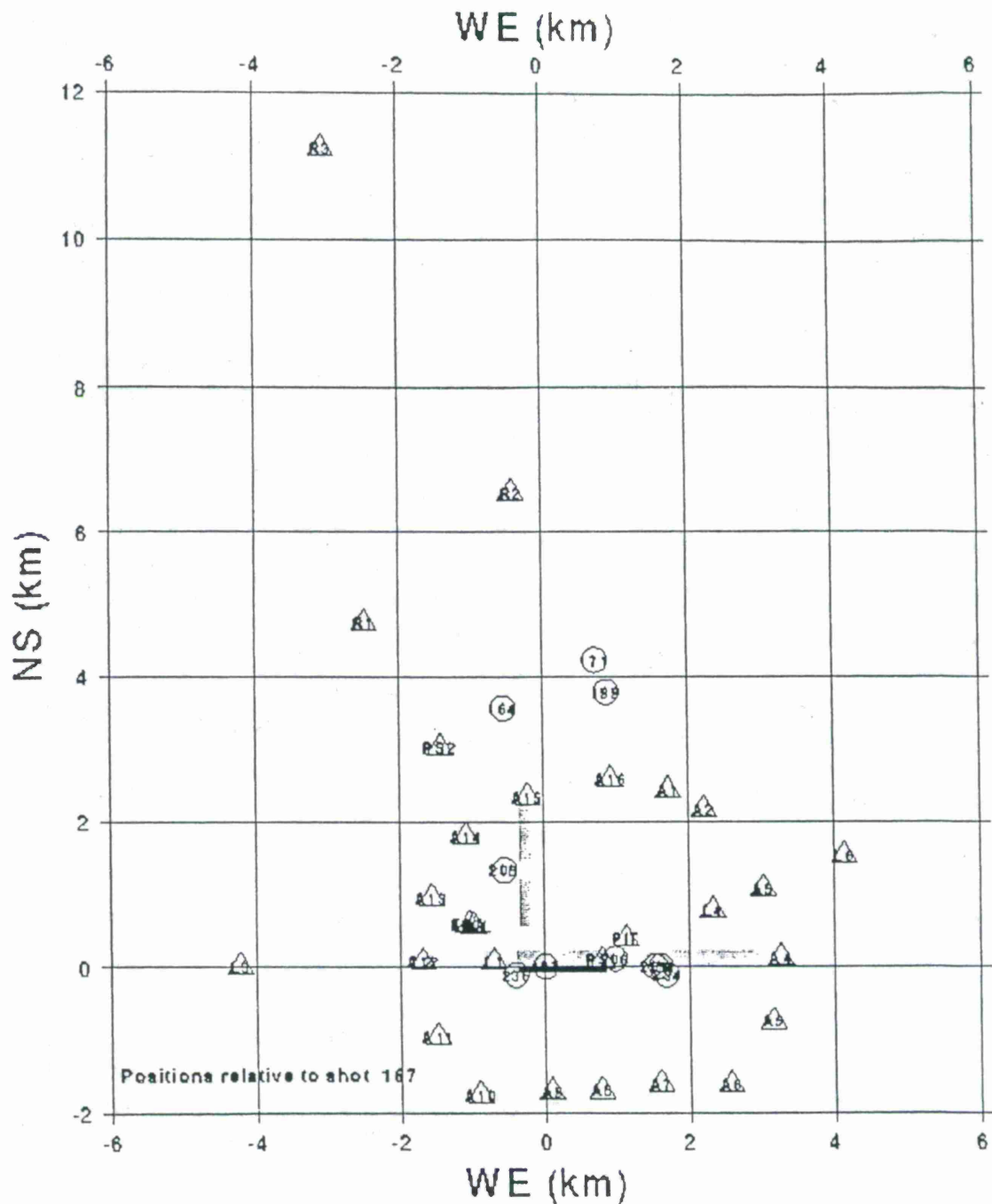


Figure 1. Locations of shots (circles) and recorders (triangles) relative to shot 167. The west and South Pits are shown as stippled areas.

We have used the source model in Barker, et al., (1993) to compute synthetic seismograms at station R3, which is 11.6 km NNW of shot 167. This model consists of an explosive component and a spall or mass movement component. An earth structure was derived by comparing synthetic with observed seismograms for the simultaneous coal shot (167). Absolute timing was unavailable so structure could not be obtained from travel

times. Although the records appear to be dominated by surface waves, narrow-band filter analysis yielded no consistent dispersion. The synthetic seismograms, which are dominated by 1 Hz energy, were sensitive to structure to a depth of about 200 m. The procedure was to vary the velocities in a model in which the upper 4 layers had thicknesses of 50 m, compute synthetic seismograms and compare the results to data. The shear velocities β of the layers were varied at 100 m/sec increments from 200 m/sec to 1000 m/sec, with the condition that the velocities increase with depth. Propagation Green's functions were computed using the full-wave integration code PROSE. The computed seismograms were most sensitive to β and Q_β , and nearly insensitive to compressional velocity α and Q_α , so the compressional values were set to be a multiple of the shear values. In spite of the relative insensitivity to α , it was possible to infer that the Poisson's ratio is high. The simultaneously detonated coal shot is modeled as a grid of 5 rows (parallel to the shot face) by 3 columns of charges of equal yield for a total yield of 40,000 pounds. Charges are spaced at 10 m intervals. The purpose of a coal shot is to bulk the material and a significant amount of movement of the overburden is observed. Thus, a signal due to spall is added to a signal from the explosive detonation for each charge. The initial vertical velocity of the spalled material is assumed to 3.5 m/sec. The tangential motion at station R3 is observed to be comparable to the radial motion, so we further assume that the spall involves horizontal movement as well as vertical. The formulation for combining the spall and explosive time functions with the Green's functions is given by Barker, et al. (1995).

The Green's functions were convolved with the source functions and the results compared visually to the observations. The diagnostic features used to judge the goodness of fit were signal duration and relative timing of apparent phases on the records. The structure derived in this manner is shown in Figure 2. The structure in the surficial 100 m was verified by borehole measurements made recently in the vicinity (R. Nigbor, Agbabian Associates, personal communication).

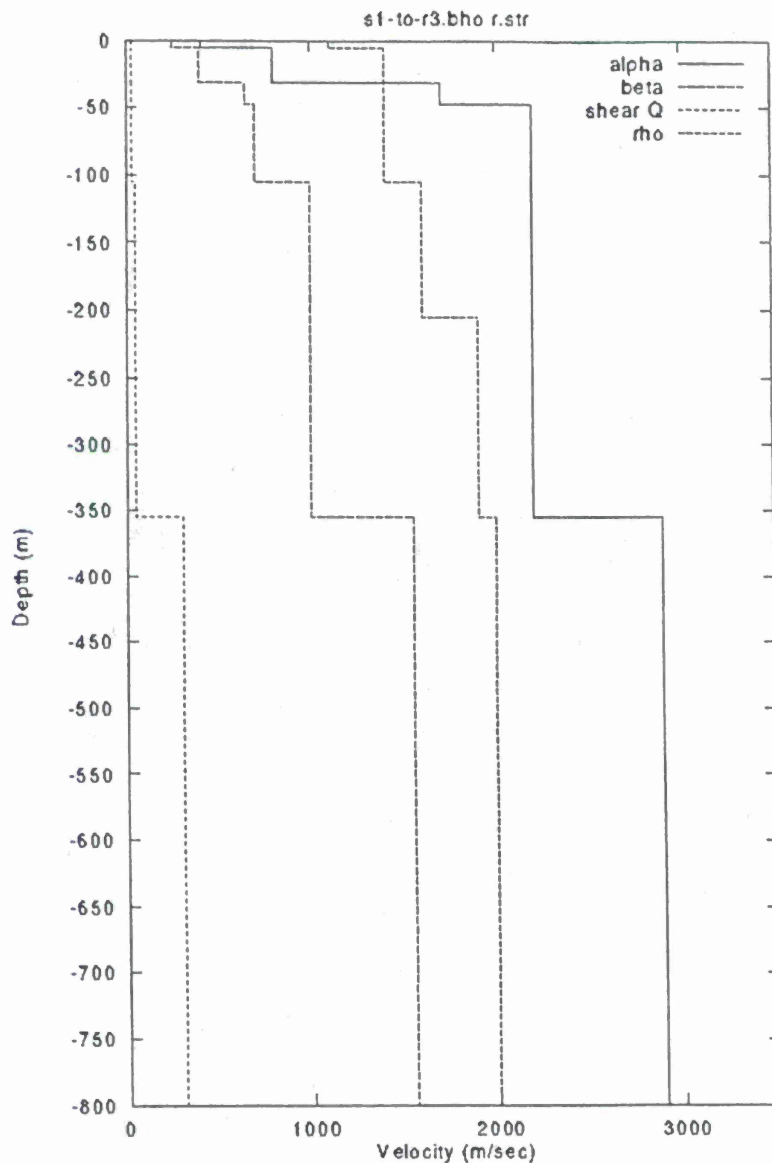


Figure 2. Earth structure used in the calculation of synthetic seismograms.

The cast blast (167) was modeled using 8 rows by 88 columns of charges, again at 10 m intervals. Time intervals followed the shot log design values which were that charges within columns were detonated at 35 ms intervals while rows were fired at times 125, 300, 500, 700, 900, 1200 and 1400 ms after the first row (Craig Pearson, LANL, personal communication). The initial velocity of the spalled material was assumed to be 3.5 m/sec with an initial angle of 30° from the horizontal. The shot was designed to throw material to the NE, which we assume to have occurred.

Tangential synthetic and observed seismograms from coal shot 236 at R3 are compared in Figure 3. The data provided to us had been processed to remove the instrument response, which introduced a long period component, which detracted from this analysis. Thus, we have high pass filtered the time series at a corner frequency of 1 Hz to remove long period artifacts. The peak ground displacements from the synthetic record

are within a factor of three of the observed record. The duration is matched fairly well, except for a small wave train after 25 sec. There is a phasing in the observed record that is roughly duplicated by the synthetic.

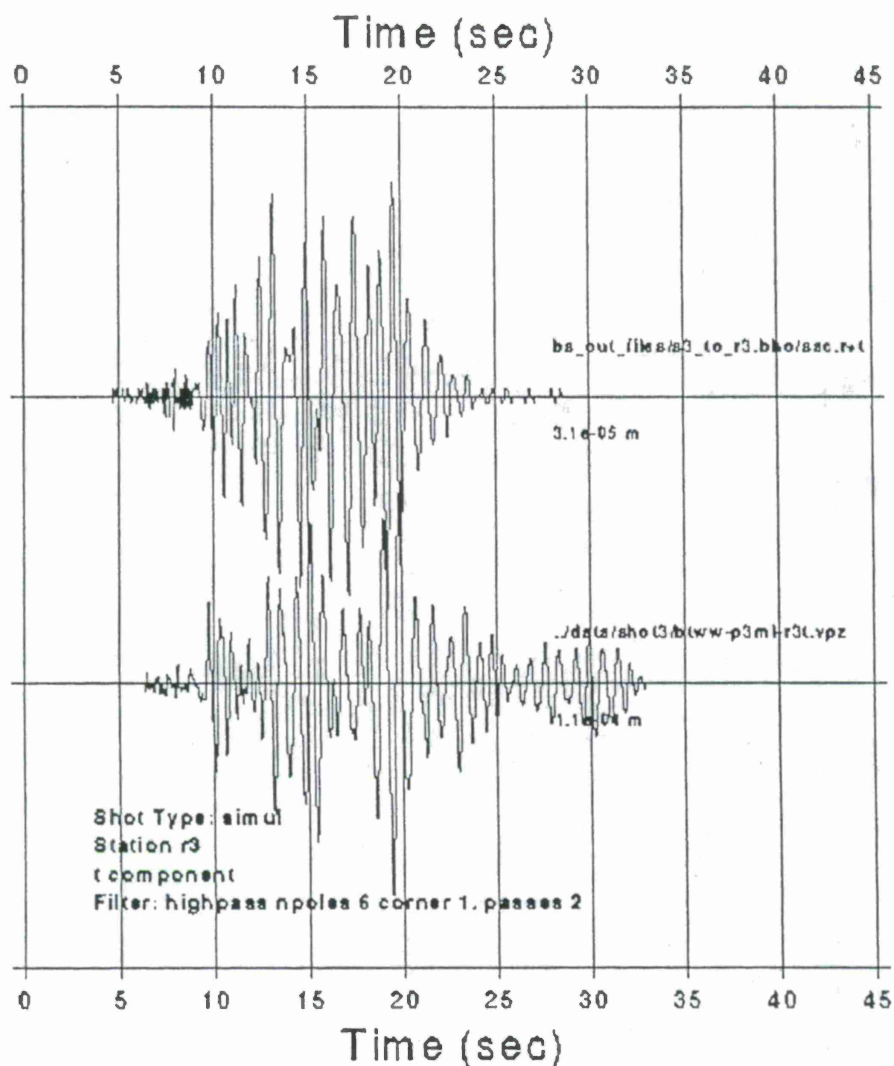


Figure 3. Tangential synthetic (upper) and observed (lower) displacement seismograms from coal shot 236 at R3. Peak displacements are indicated by the numbers below the time series (at the 30 sec line).

The corresponding vertical motions from the coal shot at R3 are shown in Figure 4. The synthetic vertical component seismograms include the explosive and vertical spall contributions. As with the tangential motions, the calculated peak displacement is about one third the observed value and the amplitude of the calculated signal arriving after 20 seconds is too small. To increase the amplitude of this late arriving energy, we tried increasing the values of Q in the surficial layers, but this did not produce the desired effect. We were unable to reproduce this late signal strength with reasonable values of seismic velocity in the shallow layers at this receiver location or at the closer station R2. Two explanations for this are (1) non-plane-layer propagation and (2) the actual source duration was longer than designed. A more complicated earth structure would not be

expected to increase signal strength at both distances, so we hypothesize that the signal duration was longer than designed. The large high-frequency signal at the start of the observed record is probably caused by charges that did not fire according to the planned intervals. Because the calculated amplitudes are smaller than observed for both tangential and vertical components, we conclude that explosive coupling is higher than in the model and that there is significant conversion of P to S energy from the explosives. The mode conversion is consistent with calculations showing the effect of the quarry bench (Barker, et al., 1994, McLaughlin, et al., 1994 and McLaughlin, et al., 1996).

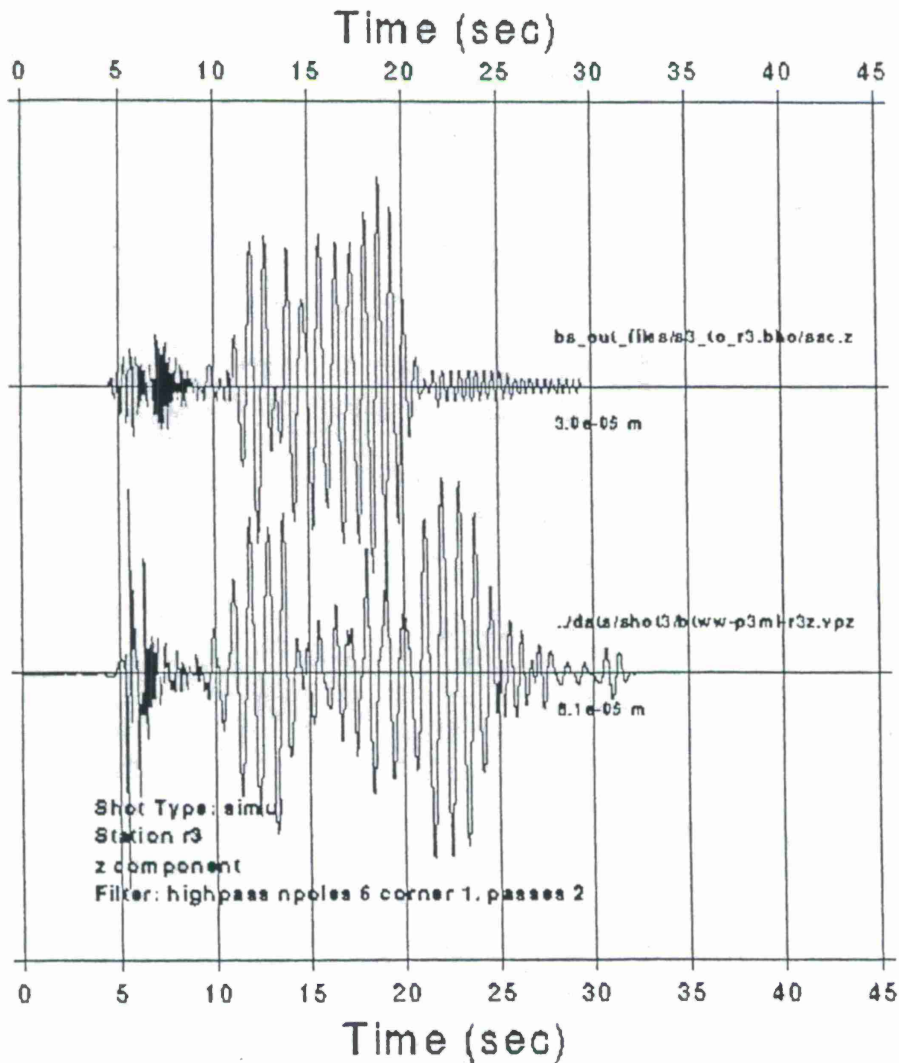


Figure 4. Vertical synthetic (upper) and observed (lower) displacement seismograms from coal shot 236 at R3. Peak displacements are indicated by the numbers below the time series (at the 30 sec line).

We now consider the cast blast 167. Figure 5 shows tangential synthetic and observed seismograms from this shot at R3. The peak displacement is about one-fifth the observed value. The duration of the signals is longer than the coal shot 167, consistent

with the increased duration of the blasting sequence. As with the coal shot, the relative amplitude of the late arriving signal (after 25 sec) is too small.

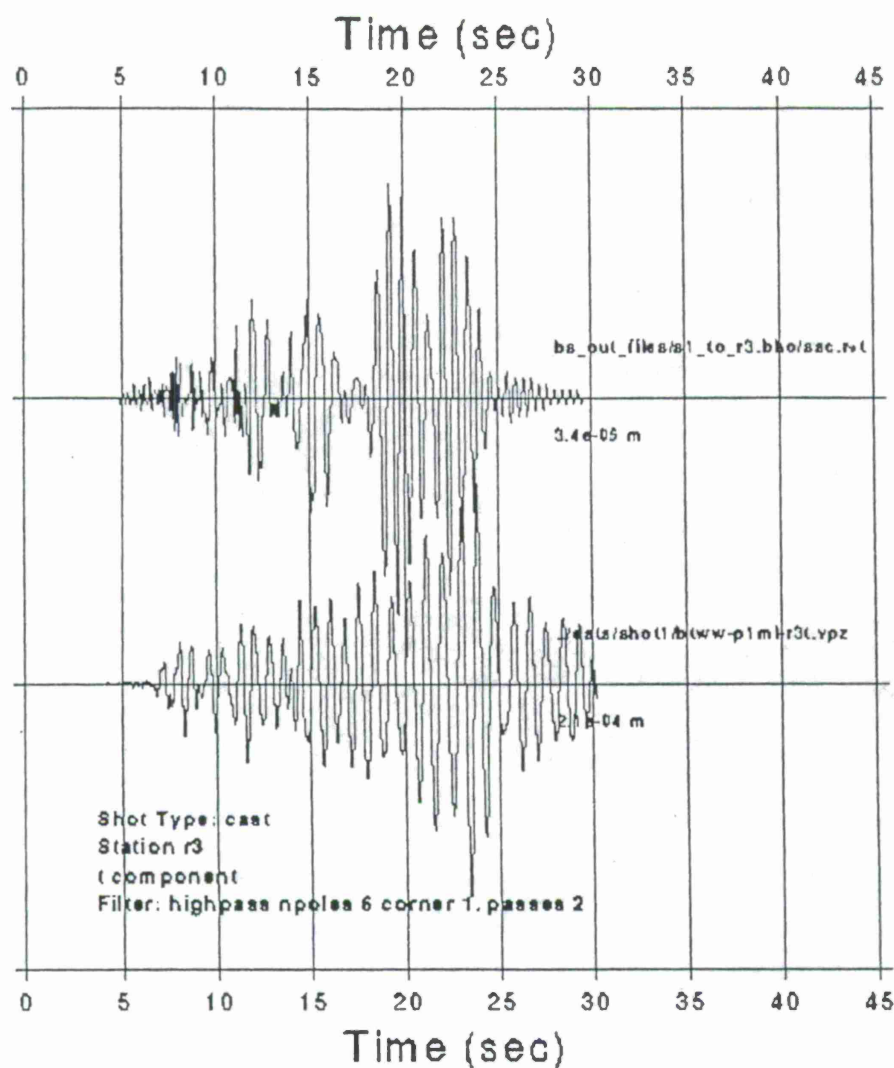


Figure 5. Tangential synthetic (upper) and observed (lower) displacement seismograms from cast blast 167 at R3. Peak displacements are indicated by the numbers below the time series (at the 30 sec line).

The vertical motions for the cast blast are shown in Figure 6. Again, the calculated peak amplitude and relative amplitude of late-arriving energy are less than observed. We conclude that we can achieve better agreement with observations by (1) increasing the source duration and (2) include P to S conversion from the explosive component of the source. We will make these modifications as well as examining other source-receiver combinations.

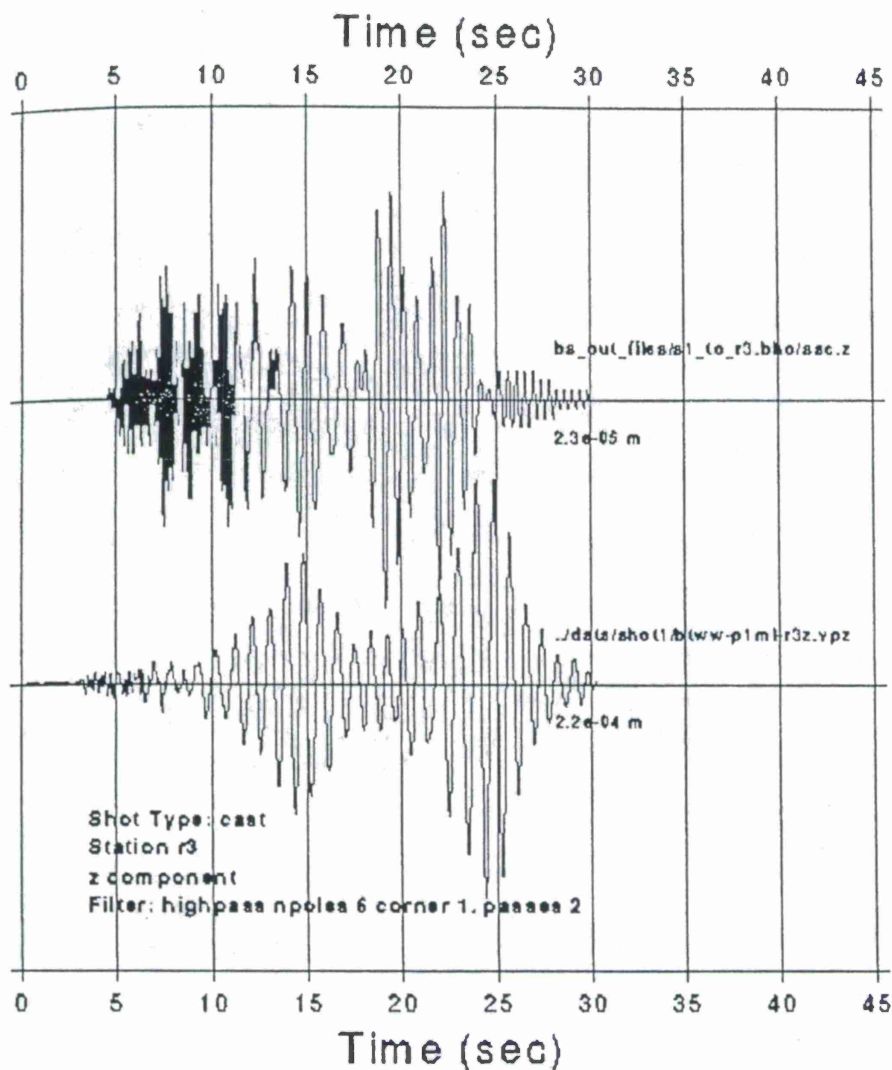


Figure 6. Tangential synthetic (upper) and observed (lower) displacement seismograms from cast blast 167 at R3. Peak displacements are indicated by the numbers below the time series (at the 30 sec line).

CONCLUSIONS AND RECOMMENDATIONS

Using synthetic seismogram methods, we have inferred earth structure at the Black Thunder mine site. We can achieve better agreement with observations of near-field data by (1) increasing the source duration and (2) include P to S conversion from the explosive component of the source. We will make these modifications as well as examining other source-receiver combinations

REFERENCES

Barker, T.G., K.L. McLaughlin and J.L. Stevens (1993), "Numerical Simulation of Quarry Blast Sources", Laboratory, SSS-TR-93-13859.

- Barker, T.G., K.L. McLaughlin, J.L. Stevens and S.M. Day (1993), "Numerical Models of Quarry Blast Sources: the Effects of the Bench", S-CUBED Semiannual Report to Phillips Laboratory, SSS-TR-93-13915.
- Barker, T.G., K.L. McLaughlin J.L. Stevens (1996), "Physical Mechanisms of Quarry Blast Sources", Proceedings of the 18th Annual Seismic Research Symposium on Monitoring a Comprehensive Test Ban Treaty, edited by J.F. Lewkowitz, J.M. McPhetres and D.T. Reiter, Annapolis MD.
- Day, S.M. and K.L. McLaughlin (1991), "Seismic source Representations for Spall", Bull. Seism. Soc. Am., 81, pp. 191-201.
- Hedlin, M.A.H., F.L. Vernon, J.B. Minster and J.A. Orcutt (1996), "Experiments in Regional Monitoring of Small Seismic/Acoustic Events", Proceedings of the 18th Annual Seismic Research Symposium on Monitoring a Comprehensive Test Ban Treaty, edited by J.F. Lewkowitz, J.M. McPhetres and D.T. Reiter, Annapolis MD.
- McLaughlin, K.L., T.G. Barker and J.L. Stevens (1994), "Numerical Simulation of Quarry Blast Sources", S-CUBED Final Report to Phillips Laboratory, SSS-TR-94-14418.
- McLaughlin, K. L., J. Bonner and T. G. Barker (1996), "Seismic Source Mechanisms for Quarry Blasts Observed Rayleigh and Love Wave Radiation Patterns from a Texas Quarry", submitted to *Bull. Seism. Soc. Am.*
- Stump, B.W. and R.E. Reinke (1988), "Experimental Confirmation of Superposition from Small-Scale Explosions", Bull. Seism. Soc. Am., 78, pp. 1059-1073
- Stump, B.W., D.C. Pearson, R.L. Martin, P.E. Harben, C.L. Edwards, D. Baker, K. Kihara, K. Dalrymple, J.P. Lewis, D. Rock and R. Boyd, "The Black Thunder Regional Seismic Experiment", LANL Report LAUL-95-3980.

MODELS OF NONSPHERICAL UNDERGROUND NUCLEAR EXPLOSIONS IN NONLINEAR AND INHOMOGENEOUS ENVIRONMENTS

Ari Ben-Menahem

Faculty of Mathematical Sciences
Weizmann Institute of Science
76100 Rehovot, Israel

ABSTRACT

It is proposed that between the permanently deformed volume and the linear zone there exist a micro fractured boundary layer having the constitution of a five-parameter Murnaghan solid, exhibiting both geometrical finite-strain and physical cubic terms in the energy density function. Alternatively, a regime with infinitesimal strain, fixed Landau-parameters, and strain-dependent Lamé parameters can be adopted, both paradigms obeying the same nonlinear wave equation. Waves excited by the source carry the signature of the boundary layer into the linear zone, all the way to the far field.

The mathematical realization of this program consists of the application of the longwave Born-Rayleigh approximation to the Landau-Goldberg equation. The perturbed field, governed by an additional force-system, is represented as a multiple expansion of eigenvector spherical harmonics of the unperturbed background field.

It is revealed that the boundary layer tends to amplify the source-field by a factor which may reach 2 for explosions in preexisting cavities and 1.5 for earthquakes. Hence, the frequency-independent amplification will effectively limit the true seismic decoupling of underground nuclear explosions to a limiting value under 70 and tend to inflate the true seismic-moments of earthquakes. In general amplification is more pronounced for compressional sources than for shear sources. In the latter case, the nonlinear theory suggests the introduction of two new source parameters: a virtual radius associated with the *yield-limit* of rocks and a larger radius associated with the *elastic-limit* of rocks.

Keywords: Nonlinearity, earthquakes, source-mechanism, elastic-wave theory, nuclear explosions.

OBJECTIVE: To obtain new criteria for the identification of clandestine underground nuclear explosions in the magnitude range $3 \frac{1}{2}$ - $5 \frac{1}{2}$. These criteria are based upon the following physical and geometrical differences between natural earthquake sources and nuclear explosion sources and environments:

- I. *Geometry* of linear two-dimensional faults vs non-spherical cavities.
- II. Scattering characteristics due to *inhomogeneities* in the source environment
- III. Effects of a *nonlinear* boundary layer at the source.

RESEARCH ACCOMPLISHED:

- I. Effects of geometry are solved in paper 1 (see list of references).
- II. Effects of scattering due to inhomogeneities are solved in paper 2 (see list of references).
- III. Effects of Nonlinearity are preliminarily treated in paper 3.

CONCLUSIONS:

- a. In fully decoupled explosions, the size of the cavity is deducible from the spectrum of far-field displacement signals. In contradistinction of earthquake sources, explosions in nonspherical cavities behave strongly like non-double-couple earthquakes. (Paper 1.)
- b. Scattering caused by source-induced *inhomogeneities* generate SH, Lg and Love waves such that Sg/Pn spectral ratios can be employed as a diagnostic tool in the discrimination of explosions from natural seismic events. Provided that an adequate inversion procedure is formulated, the spectral ratios can be used to obtain the explosion source parameters (Paper 2.)
- c. Assuming the existence of a *nonlinear* boundary layer, it is revealed that the boundary layer tends to *amplify* the source-field by a factor which may reach two for explosions in preexisting cavities. Hence, decoupling will be limited to a value of 70 or so.

RECOMMENDATIONS:

Reopen the study of *decoupling*, taking into account strain-dependent Lamè parameters in the region between the permanently deformed volume and the linear zone, extending my proposed theory to fifth order terms in the energy density function.

Study in greater detail the radiation of waves from cavities of *special geometrical form*, in an effort to achieve maximal decoupling and/or extreme SH signals. In particular, it is of interest to know how close can a predesigned cavity mimic a shear dislocation.

Study in greater detail the effects of *pre-stress* fields at the sources neighborhood on the near-field amplitudes. This is of importance if the cavity's symmetry axis is not aligned with the principal direction of the pre-stress tensor.

References

1. Ben-Menahem, A. and O. Mikhailov, Multipole radiation of seismic waves from explosions in nonspherical cavities and its application to signal identification. *Journ. Acoust. Soc. Amer.* 97, 2675-2698. AFOSR, Grant No. F49620-93-1-042DEF.
2. Ben-Menahem, A., Seismic source functions for explosions in a non-spherical cavity embedded in a scattering environment: application to the regional discrimination of nuclear explosions and earthquakes. *Geophysical Journal International* 128, 97-124, 1997.
3. Ben-Menahem, A., Effect of a nonlinear boundary layer on the radiation from earthquakes and explosions. *Geophysical Jour. International* 129, 1445-1466, 1997.

LOW AND HIGH FREQUENCY Lg FROM EXPLOSIONS - NEW INSIGHTS

Indra N. Gupta and Robert A. Wagner

Multimax, Inc.

1441 McCormick Drive, Largo, Maryland 20774

Sponsored by U.S. Department of Energy
Office of Nonproliferation and National Security

Office of Research and Development

Contract No. F19628-95-C-0176

ABSTRACT

Most discriminants make use of the prominent regional phase Lg, and so a clear understanding of the generation of both low and high frequency Lg from explosions is essential for improved and reliable monitoring of the Comprehensive Test Ban Treaty. Our research provides valuable new information regarding the origin of both low and high frequency Lg. The low-frequency (up to about 2 Hz) part of the Lg spectra (including the most prominent peaks and nulls) appears to be due to the near-source scattering of explosion-generated Rg into S. The spectral peaks seem to be associated with resonance caused by sharp impedance contrast in the source region, whereas the spectral nulls seem to be due to the CLVD source associated with the explosion sources. The high-frequency Lg appears to originate from explosion generated cracks around the source region. Evidence for these results comes mostly from analysis of broadband regional data from over 40 Nevada test site (NTS) explosions and several explosions from the Kazakh test site (KTS).

Near-field data from the Yucca Flat (NTS) explosion Starwort (26 April 1973) shows resonance at a period associated with the group velocity minimum in Rg which occurs close to a period equal to four P-wave transit times between the free surface and the Paleozoic rock surface. The Lg spectra show a prominent peak at the same resonance frequency, suggesting near-source scattering of Rg into S. Such a mechanism appears to be occurring for other NTS explosions as well, as evidenced by significant correlation between the period of the observed peak in the network-averaged Lg spectra and known depths of the Paleozoic layer for 27 Yucca Flat explosions. In agreement with earlier research, the observed null frequencies in the Lg VD spectra are in excellent agreement with those expected from Rg due to a CL source at about one-third the shot depth. A comparison of the phase ratios, Pg/Lg and Pn/Lg from the explosion Dalhart (13 October 1988), nearly surrounded by earlier shots with their estimated damage zones intersecting its shot point, with those from the earliest shot Hearts, suggests that the high frequency (about 8 to 16 Hz) S or Lg from explosions is due to the generation of new cracks created by a tamped explosion. Evidence supporting a cracking mechanism also comes from a comparison of deeper and shallower shots for their frequency dependence of Pg/Lg and Pn/Lg for shots at NTS and KTS, respectively. By improving our understanding of broadband Lg from explosions, these results make significant contribution to seismic monitoring of the CTBT.

Keywords: Lg, explosions, resonance, cracking, Lg/P, regional phases, scattering of Rg, source discrimination, seismic monitoring, NTS, Kazakh, CTBT

OBJECTIVE

The phase ratio Lg/P has been known to be an effective regional discriminant but the mechanisms of generation of neither low nor high frequency Lg from explosions are fully understood. An improved understanding of the generation of broadband Lg will therefore significantly improve seismic monitoring of the Comprehensive Test Ban Treaty.

RESEARCH ACCOMPLISHED

Resonance in Rg and Spectral Peak in Lg from Yucca Flat Explosions

Near-field displacement time histories from several nuclear tests in the Yucca Flat region suggested vertical compressional-wave resonance with the resonance period independent of explosion yield and depth (Rodean, 1981). There is a considerable impedance mismatch between the Paleozoic rocks and the overlying alluvium and tuff. The wave period was found to be equal to four P-wave transit times between the free surface and the Paleozoic rock surface (Rodean, 1981). This resonance phenomenon may be related to Rayleigh wave generation by explosions because, as noted by Hudson and Douglas (1975), when a sharp impedance contrast exists in a plane-layered model of the crust, the Rayleigh wave group velocity minimum in the fundamental mode occurs close to a period equal to four times the travel times of P-waves from the surface to the interface. An example of such resonance, as observed in the Fourier spectrum of displacement time history from a near-field velocity gauge for the Yucca Flat explosion, Starwort (26 April 1973), is shown in Figure 1a (after Rodean, 1981, Fig. 3). Multi-tapered Lg spectra of Starwort, as recorded at the four broadband stations (MNV, KNB, LAC, and ELK) of the Lawrence Livermore National Lab's (LLNL) network, were obtained by using 51.2 sec long windows and corrected for attenuation (more details are given in Gupta *et al.*, 1997). These spectra clearly indicate distinct peaks at the same resonance frequency of about 0.5 Hz (Figure 1b) at each of the four stations as well as in the network-averaged spectrum, known to suppress path effects and enhance source effects (Blandford, 1981). These results suggest near-source scattering of Rg into S and Lg, similar to that indicated by earlier studies of low-frequency Lg from explosions (*e.g.* Gupta *et al.*, 1992; Patton and Taylor, 1995; Gupta *et al.*, 1997).

In order to investigate the possibility that such a mechanism involving resonance and the scattering of Rg into S may be operating for other Yucca Flat explosions as well, we analyzed Lg from 29 Yucca Flat explosions well recorded at the LLNL network (Figure 2a). There is considerable variation in the thickness of low velocity sediments overlying the higher velocity Paleozoic layer in the Yucca Flat region (see, *e.g.* Gaffet, 1995, Figs. 2 and 3). An approximately east-west vertical cross-section across the region (Gaffet, 1995, Fig. 3) shows large lateral variations in the depth of the Paleozoic layer. The shot locations in Figure 2a include eight shots approximately along a vertical section, as shown in Gaffet (1995, Figure 3), in which the depth of the Paleozoic layer first gradually increases and then decreases. The network-averaged spectra of these eight shots show prominent peaks (marked by arrows pointing down) at frequencies that initially decrease with increasing depth of the Paleozoic layer and then increase as depth of the Paleozoic layer decreases (Figure 2b). It seems therefore that

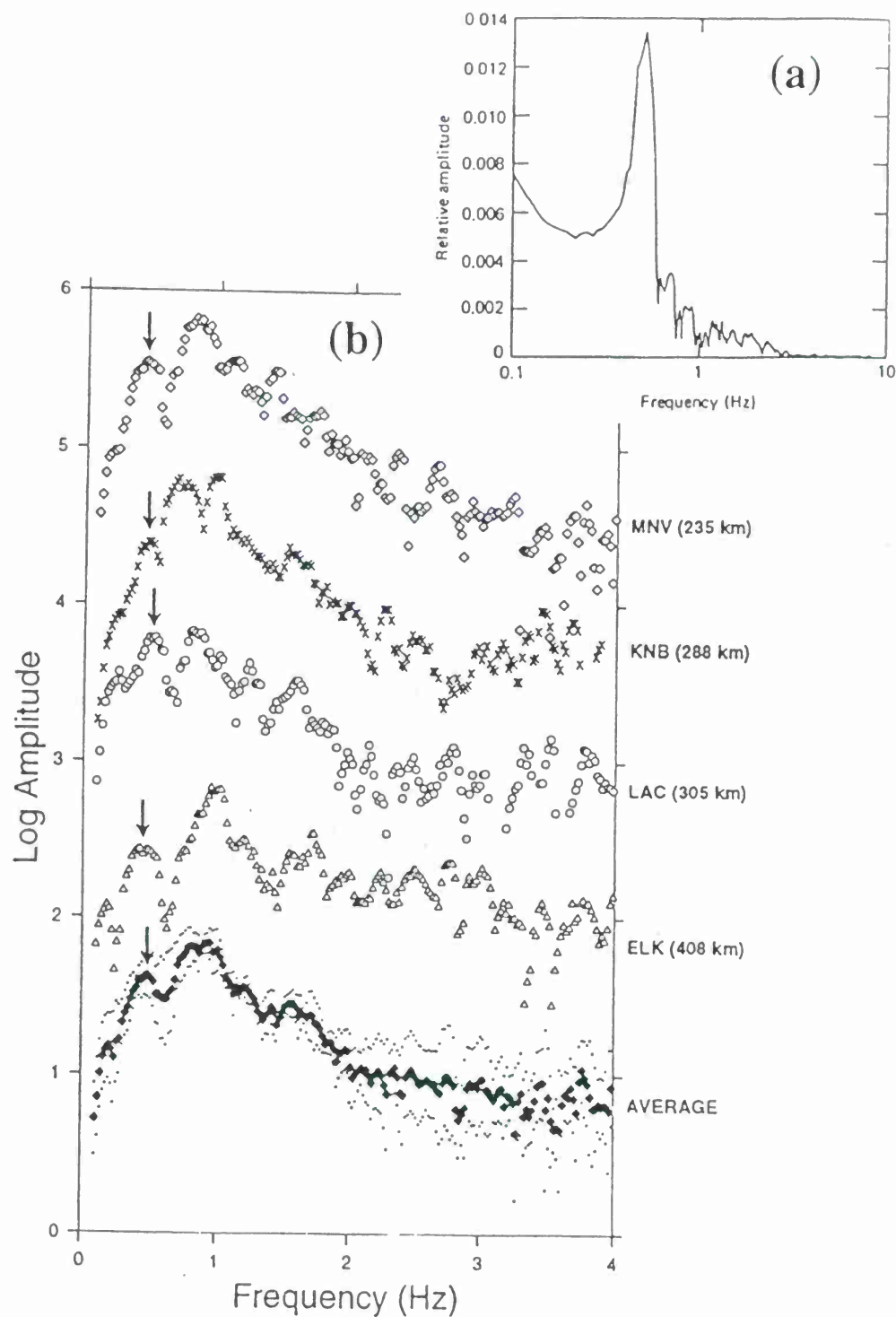


Figure 1. (a) Fourier spectrum of near-field data from Starwort indicating resonance at frequency of about 0.5 Hz. (b) Single-station and network-averaged Lg spectra, based on LLNL stations, for Starwort, each indicating a spectral peak at about 0.5 Hz.

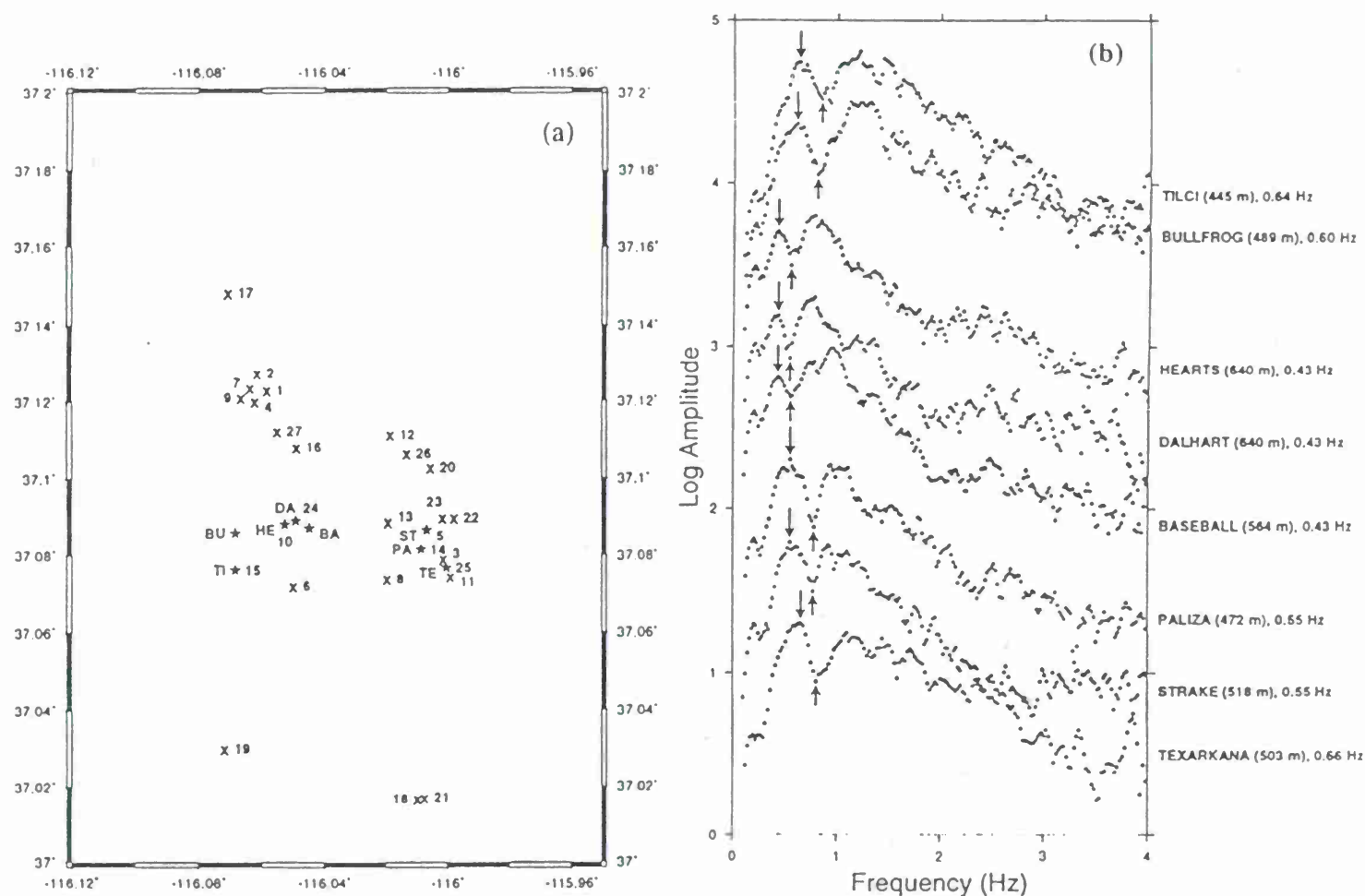


Figure 2. (a) Location map of 29 Yucca Flat explosions used in study of spectral peaks in Lg, including eight approximately along a vertical profile (indicated by \star). (b) Network-averaged Lg spectra of eight shots showing prominent peaks (marked by arrows pointing down) with spectral variation correlating with depth of the Paleozoic layer. The explosion names are given along with their shot depths and frequency of the observed peak in Lg spectra.

the Lg spectra of these eight explosions show prominent peaks with spectral variations consistent with resonance and the scattering of Rg into S, similar to those observed for Starwort.

Data for calculating the exact P-wave transit times between the free surface and the Paleozoic rock surface are not available for the Yucca Flat explosions. Furthermore, the large lateral variations in the sub-surface of the shot region makes the validity of P waves propagating through plane-parallel layers and leading to resonance questionable. However, one would expect generally larger transit times when the Paleozoic layer is deeper so that the resonance period should generally increase with depth of the Paleozoic layer. This does seem to be the case as shown by the linear regression plot in Figure 3a, based on data from 27 Yucca Flat explosions for which ground truth (including depth of the higher-impedance Paleozoic layer) was known. It seems therefore that the low-frequency peaks in the Lg spectra of Yucca Flat explosions are due to resonance and scattering of Rg into S.

Spectral Nulls in Lg from Yucca Flat Explosions

Following our earlier work suggesting that near-source scattering of explosion-generated Rg into S is responsible for the low-frequency Lg from nuclear explosions at both NTS and Kazakh test sites (Gupta and Zhang, 1996; Gupta *et al.*, 1997), we investigated the dependence of spectral nulls in Lg on shot depths for the same 27 Yucca Flat explosions. The same network-averaged spectra as used for determining the resonance peaks were used to observe the spectral null frequencies. Patton and Taylor (1995) suggested that the explosion-generated Rg must originate mainly from a compensated linear vector dipole (CLVD) source and the low-frequency null in the observed Lg is due to an excitation null in Rg from a buried CLVD source. For a homogeneous semi-infinite medium, the CLVD spectral null frequency, $f(\text{NULL})$, occurs approximately at $V/(16h)$ where V is the P-wave velocity and h is depth of the CLVD source so that the null period is directly proportional to source depth and inversely proportional to medium velocity. Moreover, a plot of $V/f(\text{NULL})$ versus h should have a slope of about 16 and zero intercept. In order to test these theoretical considerations, strictly valid only for a homogeneous half-space, we plotted the observed null periods versus shot depth (Figure 3b) and $V/f(\text{NULL})$ versus shot depth (Figure 3c). The linear regressions, with zero intercept, show significant correlations on both plots. Moreover, the slope in Figure 3c has a value of about 4.63, which is $4.63/16$, or approximately one-third of the slope expected on a plot based on depth of the CLVD source. This means, in agreement with our earlier results (Gupta *et al.*, 1997), that the depth of the CLVD source is about one-third of the shot depth, and a determination of the Lg null frequency of an explosion may provide an estimate of its shot depth.

High Frequency Lg from Explosions

It is important to understand the origin of high frequency S from explosions so that the scope and limitations of the regional discriminant Lg/P, often reported to perform better at higher frequencies, are clearly known. A suggestion has been made that the high frequency S or Lg from explosions may be due to the generation of new cracks created by a tamped explosion (Blandford, 1995). However, the evidence presented so far has probably not been fully

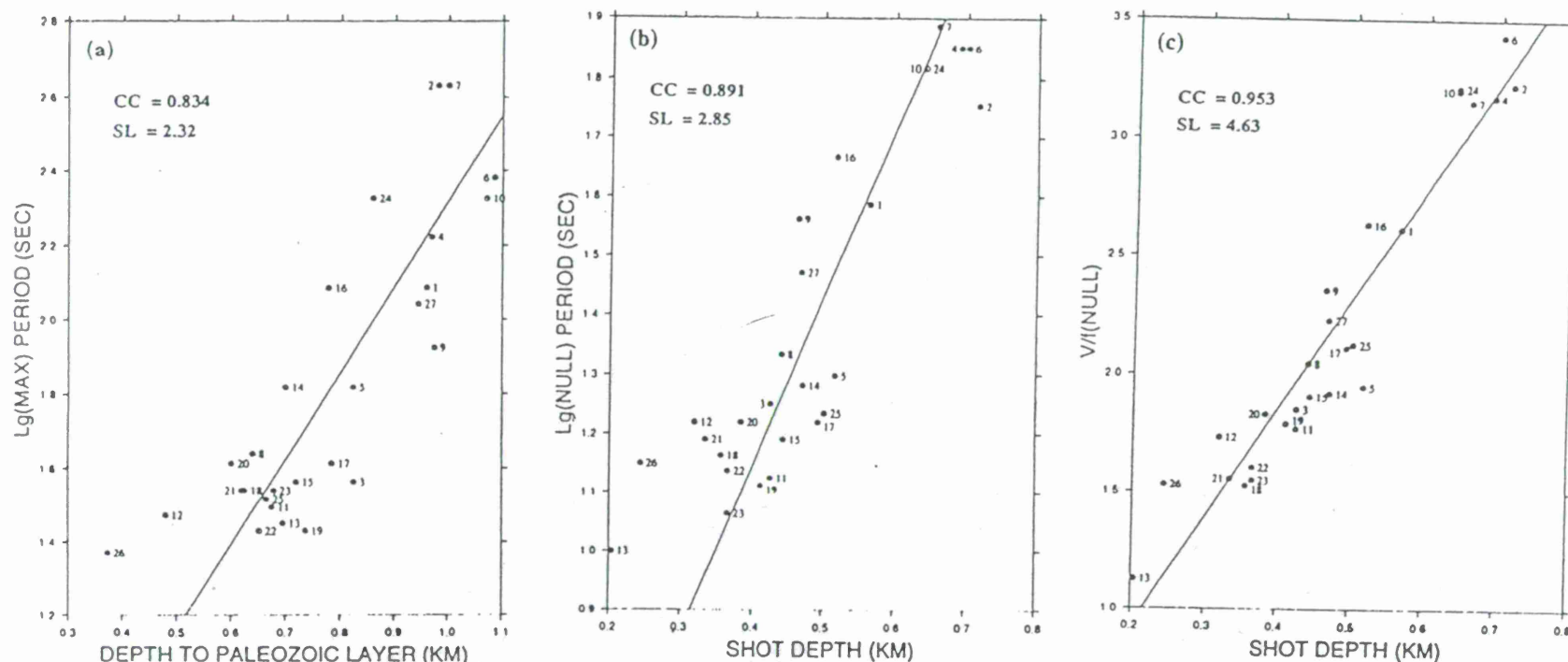


Figure 3. (a) Plot of $\text{Lg}(\text{MAX})$ Period versus depth of the Paleozoic layer for 27 Yucca Flat explosions. Linear regression, with zero intercept, shows a correlation coefficient of 0.834 with mean slope of 2.32; (b) Plot of $\text{Lg}(\text{NULL})$ Period versus shot depth for the same 27 explosions. Linear regression, with zero intercept, shows a correlation coefficient of 0.891 with mean slope of 2.85; (c) Plot of $V/f(\text{NULL})$, where V is the overburden velocity, versus shot depth for the same 27 explosions. Linear regression, with zero intercept, shows a correlation coefficient of 0.953 with mean slope of 4.63.

convincing (Murphy and Barker, 1995). We examined the origin of high frequency S from explosions by analyzing the regional phases Pn, Pg, and Lg from several closely-located and other Yucca Flats (NTS) explosions recorded at common stations so that path effects are minimized.

The Yucca Flat explosion, Dalhart (13 Oct. 88) is nearly surrounded by several earlier shots with their estimated damage zones intersecting its shot point (Figure 4). A comparison of the spectral ratios Pg (12.8 sec)/Lg (25.6 sec) and Pn (3.2 sec)/Lg (25.6 sec) from Dalhart, with those from the earliest shot Hearts, is shown in Figure 5. Nearly all stations and their average show significant differences at higher (above 8-10 Hz) frequencies. Similar comparison between Hearts and Baseball, with their damage zones well separated from each other, showed no such differences. A possible explanation for the relative deficiency of higher frequency Lg from Dalhart is lack of new explosion-generated cracks because its shot-point lies within the previously damaged zone.

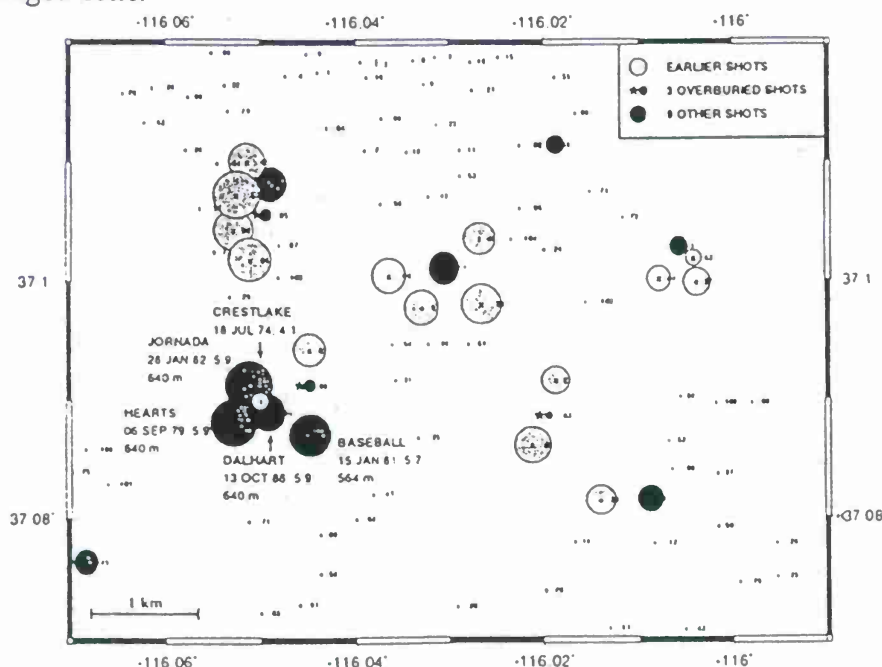


Figure 4. Location map of 106 explosions in the northern Yucca Flat region. The size of damage zone (assumed to be three times the cavity radius) is shown for Dalhart, 12 other shots, and for earlier shots with epicenters within 500 m. At least four earlier shots were so close to DALHART that their damage zones probably produced a highly fractured region around its shot point.

Evidence supporting a cracking mechanism also comes from a comparison of deeper and shallower shots for their frequency dependence of Pg/Lg, derived by linear regression of average Pg/Lg versus shot depth for the nine Yucca Flat shots with locations shown in Figure 4. As suggested by the results in Figure 6, differences in Pg/Lg due to variation in shot depth are larger for both high (greater than 6 Hz) and low (less than 4 Hz) frequencies. The increasing difference at higher frequency may be due to the generation of high frequency S by explosion-generated cracks that are inhibited by overburden pressure, as suggested by Blandford (1995). Similar results were obtained from analysis of Pn/Lg from 14 Kazakh shots recored at WMQ

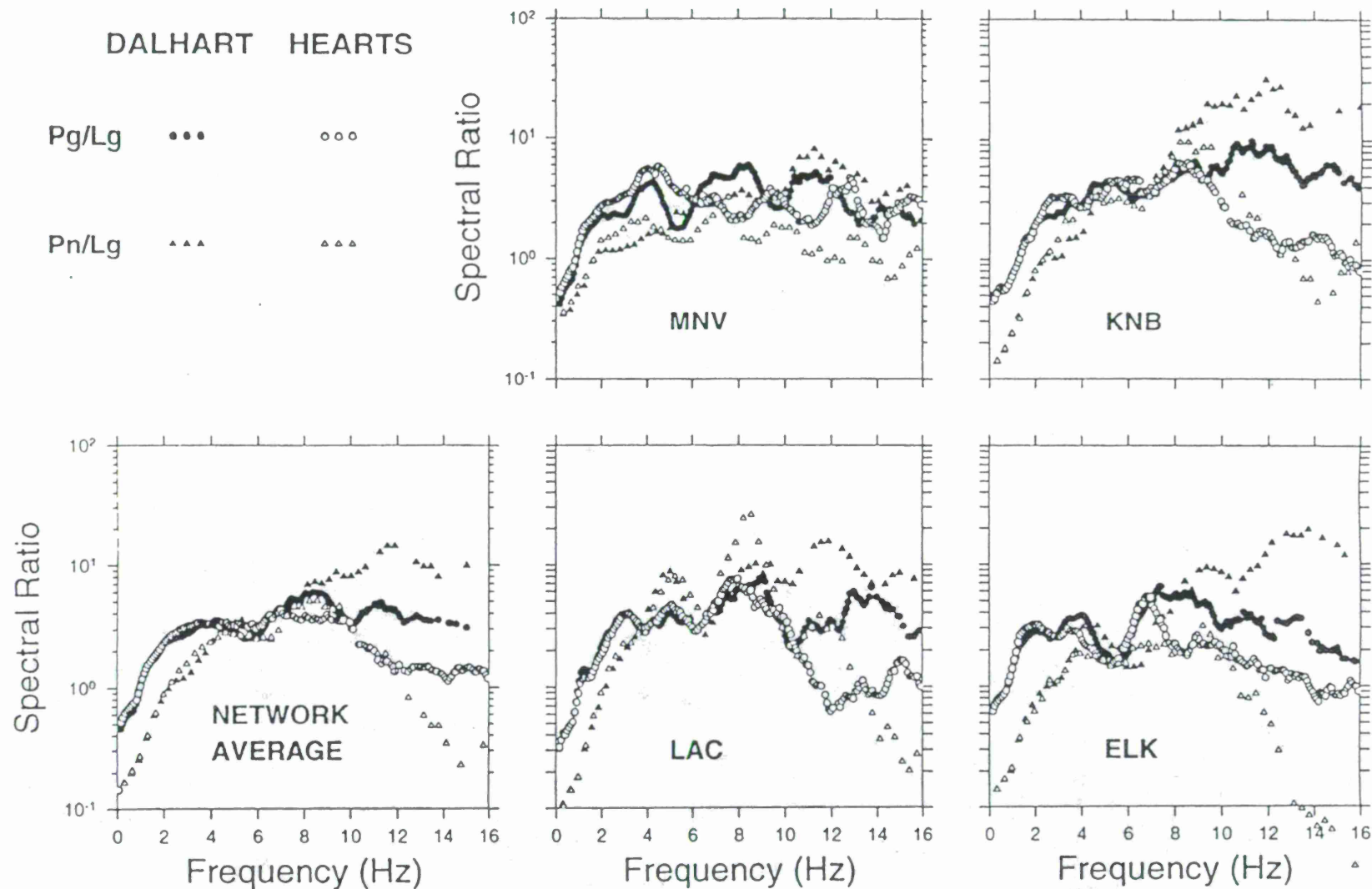


Figure 5. Spectral ratios of Pg/Lg and Pn/Lg indicating large differences at higher (above 8-10 Hz) frequencies between Dalhart and Hearts at nearly all stations. The relative deficiency of higher frequency Lg from Dalhart is probably due to lack of new explosion-generated cracks because of the damage zones from earlier shots intersecting its shot point.

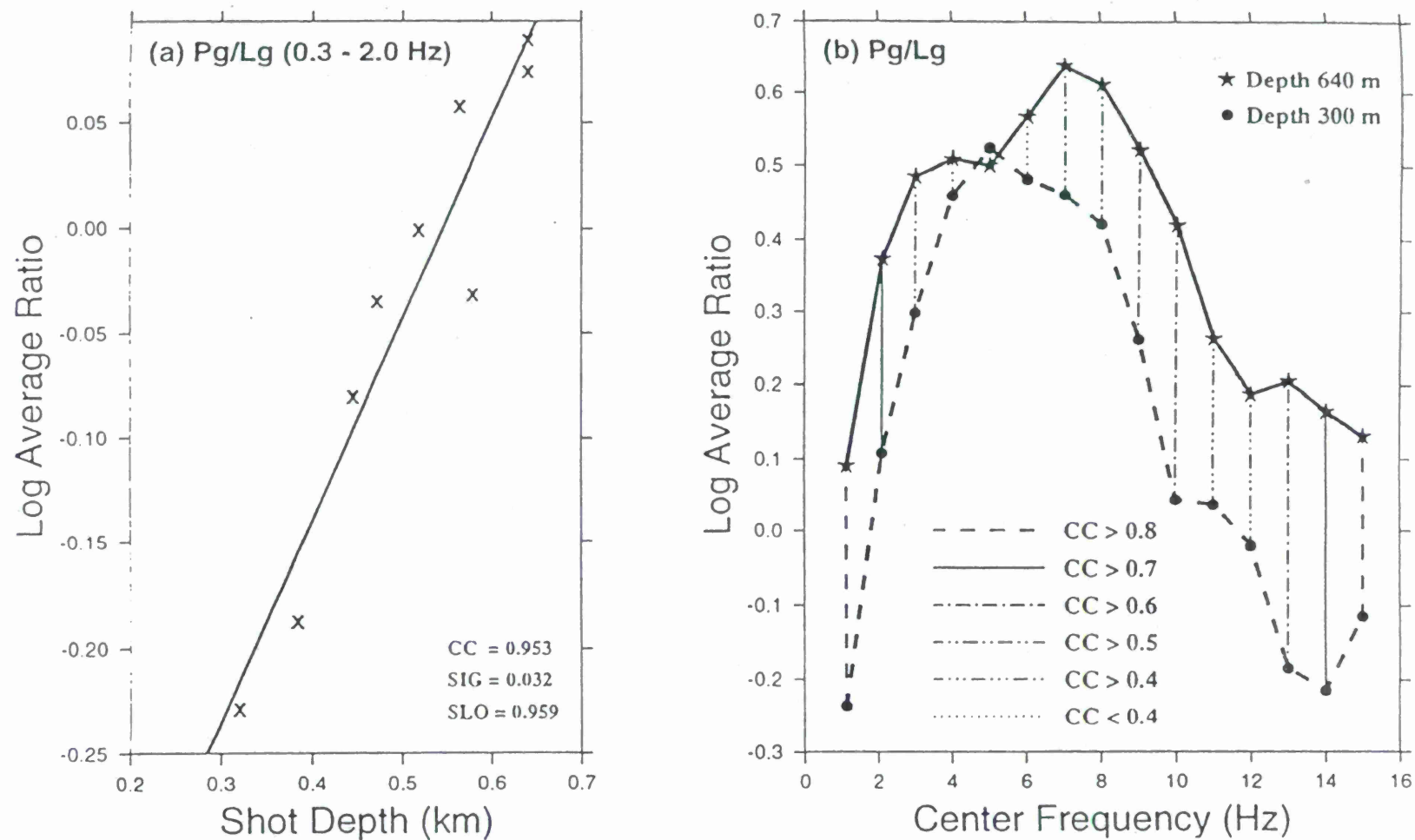


Figure 6. Network-averaged spectral differences in Pg/Lg for shallow (depth 300 m) and deep (depth 640 m) Yucca Flat explosions obtained by linear regression of average ratio versus shot depth for nine shots. An example of regression is shown in (a); each frequency band is about 2 Hz wide. Differences in Pg/Lg appear to be larger for both high (greater than 6 Hz) and low (less than 4 Hz) frequencies. The increasing difference at higher frequency may be due to the generation of high frequency S by explosion-generated cracks that are inhibited by overburden pressure, whereas that at lower frequency is probably due to scattering of explosion-generated Rg into S.

CONCLUSIONS AND RECOMMENDATIONS

Remarkable agreement between the observed resonance frequency in the near-field data and prominent peak in the Lg spectra at regional distances of Starwort, combined with the observed increase in the period of Lg(MAX) with depth of the Paleozoic layer for many Yucca Flat explosions, provide further support to the Rg-to-S scattering mechanism. These results lead to new insight into the generation of the low-frequency Lg from Yucca Flat explosions by providing an understanding of both peaks and nulls in their spectra. Comparison of Pg/Lg and Pn/Lg and their dependence on shot depth, for explosions at both NTS and KTS, suggest that the high frequency Lg is due to explosion-generated cracks, in agreement with Blandford's (1995) hypothesis. A clear understanding of the broadband characteristics of regional phases and their dependence on various near-source parameters is essential if successful seismic monitoring techniques developed in one region are to be transported to other locations. It is recommended that the broadband characteristics of Lg be further investigated for regions other than the NTS so that the role of near-source scattering of explosion-generated Rg is clearly understood and exploited for deriving source and near-source information.

References:

- Blandford, R. R. (1981). Seismic discrimination problems at regional distances, in *Identification of Seismic Sources - Earthquake or Underground Explosion*, E. S. Husebye and S. Mykkeltveit, Editors, D. Reidel Publishing Co., Dordrecht, The Netherlands, 695-740.
- Blandford, R. R. (1995). Discrimination of mining, cratering, tamped, and decoupled explosions using high frequency S-to-P ratios, AFTAC-TR-95-002, Patrick AFB, Florida.
- Gaffet, S. (1995). Teleseismic waveform modeling including geometrical effects of superficial geological structures near to seismic sources, *Bull. Seism. Soc. Am.* 85, 1068-1079.
- Gupta, I. N., W. W. Chan, and R. A. Wagner (1992). A comparison of regional phases from underground nuclear explosions at East Kazakh and Nevada test sites, *Bull. Seism. Soc. Am.* 82, 352-382.
- Gupta, I. N. and T. R. Zhang (1996). Study of low-frequency Lg from explosions at Nevada, Kazakh, Lop Nor, and Azgir test sites, *PL-TR-96-2153*, Phillips Laboratory, Hanscom Air Force Base, Massachusetts, 328-337.
- Gupta, I. N., T. R. Zhang, and R. A. Wagner (1997). Low-frequency Lg from NTS and Kazakh nuclear explosions - observations and interpretation, *Bull. Seism. Soc. Am.* 87, October.
- Hudson, J. A. and A. Douglas (1975). Rayleigh wave spectra and group velocity minima, and the resonance of P waves in layered structures, *Geophys. J. R. astr. Soc.* 42, 175-188.
- Murphy, J. R. and B. W. Barker (1995). A comparative analysis of the seismic characteristics of cavity decoupled nuclear and chemical explosions, *PL-TR-95-2177*, Phillips Laboratory, Hanscom Air Force Base, Massachusetts.
- Patton, H. J. and S. R. Taylor (1995). Analysis of Lg spectral ratios from NTS explosions: implications for the source mechanisms of spall and the generation of Lg waves, *Bull. Seism. Soc. Am.* 85, 220-236.
- Rodean, H. C. (1981). Inelastic processes in seismic wave generation by underground explosions, in *Identification of Seismic Sources - Earthquake or Underground Explosion*, E. S. Husebye and S. Mykkeltveit (eds), D. Reidel, Dordrecht, Holland, 97-189.

Waveform Correlation Methods for Identifying Populations of Calibration Events

David B. Harris
Lawrence Livermore National Laboratory

Sponsored by U.S. Department of Energy
Office of Nonproliferation and National Security
Office of Research and Development
Contract W-7405-ENG-48
Comprehensive Test Ban Treaty Research and Development Program, ST482B

ABSTRACT

An approach is presented for systematically screening large volumes of continuous data for repetitive events identifiable as mining explosions on the basis of temporal and amplitude population characteristics. The method extends previous work of Israelsson (1991) and Riviere-Barbier and Grant (1993) on event clustering through waveform correlation with a new source-region-specific detector. The new (signal-subspace) detector generalizes the matched filter and can be used to increase the number of events associated with a given cluster, thereby increasing the reliability of diagnostic cluster population characteristics.

The method can be applied to obtain "bootstrap" ground truth explosion waveforms for testing discriminants (see Walter et al., this volume), where actual ground truth is absent. The same events, if associated to a particular mine, may help calibrate velocity models. The method may also assist earthquake hazard risk assessment by providing what amounts to blasting logs for identified mines. These cluster event lists can be reconciled against earthquake catalogues to screen explosions, otherwise hard to identify, from the catalogues.

The method is demonstrated with data from the Gafsa, Tunisia MEDNET station (GFA). From 88 days of intermittent continuous data, 5 clusters were identified with 4 containing 106 probable explosions and the fifth containing 10 probable earthquakes and aftershocks.

Keywords: Waveform correlation, ground truth, calibration, detection, matched filter, event clustering, Middle East, North Africa.

The author would like to acknowledge Dr. M. Hfaiedh of the Tunisian National Institute of Meteorology for supplying information on several earthquakes recorded by GFA.

OBJECTIVE

The objective of this research is to develop reliable, automated procedures for acquiring explosion event data in the absence of hard ground-truth information. The specific target events are repeatable mining explosions conducted over periods of months or years. The CTBT applications are to develop efficient algorithms for screening mining explosions, and to create libraries of ground-truth events for developing travel-time calibrations and testing discriminants.

This study extends previous work by Israelsson (1991) and Riviere-Barbier and Grant (1993) on event clustering through waveform correlation. These methods rely upon the observation that events at a single mine often produce highly repeatable seismic waveforms. Waveform correlation measurements identify repeatable waveforms, and cluster analyses of those measurements identify groups of events presumed to originate at discrete source locations. These event groups may be associated with particular mines by estimating the event locations and comparing these locations with a list of known mine positions. The result is a set of ground-truth events suitable for testing and calibrating location algorithms and discriminants.

Pursuing this cluster identification approach is difficult when the existence of mines in a particular region is unknown or the mine positions are uncertain. If the region is also a source of natural seismic activity, it may be difficult to rule out the possibility that observed event clusters are aftershock sequences. Attributing event clusters to mines also may be difficult when the events are small and observed by a single three-component station. Single station locations may not be sufficiently accurate to correlate estimated event locations with known mine positions.

A solution to the source identification problem might be found by examining several population characteristics of event clusters. The distribution of events by hour of day (Walter and Harris, 1997) is an especially potent clue. Mining events usually occur during working hours; earthquake origin times are random. The long-term temporal distribution of events is also diagnostic of source type. Explosions should occur more or less regularly at a mine when viewed on the scale of months or years, but earthquakes will be highly episodic with an exponential decay in frequency of occurrence (following Omori's law). The magnitude distribution of events also may be diagnostic. Explosions may have a restricted range of sizes corresponding to economically viable scales of production; aftershock magnitudes should exhibit a wider, logarithmic magnitude distribution with no minimum (other than that set by the detection floor of the station).

The reliability of cluster identification improves as the number of events in a cluster increases. This study introduces a method for systematically screening large volumes of continuous data to identify larger numbers of events belonging to defined clusters. The principal innovation is a detection algorithm, generalizing the matched filter, which is sensitive only to events from specific source regions. The detector is generated from master events chosen to represent a specific event cluster. By virtue of its pattern-matching design, the algorithm is substantially more sensitive than STA/LTA algorithms at negligible false alarm rates.

RESEARCH ACCOMPLISHED

Procedure

The proposed procedure for acquiring large number of clustered events is outlined in Figure 1, and has been applied to data from the MEDNET station GFA in Tunisia. The general strategy is to obtain a "seed" pool of about 200 events by conventional means for initial definition of

event clusters, then to construct specialized detectors (one for each cluster) designed to "sweep up" all of the events originating from the cluster sources. For the collection of the initial event pool, any suitable detector may be used. Experience with GFA and another MEDNET station MDT (see Walter et al., this volume) has shown that a simple STA/LTA detector applied to about 3 months of data results in about 400 - 500 detections that can be culled to about 200 legitimate events for initial clustering.

Hierarchical agglomerative algorithms are suitable for defining event clusters (single-linkage, Israelsson, 1991; complete-linkage, Riviere-Barbier and Grant, 1993). These procedures require waveform correlation calculations for all distinct pairs of events. A computer program was prepared to compute the correlations for the available three-component data from GFA using the method outlined in Harris (1991). This method compensates for small errors of alignment and some variations in source time function between waveforms. The program requires P arrival times to be picked to an accuracy of about 1 second. It then extracts and correlates waveform segments beginning before the pick time (5 seconds before for the GFA data) and extending beyond the last significant arriving energy (for a total duration of 75 seconds in the GFA data). A single-link algorithm was applied to the GFA correlation measurements to define clusters. This algorithm sorts the available correlations into descending order, then groups events sequentially using correlation measurements as links. The grouping begins with the largest correlation, then proceeds to successively smaller correlations until a stopping threshold level is reached.

Once the clusters are defined, special detectors, referred to here as signal-subspace (or just subspace) detectors, are derived for each cluster from representative master events. These detectors are extensions of matched filters and are designed to trigger on waveforms representable as linear combinations of the master event waveforms (Harris, 1991). Conventional matched filters operate by correlating successive segments from a continuous data stream against a single representative waveform. Subspace detectors operate by correlating successive segments against the best linear combination of master event waveforms from a collection of events (best in the sense of maximizing the correlation). The term "signal-subspace" refers to the fact that the master event waveforms can be thought of as a basis for a subspace in the vector space of all signals.

Subspace detectors may have an advantage over matched filters, because a single master event waveform may not always represent well the range of Green's functions, mechanisms and time histories that may occur for sources within even a very small geographic area (such as a single mine). By synthesizing a range of Green's functions, source mechanisms, and time histories from the master event basis, these algorithms have the potential to match and detect more events originating in the region being characterized.

Subspace detectors can be used to reprocess the continuous data stream to increase the number of events belonging to the clusters already defined. Typically, these events are smaller than those detected with the STA/LTA algorithm with lower SNR. Nevertheless, their presence increases the reliability of discerned patterns in the cluster populations that identify source type.

Results

Figure 2 shows the position of the MEDNET station GFA used as a test case for the new procedure. The figure shows the known (primarily phosphate) mines in the region, and the location of one earthquake identified by the procedure. The waveforms of two representative clusters are shown in Figure 3; the first cluster corresponds to a nearby (31 km) mine at the major phosphate mining district of Mdhila. Waveforms of this cluster frequently show marked air waves.

Although the P and S phases are not well separated in these events, the presence of air waves (A) permits an accurate estimate of range (from A-P times).

In all, 5 clusters were chosen for detailed examination. Subspace detectors were derived for these five, then applied to the same 88 days of data originally screened by the STA/LTA detector. The detection threshold was set low enough to trigger on events smaller than those detected by the STA/LTA algorithm, yet no false alarms occurred. Frequently, the number of new events discovered by the subspace detectors significantly increased the size of the clusters (for example, by a factor of two for Cluster 4 shown in Figure 3).

Events in 4 of the 5 clusters are regularly distributed, suggesting continuing mine operations. Figures 4 and 5 show the distribution of detected events over the entire period for which data are available from GFA. The detail plot in Figure 5 suggests that the larger mines shot frequently, almost daily. The events of Cluster 4, however, fall within a narrow time range and are not uniformly distributed. The disparity between this cluster and the other 4 is most clear in Figure 6a, which shows the distribution of events by hour of day. Events of the 4 regular clusters all fall within normal working hours; Cluster 4's events are scattered at random throughout day and night. Cluster 4 also exhibits an anomalous amplitude distribution; it has the largest and the smallest events, with most events concentrated at the low end of the amplitude scale. The temporal and amplitude patterns of this cluster are more consistent with an aftershock sequence than with normal open-pit mining.

CONCLUSIONS AND RECOMMENDATIONS

Calibration of seismic discriminants and travel times is hampered in regions of the Middle East and North Africa by the paucity of ground truth information. The waveform correlation procedure presented in this paper provides one means of "bootstrapping" ground-truth information from as little as three months of data (provided nearby mines are consistently active). The method shows promise for identifying the number of mines (or at least mining complexes) in a region and, perhaps, even providing a surrogate blasting log for each distinguishable mine. The key is to identify enough events in each cluster that statistical analyses of temporal and amplitude patterns provide reliable clues to the origins of the clustered events.

Future work will concentrate on the systematic application of this procedure to stations in the Middle East and North Africa which provide continuous data. The results of this procedure also are applicable to earthquake hazard risk assessment (by keeping earthquake catalogs clean of blasting events), and may form the basis for collaborative work with regional seismologists.

References

- Harris, D. (1991) A waveform correlation method for identifying quarry explosions, *Bulletin of the Seismological Society of America*, Vol. 81, No. 6, pp. 2395-2418.
- Israelsson, H. (1991), Correlation of waveforms from closely spaced regional events. *Bulletin of the Seismological Society of America*, Vol. 81, No. 6, pp. 2177-2193.
- Riviere-Barbier, F. and L. Grant (1993), Identification and location of closely spaced mining events, *Bulletin of the Seismological Society of America*, Vol. 83, No. 5, pp. 1527-1546.
- Walter, W. and D. Harris (1997), Calibration of CTBT monitoring stations for event identification: MDT, Morocco, abstract for SSA '97 92nd Annual Meeting in *Seismological Research Letters*, Vol. 68, No. 2, pp 294.

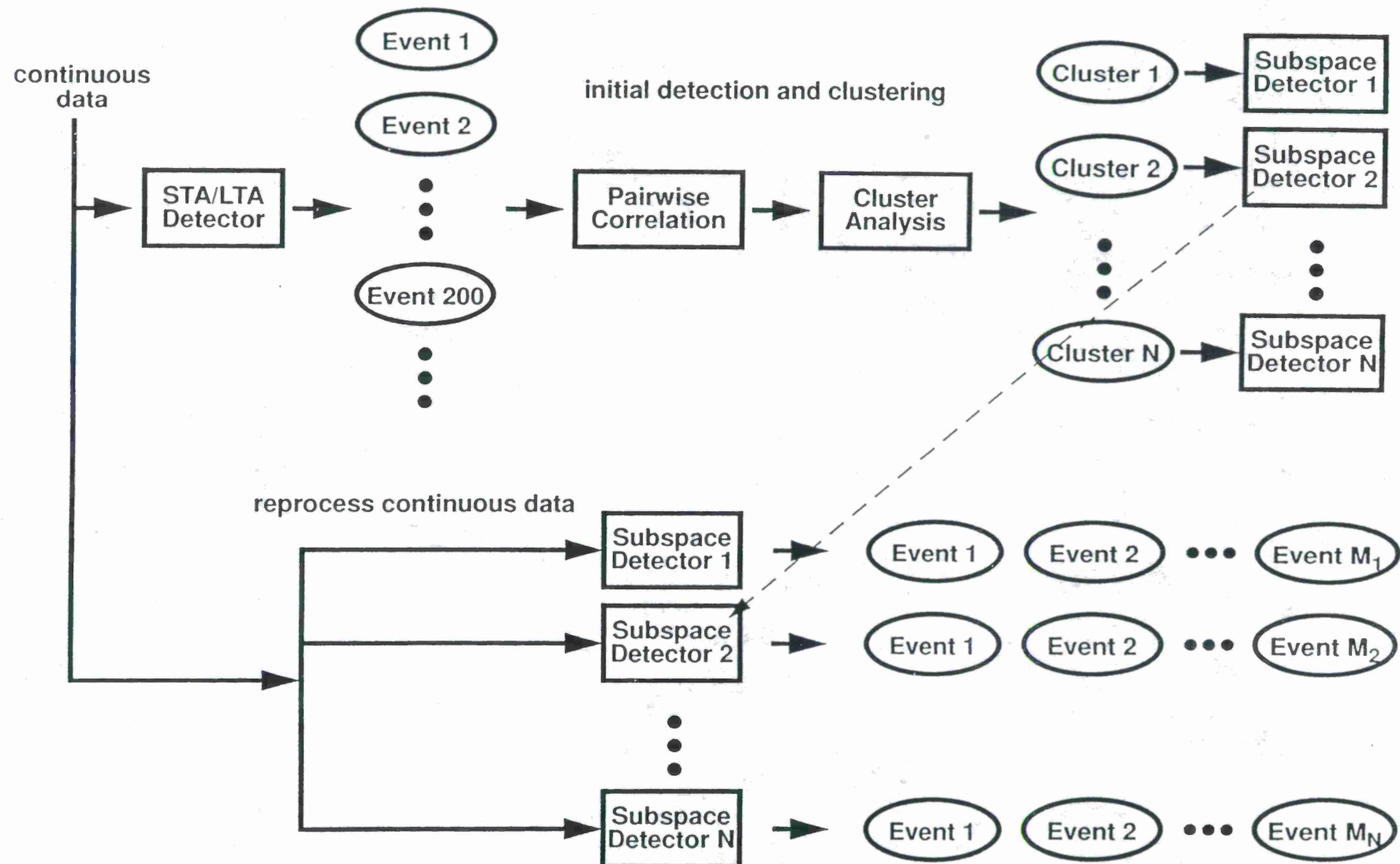


Figure 1 Schematic of procedure for detecting large numbers of clustered events. The method has three main steps: detect, cluster and reprocess (with specialized detectors). The first two steps are essentially the same as previous waveform correlation methods; the third enhances sensitivity to smaller events.

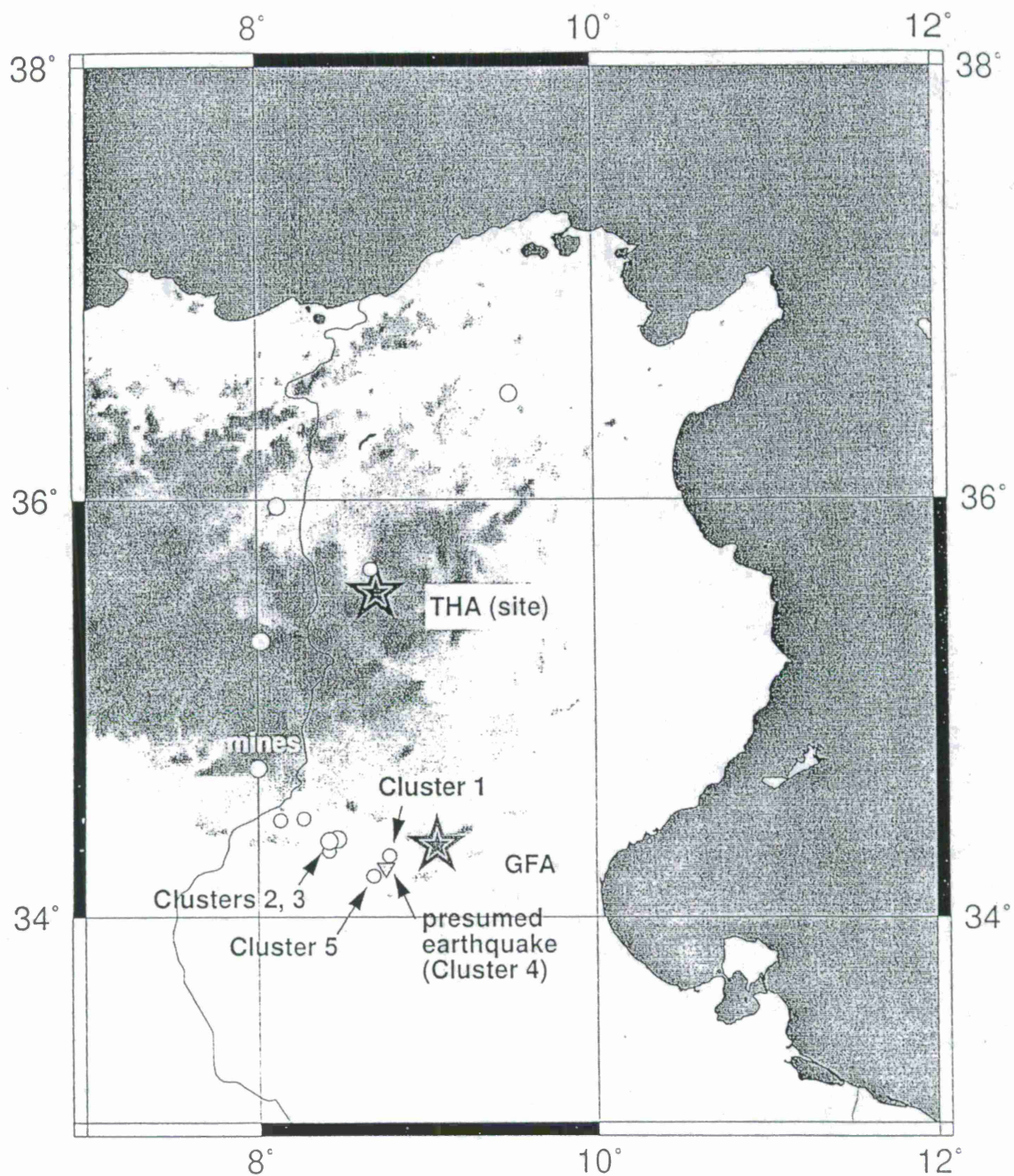
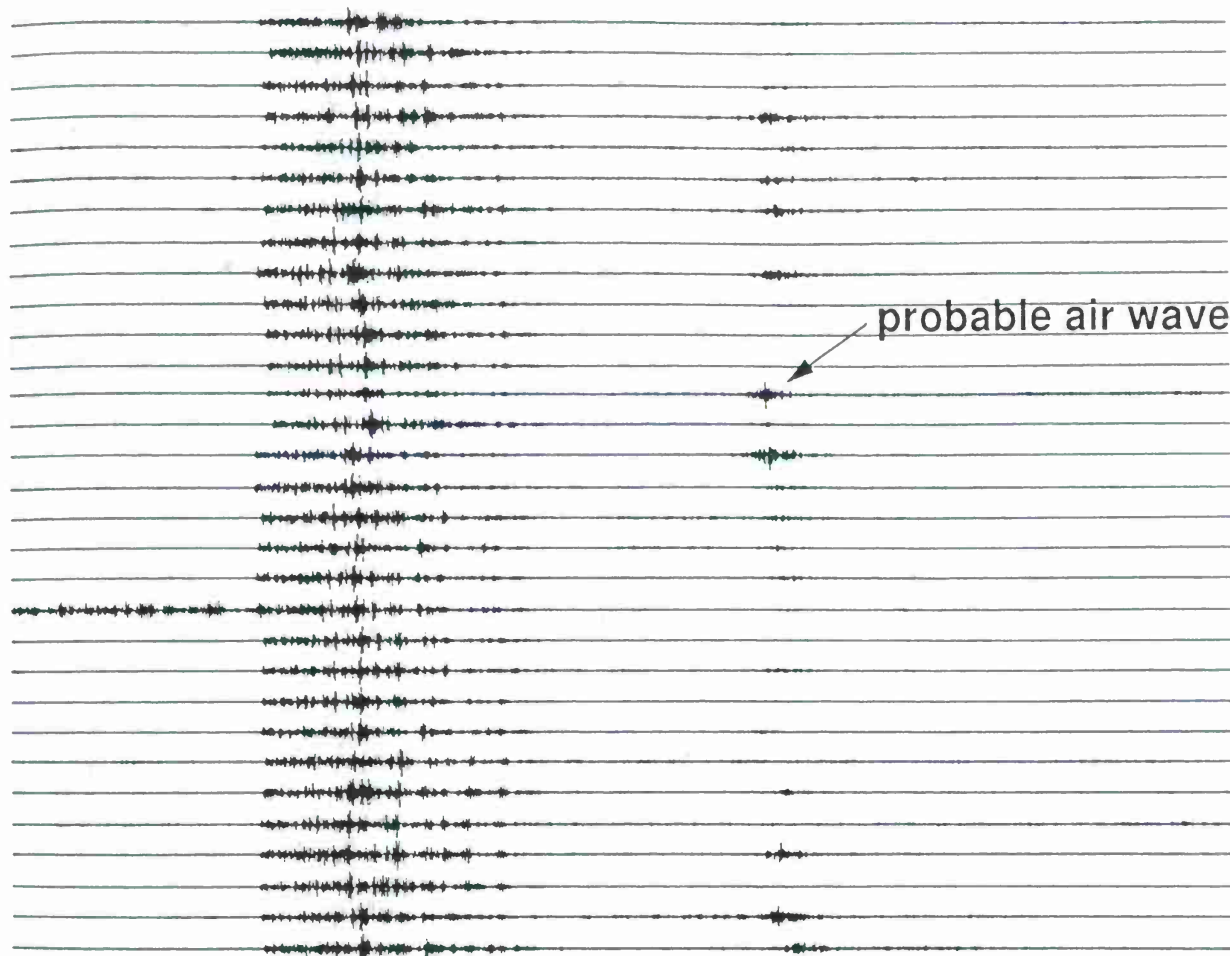
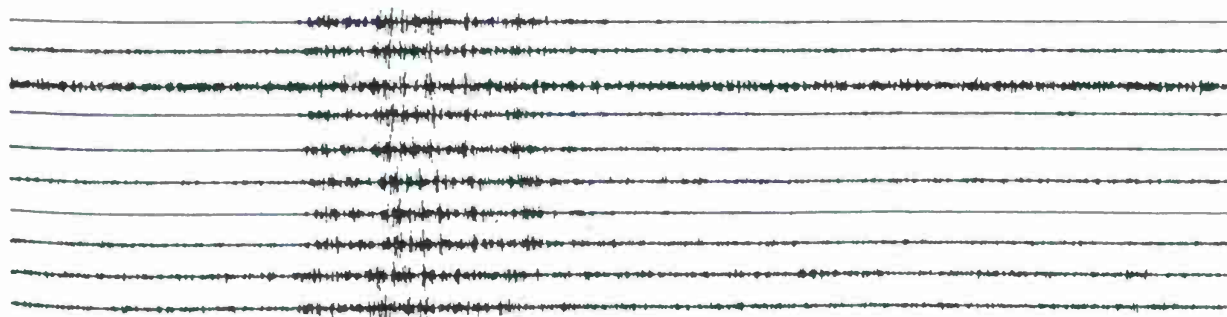


Figure 2 Map of the known mines (circles), stations (stars) GFA and IMS (site) THA, and location of presumed earthquake (inverted triangle) in north and central Tunisia. The correspondence of the clusters with mines (see remaining figures) is made on the basis of range estimates calculated from the separation of air and P waves. The earthquake location (largest Cluster 4 event) was supplied by the Tunisian national seismic network.

Cluster 1



Cluster 4



200 seconds

Figure 3 Event waveforms for two clusters defined by single-link analysis followed by reprocessing the data with subspace detectors. The first cluster of events probably originate at the phosphate mining complex of Mdhila 31 kilometers from the station, based upon a range estimate made from the evident air waves and P phases. The second cluster (Cluster 4) may be an after-shock sequence based upon the population analyses of the next three figures. The Tunisia national seismic network located the largest of these events (Ml 3.3) near Mdhila.

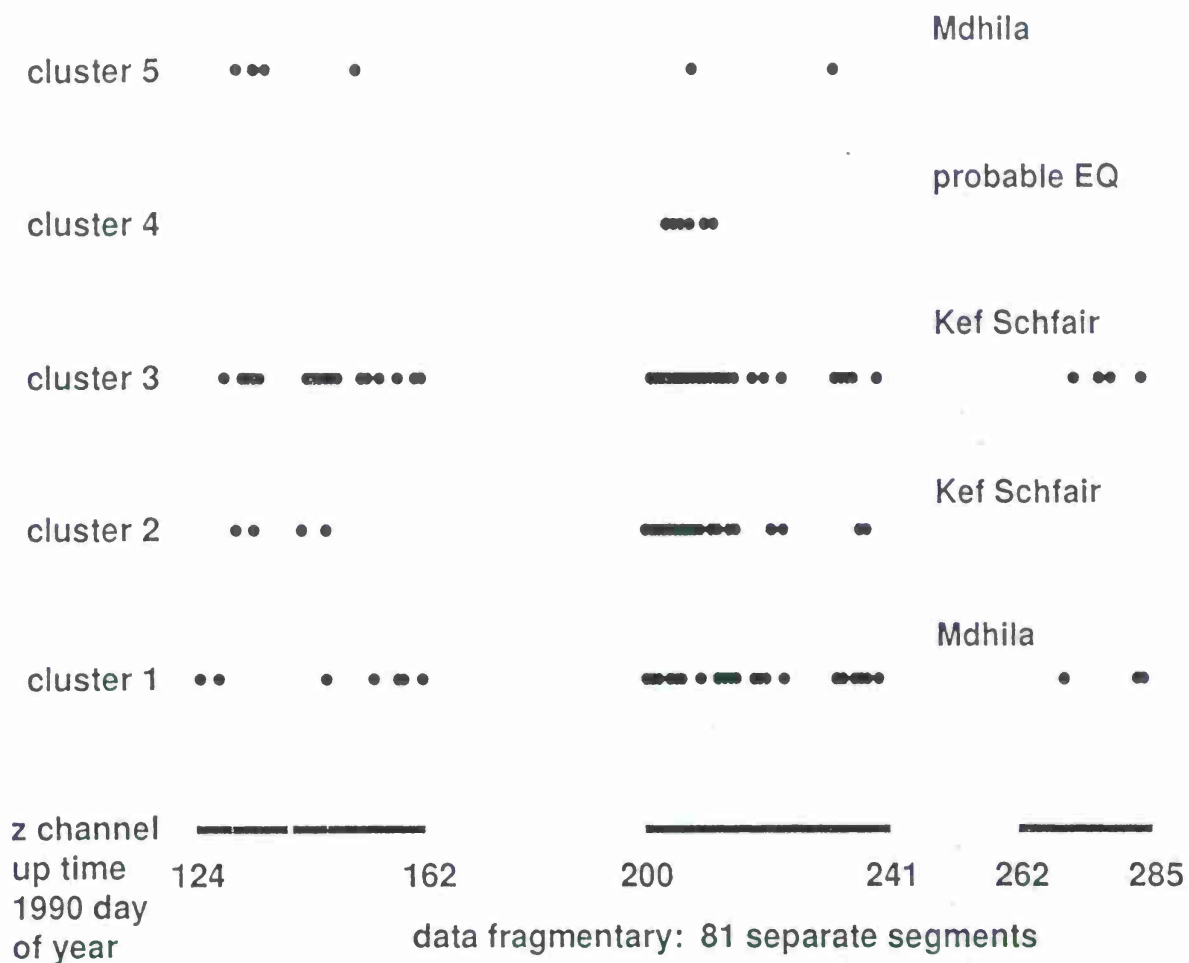


Figure 4 Long-term observations of event distribution in clusters may be a powerful tool for determining the identities of the sources. This figure shows the temporal distributions of events triggering subspace detectors designed for each of the five clusters studied. The clusters show regular event occurrence in four of five cases. The clusters are tentatively associated to major mining districts (Kef Schfair and Mdhila, central Tunisia) based upon ranges estimated from air wave - P times. The horizontal bars along the bottom of the figure indicate the periods for which data were available from GFA.

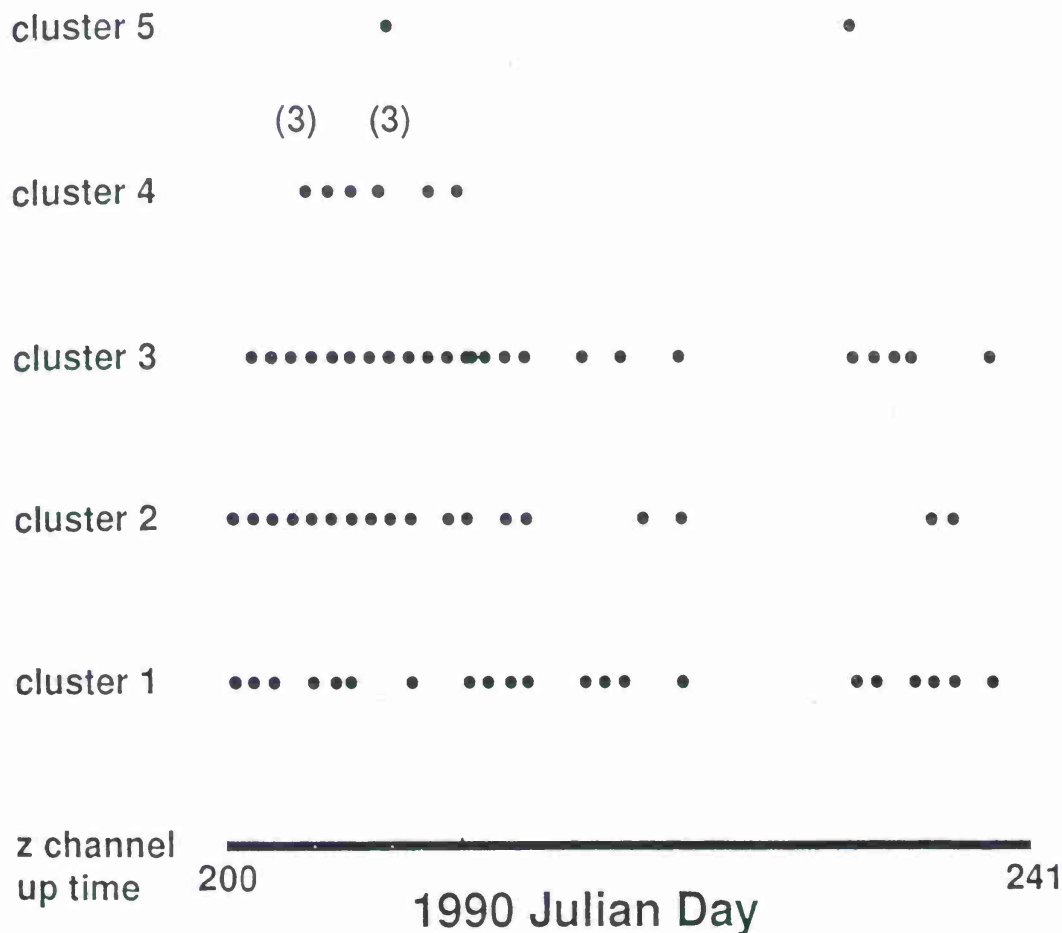
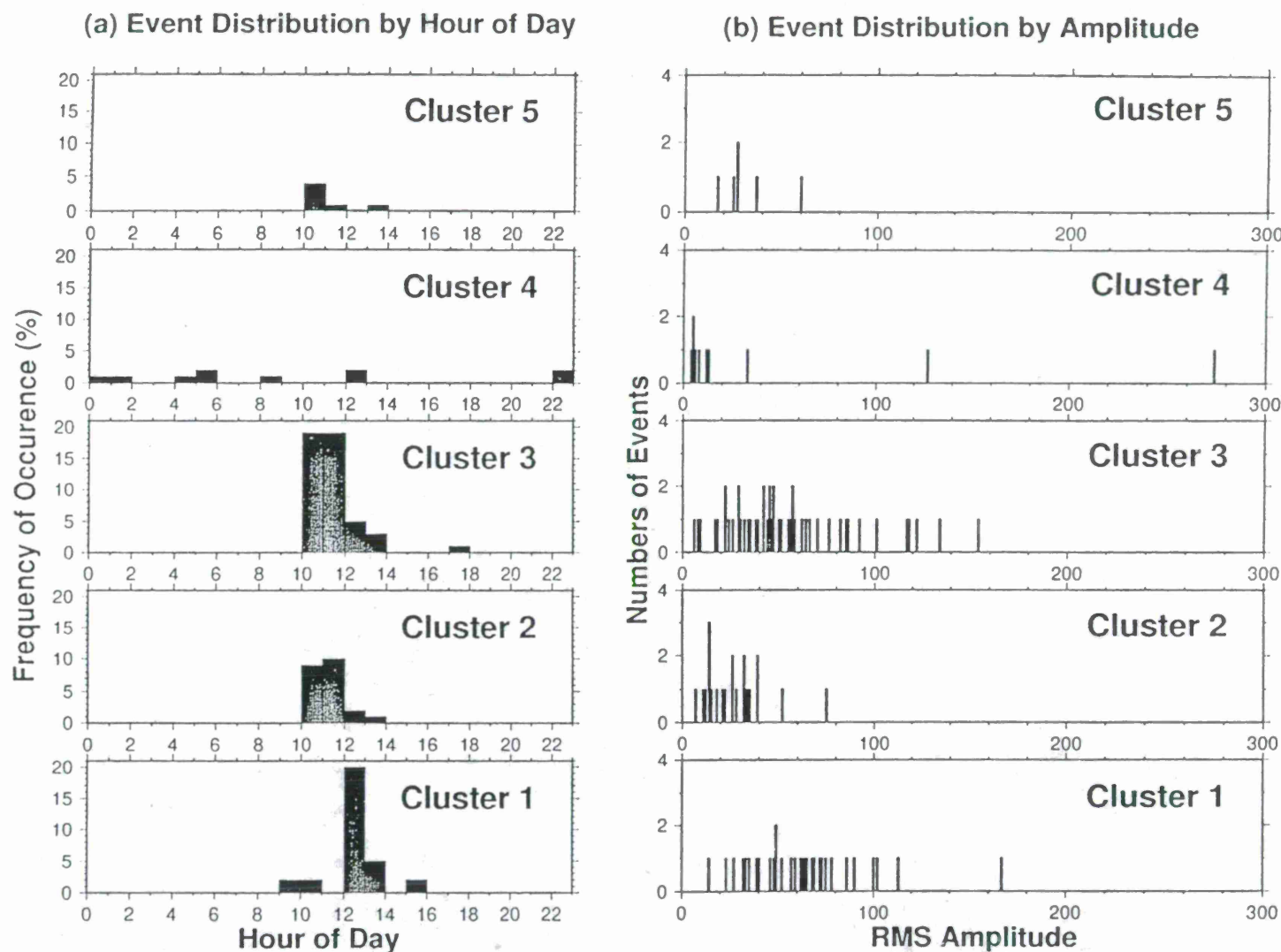
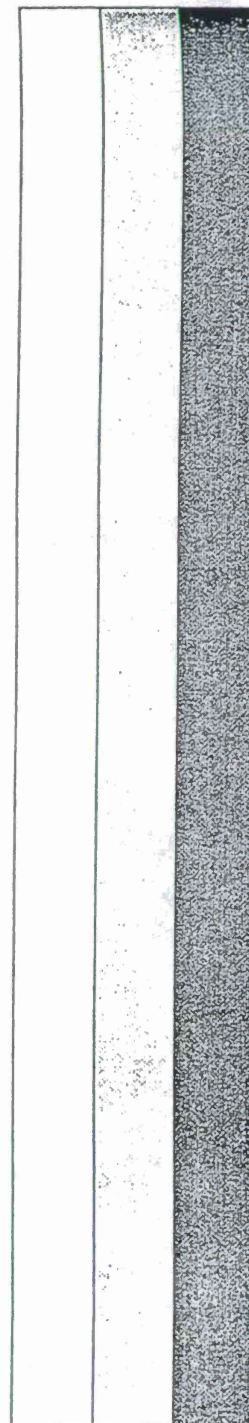


Figure 5 Detail of the time period from day 200 to day 241 shows the regularity of the events in clusters 1, 2 and 3. It appears that the mines corresponding to these clusters detonate explosions frequently, even daily. This fact suggests that the size of the charges is probably small. The Cluster 4 events all occur within an eight day period, and appear episodic. Two episodes each have three events that appear to occur simultaneously on this scale. This more random distribution is consistent with an earthquake source.



Figures 6 Event distributions by (a) hour of day and by (b) amplitude indicate that Cluster 4 is a distinct outlier. Events in Clusters 1,2,3, and 5 all occur during normal work; the events of Cluster 4 are random. The amplitudes of events in Cluster 4 show the largest dynamic range having both the largest and smallest events, with events most frequent at the smallest amplitudes. The other clusters are more concentrated in mid-amplitude ranges. The amplitudes are plotted linearly and are uncorrected for distance.



CALCULATING SEISMIC RADIATION PATTERNS FOR EXPLOSIONS IN AND AROUND CAVITIES

Matthias C. Imhof and M. Nafi Toksöz

Earth Resources Laboratory
Department of Earth, Atmospheric, and Planetary Sciences
Massachusetts Institute of Technology
Cambridge, MA 02139

Sponsored by Air Force Technology Applications Center
Contract No. F19628-95-C-0091

ABSTRACT

Seismic sources can be located in an underground complex of tunnels and cavities. Examples of such sources are chemical or nuclear devices as well as mining related events. Cavities are very strong scatterers which affect radiation patterns and conversions between different wave-type. We use a 2-D multiple multipole method to calculate source radiation patterns and scattering from cavities.

Seismograms recorded during the Non-Proliferation Experiment (NPE) show strong azimuthal variations in waveforms and amplitudes which can be explained only partially by heterogeneities along the path of propagation or near the receiver. Near the NPE source, there was a large complex of tunnels and cavities. Synthetic seismograms for a simplified NPE geometry correlate nicely with data observed around the arrival of S-waves generated at or near the source. By including near-receiver tunnels into our model, we also obtain the observed coupling between the radial and transverse component.

Keywords: radiation patterns, sources in and near tunnels, Non-Proliferation Experiment

Objective

Discrimination between seismic sources such as earthquakes, quarry or mine blasts, and nuclear explosions becomes increasingly difficult as the magnitude of the events decreases (Li *et al.*, 1996). The ability to extract useful information about seismic sources from seismic waveform data is limited by the complexity of the seismograms and the ability to model these complexities. For example, spall, tectonic release processes, and scattering contribute strongly to far-field seismic wave signals. The classic explosion source model, which yields an isotropic P-wave radiation pattern, cannot reproduce observed waveforms.

Signal-generated "noise" is particularly treacherous in this respect, as it typically has the transient character and frequency content which can easily be misinterpreted as due to some property of the source. For example, changes in source cavity shape and source location within the cavity influence the radiation pattern of the explosion by decoupling. Although many studies have been made, numerical (Gibson *et al.*, 1996) and analytical results (Ben-Menahem and Mikhailov, 1995) apply different assumptions and produce different results. Zhao and Harkrider (1992) developed solutions for the displacement field created by an explosion source located off-center within a sphere embedded in an infinite solid medium, a model of a fully tamped explosion. Here the loss of symmetry causes S-waves to be generated, even with the spherical cavity. Other studies have examined the effect of varying the cavity shape. Applying a combination of numerical and approximate analytical methods, Gibson *et al.* (1996) considered ellipsoidal and cylindrical cavity shapes and obtained estimates of far-field radiation patterns. They suggested that the P-wave radiation would be strongest perpendicular to an ellipsoidal cavity and that a fairly strong S-wave would be generated as the cavity aspect ratio (ratio of length to diameter) became large. Murphy *et al.* (1995) also examined an ellipsoidal cavity. However, in contrast to the other result, they concluded that at the frequencies of interest for regional wave propagation, the P-wave radiation pattern would be fairly isotropic and S-wave amplitudes comparatively small.

In the above studies, the effect of other heterogeneities has been mostly ignored. However, App *et al.* (1995) found that a horizontal discontinuity near an explosion source generated enough S-waves to influence regional waveforms, and thus cause such an explosion to appear more earthquake-like. For explosions at the Nevada Test Site, Stump *et al.* (1994) noted that at very closed-in distances, the transverse component of motion contained a source signature which relates to some type of scattering mechanism. An analysis of seismic data from the Non-Proliferation Experiment (NPE) showed that elastic wave scattering near the receiver had a significant effect upon the recorded waveforms (Johnson, 1995). Kamm and Bos (1995) calculated the effects of the layered structure on the NPE to study the scattering along the path of propagation.

Chemical or nuclear devices are commonly exploded within underground complexes with various explosions chambers as well as shafts and tunnels used for access and instrumentation (Denny and Stull, 1994). Moreover, there exist other seismic sources which occur in or

near underground complexes such as mines: e.g. rockbursts, collapses, or mining related explosions. But cavities are extremely strong scatterers which efficiently convert different wave-types into each other. The scatterers act as secondary sources with different radiation patterns and different distance dependencies than the primary waves. The discrimination between different seismic sources is made much more difficult by these secondary signals.

The objective of this paper is to study how the shape of the source cavity and the scattering by heterogeneities in the near-field of the source, such as tunnels and other cavities, affect the radiation of seismic waves. Characterizing seismic radiation from such complex source geometries requires an accurate and efficient computational method that will work for complex arrangements of cavities with a source in any part of a cavity complex. For this purpose, we developed the 2-D Multiple MultiPole (MMP) method (Imhof, 1996). In the MMP method, scattered wavefields are expanded into a set of basis functions which are solutions to the wave equation in a homogeneous medium. To find the yet unknown weighting coefficient for each basis function, we choose discrete matching points along the boundaries of the scatterers where we satisfy the boundary conditions. Each matching point provides two equations corresponding to vanishing tractions which build a linear matrix system for the unknown weighting coefficients. Typically, the chosen basis functions are scalar Helmholtz potentials of multipole form for P- and S-waves. In contrast to more traditional methods, we use multiple expansion centers and thus multiple multipoles for each scatterer. However, these basis functions are not orthogonal anymore. Hence, we will overdetermine the linear matrix system and solve it in the least-squares sense.

The paper is structured as follows. First, we demonstrate the effect of the source-cavity shape. We show the effect of a large heterogeneity in the near-field of an equivalent, isotropic explosion source. We then present the combined effect of asymmetrical source and near-source heterogeneity. Second, we apply our finding to the Non-Proliferation Experiment where we will explain parts of the observed waveforms by scattering in the near-field of the source.

Research Accomplished

Effect of Cavity Shape and Near-Source Heterogeneities

The situations we study are sketched in Figure 1. The models consist of (1) a source in a small, elongated cavity (26×10 m), (2) an explosive line source near a large cavity (60×18 m), and (3) both cavities together representing a large access tunnel with a source in a perpendicular side drift. The distance between the two cavities is 10 m. The geometry is not plane-symmetric. The small source cavity is offset by 15 m from the center of the larger one. At a distance of 750 m, we calculate the radiation patterns. As the source cavity is not axially symmetric, it will radiate both P- and S-waves. The model parameters are: density $\rho = 1800 \text{ kg/m}^3$, P-wave velocity $v_p = 2000 \text{ m/s}$, S-wave velocity $v_s = 1110 \text{ m/s}$, and

center-frequency 10 Hz.

The first numerical experiment is simply to determine the radiation pattern for the source cavity only. Thus, we omit the large cavity for this calculation. As source, we choose an instantaneous pressurization of the cavity. Figure 1(a) shows a sketch of the model and the resulting radiation patterns of P- and S-waves. The ratio between peak amplitudes of P- and S-waves is very close to unity. As expected, we obtain a large S-wave component with a radiation pattern typical for a double-coupled system of forces. For the P-waves, we see a combination of isotropic radiation (point source) and quadrupole radiation (double-coupled force system). Both in our calculation and that of Gibson *et al.* (1996), the P-wave radiation is strongest perpendicular to the elongated cavity-axis. In contrast to these results, Murphy *et al.* (1995) stated that at the frequencies of interest for regional wave propagation, the P-wave radiation patterns would be fairly isotropic and the S-wave amplitudes would be comparable small based on their finite-stress amplitude calculations. For small sources placed in cavities, elastic behavior would be a valid approximation, and our results should represent the radiation patterns.

As a next step, we determine the effects of the large access tunnel. We replace the source cavity with an isotropic, explosive line source located at the center of gravity of the source cavity. With this arrangement, there is no interaction between the scatterer and the source. A schematic of the model and the resulting radiation patterns are shown in Figure 1(b). The P-wave radiation is strongly affected by the tunnel. The tunnel effectively blocks the propagation of P-waves. The radiation pattern exhibits some degree of symmetry. However, the patterns are not aligned with the scatterer due to the asymmetrical configuration of source and scatterer. The S-wave radiation pattern still resembles a deformed double-couple. Interestingly, the ratio of S- to P-waves remains very close to unity. These two examples clearly show that both the geometry of the source cavity as well as additional cavities in the near-field of the source generate similar effects, i.e. conversion of P- to S-waves and angularly asymmetric radiation patterns.

We now calculate the combined model where we have an instantaneously pressurized source chamber with a large scatterer nearby. Thus, the source chamber radiates P- and S-waves as shown in Figure 1(a). However, these fields interact now with the large access tunnel. We expect the symmetry in the radiation patterns to diminish which is exactly what happens. Figure 1(c) shows the resulting radiation patterns for the combined model. The P-wave radiation pattern still resembles the original pattern as radiated from the source, although there is less P-wave radiation. Also, the symmetry of the radiation pattern is broken. The big difference lies in the S-wave radiation. The S-wave radiation is enhanced by a factor of at least 1.5. There is a significant increase in S-wave radiation in the diagonal direction.

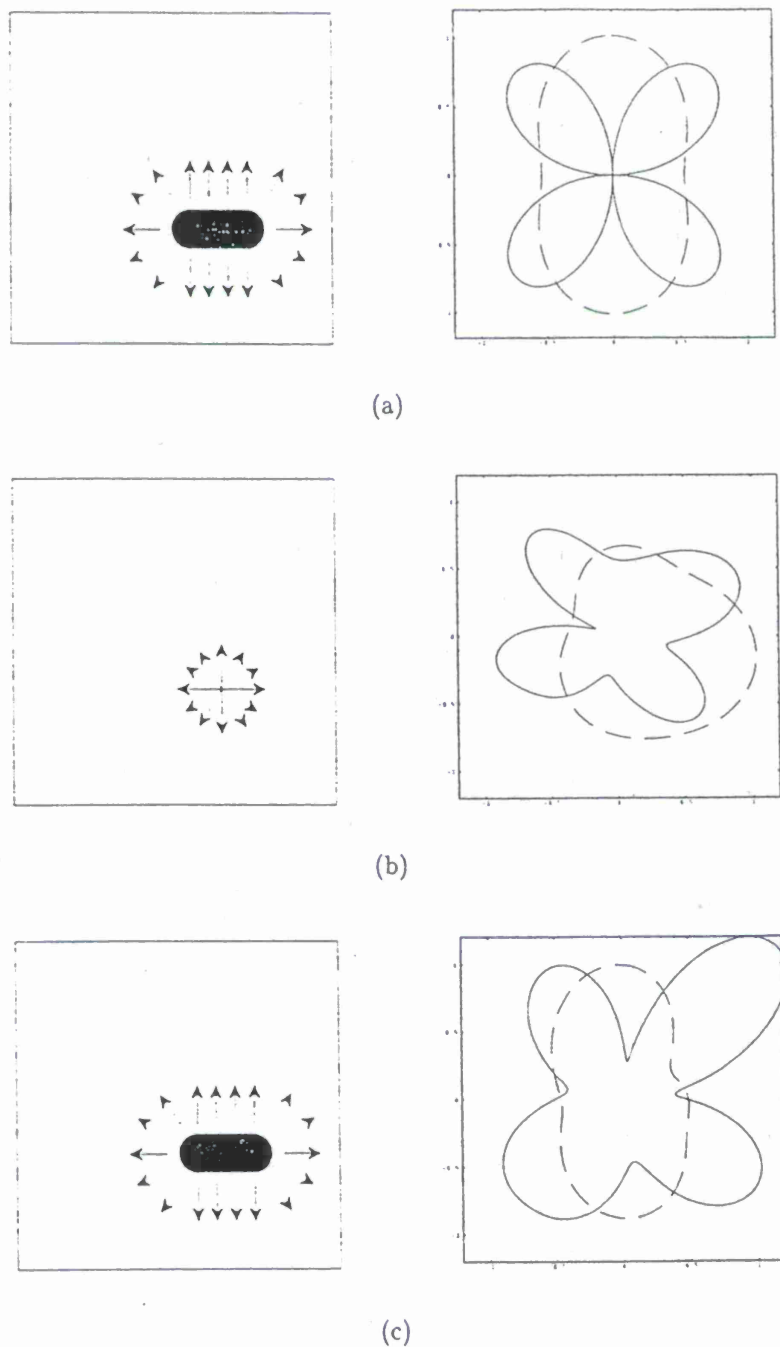


Figure 1: Radiation patterns for P-waves (dashed) and S-waves (solid): (a) for an instantaneous pressurization of the source cavity, (b) for an isotropic explosion source near a large tunnel, and (c) for an instantaneous pressurization of a source cavity near a large tunnel.

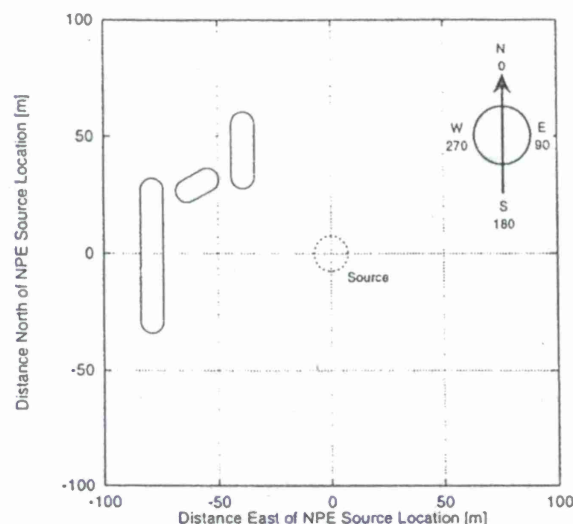


Figure 2: Cavities used for numerical simulation of NPE.

Application to the Non-Proliferation Experiment

On September 22, 1993, the Non-Proliferation Experiment (Denny and Stull, 1994) was conducted at the Nevada Test Site (NTS). A large chemical charge equivalent to 1.1 kt TNT was detonated in a cavity off from the N-Tunnel in Area 12. The purpose of the experiment was to quantify the effects of a chemical explosion of magnitude comparable to that of nuclear explosions. The charge was emplaced in a cylindrical cavity of nominal height of 5.2 m and diameter 15.2 m at a nominal depth of 389 m. The source was embedded in zeolitized tuff with $v_p = 2400.0$ m/s, $v_s = 1180.0$ m/s, and $\rho = 1800.0$ kg/m³ (Denny and Stull, 1994).

We used the 2-D MMP technique (Imhof, 1996) to analyze the effect of the caverns and tunnels. The complicated NPE geometry shown in Denny and Stull (1994) was simplified to the model shown in Figure 2. To calculate seismograms, we choose a Gaussian source potential with the spectrum $S(f) = \exp\{-(f/f_0)^2\}$ where $f_0 = 27$ Hz. Figure 3 shows a comparison between observed accelerations recorded in the tunnel complex and the synthetics neglecting the effect of near-receiver heterogeneities. The observed accelerations are plotted in [m/s²]. For the comparison, the observed traces are bandpass filtered to contain a frequency content similar to the synthetics. As a filter, we use the Fourier transform of a zero-phase Ricker wavelet with the spectrum $S(f) = (f/f_0)^2 \exp\{-(f/f_0)^2\}$ where $f_0 = 27$ Hz. All synthetic traces are scaled equally preserving the true amplitude ratios between the different receivers and components. For all four stations, synthetics and observations correlate well for early arrivals on the radial component. These arrivals correspond to the initial P-wave and its reflections from heterogeneities along the path of propagation. On

the transverse component, observed and synthetic traces correlate well around the arrival of S-waves generated near the source. These events propagated most of their path with S-wave velocities. Not only are the envelopes of the amplitudes comparable, but also their phases. In the synthetics, these S-waves dominate the transverse component.

However, these synthetics do not explain the prominent transverse arrivals at or near the P-wave arrival time. The accelerometers were grouted into small holes near access tunnels which act as near-receiver scatterers. To show their effects, we repeat the calculations but including near-receiver tunnels. As shown in Figure 4, synthetics and observations correlate well for early arrivals on both components for all stations. The applied scaling is the same as in Figure 3. Although these arrivals propagated predominantly as P-waves on the radial component, the near-receiver heterogeneity couples these events to the transverse component and thus to S-waves. Similarly, transverse arrivals are imprinted onto the radial component. In conclusion, both components contain large S-wave contributions caused by near-source scattering. The components are coupled by near-receiver scattering.

Conclusions and Recommendations

Scattering from heterogeneities has a significant effect upon recorded waveforms. Both heterogeneities along the path of propagation (Kamm and Bos, 1995) as well as heterogeneities in the near-field of the receiver (Johnson, 1995) have been observed. However, heterogeneities in the near-field of the source have not found much attention. For seismic sources located in underground complexes (e.g. tunnels and cavities), we expect very strong scattering due to the large contrasts between the rock and the embedded cavities, and thus strongly different waveforms and radiation patterns. Indeed, our numerical analysis showed that scattering in the near-field of the source has a significant effect upon both the observed waveforms and the radiation patterns.

Seismograms recorded during the Non-Proliferation Experiment exhibit a strong variation in their signals as a function of receiver location. We calculated some of these traces using a simplified 2-D model of the underground test site. We found that the transverse component matches the observed data fairly well around the arrival time of S-waves generated by cavities in the near-field of the source. However, early arrivals on the transverse component are due to the scattering of P-waves by near-receiver heterogeneities. Similarly, S-waves generated near the source scatter from the transverse component into the radial one. Although scattering from near-receiver heterogeneities might mask the effects of near-source heterogeneity, we believe that near-source heterogeneities have a strong effect on the radiation patterns and waveforms received at larger distances.

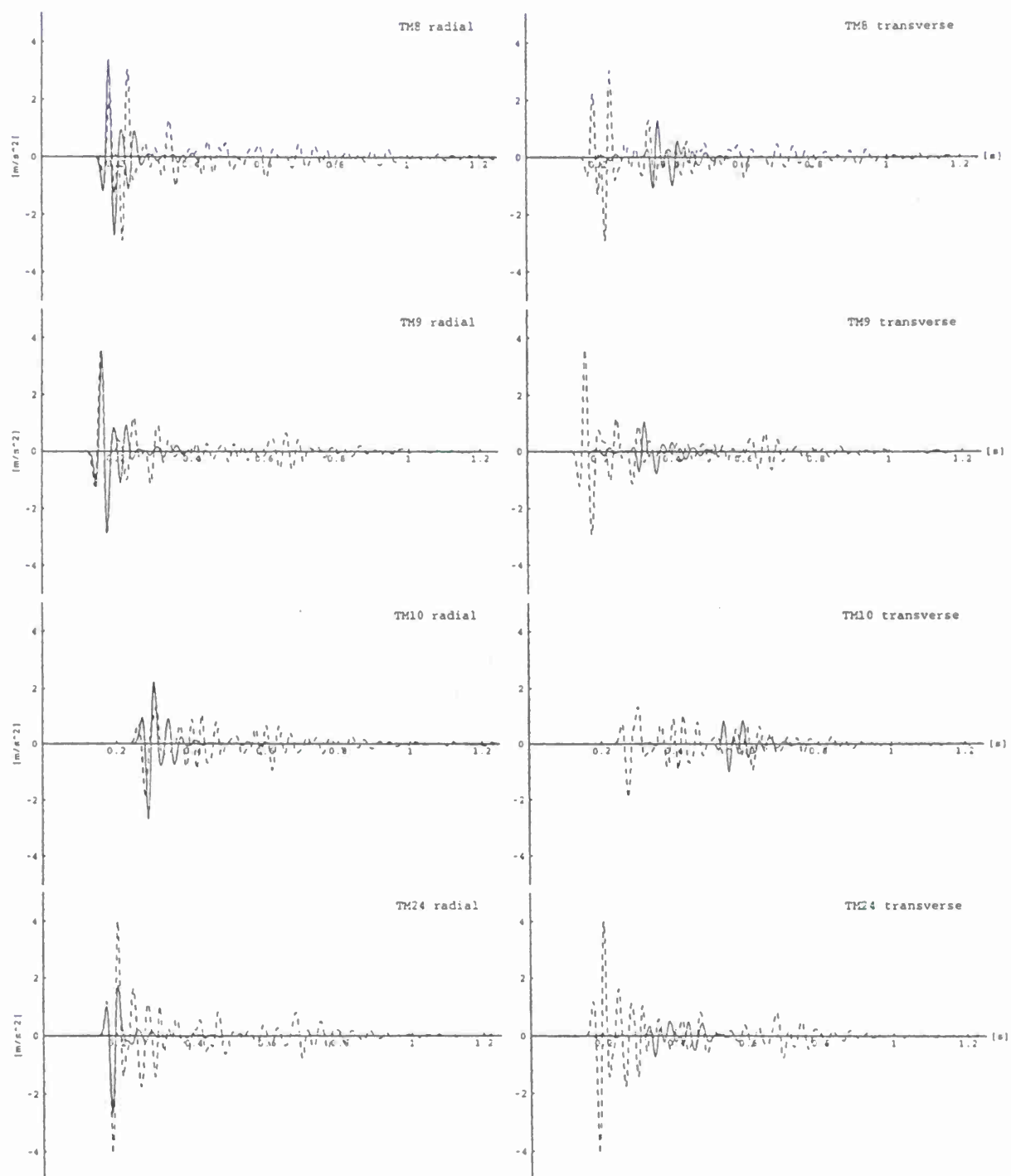


Figure 3: Observed (dashed) and synthetic (solid) accelerations at receiver stations located underground neglecting near-receiver heterogeneities.

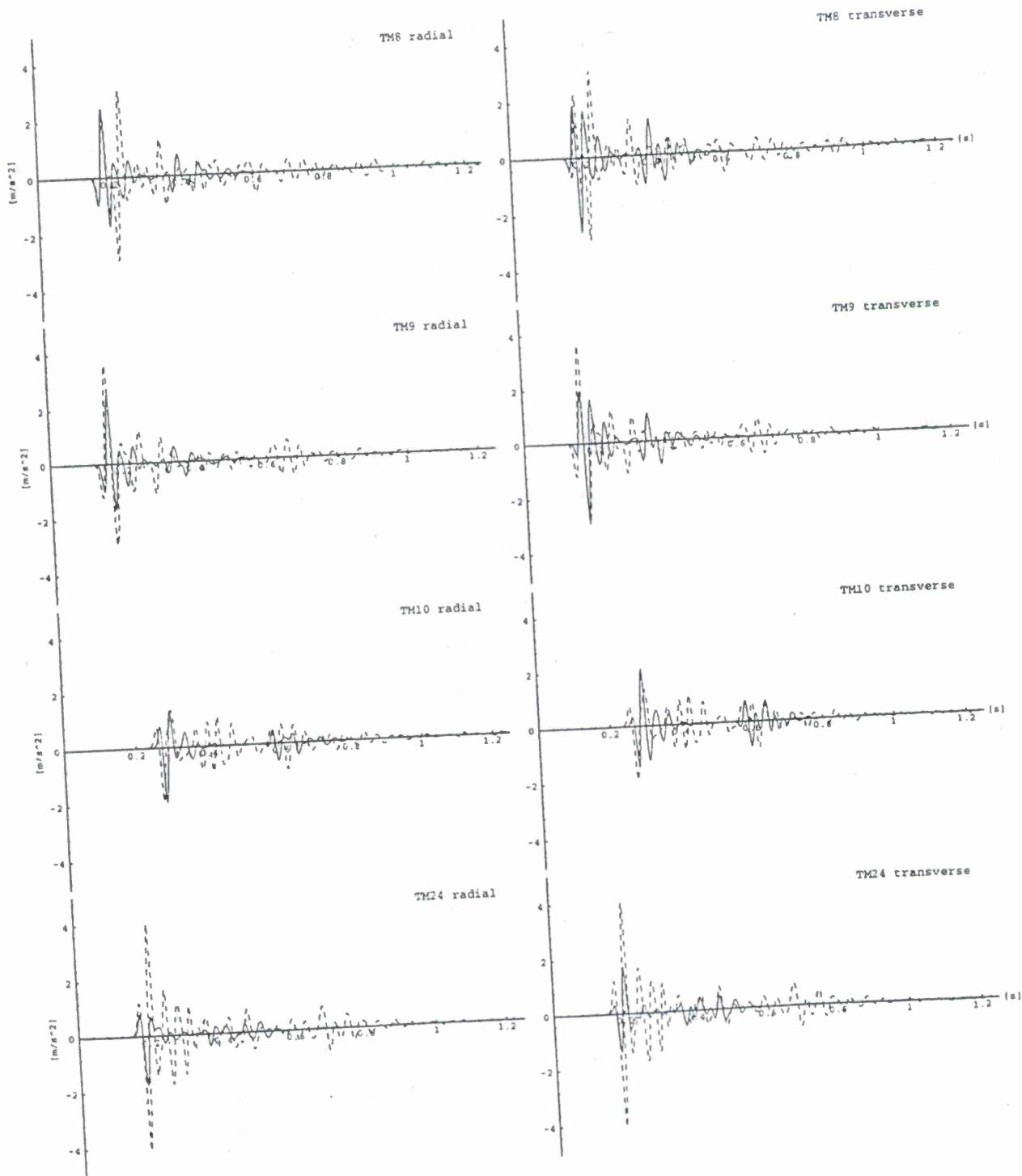


Figure 4: Observed (dashed) and synthetic (solid) accelerations at receiver stations located underground accounting for near-receiver heterogeneities.

References

- App, F. N., Bos, R. J., Dey, T. N., Jones, E. M., Kamm, J. R., and Taylor, S. R. (1995). Examining near-source effects in the far field. *Proceedings of the 17th Annual Seismic Research Symposium on Monitoring a Comprehensive Test Ban Treaty*, PL-TR-95-2108, pages 609-616.
- Ben-Menahem, A. and Mikhailov, O. (1995). Multiple radiation of seismic waves from explosions in non-spherical cavities and its application to signal identification. *J. Acoust. Soc. Am.*, **97**(5), 2675-2698.
- Denny, M. D. and Stull, S. P., editors (1994). *Proceedings of the symposium on the Non-Proliferation Experiment (NPE): Results and implications for test ban treaties*, CONF-9404100.
- Gibson, R. L., Toksöz, M. N., and Dong, W. (1996). Seismic radiation from explosively loaded cavities in isotropic and transversely isotropic media. *Bull. Seismol. Soc. Am.*, **86**(6), 1910-1924.
- Imhof, M. G. (1996). Multiple multipole expansions for elastic scattering. *J. Acoust. Soc. Am.*, **100**(5), 2969-2979.
- Johnson, L. R. (1995). The effect of near-receiver scattering on seismograms. *Proceedings of the 17th Annual Seismic Research Symposium on Monitoring a Comprehensive Test Ban Treaty*, PL-TR-95-2108, pages 421-432.
- Kamm, J. R. and Bos, R. J. (1995). Comparison of chemical and nuclear explosions: numerical simulations of the Non-Proliferation Experiment. Technical Report LA-12942-MS.
- Li, Y., Toksöz, M. N., and Rodi, W. L. (1996). Discrimination of small earthquakes and explosions. *Proceedings of the 18th Annual Seismic Research Symposium on Monitoring a Comprehensive Test Ban Treaty*, PL-TR-96-2153, pages 574-583.
- Murphy, J. R., Kitov, I. O., Rimer, N., Sultanov, D. D., Barker, B. W., and Stevens, J. L. (1995). Analyses of the seismic characteristics of U.S. and Russian cavity decoupled explosions. *Proceedings of the 17th Annual Seismic Research Symposium on Monitoring a Comprehensive Test Ban Treaty*, PL-TR-95-2108, pages 667-676.
- Stump, B. W., Pearson, D. C., and Reinke, R. E. (1994). Source comparison between nuclear and chemical explosions detonated at Rainier Mesa, Nevada Test Site. Technical Report LA-UR-94-4073.
- Zhao, L. and Harkrider, D. G. (1992). Wavefields from an off-center explosion in an embedded solid sphere. *Bull. Seismol. Soc. Am.*, **82**, 1927-1955.

GENERATION OF S WAVES BY EXPLOSIONS

Lane R. Johnson

Berkeley Seismological Laboratory, University of California,
and Center for Computational Seismology, Lawrence Berkeley Laboratory,
Berkeley, California 94720

Sponsored by the Air Force Office of Scientific Research
and the Defense Special Weapons Agency
Contract No. F49620-94-1-0197

ABSTRACT

Understanding the mechanism whereby S waves are generated by explosive sources has been a long standing problem in monitoring research. This paper investigates one mechanism which appears to be capable of generating significant S waves even in the case of a spherically symmetric explosion. It is shown that elastic waves propagating outward from an explosion can cause secondary cracking in the surrounding media. This follows from recent developments in the damage mechanics of brittle solids (Ashby and Sammis, 1990). The equivalent linear method is used to generate the stress field surrounding the explosion and criteria are then applied to estimate the increase in damage. By representing the increase in damage as a combination of a shear dislocation on an initial crack along with a tensile opening on wing cracks, it is possible to associate a source moment tensor with the damage. Secondary elastic waves are then obtained by summing up the effects of all damage caused by the outward propagating primary wave, taking into account at each point the amount of new damage, the orientation of the cracks, and the time history of motion on the cracks. The distribution and symmetry of preexisting cracks controls the amplitude of the waves generated by the damage and reasonable assumptions lead to significant amplitudes for both P and S waves. Calculations were performed for the chemical explosion detonated as part of the Non-Proliferation Experiment (NPE). For this case the calculations suggest that additional damage was caused out to distances of about 50 meters, which is almost 10 times the original source radius. The secondary P waves generated by this damage zone have an amplitude which is about 10% that of the primary waves generated by the explosion and the S waves can be even larger.

Keywords: explosion, source, damage, S waves

OBJECTIVE

The general objective of this research effort is the detection and discrimination of underground explosions through the study of radiated seismic waves. Particular emphasis is on the study of physical processes in the source region through the development of improved models for the generation and propagation of elastic waves. Such models are tested by the collection and analysis of broad-band seismic data at near and regional distances. The present paper reports on one phase of the research effort which is concerned with the interpretation of source parameters which are inferred from the analysis of waveform data. In particular, it investigates the conditions under which S waves can be generated by explosions and thus interfere with the discrimination from earthquakes.

RESEARCH ACCOMPLISHED

Introduction

The region of non-linear processes which surrounds an explosive source continues to be a subject of considerable interest, as some of the physical processes which occur in this region are still not completely understood. This study considers one such process, the question of whether the secondary cracking predicted by damage mechanics can have a significant effect upon the elastic waves generated by an explosive source.

Several different aspects of this problem have to be considered. The first involves the matter of whether the stresses generated by an explosive source are sufficient to displace and extend preexisting microcracks. The nucleation and propagation of cracks due to applied stresses will be referred to as damage, so the task is to determine the extent and characteristics of the damage zone. If this damage zone can be shown to exist, then it is of interest to investigate the properties of the secondary elastic waves which are generated by motion on the microcracks. Here it is necessary to consider the cumulative effect of motion on a large number of microcracks distributed throughout the damage zone surrounding the explosion.

In order to test the potential effect of damage on realistic explosive sources, preliminary calculations have been performed for the chemical explosion detonated as part of the Non-Proliferation Experiment (NPE) in September, 1993. This 1 kiloton explosion provides a convenient test case because of the large amount of information which is available for this explosion.

Stress field surrounding an explosion

The primary ingredient necessary for the investigation of damage surrounding an explosion is knowledge of the stress field generated by the explosion. In this study that stress field has been generated using the equivalent linear method (Johnson, 1993). While this is an approximate approach that does not incorporate all of the physics contained in complete equation-of-state approaches, it does provide a very efficient method of estimating the basic characteristics of elastic waves radiated by an explosion. The use of the equivalent linear concept allows analytical solutions developed for linear problems to be employed, thus providing a relatively simple algorithm that can be used to explore a wide variety of features associated with the explosion process.

Calculations employing the equivalent linear method were used to simulate the elastic waves generated by the NPE explosion. Source properties such as cavity size and amount of explosive are very well known for this event so the initial conditions for the calculations contain little uncertainty. Furthermore, there were large amounts of data recorded during this experiment, including the recordings of free-field motions at approximately 20 different sites. These recordings were used to check the calculations by comparing observed and calculated radial velocities out to horizontal distances of over 500 meters. The agreement was good with respect to maximum velocity and approximate with respect to waveform shape. On the basis of these comparisons it is assumed that the stress field generated by the equivalent linear method provides a reasonably accurate approximation to actual stresses that were present during the NPE.

Generation of rock damage

The basic question to be investigated is whether the elastic waves propagating outward from an explosion can cause cracks to grow in the surrounding media. Also of interest is whether these cracks can generate additional elastic waves. The problem can be approached by making use of methods developed for damage mechanics in brittle solids.

The concept of rock damage is described in Ashby and Sammis (1990) and this part of the research has been done in collaboration with Dr. Charles Sammis of the University of Southern California. In the Ashby and Sammis (1990) paper the conditions under which an initial crack can be extended under axisymmetric loading are derived. The dimensionless damage is defined as

$$D \equiv \frac{4}{3} \pi (\alpha a)^3 N_v$$

where α is a geometric term (typically 0.7), $2a$ is the dimension of the crack, and N_v is the number of cracks per unit volume. Then, given the initial damage D_0 and the major and minor stresses, σ_1 and σ_3 , the condition under which the damage will be extended by growth of the crack surface is derived. The amount of crack growth is obtained as that required to reduce the stress intensity at the crack tip to the fracture toughness of the medium. The final damage that is achieved can be determined by finding the root of a cubic equation.

The basic procedure followed in this study is to use the equivalent linear method to generate the stress field in the entire region surrounding an explosion. At each point in space the radial and tangential stresses are generated as a function of time and these are used to calculate whether additional damage has occurred. The net result is the determination of damage as a function of time and distance in the region of high stresses surrounding the explosion.

A test of this concept of rock damage were obtained by modeling the chemical explosion detonated as part of the NPE. In these simulations an increase in damage occurred in a volume that extended from the cavity radius out to a distance of 50 meters. These calculations indicate that the stresses generated by an explosive source are sufficient to cause the growth of microcracks in an extensive region surrounding the source. The calculations for the NPE suggest that:

- The zone of increased damage can extend out to 10 times the original source radius.
- The damage does not occur at the time of peak stress, but rather at a later time when the tangential stress is decreasing more rapidly than the radial stress, thus providing the imbalance of principal stresses necessary to cause an increase in damage.
- The front of the damage zone follows behind the outward propagating stress wave, having a velocity intermediate between the P and S velocity.

Damage as a source of secondary elastic waves

One of the more interesting aspects of the possibility that damage may be generated by the elastic waves propagating outward from an explosion is the potential for the microcracks to act as secondary sources of elastic waves. The damage of Ashby and Sammis (1990) is modeled as an initial crack which is extended by wing cracks. This can be represented as the combination of two separate source moment tensors, a shear dislocation on the initial crack and a tensile opening on the wing cracks. Because the damage can occur on microcracks distributed throughout a zone surrounding the explosion and having different orientations, it is necessary that the moment tensor be expressed for an arbitrary location and an arbitrary orientation. Euler angles are a convenient way of achieving this type of a representation.

In terms of the damage, the strength of the moment tensor per unit volume for the tensile crack is

$$m'_t \equiv (\lambda + 2\mu) \frac{3}{2\pi^{\frac{1}{2}}} \frac{3\lambda + 2\mu}{\lambda + \mu} \frac{K_{1c}}{\mu(\alpha a)^{\frac{1}{2}}} D_o \left[\left(\frac{D}{D_o} \right)^{1/3} - 1 \right]^{5/2}$$

where K_{1c} is the critical stress factor. For the shear crack the moment tensor strength per unit volume is

$$m'_s \equiv \mu \frac{3}{2\pi^{\frac{1}{2}}} \frac{3\lambda + 2\mu}{\lambda + \mu} \frac{K_{1c}}{\mu(\alpha a)^{\frac{1}{2}}} D_o \left[\left(\frac{D}{D_o} \right)^{1/3} - 1 \right]^{5/2}$$

After combining the moment tensor representation for the damage with an appropriate Green function, the result must be integrated over all cracks on which the damage has increased. This involves an integral over the three dimensional zone surrounding the explosion where damage has occurred and also over time, taking into account when the damage was initiated. It is assumed that the motion on each microcrack is instantaneous at the time when the damage front arrives, which seems reasonable in view of the small size of these cracks. The integration over all of the damage zone then produces the time history of secondary elastic waves caused by the damage, including their arrival time, amplitude, and frequency content. Such integrals are complicated but tractable.

This process of integrating over the damage zone will depend upon any heterogeneity or anisotropy in material properties that may be present, including the distribution or orientation of the microcracks and variations in the stress field, including the initial stress. To date, this process has been completed for two different cases, a homogeneous distribution of completely random microcracks, and a homogeneous distribution of microcracks that are aligned with a preferred orientation.

For the case of completely random cracks the most important results that emerge from the analysis are:

- Only the tensile cracks have a net moment tensor. The shear cracks make no contribution to far field wave radiation.
- The composite moment tensor for the tensile cracks is isotropic. The only contribution is from the dilatancy effect of these cracks, which is a net volume change.
- Only P waves will be radiated into the far field from this type of a source.

Calculations were performed for this case of completely random cracks and the NPE explosion. The damage zone was taken as that between a radius of 17 meters and 50 meters where the damage increased from a value of 0.1 to about 1.0. This corresponds to a dilatancy of about 3 per cent. The P waves radiated into the far field from the isotropic secondary source associated with the damage had an amplitude of about 10% the primary P waves emerging from the explosion.

The case where the microcracks are uniformly distributed but have a preferred orientation was also considered. The important results for the case of oriented cracks are:

- The tensile cracks contribute an isotropic part which is associated with the opening of the wing cracks. Its magnitude in this case is only half that for the case of completely random cracks.
- Both the tensile and shear part of the damage make non-isotropic contributions to the composite moment tensor. These contributions are identical in form, which is that of a compensated linear vector dipole.
- Both P and S waves will be radiated into the far field from this type of a source.

The far field radiation from this type of a source with oriented cracks was also estimated for the case of the NPE. As before, the damage zone was taken as that between a radius of 17 meters and 50 meters. The important results from this calculation can be summarized as follows:

- When a preferred orientation of microcracks is present in the damage zone, secondary P and S waves will be radiated into the far field which have significant amplitudes compared to those of the primary explosion.
- The secondary P waves add a small component to the tail of the primary P wave from the explosion.
- The secondary S waves have a much more significant effect, having larger amplitudes and having particle motions in directions where there is no contribution from the primary P wave from the explosion.
- The time function of the secondary S waves is quite different from that of the secondary P wave, which results from the fact that the damage front propagates at a velocity which is sub-sonic for P waves but super-sonic for S waves.
- The secondary S waves have the appearance of long period S waves radiated directly from the explosion, having the appropriate delays in time and the appropriate particle motions.

CONCLUSIONS AND RECOMMENDATIONS

With respect to the question of whether secondary cracking can occur in the region surrounding an explosive source, this study suggests that:

- The elastic waves generated by an explosive source can generate significant amounts of crack growth in an extensive region surrounding the source.
- By taking advantage of existing knowledge about damage mechanics, it is possible to make quantitative estimates of the amount of crack growth which occurs.
- For the case of the NPE, the calculations indicate that the damage zone extends out to a distance of 10 times the original cavity radius.
- The damage does not occur at the time of peak stress, which leads to a damage front following behind the outward propagating stress wave.

With respect to the question of whether an increase in damage can cause the radiation of secondary elastic waves, this study suggests that:

- While the contribution from a single microcrack is very small, the integration over the many cracks in the large zone of increased damage surrounding an explosion does lead to a composite moment tensor which may be an appreciable fraction of the moment tensor of the explosion itself.
- For an isotropic and homogeneous distribution of microcracks, the composite moment tensor is isotropic and thus radiates only P waves to the far field. This is to be expected by the basic symmetry of the problem.
- For the case where the microcracks have a preferred orientation, the moment tensor has both isotropic and non-isotropic components. Thus both P and S waves are radiated, both with their own radiation patterns.
- In this case of oriented microcracks the secondary waves caused by the damage have significant amplitudes when compared to the primary P waves generated by the explosion.
- The secondary S waves radiated by the damage have longer periods than the secondary P waves and also the primary P waves.

With respect to the basic question of whether S waves can be generated by an explosive source, this study suggests that:

- Damage mechanics appears to provide at least one possible mechanism for generating S waves of significant amplitude and period from an explosive source.

Considerable more work is needed on this problem, and potential applications of the results seem to warrant continuation. Some of the aspects which need further study are the effect of depth of burial, the effect of pre-stress such as tectonic stress, the effect of orientation of initial cracking, and the detonation of an explosion in a region which has already been damaged by a previous explosion.

References

- Ashby, M. F., and C. G. Sammis, The damage mechanics of brittle solids in compression, *Pure and Appl. Geophys.*, 133, 489-521, 1990.
- Johnson, L. R., Wave propagation near explosive sources, PL-TR-93-2118, Phillips Laboratory, 22 pp., 1993.

THE SEISMIC SIGNAL STRENGTH OF CHEMICAL EXPLOSIONS

Vitaly I. Khalturin and Paul G. Richards
Lamont-Doherty Earth Observatory of Columbia University
(also, Department of Earth and Environmental Sciences), Palisades, NY 10964

Sponsored by U.S. Department of Energy
Office of Nonproliferation and National Security
Office of Research and Development
Contract No. F19628-95-C-0100

ABSTRACT

We have compared the seismic signal strength of a variety of chemical explosions of known yield, to the signal strength expected for explosions set off under conditions similar to those of a well-contained tamped underground nuclear explosion (UNE) at the Semipalatinsk Test Site. We find that the actual signal strength of chemical explosions is typically much smaller than that expected under UNE conditions.

To quantify these observations, we define the expected signal strength under UNE conditions minus the actual strength as the *deficit*, and we document the size of this deficit using two different measures of signal strength: the energy class, K ; and the seismic magnitude (which may be the teleseismic m_b or a regional magnitude).

Our documentation covers numerous chemical explosions that include several different broad groups, mostly taken from practical experience with chemical explosions carried out on territory of the former Soviet Union.

In general, for chemical explosions carried out in the mining and construction industries, the magnitude deficit is around 1.5 to 2. There are exceptions, including cases where the deficit is smaller. These exceptions should be the focus of future work to evaluate the problems for CTBT monitoring presented by chemical explosions. But our main result, is that the problems for CTBT monitoring, associated with chemical explosions, are much smaller than might have been expected on the basis of magnitude yield relations for typical underground nuclear explosions.

Keywords: mine blasting, chemical explosions, seismic magnitudes, CTBT monitoring

OBJECTIVE

Our goal overall in this project is to document the rates of occurrence of chemical explosions of different sizes, in as many mining regions as possible, but with a focus on the observability of blasting signals originating in the former Soviet Union.

The size of a chemical explosion is expressed commonly in terms of its total charge. But in this project we are more interested in size expressed in terms of seismic magnitude, whether local, regional, or teleseismic, since our principal concern is with the *observability* of blasting activity. We are particularly interested in estimating the numbers of chemical explosions that occur in different regions and that are detected with seismic magnitudes greater than about 3. Underlying our work, is the fact that mine-blast signals are less easily discriminated from nuclear explosion signals, than are earthquake signals; so mine blast signals may require more sophisticated analysis in programs of CTBT monitoring and verification. It follows that large numbers of detectable mining blasts would represent a problem for those who must routinely identify the nature of seismic sources (whether they are earthquake, mining blast, other chemical explosion, or underground nuclear explosion).

Our project in previous years has helped to estimate the extent of this problem, by making surveys of the observability of mine blast signals of various sizes. This year, we have attempted to quantify the inefficiency of chemical explosions in generating seismic signals.

RESEARCH ACCOMPLISHED

Introduction For more than 15 years following negotiation of the Threshold Test Ban Treaty in 1974, intensive study was made of the relationship between the seismic magnitude and the yield of an underground nuclear explosion (UNE). For conditions typified by the Soviet Union's main test site (now closed) near Semipalatinsk, that relationship was demonstrated by Ringdal, Marshall and Alewine (1992) to be

$$m_b = 4.45 + 0.75 * \log Y \quad \text{for yield } Y \text{ in kilotons.} \quad (1)$$

It is well understood that this relationship can be different for different test sites, even for well-tamped contained explosions below the water table; but (1) is thought to apply to vast regions that include much of Eurasia.

When estimates began to be made, in the early 1990s, of the numbers of chemical explosions set off routinely in industrialized countries, there was concern that the seismic signals from such explosions would be so numerous, and would appear so similar to the signals expected from a small UNE, that they would swamp efforts at CTBT monitoring based on seismological methods. The reasoning behind such pessimism was that the United States, Russia, China, and numerous non-nuclear-weapon states such as Australia, Canada, Kazakhstan, and countries of South America use a total of about five megatons of chemical explosive per year. This overall total is distributed across numerous blasts of total charge size ranging above one kiloton (on the order of

a hundred per year); between 100 and 1000 tons (thousands per year); and between 10 and 100 tons (many thousands per year). These estimates are based upon Richards et al. (1992) for the U.S, Khalturin et al. (1996) for territory of the former USSR, and technical reports by W. Leith and his colleagues for other countries. If these charge sizes were interpreted via equation (1), then one would expect chemical explosions to generate about a hundred events each year with magnitude greater than 4.5; thousands of events per year in the magnitude range 3.5 – 4.5; and several events *per hour* in the range 3 – 3.5 (a magnitude range that includes the source strength expected from a fully-decoupled UNE of around 5 kilotons).

This expectation, however, leads to erroneous results, because it is clear from seismicity bulletins (global and regional), published by numerous organizations, that the actual numbers of seismically detectable chemical explosions are on the order of a hundred times smaller than what would be predicted by (1) plus information on the numbers of explosions at different yield levels.

We have attempted to resolve this issue, by collecting data on seismic signal strength and charge size (yield) for numerous different chemical explosions carried out under different conditions; and have compared the actual relationship between signal strength and charge size with that predicted by (1). We find that typical chemical explosions carried out by the mining and construction industries are highly inefficient at generating seismic signals — as compared to the predictions of (1). For quantitative purposes, we propose that this inefficiency of seismic coupling can usefully be described by the *deficit*, defined as the difference in source strength for a given chemical explosion with a particular charge size, between that predicted for a well-coupled UNE at that charge size (yield), and the actual source strength. We find that this deficit, which is subject to considerable scatter, can nevertheless be roughly estimated for different broad groups of chemical explosions.

In this short paper, we report our main results in Figures 1 and 2, and Tables 2 and 3.

Available Data, and our Method of Analysis We have acquired data on charge size, or yield, of a wide variety of chemical and nuclear explosions, together with data on the seismic source strength. Our data on source strength in some cases comes from the measurement of the energy class, K ; and in other cases it is a seismic magnitude — teleseismic m_b for large events, otherwise a regional magnitude based upon P_n or L_g waves or upon a coda measurement. It was important to include the use of energy class K in our study, because this is the only measurement of seismic source strength available for many explosions on territory of the former Soviet Union. K , equal to the value of $\log E$, where E is the seismic energy estimated in joules, is the standard measure of source strength in regional catalogs of the FSU. We appreciate that work is needed to reconcile various regional magnitudes scales with the standard teleseismic scale, m_b , but available scales are still useful for preliminary estimates of the magnitude deficit of chemical explosions.

Essentially, our approach has been to plot values of K , or magnitude, against $\log Y$ for numerous chemical and nuclear explosions, and in the case of K values to make a comparison with a line given as follows:

$$K = 11.65 + \log Y \quad \text{for yield } Y \text{ in kilotons} \quad (2)$$

that we take as a fit to the upper values of the points. For example, this line is a quite good fit to the data for single-fired well tamped chemical and nuclear explosions in hard rock. For m_b versus $\log Y$ we could have taken an equivalent approach (a line through the upper values), but the line then obtained is so similar, using our data, to equation (1), that it seems more appropriate to go ahead and use equation (1) for purposes of evaluating the magnitude deficit.

To get these equations, (1) and (2), with acceptable confidence, the observational data must be studied over as wide a range of yields as possible, including well-coupled explosions at both high and low yields. Table 1 lists information on large chemical explosions used in this study.

UPPER LIMIT OF ENERGY CLASS K VS. YIELD

To get the relationship between maximum values of K and $\log Y$, we used data as shown in Figure 1 that span the range from about 100 kilograms to 200 kilotons — more than a factor of a million. The straight line of points is the above equation (2), which divides the region of the graph that is filled with data points, from a region that has almost none. Only three points lie above the line, and they do so by amounts ΔK on the order of 0.1 – 0.2 K units — which is about the error of K determination. All nuclear explosions shown in the Figure occurred at the Semipalatinsk test site. They lie in a narrow band about the line, with K deficit typically from 0 to 1.

The range of Y values from 400 tons to 4000 tons is common to big chemical explosions and to small nuclear explosions. For chemical explosions it appears that the K deficit may be a little larger. The chemical explosions used to create dams or canals were not fired as single charges but were distributed in space in order to move large amounts of rock, and such sources are not as compact as UNEs. But typically the total charge of each of these blasts was fired within a very short period of time, like a singly fired explosion. Their deficit is seen to be small, varying between 0 and 1.5 to 2.0, and is about 1.0 on average.

Five events that were single fired explosions on the surface, without any covering materials, have deficit amounting to about 2 to 3 K units.

There is a "gap" in the values of K , for Y about 100 tons. This is probably due to an important difference in seismic coupling efficiency, between big single-fired and big ripple-fired industrial explosions in quarries. This latter type of explosion occurs in Apatity (Kola Peninsula, Russia); Krivoi Rog (Ukraine); and Tyrnauz, (South Caucasus, Russia). Taking the ripple-fired explosion data together, we get the impression that over a wide range of Y values, from 0.5 to 500 tons, the energy class K does not depend on Y at all. For all these events K is about the same: about 6.5 on average, and is scattered between 5 and 8, with deficit reaching 4 to 6 units.

Only 5 explosions were available from Krivoi Rog, Ukraine. They are of nearly the same Y value, about 600 to 800 tons. Their K value is as small as 6.5 to 8, with deficit 2.5 to 3.5.

The left side of Figure 1 is dominated by data from small industrial explosions. These occur at Almaty and Kotur-Bulak (Kazakhstan) and Medeo (Northern Tien Shan). The Medeo explosions are not quarry blasts, but were carried out to increase the elevation of a dam.

Table 1:

WELL DOCUMENTED CHEMICAL EXPLOSIONS

Location	Year	Mo	Da	Ho	Mi	Latit	Long	Y	kt	K	mb*	MPA	MLH	M**
Pokrovsk	1959.	3	25	9:	0	60.20	59.90	3.100	11.90			5.0	4.0	
Tuya-Muyun	1959.12	31	6:	0	40.35	72.59	.190	9.90				4.8	3.3	
Tuya-Muyun	1960.	3.	3	9:	0	40.35	72.59	.660	10.40			5.1		
STS D	1961.	6.	5	3:50	49.77	77.98	.660	10.90						
Dzhezkazgan	1965.11	20	7:	0	48.00	67.00	1.152	9.50						
Medeo-1	1966.10	21	4:59	43.15	77.06	1.689	11.40							
Medeo-2	1966.10	21	5:	0	43.15	77.06	3.604	11.80				5.1	3.7	
Medeo-3	1967.	4	14	6:	0	43.15	77.06	3.941	11.35			4.8		
Baipasa	1968.	3	29	6:48	38.24	69.15	1.854	10.40						
Akh-Su	1972.12	26	14:28	42.96	46.87	.552	9.40							
Medeo-4	1973.11.	3	6:22	43.15	77.06	.020	8.70							
Medeo-5	1973.11	20	5:	0	43.15	77.06	.200	9.82						
Burlykia	1975.	2.	8	7:59	41.88	73.26	.702	10.47	4.10				3.8	
Tyrnyaus	1977.12	31	11:59	43.39	42.88	.833	9.40	4.00						
STS D	1978.	7	31	8:	0	50.25	77.87	5.000	10.17	3.96				
Massa	1981.11	28	2:31	43.80	76.85	.288	8.22							
Tyrnyaus	1981.12	27	7:44	43.36	42.83	1.075	10.20							
Urgench	1982.12	26	5:29	40.92	61.63	2.550		4.80						
Bukhara-1	1983.	3	23	11:	7	39.24	64.13	1.960	11.03	4.60		4.5		
Bukhara-2	1983.	4	22	3:56	39.49	64.27	5.426	11.37	4.80			4.8	3.9	
Bukhara-3	1983.	5	16	12:	7	39.38	64.26	1.690	11.30	4.70				
Bukhara-4	1983.	5	26	12:46	39.22	64.28	3.830	10.65	4.60				3.8	
Bukhara-5	1983.	6	15	13:34	39.39	64.29	4.140	12.03	4.80			4.9		
Kosh-Bulak	1983.	6	25	20:35	41.02	61.61	2.620	11.93	4.50			4.7		
Bukhara-6	1983.	7.	2	11:42	39.44	64.34	2.560	11.45	4.80			4.7	4.2	
Bukhara-7	1983.	7	11	14:47	39.42	64.34	3.460	11.10	4.65					
Bukhara-8	1983.	8	27	5:	4	39.13	64.30	2.280	11.15	4.55			4.1	
Alindgachay	1984.	4.	9	10:	0	39.23	45.70	.689	10.40					
Quisa	1984.12	16	14:	0	42.52	43.64	.437	10.00						
STS D	1985.	6	27	11:57	49.73	78.10	.500	8.50						
STS D	1987.	6	29	4:55	49.73	78.10	.500	8.50						
Karaganda	1987.	9.	2	7:	0	50.28	72.17	.009	8.85				3.05	~
STS	1987.	9.	2	9:27	50.00	77.34	.020	8.40					2.70	~
Karaganda	1987.	9.	3	7:	0	50.28	72.17	.009	9.00				3.10	~
Uch Terek	1989.	6	11	6:59	41.72	73.25	1.915	11.11	4.85	4.7	4.3			
Arkhangelsk	1991.	2	27	11:25	62.95	41.88	1.000					4.5		#
Lebedinsky	1992.	5	22	8:	3	51.33	37.67	1.222				2.9		@
												3.6		#
Stoliensky	1995.	8.	4	10:	8	51.33	37.67	.299				2.6		#
Stoliensky	1995.	8	18	9:57	51.33	37.67	.156					2.39		@
												2.2		#
Lebedinsky	1995.	8	24	8:10	51.33	37.67	.834					2.15		@
KMA	1995.	8	26	20:	50.80	36.50	.037					2.0		#
Michailovka	1995.	9.	1	8:	52.25	35.33	.106					2.3		#
Stoliensky	1995.	9.	1	10:	3	51.33	37.67	.872				2.5		#
Lebedinsky	1995.	9.	7	8:34	51.33	37.67	.710					3.0		#
Michailovka	1995.	9.	8	8:	52.25	35.33	.320					2.8		#

COMMENTS ON TABLE 1:

mb* values are taken from the ISC or NEIC (or the average of these if both are available).

M** are: magnitudes from NORSAR (denoted by @); or Adushkin et al.(1997) (#); or ML (~).

MPVA is a Russian magnitude scale, similar to mb, but gives slightly higher values because of the different response of the SKM (Russian) sensor vs. Benioff. Approximately, $MPVA = mb + 0.3$.

MLH is a Russian scale similar to Ms, and is based on A/T of surface waves; $MLH = Ms + 0.15$.

The Medeo region is composed of hard granitic rocks. The *K* deficit for these Medeo explosions, with yield from a few tons to a few tens of tons, is never more than 2, and some of them have deficit close to 0. There was no technical reason for these small events to be divided into many smaller explosions (as is often the case at large yield), and the explosions were single-fired.

In Table 2, the *K* deficits (min, max and average) are pointed out for various different groups of chemical explosions, and for UNEs.

Table 2: THE ENERGY CLASS DEFICIT FOR SEVERAL SETS OF EXPLOSIONS

Group of data	N	K		Y, tons		K Deficit		
		min	max	min	max	min	aver.	max
UNE STS	22	10.0	15.0	250	200,000	0.0	0.7	1.3
Canal, dam	18	9.3	12.1	200	5,000	0.5	1.0	2.0
Surface	5	8.0	10.2	300	5,000	2.4	2.7	2.9
Sci.experimental	6	9.9	10.6	200	1,100	0.8	1.25	1.7
Tyrnauz	37	6.0	10.2	10	1,100	0.7	2.0	3.2
Apatity	188	4.5	7.9	4	500	2.8	4.5	6.0
Medeo	57	4.6	8.7	0.3	20	0.08	1.0	2.2
K.Bulak, Almaty	39	5.0	8.2	0.08	30	0.0	1.5	3.0

UPPER LIMIT OF MAGNITUDE VS. YIELD

Figure 2 shows our data on magnitude and log *Y* for numerous chemical and nuclear explosions. We found $M = 4.64 + 0.73 * \log Y (kt)$ for the straight line representing the upper level of magnitude, but this is so similar to the line given by equation (1), which was the result of such an extensive series of studies, that we have chosen to plot equation (1) with our data, and to use this latter line to assign values of the magnitude deficit for chemical explosions.

Equation (1), namely $mb = 4.45 + 0.75 * \log Y (kt)$, does run quite closely through the 3 small single chemical explosions in Kazakhstan (these were the calibration shots close to the

Semipalatinsk test site, arranged in 1987 by the Natural Resources Defense Council), and runs also through the UNE data and most of the large single-fired chemical explosions.

Some of the detailed features pointed out in Figure 1 are present also in Figure 2. For example, the increase in the magnitude deficit is substantial when going from well-coupled large single-fired explosions, to distributed ripple-fired explosions associated with a different practice of industrial blasting. The deficit increases abruptly by 1.5 magnitude units near $Y = 1000$ tons. In Table 3 the magnitude deficit and magnitude and Y intervals are listed for several sets of data.

Table 3: THE MAGNITUDE DEFICIT OF EXPLOSIONS FROM SEVERAL SETS OF DATA

Group of data	N	mb/ML/Mc		Y, ton		M Deficit		
		min	max	min	max	min	aver.	max
UNE STS	20	4.5	6.2	1,700	180,000	-0.2	0.0	0.2
Big.chemical	14	4.8	4.95	700	5,500	0.0	0.3	1.0
KMA, Krivoi Rog	13	2.0	3.2	37	1,200	1.2	1.5	1.8
Apatity	108	1.8	3.1	12	360	0.8	1.2	1.4
small single ChemEx	3	2.7	3.1	9	20	-0.2	0.1	0.5
Gold mine, Nevada	61	0.3	2.0	3	800	1.3	2.5	3.3
NPE, Nevada	1		4.1		1,300		0.4	
Zhuhai, China	1		3.1		11,000		2.1	

The magnitude deficit is from 1 to 2 for large explosions (fired almost simultaneously in long rows) in mines in the Kursk Magnetic Anomaly region (south of Moscow) and at Krivoi Rog (Ukraine). It reaches 2 to 3 for gold mine explosions in the Western U.S. (Jarpe et al., 1996) and is much less for small explosions in Israel, produced in quarries and for road construction (Gitterman et al, 1993 & 1996). The magnitude deficit for the shots in Israel is 0.1 to 1.5.

The NPE in Nevada (using mb from the ISC) has magnitude deficit about 0.4. But if we take into account the difference in attenuation between Nevada and the Kazakh Platform, intensively studied from UNEs at both test sites, a magnitude bias correction of about 0.35 magnitude units can be made. If so corrected, the magnitude deficit for the NPE event is very small. In the same way, a part of the large magnitude deficit for the gold mine explosions (in Nevada, as reported by Jarpe et al., 1996) is due to magnitude bias.

The explosion in Zhuhai, China, was made to level a hilltop for a new airport near Macow. Its magnitude deficit is 2.1, indicating that its huge charge was probably widely distributed.

Note that the magnitude deficit for Apatity shown in Figure 2 (using magnitudes from Mykkeltveit, 1992) is much less then would be expected from the K deficit in Table 2, since normally we expect $\Delta M = 0.47 * \Delta K$ but the Tables give $\Delta M = 1.2$ and $\Delta K = 4.5$. The K values were calculated from data on amplitudes, also published by Mykkeltveit (1992). The

scaling between different regional magnitudes used for different types of events (earthquakes, explosions) is not yet known with confidence.

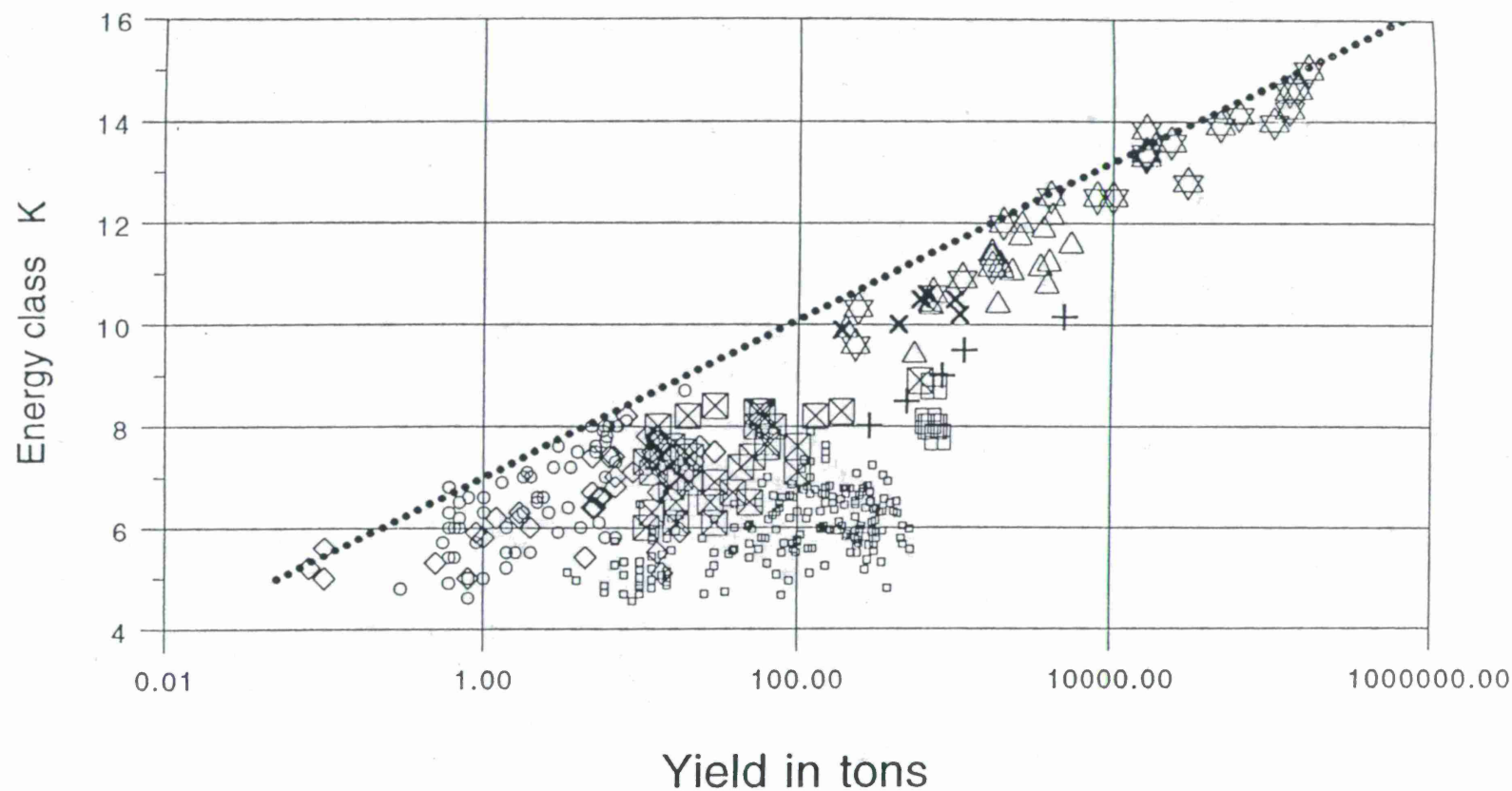
CONCLUSIONS AND RECOMMENDATIONS

We have defined the deficit of an explosion as the amount by which its seismic signals are smaller than would be expected if the explosion were carried out under conditions similar to that of most underground nuclear explosions at the Semipalatinsk test site. The deficit is a quantitative measure of the inefficiency of generation of seismic signals. We find the deficit is typically around 1.5 to 2 magnitude units for chemical explosions carried out in the mining and construction industries. This is the reason that the great majority of blasts that would be counted as large in terms of charge size, are in fact not detected seismically. The reason for the inefficiency of coupling, is presumably because the usual commercial purpose of chemical explosions entails the need to fracture rock into small pieces — which necessitates firing practices (such as ripple-firing) in which much of the explosive energy goes into rock fragmentation. A smaller fraction is then radiated seismically, than would be the case for a well-tamped single-fired shot.

We recommend: (A) that regions where the deficit is low, such as the Kuzbass mining region of Russia, and the region near Abakan further to the east, be made the subject of special studies in seismic discrimination, since explosions with magnitude greater than 3.5 in these regions are likely to be detected a few times each month (or more often); and (B) that relationships between various regional and teleseismic magnitudes be developed for different source types.

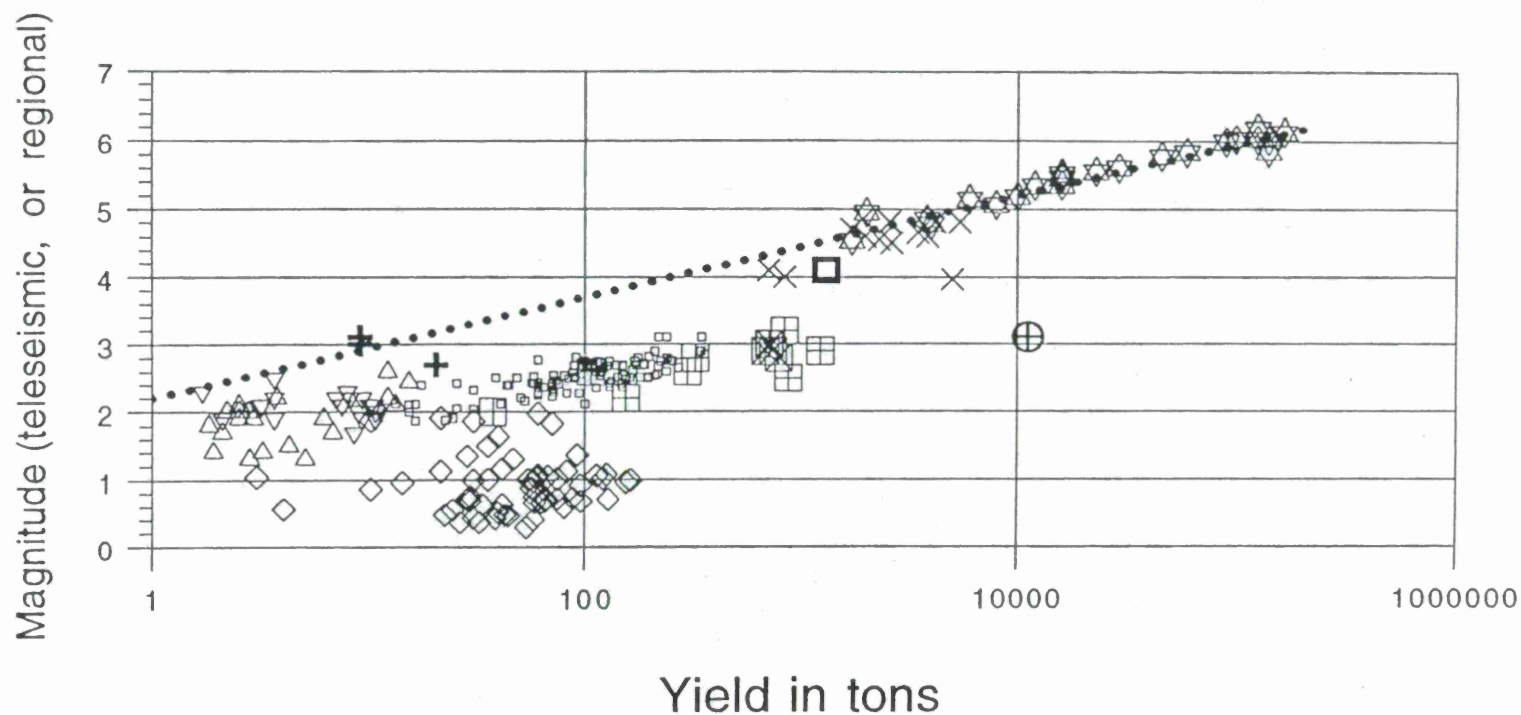
REFERENCES

- Adushkin, V., A. Spivak, W. Leith, Large-scale industrial blasts and CTBT monitoring problems, unpublished manuscript, 1997.
- Gamburzev A.G. et al., Seismic monitoring of Central Asian Lithosphere by explosions. Atlas of Temporal Variations of Natural Processes, Chap.6, pp48-90, 1996.
- Gitterman Ye., T. van Eck, Spectra of quarry blasts and microearthquakes recorded at local distances in Israel, Bull.Seism.Soc.Am., 83, pp1799-1812, 1993.
- Gitterman Ye., Pinsky V., Shapira A., Discrimination of seismic sources using Israel seismic Network, Scientific Report PL-TR-96-2207, AF Phillips Lab., 1996.
- Jarpe, S.P., B. Moran, P. Goldstein et al., Implication of mining practice in an open-pit Gold Mine for monitoring a Comprehensive Test-Ban Treaty. CTBT Seism.Monit.Task S7.2, 1996.
- Khalturin, V.I., T.G. Rautian, P.G. Richards, Statistics on mine blasting and blasting signals, Proceedings of the Annapolis conference on CTBT monitoring, 1996.
- Mykkeltweit S., Mining explosions in the Khibiny Massif (Kola Peninsula, Russia) recorded at the Apatity three-component station. Sci. Report PL-TR-92-2253, AF Phillips Lab., 1992.
- Richards, Paul G., Douglas Anderson, and David Simpson, A Survey of Blasting Activity in the United States, Bulletin of the Seismological Society of America, 82, 1416-1433, June 1992.
- Richards, Paul G., Blasting Activity of the Mining Industry in the United States, in Proceedings of a Symposium on the Non-Proliferation Experiment: Results and Implications for Test Ban Treaties, sponsored by LLNL/Dept of Energy, CONF-9404100, pp. 2-16 to 2-35, April 1994, Rockville, Maryland, ed. M.D. Denny, 1995.
- Ringdal, F., P.D. Marshall and R.W. Alewine, Seismic yield determination of Soviet underground nuclear explosions at the Shagan River test site, Geophysical Journal International, 109, 65-77, 1992.



- | | | |
|---------------------------------------|-----------------------------------|--|
| □ Apatity mine blasts, Kola peninsula | ☆ UNE at Semipalatinsk | ⊠ Tyrnauz mine blasts, S. Caucasus |
| ○ Medeo small ChemEx | × Single ChemEx, underground | • $K = 11.65 + 1.55 \cdot \log Y \text{ (kt)}$ |
| ◇ Quarry blasts, SE Kazakhstan | + Single ChemEx, surface | |
| △ Canal and Dam construction | ⊞ Krivoi Rog mine blasts, Ukraine | |

Figure 1: Energy class (K) vs. Yield, for chemical explosions (ChemEx) and underground nuclear explosions (UNE). The line $K = 11.65 + 1.55 \cdot \log Y \text{ (kt)}$ is a useful reference, against which to evaluate the inefficiency of chemical explosions.



- Apatity mine blasts, Kola peninsula
- + small single ChemEx, Kazakhstan
- ⊕ Zhuchai construction blast, China
- ◇ WUS gold mine
- △ Israeli quarry blasts
- ▽ Israeli road construction
- ⊗ Krivoi Rog mine blasts, Ukraine
- ⊞ Kursk M. A. mine blasts, Russia
- ☆ UNE at Semipalatinsk
- × large single ChemEx, FUSSR
- ChemEx (NPE) at NTS
- $mb = 4.45 + 0.75 \cdot \log Y \text{ (kt)}$

Figure 2: Magnitude vs. Yield, for chemical explosions (ChemEx) and underground nuclear explosions (UNE). The line $mb = 4.45 + 0.75 \cdot \log Y \text{ (kt)}$ is from Ringdal et al. (1992). Industrial blasting is seismically inefficient.

THE KIROVSKIY EXPLOSION OF SEPTEMBER 29, 1996:
EXAMPLE OF A CTB EVENT NOTIFICATION
FOR A ROUTINE MINING BLAST

William Leith
U.S. Geological Survey
Reston VA 20192

Douglas Baumgardt
ENSCO, Inc.
Springfield VA 22210

Nikolai M. Syrnikov
and
Yjuri S. Rybnov
Institute for Dynamics of Geospheres,
Russian Academy of Sciences, Moscow, Russia.

ABSTRACT

On September 29, 1996, a routine mining blast of about 390 metric tons was detonated underground at the Kirovskiy mine in the central Kola Peninsula. The US was notified two weeks in advance that the blast was to take place and was given the date, approximate time, location and total charge. The explosion was detected and located by the prototype International Data Center, and published in the Reviewed Event Bulletin. Analysis of this event provides a detailed picture of a type of underground mining explosion that will be detected by the CTBT International Monitoring System, and provides evidence of the need for regional calibration.

From a CTBT verification perspective, the Kirovskiy blast is of special interest because:

- it is the first example of a government-to-government, advance notice of a routine mining blast;
- the blast occurred underground (at nuclear test containment depths), in a region of intense mining activity, with both surface and underground mining operations and underground cavity creation;
- the event was located by the PIDC and had a large magnitude for an underground blast;
- the error ellipse of the event did not contain the blast site (but included another mining area);
- the mining technique employed is relatively common, and therefore represents a potential source of network-locatable underground events.

Detailed information on the blast, including the type and depth of mining operation, the underground charge configuration, and the blasting delay pattern, is reviewed and combined with a seismological analysis of the event. The seismic analysis implies that there was an associated tectonic component to the blast -- a rock burst or induced tremor -- indicated by small Pn/Sn and Pn/Lg amplitude ratios at high frequency. While this discriminant might identify the event as an earthquake, the spectral/cepstral analysis of the event clearly shows the ripple-fire delays. Considering the potential for evasion at this site, the fact that mine blasts can look like mine tremors or earthquakes to standard discrimination techniques is not problematic, since ripple-fire can usually be detected. However, if a nuclear test was decoupled in a cavity so that its signal was similar in size to aggregates of mine blasts, combined with induced mine tremors, it could be made to resemble a "normal" mining blast. Special attention might then be directed towards large events ($M_L > 3.5$) occurring at or near underground mines, even if they produce large shear waves and have evidence of ripple-fire.

keywords: mining, explosion, blasting, calibration, confidence-building.

OBJECTIVE

On September 29, 1996, a routine mining blast of about 390 metric tons was detonated underground at the "Rudnik" shaft of the Kirovskiy mining combine, located in the central Kola Peninsula (Fig. 1). This blast was unusual, in that the US was notified¹ two weeks in advance that the blast was to take place and was given the date, time, location and approximate total charge. The explosion was detected and located by the prototype International Data Center, and published in the Reviewed Event Bulletin. Having occurred only days after the adoption of the Comprehensive Nuclear Test Ban Treaty (CTBT) by the United Nations, this event is therefore the first example of the pre-notification of an explosion under the voluntary confidence building measures of the CTBT.

Analysis of this event provides a detailed picture of a type of underground mining explosion that will be detected by the CTBT International Monitoring System, and provides evidence of the need for regional calibration. We have collected detailed information on the Sep. 29 blast (hereafter, the "Kirovskiy blast"), including the type and depth of mining operation, the underground charge configuration, and the blasting delay pattern. We have also completed a detailed seismological analysis, including the evaluation of spectral discriminants and cepstral analysis.

RESEARCH ACCOMPLISHED

Mining Operations

The Kirovskiy mine is located in the Khibiny Mountains of the central Kola Peninsula (Fig. 1). In this heavily mined area, rich apatite (calcium phosphate) and related ores are excavated as the principal raw material for Russia's super-phosphate industry. Khibiny operations accounted for 70% of all phosphate mined in the former Soviet Union (Levine, 1989). The Kirovskiy mine is one of the largest underground mining enterprises in Russia, in terms of production capacity, and the ores are excavated from the greatest depths of underground development in the Khibiny massif.

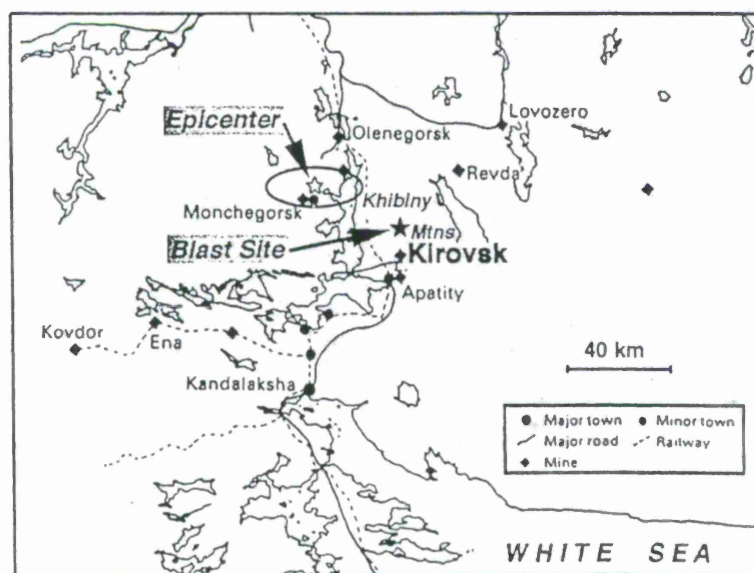


Fig. 1. Map of the southwestern Kola Peninsula, showing the locations of major mines, the Kirovskiy blast of Sept. 29, 1996, and its seismically-determined epicenter and error ellipse.

¹ The US was notified on Sep. 18, by facsimile from the Russian Ministry of Defense, Special Monitoring Service, to the US Deputy Asst. Secretary of Defense for Nuclear Treaty Programs.

The underground ore body is elongate, 12 km in length, with a thickness from 50 to 300 m. The rock massif is distinguished by the high strength of the rocks (approaching that of granites); structural irregularities of various scales (from the Saam fault, with a thickness 2-5 m, to a network of small fractures, with spacings from 0.1 to 1 m); and a high level of tectonic stresses, ranging from 30 to 80 MPa. Rockbursts are well documented there, and there is evidence for tectonic stress release accompanying underground mining blasts (Syrnikov and Rybnov, 1997).

The ore is mined by a method known as blasthole stoping (sublevel stoping), in which multiple, large-diameter, long (up to 60m), vertical holes are drilled for emplacing the explosives (see Hustrulid, ed., 1982, p.95). The use of this relatively new mining method employs large charge sizes in comparison with most underground mining operations, ranging from 150 to 400 tons. The dimensions of a single excavated block are normally 50x50x70 m, which is drilled with a complex system of holes, usually numbering about 1000, defined by the particular blast design.

Delays are used to decrease the seismic effect of the blasts on underground openings. The charged holes are exploded in groups, with up to 20 delay steps. The time interval for each delay is normally 23 msec. In this manner the blast energy is dispersed in space and in time.

Examples of Earlier Blasts

The blast on December 6, 1989, was detonated at 9.33 am local time (Moscow), with a total charge of 320 t (including 80 t at the horizon +322 to the north; see Fig. 2). The charges were exploded simul-taneously, with normal delay intervals between the blast holes. The block dimensions in plan are 30x90 m, with a height of 90 m. The thickness of undisturbed rock above the block was about 400 m. An extremely high level of aftershocks occurred in the 72 hours after the detonation. Dates of blasts at the Kirovskiy mine in 1989 are given in Table 1.

Table 1. Dates, times, total charges and magnitudes of underground mining explosions at the Kirovskiy mine in 1989.

<u>Date (d.m.y)</u>	<u>Time(Mos.)</u>	<u>Charge (t)</u>	<u>Magnitude (Ml)</u>
15.01.89	07.20	100	2.5
26.02.89	06.34	220	3.1
09.04.89	08.46	160	2.7
30.04.89	09.55	259	2.8
30.07.89	08.50	159	2.9
26.11.89	09.35	180	2.6

The blast of December 5, 1993, at 9.50 local time (Moscow) was situated on hanging side of the ore body under previously collapsed covering rocks. The thickness of rock mass over the block was about 500 m. The block dimensions in the plan (see Fig. 2) are approximately 80x55 m, the height was 70 m (for a total voluke of ~310,000m³). The total charge was 255 t. The blast was carried out in 16 stages, each with a 23 msec delay; i.e. total duration of the blast was approximately 0.35 sec. The results of measurements of the displacements and geoelectric potential at this blast were given by Syrnikov *et al.* (1996).

The Blast of Sept. 29, 1996

In September, 1996, instrumental measurements were carried out during a large blast with a total charge of 389 t and 18 delays. The blast was detonated on Sep. 29 at 10.05.46, local time (Moscow). A plan view of the blasting design at hauling horizon +252 is given in Fig. 2, which also shows the locations and dates of previous blasts. The zone depicted shows the massif in a domain limited in the plane by those zones to the north and south in which, before 1989, the ore had been already excavated. This is the so called "pillar-block" (Kozyrev & Panin, 1993).

The vertical section of the block for this blast (charge-hole groups) is given in Fig. 3. The distribution of charges in delay steps is presented in Table 2. This blast successfully separated the pillar-block from the ore handling side and did not create any significant damage to the mine. Maximum velocity values in this case do not exceed 0.25 m/s.

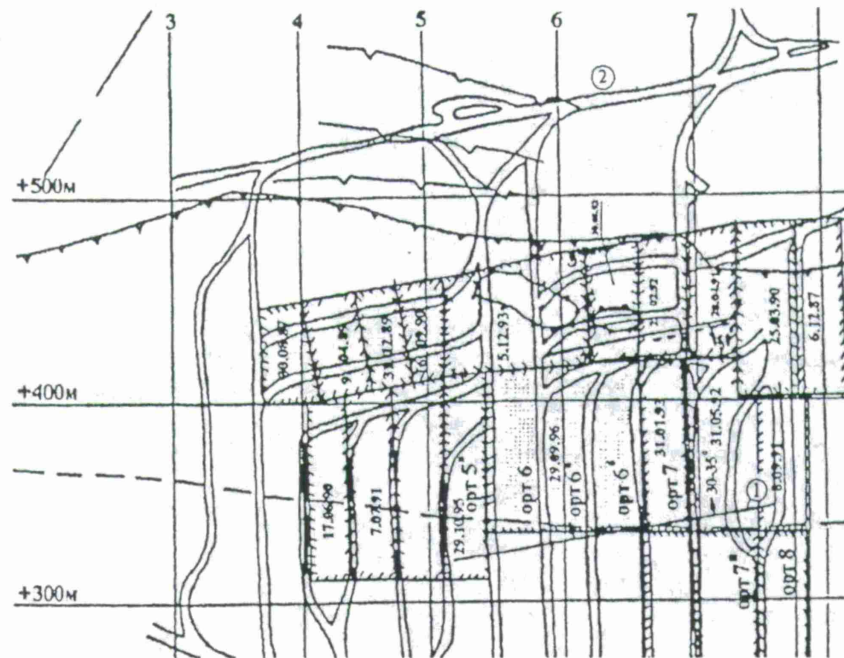


Fig. 2. Plan view of the underground configuration at the Rudnik mine, showing the location of the Sept 29 blast (shaded). This view is of a part of the hauling horizon (at the "pillar-block"); note the locations of previous, similar blasts at the mine (dates). Numbers in circles refer to: 1 - fault, 2 - east haulage drift.

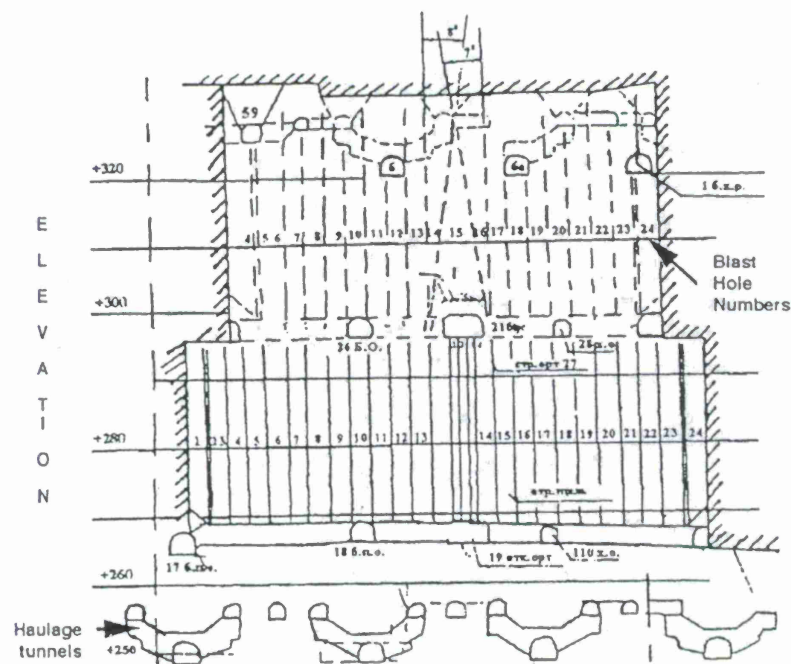


Fig. 3. Cross-section of the drillhole and delay pattern for the Sept. 29 blast. Numbered holes can be referred to the charge-delay sequence, given in Table 2. The block is approximately 100m across (see Fig. 2), and the surface elevation is about 800 m.

Table 2. Delay sequence of the underground blast of Sep. 29, 1996. The delay interval is 23 msec. The upper level holes were detonated first (see Fig. 3).

<u>delay no</u>	<u>holes fired</u>	<u>charge increment (t)</u>
0	1,2,23,24	29100
1	3,22	22478
2	4,5,23,24	30357
3	5,21	18221
4	6,6	17447
5	20,22	17911
6	7,7	16786
7	19,21	17430
8	8,8	17447
9	18,20	17351
10	9,9	14790
11	17,19	17077
12	10,10	15366
13	16,18	16312
14	11,11	15900
15	15,17	16398
16	12,12	16561
17	13,14	18221
18	13,14,14',16, 15,15'	34055 <u>16287</u>
		389175 total charge

The rock broken by the detonation of the first groups of blast holes provides an attenuating effect with respect to the subsequent groups. The velocities of the blast wave at the hauling horizon were relatively small, ranging from 1 m/s, directly against the block, up to 0.1-0.2 m/s further away. In those areas where the instruments were located, the seismic measurements were characterized by velocities in the range of 0.1-0.3 m/s, with frequencies in the range of 20-80 Hz.

Alpha Stations Recording Kirovskiy Explosion, September 29, 1996

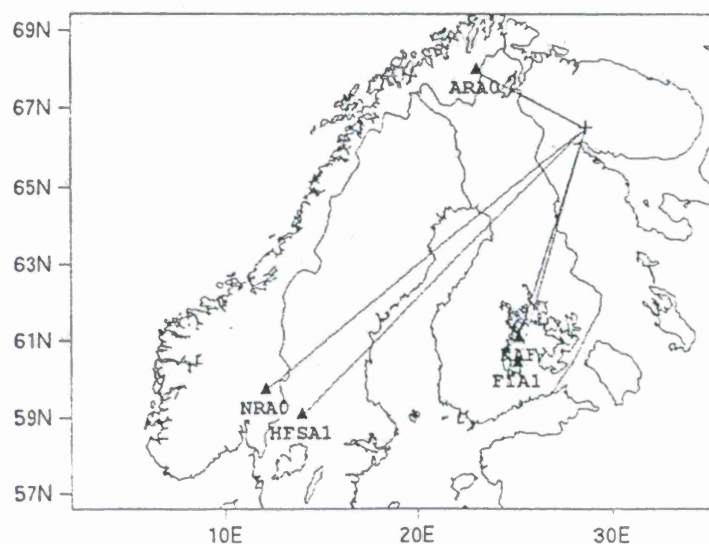


Fig. 4: Location of the event and the stations which recorded the best signals.

Seismic Waveform Characteristics

Fig. 4 shows a map of the location of the Kirovskiy blast and the nearest stations which recorded the best signals from the event. The explosion was recorded by 6 regional stations that reported to the prototype International Data Center (PIDC), and had an estimated local magnitude (M_L) of 3.4. Fig. 5 shows a record section of vertical component short period waveforms for the stations shown in Fig. 4. The waveforms have been filtered in two bands, 2-4 Hz and 4-6 Hz, using 3rd order Butterworth filters. The plots are in distance order, which ranges from 382 km for ARCESS, to 1280 km for NORESS. Lines mark the primary phases, P_n , S_n and L_g .

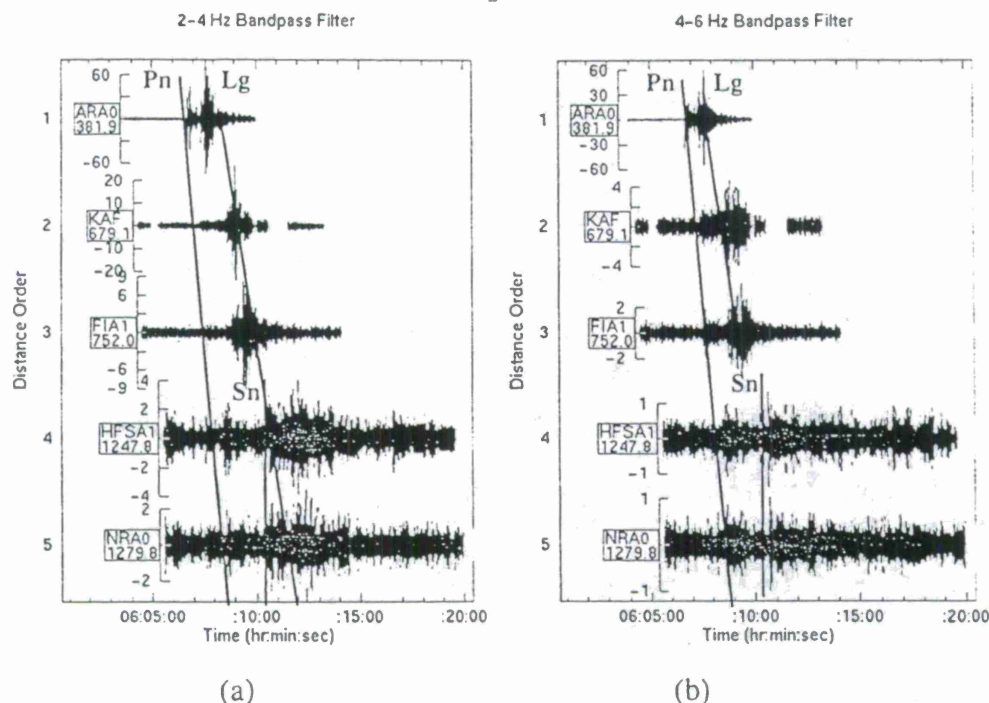


Fig. 5: Waveforms from the Sep. 29, 1996, Kirovskiy blast recorded at the six nearest stations. Waveforms are plotted in distance order. (a) 2-4 Hz filter, (b) 4-6 Hz filter. Note that L_g only appears at ARCESS and KAF at high frequency (4-6 Hz). At Hagfors and NORESS, S_n is the dominant shear wave at high frequency.

Obviously, the best signals were recorded at the stations closest to the event. For the more distant stations, Hagfors (HFSA1) at 1248 km and NORESS (NRA0) at 1279 km, the signal-to-noise ratios were low, although all three phases are visible in the low frequency band (2-4 Hz). In the higher-band (4-6 Hz), only P_n and S_n were recorded and L_g has been strongly attenuated. However, it is notable that for all distance ranges, the amplitudes of the shear waves (S_n and L_g) are larger than the P_n wave amplitudes.

ARCESS recordings had the highest signal-to-noise ratios and therefore were chosen for more in-depth analysis. Fig. 6 shows the results of a bandpass filter analysis of the seismogram recorded by the ARA0 array element of ARCESS. The filters were applied in successive bands covering the range from 0.5 to 2.5 Hz, which is best for R_g detection, and 7 other frequency bands up to 8-10 Hz. Also shown on the plot are the times of the identified main regional phases.

The analysis in Fig. 6 shows clearly that 5 main phases, P_n , P_g , S_n , L_g , and R_g , can be identified. As mentioned above, the shear waves (S_n , L_g , and R_g) have the highest amplitudes. Particularly striking are the energetic S_n and early L_g arrivals in the high-frequency (8-10 Hz) band.

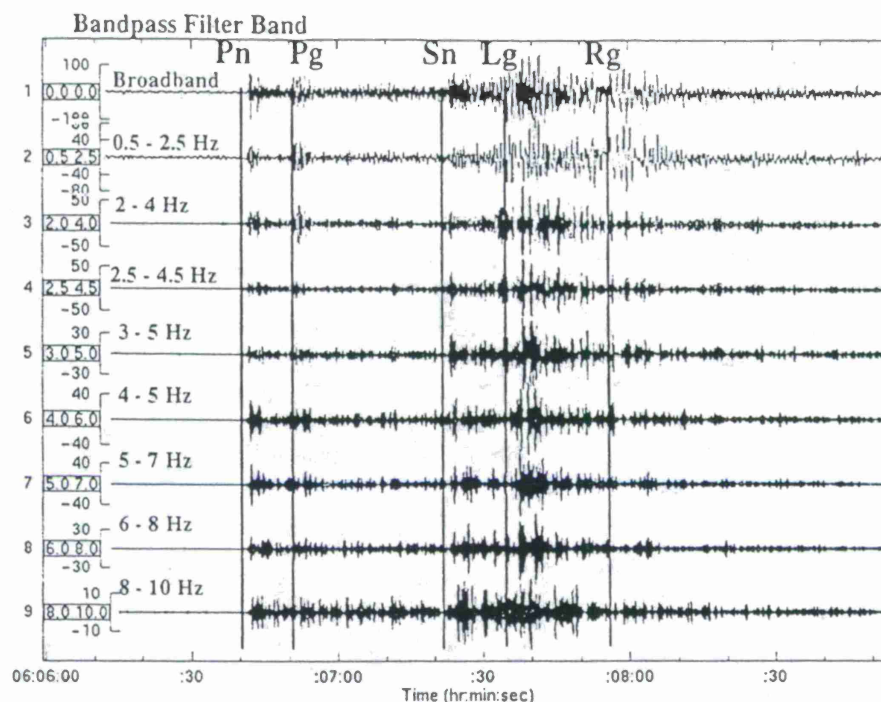


Fig. 6: Bandpass filter analysis of the waveforms recorded at the ARA0 vertical component of ARCESS from the Sep. 29, 1996, event with major phases indicated on the top broadband trace. Note large *Sn* and *Lg* wave amplitudes relative to the *Pn* across the entire frequency band and especially in the 8-10 Hz band.

Discrimination Feature Analysis

Waveform features were extracted from the ARCESS waveforms using the Intelligent Seismic Event Identification System (ISEIS) using techniques described by Baumgardt et al (1991). Two important features used in seismic discrimination are the *P/Sn* and *P/Lg* amplitude ratios in multiple frequency bands. Most studies indicate that these ratios are higher for blasts than earthquakes, presumably because earthquakes are shear sources and produce stronger shear waves than explosions that are primarily compressional sources.

ISEIS measures amplitude ratios for regional arrays like ARCESS by first measuring phase amplitudes from incoherent beams, computed by time-averaging rms amplitudes in one second windows on each array element trace, after applying bandpass filters, and then averaging the amplitudes across all the array waveforms. Amplitude ratios for *Pn/Sn* and *Pn/Lg* are then computed in the same frequency bands using these amplitude estimates.

Fig. 7 shows examples of these measurements of *Pn/Lg* ratio as a function of distance from the array (a) and the *Pn/Sn* ratio as a function of frequency (b). Also shown on the plots are ratios measured for other nearby reference events including other mine blasts (circles) on the Kola Peninsula, earthquakes (squares) in northern Norway and Sweden, and for the *Pn/Sn* ratios, nuclear explosions on Novaya Zemlya. For the *Pn/Sn* ratio plot against frequency in Fig. 7(b), each point represents the average ratio for each class and the error bar through each point indicates the standard deviation. The asterisk indicates the Sep. 29, 1996, Kirovskiy blast and is connected by a line in Fig. 7(b). Also plotted in Fig. 7(b) are measurements for the *Pn/Sn* ratio from the January 31, 1992 event at Novaya Zemlya, which was studied by several investigators with the general consensus that the event was an earthquake (Ryall et al, 1996). (Note: No *Lg* phases were recorded for the Novaya Zemlya events which is why there are no points for nuclear explosions shown in Fig. 7(a).

Generally, in most frequency bands, the Pn/Lg and Pn/Sn ratios for the Kirovskiy blast sequence are comparable with most Kola mine blasts. However, nuclear explosions clearly have higher values of Pn/Sn ratio than many mine blasts and earthquakes. Fig. 7(b) shows a striking dip in the Pn/Sn ratio for the Kirovskiy blast sequence in the frequency band above 8 Hz that falls into the earthquake category. This dip is caused by the large Sn amplitudes in this frequency band discussed earlier. Moreover, as pointed out by Baumgardt (1995) and Ryall et al (1996), mine blasts on the Kola Peninsula generally have ratios which strongly overlap measurements for earthquakes and may make clear discrimination of mine blasts and earthquakes problematic.

As we have pointed out here and elsewhere (Baumgardt, 1996), many of the mines in the Khibiny Massif and Apatity region have a history of rock bursts. It is possible that many explosions in these regions may have had associated rock bursts or induced mine tremors. Recent discrimination studies of mine tremors and rock bursts throughout the world (e.g., Bennett et al, 1994; Bennett et al, 1995) have shown that discrimination features of these events more closely resemble earthquakes than nuclear explosions which lack an associated tectonic component. We suggest that the Kirovskiy blast falls in the category of combined mine blast and mine tremor, perhaps induced, that caused the enhanced shear waves due to the tectonic component.

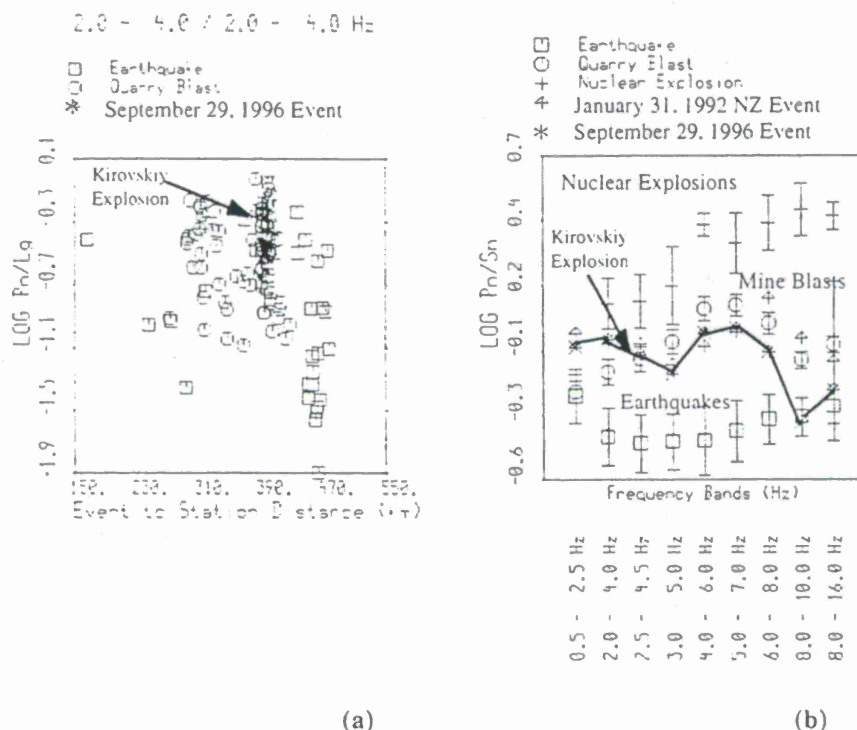


Fig. 7: Scatter plots of Pn/Lg amplitude ratios versus distance (a) and Pn/Sn amplitude ratios versus frequency band (b).

Spectral and Cepstral Features - Ripple Fire

We now explore the spectral and cepstral characteristics of the Kirovskiy blast data, which can provide information about ripple fire sequence of the shots. Baumgardt and Ziegler (1988) have shown that ripple-fire produces time-independent scalloping features and also consistent, time-independent cepstral peaks for all phases. The Kirovskiy shot sequence consisted of eighteen 23 ms shot delays spread over a horizontal region of about 140 m and depth range of about 60 m. The ARCESS sampling rate of 40 Hz precludes resolution of 23 ms, but the aggregation of shots will produce longer shot delays which can be resolved.

Fig. 8(a) shows spectra for each of the phases in the range of 1 to 16 Hz and Fig. 8(b) shows the cosine cepstra computed for each spectrum (see Baumgardt and Ziegler, 1988). The spectra

were computed by averaging across the array individual spectra on each array-element waveform, for 10 second windows, starting at the picked phase times and smoothed with a Parzen time window. The ARCESS instrument response was deconvolved from each spectrum. Cepstra were computed from the spectra by Fourier transforming the power spectra in the band from about 1 Hz to 19 Hz, with smoothing to eliminate end effects and removal of the polynomial trend. The same analysis was also applied to the noise ahead of the P_n phase.

The spectra for the five detected phases, Fig. 8(a), has scalloping not present in the noise, but the pattern is very complex. However, the cepstra plotted in Fig. 8(b) are much simpler and show at least 5 sets of consistent cepstral peaks (vertical lines). Note that these peaks do not appear in the noise cepstrum; this indicates that the peaks result from spectral modulations caused by the source.

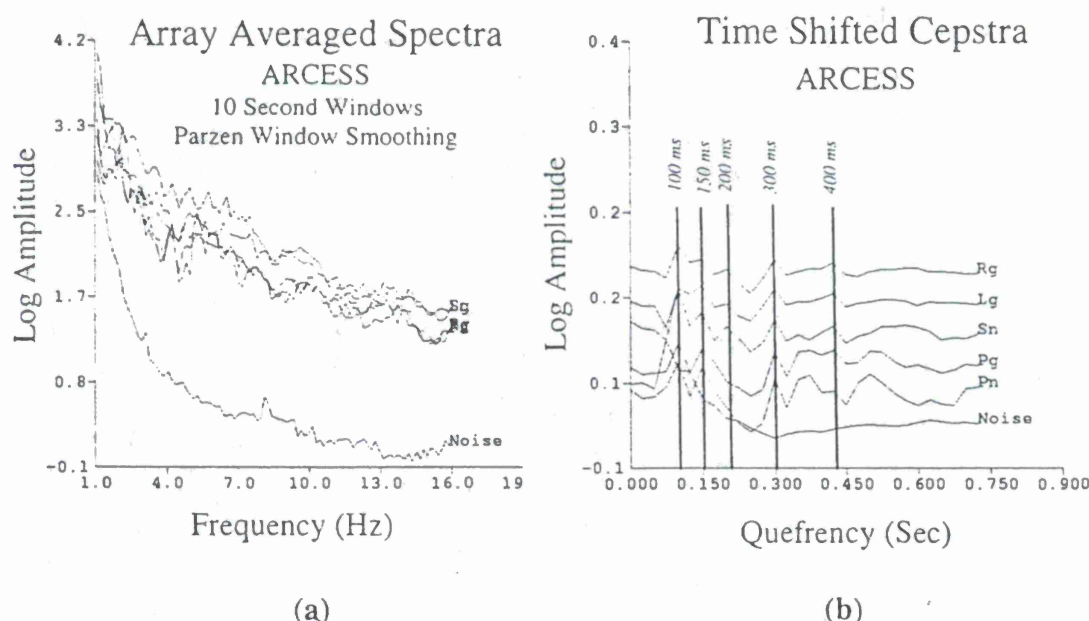


Fig. 8: Array-averaged spectra (a) and cepstra (b) for the Sep. 29, event recorded at the ARCESS array. Vertical lines in (b) indicate consistent time independent cepstra caused by the ripple-fire delays.

The delay times for these peaks range from 100 to 400 ms. The 400 ms time is close to 18 times 23 ms or 414 ms and gives the approximate overall shot duration. However, other stronger peaks are apparent at lower delay times, particularly at 100 and 300 ms.

Baumgardt (1995) has argued that the strength of spectral modulations, and the resulting cepstral peaks, are strongly associated with the correlation distances between the shots. Because the 400 ms delay corresponds to the largest shot separation, which is over 100 m and this large separation decorrelates the signals, the weak cepstral peak for the longest delay, or the total duration, may have been caused by this decorrelation. The shorter delays come from shot aggregations that are closer together spatially, and the larger cepstral peaks result from the signals being better correlated. Thus, not only does cepstral analysis give an indication of the shot duration and some of the individual shot aggregation times, but also the cepstral peak amplitude distribution is a direct indication of the ripple-fire spatial distribution and size.

CONCLUSIONS AND RECOMMENDATIONS

From a CTBT verification perspective, the Kirovskiy mining blast is of special interest because:

- it is the first example of a government-to-government, advance notification of a routine mining blast;

- the blast occurred underground (and at nuclear test containment depths), in a region of intense mining activity, with both surface and underground mining operations and underground cavity creation;
- the PIDC calculated a location and a relatively large magnitude for an underground blast;
- the error ellipse of the event did not contain the blast site (and actually included another mining area) --this has important implications for approaches to on-site inspection and points out the need for improved network calibration;
- the mining technique employed was not unique, and therefore represents potential source of network-locatable underground events.

The seismic analysis implies that there was an associated tectonic component to the blast --a rock burst or induced tremor-- indicated by small Pn/Sn and Pn/Lg amplitude ratios at high frequency. This discriminant might identify the event as an earthquake. However, the spectral/cepstral analysis of the event clearly shows the ripple-fire delays. The fact that mine blasts can look like mine tremors or earthquakes is not a serious issue since ripple-fire can usually be detected. Single nuclear explosions would be identified as having large Pn/Sn or Pn/Lg ratio and no evidence of ripple-firing. However, if a nuclear explosion was partially decoupled (in a cavity) so that its signal was comparable in size to aggregates of conventional mine blasts, combined with induced mine tremors, it could be made to resemble a "normal" mining blast. Special attention might then be directed towards large events ($M_l > 3.5$) occurring at or near underground mines, even if they produce large shear waves and have evidence of ripple-fire.

REFERENCES

- Baumgardt, D.R., and others (1991). Design and development of the intelligent event identification system, *PL-TR-91-22298(I)*, Final Rep., vols. I, II, and III, ENSCO, Inc., Springfield, VA.
- Baumgardt, D.R. (1995). Case studies of seismic discrimination problems and regional discriminant transportability, *PL-TR-95-2106*, Final Report, ENSCO, Inc., Springfield, VA.
- Baumgardt, D.R. and K. Ziegler (1988). Spectral evidence of source multiplicity in explosions: application to regional discrimination of earthquakes and explosions, *Bull. Seism. Soc. Am.*, Vol. 78, 1773-1795.
- Bennett, T.J., and others (1994). Characteristics of rockbursts for use in seismic discrimination, *PL-TR-94-2269*, Final Report, Maxwell Laboratories, Inc., S-CUBED Div., La Jolla, CA.
- Bennett, T.J., and others (1995). Investigations of the seismic characteristics of rockbursts, *PL-TR-95-2169*, Sci. Rep. #1, Maxwell Laboratories, Inc., S-CUBED Div., La Jolla, CA.
- Hustrulid, W.A., ed., 1982, *Underground Mining Methods Handbook*, Soc. Mining. Engrs., New York.
- Kozyrev A.A., and Panin, V.I. 1993. Effect of large-scale mining operation on the geodynamic behavior of the area, and mine-induced seismicity manifestation. *Proc. ISRM Int. Symp. Eurock '93*.
- Levine, R.A., 1989, *Mineral Development on the Kola Peninsula, Present Conditions and Future Prospects*, Norw. Atlantic. Comm, Security Policy Lib. No.9-1989, 22pp.
- Ryall, A. S., and others (1996), Resolving regional discrimination problems: some case histories, in *Monitoring a Comprehensive Test Ban Treaty*, Ed. E.S. Husebye and A.M. Dainty, NATO ASI Series, pp 721-741.
- Seismic events in Northern Europe*, 1989. Helsinki University, N6.
- Syrnikov, N.M., and others, 1996. On some exhibitions of structure heterogeneities in rock massif as the effect of large-scale action. *Proc. ISRM Symposium EUROCK'96*, Torino, A.A.Balkema, Rotterdam, v.1, p.483-490.
- Syrnikov, N.M., and Rybnov, Y.S., 1997, *On Rock Massif Instability From Blasting*, preprint, Russian Acad. Sci., Inst. Dynam. Geospheres, 12pp.

MOMENT TENSOR INVERSION CODES FOR THE INTERNATIONAL DATA CENTER USING REGIONAL AND TELESEISMIC BROADBAND DATA

Michael Pasyanos, Doug Dreger, and Barbara Romanowicz
Seismological Laboratory, University of California at Berkeley

Contract No W2-6-B102600-01
Sponsored by Advanced Research Projects Agency (ARPA)

Abstract

Methods of calculating moment tensor solutions using regional and teleseismic broadband data have been implemented at the International Data Center (IDC). Using methodologies adapted from regional inversion procedures, we have been able to readily determine the source parameters for large teleseismic events using data available from the IDC. As we attempt to apply these techniques to smaller earthquakes, the problem is complicated by fewer recording stations, lower signal-to-noise ratio, and more heterogeneous earth structure at shorter periods. There appears to be significant interest in making long period data for beta stations available, which should increase the number of stations available for the inversion. We are beginning to test various laterally heterogeneous earth models to account for propagation. This is a report outlining the methods, our results for large teleseisms, and progress that is being made for its implementation for smaller sources.

keywords: seismic sources, moment tensor solutions, surface waves, phase velocity, waveform inversion

Objective

The International Monitoring System (IMS) has taken a multi-disciplinary approach to ensure the verification of the Comprehensive Test Ban Treaty (CTBT). Calculating moment tensor solutions appears to be a promising method of adding to the number of detection tools available to monitor the treaty. Moment tensors can be of interest to the monitoring community for several reasons: centroid depth estimation, moment magnitude as a long period / short period seismic discriminant, robust determination of earthquake size, and the determination of the non-double couple component of the moment tensor. Towards this goal, we are adapting regional moment tensor inversion procedures developed at UC Berkeley for the conditions that are needed for global monitoring. Two different methodologies are being tested for implementation at the IDC, a frequency-domain surface wave inversion method and a time-domain waveform modelling method. In recent years, these methods have been successfully employed at the regional scale to retrieve earthquake source parameters (Romanowicz *et al.*, 1993, Pasyanos *et al.*, 1996). This report outlines the two methods, their application to large global events and their extension to smaller earthquakes.

Research Accomplished

Surface Wave Methodology

In the surface wave inversion method we invert Love and Rayleigh waves using a two-step inversion procedure (Romanowicz, 1982). The waveforms are rotated into a earthquake reference frame in order to isolate the Love waves on the transverse horizontal component. Appropriate group velocities are used to window the Rayleigh waves on the vertical component and Love waves on the transverse component, and the windows are then transformed to the spectral domain. The period used in the inversion is based upon the size of the event. Long period waves (~ 150 sec) can be used for large earthquakes that are recorded teleseismically, but moving to intermediate periods (< 50 seconds) is necessary for smaller regional events. We make a phase velocity correction applicable for the particular propagation path, in order to account for lateral heterogeneity.

Finally, after correcting the selected stations for propagation, the two-step frequency-domain surface wave inversion is performed. This method relies on the simple azimuthal radiation pattern of surface waves from earthquake sources to screen out unmodelled short wavelength variations of structure along source-receiver paths. In the first step of the inversion, azimuthal coefficients of the radiation pattern and half-duration of the source are determined from a least square inversion of the complex spectra for a discrete set of frequencies. Testing a range of source durations, including negative source durations, also allows us to account for any large errors in origin time. In the second step, the azimuthal coefficients are inverted at a series of trial centroid depths to obtain estimates of the moment tensor M and centroid depth h (Romanowicz and Monfret, 1986).

Complete Waveform Methodology

In the time-domain method complete waveforms are used. While the long-period waves that are used ($\text{freq} \leq 0.1$ Hz) are relatively insensitive to the details of crustal structure, they are sensitive to changes in crustal thickness, average crustal velocity, and near surface velocity gradient. Region specific velocity models are calibrated by forward modelling broadband technique (Dreger and Helmberger, 1990; Helmberger *et al.*, 1993). Green's functions for each model are then generated for a range of distances and source depths. The inverse procedure then fits the Green's functions to the data yielding the seismic moment tensor, and differs from other CMT type inversions in that only the high frequency location is used, the data are not aligned according to the event origin

time, and a revised centroid location is not solved for. Rather, the Green's functions are optimally aligned to the data using a cross-correlation function. This level of approximation affords a greater level of flexibility in rapid source parameter determinations when event locations and origin time are preliminary.

Source depth is found by iteration and evaluating an objective function which depends upon both the RMS of the difference between the data (d) and the synthetic waveforms (s) divided by the percent double couple (pdc): Smaller numbers indicating better fits are obtained when both the waveform misfit $\text{RMS}(d - s)$ is small and the pdc is large. Although three component waveform inversion of a single station may resolve the moment tensor parameters (Dreger and Helmberger, 1991), the use of multiple stations improves the stability of the results.

Application to Large Global Events

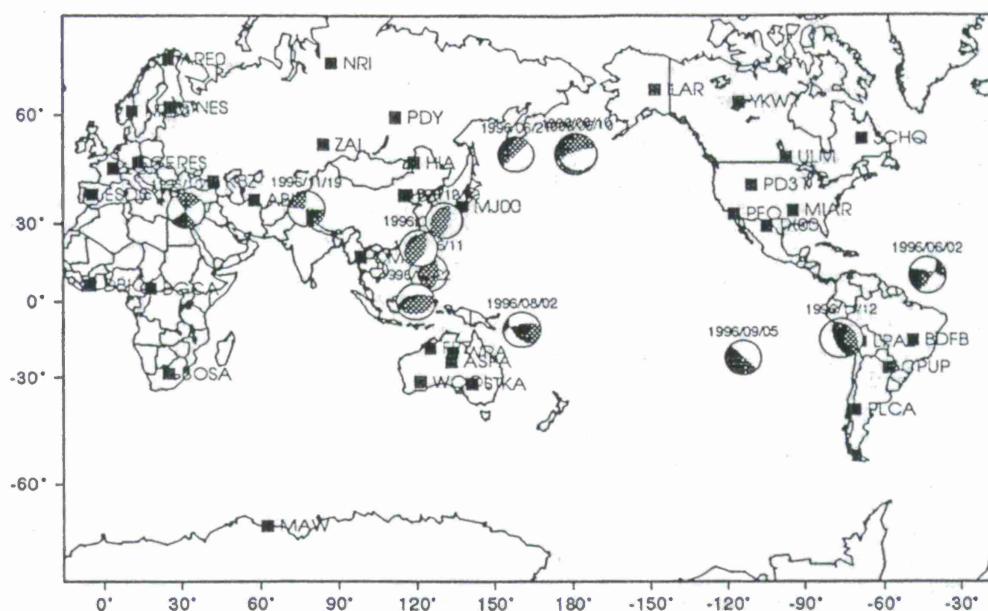
In order to extensively test how well the codes performed for the largest global events, we calculated moment tensor solutions for every event from June 1996 through December 1996 having a surface wave magnitude greater than 6.5. There were a total of 14 events over this time interval. Most of the events were located in the western Pacific, although events also occurred in the North Atlantic, Easter Islands, Cyprus, Peru, and Eastern Kashmir.

Moment tensor solutions for the rest of the earthquakes during this time period are shown in figure 1a. This map shows the location and moment tensor solution of the events along with the location of the primary stations in the IDC network. The moment tensor solutions for each of these events are then compared with solutions determined using the Harvard CMT method (figure 2). For each of the events, we make a side-by-side comparison of the mechanism computed using the surface wave method and IDC data (left column) with the Harvard CMT mechanism (right column). In the case of several events, there is either a slight rotation in strike (i.e. event 691912 - North Atlantic Ridge) or more commonly, differences in the dip (i.e. event 718715 - Kamchatka Peninsula). However, for the most part, the moment tensor solutions computed using the different methodologies and datasets compare very well.

Finally, in figure 1b we proceed to compare the moment magnitude (M_w) determined using the Harvard CMT method to three other magnitude estimates. The first is a comparison to the surface wave magnitude (M_s) estimated at the IDC. These compare very well for most of the events over the range of magnitudes that we considered, although it is possible that this methodology might break down for the largest events. We performed a second comparison to body wave magnitude (m_b), also estimated at the IDC. These events appeared to be saturated at about the magnitude 6 level and generally fell 1 - 2.5 magnitude units below the moment magnitude values. The next comparison was with local magnitude (M_L). Only 4 of the events that we considered had values for local magnitude in the database. Those events, however, showed very similar characteristics to the estimates of body wave magnitude. Again, the magnitudes appear to be saturated and fall well below the moment magnitude estimate. Finally, we compared the moment magnitude estimated using the surface wave method and IDC data to the Harvard magnitude estimate. This appears to compare very well over the range of magnitude considered.

Extension to Smaller Events

It appears that the inversion codes are working well for large global events. As we investigate smaller events and move to shorter periods, a laterally homogeneous earth model will be insufficient. Additionally, the lower signal-to-noise ratio will only allow the closest stations to be utilized in the inversion. For these smaller events, it may be necessary to include long period (LP) data from beta



Moment tensor solutions for events $M_s > 6.5$ from 6/96 - 12/96 using IDC data

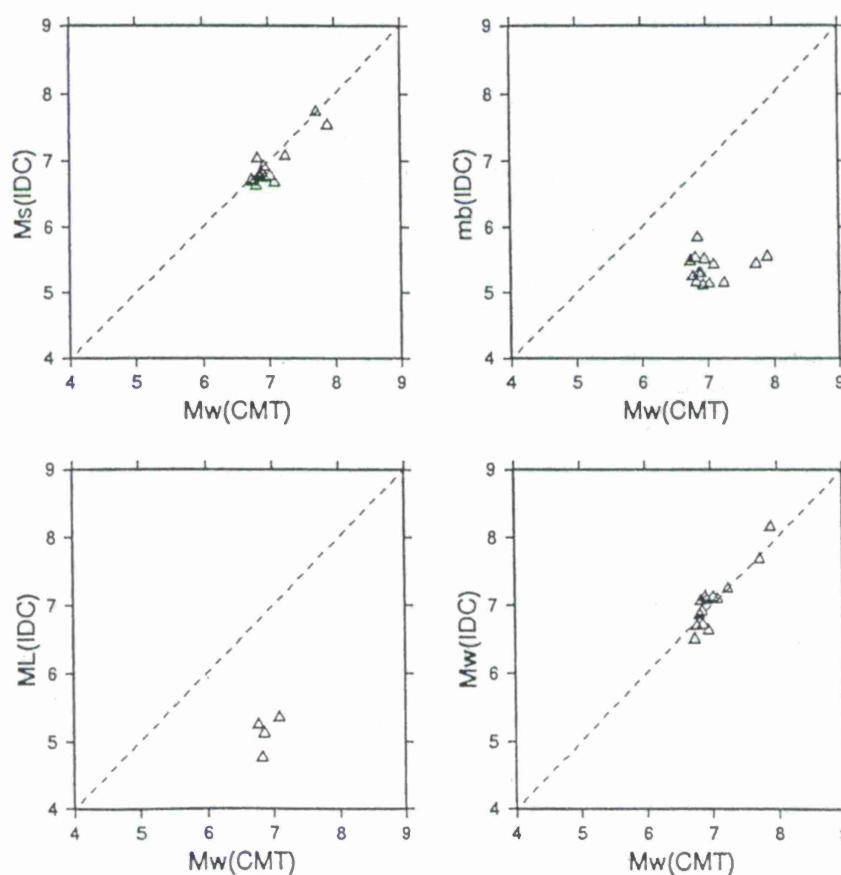


Figure 1: a) Map showing IDC stations and moment tensor solutions for events. b) Comparison of IDC M_s , m_b , M_L , and M_w magnitudes to Harvard CMT M_w .





























Event	IDC		CMT	
691912 North Atlantic Ridge		$M_w=6.63$		$M_w=6.95$
705672 Andreanof Islands		$M_w=8.15$		$M_w=7.90$
703939 Andreanof Islands		$M_w=7.25$		$M_w=7.25$
709429 Philippine Islands		$M_w=7.09$		$M_w=7.09$
718715 Kamchatka		$M_w=6.50$		$M_w=6.74$
750925 Minahassa Peninsula		$M_w=7.12$		$M_w=7.02$
759544 Solomon		$M_w=7.08$		$M_w=6.93$
789156 Easter Island		$M_w=7.13$		$M_w=6.90$
791489 Philippine Islands		$M_w=6.86$		$M_w=6.81$
825960 Cyprus		$M_w=6.91$		$M_w=6.85$
836171 Kyushu, Japan		$M_w=7.06$		$M_w=6.83$
860359 Peru		$M_w=7.68$		$M_w=7.73$
865344 Eastern Kashmir		$M_w=6.71$		$M_w=6.86$
875803 Kyushu, Japan		$M_w=6.69$		$M_w=6.77$

Figure 2: Comparison of IDC and CMT solutions for large teleseismic events in the latter half of 1996. Moment tensor solution and moment magnitudes are shown for each event.

station, which should be available shortly. We feel that this may be necessary in order to take the method down to lower magnitude levels. We chose the Middle East as our test area since it is a region of monitoring interest, active seismicity, varied earthquake mechanisms, and a reasonable distribution of stations available at the IDC. We selected all events in our test area in the first six months of 1997 with surface wave magnitude greater than 4.5 (figure 3a). Most of the seismicity in the region is confined to events along the compressional boundary between the Eurasian and African Plates, from the Eastern Mediterranean to Zagros Mts. There is also extension occurring between the African Plate and Arabian subplate along the Red Sea, as well as compression along the Eurasian/African boundary region in India. Nearby stations are shown in figure 3b.

One model that we are currently testing is the mantle earth model of Li and Romanowicz (1996) (hereafter referred to as the SAW12D model). This model is a three-dimensional shear velocity model of the whole mantle developed using SH waveform data and utilizes the nonlinear asymptotic coupling theory in the inversion. The model is expressed horizontally in degree 12 spherical harmonics and vertically in degree 5 and degree 7 Legendre polynomials in the upper and lower mantle, respectively. To correct for variations in the crust, we add a topography-bathymetry model (ETOPO5, 1992) and a Moho depth model that reflects the difference in continental and oceanic Moho depths. The overall model is used to generate phase velocities along each source-receiver path and make the necessary propagation corrections for each path. In the future, we plan on testing other earth models, such as a model developed by Jeff Stevens from surface wave phase velocities.

Figure 4 shows the dispersion curves for Love and Rayleigh waves between 30 and 500 seconds calculated using the SAW12D model for paths from an earthquake in Syria. Note that there is about a 0.1 km/s spread in the phase velocities. This variation can produce very large differences in the propagation phase when integrated over the path length. Since $\phi = \omega x/c = 2\pi f x/c$, then $\delta\phi = 2\pi f x \delta c/c^2$. Hence, a 0.1 km/s difference in 50 second Rayleigh waves (~ 4.0 km/s) for a 4000 km epicentral distance will result in a π phase shift.

Example

An example of the surface wave codes for the smaller earthquakes is shown for an event located in Syria (figure 5). The top figure represents the moment tensor solution generated using the PREM model (figure 5a) while the bottom figure uses the SAW12D model (figure 5b). On the left side of each figure, the amplitude and phase of 85 second Rayleigh waves are plotted as a function of azimuth. The amplitude and phase recorded at each station are shown with triangles and circles, respectively, while the station names are shown above each of the symbols. The results of the inversion are shown on these figures with a solid line. To the left of each figure is a beachball of the moment tensor solution along with a residual-depth curve.

Using the PREM model, the solution produces a thrust mechanism. The phase fits are truly poor, however, owing to the inappropriate propagation model. We would expect that, at the frequencies of the inversion (40 – 90 seconds), we must make use of phase corrections for specific paths instead of using a single globally-derived model. While a minimum in the residual-depth curve occurs at shallow depths, the depth is not well resolved. Estimates of depth from other sources were all fixed at shallow depths of 10 and 15 km. Finally, even with such a poor solution, the moment magnitude for this event was calculated to be 5.3. Compare this to m_b 5.4, M_S 5.4, and Harvard CMT M_w of 5.7.

When we employ the SAW12D model, however, we see a change in the solution from a thrust to strike-slip mechanism. In this case, we are fitting both the phase data (which changed with the new model) and the amplitude data (which did not) better with the new mechanism. We also find

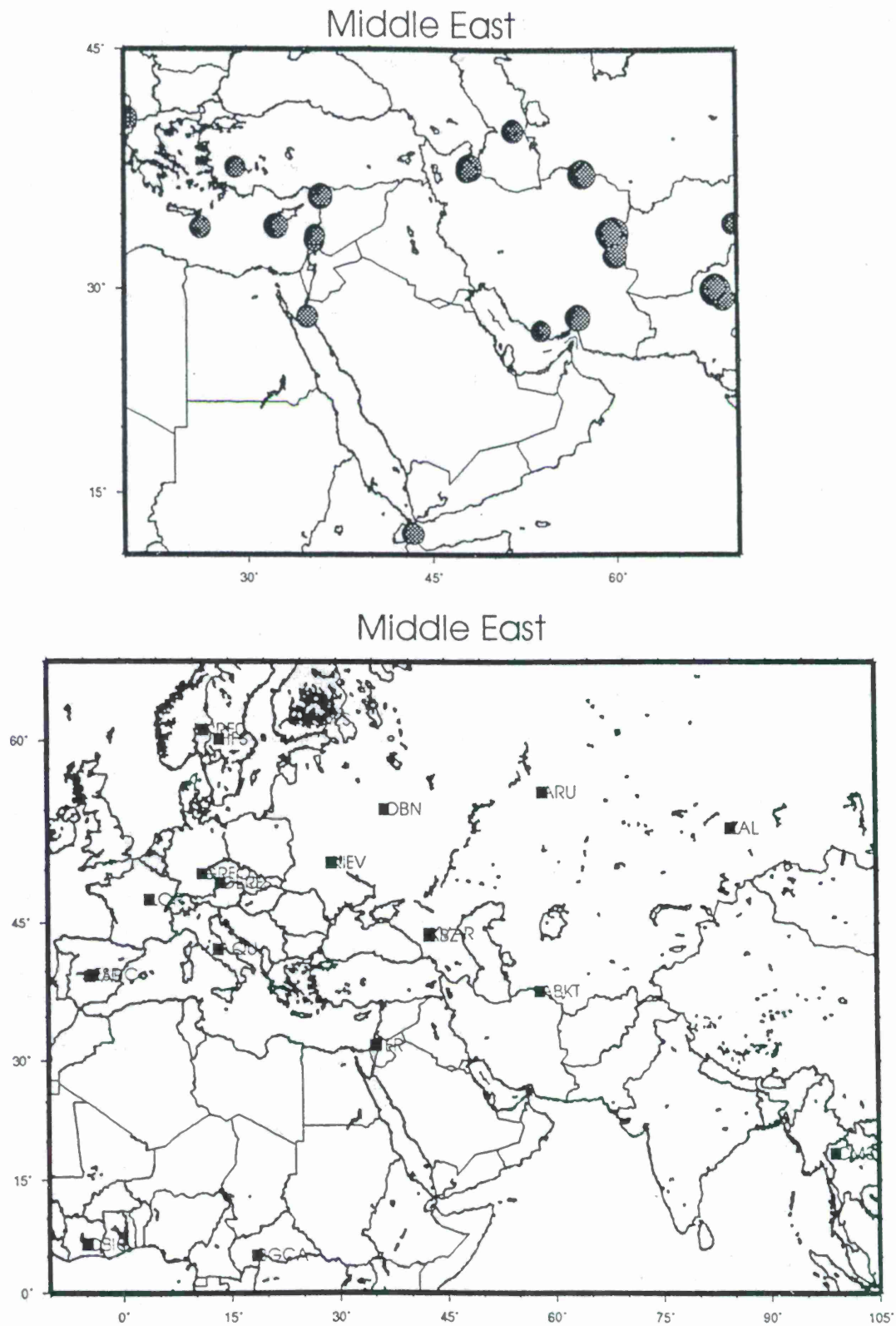


Figure 3: Seismicity and nearby stations for our test region. Earthquakes with surface wave magnitude > 4.5 occurring in top region were selected.

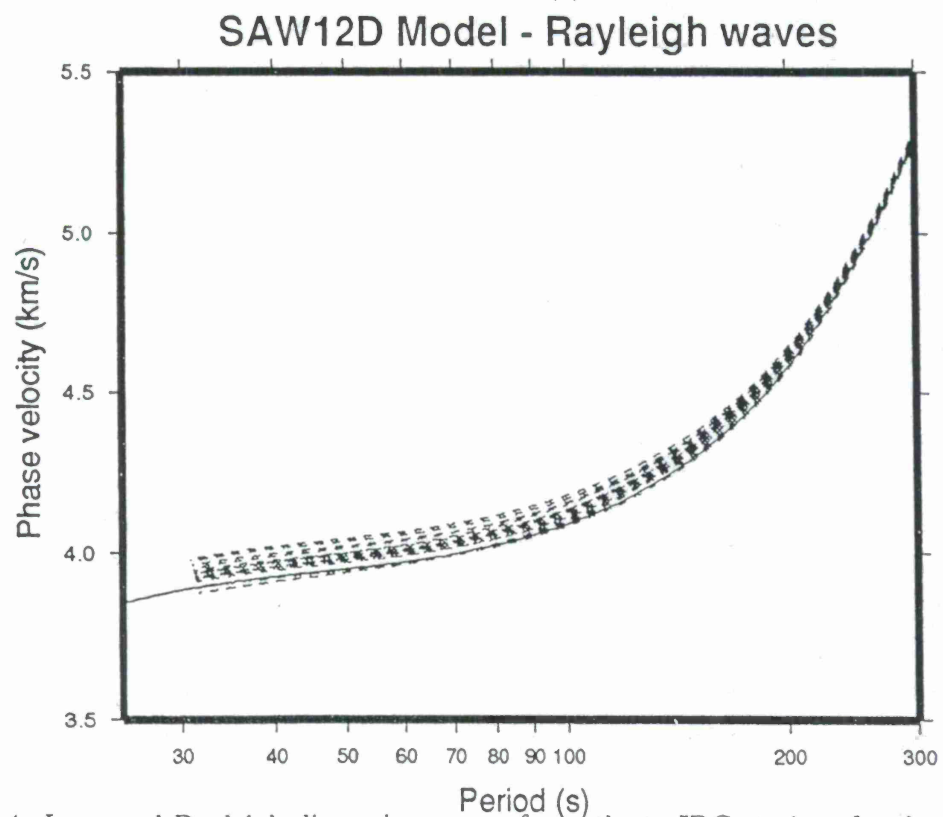
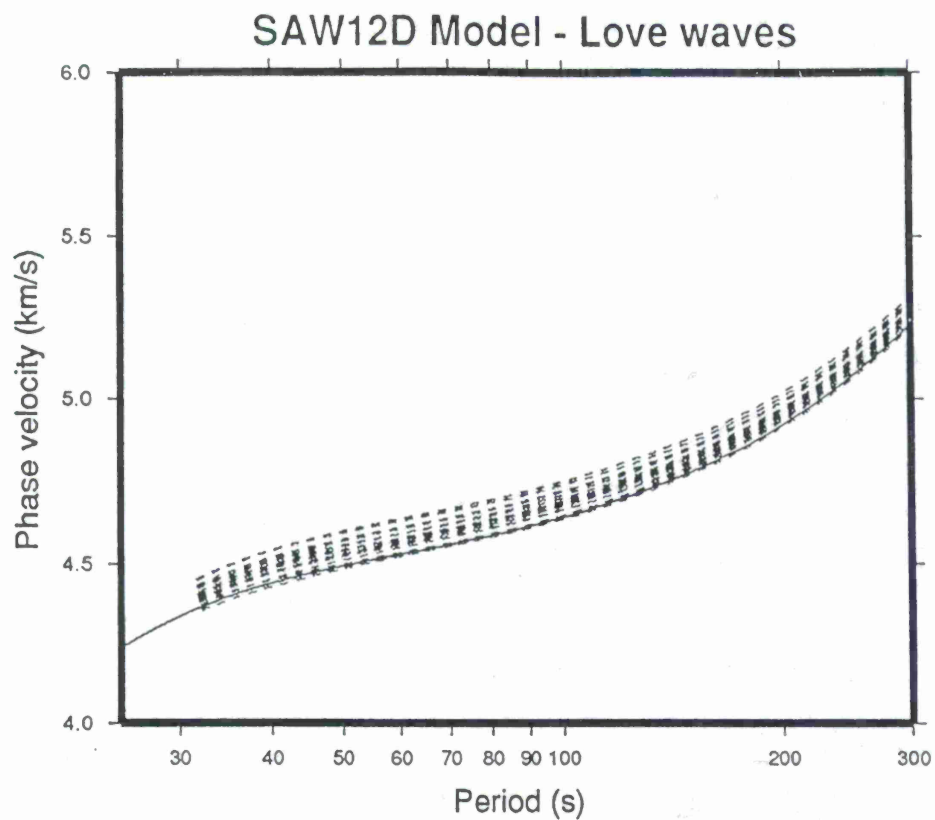


Figure 4: Love and Rayleigh dispersion curves for paths to IDC stations for the 01/22/97 Syrian earthquake. The solid line on each figure indicates the PREM model.

a much sharper minimum in the depth-residual curve at shallow depths. Furthermore, this solution is consistent with other mechanisms determined for this event. The seismic scalar moment from the second inversion drops slightly resulting in a moment magnitude of 5.2. This example should illustrate the importance of 3D path corrections for the periods used in the inversion for events of this magnitude

While this solution is stable for long periods, it starts to break down as we shift the periods used in the inversion to less than about 40 seconds. This suggests that while the model appears to be successful at generating appropriate adjustments at intermediate periods, the model starts to break down at shorter periods. For even smaller events where we need to rely on short period data, we must either employ global models that are sensitive to shorter wavelength structure or rely on regional earth models.

Conclusions and Recommendations

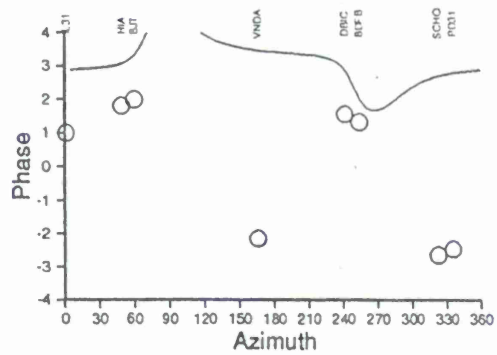
The moment tensor methods work well for the largest earthquakes using long period waves and simple laterally homogeneous earth models. We are currently working towards a similar goal with smaller sources. We have demonstrated that laterally homogeneous models are insufficient to generate adjustments for the short period data of these earthquakes. Towards this goal, we are just beginning to test various earth models which account for the more complicated wave propagation at higher frequencies. In the future, we expect to improve our results by employing more beta stations, selecting earth models which are most appropriate, and testing, modifying and developing new earth models.

References

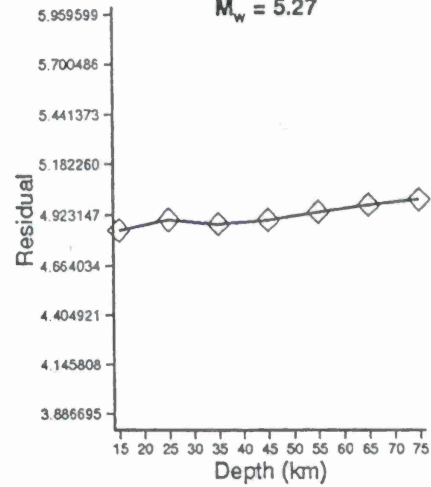
- Dreger, D. S., and D. V. Helmberger (1990), Broadband Modeling of Local Earthquakes, *Bull. Seism. Soc. Am.* **80**, 1162-1179.
- Dreger, D.S., and D.V. Helmberger (1991), Complex Faulting Deduced from Broadband Modeling of the 28 February 1990 Upland Earthquake ($M_L=5.2$), *Bull. Seism. Soc. Am.* **81**, 1129-1144.
- Helmberger, D., D. Dreger, R. Stead, and H. Kanamori (1993), Impact of Broadband Seismology on the Understanding of Strong Motions, *Bull. Seism. Soc. Am.* **83**, 830-850.
- Li, X.D., and B. Romanowicz (1996), Global mantle shear velocity model developed using nonlinear asymptotic coupling theory, *J. Geophys. Res.* **101**, 22,245-22,272.
- Pasyanos, M.E., D.S. Dreger, and B. Romanowicz (1996), Toward Real-Time Estimation of Regional Moment Tensors, *Bull. Seism. Soc. Am.* **86**, 1255-1269.
- Romanowicz, B. (1982), Moment Tensor Inversion of Long-Period Rayleigh Waves: A New Approach, *J. Geophys. Res.* **87**, 5395-5407.
- Romanowicz, B. and T. Monfret (1986), Source Process Times and Depths of Large Earthquakes by Moment Tensor Inversion of Mantle Wave Data and the Effect of Lateral Heterogeneity, *Annales Geoph.* **74**, 271-283.
- Romanowicz, B., D. Dreger, M. Pasyanos, and R. Uhrhammer (1993), Monitoring of Strain Release in Central and Northern California Using Broadband Data, *Geophys. Res. Lett.* **20**, 1643-1646.

926006 01/22/97

Rayleigh waves - 85.33 sec

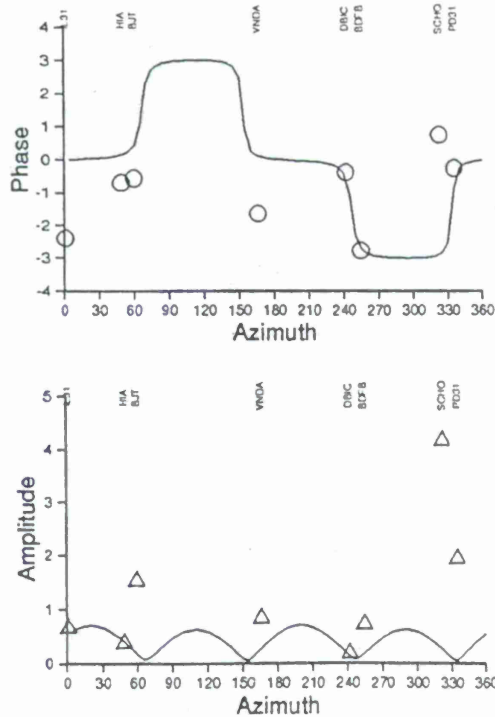


110/29/312 244/69/-69
 $M_0 = 9.10 \times 10^{23}$ dyne-cm
 $M_w = 5.27$



926006 01/22/97

Rayleigh waves - 85.33 sec



246/76/10 154/81/166
 $M_0 = 7.81 \times 10^{23}$ dyne-cm
 $M_w = 5.23$

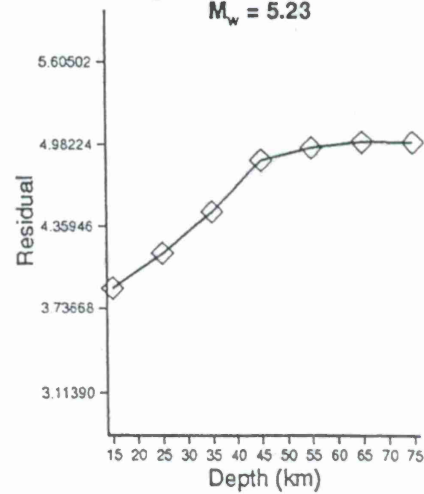


Figure 5: Output from moment tensor codes for an event in Syria. Both figures show Rayleigh waves at 85 seconds. Top figure is the solution produced using PREM model, while the bottom figure is the solution produced using SAW12D model.

OBSERVATIONAL CONSTRAINTS ON NON-LINEAR SOURCE MODELS IN THE DAMAGE REGIME

Charles G. Sammis
Department Of Earth Sciences
University Of Southern California
Los Angeles, Ca 90089-0740

Sponsored by the Air Force Office of Special Research
Contract No. F49620-93-1-0284

ABSTRACT

Crystalline rock massifs in the earth's crust are heterogeneous over a wide range of scales from microcracks in grains at the micron scale to faults and joints which span many tens of kilometers. It has been observed that this fracture heterogeneity is responsible for nonlinear effects near the source of underground explosions which affect seismic coupling and the resultant seismic waveform. Very near the source, preexisting cracks nucleate new fractures which can produce significant deviations from numerical computer simulations which assume a simply connected elastic continuum. Such effects were found to be important when computer models of nuclear explosions in granite failed to simulate the "pulse broadening" observed in the seismic signatures, even though the stress-strain behavior of the crystalline source rock was measured in the laboratory. Explosions in large (meter scale) samples also failed to exhibit the pulse broadening observed in the field, but were in good agreement with the computer simulation based on laboratory rheology. The solution to this apparent discrepancy was one of the early successes of our micromechanical model-based damage mechanics. It turns out that failure in compression, like failure in tension, is a scale-dependent phenomenon where strength decreases as the square root of the size of the heterogeneities which nucleate the fractures. The preexisting heterogeneity (cracks and pores) in the laboratory specimens - even the meter sized ones were too small to nucleate the extensive fracturing which occurs in the field and which is responsible for the observed pulse broadening. Simple models for the propagation of a sinusoidal pulse through a material which exhibits the damage mechanics rheology do indeed produce significant broadening. The question is the size of the effect. Over the past several years, we have distilled the damage mechanics to a simpler form which can be incorporated in the numerical codes currently used to simulate underground explosions while still retaining the important relations to the density and scale of preexisting fractures. We have incorporated our damage mechanics into two source models: the effective medium source model recently developed by Lane Johnson and the more traditional finite difference model used by Jeff Stevens and his collaborators at Maxwell Labs in San Diego. These models make testable predictions of how the waveform of radiated seismic energy depends on the depth of burial, the presence of ground water, and the size and density of preexisting fractures. They also predict the extent of damage which can be verified using extensive data sets on the density and morphology of the near-source fracture sets generated by several large chemical and nuclear explosions detonated in crystalline rock in the Soviet union. An intriguing implication of the damage model is that any preferred orientation of the preexisting fracture sets (fabric) may generate significant S wave energy which could effect source detection and discrimination algorithms. In our damage mechanics model, it is slip on preexisting fractures and faults which nucleates and drives new damage in crystalline rock. If the distribution of these slipping fractures are not isotropic, S wave radiation should result.

Keywords: seismic source, damage mechanics, seismic waveform, non-linear rheology

OBJECTIVE

The overall objective of this research program has been to incorporate damage mechanics in the numerical codes used to simulate underground nuclear explosions. This work is motivated by discrepancies between theoretical and observed seismic waveforms produced by explosions in crystalline rock which have tentatively been ascribed to the extensive fracturing and granulation of the rock in the non-linear source region. It is also possible that such fracturing in an initially anisotropic medium will generate significant S wave energy.

This research is relevant to the Comprehensive Test Ban Treaty because recent advances in seismic discrimination and yield estimate of underground nuclear explosions have been based largely on high-frequency local phases such as L_g and higher-mode surface waves. This shift in focus to higher frequencies has stimulated new interest in understanding the non-linear seismic coupling near the source, and in the mechanics of near-surface spallation.

While current numerical source models give an adequate representation of coupling and spall for sources buried in alluvium, significant discrepancies have been observed between model predictions and observed ground motions near explosions emplaced in hard rock like tuff and granite. These discrepancies usually involve the observation of a much broader pulse than predicted by the simulation (Rimer et al., 1987), and significantly lower displacement amplitudes (App and Brunish, 1992). App (1993) has recently identified the shear strength as the most important property of near-source rocks in shaping the seismic source function.

The problem appears to be that the numerical programs, which do a good job of modeling the compaction processes which dominate non-linear coupling in sediments, do not adequately describe the processes of crack growth and fragmentation which dominate non-linear coupling in hard rock. Crack growth is poorly modeled by current simulation programs for two reasons. First, the strength of a cracked rock is scale dependent -- strength decreases as the square root of crack length. The strength of granite measured in the laboratory is significantly larger than the strength of a granitic mass in the field simply because the length of preexisting cracks are limited by the size of the lab specimen. Hence laboratory mechanical data can not be used directly in the simulation programs. Also, the strength of the rock decreases as cracks grow during loading. A second problem has to do with the fact that, where compaction is a strengthening process which leads to a homogenization of the strain field, crack growth is a weakening process which leads to shear localization.

These same scaling problems may also explain why numerical simulations of spallation in hard rock do not seem to be as successful as those in sediments (App and Brunish, 1992). Whereas a local tensile failure criterion may work for sediments, size effects inherent in the fracture controlled tensile strength of hard rock become important.

What is needed for a more accurate numerical simulation of explosions in hard rock is a rheology which explicitly accounts for the effects of nucleation, growth, and interaction of fractures on the elasticity and strength of rock in the source region. Such rheologies are generally categorized as being "damage-mechanics" based, where "damage" is a measure of the size and density of fractures. Damage mechanics rheologies can be roughly divided into two groups: empirical formulations which are based on fracture mechanics but which have many adjustable parameters (Costin, 1983, 1985), and those which are based on a micromechanical modeling of the nucleation, growth, and interaction

of fractures growing from preexisting cracks in the rock (Ashby and Sammis, 1990). The advantage of model-based damage mechanics is that it explicitly accounts for the initial fracture spectrum in the source rock, and thus deals with the scaling problem discussed above. In Ashby and Sammis (1990), we have shown that our model gives a good description of the failure surface for a wide range of rock types with no unphysical adjustable parameters.

The source region of an underground explosion is commonly modeled as a nested series of concentric shells as illustrated in Figure 1. In the innermost "hydrodynamic regime" pressures and temperatures are sufficiently high that the rock deforms as a fluid and may be described using a PVT equation of state. Just beyond the hydrodynamic regime, is the "non-linear regime" in which the rock has shear strength but the deformation is nonlinear. This regime extends out to the "elastic radius" beyond which the deformation is linear. The objective of source models is to compute the elastic wave field at the elastic radius since this field may then be propagated to any distance using elastic wave theory.

We divide the non-linear regime into a "damage regime" in which the stresses are sufficiently high to nucleate new fractures from preexisting ones and a "crack-sliding" regime where motion on preexisting cracks produces amplitude dependent attenuation and other non-linear effects, but no new cracks are nucleated. The boundary between these two regimes is called the "damage radius" which may be computed directly from the damage mechanics expression for the nucleation of fractures (Sammis; 1990,1993).

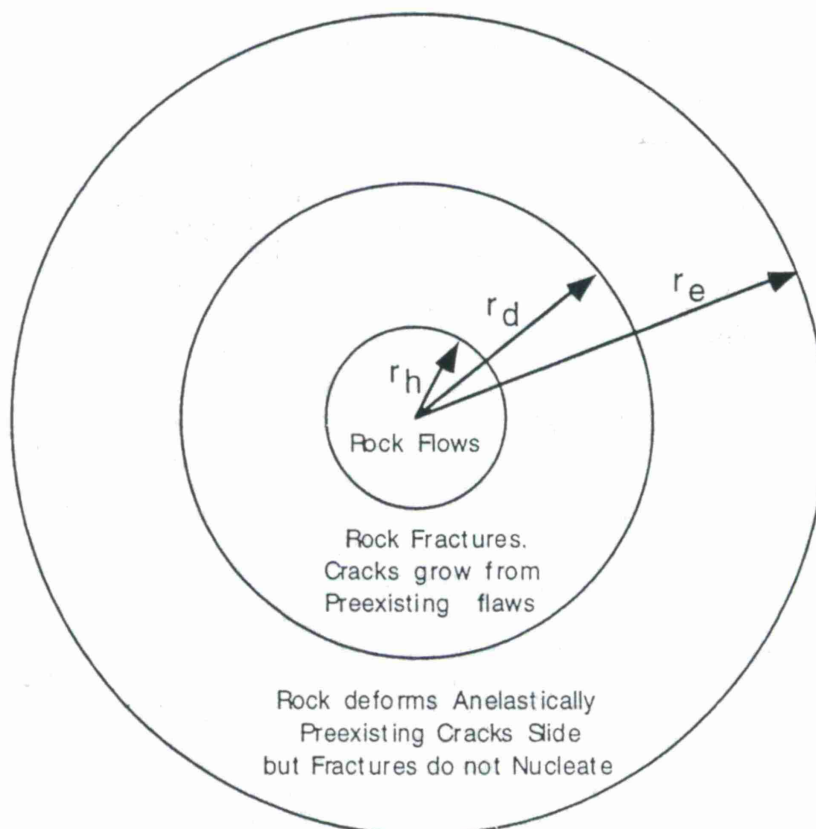


Figure 1 Deformation regimes in the nonlinear source region of an underground explosion. For distances less than the hydrodynamic radius r_h rock flows plastically. For distances between r_h and the damage radius r_d new fractures nucleate at and grow from preexisting fractures. For distances between r_d and the elastic radius r_e frictional sliding on preexisting fractures produces non-linear attenuation, but the stresses are too low to nucleate new fractures.

RESEARCH ACCOMPLISHED

Over the past few years, we have been making significant progress in casting our model-based damage mechanics into a form which can be incorporated into the numerical codes which simulate underground explosions. We have been developing these source models in collaboration with Lane Johnson at Berkeley and, in a parallel effort, with Jeff Stevens and the group at Maxwell Labs (formerly S³) in San Diego. The two source models are quite different.

Johnson (1996) has developed an equivalent elastic source model which incorporates our damage mechanics. The equivalent elastic method calculates the stress field in the entire region surrounding an explosion. At each point in space the radial and tangential stresses are generated as a function of time and these are used to calculate whether additional crack damage has occurred. The net result is the determination of damage as a function of time and distance in the region of high stress surrounding the explosion. For the well-characterized 1 kiloton chemical explosion detonated in September 1993 and known as the Non-proliferation Experiment (NPE), Johnson calculates that the damage extends out to about 50 meters (almost 10 source radii) and that the dilatation associated with the new cracking contributes about 10% to the total dilatational moment of the explosion. The model waveforms and maximum velocity were also approximately correct. However, while this approximate approach provides a very efficient method of estimating the basic characteristics of elastic waves radiated by an explosion, it does not incorporate the changes in elasticity and strength caused by the increased damage and their feedback to the source dynamics.

In order to model the effects of changing rheology due to the increasing damage, we have to incorporate the damage mechanics into a full finite difference source code so that the changes associated with increased damage can be incorporated at each time step. In order to do this we have, with Jeff Stevens and the group at Maxwell Labs, developed an algorithm which incorporates damage mechanics into their spherically symmetric "one dimensional" code SKIPPER. We are about to run a first test case for comparison with Johnson's more approximate model.

One complication which has delayed the implementation of damage mechanics in the numerical source codes has been the fact that the effective elastic modulus during a time step is not a simple function of the damage. The elastic modulus is slightly lower if damage increases during the time interval. The calculation to find the elastic modulus which accompanies the accumulation of damage is quite complicated and not suitable for numerical implementation. We have solved this problem by introducing an empirical reduction factor to the elastic modulus and fixing its value using laboratory data. We have been assisted in this by Dr. G. Boitnott at New England Research who has generated experimental stress-strain curves for granite extending through the damage regime up to failure. We plan to continue this collaboration to assure that the damage mechanics is firmly tied to laboratory data. Again, it should be emphasized that model-based damage mechanics is the proper framework to compare laboratory and field data since the scaling associated with crack size is built in.

The damage mechanics source model makes several testable predictions. The first is the amplitude and waveform of the seismic radiation. As mentioned above, Johnson(1996) was successful in modeling the peak velocity and waveform generated by the 1 kiloton NPE explosion using his rather crude implementation of the damage model.

A second testable prediction is the distance to which damage extends (the damage radius in Figure 1). Johnson (1966) predicted that the damage radius for the NPE explosion should extend to 50 meters (about 10 times the hydrodynamic radius). Unfortunately, the actual damage radius for this explosion was not measured. However, a new and important data set has recently become available. Dr. G. G. Kocharyan and his group in Moscow have extensive data sets on the density and morphology of the near-source fracture sets generated by several large chemical and nuclear explosions detonated in crystalline rock in the Soviet union. Based on these data, they have developed empirical relations which scale rock damage with distance and yield. For example, they find that the damage zone extends $85\text{-}140 \text{ m/kt}^{1/3}$, slightly larger than but in approximate agreement with Johnson's (1996) estimate. If our micromechanical models are realistic, they should produce these observed scaling relations. Dr. Kocharyan's group has been working closely with Jack Murphy and the Maxwell Labs group. We are currently working with Dr. Murphy and the Russian group to collect and assess these Russian data sets in preparation for modeling.

A third testable prediction is the effect of depth of burial on the seismic radiation. For deeper events, crack growth and hence damage accumulation should be suppressed and higher frequency radiation should result.

A fourth testable prediction is the effect of ground water on the seismic radiation. To first order, ground water reduces the coefficient of friction on the sliding starter cracks by reducing the normal stress according to the effective stress law, and thus explosions below the water table produce a larger damage radius and lower frequency seismic radiation than do explosions above the water table.

Finally, a fifth testable prediction of the damage model is that any preferred orientation to the preexisting fracture sets (fabric) should generate significant S wave energy. In our damage mechanics model, it is slip on preexisting fractures and faults which nucleates and drives new damage in crystalline rock. If the distribution of these slipping fractures is not isotropic, S waves radiation should result. The Soviet group has already documented that such movement on preexisting faults and joints is so widespread that they have questioned whether elastic continuum models are appropriate, even at distances which would normally not be considered to be in the non-linear near-field regime. A quantitative estimate of the contribution of this distributed S wave source to the overall S wave field is one of our proposed tasks.

CONCLUSIONS AND RECOMMENDATIONS

As discussed above, the damage model predicts that any preferred orientation of the preexisting fracture sets in crystalline rock may generate significant S wave energy which could effect source detection and discrimination algorithms. Also, expected products of this research such as quantitative relations between the seismic radiation and the initial fracture distribution in the source rock, the depth of burial, and effects of groundwater should improve existing detection and discrimination algorithms by allowing them to take known geology at the source into account.

REFERENCES

- App, F.N., Sensitivity of the close-in seismic source function to rock properties, Los Alamos National Laboratory Report LAUR-93-1884, May, 1993.
- App, F.N., and W.M. Brunish, Modeling surface motion and spall at the Nevada test site, Los Alamos National Laboratory Report LAUR-92-400, January, 1992.

- Ashby, M.F., and C.G. Sammis, The damage mechanics of brittle solids in compression, *PAGEOPH*, 133, 489-521, 1990.
- Costin, L.S., A microcrack model for the deformation and failure of brittle rock, *J. Geophys. Res.*, 88, 9485-9492, 1983.
- Costin, L.S., Damage mechanics in the post failure regime, *Mechanics of Materials*, 4, 149-160, 1985.
- Johnson, L.R., The effect of damage on explosion generated elastic waves, *Proceedings of the 18th annual seismic research symposium on monitoring a comprehensive test ban treaty*, 4-6 September 1996, 195-198, 1996.
- McEvilly, T.V., and L.R. Johnson, Regional studies with broadband data, *GL-TR-89-0224*, Phillips Lab, 56pp., 1989.
- Rimer, N., J.L. Stevens, and S.M. Day, Effect of pore pressure, fractures, and dilatancy on ground motion in granite, *S-Cubed Report SSS-R-87-8670*, 1987.
- Sammis, C.G., The formulation of a spherically symmetric source model based on a damage mechanics rheology, *Proceedings of 12th DARPA/GL Seismic research Symposium*, Key West Florida, 347-352, 1990.
- Sammis, C.G., Incorporating damage mechanics into explosion simulation models, in *Proceedings of the Nuclear Modeling for Underground Nuclear Test Modeling Symposium*, edited by S.R. Taylor and J.R. Kamm, Los Alamos National Laboratory Publication LA-UR-93-3839, pp. 65-93, 1993.

COMPARISON OF SINGLE-FIRED AND DELAY-FIRED EXPLOSIONS AT REGIONAL AND LOCAL DISTANCES

Brian W. Stump and D. Craig Pearson
Southern Methodist University, Department of Geological Sciences
and Geophysics Group - EES-3, Los Alamos National Laboratory

Sponsored by U.S. Department of Energy
Office of Nonproliferation and National Security
Office of Research and Development
Contract No. W-7405-ENG-36
LA-UR-97-2646

ABSTRACT

A wide range of blasting practices are utilized by the US mining industry resulting in dramatically different local and regional seismic signatures. This variability in blasting and resulting seismograms suggests that no single discriminant may be appropriate for identifying this class of sources. A range of blasting styles are identified in this paper and the distinguishing characteristics at regional distances are determined. The blasting styles are quantified with the help of mining company records and close-in acoustic, seismic and videographic data. The regional data consists of portable deployments of high frequency and broadband sensors as well as data from the International Monitoring System Primary Array at Pinedale, Wyoming.

Critical to the success of this study is the comparison of regional data from the mining explosions to data from contained, single-fired explosions. Two types of single-fired explosions are utilized, the first a *calibration* explosion (8 vertical boreholes with 5,000 lbs of explosives each) fired simultaneously. The second, single-fired explosion consists of a number of boreholes detonated simultaneously in the mine for the purpose of pre-splitting the material (driving fractures between boreholes) prior to a large cast shot. Data from these explosions provide the basis for identifying the source signatures of the more typical delay-fired explosions.

At high frequencies the single-fired and delay-fired explosions exhibit very similar waveforms at regional distances. Both event types show a high P/L_g ratio at the highest frequencies with L_g dominating at lower frequencies. Mining explosions that cast material show an enrichment in surface wave energy at relatively long periods of 4-12 seconds. Timing anomalies are identified in a high percentage of mining explosions designed to cast material. The accidental, simultaneous detonation of a number of boreholes has been observed in 2 of 9 carefully instrumented cast blasts. These produce regional waveforms that can have the characteristics of a single-fired explosion. Spectral scalloping is observed from some delay-fired explosions while not from others. The existence of these characteristics is dependent on the exact delay pattern utilized. Data from a single-fired explosion allows the assessment of local receiver effects that might appear as a characteristic of delay-firing.

Key Words: Mining explosion, single-fired, delay-fired, identification

OBJECTIVE

A number of mining explosions in the Powder River Basin of Wyoming are triggering the Prototype International Monitoring System. One of the largest events formed by the PIDC was a cast blast (designed to remove overburden) that included the simultaneous detonation of a significant amount of explosives (1 Aug 96). This event was identified as single-fired like with both the close-in observations (video and ground motion) as well as the regional observations. The event was observed at teleseismic distances and had magnitude estimates of $m_b = 4.0 \pm 0.1$ (2 measurements) and $M_L = 4.5 \pm 0.2$ (3 measurements). Cast blasts that perform normally (i.e. no sympathetic detonation or single-fired characteristic) appear to have M_L 's that are between 0.5 to 1.0 magnitude units smaller. Few if any of the coal shots (designed to fracture the coal) appear to trigger the PIMS. This observation is consistent with the experimental observation that the coal shots are a factor of 3 to 5 smaller in amplitude than the normally performing cast shots. This would suggest that they are 0.5 to 0.7 magnitude units smaller than the cast shots making them in the high 2's to low 3's. This magnitude is below that expected threshold of the IMS.

The purpose of this work is develop a collection of tools that can be used for identifying the different types of mining explosions that will be observed by the International Monitoring System. Fundamental to this study is the development of a physical understanding of these identifying characteristics so that their applicability in a range of different environments can be assessed. In order to reach this goal, a series of data sets have been developed that combine mine records, close-in observations of the mining explosions and regional seismograms. These data sets are utilized to assess identifying characteristics of the different explosion types.

RESEARCH ACCOMPLISHED

Experimental Design

In order to accomplish the objectives of this research program, a combination of portable and permanent seismographic stations were deployed to study signals from two mines in Wyoming. The mine locations, permanent stations (PDAR and RSSD) and portable stations (BHS, TIS, MON) are illustrated in Figure 1. PDAR is the IMS Primary Array. Additional instruments were deployed in each mine in order to quantify physical processes accompanying each explosion. Ground acceleration, velocity, acoustic and videographic data were recovered from within each mine. The cooperating mines provided explosive design information as well as access to mine property.

A number of different types of mining explosions were conducted in each mine. Both are recovering coal at depths between 20 and 60 m. Each removes the overburden with cast blasting. Pre-split explosions are employed at one of the mines. In this case, explosives are emplaced in boreholes along the back row of a cast blast and detonated simultaneously, prior to the associated cast blast. These explosions are designed to drive fractures between boreholes in the back row so that when the cast blast is detonated a competent high wall is produced. A single-fired *calibration* explosion was conducted at one of the mines for purposes of positively identifying the effects of delay-firing observed from the other

explosions. Smaller explosions are detonated in the exposed coal for the purposes of fragmentation and improved resource recovery.

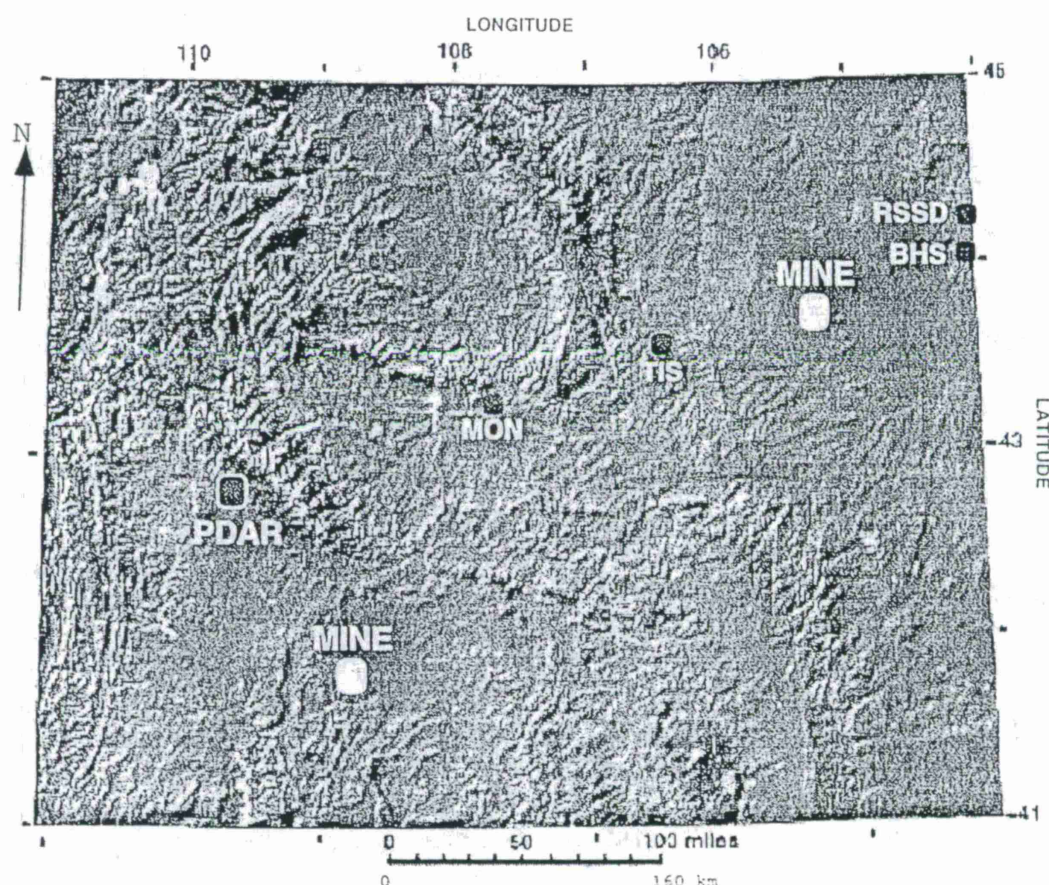


Figure 1: Location map including the permanent seismic stations (PDAR and RSSD), the portable stations (MON, TIS, BHS) and the two mine locations.

Peak Amplitudes

P and L_g amplitudes for both coal and cast shots were measured and compared to total amount of explosives detonated (Figure 2). For both the coal and the cast shots there was no apparent increase in peak amplitudes for either phase as a function of explosive weight. Standard delay-firing techniques which are designed to reduce peak amplitudes in the near-source region apparently also control peak regional amplitudes. The coal shots ranged in explosive weight between a few thousand pounds to several hundred thousand pounds while the cast shots ranged from over a million pounds to over eight million pounds. The population of coal shots were a factor of 3-5 smaller in peak amplitude than the cast shots indicating that the style shooting may effect the absolute amplitudes. The two cast shots that had single-fired characteristics were the exception to this rule. These anomalies produced the largest regional amplitudes in both P and L_g , as much as a factor of 3 to 4 greater amplitude than the cast blasts with normal performance.

AMPLITUDE vs. YIELD at PSRF

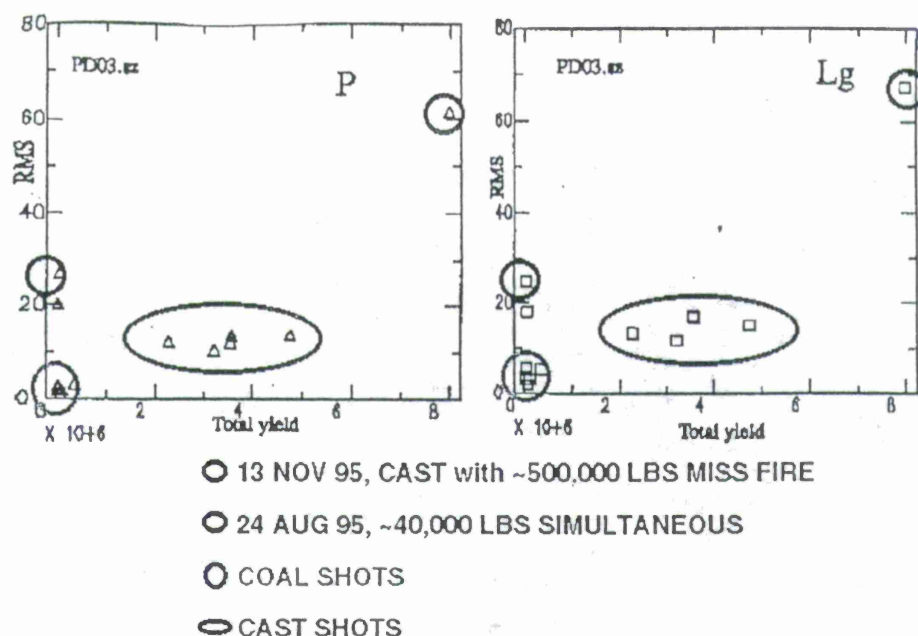


Figure 2: Comparison of peak P and L_g amplitudes from cast, coal and single-fired explosions observed at a single element of the Pinedale array (provided by V. Hsu)

High Frequency Discriminants

Large scale cast shots (and coal) excite P and L_g in a similar way to a contained single-fired explosion (Figure 3). At high frequencies ($>4-8$ Hz) the waveforms are dominated by P wave energy relative to L_g . The L_g amplitudes dominate at lower frequencies (1-2 Hz). This observational result is consistent with the success of high frequency P/ L_g discriminants for single-fired nuclear explosions in other parts of the world. The key to this comparison was the detonation of a modest size (~40,000 lbs.) single-fired contained explosion in the same mine where normal mining explosions were being detonated. These results further suggest that larger mining explosions might be utilized as a surrogate for developing high frequency discriminants for single-fired explosions.

Surface Wave Generation by Mining Explosions

There are observational differences between single-fired explosions and the large cast explosions in the mine. The large mining explosions generate surface waves in the period range of 4 to 12 seconds (Figure 3). No energy in this period range is observed above background noise for the single-fired explosion. The high frequency P/ L_g ratio can be used to identify the explosions and the existence of the long period regional surface waves may provide the opportunity to separate the large cast shots. Additional analysis of earthquake signals from the same region may provide the opportunity to compare these explosion generated regional surface waves to those resulting from earthquakes.

Anomalous Mining Explosions

The existence of regional waveforms from a contained, single-fired explosion provides a calibration event for the area of interest. The regional seismograms generated by this event

Black Thunder Single and Cast Shots at Pinedale (~ 360 km)
Short Period Array Element PD03.sz
different frequency bands

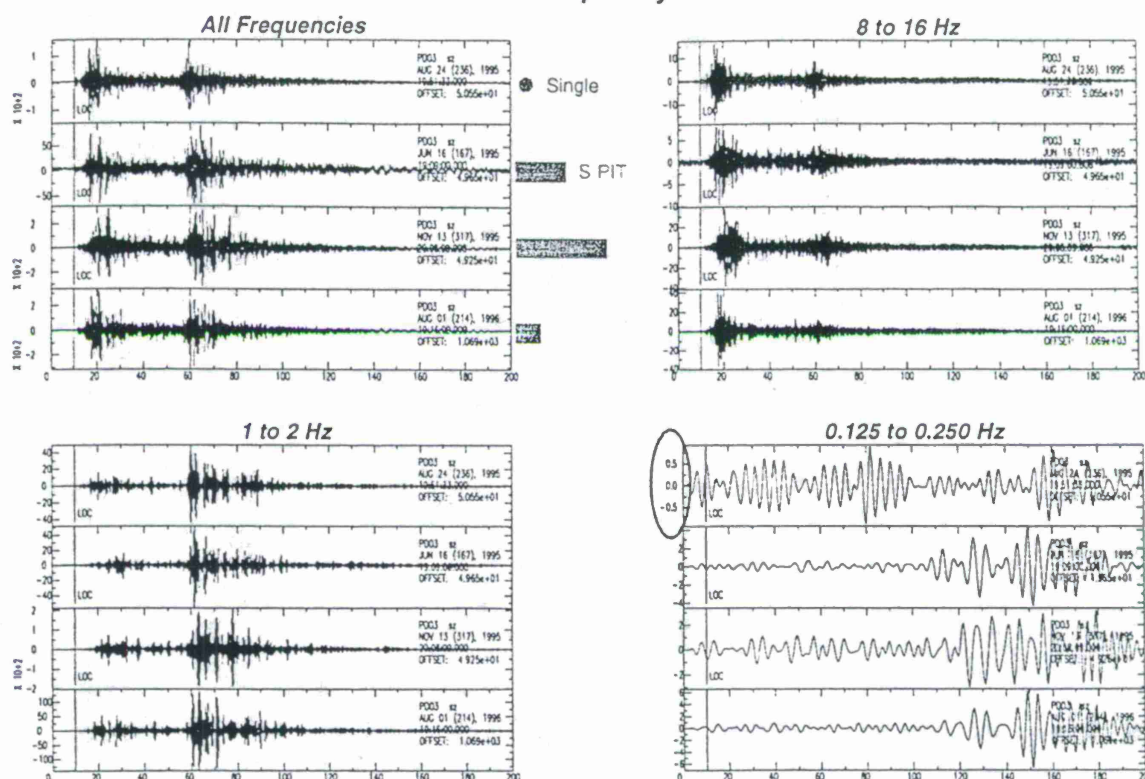


Fig 3: Comparison of vertical seismograms of the single-fired explosion and three cast blasts observed at one element of the Pinedale Array.

can then be compared to waveforms from standard mining explosions in order to identify single-fired explosion characteristics. Correlation analysis was performed on both P (Figure 4) and L_g parts of the regional waveforms. The P wave cross correlations suggest that two of the nine cast shots have impulsive characteristics. The anomalies have a very impulsive character indicating that a moderate to large amount of explosives was simultaneously detonated during the mining explosions. Close-in ground motion, acoustic and videographic data from these two shots support this interpretation.

Typical mining explosions are designed with a number of small explosions that detonate sequentially. This detonation pattern is intended to reduce ground motions from the cumulative explosive while fracturing and breaking rock in an optimal way. This explosive design results in waveform characteristics that are quite distinct from a single-fired explosion. The accidental detonation of a significant amount of explosives simultaneously during typical mining explosions have been documented in this study of mining explosions. Two of the nine cast blasts that have been studied show single-fired explosion characteristics that are a factor of 3 to 4 larger than the largest amplitudes from the parts of the explosion that performed as designed. These results suggest that in a monitoring environment that such anomalies will have to be identified. One explosive engineer

estimates that as many as 1 in 20 carefully instrumented shot shows some abnormal performance.

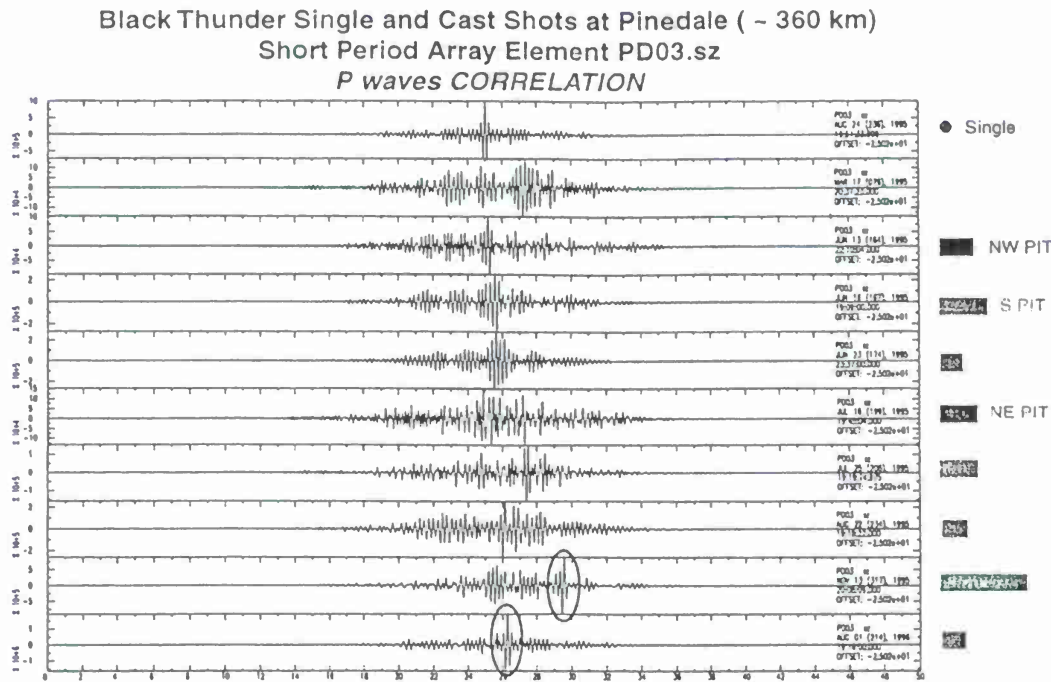


Figure 4: Cross correlation function between seismic P observations at Pinedale. The single-fired data is cross correlated with itself and data from each of nine cast blasts. Two of the cast blasts have a significant single-fired component in the P waves.

Spectral Scalloping

The entire suite of cast blasts were investigated for evidence of spectral modulation using data from the Pinedale array (mine to the NE of Pinedale, Figure 1). The bandwidth of the observational data at these stations (~360 km) limited analysis to approximately 10 Hz and below (Figure 5). Two approaches were followed in analyzing the data. Standard time varying spectral estimates with overlapping windows were first applied. A variety of window lengths and smoothing functions were applied with limited success in identifying consistent patterns of spectral scalloping. The single-fired explosion was used as a reference point as it contained the effects of propagation path that were common to all the shots (Figure 6). No consistent pattern of spectral scalloping was identified in the cast shots that could be associated with the blasting process in a predictive manner. Qualitatively the cast shots produced spectra that had more variation as a function of frequency than the smoother single-fired explosions. A mean spectral estimate for each regional seismogram was also computed by summing all the individual spectra from the moving window estimates. The resulting spectrum were then searched for spectral holes and enhancements. There was some indication of effects at the lower frequencies (<4-5 Hz) although no consistent pattern developed between the different cast shots. It is not surprising that high frequency spectral scalloping is not observed since these mining shots used 35 ms delays between shots in a hole and typically delays of 125, 400, 600, 800, 1000, 1200 and 1400 ms between rows. The cast shots which were anomalous produced relatively smoother spectra not unlike those observed from the single shot.

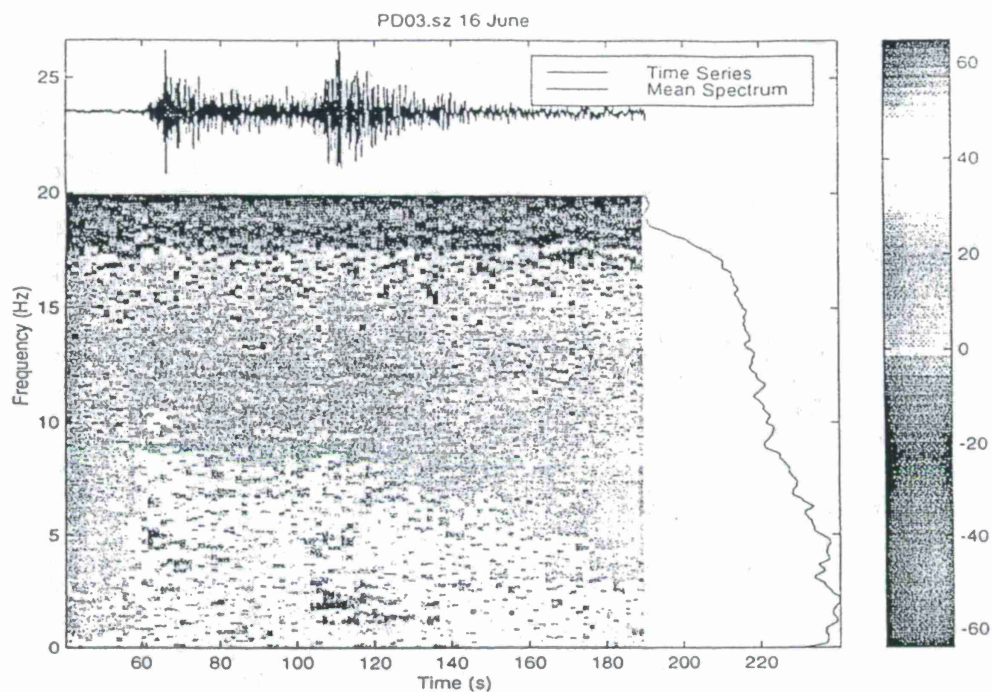


Figure 5: Time varying spectral estimates from a cast blast (mine NE of Pinedale) that was delay-fired observed at the Pinedale Array.

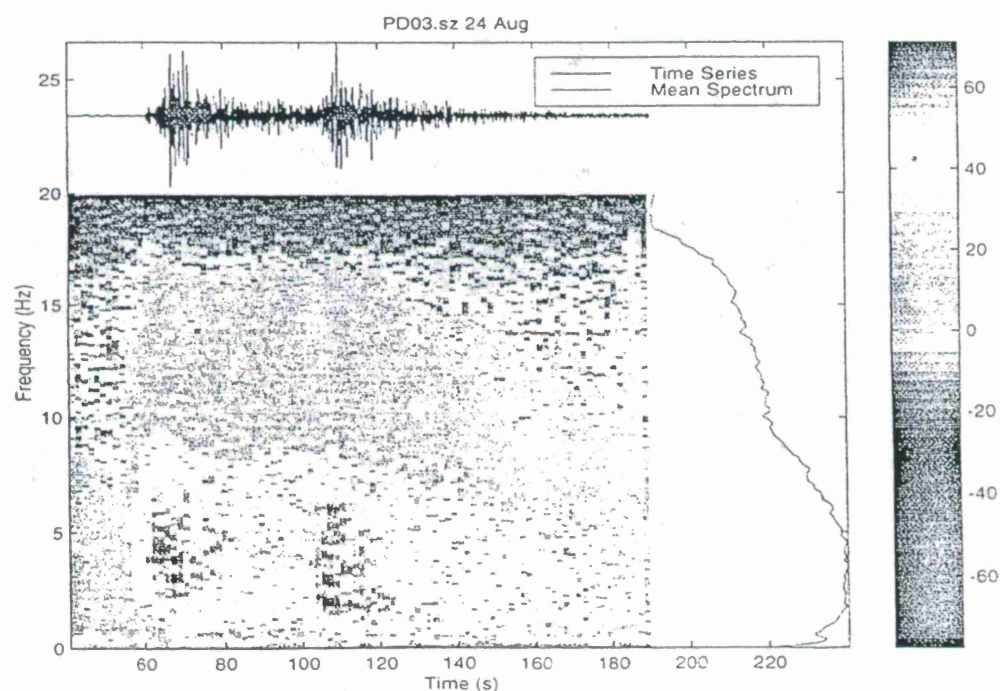


Figure 6: Time varying spectral estimates from a single-fired explosion (mine NE of Pinedale) observed at the Pinedale Array.

Mining explosions with simple detonation patterns do produce spectral scalloping that can be identified. The mine to the SE of Pinedale (Figure 1) employs a simpler timing pattern

in its cast blasts. One explosive hole from each row is detonated every 100 ms. As Figure 7 illustrates, the result is an enhancement of spectral energy just above 10 Hz. Data taken from within the mine where the bandwidth is greater supports this interpretation and shows a second peak above 20 Hz.

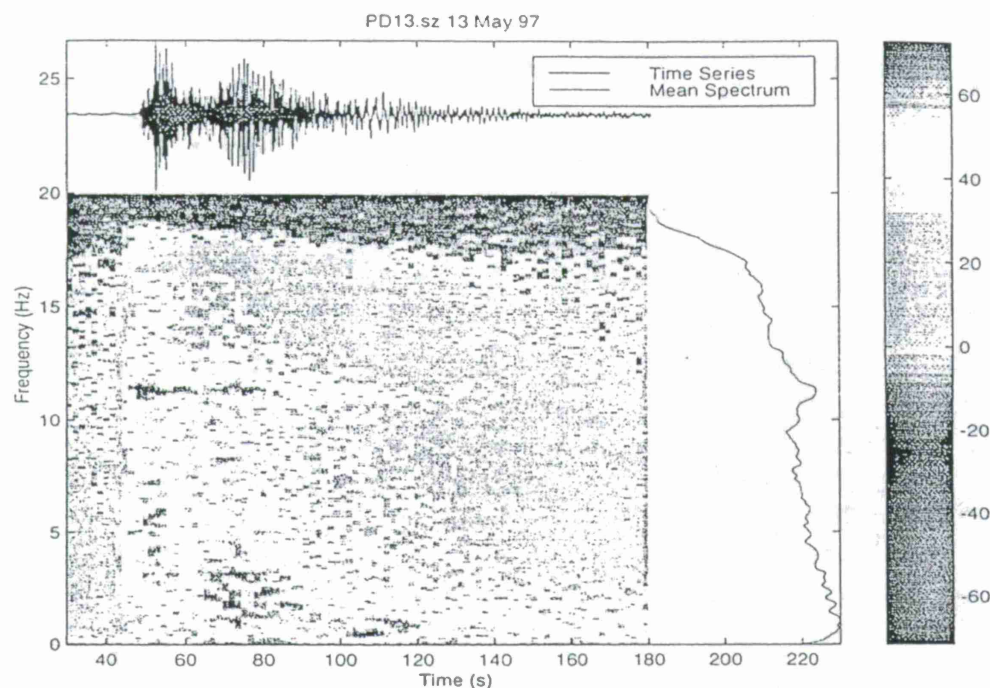


Figure 7: Time varying spectral estimates from a cast blast (mine SE of Pinedale) that was delay-fired observed at Pinedale.

At the same mine SE of Pinedale, single-fired explosions are conducted on a regular basis for pre-splitting the back row of a cast prior to the cast blast. This mining practice consists of drilling a series of holes in the back row of the proposed cast blast and loading them with explosives. Some time-period before the cast blast (days) these holes are simultaneously detonated. The purpose of this type of explosion is to drive fractures between the boreholes. These fractures then allow for a well controlled high wall after the cast blast. Comparison of the vertical seismograms from the cast blast (Figure 7) and the Pre-Split explosion (Figure 8) illustrates that the generation of these fractures between boreholes results in enhanced shear waves. Comparison of the time varying spectra from these two explosions illustrates that the high frequency enhancement observed in the cast blast (~10 Hz) is not observed from the simultaneously detonated explosion. As illustrated in the previous example, the spectra from the simultaneously detonated explosion is much smoother than that observed from the delay-fired explosion.

Near-source and Regional Comparisons

A number of comparative studies were made between near-source observations and the regional seismograms for the purposes of quantifying the importance of source processes that contribute to the regional seismograms. It is this aspect of the study that is unique in

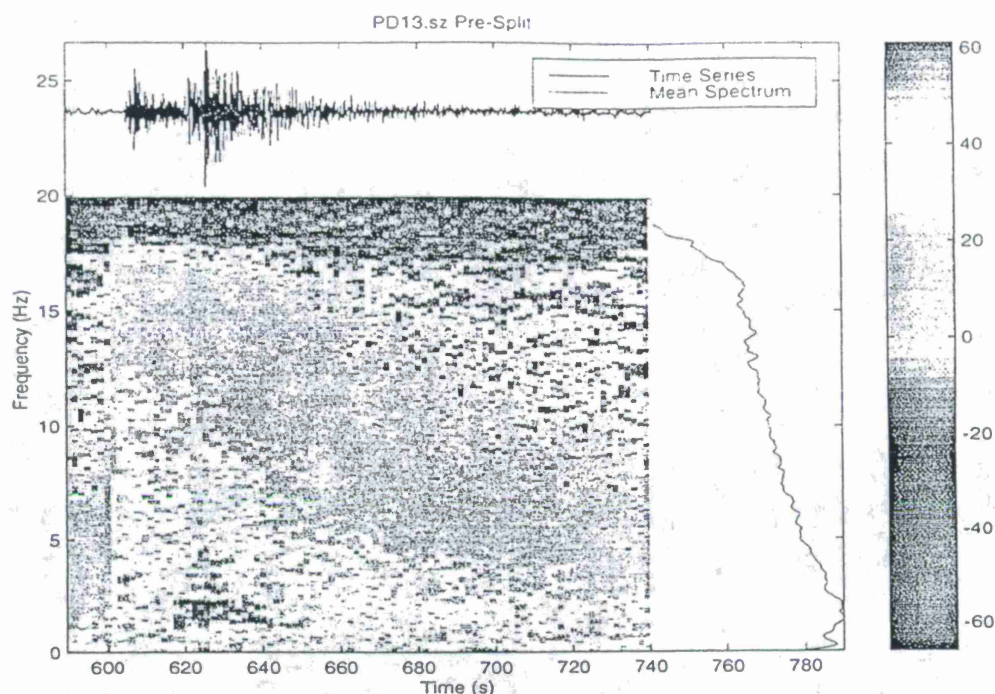


Figure 8: Time varying spectral estimates from a Pre-Split explosion (mine SE of Pinedale) that was simultaneously detonated.

determining the efficacy of regional discriminants and may provide a physical basis that can be used to assess possible tools for other regions of the world. The near-source data includes the design parameters of the explosive arrays, the three-dimensional topography of the source region, video of the explosion, ground velocity and acceleration, acoustic measurements and pre and post shot surveys of the material. One useful tool has combined the video, ground motion, acoustic and design information into a visualization tool of the explosion. The video images of the explosion are combined with the motion/acoustic data as well as a model of the detonation process (Figure 9). Time aligned images allow one to interpret how the progression of the detonation process generates the near-source wavefields. This visualization provided the first evidence of the accidental simultaneous detonation of a large amount of explosives at the end of one cast shot. This same event produced regional seismograms that were most like the single-fired explosion that was part of this experiment. These visualizations also illustrate the long source duration of these cast shots that must be taken into account in any attempt to model these events. The material that is cast into the pit following the initial detonation of the explosives can increase the source duration by 50% or more. The video in combination with the ground motion records provides the mechanism for quantifying the timing and strength of these secondary effects.

CONCLUSIONS AND RECOMMENDATIONS

Results from an empirical study identifying characteristics of seismic signals from mining explosions have been presented and support the contention that a suite of identification tools will have to be employed in order to effectively characterize these events. The need for this collection of tools is the wide variety of mining practices employed not only in the U.S. but throughout the world.

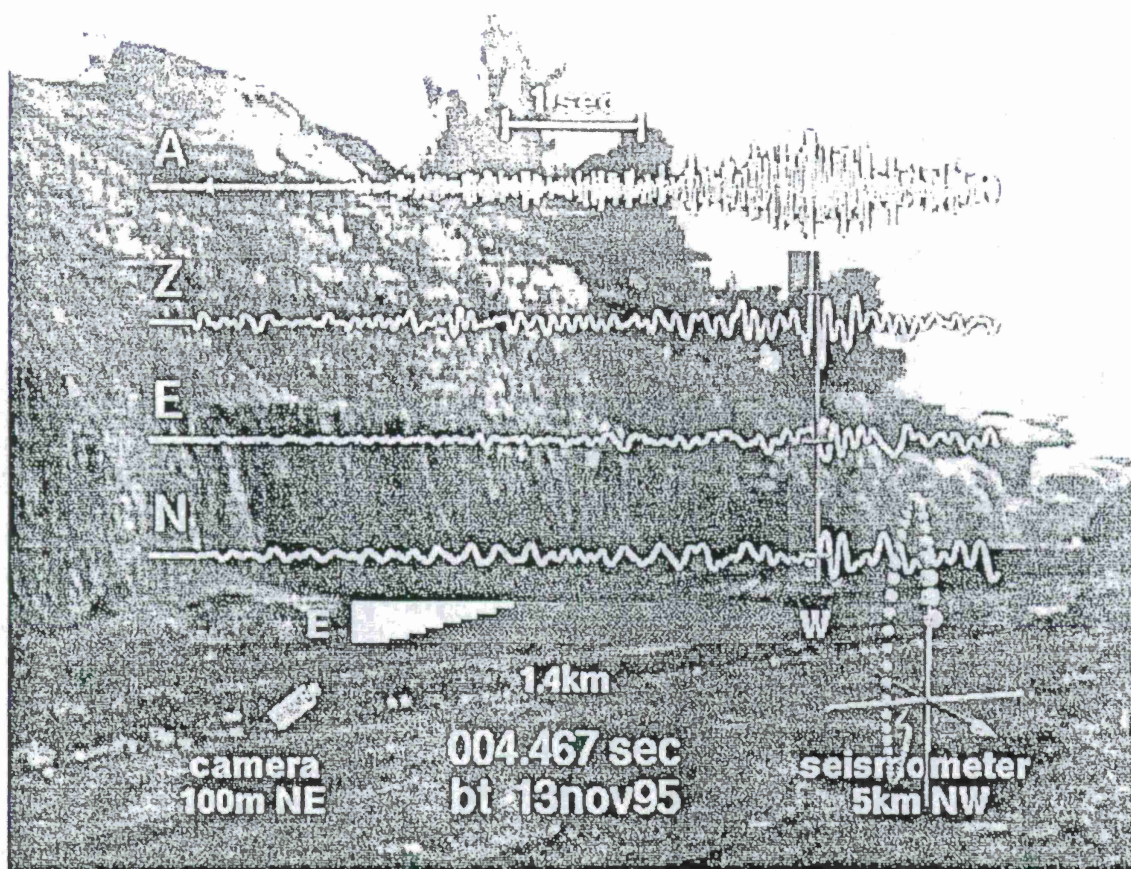


Figure 9: Single frame of combined video, ground motion (Z-vertical, E-east to west, N-north to south), acoustic (A) data along with a model of the design detonation pattern. In this frame at 4.467 s the shot is over three quarters complete. The large amplitude at this time, vertical bar across all time traces, is a result of the accidental simultaneous detonation of a significant number of boreholes at the end of the shot pattern.

A partial list of possible tools has been investigated. These include: (1) A high P/L_g ratio at the high frequency; (2) Enrichment in surface wave energy at relatively long periods of 4-12 seconds; and (3) Spectral scalloping from some delay-fired explosions.

Data from single-fired explosions is critical to the assessment of these discriminants. Pre-splitting explosions may be a source of such data. Relatively large, simultaneous detonations have also been identified to occur accidentally during a typical delay-fired explosion.

Seismic Signals from Underground Cavity Collapses and Other Mining-Related Failures

William R. Walter, Francois Heuze, and Douglas Dodge
Geophysics and Global Security Division, Lawrence Livermore National Lab

Sponsored by U.S. Department of Energy
Office of Nonproliferation and National Security
Office of Research and Development

Sponsored by U.S. Department of Energy, Contract W-7405-ENG-48
Comprehensive Test Ban Treaty Research and Development Program, ST482B

ABSTRACT

The sudden collapse of man-made underground cavities have generated seismic signals as large as magnitude 5.4. Collapses are just one of the many types of mining associated seismicity including coalbumps and rockbursts, which need to be identified and distinguished from potential clandestine nuclear explosions under the recently signed Comprehensive Test Ban Treaty (CTBT). Collapses, coalbumps and rockbursts are of concern for seismically monitoring a CTBT for a number of reasons. First, they can look like explosions when using some seismic discriminant measures, such $M_s:m_b$, $M_o:m_b$, regional P/S ratios and depth. Second, underground nuclear explosions themselves produce cavities that might collapse, possibly aiding in the detection of a clandestine event. Finally, because many mine-related events occur in the vicinity of underground cavities, they may come under special scrutiny because of the concern that very large, specially constructed cavities could be used to evasively decouple a clandestine test. For these reasons mine-related seismicity in both active and former mining regions has the potential to become false alarms under a CTBT.

We are investigating techniques to identify underground cavity collapses, either directly via waveform modeling, or indirectly by combining several seismic discriminants. We are also investigating the source mechanisms of coalbumps and collapses to better understand the performance of seismic discriminants for these events. In particular we have found similarities in point source models of some long-wall coalbumps, room-and-pillar mine collapses and NTS nuclear explosion cavity collapses. In order to understand coalbumps we are analyzing events from central Utah recorded at regional distances in Utah and Nevada including at the auxiliary station ELK. Some of these have anomalous, explosion-like high frequency P/S ratios. We are combining this new study with results from previous field work done in 1995 at a Colorado long-wall coal mining operation. Similarly to long-wall coal mines in Utah and elsewhere, this Colorado mine completely excavates a 3m high coal seam in 250m wide panels leaving the material above unsupported. The roof material above the excavated seam eventually collapses resulting in seismic events.

Key Words: seismic, source, collapse, mining, discrimination, coalbump, rockburst

OBJECTIVES

To reduce potential seismic false alarms under the Comprehensive Test Ban Treaty (CTBT) by improving our understanding and ability to uniquely identify mine-related seismicity from coalbumps, room-and-pillar collapses and rockbursts. To better understand and discriminate post-nuclear-test cavity collapses from industrial mine-related seismicity.

RESEARCH ACCOMPLISHED

As part of the overall Department of Energy CTBT Research and Development program, LLNL is pursuing a comprehensive identification research effort to improve our physical understanding and ability to seismically characterize and discriminate potential underground nuclear tests from other natural and man-made sources of seismicity. Here we focus of understanding and discriminating mine-related seismicity and underground cavity collapses. We present preliminary results in three parts: 1) Mechanisms for underground cavity collapses from both large accidental mine failures and post-nuclear shot collapses via waveform modeling; 2) Investigation of longwall coal mine seismicity in Colorado and Kentucky; 3) Investigation of discriminant performance of central Utah coalbumps.

Point Source Mechanism from the Collapse of Underground Cavities

Ground failures in underground mines are examined and categorized in quite different ways by mining engineers and seismologists. Mining engineers distinguish events based on rock type (hardrock rockbursts vs. coal bumps); by whether the event was planned (first caves, block caves, controlled pillar failure) or not (rockbursts, coal bumps, cascading pillar failure); and by whether any damage occurred in the mine. Seismologists distinguish subsurface mine events by their point source mechanism (e.g. Gibowicz, 1990; Knoll and Kuhnt, 1990; Wong and McGarr, 1990). Type 1 events, occur in the direct vicinity of mine openings and the source of energy is the rock mass at or surrounding the rock opening. These events tend to have a large implosional component leading to all dilatational first motions. Type 2 events are associated with shear slip along fault planes hundreds of meters to kilometers away from mining. They have normal earthquake focal mechanisms. Discrimination of type 1 and 2 is non-trivial and depends critically on being able to resolve the precise location of the event and the focal mechanism of primary energy release. From the point of view of monitoring a CTBT, type 2 events are shallow earthquakes while type 1 events with their unusual mechanisms may pose more of a challenge to identify. This extended abstract focuses on Type 1 collapses.

Over the last couple of years we have found that some of the largest known accidental mine collapses, reaching up to $m_b=5.4$, can be well fit with a closing tensile crack point source mechanism. Examples include the February 3, 1995 Wyoming mine collapse (Pechmann et al. 1995); the January 5, 1995 event near the Urals in Russia (Walter, 1995) and the March 13, 1989 Volkershausen event in Germany (Bowers and Walter, manuscript in preparation). We have also found that this model fits some of the larger coalbump events as will be discussed in the next section. We will show several examples at the meeting.

The closing tensile crack source is basically the same as the tabular collapse under gravity model used by Taylor (1994) for a Central Utah mine collapse near Gentry Mountain in 1984. The Taylor (1994) study reduced the collapse to vertically oriented point forces which can be shown to be mathematically similar to a shallow closing tensile crack (Day and McLaughlin, 1991). To examine the differences between pure implosional models and the closing crack models we examined a post NTS shot collapse (Walter, 1995). The 1982 NTS shot ATRISCO was followed

twenty minutes later by a cavity collapse large enough to generate surface waves at near regional distances. Figure 1A shows the synthetic fits of a pure spherically symmetric explosion source to the explosion records and a similarly good fit of the closing crack model to the collapse records at the planned primary station MNV. Note that this closing crack mechanism differs from a pure implosion (the opposite of the explosion source) since the M_{zz} couple is larger in magnitude than the M_{xx} and M_{yy} . Figure 1B shows a comparison of the data (left) and synthetics (right) for the explosion and collapse at the planned auxiliary station ELK. We have multiplied the collapse by a negative quantity to match the Rayleigh waves. Note that the Pnl waves do not match up, as would be expected if the collapse were a pure implosion or negative explosion. The change in the Pnl comes from $M_{zz} > M_{xx} = M_{yy}$ in the closing crack or tabular collapse source. With a very well calibrated structure (or an explosion for comparison) this phase shift can be used to discriminate between pure implosional and closing crack models. In all the mine-related collapses examined so far the closing crack appear to fit better than a pure implosion.

Coalbumps from Longwall Mines

To learn more about the seismic characteristics of long-wall collapse events, LLNL designed and conducted an experiment in cooperation with the Cyprus Amax Company at their Twentymile Coal Mine (Walter et al., 1996). This longwall mine held the world record for monthly underground coal production (534,557 tons in September 1994), and set a new world record during our experiment in September 1995. The experiment consisted of an 11-station seismic deployment, covering the immediate vicinity of the mine and extending to a distance of roughly 100 km. We recorded all the seismicity associated with the mining of a new panel, beginning with the "first cave" of an estimated 25,000 m² roof panel, and continuing with the monitoring of aftershocks and subsequent collapses for an approximate three month period.

The Twentymile operation completely excavates the 3 meter (10 foot) high Wadge coal seam at a depth of approximately 350 m (1100 feet) underground in 244 m (800 foot) wide panels. The roof rock above the coal seam is supported hydraulically in the immediate vicinity of the area of active mining. The entire mining machinery moves forward as the coal is removed and the region behind the active mining is allowed to collapse as shown in Figure 2A. It is believed that the softer shale rocks collapse until reaching the more competent sandstone layers, which can support more weight. It is the failure of these sandstone layers that LLNL believes leads to the $M \approx 2-3.5$ seismic events which have been detected by the U. S. Geological Survey station 160 km away in Golden Colorado. These seismic events do not cause significant air waves underground and do not generally impede the operation of the mine. After failure of the sandstone layers, the collapsed zone spreads up to the surface, where the ground above the region that has been mined eventually subsides about 1.4 m (4.5 feet). This surface settling tapers near the edges and is not easily detectable by the naked eye (see Figure 2B), it would require a leveling survey or similar measurement to quantify. On the other hand, the thick outcropping Twentymile sandstone bed can exhibit distress due to the subsidence from the underground mining. This has taken the form of substantial cliff collapses.

During the experiment (August to November, 1995) LLNL recorded hundreds of seismic events. The largest event was an ML(Coda) 2.9 (K. Mayeda pers. comm.) and there were five events between magnitude 2 and 3. The seismic records indicate they were shallow and occurred in or above the active mining panel. Seismometers on top of the mine indicated downward first motion consistent with either a shallow normal earthquake or a collapse mechanism (block collapses vertically under gravity). A comparison of the seismic waveforms with calculated indicates the gravity driven collapse model fits these large events better than normal earthquake

model as shown in Figure 3. Thus the larger seismic events coming from the long-wall mine have a similar point-source seismic mechanism as the larger accidental collapses described above. Although these events have not been tested using seismic identification algorithms, we expect their behavior to be similar to the large unplanned collapses based on their shallow depth and collapse mechanism. We examine the discrimination performance of what we believe to be similar events in Utah in the next section.

Coalbumps from longwall mines can get much larger than observed at the Twentymile mine in Colorado. For example three events in 1995-1996 with $m_b > 3.5$ are shown in Figure 4A. All were large enough to be detected teleseismically, for example the March 11, 1995 event was given an m_b of 4.2 (NEIC). The three events show a high degree of correlation indicating similar locations and mechanisms. All three are associated with a particular longwall mine in Kentucky. Discussions with mine personnel indicated that these events produced relatively little damage inside the mine for the size of the events. We believe that like the Twentymile mine, the larger events are associated with collapses that occurred above the previously mined out regions. To examine the mechanisms of these events we have been comparing the surface wave data with synthetics at available broadband stations such as those of the National Seismic Network. An example of the fit of the collapsing crack model is shown in Figure 4B. The fit is quite good except at MCWV which is dominated by noise. In particular the absence of Love waves on the transverse components is indicative of these collapse type mechanisms.

Discrimination Performance of Central Utah Coalbumps

One of the most active regions in the U.S. for coalbumps is central Utah. More than 30 coalbumps with $M_L > 3$ have occurred since 1962 (W. Arabasz and S. Nava, written comm.). The largest event was the 1984 Gentry Mountain collapse studied by Taylor (1994) who noted that it failed many regional discriminants. Patton and Walter (1993, 1994) also found this event failed the $M_o:m_b$ discriminant measure. Given the shallow depth, possibility for non-double couple mechanism and concerns for evasion (e.g. Heuze, 1995), mine-related seismicity has the potential to be a significant source of false alarms under a CTBT. For these reasons we have begun a study to examine the regional discriminant performance of these Utah events at the LLNL run stations in the Western U.S. (see top of Figure 5). These stations were previously used for a major discrimination study of earthquakes and explosions at NTS (Walter et al. 1995). By using the same stations we can compare the coalbumps with our large databases of Western U.S. earthquakes and explosions. In addition these studies help calibrate the proposed IMS stations at MNV and ELK.

The initial study of the Utah coalbumps reveals they have larger high-frequency P/L_g ratios than nearby earthquakes as the examples at the bottom of Figure 5 show. Large P/L_g ratios are a characteristic of nuclear explosions and can be used to discriminate them (e.g. Walter, et al. 1995). The Utah events occur in very similar geology to the Twentymile mine in Colorado and it seems plausible to think they may have similar mechanisms. The closing crack type mechanisms as we observed for coalbumps in Colorado and Kentucky should have higher P/S ratios than double couple events (e.g. Walter and Brune, 1993). Bennett et al. (1996) have noted that rockbursts and coalbumps in general have P/L_g ratios in between that of earthquakes and explosions but it is not clear whether this is due to mechanism depth, time function or other phenomena. By determining mechanism, depth, time functions and path corrections to these data, so that we may compare them to our large Western U.S. dataset of earthquakes and explosions, we hope to sort out the relative contributions of each to the observed P/S ratios. We will report initial results of this study at the meeting.

CONCLUSIONS AND RECOMMENDATIONS

Mine-related seismicity including collapses, coalbumps and rockbursts can look like explosions, based on some regional and teleseismic discriminants and therefore have the potential to be false alarms under the CTBT. In addition, because they involve underground cavities they raise evasion concerns and need more careful study. In order to better understand the empirical discrimination performance of these type of events, as well as model their physical source processes, we are investigating regional records of coalbumps in Utah. When combined with previous coalbump field work and western U.S. discrimination studies we hope to greatly improve our understanding of these events. We are continuing to collect and analyze the best data available from collapses, rockbursts and coalbumps worldwide to continue to improve our physical models for these types of events.

References

- Bennett, T. J., M. E. Marshall, B. W. Barker, and J. R. Murphy, (1996). Seismic investigation of rockbursts, *Proceedings of the 18th annual seismic research symposium on a monitoring a comprehensive test ban treaty* Phillips Laboratory, PL-TR-96-2153, 901-907.
- Day, S. M. and K. L. McLaughlin (1991). Seismic source representations for spall, *Bull. Seism. Soc. Am.*, **81**, 191-201.
- Gibowicz, S. J. (1990). Keynote Lecture: The mechanism of seismic events induced by mining, in *Rockbursts and seismicity in mines*, C. Fairhurst, Editor, A. A. Balkema, Rotterdam, 3-27.
- Heuze, F. E., (1995). Rockbursts and coal bumps as opportunities for evasive nuclear testing, *Lawrence Livermore National Laboratory report*, UCRL-JC-120945.
- Knoll, P. and W. Kuhnt (1990). Seismological and technical investigations of the mechanisms of rockbursts, in *Rockbursts and seismicity in mines*, C. Fairhurst, Editor, A. A. Balkema, Rotterdam, 129-138.
- Patton, H.J., and W. R. Walter, (1993). Regional moment:magnitude relations for earthquakes and explosions, *Geophys. Res. Lett.*, **20**, 277-280.
- Patton, H.J., and W. R. Walter, (1994). Correction to "Regional moment:magnitude relations for earthquakes and explosions", *Geophys. Res. Lett.*, **21**, 743.
- Pechmann, J. C., W. R. Walter, S. J. Nava and W. J. Arabasz, (1995). The February 3, 1995 =5.1 seismic event in the trona mining district of southwestern Wyoming, *Seism. Res. Lett.*, **66**, 25-34.
- Taylor, S. R. (1994). False alarms and mine seismicity: an example from the Gentry Mountain mining region, Utah, *Bull Seism. Soc. Am.* **84**, 350-358.
- Walter, W. R. (1995), Status report on new whole waveform discriminants and preliminary results, UCRL-ID-123227.
- Walter, W. R., and J. N. Brune, (1993). Spectra of seismic radiation from a tensile crack, *J. Geophys. Res.* **98**, 4449-4459.
- Walter, W. R., K. M. Mayeda and H. J. Patton, (1995). Phase and spectral ratio discrimination between NTS earthquakes and explosions Part I: empirical observations, *Bull Seism. Soc. Am.*, **85**, 1050-1067.
- Walter, W. R., S. L. Hunter, and L. A. Glenn, (1996). Preliminary report on LLNL Mine seismicity deployment at the Twentymile Coal mine, UCRL-ID-122800.
- Wong, I. G. and A. McGarr (1990). Implosional failure in mining-induced seismicity: a critical review, in *Rockbursts and seismicity in mines*, C. Fairhurst, Editor, A. A. Balkema, Rotterdam, 45-51.

The NTS explosion ATRISCO (mb=5.7, Ms=4.2) was followed 20 minutes later by a collapse (mb=4.0, Ms=3.5)

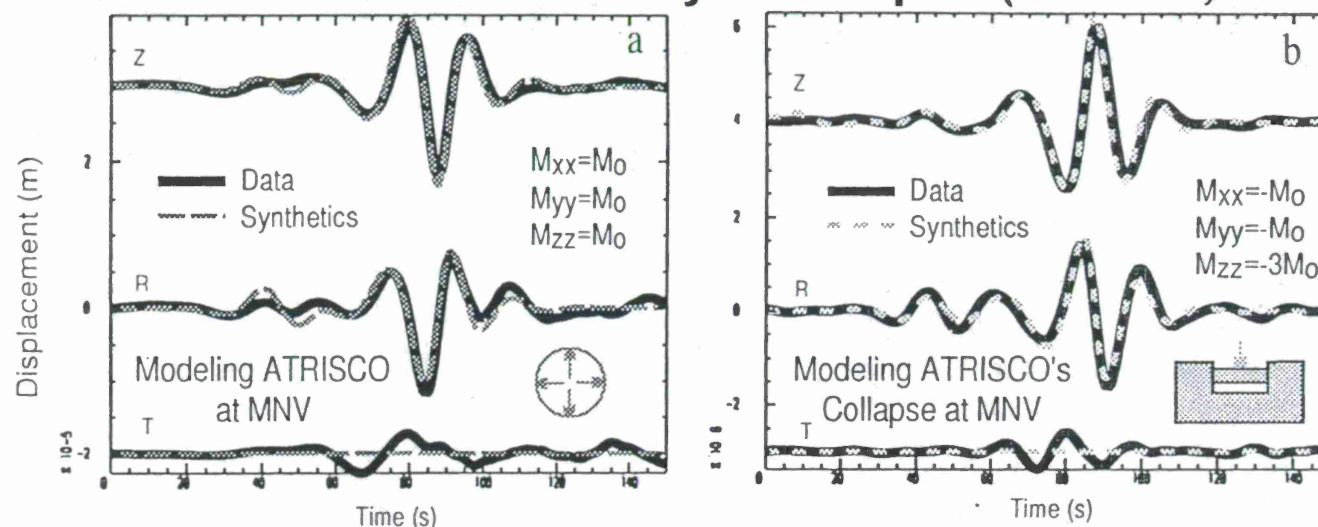


Fig. 1A. Waveform modeling indicates ATRISCO is consistent with explosion point source while its collapse has a similar mechanism to that found for large room-and-pillar mine collapses: a tabular gravity-driven failure.

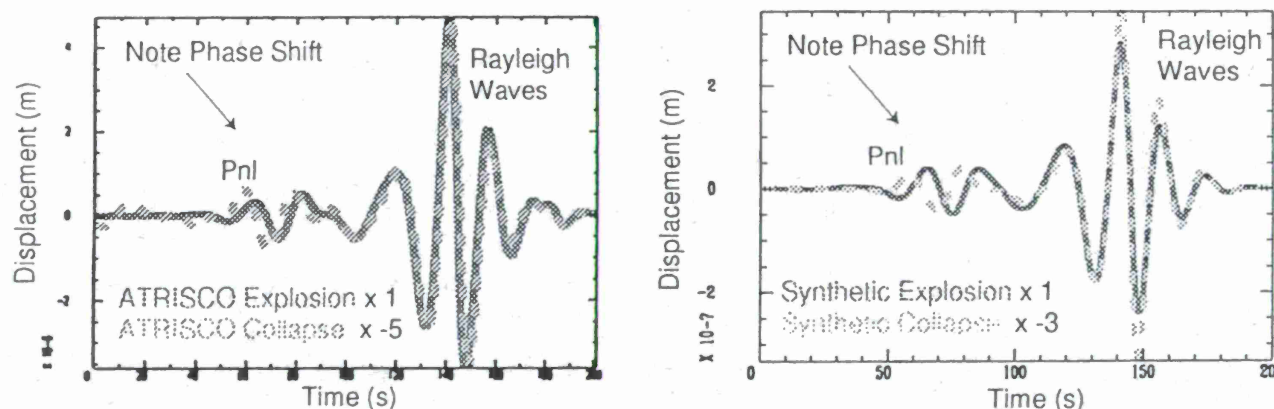


Fig. 1B. A comparison of the ELK radial component long period (15-40 s) data (left) and synthetic (right) seismograms from the NTS explosion ATRISCO and its associated cavity collapse (dashed lines) about twenty minutes later. The Rayleigh waves are out of phase for these two events. We can match the Rayleigh waves of the two events if we multiply the data collapse trace by -5 as shown on the left or for the same M_o by -3 in the synthetic trace on the right. However the long period body wave phase P_{nl} does not match, indicating the collapse is not an implosion (opposite of an explosion) but more consistent with a tabular gravitational collapse mechanism. (Figure after Walter 1995).

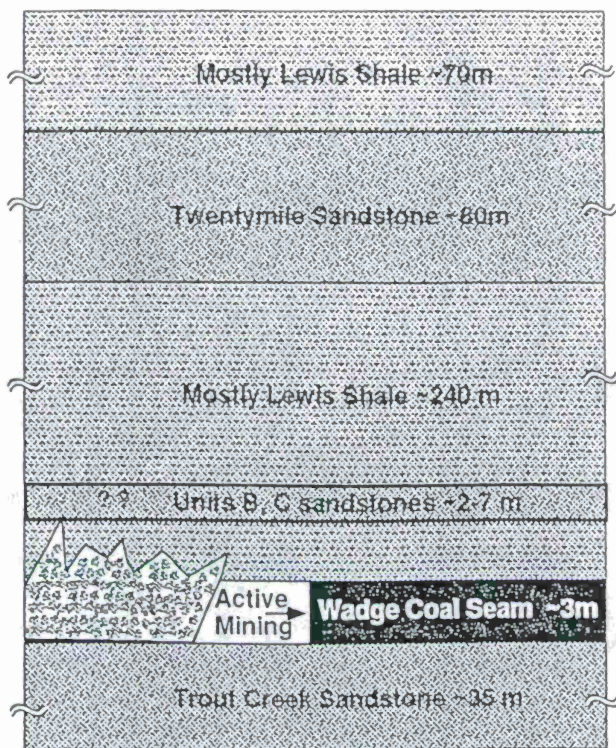


Fig 2A. Simplified schematic cross section of Twentymile coal mine and some of the major rock units. The 3m (10 ft.) high Wadge coal seam is completely excavated within the mining panels and the weak shale rocks are allowed to collapse behind the advancing face of active mining. It is hypothesized that the roof rock collapses until it reaches the stronger sandstone rock layers which can support more weight before failure. It is believed to be the failure of these sandstone layers, either units B, C or the thicker Twentymile sandstone layers that are responsible for the largest seismic events. (Simplified from detailed cross sections provided by Twentymile coal mine).

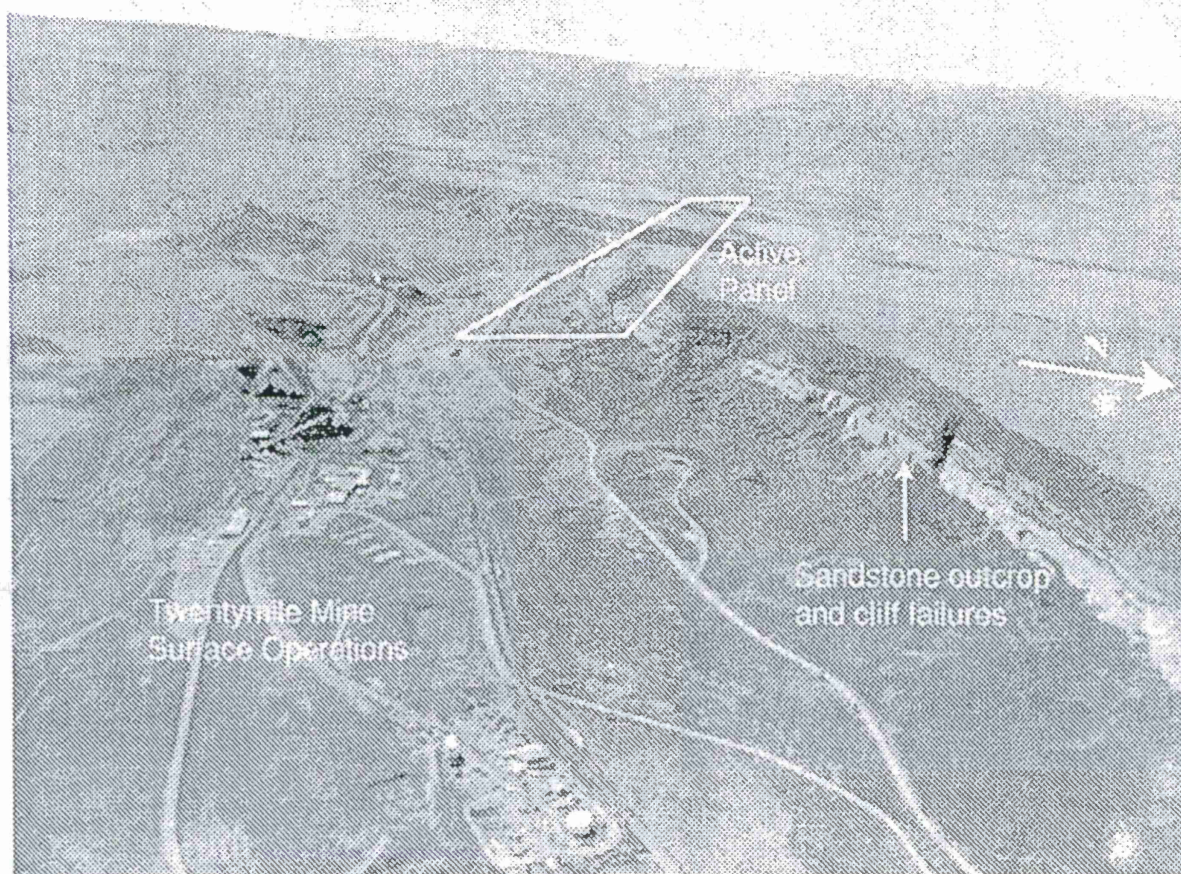
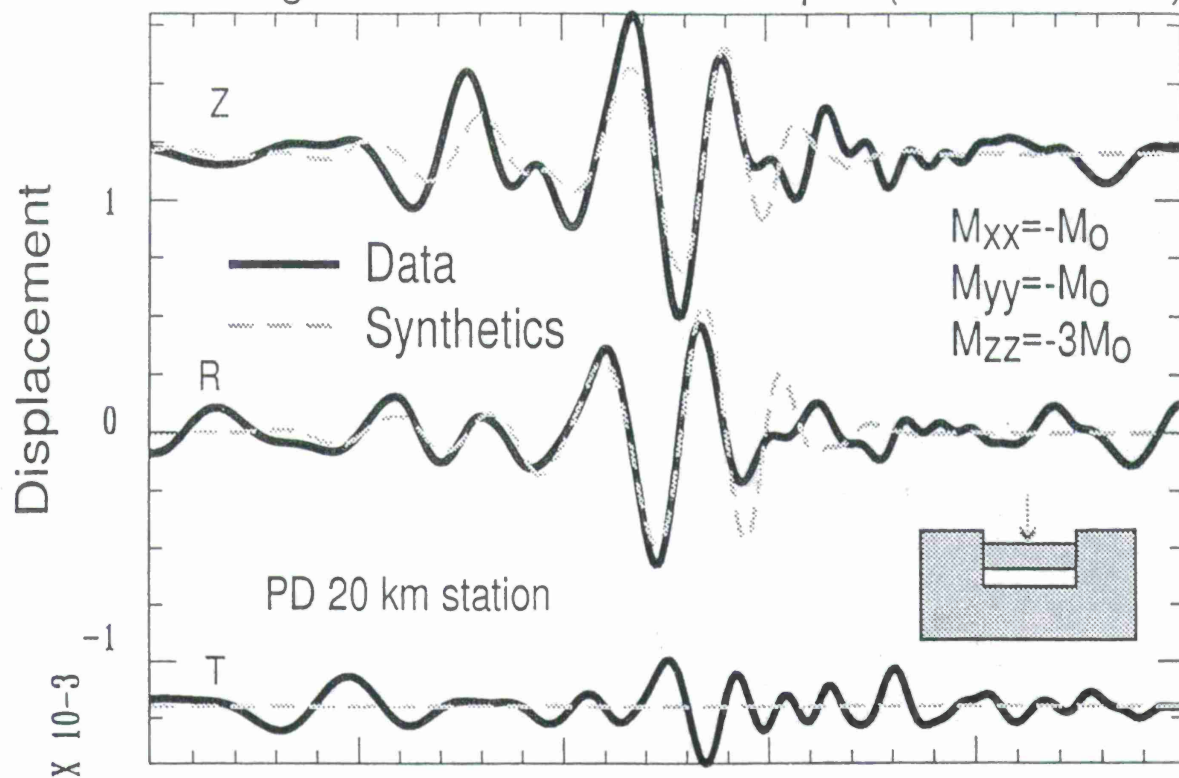


Fig. 2B. Aerial photo of Twentymile Coal Mine area. A surface projection of the mining panel active during the LLNL seismic deployment is superimposed on the picture. The ground above the active panel and previously mined panels to the north has subsided 1.4 m but this is not easily visible to the naked eye. The Twentymile sandstone layer is visible where it outcrops and does show response to the undermining in the form of cliff failures. (Photo by François Heuze).

Modeling 10/2/95 Event as a Collapse (reasonable fit)...



...Or a Normal Earthquake (poor fit).

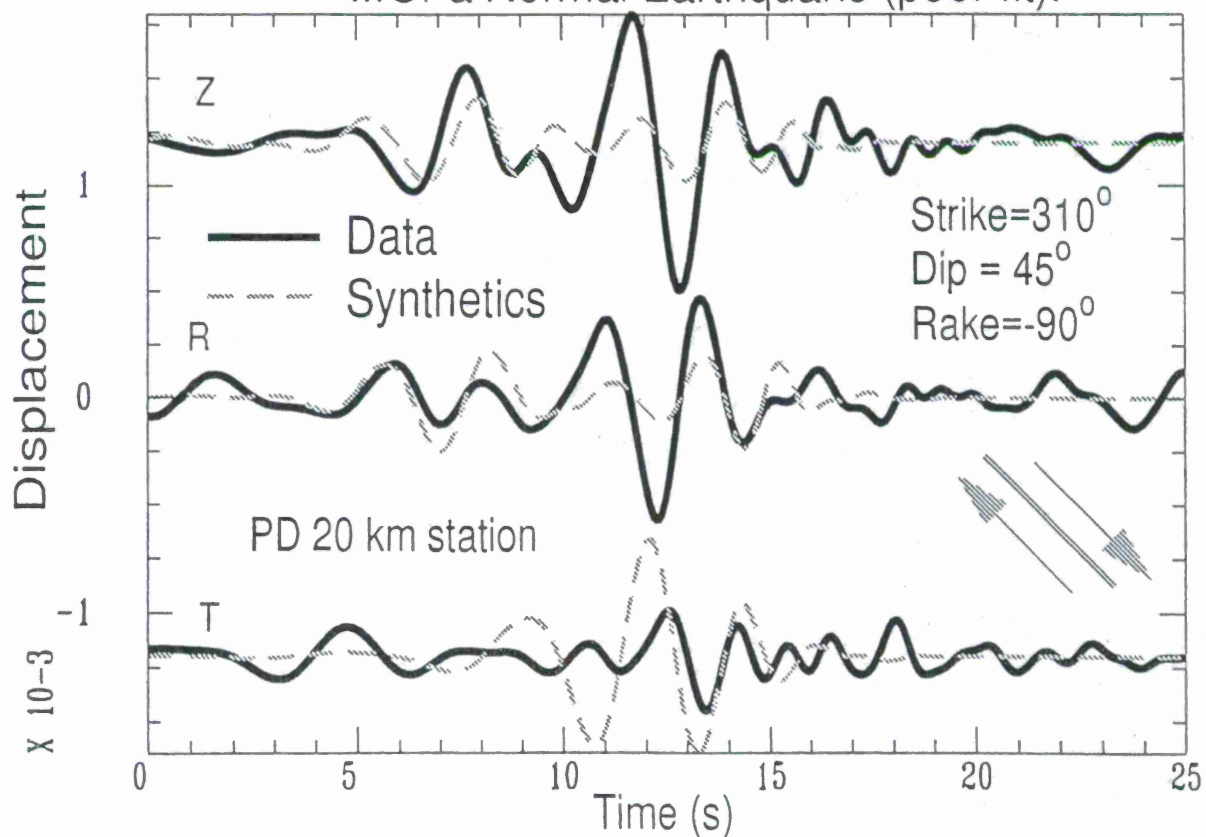


Fig. 3. Preliminary waveform modeling indicates the point-source mechanism for the largest events are more consistent with a gravitational collapse mechanism than a normal earthquake mechanism. This figure compares 3 component, 2-5 s period fits of synthetic seismograms for both mechanism types to the data recorded at a station 20 km away towards Pinedale, Wyoming. (after Walter et al., 1996).

Three Kentucky Coalbumps recorded at NSN station CEH, Chapel Hill, NC

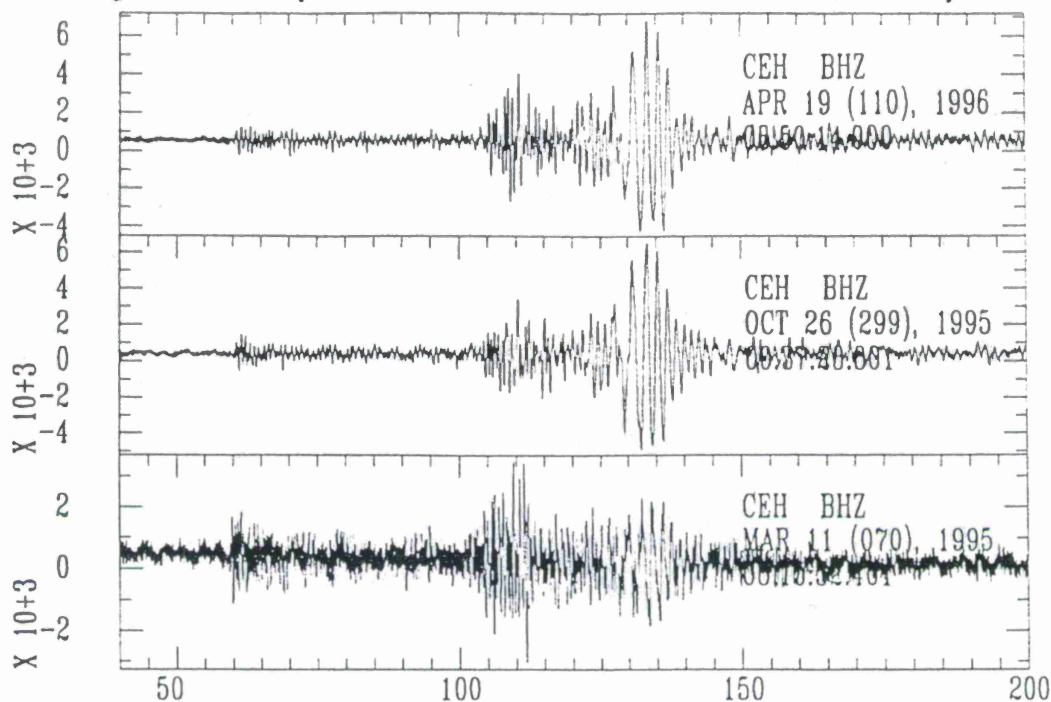


Fig. 4A. Seismic records from three coalbumps associated with the Lynch 37 longwall coal mine in Kentucky show strong correlation indicating similar source mechanisms and locations.

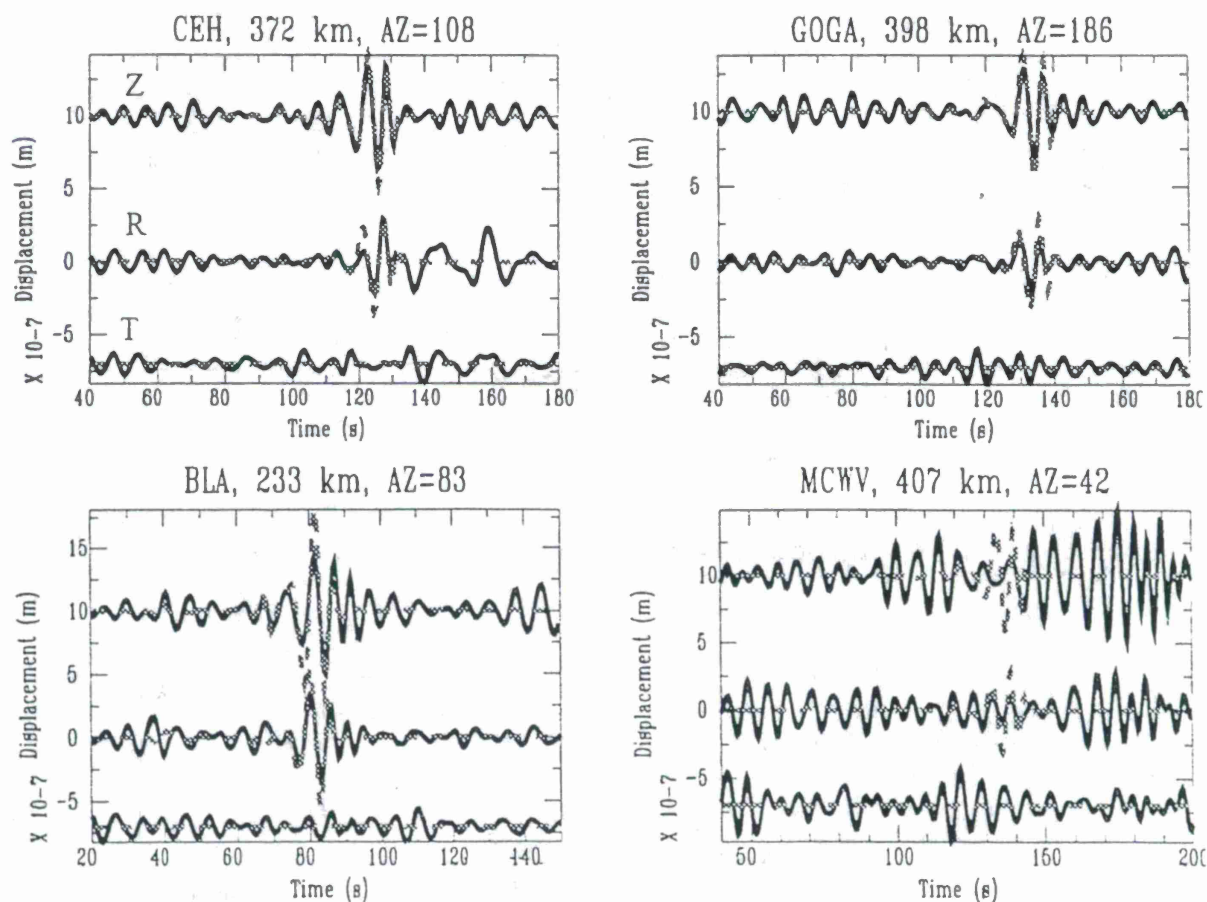


Fig. 4B. Preliminary waveform fits using closing crack mechanism (dashed lines) to regional broadband data from Kentucky coalbump on April 19, 1996 in bandpass from 5-15s period.

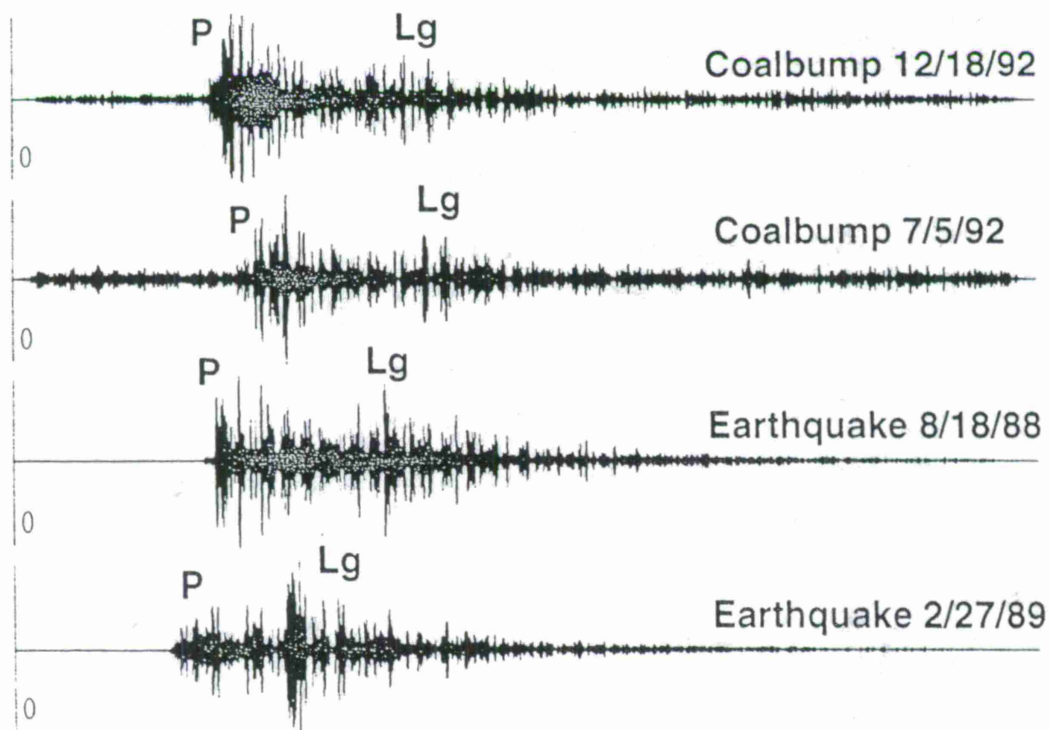
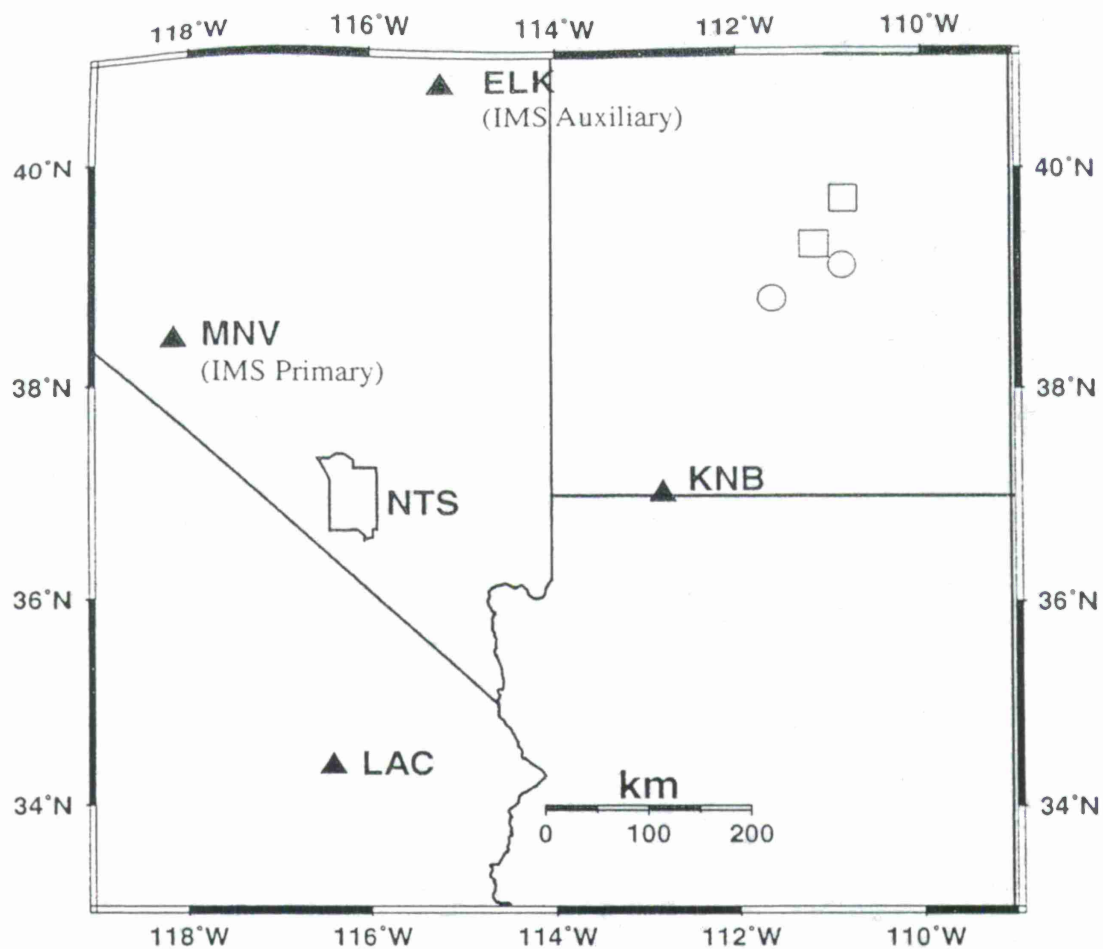


Fig. 5. Top map shows locations of LLNL run stations and central Utah earthquakes (circles) and coalbumps (squares). Bottom shows events at KNB bandpass filtered between 6-8 Hz. Note the relatively high P/Lg values for the coalbumps similar to that observed for NTS explosions.

QUANTIFICATION OF REGIONAL WAVE EXCITATION AND PROPAGATION IN CENTRAL ASIA

Jiakang Xie
Lamont-Doherty Earth Observatory, Columbia University
Route 9W, Palisades, NY 10964

Sponsored by U.S. Department of Energy
Office of Nonproliferation and National Security
Office of Research and Development
Contract No. F19628-95-K-0004

ABSTRACT

In the past year we have continued to improve the methodology to better estimate source and path spectral parameters using high-frequency regional waves, particularly Pn, Pn coda and Lg. We have also collected and processed several hundred Pn and Lg spectra from eight Lop Nor Test Site (LTS) explosions and many earthquakes, recorded by broad-band seismic stations in central Asia. Spectral ratios of larger with respect to small, nearby events are formed to estimate the source moment (M_0) ratios and corner frequencies (f_c), which are used as *a priori* knowledge in the subsequent spectral inversions. For LTS explosions, Pn spectral ratios tend to have more pronounced overshoot, whereas the Lg spectral ratios appear to have nulls at frequencies at, or slightly above, 1 Hz. These features of spectral ratios support previously proposed, different excitation mechanisms of both phases.

The improved inverse method, which estimates Q with higher numerical stability and incorporates *a priori* information on inter-station Q and source f_c values, are being applied to the Pn and Lg spectra collected. The on-going research is yielding source M_0 , f_c and path Q_0 , η values for Pn from the many LTS explosions and earthquakes. Pn Q_0 , η estimates for individual paths should vary drastically, due to 3D structural complexities. The path-averaged values, on the other hand, should reflect the areal average of Q rather robustly. At the end of this study, the M_0 , f_c , Q_0 , η values obtained using the Pn wave will be jointly interpreted with those obtained using the Lg wave, leading to a strong constraint on why the P/Lg ratio can be used as a discriminant between explosions and earthquakes.

Keywords: Pn spectra, Lg spectra, Q , source parameters, explosion discrimination, Central Asia

OBJECTIVE

Xie (1993) and Xie *et al.* (1996) developed and applied a nonlinear inverse method to simultaneously estimate the source seismic moment (M_0), corner frequency (f_c) and path-variable Q_0 and η (Q at 1 Hz and its power-law frequency dependence, respectively) using Lg spectra from explosions. The method has also been applied to earthquakes (Cong *et al.*, 1996), although the success is somewhat limited. The main objective of this research is to modify that method to analyze spectra of Pn and Lg from both explosions and earthquakes. The analysis should yield Pn and Lg source M_0 , f_c , and path Q_0 , η values. These values will advance our fundamental understanding on how the excitation and propagation of Pn differ from those of Lg. By comparing the $M_0 \sim f_c$ scalings derived using Pn from explosions and earthquakes with those derived using Lg, we will investigate if, when and why the Pn/Lg ratio works as a discriminant between explosions and earthquakes.

The proposed research is composed of several tasks. The first is to develop a relatively reliable and robust method to measure the source M_0 , f_c , and path Q_0 , η values using the Pn phase. This task is difficult due to the effects of source radiation pattern and 3D path structural complexities in the Pn spectra. The second task is to analyze, with the method developed, Pn spectra from many events to obtain their M_0 and f_c values, as well as the Q_0 and η values for central Asia. The third task is to compare the $M_0 \sim f_c$ scalings for earthquakes and explosions, derived using Pn, with those derived using Lg, to obtain the differences in those scalings.

This research provides important input to the implementation of a new Comprehensive Test Ban Treaty, since P/Lg amplitude ratio is one of the most promising discriminants between explosions and earthquakes.

RESEARCH ACCOMPLISHED

Over the past year (since the 18th seismic symposium), we have made several accomplishments, which are summarized in the following paragraphs.

Further modification of inverse algorithm

There are three fundamental problems that may occur in a spectral inversion using regional waves. The first problem is that at smaller distances the effect of finite Q may not be significant in reducing the amplitude spectra, resulting in an unstable Q estimate (the "negative Q " problem). The second problem is that the model parameters describing source spectra (M_0 , f_c) and path Q_0 , η tend to trade-off. The third problem is that the forward model used for high-frequency spectra is typically imprecise in that (a) it simplifies the source spectra by with a simple, ω^2 model, which does not fully describe effects of the complex source geometry and rupture processes, (b) it uses an idealized geometrical spreading term derived from simplified 1D models; (c) it does not fully account for the complex site response and the occasional instrument miscalibrations. In the spectral inversions, effects of these problems may be coupled to bias the result.

To tackle these problems, in the last symposium paper (Xie, 1996a) I have reported two modifications to the inverse algorithm of Xie (1993), for simultaneous determination of source M_0 , f_c and path-variable Q_0 and η values. The first modification was to use a more stable Q estimator, and the second was to incorporate *a priori* knowledge on the average interstation Q_0 and

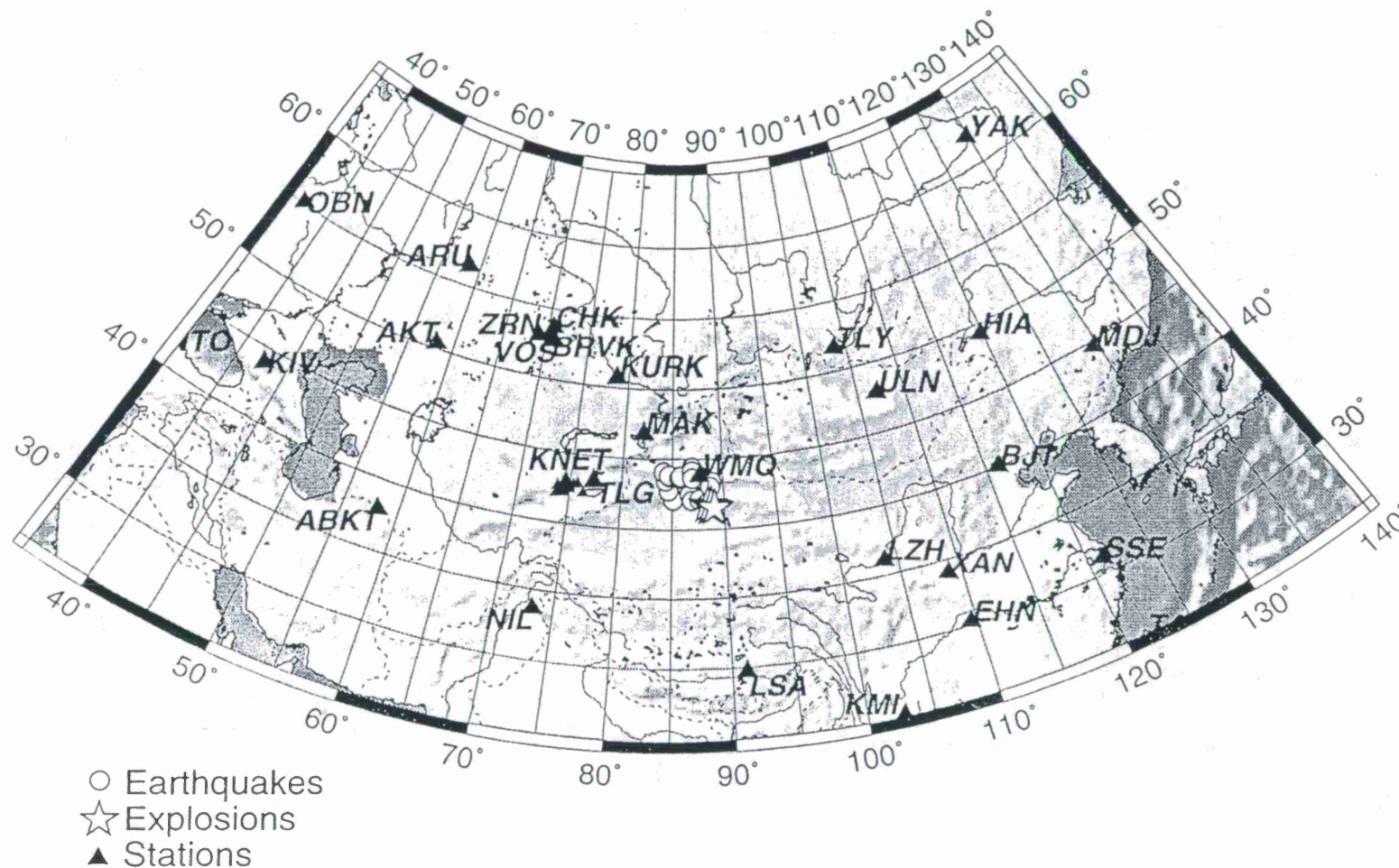


Figure 1. Locations of the explosions and earthquakes in and around the Lop Nor Text Site used in this study. Also shown are locations of the broad-band Kyrghistan Network (KNET), Kazakhstan Network, IRIS and CDSN stations. The KNET has about ten stations with an aperture of about 200 km.

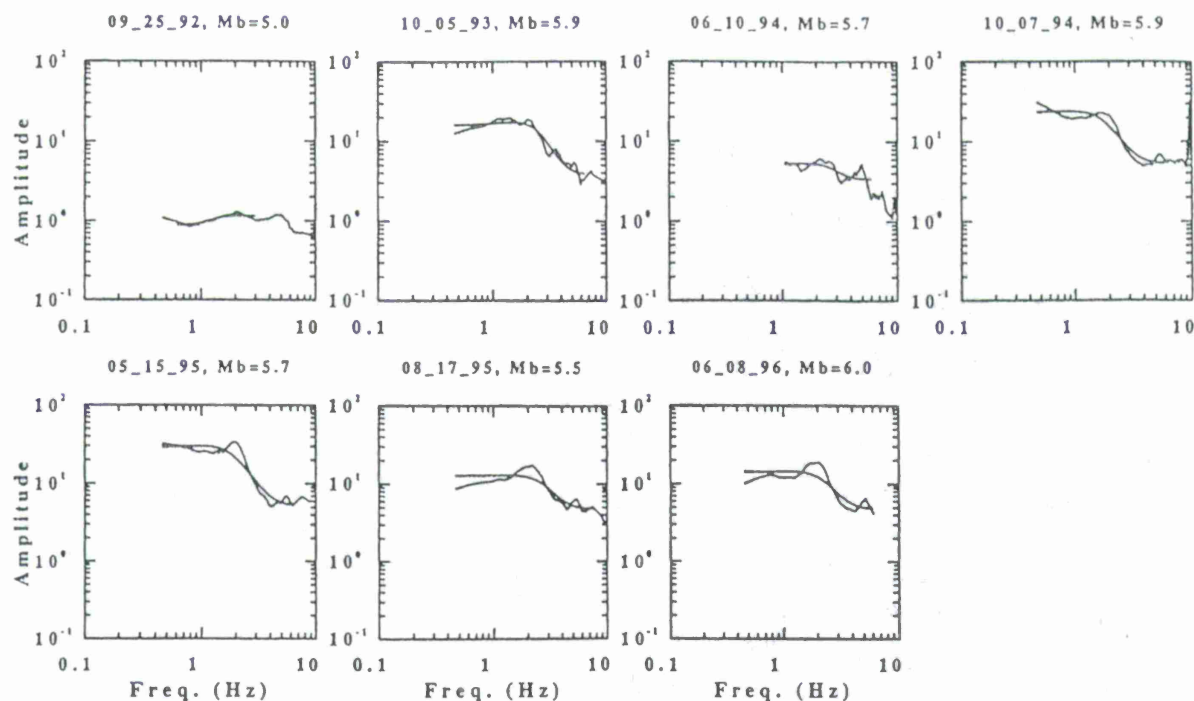


Figure 2. Pn spectral ratios of seven Lop Nor Test Site explosions with respect to a small explosion (July 7, 1996, $M_b = 4.9$), and non-linear fitting of the spectral ratios by the modified Mueller-Murphy (M.M.M.) source model. Note that for events with $M_b \geq 5.5$, there are more pronounced overshoot effect than predicted by the M.M.M. model.

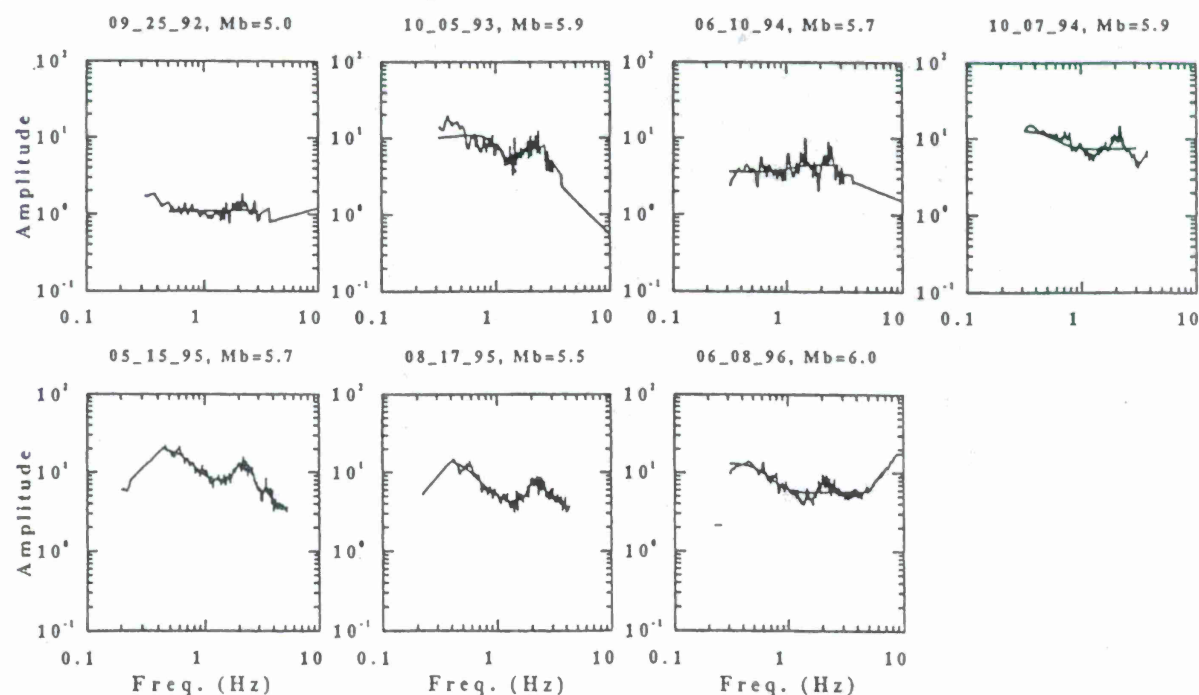


Figure 3. Lg spectral ratios of seven Lop Nor Test Site explosions with respect to a small explosion (July 7, 1996, $M_b = 4.9$), and non-linear fitting of the spectral ratios by the modified Mueller-Murphy (M.M.M.) source model. Note that for all events with $M_b \geq 5.5$, the spectral ratios tend to have nulls at frequencies that are about, or slightly above, 1 Hz.

η values as a constraint to the spectral inversion. Recently I have modified that algorithm again by using *a priori* knowledge on source spectral parameters (mainly f_c), obtained using the empirical Green's function (EGF) approach, to further constrain the spectral inversion. The use of the EGF is not new, but the numerical implementation to use it in my algorithm has only been recently done.

I have also formulated the modified algorithm formally in the theoretical framework of Tarantolla (1987), in which a general inverse problem is stated as the problem of maximizing the *a posteriori* marginal probability density function, which incorporates the *a priori* information.

Another development toward a better inverse scheme is that I have implemented the software to get moving window average of Pn coda spectra, which, compared to Pn spectra, are more stable. Currently, I am using averaged spectra of Pn /Pn coda windows, instead of Pn spectra obtained by a single window, in the inversions.

Data collection and processing

In the past year, this research has mainly focused on data collection, processing and spectral inversions, using the modified algorithm.

To date I have collected and processed several hundreds of Pn, Lg spectra from all of the eight underground nuclear explosions detonated in the Lop Nor Test Site (LTS) since September, 1992, and from many earthquakes that occurred in and around that test site. Records from the broad-band Kyrghistan Network (KNET), Kazakhstan Network (KZNET), IRIS and CDSN network stations are used for earthquakes. For explosions, records from the CDSN stations are not available. Figure 1 shows the locations of the events and stations used.

As discussed by Xie (1996a,c), Pn spectral inversion is more vulnerable to the fundamental problems in the spectral inversions, such as source radiation pattern and 3D structural effects. Therefore it is more important to obtain and use the *a priori* knowledge in Pn spectral inversion. As part of the *a priori* knowledge we have estimated the corner frequencies for many larger events using the empirical Green's function approach, when nearby smaller (empirical Green's function) events are available. Assuming that the path Green's functions of a larger and its nearby small event are stochastically the same, the spectral ratio of the two events gives the source spectral ratio and can be modeled as ratios of two ω^2 source spectra. We can therefore fit the spectral ratio with optimal values of the M_0 ratio and f_c values of both the larger and smaller events (although the f_c value of the smaller event is typically not reliable), thus obtaining the *a priori* knowledge on f_c for the larger events. As shown in the next section, the source spectral ratios contain more information than just the values of M_0 ratio and f_c . Therefore in the next section I will present, and discuss in detail, some examples of the spectral ratios.

Source spectral ratios

Figure 2 shows Pn spectral ratios of seven larger Lop Nor explosions, with respect to the smallest explosion (July 29, 1996, $M_b=4.9$). For events with M_b equal or greater than 5.5, the spectral ratios in Figure 2 tend to follow an ω^2 model at lower frequencies, a phenomenon to be expected if the path effects are canceled in the spectral ratios. We fitted the spectral ratios by the modified Mueller-Murphy (M.M.M.) model (Serenio *et al.*, 1988) to obtain the M_0 ratio and

f_c values. The fit for the larger explosions ($M_b \geq 5.5$) is quite good, except that the overshoot in the observed spectral ratios tend to be more pronounced than that predicted by the M.M.M. model.

We have obtained Lg spectral ratios for the same explosions. Figure 3 shows the Lg spectral ratios of the seven Lop Nor explosions with respect to the smallest Lop Nor explosion, together with the fit for values of M_0 ratio f_c with the M.M.M. model. Contrary to Figure 2, in Figure 3 the larger explosions do not have more significant overshoot effects than that predicted by the M.M.M. model. Another noticeable difference between Figures 2 and 3 is that the spectral ratios in Figure 3 tend to have nulls somewhere between 1 and 2 hz. Patton and Taylor (1995) observed nulls at lower frequencies of about 0.55 hz for spectral ratios from some Nevada Test Site (NTS) explosions. They proposed that Lg from the NTS events may be largely composed of scattered Rg, which is excited by CLVD sources accompanying the explosions and is associated with spectral nulls near 0.55 hz. If that mechanism is valid for the LTS explosions, the shift of the frequencies of the spectral null from 0.55 Hz (in the NTS) to above 1 hz (in the LTS) may be explained by the difference of shallow structures at both test sites.

We have also obtained spectral ratios of larger earthquakes in and round the LTS, with respect to nearby smaller earthquakes. Figure 4 shows an example of such ratios for Pn and Lg. The Lg spectral ratios do not show a pronounced null, and both Lg and Pn spectral ratio can be fitted by an ω^2 source model reasonably well.

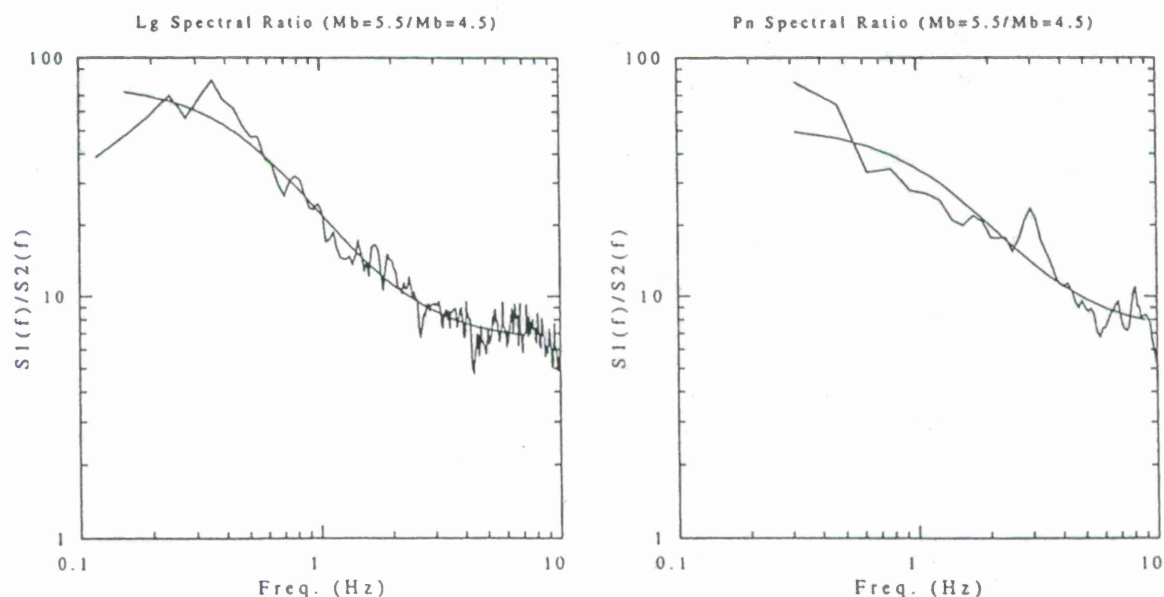


Figure 4. Lg (left) and Pn (right) spectral ratios of an $M_b = 5.5$ event (May 2, 1995, 11:48:11.6 UT, 43.78°N, 84.66°E), with respect to an nearby $M_b = 4.5$ earthquake.

Spectral inversions

For Pn from explosions and earthquakes, *a priori* information on interstation Q between BRVK and KUR is estimated, using the standard two-station spectral ratio method. This *a priori* information is used together with those on the f_c values (the last section) in Pn spectral inversions. Figure 5 shows an example of Pn spectral inversion with the *a priori* information applied. The Q_0 values estimated for the KNET stations varies between 206 (station AML) and 600 (station KZA), and η values between 0.1 (station UCH) and 1.0 (station USP; note that MAK, at which η is even higher, is not a KNET station). These variations do not reflect the true variation of Pn Q . Rather, they are caused by the drastic amplitude variation across the KNET (Xie, 1996a), probably caused by some deep-seated, 3D structural anomalies. This example shows that by the end of this study, we will likely resolve strong lateral variations in apparent Pn Q , which will not reflect the variations in true Pn Q . On the other hand, the path-averaged Q_0 and η values will probably be close to the areal averaged values of true Pn Q .

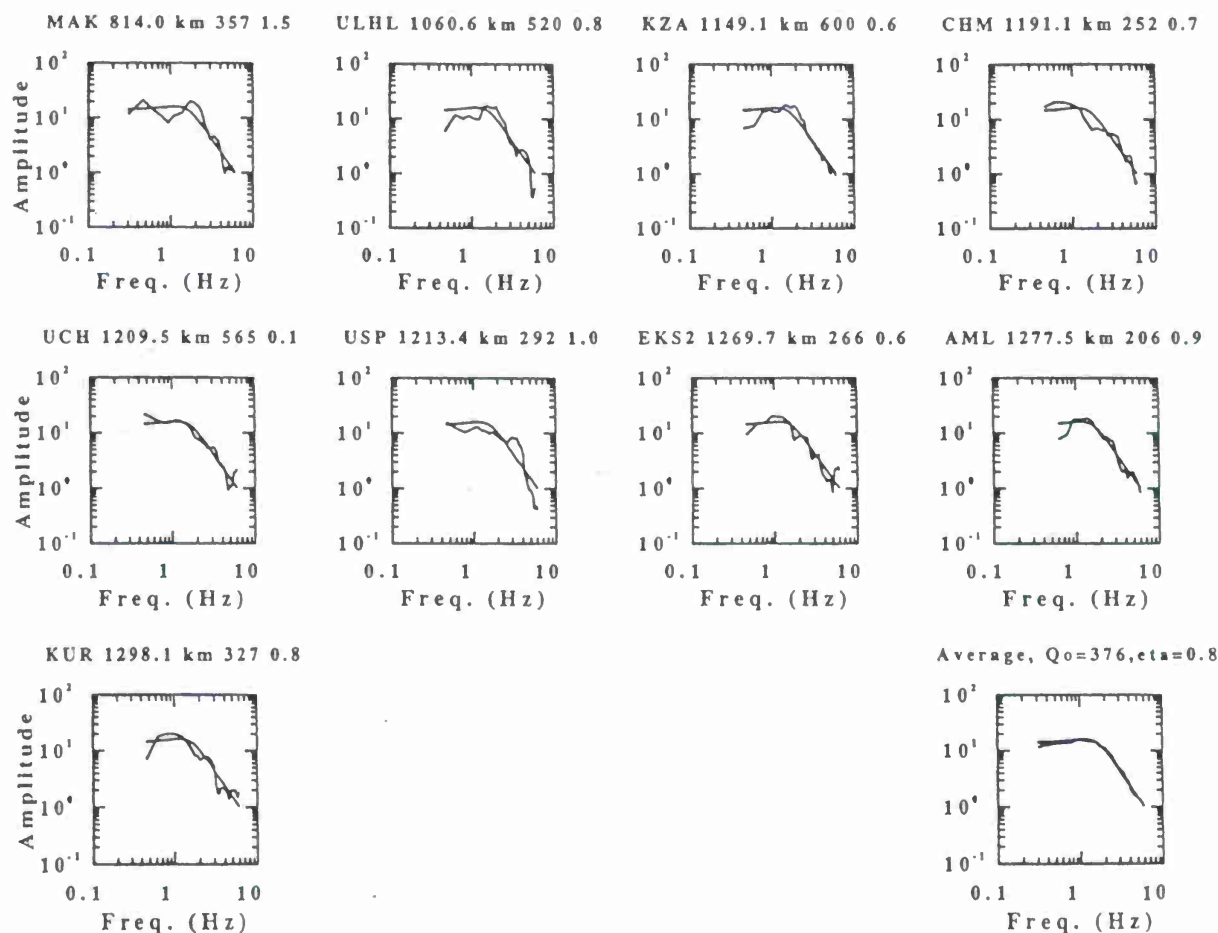


Figure 5. Synthetic Pn source spectra for KNET and IRIS stations recording the Oct. 7, 1994, Lop Nor explosion, versus the observed. The lower right panel is the station average. The synthetic spectra are calculated using a β of 1.0 and the optimal source spectral parameters ($M_0 = 3.5 \times 10^{23}$ dyne-cm, $f_c = 1.6$ Hz) obtained using the modified inverse method. The distance, Q_0 , η and values are written on the top of the panels. The unit of the amplitude is the same as that of Figure 3 of Xie *et al.* (1996).

We are currently inverting for path Q_0 , η and source M_0 , f_c values for all of the explosions and earthquakes plotted in Figure 1, with the modified inverse method and *a priori* information on two-station Q_0 , η and source f_c . The spectral inversions are expected to be completed within a few months.

CONCLUSIONS AND RECOMMENDATIONS

In the last symposium paper (Xie, 1996a), I have summarized much of the theoretical and observational work on (a) the Pn spectral complexity and modelisation errors in Pn spectral inversion, and (b) significant improvement of the spectral inverse method of Xie (1993). In the past year, I have continued those work, but most of the time has been devoted to a massive effort to collect, process, and invert the Pn and Lg spectra from numerous underground explosions and earthquakes in and around the Lop Nor Test Site (LTS). Many important findings have started to emerge. When completed, this research should yield the following result:

- (1) Apparent Pn Q_0 , η averaged over groups of paths around the LTS.
- (2) Variations of apparent Pn Q_0 , η among paths that are close to one another, reflecting the uncertainty of Pn amplitude measurement for paths crossing complex structures, such as the Tien Shan Mountain.
- (3) Pn source M_0 , f_c of the eight LTS explosions with the M.M.M. source model.
- (4) Pn source M_0 , f_c of the twenty plus earthquakes in and around the LTS.
- (5) Lg source M_0 , f_c values for the same explosions and earthquakes.

These results, plus the results of the earlier works on path-variable Lg Q_0 , η values (Xie, *et al.*, 1996) should allow us to put a strong constraint on why the P/Lg spectral ratio can be used as an explosion discriminant. This is so because for the P/Lg spectral ratio discriminant to work, either the apparent source M_0 , f_c values or apparent path Q_0 , η values have to exhibit some systematic variations with the varying source types (from explosions to earthquakes) and phases (Pn to Lg).

Research so far suggests that a fundamental understanding of the excitation and propagation of high-frequency regional wave has not yet been achieved. This fundamental understanding will be crucial in future monitoring of underground explosions. There are many regions in the world where there is no sufficient empirical data base to be used to judge if an event is a underground explosion. In the current study we are already revealing the striking differences between the NTS and LTS in many aspects of the excitation and propagation of Lg and Pn. The knowledge we have for the LTS is still limited due to the lack of ground truth information. For many other regions of interest in the world, even less is known. A fundamental understanding on how different sources excites different regional phases differently, and on how different regional phases propagates, will enhance the US capability in monitoring nuclear explosions on all major continents under the current political environment.

References

- Cong, L., J. Xie & B.J. Mitchell, 1996. Excitation and propagation of Lg from earthquakes in Central Asia with implications on explosion/earthquake discrimination, *J. Geophys.*

Res., **101**, 27779-27810.

- Patton, H., & S. Taylor, 1995. Analysis of Lg spectral ratios from NTS explosions: Implications for the source mechanisms of spall and the generation of Lg waves, *Bull. Seism. Soc. Am.*, **85**, 220-236.
- Sereno, T.J., S.R. Bratt and T.C. Bache, 1988. Simultaneous inversion of regional wave spectra for attenuation and seismic moment in Scandinavia, *J. Geophys. Res.*, **93**, 2019-2036.
- Tartantola, A., 1987. *Inverse Problem Theory: Methods for Data Fitting and Model Parameter Estimation*, Elsevier, Amsterdam.
- Xie, J. 1993. Simultaneous inversion of source spectra and path Q using Lg with applications to three Semipalatinsk explosions, *Bull. Seism. Soc. Am.*, **83**, 1547-1562.
- Xie, J., 1996a., Excitation and propagation of Pn in central Asia, in *Proc. 18th Seis. Res. Symposium on Monitoring a Comprehensive Test Ban Treaty*, edited by J.F. Lewkowicz, J.M. McPhetres, and D.T. Reiter, Air Force Phillips Laboratory, PL-TR-96-2153, pp. 419-428.
- Xie, J., 1996b. Lg Excitation and Propagation from the 1995, Western Texas Earthquake Sequence (Abs for the 1996 Fall Meeting), *EOS-AGU Trans.*, **77**, No. 46, F14.
- Xie, J., 1996c. Synthetic and observational study of Pn excitation and propagation in central Asia, Scientific Report No. 1, PL-TR-96-2270, Phillips Laboratory, Hanscom Air Force Base, MA, 24 pp.
- Xie, J., L. Cong & B.J. Mitchell, 1996. Spectral characteristics of the excitation and propagation of Lg from underground nuclear explosions in Central Asia, *J. Geophys. Res.*, **101**, 5813-5822.

THE UNIQUE SOURCE MECHANISM OF AN EXPLOSIVELY INDUCED MINE COLLAPSE

Xiaoning Yang, Brian W. Stump, W. Scott Phillips
Geophysics Group - EES-3, Los Alamos National Laboratory

Sponsored by U.S. Department of Energy
Office of Nonproliferation and National Security
Office of Research and Development
Contract No. W-7405-ENG-36

ABSTRACT

Mining explosions and collapses, in addition to earthquakes, may trigger the future Comprehensive Test Ban Treaty (CTBT) monitoring system. Most naturally occurring mine collapses have source mechanisms similar to a closing void which might provide a physical basis to discriminate them from explosions.

In this study, an explosively induced mine collapse is investigated. The collapse occurred immediately after the support pillars of an underground mine opening were destroyed by explosives. We estimated the time-dependent source moment tensor of the collapse by inverting the surface ground motion data (<1200 in). The results indicate that the source mechanism of the collapse can be represented by a horizontal crack. A unique source characteristic of the induced collapse is that, unlike natural collapses, the induced collapse initiated as a tensile crack. Because of the initial expansion source mechanism, induced mine collapses may pose some difficulties to the seismic discrimination problem. On the other hand, the collapse has a more band limited source spectrum than a typical underground explosion.

Key Words: explosively induced, mine collapse, tensile crack, expansive

OBJECTIVE

The objective of this study is to understand the source mechanism of an explosively induced mine collapse which generated regional seismic signals (Pearson *et al.*, 1996). These kinds of events are of interest to the monitoring of a Comprehensive Test Ban Treaty (CTBT) because of their similar source characteristics to underground explosions and their ability to trigger the CTBT monitoring system.

RESEARCH ACCOMPLISHED

Experiment and Data

Data used in this study were collected in a controlled field experiment conducted at the White Pine Copper Mine near Lake Superior on the Upper Peninsula of Michigan. Figure 1 is the map showing the location of the mine. The plan view of the test area and the layout of a

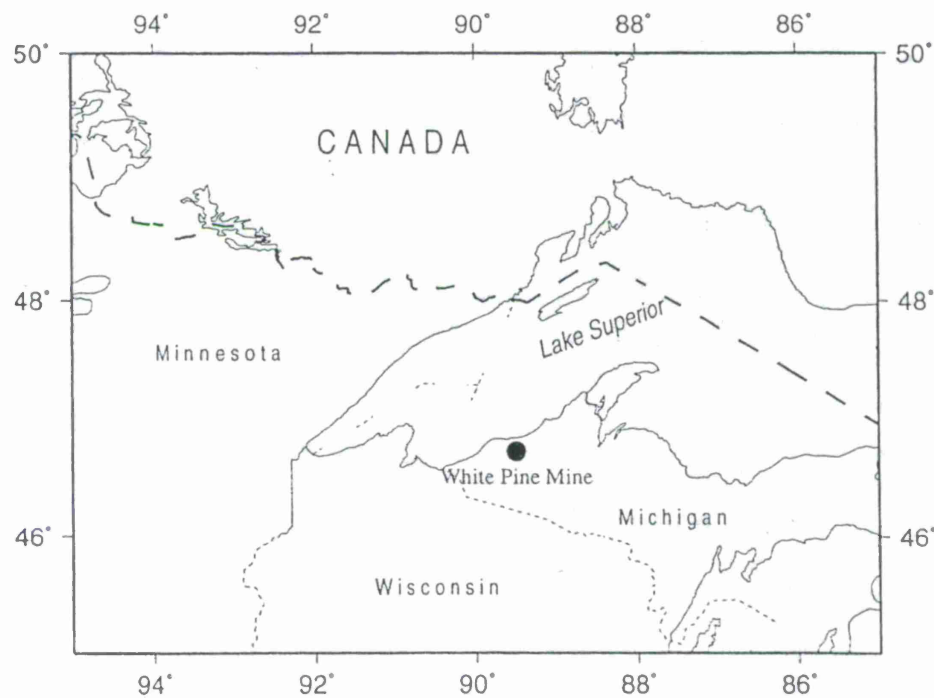


Figure 1 Location of the mine where the explosively induced collapse experiment was conducted.

near-source, surface, three-component seismometer array are presented in Figure 2. The horizontal and slant source-receiver distances and receiver azimuths are listed in Table 1. Detailed documentation of the mine, the experiment and the data acquisition can be found in Pearson *et al.* (1996).

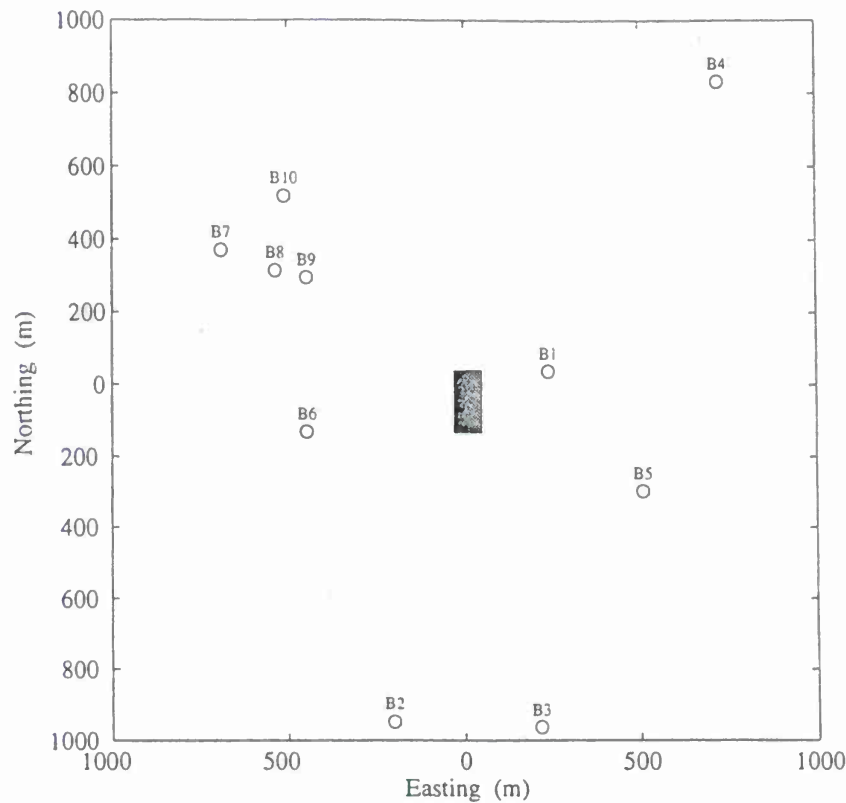


Figure 2 Plan view of the test area. The rectangle marks the collapsed panel. Instrument array is indicated by the open circles.

The section of the underground working designated for the experiment was a rectangular panel at 320 m depth. The area was roughly 20000 m² with a room height of 3 m. During the experiment, explosives were emplaced in the supporting pillars in the section and detonated. The pillars were destroyed by the explosion and the roof collapsed a fraction of a second after the explosion. A millisecond-delay firing pattern, 325 ms in length, was used to minimize ground vibration.

Ground motion from the collapse was recorded by the seismometer array and transformed into vertical, radial and transverse components. Instrument response was removed from the data. Figure 3 shows an example of the data set and its spectra.

Table 1 Source to receiver distances and receiver azimuths from north

Receivers	Slant distance (m)	Horizontal range (m)	Azimuth* (°)
B1	402	244	81.3
B2	1018	967	192.1
B3	1039	988	167.4
B4	1149	1104	41.0
B5	669	588	120.3
B6	563	463	253.7
B7	843	780	298.4
B8	698	620	300.6
B9	623	534	303.7
B10	793	726	315.6

* measured with reference to the center of the array of pillars

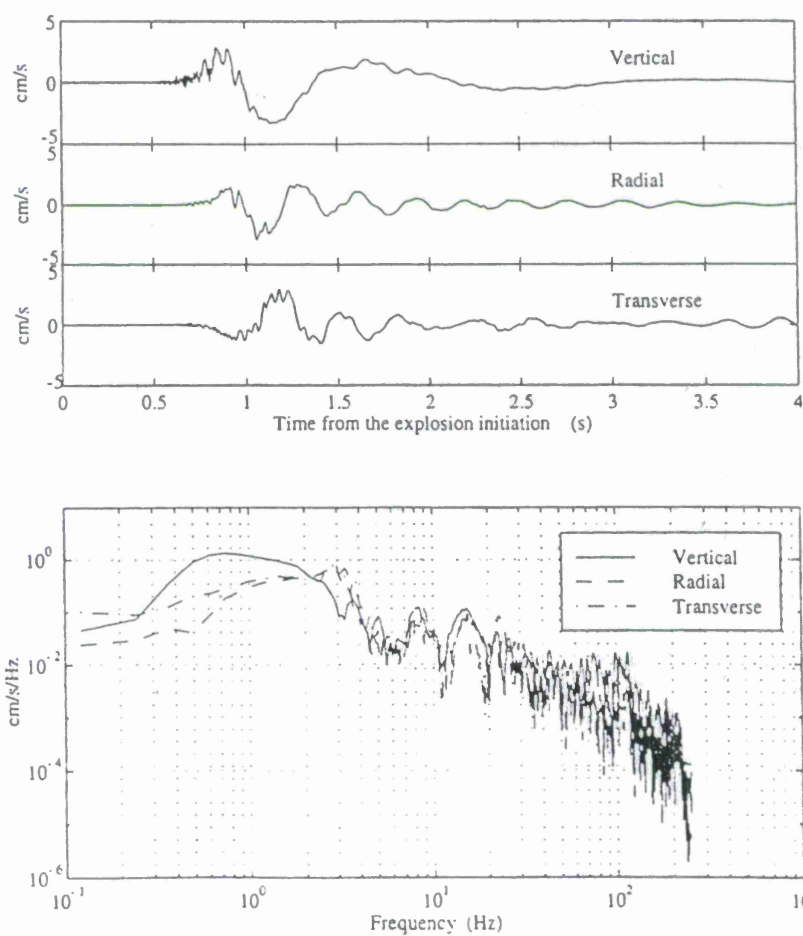


Figure 3 Ground velocities recorded at station B1 and their spectra.

Source Moment Tensor Inversion

To investigate the source characteristics of the induced mine collapse, we estimated second order source moment tensor of the collapse with the linear inversion method described by Stump and Johnson (1977). The basic assumption behind the moment tensor representation is that the wavelength of interest is much longer than the dimension of the source so that the source can be treated as a point source. In our case, the dominant wavelengths of the source signal are between 1600 and 2900 m, 8 to 14 times longer than the dimension of the source, thus satisfying the point source assumption.

The inversion was performed in the frequency domain to take advantage of the linear relationship between the source and observations, thus recovering source phase and modulus. Green's functions were calculated with the velocity model listed in Table 2. The velocity model was derived from the results of a reflection survey (Geosphere, 1995) and aftershock *P* and *S* arrival times. The singular value decomposition method (Lanczos, 1961) was employed to solve the set of equations relating the source moment tensor to the ground motion. The time dependent source moment tensor of the induced collapse was recovered by the inverse Fourier transform of the frequency domain results and is presented in Figure 4.

Table 2 Velocity model used in the inversion

Thickness (m)	V_p (m/s)	V_s (m/s)	ρ (g/cm ³)
140	3660	2000	2.2
180	4270	1800	2.5
∞	5460	3070	3.2

The moment tensor is dominated by its diagonal components. On average, the amplitudes of the off-diagonal components are only about 13% of the amplitudes of the diagonal components. Among the diagonal components, the vertical dipole M_{33} is the largest. These moment tensor components are consistent with a horizontal crack model. The diagonal components of the moment tensor estimates have similar time histories. They have sinusoidal behavior with a period of about 0.8 s. The first motions of the time histories are all positive which imply an initially expanding source.

The isotropic spectrum of the time derivative of the moment tensor, or the moment rate tensor, was calculated as the trace of the moment rate tensor spectra and is shown in Figure 5. Unlike the typical explosion source spectrum, the collapse spectrum is peaked at 1 Hz. The corner frequency is not well defined. This peaked nature corresponds to the sinusoidal behavior of the moment tensor in the time domain.

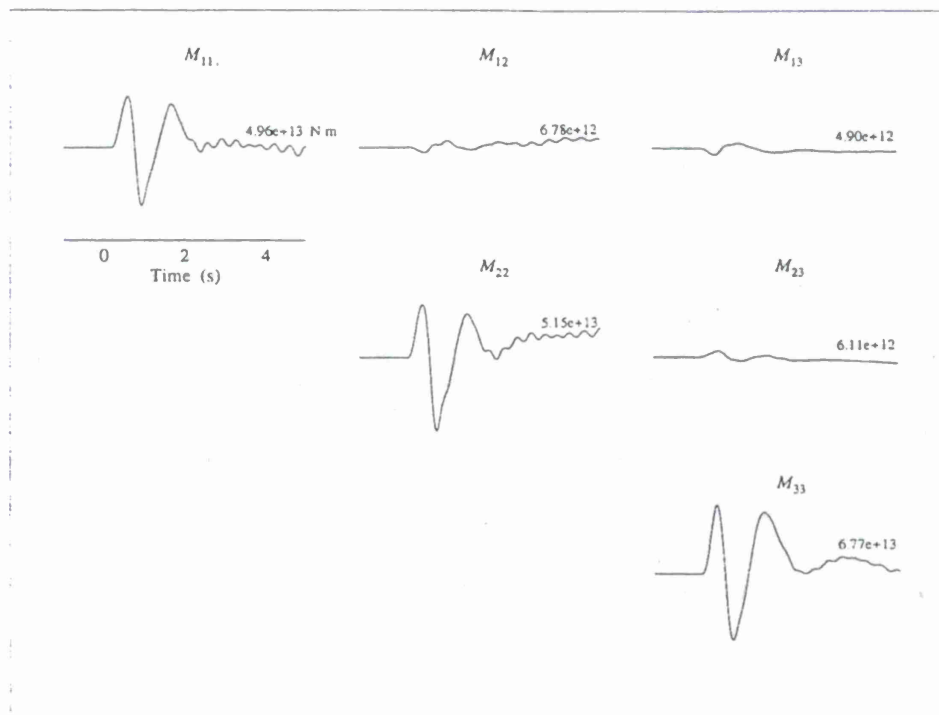


Figure 4 Source moment tensor estimates of the induced mine collapse. The maximum amplitude of the first positive peak in each component is labeled above the component.

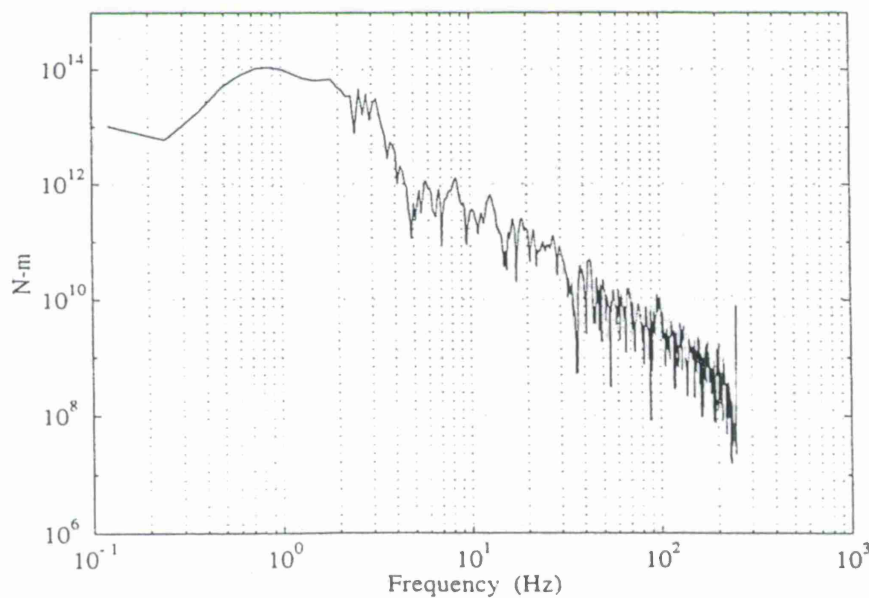


Figure 5 The isotropic source moment rate spectrum. The spectrum is peaked at about 1 Hz. Ground noise analysis indicates that the amplitude increase below 0.2 Hz is probably noise related. High frequency spectrum is estimated to decay as f^{-2} .

Interpretation and Discussion

The moment tensor estimates are dominated by the diagonal components and the time histories of the diagonal components are in phase with one another, suggesting that the induced collapse behaved like a volumetric source. The source is not completely isotropic. The vertical dipole, M_{33} , is the largest among the diagonal components while the amplitudes of the two horizontal diagonal components are about the same, consistent with a horizontal crack model.

One phenomenon particular to this induced collapse is that the source is initially expansive with all diagonal moment tensor components positive. Different results have been obtained in the natural collapse studies (Stump, 1979; Walter *et al.*, 1996). For example, Stump (1979) estimated the source moment tensor of a cavity collapse following an underground nuclear explosion. His results suggested negative first motions for all the diagonal moment tensor components (Stump, 1979; Fig. 7-23).

We reviewed the ground motion data from a natural underground mine collapse. The collapse occurred in a coal mine which employed the long-wall mining method at the depth of about 350 m underground. The collapse was an integral part of the mining activity (Walter *et al.*, 1996). The vertical component seismograms from the collapse recorded by a small aperture array are reproduced in Figure 6. Receivers in the array were distributed along the circumference of a

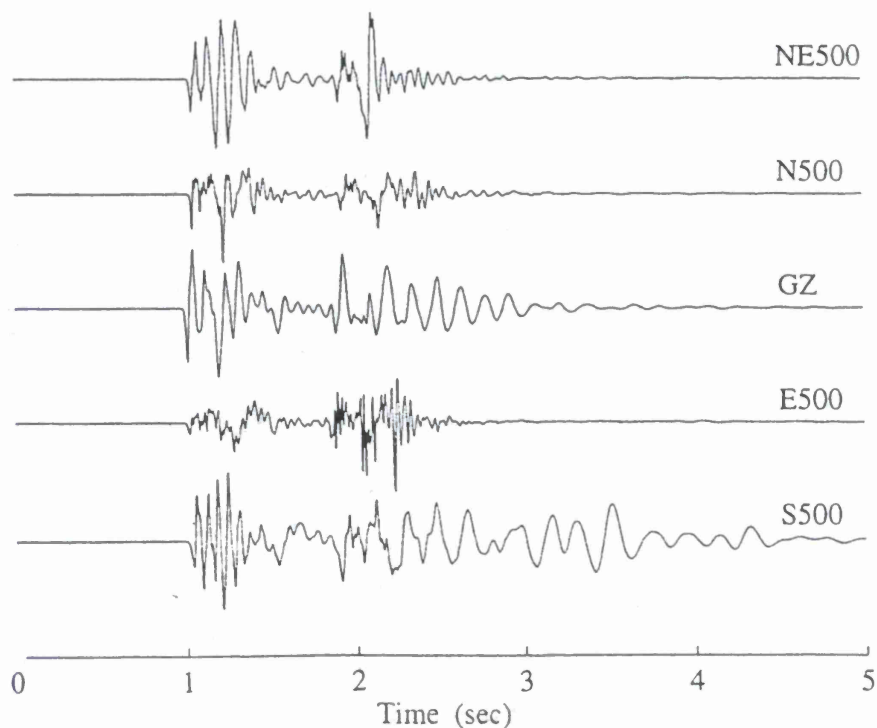
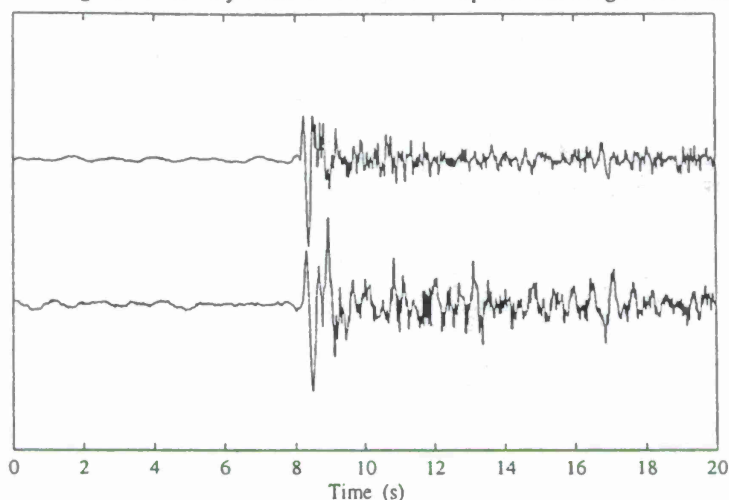


Figure 6 The vertical component near-source seismograms from a natural mine collapse. Station names are written above the corresponding records. Data are from Walter *et al.* (1996).

circle, 500 m in radius, with one receiver, GZ, at the center. The collapse was believed to have occurred under receivers NE500, N500 and GZ, and the hypocenter was shallow (< 500 m) (Walter *et al.*, 1996). The coda magnitude of the collapse is 2.8. In contrast to the positive vertical first motions recorded from the induced collapse (Figure 3), the vertical first motions from the natural collapse are all sharply negative. Near-regional records from these two types of collapses also show opposite first motion polarities: positive for the induced collapse and negative for the natural collapse (Figure 7).

Vertical ground velocity from the induced collapse at the range of 200 km



Vertical ground velocity from the natural collapse at the range of 20 km

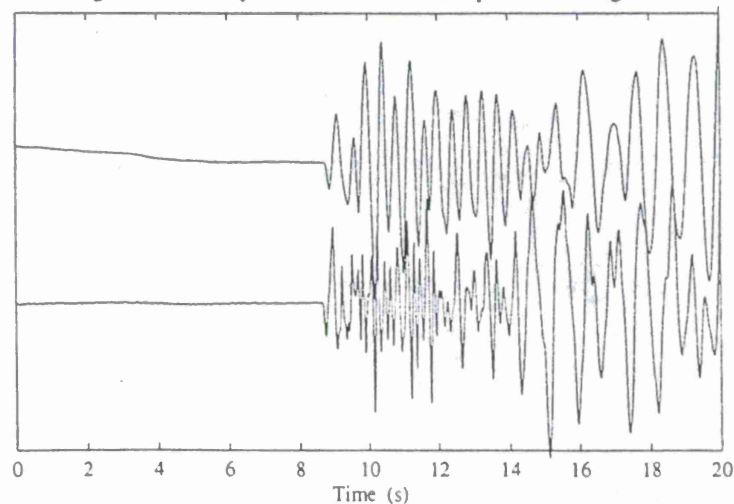


Figure 7 The vertical seismograms from the induced collapse and the natural collapse recorded at near-regional distances. Natural collapse data are from Walter *et al.* (1996).

The discrepancies observed between the explosively induced collapse and natural collapses may reflect differences in the source processes of these two categories of collapses. One possible difference is that in natural collapses, the failure process of the collapsed material takes a relatively long time because of the static loading of the collapsed material, while the material failure in an induced collapse is almost instantaneous due to the dynamic loading. In a natural collapse, after the cavity is excavated, the weight of the collapsed mass and the traction imposed by the surrounding medium are in equilibrium at first. Then micro-cracks form gradually due to small perturbations to this equilibrium. The time it takes for the material to reach its final failure as the cracks form may be far below the lowest observable frequency with seismic instruments. On the other hand, during an induced collapse, after the instant loading of the collapsed mass due to pillar removal, the equilibrium may never be realized and cracks form rapidly. The material failure threshold is reached in a time period within the observed seismic frequency band. This crack forming process can be modeled as an opening crack with a volumetric expansion, although in a natural collapse, its period is too long for it to be observed.

Based on this argument, we propose a source model for the explosively induced collapse which is shown diagrammatically in Figure 8. First the source is modeled as a vertically opening crack representing the failure process of the collapsed mass. Then the collapsed mass enters free fall and finally impacts the rest of the medium. The basic difference between this model and previous natural collapse models used by other investigators (Taylor, 1994; Pechmann *et al.*, 1995) is the inclusion of the opening crack which seems to have significant contribution to seismic wave generation. The moment tensor representation of this source model would be similar to that of the spall model accompanying an underground explosion although the crack opening and closing do not occur at exactly the same depth in a collapse.

By including the opening crack as an effective seismic source process, we can explain the initial expansion of the source estimates obtained in the inversion and the compressional first motions observed in the data.

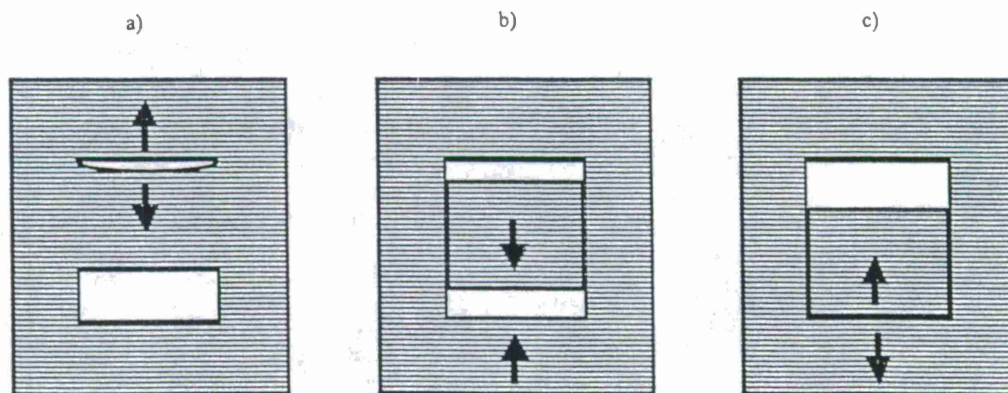


Figure 8 An induced collapse source model. The process undergoes three phases. a) Due to the sudden loading of the collapsed mass after pillar removal, an opening crack forms; b) The collapsed mass is detached from the rest of the medium and goes into free fall; c) The collapsed material rejoins the medium.

CONCLUSIONS AND RECOMMENDATIONS

The source characteristics of an explosively induced mine collapse were investigated with source moment tensor inversion. The results indicate that the source characteristics of the collapse is similar to that of a horizontal crack.

The time histories of the moment tensor estimates illustrate an initial expansion at the beginning of the source. This phenomenon and the observation that the first motions of the observed data are compressional everywhere are in conflict with the implosional nature of traditional collapse models. To explain this, we propose an induced collapse source model which includes an opening crack at the beginning of the source. With this model, the moment tensor time histories recovered by the inversion and the compressional first motions observed in the data can be explained. Because of the initial expansion and volumetric source characteristics of the explosively induced collapse sources, this kind of source may further complicate the discrimination problem. On the other hand, the peaked nature of the isotropic moment rate spectrum could be a diagnostic signature of collapses.

This study is the case study of one explosively induced mine collapse. More analyses on these kind of collapses are needed in order to validate the conclusions reached in this study. The results can be applied to regional distances to investigate the effects of different source models on regional observations.

REFERENCES

- Geosphere, Inc. (1995). Seismic reflection survey for northeast mine expansion planning, White Pine Mine, *Report to Copper Range Company*.
- Lanczos, C. (1961). *Linear Differential Operators*, D. Van Nostrand Co., London, Britain.
- Pearson, D. C., B. W. Stump and W. S. Phillips (1996). The White Pine Mine explosively induced, controlled collapse experiment, *Proc. 18th Annual Seismic Research Symposium on Monitoring A Comprehensive Test Ban Treaty*, 4-6, September, 1996, 937-946.
- Pechmann, J. C., W. R. Walter, S. J. Nava and W. J. Arabasz (1995). The February 3, 1995 M_L 5.1 seismic event in the Trona Mining District of southwestern Wyoming, *Seism. Res. Let.*, 66, 25-34.
- Stump, B. W. and L. R. Johnson (1977). The determination of source properties by the linear inversion of seismograms, *Bull. Seism. Soc. Am.* 67, 1480-1502.
- Stump, B. W. (1979). Investigation of seismic sources by the linear inversion of seismograms, *Ph.D. Thesis*, University of California, Berkeley, California.
- Taylor, S. R. (1994). False alarms and mine seismicity: an example from the Gentry Mountain mining region, Utah, *Bull. Seism. Soc. Am.* 84, 350-358.
- Walter, W. R., S. L. Hunter and L. A. Glenn (1996). Preliminary report on LLNL mine seismicity deployment at the Twentymile Coal Mine, Lawrence Livermore National Laboratory, Livermore, California, UCRL-ID-122800.

USE OF SEISMIC MICROARRAYS FOR ON-SITE INSPECTION MONITORING

Vitaliy V. Adushkin
Alexandr A. Spivak
Institute of Dynamics of Geospheres
Russian Academy of Sciences
Moscow, Russia

ABSTRACT

In order to create an active monitoring system for small seismic events, operative microarrays have been tested. The principal demands of the system under development were as follows: (1) the possibility of rapid (days) arrangement of time-continuous microseismic observations, (2) simplicity of operation, (3) mobility of relocation, (4) high sensitivity for detection of very weak seismic signals.

The system of operative microseismic monitoring was tested in numerous applications, including: observations of residual seismic effects of underground nuclear explosions, including low yield explosions (Semipalatinsk test site); monitoring geological media at sites of underground radioactive liquid waste disposal; assessment and prognosis of the long-term mechanical stability of a rock massif designated for the construction of a nuclear (breeder) reactor for hot water supply (Kola peninsula, Russia) and for underground radioactive waste storage (Chelyabinsk District); during the monitoring of the mechanical stability of local areas of the Earth's crust (Kola, Voronezh and Kursk regions of Russia). For these measurements, special equipment was developed, located in microbus together with means of life-support.

The system has been completely tested, including the rapid arrangement of observations in a foreign country (Valtellina, Italy, in the Southern Alps). Operational seismic monitoring established in 3 days, and completed in 8 days from the beginning of work. The microarray included a three-component, central seismic station and 2 additional stations to complete the small aperture array. The stations were connected by cables, radio channels and telephone lines for data acquisition and information transmission. Solar panels and batteries were used for the electric power supply. Seismic observations were three months long.

Results of the test (including multiple, quick relocations of the recording stations) prove a high performance capability of the operative system of microseismic monitoring, especially for revealing inhomogeneities within rock massifs from recordings of background seismic noise.

Keywords: on-site inspection, seismic, array, portable

OBJECTIVES

Currently, the dominant concept is that of global seismic monitoring for nuclear tests; that is, the monitoring of both land and ocean areas without exceptions. Even in the case of a wide network of seismic stations, there exist problems related, first, to an inappropriately low threshold for the identification of seismic events that can be interpreted as a nuclear test and, second, to the existence of uncertain control zones.

It is known that reliable and identification of seismic effects from the underground explosions, including low yield explosions, is accomplished at regional distances. For economic reasons, the international community always fails to achieve a high density of global seismic monitoring network.

Since technical monitoring is only an auxiliary approach, allowing confidence in the fact of creating nuclear weapons (the basic way to control the nuclear activities of CTBT members is to analyze the technical policy in nuclear and dual technologies), then the monitoring of nuclear testing via regional seismic stations becomes quite realistic.

If the monitoring of authorized nuclear activities performed by international organizations and analysis of data in acquisition, utilization and intermediary efforts relating to nuclear materials and technologies reveals that a CTBT member develops a nuclear device, it is possible to organize regional monitoring in an accessible region where the reliable control over potential nuclear tests can be provided.

Instead of stationary (observatory-type) stations, temporary monitoring stations can be organized that may be disassembled, if necessary, and transported to another region. It is clear that this approach to monitoring significantly increases the detection and identification probability for underground nuclear explosions, via the location of seismic stations in assured recording zones, and will require less CTBT funding.

This approach to the monitoring of nuclear testing, in addition to the benefits obtained from the cost reduction and credibility increase, would at the same time address more closely address other problems that are not completely solved in establishing the appropriate monitoring level when measures are undertaken to hide nuclear explosions.

"Concatenated," small-aperture, seismic microarrays of non-observatory type, consisting of 4-6 recording points, can be successfully used to monitor the compliance of nuclear weapons owners with "zero-yield" CTBT. In this case, seismic arrays would be located near previously active test sites (or reside within their boundaries). Other considerations apart, these microarrays are suitable for on-site inspection. In the present work, the experience of use of microarrays with different purposes is described.

At the beginning of the negotiations connected with preparing Test Ban treaties it was clear that it would be necessary to develop techniques for operative geological medium monitoring, aimed at determining of the location of a probable nuclear test.

Practically, on the basis of the available data and examination of estimates, we came to the conclusion that the best results should be expected from seismic methods.

Therefore, coeval with studies of changes of bacterium composition, residual electric and magnetic effects, regimes of underground gases, etc., the most attention was paid to the development of a method for the detection and discrimination of residual seismic effects. At that time, residual seismic effects were associated only with aftershocks. It was known that the amplitudes and duration of aftershocks depended not only on the explosion yield, but also on properties of the geological medium.

Also it was known that it is necessary to create a monitoring system for recording residual seismic phenomena resulting from low yield underground explosions, conducted in geological media with complex structure. In this case, residual seismic effects are not aftershocks, which are classic seismic events and which are well marked out on the microseismic background, but weak events which should be called relaxation-type seismic impulses.

As a result, the following demands for a monitoring system have been formulated:

- (1) a possibility of a quick (first days) arrangement of continuous microseismic observations;
- (2) simplicity of operation;
- (3) mobility of relocation, since it may be necessary to investigate a relatively large area during a short period of time, even if the seismic effects are weak;
- (4) high sensitivity, for detection of very weak seismic signals.
- (5) the system and measurements should be inexpensive.

Two systems were tested: one system used a multi-channel, digital seismic station of traditional construction; the second system used an analog tape-recorder with seven channels and good characteristics. In all cases, small aperture microarrays were used. For measurements under field conditions, a specially-developed system was used, located in microbus together with means of life-support.

The microseismic monitoring system was tested under various conditions. In some cases, continuous recordings of residual seismic effects due to large scale underground nuclear explosions were conducted (Adushkin and Spivak, 1996; Spivak, 1996). In this case residual seismic effects were sufficiently large, therefore location of recording points were not changed. In other cases microseismic array were dislocated along given route and regime measurements of the geological medium micro-oscillations were being conducted during several hours or several days. For example, in 1993 and 1994, an expedition covered distance from Moscow to Kirovsk (Kola region of Russia) and back, and carried out measurements of relaxation regime at the earth crust local plots at 15 points (Spivak and others, 1997).

In this way, local areas of the Earth crust were investigated in the following cases: (1) instrumental observations of aftershocks due to underground nuclear explosions; (2) studies of microseismic noise near underground nuclear explosions; (3) during underground radioactive liquid waste disposal near Krasnoyarsk-26 (Zheleznogorsk) and Dimitrovgrad; (4) during assessment and prognosis of long-term mechanical stability of a rocky massif for construction underground radioactive waste storage on the territ-

of PO "Mayak" (Chelyabinsk-65, now Ozersk); (5) during assessment and prognosis of long-term mechanical stability of a rocky massif for construction of a nuclear reactor (breeder) for heat water supply (Kola peninsula, Russia); (6) during profiling of tectonic faults according to their activity, on the territory of the Novo-Voronezh nuclear power station. All these experiments allowed the accumulation of a large working experience with these monitoring systems.

For instance, consider the data obtained in researching the relaxation regime of the geological medium due to underground nuclear explosions. The following results were obtained as the result of the measurement of microseismic noise and microseismic impulses in the near field around a borehole or tunnel in which nuclear explosions were conducted:

- (1) the number of impulse microseismic effects increase considerably in the explosion area (see Fig.1),
- (2) the amplitude of impulse events of relaxation type increase considerably;
- (3) it should be noted that the number of events decrease in time;
- (4) histograms of time intervals between aftershocks and histogram of amplitude differ from event distribution;
- (5) the spatial distribution of impulse sources has the appearance of a cloud (Fig.2), and not separate clusters which change form and location in time (which takes place when the medium is in a natural state; i.e., the relaxation regime is normal);

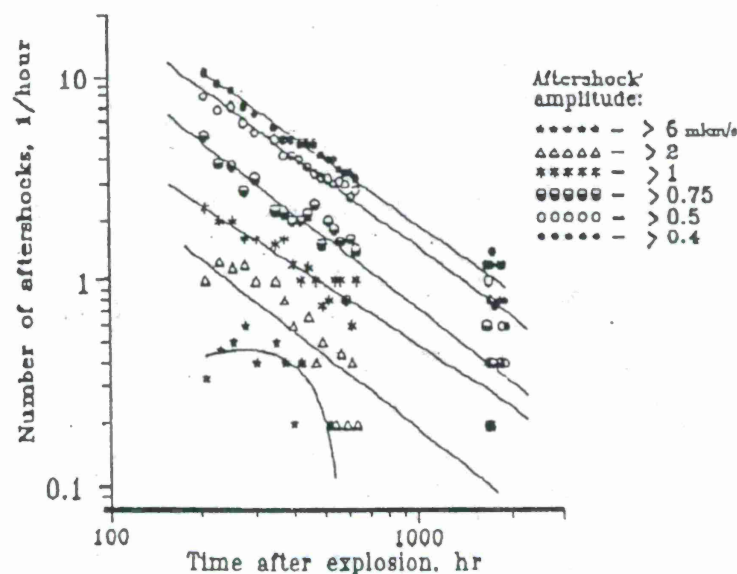


Fig. 1. Aftershocks emission intensity vs. time, for events of different amplitudes (example of a nuclear explosion conducted in a borehole at the Semipalatinsk test site, July 08, 1989).

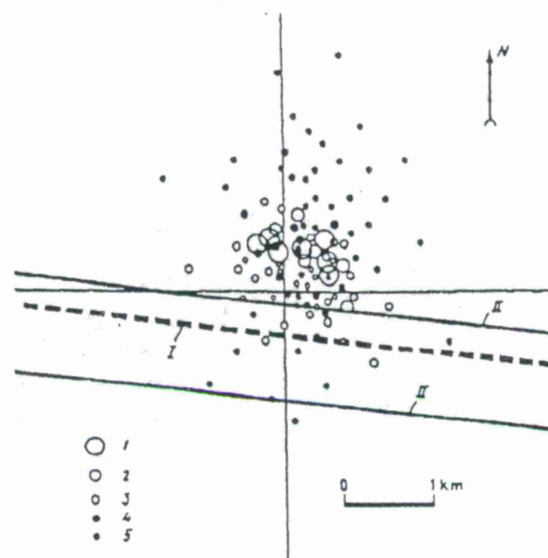


Fig. 2. Epicenters of aftershocks triggered by a nuclear explosion at Balapan, STS (July 08, 1989). Aftershock amplitudes (at the source), nm/s: (1) above 5000; (2) 2500-5000; (3) 1500-2500; (4) 750-1500; (5) under 750; I - Kalba-Chingiz tectonic fault; II - tectonic faults of higher order.

- (6) impulse microvibration sources are concentrated at the depth of explosion (taking into account location accuracy along the depth);
- (7) stress drop due to triggered relaxation is greater than due to natural relaxation;
- (8) dependence between medium relaxation and underground water regime is noted. At the same time seismic noise characteristics were researched in explosion region.

As a result of microseismic noise researching the following results were obtained:

- (1) heterogeneity of geological medium like underground cavity and damage zone of underground explosion influence the spectral characteristics of local microseismic oscillations: measurements of background micro-oscillations in the point located in the epicenter area around explosion, borehole zone show heightened ratio of vertical component of micro-oscillations to horizontal component (Fig.3);
- (2) epicentral zone characterized by heightened high frequency components is marked out. Fig.4 shows that ratio between energy in high frequency spectrum range and energy in low frequency range increase near explosion epicenter, which are marked by arrow.

Measurements carried out in low yield explosions conducted at not large depths with considerable influence of weathered layer are of special interest.

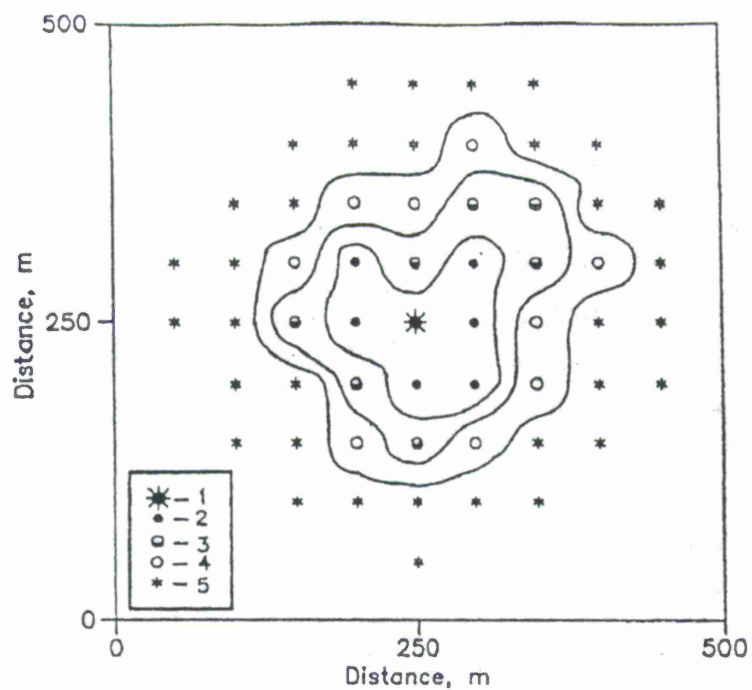


Fig.3. Ratio of vertical to horizontal spectrum component in microseismic noise measured in one month after the UNE (Oct 2, 1989; 4 kt yield; 402 m depth); (1) explosion epicenter; (2)-(5) ratio: above 1.3 (2); 1.2-1.3 (3); 1.15-1.2 (4) and under 1.15 (5).

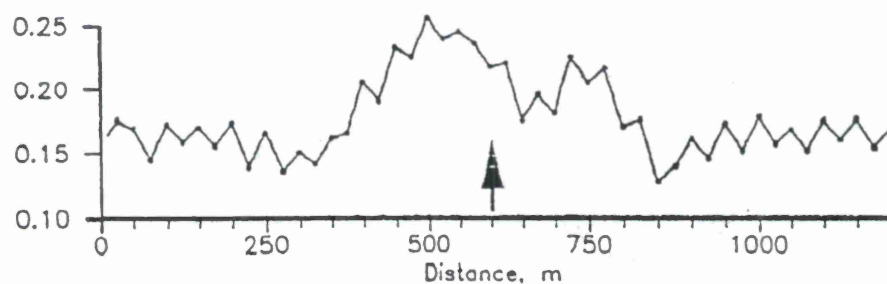


Fig. 4. Ratio of the spectrum energy of microseismic noise for different frequency ranges: 2-12 Hz and 12-22 Hz (UNE 02/09/1989); arrow shows explosion epicenter.

As a result of research the following results were obtained:

- (1) As well as in the case of large yield explosions in the case of low yield explosions change of the medium relaxation regime is recorded (numbers and amplitude of impulse micro-manifestations are considerably higher than natural values). For example, Fig.5 shows results obtained due to small nuclear explosion 132 repeated of 0.4 kt yield in the tunnel at the depth of 69 meters. For information: the thickness of the weathered rock layer is about 30 meters.
- (2) As well as large yield UNE impulse sources concentrate in zones of a least medium faulting at the distances which don't exceed 1000 m per 1 kt of explosion (it should be noted that on the first day after explosion high amplitude impulse in damage zones of preceding explosions are recorded. Triggered impulse zone is located in zone of radioactivity manifestation. It makes it possible to speak that problem of seismic inspection can be solved (let's recall that general aim of on-site inspection is to determine the place where radioactive analysis will be done).
- (3) Impulse sources concentrate in the layer located slightly deeper than layer of weathered rock, and also near boundaries between different kinds of rock;

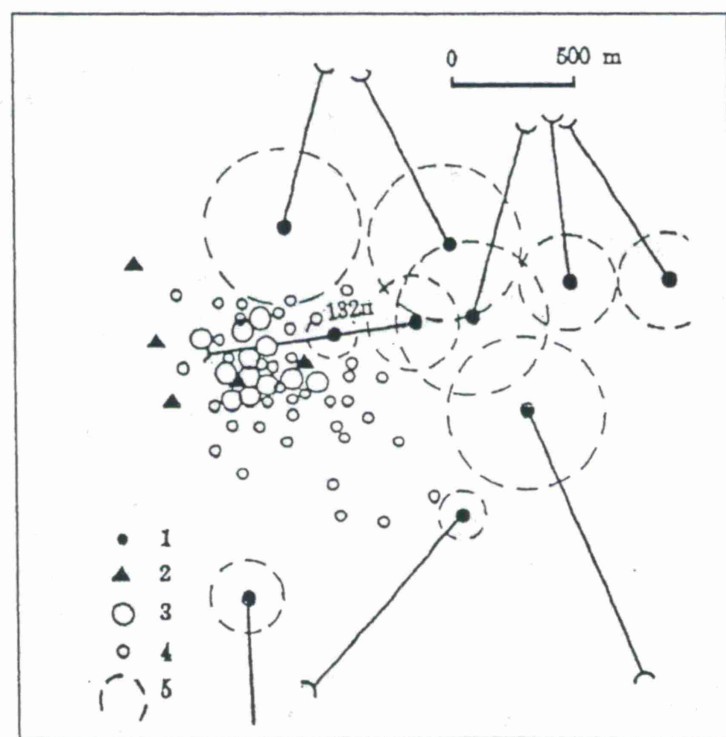


Fig.5. Epicenters of aftershocks triggered by a nuclear explosion in a tunnel; (1) epicenter of preceding UNEs; (2) seismic recording points; (3),(4) epicenters of microseismic impulse manifestations with amplitudes, nm/s: 250-500 (3); more than 500 (4); (5) damage zone boundaries.

- (4) Temporal spatial variability of relaxation processes agrees with spatial variability of underground water regime.

The considered system of operative microseismic monitoring has been tested completely (quick arrangement of observations in a foreign country) in the Southern Alps (commune Grosio, Valtellina, Italy). Monitoring of the slope phenomena was a legend for this work. Operative seismic monitoring has been arranged by 3 days, and permanent in 8 days from the work beginning. The microarray included a three-component central seismic station and 2 extra station completing the small aperture array. The stations were connected by cables, radio channels and telephone line for data acquisition and information transmission. Solar batteries and accumulators were used for electric power supply. Total time of seismic observation was conducted during about three months.

As a result of recording the following results were received: (1) one moved off and local weak earthquakes were recorded; (2) local microseismic impulses were recorded reliable; (3) ranging of mountain slopes according to mechanical stability degree was carried out on the basis of medium relaxation regime; (4) special geological researching conducted by our geologist and local geological service (Sondrio town) confirms conclusions which were made on the basis of our microseismic measurements.

Results of the test (including multiple quick relocation of recording stations) prove a high performance capability of the operative system of microseismic monitoring, in particular for revealing of contrast inhomogeneities in rocky massifs from background seismic noise.

CONCLUSIONS AND RECOMMENDATIONS

On the basis of the results of work carried out, it is possible to draw the following conclusions:

- (1) Underground explosions of even low yield change the relaxation regime of geological media;
- (2) Change of the relaxation regime can be measured by operative monitoring seismic microarray;
- (3) the epicentral zone of an underground explosion is characterized by a intensity heightened of the rock relaxation processes. Numbers of recorded vibration impulses increase more than ten times in comparison with the natural medium state;
- (4) Difference of triggered relaxation process lies in the concentration of sources cloud near one area.
- (5) In contrast to accidental character of temporary distribution of numbers and amplitude of natural impulses triggered impulses are characterized in time

by strongly pronounced decreasing of impulse numbers per time unit and amplitudes decreasing.

- (6) In contrast to natural background impulse amplitudes and time intervals between triggered impulses aren't described by event distribution (they are characterized by several maximums on the histograms).
- (7) Epicentral zone of underground explosion is characterized by stable changes of relative characteristics of microtremors.
- (8) Scheme of implementing instrumental observations showed possibility of its usage in on-site inspection.

REFERENCES

- Adushkin V., Pernick L., Spivak A. "Mechanical effects of the large-scale chemical blasts", Institute for Dynamics of Geospheres Russian Academy of Sciences, 1997, 63 p. (in Russian).
- Adushkin V., Pernick L., Spivak L. Degelen mountain chemical explosion cratering experiments, USGS, 1997, 110 p. 1.
- Adushkin V., Spivak A. Characterization of the aftershock emission caused by underground nuclear explosions. Journal of Earthquake Prediction Research, 1996, V.5, No.4, pp.443-469.
- Spivak A. Residual seismic phenomena due to underground nuclear explosions. Geoecology, 1996, No.6., pp.27-42 (in Russian).
- Spivak A., Spungin V., Dubinya V. Operative estimation of microseismic background on the basis of the mobil recording complex. Physics of the Earth, 1997, No.1, pp.79-83.

CHARACTERIZATION OF T-WAVES FROM SMALL EARTHQUAKES IN THE NORWEGIAN SEA

Donna K. Blackman and John A. Orcutt
Institute of Geophysics and Planetary Physics
Scripps Institution of Oceanography CA 92093-0225

Sponsored by Air Force Office of Scientific Research
Contract No. F49620-94-1-0041

ABSTRACT

The archive of continuously-recorded, beam-formed data from U.S. Navy hydrophone arrays in the Norwegian Sea documents activity for the period February 1995-September 1996. The recording system set up by the Naval Research Laboratory, Washington D.C., was upgraded in November 1995 and the site was shut down by October 1996, so we have 11 months of useful data. Several natural events occurred during this period that are of interest for the study of T-waves associated with regional sources in an ocean basin. Characterization of the acoustic arrivals in terms of their spectral content, duration and difference/similarity between recording sites constitutes the bulk of our investigation to date. In some cases we are able to constrain better source locations by combining the offshore and onshore observations. In order to illustrate T-wave signatures and the extent to which hydrophone arrays can supplement the ability to locate and characterize small oceanic seismic events, we focus mainly on an earthquake swarm that began on the Mohns ridge in November 1995.

A new phase of our research is beginning as data from a few Pacific arrays are archived at Scripps' Marine Physics Laboratory (MPL). The acquisition system is currently being installed and tested and we expect to be able to report on initial observations at the meeting in September.

OBJECTIVE

At this stage, the goal of our investigation in the Norwegian Sea is to complete the characterization of acoustic arrivals recorded on U.S. Navy hydrophone arrays and to continue comparison of this information with corresponding source characteristics as determined from seismic arrays onshore. In addition, we aim to assess the extent to which these hydrophone arrays improve event locations in a small oceanic basin through use of joint seismic-acoustic location inversions (combining onshore P arrival time picks with less certain, but geographically important, offshore T 'picks'). Finally, an estimate of the detection threshold of this offshore system can be compared with that known for the onshore seismic arrays in the Norwegian Basin for the period of recording overlap.

The research objective will shift as we complete the Norwegian Sea data analysis and begin to incorporate Pacific hydrophone data in our catalogue of T phases and associated sources. The subsequent modeling portion of this study is designed to use known variations in near-source geology and bathymetry to predict changes in T-phase character for seismo-acoustic events from several key geographic/tectonic regions. Comparison of the predicted vs observed waveforms will guide incremental steps in model complexity.

RESEARCH ACCOMPLISHED

The hydrophone array data for the Norwegian Sea project was archived by the Naval Research Lab (Nishimura and Conlon, 1994) mid February, 1995, to September, 1996. Sixteen channels monitored pre-formed beams. Our choice of archived beams reflects an emphasis on the Mohns ridge and its intersection with the Jan Mayen transform fault (Figure 1). Several beam directions from more than one location were used. During the first eight months of recording we obtained data useful for initial work but, due to problems at the acquisition site, the usefulness of the archive was reduced by noise and electronic crosstalk between channels. Most of these problems were sorted out in November, 1995, and by February, 1996, a GPS clock was integrated into the system to provide a more accurate time stamp.

The hydrophone data record regional T-waves, body waves from large teleseismic earthquakes, and P-waves, and seafloor-reflected P-waves, from local events. When both P and T arrivals are recorded for a single event at a given site, we can estimate the distance between source and receiver and compare this arc with the epicenter determined using onshore seismic arrays alone. When T arrival times can be picked with enough accuracy at multiple sites, we can constrain event locations using the offshore data alone as well as in combination with onshore body-wave travel-times. For comparison of onshore vs offshore detection levels, we concentrate on the 6-month period from mid-November, 1995 to mid-May, 1996 since we have these hydrophone data here at Scripps and can analyze them in the classified facility operated at MPL.

The International Data Center (IDC) lists 109 events in the Norwegian Basin during the 6-month period (Figure 1). Forty-nine of these events were also recorded on the Global Seismic Network and reported by the NEIC. Epicenters in the two bulletins agree to within 19 ± 22 km for the co-listed events. The largest misfit (119 km) is associated with one of the Mohns

ridge swarm events as discussed below. The other large epicenter misfit (90 km) is for an event that the NEIC locates in Svalbard but the IDC locates on the shelf offshore.

As reported last year (Blackman and Orcutt, 1996), a swarm of earthquakes on the Mohns Ridge began November, 1995. Earthquake activity detected by the onshore arrays was concentrated in a 2-week period and event magnitudes were listed as 3.5-4.8 m_b . During the subsequent year, several isolated events were also reported from the area.

Analysis of SOSUS data for this period shows over 7000 events occurred during the earthquake swarm (Figure 2). Recorded arrivals include P-waves, water-borne T-waves, PT pairs and P-waves reflected at the seafloor. Activity started before mid-November, 1995, (we cannot document the start precisely due to a recording problem at the time) and continues into January, 1996. The greatest number of events ($> 40/hr$) occurred over a 3-day period in the middle of the 70-day duration of the activity.

Separation in time of P- and T-waves recorded at the SOSUS arrays are used to determine relative locations of events and their spatial evolution throughout the swarm. For our initial analysis a land-determined epicenter was used as a master event and SOSUS-determined relative shifts were simply projected along the trend of the ridge axis. The locus of activity shifts by 30-40 km (Figure 3) during the swarm but no apparent steady migration of activity is seen in contrast, for example, with the migration of seismicity observed in Iceland during an eruption of Krafla (Einarsson and Brandsdottir, 1980). This suggests that surface breaks during dike injection did not occur or, at least, did not generate T-waves or that the swarm was not associated with a simple dike emplacement along the ridge. The time history of the activity, on the other hand, is quite similar to that seen associated with two known volcanic events on the Juan de Fuca and Gorda ridges (Fox et al., 1993; NOAA VENTS web page).

The IDC listed swarm epicenters extending as much as 100 km down the flank of Mohns ridge. Analysis of the T-P separation times indicates that the events must have occurred within at least 50 km of the ridge axis. Also, the NEIC places the epicenter located furthest off axis by the IDC as being much closer to the ridge axis (Figure 1 shows line connecting the two estimates).

Absolute event locations should be improved by combining onshore seismic arrival times with acoustic arrival times on SOSUS for a joint location inversion. Initial work suggests that a few dozen events during the swarm will be useful in offshore (alone) inversion for source location. About twenty of these events will be used in our attempts at combined onshore/offshore epicentral re-location. We have transferred seismic waveform data from CMR to Scripps for these events, as well as several other non-swarm events during the 6 month study period. We expect to have results from this combined re-location analysis at the meeting in September.

Part of our efforts during the past year have gone into setting up a secure facility at Scripps Marine Physics Laboratory for archiving of newly-acquired Pacific hydrophone data. Tapes of the Norwegian Sea SOSUS data have been shipped to MPL and we will now be able to complete our analysis locally. Archiving of the Pacific data should begin in July 1997 so we will report on related progress at the meeting.

CONCLUSIONS AND FUTURE RESEARCH

The news that our recording site for the Norwegian Sea SOSUS data had been shut down was certainly a disappointment this past year. Fortunately, in the year we were able to archive data with a decent time stamp, enough events occurred to make the study worthwhile. Also, as the new facility for recording Pacific array data comes on-line at Scripps Marine Physical

Laboratory, we will continue our characterization of T-waves from different events in various geological settings. The data provide critical constraints as we enter the modeling stage of our study during the coming year. Details of both local bathymetry and geologic conditions at the source will be incorporated as we test for dependence of T-wave character on parameters other than source magnitude. Initial analysis by de Groot-Hedlin and Orcutt (1996) shows there is not a simple correlation between signal-to-noise ratio of recorded T and the magnitude of large Pacific earthquakes.

REFERENCES

- Blackman, D.K., C.E. Nishimura, J.A. Orcutt, Volcano-tectonic event on the Mohns Ridge, EOS Transactions AGU 77, pF723, 1996.
- Blackman, D.K. and J.A. Orcutt, Seismoacoustic studies of the Norwegian Sea, Proceedings of the 18th Seismic Research Symposium, 826-832, 1996.
- de Groot-Hedlin, C. and J.A. Orcutt, Observations of T phase arrivals from north Pacific events, Proceedings of the 18th Seismic Research Symposium, 853-860, 1996.
- Einarsson, P. and B. Brandsdottir, Seismological evidence for lateral magma intrusion during the July 1978 deflation of the Krafla volcano in NE Iceland, J. Geophys. 47, 160-165, 1980.
- Fox, C.G., W.E. Radford, R.P. Dziak, T-K. Lau, H. Matsumoto, A.E. Schreiner, Acoustic detection of a seafloor spreading episode on the Juan de Fuca Ridge using military hydrophone arrays, Geophys. Res. Lett. 22, 131-134, 1993.
- Nishimura, C.E. and D.M. Conlon, 1994, IUSS dual use: monitoring whales and earthquakes using SOSUS, Mar. Tech. Soc. 27, 13-21.

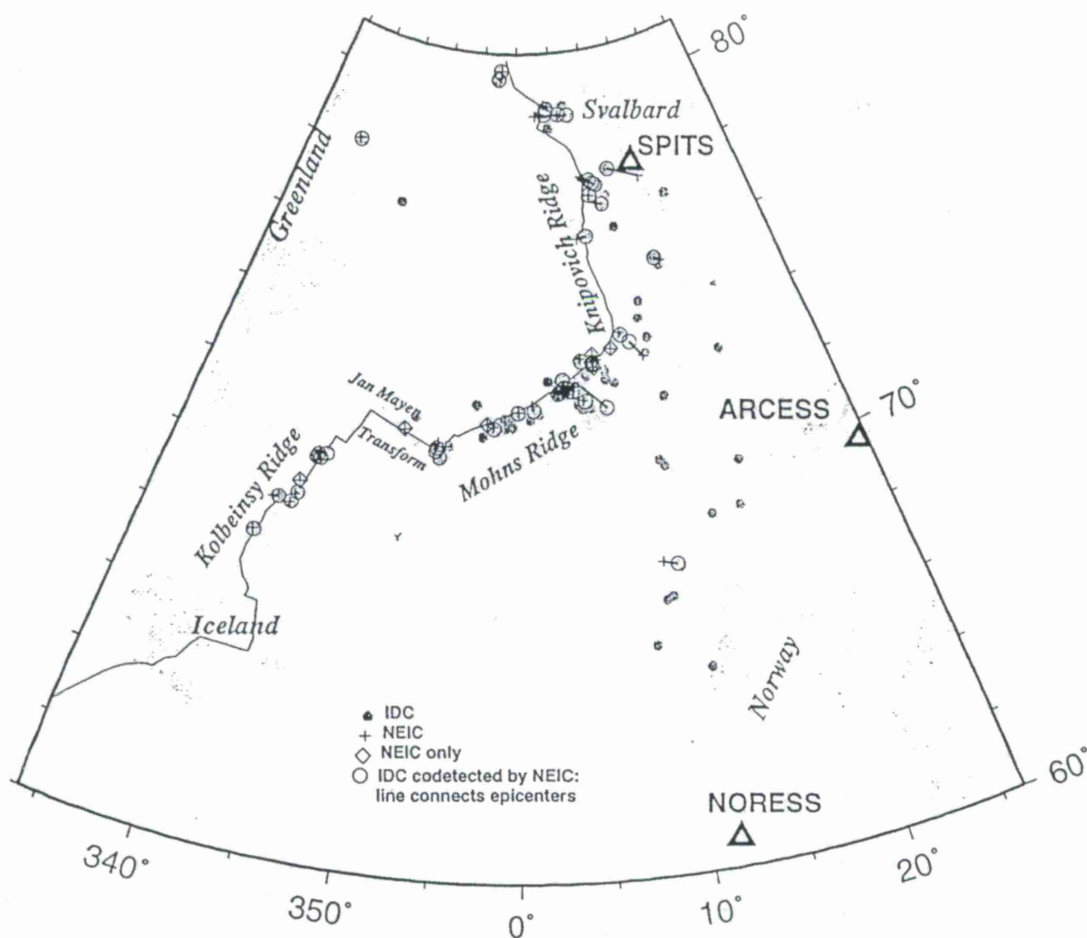
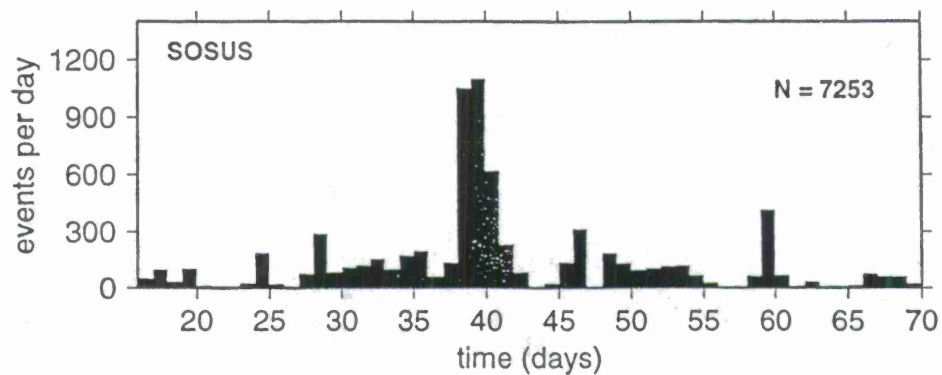


Figure 1. Location map of the Norwegian Sea study area. Plate boundary is shown by solid line; onshore seismic arrays are shown by triangles; earthquakes listed by the IDC and NEIC, respectively, are shown by the symbols which are explained in the legend. Seismicity shown is for the 6 month period November, 1995-May, 1996.

Mohns Ridge Activity Nov/Dec 1995



Land-Recorded Events

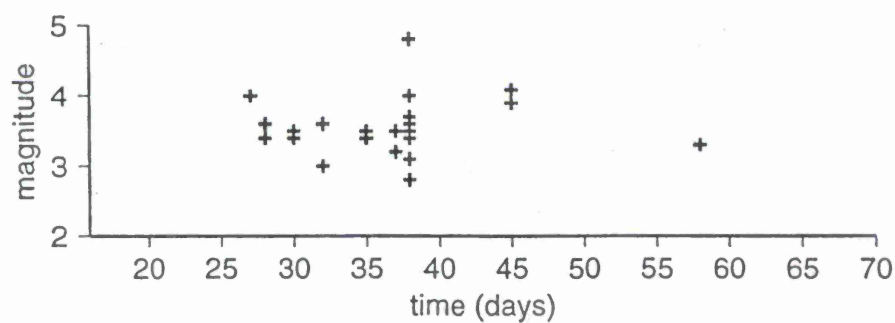


Figure 2. History of earthquake activity associated with the Mohns Ridge swarm. Top panel shows the number of events recorded by SOSUS arrays. Arrivals are a mix of P-waves and T-waves. Bottom panel shows the events listed by the IDC for the same time period.

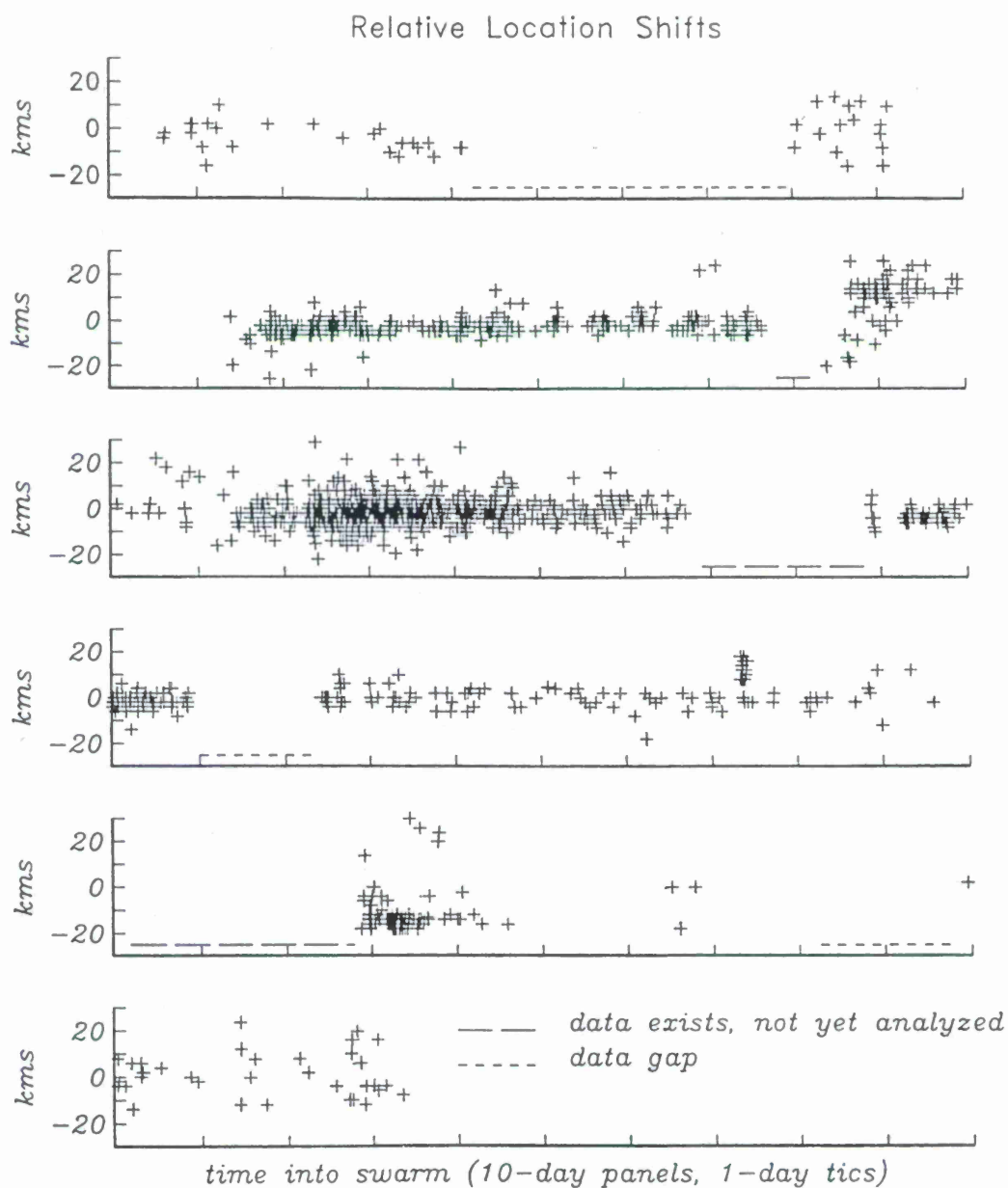


Figure 3. Relative shifts in event location as a function of time during the swarm. Shifts are referenced to land-determined master event location and are based on difference in P and T arrival times for the 1740 events in which both phases could be picked (minimum distance model takes straight-line P path so actual shift is somewhat greater). Time increases from top panel to bottom panel.

Energy Coupling of Nuclear Bursts in and above the Ocean Surface: Source Region Calculations and Experimental Validation

Douglas B. Clarke, Philip E. Harben, Donald W. Rock and John W. White,
Lawrence Livermore National Laboratory, and

Andrew Piacsek, Central Washington University

Sponsored by U.S. Department of Energy
Office of Nonproliferation and National Security
Office of Research and Development
Contract W-7405-ENG-48

ABSTRACT

In support of the Comprehensive Test Ban, research is underway on the long range propagation of signals from nuclear explosions in the deep underwater sound (SOFAR) channel. Initially our work at LLNL on signals in the source region considered explosions in or above the deep ocean. We studied the variation of wave properties and source region energy coupling as a function of height or depth of burst. Initial calculations on the CALE hydrodynamics code were linked at a few hundred milliseconds to a version of NRL's weak shock code, NPE, which solves the nonlinear progressive wave equation. The simulation of the wave propagation was carried down to 5000 in depth and out to 10,000 in range. We have completed ten such simulations at a variety of heights above and depths below the ocean surface. The results form a so-called "energy coupling curve" of coupled energy versus height or depth of burst. We have derived "starter fields" for calculations on a linear acoustics code which are available to others to extend the propagation to ocean basin distances. More recently we completed calculations to evaluate environmental effects (shallow water, bottom interactions) on signal propagation. We compared results at 25 km range from calculations of the same 1 kiloton burst (50 in height-of-burst) in different environments, namely, deep water, shallow water, and cases with shallow water sloping to deep water. In this shallow water study, we found that propagation through shallow water complicates and attenuates the signal; the changes made to the signal may impact detection and discrimination for bursts in some locations.

We are continuing to make improvements in our understanding our source region signals. Besides the simulations of propagation with bottom interactions referred to above, we are making improvements to our calculational tools and planning small-scale explosive experiments to validate our calculations of source region energy coupling. We have under development a new version of the NPE code which will have improved capability to propagate signals away from the horizontal. We are also planning a series of 1/50-scale (15 lb. HE) experiments in a lake in Wyoming. These experiments, currently scheduled for August 1997, will provide data that can be applied to the full scale. We will present results of the experiments and compare with predictions.

Key words: hydroacoustic, ocean monitoring, underwater signal propagation, energy coupling, NPE, shallow water

OBJECTIVE:

The planned International Monitoring System will have an ocean monitoring component whose principal function will be to detect and identify clandestine nuclear explosions in the broad ocean areas. The overall goal of our research supported by NN-20 is to increase the understanding of phenomena affecting the ability of the ocean monitoring system to accomplish its task and to establish the long-range signature of large explosions to assist in detection and discrimination wherever the explosion may be, including underwater explosions or explosions in the low atmosphere. Our calculations in the source region for nuclear explosions above and below the ocean surface are part of a continuing effort at Lawrence Livermore National Laboratory to understand how the source region phenomena contribute to the signals which would be detected at ocean basin distances. In particular, we are interested on how much acoustic signal energy will result from a nuclear explosion under various oceanic burst conditions and environments.

The usual analysis of signal propagation from an explosion in (or above) the ocean begins by dividing the ocean into two regions, a region relatively near the burst location—the source region—and another much larger region in which the signal propagation is affected by oceanic conditions such as the bathymetry over thousands of kilometers. Signals in the source region involve high pressures and shock waves near the burst and non-linear wave propagation; the burst height, the ocean depth, and the properties of the bottom materials will all modify the acoustic signals in various ways.

We have completed calculations and analysis for one kiloton explosions in a variety of environments. In previous work we considered bursts in and above a 5000 m deep ocean; more recently we have been evaluating the effects of shallow water and bottom materials on signals in the source region.

RESEARCH ACCOMPLISHED

The initial high temperature, high pressure non-linear phase of our calculations was completed using the LLNL hydrodynamics code CALE (Tipton, 1995). After a time, typically a few hundred milliseconds, the pressures drop to less than 100 atmospheres (10^7 Pa). At this stage the motion was "linked" (transferred) to the weak-shock propagation code, NPE (Nonlinear Progressive wave Equation), developed by Ed McDonald and others at the Naval Research Laboratory⁴⁻⁶. With NPE, the calculations can be extended to distances of tens of kilometers (or times of tens of seconds), at which point the near-source-region phase has been completed.

Earlier we completed a set of ten calculations of one-kiloton explosions at various positions in or above the deep ocean. One advantage of beginning our simulations with the deep (5000 m) ocean was the simple geometry. The great depth allowed us to make the approximation that interaction with the ocean bottom was a minor effect compared to the explosion and the development of the main shock wave. With these deep ocean calculations we have made predictions for the amount of energy coupled by an explosion within 1000 m of the ocean surface. The burst location was varied from 1000 m below the surface (fully coupled) to 1000 m above the surface. We compared the total wave energy in the NPE grid at approximately 10,000 m range. (See Figure 1.) This distance was chosen because it was twice the simulated ocean depth. It was expected that when the signal reached this range, the energy coupling and evolution into a deep ocean signal would be essentially complete. The results formed the so-called coupling curve (Fig. 1) for bursts in or above the deep ocean and show that the coupling efficiency declines precipitously as the burst point is raised through the ocean surface. The results from the

ten calculations in the Deep Ocean study are being made available to other contractors in the form of "starting fields" for studies of long range propagation in ocean environments. Some results from this work were reported in the first two references (Clarke, White and Harris, 1995; and Clarke, 1996).

Despite the large decrease in coupled energy for bursts above the ocean surface, we predict that explosions above the ocean surface will produce observable hydroacoustic signals, and that these signals will be unusual for their short duration and relatively low frequency content.

More recent work has focused on simulations of near-source region signals in complex environments; that is, those in which interaction with the ocean bottom is important for the signal propagation. An example might be a burst in or above shallow water, perhaps on or near the edge of the continental shelf. The weak shock wave from a nuclear burst near the surface will interact with the mud, sand or rock in the sea bed fairly quickly, so that the signals that arrive at a given location (e.g. 10 km away) will be strongly affected by the bottom materials. The goal was to evaluate the effects of the water environment (shallow or deep) and the effects of propagation in and attenuation by the mud or rock.

In the past year we have moved from modeling a uniformly deep ocean, to considering simple models of a shallow water environment. We have completed a new set of source region calculations with either a flat or a sloping bottom and a choice of bottom materials. (See summary, Figure 2.) The NPE code was modified to include a sea bed depth that varies with range and which provides for a specification of sound speed gradients in the bottom as well as in the water column. In these simulations, the bottom is modeled with a sound speed profile that corresponds to mud and silt overlying a weak bedrock; an attenuation coefficient of 0.6 dB per wavelength is applied throughout the bottom.

We have completed a series of NPE calculations with the modified code in which waves from the same 1 kiloton burst (50 m height-of-burst) were propagated in water over a flat mud/sand bottom; only the depth was varied from calculation to calculation. We also completed a calculation with a sloping ocean floor and the same bottom materials. The NPE calculations were stopped after propagation for 17 seconds, equivalent to about 25 kilometers, a distance still much smaller than ocean basin distances. Comparing the signals at 17 s, we found that propagation through shallow water complicates and attenuates the signal. The case with the shallowest flat bottom (uniform 200 m depth) showed significant loss of energy, a peak pressure about 10 times lower than the other cases, signal dispersion and a shift toward low frequencies in the spectral shape. All the shallow water cases had more structure in the waves than the deep case. The large loss of energy in the case of a shallow (200 m deep) ocean suggests that there is a "cliff" in the curve of energy transmission versus water depth such that as the water gets gradually shallower at a certain depth the attenuation suddenly becomes much larger so that, at that depth, the transmitted signal suddenly becomes much weaker. Some of the results of this study were discussed at the Informal Hydroacoustic Workshop at the CMR in November 1996, and were included in a recent document (Clarke, Piacsek and White, Dec. 1996)⁷

Work is continuing at LLNL on further NPE calculations of waves propagating downslope in a variety of shallow water and/or littoral environments. At this time, results indicate that a significant fraction of the acoustic energy will generally reach deep water off the continental shelf, although this is strongly influenced by the water depth at the source and the distance of shallow water propagation leading to the shelf. In addition, the strong refraction of the pulse in the upper sea bed layers and the subsequent reradiation into the water column generates head waves that are generally preserved into the deep

water. This feature may potentially serve as a discriminant between seismic and explosive sources and, in the latter case, to characterize the source environment.

With our calculations of signals in shallow water, we are beginning to understand the properties of explosion signals in the near-source region in a variety of environments. The changes made to the signal by propagation through shallow water may impact detection and discrimination for bursts in some locations. As this research develops, our calculations for shallow ocean environments could provide data to create starter fields for long range propagation.

The original formulation of the NPE (Non-linear Progressive Equation) code made the assumption that the signals of interest were propagating at a angle close to the horizontal. This so called "narrow-angle approximation" is a limitation on NPE. Using the CALE hydrodynamics code, which has no such limitation, we have made estimates of wide-angle versus narrow-angle effects on source region signal propagation in the deep ocean. Work is continuing on a newer "wide-angle" version of NPE, which will allow us to evaluate to what degree the narrow-angle limitation has affected our results. If necessary, improved calculations will be completed to provide an adjusted coupling curve, but based on the results from the CALE, the changes are expected to be modest. It is not yet known to what extent the narrow angle limitation has affected the shallow water calculations.

Although we can use computer calculations to model explosion effects and estimate the coupling from detonations above and below the water surface, experimental validation of the modeling results is crucial in the process of refining and extending our modeling capabilities. If our calculations methods can be experimentally validated using small explosions, then scaling relations will allow similar full scale calculations to be applied with some reliability to predict coupling and energy partitioning from large explosions--explosions that are too large to conduct for the sake of model validation. Figure 3 is a summary of our plans for validation of our model calculations.

The Wyoming Field Experiments will attempt to provide source coupling model validation by conducting a number of explosive tests at various depths above and below a body of water. The charge size (15 pounds or 6.82 kg of Pentolite 50/50) will result in an explosion which is at approximately 1/50 length scale (1/125,000 in explosive energy) relative to a one-kiloton nuclear burst. The experiments will take place in an isolated biologically dead lake associated with an abandoned uranium mine in south central Wyoming. A single hydrophone string located about 60 meters from the explosion points will monitor the acoustic energy coupled into the water using 8 piezoelectric sensors spaced from near-surface to about 30m depth. The experimental data will be compared with computer predictions.

CONCLUSIONS AND RECOMMENDATIONS

Validation of source region coupling model calculations is the single most important goal of near-future efforts. In particular, experimental measurements of larger explosions near and below the water surface need to be compared to model calculations. This is necessary to demonstrate the validity of using scaling relations to conduct model validation using small explosions and to test the robustness of the model results in a number of different source regions and scales (Fig. 3). This will be approached in two ways: 1) by taking advantage of events of opportunity such as a series of upcoming ship-shock trials off the coast of Florida by the US Navy and by 2) mining the archived data on old US and French atmospheric nuclear tests over and in the open ocean where hydrophone signal data still exists. Modeling calculations can be run using the same source region and yield to generate acoustic pressure signals that can be compared with actual data.

In summary then, the LLNL research in ocean monitoring will proceed in two directions. We will be continuing calculations of source region signals in a variety of environments to increase our understanding of the effects of shallow water and bottom materials on the signal propagation. In work to validate our modeling calculations, we will be comparing experimental measurements with calculational predictions for explosions at small and large scales.

REFERENCES

1. Clarke, D. B., J. W. White and D. B. Harris, "Hydroacoustic Coupling Calculations for Underwater and Near Surface Explosions," UCRL-ID-122098, Sept. 1995, (U)
2. Clarke, Douglas B., "Pressure Time Histories Derived From Hydroacoustic Coupling Calculations: The Transition to Long Range Linear Acoustics," UCRL-ID-122595, December 1996, (U).
3. Tipton, Robert, "CALE Users Manual, Version 950101," LLNL Internal Report, March 1995. For further information on CALE, contact D. B. Clarke, LLNL, P O Box 808, L-200, Livermore CA 94551. — (510) 422-6593 · Email: clarkel@llnl.gov.
4. McDonald, B. E. and W. A. Kuperman, "Time-Domain Solution of the Parabolic Equation Including Non-Linearity," *Comp. and Maths. with Appls.*, Vol. 11, pp. 843-851, Pergamon Press Ltd., UK (1985)
5. McDonald, B. E. and W. A. Kuperman, "Time Domain formulation for pulse propagation including nonlinear behavior at a caustic," *J. Acoustic Soc. Am.*, Vol. 81, pp. 1406-1417 (1987)
6. Ambrosiano, J. J., D. R. Plante, B. E. McDonald and W. A. Kuperman, "Nonlinear Propagation in an Ocean Acoustic Waveguide," *J. Acoustic Soc. Am.*, Vol. 87 (4), p. 1473-1482 (1990).
7. Clarke, D. B., Andrew Piacsek and John. W. White, "Predictions of acoustic signals from explosions above and below the ocean surface: source region calculations," UCRL-ID-125914, CTBT Ocean monitoring Research Deliverable No. H2.2.1, December 1996. (U).



Total wave energy in NPE at 10 km range

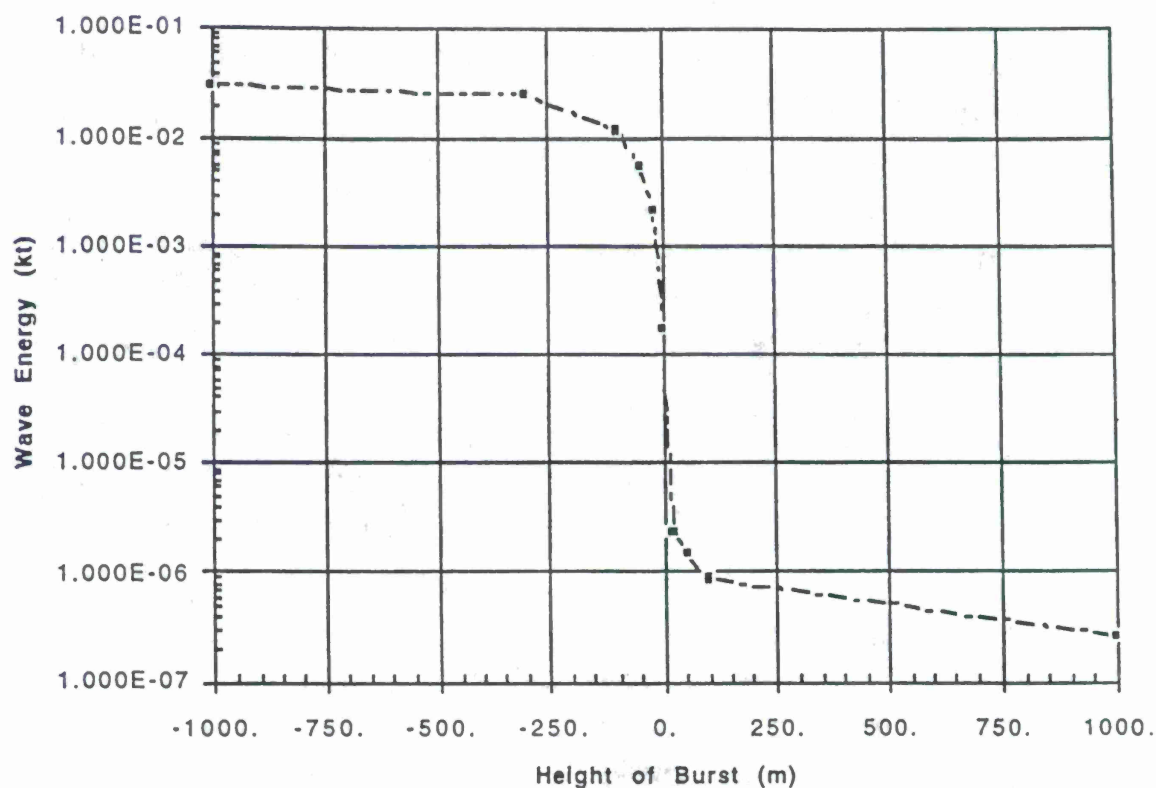


Figure 1. This figure shows results from a series of ten CALE/NPE calculations of one-kiloton nuclear explosions at different heights above (or depths below) the ocean surface. The energy coupled by the explosion at each height is measured by the total wave energy in the water at a range of 10,000 m. The calculated energy coupling is sharply reduced for burst locations near and above the water surface. However, current estimates are that signals from such decoupled explosions are still expected to be easily observable above background noise. At 10 km range, the peak pressures in these simulations range from 100,000 Pa to about 200 Pa.



LLNL Hydroacoustic Computational projects are moving toward modeling near-source region signals in complex environments

- Initial efforts focused on source region signals for a simple Deep Ocean case (depth = 5000 m)
 - Major result: Energy Coupling Curve
- Recent work is focusing on environmental effects such as depth near the source region and effects of bottom materials (mud/silt/sand layers)
- Using an enhanced version of NPE with improved treatment of bottom materials, based on work of Ed McDonald, we have completed calculations to study depth and bottom effects
- Compare results at 17 seconds from the same source
 - Shallow water (flat bottom) 200 m depth, also 1000 m depth
 - Shallow water, sloping from 200 m to 2200 m over 25 km
 - Flat bottom, 5000 m deep case, also with bottom materials
- Results show that the ocean bottom configuration has a drastic effect on the pulse leaving the source region, including reduced signal amplitude, dispersion and alteration in spectrum

Figure 2.



Validation of source region coupling model calculations is the single most important goal of near-future efforts

- Planned validation efforts will cover signals from explosions at several scales from under 10 kg HE to large explosions
- Compare experimental measurements of signals with model calculations to
 - Demonstrate the validity of scaling relations
 - Test the robustness of model results in a variety of source regions and scales
- Small scale (1/50) coupling experiments in dead lake in Wyoming
 - 15 lb. HE charges at several locations above or below surface
 - Compare results to calculations (small and full scale)
- Signals from U S Navy ship shock trials (multi-ton HE) near Florida coast (working with BBN)
- Analyze where available the archived data on old atmospheric nuclear tests over and in the open ocean

Figure 3.

OBSERVATIONS OF T-PHASES FROM NORTH PACIFIC EVENTS: DETERMINATION OF EPICENTRAL LOCATIONS FROM T-PHASES

Catherine D. deGroot-Hedlin and John A. Orcutt
IGPP, Scripps Institution of Oceanography, University of California, San Diego

Sponsored by U.S. Department of Energy
Office of Nonproliferation and National Security
Office of Research and Development
Contract No. F19268-95-K-0011

ABSTRACT

T-phase source locations were determined for 54 sub-oceanic earthquakes in the North Pacific. It was found that picking T-phase onset times is complicated by multiple arrivals within the T-phase coda. To resolve ambiguity in T-phase onset, we picked T-phase amplitude maxima in the 10-20 Hz band. Using travel times determined by integrating SOFAR channel velocities along geodesic paths, it was found that T-phase source locations are generally not coincident with epicentral location. NEIS and T-phase source locations generally agree to within two degrees, but there is a consistent bias between NEIS and T-phase source locations, that is, the acoustic source is generally located in regions of shallower bathymetry than the earthquake epicenter.

We found that the length and onset times of the T-phase coda are consistent with seismic/acoustic coupling over shallow regions of the ocean floor in the vicinity of the earthquake epicenter. We modeled T-phase amplitudes using a simple expression involving seafloor depth, depth of the SOFAR channel, and the distance from the earthquake hypocenter to the seafloor. We found that we could model T-phase onset times and durations reasonable accurately with this simple expression.

Keywords: T-phase, source location, seismic/acoustic coupling, hydroacoustic propagation.

Objective

The purpose of the hydroacoustic monitoring system for the CTBT is to detect and locate both underwater events and suboceanic events. Although observations at at least three stations are usually required to accurately locate an event, only two hydroacoustic stations, at Wake Island and Pt Sur, are in place for detection of hydroacoustic events in the Pacific. Thus event source location in the Pacific will generally rely on the analysis of a combination of seismic and hydroacoustic data types. However, it has been noted by numerous authors (*e.g.* Johnson, 1966) that the seismic/T-phase coupling may occur at locations other than at the earthquake epicenters. Therefore the success of an integrated seismic/hydroacoustic analysis will depend on whether the locus of T-phase excitation is coincident with the locus of P and S-wave excitation, *i.e.* at the earthquake epicenter. One of the objectives of this paper is to determine T-phase source locations using hydroacoustic data from Pt Sur and Wake, and compare them with source locations as determined by the NEIS. This will indicate the magnitude of location error which results from assuming that the T-phase source is coincident with the earthquake epicentral location.

A second objective is to explore methods of locating T-phase sources using T-phase coda observed at a small number of receivers. It has been observed by Walker *et.al.*(1992) that the character of the T-phase coda is strongly dependent upon the bathymetry of the ocean floor in the region in which seismic to acoustic coupling takes place. Thus earthquakes from the same geographic area generate similar T-phase coda. We demonstrate an approximate method of simulating the T-phase coda. This may lead to methods of T-phase source location using only one or two receivers.

Research Accomplished

Data

We assembled a suite of records from 54 events for which hydroacoustic data were available from stations at both Pt. Sur and Wake Island. The recordings were obtained from the Center for Monitoring Research (CMR) for an 8-10 minute band about each expected T-phase arrival. Event parameters were obtained from the near real-time Earthquake bulletin, provided by the National Earthquake Information Service (NEIS). Only events with accurately determined hypocentral locations were used.

T-phase source locations

Johnson (1966) published a method for "routinely" determining T-phase source locations, but noted that these locations were not necessarily coincident with earthquake epicentral locations. In this method, the T-phase onset time was taken as the largest T-phase amplitude in the frequency range from 1-15Hz. Application of Johnson's method to a large series of earthquakes with known epicentral locations occurring over a fairly uniform area showed that the T-phase energy appeared to be generated at several distinct regions (Johnson and Norris, 1968), suggesting that T-phases were being generated only at

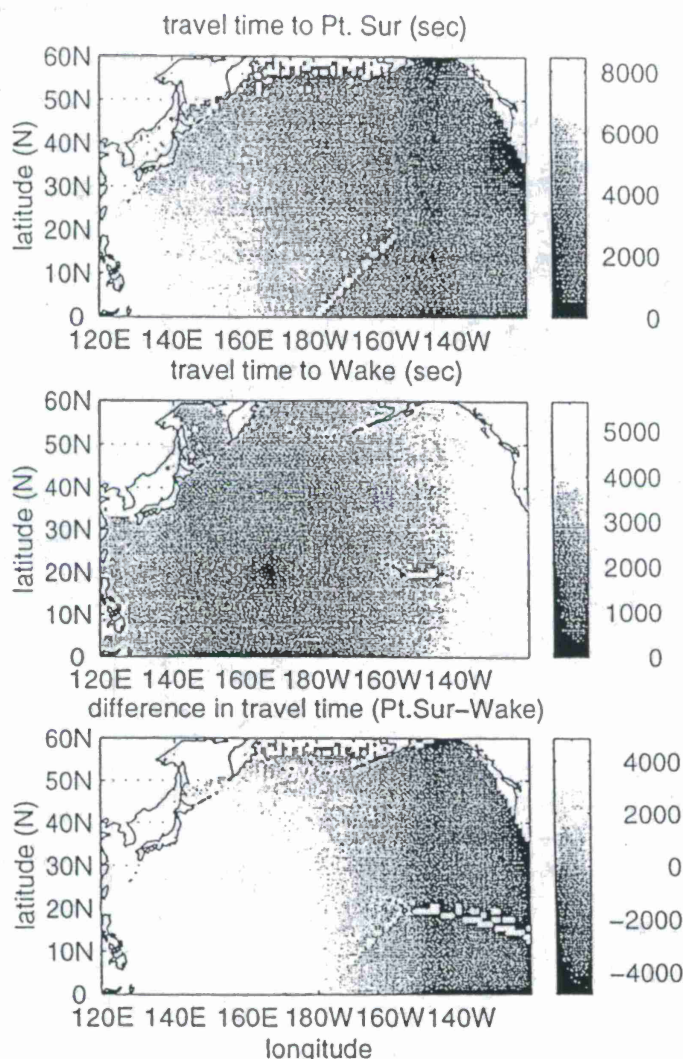


Figure 1. Travel times to Pt Sur (top), Wake (middle) and the difference in travel time (bottom). Travel times are computed by integrating SOFAR channel velocities along geodesic paths. Shadow are indicated by white patches; these were computed approximately as regions where bathymetry along the geodesic path intersects the surface.

and Pt Sur, we integrated SOFAR channel velocities along geodesic paths. Seasonal databases of the SOFAR channel velocities were provided by Farrell and LePage (1996). We used the annual averages of the SOFAR channel velocities; negligible differences were noted between travel times computed at different seasons. Note that 3-D acoustic effects, *i.e.* the horizontal refraction of acoustic energy near islands and seamounts, were not taken into account.

Travel times to Wake and Pt Sur are shown in the top two panels of Figure 1. Shadow zones regions are roughly indicated by the white patches; these are regions where the bathymetry along the geodesic path intersects the ocean surface. Travel time differences are shown in the bottom panel of Figure 1. Note that, without supplemental seismic or T-phase information (from island T-phase stations, for instance),

isolated locations along the ocean floor. Furthermore, it has been shown that seamounts and islands act as secondary generators of low frequency T-phase energy (Walker *et al.*, 1992; Northrup, 1973, 1974). Thus accurate source location becomes complicated in locations where phases associated with secondary sources are of the same order of magnitude as the primary T-phase radiator.

We computed envelopes of the T-phase coda for several frequency ranges. We noted that for several events, T-phase onset times, as defined by the time of the largest T-phase amplitude, were strongly dependent on the frequency range examined. This occurred where secondary sources generated larger low frequency T-phases than the primary, *i.e.* near-source, radiator. To resolve the ambiguity in T-phase onset, we chose the maximum amplitude arrival in the 10-20Hz frequency range. Onset time picks are accurate to 2 seconds.

To determine travel times for arbitrary source locations to the receivers at Wake

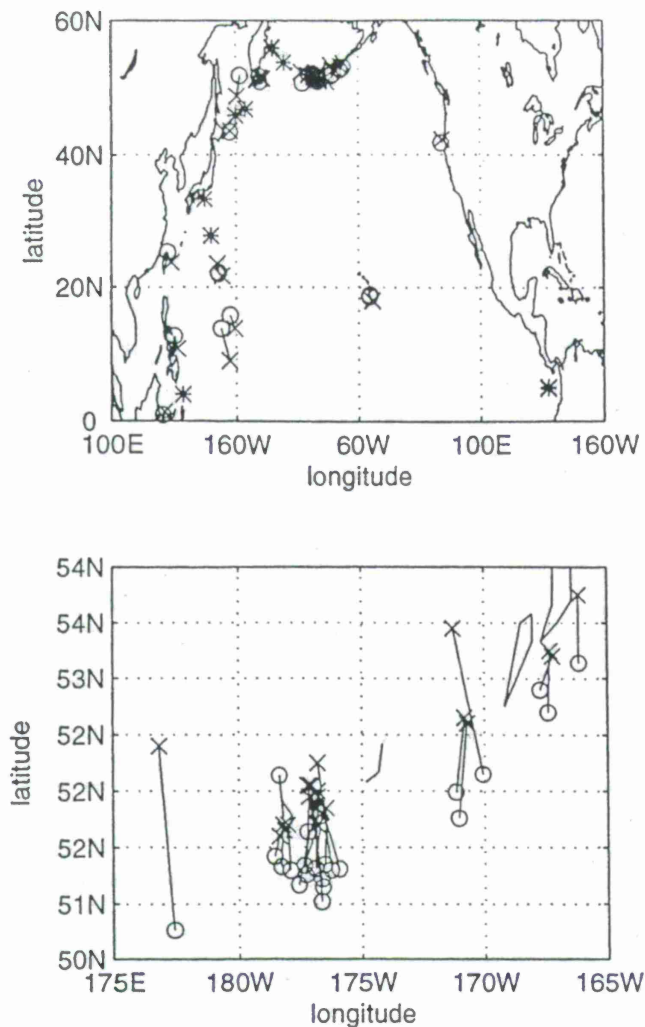


Figure 2. NEIS determined epicenters (circles) and T-phase source locations (x'es) determined in this study. NEIS-determined epicenters that were not observed at Wake or Pt Sur are indicated by asterisks. A blowup of the Aleutian Island region is shown below. Note that T phase source locations are consistently biased to the north (i.e. in shallower bathymetry) of the NEIS locations.

the difference in T-phase onset times at Pt Sur and Wake are the only information available to determine source location. This will be the case for most small oceanic and sub-oceanic sources because T-phases can generally be more reliably detected than seismic body waves (Brocher, 1983; Shurbet, 1962), due to the extremely efficient propagation of acoustic energy through the ocean. In this case, note that the longitude of the T-phase source is much more clearly resolved than the latitude over most of the Pacific. Resolution is even worse for regions to the southeast of Wake Island.

T-phase source locations were determined using the travel time as given above, as well as the given NEIS origin times and T-phase onset times defined above. Travel times through the crust were neglected in determining source locations. A comparison between NEIS epicenters (circles) and T-phase source locations (x'es) is shown in Figure 2. For several events near coasts, no accurate T-phase

source location could be determined. Two possible causes for this are that either (1) horizontal refraction must be accounted for near the coasts, or that (2) peaks corresponding to a near-source radiator was picked for one station, whereas a peak corresponding to a secondary source was picked for the other station. Several NEIS events, indicated by asterisks, were not located using T-phases as they were not observable at one of the stations. The bottom panel of Figure 2 shows a blowup of the Aleutian Island area. Note that the T-phase source locations are consistently biased to the north of the NEIS locations, in regions of shallower water.

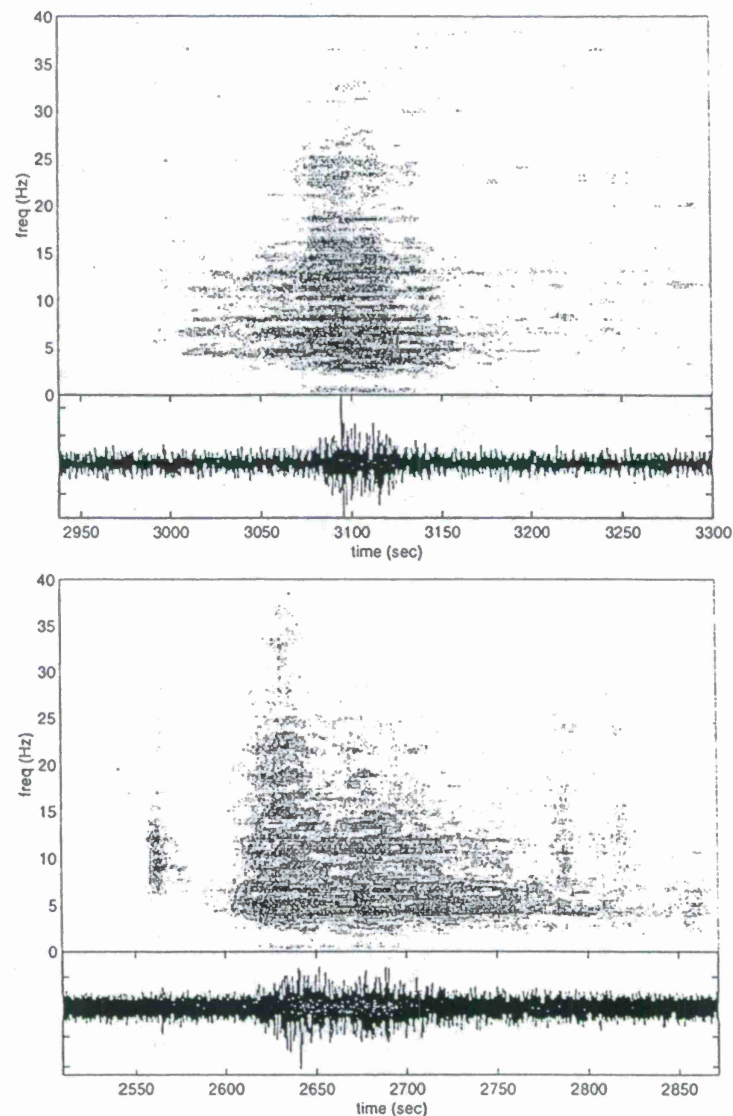


Figure 3. Sonograms and traces for event at 51.32N, 183.11E. Pt Sur is shown at top, Wake is shown in the bottom panel. Sonograms have been de-trended in the frequency domain so that signal-to-noise ratios in each bandwidth can be observed more clearly. The Pt Sur coda is relatively symmetric, whereas the Wake coda shows a sharper onset, followed by a very gradual decrease in energy.

Modeling T-phase coda

To determine whether peaks in the T-phase coda could be identified with specific bathymetric features, we computed T-phase sonograms for an event at 51.32N, 183.11E. The sonograms for Pt. Sur and Wake are shown in the top and bottom panels of Figure 3, respectively. Bathymetry for this region is shown in Figure 4. Superimposed on the bathymetry are contours of the travel times to Pt Sur (shown as the dashed line) and to Wake (solid line). Travel times from the hypocenter are given by the summation of T-phase travel times (computed as described above) and the travel time through the crust (using a crustal velocity of 8km/sec).

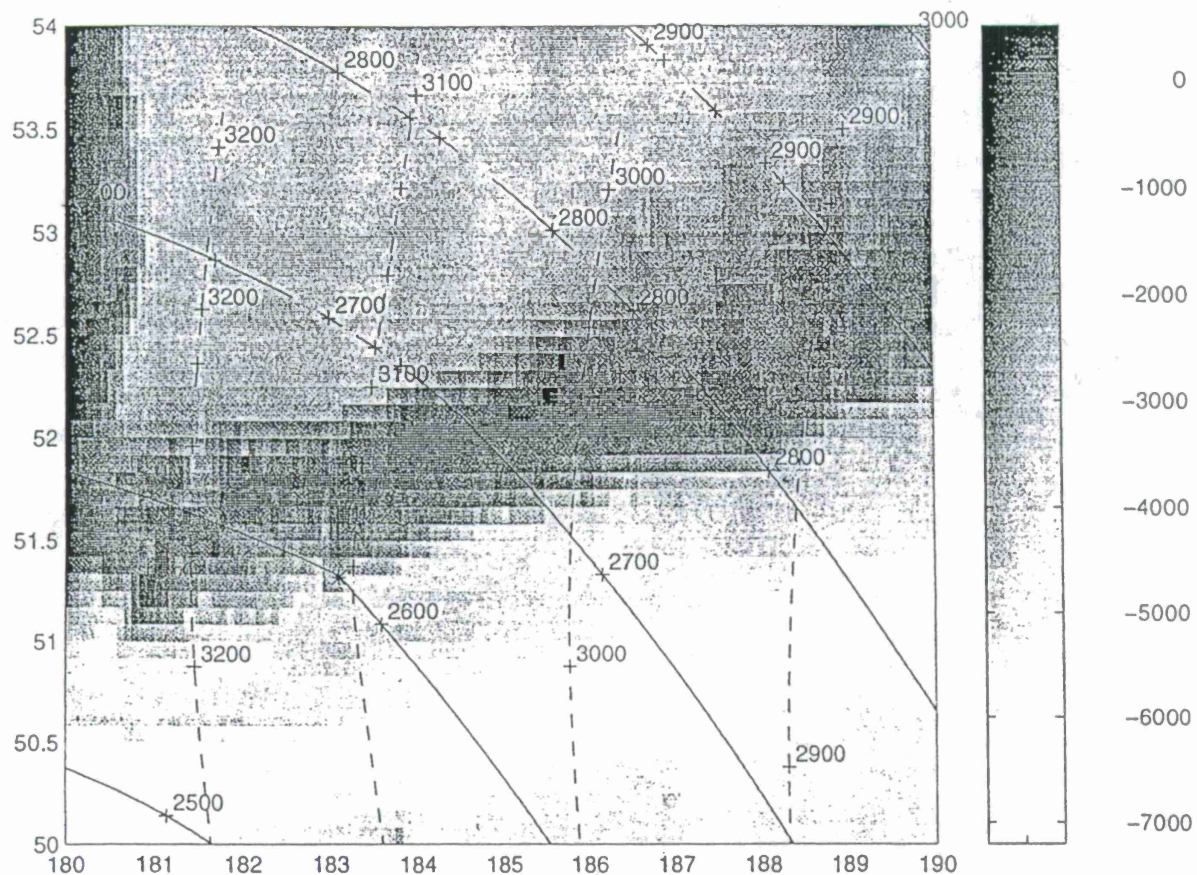


Figure 4. Bathymetry map for the Aleutian island region in the vicinity of the 51.32N, 183.11E earthquake. Dark areas indicate shallow regions. The travel time from the earthquake epicenter to the seabottom, and from the seabottom to receiver are indicated by the contour lines. Solid contour lines correspond to travel time to Wake, dashed contour lines correspond to travel time to Pt Sur. The NEIS epicentral locations is indicated by an asterisk,

If the T-phase source location were coincident with the epicentral location, the expected travel time to Wake would be 2600 sec, and to Pt Sur would be 3106 seconds. As indicated in Figure 3, the T-phase onset at Wake is considerably delayed with respect to the expected travel time. Thus the onset time is consistent with seismic energy travelling through the crust to a shallower region slightly north of the epicenter, then being converted to acoustic energy.

Several authors have theorized (Tolstoy and Ewing, 1950; Johnson *et al.*, 1963) that transformation of P to T waves takes place along the continental slope. We hypothesize that the T-phase coda may be approximately modeled as the weighted sum of seismic/acoustic conversion over all shallow regions near the epicenter, with attenuation of seismic energy increasing with distance from the epicenter. Thus, from Figure 4, fairly symmetric T-phase coda are expected at Pt Sur, since seismic energy travelling west along the Aleutian chain would be advanced with respect to the onset; seismic energy initially travelling east along the chain would be delayed. Conversely, one might predict a fairly short rise time

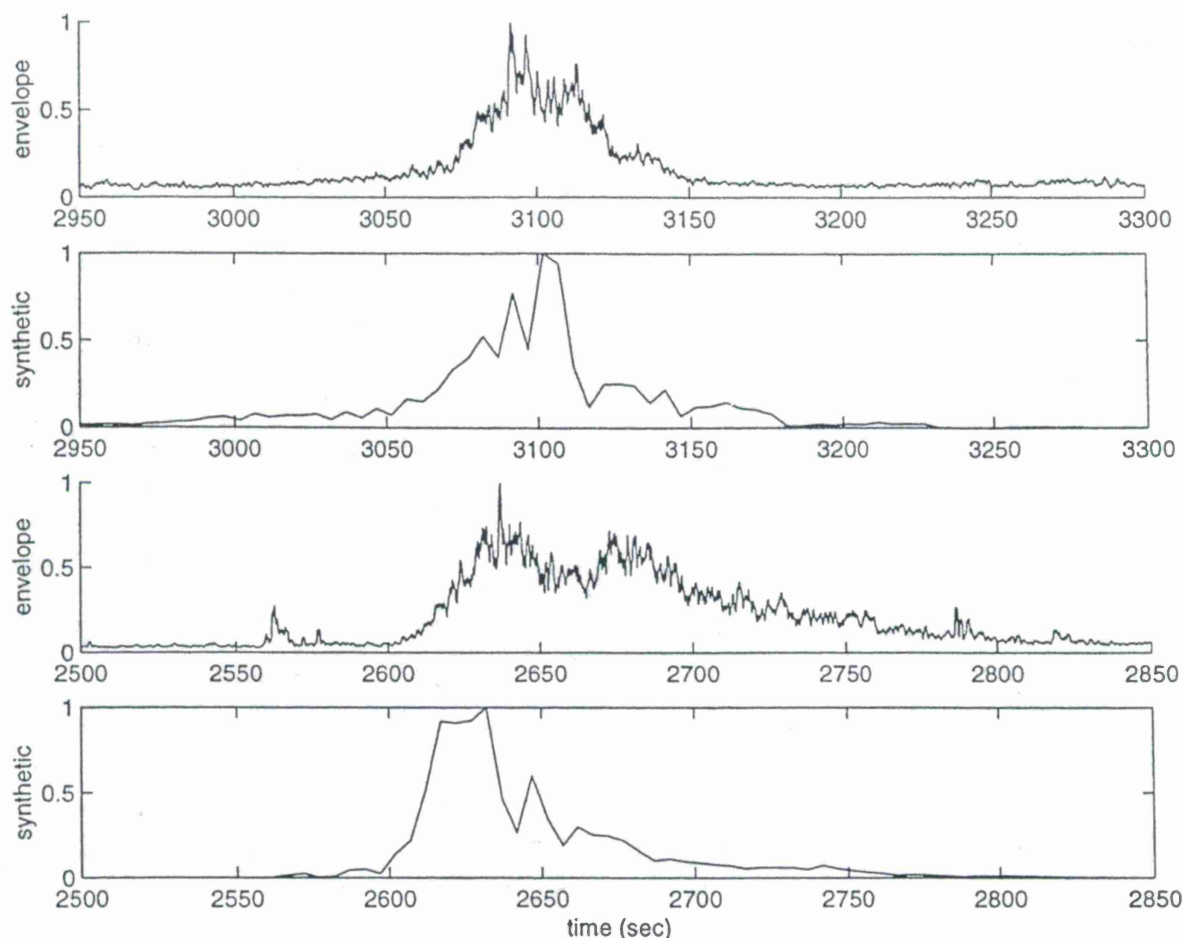


Figure 5 Comparison of T-phase envelopes over a 0.1-20Hz band, and synthetic T-phase coda amplitudes computed using the method described in the text. Results for Pt Sur are shown in the top two panels, results for Wake are shown in the bottom panels. Note that the gradual rise time of Pt Sur and the sharper onset at Wake are modelled reasonably accurately. The delayed arrival time at Wake (with respect to what would be expected for a source at the earthquake epicenter) is also modelled quite accurately. Dropoff times at both receivers are poorly modelled.

and long drop-off time at Wake. This is confirmed in Figure 3. Note that the T-phase coda is shorter in duration and has lower maximum frequency at Pt. Sur than at Wake. This is probably due to higher noise levels at Pt Sur.

We choose the following trial form for the amplitude of T-phase energy emanating from each point in the region of the earthquake epicenter:

$$\text{amplitude} = \exp(-\text{bathymetric depth}/\text{SOFAR depth})/(\text{crustal_distance}^2).$$

Amplitudes are set to zero in shadow zones and on land. This equation states that the T-phase amplitude from each point decreases with increasing depth and that energy conversion is more efficient in regions where the SOFAR channel is deeper. Furthermore, the amplitude decreases with the square of the

distance travelled through the crust, *i.e.* we assume cylindrical spreading of seismic energy within the crust. Path propagation effects are not taken into account, aside from zeroing out energy from shadow zones. Travel times are as given in Figure 4. Furthermore, the degree and direction of slope are not taken into account in this formulation. To compute the synthetic T-phase envelopes we sum amplitudes within 5 second bins.

Real and synthetic T-phase envelopes for both Pt Sur and Wake are compared in figure 5 for this event. Envelopes for the real data are computed over a 0.1-20Hz bandwidth. Note that the slow rise time of the Pt Sur coda has been effectively modelled, however the slow dropoff time is less effectively modelled. For the Wake event, the sharp rise time, and delay with respect to the expected T-phase onset time has been accurately modelled, however the very gradual dropoff of energy is less effectively modelled.

Conclusions and recommendations

- T-phase sources in the Pacific cannot be accurately located using only onset times at the Pt Sur and Wake stations.
- There is a systematic difference between T-phase source location and earthquake epicentral location. The acoustic energy is excited in shallow areas. This implies that only an approximate epicentral location can be determined from a joint analysis of seismic and hydroacoustic data.
- T-phase source location tends to be less accurate near ocean/continent boundaries. This may be due to either generation of T-phases at several locations along the coast, or due to 3-D acoustic effects, such as horizontal refraction of T-waves.
- The T-phase onset time is consistent with seismic/T-phase conversion at relatively nearby shallow structures. The lengthened arrivals are consistent with a super-position of T-phases generated over shallow regions near the earthquake epicenter.
- T-phase amplitudes can be modeled approximately using a simple method which assumes that the amplitude of seismic/T-phase coupling at any location is dependent upon the SOFAR channel depth, the depth of the seafloor, and the distance from the earthquake epicenter. Future plans call for taking into account propagation effects such as cylindrical spreading, blockage or partial blockage of acoustic energy, slope effects, and seafloor characteristics.
- Once a more accurate formulation for T-phase amplitudes has been determined, it will be possible to locate epicenters by correlating observed T-phase coda with synthetics, for a number of trial

source locations. This could lead to an accurate method of source location using only two receivers. Note that it is necessary for this purpose to find a simple expression for the T-phase coda so that a rapid estimation of source location may be made.

References

- Brocher, T.M., T-phases from an earthquake on the mid-Atlantic ridge at 31.6N, *Mar. Geophys. Res.*, **6**, 39-49, 1983.
- Farrell, T., and K. LePage, Development of a comprehensive hydroacoustic coverage assessment model, *Final report*, Sept.1996.
- Johnson, R.H., J.Northrup, and R.Eppley, Sources of pacific T-phases, *J. Geophys. Res.*, **83**, 4251-4260, 1963.
- Johnson, R.H., Routine location of T-phase sources in the Pacific, *Bull. seism. Soc Am.*, **56**, 109-118, 1966.
- Johnson, R.H., and R.A. Norris, T-phase radiators in the western Aleutians, *Bull. seism. Soc Am.*, **58**, 1-10, 1968.
- Northrup, J., T-phases from the Hawaiian earthquake of April 26, 1973, *J. Geophys. Res.*, **79**, 5478-5481., 1974.
- Northrup, J., T-phases radiation from the Cannikin Explosion, *J. Geophys. Res.*, **78**, 1809-1817., 1973.
- Shurbet, D.H., Note on use of a SOFAR geophone to determine seismicity of regional oceanic areas, *Bull. seism. Soc Am.*, **52**, 689-691, 1962.
- Tolstoy, I., and M.W. Ewing, the T-phases of shallow focus earthquakes, *Bull. seism. Soc Am.*, **40**, 25-51, 1950.
- Walker, D.A., C.S. McCreery, and Y. Hiyoshi, T-phase spectra, seismic moments, and tsunamigenesis, *Bull. seism. Soc Am.*, **82**, 1275-1305, 1992.

COMPONENTS OF THE HYDROACOUSTIC KNOWLEDGE DATABASE

Ted Farrell, Jeff Angell, Kevin LePage and Rob Gibson
BBN Systems and Technologies

Sponsored by U.S. Department of Energy
Office of Nonproliferation and National Security
Office of Research and Development
Subcontract No. B334423

Sponsored by the Department of Energy through
the Lawrence Livermore National Laboratory

ABSTRACT

As part of the CTBT hydroacoustic research and development program, oceanographic databases, predicted acoustic mode structures and the expected characteristics of hydroacoustic propagation paths are being integrated into a knowledge database. During this year's effort, BBN is using the Hydroacoustic Coverage Assessment Model (HydroCAM) to generate geographic grids containing hydroacoustic mode characteristics, travel times, and path amplitudes to contribute to this database. In addition, we are working to develop approaches for predicting hydroacoustic waveform envelopes that include both source effects and geographically varying acoustic environments.

Keywords: CTBT, hydroacoustics, knowledge database, travel time

OBJECTIVE

The primary functions of the hydroacoustic segment of a monitoring network are to provide discrimination and to improve location estimates of nuclear events detected by other monitoring technologies. Both of these functions rely on the ability to detect explosive events at long ranges. In general, the high source levels from nuclear tests and the efficiency of acoustic propagation in the SOFAR channel should result in excellent detection performance. In addition, the channel sound speed in many areas is relatively constant so that energy in the channel travels along stable geometric paths, resulting in predictable travel time and localization performance. However, challenges occur when the channel is partially or completely blocked by bathymetric features, when energy is horizontally refracted as it traverses into colder Antarctic waters, when the continuously changing temperature and salinity structure of the ocean is accounted for, or when sources do not fully couple their energy into the SOFAR channel, such as atmospheric and coastal tests. In a sparse global network like the currently proposed IMS, information derived from each sensor is critical to the performance of the network. Processing and interpretation of hydroacoustic data will therefore require a knowledge database that contains accurate ocean characteristics, travel times, path amplitudes and ultimately spectral characteristics of received waveforms. The goal of this effort is to use HydroCAM to develop the primary components of this database.

The specific goals for this year were:

1. To develop geographic grids containing predicted travel times and path amplitudes to each station in the monitoring network.
2. To validate the grids by comparing predictions with measured data.
3. To determine the feasibility of predicting the envelopes of hydroacoustic waveforms.

The progress toward each of these goals is summarized in the following sections.

RESEARCH ACCOMPLISHED

Approach to Propagation Modeling

HydroCAM is a hydroacoustic network performance prediction program that contains oceanographic databases, acoustic propagation models, network performance models, and software tools to perform a variety of processing, analysis and display functions [1,2]. Global-scale low-frequency propagation models in HydroCAM account for the ellipsoidal nature of the earth, effects of bathymetric features, and geographic and seasonal variations in sound speed. Two general options for characterizing the ocean waveguide are provided. The first assumes that

all energy propagates in the SOFAR channel. The second, more accurate approach is to treat the vertical component of the problem with the method of normal modes, in which environmental data at each location in an ocean grid is used to calculate the local mode structure and thus the waveguide properties. Two models are available for computing the mode structure at each point; a well known normal mode code called Kraken from NJIT, and a WKB approximation developed by BBN. Kraken calculates exact eigenvalues for as many modes as are necessary locally, while the WKB code rapidly calculates approximate eigenvalues for only those modes requested.

Investigation of modeling approaches has indicated that, to obtain sufficient accuracy in the geographic grids, the effects of horizontal refraction must be considered for cases where paths interact with bathymetric features such as continental shelves, islands and seamounts, and when paths traverse rapidly changing water, such as the Antarctic convergence. Furthermore, modal phase speeds, rather than simply the SOFAR channel sound speeds, are required to accurately predict the horizontal refraction [3].

Several test cases were conducted comparing results from Kraken to those from the WKB model over both world-wide grids and high-resolution subsets. Agreement between the models was excellent, resulting in the selection of the WKB model to generate all of the geographic grids, given the substantial savings in execution time. To speed execution further, it is assumed that only the first mode, which has the least interaction with ocean surface and bottom, is necessary to characterize the ocean waveguide for the purposes of travel time determination.

Three models are incorporated in HydroCAM for predicting acoustic paths. The model that was chosen for use in grid generation is a horizontal ray-tracing approach with an interpolation scheme included in cases where multiple paths are determined to exist. (An eigenray search method was not used due to convergence problems in certain cases, and a "bender" method, in which path boundary values are specified, was not used due to the number of calculations required.)

Components of the Geographic Grids

The geographic grids generated for the knowledge database contain propagation data from all potential source locations on a world-wide grid to a given hydroacoustic monitoring station. Grids have been produced at two frequencies, 10 Hz and 50 Hz, for all four seasons. The four *propagation grids* consist of travel time, range, path attenuation and travel time standard deviation. An intermediate step in the generation of the propagation grids is calculation of *modal property grids*, which contain phase speed, group speed, modal attenuation and modal slowness variance.

Modal Property Grid Resolution

A nominal resolution of 1° was chosen for world-wide modal property grid generation. However, in certain regions where the acoustic paths are likely to be significantly affected due to rapid changes in bathymetry or sound velocity structure, higher resolution is required to obtain more accurate results. These high-resolution areas include shallow regions near islands or coastlines,

where ray paths originating from monitoring stations are likely to be refracted or blocked. Candidate high-resolution regions were initially identified by inspection of coverage maps for each of the proposed IMS stations. Those regions where fluctuations in bathymetry or sound speed were not adequately characterized by 1° databases were identified as high-resolution areas. Figure 1 shows the geographic locations of the fifty-one regions so identified.

The effects of different grid resolutions were analyzed by shooting several closely spaced rays from one of the monitoring stations (Crozet Island) through a high-resolution area (around the Cape of Good Hope) to a distant location (the eastern seaboard of the US). Grid resolution in the high-resolution areas was varied from 30 minutes to 5 minutes, and the resulting spread in the end points of the paths was observed. The ray paths within the high-resolution area differed markedly with each choice of grid resolution, and the locations of the ends of the ray paths were more closely spaced with higher grid resolution. Based on these results and the assumption that finer resolution yields more accurate estimates, a resolution of 5 minutes was chosen for generation of the high-resolution modal property grids.

Determination of Modal Properties

Environmental databases are used to determine the modal properties. Various databases were investigated and compared with respect to coverage, resolution, and accuracy. The primary bathymetry database used for grid generation is ETOPO5 (Earth Topography, 5 minute resolution). However, since this database is known to have deficiencies in some areas [4], it was supplemented with a recent database from the Scripps Institute of Oceanography [5] in certain regions. The primary database used for sound speed is the World Ocean Atlas (WOA) Analyzed database from NOAA [6], supplemented in certain regions by data from the Generalized Digital Environmental Model (GDEM) from the Naval Oceanographic Office [7]. Sound speed variance from the WOA Analyzed database is used to determine modal slowness variance.

Capabilities for calculating various types of attenuation have recently been incorporated into HydroCAM's WKB software. Transmission loss due to the bottom is determined using a simple fluid half space model which assumes constant bottom sound speed, density and attenuation, similar to an approach used in [8]. Attenuation due to ice cover is determined from an empirical model previously developed by BBN, based upon experiments performed in the central Arctic [9]. Geographic extent of ice cover is obtained from a database of ice concentration estimates from the National Snow and Ice Data Center (Boulder CO). For the low frequencies of interest, attenuation due to wind-speed related surface roughness was studied and determined to be negligible compared to other transmission losses.

Summary of Propagation Grid Generation Technique

The overall propagation grid generation procedure consists of three steps, as shown in Figure 2. First, the mode structure is determined and modal property grids are generated for each frequency and season, using the environmental databases incorporated in HydroCAM. Second, the modal property grids are used to compute the travel time, path attenuation and travel time

standard deviation by performing path integrals of the appropriate grid database quantity along horizontally refracted paths to each station in the monitoring network. Transmission loss due to ice cover is added to the integrated bottom attenuation along each path. Third, the non-uniformly sampled path data are then interpolated onto a regular latitude/longitude grid with 1° resolution.

Validation of the Propagation Grids

During the development of HydroCAM, three available cases of measured travel time data were used for model validation [1]. Further efforts to validate travel time, amplitude and travel time variance are currently underway. Among the measured data sets being considered are ship shock trials, Aleutian tests and historical nuclear shot data. Additionally, predictions from HydroCAM are being compared with those from IVSEM (Integrated Verification System Evaluation Module), a fast, PC-based model, developed at Sandia National Laboratories, for evaluating performance of all four monitoring technologies [10]. At the time of writing, grid validation is not yet complete. Details of these studies will be provided in the project Final Report.

Feasibility of Waveform Prediction

In addition to travel time and path attenuation it is desired to develop a knowledge database of hydroacoustic waveform envelopes for explosive sources. Such a database has several possible functions: from sophisticated automatic algorithms for detection and discrimination to display formats that allow operators to compare predicted waveforms with measured waveforms from a particular event. BBN has been investigating technical issues associated with waveform grid generation in order to assess the feasibility of such a database.

A narrow band approximation of the envelope of the signals for the individual normal modes has been developed. This approach, consistent with the normal mode basis used throughout these investigations, is suitable for use at low frequency. The approximation technique is based upon a frequency integral over a finite bandwidth, summed over a truncated spectrum of normal modes, to obtain an approximate time series. Modal eigenvalues are then expanded to second order about the center frequency of the band. The results of the narrow band approximation were compared with results from Kraken for both shallow water and SOFAR channel sound speed profiles. Figure 3 shows a comparison between an analytically determined narrow band synthesis of the arrival structure summed across all modes and the approximate envelope prediction. The overall form of the arrival envelope is generally predicted quite well, and better for narrower frequency bands than for wider ones.

Based upon these initial conclusions, the prognosis is good for developing a computationally efficient technique for generating waveform grids in the future. Other issues which are currently being investigated include the time/frequency and spatial sampling needed for accurate predictions, the sensitivity of prediction approaches to environmental variability, and the effects of specific sources and scenarios.

CONCLUSIONS AND RECOMMENDATIONS

A hydroacoustic network performance prediction model has been successfully applied to the generation of world-wide geographic grids of propagation data, which will form an important part of the hydroacoustic knowledge database. Calculation of the grid data includes the effects of horizontal refraction and of seasonal and geographic changes in sound speed. Verification of the grids is underway. A technique has been developed for efficiently predicting approximate envelopes of hydroacoustic waveforms. In the coming years, further attention should be given to developing the waveform knowledge base, validating it through comparison with measured data, incorporating measured waveform data into the knowledge database, and potentially integrating the hydroacoustic model with models for other techniques, such as infrasound.

REFERENCES

- [1] T.R. Farrell and K.D. LePage, *Development of a Comprehensive Hydroacoustic Coverage Assessment Model*, PL-TR-96-2248, September 1996.
- [2] T. Farrell, K. LePage, G. Duckworth, *Development of the Hydroacoustic Coverage Assessment Model (HydroCAM)*, Proceedings of the 18th Annual Seismic Research Symposium on Monitoring a CTBT, PL-TR-96-2153, September 1996.
- [3] K.D. Heaney, W.A. Kuperman, B.E. McDonald, *Perth-Bermuda Sound Propagation (1960): Adiabatic Mode Interpretation*, JASA 90(5), Nov. 1991, p.2589.
- [4] L.W. Row III, D.A. Hastings, P.K. Dunbar, *TerrainBase, Worldwide Digital Terrain Data, Documentation Manual*, US Department of Commerce, National Oceanic and Atmospheric Administration, April 1995.
- [5] W.H.F. Smith, D.T. Sandwell, *Global Seafloor Topography from Satellite Altimetry and Ship Depth Soundings*, recently submitted to Science.
- [6] Levitus and Boyer, *World Ocean Atlas 1994, Volume 4: Temperature*, NOAA Atlas NESDIS 4, Washington DC, June 1994.
- [7] *Database Description for the Master Generalized Digital Environmental Model (GDEM) Version 5.0*, OAML DBD-20F, Naval Oceanographic Office, Stennis Space Center, MS, September 1995.
- [8] I.A. Fraser and P.D. Morash, *Observation of the Heard Island Signals Near the Gulf Stream*, JASA 96(4), p. 2448-2457, 1994.
- [9] G. Duckworth, T. Farrell, K. LePage, C. Atkinson, *Arctic LFA Program Final Report (U)*, BBN Technical Report No W1226, ONR/AEAS Technical Report 94-S102, September 1994 (SECRET/NOFORN Report).
- [10] M.W. Edenburn, M.L. Bunting, A.C. Payne, R.R. Preston, L.C. Trost, *Synergy Among International Monitoring System Technologies*, Proceedings of the 18th Annual Seismic Research Symposium on Monitoring a CTBT, PL-TR-96-2153, September 1996.

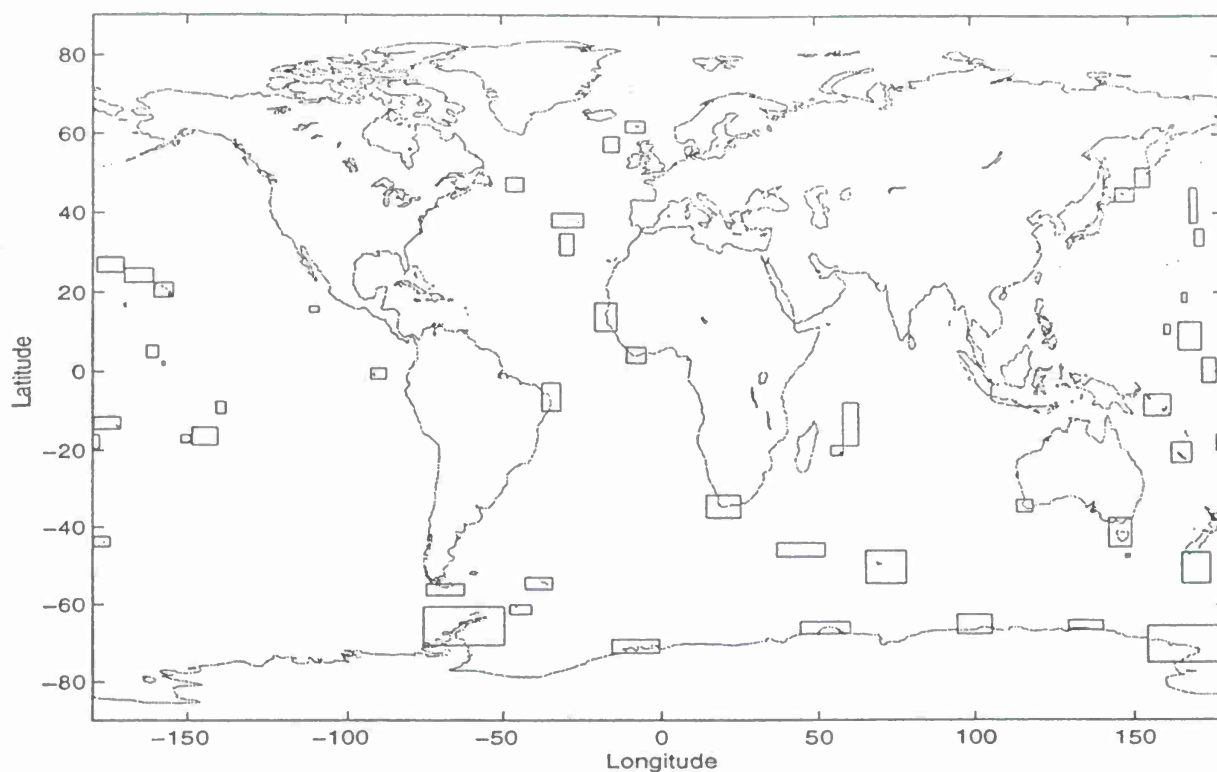
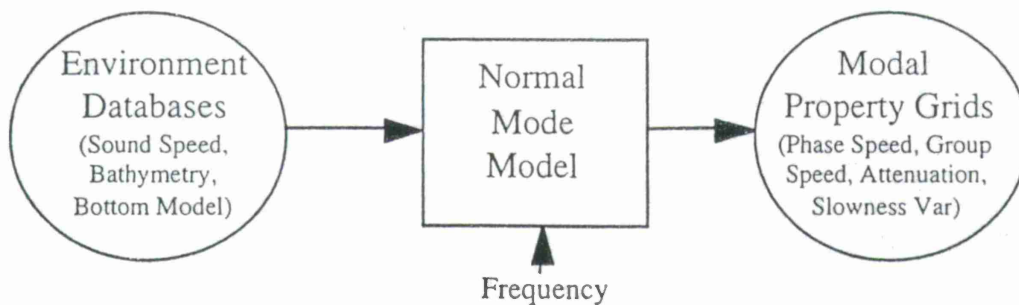
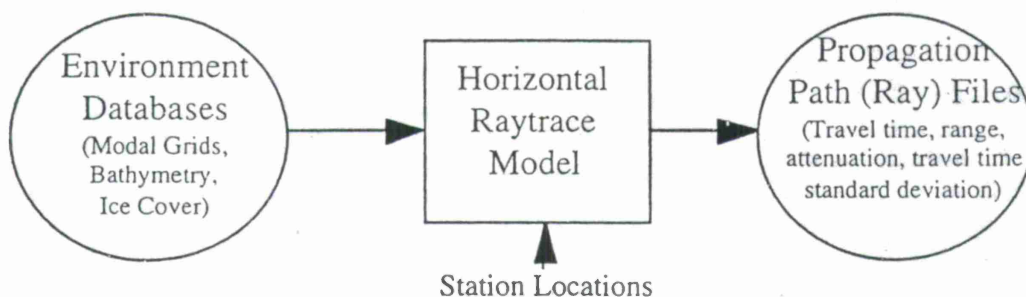


Figure 1: Identification of High-Resolution Areas. These fifty-one regions require modal property grid resolution greater than 1° in order to obtain sufficient accuracy in determination of acoustic paths and travel times. Five minute resolution was used in grid generation.

STEP 1: Generate Modal Property Grids



STEP 2: Calculate Refracted Paths



STEP 3: Interpolate onto lat/lon Grid

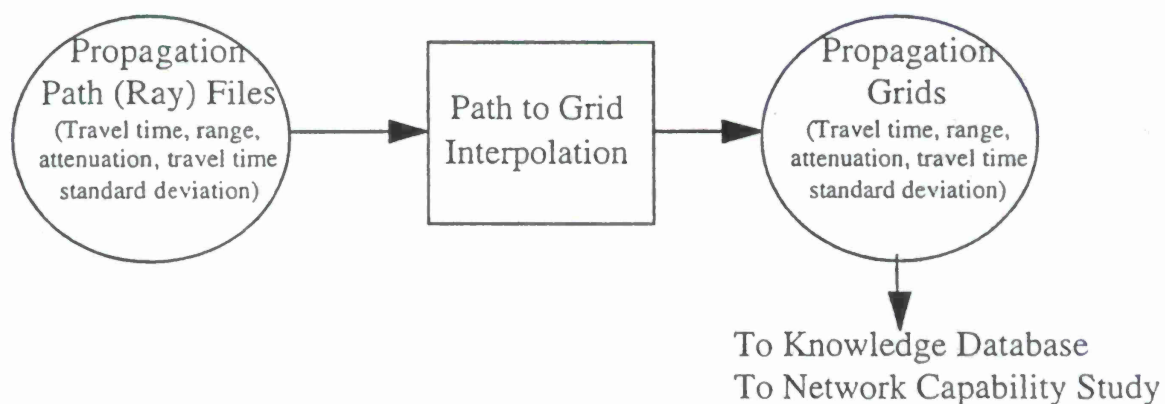


Figure 2: Summary of Grid Generation Procedure.

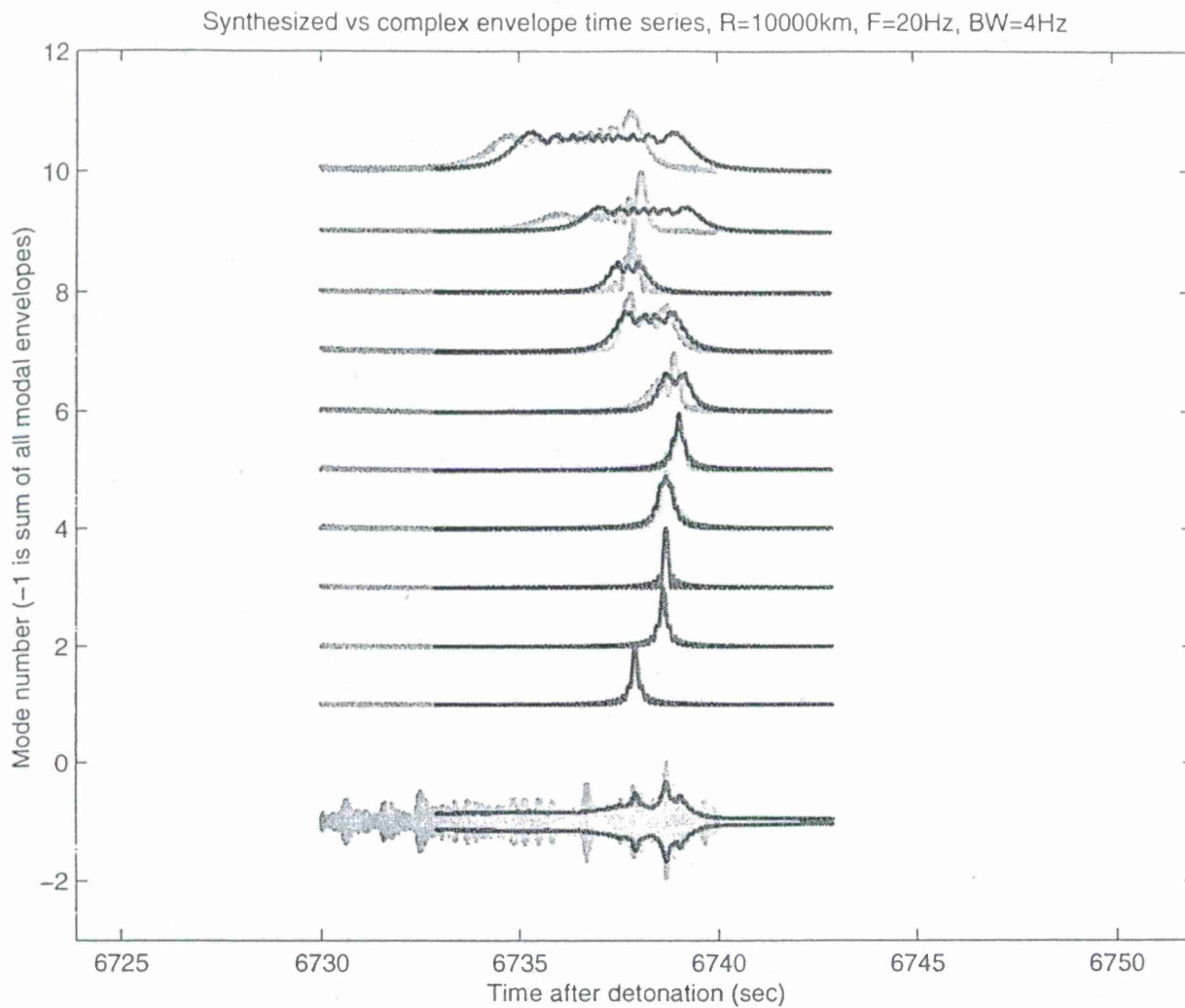


Figure 3: Comparison of Approximate Arrival Envelope to Analytical Modal Synthesis. Center Frequency is 20 Hz, bandwidth is 4 Hz, and range is 10000 km. The darker traces are the approximate modal envelopes and the lighter traces are the corresponding synthetic envelopes. The bottom pair of traces (mode number -1) compares the approximate envelope with the actual synthetic time series summed across all modes.

Accurate Arrival Azimuth Estimates for Earthquakes using T-phase Waveforms from a Large Aperture Hydrophone Array

Jeffrey A. Hanson and Holly K. Given

Cecil H. and Ida M. Green Institute of Geophysics and Planetary Physics
Scripps Institution of Oceanography, UCSD, La Jolla, CA 92093

Intra-University Agreement B334398 between Lawrence Livermore National Laboratory and
University of California San Diego

ABSTRACT and OBJECTIVE

Data from oceanic hydrophones deployed originally for military reconnaissance purposes are increasingly being applied to studies of underwater geophysical phenomena such as earthquakes and volcanic eruptions. As one component of the International Monitoring System, a global network of sensors to be established under the Comprehensive Nuclear Test Ban Treaty, hydrophones will monitor the ocean basins for underwater nuclear explosions and natural events such as earthquakes that could be confused with explosions. These applications require the development of methods using hydrophone data that provide accurate information about the event of interest. We have developed a simple method whereby station-to-source azimuths are estimated by fitting a plane wave to envelope functions of T-phases observed on a 5-element hydrophone array around Ascension Island, South Atlantic Ocean. When applied to a data set of 55 earthquakes of known location ranging between 2 and 45 degrees distance from Ascension Island, estimated azimuths have a standard deviation of 3.6 degrees from reference azimuths when 3 or more hydrophone elements are used. The standard deviation decreases to 1.8 degrees if T-phase data from all 5 hydrophone elements are used. We also investigate variations in azimuth estimation accuracy for different sub-array geometries (that is, different combinations of the 5 Ascension Island hydrophones) and arrival azimuths. Although there is a decrease in the standard deviation of azimuth misfit as more elements are used, a general conclusion is that a 3-element array centered on Ascension island with a spacing of 25 km will provide azimuth estimates that are accurate to within 5 degrees. For cases where the plane wave approximation is inaccurate, usually because the event is too close to the array, we show that a cylindrical wave fit to the envelope time lags will provide accurate azimuth estimates if independent information about the event's distance (e.g., from arrival times of seismic phases recorded by an island seismic station) is available.

Our method is amenable to automation and can easily be incorporated into a global monitoring system; it is also transferrable to comparable instrumentation in other parts of the world's oceans. (Note: In this paper, we use the terms "array" and "elements" loosely, referring to the hydrophones around Ascension Island which have spacing of around 25 km. Others may call this configuration a "network" with individual "stations". However, much like traditional array processing, we use correlation methods to estimate azimuths to events well outside the area of the instruments.)

Key Words: hydroacoustic, T-phase, azimuth estimates, Ascension Island, hydrophone array, hydrophone network

RESEARCH ACCOMPLISHED

T-phases generated by earthquakes are acoustical disturbances in the ocean caused by co-seismic displacement of the ocean floor near the epicenter which propagate for long distances in the oceanic sound (SOFAR) channel. Figure 2 shows a 25-minute data window containing T-phases from several earthquakes seen by 5 elements of the Missile Impact Locating System (MILS) hydrophone array deployed around Ascension Island in the south Atlantic Ocean (Figure 1). The azimuth to a seismic event is estimated by fitting a plane wave to the relative times between the T-phases observed on the individual hydrophone elements via a simple inversion.

The T-phase is a wave-packet with a typical duration on the order of 100 seconds. The underlying signal frequency content ranges from approximately 1 Hz to more than 60 Hz. The T-phase signal is not highly coherent between elements, but the shape of the overall wave packet is. We compute envelope functions from the waveforms which are then cross-correlated to find the time lag between element pairs. Figure 2 shows an example of an envelope function corresponding to one of the T-phase waveforms.

We find the best fitting plane wave for the estimated time lags between element pairs as an overdetermined inverse problem. The forward problem is a simple projection of the position vectors onto the slowness vector of the plane wave. For example, the forward problem for a four-element array would be

$$\begin{bmatrix} x_{2-1} & y_{2-1} \\ x_{3-1} & y_{3-1} \\ x_{3-2} & y_{3-2} \\ x_{4-1} & y_{4-1} \\ x_{4-2} & y_{4-2} \\ x_{4-3} & y_{4-3} \end{bmatrix} \cdot \begin{bmatrix} k_x \\ k_y \end{bmatrix} = \begin{bmatrix} \delta t_{2-1} \\ \delta t_{3-1} \\ \delta t_{3-2} \\ \delta t_{4-1} \\ \delta t_{4-2} \\ \delta t_{4-3} \end{bmatrix}$$

where x_{2-1} and y_{2-1} indicate the difference between the latitudes and longitudes respectively of elements 2 and 1. Likewise δt_{2-1} is the time lag between elements 2 and 1, while k_x and k_y are the components of the slowness vector. We invert for the slowness vector using a weighted least-squares algorithm with the weights based on the cross-covariance of each element pair. The direction opposite of the slowness vector provides the azimuth to the event, and the inverse of the slowness vector's length is an estimate of the velocity of the T-phase.

The method described was used to determine arrival azimuths at Ascension Island to 55 earthquakes in the Atlantic Ocean using data from the MILS hydrophone array which surrounds the island (Figure 1). Most of the earthquakes are on the mid-Atlantic ridge, and ranged from 2° to 45° distance from the array. The median signal-to-noise ratio of the T-phases used was 12, and the smallest signal-to-noise ratio (used for less than 5 observations) was 2.

We compare our azimuth estimates to the known azimuths from earthquake locations either in the NEIC's *Preliminary Determination of Epicenters* or the Center for Monitoring Research's *Reviewed Event Bulletin*. Figure 3a shows a histogram of the differences between the reference azimuths and our calculated azimuths, 95% of which are within 5°. T-phase records from all 5

hydrophone elements were used whenever possible, but in more than half the cases fewer elements were available, either due to instrumental problems or because the T-phase was blocked for certain hydrophones by Ascension Island. An example of natural blockage can be seen in Figure 2, where the third and sixth events have almost no appreciable T-phase on element U29 even though it is well recorded on the other array elements. Figures 3*b-d* show how the azimuth residuals change when 3, 4, or 5 elements were used. Even when only 3 elements were used in the azimuth estimate, the results were still within 5° of the reference azimuth 85% of the time.

The accuracy of the azimuth estimate can be affected not only by how many array elements were used, but also the apparent aperture and element spacing of the array which depends on "look angle" and the array geometry. To illustrate how this may affect results, Figure 4 (left column) shows predicted standard deviations versus azimuth for some possible combinations of 3-element sub-arrays of the 5 Ascension Island hydrophones. We have assumed errors in the measured time delays are normally distributed with a 1 second standard deviation which is a typical RMS time residual to a plane wave fit of our data. Not surprisingly, sub-arrays that use element U26 have strong minimums in predicted error for events arriving from the east or west since the array aperture is maximum from these directions. The left column fails to show that the sub-arrays do not record events arriving from every azimuth on all 3 elements, either because of instrument problems or T-phase blockage. Figure 4's right column shows histograms of residuals of our estimates using data from the same sub-arrays. On average, a particular sub-array records about 25 of the 55 earthquakes. U19-U21-U26 records the most events, but because the events are arriving mainly from the north and south the estimates for this sub-array have the worst standard deviation. It is difficult to directly compare the predicted and observed results because events arriving from different azimuths have different error distributions; however, the general similarity implies that the combination of arrival azimuth and sub-array geometry has a major effect on the accuracy of the azimuth estimate.

Some error in our solution is introduced for nearby events by using a plane wave approximation that is most appropriate for large distances. In allowing the velocity to vary, our inversion has an added degree of freedom which can absorb some of the error, but the solution then becomes more sensitive to random error. Even with this trade-off we have found the added degree of freedom generally results in better azimuth estimates; the standard deviation of the residuals decreases by 25% when we invert for the velocity and azimuth compared to inverting for the azimuth while keeping the velocity fixed. As an example Figure 5 shows various solutions for an earthquake that occurred 215 km from Ascension Island. The solid straight lines indicate the reference azimuth and our best estimate of the T-phase velocity from various inversion configurations. The "+" shows the estimate solving for both the velocity and azimuth assuming a plane wave. The low velocity, 1.31 km/s, indicates that our approximation is inadequate, which is expected for an event this close. For comparison, the "x" is the solution obtained for a plane wave assuming a fixed velocity; the azimuth estimate is now significantly worse. To evaluate our solution against a cylindrical approximation we calculate the expected delay times for a cylindrical wave at a distance of 215 km for a variety of azimuths and velocities. The relative RMS misfit between these and the measured delay times is shown as the contours in the figure. The circle in the center of the contours indicates the best fitting solution. The azimuth is no better than our original solution although the velocity is more realistic. By using the higher order approximation we have added too many degrees of freedom for the amount of data to accurately determine the full solution, but by constraining the velocity to its "known" value we estimate a significantly better

azimuth, shown as the other circle in Figure 5. This is an example of how our method can do a remarkably good job even for events at close range using the inaccurate plane wave approximation.

In an earlier paper, we discussed how elements of the Ascension Island hydrophone array could be used in conjunction with the IRIS/IDA broad band seismographic station ASCN on the island as a small network for locating earthquakes on the nearby mid-Atlantic ridge and Ascension fracture zone (Hanson et al, 1996). In that study, only P-phases seen on the hydrophones were used, and as with a conventional local seismic network, location ability degrades quickly for events farther than a few network widths. A different approach for event location using the combined seismic/hydrophone data set would be to use the hydrophone data for an azimuth estimate and the seismic data to provide a distance estimate from the difference of times of seismic phases, such as S-P, Lg-Pn, or (seismic) T - R, somewhat similar to the practice of locating events with two or more regional seismic arrays (e.g. Bratt and Bache, 1988). Earthquake locations made this way would be of inherently poorer quality because a given azimuth uncertainty translates into a larger geographical uncertainty with increasing distance. However, such a method could be applicable to earthquakes from the entire Atlantic region since T-phase amplitudes maintain a high signal-to-noise ratio at large distances. Location estimates could then be used as input into a global location system for a more accurate epicenter calculation.

The dependence of the accuracy of azimuth estimation on the number of array elements is of particular interest to the monitoring community. We showed in Figure 4 that a sparse 3-element array can provide azimuth estimates as accurate as the 5-element array in many cases, which argues for deployment of cost-effective 3-element hydrophone arrays. However, there would always be cases when only two elements were available due to instrument problems or blockage by a central island landmass. It is possible to estimate the arrival azimuth with only two elements by assuming a plane wave and a velocity, but there will be an ambiguity between two solutions which are symmetric about an axis connecting the two elements. It may be possible to eliminate the ambiguity by considering other factors such as arrival times at other T-phase stations or it may be that one of the arrival azimuths is impossible due to island blockage and can be eliminated. In our study we know the locations of the events, and hence we are able to pick the "correct" solution and determine azimuth residuals. Even after eliminating the ambiguity there are still a few large residuals greater than 50° . After removal of these outliers, 95% of the residuals are within $\pm 22^\circ$. Figure 6 shows the 95% confidence limits of azimuth estimates versus the number of array elements used. The 2-element arrays are nearly 3 times as poor as any of the other combinations, even after eliminating the ambiguity between the 2 solutions. Improvements in the confidence limits from 3 elements to 5 elements are less dramatic, starting at 8° and decreasing to 4° .

CONCLUSIONS AND RECOMMENDATIONS

We have shown that earthquake azimuths can be accurately estimated from the relative arrival times of T-phase waveform envelopes recorded on a widely spaced 5-element hydrophone array using a nearly automated inversion assuming plane wave propagation. When observations on three or more elements were available, the standard deviation of the azimuth misfit was 3.3° , with 51 of 55 estimated azimuths being within 5° of the reference azimuth from the catalog location. When all five elements were used, the standard deviation decreased to 1.8° . We studied the effect

of using only 3 of the 5 elements on the accuracy of the azimuth estimates. The standard deviation of azimuth misfits using 3 elements increased, but there are many individual cases where azimuths estimated using 3 elements only are as accurate as those using 5 elements for the same event. The amount of improvement made by using more elements depends on the geometry of the array relative to the incoming direction of the T-phase. In general, however, azimuth estimates within 5° can be obtained by a 3-element array centered on Ascension Island with a spacing of 25 km.

Hydrophone arrays can be applied to various monitoring scenarios such as those being developed under the Comprehensive Test Ban Treaty. The method presented here is already fairly automated and has been developed using functions and scripts written for the software package MATLAB®. When a signal with T-phase characteristics is detected, an azimuth estimate to the likely causative event can be calculated quickly and automatically and used as an input data point to a more precise inversion for location calculated by a global monitoring system using multiple kinds of sensors. This will be very important for events in the ocean basins where location ability is inherently poorer than for continental regions due to the lack of nearby seismographic stations.

References

- Bratt, S.R., and T.C. Bache, Locating events with a sparse network of regional arrays, *Bull. Seismol. Soc. Am.* 78, 780-798, 1988.
- Hanson, J.A., H.K. Given and J. Berger, Earthquake activity near Ascension Island, south Atlantic Ocean, as seen by a combined seismic/hydrophone array, *Geothermics* 25, 507-519, 1996.
- LeBras, R., and T.J. Sereno, Monitoring nuclear explosion testing in underground and underwater environments, *EOS Trans. Amer. Geophys. Union* 77, p.F-7, 1996.

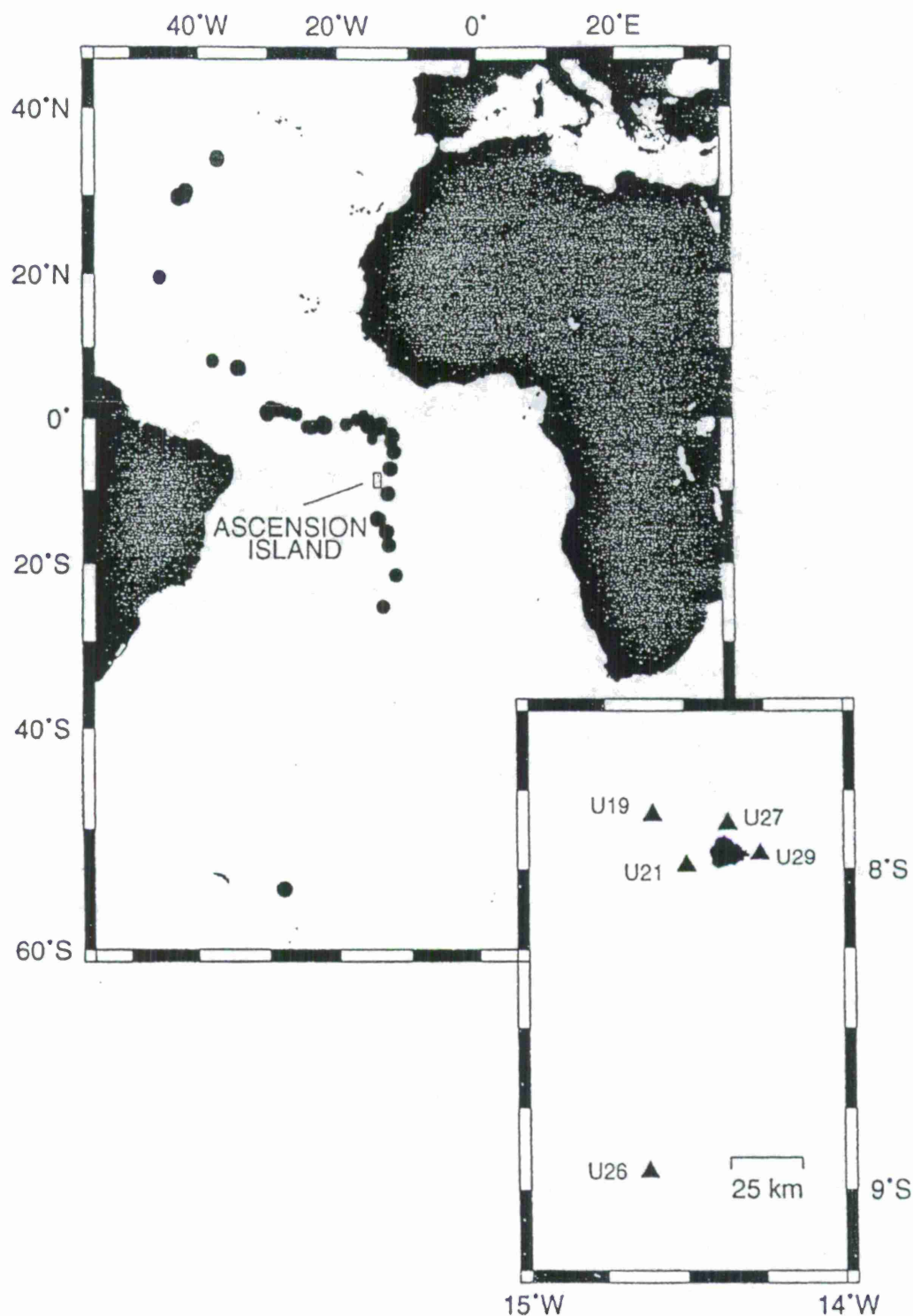


Figure 1. The 55 earthquakes (solid circles) used in this study occurred along the Mid-Atlantic Ridge at distances between 2° and 45° from Ascension Island, located at about 8° South. The earthquake magnitudes range from below 4.0 to 6.6 with a median of 4.7. The insert shows the 5 elements of the hydrophone array (solid triangles), part of the Missile Impact Locating System, relative to Ascension Island.

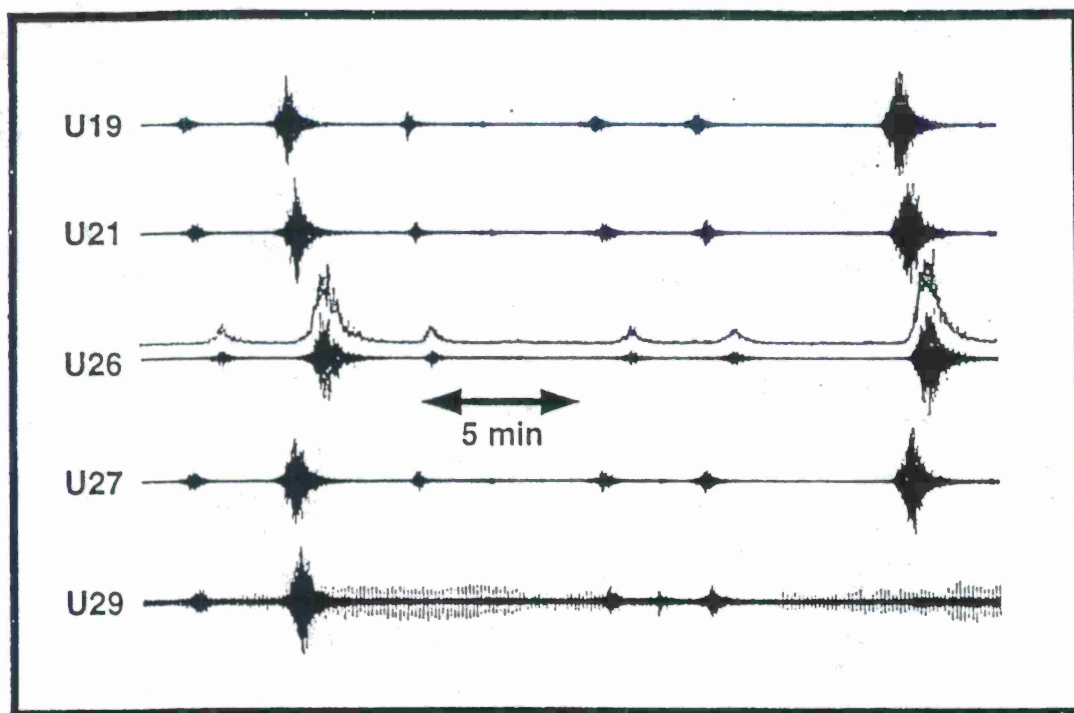


Figure 2. Hydrophone records showing T-phase arrivals from six earthquakes. Events 1, 4, and 5 appear to be foreshocks/aftershocks of Event 2 while Event 3 is a likely foreshock to Event 6. The reference azimuths for Events 2 and 6 are -33.4° and -53.4° . Events 3 and 6 are not recorded on element U29 due to island blockage. The grey line above the U26 record shows the envelope function calculated from this waveform.

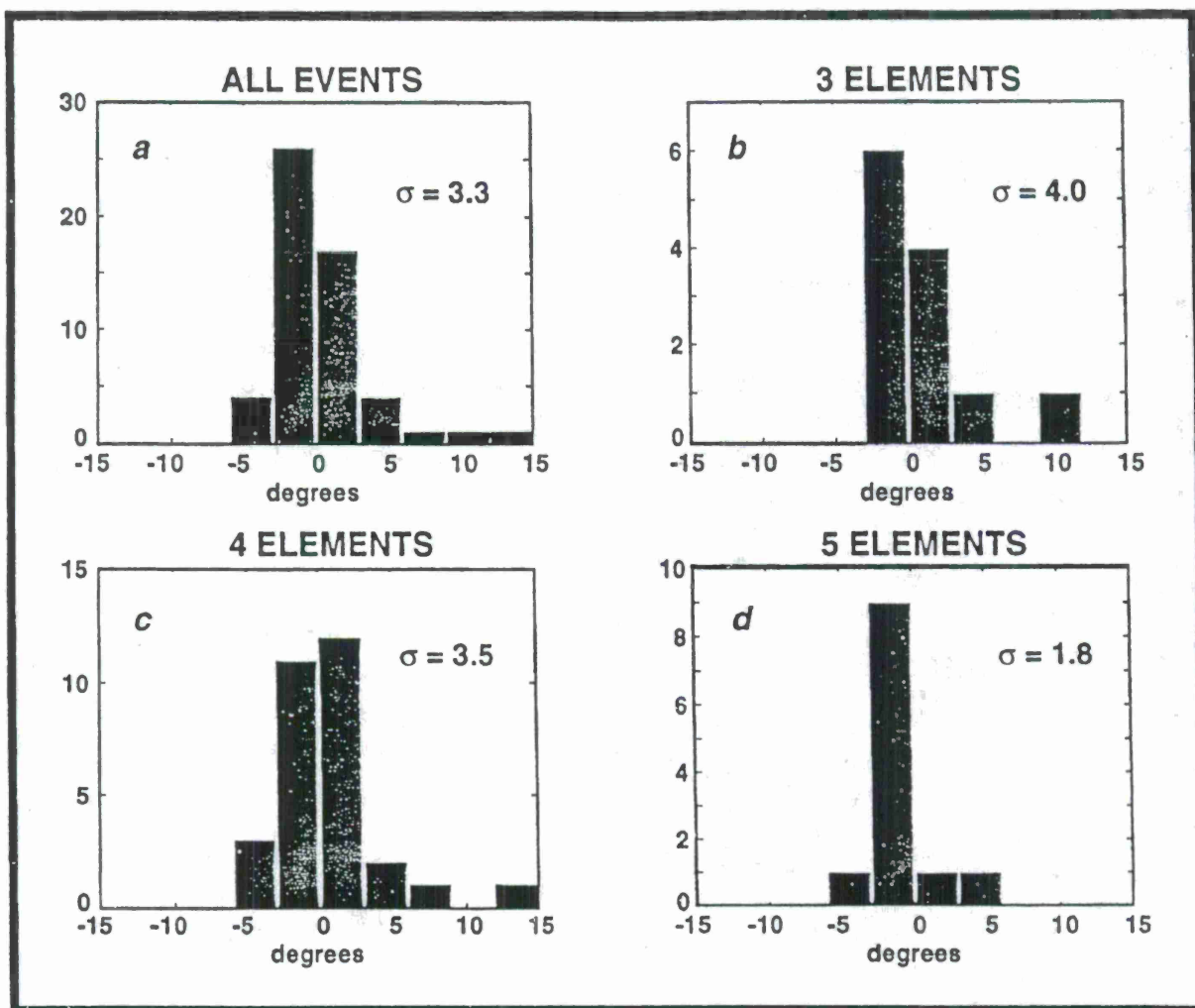


Figure 3. Histograms of residuals between azimuths from catalog locations and those estimated from T-phases, with standard deviations. Figure *a* shows results from all 55 events used in the study. Figure *b* shows the residuals for events that were recorded on 3 hydrophone elements only. Figures *c* and *d* are the azimuth residuals for events recorded on 4 and 5 elements respectively. The standard deviation decreases with increasing number of elements.

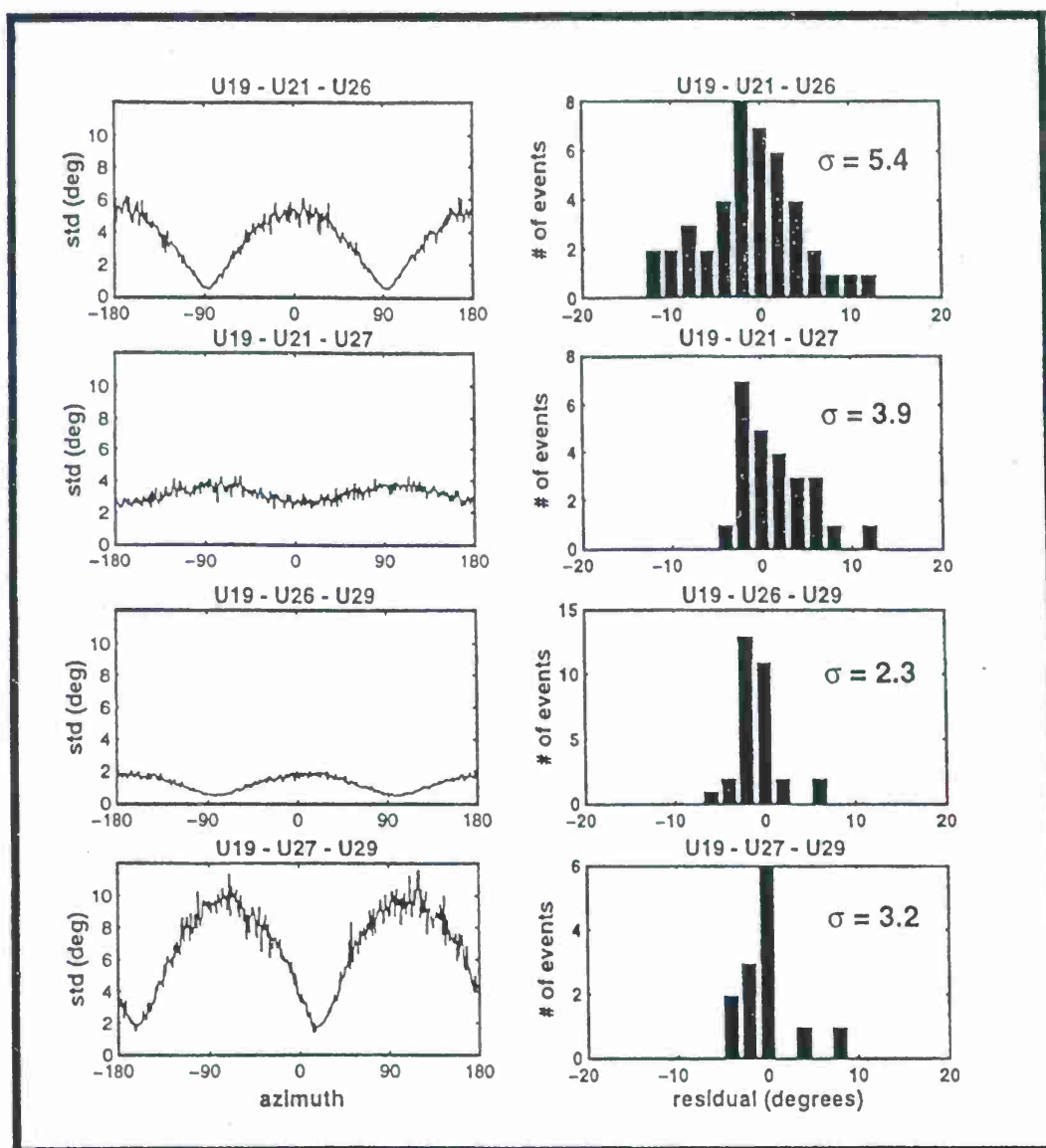


Figure 4. *Left column:* Predicted standard deviations for selected 3-element sub-arrays as a function of azimuth. The standard deviations were calculated by creating synthetic data, adding normally distributed noise, and then running that data through our inversion scheme. A majority of the earthquakes in this study range in azimuth from -60° to 0° which typically is neither the best or worst "look angle" for these sub-arrays. *Right column:* Histograms of observed azimuth estimate standard deviations on the same sub-arrays. The general similarity to the predictions in the left column shows that array geometry is a factor in the accuracy of azimuth estimates from T-phases.

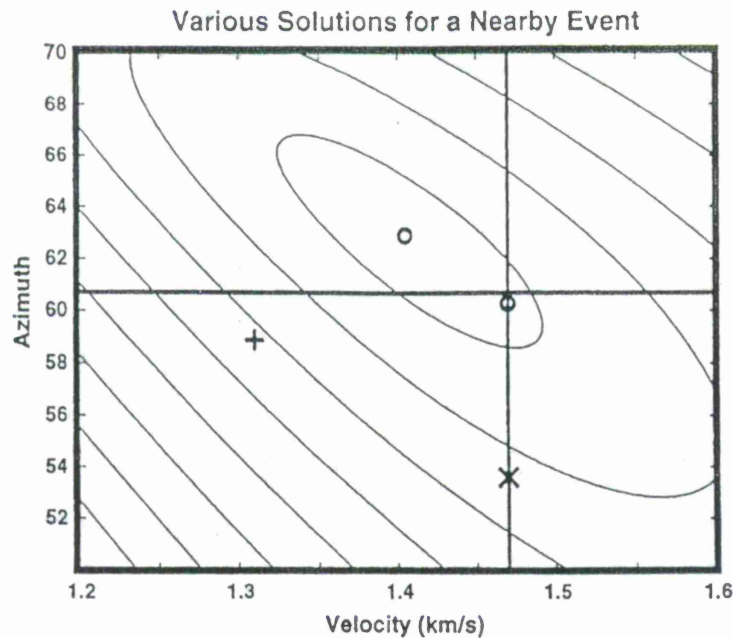


Figure 5. Various azimuth/T-phase velocity solutions for an earthquake 215 km from Ascension Island. The solid lines indicate the known azimuth and a realistic value for the T-phase velocity. The "+" is the plane-wave solution that solves for both azimuth and velocity; the "x" is the solution with the T-phase velocity fixed. The contours show the relative RMS misfit using a cylindrical wave solution. The circle at the center of the contours shows the best fitting solution and the circle on the solid line is the best solution for a fixed velocity. The plane-wave solution (+) estimates the azimuth quite well by mapping much of the error into the T-phase velocity. The cylindrical wave solution is poorly constrained so that fixing the velocity returns a better azimuth.

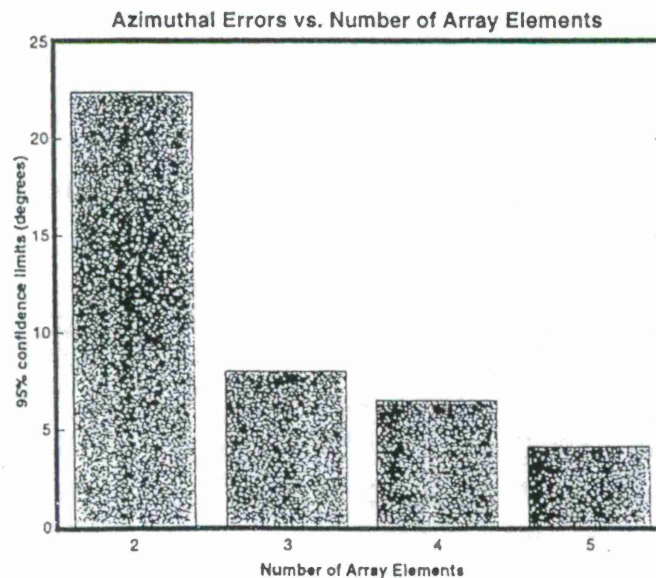


Figure 6. 95% confidence limits of azimuth estimates vs. the number of hydrophone elements used. For the 2-element solutions, the ambiguity has been eliminated by using the known locations, and large outliers ($>50^\circ$) were thrown out (see text).

SOURCE IDENTIFICATION USING METEOROLOGICAL AND STATISTICAL MODELLING

**Stephen E. Masters
ENSCO, Inc.,
445 Pineda Court
Melbourne, FL
stevem@fl.ensco.com**

**Contract No.: F08606-92-C-0004
Air Force Technical Applications Center
Patrick AFB, Florida**

ABSTRACT

This report documents one approach to estimating the location, time, and size of a release based on atmospheric modelling. A grid of virtual sources is defined over the region covering the suspected source. Simulated releases from each source are tracked using an atmospheric transport-dispersion model. At each real sampler the concentration of material released from each virtual source is calculated as a function of the sampling period. The correlation between the predicted and observed concentrations is calculated using a statistical regression procedure. The areal and temporal patterns of the correlation are examined to determine the most likely event time and location.

The Across North America Tracer Experiment (ANATEX) provided the data for this study. During ANATEX, perfluorocarbon tracers were released from two widely-spaced sources at regular intervals during the winter of 1987. A wide-ranging network of samplers collected data at daily intervals during the experiment. For this study, a subset of samplers were selected to roughly simulate the CTBT detection network.

OBJECTIVE

A network of xenon sampling units is being deployed world-wide to support the Comprehensive Test Ban Treaty (CTBT). The purpose of these samplers is to collect and measure any radioactive xenon isotopes released in a nuclear explosion. The network configuration is designed to make it difficult for any nation to test a nuclear weapon without detection. If a xenon plume from a suspected weapons test is detected by the network, the location of the test must be identified. In addition to locating the test through seismic methods, meteorological modelling can be combined with an analysis of the xenon plume collections to attempt to identify the source. This report documents one approach to estimating the location, time, and size of the event based on atmospheric and statistical modelling.

RESEARCH ACCOMPLISHED

The ANATEX Experiment

The Across North America Tracer Experiment was conducted between 05 January and 29 March 1987. A total of 33 tracer releases were conducted from Glasgow, Montana (GGW) and St. Cloud Minnesota (STC). Distinct perfluorocarbon tracers were released simultaneously from each source every 60 hours. Ground level air samples were collected from 76 sites during the span of the experiment. Each sampler collected a 24-hour, ground level sample starting at 1400 UTC each day. The tracers were inert and had no significant background. More detailed information about the experiment and data processing may be found in References 1 and 2. For this study, five widely-separated samplers were selected from the 76 active sites. Because of their separation, at no time did all five of the samplers detect a particular release. In general, only one or two samplers measured significant concentrations from a release on any given day. Even though the five samplers have a closer separation than the CTBT xenon network, their spacing still represents an adequate simulation of the data structure likely to be encountered by the CTBT analyst. Table 1 lists the stations selected for this study.

From the 33 ANATEX releases, four periods were selected for this study. Each of the chosen releases could be readily followed from the time of release for at least three days and exhibited minimal mixing with previous or subsequent events. Table 2 lists the releases selected for this study. Several significant concentration measurements that were clearly from a previous or subsequent release to the one being examined were set to zero. This was done to determine the skill of the technique in detecting single releases. The conclusions section of this report discusses the impact of "spurious" concentrations not a part of the release being studied.

The primary weather data source for the atmospheric transport-dispersion model was the standard rawinsonde network over the United States and Canada. A few additional rawinsonde observations were taken during the experiment (see Reference 1). To augment the standard network over the oceans or during periods with missing data, the gridded NCAR-NCEP Reanalysis data (Reference 3) were utilized. This dataset provided 6-hourly analyses at mandatory pressure levels at 2.5-degree latitude-longitude intervals.

Table 1: ANATEX Samplers Used for this Study

Sampler	City	Latitude (°N)	Longitude (°W)
1005	Huron, SD	44.38	98.22
1603	Oklahoma City, OK	35.40	97.60
2006	Fenton, MI	42.86	83.75
2352	Faribault, QE	49.77	74.53
3006	Pleasantville, NJ	39.45	74.57

Table 2: ANATEX Releases Used for this Study

Release Period			Tracer Released (kg)	
Release	Date	Time (UTC)	Glasgow	St. Cloud
3	10 Jan 87	1700-2000	83.5	50.8
4	13 Jan 87	0500-0800	83.9	50.6
16	12 Feb 87	0500-0800	83.7	47.0
23	01 Mar 87	1700-2000	83.7	46.9

GAMUT Transport-Diffusion Model

The Global Atmospheric Multi-layer Transport Model (GAMUT, Reference 4) produced the transport and diffusion estimates for this project. This model has been in operational use at the Air Force Technical Applications Center (AFTAC) since 1988. GAMUT simulates continuous or discrete releases of inert material over synoptic-scale distances. Trajectories are calculated within fixed layers between the surface and 12 km above ground level. Ground-based mixing depths are calculated twice daily and are used to drive the material redistribution process within the model. Synoptic-scale vertical motion is calculated using static energy as a conservative tracer. Ground-based concentrations are calculated using a Gaussian diffusion methodology, with impacts from the vertical material distribution and local mixing depths accounted for. Early versions of GAMUT were evaluated by outside agencies using ANATEX data (Reference 5).

Source Grid and Meteorological Model Configuration

A fixed grid of virtual sources was defined covering much of North America. Sources were located at 1-degree latitude and longitude intervals between 30°N-60°N, 70°W-120°W, a total of 1581 locations. The grid configuration is shown in Figure 1.

In modeling each of the periods selected for this study, a fixed amount of material (2 kg) was released from each source at 2-hour intervals. The material was tracked for 144 hours (6 days) following the release time. During this period, the material was allowed to mix to higher levels and loft or sink according to the synoptic patterns. Concentrations at each of the five

selected samplers were calculated for each source and release time. The calculated concentrations were 24-hour average values starting at 1400 UTC each day, corresponding to the actual ANATEX sampling period.

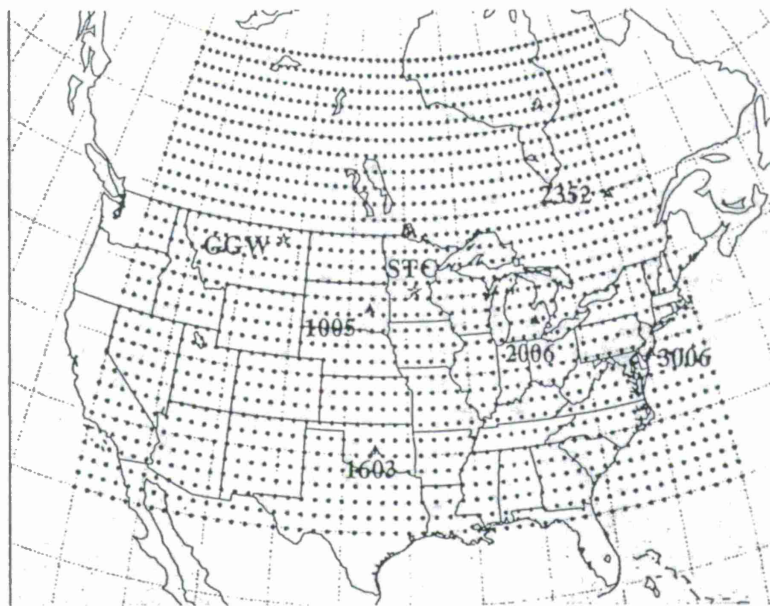


Figure 1: Virtual Source Grid. The ANATEX sources and samplers used in this study are also shown.

Least Squares Regression Modelling

To objectively determine the areas of the grids most likely to contain the real sources, a least-squares regression model was applied to the data (Reference6). A simple linear model was used, of the form

$$Y = \beta_0 + \beta_1 X + e \quad (1)$$

where Y is an n -element vector containing the measured perfluorocarbon concentrations at each sampler and sample date,

β_0 and β_1 are the computed regression parameters,

X is an n -element vector containing the concentrations computed by GAMUT for the corresponding sampler and sample dates.

To apply this statistical model, the GAMUT concentration calculations (X) for each sampler from each virtual source and release time were merged with the corresponding sampler data (Y). Both the GAMUT calculations and the measured concentrations were handled in units of pg/m^3 . Then, the regression calculations were performed on the merged data. The computed β_1 parameter from the regression calculations is then an estimate of the tracer release rate in grams per hour.

It is important to note that the statistical model uses "simple regression," that is, each source is considered independently of the others. Since it is known that only one source existed in each case (Glasgow and St. Cloud released distinct tracers), it is not necessary to consider a

multiple regression model. If it is known that more than one source may be simultaneously emitting material, a multiple regression approach may prove useful in separating the sources.

Regression calculations were performed for each case, trajectory start time, and virtual source location combination. The β_1 release rate term was saved, as was the standard correlation coefficient of the regression. For a particular case and trajectory start time, the patterns of the correlation and the release rate values were plotted on maps to determine the most likely source areas.

Of the eight release events selected for this study (four periods from two sources), two are described in some detail in the following sections. Releases 3 and 23 from St. Cloud were both successfully handled by the technique. A set of locations near the actual release sites was identified as the probable source region near the actual release times. Release 23 from Glasgow was not predicted correctly by this approach, as the source location was identified near Oklahoma City. The reasons for the failure in this case are examined. The results for the five other release events are then briefly summarized.

St. Cloud Release 23

Release 23 from St. Cloud commenced at 1700 UTC 01 March. It was embedded in northwesterly flow behind a low pressure center over Michigan. This flow carried the plume towards the middle Atlantic coastline near Chesapeake Bay. Measurements from samplers south of St. Cloud indicate that the plume may have split near or shortly after release time, with some material moving southward more slowly over several days. Of the five samplers used in this study, sampler 3006 measured the highest concentrations, with smaller concentrations observed at sampler 2006 and 1603.

Figure 2 shows the pattern of correlation and release estimates from the virtual source grid for simulated releases 24 hours before the real release. Large colored squares show locations with a positive correlation between the predicted concentrations from the model and the observed concentrations at the five selected samplers. The color of the square shows the degree of correlation as well as the calculated model release required to produced the best fit to the measured concentrations. In the black and white reproduction in this volume, darker colors depict the points with the combination of high correlation and small release rate. [The full color versions of these figures are available from the author.] Yellow areas denote areas of low correlation and very high release rates; red areas show low release rates but low correlation; green areas have high correlations but high release rates. The blue squares show source locations where the model-measured concentrations are highly correlated and a small release rate is estimated. These are the locations that most likely are near the real source. Grid locations denoted by small gray squares are source locations with a negative correlations between the modelled and measured concentrations. The white squares denote source locations that failed to cause positive concentration estimates at any of the five sampler locations for the release time shown. The locations of the actual source (blue stars) and selected samplers (red triangles) are also shown.

While a wide area of virtual sources have a positive correlation at 1800 UTC 28 February, most have small correlations and/or unrealistically high release estimates. At this time, several points over Lake Superior (shown in a dark purplish color) appear to be highlighted. For modelled releases at 0800 UTC 01 March (not shown), points immediately near and northeast of St. Cloud have high correlation and low release estimates. At the time of the release (Figure 3), several point very near St. Cloud are again highlighted.

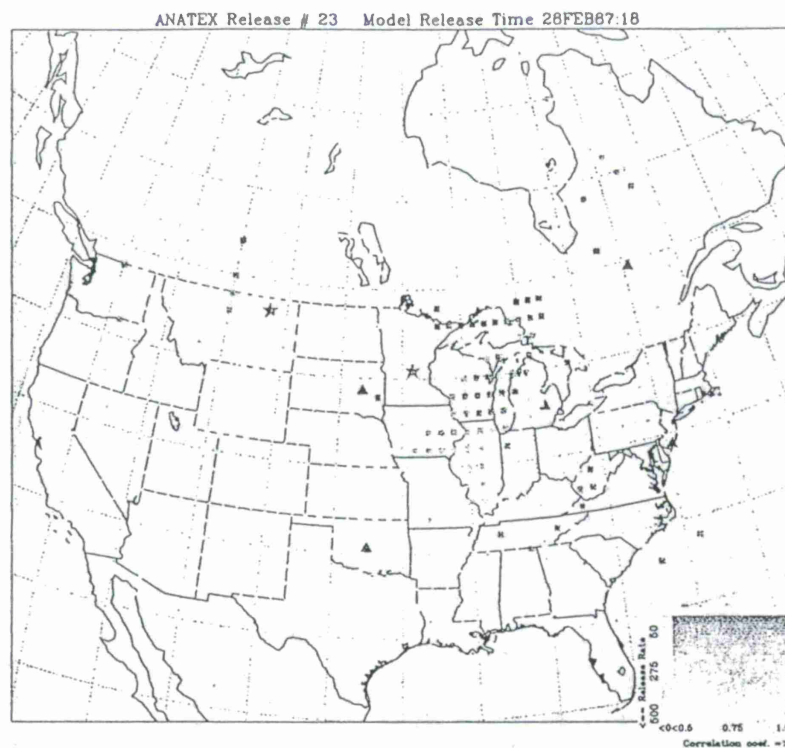


Figure 2: Correlation/release rate pattern for release starting at 1800 UTC 28 February 1987. The actual release location is St. Cloud. See the text for a description of the plot.

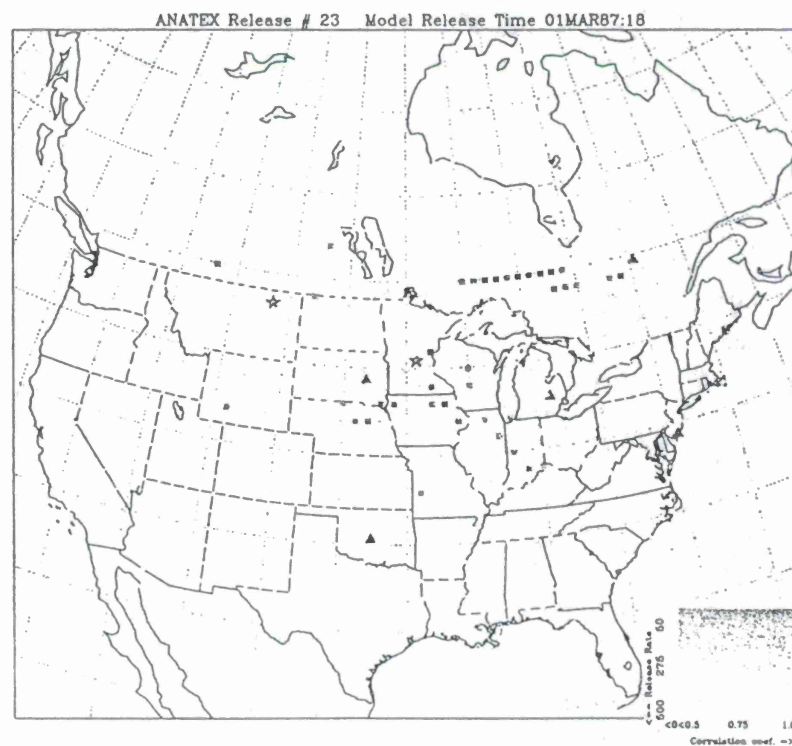
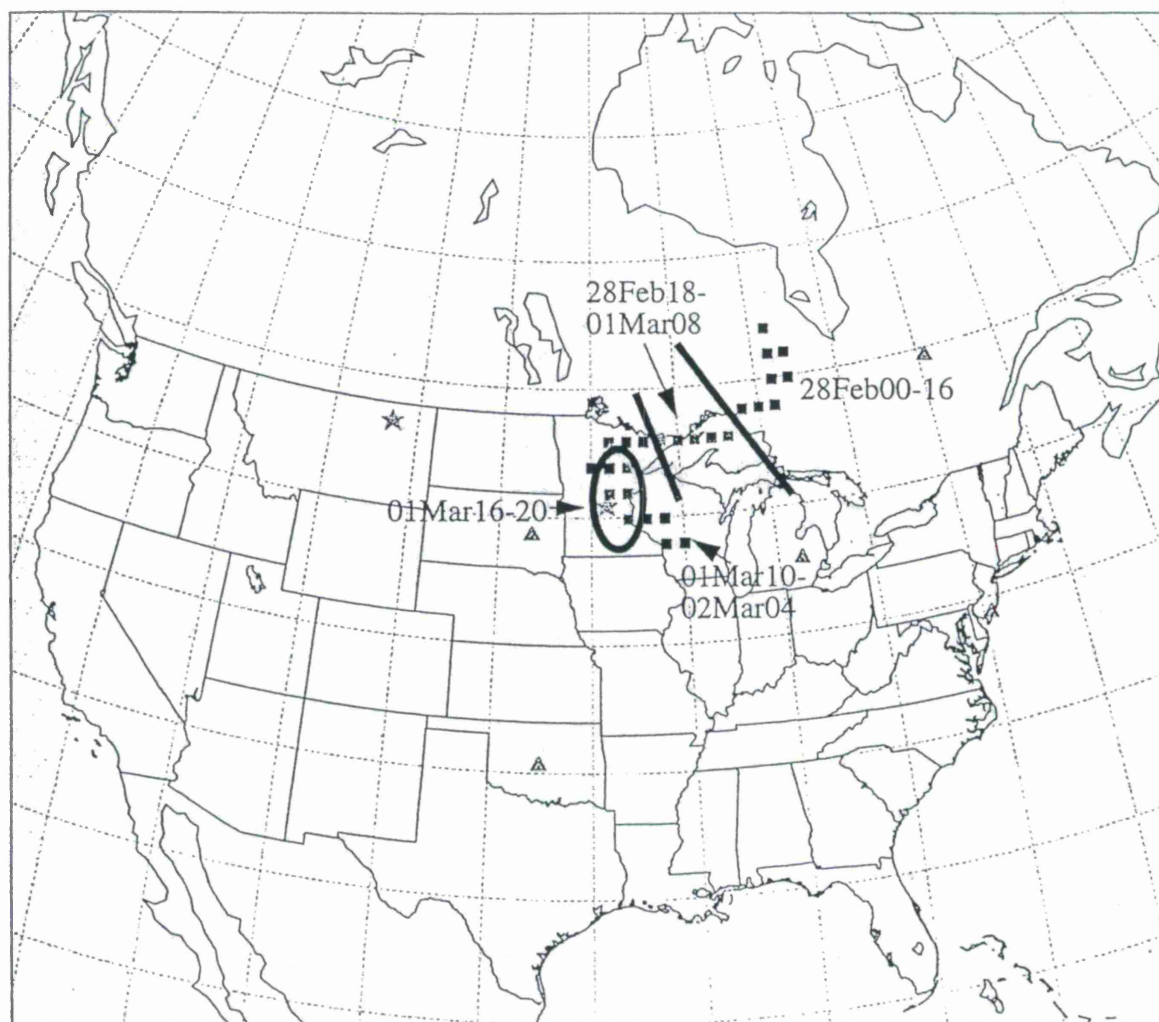


Figure 3: Correlation/release rate pattern for release starting at 1800 UTC 01 March 1987. The actual release location is St. Cloud.

From these and other figures, the set of points that have high correlation and low release estimates can be determined and plotted on a single map. Figure 6 shows these points, color-coded by the time period of the indicated release. The area covered by the highlighted points form a narrow, winding band from west of James Bay to western Wisconsin. The time window containing the points is between 0000 UTC 28 February through 0400 UTC 02 March. Most points are within 24 hours of the actual release time, Between 1600 and 2000 UTC 01 March, points very close to St. Cloud are highlighted. In this case, the actual location and time of the release was predicted fairly well.



- 28Feb 0000-28Feb 1600
- 28Feb 1800-01Mar 0800
- 01Mar 1000-02Mar 0400
- 01Mar 1600-01Mar 2000 (release time)

Figure 4: Virtual source locations where the model-measured concentration correlation is greater than 0.90 and the estimated release rate is less than 200 kg/hr, St. Cloud Release 23. The color of the square shows the estimated release time for the virtual source.

St. Cloud Release 3

For release 3 from St. Cloud, a rather broad area was identified as the source region over a 36-hour span (Figure 5). As with the successful case above, the actual source was included in the area identified during the period of the actual release. It is interesting to note that the total area identified as the possible source region is bounded by the two samplers 1005 and 2006. This pattern was noted in several cases.

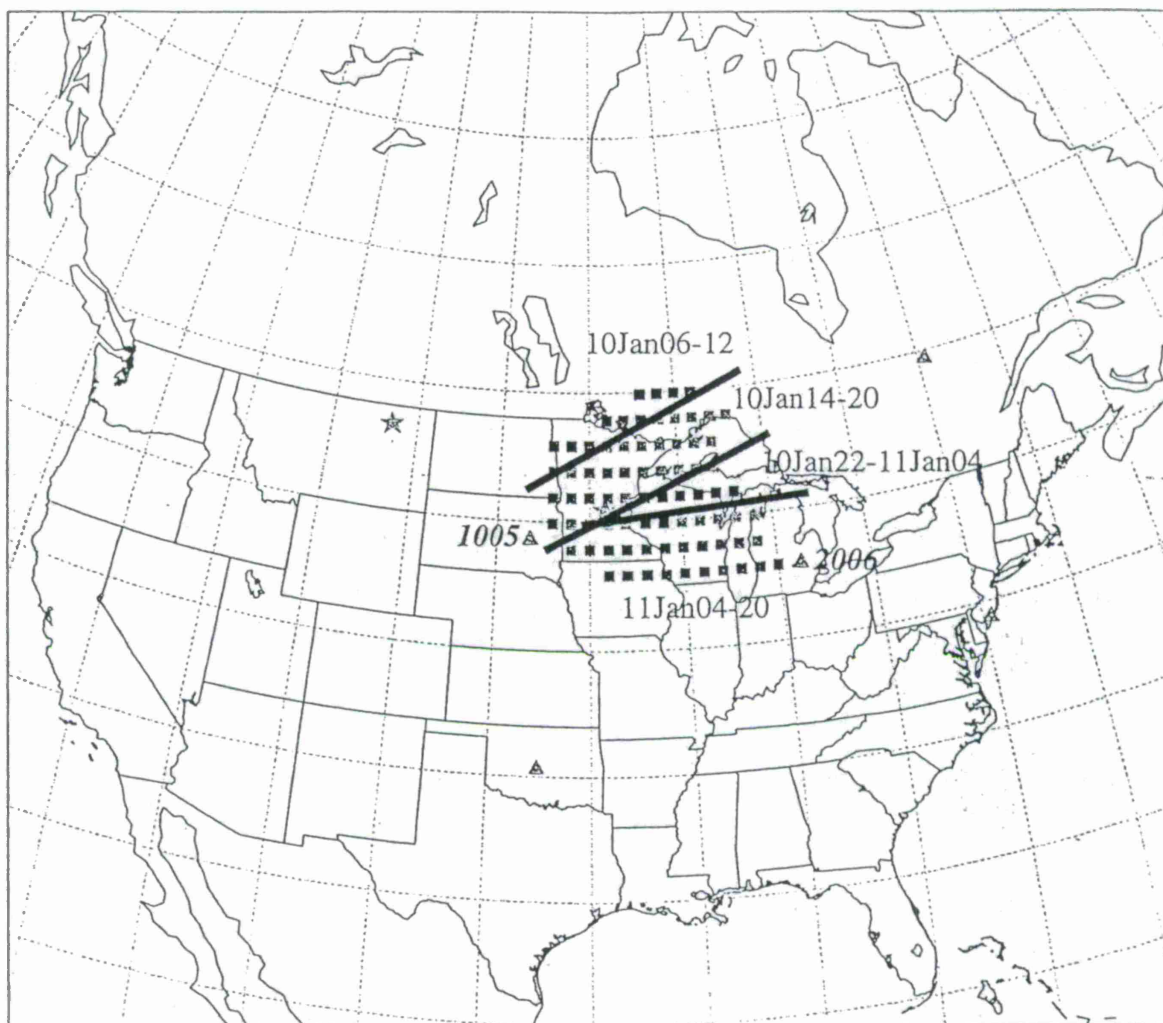


Figure 5: Virtual source locations where the model-measured concentration correlation is greater than 0.95 and the estimated release rate is less than 100 kg/hr, St. Cloud Release 3. The color of the square shows the estimated release time for the virtual source.

Other Releases

Not all releases were modelled successfully in this study. For Glasgow Release 23, the source was incorrectly placed near Oklahoma City. Careful examination of the data indicated a large observed concentration at the Oklahoma City sampler on March 3 was not predicted by the meteorological model. As a result, the statistical model placed the source far from the actual

release location. This example highlights the need for accurate measurements and meteorological modeling for this procedure to succeed.

In Table 3 below is listed a summary of all of the cases examined and the degree of success in identifying the source.

Table 3: Summary of Results for the Eight ANATEX Release Events in this Study.

Release	Source	Success of location/time identification
3	Glasgow	Good location and time identification and correspondence
3	St. Cloud	Broad location identification. Good time/location correspondence
4	Glasgow	Source identified over western South Dakota; Time prediction 6 hours late
4	St. Cloud	No clear source identified. High concentration at 1603 does not correlate with actual release.
16	Glasgow	Excellent location identification. Time prediction about 24 hours off. This release was seen by only one of the five samplers.
16	St. Cloud	Good location identification. Time prediction about 24 hours off.
23	Glasgow	Source identified in Oklahoma. Uncorrelated measurement at sampler 1603 the likely cause.
23	St. Cloud	Good location and time identification and correspondence.

CONCLUSIONS AND RECOMMENDATIONS

From an examination of the eight cases studied for this report, these conclusions may be drawn concerning this technique.

1. The combined meteorological and statistical technique was often successful in identifying the general area and time of the actual release. In six of the eight cases, the general location was correctly identified; in four of those six, the proper time of the release was correctly found.
2. If the actual time of the event is known through other means, the location of the source can often be estimated with greater precision. If the event timing is totally unknown, the area flagged as the probable source location is often bounded by samplers that were impacted by the release. When information concerning the release time is added, the flagged area is often quite small and usually includes the actual source location.
3. Erroneous data or data from other events can cause the technique to incorrectly identify the release location and time. This is particularly true if the measured concentrations in question have a high magnitude compared to other data.
4. The meteorological model used to produce the concentration estimates from the virtual sources must possess sufficient skill to reasonably simulate the actual transport and dispersion that is occurring. If the model fails to produce reasonable downwind concentration estimates, the measured data may appear to be erroneous leading to the problem in item 3 above.

The results presented here are encouraging. In many of the cases, even with only one or two samplers observing the effluent plume, the source was still accurately identified. Several avenues of further investigation are suggested by these results.

1. The results from several cases suggests that the precision of this technique in determining the source location is related to the sampler spacing. The sampling period likely limits the precision of the estimate of the event time. Examination of more ANATEX releases could help to quantify the precision that can be expected with a sparse sampler network.
2. Alternate meteorological models could be applied to this problem. A medium-range model using surface data may provide more accurate transport predictions, particularly in the first one or two days after the release. A study could be performed comparing the predictions derived from several models.
3. A total of 76 samplers were active during ANATEX. While the CTBT network will be nowhere as dense as the ANATEX network, a study could be performed to determine the impact of adding more samplers. The increased accuracy in source identification when a plume is observed by three or more samplers (instead of the one or two common in these cases) could be determined.

REFERENCES

1. Draxler, Roland R., 1991. The Accuracy of Trajectories during ANATEX Calculated Using Dynamic Model Analyses Versus Rawinsonde Observations. *Journal of Applied Meteorology*, 30, 1446-1467
2. Draxler, Roland R., and J. L. Heffter, eds., 1989. Across North America Tracer Experiment (ANATEX) Volume I: Description, ground-level sampling at primary sites and meteorology. NOAA Tech Memo. ERL ARL-167, 88 pp. and Appendices. [Available from National Technical Information Service, Springfield, VA.]
3. Kalnay, E., and coauthors, 1996. The NCEP/NCAR Reanalysis Project. *Bulletin of the American Meteorological Society*. 77. 437-471.
4. ENSCO, Inc., *Software Requirements Specification for the Global Atmospheric Multi-Layer Transport Model (GAMUT) CSCI of the Integrated RPP Evaluation System (IRES)*. Prepared for the Air Force Technical Applications Center, Patrick AFB, FL, July, 1993
5. Clark, T. L., and R.D. Cohn, 1990. *The Across North America Tracer Experiment (ANATEX) Model Evaluation Study*. EPA/600/3-90/051, 99 pp. [Available from Atmospheric Research and Exposure Assessment Laboratory, United States Environmental Protection Agency, Research Triangle Park, NC.]
6. Neter, J. and Wasserman, W. 1974. *Applied Linear Statistical Models*, Homewood, IL: Irwin.

RADIONUCLIDE MEASUREMENTS FOR THE COMPREHENSIVE TEST BAN TREATY

H.S. Miley*, K.H. Abel, S.M. Bowyer, T.W. Bowye, C.W. Hubbard, A.D. McKinnon,
M.E. Panisko, R.W. Perkins, P.L. Reeder, R.C. Thompson, R.A. Warner

Pacific Northwest National Laboratory

Sponsored by U.S. Department of Energy
Office of Nonproliferation and National Security
Office of Research and Development
Contract DE-AC06-76RLO 1830

Comprehensive Test Ban Treaty Research and Development Program, ST-27 1, ST-5 83

ABSTRACT: The Comprehensive Test Ban Treaty is designed to end nuclear weapons tests forever. However, like all treaties, this treaty must have a robust and credible verification method. For this reason, the International Monitoring System (IMS) has been created to define and maintain a worldwide array of sensors of several types; seismic, hydroacoustic, infrasonic, and radionuclide. The vibrational measurement systems are all able to detect and localize explosions within a few minutes of the event. However, only radionuclide systems can verify that an event was indeed nuclear. This is accomplished by capturing an extremely small portion of the weapon itself and using the distinct nuclear signature of the appropriate radionuclides to rule out other possible sources. This determination must discriminate weapons debris from reactor products, medical isotopes, or industrial isotopes. Further, the measurement must be sufficiently sensitive to detect explosions at great distances, and must report results in a sufficiently timely manner to allow reasonable on-site inspections.

The radionuclides of interest to the CTBT include xenon isotopes, which are the most likely radionuclides to escape an underground test, and radionuclide aerosols, which create an abundant and distinctive signature in atmospheric weapons tests. The work reported in this paper is the development of radionuclide measurement systems at Pacific Northwest National Laboratory under the direction of the Department of Energy Office of Research and Development. This development has resulted in a Radionuclide Aerosol Sampler/Analyzer (RASA) and an Automated Radioxenon Sampler/Analyzer (ARSA). The function of these proposed components of the IMS is to verify worldwide CTBT compliance by monitoring the atmosphere for radionuclides indicative of a weapon.

The development of the RASA and ARSA instruments is complicated by the fact that a number of the selected sites are remote, their power may be unreliable, and suitable operators may be unavailable to make daily site visits. For these reasons and others, the RASA and ARSA have been designed as automatic, unattended sampler/analyzers with remote control and reporting capabilities. It is envisioned that a network of RASA and ARSA systems could both provide an effective radionuclide component of the IMS, and provide it in a convenient, cost effective form.

Both the RASA and ARSA are on a fast track to commercial availability; the ARSA is currently being subjected to a substantial field test at the Environmental Measurements Laboratory (EML) in New York and RASA is currently undergoing a brief Engineering Manufacturability Development as a precursor to commercial availability.

OBJECTIVE

The objective of the research activity reported here is to develop CTBT verification technology for collection and sensitive measurement of nuclear debris. However, while this objective is fundamental, a number of other requirements have to be addressed to make a practical, affordable, and credible IMS. Firstly, since several of the interesting isotopes are short-lived, near-real time measurements must be made. Since the CTBT requires daily measurements, this all but mandates automated systems, although some nations may elect to use pre-existing manual systems for aerosols. In addition, the remote nature of many IMS radionuclide sites means that frequent operator access is unlikely. Thus the systems must operate for long periods without operator intervention. This requirement mandates remote controls, remote reporting, state-of-health (SOH) sensors. Finally, the infrastructure of these remote, unattended sites is expected to be lacking. This means that the systems must be power-failure-tolerant, communication-failure tolerant, and require only small quantities of power and space. Finally, to be cost effective, the systems should be compatible with highly-organized, depot-level maintenance facilities.

RESEARCH ACCOMPLISHED

At the inception of the radionuclide measurement research and development program at PNNL, the basic science of a sensitive aerosol measurement system was well understood; detection of aerosol debris from distant nuclear detonations had been made at PNNL (Perkins et al) and elsewhere for over 30 years. The challenge in the aerosol field was to make the measurements without a radon-daughter decay time to facilitate cheap, low-resolution detectors. The use of mechanically-cooled germanium detectors solved this problem, and left only the development of appropriate automation techniques to surmount the aforementioned CTBT logistical hurdles. As a result, the RASA is the most sensitive automated radionuclide aerosol sampler/analyzer system ever reported.

However, in the xenon case, the ARSA is the first automated xenon sampler/analyzer and the most sensitive xenon system of *any* kind, manual or automatic. For this reason, many of the facets of the ARSA are in previously unexplored territory and have required more development effort.

Radionuclide Aerosol Sampler/Analyzer (RASA)

The RASA was designed to reasonably reproduce many features of a laboratory-based radionuclide aerosol measurement. The RASA employs a large, 0.25 m² filter surface through which about 20,000 standard cubic meters (SCM) of air is drawn per day. The filter is allowed to decay for 24 hours to reduce radon-daughter concentrations, then the residual radionuclides are measured using a large, (90% relative efficiency) mechanically-cooled germanium gamma-ray spectrometer. In this way the RASA achieves CTBT sensitivity requirements of L_d (as defined by Currie) at 30 μBq/SCM of ¹⁴⁰Ba within 72 hours from the start of sample acquisition, therefore in

the presence of radon-daughters. A real filter plus mocked-up weapons debris as measured by a germanium and NaI(Tl) detector are shown in Figure 1.

What makes the RASA differ from a conventional laboratory measurement is that the filter is composed of six segments exposed in parallel to an air stream. The segments are fed from six rolls into a patented sample head such that this large air volume can be collected by the use of a low-power, low-noise centrifugal blower. Another difference is that rather than mechanically compacting the filter to a button geometry for a highly improved counting efficiency, the filter is simply led in a path which wraps around the detector. This results in a modestly improved counting efficiency, yet allows the entire system to be automated by the use of a single drive motor and fits into a 1 m x 2m floor space (see Figure 2). This system requires about 1600W and produces only about 75 dBA at 1 meter from the system enclosure.

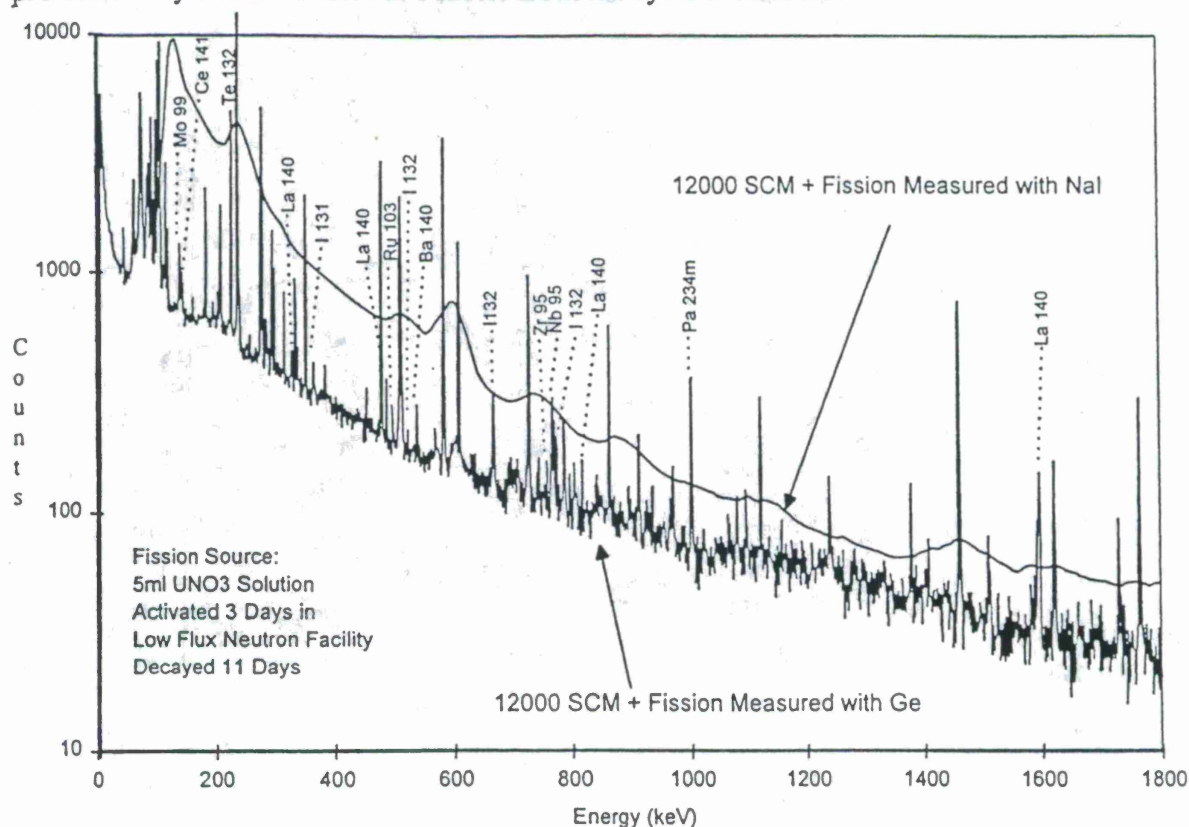


Figure 1: Comparison of germanium and NaI detector gamma spectra resulting from the measurement of exposed air filter doped with fission products in order to mock-up a sample of the expected collection of radioactive debris from a nuclear detonation in the presence of the naturally occurring radon background.

A calibration source may be introduced to the detector at any time to provide a system check. This is accomplished using a small, traceable source which is mounted on the end of a threaded rod which is extended and retracted by a small stepper motor. The stepper motor is controlled by small optical sensors to allow reproducible positioning of the source.

Each sample is sealed between two continuous polyester strips as it exists the sample head to ensure that the samples are not tampered with and cannot contaminate the detector. One of the

polyester sheets is printed every 50 cm with an optical position bar and a sequential barcode. The optical bar is detected by a sensor which allows extremely accurate advancing of the filter strips. The bar code is read each time the samples are advanced to associate the electronic measurement results (i.e. the gamma-ray spectrum) with a physical filter. In this way, any filter which shows an interesting spectrum may be retrieved.

To automate the hardware and achieve CTBT goals of remote control, automatic reporting, remote maintenance, SOH logging, and network management for lower operational costs, a real-time operating system was selected. A robust control program was developed (Hubbard, et al) based on a State Machine concept. This easily maintainable code automates all the routine functions within the RASA. In addition, a separate Graphical User Interface can interrogate and control the RASA and provides access to stored data, both gamma-ray spectra and SOH sensor data.

The automatic transmission of the RASA data has been accomplished (Mckinnon, et al) using automated file-transfer protocol (FTP), automated electronic mail, and automated network-news-transfer protocol (NNTP) is under development. The basic principle is that the contents of a certain subdirectory is inspected periodically. The presence of any new files triggers a transfer. Subsequently, the files are moved to an archive area. These methods are error-free, robust against temporary loss of telephone or internet communications, make use of ubiquitous internet-service-provider infrastructure, and should provide compliance with current and future National/International Data Center communications methods.

In addition, an automated simple-network-management protocol (SNMP) communications scheme is under development to allow direct use of existing SNMP network management utilities for logistical management and coordination of large networks of RASA and ARSA units. This should allow easy detection of malfunctioning systems. With the addition of simple process control systems, an SNMP system should be able to certify that a system is under control and

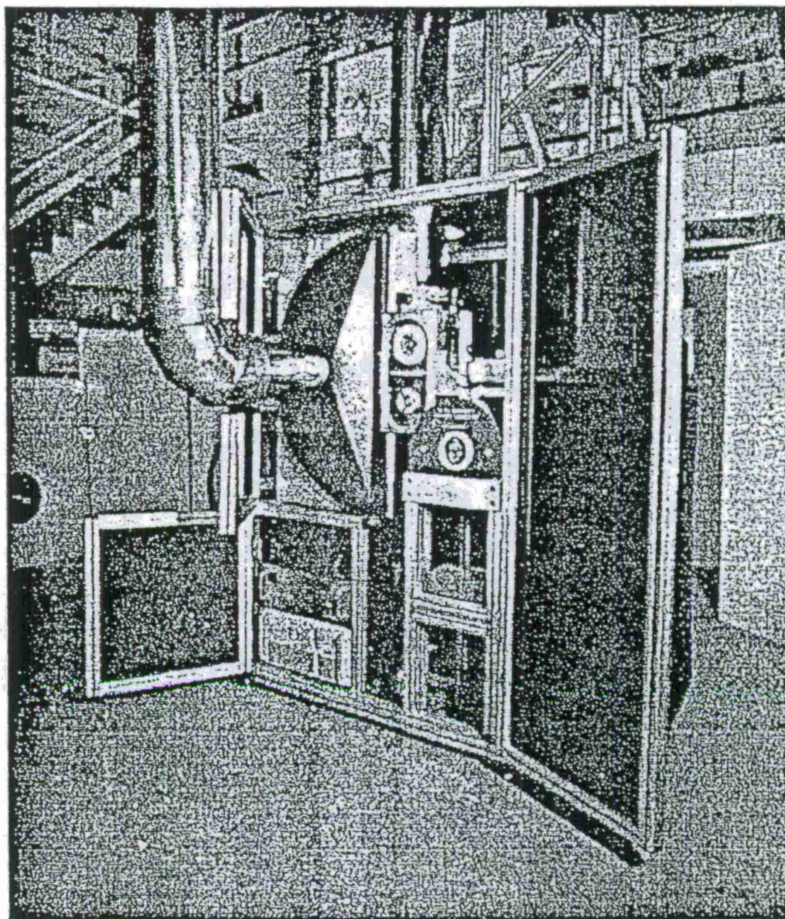


Figure 2. Radionuclide Aerosol Sampler/Analyzer

even predict component failures far enough ahead to allow component swap-out with minimal down time.

Atmospheric Radioxenon Sampler/Analyzer (ARSA)

The ARSA permits the continuous measurement of atmospheric ^{131m}Xe , ^{133m}Xe , ^{133}Xe and ^{135}Xe . By measuring these concentrations, it is possible to differentiate between vented material from a subsurface nuclear detonation (or other nuclear detonation where aerosol radionuclide release is minimal) and emission from nuclear reactors, fuel reprocessing, and medical isotopes production and usage. The ARSA is the first automatic system developed for the measurement of atmospheric xenon radionuclides and allows a 100- to 1000-fold greater sensitivity for the short collection/analysis periods of interest than previously reported laboratory-based analytical methods.

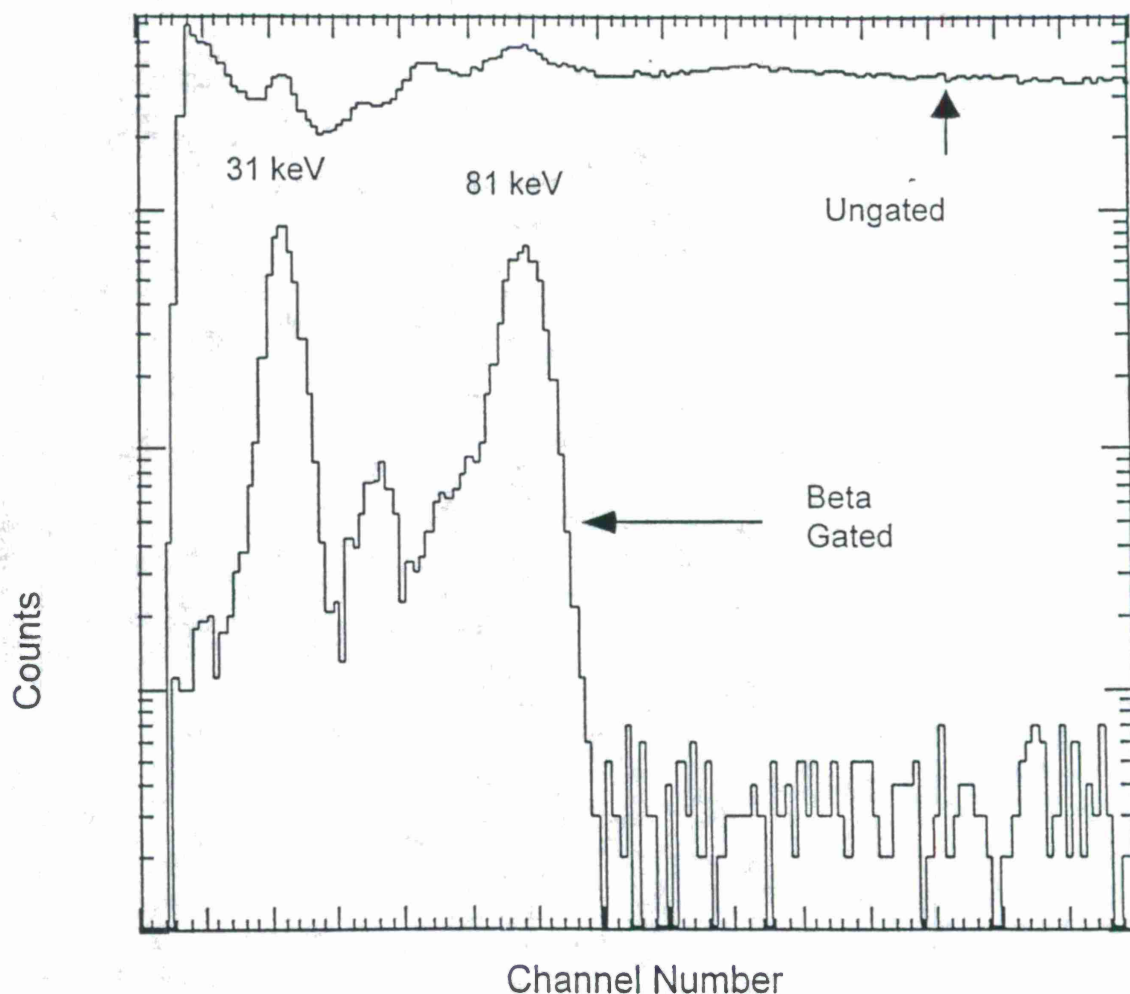


Figure 3. Plot of ^{133}Xe from our beta-gamma coincidence spectrometer. The 31 to 36 keV x-rays and the 81 keV gamma ray from ^{133}Xe are used to identify the isotope

Evaders of a CTBT may attempt to carry out a nuclear test in a manner that minimizes signatures associated with such an event. For example, conducting a test underground, underwater, or over the ocean in a rainstorm could minimize or eliminate some signatures, including the aerosol radionuclides.

Under such conditions, only the noble gas radionuclides may enter or remain in the atmosphere in significant quantities. Of the noble gas radionuclides, the xenon radionuclides are by far the most abundant at a few days after a detonation. Therefore, the measurement of xenon radionuclides could provide confirmation that an event was nuclear rather than seismic in origin.

The ARSA allows rapid separation of atmospheric xenon from about 5 m³ of air per hour and prompt subsequent radioxenon measurement. The demonstrated sensitivities for the radioxenons are about 90 $\mu\text{Bq}/\text{m}^3$ based on a 8-hr collection and a 24-hr analysis period. These measurements of extremely low concentrations require a very low background and highly-selective, efficient counting system which is provided by the beta (and/or conversion electron) gamma (or x-ray) coincidence detection systems as described below. While sensitivity requirements for possible radioxenon monitoring of a CTBT are not specified, it is clear that high sensitivities will be essential to detect the very low yields which will be prohibited by a "zero yield" test ban.

The sampling and subsequent analysis is accomplished in three steps. First, xenon is adsorbed from an air stream on a cooled, activated charcoal at a flow rate of about 100 standard liters of air per minute (slpm). Second, the xenon trapped on the charcoal bed is thermally desorbed and purified to remove traces of radon and CO₂. Third, the purified sample is transferred to a nuclear counting system, counted, and then assayed using a residual gas analyzer, so that the stable xenon concentration can be determined.

The decay of the three xenon radionuclides of primary interest, ^{133m}Xe, ¹³³Xe and ¹³⁵Xe, as well as that of ^{131m}Xe, is by coincidence emission of a beta particle and/or a conversion electron in coincidence with a gamma ray or a cesium or xenon x-ray. In order to simultaneously measure these with very high sensitivity and selectivity, it is necessary to measure the photon energy in coincidence with a high-efficiency electron detection. To accomplish this in a manner which was compatible with the

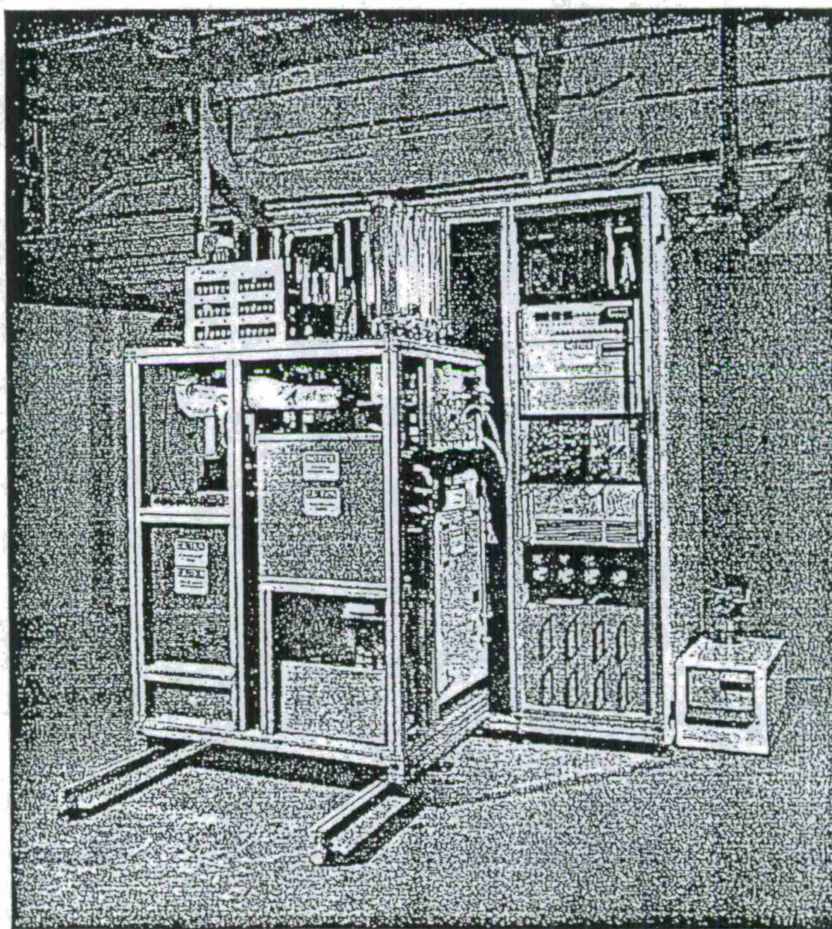


Figure 4. Atmospheric Radioxenon Sampler/Analyzer

automatic separation process, a gas cell scintillation counter was developed and described in detail in elsewhere (Reeder, *et al*).

The photons are detected in one of two NaI(Tl) crystals completely encasing the gas cell scintillation counters. The detection system accommodates four gas cell scintillation counters for the simultaneous counting of four xenon gas samples. The xenon gas samples which are collected during consecutive 8-hr periods are transferred into the gas cell scintillation counters and their xenon radionuclide content measured by beta and/or conversion electron - gamma or x-ray coincidence counting. Since a beta and/or a conversion electron event in a given gas cell triggers storage of an associated gamma ray or x-ray as part of a specific gamma-ray spectrum, four spectra or more could be measured simultaneously without interference. We have observed that using beta and/or conversion electron and gamma or x-ray coincidence counting provides a 10^3 - to 10^4 -fold background reduction over standard gamma-ray spectrometry. Since essentially all of the beta and conversion electron emissions are observed in the gas cell scintillation counter, the gamma-ray and x-ray counting efficiencies are not significantly reduced by requiring a coincidence event. Figure 3 illustrates a beta coincidence gamma-ray spectra of a ^{133}Xe spike taken with our counting system with and without the coincidence requirement. The extremely low gamma-ray background provided by the coincidence requirement permits xenon measurement of just a few disintegrations per hour.

Figure 4 shows a photograph of the engineering field model that began a several month field test at the Environmental Measurements Laboratory (EML) in March, 1997. All of the operations are automatic and computer-controlled, including state-of-health, safety, power recovery, remote programmability, transmission of gamma-ray spectral data, etc. The spectral data, together with gas composition and radionuclide composition, permit calculation of the radioxenon concentrations and all of these data are automatically transmitted to a data center at the conclusion of each analysis.

Current Status and Future Availability

The development and commercialization of the RASA and ARSA being coordinated between the US DOE Office of Research and Development and the US National Data Center (NDC). This process has been designed to move as rapidly as possible from the initial statement of the problem to reliable hardware operating in the field. Currently the RASA is in a brief Engineering manufacturability Development (EMD) Phase and the ARSA is simultaneously engaged in a Field Test and Design Review.

CONCLUSIONS AND RECOMMENDATIONS

The RASA and ARSA systems will become commercially available and should provide an important part of the IMS. However, further modest efforts can make these systems more cost effective, perhaps more cost effective than pre-existing manual systems in the case of the RASA. These efforts will include a series of watchdog applications which actively monitor key processes and generate warnings or issue system commands when certain conditions are met. For instance, if the RASA detected gross amounts of radioactivity in a filter, a message could be sent within 10 minutes, thereby saving a day of transit time for sample recovery and potentially warning of public health hazards.

In addition to efforts aimed directly at system development, the samples acquired by the RASA and ARSA will require confirmatory analysis at a regional laboratory for QA purposes and to doubly confirm a positive measurement of a nuclear explosion. The ability to recover these samples from the RASA and ARSA has already been assured by design of the filter bundle and archive sample bottles, respectively. However, the laboratory procedures needed to perform QA or confirmatory measurements should be worked out for these unique sample matrices and form factors.

Finally, the developers of the RASA and ARSA have been contributing to the technical groups directly tasked with the job of formulating CTBT planning for subjects ranging from IMS operations manuals to IMS Site Survey requirements and procedures.

In summary, the RASA and ARSA have achieved levels of radioanalytical capability sufficient to satisfy or exceed IMS requirements, and a process culminating in universal RASA and ARSA availability has begun.

ACKNOWLEDGEMENTS

Pacific Northwest Laboratory is operated by Battelle Memorial Institute for the US Department of Energy under Contract DE-AC06-76RLO 1830.

REFERENCES

Currie, L. Analytical Chemistry

Hubbard, C. W., McKinnon, A. D. IEEE Transactions on Nuclear Science, Vol 44, Number 3 (1997) 783-787.

McKinnon, A. D., Hubbard, C. W. IEEE Transactions on Nuclear Science, Vol 44, Number 3 (1997) 1062-1064

Bowyer, T.W., K.H. Abel, W.K. Hensley, M.E. Panisko, R.W. Perkins. Ambient Xe-133 Levels in the Northeast U.S., in print, Journal of Environmental Radioactivity (1996).

Reeder, P.L., Bowyer, T.W., and Perkins, R.W., "Beta-Gamma Counting System for Xe Fission Products", Proceedings of the Marc IV conference, paper #97-157, Kailua-Kona, Hawaii (1997).

A FLUID-BASED MEASUREMENT SYSTEM FOR AIRBORNE RADIOXENON SURVEILLANCE

B. Rooney, K. Gross, and R. Nietert
Argonne National Laboratory
and

J. Valentine and W. Russ
University of Cincinnati

Sponsored by U.S. Department of Energy
Office of Nonproliferation and National Security
Office of Research and Development
Contract No. ANL-97-248N

ABSTRACT

A new and innovative technique for concentrating heavy noble gases from the atmosphere and subsequently measuring the radioactive xenon isotopes has recently been developed at Argonne National Laboratory. The concentration technique is based on the discovery of a phenomenon where certain organic fluids absorb heavy noble gases with very high efficiency at room temperature and release the noble gases when slightly warmed (about 60°C). Research has been conducted to study the application of this technology to the design of an ultra sensitive radioxenon measurement system. Such a system could be used to monitor or sample the atmosphere for noble gas fission products (^{133}Xe , $^{133\text{m}}\text{Xe}$, and ^{135}Xe) generated by nuclear testing. A system that utilizes this fluid-based technology provides a simpler, more portable, less expensive means of concentrating xenon than current cryogenic techniques and avoids some of the complications associated with charcoal-based systems. Preliminary experiments to demonstrate the feasibility of utilizing this fluid-based technology in the design of an atmospheric radioxenon measurement have been very promising and research is continuing toward applying this technology to monitoring activities which support the Comprehensive Test Ban Treaty (CTBT).

Keywords: xenon, noble gas, radioxenon, radionuclide, CTBT

OBJECTIVE

Radionuclide monitoring technologies have become increasingly important for ensuring compliance with the Comprehensive Test Ban Treaty (CTBT). In a nuclear test, many different radionuclides are produced that are unique to the fission process. Detection of these radionuclides can positively confirm a nuclear detonation. Underground nuclear testing, however, prevents most fission products from getting into the atmosphere. In the event of an underground nuclear test, noble gas fission products emanating from the ground may be the most significant source for radionuclide monitoring. Among the noble gas radionuclides, xenon is the most abundant a few days after detonation [1,2]. By measuring the atmospheric activities of different xenon radioisotopes (^{133}Xe , $^{133\text{m}}\text{Xe}$, and ^{135}Xe) as a function of time, a nuclear detonation can be confirmed based on the ratio of these radioxenons exceeding normal ambient values. Ambient levels of radioxenon in the atmosphere are the result of nearby nuclear reactor operations. The radioxenon ratios from nuclear testing are expected to be orders of magnitude higher than ambient levels from nuclear reactors [3,4].

Significant efforts have been undertaken to design detector systems capable of monitoring airborne radioxenon [1-4]. Detection of very small quantities (or activities) requires large atmospheric samples be processed with the xenon being separated and concentrated so detection of the radioxenon using gamma-ray and X-ray spectroscopy is possible. Current technology requires using activated charcoal which has been cooled to temperatures below -70°C to separate the xenon from the atmospheric samples. Heating of the charcoal then releases the xenon gas, thus providing a means for concentrating the xenon for isotopic analysis. This procedure requires both cryogenic and heating equipment to concentrate xenon, as well as measurement instrumentation for analysis of the radioxenon. While this technique can be very effective in a laboratory or for a stationary monitoring system, it can be costly, bulky, and difficult to use in the field.

A new technique for concentrating heavy noble gases (radon and xenon) from the atmosphere has recently been developed at Argonne National Laboratory (ANL). This concentration technique is based on a phenomenon where certain organic fluids have a high affinity for absorbing heavy noble gases at room temperature. These same fluids also release the trapped noble gases when slightly warmed ($\approx 60^\circ\text{C}$) or agitated. Efforts to apply this technology in the design of an ultra sensitive radioxenon detection system have been investigated collaboratively by Argonne National Laboratory and the University of Cincinnati.

RESEARCH ACCOMPLISHED

The focus of this research has been to study the phenomenon of heavy noble gas absorption/desorption within a specific biologically benign organic fluid and to design a measurement system that integrates xenon concentration and subsequent analysis of the radioactive xenon isotopes (radioxenon). Herein, this organic fluid will be referred to as the working fluid. Public release of the specific working fluid chosen for this research is pending patent applications associated with this fluid-based technology. Applying this technology to a noble gas (xenon) measurement system offers several advantages. First, such a system has the advantage of eliminating the costly cryogenic charcoal methods for xenon concentration. In

addition, the working fluid acts only as a transfer medium, not a retention medium as in a charcoal system. Thus, the working fluid can be cycled through both absorption and degassing sections, continuously concentrating the radioxenon and providing true real time analysis. Consequently, the ability to build a low cost, compact, field deployable radioxenon measurement system using this fluid-based technology provides significant promise.

Scientific Concept

On a molecular level, the mechanism responsible for the strongly temperature-dependent noble gas absorption/desorption phenomenon in certain organic fluids is not fully understood. It is postulated that there may be a clathrate effect, wherein the heavy monatomic noble-gas atoms are being trapped in the interstitial spaces of the much larger fluid molecules. This effect is consistent with ANL's observations that the mechanism works only with the heavy noble gases (Rn, Xe, Kr) and not the lighter noble gases (He, Ne, Ar). Clathrates are known to trap only those atoms and other molecules with a range of sizes that "fit snugly" into the host's interstices. An alternative hypothesis is that there is an unknown temperature-dependent solubility phenomenon that fortuitously absorbs and releases these noble gases between the convenient temperatures of 20 and 60 °C.

Design of a Measurement System

Incorporating this fluid-based technology into an atmospheric radioxenon measurement system is currently being studied. A proposed monitoring system would involve three integrated sections; 1) an absorption section for atmospheric sampling; 2) a degassing section for concentrating the xenon; and 3) a radionuclide detector for radioxenon quantification. A possible measurement system which has been designed during the course of this investigation and which uses this fluid-based technology for radioxenon measurement is illustrated in Fig. 1.

The absorption section in Fig. 1 consists of a counter-current absorption tower. Atmospheric air is filtered for particulates and then enters the bottom of the tower flowing up across structured packing material. This structured packing material is designed to optimize the surface to volume ratio of the fluid/gas flow and increase the absorption efficiency of xenon into the working fluid. The sampled air is then vented at the top of the absorption tower back into the atmosphere. The working fluid flows in a reverse direction to that of the sampled air, entering the top of the tower, and down the packing material into a small reservoir. From the tower reservoir, the working fluid flows into the degassing section. The fluid, with trapped xenon, is preheated and pumped into a degassing unit. The degassing unit continues to heat and agitate the fluid allowing trapped xenon to vent into the detector loop. The working fluid exits the degasser and then is circulated through a cooling radiator (or heat exchanger) before flowing back into the top of the absorption tower.

The vented off-gas from the degassing section in Fig. 1 enters a closed detector loop designed to filter and quantify the concentrated radioxenon. Gas in the detector loop is continually circulated through a sub-micron filter and then through a beta/photon coincidence detector for radioxenon measurement. The filter removes any fluid vapors from the degassing section as well as removing daughter products resulting from radon being concentrated in the detector loop. The radioxenon detector continuously measures and quantifies the radioxenon flowing through the detector loop. A detailed description of the radioxenon detector is given below.

Absorption Experiments

A series of experiments has been conducted to test the absorption of xenon in the working fluid. The basic experimental arrangement for the absorption experiments is shown in Fig. 2. In these experiments, a 20 liter double lined saran bag was filled with standard air along with a known activity of radioactive ^{133}Xe . The ^{133}Xe /air mixture flowed into the bottom of the absorption tower, that consisted of a 7 cm diameter by 35 cm long cylindrical tube filled with 0.64 cm Raschig rings. The air was vented near top of the tower into the detector. The detector consisted of a flow-through chamber with a windowed gas-filled proportional counter on one side of the flow-through chamber. The calibrated proportional counter was used to monitor the ^{133}Xe activity in the flow-through chamber.

After starting the flow of the ^{133}Xe /air mixture through the tower, the count rate in the detector was allowed to stabilize. The working fluid was then introduced, flowing at a constant rate through the tower until the count rate in the detector stabilized after a few minutes. The reduction in ^{133}Xe activity at the tower outlet indicated the removal efficiency for that specific experiment. Several experiments were performed using this method with both different ^{133}Xe activities and different flow rates. A removal factor as much as a 57% was measured during these tests. The packing material height (35 cm) in the absorption tower was constrained by the height of the charcoal-filtered hood where these experiments were conducted. Using either a taller bed of packing material or multiple absorption towers should result in significantly better absorption efficiencies. This assumption is substantiated by previous experimental results by Steinberg and Manowitz where a 100 cm tall column was used for xenon absorption with over 99% of xenon being absorbed in one pass [5],[6]. Additional absorption experiments with the 35 cm tower are planned by replacing the 0.64 cm Raschig rings with a commercially manufactured structured packing material. This structured packing material is designed to optimize gas-to-liquid absorption in typical applications.

Similar experiments to those mentioned above have been accomplished to study radon absorption in the same working fluid [7]. These absorption tests with radon have included the study of introducing two contaminant gases (CO_2 and water moisture) and the associated effects on the absorption process. The presence of these additional gases was a concern for competing with the noble gas absorption phenomenon or decreasing the noble gas absorption capacity of the working fluid. However, it was found that CO_2 has no affect upon the radon removal capacity. These tests also showed only a very slight decrease in the noble gas concentration factor in the working fluid when the inlet air stream had a relative humidity of 100% [7]. Similar results are expected when the noble gas absorbed by the working fluid is xenon. These excellent findings are in sharp contrast to the behavior of conventional cryogenic charcoal concentration systems, which can be plugged and rendered inoperable by small humidity levels.

Degassing Section

When the working fluid is heated above 60 °C, it has a significantly reduced affinity for noble gas absorption and eventually releases most of the trapped xenon. This degassing effect is further promoted by agitation of the working fluid. In the proposed degassing loop, shown in Fig. 1, the working fluid from the absorption tower is first preheated. From the preheater, the fluid is directed into the degassing unit where it is further heated and agitated, resulting in the previously trapped gas (xenon) being vented and concentrated in the detector loop. After leaving

the degassing unit, the working fluid is directed through a passive cooling radiator (or a heat exchanger with the incoming fluid when minimal energy utilization is a primary functional requirement) before being recycled back into the absorption tower.

A commercially-available flow cell and sonicator (ultrasonic transducer and amplifier horn) is among other methods currently being investigated for the removal of xenon trapped in the working fluid. In this apparatus, the working fluid is forced across the tip of a 1/2 inch vibrating sonicator probe. The large amplitudes of the sonicator (120 μm) produce cavitation in the working fluid allowing the trapped gases to coalesce and rise to the surface. The use of both heat and sonication has been demonstrated to remove xenon at a faster rate than heating alone. Another potential method to be examined for heating and degassing involves the use of microwaves.

The study of the degassing phenomenon in the working fluid is ongoing. One concern in the degassing stage of this system is radon (and daughter) buildup in the detector loop. It has been shown that this fluid-based technology also effectively absorbs radon [7]. Since ambient levels of radon can exceed 10 mBq/l, buildup of radon may cause excessive background in the radioxenon detector, lowering its sensitivity to radioxenon. However, available data on the temperature-dependent solubility coefficients for radon and xenon differ for similar fluids [8]. This characteristic may be utilized to degas the majority of one constituent at a lower temperature without significantly degassing the other constituent. This procedure is called fractionation. Studies of the requirements and possible fractionation schemes are currently being evaluated for mitigating the effects of radon in the detector loop.

Radioxenon Detector

Several detector technologies are being considered for quantifying the radioxenon concentrated in the detector loop. Currently, a measurement system that utilizes both a gas-filled proportional counter and a NaI(Tl) scintillator is being investigated. This detector system, as shown in Fig. 3, consists of a flow through chamber centered between two gas-filled proportional counters and surrounded by two NaI(Tl) scintillators. The off-gas from the degasser is continuously filtered and cycled through the flow-through chamber. Signals from both the gas-filled proportional counters and NaI(Tl) scintillators are analyzed using coincidence electronics resulting in a beta/photon coincidence detector that is described in more detail below.

The radioxenons of interest, ^{133}Xe , $^{133\text{m}}\text{Xe}$, and ^{135}Xe , decay by either beta particle emission or internal electron conversion. There are also finite probabilities that each decay involves the emission of one or more photons (gamma ray or X ray) with the emitted electron. It is the energy of these photons that most effectively determines which xenon isotope was involved in the decay. Detection of these photons is accomplished by using the NaI(Tl) scintillators. However, the background associated with typical NaI(Tl) scintillators can easily obscure the valid photon data from radioxenon at very low concentrations. Therefore, it is desirable to record only those photon events in the scintillator when the associated energetic electron is also detected. Most of the scintillator background can be eliminated by using coincidence mode detection, thus permitting the ability to quantify radioxenon at much lower activities.

To detect the energetic electrons emitted by the xenon and to provide the required coincidence timing signal, gas-filled proportional counters were used. For this study, a single gas-filled proportional counter was placed on one side of the flow-through chamber. Using this configuration, detection efficiencies of 35% for ^{133}Xe were measured. Therefore, a system with

two counters should result in total detection efficiency of 70%. In addition, the proportional counter provides information on the energy deposited in the gas filled chamber. This energy information is useful for discriminating against other radionuclides that decay by emitting alpha particles. This discrimination capability may be important for minimizing the influence of radon in detector loop.

Using the signal from the proportional counter to trigger (or gate) the NaI(Tl) scintillator, results in photon interactions in the NaI(Tl) scintillator being recorded only when a valid signal is simultaneously recorded by the counter. This method of gating the NaI(Tl) scintillator eliminates most of the background associated with the detector. As much as four orders of magnitude reduction in scintillator background can be achieved with this technique. This reduction was demonstrated by using half of the system shown in Fig. 3 (i.e., one flow through chamber, one proportional counter, and one NaI(Tl) scintillator). Fig. 4 shows the pulse height spectra recorded from the NaI(Tl) detector when it was both gated by the gas-filled proportional counter and ungated. The spectra in Fig. 4 were recorded over the same time period (12 hrs). As can be seen in the ungated NaI(Tl) spectrum, the 81 keV gamma rays emitted by the decay of Xe-133 are unresolvable. However, when the scintillator is gated by the gas-filled proportional counter, both the 81 keV gamma ray and 31 keV X ray peaks are very distinct and quantifiable.

While this detector system is still being evaluated for optimal geometry and size, it is estimated that concentrations in air of 0.005 Bq/liter may be measurable. Assuming a xenon concentration factor of 1000, as compared to atmospheric levels, then airborne radioxenon concentrations down to 5 μ Bq/l should be measurable with a fluid-based measurement system.

CONCLUSIONS

Initial experiments and feasibility studies of this fluid-based technology for radioxenon measurement have been promising and research of this technology is continuing. Plans to design and test a prototype system are being pursued at Argonne National Laboratory and the University of Cincinnati. Three patents by ANL (one jointly with the University of Cincinnati) have been submitted based on this technology. A fluid-based measurement system, incorporating absorption, degassing, and concentration sections, integrated with a sensitive gamma-ray and X-ray spectroscopy detector should permit the real-time atmospheric measurement of ^{133}Xe , $^{133\text{m}}\text{Xe}$, and ^{135}Xe . As described in previous publications [3],[4], measuring elevated ratios of these xenon isotopes in the atmosphere can confirm the occurrence of a nuclear test where other methods may be inconclusive.

The fluid-based system avoids some of the limitations associated with charcoal-based systems and offers additional advantages. The simplicity and size of such a system may offer the most attractive advantages in monitoring applications which support the CTBT. As the absorption and degassing research progresses, larger concentration factors will likely be achieved, thus improving the minimum sensitivity. While experiments using proportional counter and scintillator technology for the measurement of radioxenon have been very successful, other detector types are also being considered. An optimal detection scheme will likely further reduce the minimum sensitivity. Consequently, the fluid-based technology holds much promise for providing a cost-effective radioxenon measurement system for CTBT applications.

REFERENCES

- [1] T.W. Bowyer, K.H. Abel, W.K. Hensley, C.W. Hubbard, A.D. McKinnon, M.E. Panisko, R.W. Perkins, P.L. Reeder, R.C. Thompson, R.A. Warner, "Automatic Radioxenon Analyzer for CTBT Monitoring," *PNNL-11424, UC-713*, Dec. 1996.
- [2] T.W. Bowyer, K.H. Abel, W.K. Hensley, C.W. Hubbard, A.D. McKinnon, M.E. Panisko, R.W. Perkins, P.L. Reeder, R.C. Thompson, R.A. Warner, "Automatic Radioxenon Analyzer for CTBT Monitoring," *PL-TR-96-2153*, p. 834, Sept. 1996.
- [3] R.W. Perkins, H.S. Miley, and W.K. Hensley, "DOE Radionuclide Monitoring Systems for CTBT Verification," *PL-TR-95-2108*, p. 984, Aug. 1995.
- [4] R.W. Perkins, L. Casey, "Radioxenons: Their Role in Monitoring a Comprehensive Test Ban Treaty," *DOE/RL-96-51*, Jun. 1996.
- [5] M. Steinberg and B. Manowitz, "An Absorption Process for Recovery of Fission Product Noble Gases," *BNL 493 (T-115)*, Feb. 1958.
- [6] M. Steinberg and B. Manowitz, "Recovery of Fission Product Noble Gases," *Ind. and Eng. Chem.*, vol. 51, pp. 47-50, 1959.
- [7] K.V. Liu, J.D. Gabor, R.E. Holtz, and K.C. Gross, "Fluid-Based Radon Mitigation Technology Development for Industrial Applications," *Proc. 1996 Chinese American Academic and Professional Conference.*, Ottawa, Canada (June 29 - July 2, 1996).
- [8] H. Lawrence Clever, "Solubility Data Series; Vol 2: Krypton, Xenon and Radon Gas Solubilities," Pergamon Press, 1979.

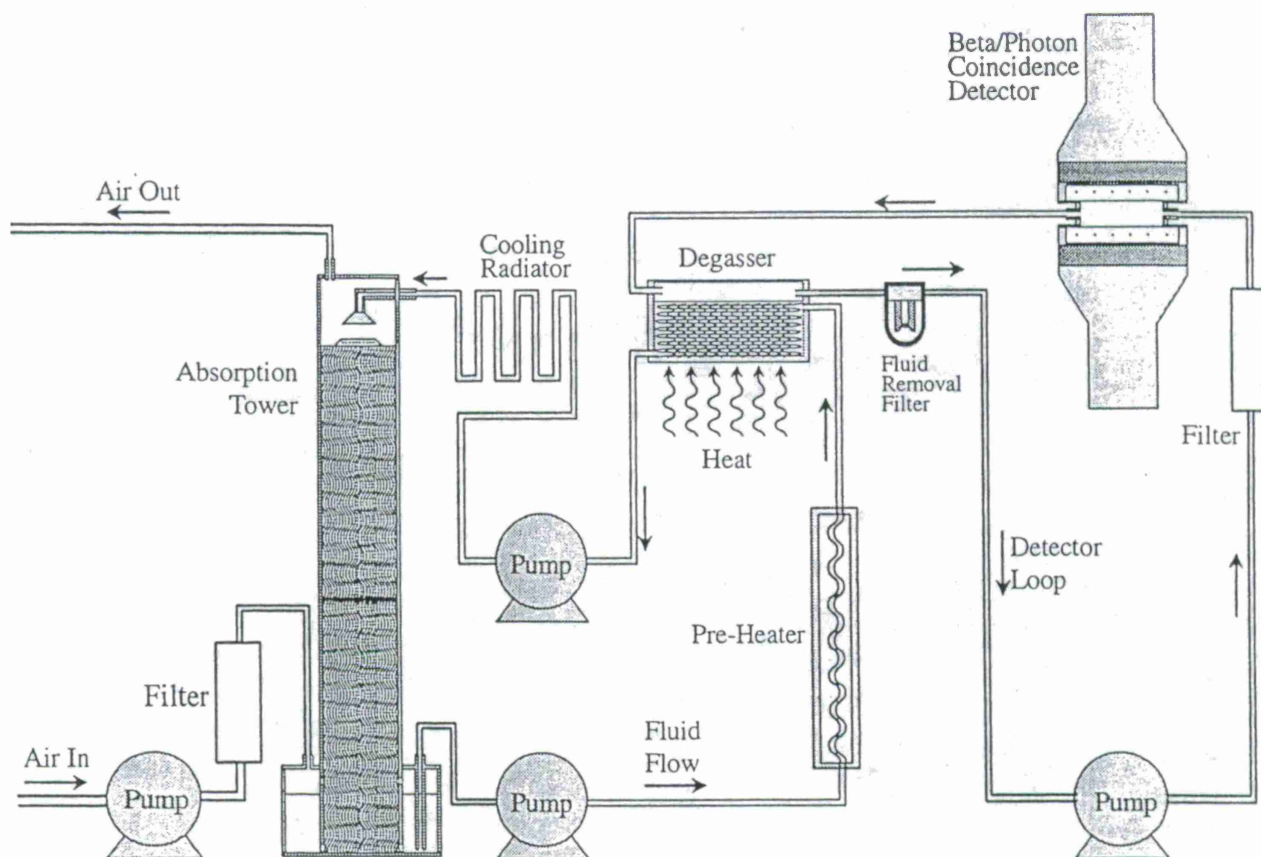


Fig. 1. Diagram showing an airborne radioxenon measurement system utilizing fluid-based noble gas absorption technology.

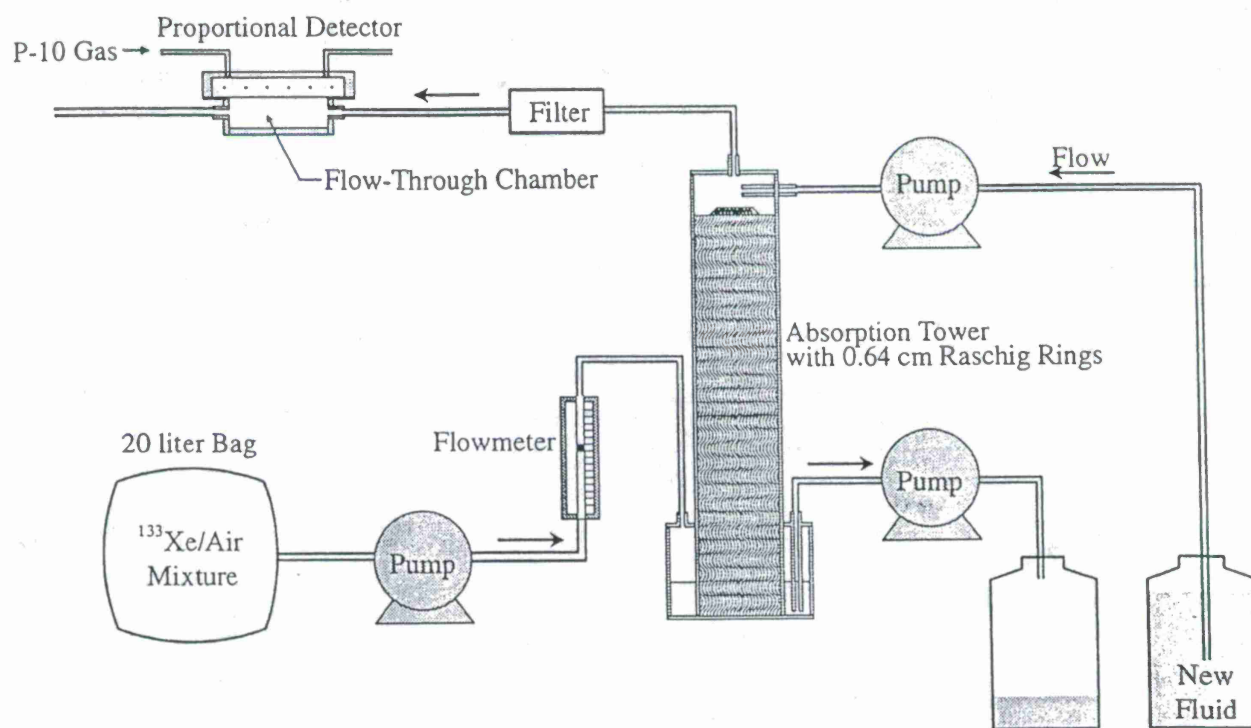


Fig. 2. Experimental apparatus used to test the absorption of xenon in a fluid-based system.

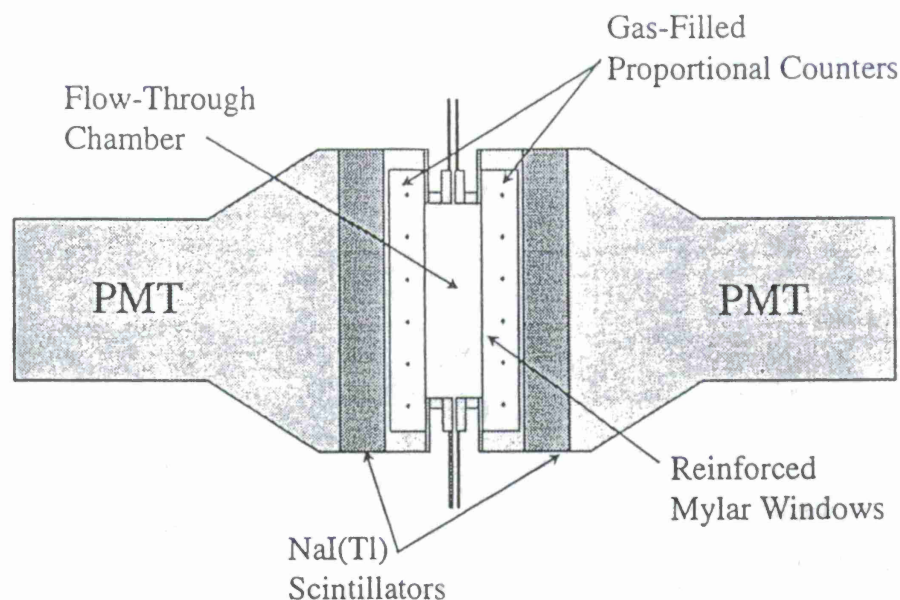


Fig. 3. Radioxenon spectroscopy detector utilizing gas-filled proportional counters, NaI(Tl) scintillators, and coincidence electronics.

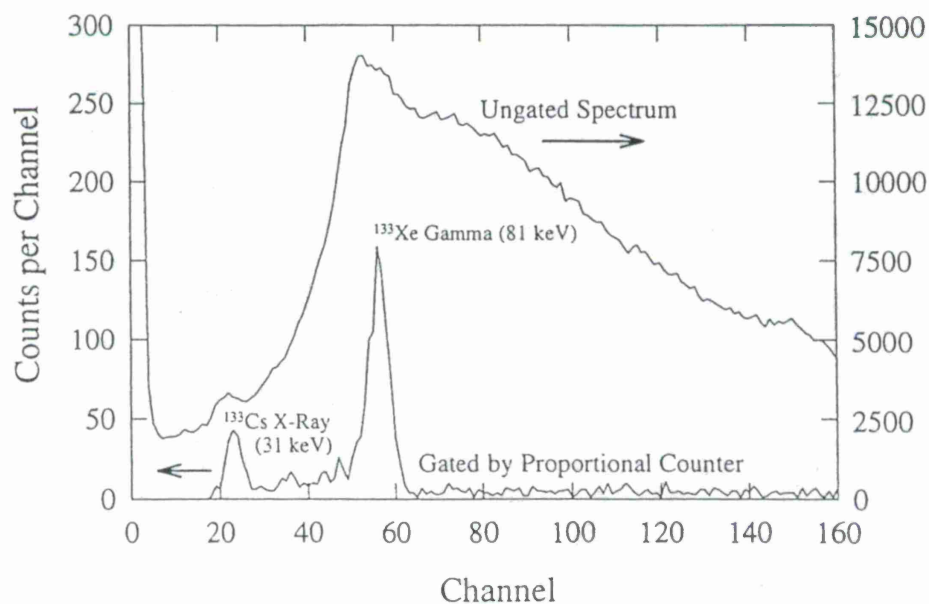


Fig. 4. Photon spectra from a NaI(Tl) scintillator with ^{133}Xe . The upper (ungated) spectrum was recorded without using the coincidence signals from the proportional counter. The lower spectrum was recorded using the proportional detector to gate the NaI(Tl) scintillator.

EVALUATION OF A PROTOTYPE INFRASOUND SYSTEM

Rod Whitaker
Tom Sandoval (Contractor)
Los Alamos National Laboratory
Contract # W7405-ENG-36

Dale Breeding, Dick Kromer
Tim McDonald (Contractor)
Sandia National Laboratories

Sponsored by U.S. Department of Energy
Office of Nonproliferation and National Security
Office of Research and Development
Contract DE-AC04-94AL85000

ABSTRACT

Under Department of Energy sponsorship, Sandia National Laboratories and Los Alamos National Laboratory cooperated to develop a prototype infrasonic array, with associated documentation, that could be used as part of the International Monitoring System. The United States Government or foreign countries could procure commercially available systems based on this prototype to fulfill their Comprehensive Test Treaty (CTBT) obligations. The prototype is a four-element array in a triangular layout as recommended in CD/NTB/WP.224 with an element at each corner and one in the center. The prototype test configuration utilize an array spacing of 1 km.

The prototype infrasound system has the following objectives:

- Provide a prototype that reliably acquires and transmits near real-time infrasonic data to facilitate the rapid location and identification of atmospheric events.
- Provide documentation that could be used by the United States and foreign countries to procure infrasound systems commercially to fulfill their CTBT responsibilities.

Infrasonic monitoring is an effective, low cost technology for detecting atmospheric explosions. The low frequency components of explosion signals propagate to long ranges (few thousand kilometers) where they can be detected with an array of sensors.

Los Alamos National Laboratory's expertise in infrasound systems and phenomenology when combined with Sandia's expertise in providing verification quality systems for treaty monitoring make an excellent team to provide the prototype infrasound sensor system.

By September 1997, the prototype infrasound system will have been procured, integrated, evaluated and documented. Final documentation will include a system requirements document, an evaluation report and a hardware design document. The hardware design document will describe the various hardware components used in the infrasound prototype and their interrelationships. Final versions of all documents should be available from the bibliography on the CTBT R&D web site, URL:
<http://www.ctbt.rnd.doe.gov/>

Sandia is a multiprogram laboratory operated by Sandia Corporation, a Lockheed Martin Company, for the United States Department of Energy.

OBJECTIVE:

The prototype infrasound system has the following objectives:

- Provide a prototype that reliably acquires and transmits near real-time infrasonic data to facilitate the rapid location and identification of atmospheric events.
- Provide documentation that could be used by the United States and foreign countries to procure infrasound systems commercially to fulfill their CTBT responsibilities.

RESEARCH ACCOMPLISHED

Background

Sandia and Los Alamos initially held several technical interchange meetings to define programmatic responsibilities for the development of the prototype infrasound system. They jointly developed the "Program Plan for the Infrasound Prototype Development" and "System Requirements for the Infrasound Prototype," and received comments on the plan and requirements at a technical interchange meeting with Air Force Technical Applications Center on April 12, 1996.

Several hardware options were developed that could satisfy the requirements. The Department of Energy held a design review May 22, 1996 to discuss the hardware options for the prototype. Based on discussions during and after the review, the decision was made to bid the data acquisition system. A request for proposals was distributed to potential suppliers in July. After reviewing the two bids received, a contract was awarded for the data acquisition system in September 1996. The data acquisition system was delivered in early May.

Prototype Features

A block diagram of the infrasound prototype is shown in Figure 1.

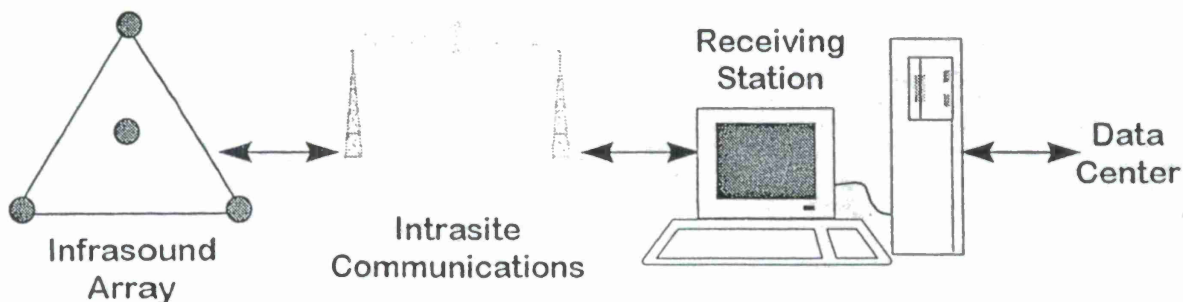


FIGURE 1. BLOCK DIAGRAM OF THE INFRASOUND PROTOTYPE

The triangular array layout was recommended in the Conference on Disarmament/Ad Hoc Committee on a Nuclear Test Ban/Working Paper 224 and 283. The infrasound array elements are located in a triangle (one at each corner and one in the center). The prototype spacing will be 1 km on a side, however, the Conference on Disarmament working papers provide for an optional spacing up to 3 km.

A block diagram of the components that make up the infrasound prototype is shown in Figure 2.

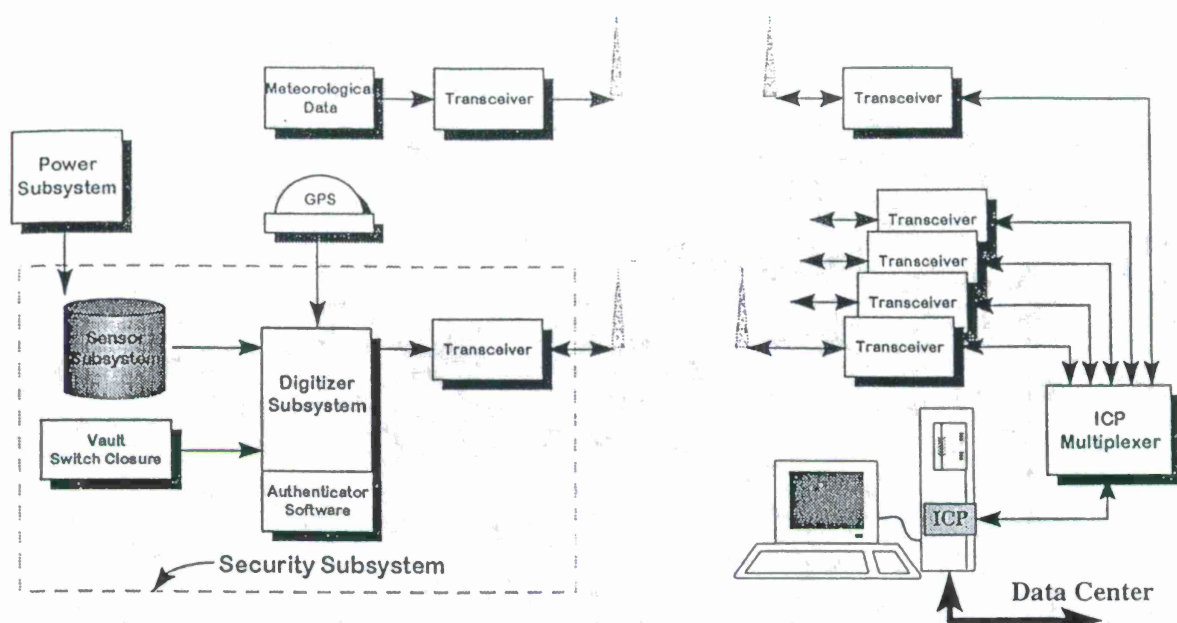


FIGURE 2. DETAILED BLOCK DIAGRAM OF THE INFRASOUND PROTOTYPE

The physical layout at an array element is shown in Figure 3.

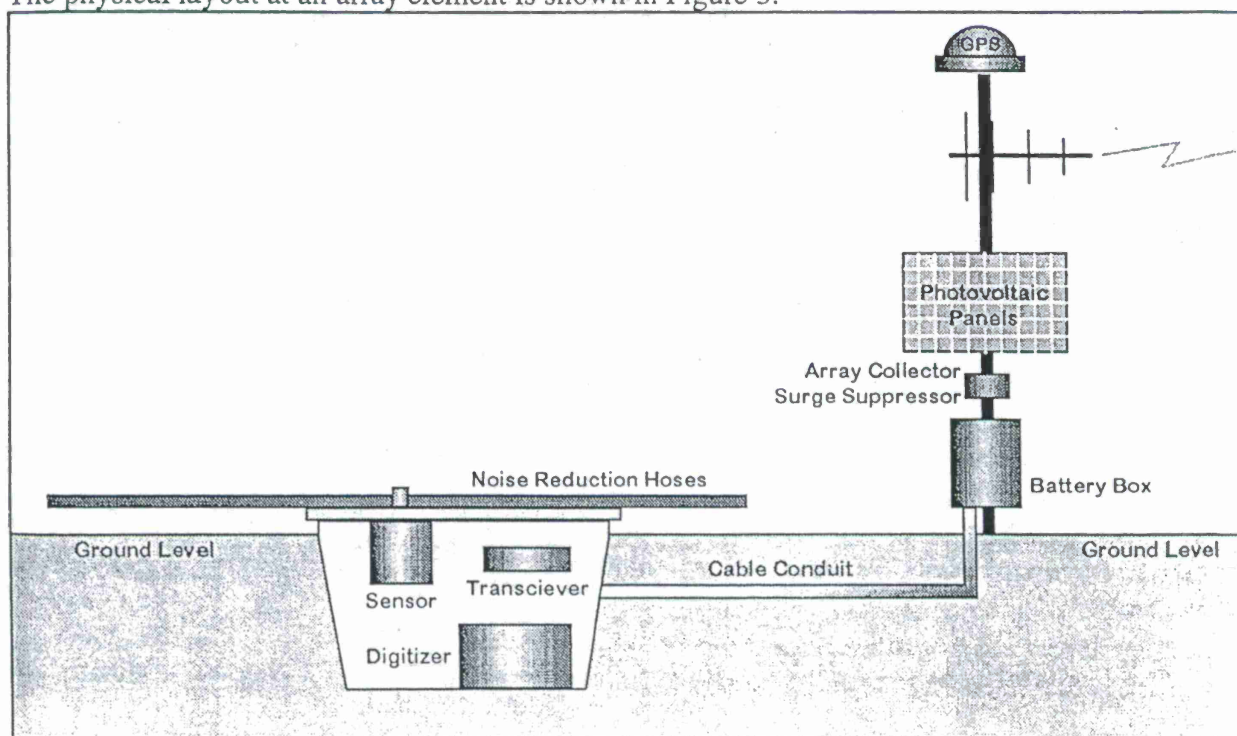


FIGURE 3. LAYOUT OF AN ARRAY ELEMENT

Sensors

The prototype infrasound sensor (Figure 4) is a microbarograph model 4.11 from Chaparral Physics Inc., Albuquerque, NM. Chaparral Physics re-packaged the sensor to accommodate the

infrasound prototype data surety features. The microbarograph can be calibrated remotely with a step function to verify the sensor electronics response and to confirm system operation.

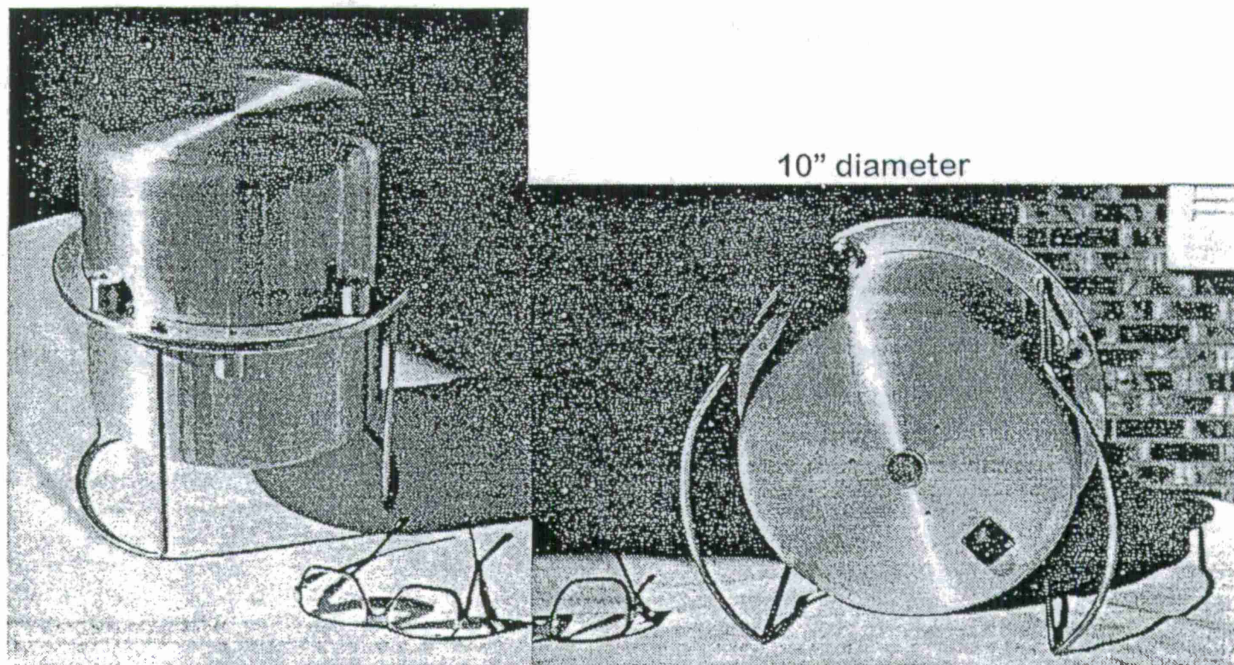


FIGURE 4. PHOTOGRAPHS OF THE MICROBAROGRAPH

Los Alamos calibrates the microbarograph utilizing a piston phone calibration chamber to:

- Set the calibration constant to 0.04 volts per μ Bars (0.004 volts/Pa) at the low gain setting.
- Verify a flat response over the frequency range from 0.16 to 4.0 Hz.

In addition, Sandia has performed side-by-side sensor coherence testing to determine the broadband sensor noise, sensor dynamic range, and relative amplitude & phase between sensors. Testing shows that the sensor self noise is down better than 80 dB from clip @ 1.0 Hz.

Complete results of the sensor testing will be presented at the symposium.

System and Data Surety

The prototype data surety features are provided by a two fold thrust: authentication and tamper protection.

- Data authentication is performed in software in the digitizer utilizing a Digital Signature Algorithm furnished by Sandia. Sandia obtained data from the vendor and has validated the signature.
- Tamper protection is provided by both active and passive indicators on the enclosure housing the sensor and digitizer. An active switch closure signal is transmitted with the data to the National Data Center. The passive indicator is a seal on the enclosure. During maintenance, personnel can determine whether the enclosure seal has been broken.

Complete results of the system and data surety testing will be presented at the symposium.

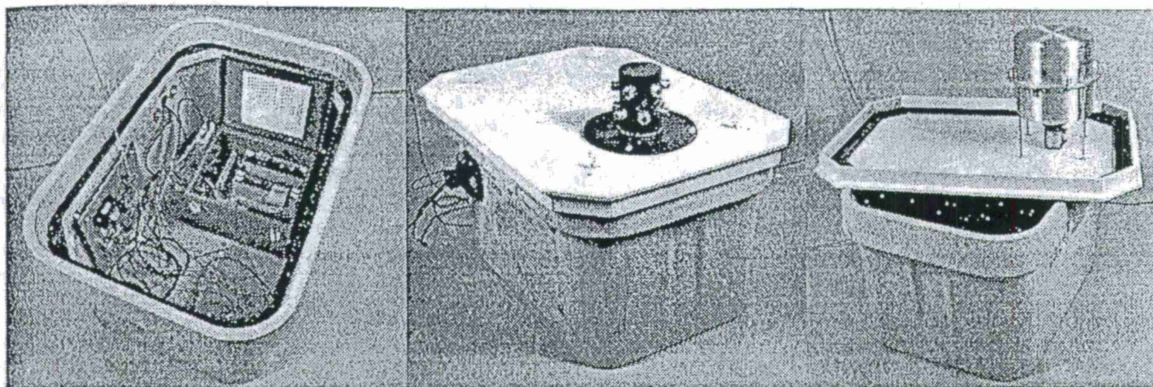


FIGURE 5. THREE VIEWS OF THE ARRAY ELEMENT ENCLOSURE

Figure 5 shows three views of the array element enclosure. Once buried (as in Figure 3) the enclosure (center, above) accommodates both active and passive tamper protection. The noise reduction hoses connect to the manifold shown on the top. The sensor (right) mounts to the bottom of the cover. The enclosure with the top removed is shown on left.

Data Acquisition System

The Data Acquisition System (Figure 6) consists of the digitizer, intrasite communications, and a host processing system. These components are commercially available from Geophysical Services and Products (GSP). Their subcontractor is Teledyne Brown/Geotech Instruments.

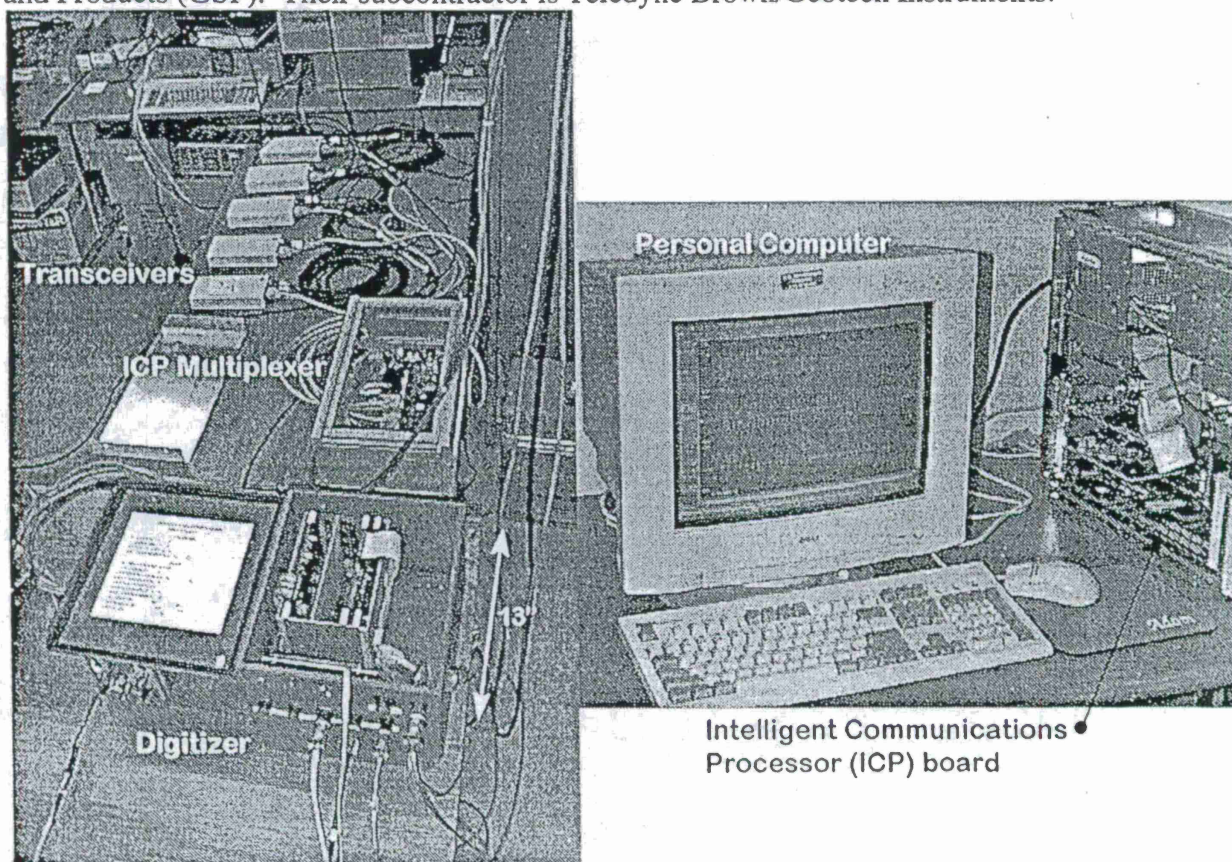


FIGURE 6. PHOTOGRAPHS OF THE DATA ACQUISITION SYSTEM

Testing indicates that the digitizer meets or exceeds requirements. Some salient features include a:

- Dynamic range measured at better than 120 dB.
- Resolution measured at better than 20 bits.
- Bandpass measured from DC to 4 Hz at 10 sps.
- Accuracy measured to better than 1%.
- GPS timing accuracy measured to better than 1 ms.

Complete results of the data acquisition system will be presented at the symposium.

The primary features of the infrasound prototype data processing system have been demonstrated. These include:

- Storing data in the CSS 3.0 flat file format as verified by Los Alamos.
- Authenticating the Alpha protocol as verified by Sandia.
- Transmitting the infrasound data in the Alpha protocol as verified by the National Data Center.

CONCLUSIONS AND RECCOMENDATIONS

Test and evaluation of the prototype infrasound system should be completed by the end of July 1997. Final versions of all prototype documentation will be available on the DOE CTBT R&D web site, URL: <http://www.ctbt.rnd.doe.gov/>.

Technical Reports

- LANL, SNL, *Program Plan for the Infrasound Prototype Development*, SNL-CTBT-0001, dated 8/12/96
- LANL, SNL, *System Requirements Document for the Infrasound Prototype*, SNL-CTBT-0002, dated 8/16/96
- LANL, SNL, *System Test Plan for the Infrasound Prototype*, dated 7/31/97
- LANL, SNL, *Test Procedures for the Infrasound Prototype*, dated 7/31/97
- LANL, SNL, *Evaluation of the Infrasound Prototype*, dated 8/15/97
- LANL, SNL, *Hardware Design Document for the Infrasound Prototype*, dated 8/15/97

The Hardware Design Document identifies all hardware components in the prototype. Commercial components are listed by quantity, manufacturer, and part number. Modifications to commercial components are also included in the listing. If alternate components are recommended, they are also identified in the listing. Non-commercial components (cables, etc.), manufactured locally, are identified with drawing number. All drawings are included in the document.

Distribution of International Monitoring System Data to the General Research Community

Tim Ahern, Incorporated Research Institutions for Seismology
Tom McSweeney, Incorporated Research Institutions for Seismology
NSF EAR - 9529992

Sponsored by National Science Foundation

ABSTRACT

With the signing of the Comprehensive Test Ban Treaty, and the installation of several high quality state-of-the-art seismic networks to monitor CTBT compliance, the seismological research community is about to gain access to an enormous amount of seismological data. In 1995 the Advanced Research Projects Agency (ARPA) commissioned the National Research Council to address issues associated with establishing an International Seismic Monitoring System for monitoring a CTBT. Among its various recommendations was the recommendation that the data would best be distributed to the wider seismological community through the IRIS Data Management Center working closely with the US National Data Center at Patrick Air Force Base (AFTAC).

Driven primarily by the broader research community's interest in gaining access to the ISMS data, IRIS installed computer and communications equipment at the US NDC in January, 1997 enabling the IRIS DMC to receive data from stations reporting to the US NDC essentially in real time. At the US NDC, IRIS placed an Ultrasparc and a 9 gigabyte disk to provide local buffering. The UNIX workstation is connected to a Cisco router and a 256 kilobit/second Frame Relay Circuit that connects AFTAC with the IRIS DMC. At the DMC, data are received by an Ultrasparc 2 workstation with 100 gigabytes of disk buffer. All data communication between AFTAC and IRIS is performed using alpha protocol as used by the ISMS. AFTAC is running AlphaSend processes and IRIS has developed its own Alpha Connection manager to receive the data.

At the DMC, data are buffered, sorted, infinite velocity stacks for the vertical array elements are formed, data are converted to SEED format and then archived in a manner identical to how the IRIS DMC archives data from the IRIS GSN and PASSCAL programs. All standard request mechanisms at the DMC will be able to provide access to the ISMS data. Data from individual array elements will only be made available as network day volumes in SEED format.

This poster will summarize the current status of the project to provide data from the ISMS through a cooperative project between the US NDC at AFTAC and the IRIS Data Management Center.

Key Words: Data Distribution, ISMS, CTBT, Communications Circuits, Frame Relay, SEED, Alpha Format

The recent signing of the Comprehensive Test Ban Treaty offers an unprecedented opportunity for a large amount of data to be made available to the seismological research community. In the ISMS structure, National Data Centers (NDCs) in a host country act as data concentration points for all seismic data collected within that country. The NDCs will forward all data to the International Data Center (IDC) that is being established in Vienna, Austria. The IDC will provide all requested data back to any NDC. For individual researchers or organizations access to the data will be provided by the NDC located in the country where the data requester lives. In the United States the National Data Center is AFTAC located at Patrick Air Force Base, Florida.

A 1995 NRC study commissioned by ARPA studied various aspects of the "Seismological Research Requirements for a Comprehensive Test-Ban Monitoring System". Among the issues studied was the preferred method of distributing data within the United States. The recommendation of the NRC study was that all ISMS data received at the US NDC "should be archived in and made accessible on various media through the Incorporated Research Institutions for Seismology's Data Management System". IRIS began working with AFTAC in 1996 to develop this capability. At the present time, the system is in development and a limited amount of data are routinely arriving from AFTAC operated stations and arrays at the IRIS DMC in real time.

The ISMS Data Sources

The current ISMS network consists of 135 primary and auxiliary stations and arrays. The Primary Network consists of stations and arrays that are connected to the IDC with continuous real time telemetry links. These data are augmented by an auxiliary network of stations accessed by the Internet or by dial-up as needed. Figure 1 shows the primary network from which AFTAC has agreed to supply data to the IRIS DMC. The primary network currently consists of 42 3-component stations and 15 arrays.

Figure 2 shows the current auxiliary network that is operating as part of the ISMS network. This network consists of 76 3-component stations and 2 arrays. The majority of the auxiliary stations are operated as part of the IRIS GSN or by members of the Federation of Digital Seismographic Networks (FDSN). The IRIS DMC is the FDSN Data Center for continuous data and as such receives much of this data after it has been quality controlled but with a delay of weeks to sometimes months. The ISMS data will be used to meet real time needs of IRIS DMC data requesters. When quality controlled data for these stations are received through normal IRIS/FDSN channels the quality controlled data will be distributed unless otherwise requested.

After compression, we estimate that the data from the ISMS data sources will generate about 5 terabytes per year of new data flowing into the IRIS DMC. This is a very significant amount of seismic data and represents roughly twice as much data as the IRIS DMC archived from all sources in 1996. We do not anticipate reaching this data volume for another few years however giving the IRIS DMC time to develop the infrastructure to increase the archiving capacity.

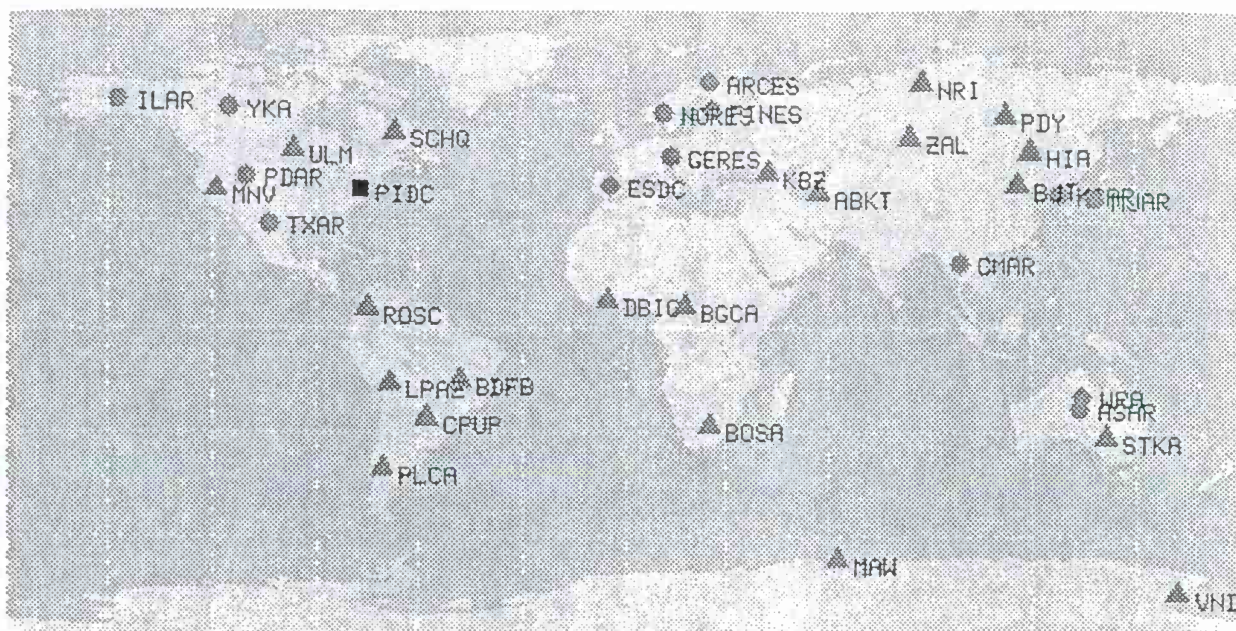


Figure 1. The ISMS Primary Network. Arrays are designated as circles and 3-component stations as triangles. (Figure reproduced from WWW pages of Prototype IDC).

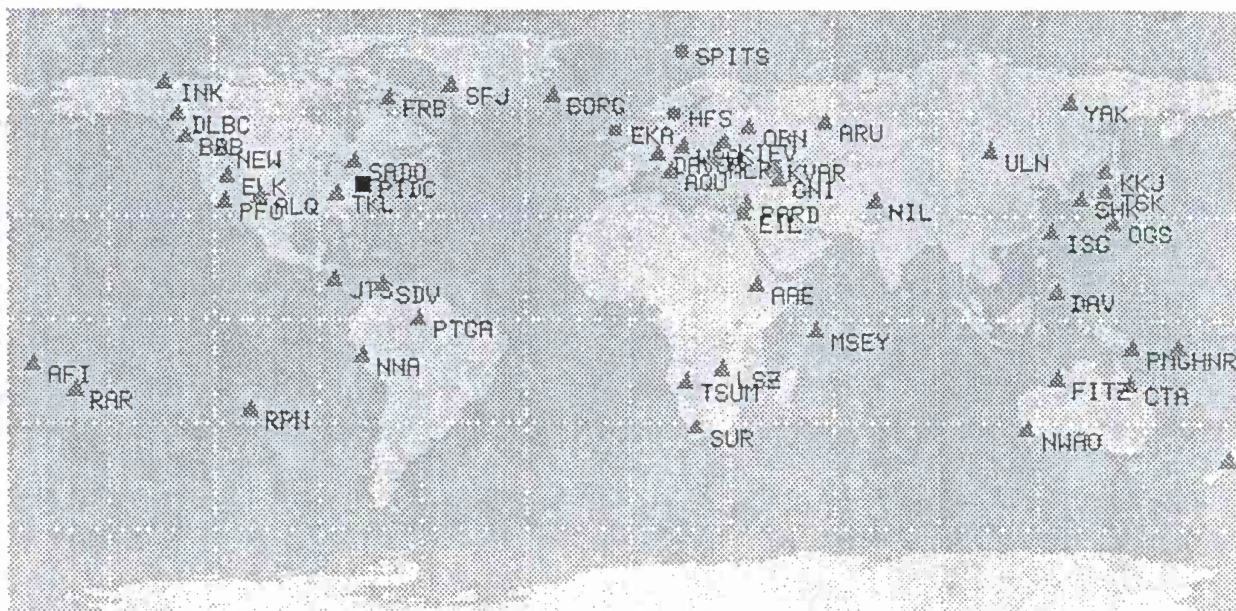


Figure 2. The Auxiliary Network of the ISMS is shown on this figure. It consisted of 76 3-Component stations (represented by triangles) and 2 Arrays (represented by circles). Auxiliary stations are accessed as needed by the IDC to characterize events detected by the Primary Seismic Network. (Figure reproduced from WWW pages of Prototype IDC)

The Anticipated Data Volume

At the present time we anticipate that there will be a total of 1.8 terabytes of new data flowing to the IRIS DMC from the existing ISMS stations. This is after compression using standard Stein compression algorithms. By new data we mean data from stations not presently arriving at the DMC through another data path.

Plans for the ISMS arrays and stations are nearly finalized and figure 3 shows the locations of current and proposed stations. AFTAC has estimated the data volume will be about 15 terabytes per year before compression and based upon our experience we believe that this volume will reduce to about 5 terabytes/year after standard compression schemes used at the DMC. We have built a system capable of archiving data at that rate. Of course the majority of these data are data from individual array elements and these data will be handled differently to minimize the impact upon our mass storage systems. The data volume estimates have been made assuming roughly 50 continuously recording arrays and roughly 100 auxiliary stations, half of which the IRIS DMC receives via alternative paths.

We anticipate data flow from the ISMS will be roughly equal to the data flow from all other IRIS DMC sources. This means that the DMC is well within its capability to handle this increased data flow.

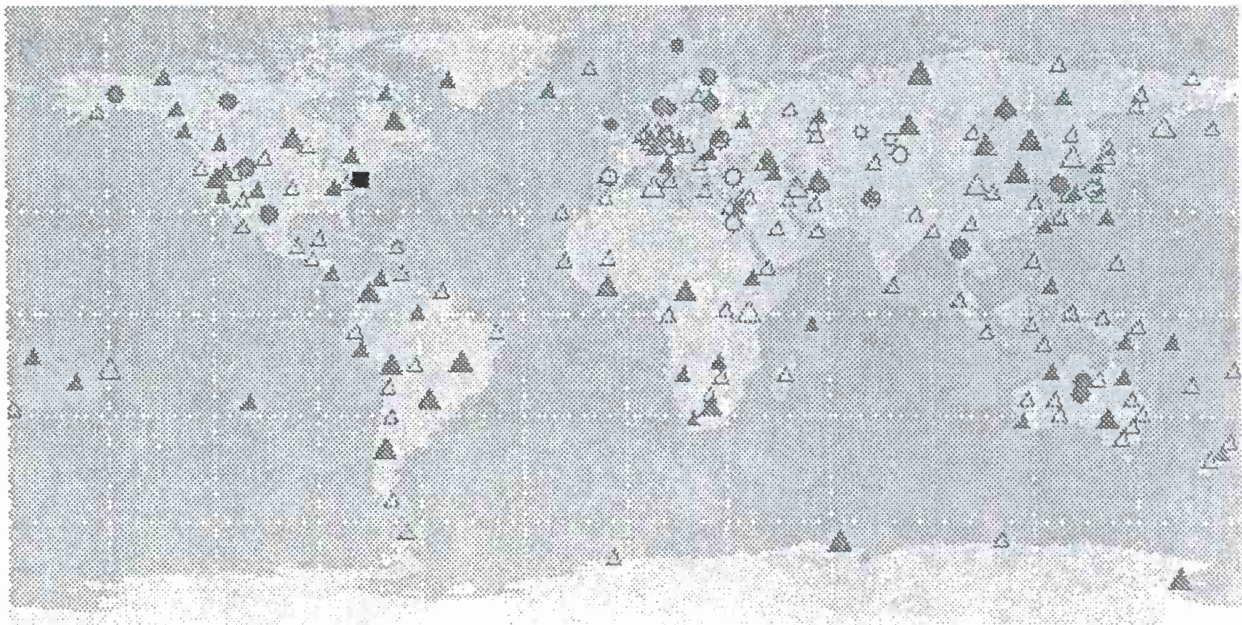


Figure 3. This figure shows existing (Closed Symbols) arrays (circles) and 3-component stations (triangles) from both the primary and auxiliary seismic networks. The primary network elements are shown as slightly larger symbols. This figure was reproduced from the WWW pages at the Prototype International Data Center at the Center for Monitoring Research.

The IRIS Plan for Data Archiving and Distribution

In the United States, the NDC is operated by AFTAC at Patrick Air Force Base. AFTAC is working with IRIS to provide data to the general research community through the IRIS Data Management Center (DMC) in Seattle, Washington. IRIS has requested all data from all elements for all arrays and three component stations generated by the ISMS. IRIS will transmit the data from AFTAC to Seattle over a dedicated Frame Relay communications circuit using the alpha protocol developed for the IMS.

When these data are received in Seattle, they will be temporarily buffered in a 100 gigabyte disk buffer and within a few minutes translated from Alpha format to miniSEED format and left in another buffer. These disk buffers are large enough to hold about one month of data at current data rates. After a few weeks, the data will be removed from the 100 gigabyte buffer and moved into the main IRIS DMC archive systems, presently a METRUM RSS-48 with a near-line capacity of 1 terabyte and an off-line capacity exceeding several petabytes. Ultimately we hope to migrate the data into a new mass storage system with a capacity of several tens of terabytes (50 tbyte - 75 tbyte) in a fashion that is identical to the way in which we archive IRIS GSN, IRIS PASSCAL and FDSN data. All data will be stored in SEED format and identical database structures to those for the GSN and PASSCAL sources will be used to store the metadata related to the ISMS data.

To begin the development of the software required, AFTAC has begun sending data from four sources in real time. Figure 4 shows the locations of these data sources. At the present time only data from US sources are being transmitted as protocol issues within the IMS are resolved. The present four stations provide significant variety in the types of data and problems that can exist. Two of the data sources are arrays and will allow us to develop the beam forming software and conversion to SEED, Wake Island provides hydrophone data and Attu is a broadband 3-component station.

Our initial experience with these data indicate that delays through the entire system are very acceptable. Data from TXAR are received with a typical delay of 50 seconds, Pinedale in about 3 minutes, Wake Island in about 30 seconds and Attu is significantly delayed by more than eight minutes. We believe many of the delays are understandable in terms of times necessary to fill buffers.

We anticipate eventually receiving all data from all ISMS primary stations in real time from the NDC. As mentioned data from the 3 component stations will be handled in the same manner as we handle existing IRIS GSN data. Arrays will be beam formed into a single beam looking directly under the station to improve signal to noise ratios. All array element data will be stored as individual time series in SEED format and available as assembled SEED volumes for an entire array day. Depending on future request patterns we may alter the manner in which we handle all types of ISMS data, paying particular attention to the voluminous individual array elements.

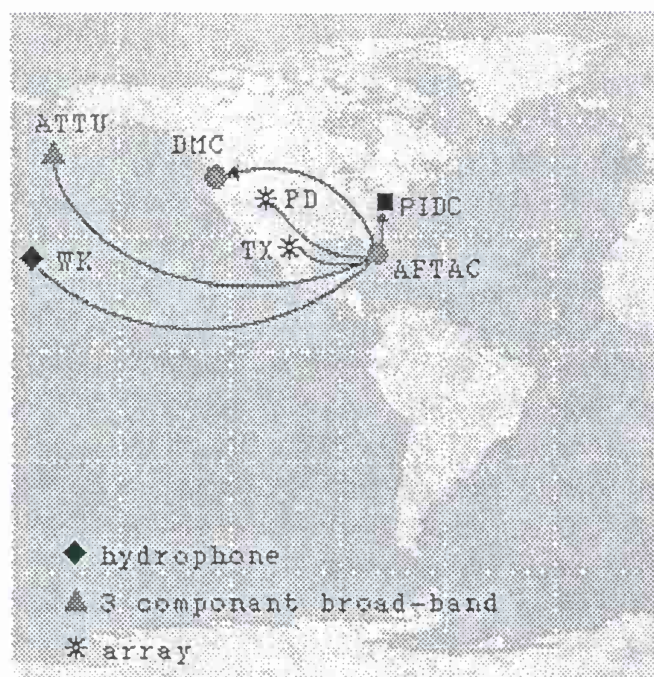


Figure 4. This figure shows the four locations the IRIS DMC is receiving from AFTAC in real time for development of the data distribution system. AFTAC forwards these data to the Prototype IDC in Arlington, VA as well as forwarding them to the IRIS DMC in real time over the dedicated Frame Relay circuit.

At the present time (7/97) the ISMS consists of 135 stations and arrays. Data from the Primary seismic network are telemetered in real time to the International Data Center. Currently there are 15 primary arrays and 42 primary 3 component stations. As needed, auxiliary stations are contacted and waveform segments extracted to further characterize events detected by the primary network. At the present time there are 76 auxiliary 3 component stations and 2 auxiliary seismic arrays. We would hope to have data from these existing stations flowing routinely to the DMC by the end of this year.

We wish to express our appreciation to Mr. Bruce Varnum, Director of the US NDC, and Dr. Ellen Herron for their cooperation in establishing the initial capability between IRIS and AFTAC. Assistance from Tad Glines and Jon Sessions has also been very useful. We would also like to thank Mr. Richard Baumstark and Rick Braman for their technical assistance in this project. A final thanks to Dr. Steve Bratt of ARPA who has made available necessary software to transmit and handle data in Alpha format.

OBJECTIVE: Access to the ISMS data in a flexible and well known manner is of great interest to a very large portion of the academic community as well as others. By merging the ISMS data set into the data from the IRIS and FDSN Broadband networks, the power of the IRIS DMC archive to address many different types of problems related to nuclear test monitoring as well as other scientifically interesting problems is increased. Our goal is to provide data from as many high quality seismic networks as possible in a timely and efficient manner.

RESEARCH ACCOMPLISHED: It is not the objective of IRIS to do research, rather it is our mission to develop the infrastructure to allow others to improve efficiency in gaining access to a variety of different data sources. This project should facilitate a considerable amount of research to be accomplished both within the defense community and the academic research community.

CONCLUSIONS AND RECOMMENDATIONS: With the cooperation of AFTAC it is clear that IRIS can effectively acquire, archive and distribute data from the ISMS networks. We would recommend continued close cooperation between the Defense community and IRIS to coordinate activities in data distribution.

FISSURES - A New Approach in Software Development

Tim Ahern, Incorporated Research Institutions for Seismology
Ken Creager, University of Washington

NSF EAR - 9529992

Sponsored by National Science Foundation

ABSTRACT

In the IRIS 2000 proposal to the NSF, the IRIS Data Management System (DMS), proposed to develop a software framework to assist the research community in fully utilizing the large amounts of seismic data now available from a variety of sources. To initiate discussion the Framework for Integration of Scientific Software for University Research in Earth Sciences (FISSURES) workshop was held in May, 1997 in Chicago and was attended by 49 people. Approximately forty of these were seismologists. The workshop was attended by members of the academic community, Department of Defense, Department of Energy, Department of the Interior, international organizations as well as representatives from the non-profit and for-profit software industries.

Following the FISSURES workshop, a Special Interest Group, SIG, was held during the IRIS Workshop in Breckenridge, Colorado in early June. The SIG was attended by about 70 people. The results of the FISSURES workshop were summarized and recommendations as to how to proceed with the FISSURES development resulted. The majority of attendees at the SIG felt that the basic concepts of the FISSURES initiative should be pursued by IRIS.

This poster will summarize the present thinking concerning the FISSURES development. Several key features of the design process are to move software development to an object oriented framework and as such invoke a "paradigm shift" in software development in the academic seismological community. Great interest in developing new code in JAVA was expressed. This system must preserve the existing applications (legacy applications) since they are widely used within the seismological research community. The Common Object Request Broker Architecture (CORBA) is a commercially available approach that allows one to enclose existing applications within "object wrappers" and make them appear as objects. A primary design goal is to provide interoperability such that researchers can transition between a variety of applications in a seamless and productive manner.

It was felt that the heart of FISSURES would be a database schema built upon the CSS3.0 model. IRIS wishes to work with its colleagues in the Departments of Defense and Energy to develop a cohesive software framework that is beneficial to all.

Key Words: Software, Interoperability, Software Frameworks, Object Oriented, CORBA, JAVA

The Framework for Integration of Scientific Software for University Research in Earth Sciences (FISSURES) is an initiative by IRIS to help coordinate the development of software for the seismological community. If successful FISSURES will help existing applications communicate with other existing tools as well as initiate a new paradigm for future software development.

Figure 1 shows a diagram of the FISSURES tree that helps identify various components of the FISSURES structure and how they relate. This tree serves as a reference model for the concepts that are being discussed within FISSURES. The leaves of the tree represent the applications, the roots contain information and waveforms in database tables. Information flows from the leaves to the roots through the trunk of the tree and information can flow directly between applications through the limbs and branches as well. The various components of the tree are self contained objects that communicate through messages.

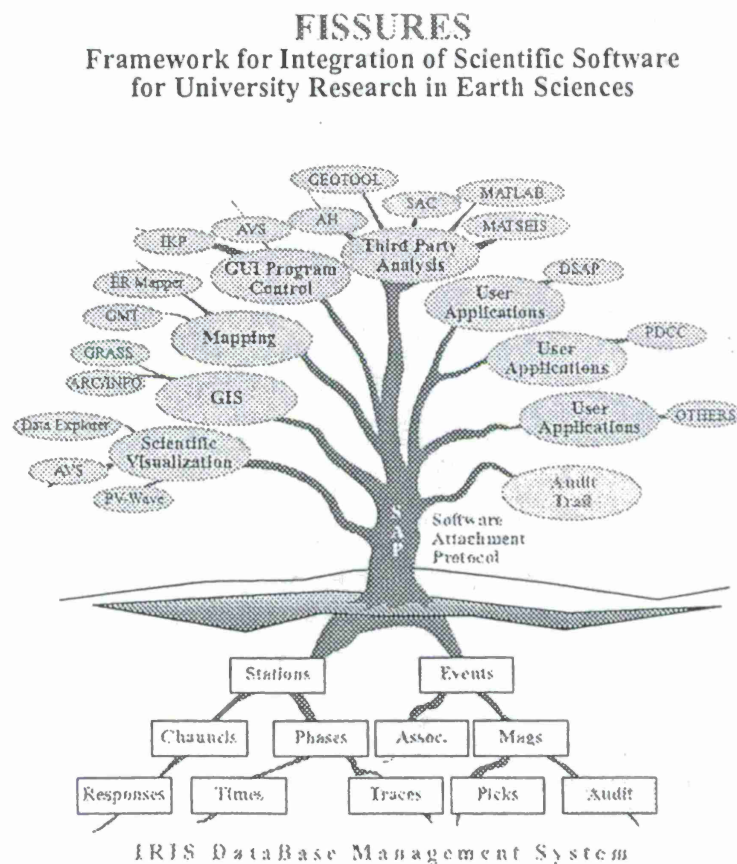


Figure 1. The FISSURES Tree. This diagram shows the various components of the FISSURES tree and how the components relate to each other. Obviously the database tables are fictitious.

The method of attaching new applications was dubbed the Software Attachment Protocol (SAP) is an essential ingredient of the model and at the time of the first FISSURES workshop it was not well defined. We now believe that an Object Request Broker method would be applicable.

At the present time there are several areas where there is general agreement concerning the following topics addressed by FISSURES.

- The community needs a way to interconnect applications so that information can flow easily between applications and between database tables and applications. For instance processing done in one application, such as SAC, could move to another application such as MATSEIS and back again, freely exchanging parametric information and waveform data. In other words applications need to be made INTEROPERABLE.
- A database management system (DBMS) approach should be used. Further there was general agreement that the CSS3.0 schema provides the obvious starting point for the needed schema. It was generally believed that the CSS3.0 schema would need some minor modification but would certainly serve as the best starting point.
- It was felt that the solution must be future-proofed. Although this is a motherhood concept, the implication is that to every extent possible the FISSURES framework should use industry standards so that, when needed, new modules can replace obsolete software with a minimum of effort. The concept of component-ware discussed by several industry representatives addressed this need.
- There was general agreement that modern computing practices had passed most of the seismological community by. Seismologists are still primarily FORTRAN programmers and the seismological programming gurus are C programmers. Clearly industry has moved from such languages to object oriented approaches such as C++ and more recently JAVA. There was a general feeling that getting some "expert" help to look at our problem would be useful and perhaps the expertise to develop the framework does not exist within the seismology community.
- Industry experts indicated that it would be possible to build "wrappers" around existing applications in order to make them appear to be "objects". This should allow existing applications to be moved into an object oriented framework in relatively short order. Estimates as to the time to do this varied from a few months (3-4) to no more than one year. Hybrid solutions have already been used successfully in other fields.
- Initial effort should be spent defining seismic "objects" or classes that are used by our community. Industry experts again indicated that the expertise to do this existed within our community, since we are the "domain experts". Industry experts indicated the existing record structure within the CSS3.0 database might be a good first attempt at object definitions.
- The need to keep track of what has been done to a given seismogram in the processing sequence was generally accepted. This audit trail may be complex but it is believed that a well defined Object Request Broker implementation of the SAP might address this problem. Also, in an object oriented environment, the messages passed between objects offer an interesting method to create the "audit trail" through an audit object.

- IRIS should not concentrate on developing applications. That should be left for the scientific community during the course of their normal research activities. However IRIS, consistent with its mission to develop seismological infrastructure, can develop procedures and practices that can enable the development of a software framework that can provide application interoperability and logical connections between applications, parametric information and time series data. IRIS can help to define a set of standard seismic classes.
- There was a general feeling that if something is going to be done it must be able to show some results within one year from the beginning of the project.

Are There Any Solutions Readily Available?

Developments that are taking place within the software industry seem to be directly applicable to the software problem within our community. The CORBA (Common Object Request Broker Architecture) system will allow legacy applications to be brought into an object oriented framework. The development of componentware that should allow future-proofing, is now becoming a reality as JAVA and other object oriented programming approaches are reaching maturity. By embracing an object oriented approach to software development, the development of reusable objects should improve the efficiency of future seismological code development. At the present time it requires significant effort to integrate applications. There is relatively little coordination and cooperation taking place between seismological software developers.

Sessions at the FISSURES workshop that were dominated by the software industry, indicated that object oriented approaches could provide the interoperability that FISSURES needs to provide. The motivations of the industry are obviously quite different, they are interested in object oriented approaches to minimize their cost in developing and maintaining applications. Similarly the seismological research community is interested in improving efficiency in software development so that our community can spend its time doing seismological research instead of writing software. Efficiency for the research community is not in terms of financial profit, rather it is in terms of minimizing the time between the scientific idea and the scientific result. The "profit" for a research scientist is maximizing the number of peer reviewed publications.

There appear to be two complimentary technologies that are common in the commercial software arena that might apply to the general problem of software development and maintenance within the IRIS community. These are Common Object Request Broker Architecture (CORBA) and object oriented programming languages such as Smalltalk, C++ and more recently JAVA. CORBA does not require use of a specific language making it attractive to our community. JAVA is a truly object oriented language that might be appropriate for development of our objects and general framework. We believe IRIS should pursue both CORBA and Object Oriented Programming techniques such as JAVA.

CORBA - Common Object Request Broker Architecture

In general, software applications in seismology and other areas, perform some limited range of functions. However various applications do not interoperate well. Integration when it does exist is insufficient and does not evolve as technology changes. CORBA is an industry standard

infrastructure tool for systems integration. Its most obvious benefit for the IRIS community is that it allows interoperability between applications. Additionally, it appears that CORBA might be able to wrap data in object wrappers so that data can become interchangeable. CORBA brings the hope of future-proofing since it brings component interoperability into the framework.

There are significant benefits of CORBA including

1. CORBA simplifies distributed computing and application integration. It is easier to use than other efforts in this area.
2. Because CORBA is a standard, it holds the promise of interoperability and component interchangeability.
3. Because CORBA is a framework based solution, to link N applications together (make them interoperable) it only requires N interfaces to be developed. In the traditional custom interface solution to software architecture it would require $N*N$ interfaces.
4. CORBA fully supports the concept of object wrappers that will allow the legacy applications and data to be adapted to the new software architecture with minimal effort.
5. CORBA encourages reuse of objects developed by the entire seismic community.

At the FISSURES workshop, the concept of Object Wrappers was introduced and our industry experts said that it is a viable solution. Our problem, as is the problem with most established fields, is that there are a large number of existing components/applications with a long history. Object wrapping is the practice of implementing a software architecture, given pre-existing components (often referred to as legacy systems). This provides an approach whereby existing non-object oriented applications and data can be "wrapped" and made to appear as objects. Object wrapping allows access to a legacy system through an encapsulation layer. The wrapper serves as an interoperability bridge between our legacy systems and a new CORBA compliant software architecture. It may also be obvious to those knowledgeable in object techniques that future implementations of an application could be developed using traditional object oriented techniques and at a later date the legacy applications could be replaced. Without going into the details of CORBA, let it be stated that object wrappers are a well defined and mature concept in the CORBA standard and appears to offer a solution to several of the consensus items previously mentioned. We believe IRIS can and should develop an approach whereby applications, written in any language, can be made CORBA compliant.

CORBA is a standard driven by the Object Management Group (OMG). It is targeted toward using object oriented system architectures for software development. It appears that this technology might serve the IRIS community very well.

Object Oriented Programming - The case for JAVA.

Object technology is computing that models the real world. The difficulty is that the real world is fairly complex. The approach used in object oriented computing is to identify problems, define solutions in terms of portions of the problem and make each component small enough to actually solve and maintain. The monolithic programming approaches of the past must be

replaced by more modern, manageable programming practices. Object Oriented Programming address four major problem areas in computing.

1. Programs are difficult to change or extend. By defining the problem in terms of smaller objects, programmers can focus on only those objects that need modification. The "house of cards" problem is eliminated.
2. Programs are difficult to maintain. Traditional programming approaches split data (variables) and procedures (functions). This almost guarantees that maintenance fixes can have unpredictable results.
3. Programs take too long to write. Well designed objects are more likely to be recognized and reused by a new developer thus reducing redundant programming effort. For instance an AUDIT OBJECT could be written once, and the difficult task of tracking what has been done to a seismogram can be solved in a uniform manner. In general well written objects can be reused as written. The idea of an object oriented seismological toolkit is a reality that IRIS should consider pursuing.
4. Objects are components. The concept of component-ware is an obvious outgrowth of object oriented programming approaches. As techniques evolve, one component/object can be easily removed and its replacement easily inserted. The concept of polymorphism (standard messaging) makes this possible.

The most obvious difficulty in object oriented programming, for the seismological community, is that the way of thinking about software development is very different than the paradigm most scientific programmers have been using. However, that is not to say that the migration to modern programming practices should not begin. CORBA offers a way to encapsulate existing applications inside object wrappers to make them appear as objects. If IRIS was to begin development of a software framework in a modern object oriented language, most likely JAVA, then we would begin moving towards an object oriented solution to the seismological software needs identified at the FISSURES workshop. With essentially no interoperability existing today it is clear that such a change in strategy is needed.

Objects are discrete software components that contain data. Objects also consist of methods that manipulate the data contained within that object. The data can be manipulated by only the object that contains it. Other objects send messages to a specific object to manipulate data and that object returns messages to the calling object along with responses. We have given some thought about examples of seismic classes, one of which might be the class seismogram. We believe it is straightforward to define a series of sub-classes of the class seismogram such as seismogram_plot, seismogram_filter, seismogram_pick, etc. and then to define objects built upon these sub-classes that will allow seismic data analysis to proceed in a more rational, object-oriented approach. An object built from the sub-class of seismogram_plot would contain time series data, the metadata (header values) that describe the data, and a variety of plotting procedures. To plot a particular seismogram in a particular manner, an object would send a message to the particular instance of the seismogram object. Other objects would be objects that manipulate the information in database tables. Instead of interacting directly with the database through Structured Query Language (SQL) the database interaction could be handled in

appropriate objects that in turn generated SQL calls to a relational database. The incorporation of Relational Databases into Object Oriented Frameworks is fairly well established using commercial databases.

An object oriented approach can be a very natural way to develop the framework of the FISSURES system as well as developing new tools (objects) that have more chance of being re-utilized at a later date. C++ and JAVA are languages that should be considered for the development of a seismological framework. JAVA has the advantage that it will allow distributed concepts to be imbedded in the FISSURES structure and this seems to be an important factor to consider in the development of software systems for the next decade.

What should IRIS Do?

Here are some specific things that IRIS is considering doing.

1. Organize a workshop to define the seismic classes from which seismic objects will be built.
2. Work with the Defense Community to modify the CSS3.0 schema as needed.
3. Initiate a pilot project to "wrap" applications such as SAC and MATSEIS into CORBA compliant object wrappers.
4. Develop database objects that would interact with information in database tables and various applications. Details of SQL should be hidden.
5. Attach the database object and the wrapped SAC and MATSEIS applications into the first FISSURES tree.
6. Design the AUDIT object that can be called by application/database objects.
7. Begin developing a JAVA based set of seismological objects to form the basis of a seismological toolkit.
8. Develop a template approach allowing applications written in any language to be CORBA compliant.

It is our belief that IRIS should not develop the applications but rather try to develop a more effective structure/environment in which future software development might occur more efficiently.

Listserver

The IRIS DMC is running a mail listserver related to the FISSURES initiative. You can subscribe to this list by sending the following to

majordomo@iris.washington.edu

Leave the subject line blank and in the body of the mail message include the line
subscribe fissures

to remove yourself from the listserver send e-mail with this line in the body
unsubscribe fissures

For more complete information on commands that you can send to majordomo simply send e-mail to majordomo@iris.washington.edu with the word help in the message body.

You can make contributions to the FISSURES listserver by sending e-mail to
fissures@iris.washington.edu

OBJECTIVE: The objective of FISSURES is to provide a software framework that allows existing seismological applications to interoperate. An additional objective is to improve the efficiency of software development by moving to object oriented techniques allowing better reuse of existing software and an environment that encourages coordination in software development.

RESEARCH ACCOMPLISHED: FISSURES is still in the early stages of development. Initial software systems may not be available for an additional year.

CONCLUSIONS AND RECOMMENDATIONS: FISSURES would benefit by having close cooperation between the academic and government seismological communities. As much as possible IRIS feels that the two communities can both gain from a unified software framework and coordination of efforts in the development of database schemas, definition of seismic classes and the promotion of standards.

**THE BROWSER PROTOTYPE
for the
CTBT KNOWLEDGE BASE**

Hillary M. Armstrong and Ralph G. Keyser

Sandia National Laboratories

Sponsored by U.S. Department of Energy
Office of Nonproliferation and National Security
Office of Research and Development
Contract No. DE-AC04-94AL85000

ABSTRACT

As part of the United States Department of Energy's (DOE) Comprehensive Test Ban Treaty (CTBT) research and development effort, a Knowledge Base is being developed. This Knowledge Base will store the regional geophysical research results as well as geographic contextual information and make this information available to the Automated Data Processing (ADP routines) as well as human analysts involved in CTBT monitoring.

This paper focuses on the initial development of a browser prototype to be used to interactively examine the contents of the CTBT Knowledge Base. The browser prototype is intended to be a research tool to experiment with different ways to display and integrate the datasets. An initial prototype version has been developed using Environmental Systems Research Incorporated's (ESRI) ARC/INFO Geographic Information System (GIS) product. The conceptual requirements, design, initial implementation, current status, and future work plans are discussed.

Keywords: ARC/INFO, ArcView, browser, CTBT, data integration, data visualization, Knowledge Base, GIS

Sandia is a multiprogram laboratory operated by Sandia Corporation, a Lockheed Martin Company, for the United States Department of Energy.

INTRODUCTION

The purpose of this document is to introduce the Knowledge Base Browser prototype. There are several motives behind development of a browser. Number one is the need for the various users to be able to browse the data in the Knowledge Base during all phases of development. An early benefit of this has been the realization that accurate metadata is essential to effectively work with large volumes and many different types of data. Dealing with that issue has, in turn, helped with the development of a draft data dictionary [Shepherd 1997] and associated draft dataset delivery specifications [Armstrong 1997]. Another motive is to experiment with different ways of accessing and displaying the different types of data. This will lead to discovery of optimal ways to handle each datatype. Yet another motive is to look at several commercial software packages to do the best job in developing the browser. This experimentation will point to which one is best suited to development of the browser, as well as other applications in the future. Thus, the browser prototype is an experimental tool to explore different ways to display and integrate datasets of varying type and format, residing in the Knowledge Base.

CONCEPTUAL REQUIREMENTS

While developing an experimental prototype, it is important to keep potential functional requirements in mind to guide the development. The items in the following list describe some of the capabilities the browser prototype will need to provide. It is by no means an exhaustive list, but is a starting point. Development of the prototype will point out additional requirements. The current list reflects what potential users may be doing with the Knowledge Base. These users could be researchers, evaluators, or others who have either provided or are otherwise familiar with the data. Other types of users might be application developers who currently are or will be putting together applications which access, manipulate, or maintain the data in the Knowledge Base.

- o Allow access to and examination of the data in the Knowledge Base for such things as identification and reconciliation of disparate datasets covering the same or adjacent areas
 - o Handle large datasets quickly and efficiently
 - o Provide access to information about the datasets in the Knowledge Base (metadata)
 - o Display a wide variety of data types and formats (e.g., imagery, oracle tables, Spatial Database Engine (SDE) tables, ARC/INFO coverages)
 - o Provide access to a theoretically infinite number of datasets
-

- o Facilitate user interface design discussions for other applications
- o Have a shallow learning curve for users
- o Be relatively easy to understand, from an application developer's point of view
- o Be used as reference on ways to access and display data and, if appropriate, as a starting point to develop other more specialized applications, such as a maintenance interface
- o Be composed of modular and well documented code so that pieces may be replaced and updated or used as parts for development of other applications

CONCEPTUAL DESIGN

The following design characteristics come out of the conceptual requirements listed above. Their proper implementation will help satisfy those requirements.

- o All datasets should be available to the user simultaneously
This implies that the user should be able to access any dataset from the top or major level in the application. In order to make this useful and not overwhelm the user, the datasets should be presented in a logical and organized fashion.
- o Functions that control the datasets of a datatype should be grouped together and available only at the appropriate time, and functions that apply to all datatypes in general should be available all the time
This implies grouping the functions such as the ones that turn specific datasets on and off, but having ones that apply to the general session environment, like redraw all, be accessible all the time. When dealing with global datasets in applications such as this, it is essential that users have control over when the datasets are drawn.
- o The user should be able to control the appearance of the data
This implies letting the user change the symbols and colors of features in a dataset to facilitate examination of the data.
- o The user should be able to easily and directly access the datasets' metadata and attributes
An online connection to metadata is one possibility here. The ability to display the attributes of selected features is essential.

- o **The user should be able to move around and zoom in and out at will**
The ability to go quickly to an area of interest is important. Also, the user needs to know ahead of time if what they are requesting will take a long time to draw.
- o **The user should be able to analyze the data and then save and output these results**
This implies provision of spatial analysis tools and hard and softcopy output tools.
- o **The prototype needs to be as generic and consistent as possible in the way it accesses and handles the datasets**
This will facilitate modifying the user interface to accommodate adding new and different types of datasets as they become available. The more commercial off the shelf (COTS) software can be used, the less "custom" the interface will be, and the easier it will be to maintain. The amount of customization necessary depends on the application software being used for development together with the user requirements.
- o **The application and code should be developed and documented to some reproducible, commonly available standard**
Doing this will make the application much easier to maintain. The application will also be more useful either as a reference for an application developer, or as a parts for a new system, since it will be easy to interpret and evaluate fitness for a specific use.

PHYSICAL DESIGN AND IMPLEMENTATION

Since this browser is a prototype, it will continue to evolve as feedback is received from the users and new types of datasets are hooked up. It will start out to be very basic with hooks to just a few datasets and will end up being a fully functional browser with access to all the datasets in the Knowledge Base. One of the risks of this type of prototype development is that, due to lack of precise implementation requirements and scope at the beginning, the system will outgrow its original design and evolve into a kludge. That is why it is usually a bad idea to expect prototypes to be used as or evolve into production systems. One good way to help lower the above mentioned risk is to use COTS software packages as much as possible. That way, time is not spent developing basic parts that already exists commercially. This frees the developer up and allows more time to experiment with different ways of developing the unique and interesting parts of the system. Another "plus" of using COTS software is that the system will more likely to work with new releases of the COTS software package (be upwardly compatible). Although using COTS software is a good idea, it is rare to find one package that meets all development needs. When custom code does need to be developed, it should be well documented, written to a commonly available software development standard, and contain as little operating-system dependent code as possible. The more system dependent the code, the more work it will be to port the system to another hardware platform in the event that a hardware change is needed or support for an additional platform is required. These are all important considerations, because at

the initial prototyping stage, nothing has been "set in concrete" and therefore anything can change. In fact, things should change as a result of the prototyping phase if it is well executed.

Prototype development software

When looking at COTS development packages, the idea is to balance familiarity, capability, flexibility. ARC/INFO was chosen as the initial prototyping package both because we were familiar with it and knew it could do the job, our customer had expressed interest in it, and at the time ArcView didn't have all of functionality we were looking for. With ArcView 3.1, slated for release in "late summer 1997" [ESRI 1997], it now looks like a good choice as well. It may even have some advantages over ARC/INFO for browser prototype development. Capabilities like interfaces to handle more of the military data formats, a new image handling and analysis package called Image Analyst which was developed in close collaboration with ERDAS, Inc. (a leading image-processing software vendor), and the Dialog Designer Extension which makes it much easier to customize ArcView make it a very attracting prototyping tool.

Browser structure

As mentioned above, the browser is currently implemented as an ARC/INFO application. ARC/INFO is a GIS toolbox containing a wide variety of low level tools. These tools may be assembled into a collection of programs called using ESRI's custom Arc Macro Language (AML) application programming interface (API) together with menus to create a graphical user interface (GUI). ARC/INFO provides a high degree of capability as well as design flexibility. Because the API is so flexible, AMLs can become fairly complex. Though not as complex as those developed in a language such as C++ and an X windows package, the AMLs and menus must be designed to work together as a system, which requires significant investment in upfront requirements analysis and design, even in this type of prototype development.

The browser prototype needs to provide fairly rapid access to a theoretically infinite number of datasets in a variety of formats and varying sizes, and be easy to understand from an application developer's point of view. To this end, significant effort was put into the underlying structure of how the application interacts with those datasets. Managing the complexity of dealing with so many datasets ranging from raster to vector to flat files, in a variety of different formats (e.g. ARC/INFO coverages, ArcView shapefiles, oracle tables, SDE tables, Vector Product Format (VPF), ASCII, etc.), will determine how easy it is to add new datasets, change the way the dataset appeared in a display, etc. In order to help manage this complexity, each data type (e.g., event sources, meteorology, depth to moho, etc.) is loosely treated as a class of objects, with the datasets being instances of that class (i.e., objects). Although AML does not have object oriented extensions, it is possible to structure the code in a fashion that reflects this way of thinking. The assumption was made that datasets of the same type are similar enough that it makes sense to group the functions which handle them together. Handling datasets in this way has helped to manage the complexity of accessing and displaying a large number of datasets by making it easier to find and change the code that controls a particular type of data. Physically, these ideas have been implemented as described in the following paragraphs.

Datasets of each datatype are accessed via a menu like the Digital Chart of the World menu shown in Fig. 1. The menu is controlled by an AML which takes one argument. This argument is the name of the routine (a separate block of code placed at the end of the AML) to be run by the AML in order to tell the datatype to do something (e.g., initialize its menu, draw one of its datasets). These routines are analogous to the methods of an object. The routine name is also an indication of the state of the dataset. For example, when the user selects the "Digital Chart of the World" option from the "GEOGRAPHICAL" datatypes pulldown menu, `dcw.aml` is run with `menu_init` as the argument, telling the datatype to initialize and display its menu. If a dataset is then turned on and the "APPLY" button is selected, `dcw.aml` is called again, this time with "apply" as the argument which runs the apply routine which sets the appropriate status variables and calls the draw routine to draw the dataset which has been turned on.

Structuring the application in this way has made modifications to the code, such as adding new datasets much more straightforward. For example, to add a new dataset of an already existing datatype, add the dataset name to the global initialization routine and code specifying how the new dataset should be drawn to the global initialization and draw routines, and then add an "ON/OFF" button for the new dataset to the menu for that datatype to give the user access to the new dataset.

Another factor which has helped make development and modification easier is that the prototype has been developed following the ESRI's applications programming standards [ESRI 1992]. Among other guidelines, this standard recommends fully documenting the AMLs and menus to include a documentation header, which it provides a sample of. Although time-consuming to create, this documentation has already proven to be extremely valuable in adding new and modifying existing functionality in the prototype.

CURRENT STATUS

A first cut of the browser prototype has been developed using ARC/INFO. It has access to 43 datasets. Some of these datasets are global and some are regional. They range in size up to 3 gigabytes. Raster and Vector datasets are represented. Basic functions, such as turning datasets on and off, changing symbol and color, and panning and zooming are available at this time. (Fig. 2)

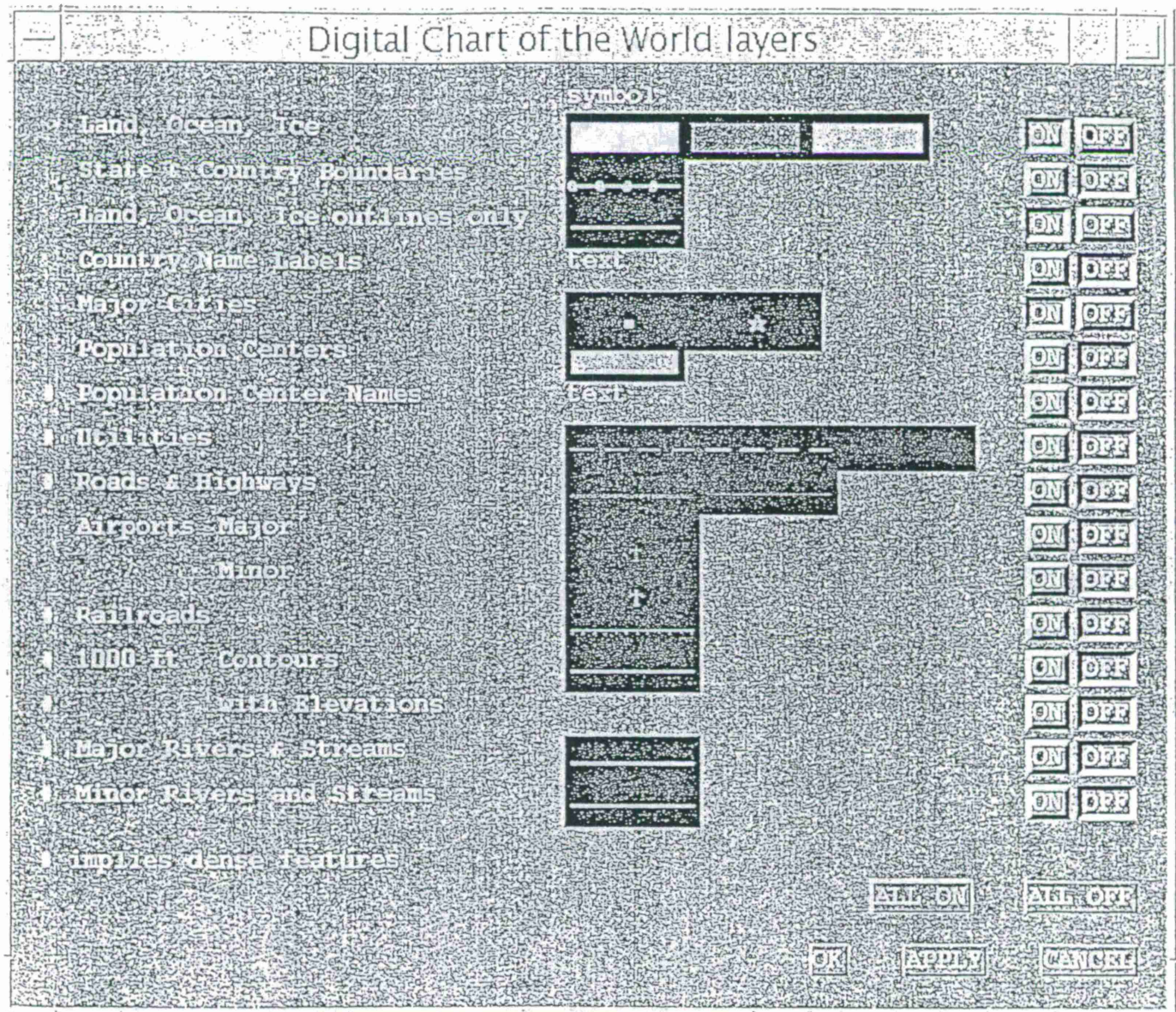
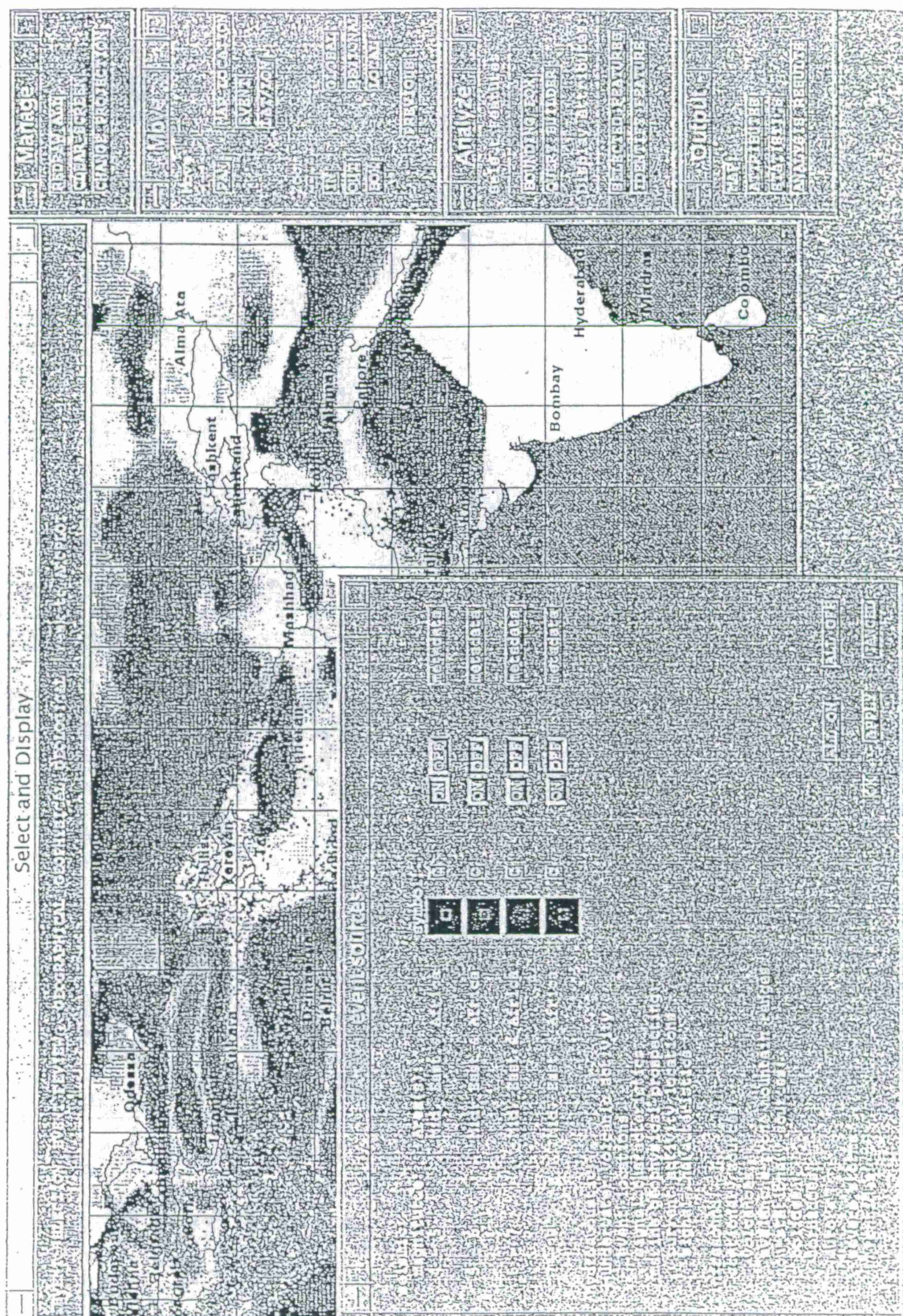


Fig. 1: The Digital Chart of the World access menu



816

FUTURE WORK

Experiment with ArcView 3.1

It appears that ArcView 3.1 contains some previously unavailable but needed functionality. The fact that it could be bought with ArcView and then would not have to be developed in ARC/INFO would not only save valuable development resources, but would also result in a more purely COTS application (i.e. less custom code) than ARC/INFO. Additionally, more effort could then be put into the task of developing new ways to use the existing ArcView tools to access and display the data, rather than developing the tools themselves. The generic GUI which come with ArcView could be used first, and then gradually customized to meet the users' needs. In contrast, even the most generic ARC/INFO interface will be custom to some degree, because of the nature of ARC/INFO application development. A big tradeoff here would be that the generic interface from ArcView would probably not be as easy to use as a custom one developed with ARC/INFO, but it could be had much faster and may be suitable as a prototype. Thus, it would be worth the effort to look into using ArcView to develop the next version of the browser prototype.

Hook up more datasets

As the research entities deliver more and more datasets for inclusion in the Knowledge Base, they will be hooked up to the browser. This will be an ongoing effort. During this period, the suitability of the metadata delivered with the datasets will be evaluated, as it will be used to install the datasets in the Knowledge Base. Eventually, users will have access to spatial datasets like bathymetry, seismic events, correction surfaces, hydroacoustic event, to name a few.

Demo to users and refine user interface

Development of the browser has been and will continue to be user-driven. Thus, we will continue to periodically give demonstrations to and solicit comments from the users. Comments and questions will continue to influence things like the look, feel and features of the browser.

References

Shepherd, E., R. Keyser, H. Armstrong, E. Chael, C. Young. Draft Data Dictionary for CTBT Knowledge Base, Revision 1. April 21, 1997.

Armstrong, H., R. Keyser. ARC/INFO Dataset Delivery Specifications. February 3, 1997.

Environment Systems Research Incorporated. Arc News. Spring 1997.

Environment Systems Research Incorporated. Applications Programming Coding Standards. ESRI Applications, March 1992.

SOFTWARE DESIGN AND OPERATIONAL MODEL FOR THE WCEDS PROTOTYPE

Judy I. Beiriger, Susan G. Moore, Julian R. Trujillo, and Chris J. Young
Sandia National Laboratories

Sponsored by U.S. Department of Energy
Office of Nonproliferation and National Security
Office of Research and Development
Contract No. DE-AC04-94AL85000
Comprehensive Test Ban Treaty Research and Development Program

ABSTRACT

To explore the potential of waveform correlation for CTBT, the Waveform Correlation Event Detection System (WCEDS) prototype was developed. The WCEDS software design followed the Object Modeling Technique process of analysis, system design, and detailed design and implementation. Several related executable programs are managed through a Graphical User Interface (GUI). The WCEDS prototype operates in an IDC/NDC-compatible environment. It employs a CSS 3.0 database as its primary input/output interface, reading in raw waveforms at the start, and storing origins, events, arrivals, and associations at the finish. Additional output includes correlation results and data for specified test case origins, and correlation timelines for specified locations. During the software design process, the more general seismic monitoring functionality was extracted from WCEDS-specific requirements and developed into C++ object-oriented libraries. These include the master image, grid, basic seismic, and extended seismic libraries. Existing NDC and commercial libraries were incorporated into the prototype where appropriate, to focus development activities on new capability. The WCEDS-specific application code was built in a separate layer on top of the general seismic libraries. The general seismic libraries developed for the WCEDS prototype can provide a base for other algorithm development projects.

Keywords: waveform correlation, software design, rapid prototype, seismic processing

OBJECTIVE

The Waveform Correlation Event Detection System (WCEDS) project was initiated in the Spring of 1995 specifically to investigate the potential utility of a waveform correlation-based approach to the CTBT event detection and location problem. While the primary goal of the software design for the project was to develop the WCEDS prototype, an additional goal of the software design effort was to develop a general software base to support rapid prototyping and proof-of-concept testing for CTBT advanced data processing research. To facilitate this, the software design separates the WCEDS-specific software entities and functions from more general seismic software. The two most important requirements for the software system were operation in an IDC/NDC-compatible environment, and incorporating existing IDC/NDC software and commercial third-party libraries to avoid spending development effort for capabilities that could be obtained readily elsewhere.

The WCEDS prototype software development task is primarily a research effort, not a production software development project. Consequently, the software design choices emphasized flexibility, access to intermediate processing results, adaptability to changing requirements, and generality to seismic monitoring. Production software requirements such as execution speed and robustness, though not ignored, were treated as lower priority and developed less fully than for an operational system.

RESEARCH ACCOMPLISHED

The first step of the WCEDS software development effort focused on porting the original code (Shearer 1994) to our system and modifying it to function in an IDC/NDC-compatible environment. The largest portion of this task involved interfacing the code to a CSS 3.0 Oracle database to read waveform data. This initial WCEDS code was used to begin exploring the waveform correlation concept for CTBT application, and provided valuable insight into how to structure a correlation-based prototype detector.

The WCEDS prototype software design began with an analysis of the waveform correlation detector requirements in the context of the general CTBT monitoring problem. The software analysis was based on an object-oriented modeling approach, primarily employing the design process and conventions known as the Object Modeling Technique (OMT) (Rumbaugh, et. al. 1991). The WCEDS analysis model describes what the system is to do, exclusive of considerations of how it might be implemented; it describes the static structure, temporal relationships and behavior, and data transformations required of the system.

After the analysis was completed, we began the WCEDS software system design. This system design describes how the system is structured to meet its requirements, defining the major software components and their organization. We defined the strategy for making design decisions and provided a framework for detailed design and implementation. The system design discusses the components, interfaces, information flow, concurrency, data store implementation, task allocation, resource access, system control, and user interaction. Care was taken to separate WCEDS-specific components and functions from more general seismic monitoring components and functions.

The detailed design and implementation phase is nearing completion. The WCEDS prototype is a fully-developed detection system, reading in waveforms at one end and reporting events and associated arrivals at the other. Other analysis output is possible, such as the waveform correlation and detection threshold comparisons for a specified testcase time and location, a snapshot of the correlation at each grid point at a specified point in time, and a timeline of the correlations at a specified grid point. The detector operation is managed through a Graphical User Interface (GUI); work is continuing to allow the GUI to manage detector parameter configuration and utility program execution as well. A user's manual explains how to use the GUI to run the various application and utility programs.

SYSTEM OVERVIEW

The WCEDS prototype system consists of a set of related executable programs that are accessed and controlled through the WCEDS GUI. This compartmentalized approach allowed the major processing phases of the waveform correlation technique (that is, preprocessing, correlation, and detection) to be developed and investigated independently. It is also an arrangement compatible with the IDC/NDC pipeline scheduling. Operation of the WCEDS prototype is illustrated by tracing a typical data interval through the system from raw waveforms to detected events. The data flow through the system is summarized in Figure 1.

The WCEDS executable programs operate on one data interval and then terminate. They are scheduled and launched with the appropriate input parameters, so that successive data intervals are sequenced through all of the specified processing steps. To initiate a run, the user must first specify the desired configuration and operational parameters to be applied to all of the executable programs during a single WCEDS run. These include:

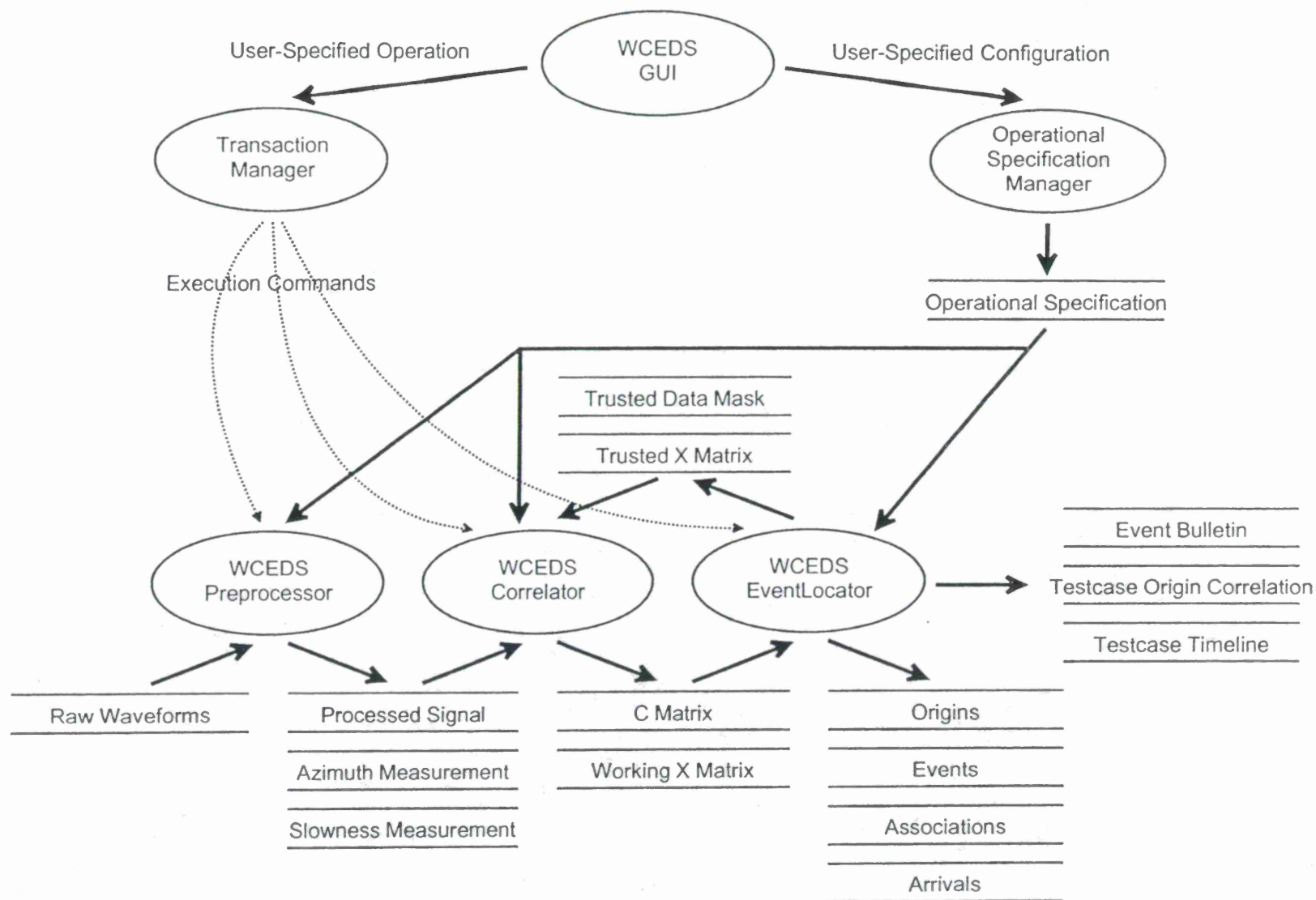
- the set of phases and time and distance resolution for the travel time models,
- the time and distance resolution for candidate event locations,
- the set of sites to use for seismic data input, and site-specific information for each site, such as channels, site/channel groups, algorithms, filters, recipes, and recipe parameters,
- seismic event and arrival detection thresholds, and optional azimuth and slowness criteria,
- the database interface,
- optional testcase origins,
- the desired start time,
- either continuous operation or a fixed duration,
- which processing steps to perform,
- and preprocessing, correlation, and location interval sizes.

In a typical research scenario, preprocessing, correlation, and event detection are to be performed on a particular block of waveform data. There may be known locations and times of interest. The set of sites includes both arrays and three-component stations, which require different waveform processing algorithms. The block of waveforms is broken into smaller time segments, which are processed consecutively by separate invocations of the appropriate executable program. The executables do not coordinate directly, but are loosely coupled; each starts when its input data becomes available.

First, the waveforms are preprocessed to provide the signal, azimuth, and slowness measurements. The preprocessing interval size specifies the time interval of waveform data for the WCDPreprocessor program, say 15 minutes. The WCDPreprocessor reads the recipes defined for each site and performs the specified processing. Desired processing differences between sites - different filter bands, different algorithms, different input parameters for the same algorithm, etc. - are achieved by defining different recipes. The typical sequence is bandpass filtering of all the waveform channels, a multichannel signal detection method like spatial coherence, scaling of the processed signal, and f-k analysis to take azimuth and slowness measurements at each output data sample time. For each recipe, three processed data streams are stored in the CSS database as waveforms: the processed signal, stored using the recipe name as the channel name, and the azimuth and slowness measurement streams, stored with an 'A' or an 'S', respectively, appended to the recipe name. The WCDPreprocessor program then terminates. When the next 15-minute interval of raw waveforms is available, another WCDPreprocessor program is started.

Once sufficient preprocessed data becomes available, a WCDCorrelator program is started for the first location interval. The epicentral distance interval from 0 to 180 degrees is discretized to a specified spacing, and the travel time curve for a particular phase is presented as boxcars of finite duration centered at the expected travel time for each discrete distance. The correlation time interval specifies the length of the processed waveforms that are to be correlated against the expected travel time curves, yielding a correlation result for a single postulated origin time. The correlation interval must be long enough to encompass the phases of interest, say 1 hour. The location interval size specifies the time interval of postulated origin times for which trusted correlations will be

FIGURE 1. WCEDS Information Flow.



made. Trusted correlations are those for which processed data were available for the full correlation time interval. The WCDCorrelator program needs processed data for the location interval plus the correlation interval to compute results for the location interval. It actually produces correlations for postulated origin times as far out as it has data, though results beyond the location interval can not be trusted since full correlation was not possible. The need for the trusted/untrusted model for resolving false correlations near the end of the location interval due to an event in the succeeding interval (see Young, et. al. 1996) became apparent during the initial WCEDS prototype testing.

The desired behavior of the waveform correlation detector is that, for a given postulated origin (grid point and time), the processed signals for each site are correlated with specified phases of the travel time curve at the corresponding site-to-grid point distance and added together to yield a single correlation value for the postulated origin. For performance reasons, the software implementation splits the distance correlation and the summing into two steps. Since any site is expected to be at each of the discrete correlation distances from at least one grid point, and at the same distance from many grid points, its correlation at each discrete distance is computed once and saved. There is also a data mask channel for each processed signal channel that could block segments of the processed waveform from being correlated. Blocked segments could include previously-identified arrivals or data that failed quality control criteria. (Quality control is not implemented in the WCEDS prototype.)

The results are saved in a Correlation Matrix (C Matrix). The C Matrix originally contained, for each origin time, a column for each site and a row for each distance. Each cell contained a single summed value for all of the phase correlations for all of the processed recipe channels for the corresponding site and distance. The C Matrix has since been generalized to hold separate correlation values for individual phases and channels, as well as azimuth and slowness measurements, and to allow different (possibly overlapping) distance ranges for different channels. The azimuth and slowness measurements corresponding to an individual phase correlation are determined as the data samples of the azimuth and slowness channels at the time of maximum correlation between the travel time pulse and the processed signal. In addition, the C Matrix contains a correlation mask (X Matrix). If the phase correlation value does not exceed the specified threshold, the X Matrix is set to prevent it from being included in a sum for some grid point. The user may optionally specify a slowness check for individual phases. If slowness checking is requested, the WCDCorrelator program compares the slowness measurement to the expected travel time slowness for the specified phase. If the slowness values differ by more than the specified threshold, the X Matrix is set to mask that phase correlation value. After the X Matrix is stored, then the WCDCorrelator program terminates. Another will not start until preprocessed data for the next location interval plus correlation interval are available. Correlation intervals after the first will also need phase identification information from the WCDEventLocator, provided as initial X Matrix and data masks for the interval, before they can run.

When a location interval of trusted correlation data (and its corresponding untrusted correlation data) becomes available, a WCDEventLocator program is started. It proceeds by computing, for each postulated origin time in the trusted and untrusted intervals, the correlation sum for each grid point. A C Matrix map defines the summing path for each grid point. The map is a set of offsets from the start of the C Matrix to the individual phase correlations for each site channel at the appropriate site-to-grid point distance. The X Matrix has the same structure, so it may be navigated with the same map. At each map offset, if the X Matrix value allows, the C Matrix phase correlation value is added to the grid point sum. The user may optionally specify an azimuth check for individual phases. If azimuth checking is requested, the WCDEventLocator program compares the azimuth measurement to the site-to-grid point azimuth for the specified phase. If the azimuth values differ by more than the specified threshold, the phase correlation value is not included in the sum.

If the maximum of the correlation sums exceeds the specified threshold, it is considered an event. Associated phases are then identified. Phase identification is accomplished by duplicating the correlation process for the event time and location, but using the phase identification and screening configuration, rather than the detection configuration, of the phase set and the azimuth

and slowness criteria. The screening configuration must at least guarantee that the detected signals will be claimed by this event. Typically, the screening phase set is much larger than the detection set, and the azimuth and slowness checks are much less stringent. A phase correlation that meets the threshold criteria is considered an arrival at the time corresponding to the peak correlation with the travel time boxcar. The WCDEventLocator program stores the event information in the CSS database origin, arrival, and assoc tables. The author, algorithm, and velocity model fields are set to indicate that the record was created by WCEDS. Possible event types are trusted, untrusted, or testcase. Events with times in the trusted interval are also inserted into the event table.

WCEDS tracks the start and stop times corresponding to the travel time boxcar to identify the data segments claimed by arrivals. The data mask for a claimed data segment must be set properly so this arrival will not add into other computations. Similarly, the X Matrix must be set to mask travel time correlations with the data segment. This is done by computing the origin times when the data segment correlated with any phase in the detection travel time model, and masking that phase correlation value. For trusted events, separately-maintained trusted data and X Matrix masks are updated. These trusted masks are used by the WCDCorrelator and WCDEventLocator programs operating on the next location interval. Using the new X Matrix, the WCDEventLocator program then repeats the process of finding the maximum correlation sum. When the maximum sum falls below a specified threshold, or a specified number of events has been found in the interval, the program stores the trusted mask information and terminates. Another WCDEventLocator program will be started when the next location interval of trusted correlation data becomes available.

The user may optionally specify testcase origins or locations for which additional output is produced for analysis. An "event" testcase specifies a target latitude, longitude, and time. The closest grid point and postulated origin time used by the detector are treated as an event, and both the detection and screening correlations are performed. The user may choose to see all phase correlation results, or only those that pass the threshold criteria. A "timeline" testcase specifies a target latitude and longitude. The correlation sum for the closest grid point is output for each postulated origin time, so the seismic activity at that point can be watched in time. A separate utility program, CorrSnapshot, stores the correlation sum for all grid points for a set of origin times and outputs the data so it can be viewed by an animation program.

SYSTEM DESIGN

Architecture

The WCEDS prototype is organized into several subsystems, each providing a particular service to the system through a well-defined and relatively small interface. A subsystem is a package of interrelated software components, associations, and operations that can be designed and implemented independently of other subsystems.

The WCEDS system is structured as a closed architecture of layers and partitions, as shown in Figure 2. The bottom three layers encompass the hardware system and available resources: a distributed network of Sun workstations running the Solaris 2.5.1 operating system, with the Network File System (NFS) and an Oracle database. The top layer provides the WCEDS application - the global capabilities and services - to the user. In between is a layer encompassing the WCEDS prototype functionality, divided into three vertical partitions. The Object Specification Manager Subsystem manages the user specification of the WCEDS components and analysis parameters, providing them to the user interface for display and editing, and providing them to the detector code for operation. The Transaction Manager Subsystem manages the execution of the WCEDS detector according to the user specification; several detector application and utility programs are available. The WCEDS Capabilities Subsystem provides the high-level WCEDS functions and executables that can be launched by the Transaction Manager. It is built upon the Seismic Domain Subsystem, which provides seismological information and processing services. The Seismic

Domain Subsystem is further subdivided into Travel Time Model, Earth Model, Base Seismic Data, Extended Seismic Data, and WCEDS Seismic Domain Subsystems.

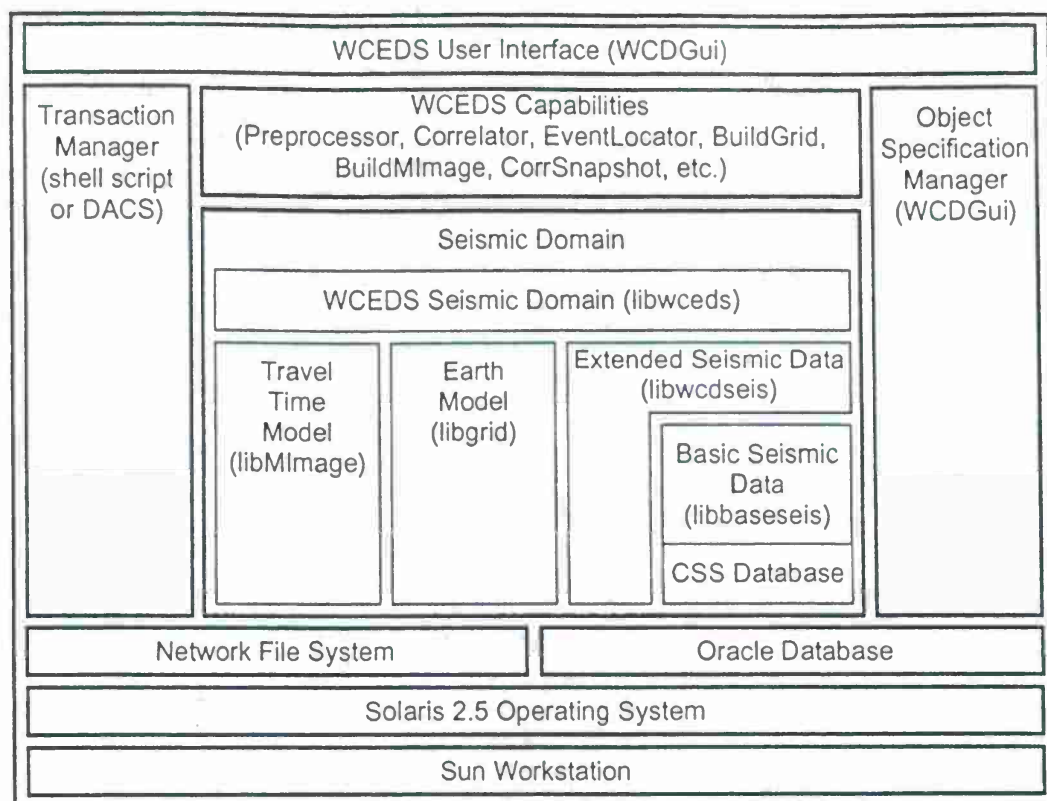


FIGURE 2. WCEDS Subsystems Block Diagram

Relationships between the layers are one-way, client-server relationships: a layer knows about the layer immediately below it, but not above it. The WCEDS User Interface Subsystem requests services of the Object Specification Manager Subsystem interactively. It "requests" services of the Transaction Manager Subsystem indirectly, and through it services of the WCEDS Capabilities Subsystem, by specifying parameter files and launching execution. The WCEDS Capabilities Subsystem requests services of the Seismic Domain Subsystem by directly invoking object operations.

Relationships between partitions may be one-way or two-way relationships: a partition knows about the other partitions in the same layer. The relationships between the Object Specification Manager Subsystem and each of the other subsystems in that layer are one-way relationships: the Object Specification Manager provides the operational specification to the other subsystems in a data store. The relationship between the Transaction Manager Subsystem and the WCEDS Capabilities Subsystem is a two-way, peer-to-peer relationship: these subsystems interact through asynchronous, message-based communications. (Currently, this is a one-way interaction: the Transaction Manager launches a WCEDS executable.) The various executables in the WCEDS Capabilities Subsystem, such as the preprocessor, correlator, and locator executables, do not relate to each other directly: they interact indirectly through data maintained in the Seismic Domain Subsystem.

Subsystems

The WCEDS user interaction and object specification management are implemented in the WCEDS GUI executable. The GUI allows the user to view and set the operational control param-

eters for the WCEDS prototype detector: detector start time and duration, which of the preprocessing, correlation, and location steps are to be performed, preprocessing, correlation, and location interval sizes, and whether to start fresh or use event history information. The GUI capability is currently being extended to also manage the WCEDS configuration parameters such as the set of sites, preprocessing recipes, testcase locations, master image configurations, etc. The design allows a user to set configurations, and then store and recall them by name. The WCEDS GUI provides the operational specification to the detector code through a data store. Information for launching WCEDS executable programs is provided to the transaction manager.

The transaction manager is currently implemented as a shell script. It receives user-specified information from the GUI to launch and sequence the executable programs. It is responsible for ensuring that the requested data intervals receive the requested processing, but is not robust. The WCEDS design plans for the transaction manager to be the Distributed Applications Control System (DACS) developed by SAIC for the NDC. We performed some simplified prototyping to verify proof-of-concept, but have not implemented the DACS interface.

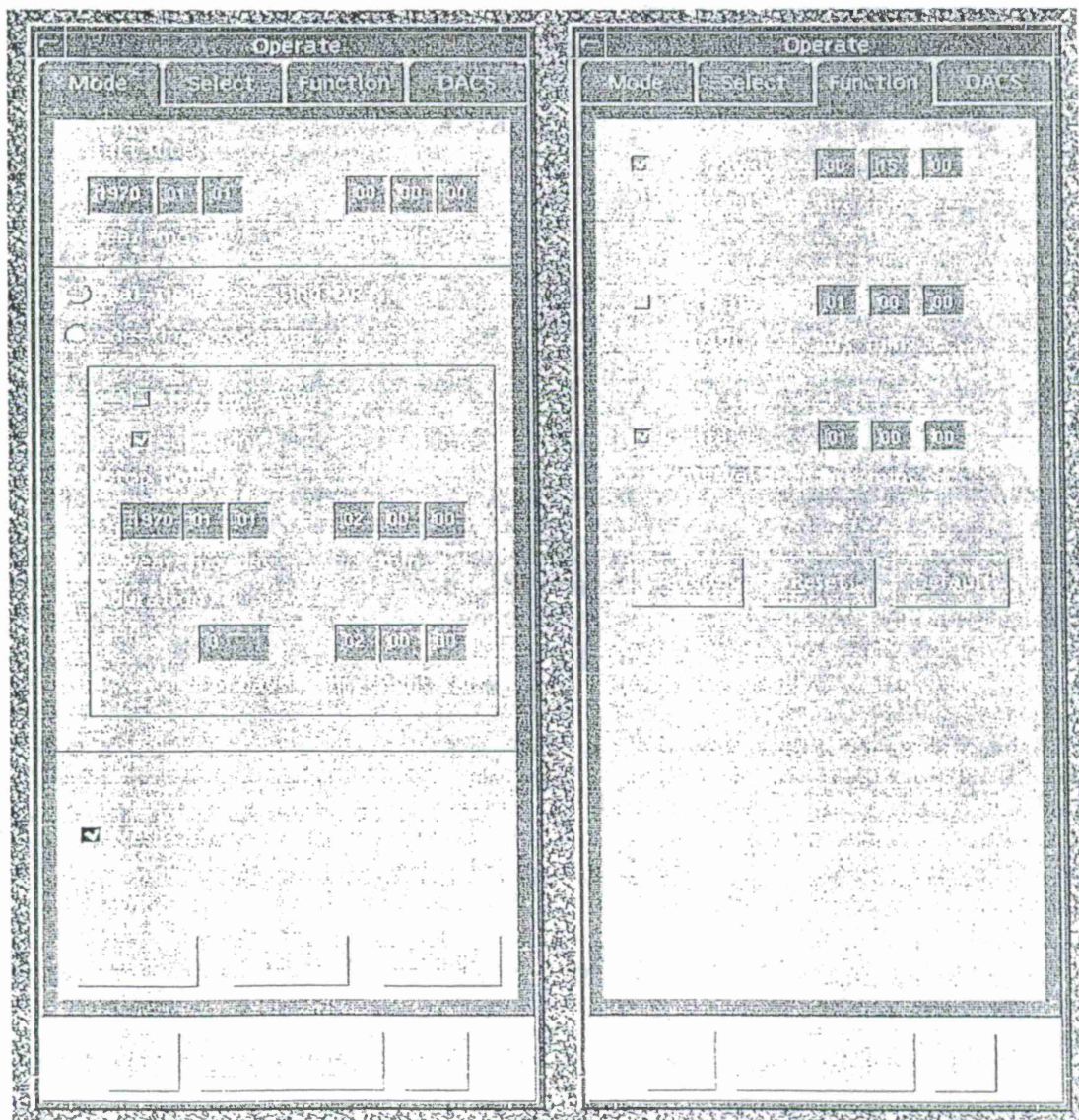


FIGURE 3. Example WCEDS GUI windows.

WCEDS capabilities are implemented as separate, but related, executable programs. Coordination and consistency between the programs is provided by the operational specification data store and the scheduling and launch parameters provided by the transaction manager. The major seismic event processing is provided by the programs WCDPreprocessor, WCDCorrelator, WCDEventLocator. There is another variation, WCDCorrLoc, which combines correlation and detection if the interim results are not wanted. In addition, several utility programs for managing the WCEDS prototype have been developed, including programs to build grids and master images, and programs to manage the database.

The travel time model is implemented as a library package called the master image library (libMImage). Travel time information from a known source, such as the IASPEI 91 tables or empirical data collected by UCSD, is interpolated and reformatted to provide expected travel time data at an arbitrary, specified time and distance spacing. The master image uses a specified shape function to spread the expected travel time from a point to a finite-width pulse; for example, the expected time for P to travel 1 degree could be spread from 19.17 seconds to an arbitrarily-shaped pulse with a duration from 14 to 24 seconds. The master image was designed to be a general use library, independent of WCEDS. It has a set of operations that can be called to present the travel time information for requested phases to an application program. The master images used for the WCEDS detector operation to date have been based on the IASPEI 91 travel time curves. At the beginning of the project, we experimented with various time and distance spacings and pulse widths and shapes for the WCEDS application, and eventually settled on a 1-second, 1-degree spacing and a square pulse (boxcar) of variable width chosen so that the phase may span the distance between grid points.

The earth model is implemented as a library package called the grid library (libgrid). It presents geographic location information as a set of discrete grid points (latitude, longitude, and depth) with a specified spacing. It was designed to be a general-use package. It provides geographic functionality such as calculating the distance and azimuth between a station and a grid point and finding the closest grid point to a specified target location, but not WCEDS-specific uses of the grid.

Seismic information is implemented in two library packages, a basic seismic library (libbaseseis) and an extended seismic library (libwcdseis). The base seismic library provides the CSS 3.0 database tables and relations as objects for use by an application program. The complete CSS 3.0 database has not been implemented, but the fundamental tables, such as wfdisc, origin, event, arrival, assoc, site, sitechan, etc. have. The extended seismic library is built on top of the base seismic library, and provides seismic information and functionality beyond the CSS database. In some cases, this is simply adding an attribute or relation to a CSS object. Other common seismic objects like filters, signal processing algorithms, recipes, and station/channel groups are located in this library.

Specific application or implementation uses of the more general seismic domain information is implemented in an application library (libwceds). This includes functions like translating the user specification into operations on the general seismic objects, or customizing them in some way. For example, the WCEDS application allows optional variations of the master image, such as distance-dependent phase scaling or modification of overlapping phases, and uses the grid points as candidate seismic event locations. Libwceds also provides the correlation mappings between the grid points, seismic monitoring stations, and master images, performance-enhancing implementation objects like the C Matrix, non-CSS uses of the Oracle database, and mechanisms for coordinating among the separate WCEDS executables.

Miscellaneous general purpose utility functions are provided in a separate library (libgpu). These include directory path and file name manipulation, string matching functions, file utility functions such as stripping comment lines from input files, and date/time utilities.

Where appropriate, the WCEDS prototype incorporates some other libraries not developed at Sandia. A number of NDC libraries are used for seismic functions; examples include waveform filtering, f-k analysis, and input parameter parsing. To minimize the resources spent developing software not fundamental to the waveform correlation or general seismic monitoring problems, commercial libraries were used for a few specific, ancillary purposes. BXPro from Integrated

Computer Solutions allowed a simple GUI to be implemented quickly. DBTools from RogueWave allowed quick development of database access functions. The MATLAB Library and Compiler from The Math Works allowed signal processing algorithms to be developed quickly in the MATLAB environment, and then compiled into the WCEDS executable. The commercial libraries primarily support rapid prototyping; their use in an operational environment would need to be reviewed.

CONCLUSIONS AND RECOMMENDATIONS

The WCEDS software design effort has produced a successful prototype for investigating waveform correlation techniques for CTBT, and has been used in numerous experiments. The WCEDS prototype incorporated existing NDC and commercial software, where appropriate, to concentrate development activities on new capability. Output from the WCEDS prototype includes an event bulletin, origins and associated arrivals inserted into the database, correlation results and data for specified testcase origins, and correlation timelines for specified locations. The WCEDS software development focused on research priorities, such as flexibility and access to intermediate processing results, and not on operational requirements. No concerted effort was made to optimize performance, and it is anticipated that considerable gains could be made in this area. As part of the software development effort, the more general seismic monitoring functionality was separated into a C++ object-oriented library, with the WCEDS-specific application code built on top. In a similar fashion, the general seismic library can provide a base for other algorithm development projects.

REFERENCES

- [1]. Beiriger, J., S. Moore, and J. Trujillo (1996). Waveform Correlation Event Detection System Analysis Document, Sandia National Laboratories, Decision Support Systems Department 9432, August, 1996.
- [2]. Beiriger, J., S. Moore, and J. Trujillo (1996). Waveform Correlation Event Detection System Design Document, Sandia National Laboratories, Decision Support Systems Department 6532, November, 1996.
- [3]. Beiriger, J., S. Moore, and J. Trujillo (1997). Waveform Correlation Event Detection System User's Manual, Sandia National Laboratories, Decision Support Systems Department 6532, May, 1997.
- [4]. Beiriger, J., S. Moore, and J. Trujillo (1997). Waveform Correlation Event Detection System Object Design Document, Sandia National Laboratories, Decision Support Systems Department 6532 (DRAFT).
- [5]. Rumbaugh, J., M. Blaha, W. Premerlani, F. Eddy, W. Lorensen (1991). *Object-Oriented Modeling And Design*, Prentice-Hall, Inc., Englewood Cliffs, NJ, ISBN 0-13-629841-9.
- [6]. Shearer, P. M. (1994). Global seismic event detection using a matched filter on long-period seismograms, *J. Geophys. Res.*, 99, 13713-13725.
- [7]. Young, C. (1997). Status Report On The Waveform Correlation Event Detection System (WCEDS) Project, May, 1997.
- [8]. Young, C., M. Harris, J. Beiriger, S. Moore, J. Trujillo, M. Withers, and R. Aster (1996). The Waveform Correlation Event Detection System Project, Phase I: Issues in Prototype Development and Testing, *SAND96-1916*.

AUTOMATIC PHASE IDENTIFICATION AND ONSET TIME ESTIMATION AT REGIONAL DISTANCES USING THE CUSUM ALGORITHM AND GENERALIZED POLARIZATION ANALYSIS

Zoltan A. Der
ENSCO Inc, Springfield, VA.

Sponsored by U.S. Department of Energy
Office of Nonproliferation and National Security
Office of Research and Development

ABSTRACT

This paper explores two approaches to the automation of processing of regional events. One of these methodologies, the CUSUM algorithm, was designed to detect the onset times of arrivals by exploiting sudden changes in the various relevant statistics associated with changes in spectral content, amplitude and polarization. This methodology, originally applied in industrial control systems, was found to be effective to pick onset times of poorly defined and emergent phases in regional seismograms.

The second method, the generalized polarization analysis, is designed to identify automatically the nature of various main wave groups in the regional seismograms as various phase types such as Pn, Pg, Sn and Lg. This method automatically learns the polarization-slowness patterns from previously recorded events along similar propagation paths and uses these to tag wave groups in new events. This method performs better than conventional slowness-polarization analyses based on analytical signal models because the unpredictable site transfer functions are also learned.

The two methodologies can complement currently used array signal processing methods in processing seismic events. They have the potential for full automation of several routine tasks in analyzing regional seismograms, thus greatly reducing the work load on personnel.

Keywords: detection, travel times, location, discrimination, regional

OBJECTIVE

The purpose of the work presented is to develop automated methods for identifying regional arrivals at small seismic arrays and automatically estimate their onset times. Automation of these tasks would relieve the analyst from routine tasks and make it also possible to automate some spectral amplitude discriminant analyses.

RESEARCH ACCOMPLISHED

Background.

Automatic phase arrival identification and onset time estimation is of considerable interest because of the need for rapid location and identification of numerous seismic events by networks and arrays monitoring a Comprehensive Test Ban Treaty. Regional seismic arrivals are commonly identified by spectral matrix eigenvalue-based polarization analyses (Jurkevics 1988), slowness estimates and the arrival time sequence. It was found, however, that phase identification based on polarization-slowness characteristics have a very high error rate at small regional seismic arrays, especially for later arrivals such as Pg, Sn and Lg (Suteau-Henson 1991, Kvaerna and Ringdal 1992). Another approach that, instead of identifying regional phase arrivals by their expected analytical characteristics, uses empirical fits to previously observed events can more reliably identify the individual regional phase arrivals (Der et al 1993).

Onset times of seismic "phase" arrivals are defined as times where some visible characteristic, such as amplitude, frequency content or wave polarization changed in some recording. Again, this is a difficult task at regional distances where most of the later arrivals are emergent and poorly defined. Humans are very effective detectors of changes in the properties of seismograms, especially when they are aided by appropriate frequency filtering and display routines. The automated equivalent of such subjective human operation requires the definition of some statistics (e.g. amplitude, AR model, polarization parameters) and some algorithm that can define the time when changes in such parameters occurred. The standard short-term average over long-term average ratio (STA/LTA) algorithm is well suited for arrival detection but not for precise arrival time estimation because of the long delay associated with any significant change in the STA. Most methods proposed for precise arrival time estimation typically attempt to find the first point where some statistic suddenly changes. Many of these work well for most first arriving Pn if the signal is impulsive, but do poorly with emergent phases or secondary arrivals typically seen at regional distances.

The CUSUM algorithms described in Basseville and Nikiforov (1993) were designed for pinpointing the time of a change in a system and have their primary applications in quality control and machine diagnostics. The basic idea is detecting changes in the trends of the cumulative sum of some suitable statistic that abruptly

changes with time as the properties of the time series change. It is much easier to see and quantify a change *in a trend*, than to pinpoint the exact time of the *first point* where the change occurred. The most appropriate statistic to be used depends on the particular change to be detected and will be varied. In the case of seismic arrival onset determination case we look for changes in signal amplitudes, spectral contents (AR model residuals) and polarization (cross-extrapolation residuals) or any combinations of these. A simple application of the method is to compute the cumulative sum of the chosen statistic and subtract a linear ramp from it. This way the changes in the trend of the CUSUM are converted into minima. Numerous methods for automatic finding of minima for empirical functions exist already. The simplest is to find absolute minima in the time windows where the arrival times of phases were expected. Such time window can be provided by the generalized polarization method mentioned above.

The generalized polarization method, developed by Der et al (1993), memorizes the slowness-polarization characteristics of observed regional arrivals by encoding these into a multichannel transfer function that extrapolates the motion on one recorded channel from the rest. It is typically applied to some subconfiguration of a regional array that may include three-component sensors. The encoding of the signal characteristics into some digital filter is fairly standard in other fields (such as speech processing) but has not been applied to seismic data previously. The advantage of this approach is that site effects that cause signal "decorrelation" and distortion of polarization relative to analytical P and S wave models are automatically included. The result is that the method often works better than those based on analytical signal models.

It is possible to design such a multichannel filters from the data by using the standard frequency domain formulation of the Wiener-Hopf equation (Figure 1)

$$\mathbf{h} = \mathbf{S}^{-1} \mathbf{c} \quad (1)$$

where \mathbf{h} is the complex multichannel transfer function (an $n-1$ by 1 vector) and \mathbf{S} is the $(n-1) \times (n-1)$ complex spectral matrix of the time series recorded at the various sensors, excluding the one to be extrapolated, and \mathbf{c} is the $n-1$ by 1 complex column vector of the cross spectra between the $n-1$ input processes and the channel to be extrapolated. Both \mathbf{S} and \mathbf{c} are obviously parts of the total spectral matrix \mathbf{A} of the array data and can be computed directly from the array recordings. As long the makeup of the signals are similar one can compute \mathbf{S} by averaging the cross products of the Fourier transform components over suites of n events

$$S_{ij} = \sum_n f_{in}(\omega) f_{jn}^*(\omega) \quad (2)$$

where the * denotes complex conjugation. In order to weigh the various events with varying event magnitudes equally we normalized the average absolute amplitudes of each event to the same value but kept the relative amplitudes and phases among sensors the same for the same suite of events.

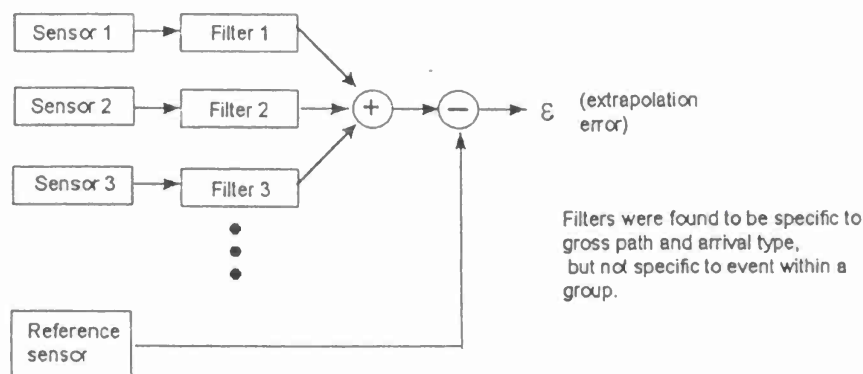


Figure 1. Processing flow of the small array polarization processor.

Application of the CUSUM method to onset time estimation.

To test the CUSUM method we have taken numerous individual traces recorded at ARCESS for regional events located in the Khibiny massif in the Kola peninsula. The purpose of the exercise was to decide how well such an approach performs compared to identification of an arrival by visual inspection of the same traces. Since many of the raw data traces are quite noisy we have applied a 13 point adaptive AR filter to each trace to reduce the low frequency noise prior to the Pn arrival, and emphasize any spectral changes at the arrival of the later phases (Taylor et al 1992). We could have used some fixed band-pass filter to enhance the high frequency regional arrivals with similar efficiency. The resulting traces were rectified and the cumulative sum of the result was computed and the minima identified as phase arrival times. Four examples of such processing are shown in Figure 2. Despite the poor definition of each arrival, and the emergent nature of many of them, the individual minima seem to be surprisingly well defined.

Instead of finding an absolute minimum in the CUSUM-linear trend sum the minimum could also be located by randomized search methods. Simulated annealing (SA) is a suitable technique for finding global minima of irregular functions where many other local minima may exist. It tends to disregard minor local minima and converge to the lowest points. It uses a random search algorithm (the Metropolis algorithm) which is based on a thermodynamic analogy (Press et al 1986). Initially it

allows the search using large steps in the independent variables which may even be associated with increased values of the function. This allows the solution to "jump out" from local minima and resume search for deeper minima. As "cooling" occurs such steps are accepted less and less and finally the solution will settle in broad global minima. Since there is a possibility that occasionally local minima may be located, a few rules are needed to restart the algorithm. The algorithm is extremely fast and can be run many times to narrow down on the actual arrival times and assess their mean error empirically.

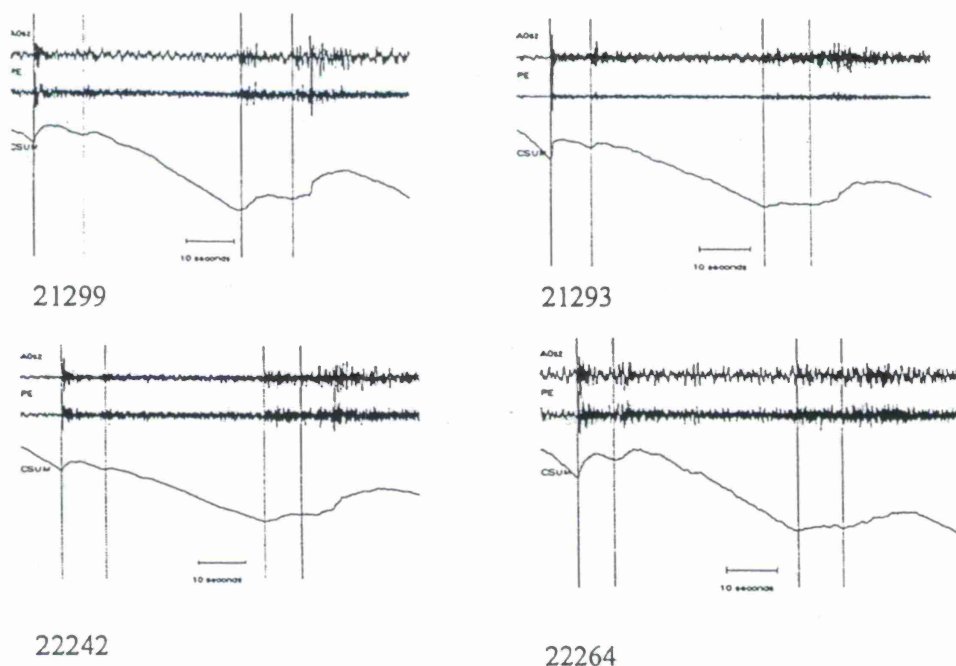


Figure 2. Application of the CUSUM method to four events in the Khibiny data set. The top trace is the original single sensor output, below it is the adaptive AR filtered version. At the bottom is the cumulative sum of the absolute values of the second trace with the time picks (vertical lines) for Pn, Pg, Sn and Lg. Note that in spite of the ill-defined beginnings of each phase the minima are quite well defined. Absolute minima in certain time frames were picked. These examples of onset time estimation are based on both amplitude and frequency content changes enhanced by the AR filter.

Repeated applications of the SA algorithm result in clusters of picks close to the actual arrival times as a seismologist would choose them (Figures 3 and 4). Various strategies can be used for picking the best onset time from such clusters. One could take the median of such clusters, or one could take the leftmost part of the main clusters to compensate for occasional bias caused by the fact that the actual minimum tends to be late for emergent arrivals. The development for the best strategy should be the subject of additional work. Heuristics specially adapted to such results could also help in phase identification, similarly to presently existing systems.

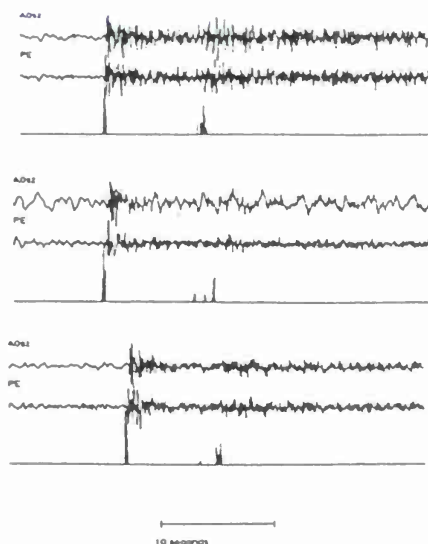


Figure 3. Very stable arrival time picks were obtained using simulated annealing. Adjustments of various parameters (initial temperature and cooling rates) in the algorithm remedied many earlier problems. A few additional criteria were added to restart the procedure if the solution settled in a local minimum. These are displays of histograms of 300 independent SA searches vs. the original and AR filtered seismograms, we are attempting to pick the emergent Pn and Pg phases on SPZ seismograms from the CUSUM.

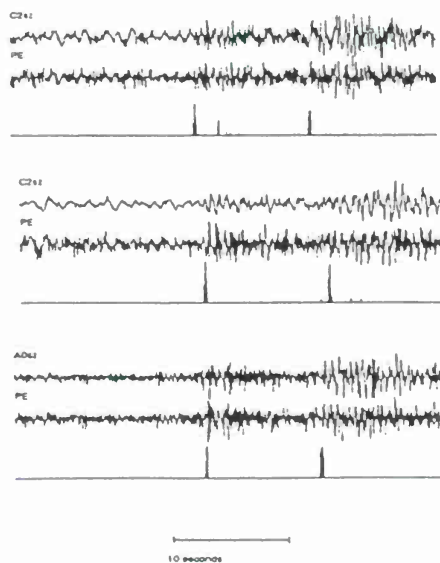


Figure 4. These are displays of histograms of 300 independent SA searches vs. the original and AR filtered seismograms, we are attempting to pick the emergent Sn and Lg phases on SPZ seismograms from the CUSUM.

The scatter in the individual clusters can be used as measures of onset time uncertainty. Moreover, where there is ambiguity, the human analysts would also hesitate. The examples of more difficult picks are shown in Figure 5.

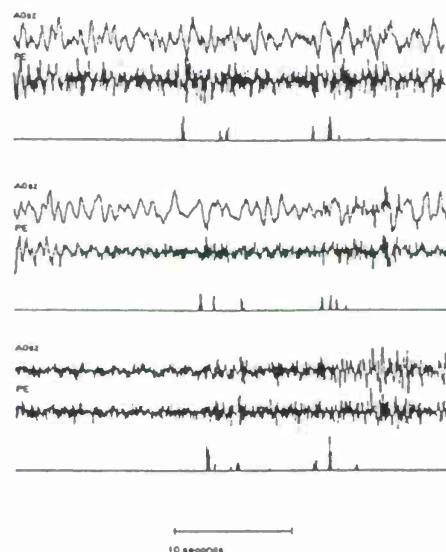


Figure 5. The method has problems with some seismograms. These noisy examples contain poorly defined arrival onsets an analyst would also have trouble with. We still have clusters beginning at the proper arrivals.

Testing of the generalized polarization method on a set of Kola explosions.

We present below some of the results of generalized polarization analyses performed on a data set of Kola peninsula quarry blasts as recorded at ARCESS. All the events, quarry blasts, occurred during 1990. The quarry blasts were grouped into event sets with respect to their locations as determined by the Intelligent Monitoring System also considering their visible characteristics as originating in areas (quarries) named K1, K2, K3, K4, K5 and K8. There is no other independent confirmation, "ground truth", of the validity of these groupings, and they may be in error. The K1, K3, K2 and K5 events together form an overlapping cluster located in a limited area of about 40X40 km 350 km WSE from ARCESS. The K8 and most of the K4 events are grouped at two distinct locations compared to this cluster. We had seven events at K1, ten at K2, eleven at K4, five at K5 and five at K8.

We used six-element arrays, subsets of ARCESS, in two major configurations, the "mini-array" used in Der et al (1993) which consists of a three-component combination at A0 combined with three vertical components in the C ring, and an "all vertical" array that combines the vertical component at A0 with two vertical components

in the B ring and three in the C ring. The choice of these combinations of sensors was dictated by the commonality of error free traces among events and mines. We tried to maximize the amount of data, common error free traces, available. In processing the data we extrapolate the trace A0 from the rest using a five-channel multichannel filter.

In all the processing we have used the "leave-one-out" selection that leaves out the event to be processed from the learning data set used for the design of the filters. This was done in order to exclude the possibility that the exact properties of that event are learned by the processor.

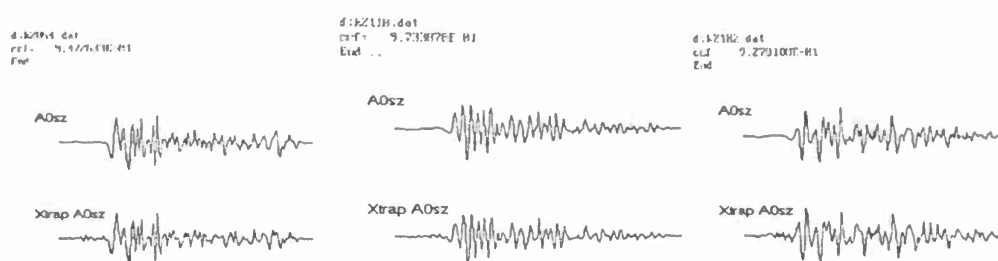
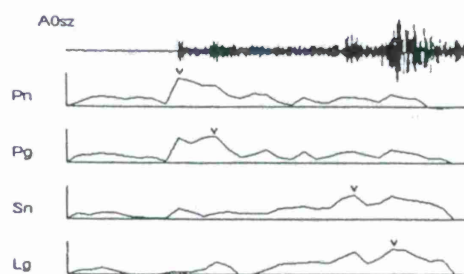


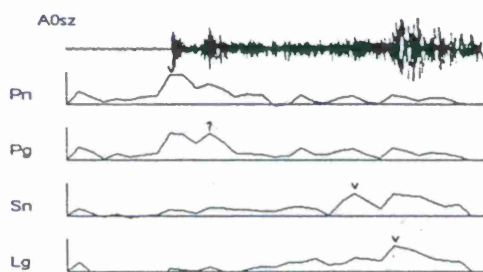
Figure 6. Examples of Pn waveform extrapolations using the "mini-array" and the leave-one-out method. All of the waveform matches between the original A0 waveforms (top) and the waveform extrapolations (below) are excellent. Event identifications and correlation coefficients are plotted above each pair of waveforms. The time length of these waveform segments is 6.4 seconds.

Figure 6 shows examples of Pn extrapolations produced for some K2 mine events. Note the fine details in these waveforms that are reproduced. Such results could not be produced by beamforming or some other simple-minded method. Waveform extrapolations of similar quality can be produced for Pg and Sn. The waveform extrapolations are worse for Lg due to the complexity of this phase (Der et al 1993).

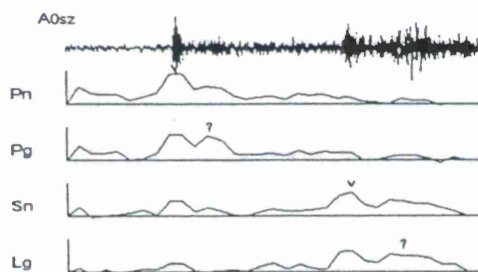
Nevertheless, the method performs well for most events in the tight K1, K2, K3 and K5 cluster even though the processors we designed were based on the nine K2 events only. This shows that the methodology is applicable over sets of events in a wider area than the vicinity of a single quarry. Figure 7 shows examples of processed events for K2 using the leave-one-out method. In these figures we show the A0 trace, to be extrapolated, on the top. The successive four traces below are the plots of the normalized correlation coefficient between this reference trace and the extrapolated traces derived by using multichannel filters over overlapping windows of 256 point (6.4 sec) length. These were designed from the Pn, Pg, Sn and Lg phases, respectively, of the learning event set. The vertical line on the left shows the 0-1 range. Note that the maxima in the normalized correlation coefficient tend to occur at the time of the main wave group of the phase the filter was designed for. Sometimes, even if the absolute maximum is elsewhere, the correlation coefficient for the proper phase is increased relative to the other processing results (bottom example), a possible additional criterion for identification.



Event k2054



Event k2110



Event K2219

Figure 7. Examples of K2 events processed by the leave-one-out technique. The records processed in this figure had the duration of 102.4 seconds.

On the other hand, when we applied the K2 filters to the K4 and K8 events the method did not work, since the slownesses, polarizations and site effects at ARCESS are expected to be different for these quite different event locations. Final implementations will require, similarly to the current systems, the inclusion of some intelligence in the form of appropriate heuristics and rules specially designed to enhance phase identification.

References

- Basseville, M. and I.V. Nikiforov (1993), *Detection of Abrupt Changes: Theory and Application*. Prentice Hall Information and System Science Series, Prentice Hall, Englewood Cliffs, NJ.
- Der, Z.A., Baumgardt, D.R. and R.H. Shumway (1993), The nature of particle motion in regional seismograms and its utilization for phase identification. *Geophys. J. Int.*, **115**, 1012-1024.
- Jurkevics, A. (1988), Polarization analysis of three-component array data. *Bull. Seism. Soc. Am.*, **78**, 1725-1743.
- Kvaerna, T. and F. Ringdal (1992), Integrated array and three-component processing using a seismic microarray. *Bull. Seism. Soc. Am.*, **82**, 1725-1743.
- Press, W.H., Flannery, B.P., Teukolsky, S.A. and W.T. Vetterling (1986), *Numerical Recipes: The Art of Scientific Computing*. Cambridge University Press.
- Suteau-Henson, A. (1991), Three-component analysis of regional phases at NORESS and ARCESS: polarization and phase identification. *Bull. Seism. Soc. Am.*, **81**, 2419-2440.
- Taylor, D.W.A., Ghalib, H.A.A. and R.H. Kimmel (1992), Autoregressive analysis for seismic signal detection and onset time estimation. DCS-92-90. ENSCO Inc., Melbourne, FL.

CONCLUSIONS AND RECOMMENDATIONS

Most of the tests of the CUSUM method applied jointly with adaptive AR filtering showed it to be quite effective for automatic onset time picking in regional seismograms with performance approaching that to a human analyst even for poorly defined, emergent arrivals. In the cases where it did not do well the waveforms were ambiguous, with multiple possible phase onsets, trained seismologist would also have difficulties in defining the onset times of arrivals.

Tests of the generalized polarization analysis showed that it worked well at ARCESS for a set of fairly widely distributed area in the Kola peninsula at a distance of about 350 km when events in this area were used as the learning event set. As it is to be expected, the processor did not work for events farther outside this area. This work has validated the performance of this method on a data set larger than the original one used for its development. It is thus a viable potential alternative to slowness-rectilinearity analyses

We recommend that these methods be implemented and tested in one of the current monitoring systems and their performance is tested against more conventional methods.

DEVELOPMENT OF A LITHOSPHERIC MODEL AND GEOPHYSICAL DATA BASE FOR NORTH AFRICA

Diane I. Doser, G. Randy Keller, Paul Dial, Kate C. Miller and Steven Harder, Department of Geological Sciences, University of Texas at El Paso, El Paso, TX 79968-0555

Sponsored by U.S. Department of Energy
Office of Nonproliferation and National Security
Office of Research and Development
Contract Number F19628-95-C-0104

ABSTRACT

We have collected seismic, geologic, gravity and other potential field data to develop a model of the North African lithosphere via an integrated approach. We have modeled gravity data along three transects across North Africa: 1) from north central Egypt across Libya to the Hoggar Uplift, 2) from north central Tunisia across northern Algeria to the Atlantic coast of Morocco, 3) from north central Algeria across the Hoggar Uplift to northern Chad. The gravity models are constrained wherever possible by geologic and other geophysical information. Crustal thicknesses we have obtained for the Hoggar Uplift (38 km) agree well with preliminary results of seismological studies by other research groups. Our modeling results also suggest that the mantle anomaly under the Hoggar Uplift is relatively small (200-300 km wide, less than 60 km in vertical extent) compared to mantle anomalies associated with other hot spots and rift zones. A Bouguer gravity map, filtered Bouguer gravity map, and the three interpreted gravity profiles can be accessed at the web site: <http://www.geo.utep.edu/nafr/nafr.html>.

We have collected Worldwide Standardized Seismograph Network (WWSSN) seismograms from stations located at regional distances for magnitude > 5.0 earthquakes occurring within North Africa (between 1963 and 1988) and their associated aftershocks. We are currently modeling these seismograms. First we construct a preliminary 1-D velocity model based on crustal structure determined from our gravity models. We then utilized a reflectivity code to generate synthetic seismograms. Our results from a propagation path between Algeria and recording stations in Spain and Portugal using aftershock recordings of the 1980 El Asnam, Algeria, earthquake sequence match the initial waveform (P, PL) character well, but overestimate surface wave amplitudes. This may suggest backscattering of surface wave energy by structural changes along the propagation path. Results of our preliminary modeling may also be accessed at our web site.

We have collected travel time delay and magnitude information for over 70 earthquakes occurring in North Africa between 1960 and 1992 from ISC and ISS bulletins. We are utilizing the older (WWSSN) events to increase coverage in regions with little recent (post-1985) seismicity. In addition to standard plots showing map views of travel time delays, we have been examining the utility of plane-parallel coordinate plots to display delay and magnitude variations with distance and azimuth.

Keywords: geophysical data base, North African lithosphere, gravity models, regional seismograms

OBJECTIVE

We will develop a model of North African lithosphere via an integrated analysis of seismic, potential field, and geologic data. In particular, we will construct detailed 2-D models from known earthquake source regions to key seismic monitoring stations in the region. An outgrowth of this effort will be a data base of geological and geophysical information which will be made available to the scientific community through electronic access.

RESEARCH ACCOMPLISHED

A first step in our study of North African lithosphere was the collection of pertinent geological and geophysical information for our data base. We have digitized the locations of numerous geological features within the North African region to aid in our interpretation of gravity and seismic data. These features include: surface exposures of Precambrian rocks in the major uplifts, depth to Paleozoic and Mesozoic basement within the Sirt Basin of Libya, surface faults within the Sirt Basin, the location of Pan-African suture zones and Cretaceous and Cenozoic age rifts, and the boundaries of West and Central African rift basins. Many of these maps can now be accessed electronically from our web site at: <http://www.geo.utep.edu/nafr/nafr.html>.

We have collected gravity data from a number of sources including the unclassified data from the global data base maintained by the Defense Mapping Agency (36,000 points) and additional data from Libya that were compiled by one of our graduate students (Suleiman, 1993; 5,000 points). A third set of data was obtained in the form of a 5' by 5' Bouguer gravity anomaly grid from GETECH, which is associated with Leeds University. We are only free to use these data in the form of maps which are contoured at intervals of 10 mGal or greater. Details on the availability of these data, along with filtered and unfiltered gravity maps in full color, can be found at our web site.

We have modeled three gravity profiles across the region (Figure 1). These profiles represent important propagation paths between earthquakes and seismograph stations located within North Africa. Profile 1 extends from central Egypt, the site of several recent earthquakes and seismograph stations, across central Libya where we have good geological and geophysical control on crustal structure (e.g. Suleiman, 1993; Nyblade et al., 1996) to the Hoggar Uplift, site of several French nuclear tests in the early 1960's. Profile 2 extends across the Atlas Mountains from the Atlantic coast of Morocco to central Tunisia. Earthquakes and seismograph stations are located throughout the region. Profile 3 extends from north central Algeria across the Atlas Mountains to the Hoggar Uplift. A preliminary velocity model has been obtained by McNamara et al. (1996) from regional seismograms whose waves propagate along paths that parallel Profile 3.

An interpretation of Profile 3 is shown in Figure 2. Here the shallow upper crustal structure is constrained from knowledge of basin geometries and thicknesses (e.g. Schurmann, 1974; Lesquer et al., 1988). The Moho depth at the northern end of the profile is constrained by the results of the European Geotraverse (Ansorge et al., 1992). The crust appears to rapidly thicken beneath the Atlas Mountains, then gradually thin to the south. The Hoggar Uplift can be modeled with a 38 km thick crust. A gravity low over the uplift suggests the presence of an upper mantle anomaly with width of 200 to 300 km and depth of 40 to 60 km, much smaller than observed under the Ethiopian and Kenyan domes. Interpretations of all three profiles can be found at our web site. Our collection of gravity data and results from other crustal/mantle studies has also allowed us to develop a crustal thickness map for Africa (Figure 1).

We have collected pre-digital seismic recordings at regional distances to increase data coverage across regions of North Africa with little recent (post-1985) seismicity and where no digital station coverage is currently available to constrain certain propagation paths. We begin the waveform modeling process by constructing preliminary 1-D models based on crustal structure determined from gravity models and other geophysical studies. We then use a reflectivity code (Randall, 1989) to generate synthetic seismograms.

One of our first modeling studies has focused on aftershocks of the 1980 El Asnam sequence of northern Algeria as recorded at MAL, TOL, and PTO (Figure 3). The propagation

paths for these events include 300 to 500 km of the Mediterranean Basin and as much as 700 km of continental crust in Spain and Portugal. Seismograms for the aftershock sequence were hand digitized and 88 seismograms from this sequence have been modeled. We developed a simple 1-D velocity model (Figure 4) for the propagation path based on the velocity model obtained from receiver function studies at TOL (Seeber et al., 1996) and crustal structure studies of Geiss (1987). We have focused on matching the relative amplitudes of the initial portion of the observed waveforms (P,PL). The degree of time shifting to match the waveforms varied, but was < 10 sec for 75% of the seismograms. An example of waveform modeling for an aftershock recorded at TOL is shown in Figure 4. Note that the synthetic surface wave amplitudes (dashed) overestimated the observed amplitudes within the latter portion of the wavetrain. We have found this to be true of many of our seismograms. This may suggest structural changes along the propagation path unaccounted for by the 1-D model. The tangential component of motion at these stations is also large, suggesting dipping layers. Some results of our modeling studies can be found at our web site.

Travel time delay and magnitude information for over 70 earthquakes occurring between 1960-1992 in the region were also collected. We have focused on magnitude > 5.0 events (whose focal mechanisms, epicentral locations and focal depths are fairly well determined) and their associated aftershock sequences. In addition to standard travel-time delay plots, we have examined the utility of plane-parallel coordinate plots to display delay and magnitude variations. Figures 5a and 5b show standard travel-time delay plots for WWSSN stations PTO and TRI from aftershocks of the El Asnam earthquake sequence. Note most delays at PTO are negative, whereas TRI has more positive delays. Figure 5c illustrates how the delays at several stations from the same earthquake sequence can be looked at simultaneously using a plane-parallel coordinate representation of station distance, azimuth from earthquake to station, delay time and earthquake magnitude. We feel this representation approach provides a way to rapidly evaluate variation in delay values at a several stations and to determine how this variation relates to azimuth, distance and earthquake magnitude.

CONCLUSIONS AND RECOMMENDATIONS

We are continuing our modeling of regional seismic phases. In addition to the El Asnam sequence, we are currently concentrating on a sequence in the Red Sea. We are in the process of transferring our delay-time and magnitude variation information to our web site, as well as determining which combination of coordinate axes for plane-parallel coordinate plots provide the best displays of magnitude and delay information.

REFERENCES

- Ansorge, J., D. Blundell, and St. Mueller, 1992. Europe's lithosphere-seismic structure, in *A Continent Revealed: The European Geotraverse*, D. Blundell, R. Freeman and St. Mueller (eds.), Cambridge University Press, 33-69.
- Geiss, E., 1987. A new compilation of crustal thickness for the Mediterranean area, *Annales Geophysicae*, 5B, 623-630.
- Lesquer, A., A. Bourmatte, and J. M. Dantria, 1988. Deep structure of the Hoggar domal uplift (central Sahara, south Algeria) from gravity, thermal and petrological data, *Tectonophysics*, 152, 71-87.
- McNamara, D.E., W.R. Walter, C. Schultz and G. Goldstein, 1996. Regional phase propagation in Northern Africa and the Mediterranean (abstract), *Seismo. Res. Lett.* 67, 47.

Nyblade, A.A., I.S. Suleiman, R. Roy, B. Pursell, A.S. Suleiman, D.I. Doser, and G.R. Keller, 1996, Terrestrial heat flow in the Sirt Basin, Libya, and the pattern of heat flow across northern Africa, *J. Geophys. Res.* 101, 17,737-17,746, 1996.

Randall, G.E., 1989. Efficient calculation of differential seismograms for lithospheric receiver functions, *Geophys. J. Int.* 99, 469-481.

Schurmann, H.M.E., 1974, *The Precambrian in North Africa*, E.J. Brill, Leiden, The Netherlands, 351 pp.

Seeber, D., E. Sandoval, M. Vallve, G. Brew, and M. Barazangi, 1996. Development of a geological and geophysical information system and seismological studies in the Middle East and North Africa, *Proc. 18th Ann. Seis. Res. Symp. on Monitor. a CTBT*, 1026-1035.

Suleiman, A.S., 1993. Geophysics of the rifts associated with the Sirt Basin (North Africa) and the Anadarko Basin (North America), Ph.D. Dissertation, The University of Texas at El Paso, 150 pp.

Depth to Moho in Africa

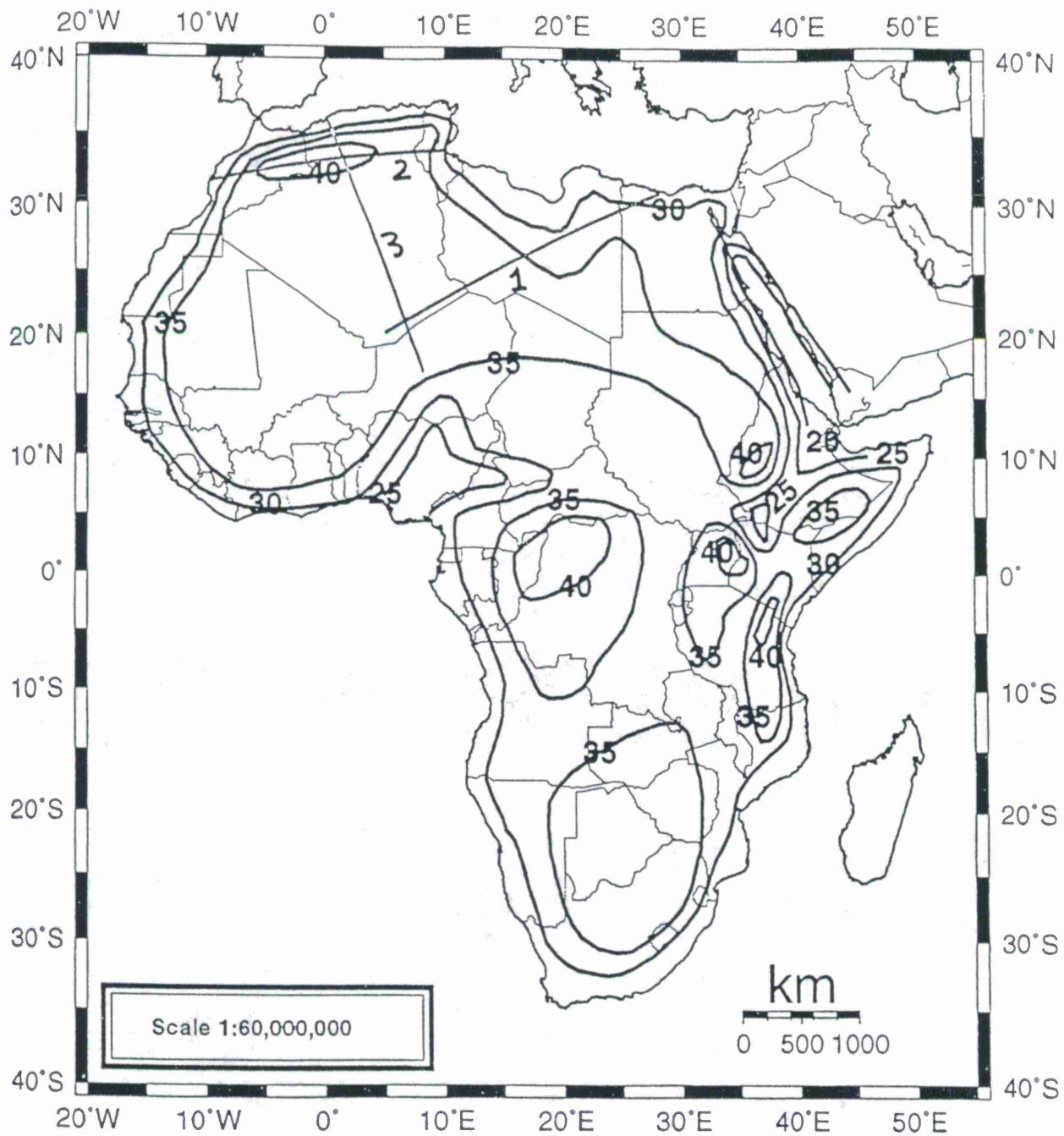


Figure 1. Crustal thickness map of Africa. Profiles 1, 2, and 3 are profiles used in gravity modeling study.

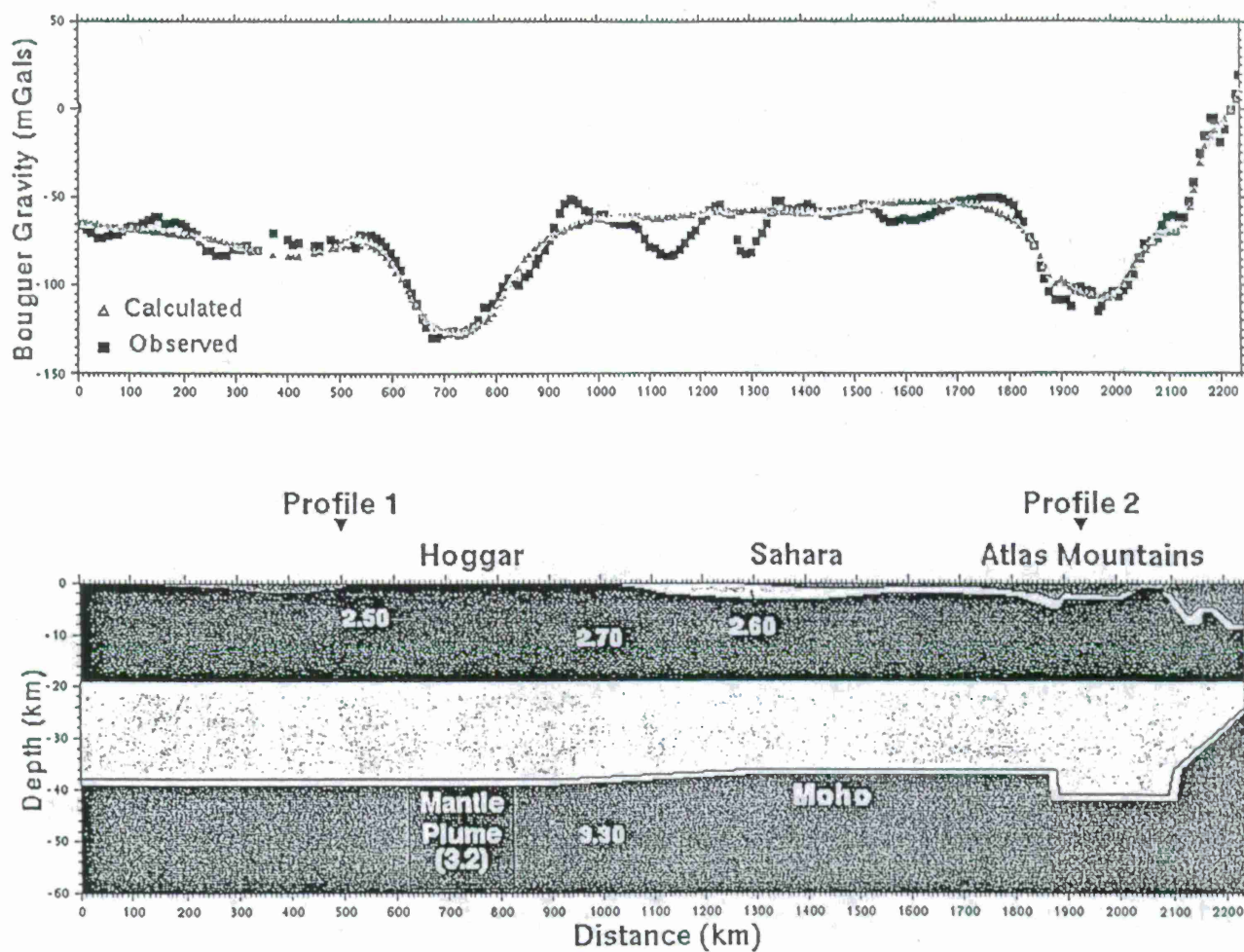


Figure 2. Lithospheric model for Profile 3 (southern Algeria to northern Algeria). Numbers are densities in g/cc. The upper two units of the model which are not labeled are Mesozoic and Paleozoic sedimentary rocks with densities of 2.5 and 2.6 g/cc, respectively.

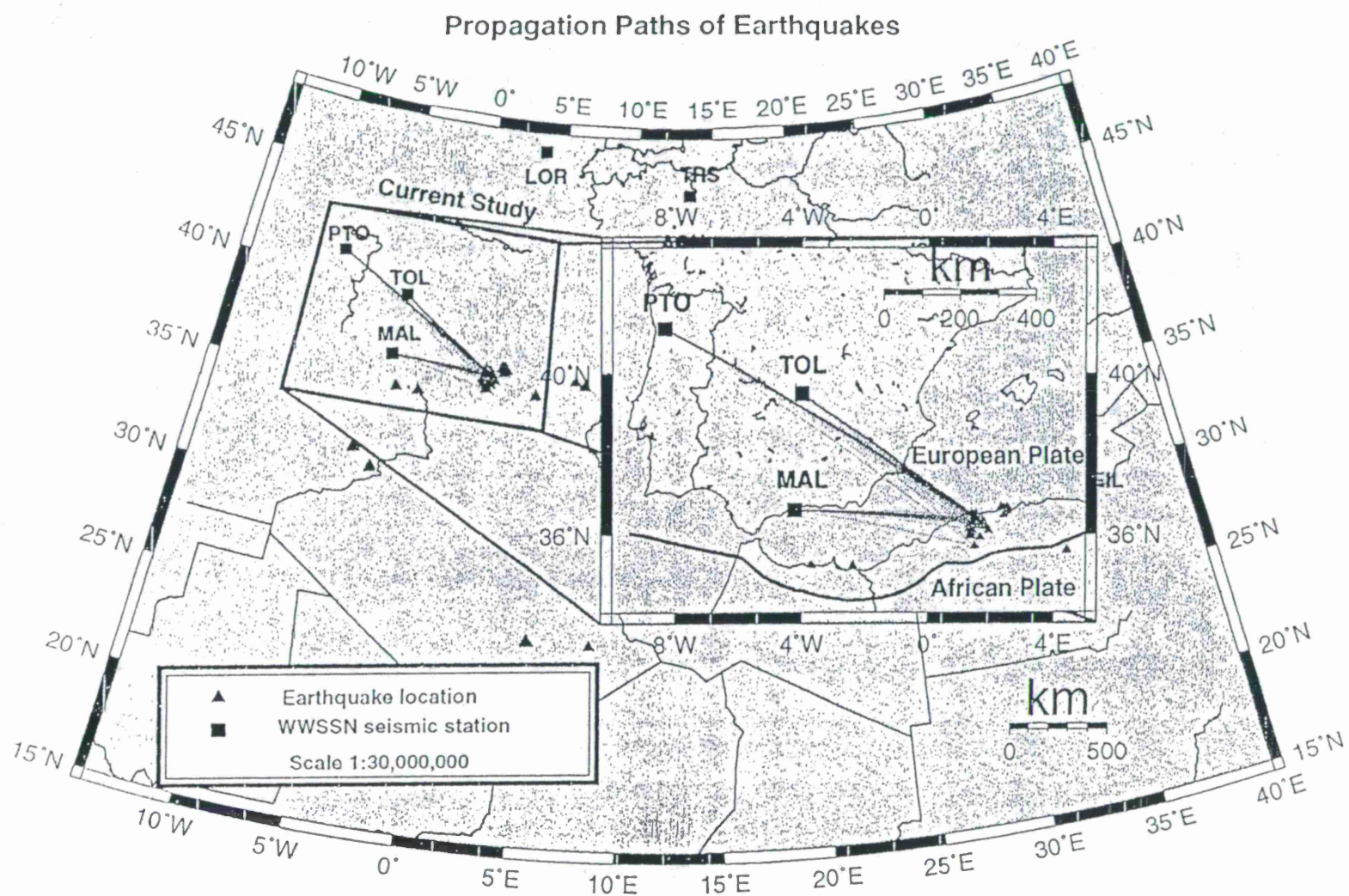


Figure 3. Propagation paths of earthquakes of the El Asnam sequence to WWSSN stations in Portugal and Spain.

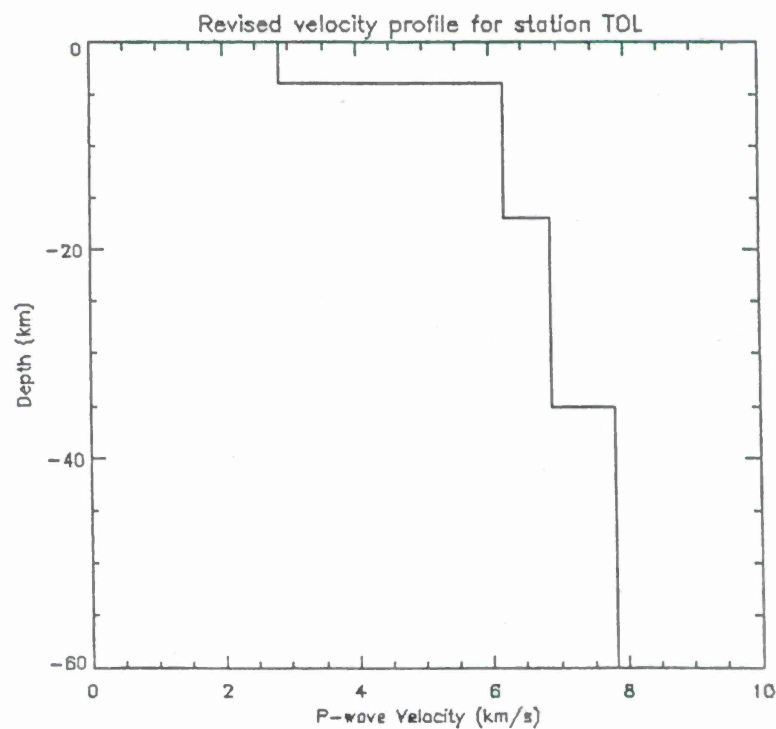
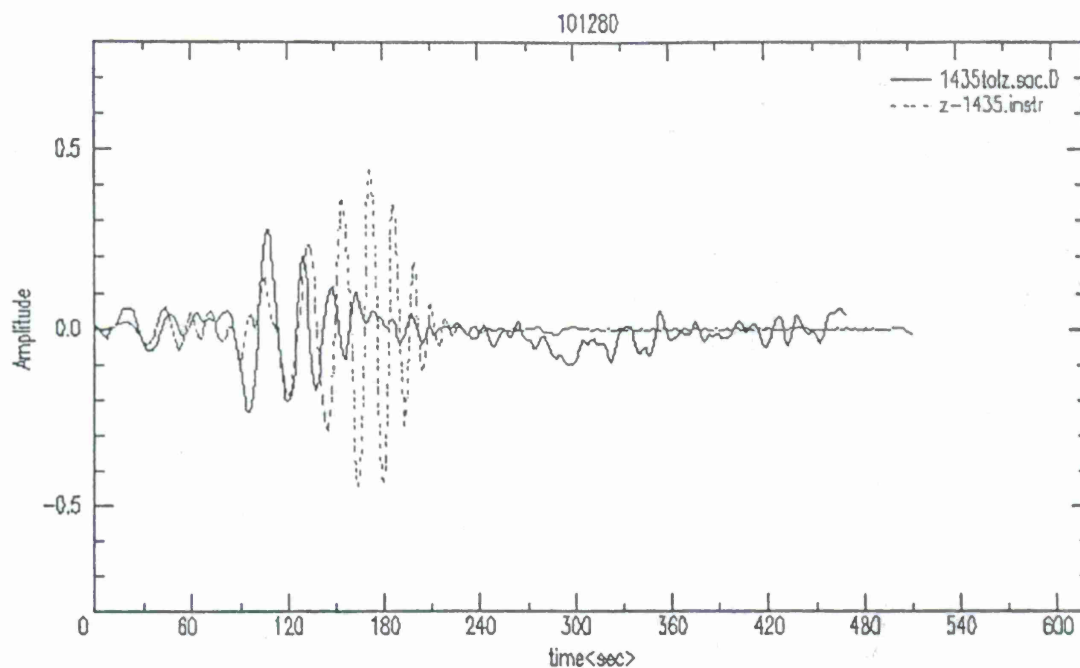


Figure 4. Comparison of observed (solid) and synthetic (dashed) seismogram for an aftershock of the El Asnam Algeria sequence occurring on 10/12/80 as recorded at TOL (Toledo, Spain). The velocity model of 4-layers with a crustal thickness of 35 km is shown at bottom.

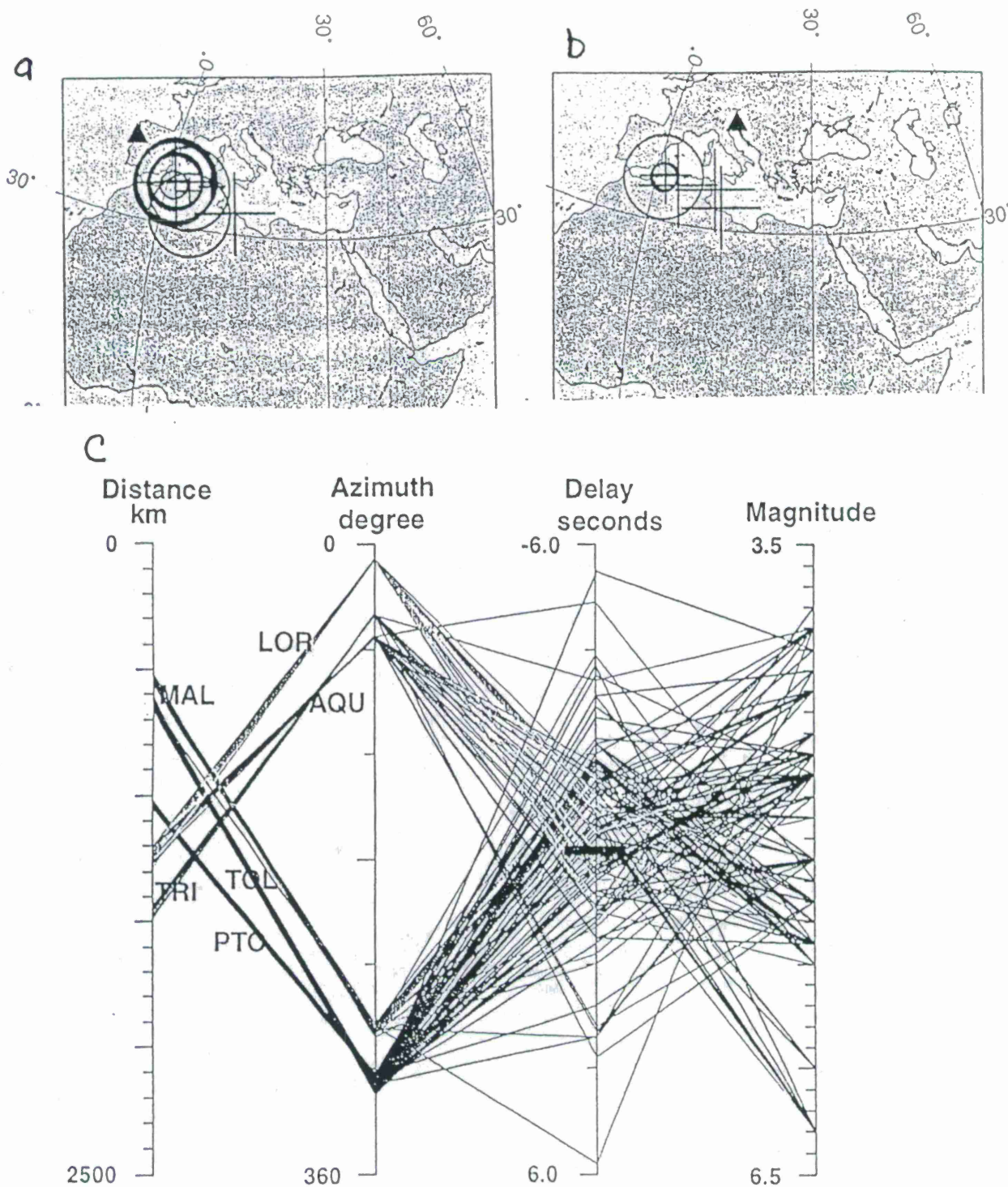


Figure 5. Travel time delays of aftershocks of the El Asnam sequence as observed at PTO (a) and TRI (b). Circles indicate negative delays, pluses positive delays. Size of symbol is related to magnitude of time delay. (c) Plane-parallel coordinates plot illustrating variation in time delay with distance, azimuth and magnitude for aftershocks of the El Asnam sequence. Each set of observations for a particular WWSSN station is labeled.

VISUALIZATION TOOLS FOR COMPREHENSIVE TEST BAN TREATY RESEARCH

Tony L. Edwards, J. Mark Harris, Randall W. Simons, Christopher J. Young
Sandia National Laboratories

Sponsored by U.S. Department of Energy
Office of Nonproliferation and National Security
Office of Research and Development
Comprehensive Test Ban Treaty Research and Development Program
Contract No. DE-AC04-94AL85000

ABSTRACT

This paper focuses on tools used in Data Visualization efforts at Sandia National Laboratories under the Department of Energy CTBT R&D program. These tools provide interactive techniques for the examination and interpretation of scientific data, and can be used for many types of CTBT research and development projects. We will discuss the benefits and drawbacks of using the tools to display and analyze CTBT scientific data. While the tools may be used for everyday applications, our discussion will focus on the use of these tools for visualization of data used in research and verification of new theories. Our examples focus on uses with seismic data, but the tools may also be used for other types of data sets.

Keywords: data visualization, scientific visualization, Comprehensive Test Ban Treaty, CTBT.

1. Introduction

Scientific visualization is one of the many reasons that computer graphics is used heavily today. Scientists are not artists, but they do need to view their data graphically, and their data sets exist on computer systems, so it is natural to display this data on the computer.

Visualization often helps people extract information from data faster and more efficiently. The large volumes of event data and the wealth of contextual information to support decision making make data visualization a portion of CTBT research.

Three-dimensional visualization is currently a popular method for displaying scientific data. This method gives a user an unlimited range of views for their data. They may look at the data from any angle, zoom in or out, and slice volumes of data into single planes. Often, new information about the data is gleaned from this highly flexible method of examining the data.

The following sections will provide an overview of applications available commercially and via the Internet that were used by the Data Visualization Team at Sandia National Laboratories. These tools provide the capabilities to display data in 2-D and 3-D. Some of the tools are best suited to rapid prototyping, while others are better for high speed visualization. The tools to be discussed are: AVS Express, The Visualization Toolkit, OpenGL, and MATLAB.

2. Research Environment

Our research environment consists of Sun Ultra1 and Ultra2 workstations with Creator3D graphics. The Ultra1 workstations contain a 167mhz processor and the Ultra2 workstations contain two 200mhz processors. The Creator3D graphics cards contain hardware enhancements for accelerated 24-bit, double- and Z-buffered 3-D rendering. Many of our visualization efforts use GSETT II data (Group of Scientific Experts 1992) and GSETT III reviewed event bulletins from the International Data Center.

3. Advanced Visual Systems (AVS) Express

AVS Express is a data visualization application that is available from Advanced Visual Systems (<http://www.avs.com>). This product allows for rapid visualization of data via a large set of predefined modules. These modules provide image processing, picking, graphing, hardcopy output, GIS, Database, GUI creation, math routines, etc. Most of what the user needs is here and if it is not available you can create your own through C, C++ or FORTRAN. AVS Express will run on Unix and Windows NT and 95 platforms. AVS Express takes advantage of hardware acceleration if available or uses a software renderer otherwise.

AVS Express uses a visual network editor (see Figure 1) to develop an application. All of the user's modules are networked together via input and output data ports. The data flows from files and databases through the different modules and finally into a two or three dimensional viewer. Different filters (slice, orthoplot, etc.) may be applied to the data before it is displayed.

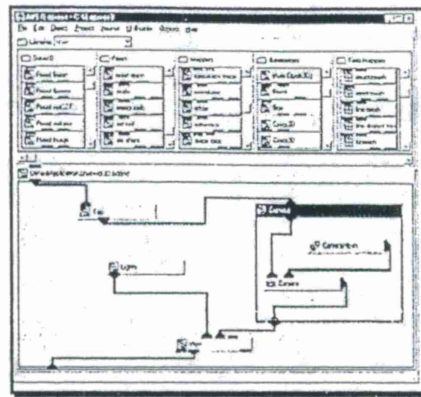


Figure 1. AVS Express Network Editor

We used the GIS and database modules to visualize data from a CSS 3.0 database from GSETT II data(Anderson, et. al. 1990) (See Figure 2). We were able to create spherical and 2-D mapping projections of GIS data sets supplied and use the database module to access an Oracle database (Simons, et. al. 1996). The GIS modules provide access to CIA World Data Bank II and Digital Elevation Map (DEM) data. You may also read data from other data files or via remote processes.

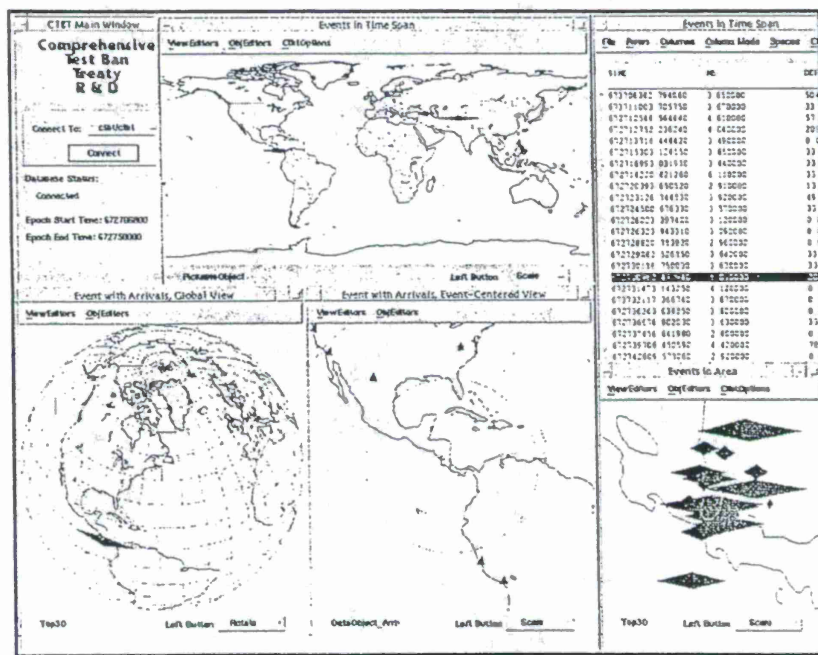


Figure 2: Data Visualization with AVS Express

AVS Express is a relatively expensive product, but it does offer a rich suite of tools to visualize any data. This product did run slow on our machines due to the amount of data and the fact that AVS Express does not support OpenGL on the Sun platforms at the time of this writing. Much of the poor performance could be due to the overwhelming module support the product contains. If the data set is small and specialized, this product is

overkill. If you view many types of data and need fast prototyping or visualization, this product could be a great tool for your research.

4. The Visualization Toolkit

The Visualization Toolkit (VTK) is a 3D graphics package that grew from research at the General Electric Corporate R&D Center. It is still supported by the staff at General Electric. The product is freely available via the Internet (<http://www.cs.rpi.edu/~martink/>) or may be purchased with the official book (*The Visualization Toolkit: An Object Oriented Approach to 3D Graphics*, Will Schroeder, Ken Martin, Bill Lorensen, Prentice Hall). The software in the book is several versions old now, but the book is still great hardcopy reference. The software has support for many graphics libraries and platform support for Unix and Windows NT and 95 based PCs.

VTK was written in C++ (you will need a C++ compiler to compile the package) in order to take advantage of the object-oriented capabilities of the language. You may write code in C++ or use the Tcl Interpreter (information on Tcl can be found via the Internet at <http://sunscript.sun.com>). Using the Tcl Interpreter can provide for rapid prototyping, but we found that creating an application was just as easy using C++.

VTK, like AVS Express, provides a large suite of tools for 3-D data visualization. VTK provides all of the necessary routines to create and manage cameras, geometry support, analysis routines, hard copy support, interaction, etc. There is no support for GIS mapping or database connectivity. This capability must be created by the developer of the application.

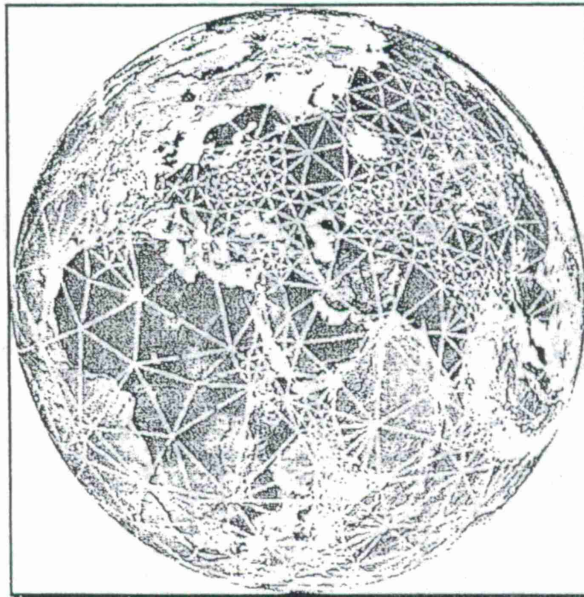


Figure 3: Visualization using The Visualization Toolkit

To investigate VTK, we created an application to view Knowledge Base data on a 3-D globe (See Figure 3). We had to create the necessary code to read coastline data and the

Knowledge Base data, but we used VTK's interaction routines, OpenGL support, and earth object to create the heart of our application. The amount of code that we had to write to support our application was minimal.

VTK also supports viewing of data with stereoscopic glasses. We used this to visualize many different data sets and found stereoscopic viewing to be a valuable asset to 3-D data visualization. We used the CrystalEyes product from StereoGraphics (<http://www.stereographics.com>) to view our data in stereo. Stereoscopic viewing is accomplished by showing the left image on the display while the right lens of CrystalEyes is closed, then showing the right image on the display while the left lens is closed. Because this happens a minimum of 120 times per second, you perceive left and right views simultaneously. The result is amazingly real depth perception.

The performance proved to be quite slow, but this is due to VTK's limited capability of taking advantage of graphics hardware. VTK has support for numerous windowing and graphics packages. This has great functionality, but it does limit performance.

5. OpenGL

OpenGL is an application programming interface (API) that is available on almost all platforms used today. OpenGL is supported by strong industry standards and conformance. Online information regarding the OpenGL standard can be found at <http://www.sgi.com/Technology/OpenGL/>.

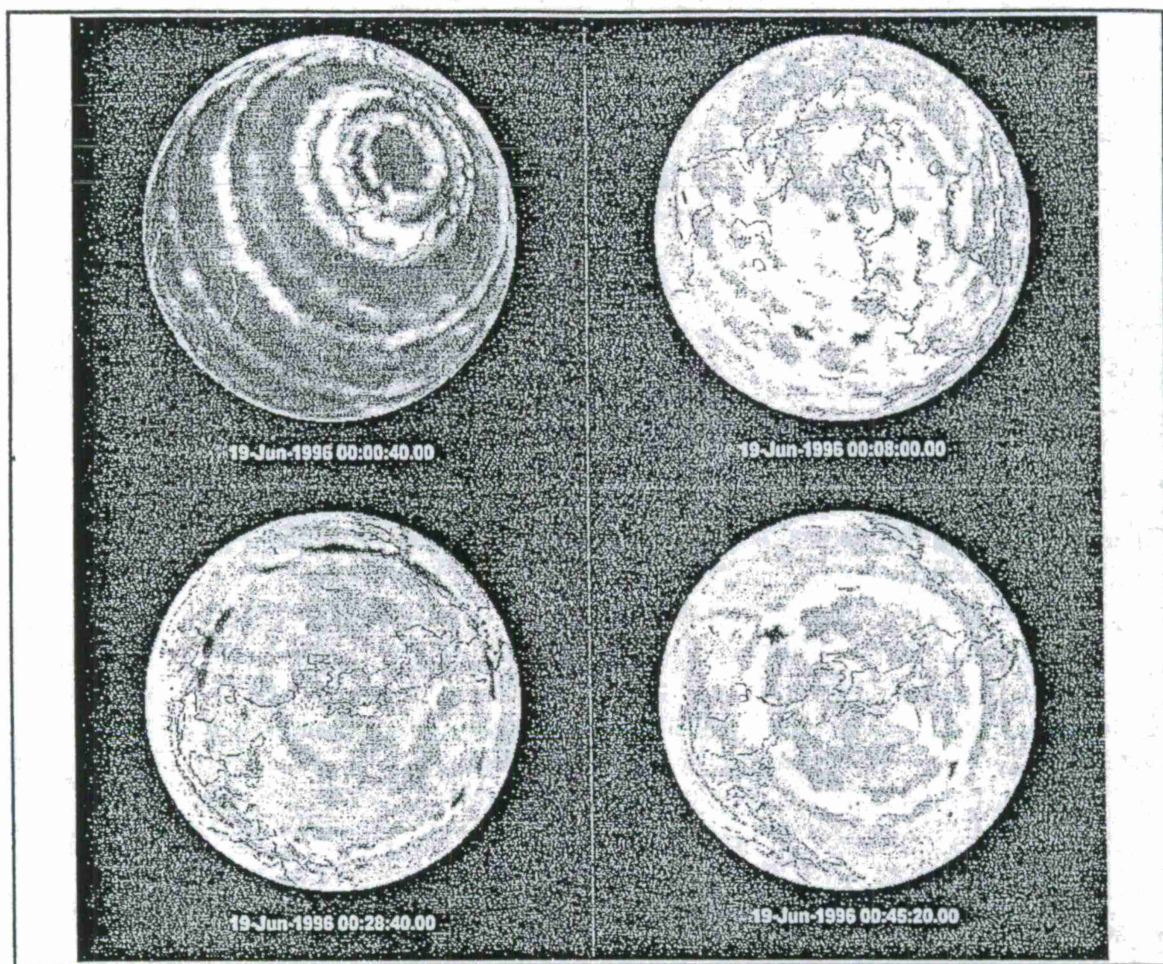
We implemented several data visualization applications using OpenGL and C++. Figure 4 shows an OpenGL application that displays output from the Waveform Correlation Event Detection System (Young, et. al. 1996). This application was created to animate the data over a set period of time. Our initial data set looked at 1 hour of data stepped at 10 second increments. The performance is excellent because we wrote software that was optimized for the graphics hardware.

Programming data visualization this way does require the developer to create all of the graphics code from scratch, but once this is done, a developer should be able to support other data sets fairly easily. We created a graphics user interface using Motif and created the necessary basic OpenGL elements (lighting, camera positions, rotation, zoom, pan, etc.). We also had to handle the GIS mapping (coastlines) and file input and output. Data input into OpenGL can be done fairly easy by inputting your data set as points, but some thought must be put into what you want to visualize. Once we created the basic elements we are able to display data in a variety of ways by changing the data set we wished to view.

By programming a visualization system by hand, a developer is able to create exactly the elements required to display their data and consequently performance is optimized. In contrast, much overhead goes into commercial and public domain packages to support the mythical average user, and performance can be affected. Clearly there is a big trade off

with the time it takes to develop an OpenGL graphics package vs. performance. There are many toolkits available to help with design, but it is still time consuming.

Figure 4: Data Visualization with OpenGL



6. MATLAB

MATLAB is a commercial product from The MathWorks, Inc. (<http://www.mathworks.com>). MATLAB is an application for technical computing that combines numeric computation, advanced graphics and visualization, and a high-level programming language. We have found MATLAB to be an excellent environment for analysis, algorithm prototyping, and application development. Many data analysis procedures, such as spectral estimation, filtering, and interpolation, are available at the command line to operate on data in matrix variables. Other processing capabilities are available from The MathWorks in the form of toolboxes. These include things such as wavelets, neural networks, and system identification.

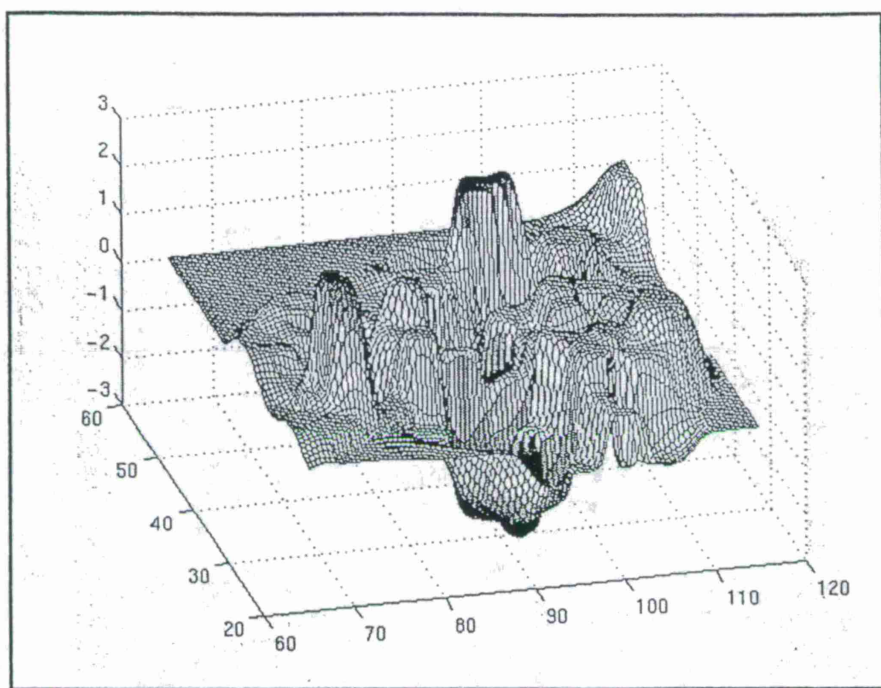


Figure 5: Spatial Data Visualization with MATLAB

We routinely use MATLAB to process and visualize spatial data, such as the interpolation of travel-time error corrections as shown in Figure 5. Using the high-level plotting commands in MATLAB, the interpolated surface may quickly be viewed and manipulated to aid in the development of the algorithms.

To support seismic waveform processing algorithm development, we developed MatSeis, a seismic analysis GUI programmed in MATLAB (<http://www.ctbt.rnd.doe.gov/ctbt/data/matseis/matseis.html>). MatSeis (Harris, et. al. 1996) makes it easier to access seismic data in MATLAB from our CSS 3.0 database. The standard MATLAB environment is available from the command window. Data displayed in MatSeis may be accessed on the command line for manual processing and the results plotted using MATLAB or entered back into MatSeis. The basic MatSeis display (see Figure 6) is an interactive data profile (time vs. epicentral distance) integrating event origin, waveform, travel-time, and arrival data, all of which are selectable objects. Graphical plot controls, data manipulation, and signal processing functions are provided. Current capabilities include filtering, beaming, spectral analysis (PSD and spectrogram). FK analysis, vespagram creation, database editing, and mapping. We continue to develop modules as needed by our group.

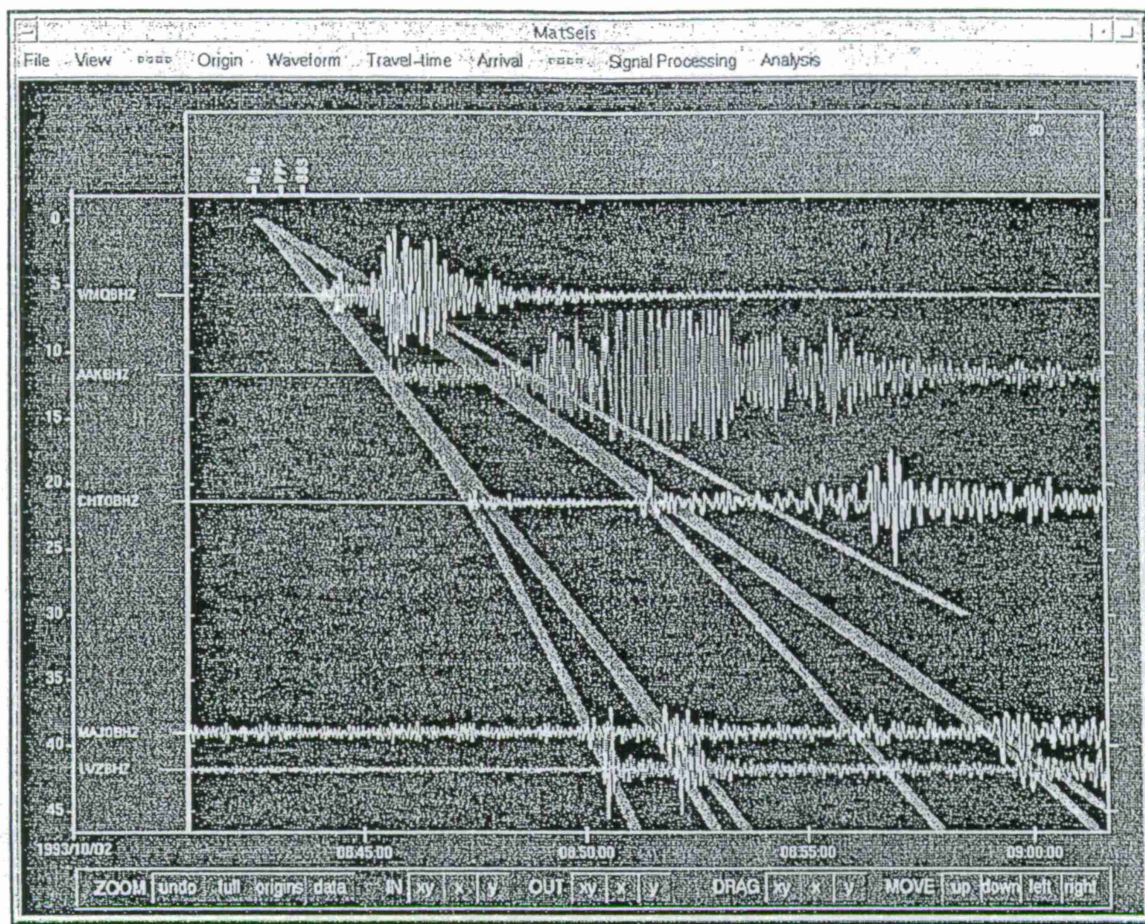


Figure 6: MatSeis Application using MATLAB

7. Conclusions

With the increased amount of data that must be analyzed to monitor the CTBT, the need for visualizing the data in more than two dimensions is becoming apparent. Interactive displays for this type of data are essential. There are many programming tools and applications available in the market today for scientific visualization. This paper discussed several tools that Sandia National Laboratories researchers used to visualize data for CTBT research. We feel that these tools could fulfill the needs of many CTBT researchers regardless of scientific field.

To aid researches in deciding which of the tools are most appropriate for them, we have categorized them according to the following criteria: cost, creation method, support, performance, and platforms available (see Table 1). The creation methods for application development were by hand coding or visual interface builder. A visual interface builder allows you to build an application by connecting individual modules together to make an application. The performance characteristics in Table 1 were based on our observations. When building any type of data visualization application, performance is driven by the amount of data to be viewed and how the application was programmed. While using OpenGL, we were able to program the software in several ways. When we programmed

the software within the specific parameters of the hardware vendor, we were able to get the highest performance.

	Cost	Creation Method	Support	Performance	Platforms
AVS/Express	\$15K+	Visual interface and/or code	Vendor	Slow to Medium	Unix, PC
Visualization Toolkit	\$0	code	Developers and Newsgroups	Slow to Medium	Unix, PC
OpenGL	\$0 to \$1000+	code	Vendor and Newsgroups	Medium to High	Unix, PC, Mac
MATLAB	\$1000 to \$4000	code	Vendor	Medium	Unix, PC, Mac

Table 1: Visualization Tool Characteristics

When starting to develop an application for data viewing, the developer must be aware of the potential end user. Who is the end user, how often will this application be used, and what systems will be used are important questions to ask. If a scientist needs to view an application only once, than a commercial off the shelf (COTS) package may be the best application for development. Conversely, if the application needs to handle real-time data and be used routinely, a COTS application may not be a good choice for development.

8. Additional Topics

There are other important areas of interest that a developer or scientist should consider while implementing a visualization application. We will discuss a few of these topics below.

For some problems, the user may wish to explore more exotic technologies. For example, large data sets could be explored with Virtual Reality technologies. Visualizing in this method gives users a better sense of depth compared to traditional display technologies. With the use of the Virtual Reality Modeling Language (VRML), it is even possible to share data viewing across the World Wide Web with other scientists.

GIS systems can also provide valuable information. For example, displaying event data on actual topological maps could prove to be a great asset. Of course a GIS is more than just maps and land formations; it also has the capability to store critical attributes about the area, such as mines, industrial areas, geological formations, etc.

We are currently developing software to view correction data used for the CTBT knowledge base. The viewing of the algorithms and the data is very important in creating an accurate application. One particular area of visualization need is in knowledge base grid editing. The grid must be checked for adequate coverage, proper interpolation, and referenced to contextual information such as geologic and political boundaries.

Another very important issue in visualization is Human Computer Interaction (HCI). The most important item you will encounter when developing your application is color (Tufte 1990). The use of color can display the correct information and can also convey the wrong information. The user must be aware of how color is used in your application.

9. Conclusions and Recommendations

We have discussed several tools used in scientific visualization at Sandia National Laboratories. While these tools ranged in cost from cheap to expensive, no tool stands out as a clear answer to all of our visualization needs. A scientist must understand his audience, data needs, visualization experience, and application's main goal to decide which tools is the best for them. There are many ideas and approaches to scientific visualization. It is important to try many different methods of visualization to make sure a user understands the data correctly. One must take into account textures, lighting, modeling approaches, proper data set creation, colors, hardware, software, etc.

Future visualization efforts at Sandia National Laboratories will focus on helping researchers and users extract information from increasingly large, complex spatially oriented data sets, such as those found in the CTBT Knowledge Base.

10. References

Anderson, J., Farrell, W. E., Garcia, K., Given, J., and Swanger, H. (1990), CSS Version 3 Database: Schema Reference Manual, Science Applications International Corporation, Arlington, VA.

Simons, R. W., Young, C. J., Edwards, T. L. (1996), Data Visualization for Comprehensive Test Ban Treaty Monitoring, Proceedings of the 18th Seismic Research Symposium on Monitoring a CTBT.

Harris, M., and Young, C. (1996), MatSeis: A Seismic GUI and Tool-box for MATLAB, Seismol. Res. Lett., 67(2), 267-269.

Young, C., Marris, M., Beiriger, J., Moore, S., Trujillo, J., Withers, M., and Aster, R. (1996), The Waveform Correlation Event Detection System Project, Phase 1: Issues in Prototype Development and Testing, Sandia National Laboratories, SAND Report SAND96-1916.

Tufte, E. R. (1990), *Envisioning Information*, Graphics Press, Cheshire, Connecticut.

RECENT DEVELOPMENTS IN SAC2000

Peter Goldstein, Doug Dodge, and Mike Firpo

Geophysics and Global Security Division, Lawrence Livermore National Laboratory

Sponsored by U.S. Department of Energy
Office of Nonproliferation and National Security
Office of Research and Development
CTBT R&D Program ST482B
Contract No. W-7405-ENG-48

SAC2000 is the rebirth and evolution of Lawrence Livermore National Laboratory's (LLNL's) Seismic Analysis Code (SAC) developed during the 1980s for a variety of geophysical applications. Primary funding for the development of SAC2000 has been through LLNL as part of the Department of Energy's (DOE's) Comprehensive Test Ban R&D program. The primary development goals for SAC2000 have been to meet the seismic signal processing and analysis needs of the DOE CTB R&D teams and the rest of the CTBT R&D community. SAC2000's strengths include its ability to process a diverse range of data types, its extensive, well-documented signal processing capabilities (both on-line and on the web at: <http://www-ep.es.llnl.gov/tvp/sac.html>), its macro language, and its ability to do both batch and interactive processing. Its extensive usage (> 300 institutions worldwide) has also made it much easier for researchers to develop collaborative research projects. SAC2000's extensive signal processing capabilities include: data inspection, signal correction, and quality control, unary and binary data operations, travel-time analysis, spectral analysis including high-resolution spectral estimation, spectrograms and binary monograms, and array and three-component analysis.

Recent developments in SAC2000 include: enhanced compatibility with the CSS3.0 database schema, complete compatibility with the widely used SEED data format instrument responses, map making capabilities via an interface to GMT, a new three-component polarization and phase identification tool, an external interface that allows users to define their own commands, and an interface to MATLAB that allows the user to use MATLAB commands and scripts on SAC data from within SAC2000. We have also implemented a number of commands to enhance user efficiency and numerous improvements and enhancements to many individual SAC commands.

Current developments in SAC2000 are motivated by the need for easy and efficient access to and processing and interpretation of large amounts of data. We are also driven by the need to communicate results from SAC2000 to our database and other programs. Based on these needs, we have begun developing a new, internal data structure for SAC2000. This new structure will be completely compatible with the standard SAC format but will also allow us to access, modify, and output all the information in CSS3.-based Oracle databases or CSS3.0 flat files. Given the variety of data types that are currently possible in SAC2000 and other programs, and the likelihood that additional data types or parameters will be needed in the future, we are designing SAC2000's new format to be easily extendable and anticipate incorporation of significant extensions to the CSS3.0 schema.

Key Words: Seismic, Data, Signal Processing, Software

Objectives

We are continuing the development of SAC2000 (<http://www-ep.es.llnl.gov/tvp/sac.html>, Goldstein and Minner, 1995, Goldstein et al., 1996) to provide the signal processing and analysis capabilities needed for Comprehensive Test Ban Treaty research and development. These efforts are utilized by a broad community of researchers and institutions including the federal government, academia, and companies (Figure 1). Our current efforts include the development of a new data structure that will allow us to access, modify, and output all the information in CSS3.0-based Oracle databases or CSS3.0 flat files. These new capabilities are essential for efficient processing and analysis of the large amounts of data that are being collected as part of DOE's seismic regionalization and identification R&D efforts. We have also focused part of our effort on implementing state-of-the-art signal processing capabilities that allow researchers to process and interpret data more accurately and efficiently. We describe a few selected developments in the next section and provide a more extensive summary in an appendix.

Research Accomplished

Three-Component Data Analysis Tool

We have developed a new, MATLAB-based tool for interactive and batch mode analysis of 3-component seismic data. This tool will improve a user's ability to detect and identify seismic phases, especially secondary phases. It has also helped us process data and identify problems with data such as incorrect sensor orientation information.

This tool has a number of capabilities including: graphical data selection and filter design, automatic back-azimuth and incidence angle estimation, interactive, graphical, three-component particle motion analysis, and maximum-likelihood probability estimates of selected wavetypes (Christoffersson et al., 1988).

Figure 2 displays a selected example of the interactive version of this three-component data analysis tool. Interactive data/window selection, phase picking, and signal rotation are done in the main window. Popup windows are used to: filter the data (no windows shown), interactively analyze particle motions (Particle motion module), and compute maximum-likelihood probabilities for selected wavetypes (ML-polarization analysis module).

Easy-to-Use MATLAB Interface

We have developed an easy-to-use interface to MATLAB from SAC2000. This interface automatically loads all the data in SAC2000's internal memory into a set of well-organized, concise MATLAB data structures. This interface allows the user to apply both MATLAB and SAC2000 commands to data from within SAC2000. Users now have the option to use both SAC Macros and MATLAB scripts for both interactive and batch processing. As an example of the use of this capability we developed a data inspection tool (Figure 3) that plots the SAC data and documents the MATLAB data structures using pull-down menus.

Access to Oracle and Flat File CSS3.0 Databases

We are developing a new data management module in SAC2000 that will provide convenient and intuitive access to both Oracle databases and flat files. This module includes a new, internal data structure that is completely compatible with the standard SAC and CSS3.0 formats but more flexible and easily extensible. The development of this new module is essential for efficient access and processing and updating of data. A schematic illustration of the new SAC data management module and its relation to the rest of SAC2000 is indicated in Figure 4.

Efficiency Enhancements

We have implemented a number of enhancements that will improve user efficiency. These include the ability to use Unix commands from within SAC2000 and a HISTORY command, similar to the Unix history command, that allows the user to inspect and repeat previously entered SAC2000 commands. DELETECHANNEL is a recently implemented data selection capability that can be used with the FILENUMBER command to identify and remove unwanted data from SAC2000's internal memory. A more extensive list of enhancements is given in the appendix to this paper.

Conclusions

We have implemented a number of new processing capabilities and enhancements in SAC2000 that will improve users' efficiency and their ability to accurately interpret data. We are also developing a new, flexible data structure for SAC2000 that will allow us to access, modify, and output all the information in CSS3.0-based Oracle databases or CSS3.0 flat files. These new capabilities are essential for efficient processing and analysis of the large amounts of data that are being collected as part of DOE's seismic regionalization and identification R&D efforts.

References

- Christoffersson, A., E.S. Husebye, and S.F. Ingate, 1988, "Wavefield decomposition using ML probabilities in modeling single-site 3-component records", *Geophys. Journal Int.*, 93, 197-213.
- Goldstein, P., Lee Minner, 1995, "A status report on the development of SAC2000: a new seismic analysis code", UCRL-ID-121523.
- Goldstein, P., C. Schultz, S. Larsen, and L. Minner, 1996, "Modeling of regional wave propagation phenomena in the Middle-East and North-Africa and new analysis capabilities in SAC2000", *Proceedings of the 18th annual seismic research symposium on monitoring a CTBT*, Annapolis, MD, September 4-6.

Appendix: Summary of New Commands and Capabilities in SAC2000

The following is a very brief summary of some of the recent enhancements to SAC2000. SAC2000 commands are indicated by words with all capital letters. More extensive documentation of these features can be found on-line by typing:

help "command name".

One of our newer features the MAT command is an interface to MATLAB that will allow you to run MATLAB scripts from within SAC2000 on data in SAC2000 memory. This interface is still undergoing development but a preliminary version is available in the latest version of SAC2000. Type "help mat" for more information.

Processing enhancements:

MAP or GMAP: High-quality maps using a command line interface to GMT.

Arraymap can be used to plot array configurations.

external_interface: Make your own SAC commands using Fortran or C subroutines.

LOAD: Loads your external commands.

MAT: Allows users to run their MATLAB scripts from within SAC.

evalresp option in TRANSFER: Transfer has been modified to incorporate/utilize SEED style responses.

TRAVELTIME: Calculates traveltimes based on the iasp91 model.

User can write a selected traveltime to a blackboard variable using the BB option.

PLOTRECORDSECTION: new version with a default portrait mode that can also plot iasp91 travel times on record sections and automatically displays travel time picks.

It is also possible to zoom in and out and it is no longer necessary to specify a timewindow with this command.

ADDSTACK, CHANGESTACK, LISTSTACK: begin and end time can now be specified.

DELETSTACK now works properly.

SPECTROGRAM: High-resolution spectrograms with properly registered seismogram.

SONOGRAM: High-resolution sonograms and binary sonograms.

IMAGE: image plots of 3-D data.

LOADCTABLE (lct): a selection of 17 colortables to use with 3-D images (e.g., spectrograms, fk, etc...).

BBFK and BEAM: Use lat and lon in headers or user7, user8, user9, to compute relative station locations.

BBFK: Wavenumber and azimuth at maximum power are written to blackboard variables.

CORRELATE: output timing made consistent with conventional applications.

CONVOLVE: convolves a master signal into itself and a number of traces.

Timing is now consistent with conventional applications.

FUNCGEN: Generates a new function consisting of a string of impulses.

LINEFIT: Fit a straight line to data

WIENER: filters data using filter design based on a window of noise.

This routine has significantly improved stability and error checking is done to make sure the noise window is within the data.

Input and Output

READCSS: read CSS2.8 and CSS3.0 data into SAC.

Recent enhancements include:

station and channel selection options

(e.g., readcss my.wfdisc station AAA).

wildcard capabilities.

Automatic loading of picks from assoc and arrival tables

Shift on or off to set the origin time to reference time (default is on)

Scale on or off to scale the data by the calib constant (default is off)

Added GSE3.0 format.

Added compressed e1 data format.

PICKPHASE: Allows the user to specify which phases/picks are loaded using READCSS.

PICKAUTHOR: Allows the user to specify authors of the picks loaded using READCSS.

WRITECSS: write CSS3.0 data from SAC (Minimal functionality, still under development).

WRITE: Write to xdr format for transformation to linux version.

kstcmp option uses to kstnm and kcmpnm to define file name.

The kstcmp option is most useful with css data that has multiple waveforms in a single wfdisc.

READ: Read from xdr format. (see write).

Documentation

HELP: on-line help contains all the SAC documentation. Type help for instructions.

Web page: <http://www-ep.es.llnl.gov/tvp/sac.html>

Ease of use and efficiency related enhancements:

UNIX: Any Unix command except rm can be specified at the command line.

HISTORY: view commands or reissue with Unix style !"command number"
(e.g., !2 to rerun the second command issued in the current SAC session).

sacnfiles (an automatically generated blackboard variable):

The number of files in memory is now listed as a blackboard variable.

CHNHDR: selectively change individual file headers.

READ: can now handle path names with wildcards and very large directories

SETMACRO: Added a new option to add more macro directories and increase maximum number of macro directories to 100.

LISTHEADER: You can now see all the header variables with the inclusive option (including those that aren't defined).

FILENUMBER ON|OFF: When this command is on the file numbers are displayed next to the traces.

DELETECHANNEL (dc): combined with file number, it allows the user to remove unwanted channels from memory.

PLOTPK: a new option to turn the bell on or off: e.g., ppk bell off. (default is on).

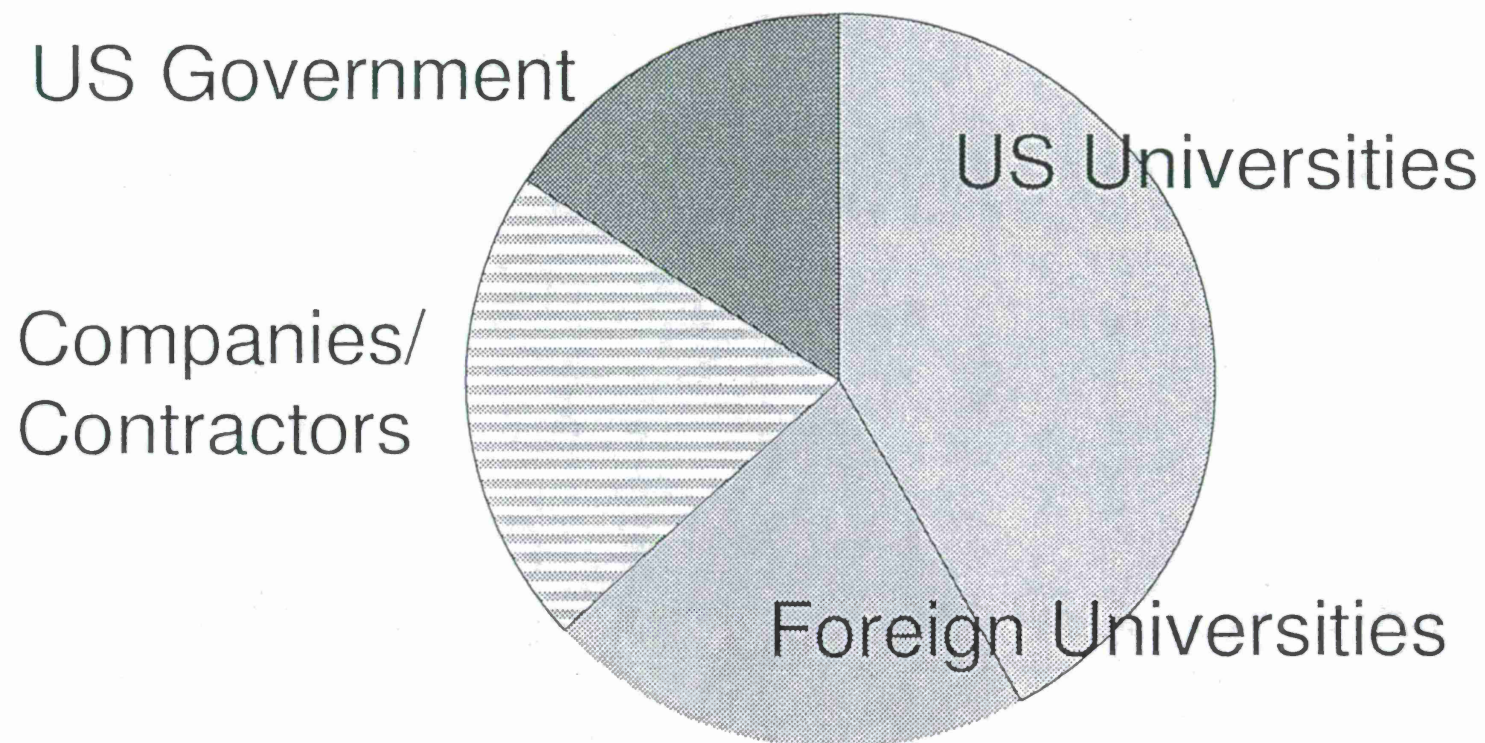


Figure 1. Pie chart indicating the types of institutions that use SAC2000. SAC2000 is used extensively by the seismological R&D community. It is used at more than 300 institutions by thousands of researchers. We have provided copies of SAC2000 to more than 150 institutions in the last year and the number of requests continues to grow.

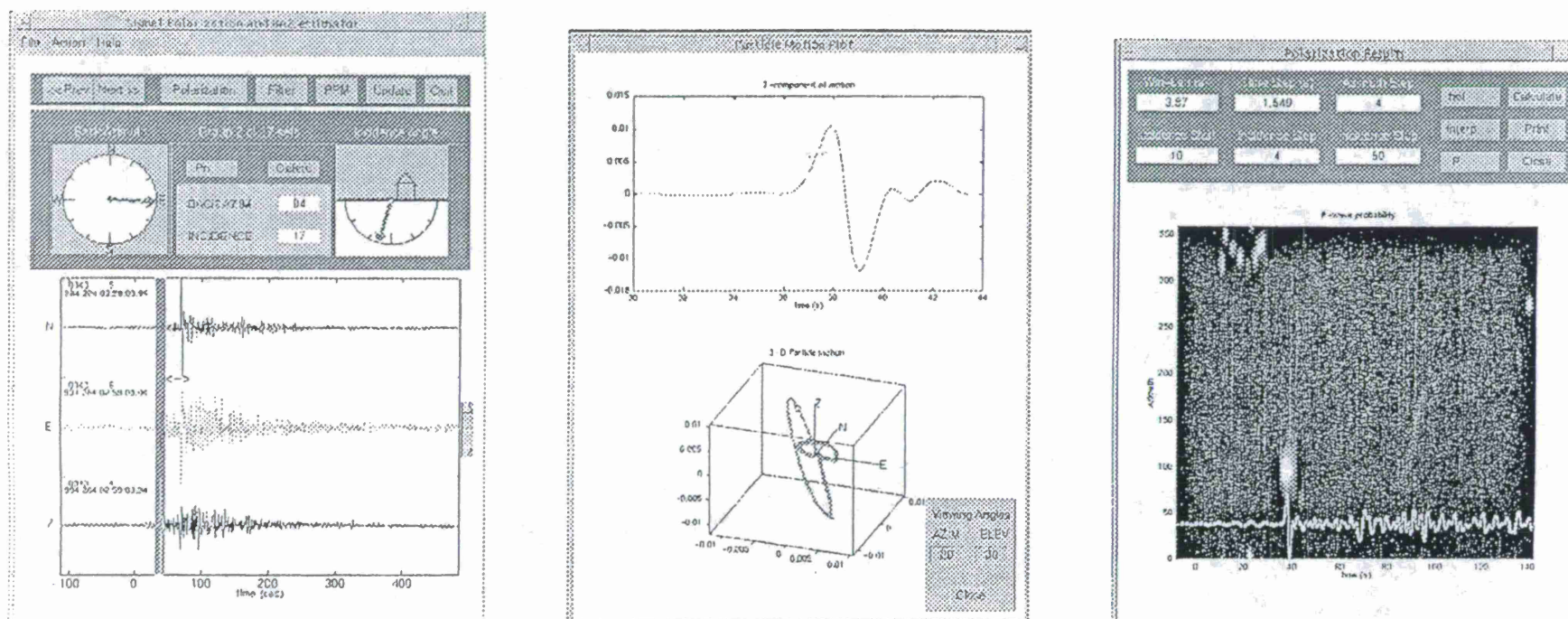


Figure 2 Interactive version of SAC2000's three component data inspection and analysis tool. The leftmost panel illustrates the main window where picking, processing, and window selections are made. The center panel indicates the vertical component window of the data and the corresponding three-dimensional particle motion. The particle motion perspective can be changed interactively by dragging on the axes of the particle motion plot or by changing the values in the text box at the lower right. The panel at the right indicates the ML probability estimate of the polarization for this window.

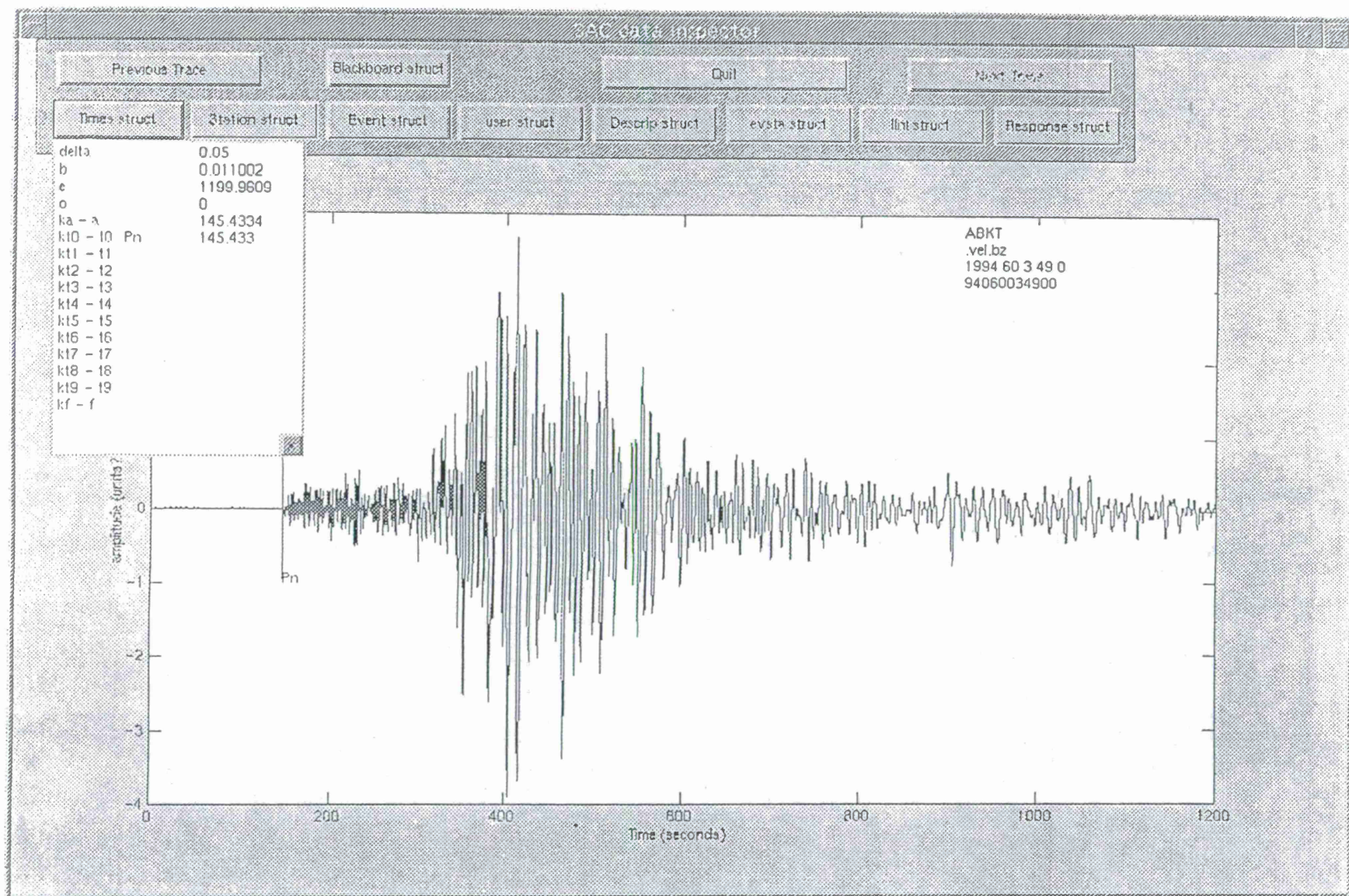


Figure 3. MATLAB based graphical user interface to data in SAC2000. Pulldown menus indicate the available data structures and data values currently in memory.

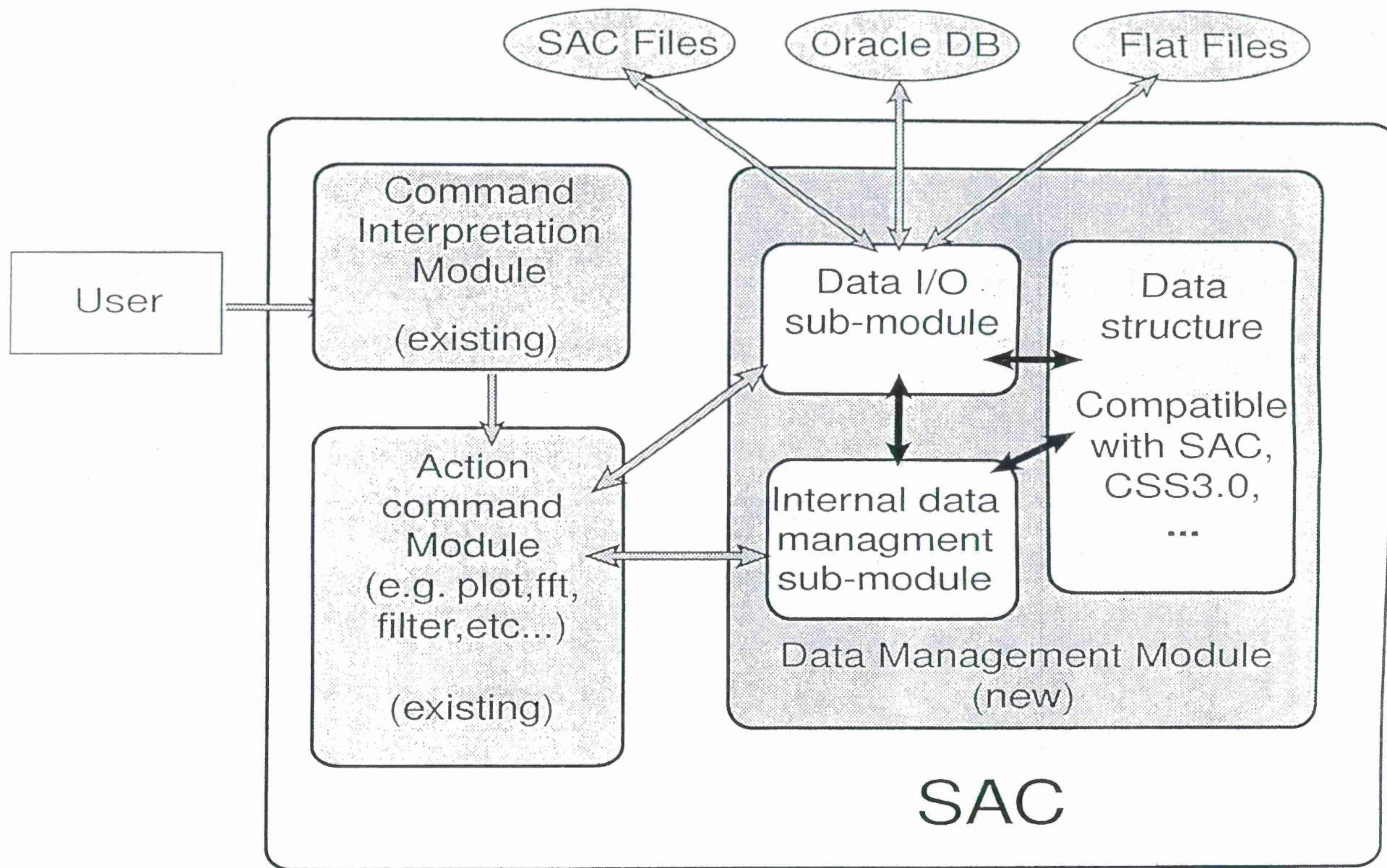


Figure 4. Schematic diagram illustrating the new SAC data management module and its relation to the command interpreter and processing commands.

GROUND TRUTH DATABASE FOR REGIONAL SEISMIC DISCRIMINATION RESEARCH IN THE MIDDLE EAST AND NORTH AFRICA

Lori Grant Robert Wagner Floriana Ryall Wilmer Rivers Ivan Henson

Multimax, Inc.

Sponsored by U.S. Department of Energy
Office of Nonproliferation and National Security
Office of Research and Development
Contract No. F19628-95-C-0094

ABSTRACT

Since January of 1996, we have provided research-ready data products to the CTBT community from the GTDB Web page at www.multimax.com. Our objective has been to collect, format, analyze and distribute waveforms, phase readings, and other information for regional events in the Middle East and North Africa (ME-NA). We include large events to serve as reference events but also include events near or below the current (global bulletin) threshold in the region. Sparse station coverage by the network of the International Data Center (IDC) has been augmented with data from other archives, primarily the IRIS Data Management Center (DMC). The result is a database rich in regional waveforms and phase arrivals sampling the diverse tectonics of ME-NA.

Our products include careful and consistent seismic data analysis: only two analysts have worked on this project, both previous Lead Analysts at the IDC. In our approach to analysis, events are grouped into geographic regions. Data redundancy helps to determine which observations are consistent in the region and which are spurious.

To date, we have processed more than 800 events and identified over 7,000 regional phases. Events are organized into distinct datasets, each having unifying characteristics such as source of waveforms or source of hypocenter information. Data are stored in one consistent format and are made available by anonymous FTP ([es2.multimax.com](ftp://es2.multimax.com)). All information for one event is packaged in a regular file in Unix compressed tar format and can therefore be delivered via FTP without interaction with a relational database management system (RDBMS). At the same time, unique identification numbers in the database tables allow any number of these events to be merged into one large dataset or loaded into an RDBMS.

Documentation for each dataset is provided on the GTDB Web site. This site features location maps, seismic bulletins, waveform and signal quality comments, analysis summaries, sample waveform plots, and references to the source of the waveform data.

Our methods of delivering research-ready data products via FTP and providing detailed documentation over the Web have facilitated research in the ME-NA region. CTBT researchers have presented numerous papers in the past year which have utilized GTDB datasets. The primary users have been Lawrence Livermore National Labs (LLNL) researchers or other scientists whose research was sponsored by DOE.

Keywords: ground-truth, regional waveforms, database, seismic bulletin, FTP, Web site

OBJECTIVES

The objective of the GTDB is to combine information about seismic events with the seismic waveforms from those events to produce research-ready data products. Our data collection efforts emphasize regional waveform data which sample the diverse tectonics of ME-NA.

RESEARCH ACCOMPLISHED

First we present several sections describing the GTDB methodology and the database organization. Then we summarize the contents of the completed datasets of the GTDB.

Method

- Identify a list of events to be included in the GTDB;
- Extract event-based waveform segments from all available archives;
- Carefully analyze waveforms, adding phase arrivals and comments;
- Correct all database table-files to conform to CSS3.0 format (Anderson *et al.*, 1990);
- Make a seismic bulletin listing event location, phase arrivals, and remarks;
- Put the completed dataset on the anonymous FTP site;
- Put documentation for the dataset on the GTDB Web page.

Source of Hypocenters

We use different seismic bulletins for different datasets, ranging from national bulletins (e.g. Spain) to global bulletins such as the Reviewed Event Bulletin (REB) of the IDC. Where possible, we reference regional bulletins to the USGS Monthly or the USGS Earthquake Data Reports (EDR).

Source of Waveforms

Several key stations in the Middle East planned for the IDC network are not yet on-line (e.g. THR in Iran, LXAR in Egypt, GEYT in Turkmenistan, FURI in Ethiopia, BRTR in Turkey). Other stations which are listed in the IDC network do not regularly contribute data to the archives. These factors have caused regional waveforms to be sparse in ME-NA relative to other regions. The IRIS database, including historical archives, was a major factor in overcoming the lack of regional ME-NA data available through the IDC.

The program ReqData (Henson and Grant, 1996) was developed to format and automatically parse autoDRM requests to the IDC and USGS. A modified ReqData was used to format Breq_Fast requests to IRIS, but the results were not automatically parsed. Additional data came from archives available over the Internet or through personal contact. Waveform data from over 270 different sites, including arrays and dense networks (e.g. KNET, ISN, ILPA), are available through the GTDB. The subset of stations located in the ME-NA region

is shown in Figure 1. Most of the stations shown in this figure provided *regional* waveforms to the database. Stations and their affiliations are listed in Table 1.

The IDC stores continuous data for Primary stations and event-segments for Auxiliary stations (PRI and AUX in column 1 of Table 1). In general, IRIS stores continuous data for the time periods shown in the next-to-last column in Table 1. Stations with a "Y" in the USGS column have segmented data available from the USGS autoDRM.

For some of the IDC stations, we had better results retrieving data from the IRIS archives than from the IDC archives for two reasons. Some Auxiliary stations in the IDC network contribute data very infrequently to the IDC bulletin (e.g. KMBO). Also, since IRIS stores continuous data, we can often obtain a more complete waveform from IRIS for a given IDC Auxiliary station (e.g. NIL). However, there is a lag time (often months) for IRIS to archive the data from some stations, whereas the IDC data are available within hours after the event.

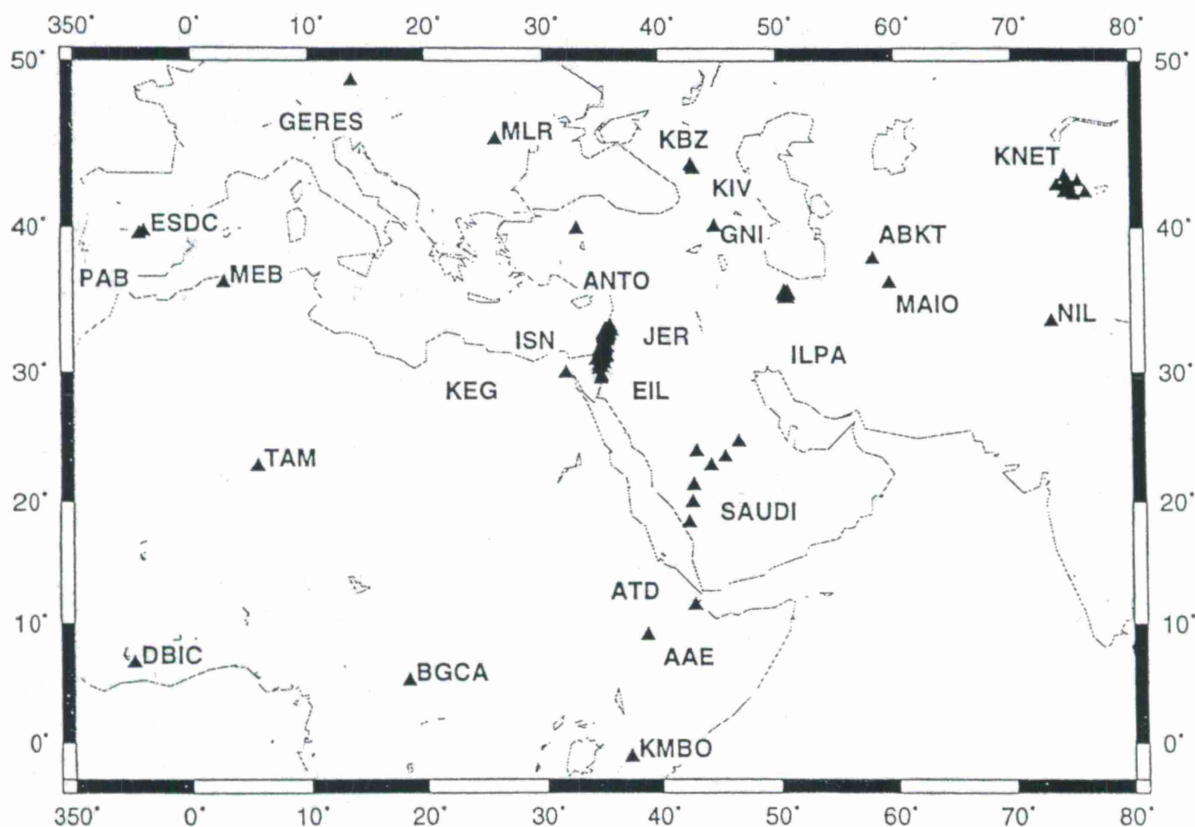


Figure 1: Stations which have contributed regional waveforms to the GTDB. Station affiliations are listed in Table 1.

Table 1. Partial Listing of Stations and Affiliations

IDC	Sta Code	Lat	Lon	Station Name	IRIS Affiliation		USGS
AUX	AAE	9.0	38.8	Addis Ababa, Ethiopia	iris/usgs(gsn)	(94-)	Y
	AAK	42.6	74.5	Ala-Archa, Kyrgyzstan	iris/ida(gsn)	(90-)	
PRI	ABKT	37.9	58.1	Alibek, Turkmenistan	irs/ida(gsn)	(93-)	Y
AUX	ANTO	39.9	32.8	Ankara, Turkey	iris/usgs(gsn)		Y
AUX	ATD	11.5	42.8	Arta Tunnel, Djibouti	geoscope	(93-)	
PRI	BGCA	5.2	18.4	Bogoin, Cent.African Rep.			Y
	BGIO	31.7	35.1	Bar Giyyora, Israel	usgs	(86-88)	Y
PRI	DBIC	6.7	-4.8	Dimbroko, Ivory Coast			Y
AUX	EIL	29.6	36.0	Eilat, Israel	usgs-gdsn	(72-79)	
PRI	ESDC	39.7	-4.0	Sonseca Array, Spain			
PRI	GERES	48.5	15.0	GERESS Array, Germany			
AUX	GNI	40.0	44.7	Garni, Armenia	iris/usgs(gsn)	(91-)	
	ILPA	35.7	50.6	Iranian LP Array	ARPA	(78-79)	
	ISN	31.7	30.2	Israel Seis. Net, incl. BGIO			
AUX	JER	31.8	35.2	Jerusalem, Israel			
AUX	KBZ	42.0	39.5	Khabaz, Russia			
AUX	KEG	29.9	31.8	Kottamya, Egypt	mednet	(90-)	
	KIV	44.0	42.7	Kislovodsk, Russia	iris/ida(gsn)	(88-)	Y
PRI	KMBO	-1.1	37.2	Kilima Mbogo, Kenya	iris/usgs(gsn)/geofon	(95-)	Y
	KNET	42.6	74.5	Kyrgyzstan Net., incl AAK	iris/ucsd		
	MAIO	36.3	59.5	Mashhad, Iran	usgs/gdsn	(75-78)	
	MEB	36.3	2.7	Medea, Algeria	mednet	(92-94)	
AUX	MLR	45.5	25.9	Muntele Rosu, Romania			
AUX	NIL	33.6	73.2	Nilore, Pakistan	iris/ida(gsn)	(94-)	
AUX	PAB	39.5	-4.3	San Pablo, Spain	iris/usgs(gsn)	(92-)	Y
	RAYN	23.6	45.6	Ar Rayn, Saudi Arabia	iris/ida(gsn)	(97-)	
	SAUDI	23.6	45.6	temporary, incl. RAYN	iris/ucsd	(96-97)	
	TAM	22.8	5.5	Tamanrasset, Algeria	geoscope	(83-)	

Table 2. Results of Interactive Waveform Analysis

Dataset	events	phases	Regional Phases (delta < 20 degrees)						Regional Stations
			all	Pn	Pg	Sn	Lg	P	
ILPA/MAIO	195	1702	1570	507	124	65	369	103	MAIO; ILPA(5)
SPAIN	152	723	723	132	140	123	61	0	ESDC, PAB, MEB, TBT
GALLILEE	50	1226	1226	104	521	2	106	0	ISN only
JSOP-I	24	85	78	21	11	16	20	0	ABKT, BGIO, KEG
JSOP-II	14	147	140	20	11	10	44	14	AAE, ABKT, ANTO, KIV, SAUDI(5)
SAUDI	156	2303	2128	460	92	278	512	84	ABKT, ANTO, ATD, BGIO, KIV, SAUDI(6)
REB EQ's	49	995	591	161	13	147	87	16	ARU, BRVK, EIL, GNI, JER, KBZ, KIV, KMBO, NIL, PAB, RAYN, KNET(9)
BATCH 1-3	144	1385	544	153	27	82	69	85	ABKT, ANTO, ARU, BGCA, EIL, ESDC, GERES, JER, KBZ, KIV, MLR, NIL, PAB
TOTALS:	784	8566	7000	1558	939	723	1268	302	

Event Directories: What You Get

The directory structure of the GTDB is based on having all waveforms and CSS3.0 tables relating to one event be located in a single directory. These directories are organized by dataset and by the geographic region within the dataset. As an example, the file *ev513.tar.Z* unpacks into the event-directory, named *ev513*, with the following contents:

Comments	<i>ev513.arrival</i>	<i>ev513.site</i>	<i>ev513.wfdisc</i>	<i>ev513.origin</i>
<i>ev513.remark</i>	<i>ev513.assoc</i>	<i>ev513.sitechan</i>	<i>ev513.wftag</i>	<i>wf</i>

These are all the files for event 513 of the Zagros region of the SAUDI Dataset. Waveforms are under the *wf* directory. Event directories are stored as Unix compressed tar files (e.g. <ftp://es2.multimax.com/pub/gtdb/saudi/zagros/ev513.tar.Z>). If event type is known, it is included in the *origin* table.

One advantage of this structure is that all the information for one event is packaged as a regular file and can therefore be delivered via anonymous FTP without interaction with a RDBMS. At the same time, unique identification numbers in the database tables allow any number of these events to be merged into one large dataset or loaded into an RDBMS.

Interactive Waveform Analysis

Each GTDB event has been reviewed by Flori Ryall or Bob Wagner to identify seismic phases and make notes about waveform and signal quality. A summary, written after completion of each cluster, gives guidelines followed during analysis which may be critical for interpreting the *assoc* and *arrival* tables. These analysis summaries are featured on the GTDB Web page.

At this writing, our database is populated with 800 events and 8,566 associated phases. Of these, 7,000 are regional phases (event-station distance less than 20 degrees). Table 2 summarizes the associated phases.

Summary of Completed Datasets

In this section we summarize the individual datasets completed under the current project. The first seven are available from the anonymous FTP site (es2.multimax.com). The last dataset can be obtained by contacting the authors. The first three datasets were the subject of our poster presentation at last year's Seismic Research Symposium (Grant *et al.*, 1996a).

ILPA/MAIO: The waveform data are from two seismic stations located in Iran and operating in the late 70's: The Iranian Long-Period Array (ILPA), located near Tehran, and MAIO, located 800 km east of ILPA. Based on USGS hypocenters regional to ILPA, we segmented the continuous waveform data for 273 events. Over 1,700 phases were timed, identified and associated with 195 events. Due to the wide (50 km) aperture of the array, individual sites were treated separately. One nuclear explosion from the Azgir test site is included (12/18/78). Events occurred between May 1978 and October 1979. Grant *et al.* (1996b) detail the construction of this dataset and present analysis observations. Baumgardt (1996) has used this dataset to confirm Lg blockage in the Caspian Sea; Sweeney (1996), to test accuracy of teleseismic event locations in ME-NA; Alexander and Yang (1996), to test improved depth determination techniques; and Gupta and Zhang (1996), to test spectral nulls in explosions.

SPAIN: Based on the bulletin produced by the Instituto Geografica Nacional (IGN, Madrid) we identified 5 clusters of interest. Available waveform data for these events are primarily from stations PAB, MEB and the Sonseca Array (ESDC). Two clusters are at the site of known mines and are believed to be quarry blasts. One event is a mine tremor. These are about 1 degree distant from ESDC. Two clusters on the north coast of Africa are presumed earthquakes. Distances to ESDC are about 4.5 degrees. These events occurred between May 1993 and July 1995. Pulli (1996) has used these events in discrimination studies.

GALILEE: The Geophysical Institute of Israel (GII) provided waveforms from the Israel Seismic Network (ISN). Twenty events were identified as quarry blasts, and 30 as earthquakes (Gitterman and van Eck, 1993). We used updated locations calculated by Gitterman *et al.* (1996). Events range in magnitude from ML 1.0 to ML 2.6, epicentral distances from less than 0.1 degree to 3 degrees, and depths from surface to 23 km. The largest of the events was recorded at 28 ISN stations, and the smallest at 4 ISN stations. Events occurred between October 1987 and May 1991.

JSOP-I: Participating countries in the first experimental period of the Joint Seismic Observation Program (JSOP-I) were: Cyprus, Egypt, Israel, Jordan, Lebanon, Saudi Arabia, Turkey, and Yemen. Phase readings were exchanged and the bulletin produced at the European-Mediterranean Seismological Centre (EMSC, 1995). We retrieved waveforms from the IRIS DMC archives for 35 events. Arrivals were associated with 24 events, half of which are located near the Gulf of Aqaba. The JSOP-I experiment was conducted between September and November of 1994.

JSOP-II: We formed this dataset based on the first three months of the JSOP-II bulletin which is currently being produced by EMSC for 1996. Out of 1230 events in that bulletin, over 1100 were aftershocks of the Ms 7.1 Gulf of Aqaba event of November 22, 1995. Because this aftershock series is represented in the Saudi Dataset (below), we collected data only for the events located outside the Gulf of Aqaba. The majority of the non-Aqaba events were contributed by Syria. For 46 Syrian events, we collected and analyzed all available regional data from IRIS. Useful signals were observable for only a handful of events due to the small magnitudes and lack of available near-regional data. Processing of another 12 non-Aqaba events contributed by other countries added another 7 events with associated phases.

SAUDI: Waveform data from a temporary network of broadband seismometers sited in Saudi Arabia has recently been made available to the CTBT research community through the IRIS DMC. These data were collected primarily by researchers from UCSD, King Saud University and Boise State University (Vernon *et al.*, 1996). Based on the bulletins produced by the USGS and the IDC, we have identified over 300 events regional to the Saudi network and occurring on days when at least one Saudi station was operational. Events occurred between November 1995 and May 1996. Saudi network data have been supplemented with data from other stations from the IRIS archives. Events have been grouped into 12 geographical clusters. The first three clusters (156 events) are complete: Zagros Thrust Belt, Strait of Hormuz, and Gulf of Aqaba (including the main shock of November 1995 which occurred the day before the Saudi network became operational). Events in the remaining nine clusters, shown as open circles in Figure 2, will be completed next.

REB Earthquake Clusters: During February and March of 1997, three earthquake sequences occurred in the Middle East and were reported in the REB. We collected all regional data from the IDC and DMC archives for these earthquake clusters located in Turkmenistan, Pakistan, and Djibouti. By combining IDC data with IRIS data, and analyzing the events with emphasis on identification of later phases, we increased the number of regional phases associated with these events. The REB had 81 regional phases associated with these 49 events, and we now have 591. About half of these are from KNET stations. The number of phases at stations JER and EIL increased 10-fold, and the number at NIL doubled. Another four series of interest occurred in April and May. These events, shown as open circles in Figure 2, will be analyzed next.

REB Batch 1-3: In addition to the above datasets, we have retrieved and analyzed about one gigabyte of waveform data from the IDC and USGS data archive for events occurring in ME-NA in 1996. For the most part, these events do not have good regional station coverage. Only stations JER, NIL, KIV, and ABKT have significant numbers of regional phases. We did not supplement the regional data from IRIS DMC for these events. Batch 1 includes two Lop Nor nuclear explosions (6/96, 7/96) and a German mine tremor (9/96). Batch 2 of this dataset is an aftershock series related to the Cyprus event of October, 1996. These data were delivered directly to LLNL for inclusion in their regionalization database. Although these data are not currently available from the GTDB FTP site, they can be obtained from the authors.

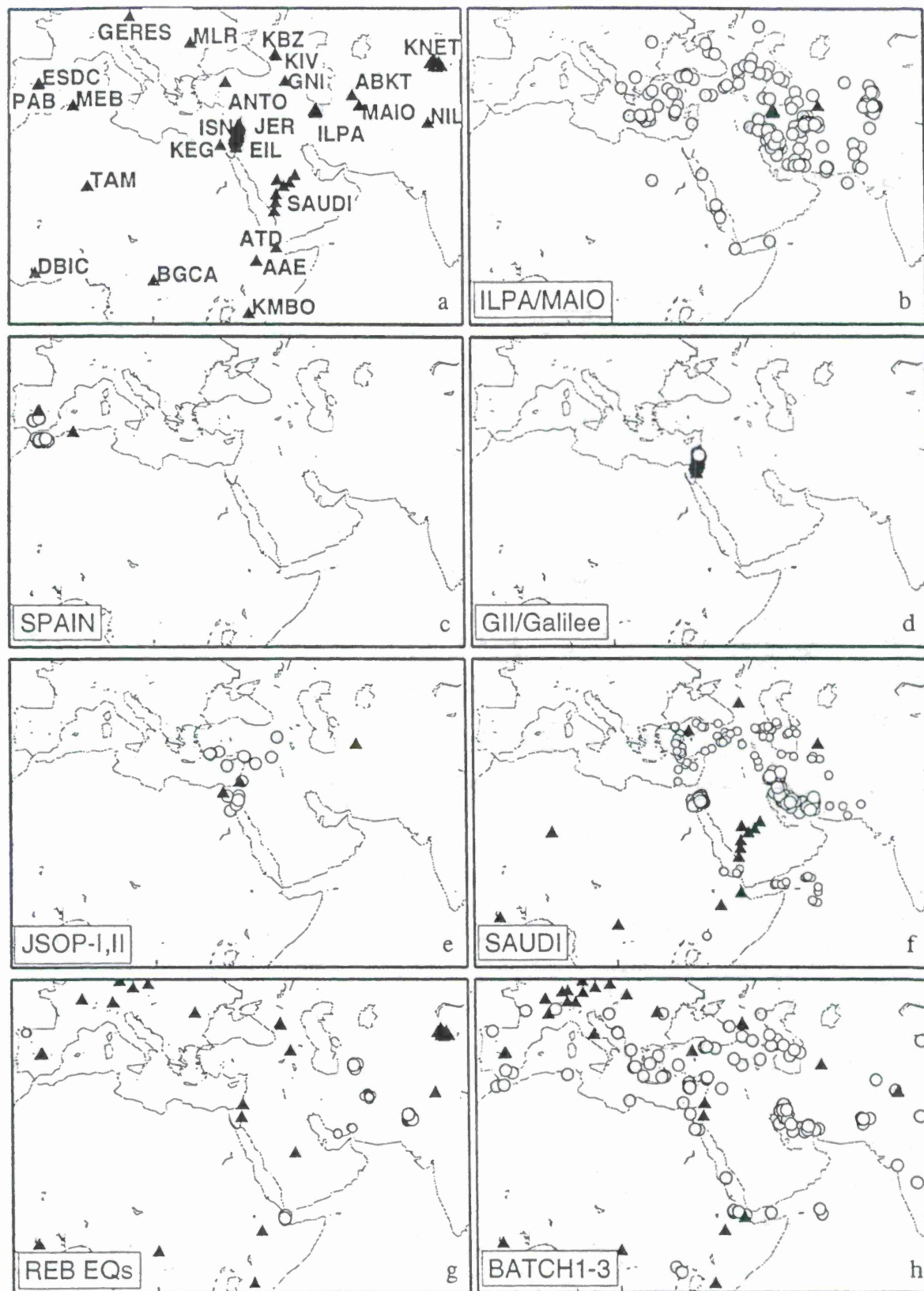


Figure 2: GTDB Datasets. a) stations; b-g) completed datasets available via FTP (es2.multimax.com/pub/gtdb); h) additional data. Open circles are events yet to be analyzed. Map boundaries are the same as in Figure 1.

CONCLUSIONS AND RECOMMENDATIONS

The total waveform data available from the GTDB exceed 2.5 Gigabytes. The database includes 800 events, most of which are located in the ME-NA region. Associated with these data are over 8,500 phase arrivals, timed and named by expert analysts. Over 4,400 of these phases are standard crustal phases (Pn, Pg, Sn, and Lg) observed at distances of less than 20 degrees.

We have developed efficient methods of retrieving and parsing waveform data from the IDC and IRIS archives. We have also developed efficient methods of documenting and distributing finished products: the GTDB Web site and FTP sites have been popular among CTBT researchers. Our data have been loaded into the research databases at LLNL, Sandia National Labs, and the Air Force Technical Applications Center (AFTAC). Our work has facilitated CTBT research in the ME-NA region by providing research-ready data products in one consistent format. Evidence for this claim is the numerous research studies utilizing GTDB data published in 1996 (e.g. Alexander and Yang, Baumgardt, Dowla *et al.*, Gupta and Zhang, Pulli, Sweeney). Recently released datasets will no doubt be the subject of more research in 1997, especially those studies focusing on propagation characteristics of regional phases.

For datasets with hypocenters taken from global bulletins, there is probable location error, especially for small, shallow events (Sweeney, 1996). Location error should be addressed before using these events for travel-time studies. We have sampled several earthquake series where abundant regional data are available for events close to one another. The SAUDI and the REB EQ datasets are good candidates for relative re-location because they include aftershock sequences recorded at several regional stations.

We believe our data are both useful and easy to use. However, if there are any questions or suggestions about GTDB data products, please contact the authors.

Lori: lori@multimax.com Bob: wagner@multimax.com Flori: flori@s160.es.llnl.gov
Wilmer: wilmer@multimax.com Ivan: ivan@multimax.com

ACKNOWLEDGEMENTS

We appreciate the availability and ease of use of the continuous data archived at the IRIS Data Management Center. The IRIS program RDSEED was used to convert IRIS data to CSS3.0 format. We appreciate being granted autoDRM access to IDC and USGS waveforms. The Datascope Seismic Analysis Package developed at IRIS's Joint Seismic Program Center was used in place of an RDBMS to manipulate CSS3.0 formatted table-files (Quinlan, 1995). Maps in this paper were made with Generic Mapping Tools (Wessel and Smith, 1995). Geotool was used for interactive analysis of the waveforms (Henson and Coyne, 1993). The SAUDI dataset was analyzed by Flori Ryall under DOE Contract No. 1143.

REFERENCE LIST

- Alexander, S. and C. C. Yang (1996). Use of the Cepstral Stacking Method (CSM) for Improved Source Depth Determinations from Combined Single-Station and Array or Network Observations at Regional Distances, *Proc. of the 18th Annual Seismic Research Symposium*, Annapolis, MD, PL-TR-96-2153, ADA313692.
- Anderson, J., W. E. Farrell, K. Garcia, J. Given, H. Swanger (1990). Center for Seismic Studies Version 3 Database: Schema Reference Manual, TR C90-01, September 1990.
- Baumgardt, D. (1996). Investigation of Lg Blockage and the Transportability of Regional Discriminants in the Middle East, Phillips Laboratory Report PL-TR-96-2294.
- European-Mediterranean Seismological Center (Centre Sismologique Euro-Mediterranean), Newsletter, No. 8, December 1995, 8 pp.
- Dowla, F., P. Goldstein, P. Harben, D. Harris, T. Hauk, S. Jarpe, E. Kansa, P. Lewis, D. McNamara, H. Patton, D. Rock, A. Ryall, C. Schultz, A. Smith, J. Sweeney, W. Walter, L. Wethern (1996). Seismic Regionalization in the Middle East and North Africa, *Proc. of the 18th Annual Seismic Research Symposium*, Annapolis, MD, PL-TR-96-2153, ADA313692.
- Gitterman, Y. and van Eck, T. (1993). Spectra of quarry blasts and microearthquakes recorded at local distances in Israel, *BSSA*, 83, No. 6, 1799-1812.
- Gitterman, Y., V. Pinsky, A. Shapira (1996). Discrimination of seismic sources using Israel Seismic Network, Phillips Laboratory Report PL-TR-96-2207.
- Grant, L., F. Ryall, I. Henson, W. Rivers (1996a). Ground Truth Database for Seismic Discrimination Research, *Proc. of the 18th Annual Seismic Research Symposium*, Annapolis, MD, PL-TR-96-2153, ADA313692.
- Grant, L., F. Ryall, W. Rivers (1996b). Ground Truth Database: ILPA/MAIO Handbook, Phillips Laboratory Report PL-TR-96-2236.
- Gupta, I. N. and T.-R. Zhang (1996). Study of Low Frequency Lg from Explosions at Nevada, Kazakh, Lop Nor, and Azgir Test Sites, *Proc. of the 18th Annual Seismic Research Symposium*, Annapolis, MD, PL-TR-96-2153, ADA313692.
- Henson, I. and J. Coyne (1993). The Geotool Seismic Analysis System, *Proc. of the 15th Annual Seismic Research Symposium*, Boulder, CO, PL-TR-93-2160.
- Henson, I. and L. Grant (1996). A Guide to ReqData: Automated Requesting and Parsing of GSE Formatted Data, Phillips Laboratory Report PL-TR-96-2272.
- Pulli, J. J. (1996). Transportable Seismic Discriminants: Stable Estimates of Spectral Ratios, *Proc. of the 18th Annual Seismic Research Symposium*, Annapolis, MD, PL-TR-96-2153, ADA313692.
- Quinlan, D. (1995). DATASCOPE: A Relational Database System for Scientists: Tutorial, Version 1.1, IRIS's Joint Seismic Program Center University of Colorado, Boulder, Colorado, (<http://jspc-www.colorado.edu/software/software.html>).
- Sweeney, J. J. (1996). Accuracy of Teleseismic Event Locations in the Middle East and North Africa, Lawrence Livermore National Laboratory, UCRL-ID-125868.
- Vernon, F. L., R. J. Mellors, J. Berger, A. M. Al-Amri, and J. Zollweg (1996). Initial results from the deployment of broadband seismometers in the Saudi Arabian Shield, *Proc. of the 18th Annual Seismic Research Symposium*, Annapolis, MD, PL-TR-96-2153, ADA313692.
- Wessel, P., and W. H. F. Smith (1995). New version of the Generic Mapping Tools released, *EOS Trans. Amer. Geophys. U.*, 76, pp. 329.

A KEY MANAGEMENT CONCEPT FOR THE CTBT INTERNATIONAL MONITORING SYSTEM

Pres Herrington, Tim Draelos and Rick Craft, Sandia National Lab¹
Ernie Brickell, Yair Frankel, and Mark Silvestri, CertCO²

Sponsored by U.S. Department of Energy
Office of Nonproliferation and National Security
Office of Research and Development
DOE Contract No. DE-AC04-94AL85000

ABSTRACT

Cryptographic authentication (commonly referred to as "technical authentication" in Working Group B) is an enabling technology which ensures the integrity of sensor data and security of digital networks under various data security compromise scenarios. The use of cryptographic authentication, however, implies the development of a key management infrastructure for establishing trust in the generation and distribution of cryptographic keys. This paper proposes security and operational requirements for a CTBT key management system and, furthermore, presents a public key based solution satisfying the requirements. The key management system is instantiated with trust distribution technologies similar to those currently implemented in industrial public key infrastructures. A complete system solution is developed.

Key words: Authentication, Public Key, Key Management, Certificate, Certification Authority, Trust

¹Sandia is a multiprogram laboratory operated by Sandia Corporation, a Lockheed Martin Company, for the United States Department of Energy.

²CertCo's help in this effort has been on a voluntary basis and no funding from DOE has been provided for this assistance.

OBJECTIVE: To develop an operational concept for management of cryptographic keys to be used in the CTBT IMS for authentication of sensor data and other digital products.

RESEARCH ACCOMPLISHED

Introduction

Data collected within the Comprehensive Test Ban Treaty (CTBT) International Monitoring System (IMS) must be both authentic and accurate in order to provide value to its user community. In fact, many electronic data networks (e.g., medical records and banking) have similar authenticity and reliability requirements to support their user base. We suggest that the IMS implement techniques commonly used in other electronic networks to provide for authenticity and accuracy of the data generated within the system. In this paper, we show how these security techniques can be effectively implemented for the IMS.

The security of electronic networks is generally analyzed by studying threat models under various attack scenarios. The potential losses for various internal and external attacks are analyzed and the final system design reflects a balanced approach taking into consideration the cost of the system and potential losses under various compromises. We suggest that a similar approach be used for the IMS. Work done to date suggests that, without safeguards, the CTBT International Monitoring System is vulnerable to modification of sensor outputs within the territory of a host country even though this may be performed without approval of the host country's government (an internal attack). Similarly, an internally-launched attack on the workstation of a data user can make fraudulent data appear to be authentic. In addition, an unprotected IMS is vulnerable to modification of any information after the data leaves the host countries (an external attack).

The most prevalent techniques currently used to protect a computer network from these types of external attacks are the use of cryptographic authentication complemented with various software and hardware shielding techniques to support the security of the cryptography. The authentication mechanisms provide a computational means in which modification of the source or the integrity of the message can be detected. The message generating entity computes an authentication element based on the entity's secret key and the message. Verification of the integrity and the source of the message is performed using an authentication key. However, cryptographic authentication provides little protection against an insider who has possession of the secret key. Placing authentication units and keys inside tamper resistant devices, ensuring redundancy in data availability, and multi-point checking of integrity provide the primary approaches to protect against insiders. It is our belief that IMS security should be designed such that there is no single point of failure – a common standard used in the design of secure systems.

It is also our belief that cryptographic authentication and proper location of sensors are complementary security mechanisms which are part of a full system security design. We suggest that cryptographic authentication be used in the IMS to protect against modification of the source and/or the integrity of the message. Redundancy and multi-point checking to minimize the consequences of "internal attacks" is already incorporated into the IMS by proper location of sensors such that modification of the data of a few sensors does not compromise the detection of nuclear tests.

The inclusion of cryptographic authentication, however, implies the development of a key management infrastructure for establishing trust in the generation and distribution of keys. Though key management is an essential component for the protection of sensor data, its design can support the securing of other IMS products, such as commands used to control sensors or event bulletins and supplementary bulletins generated by the IDC or the NDCs.

The objective of this paper is to offer a complete key management solution to support the use of sensor data authentication in the IMS as well as other communications (e.g., sensor commands and event bulletins). The proposed system recognizes the absence of a single trusted entity within the CTBT community and takes advantage of the trust as well as distrust that is present between state's parties.

Background

The basic concepts of key management, public key signatures and certification authorities are reviewed in this section.

Private/Public key signatures

An asymmetric cryptosystem is one in which knowledge of a public key does not provide any computational information about the private key. One definition of a digital signature is:

A transformation of a message using an asymmetric cryptosystem such that a person having the initial message and the signer's public key can accurately determine (1) whether the transformation was created using the private key that corresponds to the signer's public key, and (2) whether the initial message has been altered since the transformation was made.

Hence, a public key cryptosystem allows for the verification of the source and integrity of a message. Moreover, since the system is an asymmetric cryptosystem the verifier learns nothing in the verification process which would allow it to sign new messages or modify previously signed messages.

Public key signatures are the standard method to perform authenticated communication among mutually distrusting parties in banking and other electronic commerce protocols (e.g., SET, digital cash, etc.). In our suggested system, public key signatures are used to authenticate sensor data and other IMS data products as well as to establish trust in the key management protocol.

Key management supporting public key systems

The basis of security in cryptography is secret keys and therefore an infrastructure which supports the secure management of the keys is a necessary component of any system. A key management system provides the underlying policies and mechanisms for executing and maintaining a cryptographic system. It provides all the service functions needed for the cryptographic components to work and, when specified correctly, permits the operational aspects of the system to be designed on their own. Its functionality includes:

1. **Key generation:** Establishment of a secure key for entities and processes. Generally this is accomplished by the entity that will possess the key after generation but this is not always the

case. The primary concern here is that the key is known only to the entity responsible for signing information using the key.

2. **Key distribution:** Once a private key is generated the public keys must be disseminated to those who need it in a manner that permits the parties who accept the public key to trust that it is authentic.
3. **Key maintenance:** Addition, deletion & suspension of private/public key pairs is a normal operational aspect of any cryptographic authentication system. This means that the users of the system must be notified that old keys are not valid and that new keys have the functionality of the old ones. As in (2), it is imperative that this notification is performed using authenticated means.
4. **Key archiving:** When signed data is archived, it is also necessary to archive the public keys and to have a method for establishing that the public key was valid on the date that the data was generated.

Certificates and Certification Authority (CA)

A digital signature has limited utility unless the recipient can ensure the authenticity of the public key used to verify the signature. Hence, the receiver must receive the sender's public key from an authentic and trusted source. If it can not receive the public key directly from the sender, then the most common technique for the receiver to obtain the public key is from a trusted source called a "certification authority". One organization defines a certificate as:

A computer-based record which at least (1) identifies the certification authority issuing it, (2) names or identifies its subscriber, (3) contains the subscriber's public key, and (4) is digitally signed by the certification authority issuing it.

A certification authority is the standard method for establishing user trust in public keys. Currently, CAs exist for many applications including electronic banking, electronic commerce, and telephone and mail services. The CA infrastructure reduces key management to one trusted interaction with the CA and then later the CA attests to the validity of all public keys in the system by the signing of certificates. The certificates signed by the CA are used to establish the validity of public keys used in current transactions and the validity of archived public keys associated with archived data.

Security model for IMS sensor data

CTBT IMS entities, as well as those for other networks, can be categorized by the functionality which they perform with respect to the gathering and manipulation of data. Though simplistic we categorize entities as:

- an information gathering entity (e.g., sensors),
- an information retrieval entity (e.g., an NDC)
- an information processing entity (e.g., NDC, IDC),
- a data storage entity (e.g., NDC, IDC), and/or
- a network control and management entity (e.g., host countries, NDC, key management control entities).

An information gathering entity has the purpose of gathering data which will be processed by the system. The primary security considerations with this entity are that the information it gathers is accurate and has integrity. An adversary may try to attack this type of entity either with internal

attacks at its source or with external attacks as it disseminates the information it gathers. Cryptographic authentication protects against modification of data by outsiders after information retrieval, while tamper resistant devices, redundancy in data availability, and multi-point checking of integrity protect against internal attacks performed at the information gathering unit. In the IMS, therefore, protection of sensor data using both cryptographic authentication and proper placement of sensors provides a full system approach. Authentication protects against modification of data after it leaves the host country while placement provides additional information to protect against mis-information provided at the host country.

An information processing entity takes data held globally by the system and processes it. An information retrieval entity downloads data held globally by the system and displays it. Both of these entities require assurance that the information received is accurate and authentic.

A data storage entity, such as an NDC, stores the data collected by the information gathering entity or data processed by the information processing entity. This entity *may* require assurance that the data and information it receives are authentic. If so, the information it receives from information gathering entities and information processing entities must be authenticated.

Control and management entities are those that control the other entities in the system, usually by remotely generated commands. In order to assure that these controlled entities operate with integrity, the commands sent to them from control and management entities must be authenticated.

CTBT auxiliary objectives

In addition to these requirements levied on the IMS entities, an IMS security solution should also address the following objectives:

- **High degree of sovereignty:** The proposed authentication and key management technology is not limited to any single State's source of technology.
- **Multiple entities must trust the process:** No single State or entity is trusted by all States to ensure the integrity of the system. In the proposed system, trust is distributed so that any State can trust the reliability of the data by trusting only a single member of the Oversight Committee or by trusting the fact that the members will not collude.
- **Flexibility in State to State trust/dependence:** Internal relationships between States are flexible and may change over time. Membership in the Oversight Committee, as well as policy modification, can be easily changed when using the proposed system.
- **Preserve national integrity:** Ensure no false implications of event hiding, event falsification, event alteration and undermining of the IMS by allowing every State to be a part of the critical key management components. By taking a complete system security approach the host country, the Oversight Committee, and the IMS infrastructure are protected from false implication.
- **Low life cycle cost:** The primary cost in this system is the Observers during sensor installation and key generation. Since Observers must already be present during station certification, the incremental cost associated with their performance of key management functions will be minimal. Other costs in the system (e.g., Equipment & maintenance of

Oversight Committee, storage of a database of certificates on a Certificate Server, reissuing & revoking expired certificates) are minimized by using cost effective commercial off-the-shelf solutions.

Key management solution

We now discuss our concept for a key management system architecture. This architecture implements a chain of trust relationships that makes it possible for information processing entities to rely on the authenticity of data received from sensors throughout the IMS. A summary of this solution is presented in the figure at the end of this paper.

Distributed Trust CA

The first trust relationship in our key management system is between information processing entities (e.g., NDCs and IDC) and a Certification Authority. It is the job of the Certification Authority in this architecture to generate certificates that information processing entities can use to verify signatures generated by the sensor sites in the IMS.

In order for an information processing entity to trust a certificate, the entity must have trust in the Certification Authority. Since there is no single trusted entity in CTBT IMS, we suggest using a distributed trust mechanism for the Certification Authority. This can be accomplished through a technology called threshold cryptography. The certification authority function will be split among a group called the "Oversight Committee". This committee will be constituted by some process agreed to by all CTBT signatories. In order for a certificate to be issued, all members of the Oversight Committee must agree that the certificate should be issued. This is accomplished as follows:

- Each member of the Oversight Committee will have a secret partial signing key.
- When a member of the Oversight Committee approves of a certificate, that member will form a partial signature of the certificate using their partial signing key.
- After all of the members have generated partial signatures, these partial signatures will be combined into a single CA signature.

This distributed trust CA has the property that even if all but a single committee member generates a partial signature for a certificate, the final signature cannot be computed³.

Information processing entities can trust the Oversight Committee based on one of two criteria. First, they can explicitly trust the reliability of one or more members of the committee. When this criterion is used, the information processing entities believe that the committee member(s) will not allow a certificate to be created if they do not trust the authenticity and security of the cryptographic keys associated with the certificate. Second, information processing entities can trust in the distrust built into the Oversight Committee. In this case, the information processing entities may not explicitly trust any of the members of the committee but they trust that the composition of the committee is such that all of the committee members will not collude to create a false certificate.

³ While the approach being advocate here employs a "100% threshold" (e.g., 7 members out of a committee of 7 are required for signature), the total number of oversight members and size of quorum to sign is configurable. Hence, it is possible to make, for example, a 6 out of 8 system in which any 6 oversight members may work together to sign yet less than 6 can not generate a signature.

In an initialization process, there will be a public key generated for the Oversight Committee. This public key will be widely disseminated to all parties of the IMS. Although there are many cryptographic keys in the system, the CA simplifies key management by requiring an entity to store only this one public key of the CA, which is then used to maintain trust and security in all of the other keys in the system. In practice, for the sake of communications efficiency, IMS entities will likely store all sensor public keys after verifying their associated certificates using the CA's public key. If desired, the certificates could be retained and reverified on each use.

Transfer of trust to a certificate

In order for members of the Oversight Committee to certify a sensor site, the members must believe that:

- the sensor's private key is known only to the device that signs sensor data,
- the public key that is to be placed into a certificate for the site is associated with the private key in the sensor's authentication unit,
- the sensor and authentication unit are installed at that site, and
- the sensor and authentication unit are operating with integrity (i.e., that the signed data sent from the sensor accurately reflects the signals being received by the sensor).

To assure that these things are true about a given site, the Oversight Committee will charter a team of "Observers" to visit the site and to oversee the sensor's and authentication unit's initialization process. As with the Oversight Committee, these teams will be constituted using a process established by the Provisional Technical Secretariat. Similar to the previously described trust relationship, trust between a given member of the Oversight Committee and a team of Observers is established either through explicit trust in one or more of the Observers or in the belief that the composition of the Observer team minimizes the possibility of collusion.

At an appropriate time in the site installation/certification process, the team of Observers will determine whether the installation and initialization procedures have been followed correctly.

- The Observers will inspect the sensor / authentication unit installation for signs of tampering. It is assumed here that the sensor and its authentication unit will have been inspected by an agent of the CTBTO prior to their installation to ensure that they will operate with integrity.
- The authentication unit associated with the sensor will generate a public/private key pair. This process can be performed jointly with the observers to prevent bias by the sensor and make sensor key generation a mutual effort. Only the authentication unit will know the private key but its public key will be published to the Observers.
- The Observers will prepare a certificate request containing this public key and will send that certificate request to the members of the Oversight Committee. The Observers will also send authentication information so that the Oversight Committee members can verify that the certificate request came from the Observers and no-one else.
- The Oversight Committee members will approve the certificate request and a certificate containing the sensor identification information and the public key will be generated and stored on a Certificate Server (i.e., a database system) for distribution to data users.

Through the above procedure, the trust in the observers that the authentication unit was properly installed at the site has been transferred to the certificate.

Transfer of trust to the sensor data

After the sensor is in operation, the certificate will be used to transfer trust to the information processing entity. The process is as follows:

- All data from the sensor is digitally signed with the private key in that sensor's authentication unit. The digital signature is sent along with the data.
- Upon receipt of the signed data, an information processing entity verifies the signature using the public key associated with the sensor's authentication unit. The public keys for the sites of interest to the information processing entity are held locally (e.g., in RAM or on disk) by the information processing entity
- If, by chance, the signature fails to verify, then the information processing entity requests from a Certificate Server (probably located at the IDC) the certificate associated with the sensor that generated the data.
- As all authentic certificates will have been signed by the Oversight Committee, the information processing entity can verify the authenticity of the certificate using the Oversight Committee's public key.
- Once the certificate is verified, the public key contained in the certificate is then used in an attempt to verify the signature on the data.

Depending on the operational concept of the information processing entity, the requesting of new certificates and the reverification of signatures can be performed on other computers than those used to process incoming sensor data and/or can be delayed until a later time.

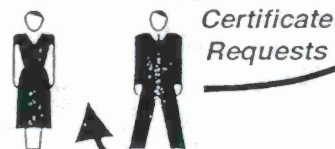
Conclusion

A CTBT IMS key management protocol is proposed using distributed trust technologies, an approach is based on technology currently being used to protect other digital networks (e.g., banking applications). The proposed solution is both secure and cost effective.

Observers

- * Act on behalf of Oversight Committee
- * Attest to fact that:
 - * Sensor and Authentication Unit not subverted
 - * Private key securely generated by Authentication Unit
 - * Public key submitted to Oversight Committee corresponds to private key
 - * Sensor and Authentication Unit securely installed at specified site
- * Each Observer submits request for certification of Authentication Unit's public key

Warramunga Array



Authentication Unit

Sensor

Sensor Data

Oversight Committee

- * Oversees Key Management in IMS
- * Functions as certification authority
- * Each committee member:
 - * Reviews certificate requests generated by Observers for a given sensor site
 - * If satisfied with the requests, creates a certificate fragment for that site
 - * Submits the certificate fragment to the Certificate Server

Moscow

Beijing

London

Tokyo

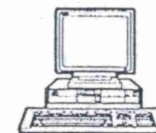
La Paz

Certificate Fragments

Certificate Server

- * Combines certificate fragments to create sensor site's certificate
- * Serves as repository for certificates and certificate revocation lists (CRLs)
- * Supplies certificates and CRLs to Data Users on request

Vienna



Data User

Certificate

- * Reviews or processes data generated at sensor sites
- * Verifies signature on data using sensors' public keys
- * Public keys not currently held at Data User's site obtained from certificates retrieved from Certificate Server

Canadian NDC



Sensor Data with Signature

Optimized Filtering of Regional and Teleseismic Seismograms:
*Results of Maximizing SNR Measurements From the
Wavelet Transform and Filter Banks*

Richard R. Leach Jr., Craig Schultz, Farid Dowl
Earth Sciences Division, Lawrence Livermore National Laboratory

Sponsored by U.S. Department of Energy
Office of Nonproliferation and National Security
Office of Research and Development
Contract No. W-7405-ENG-48
Sponsored by DOE CTBT R&D Program

ABSTRACT

Development of a worldwide network to monitor seismic activity requires deployment of seismic sensors in areas which have not been well studied or may have few available recordings. Development and testing of detection and discrimination algorithms requires a robust representative set of calibrated seismic events for a given region. Utilizing events with poor signal-to-noise (SNR) can add significant numbers to usable data sets, but these events must first be adequately filtered. Source and path effects can make this a difficult task, as filtering demands are highly varied as a function of distance, event magnitude, bearing, depth, etc. For a given region, conventional methods of filter selection can be quite subjective and may require intensive analysis of many events. In addition, filter parameters are often overly generalized or contain complicated switching. We have developed a method to provide an optimized filter for any regional or teleseismically recorded event. Recorded seismic signals contain arrival energy which is localized in frequency and time. Localized temporal signals whose frequency content is different from the frequency content of the pre-arrival record are identified using rms power measurements. The method is based on the decomposition of a time series into a set of time series signals or scales. Each scale represents a time-frequency band with a constant Q . SNR is calculated for a pre-event noise window and for a window estimated to contain the arrival. Scales with high SNR are used to indicate the band pass limits for the optimized filter. The results offer a significant improvement in SNR, particularly for low SNR events. Our method provides a straightforward, optimized filter which can be immediately applied to unknown regions as knowledge of the geophysical characteristics is not required. The filtered signals can be used to map the seismic frequency response of a region and may provide improvements in travel-time picking, bearing estimation, regional characterization, and event detection. Results are shown for a set of low SNR events as well as 92 regional and teleseismic events in the Middle East.

Key Words: constant Q filter banks, wavelet transform, calibrated seismic events, Middle East, scales, signal-to-noise

1. OBJECTIVES

The long-term objective of Lawrence Livermore National Laboratory's regionalization research is to provide the U.S. National Data Center (NDC) and the CTBT International Data Center (IDC) with the necessary calibrations and algorithms to improve detection, phase identification, location, and discrimination in the Middle East and North Africa (Dowla, et. al, 1996). To achieve these goals, filtering will play a major role, particularly in low SNR signals. This study uses pre and post-arrival SNR measurements to suggest a filter which will optimize detection and identification of an arrival. This method can be used for any phase arrival, although this study focused on the initial P arrival.

One of the principal challenges was to choose an efficient, but accurate way to decompose the original seismic signal into sub-signals or scales, each of which would emphasize a different frequency band for transient analysis. For this reason, we investigated the application of the wavelet transform as well as simple banks of constant Q filters in order to learn the advantages and drawbacks of each approach.

Our purpose was to measure the SNR with respect to the estimated P arrival in each band and develop an algorithm to identify a subset of bands which together would indicate a filter to produce maximum SNR. This approach has been successfully used to lift observed seismic signals off the background noise with little distortion (Douglas, 1997).

The algorithm was tested in two ways. First, on a small set of low SNR events which were selected by the human analyst based on their difficulty in phase picking. Second, on a set of 92 regional and teleseismic signals recorded at the station ABKT in Alibek, Turkmenistan.

2. RESEARCH ACCOMPLISHED

2.1 Wavelet transforms and constant Q filter banks We considered two approaches to achieve constant Q filtering: the wavelet transform and a constant Q logarithmic filter bank. A discussion on the rapidly growing study of wavelet theory is beyond the scope of this work, but interested readers should refer to a paper by Olivier Rioul (Rioul, et al. 1991) which contains a review, tutorial, and extensive bibliography on wavelet theory. In general, however, the wavelet transform $W(a, \tau)$ of a seismogram signal, $s(\tau)$ is given by:

$$W(a, \tau) = \frac{1}{\sqrt{a}} \int_{-\infty}^{\infty} s(t) h([(t - \tau)]/a) dt \quad (2.1.1)$$

where a represents the scale and τ time in the transform domain, and $h(t)$ is the analysis wavelet which is localized in both time and frequency (Vetterli, 1995).

One of the key ideas is the decomposition of the original signal into constant relative bandwidth or constant Q frequency bands (Rioul et al., 1991). This approach offers analysis of the data at different scales such that short windows are used at high frequencies and long windows are used at low frequencies. Seismic arrivals often occur in only one or two of the scales.

Of course, constant Q logarithmic filter banks using conventional filters can also be used to decompose seismic signals. Although comparable results are obtained, it is a less efficient approach as it represents each band of a N-point signal with another N-point signal. The discrete wavelet transform represents all scales with a single N-point set. The disadvantage of using wavelets is determining which wavelet basis function to select, and the dyadic nature of the wavelet algorithm, which limits the flexibility in selecting Q values for a given type of data. The results in this report were obtained using constant Q logarithmic filter banks. Figure 2.1.1 illustrates a signal which has been decomposed into scales or filter bands by both the wavelet transform and a 4th order Butterworth constant Q filter bank.

All data used in this study was obtained from the Incorporated Research Institutions in Seismology Data Management Center (IRIS DMC). Event location, magnitudes, and depths were obtained from the United States Geological Survey Preliminary Determination of Epicenters (USGS/PDE) catalogs. All events used are presumed earthquake signals. All events were recorded using broadband instruments. All stations were 3 element, single site installations. Only the vertical (z) component data was used in this study. RANI and AFIF had a sample rate of 40 Hz. All other stations sampled data at 20 Hz.

Five regional events were chosen by a human analyst to test the algorithm based on their low SNR and analyst difficulty in selecting a filter for picking the P arrival. These five events ranged from 848 to 2332 km. Magnitudes ranged from 3.6 to 4.6 mb. Depths varied from 0 to 79 m. Five different events were recorded at a separate stations as shown in figure 2.1.2. In addition, 92 events recorded at station ABKT in Alibek, Turkmenistan were obtained to examine regional filter clustering. Distances for the ABKT events ranged from 155.2 to 4416.6 km. Magnitudes ranged from 4.3 to 6.2 mb. Event depths varied from 9 to 273 m. A map of these events is also shown in figure 2.1.2.

2.2 Signal and Noise Windows for P arrival

Signal and noise windows were selected for each event. The goal was to obtain a noise window which characterized pre-arrival background noise and a signal window which included the P arrival and a small time period surrounding the P arrival. The IASPEI91 model was used to calculate estimated P arrivals for each event. For regional and teleseismic events (>500 km), the signal window was defined from the estimated P arrival -10s to +30s. For local events (< 500 km) the signal window was +30s centered on the estimated P arrival. The noise window was defined from the 20km/s arrival time to 9/10 of the start time of the signal window. In Figure 2.1.1, the signal and noise windows are the darkened portions of the time series plots.

The instantaneous normalized power $p(t)$ associated with a time-varying signal $x(t)$ is:

$$p(t) = x^2(t) \quad (2.2.1)$$

The average normalized power P is then obtained by a time average of $p(t)$ over a period T .

$$P = \frac{1}{T} \int_0^T x^2(t) dt \quad (2.2.2)$$

The root-mean-square (rms) value X_{rms} is defined as the constant value that produces the same average power as the given time-varying signal. which leads to

$$X_{rms} = \sqrt{P} = \sqrt{\frac{1}{T} \int_0^T x^2(t) dt} \quad (2.2.3)$$

and is denoted by S_{rms} for signal rms power and N_{rms} for noise rms power. Using equation 2.2.3, SNR for this and all other examples is:

$$SNR = \frac{S_{rms}}{N_{rms}} \quad (2.2.4)$$

2.3 Algorithm for weighing scales or filter bands

The 92 ABKT signals were bandpass filtered six times using constant Q 4th order Butterworth filters. The start and stop bands are listed in Figure 2.1.1. The Q used was 1.25 with the lowest bandpass centered around 0.12 to 0.28 Hz. All bands were considered for teleseismic data, the two lowest frequency bands were ignored for regional events, and only the three highest bands were considered for local events.

The SNR value for each band was compared to the SNR value of the original signal. All SNR

values greater than or equal to the original signal's SNR value were classified as potentially useful or 'high SNR' bands. The bands whose SNR value fell below the original signal's SNR value were classified as 'low SNR' bands. The first step was to select the highest frequency 'high SNR' band. If the next lower frequency adjacent band was also a 'high SNR' band, it was concatenated with the previous band. This process continued until a 'low SNR' band was encountered. If none of the bands were 'high SNR' bands, the dominant band was selected as the 'suggested' bandpass filter with the caveat that the signal should be reviewed by a human expert for further analysis.

The result of the above process is a 'suggested' bandpass filter whose band limits were selected to improve SNR. This filter is then applied to the original signal as the optimal filter for this event. Frequency bands which contain maximum SNR for the desired seismic phase arrival were measured and identified using equation 2.2.4.

This algorithm can be applied using constant Q filter banks, or using the wavelet transform. Analogous to the previous discussion, scales are classified into 'high SNR' and 'low SNR' wavelet scales. The rest of the algorithm is the same. A conventional filter is used based on the 'suggested' bandlimits represented by the 'high SNR' scales. This is extremely useful, as it avoids the problems associated with anticausal distortion introduced by modifying wavelet scales prior to reconstruction or synthesis.

2.4 Results for low SNR events

The events at the top of figure 2.1.1 were described by the human analyst as being difficult or impossible to pick the P arrival from the raw signal without a great amount of uncertainty. Often, the analyst had to 'hunt' for a filter which would bring out the P arrival. The analyst's final selected filter specifications are listed in Figure 2.4.1.

These events were also processed using the algorithm described previously. The filter suggested for optimized SNR was then applied to the original signal. The automatically selected filter specifications are also listed in Figure 2.4.1.

Figure 2.4.1 contains three plots for each event. The top trace is the original raw waveform. The middle trace is the result of applying the analyst selected filter. The bottom trace is the result of applying the automatically selected filter. The vertical line labeled IP is the IASPEI91 P arrival time. (Kennett et al., 1991) The vertical line labeled FP is the P arrival time picked by the analyst. The analyst used the middle trace for the FP pick, although it is also superimposed on the raw and automatic filter trace for comparison.

2.5 Results for 92 ABKT events

The filtering algorithm was applied to 92 events recorded at station ABKT. This produced a set of 'suggested' filters which could be readily clustered. Clustering revealed eight unique bandpass filters for the 92 ABKT events. A histogram, plot, and table of filter bandwidths is shown in figure 2.5.1.

From the histogram we see that the predominant filter is the third cluster, corresponding to a suggested frequency bandwidth of 0.55 to 1.52 Hz. This band, which was suggested in over half the events, is interesting in two ways. If the algorithm does indeed produce optimal filtering, then one might argue that the third cluster indicates the best general band for the region. Inspection of the other bands, however, reveals quite a wide variance which would make this approach impractical. Secondly, most of the events fall into the third and fifth cluster. These clusters represent tight bands around a specific center frequency. This suggests that an approach using fixed filter bandpass limits would do poorly in an automated system. For optimal filtering, many events require narrow bandwidths around a specific frequency. Finally, maps with filter cluster symbol size scaled by the reported magnitude and depth are plotted in figure 2.5.2.

2.6 Regional frequency response

Figure 2.6.1 is a map of the region surrounding ABKT with a contour map and a surface plot superimposed. The upper map shows the Pn velocity relative to 7.9 km/s. (Hearn et al., 1994) The lower map uses the bandwidth clusters produced by the 92 ABKT events were used to generate the topography. The contours are approximately equal to the center frequency of the cluster bandwidths. From this result, it is clear that stations such as ABKT show complex and highly variable P wave propagation.

CONCLUSIONS AND RECOMMENDATIONS

The extreme geophysical variability of regions in the Middle East as seen at ABKT illustrates the need for methods which can use existing data to produce useful information about the region. We recommend further testing of this approach at other sites in the Middle East and North Africa. It is also recommended that this method be used as a pre-processing step to lower the variance in detection and location algorithms. We recommend that the algorithm be applied to other seismic phases such as surface waves. Further study is needed to determine optimal wavelet basis functions as suggested by others (Gibb et al, 1997, Kawaldip et al. 1997, and Yomogida, 1994) and to modify the wavelet transform itself to allow a selectable Q. A study to determine the optimal Q for seismograms in general would also be very useful. Finally, the implication for CTBT monitoring is that this algorithm offers a simple, effective process which can, in general, produce filtered seismic signals with maximum SNR and bring out signals typically buried in background noise.

REFERENCES

- Douglas, A (1997) Bandpass filtering to reduce noise on seismograms: Is there a better way?. *Bull. Seis Soc Am.*, Vol 87, No. 4. pp. 770-777.
- Dowla, F. U., P. Goldstein, P. Harben, D. Harris, T. Hauk, S. Jarpe, E. Kansa, P. Lewis, D. McNamara, H. Patton, D. Rock, A. Ryall, C. Schultz, A. Smith, J. Sweeney, W. Walter, L. Wethern (1996) Seismic Regionalization in the Middle East and North Africa, Proceedings of the 18th annual research symposium on monitoring a comprehensive test ban treaty, July, 55-64.
- Grub, H. J. and A. T. Walden (1997) Characterizing seismic time series using the discrete wavelet transform. *Geophysical Prospecting*, **45**, 183-205.
- Hearn, T. and J. Ni (1994) Pn velocities beneath continental collision zones: the Turkish-Iranian Plateau, *Geophys. J. Intl*, **117**, 273-283
- Kanwaldip, S. A., and F. U. Dowla (1997) Wavelet Transform Methods for Phase Identification in Three-component Seismograms. (in preparation).
- Kennett, B. and E. Engdahl (1991) for global earthquake and phase identification. *GJInt.*, **105**, 429-465
- Rioul, O. and M. Vetterli (1991) Wavelets and signal processing, *IEEE Spectrum magazine*, October, 14-36.
- Vetterli, M., and J. Kovacevic (1995). *Wavelets and Subband Coding*, Prentice Hall, Englewood Cliffs, NJ.
- Yomogida, K., (1994) Detection of anomalous seismic phases by the wavelet transform.. *Geophys. J. Int.* **116**, 119-130.

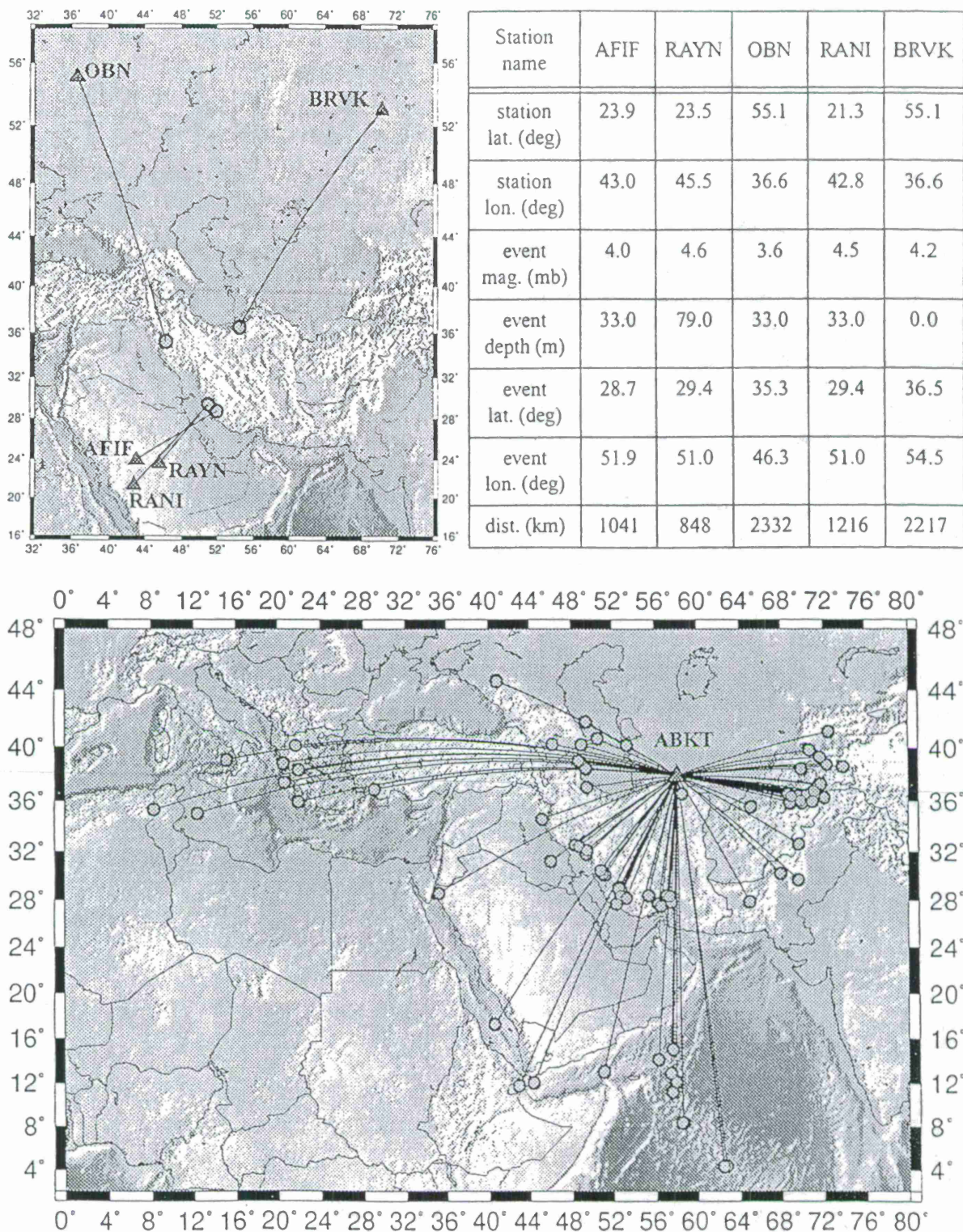


Figure 2.1.2 Map of low SNR regional event/station pairs selected by analyst based on difficulty on selecting a filter for picking the P arrival. for low SNR events.(top left) Corresponding table of values for event and station location, magnitude, distance, and depth. (top right) Location of 92 ABKT events to be filtered by the filter optimization algorithm to show regional propagation characteristics based on filter clusters. (bottom)

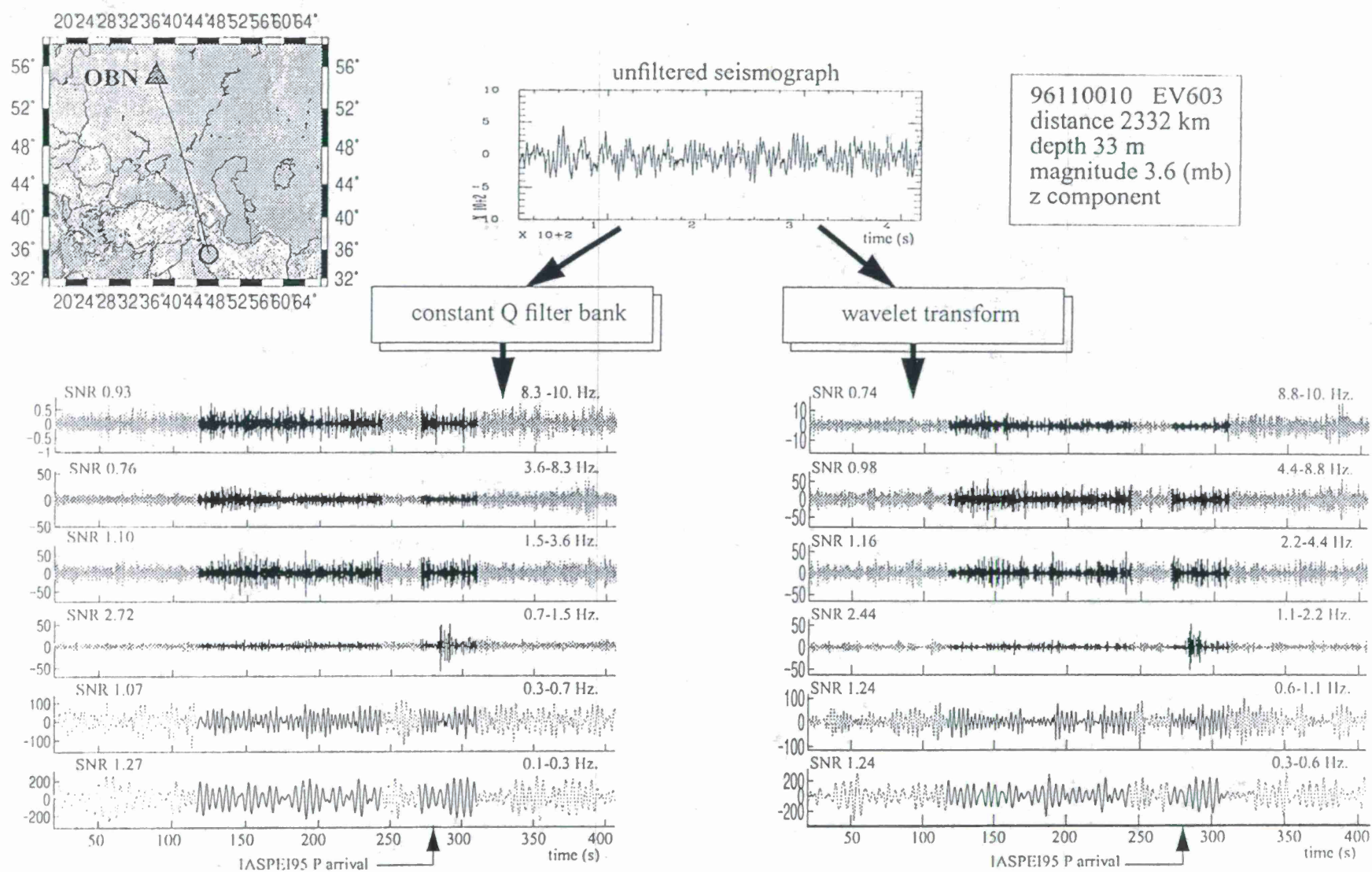


Figure 2.1.1 Decomposition of raw signal using wavelet transform (right) and constant Q logarithmic filter bank (left). In both cases, the fourth scale contains the dominant arrival energy. The wavelet scale corresponds to a 0.55-1.1 Hz filter, while the band in the filter bank is a 4th order Butterworth filter from 0.65-1.52 Hz.

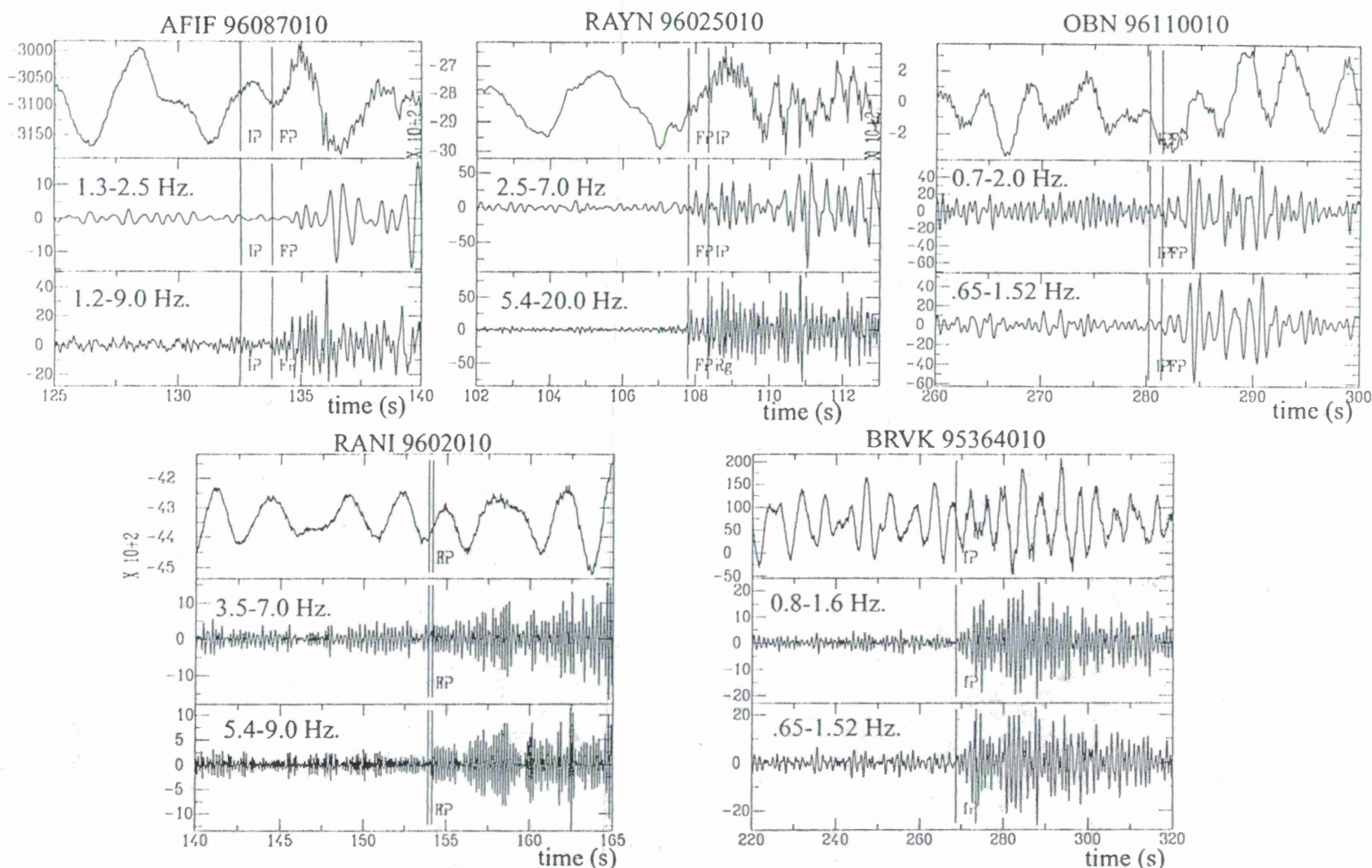


Figure 2.4.1 Five low SNR events with raw signal (top), analyst filtered signal (middle) with bandpass limits superimposed on plot, and optimization algorithm suggested filter (bottom) with bandpass limits superimposed on plot. IASPEI95 P arrival is indicated by the IP marker on each plot. Analyst pick is indicated by the FP marker. (The middle plots were used for the FP pick)

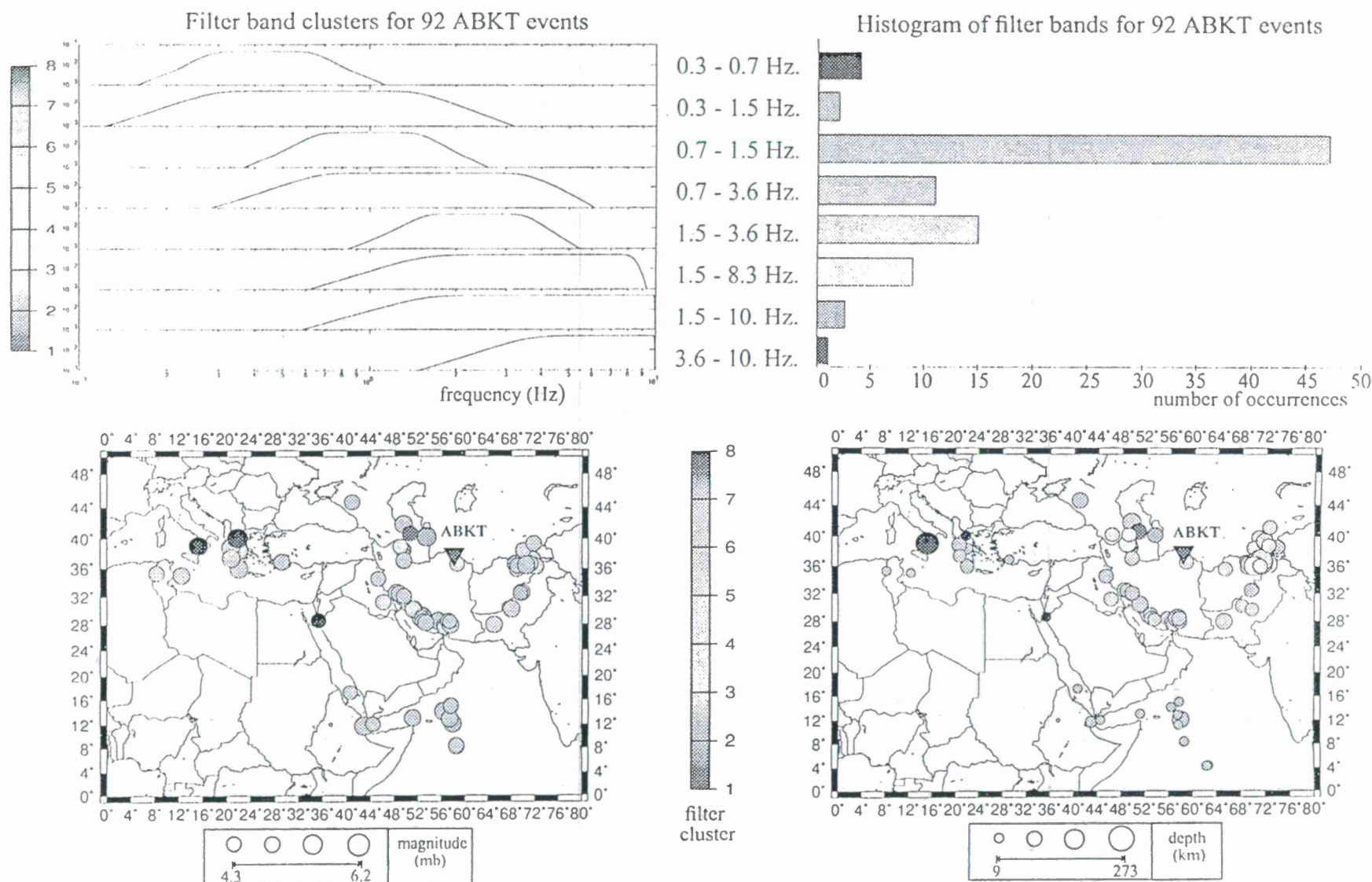


Figure 2.5.1 Clustering of 92 ABKT event bandpass filters revealed 8 unique clusters. (top left) Histogram indicates predominance for 6th filter cluster, but also shows a large variance. (top right) Maps indicate location of clusters sized by magnitude (bottom left) and sized by depth (bottom right)

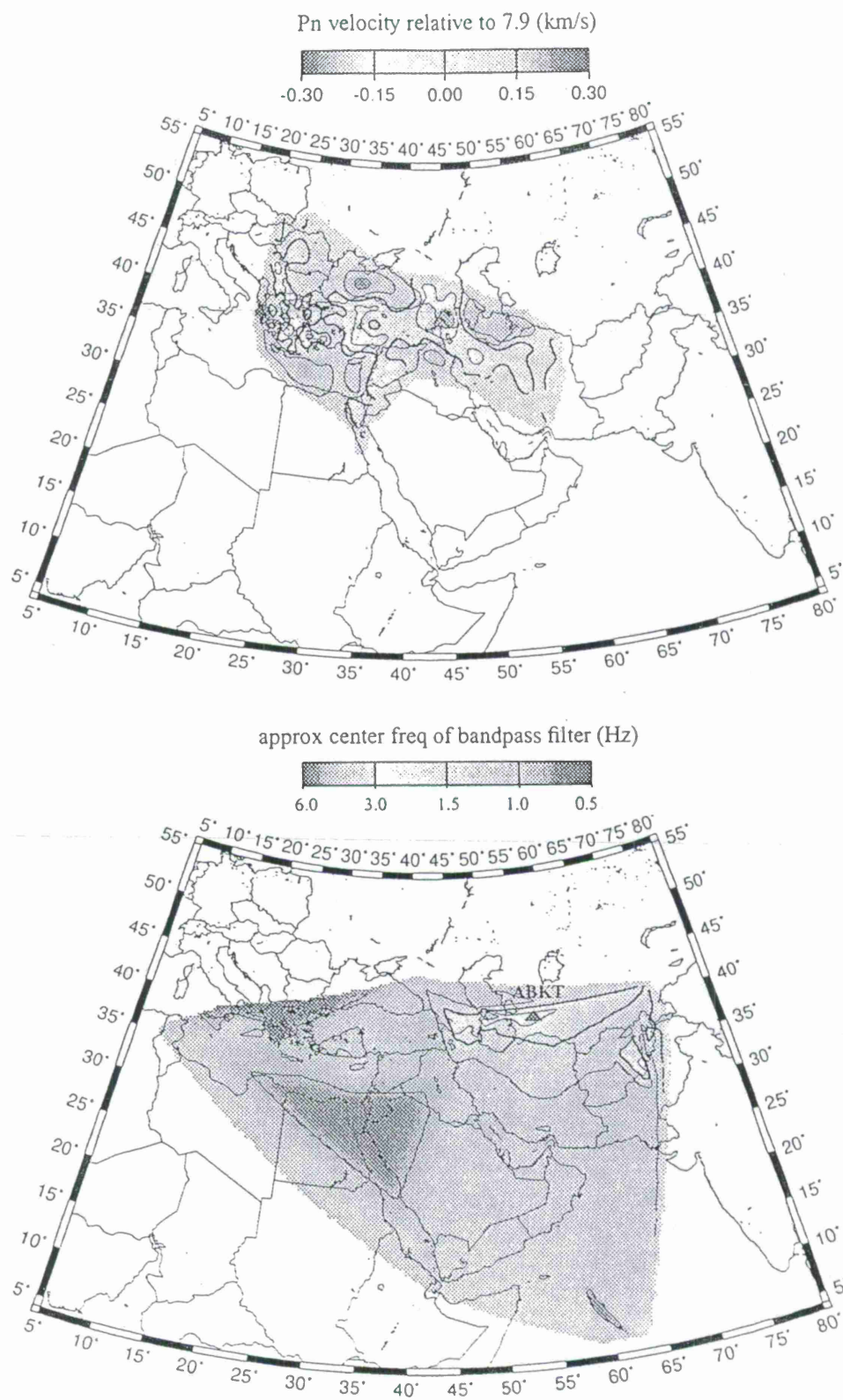


Figure 2.6.1 Plot of Pn velocity relative to 7.9 km/s (top). Contour plot of the approximate band-pass filter center frequencies for the 8 filter clusters produced by 92 ABKT events. (bottom)

LLNL MIDDLE EAST AND NORTH AFRICA RESEARCH DATABASE

Stanley D. Ruppert, Teresa F. Hauk, Richard Leach

*Geophysics and Global Security, Lawrence Livermore National Laboratory
University of California*

Sponsored by U.S. Department of Energy
Office of Nonproliferation and National Security
Office of Research and Development
Contract No. W-7405-ENG-48
Sponsored by DOE CTBT R&D Program

ABSTRACT

The Lawrence Livermore National Laboratory (LLNL) CTBT R&D program has made significant progress assembling a comprehensive seismic database (DB) for events and derived parameters in the Middle East and North Africa (ME/NA). The LLNL research DB provides not only a coherent framework in which store and organize large volumes of collected seismic waveforms and associated event parameter information but also provides an efficient data processing/research environment. The DB is designed to be flexible and extensible in order to accommodate the large volumes of data in diverse formats from many sources in addition to maintaining detailed quality control and metadata. Researchers can make use of the relational nature of the DB and interactive analysis tools to quickly and efficiently process large volumes of data. Seismic waveforms have been systematically collected from a wide range of local and regional networks using numerous earthquake bulletins and converted a common format based on CSS3.0 while undergoing quality control and corrections of errors. By combining traveltime observations, event characterization studies, and regional wave-propagation studies of the LLNL CTBT team, we are assembling a library of ground truth information and event location correction surfaces required to support the ME/NA regionalization program. Corrections and parameters distilled from the LLNL research DB will provide needed contributions to the DOE knowledge base for the ME/NA region and enable the USNDC and IDC to effectively verify CTBT compliance.

Key Words: seismic, waveform, database, metadata

Objectives

The primary objective of the LLNL research DB program is to efficiently provide large volumes of quality controlled seismic data and interactive analysis tools with connectivity to the DB in support of the LLNL CTBT Middle East and North Africa regionalization program. In the Middle East and North Africa, there is a hierarchy of ground truth that can be obtained. This hierarchy ranges from explosions with exact locations to carefully studied aftershock sequences, events located by dense local networks, and teleseismically constrained events such as CMT and EDR bulletin events. Our goal is the collection, quality checking, and conversion of tens of thousands of seismic waveforms from many different seismic networks (such as AFTAC, PIDC, IRIS/IDA, IRIS/USGS, IRIS/GEOFON, MEDNET, GEOSCOPE) to a standard format provide the necessary framework to be able to relocate and characterize each event. Location studies require synthesis of traveltime and azimuth correction surfaces, phase onset measurements and identification and depth determination. All of the waveforms compiled and integrated will be re-analyzed and quality checked by trained analysts. Event characterization requires analysis of physical basis including earth structure derived from body waves, surface waves and regional geology, and the effects of phase blockage. The research DB will provide ready access and organization to the thousands of events and associated waveforms and also provide the framework for storage and dissemination of results. Sufficient metadata (including measurement procedures, codes, comments and measurement errors) are stored at each step in the analysis process to allow recreation or verification of results at any stage in the processing flow.

In detail, the LLNL research DB must facilitate scientific analysis during all phases of the CTBT regionalization program. From exploratory data interpretation, production data analysis and distillation of standardized measurements applied to all waveforms, and Quality Assessment (QA) and delivery of research products to the DOE knowledgebase. Out of the research DB will be compiled the reference event libraries and ground truth datasets showing space and time clustering of natural earthquake and mine events, phase blockage maps, event characterization parameters necessary for the monitoring CTBT compliance in the ME/NA region.

Research Accomplished

Data Collection

Data collection for the LLNL ME/NA research database began in 1996 and continues today. Initially, large events were selected from the Harvard CMT catalog and the NEIC PDE catalog. As the database fills, we are moving to smaller magnitude events and extending our coverage of the entire ME/NA area. Detecting and characterizing small magnitude events that can be associated with mining events is a research priority. In support of this, we also have collected continuous data from several stations. Analysis of the continuous data using waveform correlation, spatial and temporal clustering by LLNL CTBT researchers to detect smaller magnitude events is currently underway. The ME/NA area from which events are chosen has grown as we've developed our database and run into research issues that require data from outside the original arbitrary bounds (e.g., ray-path coverage, structure-related phase blockage or attenuation, etc.). Source-receiver distances range from local to teleseismic. Figure 1 outlines the base data acquisition flow from data request, quality checking and integration of the waveform into the DB using a

common format, and access of the waveform from the database by LLNL CTBT researchers and analysis programs.

Our current area of interest (Figure 2) includes all seismic events located within and recorded by stations in the box bounded roughly by corners 10S, 35W and 60N, 85E. Figure 2 shows the IMS primary, auxiliary, and supplemental stations data collection from which data is currently being requested, on superimposed on NEIC seismicity between 1990 and 1996. This is the time period for which the most high-quality, easily accessible digital data were available from most stations. Certain selected events or datasets at stations operating prior to 1990 have been requested. ILPA (Iranian Long Period Array) data, for example, are used as a surrogate for the proposed IMS primary array, THR. ILPA was operational from 1977-79. Magnitude thresholds are determined by the catalog used to initiate the requests. We have certain regions for which all events down to mb4.0 in the PDE catalog are included in the current database. Our goal is to get all data for all stations and events at least down to mb4.0 or perhaps smaller. The compilation of local and regional seismic network bulletins is continuing as we move to smaller magnitude thresholds. We are also collecting large continuous data segments from some stations for specific research (e.g. clustering analysis, detection and identification of mining explosions in certain areas, etc.). The local bulletins we have obtained sometimes also include identified mining explosions which are useful for constraining location errors of small events.

As of July 1997, the number of waveforms in the DB exceeded 50,000 representing over 2200 events. As summarized in Figure 3, all of the waveforms currently in the database recorded by a particular station (open triangle) and event (small circle) pair are shown as either gray raypath where data has been loaded or as black raypath denoting where travel-time observations have been made by a LLNL or contractor trained analyst. Currently about 650 events out of the 2200 have been repicked to yield over 6000 travel-time observations made available to the LLNL CTBT research teams for location and discrimination projects. The current raypath coverage is dense enough that surface and body wave tomography studies are now underway. Augmenting the LLNL picks, we've added all ~5 million NEIC EDR phase pick observations into the DB to be used as a starting point for travel-time correction studies and correction surface generation. Statistical studies are underway comparing the variance and accuracy of the LLNL analyst picks to those from the NEIC EDR bulletins to see where using the EDR picks is most appropriate. Bulletin information many local and regional catalogs (NEIC EDR, CMT, ISC, JSOP, Greece, Turkey, Israel, AFTAC (unclassified), Saudi Arabia) have been incorporated into the DB to be used in forming event requests.

We have also derived an initial teleseismically derived ground-truth event bulletin (Schultz et. al., 1997) to be used in event requests. The work of Sweeney (1996) shows that teleseismic events can give event locations with a known uncertainty. As part of a LLNL ME/NA location study, we derived teleseismically constrained ground truth dataset using NEIC EDR phase pick information and AK135 velocity model. We relocated all EDR events that fit the azimuthal gap $< 180^\circ$ and number of phases > 50 criterion, suggested by Sweeney's aftershock studies, using the this velocity model. Relocation was done using EvLoc which operates on the LLNL Oracle database and all of the AK135 relocations shown as circles coded by particular catalog, either NEIC (light) or CMT (dark) catalog, in Figure 4 have been incorporated into the LLNL hierarchical ground truth database with a 20

km uncertainty assigned to the location. Comparisons and reconciliation of events common between bulletins and those relocated using travel-time corrections for the ME/NA region is also underway as part of the location research efforts. In addition to the teleseismically constrained ground truth events, we have begun collecting mine explosions, a very few nuclear events, and small magnitude local event well constrained by local networks. Selected events from these higher grade (i.e. better location and origin time estimates) categories are also plotted in Figure 4 as diamonds/triangles.

Surrogate stations were chosen for IMS primary and auxiliary network arrays and stations that have not yet been installed or for which little data is currently available. Supplemental data from broadband stations located in the vicinity of proposed IMS sites and from other stations in our general area of interest were also requested. The current list of stations for which there are waveforms in the database totals 296 (includes individual array elements). Figure 2 shows the stations from which we currently have waveforms from in the ME/NA region. Data windows to be requested were calculated for each station so that the criteria for all segments would be consistent (begin at origin time of event and end at arrival time of seismic waves traveling at 1 km/sec). Data was requested from five major data archival centers: AFTAC, IRIS, GEOSCOPE, GEOFON, and the PIDC. IRIS requests were submitted using the `breq_fast` batch method for a single station for a year-long period to keep the seed volumes small enough to transfer electronically. The `xretrieve` method was used to request continuous data segments that were provided on Exabyte tape. GEOSCOPE and GEOFON requests were similar. AFTAC requests were made using a modified `autoDRM` request format. Multimax, Inc., is contracted to do a portion of the data collection for the LLNL database. They obtained bulletin and waveform data from the PIDC using their `Req-Data` request routine. Multimax is responsible for collecting recent and continually occurring earthquake data while LLNL concentrates on the historic waveforms available.

Data arrive from the various data centers in, primarily, 2 different formats, CSS3.0 and SEED. The waveform data is processed and written out in CSS formats. The default origin definition (`orid`) for each waveform is the NEIC EDR monthly location solution unless a better location is available. The station location information has been found to have discrepancies between different sources. In such cases, we've gone directly to the network operators and have attempted to obtain the best information possible. There are also discrepancies in what channels are being recorded at a given station and the dates those channels are operational. Again, we have worked hard to obtain the most accurate information from the most direct sources in these instances to keep the database as accurate as possible. All available pertinent information about the event (PDE location parameters) and the station (available network station inventories, FDSN station book, IDC country book, site and sitechan tables) is examined and the verified information is added to file headers (SAC) or flat files (CSS). The processed waveform data is written to a staging disk into separate event directories prior to loading into the DB. Waveform and header data are examined to verify that the resultant CSS format files are complete. Checks are made to prevent overwriting data files in the existing database. Overlap of id numbers, such as `wfids`, is checked to ensure uniqueness in the database. Processing logs are reviewed to ensure that all available data was processed and that there were no blatant errors. The waveform data is then moved to the disk storage system as an official part of the LLNL ME/NA research database and made available to researchers.

Database structure

The basic design goals of the LLNL research DB are support the representation of diverse data types, handle large quantities of data and yet be flexible, extensible and maintainable. Data stored in the DB, along with the associated metadata and quality control information provides the raw material and is of central importance to most of the LLNL CTBT regionalization programs including event location and event characterization. Because the subsets of data must be provided in a form easily accessible to many diverse research programs having different user requirements of data and metadata, the DB access tools have been designed to utilize the power of the relational database to facilitate efficient queries and data retrieval and to hide as much of the low level database calls from the end user as possible. Hence the LLNL research DB fills the role of both data archive for the assembled seismic datasets and ground truth libraries forming the deliverables to the DOE knowledgebase, but also as an analysis tool itself enabling data analysis to be done thoroughly on over 50,000 waveforms while providing data organization and visualization results.

The core of the LLNL DB is comprised of ORACLE relational database (RDB) software running on a SUN Ultra 1/170 workstation. Integral to the ORACLE server is WWW server which provides researchers, within the LLNL intranet, interactive (GUI) access to the DB contents in addition to DB access via software tools such as SAC, MATLAB, and custom data browsers based on HTML. Many seismic analysis codes such as EvLOC can connect to the DB directly from the users workstation. Storage space for the waveforms consists of two SUN disk storage arrays holding over 250 GB of seismic waveforms, DB files, and associated metadata information. The DB is connected via 100Mb/s high speed ethernet to the researchers' workstations. The waveforms themselves and final deliverable parameter products are provided in CSS3.0 format utilizing AFTAC and NDC extensions where needed. Several LLNL custom tables are used to store intermediate research parameters, measurements, and metadata. The CSS3.0 standard with extensions was adopted for the purposes of compatibility.

Quality and metadata information is carefully maintained for the collected and corrected waveforms, on all event relocations, and on all event characterization and identification measurements. Metadata allows the processing history and quality to be assessed at any step during the processing flow (Figure 1) and will be an integral part of the derived parameters and corrections delivered to the DOE knowledgebase. Design of the metadata tables was undertaken in collaboration with Sandia National Laboratory and Los Alamos National Laboratory CTBT programs to ensure compatibility and completeness of the final deliverable products. LLNL metadata tables for internal use provide frequent cross-checks of the data collected to data and allow for efficient processing of 1000's of waveforms arriving monthly from disparate global and regional networks as well as from contractors.

An example of two types of metadata we currently generate automatically and store for each waveform in the DB is as follows. First, any defined process can generate metadata across all the signals in the database. For example, signal-to-noise (SNR) is an important parameter in many research studies. We have generated pre and post-P wave rms signal power measurements for all the signals in the database. The instantaneous normalized power $p(t)$ associated with a time-varying signal $x(t)$ is:

$$p(t) = x^2(t) \quad (1.1)$$

The average normalized power P is then obtained by a time average of $p(t)$ over a period T .

$$P = \frac{1}{T} \int_0^T x^2(t) dt \quad (1.2)$$

The root-mean-square (rms) value X_{rms} is defined as the constant value that produces the same average power as the given time-varying signal. which leads to:

$$X_{rms} = \sqrt{P} = \sqrt{\frac{1}{T} \int_0^T x^2(t) dt} \quad (1.3)$$

Using 1.3, we have generated signal and noise rms power measurements for all the signals in the database. The results along with the metadata (algorithms used and waveforms measures) were placed into the database to allow other researchers to use these results to readily obtain SNR values for any signals of interest. This was recently done on over 50,000 signals presently in the database.

Secondly we have developed an automated algorithm which can provide tailored meta information on defined subset of signals in the database. This is extremely important in areas with sporadic or poorly recorded data or in aseismic areas. For example, if the focus of a study is the P and S arrival, parameters can be set to focus on a desired time including and in the vicinity of those arrivals. A specific station or set of stations can also be chosen. The algorithm permits 18 separate error detections on the signals requested only during the time of interest. These checks include timing errors such as a negative time axis and non-existing data. They also check for zero slope areas of the data and discontinuities. Finally, in the case of multi-channel data, median filters are used to determine if the signal power, noise power, or SNR is reasonable relative to the other channels. This is useful for array data as well as three-component signals. The metadata gathered is stored in database tables for review. By applying this algorithm only during times of interest, many more events can be identified which might have been rejected using a meta filter across the entire signal.

Summary

Future work will strive to make the waveform DB complete for all stations and all earthquake events down to magnitude 4.0 in the ME/NA area in addition to as complete a bulletin as possible of mine blast and other ground truth events down lower magnitudes. Continuous data segments will also be added as requested by the location and identification researchers. Detailed summary and compilation bulletins will be produced to be used in further ME/NA research efforts including special event analysis and array installation studies. DB tables of derived location and identification parameters from these waveforms will be distilled and delivered to DOE to become part of the run-time knowledgebase.

References

Sweeney, J.J., 1996, "Accuracy of teleseismic event location in the Middle East and North Africa", Lawrence Livermore National Laboratory, UCRL-ID-125868.

Schultz, C.A., Myers, S.C., Ruppert, S.D., 1997, "Event Location in the Middle East and North Africa", Lawrence Livermore National Laboratory.

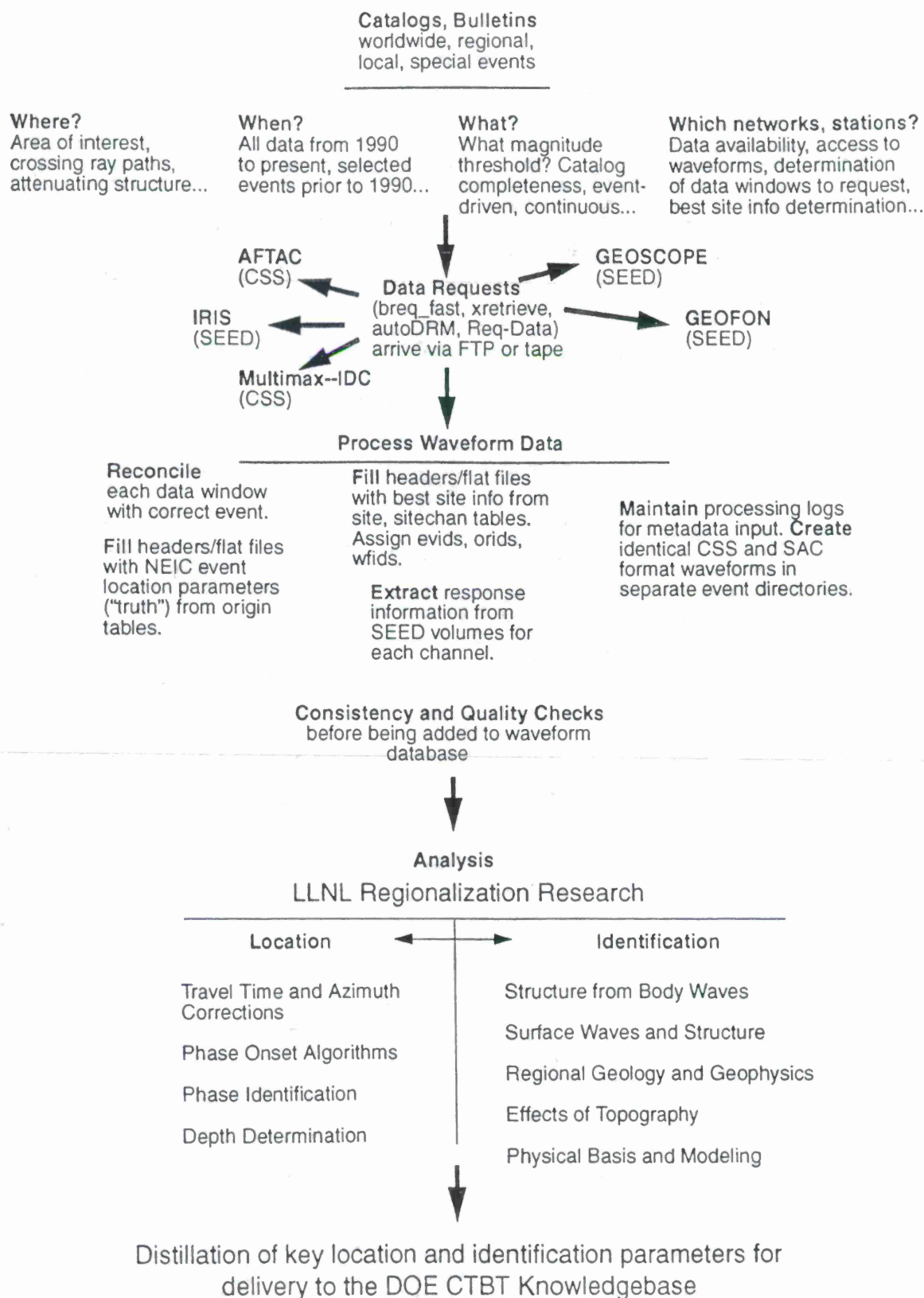


Figure 1. Flow chart for Datacollection and Quality Control.

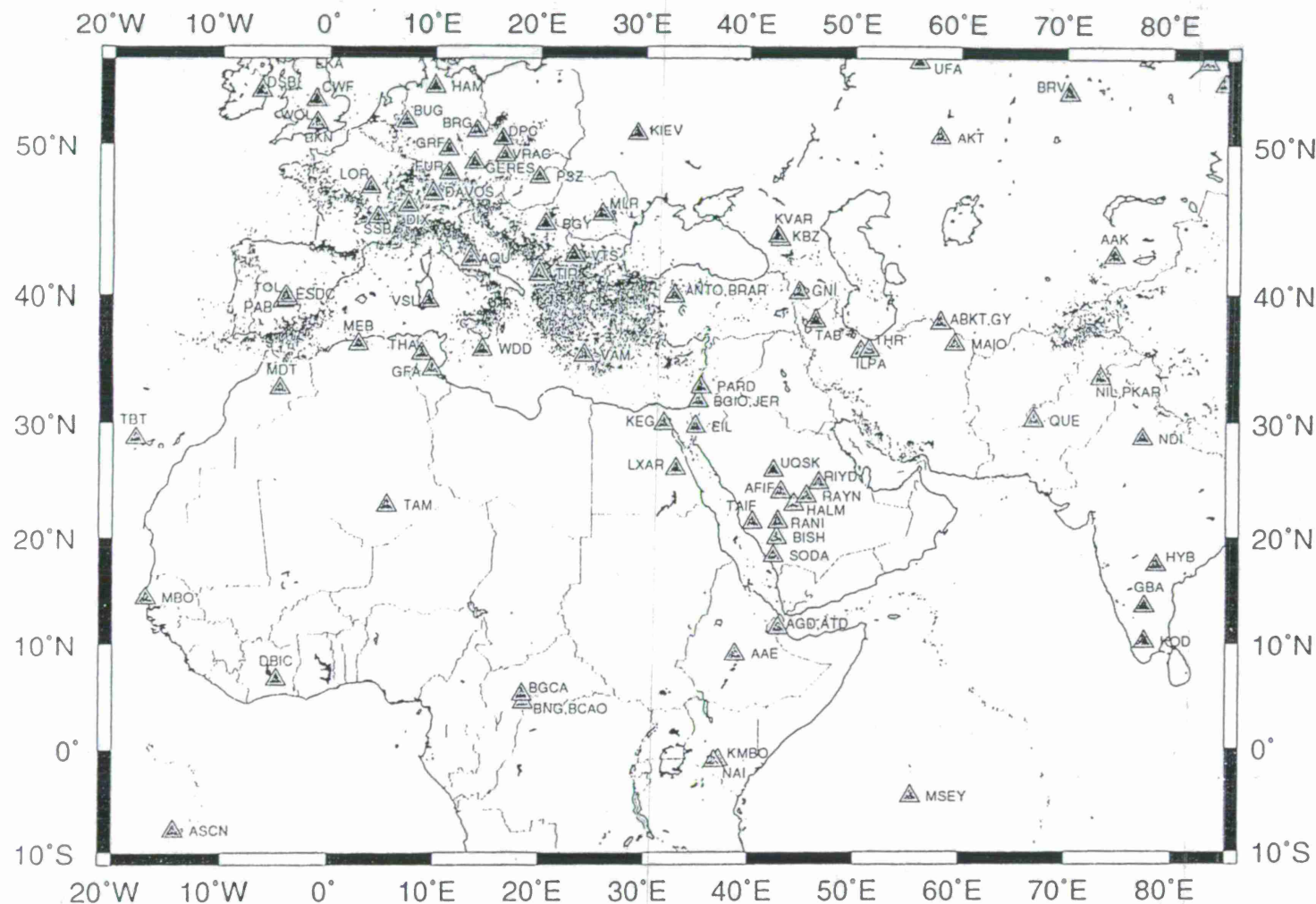


Figure 2. Middle East and North Africa seismic stations and 1990-1996 seismicity. The IMS primary, auxiliary, and other broad-band stations both current and proposed are shown plotted over 1990-1996 NEIC seismicity for the ME/NA region.

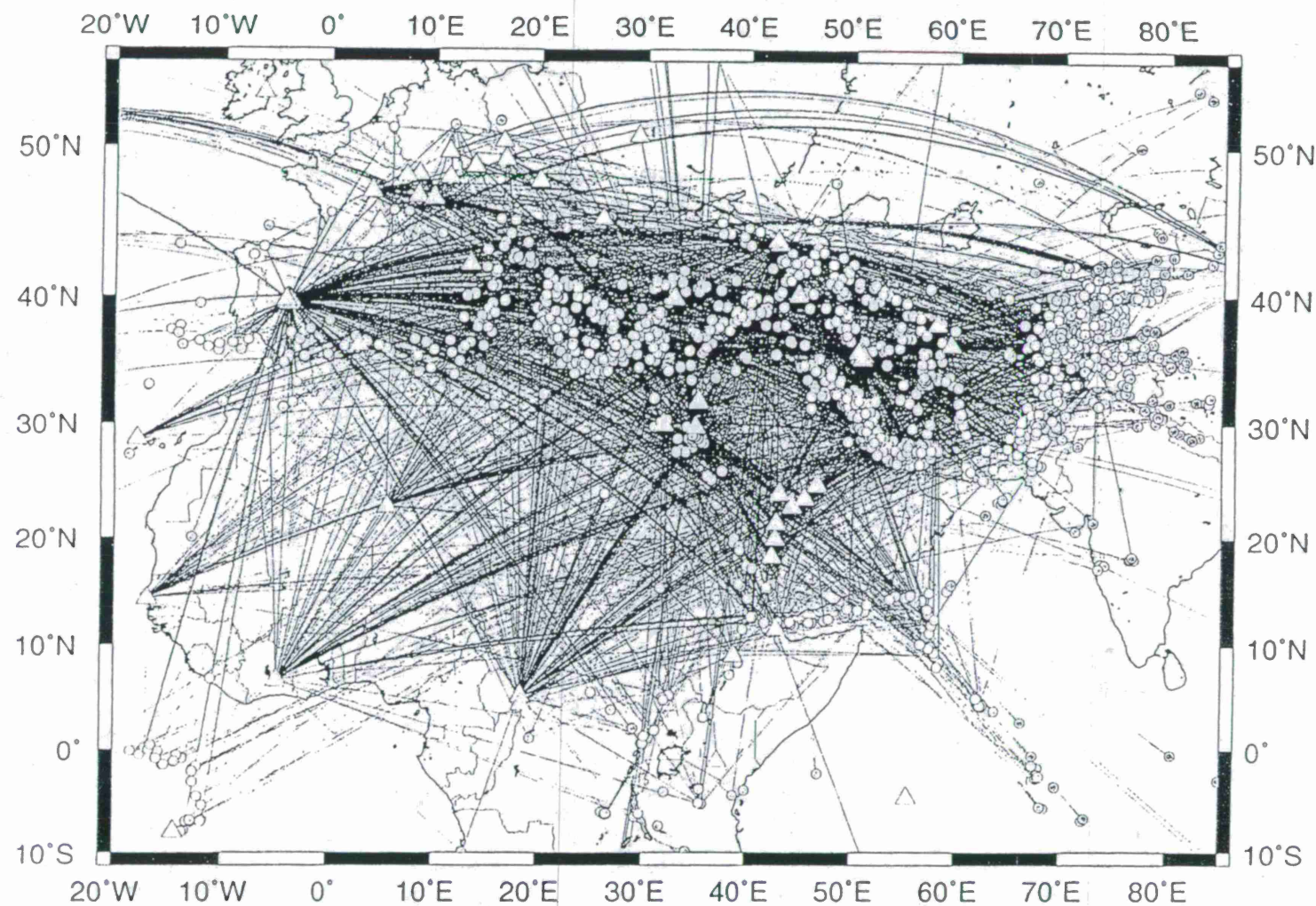


Figure 3. Database inventory plot as of summer 1997. All of the waveforms currently in the database recorded for all station (open triangle) and event (grey circle) pairs are shown as either grey raypaths where data has been loaded or as black raypaths where travel-time observations have been made. As of summer 1997 over 50,000 raypaths from 2200 events and 6000 travel-time picks have been quality checked and made available to the LLNL CTBT research teams for location and discrimination projects.

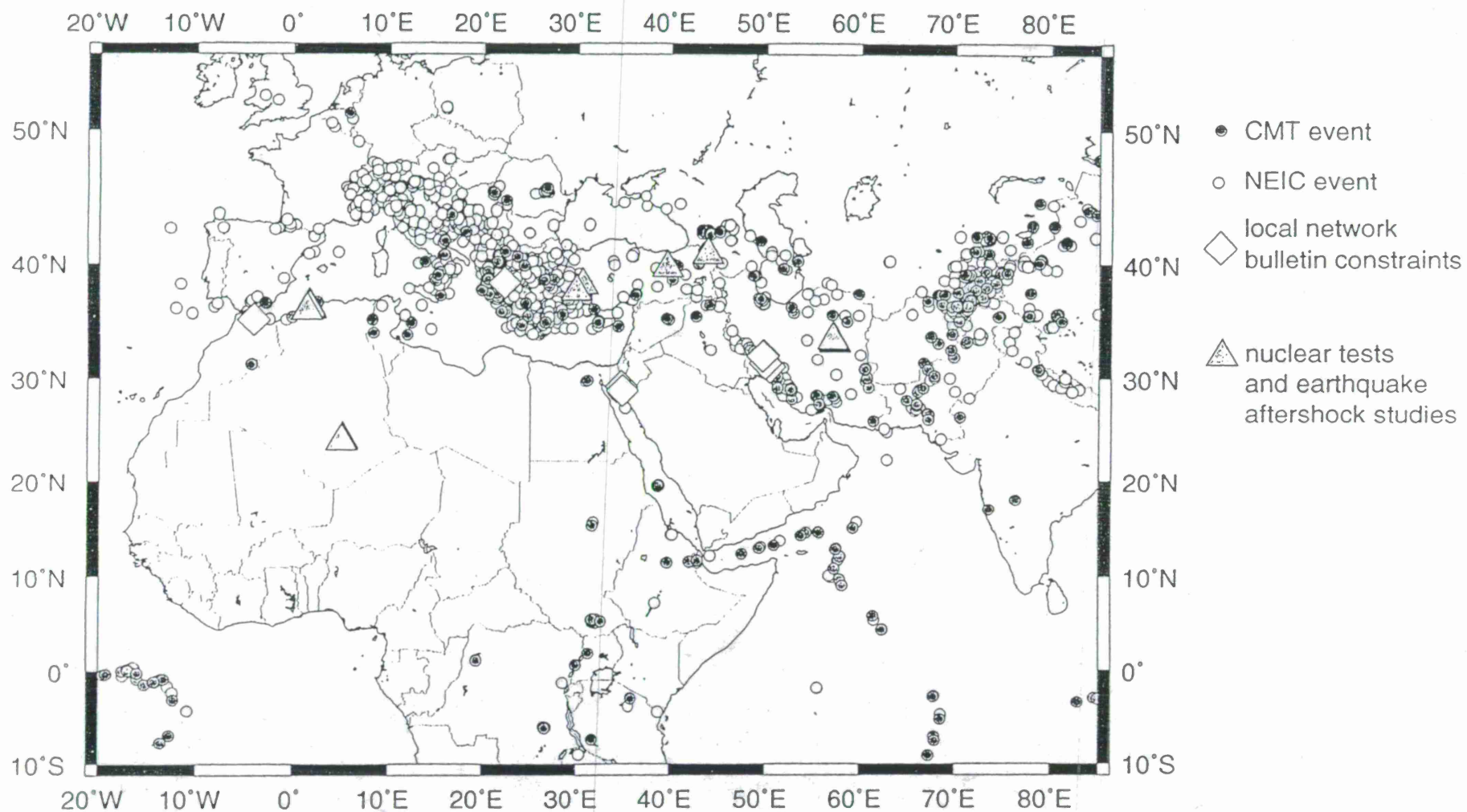


Figure 4. Map view teleseismically constrained (TC) ground truth events and selected explosion/local network events. Thus far ground truth events in the Middle East and North Africa are predominantly teleseismically constrained events based on EvLOC & AK135 relocation of NEIC events meeting the Azgap < 180° and numphases > 50 criteria. Nearly 2,000 TC ground truth events lie within the ME/NA region with far fewer reference explosion data available thus far.

7

SEISMOLOGICAL RESEARCH IN SUPPORT OF CTBT FOR THE MIDDLE EAST AND NORTH AFRICA REGION

Eric Sandvol, Dogan Seber, David Steer, and
Muawia Barazangi

Institute for the Study of the Continents, Cornell University, Ithaca, New York 14853
(e-mail: sandvol@geology.cornell.edu)

Sponsored by U.S. Department of Energy
Office of Nonproliferation and National Security
Office of Research and Development
Contract No. F19628-95-C-0092

ABSTRACT

In order to meet the rigorous monitoring requirements contained in the Comprehensive Test Ban Treaty (CTBT) it is essential to increase the current knowledge of regional-scale earth structure. Monitoring low yield nuclear explosions and discriminating them from earthquakes and other types of large chemical explosions is essential to successful enforcement of the CTBT. Current knowledge of the Middle East and North Africa is insufficient to effectively accomplish regional monitoring that would detect small yield nuclear explosions. We are using various seismological techniques and data that will provide the monitoring community robust information on the structure of the earth that will help to accomplish this very difficult problem.

In this paper, we give some examples of original seismological studies that will help in the better understanding of crustal structure and regional wave propagation in the Middle East and North Africa. We are studying the crustal structure beneath each broadband station using receiver function grid search inversion. We have also begun to look at regional wave propagation in the Middle East using seismic data from Turkish and Syrian national seismic network data. Preliminary results show that the Bitlis suture causes Lg blockage and that the northern Dead Sea fault attenuates Sn waves. We have also examined the problem of discriminating between earthquakes and chemical explosions in Morocco.

Keywords: Middle East and North Africa, CTBT, regional tectonics and geophysics, seismology.

OBJECTIVE

Multilateral zero yield treaties, such as the CTBT, will require developing credible strategies for effective monitoring, including the ability to detect, characterize, calibrate, discriminate, and verify any suspect event for any region on earth. In order to accomplish this task, fundamental observations concerning earth structure are needed. Examples of such critical observations are crustal velocities, crustal densities, regional phase propagation efficiencies, and the behavior of standard discrimination algorithms in regions where previously there has been very little work. Current knowledge of these parameters in the Middle East and North Africa is insufficient to effectively characterize and calibrate seismic events. New seismological data are required to constrain advanced theoretical modeling efforts in order to better understand the propagation of high-frequency seismic waves produced by very low yield events at regional distances. In order to make our final results available to the monitoring community we will include our work in the Middle East and North Africa GIS database.

Our objective is to constrain some of the existing geophysical/seismological information and/or provide new information on the nature of the earth in the Middle East and North Africa. We have used these data to obtain more accurate results and included them in our GIS databases. In this paper we will be giving three examples of new observations that we have made. These observations will prove critical to calibrating and discriminating seismic events in the Middle East and North Africa.

RESEARCH ACCOMPLISHED

Receiver Function Inversion for Crustal Structure

We have made estimates of crustal thickness and shear-wave velocity structure using receiver function inversion for all available broadband stations in the Middle East and North Africa. We have created over 500 receiver functions from fifteen stations in this region. We have reviewed each receiver function and eliminated all those with poor signal to noise ratios (less than 3 to 1). Of these fifteen stations we have been able to construct high quality receiver functions stacks for twelve stations. In each of the stack receiver functions we have included data from all available azimuths. This allows us to invert for average velocity structure beneath each station. In order to avoid destructive interference or artificial broadening of the P-to-S energy we have only stacked events with similar teleseismic P-wave ray parameters.

In order to invert the receiver function data for crustal and uppermost mantle shear-wave velocity structure we have employed a grid search scheme using a maximum of five layers over a mantle half-space for our model. Unlike least squares inversion schemes our

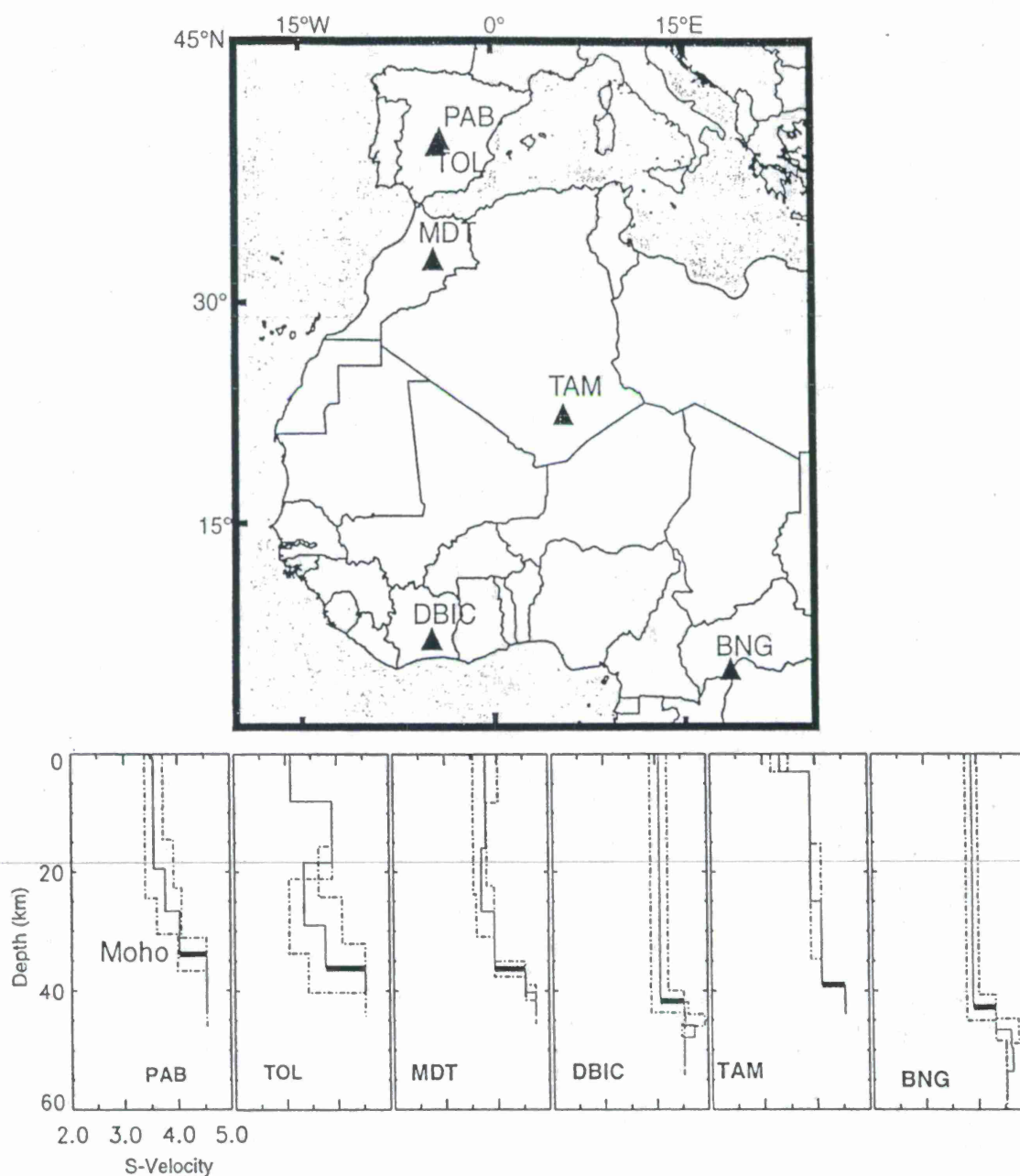


Figure 1. Shear-wave velocity models obtained from receiver function inversions of broadband data taken from permanent stations within North and Central Africa as well as Spain. The error bounds are from standard errors computed from jackknifed inversions for each station's receiver function stack.

grid search technique guarantees that we will solve only for global minima. By using only 8 to 10 model parameters (4 to 5 layers, varying both the layer velocity and thickness) in our inversion we are able to minimize the over-parameterization of this problem. We have also made estimates of errors using jackknife statistics. We resample each of the receiver

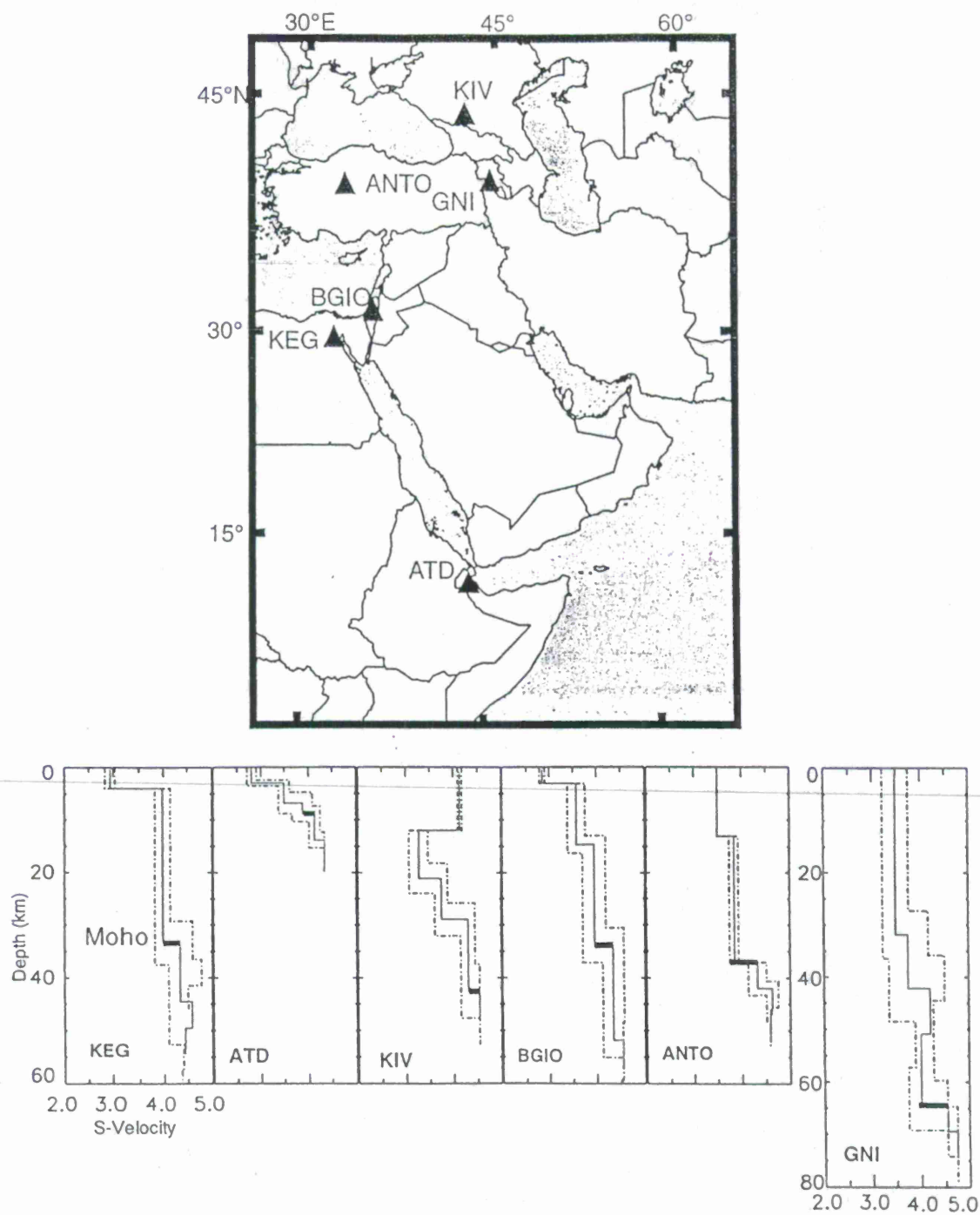


Figure 2. Shear-wave velocity models with error bounds for 6 permanent broadband stations in the Middle East. The Moho is interpreted based upon the velocity structure as well as surface geology.

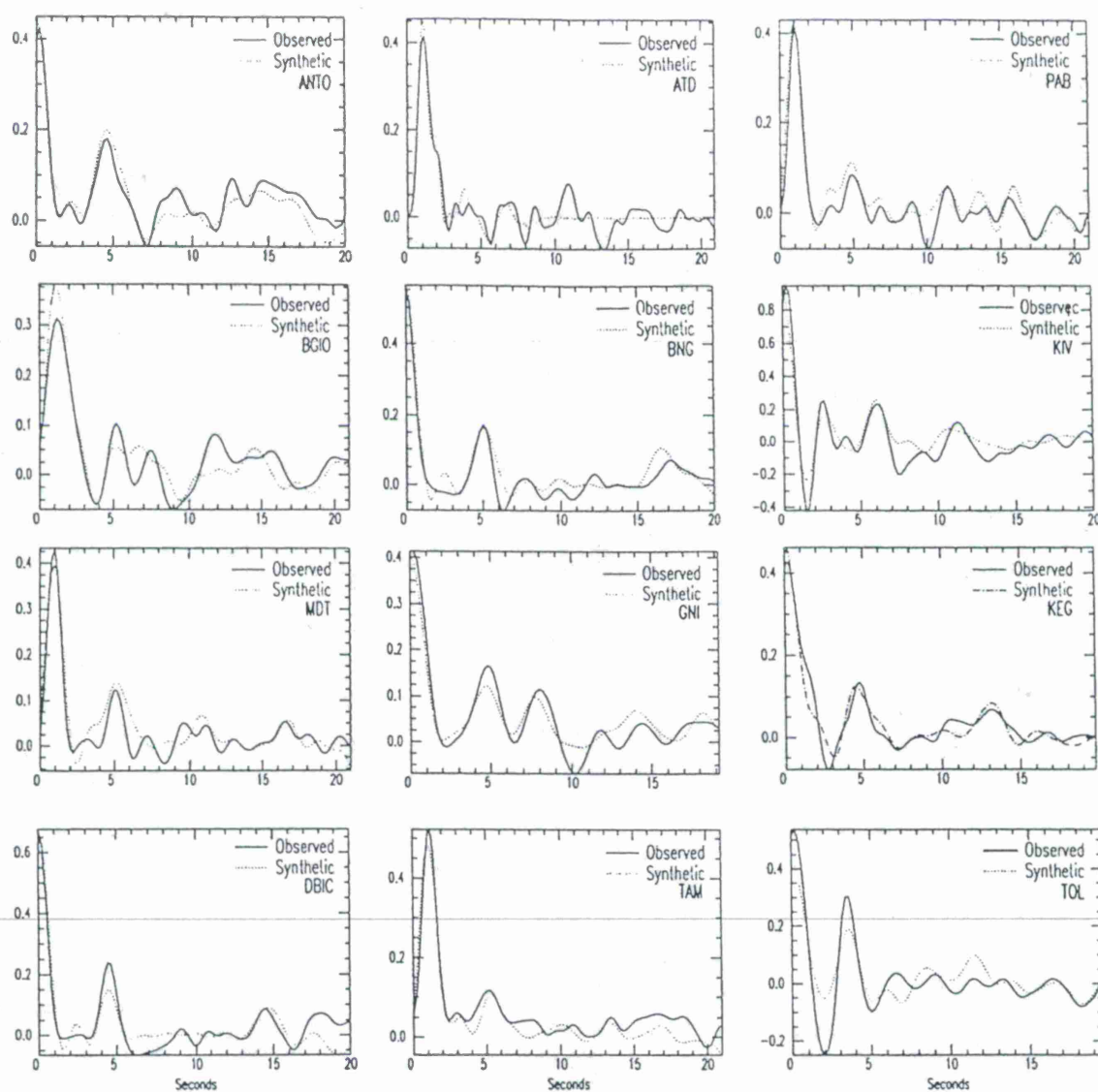


Figure 3. Observed and synthetic receiver function waveforms for all twelve stations that we have used in our study of the North Africa and Middle East. Station TOL and BGIO represent our worst fits. Station TOL has a large amount of noise in the data and station BGIO has a very complex receiver function which is not easily fit with a 5 layer model.

function stacks up to 100 times and then reinvert each of these jackknifed stacks. The subsequent distribution of model parameters can be used to determine the errors for each of the model parameters. This technique effectively tests the stability of our waveform inversion. We have also used the minimum number of layers that we qualitatively need to match the observed receiver function waveforms. In most cases we only use 2 or three layers while obtaining a reasonably good fit. By using only longer period receiver functions (~2

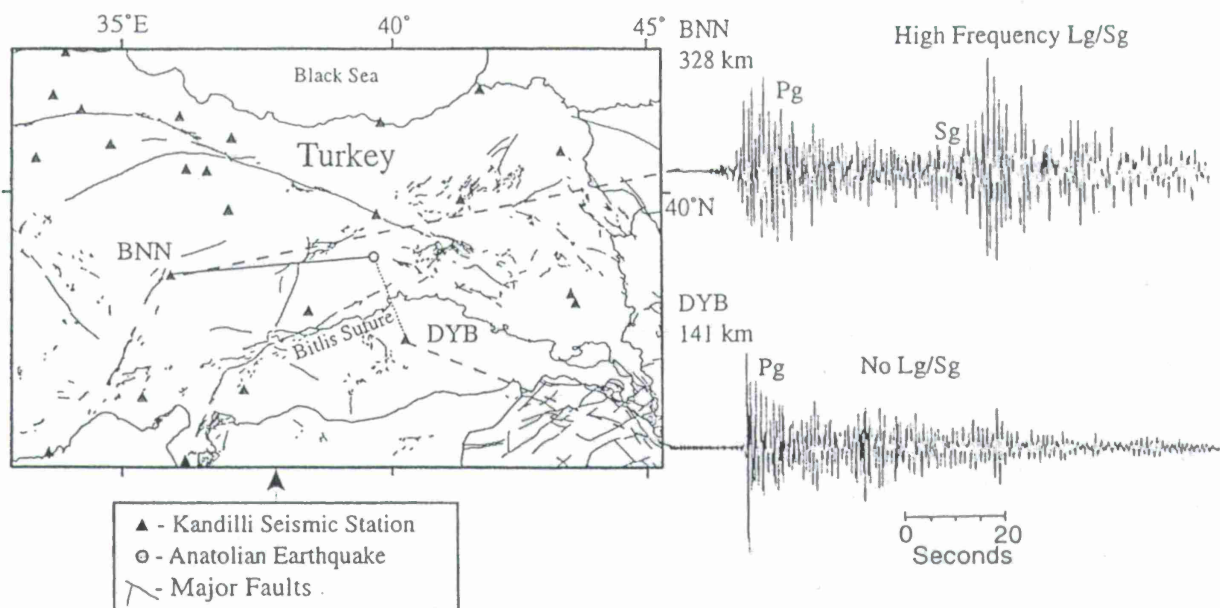


Figure 4. An example of Lg blockage across the Bitlis suture. We have used vertical component short period seismic stations in Turkey and Syria to map detailed Lg propagation efficiencies in the Middle East. These data are taken from the Kandilli Observatory stations in Turkey.

to 3 seconds) and only a few layers we have resolved the first order discontinuities within the crust.

Crustal thickness in North and Central Africa is found to be generally on the order of 30 to 41 km (Figure 1) while in the Middle East we have found a wide variety of crustal thickness values. At station ATD we have found a crustal thickness of only 8 km which is consistent with this region being on oceanic crust or young thinned continental crust. At station GNI we have found the thickest crust of over 60 km. Our results agree with available seismic refraction profile data. At station KIV in the Greater Caucasus, there is evidence of a pronounced mid-crustal low velocity zone which may be the result of having high velocity Paleozoic rocks being thrust over lower velocity Mesozoic strata.

Regional Wave Propagation in the Middle East

Collaboration with colleagues in Turkey and Syria have provided a large amount of waveform data from local networks in these two countries. These stations primarily consist of short period, vertical component seismometers. We are using these data to characterize the propagation efficiencies of the regional phases Pn, Sn, and Lg. This work should provide much more accurate maps of the zones of poor propagation. Seismic events from the Aegean sea, Zagros Mountains, Red Sea, and Caucasus Mountains have provided us excel-

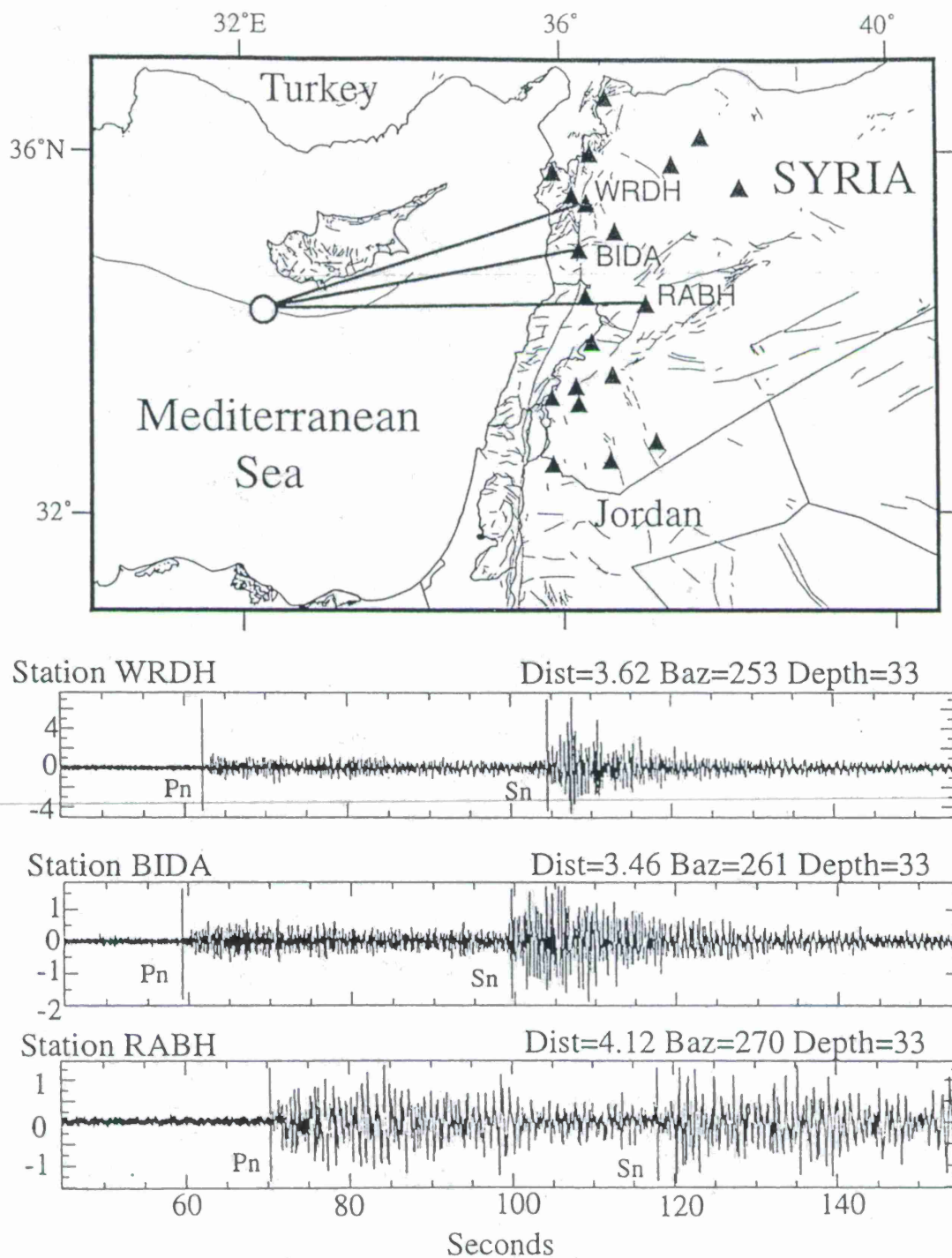


Figure 5. An example of Sn attenuation across the northern Dead Sea fault zone in northwest Syria. We have observed a number of other seismograms which strongly indicate that the upper mantle beneath the northern Dead Sea fault is attenuating and in some cases eliminating Sn. Note the change in relative amplitude between Pn and Sn phases.

lent azimuthal coverage for investigating the nature of regional wave propagation in the Middle East.

We have found regions within the Middle East that attenuate Lg in Turkey and Sn in Lebanon and northern Syria. The Bitlis suture in eastern Turkey appears to block Lg/Sg phases. Within the Anatolian Plateau we have also seen that Lg tends to propagate less efficiently over distances of greater than 500 km. In Lebanon and northwest Syria, there is strong evidence of Sn being highly attenuated. We have observed that Sn becomes attenuated and in some case completely eliminated when propagating through a region of the upper mantle beneath the northern Dead Sea fault (Figure 5). Our azimuthal control is quite good due to the large number of Syrian stations as well as Mediterranean earthquakes. Observations of low Pn velocity combined with our observations of inefficient Sn propagation indicate that the upper mantle in this region is hot.

Discrimination of Chemical Explosions in Morocco

In order to examine the limitations in the techniques for discriminating between chemical explosions and earthquakes at local and regional distances, we have applied several standard heuristics to seismic events in northwest Morocco where little *a priori* information was available. Only short period seismic stations with 1 Hz geophones that recorded both earthquakes and explosions in proportionate numbers were included in the analysis in order to account for stations effects and thus to allow direct comparisons between events. Recordings with under a 2:1 RMS signal to noise ratio were eliminated from the population. These criteria eliminated all but high quality seismograms from 8 Oud Zem phosphate mine explosions and 6 earthquakes that occurred in northwest Morocco (Figure 6). The explosions used have similar geographic locations, total charge magnitudes, and presumably ripple fired mechanisms, and yet the seismic recordings are still characterized by a surprising amount of diversity.

Time and path independent modulations, owing to the periodic source mechanisms of the ripple fire explosions, rarely unequivocally distinguish the explosions from the earthquakes in the region. Our findings imply that more often than the current literature suggests, source inconsistencies have a role in the failure of common discriminants. Furthermore, crustal seismic velocity and the attenuation structure seemed to shape the seismic signals more than the nature of the source mechanism. The 10-15 Hz Pg/Sg ratio test proved to be the most accurate discriminant, while the often-used 6-8 Hz Pg/Sg proved to be the least accurate test.

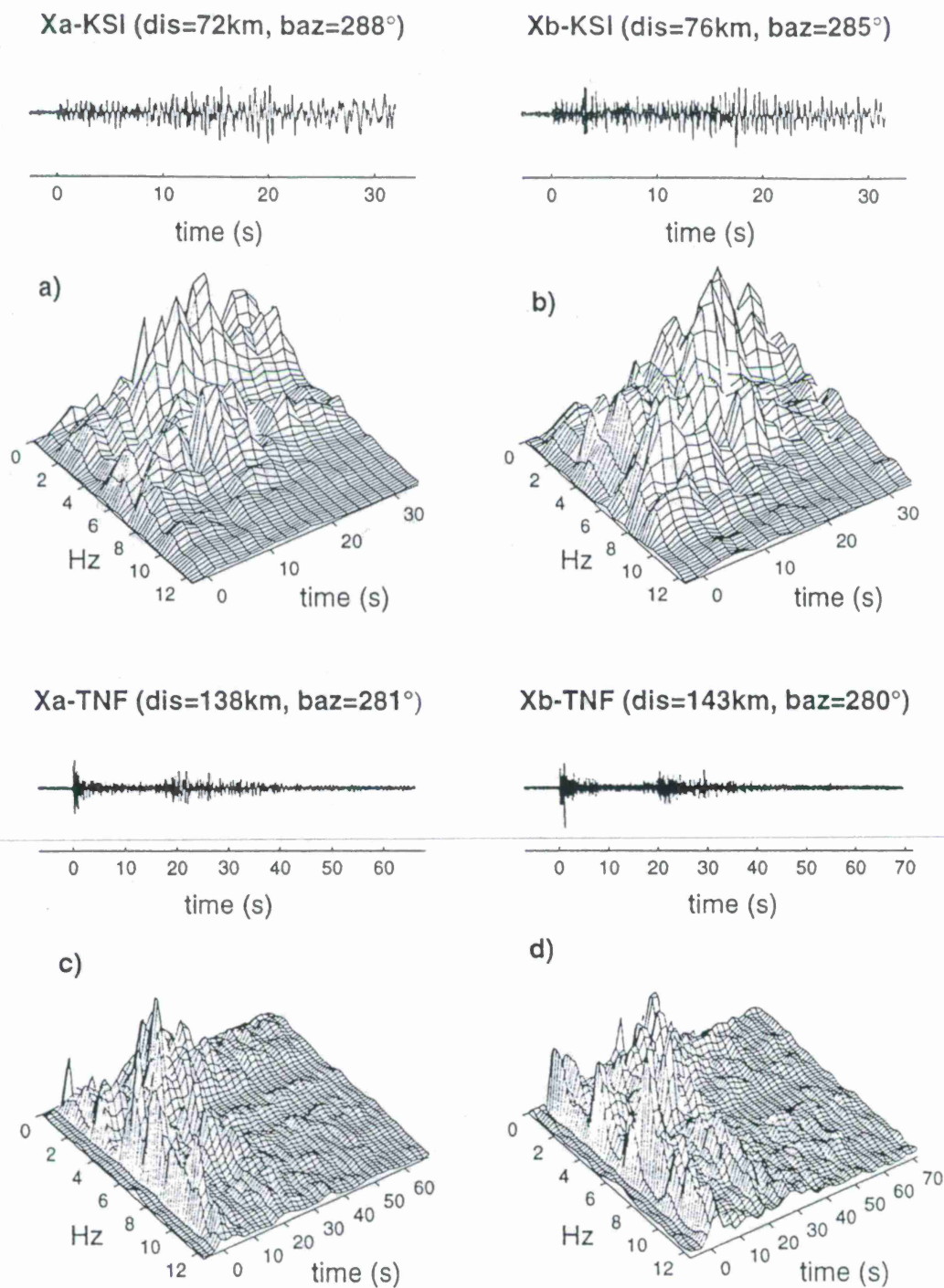


Figure 6. Examples of Mine explosions recorded by short period seismic stations of the Moroccan National Seismic Network. These seismograms and spectrograms show the complexity of the seismic waveforms in Morocco. Note the lack of banding in the explosion spectrograms.

CONCLUSIONS AND RECOMMENDATIONS

New geophysical/seismological information for the Middle East and North Africa region are an essential element in any attempt to monitor and discriminate small seismic events in the region. These critical observations will provide important information on the regional propagation efficiencies. Combining our new knowledge of the earth structure as well as detailed information on regional phase behavior will give us new and critical insight into understanding how regional seismic waves propagate and how sensitive they are to small scale earth structure.

New data are required to constrain advanced theoretical and modeling efforts in order to better calibrate the Middle East and North Africa region. It is essential that we continue to collect and improve upon our knowledge of the earth structure if we are to effectively monitor and discriminate small seismic events. This will be an iterative process as the earth is an extremely complex media and cannot be described with overly simplistic models.

DATABASE DEVELOPMENT FOR THE MIDDLE EAST AND NORTH AFRICA REGION

Dogan Seber, David Steer, Eric Sandvol, Marisa Vallvé, Christine Orgren, and
Muawia Barazangi

Institute for the Study of the Continents, Cornell University, Ithaca, New York 14853
(e-mail: seber@geology.cornell.edu)

Sponsored by U.S. Department of Energy
Office of Nonproliferation and National Security
Office of Research and Development
Contract No. F19628-95-C-0092

ABSTRACT

With the signing of the Comprehensive Test Ban Treaty (CTBT) document drafted at the Conference on Disarmament (CD) by most governments at the UN, we need to focus our attention on the operational aspects of global monitoring. Our objective is to collect and organize all available seismological, geophysical, and geological data sets for the Middle East and North Africa into a comprehensive Geographic Information System (GIS). We are distributing the organized databases in ArcInfo GIS format and menu driven access tools and with a specially designed World Wide Web (WWW) server. Among the already collected digital data sets are detailed Moho and basement maps for the Middle East region, seismicity catalogs, focal mechanisms, and tectonic maps, mine locations, and various types of geophysics/geologic/geographic data. We have also been developing metadata to document the resolution and accuracy of the already organized data sets. The developed organized system will help CTBT researchers and decision makers to reach a conclusion in a very short time, including analyses of special (suspect) events and On Site Inspection efforts. Our World Wide address for data distribution is <http://atlas.geo.cornell.edu>

Keywords: Middle East and North Africa, GIS, CTBT, Regional geology and geophysics, www.

OBJECTIVE

Concentrated efforts toward a global Comprehensive Test Ban Treaty that will ban all nuclear explosions on earth are currently underway. Effective monitoring for such a treaty is essential if all nations are to adhere to its stated articles, conditions, and guidelines. For the past few decades, emphasis has been placed on using seismological observations and techniques to monitor a limited test ban, especially to assist in the precise calibration of explosive yields at a few specific sites. The new development of multilateral zero yield treaties will require developing credible strategies for effective monitoring, including the ability to detect, characterize, calibrate, discriminate, and verify any suspect event for any region on earth. Recently, other technologies, such as radionuclide, infrasound and hydroacoustic monitoring systems, are increasingly being used and integrated with seismic monitoring system to more accurately and comprehensively monitor this agreed upon treaty.

As these varied technologies progress and the size of discrimination thresholds get smaller (< 1 kiloton), it becomes apparent that other geophysical, geological, and satellite imagery data sets, in automated digital form, could significantly contribute to the overall monitoring objectives. Specifically, this "auxiliary" information can make it possible to better characterize and calibrate recorded events in a given region by providing accurate observations that are pertinent to the region under investigation. Examples of such critical observations are crustal velocities and densities, locations and depths of sedimentary basins, locations of active faults and well located earthquake locations. In addition, new data, both seismological/geophysical and geological, are required to constrain advanced theoretical modeling efforts in order to better understand the propagation of high-frequency seismic waves produced by very low yield events at regional distances. For these monitoring efforts to be successful, researchers must be able to detect, characterize, calibrate, discriminate, and verify any suspect event for most regions on earth. As important to the success of any monitoring strategy, such data must be swiftly accessible to researchers via computer networks in order to integrate with real-time recorded events to provide ground-truth for timely verification.

Our objective is to collect and organize all available seismological, geophysical, topographical, and geological data sets for any region on earth to form a digital information system that is accessible via the INTERNET from Cornell. In cases where there are recent, unstudied data that can be used to constrain some of the existing information and/or provide new information, we use these data to obtain more accurate results and include them in our databases as new information. It is important that our digital, network-accessible information system is complete, comprehensive, multidisciplinary, unified, easy to update, and of

direct relevance to monitor the CTBT .

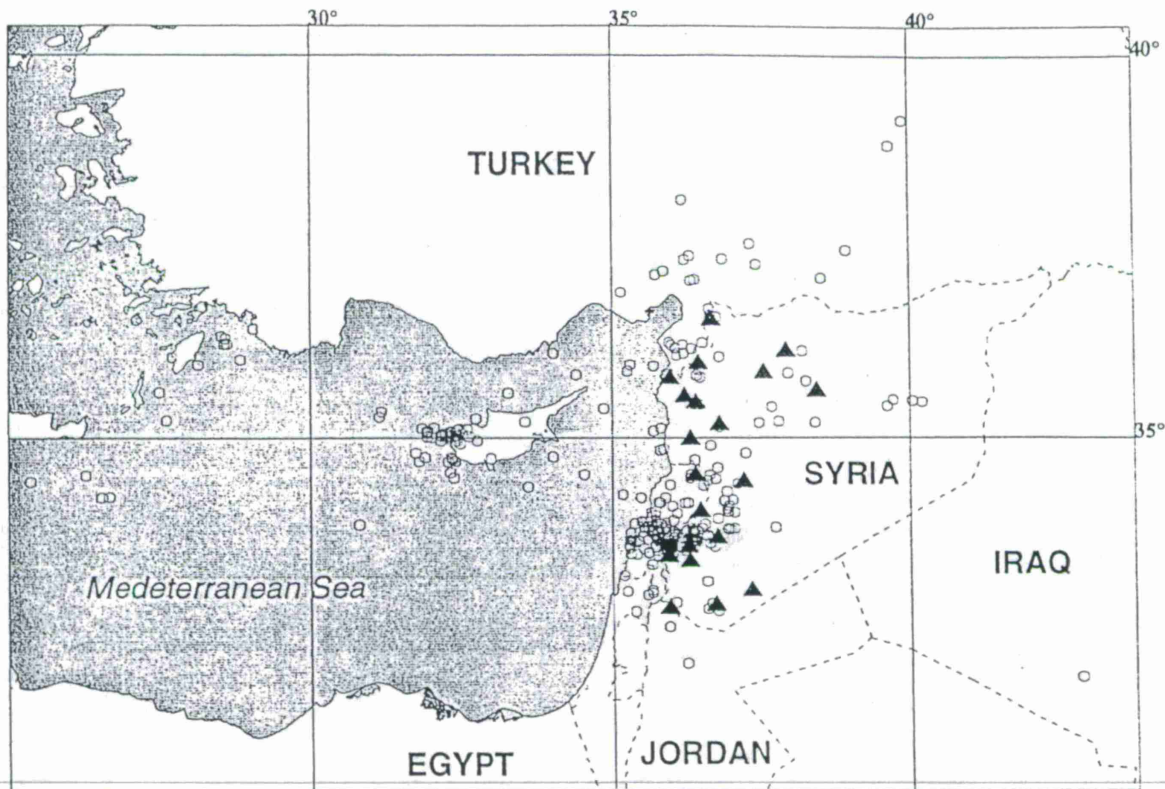


Figure 1. Example of results from one of the local seismic networks in the Middle East (Syria). Seismic station locations (solid triangles) and earthquake locations (open circles) are from the Syrian National Seismic Network Bulletin (1994-1995).

RESEARCH ACCOMPLISHED

Databases and computerized data access tools

We continuously add more information into our database in order to construct a complete crustal structure database as well as other types of geophysical and geological databases. The database system is divided into four different categories: Geographic, geologic, geophysical, and imagery. In this report, we present some of the available data and access tools that we have recently developed. The entire database system is developed on an ArcInfo Geographic Information System (GIS). All data are kept in ArcInfo format and

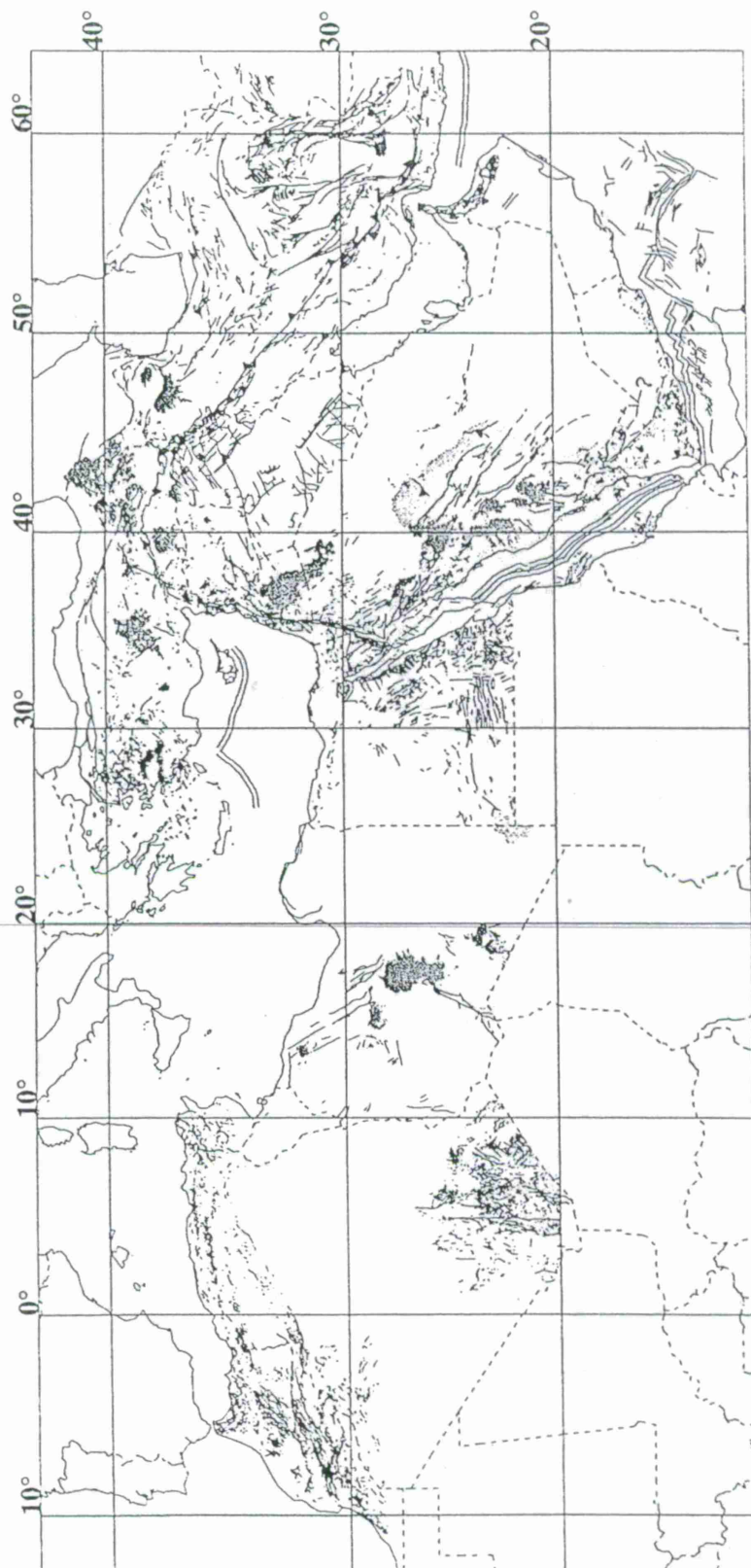


Figure 2. Digitized tectonic map of the Middle East and North Africa region. Solid lines represent faults locations, lighter shades on land areas are basement outcrops, and darker shades on land areas represent young volcanics in the region.

can be accessed through custom designed, menu-driven access tools. The entire system is self sufficient and requires no prior knowledge of ArcInfo software commands. A user can search, study, manipulate, download and make prints or slides of any part of this database using this menu-driven system. One of the biggest advantages of this newly developed system is that all the data are available on one computer and the user can select and display any parts of the various databases within a few seconds. Multiple layers of data can be displayed in the same graphic window allowing the user to comprehend the study area in its entirety.

Examples of developed databases

Local earthquake bulletins

In a year there are tens of thousands of earthquakes located throughout the globe. The number of recorded earthquakes would be increased if we were able to detect all events down to about magnitude 3.5 globally. The accuracy of these locations and their depths are also critical. It is well known that most of the events are located along major plate boundaries. However, there are numerous earthquakes located in the interior of plates such as central Asia and the Middle East. In order to obtain accurate locations we are including in our databases seismic bulletins from local government networks (Figure 1). These kinds of data can be used for studying previous small seismic events. This becomes particularly important in a situation where a "suspicious" event is located in a region. These data sets provide means of quickly obtaining information concerning the extent, depth, and exact mechanism of historical seismicity for any given region. Researchers will also be able to use these data in their studies, such as looking at velocity distribution and depth estimation of these events and their accuracies. This type of information will be critically important for decision makers who may have to issue alerts or request on-site inspections under the auspices of the CTBT.

Tectonic map of the Middle East and North Africa

Figure 2 shows fault distribution, young volcanism, and basement outcrops extracted from a recently developed tectonic map of the Middle East and North Africa region. Using this tectonic map, faults (or any other features in the map) can be used in conjunction with earthquake locations, or it is possible to study the location of a suspicious event and its

correlation with the surrounding tectonic units. The advantage of this system is that it allows a user to interactively select any item from the map and study its attributes. For example, a user can click on a fault for which attribute information is available and obtain information about style of deformation along the fault or whether or not it is active.

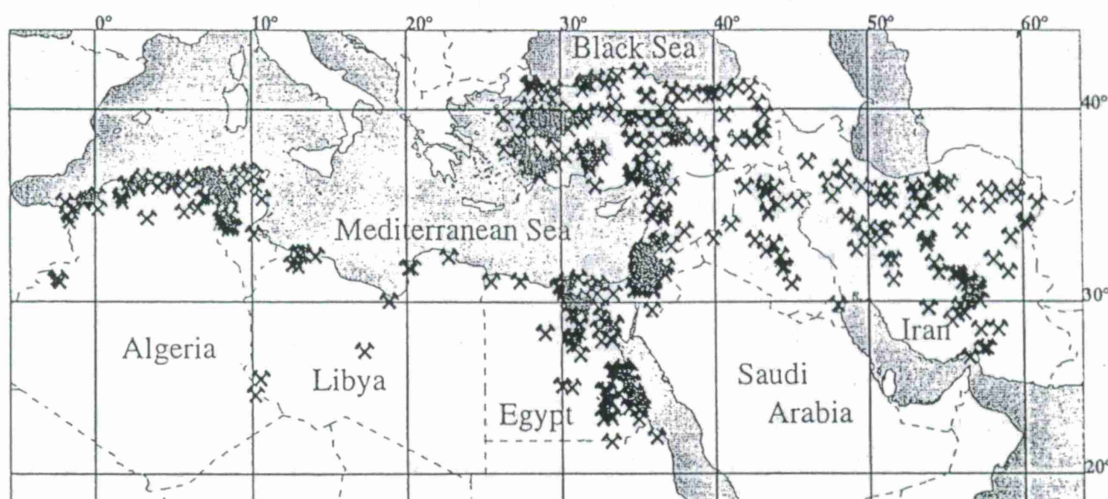


Figure 3. Producing mine locations in the Middle East and North Africa region.

Mine locations

With the collaboration of the Lawrence Livermore National Laboratory we developed a database of mine location sites for some countries (see Figure 3) in the Middle East and North Africa. This information is critical for CTBT monitoring, as many of these mines use large chemical explosions on a regular basis. In a hypothetical situation where a country might detonate a small nuclear explosion these mines sites are potential sites as there are always large explosion conducted near them. In our databases we not only recorded locations of these mines, but also their style of operation, the commodity that is mined, and whether or not these mines are active in the present time.

Additional data sets and Metadata information

There are many other data sets that are already developed and ready to be used in our database systems, including topography, basement and Moho depths, satellite imagery,

Pn velocity, seismic waveform propagation quality factors, gravity data, focal mechanisms of seismic events, geographic information such as country borders, coast lines, rivers, lakes, roads, etc. These data sets are an essential part of CTBT monitoring efforts and allow decision makers to be alert in cases there are any suspect events near mine sites.

We are also working with Sandia National Laboratories in constructing a uniform Metadata about all the data sets entered in our GIS system. Several of our databases now include standardized Metadata information. Our plan is to finalize this task within the next few months.

Access to Cornell databases

Considering that the software we are using is not freely available to research groups and decision makers, we are also developing an ArcInfo - WWW interface to access our developed databases. Our current web server has already been accessed several thousand times by hundres of researchers throughout the world. Our WWW address is "<http://atlas.geo.cornell.edu>"

Access to ArcInfo databases is provided through specially designed programs. We are striving to keep the architecture in the Web pages as close to those in ArcInfo system as possible. Although it is not possible to give as much flexibility in data manipulation, 80-90% of the menu driven system's functionality will be accomplished under this WWW system (see Figure 4).

CONCLUSIONS AND RECOMMENDATIONS

Our expanding digital geological and geophysical information system will be an essential tool in the implementation of the CTBT and nonproliferation monitoring. These databases provide important ancillary information on the structure of the crust and upper mantle that may affect the propagation of seismic phases at regional distances. In turn, this bears on the detection, discrimination, calibration, on-site inspection, and yield estimation of nuclear explosions and other suspect events.

We recommend that to monitor the multilateral comprehensive nuclear test ban and nonproliferation treaties, comprehensive digital databases be made available and accessible

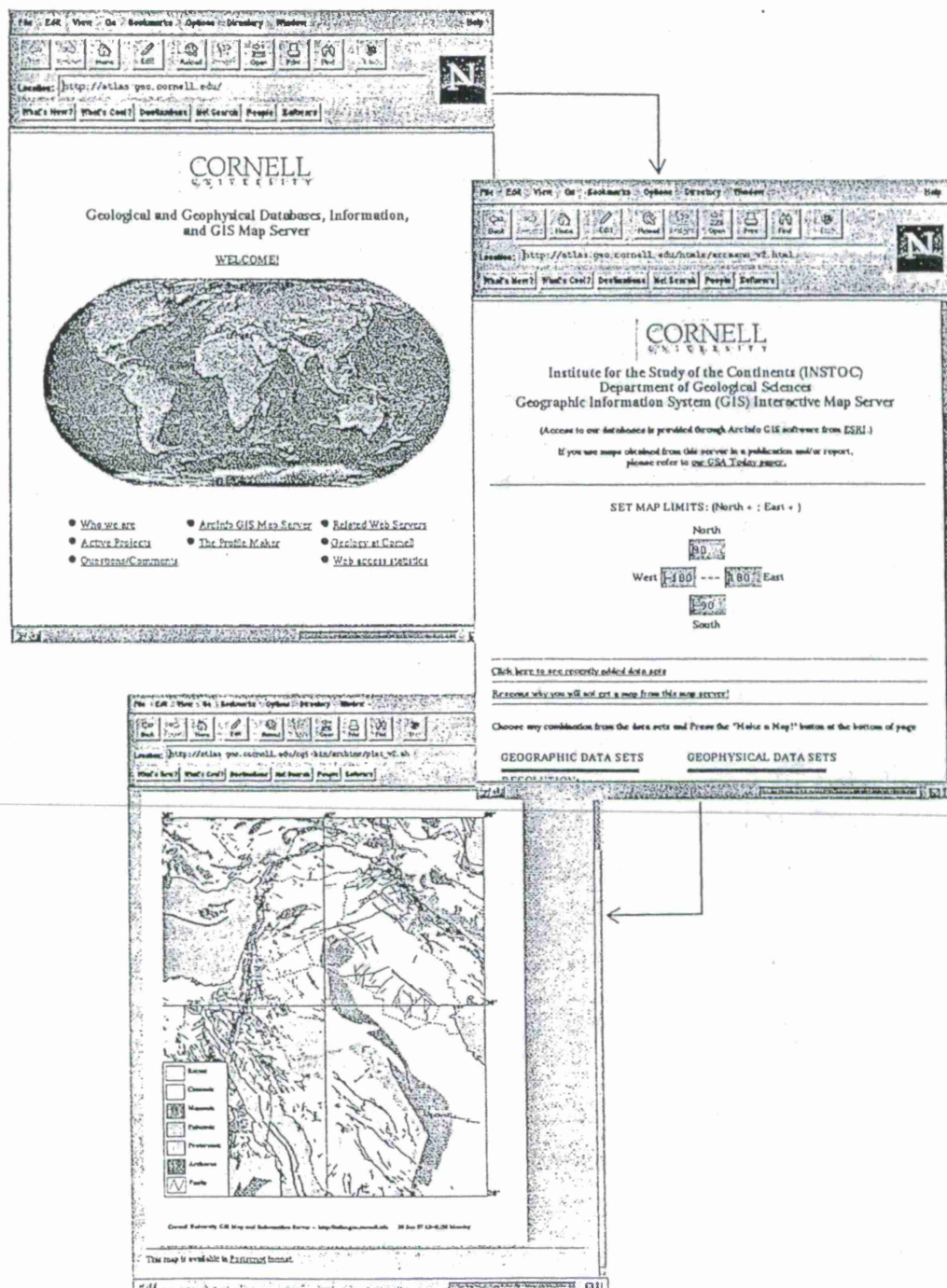


Figure 4. Sample pages from our WWW server showing how to generate a custom designed map. We are continuously updating and adding new data sets in this Web server.

in local computers of decision makers, and similar information be made available over the INTERNET for use by researchers. New data, both seismological/geophysical and geological, are required to constrain advanced theoretical and modeling efforts in order to better understand the propagation of seismic waves produced by very low magnitude events at regional distances. For these monitoring efforts to be successful, researchers must be able to detect, characterize, calibrate, discriminate, and verify any suspect event for most regions on earth. As important to the success of any monitoring strategy, such data must be swiftly accessible in digital form to researchers via networks in order to integrate with real-time recorded events to provide ground-truth for fast verification purposes.

THE DATA DICTIONARY: A VIEW INTO THE CTBT KNOWLEDGE BASE

Ellen R. Shepherd, Ralph G. Keyser, Hillary M. Armstrong, Eric P. Chael,
Christopher J. Young
Sandia National Laboratories

Sponsored by U.S. Department of Energy
Office of Nonproliferation and National Security
Office of Research and Development
Contract No. DE-AC04-94AL85000
Comprehensive Test Ban Treaty Research and Development Program

ABSTRACT

The data dictionary for the Comprehensive Test Ban Treaty (CTBT) knowledge base provides a comprehensive, current catalog of the projected contents of the knowledge base. It is written from a data definition view of the knowledge base and therefore organizes information in a fashion that allows logical storage within the computer. The data dictionary introduces two organization categories of data: the datatype, which is a broad, high-level category of data, and the dataset, which is a specific instance of a datatype. The knowledge base, and thus the data dictionary, consist of a fixed, relatively small number of datatypes, but new datasets are expected to be added on a regular basis.

The data dictionary is a tangible result of the design effort for the knowledge base and is intended to be used by anyone who accesses the knowledge base for any purpose, such as populating the knowledge base with data, or accessing the data for use with automatic data processing (ADP) routines, or browsing through the data for verification purposes. For these two reasons, it is important to discuss the development of the data dictionary as well as to describe its contents to better understand its usefulness; that is the purpose of this paper.

Keywords: knowledge base, data dictionary, datatype, dataset

Sandia is a multiprogram laboratory operated by Sandia Corporation, a Lockheed Martin Company, for the United States Department of Energy.

OBJECTIVES

In support of the Comprehensive Test Ban Treaty Research and Development (CTBT R&D) program, the United States Department of Energy (DOE) is developing a CTBT knowledge base that includes both the content and the framework for storing that content. The knowledge base is intended to improve the ability of the U.S. monitoring community to process and analyze sensor data in support of monitoring the CTBT. All phases of data processing, from automated processing through interactive evaluation of events, are expected to benefit from information contained in the knowledge base.

The data dictionary is a tangible result of the design effort for the CTBT knowledge base and is intended to be used by anyone who accesses the knowledge base for any purpose, such as populating the knowledge base with data, or accessing the data for use with automatic data processing (ADP) routines, or browsing through the data for verification purposes. It is a catalog that describes the data, its use and location, and how to access it for use in the CTBT monitoring efforts.

INTRODUCTION

The design effort for the contents of the CTBT knowledge base project has concentrated over the past year on identifying users of the knowledge base, understanding the framework for its intended use, and characterizing the constituent data components. It quickly became obvious that the volume of data to be stored in the knowledge base is enormous, so one focus of the design efforts became an issue of prioritizing which data to include initially. In addition to the sheer volume of data within the knowledge base, we also identified a large number of formats of data components such as waveforms, gridded information, CSS databases, tessellation grids, tables, and formulas. In this paper, we will summarize the development process and the resulting data dictionary that describes the design of the contents of the knowledge base.

The purpose of the knowledge base is to provide a single, comprehensive source of data required for analysis in support of the CTBT monitoring effort. The analyses may be performed via automated data processing routines such as DFX (signal detection) or GA (event association), or the analyses may be performed interactively by an analyst. Probably one of the most significant contributions of the knowledge base to the CTBT monitoring efforts is the fact that having a single, comprehensive source of data facilitates reproducibility and traceability of analysis results. Another important benefit of the knowledge base is that it is easier to maintain correctness and currency because the data shares a common indexing methodology.

DEVELOPMENT OF DATA DICTIONARY

The data dictionary was produced to reflect the design of the knowledge base; it is intended to make the knowledge base accessible to all users. To better understand the usefulness of the data dictionary, it is necessary to summarize the development of the knowledge base to date, which is accomplished in this section.

Over the past year, we have performed the following tasks with the goal of developing the contents of the CTBT knowledge base:

- *Identified users.* Users consist of anyone who accesses the knowledge base for any purpose, such as populating the knowledge base with data, or accessing the data for use with ADP routines, or browsing through the data for verification purposes. Users may be high level managers, evaluators, analysts, researchers, code developers, for example. Users were asked for input for knowledge base requirements.
- *Identified and characterized automated and interactive applications.* The interface and data requirements were identified, such as those requiring iterative queries or "fast" response time. Some applications are already well defined, while others comprise future functionality. For each application we identified specific data requirements and categories.
- *Identified sources of existing and potential research data.* These include other national laboratories, universities, and commercial sources.
- *Identified relevant metadata for each type of data.* Metadata is data about data, such as date of collection, sensors used, who collected the data, and what type of processing the data underwent. We looked to the Federal Geographic Data Committee (FGDC) for its standard that Federal agencies are instructed to use to document new geospatial data, and ensured that all datasets adhere to this standard. The data dictionary has more details on the FGDC standard and how it applies to the knowledge base contents.

While gathering data requirements for the content of the knowledge base, we also developed requirements and characteristics for the functionality of the knowledge base. These considerations helped focus the design and implementation of the knowledge base.

For example, the main activity of the knowledge base will be data retrievals, with updates being performed relatively infrequently. This influences the selection and implementation of database technology because it puts a higher emphasis on accuracy and speed of retrieval, and less emphasis on database management activities associated with transaction processing such as mirroring and transaction logging. Additionally, we imposed the requirement that the knowledge base had to accommodate different formats of datasets provided by researchers, so that the knowledge base did not introduce artificial methods of collecting data. This requirement also influenced the selection of the underlying database design and management scheme. Further, we ensured compliance with the FGDC metadata standard to facilitate data exchange with geospatial and government entities. It is readily apparent that the size of the metadata alone can match or easily exceed the size of the data itself, therefore, we had to ensure that the database management system could accommodate the volume of metadata.

In addition to the requirements we imposed on the knowledge base, we solicited analysts and other users for requirements for future analytic capability. It quickly became obvious that the volume of data to be stored in the knowledge base combined with all desired functionality is enormous, so then the focus of the design efforts became an issue of prioritizing which data and functions to include initially. We decided to support existing analysis capabilities (data and system interfaces) while planning for future capability.

After identifying all types of data--existing, anticipated, and metadata--we began to look at numerous, various methods of organizing the data for representation in the knowledge base.

Many factors were taken into account in determining an optimal representation such as anticipation of future data types; inclusion of all data types; intuitive appeal to domain experts; exploit-

ing underlying similarities in data across sensor technologies; and independence of database management system implementation.

Many representations were considered:

- traditional relational database schemas
- object oriented representations
- sensor domain representations such as points, stations, and paths
- organization by monitoring technology (for example, all data associated with seismic monitoring or with hydroacoustic monitoring)
- organization by analysis capability (for example, all data associated with event interpretation or all data associated with signal propagation).

Each of these was rejected for various reasons, either because they failed to encompass all types of data, or worse, they failed to take advantage of similarities in the data.

Finally, we derived a representation that organizes information in a fashion that allows logical storage within the computer. We developed two organization categories of data: the datatype and the dataset. The datatype is a broad, high-level category of data, and the dataset is a specific instance of a datatype. The datatype and dataset concepts are described in more detail in the following section, "Contents of the Data Dictionary." The advantage of this representation is that there is a fixed, relatively small number of datatypes, with a potentially large number of *instances* of the datatypes known as datasets. Eventually the bulk of the knowledge base, and thus the data dictionary, will be dataset definitions as new datasets are added.

The concept of datatypes and datasets facilitates development of datasets because the detailed list of defined datatypes provides a common framework for documenting datasets. The defined *datatypes* are of primary interest to *developers* of datasets because of this framework. The *dataset* definitions are of primary interest to *users* of the datasets because the definitions document the contents of the individual datasets, such as how the data was collected and how it should be used.

In addition to developing the design and the structure of the knowledge base, we evaluated and selected database management technology with which to implement the knowledge base:

- Researched underlying database technologies, evaluating for capability to handle multiple data types and custom data types; scalability; speed of retrieval; compatibility with existing platforms; data sets and applications; and technical support.
- Acquired supporting database management technologies and training. Primarily this is the Spatial Database Engine (SDE) technology combined with Oracle Database Management System.

The data dictionary represents the result of all these development stages. Most of these development details are not included explicitly in the data dictionary, but are expounded here to show the stages in designing the knowledge base and thus the data dictionary.

CONTENTS OF THE DATA DICTIONARY

As a catalog, the purpose of the data dictionary is to describe the contents of the knowledge base in context of CTBT monitoring applications and to provide a guide to the location and use of the data. The contents of the knowledge base are represented by datatypes, which are a broad, high-level category of data, and by dataset, which is a specific instance of a datatype. Therefore the data dictionary defines each datatype and then defines specific datasets.

The knowledge base, and thus the data dictionary, consist of a fixed, relatively small number of datatypes. The defined datatypes encompass all existing and foreseen data requirements, and provide the framework for developing and documenting datasets. Datatype definitions are of interest primarily to the developers of datasets because the definitions provide structure for the datasets.

As the knowledge base is populated with new datasets, the data dictionary will become thick with dataset definitions. The dataset definitions are of primary interest to users since the definitions describe the details particular to the dataset such as methods of collection, units of measure, geographical range, and restrictions on usage.

The data types for the knowledge base are defined from the computer's view to take advantage of the similarities in data types across all sensor technologies, and to remove dependencies on automated data processing functionality. An overview of the constituent data types is shown below. Brief descriptions of each data type follow; please see the data dictionary for more details and examples.

Knowledge Base Datatypes

- 1.0 CSS Information
 - 1.1 Reference Events
 - 1.2 Network and Station Information
- 2.0 Calibration Information
 - 2.1 Referenced by Lat, Lon, and Station
 - 2.1.1 Referenced by Lat, Lon, Station, and Phase
 - 2.1.1.1 Basic Grid Information
 - 2.1.1.2 Augmented Grid Information
- 3.0 Contextual Information
 - 3.1 Discrete features
 - 3.1.1 Basic Grid Information
 - 3.1.2 Augmented Grid Information
 - 3.2 Linear features
 - 3.2.1 Basic information for linear features
 - 3.2.2 Augmented information for linear features
 - 3.3 Area features
 - 3.3.1 Basic information for area features
 - 3.3.2 Augmented information for area features
- 4.0 Supporting Datatypes
 - 4.1 Tabular
 - 4.2 Formula (subroutines, algorithms)

CSS Information stands for Center for Seismic Studies Information and is a reference to the CSS 3.0 Database Schema. The CSS schema is widely used within the US monitoring community for operational databases, so there are numerous software applications that understand the CSS schema and can take advantage of data stored in that format. The CSS schema is also likely to be one of the accepted formats for the international CTBT community as well. This schema has been designed for storing event information including the associated arrivals, measurements, and station information. Because of its wide acceptance, common use, and suitability, it was chosen as the storage schema for event information in the knowledge base.

Reference Events are a linked collection of information containing as much detail as needed about a particular event. They are typically well characterized, well-located events of a particular type in an area. Metadata should include the expected use for these events, any known limitations on how they should be applied, and information about the collection and processing (also known as its "lineage") of the event data.

Network and Station Information describes the sensor stations, and provides long-term average information about the station performance and its background noise environment. This is historic or average information as opposed to current or real-time information since the knowledge base is not expected to handle rapidly changing information like the operational database.

Calibration Information has also been called correction data or gridded parameter data. It contains items such as the regional seismic travel-time corrections, hydroacoustic travel times, and other path dependent information. The datatypes defined in this area are largely intended to directly support automated processing applications such as EVLOC, magnitude calculations, etc.

Some of the datatype definitions will refer to **Gridded Information**. This is information associated with points on a grid corresponding to points on the earth, identified by latitude and longitude. The grid may be regular or irregular, depending on the method of collection or generation of data. For intermediate values in the grid, interpolation may be performed, if the provider of the dataset indicates this is permissible.

Basic grids are simple in structure, having only one or a few values associated with each point. **Augmented grids** have additional data structures (tables or an image, for example) at each point. The data structure may be referenced by a pointer. Some of the grids may be associated with a given station, and some of the grids may be referenced by station and phase.

Contextual Information is the broadest of the general information categories in the knowledge base. It contains information useful to understanding the larger context around a particular event, so most of the information in this category is intended for use by someone evaluating an event that needs a more in-depth analysis. One might also think of this category of information as "background" material since it includes everything from coastlines and city locations to depth to Moho maps and ocean temperature profiles. Within this category, there are **Discrete Features**, which are linked to a single, discrete latitude and longitude pair; there are **Linear Features** such as rift zones and faults; and there are **Area Features** such as population centers and salt deposits.

Supporting Datatypes are effectively a sub-category of datatypes, but since it could apply to any of the other datatype categories, it made sense to call it out at this level. These are simply "containers" for complex types of data such as multi-dimensional tables or mathematical algorithms. There are two types of Supporting Datatypes: **Tabular** and **Formula**. Tabular datatype is available for use by other data types as a storage mechanism. Data is stored in tables, which may be two- or three-dimensional. The format for each table is specified in an associated dataset definition, also included in the data dictionary. Formula datatype is a supporting data type, available

for reference by other datatypes. These could be executable computer codes or subroutines, interpolated or scripted software, or algorithms with parameters.

Following the datatype definitions in the data dictionary are the dataset definitions. For each dataset definition, there are three sections of information: high level description, conceptual detail, and technical detail. Each section has a specific audience, and provides detail relevant to that audience. For example, the high level description is targeted to users who are not domain experts or do not need implementation detail.

The high level description gives an overview of the dataset and lists points of contact and security information. Then there is a conceptual detail section that details the purpose of the dataset, its time period, lineage (processing steps that the dataset has undergone), and attribute accuracy. Finally, the technical detail section describes data storage description and access information.

There are three types of dataset definitions in the data dictionary: actual, preliminary, and sample. The actual data set definitions describe existing datasets. The preliminary dataset definitions define anticipated datasets; the definition may not yet be complete. A sample dataset is given for the purposes of illustration; the dataset does not really exist and is not anticipated to exist. The heading for each definition will indicate whether it is an actual, preliminary or sample dataset. Datasets that currently exist in the knowledge base are the IASPEI 91 Travel Time Tables and Digital Chart of the World (DCW).

BENEFITS OF THE DATA DICTIONARY

The data dictionary is a single, comprehensive catalog for describing the contents, location, and access methods for the contents of the CTBT knowledge base. It benefits analysts, evaluators, users who browse the knowledge base, developers, researchers who populate the knowledge base with datasets, and high level managers. There are many direct and substantial benefits from using the data dictionary:

- Since it is a single reference for all users, it provides a common framework for all research, development, and user perspectives. This is probably one of the most important benefits.
- The data dictionary helps prioritize research by making it possible to identify areas where more research data is needed.
- The data dictionary is a single source describing the contents of the knowledge base, which will make it easier to maintain currency and historical data.
- It identifies source, currency, and quality of data to aid users in selecting and using datasets.
- It contains a high level description for each datatype and each dataset so that users other than domain experts can understand the contents of the datatype or dataset.
- It describes the format for each datatype and dataset so that developers know what to expect when writing interface software.
- In most cases, the data dictionary does not require specific formats for datasets provided by researchers to avoid introducing artificial methods of collecting data. In the few cases where specific formats are required, such as CSS database formats, these instances and the associated formats are well-documented.

- It defines the requirements for metadata for each datatype and dataset so that (1) researchers will know what to provide when submitting datasets and (2) users will know the source and history of the datasets.
- It has the capability to include hyperlinks to and from browsers to provide direct viewing of the constituent data.

FUTURE DEVELOPMENT OF THE DATA DICTIONARY

Future development of the data dictionary is driven by future development of the knowledge base. As the knowledge base is refined, and as datasets are added to the knowledge base, the data dictionary will be updated to reflect these enhancements.

To help maintain viability of the data dictionary, it will become an on-line document rather than a static paper document that quickly becomes obsolete. This will help ensure currency of the data dictionary and will facilitate accessibility to all users by eliminating the need to generate and distribute paper documents.

As the single, comprehensive source describing the contents of the knowledge base, the data dictionary will be the basis for reference in tools that are being developed for accessing or browsing the knowledge base. This could be accomplished by implementing hypertext links from the browser tool into the data dictionary, so that when browsing the contents of the knowledge base, the user could immediately retrieve the associated description contained in the data dictionary. Similarly, the data dictionary could contain hypertext links to the browser, so that a user can read the data dictionary and immediately jump to viewing the dataset.

CONCLUSIONS AND RECOMMENDATIONS

The data dictionary provides a useful, accessible, and current catalog of the contents of the CTBT knowledge base. It reflects the ongoing refinements and enhancements to the knowledge base. The data dictionary defines basic datatypes that encompass all existing and anticipated data requirements; these datatypes provide the framework for documenting datasets. The data dictionary is in draft form and comments are welcome.

In order for the data dictionary to maintain its objectives for currency and usefulness, two things must happen. First, the authors have the responsibility of updating the data dictionary as new datasets are added and as refinements are made to the knowledge base. Secondly, and equally important, it is imperative that users provide feedback evaluating its usefulness.

REFERENCES

References that may be useful to developers or users of datasets.

Anderson, et al; *CSS Version 3 Database: Schema Reference Manual*, Science Applications International Corporation, September 1990. Describes the schema of the Version 3.0 database standard for data and software at the Center for Seismic Studies. When the phrase "CSS 3.0 format" is used, this is the document that is being implicitly referenced.

Armstrong, H., and Keyser, R.; *ARC/INFO Dataset Delivery Specifications*, memo dated December 10, 1996. Provides a description of what to include with delivery of research reference datasets that are in ARC/INFO coverage format, includes samples.

Hipp, J. et al; *Knowledge Base Interpolation of Path-Dependent Data Using Irregularly Spaced Natural Neighbors*, Sandia National Labs, 1996; published in *Proceedings of the 18th Annual Seismic Research Symposium on Monitoring a CTBT*, 4-6 September 1996 (Editors: Lewkowicz, McPhetres, Reiter), 17 July 1996.

Shepherd, E. R., R. Keyser, H. Armstrong, E. Chael, C. Young (1997). Data Dictionary for CTBT Knowledge Base, Revision 1, DRAFT. Sandia National Labs, April 21, 1997.

References used in developing the contents of the knowledge base.

Devlin, B., *Data Warehouse from Architecture to Implementation*, Addison-Wesley, Reading, Massachusetts, 1997.

Federal Geographic Data Committee (FGDC), "Content Standards for Digital Geospatial Metadata," June 8, 1994. URL's: <http://www.fgdc.gov/>, <http://www.fgdc.gov/Metadata/metadata-home.html>.

HQ-AFTAC, "System Requirements for the NEMS (DRAFT)." 17 June 1996.

US-DOE, "Knowledge Base Product Definition, Phase 0, Revision 8." March 1997.

USNDC, "USNDC Knowledge Base Working List" revision: 21 Jan 97 (date of fax receipt, from Mark Woods [HQ AFTAC/TT] to Hillary Armstrong).

Global Database Development for the International Data Center

David Steer, Dogan Seber, Christine Orgren, Marisa Vallve,
Muawia Barazangi

Institute for the Study of the Continents, Cornell University, Ithaca, New York 14853
e-mail: steer@geology.cornell.edu

Grant # DASG609610002

Sponsored by the Advanced Research Projects Agency (DOD)
for the Nuclear Treaty Programs Office (NTPO)

ABSTRACT

All available geophysical/geological and imagery databases must be fused with data products produced at the International Data Center (IDC) to better calibrate a given region and for improved location, verification, and discrimination between nuclear explosions and other types of similar events as envisioned under the multilateral Comprehensive Test Ban Treaty (CTBT). The effectiveness of the four monitoring technologies (seismic, radionuclide, infrasound, and hydro-acoustic) can be enhanced by merging their results in a common background and frame-of-reference provided by an appropriately scaled, global Geographical Information System (GIS). When implemented, this system, as part of the decision making process, will provide a rapid analysis tool to assist in discrimination of nuclear from nonnuclear events by placing suspect events in spatially registered displays of topography, geology, tectonic zones, faults, historical seismicity, focal mechanisms, cultural landmarks, and Landsat TM imagery. These data are combined with geophysical data such as basement depth, crustal thickness, and seismic wave velocities that are also useful for regional and global seismic wave propagation modeling and regional characterization. Metadata are also included to provide additional information describing the source, accuracy, and reliability of the data. This work provides the IDC an opportunity to use non-seismic technology that is not only of direct relevance to the ongoing efforts in the seismic technology, but that also better integrates the results of the four standard technologies. The final product provided to the IDC will include a menu-driven Arc/Info GIS that is capable of rapidly producing global or regional analyses of any region in the world and that is fully compatible with the IDC's Oracle database. Many of these data are now accessible on the World Wide Web at <http://atlas.geo.cornell.edu>.

Key Words: Geographical Information System, GIS, global, IDC, CTBT

OBJECTIVE

The objective of this work is to create state-of-the-art information and intelligent data access tools to analyze, interpret, visualize, map, graphically manipulate and merge the results of multi-dimensional, multi-technology databases produced both for and by the International Data Center's (IDC) International Monitoring System (IMS) (Figure 1). This system will include a publically available, user-friendly, on-line environment for detailed, rapid analysis of suspect events. Key short term objectives are to expand the capabilities of the IDC to include use of non-seismic databases in an interactive way to serve the objectives of the broader Comprehensive Test Ban Treaty (CTBT) verification readiness efforts. Long term objectives are to facilitate (1) analyses of suspect events and to assist in associating such events to specific geologic structures or man-made facilities, and (2) initiation of on-site inspection efforts, if warranted. Attaining these objectives will assist in the monitoring effort by providing (a) interactive access to global velocity and attenuation characteristics that will improve travel time and wave propagation calibration for any given region, (b) development of crustal and basement thickness and velocities that will assist in accurate relocation of suspect events and, (c) rapid association of anomalous events to specific geographical or geologic features such as known mines, active faults, volcanic centers, topographic fronts, or geologic terrain. The databases merged with this system will also rapidly provide the preliminary geographical, geologic, and cultural background information required to support on-site inspections if necessary.

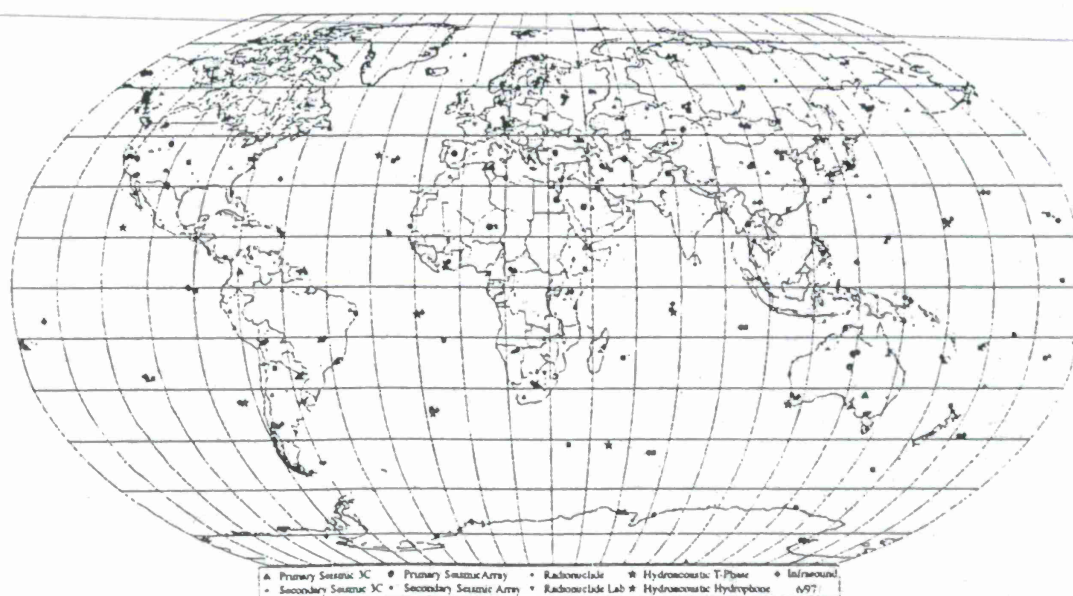


Figure 1. This map shows all the IMS monitoring stations. Annex 1 to the Protocol to the CTBT lists the required network that is comprised of 50 primary and 120 auxiliary seismic stations, 11 hydroacoustic stations, 60 infrasound stations, 80 radionuclide samplers, and 16 radionuclide laboratories.

RESEARCH ACCOMPLISHED

Graphical manipulation of very large, comprehensive Geographical Information System (GIS) databases through an easily manipulated menu-driven interface (Figure 2) will permit National Data Center (NDC) researchers throughout the world to analyze suspect events and to relate them to geologic or man-made structures. The geologic, geophysical, and geographic databases critical to the CTBT monitoring effort must be global, of the highest possible resolution, and also accessible through the World Wide Web.

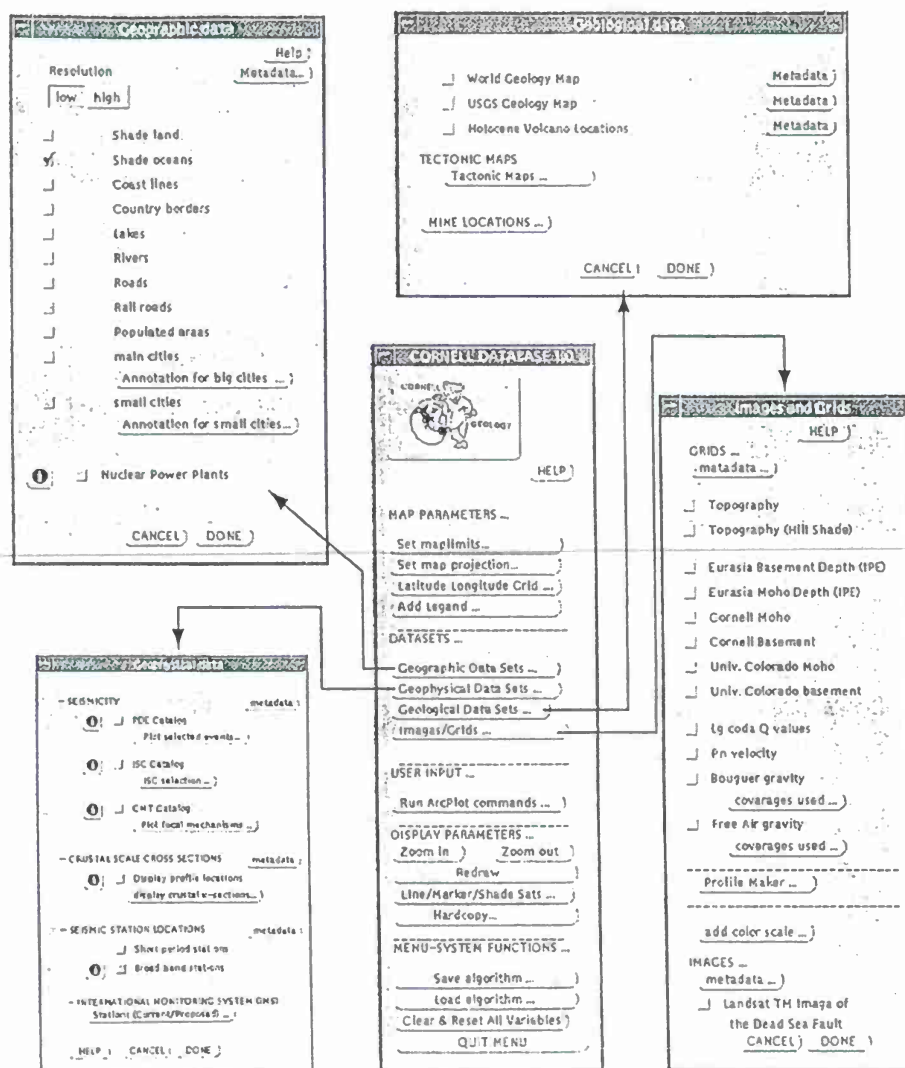


Figure 2. In order to rapidly access all available data for any region in the world, a simple menu-driven GIS is under development for use by analysts and researchers. Pull down menus such as this require little or no GIS experience for effective manipulation of these data.

Examples of critical databases that must be available for CTBT monitoring include digital elevation models (topography and bathymetry), historical and instrumental seismicity, focal mechanisms, volcanic zones, geologic maps with faults, crustal thickness and depth-to-basement, crustal and upper mantle velocities, gravity data, magnetic data, political boundaries, city locations, transportation structure, mine locations, nuclear facility locations, and weather station locations and data. These databases will be integrated with results from the four monitoring technologies at the IDC to assist in the overall monitoring efforts to distinguish possible treaty violations from the more than 25,000 seismic events per year located by the Prototype IDC (Figure 3).

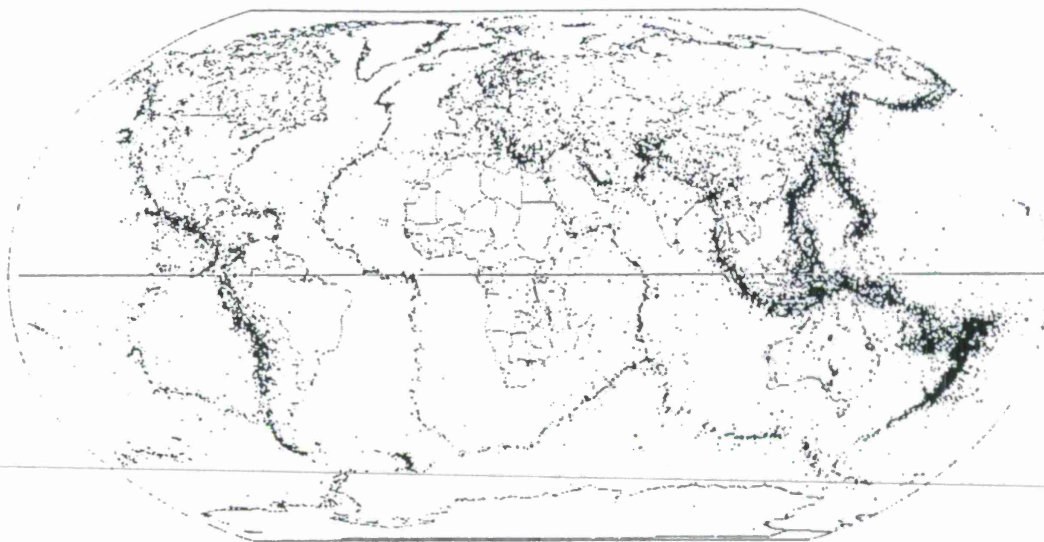


Figure 3. Over 53,500 events were located by the PIDC from January 1995 to June 1997. The GIS system under development will provide critical information required to discriminate seismic events from possible violations of the CTBT.

Accurate global grids of topography, crustal thickness and depth-to-basement, and crustal/upper mantle velocities are useful when analyzing event locations and modeling seismic wave propagation paths. A global digital elevation model with nominal 1 km precision for topography and 3 km for bathymetry has been assembled by merging data from the United States Geological Survey (USGS) 5 minute (10 km) digital elevation model (DEM) ETOPO5 data, USGS and EROS data center 30 arc-second (1 km) GTOPO30 data, and the National Oceanographic and Atmospheric Administration (NOAA) 2 minute (3 km) bathymetry of Smith and Sandwell [1994]. These data are oversampled to retain the 1 km pixel size and combined to form the most precise DEM available for public distribution that is useful for analyzing seismic events (Figure 4).

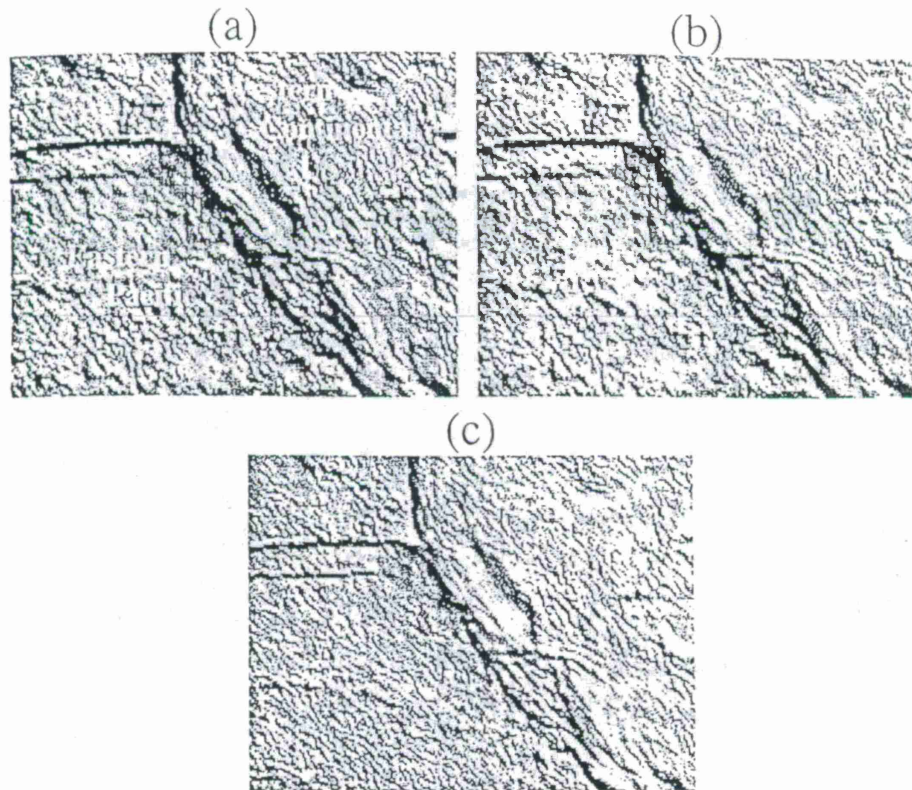


Figure 4. Digital Elevation Models (DEMs) provide essential topographic and bathymetric data that are critical to modeling seismic, hydroacoustic, and infrasound wave propagation paths. These data display the variety of scales available for general use by the CTBT community with data from (a) ETOPO5 data (10 km pixels), (b) ETOPO5 supplemented with GTOPO30 continental data (1 km pixel), and (c) 3 km bathymetric data from Smith and Sandwell[1994]. Note the improvement in resolution of the continental area from 10 km in (a) to 1 km in (b) and the improvement in the oceans from 10 km in (a) to 3 km in (c).

Crustal and basement thickness grids employ the USGS CRUST5.1 data [Mooney and Laske, 1995] supplemented with digitized data for EURASIA [Kunin et al., 1987], Europe [Meissner et al., 1987], the Middle East [Seber et al., 1997], and the United States [Braile et al., 1989] (Figure 5). These grids are useful for 2-D analyses of seismic wave travel paths in order to identify potential Sn/Lg attenuation zones that may be structurally controlled. Likewise, detailed grids of crustal and basement velocities are necessary for 3-D regional waveform modeling.

Complete analysis of an ambiguous event requires simultaneous display of geologic and geophysical information as well as geographical data. Geologic and fault maps form fundamental databases for comparing a seismic event to the geologic/tectonic setting. The Canadian Geological Survey 1:30,000,000 global geologic map [Geological Survey of Canada, 1995] provides uniform coverage that is supplemented with more detailed digital information

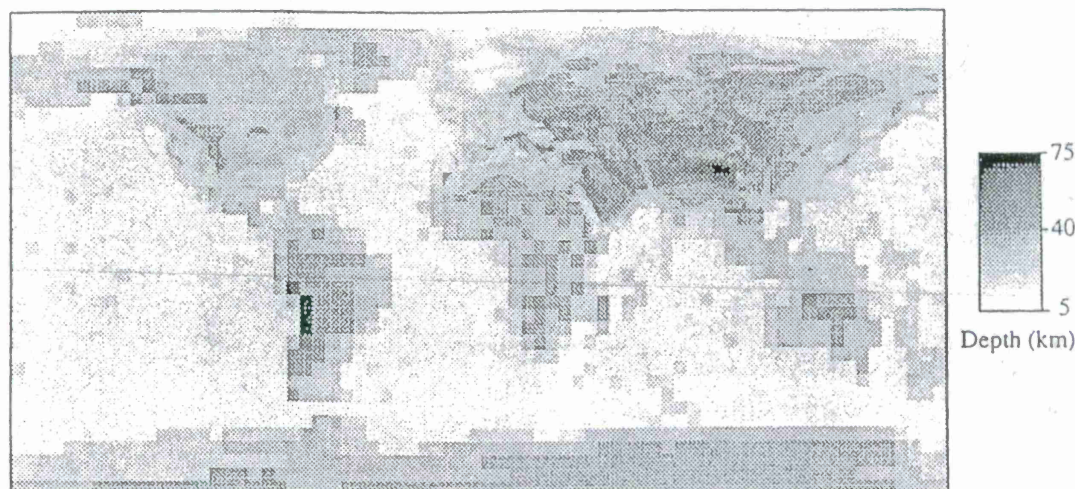


Figure 5. Monitoring of regional seismic waveforms require accurate 3-dimensional information concerning the crustal thickness. As shown above, the resolution of these data vary considerably. The global model is the 5x5 degree (550 km resolution) USGS Crust5.1 [Mooney and Laske, 1995]. Superimposed on the global model are several digitized and gridded Moho maps for various regions where more detailed data are available (US Moho from Braile et al., 1989 - 110 km resolution; Eurasia from Soviet IPE maps, Kunin et al., 1987 - 10 km; China from University of Colorado, Ritzwoller et al, 1997 - 6 km; Middle East from Seber et al., 1997 - 9 km).

such as the 1:5,000,000 USGS map. Some pertinent geographical data are political boundaries, transportation infrastructure, city locations, mine locations, and nuclear facility locations. Political boundaries, city locations, and transportation structure (roads, railroads, airfields) are extracted from the Digital Chart of the World (DCW) library. Mine locations are extracted from the DCW database and supplemented with regional data for EURASIA (USGS, USBM), Canada (CGS), Algeria, Egypt, Iran, Iraq, Israel, Jordan, Libya, Syria, Tunisia, and Turkey (DOE). The locations of nuclear facilities are obtained from the International Atomic Energy Agency and the US Nuclear Regulatory Commission.

CONCLUSIONS AND RECOMMENDATIONS

In order to enhance the efforts of the IDC to effectively monitor the CTBT, research and development of global and regional GIS databases must continue. The highest resolution topographic and bathymetric elevation models are required for regional seismic wave propagation and characterization. Also, detailed knowledge obtained from research of crustal thickness, basement depth, and upper mantle and crustal velocities is essential for regional 3-D seismic wave propagation modeling. Updated IDC, PDE, ISC, CMT, and USGS historical and instrumental data concerning regional seismicity will continue to provide an important source of information concerning the number, magnitudes, depths, and energy radiation

patterns for a given region that can be used to assist in characterizing ambiguous events. Precise locations of faults and their relation to local geology, activity level, and likely slip direction are also critically important for determining if an event is a likely violation of the CTBT and to swiftly facilitate on-site inspection efforts. Detailed geologic maps and historical and instrumental seismicity must be merged with pertinent geographical data in an on-line, unified GIS to form a comprehensive display for analysis (Figure 6). These data must also be merged with the results of supporting hydroacoustic, radionuclide, and infrasound technologies to provide a complete analysis tool for the decision maker or researcher. Clearly, work on a global GIS with uniform coverage requires additional efforts, primarily for regions in the southern hemisphere where data and information are sparse. Future work will also emphasize update of existing global databases and expansion to new regions of special interest.

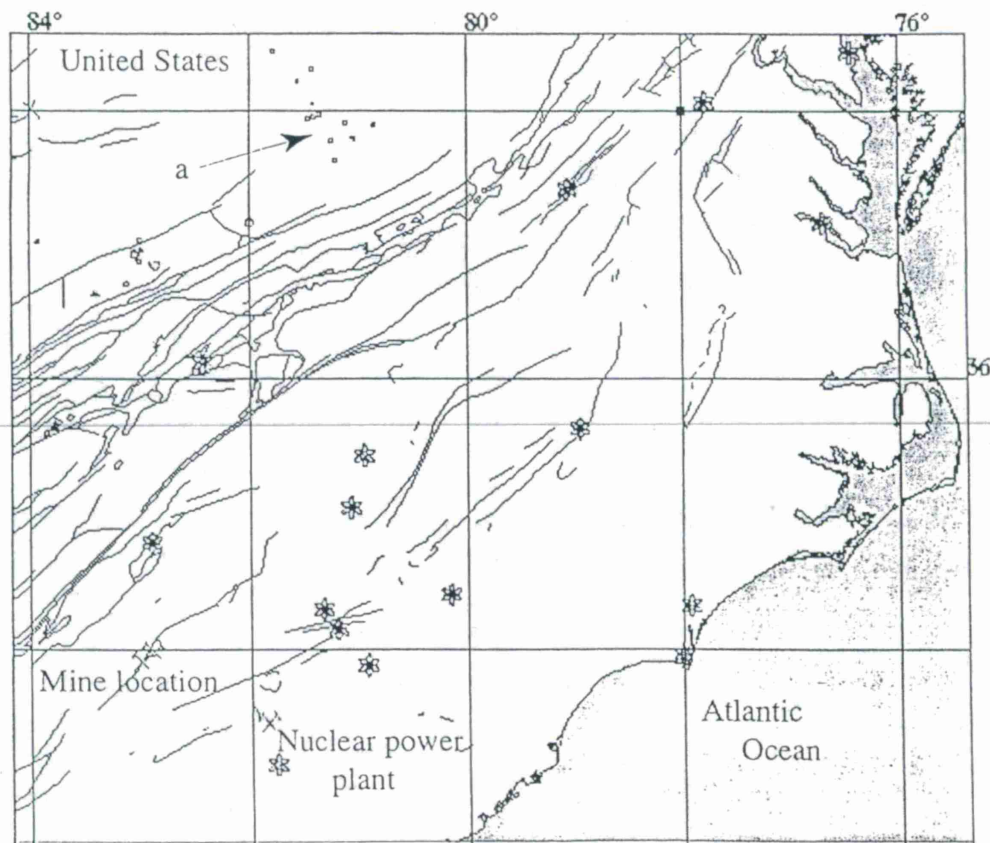


Figure 6. Faults, IDC seismicity 1/95-6/97, mine locations from the DCW database, and locations of nuclear reactors are displayed in this integrated image for the eastern seaboard of the United States. In this example case, several events occurred in a normally non-seismic region with no mapped faults or mine locations (see letter a). These data illustrate the need for very detailed geological, geophysical, and geographical information to avoid possible requests for on-site inspections and to improve transparency for all State Parties to the CTBT.

REFERENCES

- Braile, L.W., Hinze, W.J., von Frese, R.R.B., and Keller, R.G., Seismic properties of the crust and uppermost mantle of the conterminous United States and adjacent Canada, *Memior-Geol. Soc. Am.*, **172**, 655-680, 1989.
- Geological Survey of Canada, Geologic Map of the World, OF-2915d, Vancouver, B.C., 1:30,000,000 scale digital map.
- Kunin, N. and others, Map of depth to Moho and depth to seismic basement, Institute of Physics of the Earth, Moscow, 1:15,000,000 scale, 1987.
- Meissner, R., Wever, Th., and Flüh, E.R., The Moho in Europe - Implications for crustal development, *Annales Geophysicae*, **5B**, 357-364, 1987.
- Mooney, W.D., and Laske, G., A new global crustal model 5x5 degrees; CRUST5.0, EOS, *Trans. Am. Geophys. Un.*, **76**, 421, 1995.
- Ritzwoller, M., Levshin, A., and others, Surface wave tomography of EURASIA: Depth to Moho, Univ. Colorado, <http://tagg.colorado.edu/geophysics/eurasia/eurasia.html>, 1997.
- Seber, D., Vallve, M., Sandvol, E., Steer, D., and Barazangi, M., Middle East tectonics: Applications of Geographical Information Systems (GIS), *GSA Today*, **7**, 1-5, 1997.
- Smith, W.H.F., and Sandwell, D.T., Bathymetric prediction from dense altimetry and sparse shipboard bathymetry, *J. Geophys. Res.*, **99**, 21803-21824, 1994.